PROCEEDINGS OF THE

1991 SYMPOSIUM

ON THE

SUPERCONDUCTING SUPER COLLIDER

"THE PROJECT, THE PROGRESS, THE PHYSICS"

CORPUS CHRISTI, TEXAS

13–17 OCTOBER, 1991

The Superconducting Super Collider Laboratory is Operated by the Universities Research Association, Inc., for the U.S. Department of Energy under Contract No. DE-AC35-89ER40486.

ORGANIZING COMMITTEE

R. Adair
Yale University

D. Cassel
Cornell University

W. Chinowsky
University of California, Berkeley

T. Gabriel
Oak Ridge National Laboratory

F. Gilman
SSC Laboratory

P. Hale
SSC Laboratory

S. Meshkov
SSC Laboratory

F. Paige
Brookhaven National Laboratory

L. Price
Argonne National Laboratory

P. Rosen
University of Texas at Arlington

A. Sanda
Rockefeller University

R. Schwitters
SSC Laboratory

N. Tyurin
Institute for High Energy Physics, Protvino, Russia

G. Yost
SSC Laboratory

PREFACE

The 1991 Symposium on the Superconducting Super Collider Laboratory was held in Corpus Christi, Texas, October 13-17, 1991. The theme of this year's Symposium was " The Project, the Progress, the Physics." About 400 participants heard from Laboratory management about the project and the progress, and from physicists from around the world on the promise of the physics. A special address was given by Congressman Joe Barton of Texas regarding support for the SSC in Congress.

The City of Corpus Christi cooperated with beautiful weather and fine hospitality. A highlight was the sunset cruise on the Bay.

These Proceedings are presented in a new spirit. All speakers were requested to prepare a written version of their talk. In an effort to reduce publishing delays and increase completeness those talks that were not made available in written form are included as presented, as copies of transparencies. In some cases, the speakers have constructed a short introduction and guide to their transparencies. In other cases, the transparencies are simply given as they were presented. We have made an effort to reproduce them as well as possible; however, in a few cases, photographs have not reproduced well. In such cases, we have chosen to omit the photograph rather than include it in unreadable form.

We also include a selection of papers that were contributed to the Symposium.

We believe this cross between the older practice of including only written versions of the talks and the quick-and-dirty practice of including only transparencies provides the best attainable completeness and speed. We hope that our readers will agree that in those cases where an author decided not to submit a written copy, having the transparencies from a talk is superior to having nothing at all.

On behalf of the entire Symposium, we would like to thank Phyllis Hale, head of the SSC User's Office, and her tireless staff, for a smoothly organized conference. We also want to thank Terry Johnson and those who assisted him in coordinating our computing and communications. Many other people, too numerous to mention, worked behind the scenes, and we want to express our appreciation to them as well.

On behalf of the Organizing Committee,

V. Kelly and G. P. Yost

CONTENTS

SSC PROJECT

SSC Laboratory 1
R. Schwitters

Physics Research at SSCL 21
F. Gilman

SSC Project—Magnets 45
T. Bush

SSC Education 61
T. Gadsden

Parameter Selection for the SSC Trade-Offs and Optimization 77
D. Edwards and M. Syphers

Computing 103
K. Rich

Conventional Construction 111
J. Ives

SSC DETECTORS

SSC Physics Signatures 131
F. Paige

The GEM Detector for SSC 153
B. Barish

SDC 171
T. Kondo

***B* Phyics at the SSC** 225
S. Stone

Special Purpose Detectors 245
R. Stefanski

Report of the Users Organization for the SSC 263
D. Cassel

Highlights of the SSC Site Development Plan 271
J. Sanford

DETECTOR SUBSYSTEM R&D AT CERN AND SSCL

Calorimetry Subsystem R&D 303
J. Brau

Calorimetry II 335
W. R. Frisken

Research and Development for Supercollider Calorimetry: The European Scene 393
C. Fabjan

SSC Tracking Detectors Using Straw Tube Drift Chambers and Scintillating Fibers 407
A. Goshaw

High Precision Tracking: Silicon Detectors, Gas Microstrips 433
A. Seiden

Tracking III 459
H. J. Hilke

Electronics I 473
J. Dorenbosch

Front End Electronics for SSC/LHC Detectors 493
H. H. Williams

Signal Processing, Trigger and DAQ R&D at CERN 517
S. Cittolin

Muon Systems 537
J. Bensinger

SSCL R&D in Computing 555
K. McFarlane

PHYSICS

Fermilab Collider Program 573
J. Huth

The CERN Large Hadron Collider (LHC) 599
W. Hoogland

DOE: Laying the Framework for Future Support 603
J. Decker

Status of the Project 617
P. Reardon

What Lies Ahead? 651
J. D. Bjorken

CONTRIBUTED PAPERS

First Order Tune Shift Calculations for Transverse Betatron Dynamics 669
T. Garavaglia

A Fast Vertex Fitting Method for the Experiments at Multi-TeV PP Colliders 703
P. Billoir and S. Qian

Calorimeter Trigger Applications, Training, and Assessment of a Feed-forward Neural Net 707
D. Wu and M. Campbell

Development of Diamond Radiation Detectors for the SSC and LHC 737
M. Franklin, A. Fry, et al.

Conceptual Design for a Parallel Plate LAr and LKr Electromagnetic Calorimeter for GEM 753
T. Burnett, V. Cook, et al.

A Pizero Identifier for GEM 769
J. Eisenberg and P. Mockett

Importance of the $B_s^0 \rightarrow \mu + \mu -$ Branching Fraction 781
A. Fridman and A. Snyder

Adopt-A-Magnet 791
SSC Education Office

Hybrid Subsystem Progress Report for FY1991 817
Brian Kross, Stan Majewski, et al.

Study of Hadron Punchthrough and Muon Rates at the SSC 847
Y. Chang and B. Zhou

LIST OF ATTENDEES 893

SSC Laboratory

R. Schwitters

SSC

The Physics

Beyond Standard Model

The Progress

Technical
Managerial
Scientific

The Project

We are building the SSC

Why go beyond?

1) Inadequacies of Standard Model

Complexity ≥ 18 parameters
3 generations

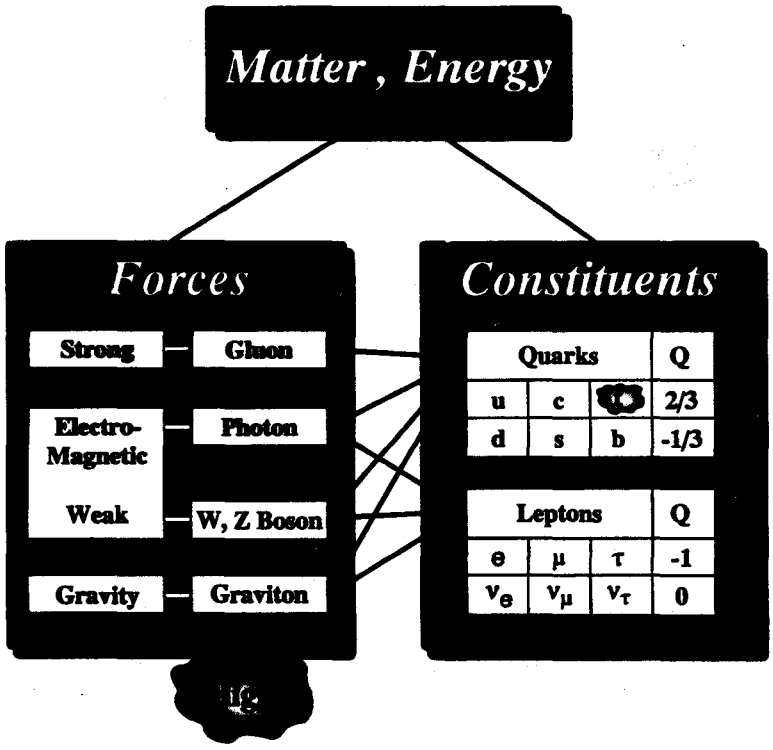
Hi-E behavior

2) New Physics at High Energy

-
-
-

Missing clue: Mechanism for electro-weak symmetry breaking

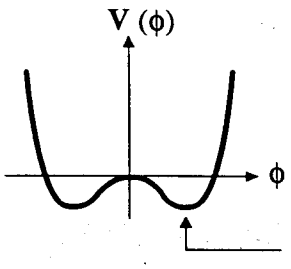
The Standard Model



TIP-01740

Scale for Studying E–W Symmetry – Breaking

(or where is the Higgs?)



$$\phi_0 = \frac{m}{\sqrt{\lambda}} = \frac{1}{\sqrt{\sqrt{2}\, G_F}} = 247 \text{ GeV}$$

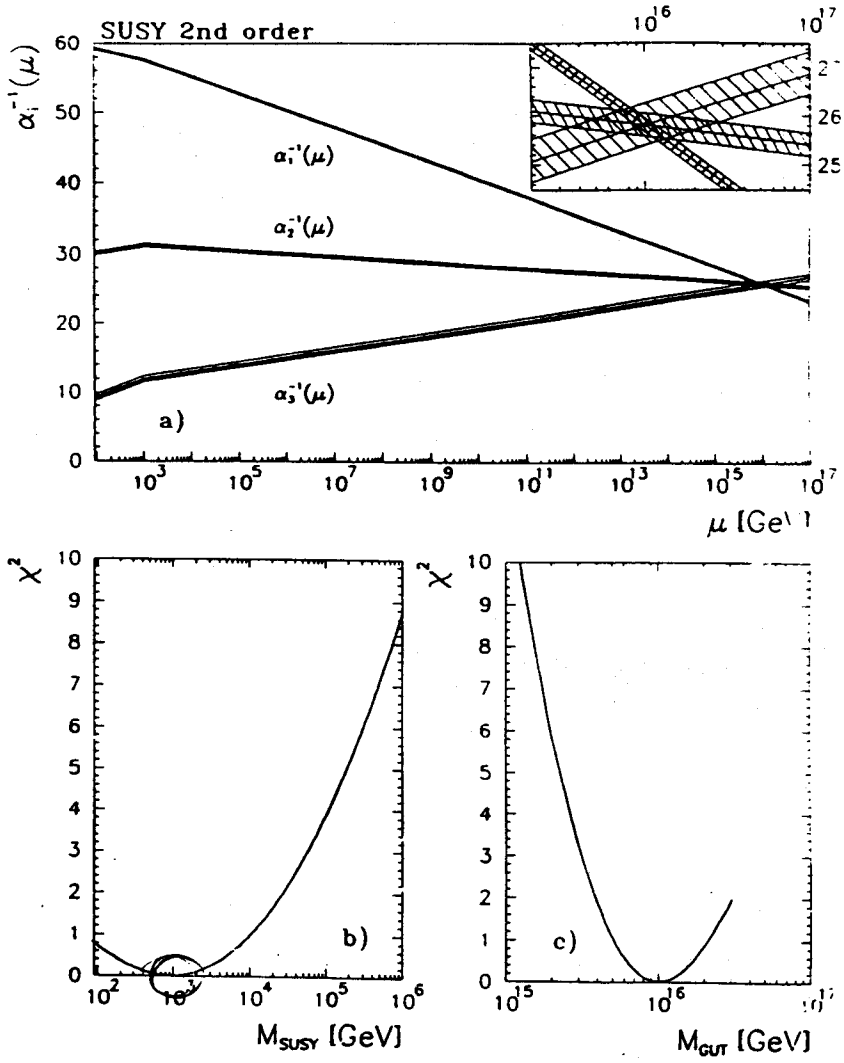
$\lambda \sim e^2$, $M_H \sim 100$ GeV

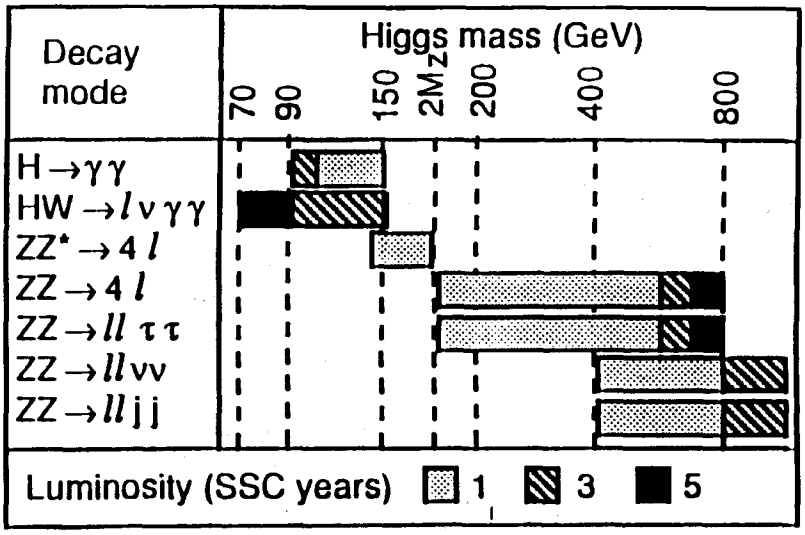
$\lambda \sim 4\pi$, $M_H \sim 900$ GeV

sum rules ⇒ "strong" WW effects
@ ~ TeV scale w/wo H.

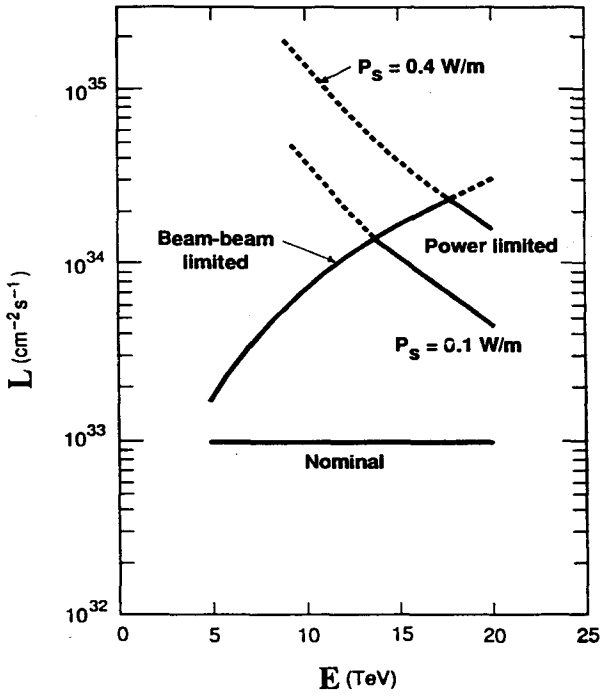
2 Choices

Elementary Composite (eg s.c.)


SUSY 2nd order
$\alpha_i^{-1}(\mu)$
$\alpha_1^{-1}(\mu)$
$\alpha_2^{-1}(\mu)$
$\alpha_3^{-1}(\mu)$
a)
μ [GeV]
χ^2
b)
M_{SUSY} [GeV]
c)
M_{GUT} [GeV]



SSC Luminosity Potential

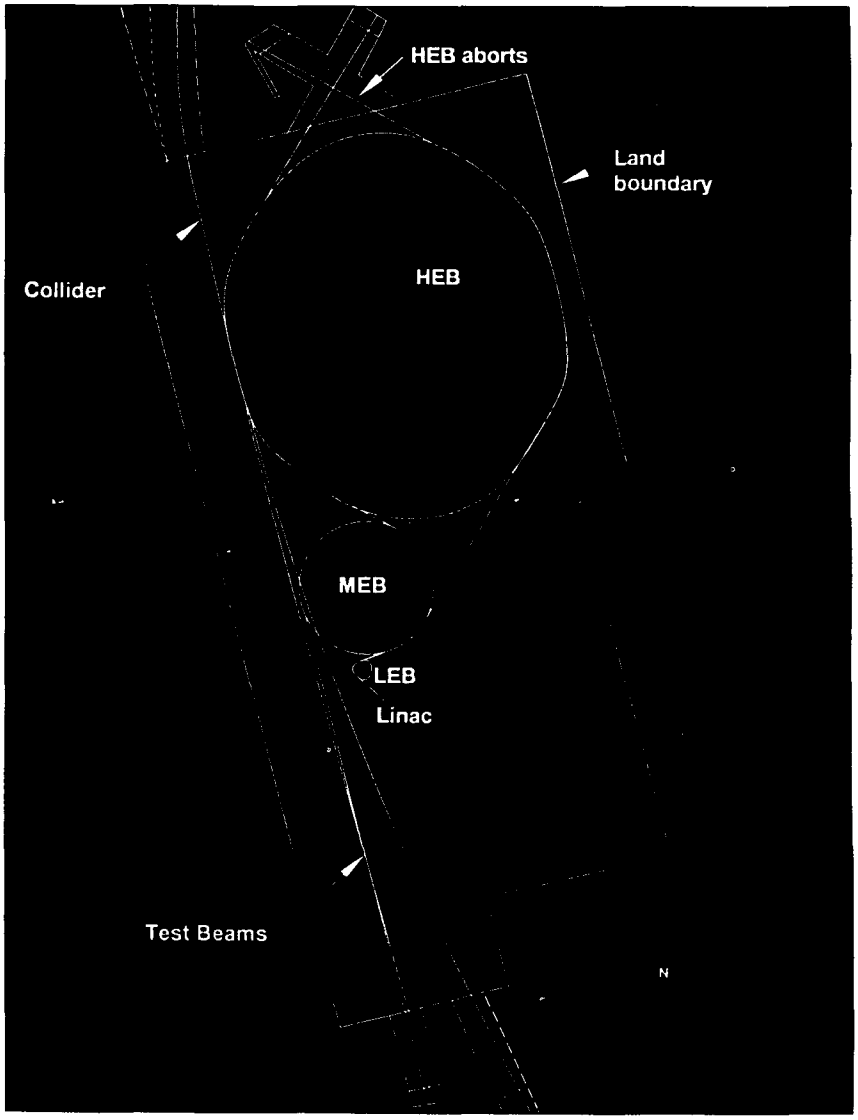


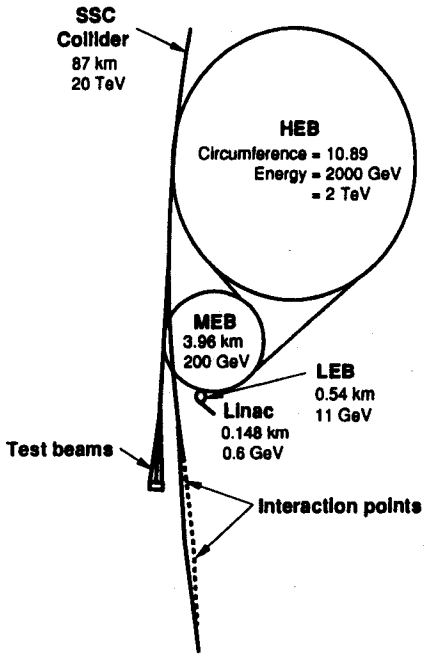
L ~ B • I

B = Brightness (N_B/ε_N)

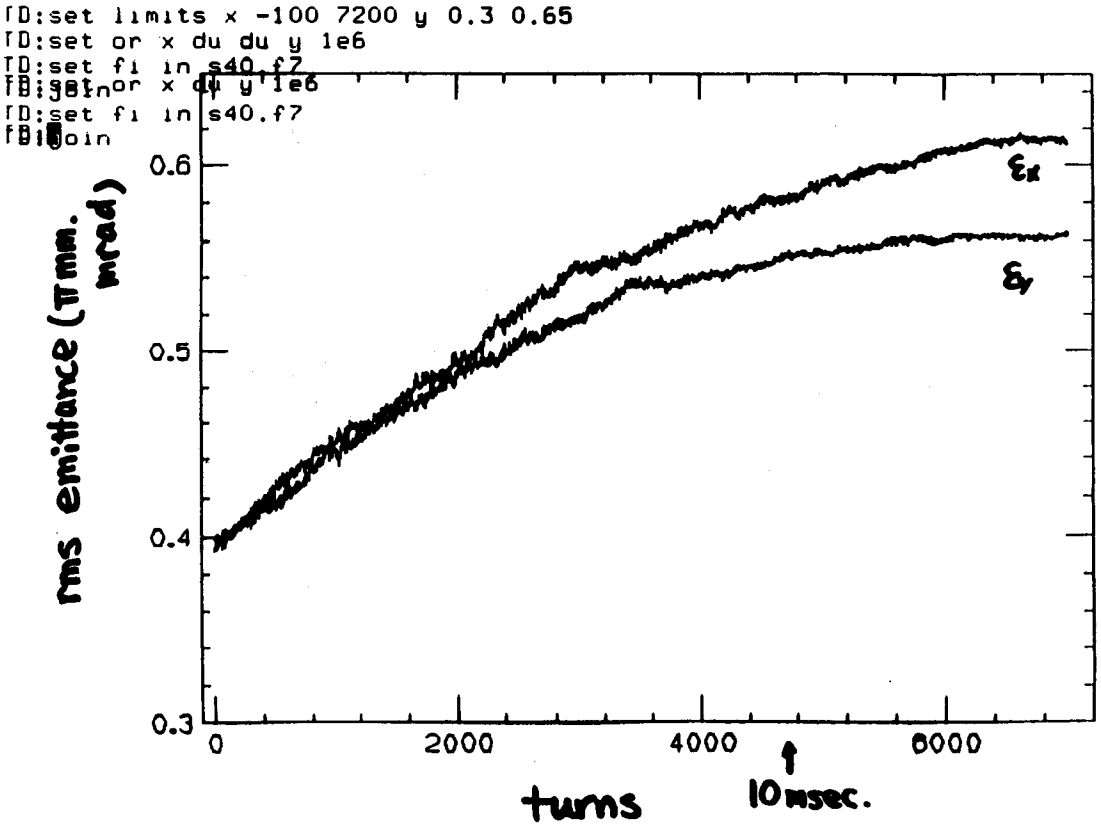
I = Total current

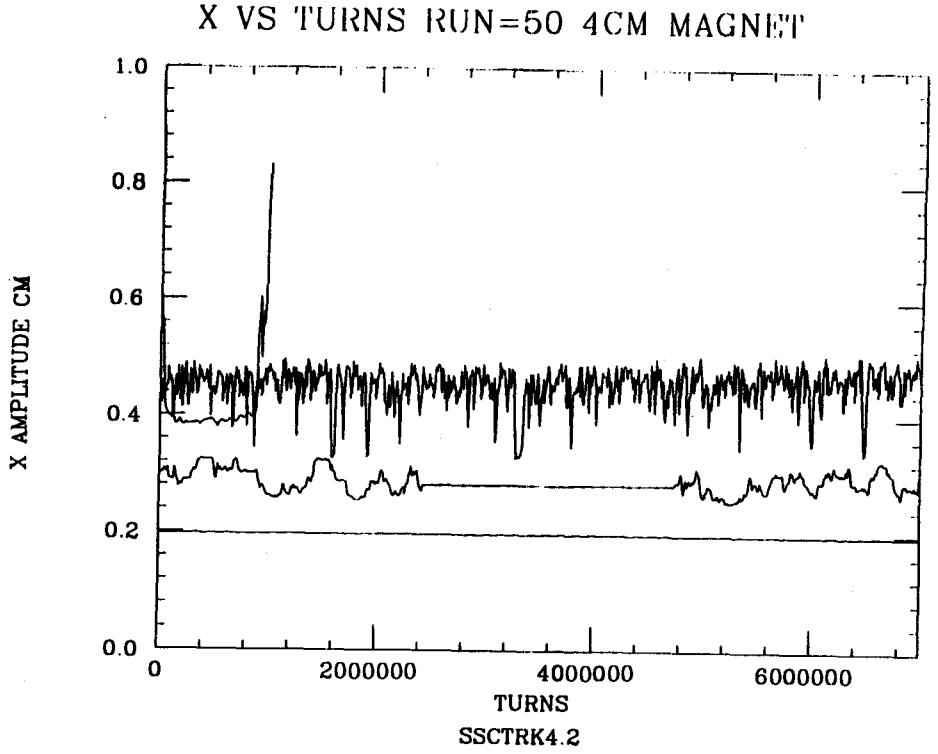
TIP-02221


HEB aborts
Land
boundary
Collider
HEB
MEB
LEB
Linac
Test Beams
N



5 Stages of Acceleration	
Linac	0 – 0.6 GeV
LEB	0.6 – 11 GeV
MEB	11 – 200 GeV
HEB	200 – 2000 GeV
Collider	2 TeV – 20 TeV

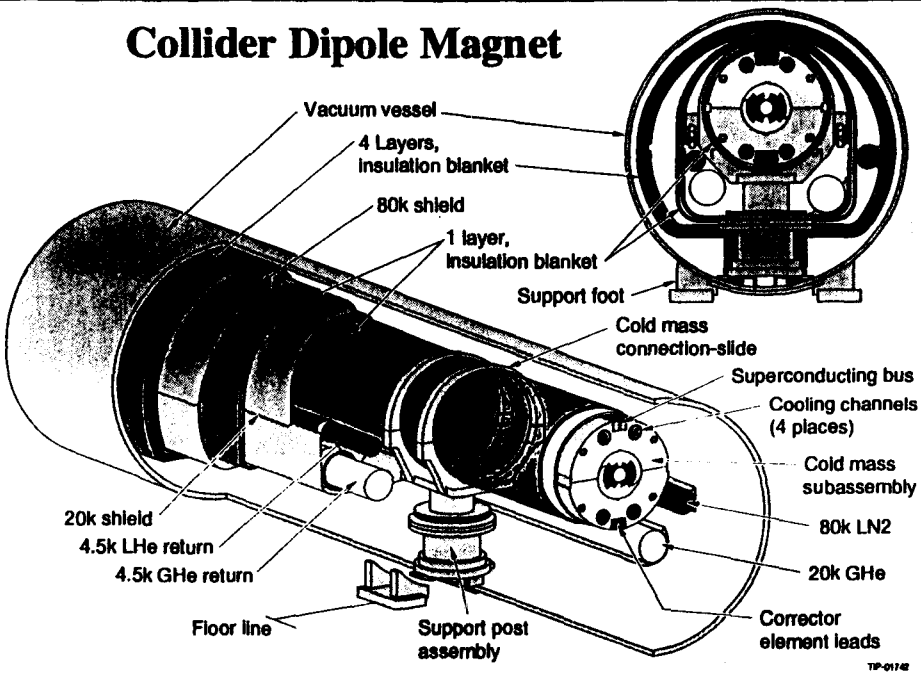


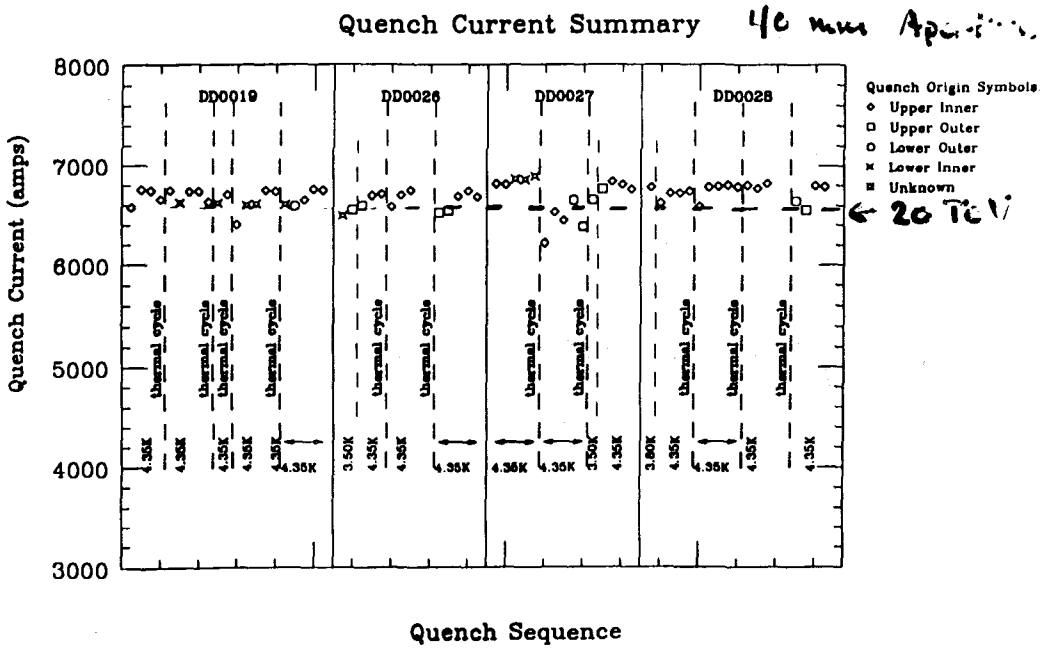


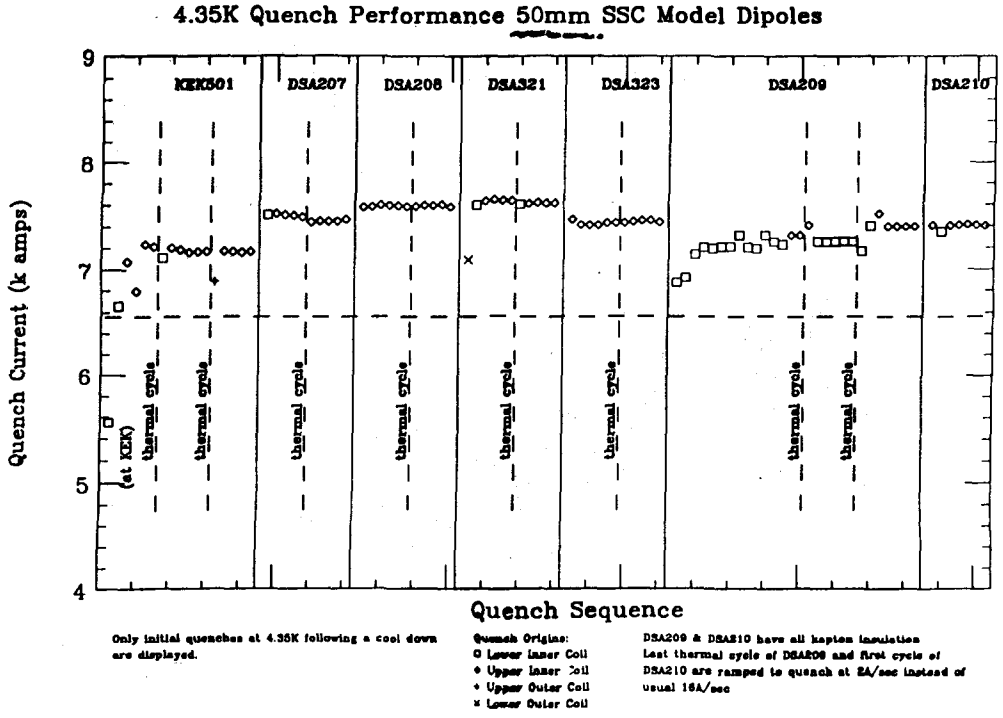


SSC Laboratory

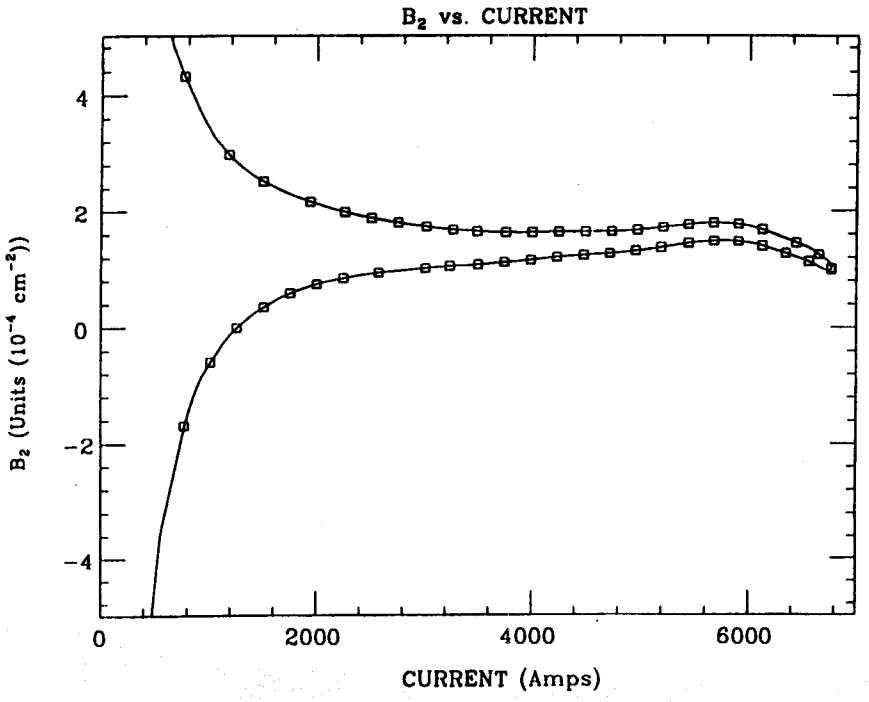
Collider Dipole Magnet




Quench Current Summary
40 mm Aperture
DD0019
DD0026
DD0027
DD0028
Quench Origin Symbols
Upper Inner
Upper Outer
Lower Outer
Lower Inner
Unknown
20 TeV
Quench Current (amps)
Quench Sequence

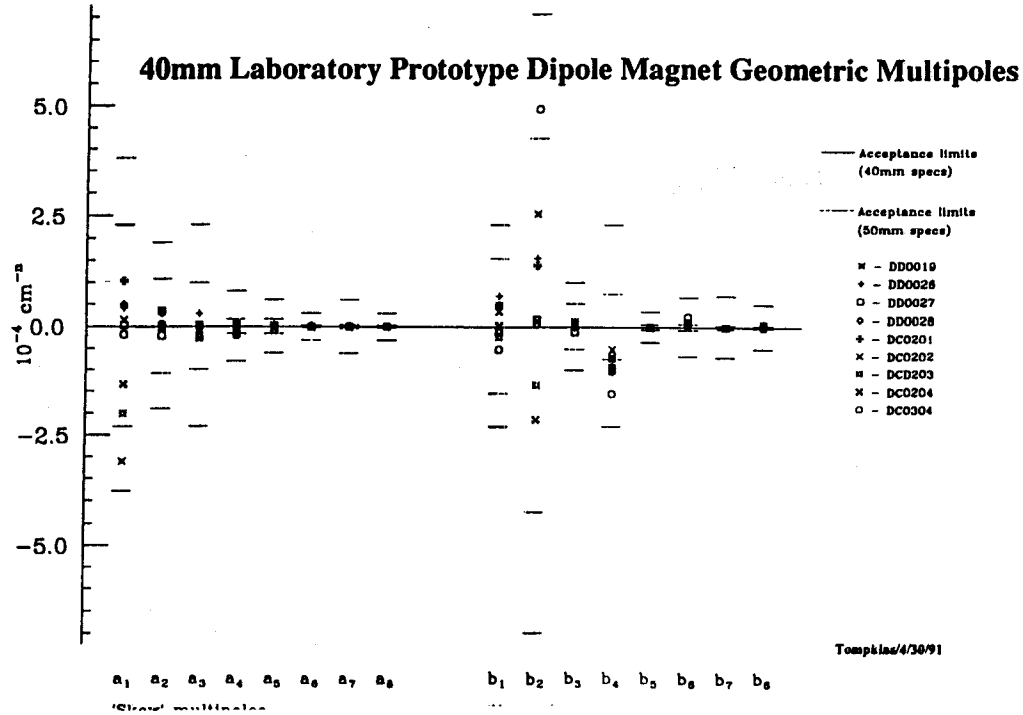

4.35K Quench Performance 50mm SSC Model Dipoles
KEK501
DSA207
DSA208
DSA321
DSA323
DSA209
DSA210
Quench Current (k amps)
Quench Sequence
Only initial quenches at 4.35K following a cool down are displayed.
Quench Origins:
Lower Inner Coil
Upper Inner Coil
Upper Outer Coil
Lower Outer Coil
DSA209 & DSA210 have all kapton insulation
Last thermal cycle of DSA208 and first cycle of DSA210 are ramped to quench at 2A/sec instead of usual 16A/sec

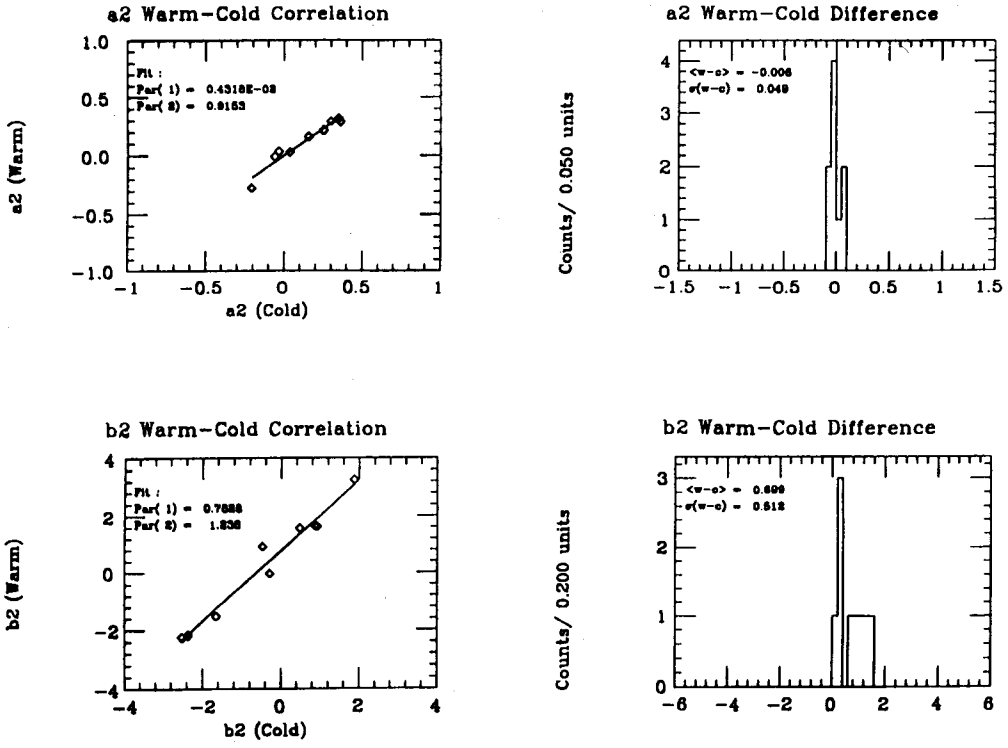
JUL 5 19



□ DD0028 36 20 Nov 1990 cold data to 7000 Amps Current loop w/ no pre-ramp
position: 7.010 meters

SSC Laboratory Magnet Systems



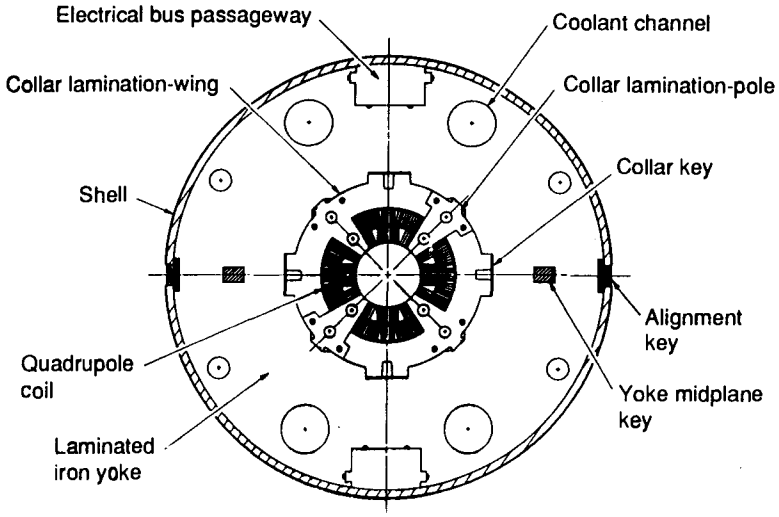


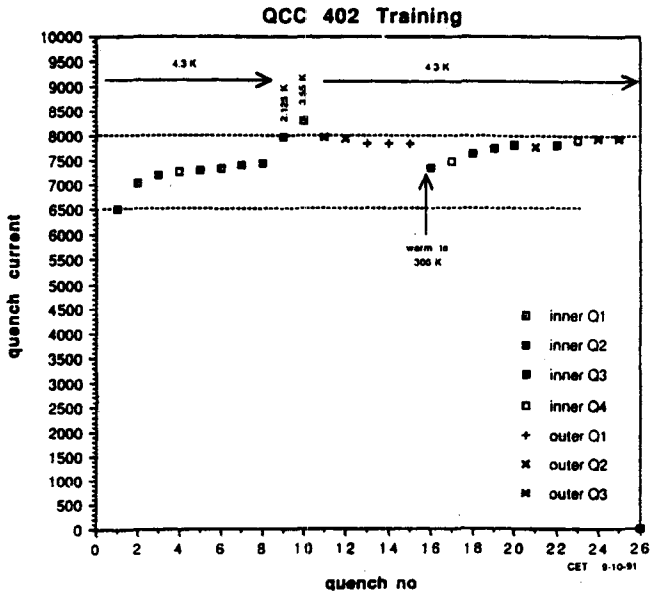


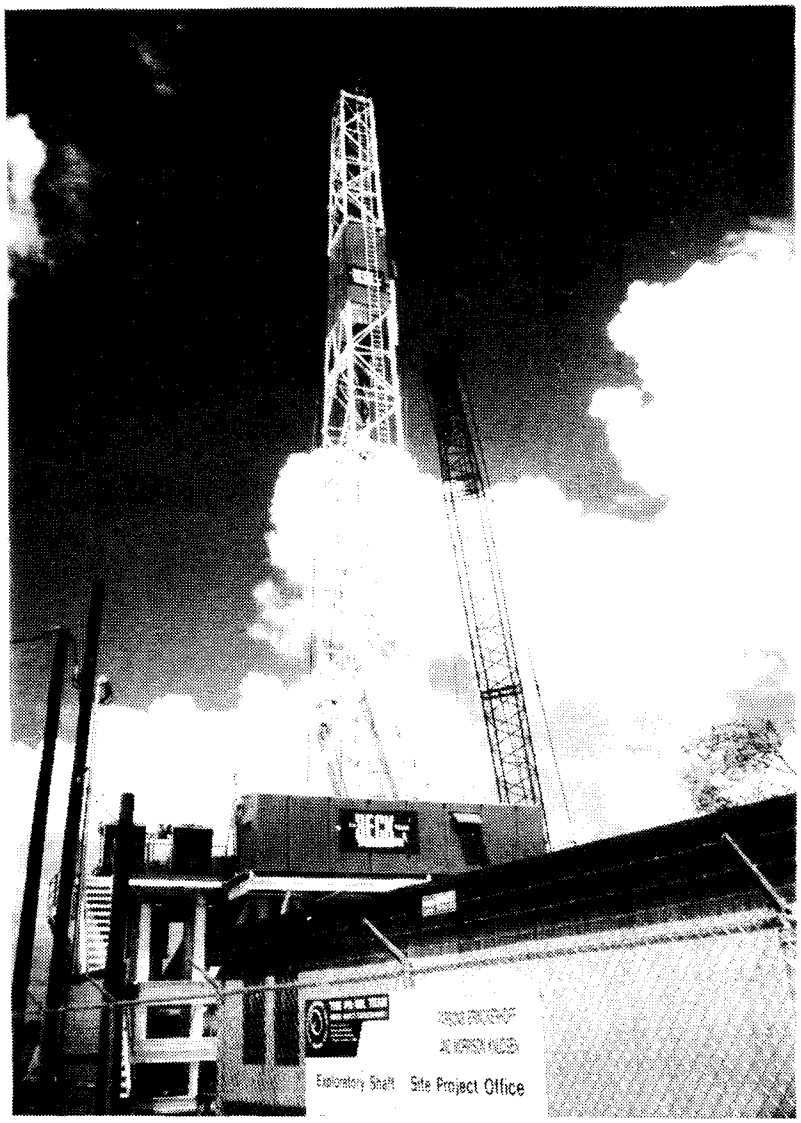
SSC Laboratory

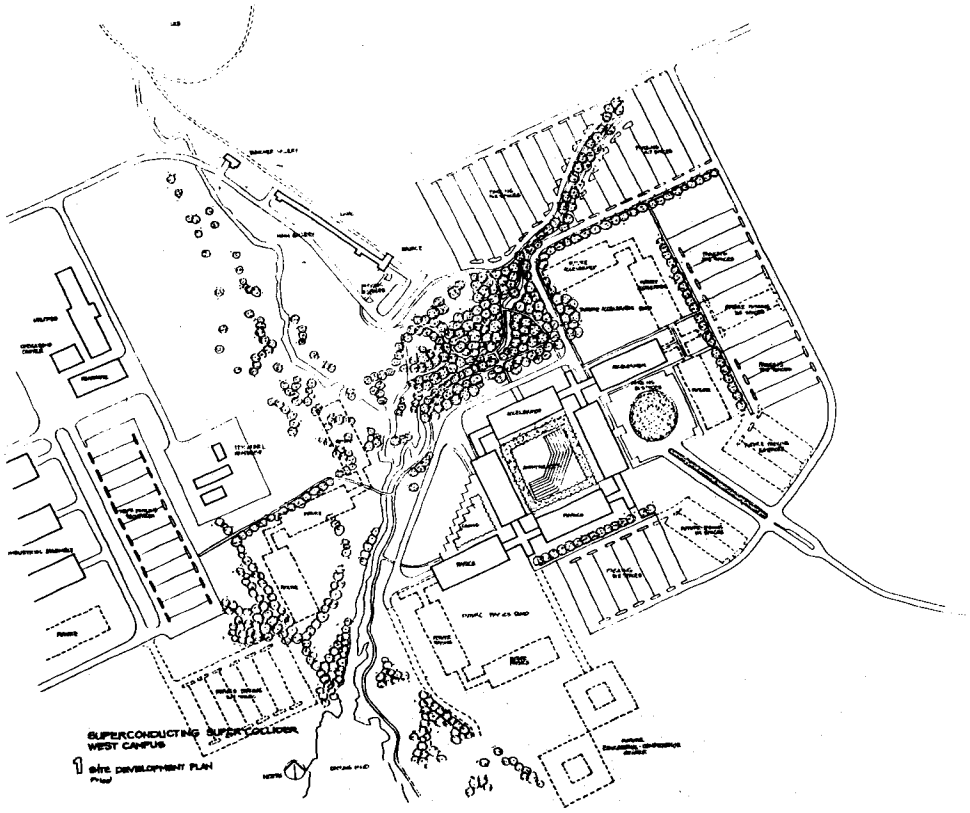
Collider Quadrupoles

- High-tech superconductivity as for dipoles




QCC 402 Training
quench current
quench no
4.3 K
4.3 K
2.125 K
3.65 K
warm to 300 K
inner Q1
inner Q2
inner Q3
inner Q4
outer Q1
outer Q2
outer Q3
CET 9-10-91


Exploratory Shaft Site Project Office



Initial Scientific Program

Proposal Driven — **First Expressions of Interest June, 1990**
20 EoI's received

2 Major, complementary detectors

Formal proposal review – 1992

SDC
GEM } **~ 700 U.S. physicists,** major foreign participation

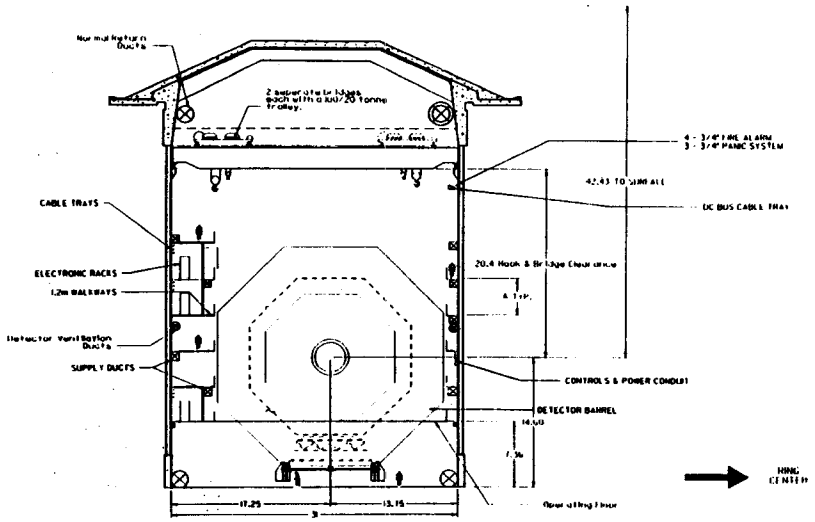
Smaller experiments

Reserve capital funds

Workshops, new calls for proposals : 1992-93

Detector R&D program

SSCL-TIP-02199



SECTION (A)

Scientific Targets of the SSC

Clarification of the nature of electroweak symmetry breaking

- **Higgs**

Searches for new physics beyond the standard model

- **Supersymmetry**
- **Technicolor**
- **Compositeness**
- •
- •
- •

Detailed studies of standard model processes

- **Top-Quark production**
- **B-Quark studies – CP violation?**

Low – Q^2 Physics

- **Elastic Scattering** } **The Pomeron**
- **Diffraction** }

- **The Vacuum**

DEPARTMENT OF ENERGY
FY 1992 CONGRESSIONAL BUDGET REQUEST
GENERAL SCIENCE AND RESEARCH
(dollars in thousands)
LEAD TABLE
Superconducting Super Collider (SSC)

Activity	FY 1990 Actual	FY 1991 Estimate	FY 1992 Base	FY 1992 Request	Program Change Request vs Base: Dollar	Program Change Request vs Base: Percent
perating Expenses.....	$69,587 a/b/	$116,000	$116,620	$103,593	$- 13,027	- 11%
apital Equipment.....	20,706	33,000	33,000	56,340	+ 23,340	+ 71%
onstruction.....	126,592	93,866	93,866	373,767	+279,901	+ 298%
Total.....	$216,885 c/	$242,866 c/	$243,486	$533,700 c/	$+290,214	+ 119%
perating Expenses.....	($69,587)	($116,000)	($116,620)	($103,593)	- 13,027	+ 11%
apital Equipment.....	(20,706)	(33,000)	(33,000)	(56,340)	+ 23,340	+ 71%
onstruction.....	(126,592)	(93,866)	(93,866)	(373,767)	+ 279,901	+ 298%
Total Program.....	($216,885)	($242,866)	($243,486)*	($533,700) * $483,700	$+290,214	+ 119%
Staffing (FTEs).....	15	58	70	89		

uthorization: Section 209, P.L. 95-91.

/ Includes $2,400,000 reprogrammed from SSC Construction for 18 additional FTEs. Does not include $838,000 in in FY 1990 General Science Program Direction support.
/ Total has been reduced by $847,000 reprogrammed to Energy Supply for SBIR.
/ Includes funding provided through appropriation process only. Non-federal contributions will permit additional activities. The size and scope of these contributions will be known after firm agreements with the State of Texas and foreign partners are completed.

* Passed by Congress, signed by President

* +~$160 M from Texas

+ ~ $130 M from Texas

U. S. Department of Energy
SSC Project



SSC BASELINE SCHEDULE
MAJOR PROJECT MILESTONES

WBS	DESCRIPTION	10-YEAR	
3.0	Baseline Validation Complete	JUL-90	
2.5.1	A-E/CM Letter Contract & NTP	AUG-90	
1.2	CDM Authorization to Incur Costs	NOV-90	
3.0	SEIS Record of Decision (ROD)	JAN-91	
5.0	Begin Conceptual Design for Detectors	FEB-91	
2.1.1	Start SSC Civil Construction	FEB-91	
5.0	Notice to Proceed (NTP) Experiment Halls	JUN-93	•
1.1.8.8.23	Accelerator String Test Complete Phase 1	SEP-92	
1.2	Full-rate Production Decision on Magnets	APR-94	
1.2	Start First Half Sector CDM Delivery	APR-94	
1.1.6	First Collider Half Sector - Start Installation	JUN-94	•
1.1.2	LINAC Start Commissioning (600 MeV)	OCT-94	
1.1.6	First Collider Half Sector - Start Cooldown	MAR-95	
1.1.3	LEB Start Commissioning	OCT-95	
5.0	Beneficial Occupancy of Large Experiment Halls	JAN-96	
1.1.4	MEB Start Commissioning	JUN-96	
1.1.5	HEB Start Installation	AUG-96	
1.1.4	MEB Test Beams Available	JAN-97	•
1.1.5	HEB Start Commissioning	SEP-98	
5.0	West Detectors - Start Commissioning	MAR-99	
1.1.6	Collider - Start Commissioning (beam)	MAR-99	
1.1.6	Beam to Exp. (End of Project/Begin Op)	SEP-99	

• CHANGED BY CCB ACTION

Summary

Scientific opportunity at SSC unmatched

- **20 x increase in energy**
- **Will explore "beyond Standard Model"**
- **Diversity of experimental areas**

The SSC is being built

- **Technology/Management issues under control**
- **Costs stable**
- **Detectors can be built to do the physics**
  - **Large collaborations working now**

SSCL-TIP-0219

Physics Research at SSCL

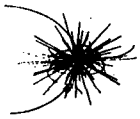
F. Gilman



SSC Laboratory Physics Research Division

PHYSICS RESEARCH AT SSCL

Fred Gilman
Corpus Christi
October 14, 1991



SSC Laboratory Physics Research Division

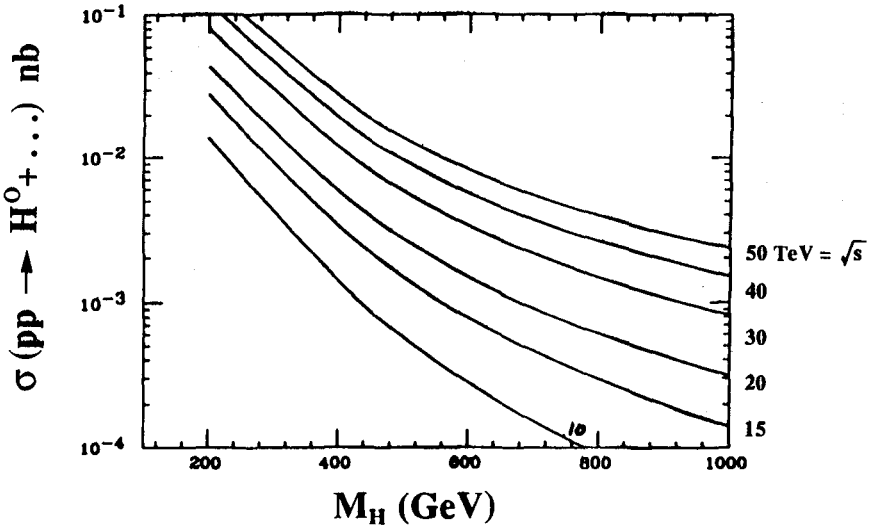
Physics of the SSC

- Uncover the nature of electroweak symmetry breaking
  Higgs: single or multiple, elementary or composite;
  More generally, discern what happens in $W_L W_L$ scattering
- Look at physics inside the Standard Model, e.g., b's, t's, QCD
- Look for physics beyond the Standard Model
  - Larger gauge sector: W′, Z′
  - SUSY
  - Compositeness
    - •
    - •
    - •

Higgs Boson

- Standard Model Higgs Boson – The benchmark for theory and experiment in electroweak symmetry breaking
- Produced primarily in gluon - gluon and W-W collisions of the constituents of the protons
- High Mass Higgs ($M_H \gtrsim 2\ M_W$)
  Very cleanly detected in $H \rightarrow Z\ Z \rightarrow 4$ leptons
- Intermediate Mass Higgs ($2M_W \gtrsim M_H \gtrsim M_W$)
- $H \rightarrow Z\ Z^* \rightarrow 4$ leptons
- $H \rightarrow \gamma\ \gamma$

Higgs Cross Section



TIP-00579 22

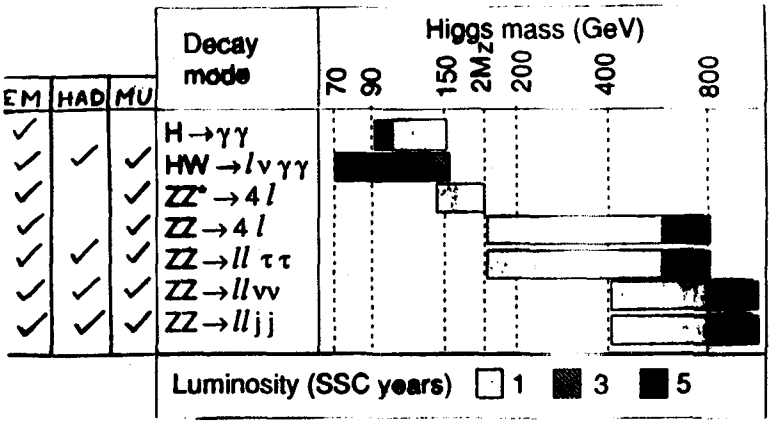
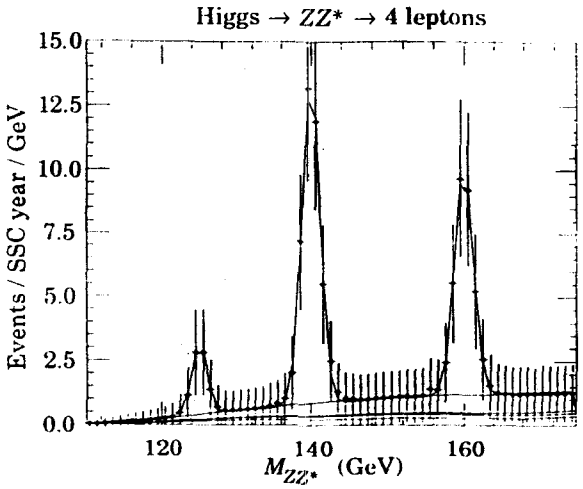
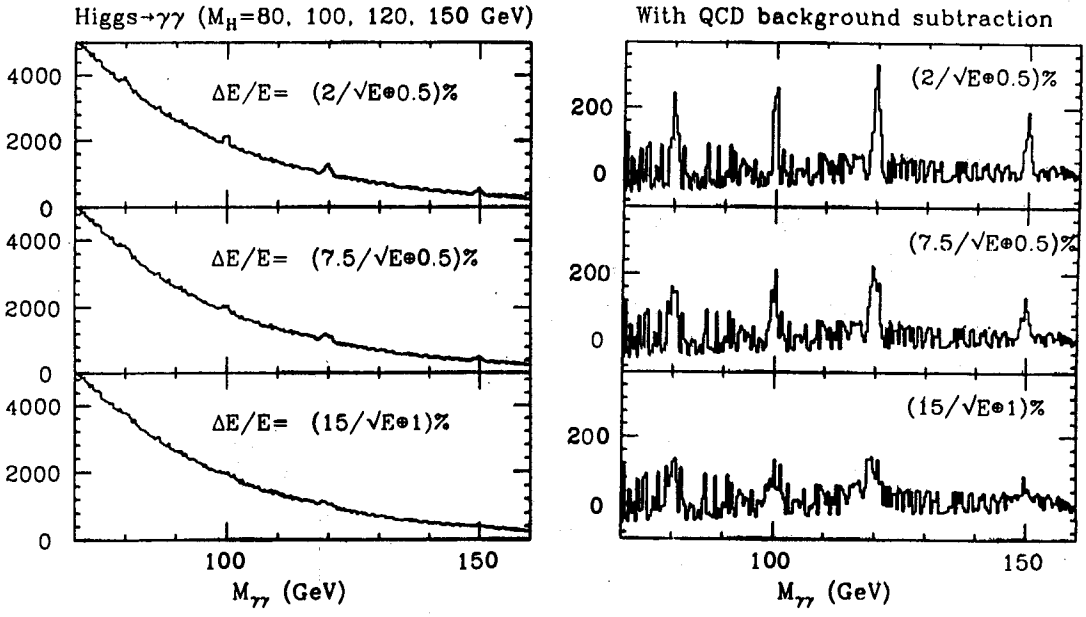
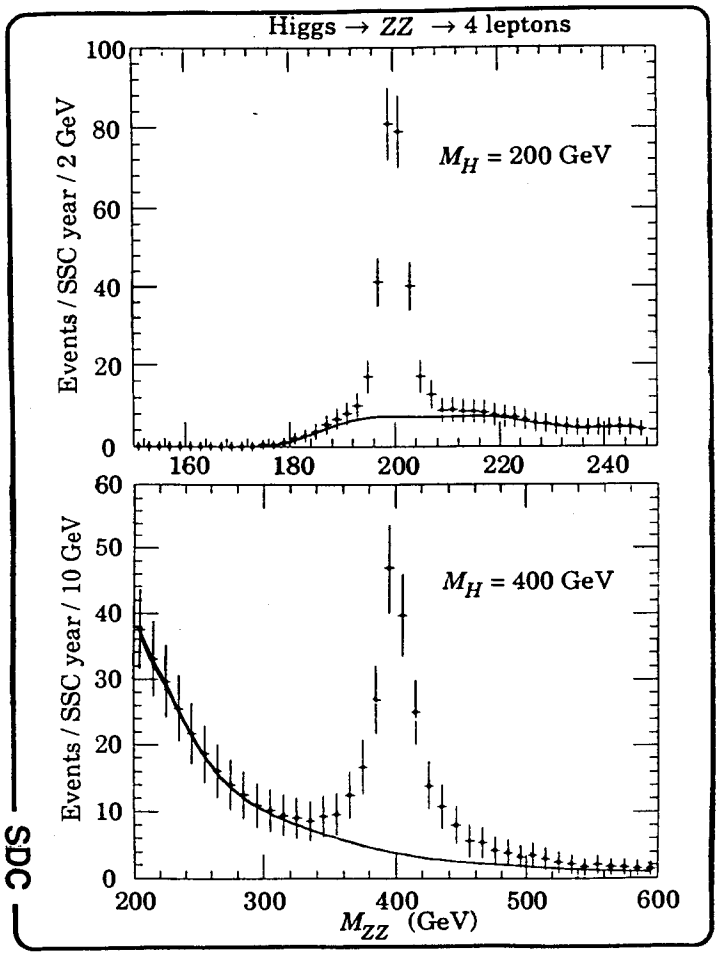


Figure 6.36 Approximate mass reach for Higgs discovery in various decay modes with the EMPACT/TEXAS detector.



Backgrounds: 1) continuum ZZ*
2) $Z + b\bar{b}$
3) $Z + t\bar{t}$
4) $t\bar{t}$


Higgs→γγ (M_H=80, 100, 120, 150 GeV)
ΔE/E= (2/√E⊕0.5)%
ΔE/E= (7.5/√E⊕0.5)%
ΔE/E= (15/√E⊕1)%
4000
2000
0
100
150
$M_{\gamma\gamma}$ (GeV)
With QCD background subtraction
(2/√E⊕0.5)%
(7.5/√E⊕0.5)%
(15/√E⊕1)%
200
0
100
150
$M_{\gamma\gamma}$ (GeV)

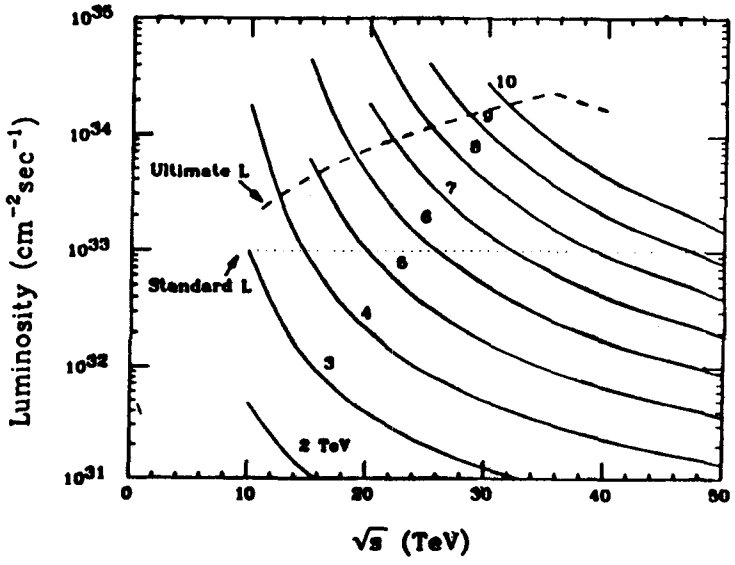

Higgs → ZZ → 4 leptons
Events / SSC year / 2 GeV
M_H = 200 GeV
160
180
200
220
240
Events / SSC year / 10 GeV
M_H = 400 GeV
200
300
400
500
600
M_{ZZ} (GeV)
SDC

Heavy Gauge Boson

- Cross Section rises rapidly with collider energy
- Detected very cleanly in $Z' \rightarrow 2$ leptons
- SSC can pursue such heavy gauge bosons to $M_{Z'} = 10$ TeV

SSC Laboratory Physics Research

100 produced Z'



The SSC is a powerful probe for surprises at enormous energies.

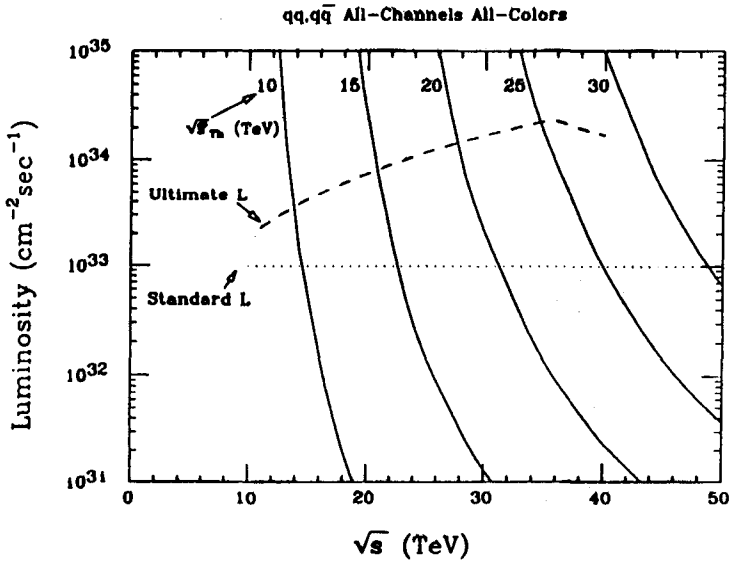
e.g., Suppose a new threshold at the parton level:

$\hat{\sigma}(\hat{s}) = (4\pi/\hat{k}^2)\,\theta(\hat{s}-\hat{s}_{thresh})$

(For $\hat{s}_{thresh} = (20\ TeV)^2$, $\hat{\sigma} \lesssim 50\ fb \sim \pi\,(1.3 \times 10^{-19}\ cm)^2$)

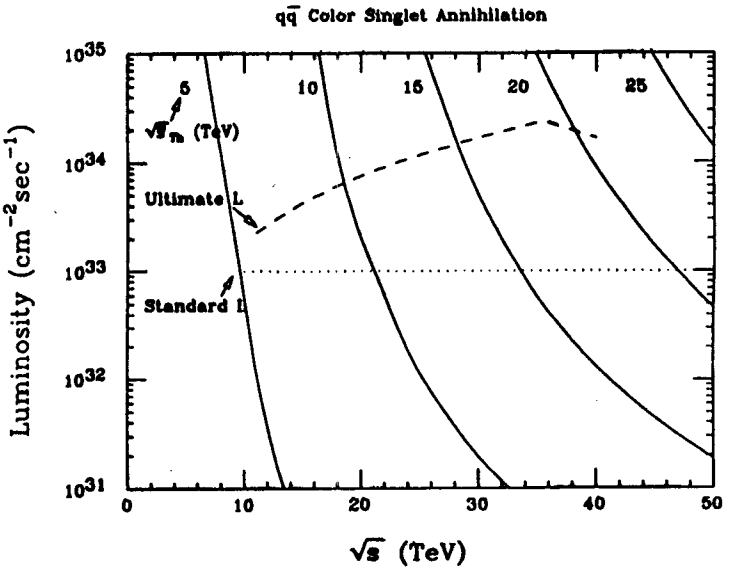
There would be a few events/year at the SSC for $\hat{s}^{1/2}_{thresh} = 20$ TeV

Five Events – New Threshold Above $\hat{s}_{TH}$



TIP-00579-5

Five Events – New Threshold Above $\hat{s}_{TH}$



The SSC Experimental Program

- First meeting of the SSC Program Advisory Committee (PAC) was on February 9–10, 1990
- Issued call and guidelines for Expressions of Interest on any type of experiment that might be part of the initial experimental program
- Initial fifteen EOIs presented and considered at PAC meetings in June and July, 1990

List of EOIs

Number	Spokesperson	Name of EOI	Number of Institutions	Number of Collaborators
SSC-EOI0001	A. Krisch	Inclusive Spin-Spin Effects and Cross Sections Near 20 TeV	3	38
SSC-EOI0002	J. Orear	Low P_t Physics at the SSC	11	20
SSC-EOI0003	G. Trilling	Solenoidal Detector Collaboration (SDC)	74	500
SSC-EOI0004	H. Sobel	A Very Long Baseline Neutrino Oscillation Experiment	11	34
SSC-EOI0005	W. Willis	High Luminosity at the SSC	4	17
SSC-EOI0006	M. Marx	Electrons Muons Partons with Air Core Toroids (EMPACT)	44	222
SSC-EOI0007	R. Lander	10^{34}	1	3
SSC-EOI0008	N. Lockyer	Bottom Collider Detector (BCD)	32	85
SSC-EOI0009	H. Kagan D. Kania S. Schnetzer	A Compact Diamond-Based Detector for the SSC	5	19
SSC-EOI0010	S. Ting	L*	66	827
SSC-EOI0011	S. Reucroft L. Sulak R. Webb	A Calorimeter-Based High-Rate Detector for the SSC (TEXAS)	15	42
SSC-EOI0012	R. Kanofsky	(Proposals to be Submitted)		
SSC-EOI0013	J. Rosen	Internal Target Beauty Physics at the SSC	1	1
SSC-EOI0014	B. Cox	Super Fixed Target Beauty Facility	36	138
SSC-EOI0015	G. Giacomelli	Search for Magnetic Monopoles		
SSC-EOI0016	M. Atiya	A High Resolution Detector for $H^0 \rightarrow \gamma\gamma$	1	2
SSC-EOI0017	H. Bryant	Relativistic Atomic Physics at the SSC	11	23
SSC-EOI0018	S. Linn	Electromagnetic and Muon Detector for the SSC	5	6
SSC-EOI0019	J. D. Bjorken	A Full-Acceptance Detector for SSC Physics at Low and Intermediate Mass Scales	1	1
SSC-EOI0020	B. Barish B. Willis	To Construct A Major SSC Detector	52	310
		Total:	373	2288

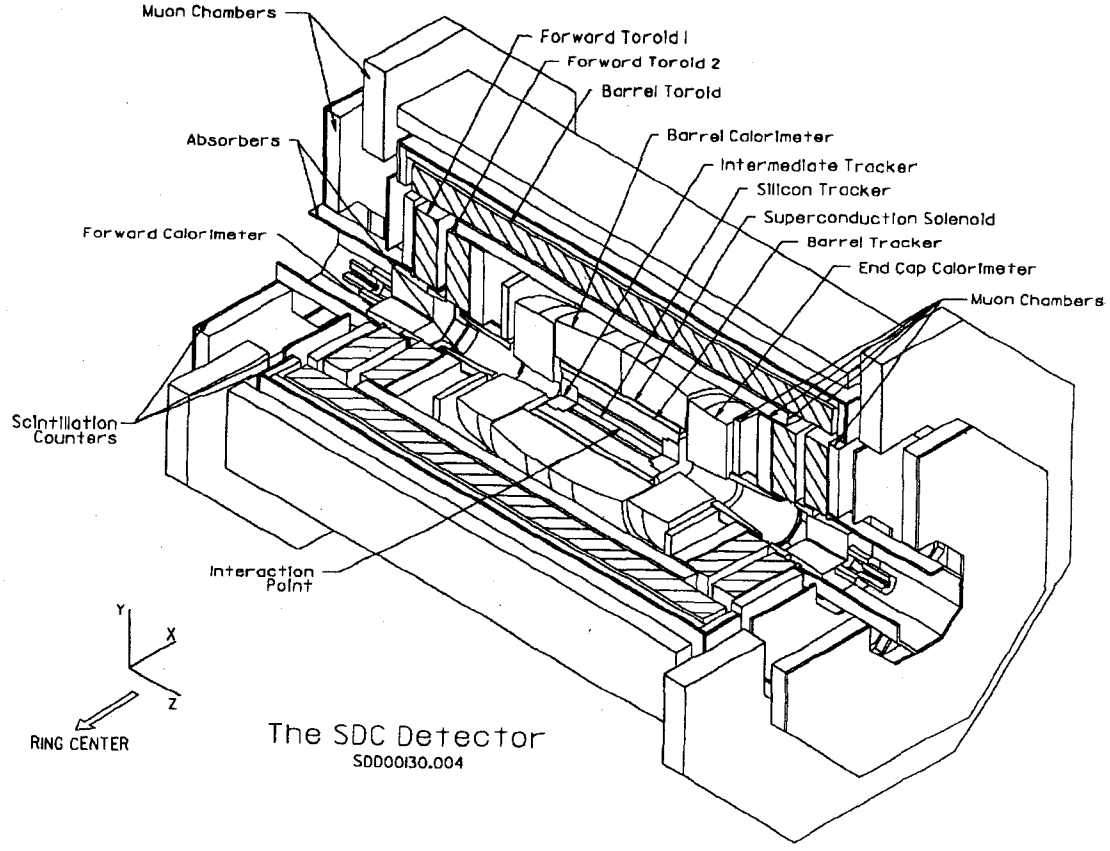
SSC Laboratory Physics Research Division

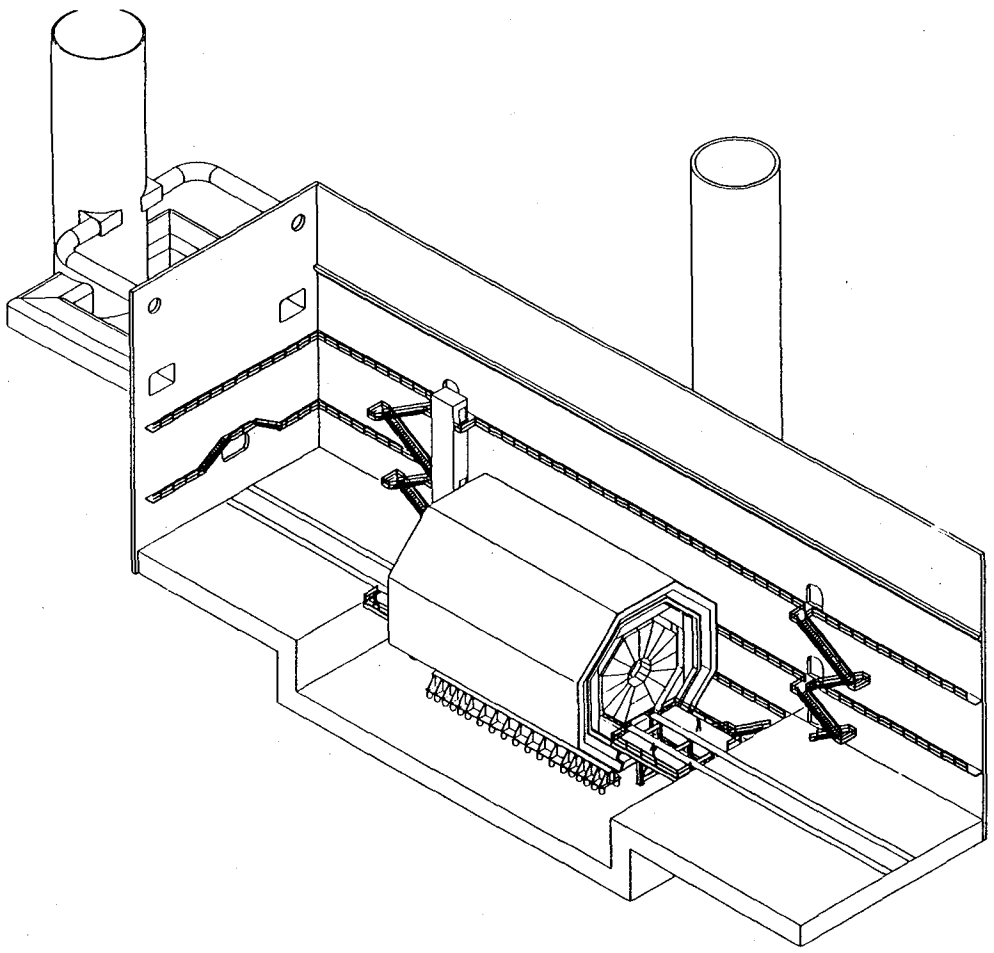
- **Call in July, 1990, for Letters of Intent for major SSC detectors**
  - **One with as broad a range of capabilities as possible**
  - **Other, competitive and complementary, emphasizing robust muon detection and calorimetry**
- **Three Letters of Intent received: SDC, L*, and EMPACT/TEXAS**
- **Focus of PAC meetings in December, 1990 and March, 1991.**

SDC

From the PAC Meeting of December 13–15, 1990

- **The SDC design goals of good central tracking, hermetic calorimetry, lepton energy measurement and identification and high resolution vertex detection satisfy the criteria for a "general purpose" SSC detector that were put forth in the Guidelines for the Letters of Intent**
- **While some important technical questions remain to be resolved through subsystem R&D, the PAC felt that the collaboration has the technical expertise to address them and build the detector**
- **Therefore, the Laboratory is supporting the SDC to proceed toward development of a technical proposal.**





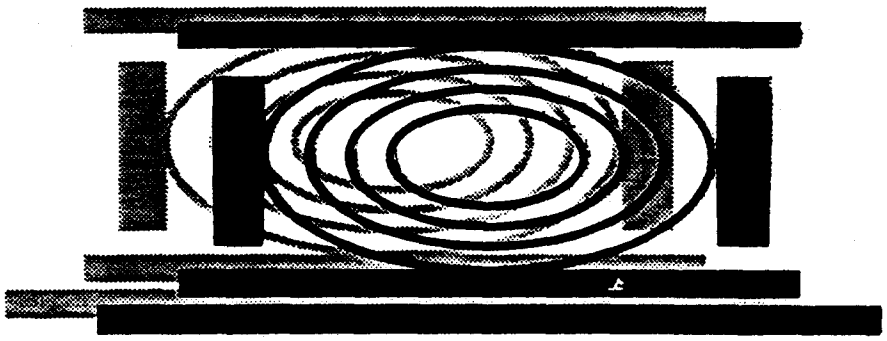
The Second Detector

- The December and March meetings of the PAC considered the EMPACT/TEXAS and L* LOIs, and then after January, 1991, just L* as the candidate for the second detector
- Unresolved questions pertaining to funding and collaboration management led the SSCL to conclude that L* should not be supported to proceed to a full technical proposal
- Much excellent technical work has been done

MEETING ON THE 2ND DETECTOR

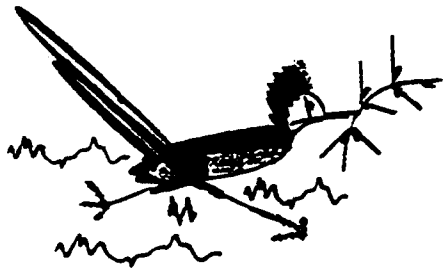
June 11 - 13, 1991

Superconducting Super Collider Laboratory - **Auditorium**



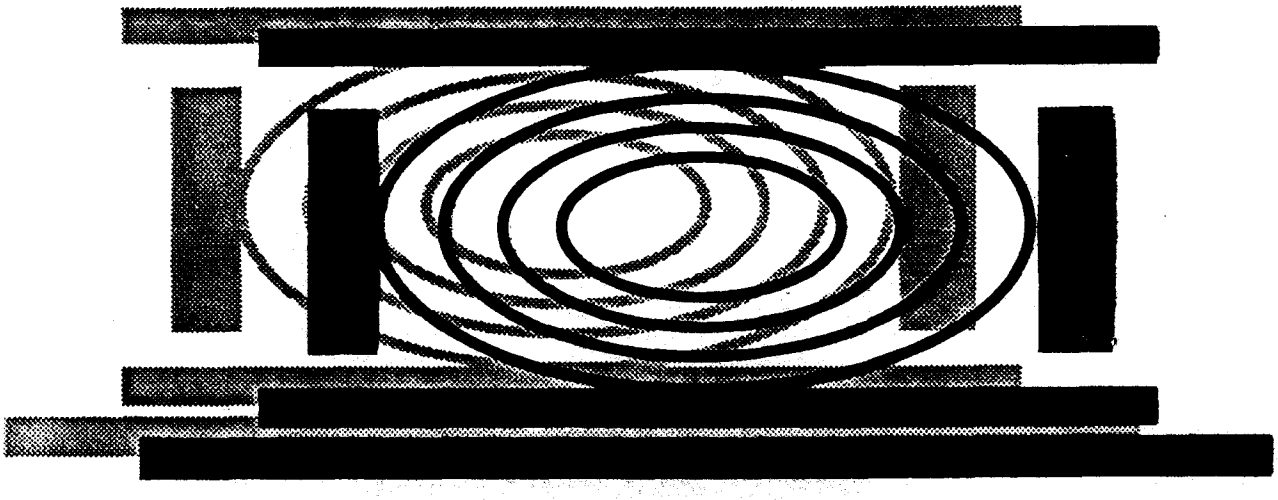
* June 14, 1991 • EOI Presentations

Contact: **SSCL Users Office**
Email: USERSOFFICE@SSCVX1
Tele: 214 708 1001
Fax: 214 708 0000



An Expression of Interest to Construct a Major SSC Detector

July 8, 1991



Overall Financial Constraints

- $752.1M(FY1990 Dollars) in SSC project funds for detector R&D, detectors, and detector-related computing
- Approximately $625M for detector themselves
- Reserve $75M for smaller experiments
- Leaves approximately $550M for the major detectors, including detector–specific project management, engineering/ R&D, etc., in SSC project funds. The remaining portion of the major detectors' financing will come from non-project funds, mostly as foreign in-kind contributions.

Engineering,Systems Integration, and Coordination Funds

- SDC, L*, and EMPACT/TEXAS each received $500K in FY90
- An additional $200K was given in December, and $300K in January, for a total of $1M to each collaboration submitting a Letter of Intent
- Support being given to SDC to proceed to a proposal — $3.5M in FY1991
- Support for GEM to move toward a Letter of Intent — $0.6M in FY1991

Results of the PAC Meeting July 8-12, 1991 (cont'd)

Smaller Experiments

- EOIs continue to be received
- Very useful but not formal proposals
- Call for proposals in late 1993 or early 1994
- SSCL to encourage and focus efforts for smaller experiments

B Physics

- Important and promising area
- SSC has special capabilities
- Significant progress in fixed target and in hadron and e^+e^- collider experiments in last year
- Hold a workshop in late 1992 to examine in depth the strategy for B physics at the SSC — collider and/or fixed target

East Campus Facilities

- Need to define hall requirements by January, 1992 for East Campus
- Preserve options in advance of proposals
- Recommend enlarging the collider tunnel to 6 meter diameter plus a small hall (approximately 10 meters diameter by 40 meters length) around the interaction point

The GEM Magnet Panel

- **Charge: To determine if the construction of a chosen baseline magnet concept consisting of a large superconducting solenoid, either as a single or double coil version, is feasible and what would be the estimated cost, manpower requirement and schedule**
- **Large, diverse composition of the Panel**
- **Panel met September 4–6 and 25–27, 1991**
  Oct 10-11

GEM Magnet Review Panel Members and Participants
September 25, 1991

Members

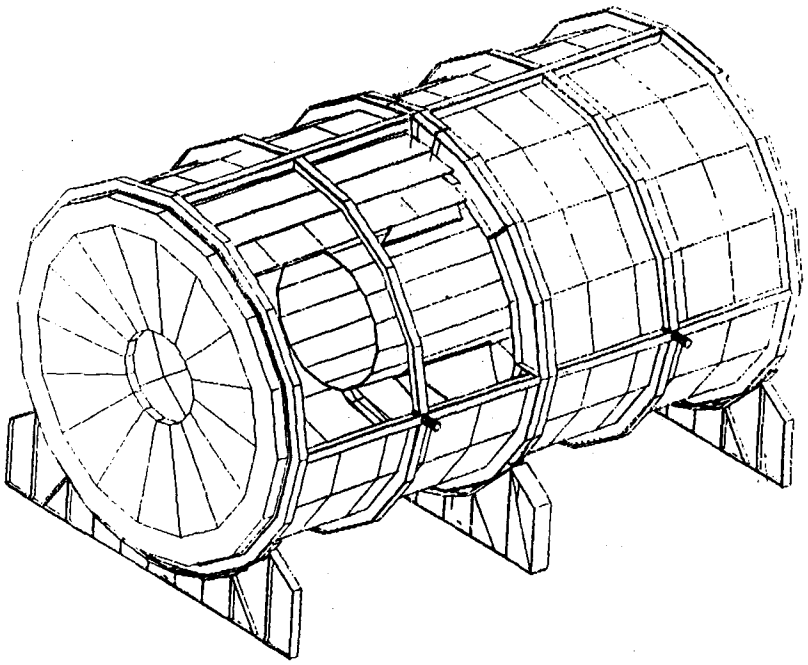
Peter Clee, Rutherford Appleton Laboratoy (second & third session)
Gary Deis, Lawrence Livermore National Laboratory
Mike Harris, SSC Laboratory
Alain Herve, CERN (only third session)
Coleman Johnson, Lawrence Livermore National Laboratory
Robert Johnson, JBc Associates
E. Klimenko, Kurchatov IAE
Dennis Lieurance, General Dynamics Space Systems
Peter Marston, Massachusetts Institute of Technology
Nickolai Martovetsky, Kurchatov IAE
John Miller, Lawrence Livermore National Laboratory
Bruce Montgomery, Massachusetts Institute of Technology (first session only)
Dr. Roberto Penco, Ensaldo Componenti
Tom Prosapio, SSC Laboratory
Robert Richardson, SSC Laboratory
Dr. Gary Sanders, Los Alamos National Laboratory
Dr. Ray Stefanski, SSC Laboratory
Dr. Richard Stroynowski, Caltech High Energy Physics
Francois Wittgenstein, CERN (only second session)
Ronn Woolley, SSC Laboratory
Phil Sanger, SSC Laboratory
Don Edwards, SSC Labortory
Jon Ives, SSC Laboratory
George Mulholland, SSC Laboratory
Ted Kozman, SSC Laboratory

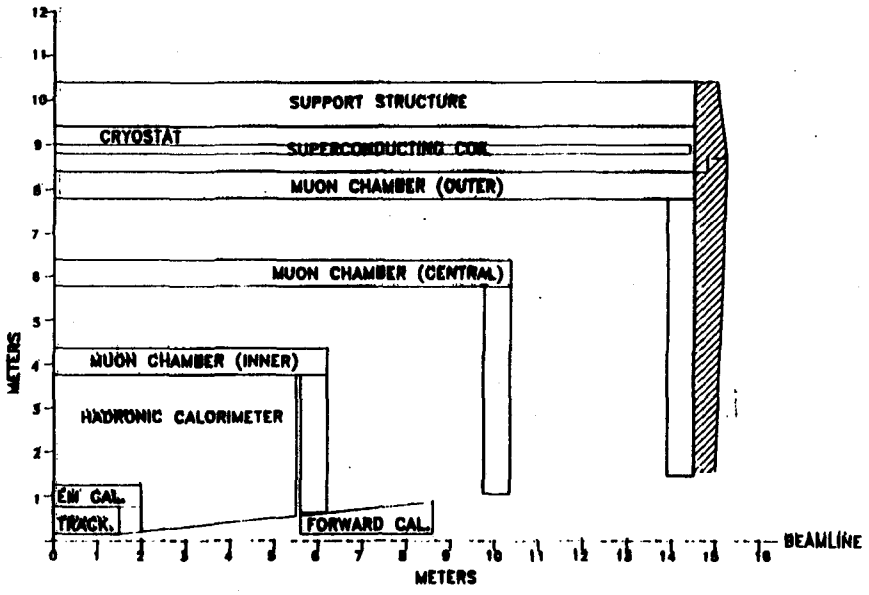
Participants

Howard Shaffer, Westinghouse Science & Technology Center
Sharad K. Singh, Westinghouse Science & Technology Center
Robert Swinderman, Pitt-Des Moines, Inc.
Yehia Eyssa, Babcox and Wilcox
Joe Heim, LLNL
Z. John Stekly, Intermag. Gen. Corp.

GEM Magnet Panel Conclusions

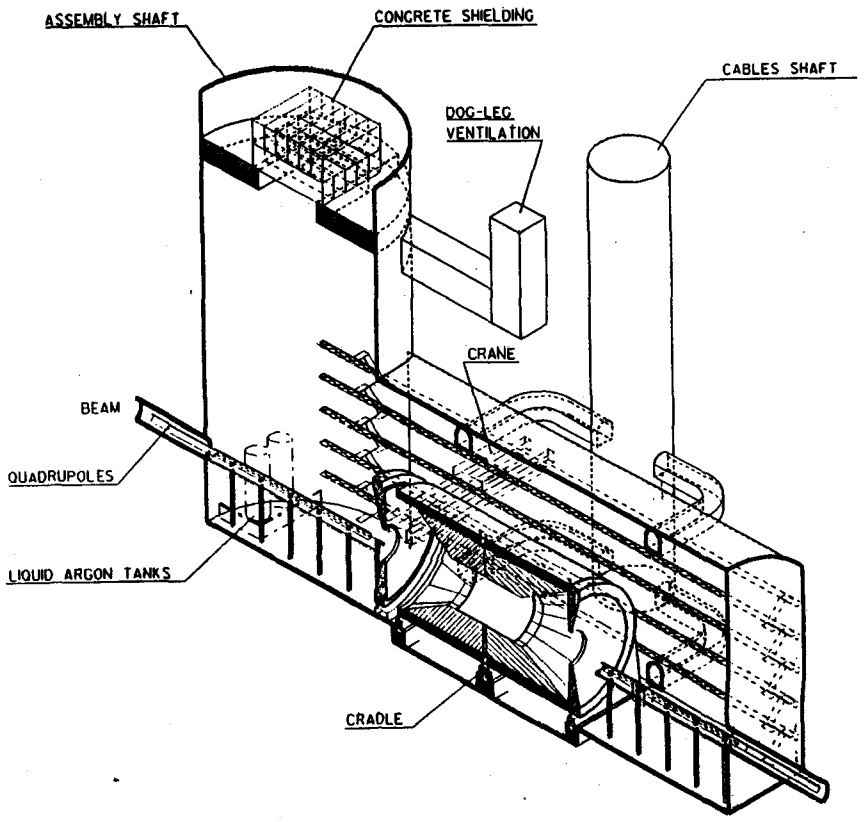
- The single coil, unshielded solenoid should be the baseline magnet configuration for the GEM detector
- It has very substantial cost, schedule, and technical risk advantages over the double coil or iron return-yoke alternatives
- Substantial engineering and R&D support for the magnet is necessary in FY1992 in order to maintain the schedule for FY1999 turn-on

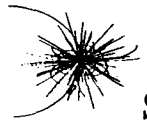




QUADRANT VIEW OF THE DETECTOR CONCEPT

ISO VIEW





SSC Laboratory Physics Research Division

MEETING OF PAC SUBCOMMITTEES

OCTOBER 3—4, 1991

- Reviewed Progress of GEM and SDC
- Pleased by progress and effort of both collaborations in narrowing technology options and planning for 1992
- PAC and Laboratory concerned with the current design of each detector having a cost larger than the sum of identified sources, cash and in-kind

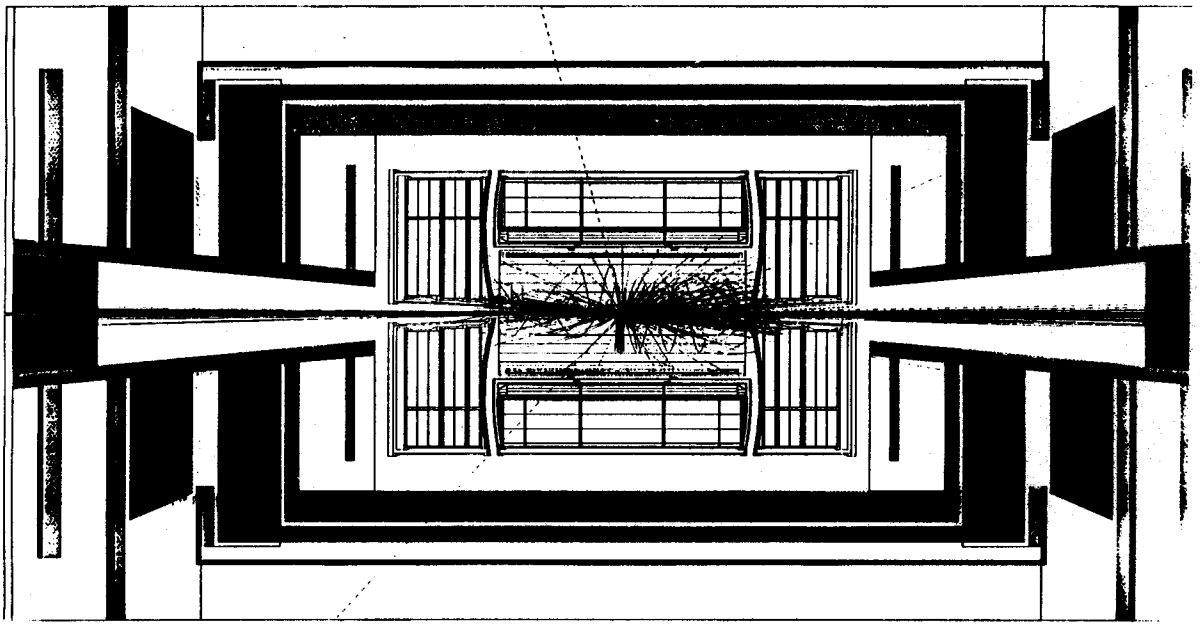


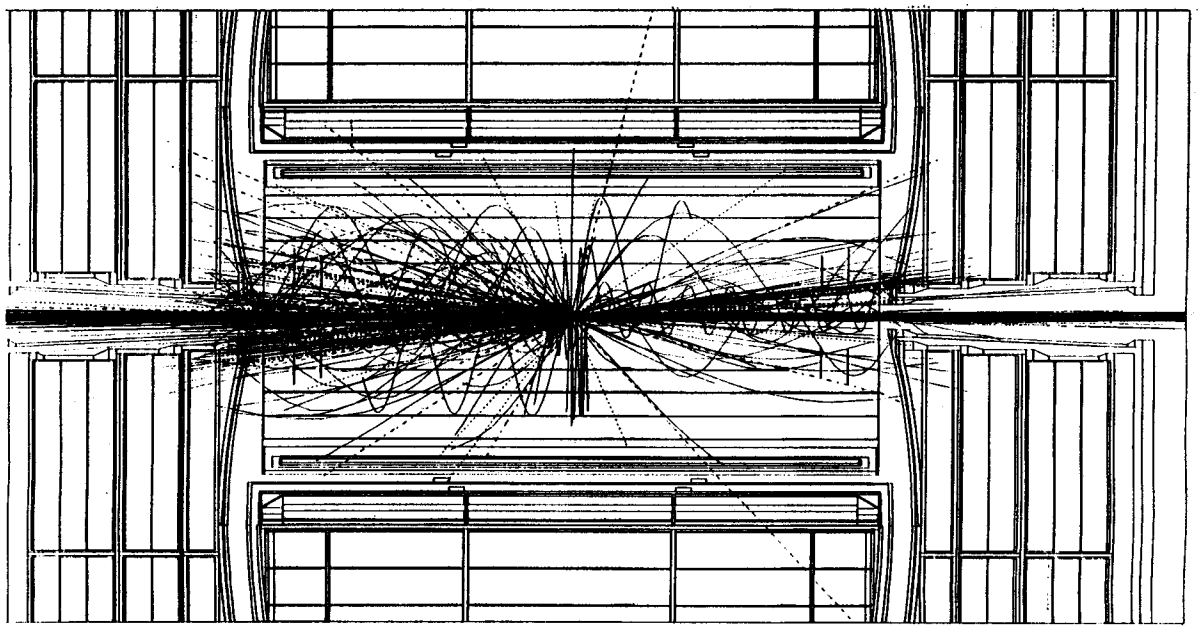
SSC Laboratory Physics Research Division

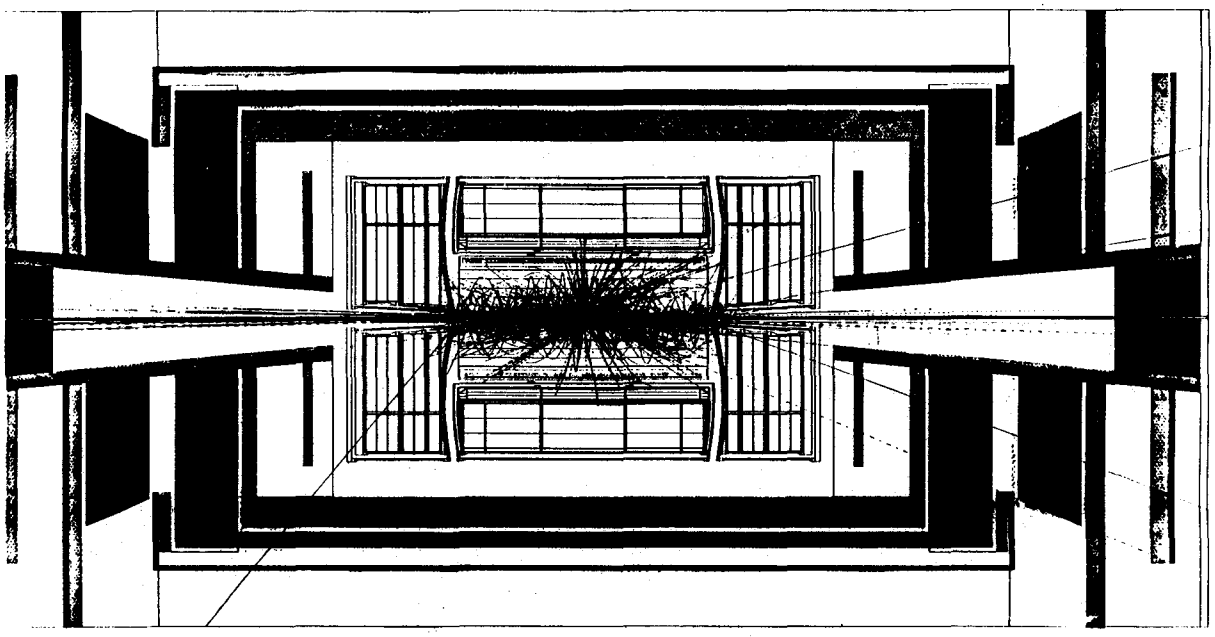
ORGANIZATION OF THE PHYSICS RESEARCH DIVISION

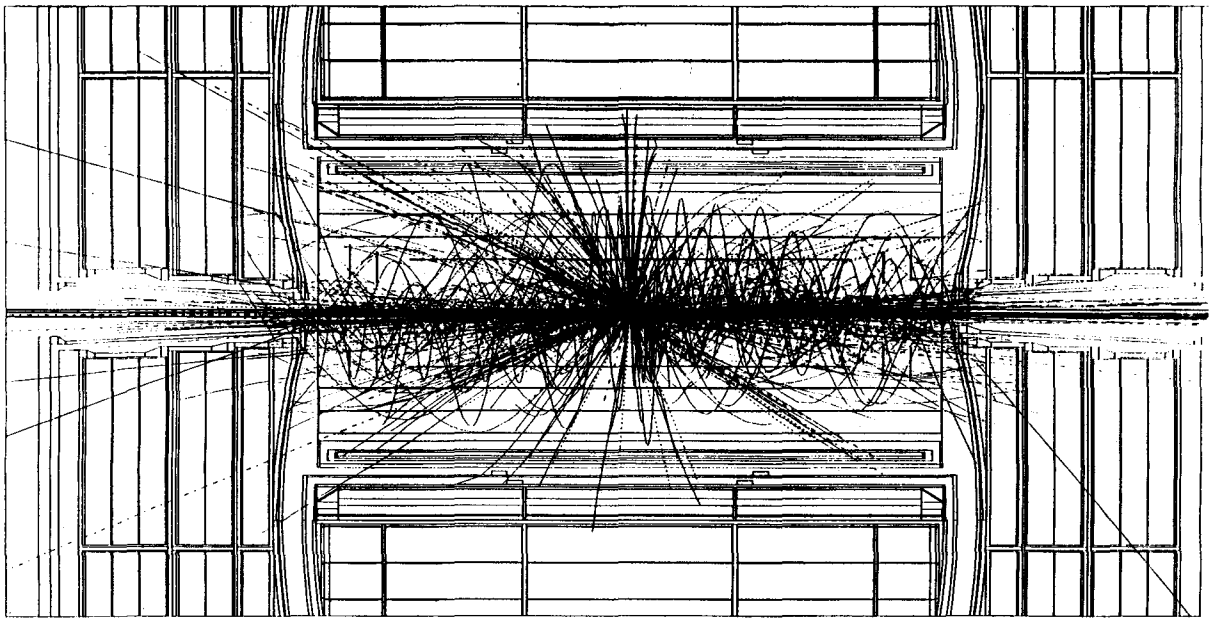
- Organized to take on responsibilities for high energy physics research and for management of detector construction
- Theoretical Physics Department established
- Experimental Physics: Includes SSC Detector R&D, on-going experimental HEP Research activities
- Interim SDC Project Management
- Computing

PDSF









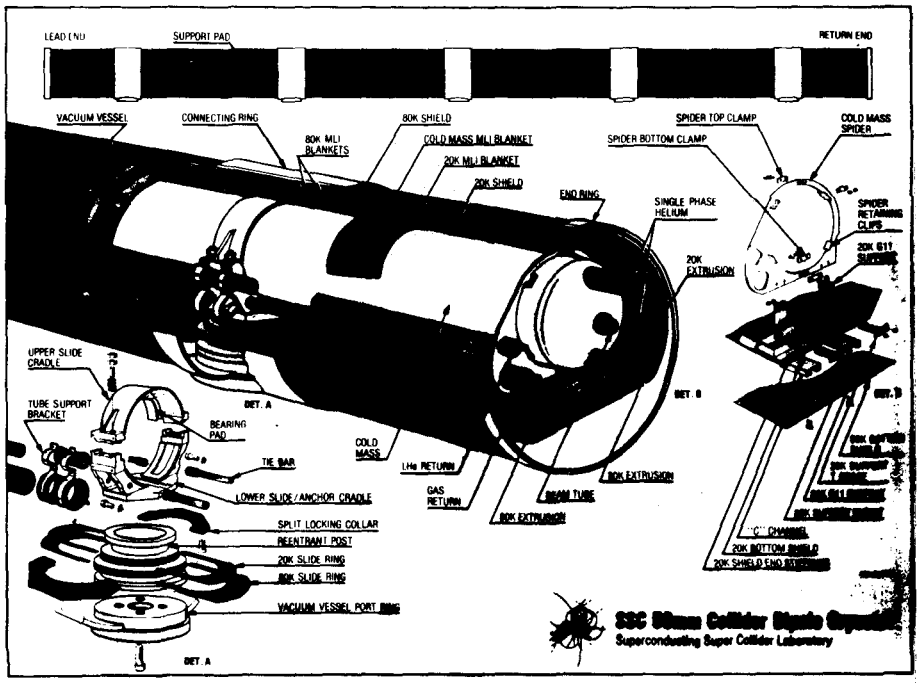
SSC Project—Magnets

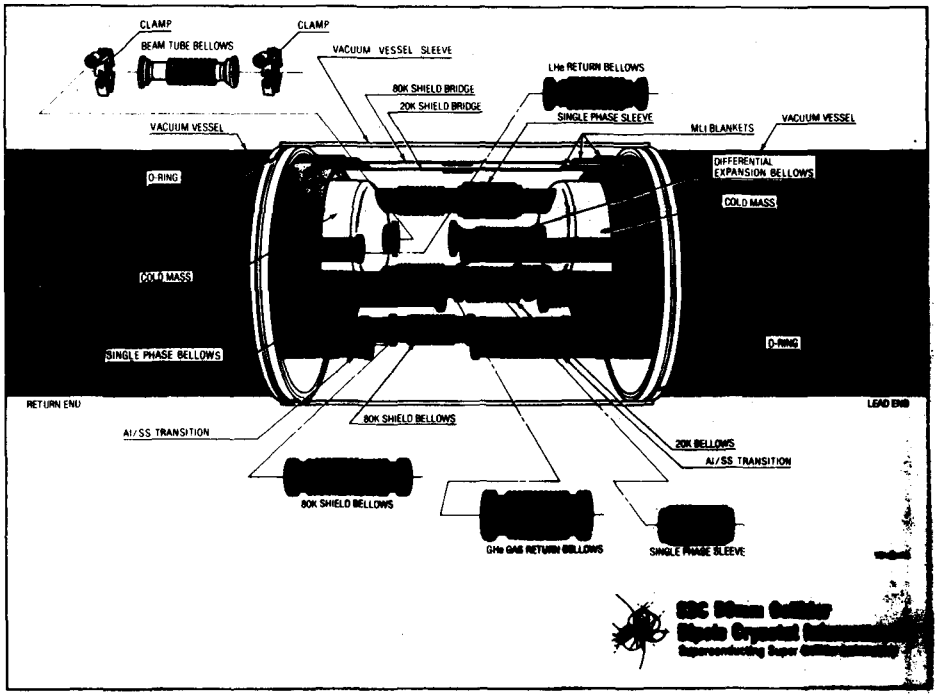
T. Bush

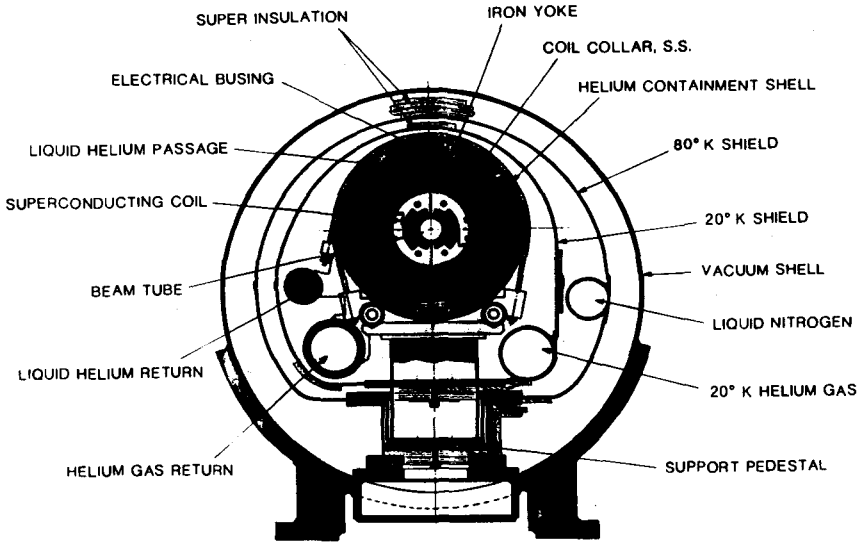
1991 Symposium on the Superconducting Super Collider

SSC Project - Magnets

Dr. T. O. Bush
October 14, 1991




CLAMP
CLAMP
BEAM TUBE BELLOWS
VACUUM VESSEL SLEEVE
LHe RETURN BELLOWS
80K SHIELD BRIDGE
20K SHIELD BRIDGE
SINGLE PHASE SLEEVE
MLI BLANKETS
VACUUM VESSEL
VACUUM VESSEL
DIFFERENTIAL EXPANSION BELLOWS
O-RING
COLD MASS
COLD MASS
SINGLE PHASE BELLOWS
O-RING
RETURN END
LEAD END
80K SHIELD BELLOWS
Al/SS TRANSITION
20K BELLOWS
Al/SS TRANSITION
80K SHIELD BELLOWS
GHe GAS RETURN BELLOWS
SINGLE PHASE SLEEVE


SUPER INSULATION
IRON YOKE
COIL COLLAR, S.S.
ELECTRICAL BUSING
HELIUM CONTAINMENT SHELL
LIQUID HELIUM PASSAGE
80° K SHIELD
SUPERCONDUCTING COIL
20° K SHIELD
VACUUM SHELL
BEAM TUBE
LIQUID NITROGEN
LIQUID HELIUM RETURN
20° K HELIUM GAS
HELIUM GAS RETURN
SUPPORT PEDESTAL

Collider Dipole Magnet Overview

40mm aperture program ending; R&D vehicles

- magnet mechanics
- quench performance
- magnetic measurements

Established a baseline design - BNL

50mm aperture program begun

- model magnets tested
- ASST magnets in production at FNAL
- BNL "back up" design also in production

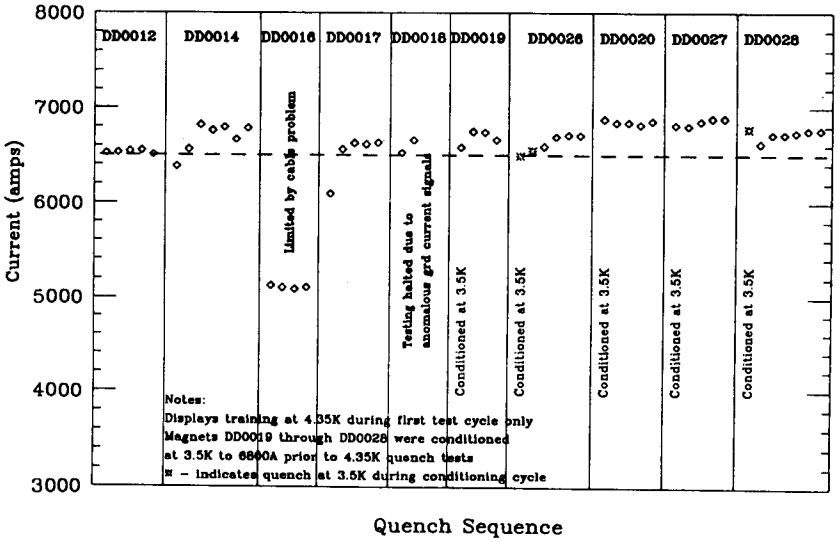
Industrial participation

- General Dynamics (leader)
- Westinghouse (follower)
- Assembly of ASST magnets

Bush/10/11/91

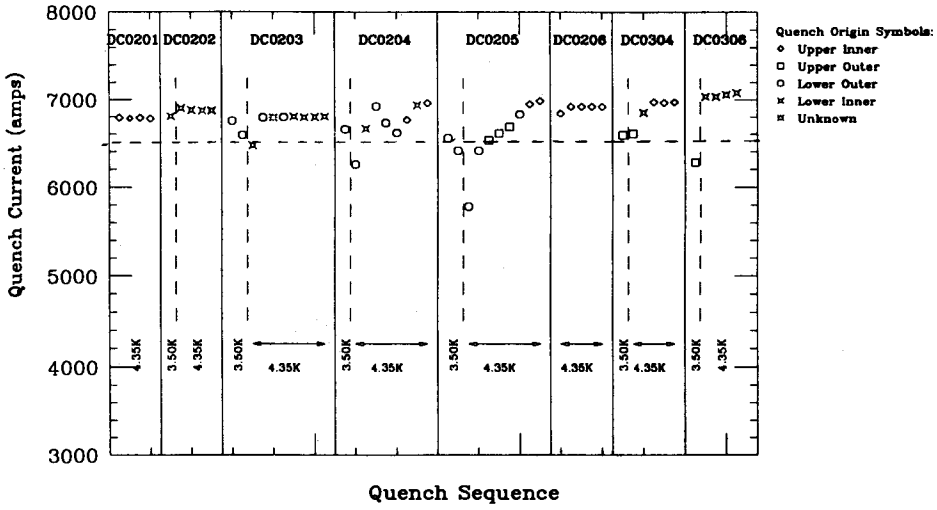
SSC Laboratory Magnet Systems

Initial Quench Performance of 40mm Full Length SSC Dipoles



Tompkins/10/7/91

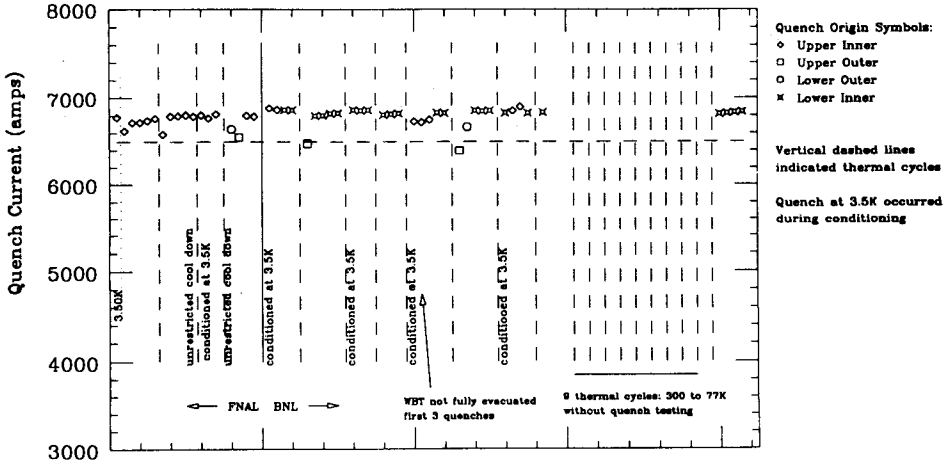
Initial Quench Performance of 40mm Full Length SSC Dipoles (cont)



All magnets conditioned at 3.5K before 4.35K tests
Quenches at 3.5K occurred during conditioning

Tompkins/10/7/91

DD0028: 4.35K Quench Behavior



Tompkins/10/11/91

Collider Dipole Design Evolution

- Collars
  strengthen to improve support of coil
  improve keying technique to reduce over pressure
- Cross section design
  better wedge mechanics
  harmonics
- Coil fabrication
  all-Kapton® insulation
  revise curing process
  improve tooling for better uniformity along length

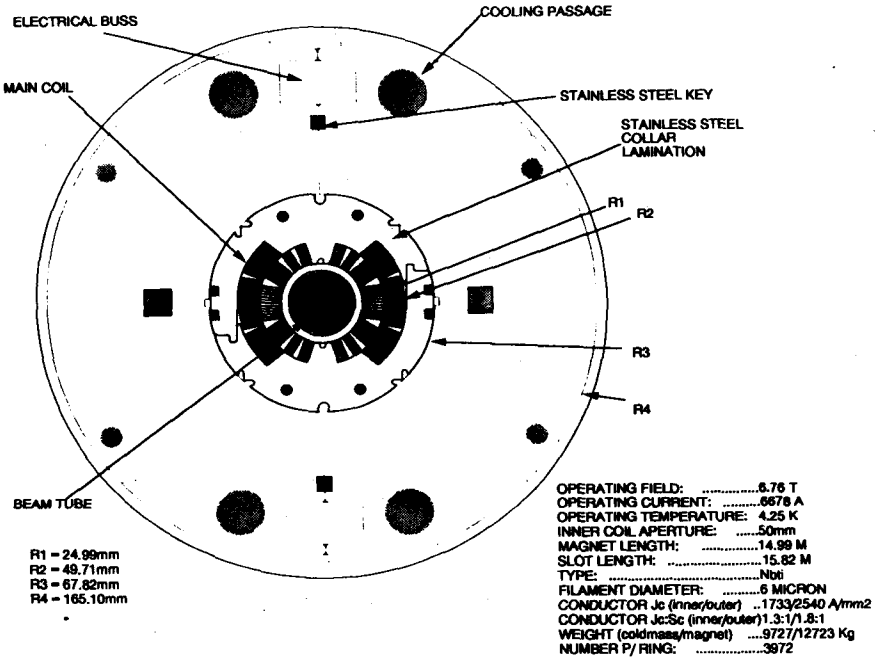
Bush/10/7/91

SSC Laboratory Magnet Systems

Collider Dipole Design Evolution (cont)

- Coil ends
  strengthen
  better radial uniformity
- Splices
  increase support
  control cable placement
- Yoke
  improve alignment, packing
  use as support element for coil

Bush/10/7/91



SSC 50mm COIL MAGNET CROSS SECTION

Current Status - Dipole Quench Performance

- Quench performance

  initial quenches near or above operating current

  very little training

  baseline mechanics well behaved up to ~7500 amps

  (force levels well above SSC operating current)

- Conditioning studies

  suppress initial training - promising

  possible procedure for starting machine after warm up

- Quench dependence - cool down

  data not conclusive. There is, at most, a weak dependence of training on cooldown rate.

- 50mm Model Dipoles

  increased margin in operating current

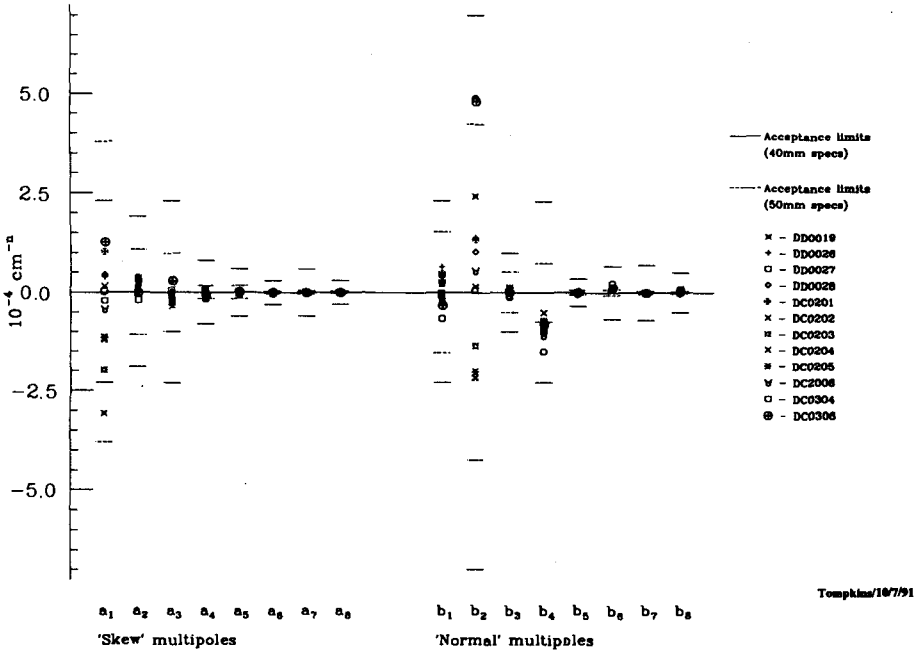
  excellent quench behavior

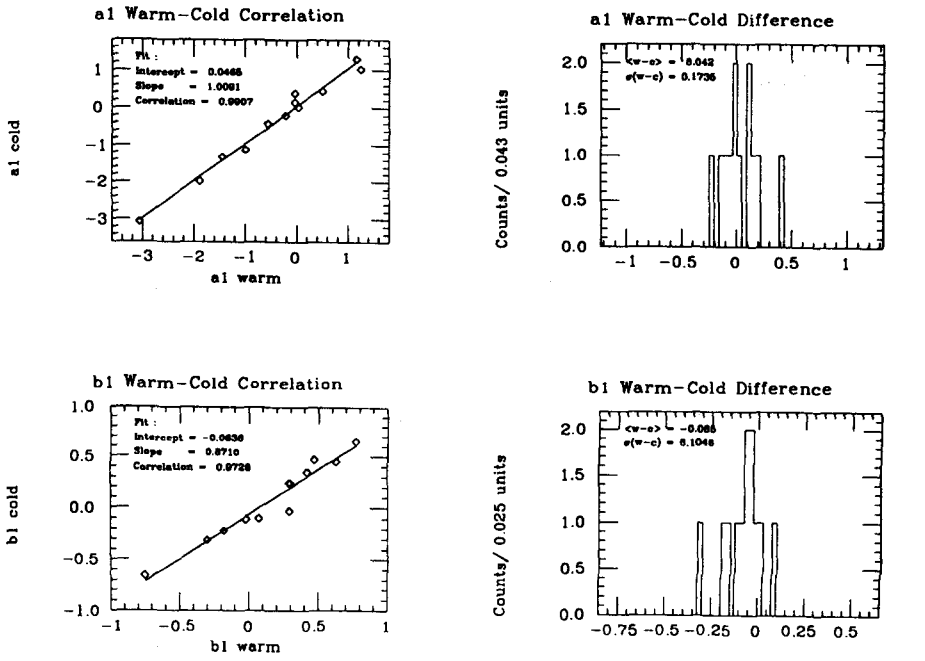
Bush/10/11/91

SSC 40mm Dipole Magnet Geometric Multipoles

2000A up ramp measurements corrected for persistent current

SSC Laboratory Magnet Systems





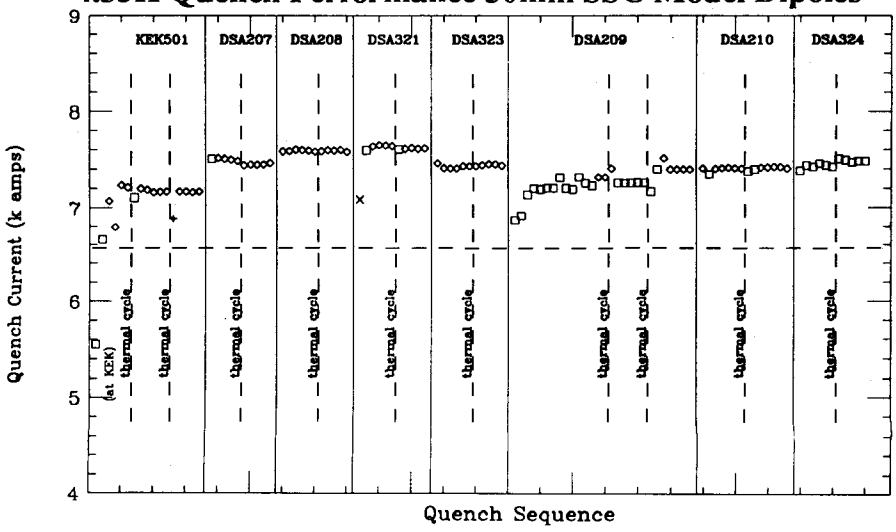
Magnetic Measurements

- Fabrication diagnostics as well as machine issues
  dipole field angle measurements
  NMR/Hall probe measurements
- Field quality
  uniformity
    point-to-point, magnet-to-magnet
  multipole content
    cold, warm, warm/cold correlation
- Stability of field, quality
  measure change with quench history, thermal cycling
- Persistent current studies
  b2 at injection
  time dependence
  spatial dependence

Bush/10/7/91

SSC Laboratory Magnet Systems

4.35K Quench Performance 50mm SSC Model Dipoles



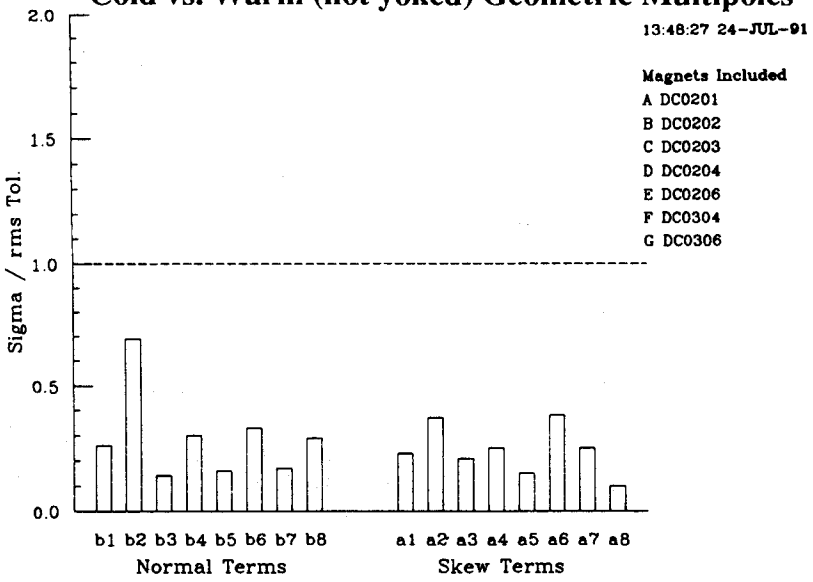
Only initial quenches at 4.35K following a cool down are displayed.

Quench Origins:
- ○ Lower Inner Coil
- ◇ Upper Inner Coil
- + Upper Outer Coil
- × Lower Outer Coil

Tompkins10/7/91

DSA209 & DSA210 have all kapton insulation
Last thermal cycle of DSA209 and first cycle of DSA210 are ramped to quench at 2A/sec instead of usual 16A/sec

Cold vs. Warm (not yoked) Geometric Multipoles



Schermer10/7/91

SSC Laboratory Magnet Systems

Collider Quadrupole Magnet Overview

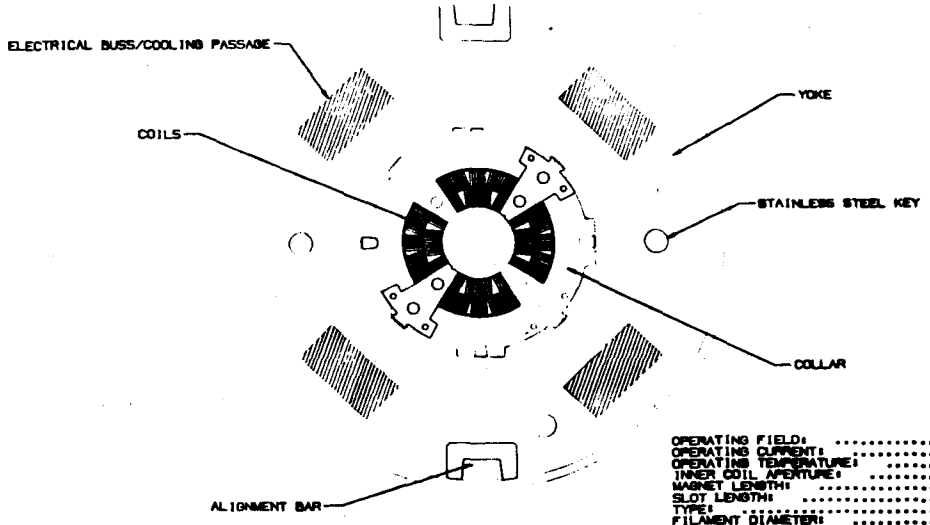
211T/m design (40mm aperture) at LBL

- **model magnets tested**
- **2 laboratory prototype quadrupoles tested**

Industrial participation

- **Babcock & Wilcox (leader)**
  - **participated in quad assembly at LBL**
- **General Dynamics (follower)**

Bush/10/11/91

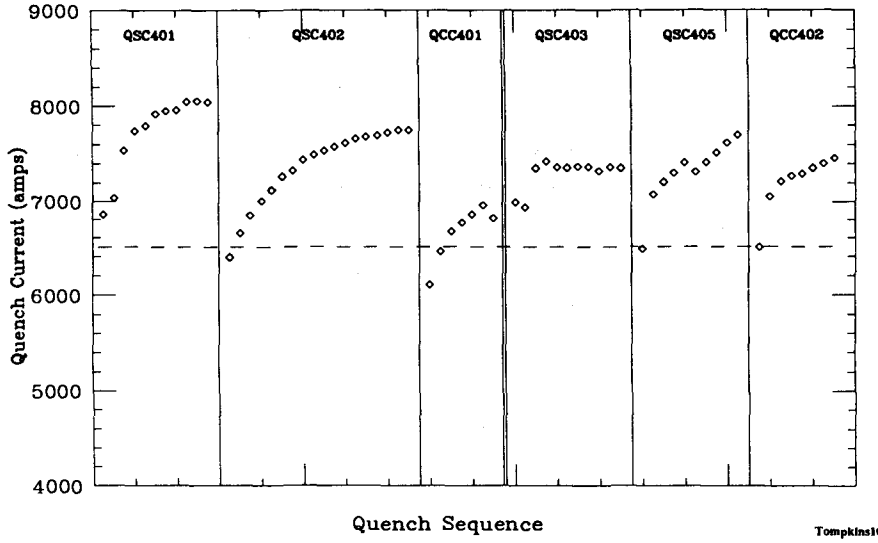


SSC 40mm QUADRUPOLE MAGNET CROSS SECTION

OPERATING FIELD:	217 T/M
OPERATING CURRENT:	6878 A
OPERATING TEMPERATURE:	4.35 K
INNER COIL APERTURE:	40 mm
MAGNET LENGTH:	4.02 M
SLOT LENGTH:	3.85 M
TYPE:	NbTi
FILAMENT DIAMETER:	9 MICRON
CONDUCTOR Jc(inner/outer):	2940 A/mm²
CONDUCTOR Jc:Sc(inner/outer):	1.8:1
WEIGHT(coldmass/magnet):	16[illegible]
NUMBER PER RING:	640

SSC Laboratory **Magnet Systems**

Initial 4.35K Quench Performance 40mm SSC Quadrupoles



Tompkins10/11/91

Short quadrupoles:
QSC401, QSC402, QSC403, QSC405

Full length quadrupoles:
QCC401, QCC402

High Gradient Quadrupole (IR Quad)

- NbTi at 1.8K is lowest risk option
- SSCL design underway (QSE101)
  - 50mm aperture
  - 180$\pm$ 10 T/m
  - 20% or better operating margin
  - available s/c cable
  - outer coil wound on inner coil (3 vice 7 splices)
  - coils and collars to be assembled with modified dipole tooling

Bush/10/7/91

High Energy Booster Dipole Overview

- Requirements include rapid cycling and bipolar operation
  - A/C losses calculated; experiments underway
  - Tests
    - at FNAL - A/C losses & bipolar operation
    - at KEK - A/C losses & fine (2.5mm) filament
- HEB dipole contractor selected
  - TBA Leader
  - TBA Follower

Bush/10/11/91



SSC Laboratory Magnet Systems 

High Energy Booster Quadrupole Overview

- Design a joint effort: SSCL & CEN, Saclay
- "Build to print" approach with vendor

Bush/10/7/91



SSC Laboratory Magnet Systems 

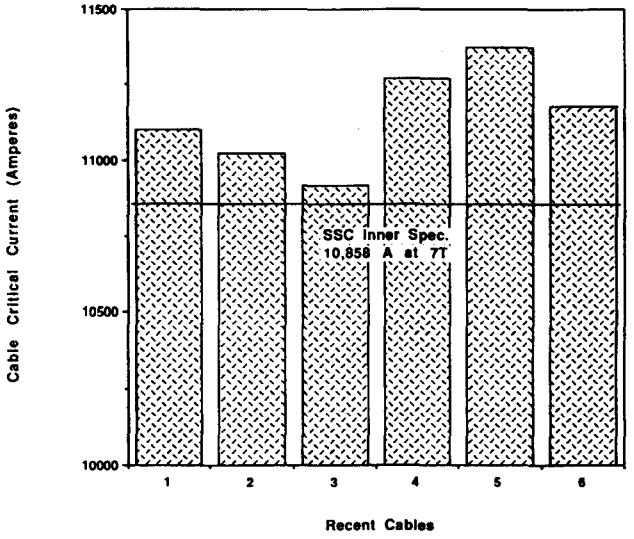
Superconductor Development

- 7 vendors selected for Phase I
  - Qualification of vendors now in progress

Inner S/C Vendors	Outer S/C Vendors
Intermagnetics General	Alsthom
Sumitomo	Furukawa
Teledyne	Oxford
	Outokumpu

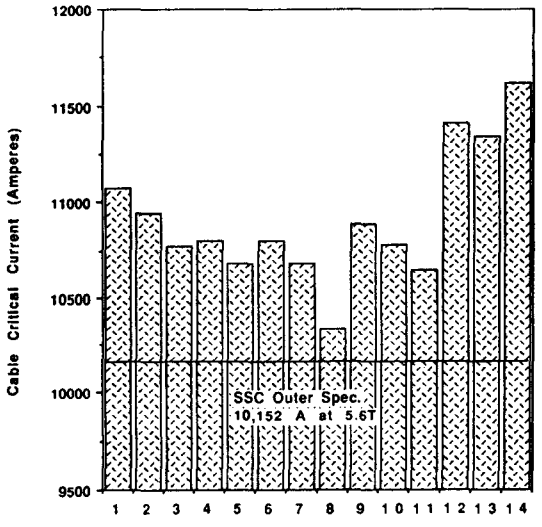
Bush/10/7/91

Inner Cable Critical Current (1.3:1 Cu/SC)



Christopherson/10/11/91

Outer Cable Critical Current (1.8:1 Cu/SC)



Christopherson/10/7/91

Coming Events

Start construction of MTL October 1991
HEB dipole vendor selection in November 1991
First ASST magnet tests in November 1991
QSE101 testing April 1992
Start magnet assembly in MDL May 1992
Start first industry prototype at General Dynamics October 1992
Five ASST magnet string test October 1992

Bush/10/7/91

SSC Education

T. Gadsden

SSC Research Associate Program

Offers educators research opportunities at the SSCL to revitalize their interest in science and understanding of new technologies.

SSC Science Academy

A two week science program for pre-college teachers to enhance their ability to teach science education. Program participants will perform and ultimately develop a number of science demonstrations and curriculum activities that they will take back to their classrooms.

Science Education Resource Program

Equipment such as small lasers and kits to demonstrate science concepts would be loaned to schools to enhance science education. Program resources also include SSCL staff accessing computer networks to disseminate information about the SSC, answer student and educator science questions, etc.

 SSC Laboratory Educational Programs

Minority Opportunities in Science and Technology (MOST)

Provides work opportunities at the SSCL to motivate minority and disadvantaged high school students towards achieving science literacy, a college degree, and perhaps, pursuing a career in science.

New Educational Initiatives



Superconducting Super Collider

Certificate of Recognition

awarded to

_____

for completion of the _____

Adopt-A-Magnet Workshop

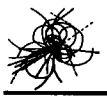
Tom Gadsden, SSCL Education Office

Sherri "Sam" Kivlighn, SSCL Education Office

Superconducting Super Collider Laboratory
2550 Beckleymeade Avenue, MS-2071
Dallas, Texas 75237

Teacher Workshop Program

Inservice workshops offer pre-college educators an opportunity to learn about SSC related science and technology while receiving accreditation for career ladder pursuits. Each workshop is individually tailored to the requesting school district's needs.

 SSC Laboratory Educational Programs

Teacher/Faculty

Adopt-A-Magnet Program

This Program uses puppets, games, songs, experiments, and interactive computer software to stimulate kindergarten - ninth grade student interest in science

SSC Laboratory Educational Programs

Kindergarten - Ninth Grade

Student Fieldtrip Program

Laboratory hosted school visits to stimulate student interest and understanding of science and the SSC.

SSC Laboratory Educational Programs

High School - Undergraduate



SSC Fellowship Program

Provides fellowships that encourage young scientists to participate in research related to the mission of the SSCL and to enhance high energy physics programs at U.S. Universities.



SSC Ph.D. Thesis Program

This program will encourage graduate students to participate in research related to the mission of the SSCL by offering high energy physics dissertation topics to students attending U.S. institutions of higher education.

Graduate Education for Minorities (GEM)

Through the GEM Program, capable minority engineering students are identified and offered graduate fellowships towards the pursuit of a masters degree.

Minority College and University Program

SSC speakers visit school campuses and make presentations to stimulate minority student interest and understanding of the SSCL and related technologies. This program includes Black Executive Exchange Program presentations at historically black colleges and universities.

SSC Technical Training Project

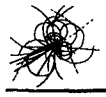
A state funded project to facilitate integration of SSC technology into community college student curriculums. This program includes a database to identify SSC industrial needs, required skill levels and educational programs for development of these skills.

SSC Technology Project

A state funded project designed to provide technology transfer to Texas community college faculty and students for the facilitation of knowledge/expertise in SSC related technical areas.

SSC Cooperative (Co-op) Student Program

Provides work opportunities at the SSC to afford undergraduate and graduate students with hands-on work experiences to integrate classroom studies with practical application in a laboratory environment.

 SSC Laboratory Educational Programs

Undergraduate - Graduate

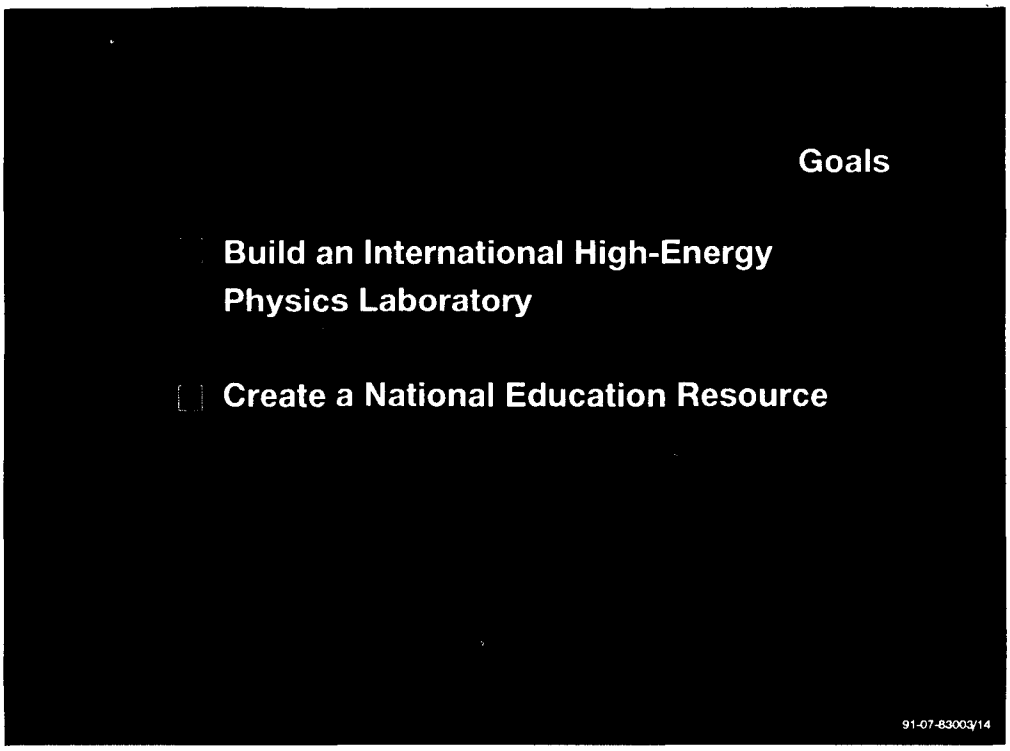
The SSC Education Office has four goals:

I. Stimulate Interest in and Promote Understanding of Science

II. Encourage Participation in Science and Technology

III. Improve the Classroom Experience

IV. Provide Leadership for Systemic Improvement



Parameter Selection for the SSC Trade-Offs and Optimization

D. Edwards and M. Syphers

Parameter Selection for the SSC Trade-Offs and Optimization

D. A. Edwards and M. J. Syphers
SSC Laboratory*
Dallas TX 75237

October 14, 1991

Abstract

In November of 1988, a site was selected in the state of Texas for the SSC. In January of 1989, the SSC Laboratory was established in Texas to adapt the design of the collider to the site and to manage the construction of the project. This paper describes the evolution of the SSC design since site selection, notes the increased concentration on the injector system, and addresses the rationale for choice of parameters.

1 Introduction

The basic parameters of the SSC shown in Table 1 were established, for the most part, some eight years ago. In the summer of 1984, a Central Design

Table 1: SSC Parameters

Particle Species	Proton	
Energy of Each Beam	20	TeV
Peak Luminosity	10^{33} cm^2 sec	
No. of Interaction Regions	up to 4 initially	
Storage Time (typical)	20	hours
Test Beam Energy	200	GeV
Availability	80	%

Group (CDG) was established at Lawrence Berkeley Laboratory to organize the

*Operated by the Universities Research Association, Inc., for the U. S. Department of Energy.

Table 2: SSC Injector Parameters

	Collider	HEB	MEB	LEB	Linac
Energy	20 TeV	2 TeV	200 GeV	12 GeV	600 MeV (K.E.)
Circumference (m)	87120	10800	3960	570	
Superconducting/Normal	SC	SC	N	N	N
Bunch Spacing	5	5	5	5	
Emittance (rms,norm., 10^{-6}m)	1.0π	0.8π	0.7π	0.6π	$< 0.4\pi$
Protons/bunch (10^{10})	0.75	1	1	1	
Cycle Time		4.5 min.	4.5 sec.	0.1 sec	

SSC design effort. Under the leadership of Maury Tigner, the CDG developed a sound design for a generic version of the SSC independent of site, yet more importantly, developed a design procedure that could be readily modified to the conditions of the selected site.

At the SSC Laboratory, effort has concentrated on tailoring the generic design to the Texas site and fleshing out the injector specifications. (See Table 2.) Additionally, SSC Laboratory personnel have felt that some steps in the direction of design conservatism should be taken. These will be described below. In the following sections we take up the various accelerators in order of descending energy.

2 Collider Parameters

Injection into the Collider is the dominant factor in determining the Collider parameters. Since 16 cycles of the High Energy Booster (HEB), each of four minute duration, are required to fill the Collider, particles must be able to endure this environment for 10^7 revolutions about the accelerator without degradation. The present Collider design parameters are shown in Table 3 together with the 1986 CDR [1] values.

2.1 Motivations for Change

Accelerator experiments performed at Fermilab and at CERN revealed long-term particle beam loss mechanisms in the presence of guide fields with a significant admixture of nonlinearity. These observations were one of the early warning signs leading to the question of long-term stability in the SSC at injection. The causes and mechanisms of the observed diffusion are still not completely understood.

Concurrently, accelerator studies took place using the Fermilab Main Ring where the injection environment is such that the natural dynamic aperture is on the order of the emittance of the incoming beam from the Booster synchrotron [2,3]. The measured geometrical admittance of the Main Ring is more than three times the equilibrium emittance arrived at by dynamical processes. After 20 years of operation the beam behavior in the Main Ring is not adequately understood. Though the Main Ring was not designed as a storage ring, experience with this synchrotron prompts one to look even more closely at the particle dynamics associated with the SSC at its injection energy.

Complementary to the experiments mentioned above were numerical simulations. A striking feature of these simulations was that in order to account, even qualitatively, for the results a rather detailed model of the synchrotron had to be developed and the tracking had to continue for orders of magnitude more turns than previously expected. Essential ingredients of the model were synchrotron oscillations, random and systematic multipole magnetic field errors, and closed orbit distortions. These results led to an extensive study of the long term behavior of particles at the injection conditions of the Collider. When this environment was first simulated for the CDR design, the resulting data indicated a dynamic aperture for 10^5 turns of only 5 mm. Simply extrapolation of the data suggests that the dynamic aperture for a particle to survive 10^7 turns would be on the order of one millimeter. Though this might be a slight underestimate, nevertheless it was hard to feel comfortable with the long-term dynamic aperture of this accelerator.

Table 3: Collider Parameters

	Present	1986 CDR	
Injection Energy	2.0	1.0	TeV
Circumference	87120	82944	m
Cell length	90	96	m
Cell phase advance	90	60	deg
Dipole Coil Diameter	50	40	mm
Dipole Field	6.60	6.60	T
Max. β in Arc	305	332	m
Max. dispersion in Arc	1.8	3.9	m
Beam-beam $\Delta\nu$ (H.O.)			
Beam-beam $\Delta\nu$ (L.R.)			
β^*	0.5	0.5	m
Crossing angle	< 150	< 150	μrad

2.2 Analytical Input

To study the parameter space of the Collider design, one needs to see the "handles" available. The three major accelerator parameters explored have been the quadrupole spacing in the arcs, the injection energy, and the coil diameter of the superconducting dipole magnets [4].

The first order effect that the quadrupole spacing has on the accelerator performance is the determination of the beam size. For a quadrupole spacing (half cell length) L and a betatron phase advance of 90° per cell, the maximum amplitude function of the cell is $\hat{\beta} = 3.41\ L$. The dispersion function varies as the square of the quadrupole spacing and $\hat{D} = 2.71\ L^2/R$, where R is the average radius of the arc. The maximum rms beam size within a cell is then

$$\hat{\sigma} = \sqrt{\frac{\hat{\beta}\epsilon_N}{\pi\gamma} + \hat{D}^2\left(\frac{\sigma_p}{p}\right)^2} \qquad (1)$$

where ϵ_N is the rms, normalized emittance, γ is the ratio of beam energy to the proton rest energy, and σ_p/p is the rms momentum spread of the beam.

In addition to the physical extent of the beam being smaller, a shorter half cell length can result in an increase in the linear aperture. For example, the chromaticity due to systematic sextupole errors varies as L^3. The higher order multipoles have even higher dependences on half-cell length; for instance, the tune shift of off-momentum particles due to decapole errors (b_4) varies as the quadrupole spacing to the seventh power.

Due to the adiabatic damping of betatron oscillations as the energy of the beam is raised, a higher injection energy for the Collider rings implies a smaller beam size and hence reduced aperture requirements. More importantly, the "persistent" current multipoles at injection will be lessened. By doubling the injection energy from 1 TeV to 2 TeV the sextupole coefficient is cut by over a factor of two and coupled with the cell length change indicated in Table 3, the chromaticity of the Collider ring due to persistent current b_2 is reduced to 700 units from 3400 units. It also relaxes the alignment requirements of the dipoles enough to eliminate the need for bore tube correctors. In addition, the betatron oscillation amplitudes of the beam particles are reduced by 30% due to adiabatic damping and, in conjunction with the new half cell spacing, the beam size is reduced by 50%.

The good field region of the Collider magnets can be increased by increasing the magnet coil diameter, keeping the field shape the same. If the transverse dimensions of the magnet (indicated by the coil radius R_o) are increased, then $b_n \sim 1/R_o^n$. This scaling law applies to the systematic, or average, multipoles in the magnets which are generated by the magnet geometry or by persistent currents.

If coil placement errors are independent of the scale of the magnet, then the rms values of the multipoles will scale like $\sigma_{b_n} \sim 1/R_o^{n+1}$. On the other hand, if

placement errors scale in proportion to the size of the magnet, then $\sigma_{b_n} \sim 1/R_o^n$. In either case the spread in the higher order multipoles are significantly reduced by increasing the coil radius. For comparison studies, the geometric mean of these two cases was used to perform the scaling of random multipoles, i.e., $\sigma_{b_n} \sim 1/R_o^{n+1/2}$.

While many effects of various design parameters on beam performance at injection can be estimated analytically, verification with long-term particle tracking is still necessary. In particular, tracking is necessary for the unraveling of magnet coil diameter dependencies as well as quantitative verification of effects of the other two changes.

2.3 Simulations and their Parameterization

In the Collider, beam tracking results of particle loss for a model based on standard cells [5,6] have been systematically analyzed in order to obtain a method of comparison from one set of tracking plots to another [7] and to reduce statistical and conceptual biases. The results then lend themselves to straightforward empirical parameterization, leading to functional relationships between aperture and number of turns to loss, with, as examples, bend and quad coil diameters, at varoius momentum, off set injection energy, cell length, on phase advance per cell as parameters. An attempt will be made to tie this parametric information to approximate cost differentials in order to gain general insight into whether or not the design is reasonably cost optimized. Similar effort is underway for the High Energy Booster injection situation, and is discussed later in this paper.

The survival plots have been analyzed to find the mean amplitude for loss and its standard deviation as a function of the number of turns. The "aperture" is then defined as the point two standard deviations within the mean. Both the mean and the standard deviation are fit as a function of the number of turns, n, and extrapolated to $n = 10^7$ to define the "10^7 n aperture."

The expressions used are

$$a(n) = Bn^{-0.065} \tag{2}$$

where a is the mean amplitude, and B is to be found for each set of data. For the standard deviation, the empirical relation is

$$da(n) = 1.8n^{-0.065} mm \tag{3}$$

Then the aperture, A, is given by

$$A(n) = Bn^{-0.065} - 2 \cdot 1.8\ mm\ n^{-0.065} \tag{4}$$

$$= (B - 3.6\ mm\ )n^{-0.065} \tag{5}$$

As the results of the analysis are given at $n = 10^7$ and $\delta p/p \approx 5 \times 10^{-4}$ $(5\sigma_p/p)$, the aperture at any other n is given by

$$A(n) = A(10^7)\frac{n^{-0.065}}{0.35} \tag{6}$$

In what follows, A will stand for $A(10^7)$.

The relationship between the bend and quadrupole coil diameters, and the dynamic aperture, was found to be approximated by:

$$\frac{1}{A} = \left(\frac{1}{A_q^2} + \frac{1}{A_b^2}\right)^{1/2} \tag{7}$$

$$A_{b,q} = C\left(\frac{d}{D_o}\right)^m, D_o = 40\ mm \tag{8}$$

$$A_b = 2.7\ mm\left(\frac{d}{D_o}\right)^{3.2} \tag{9}$$

$$A_q = 6.4\ mm\left(\frac{d}{D_o}\right)^{1.9} \tag{10}$$

The aperture as a function of coil diameter, d, could be expected to vary approximately as in Table 4 with $10\sigma = 3.8$ mm.

Table 4:

Quad Diameter	Bend Diameter	A (mm)	A/σ
4	4	2.5	6.5
4	5	4.0	10.5
5	5	4.6	12.1
4.8	4.8	4.2	11

For the basis of comparison here, a simplistic approximate cost model is used to evaluate the relative effectiveness of the incremental coil changes, injection energy changes, cell length changes, etc. It should be stressed that these approximate models are not a substitute for detailed cost estimates, but only a guideline. They try to approximately reflect the relative proportion of fixed cost to cost associated with change in diameter. For instance cryostat and labor costs do not necessarly change linearly with coil diameter. Costs associated with change in cell length are discussed below. Only the inpact on the quad has been taken tinto account, although it is known that increasing the number of bend magnets for the same intergial B·dl does increase the cost.

For the bend, quad and correctors, assume the differential cost goes like

$$\frac{\Delta cost}{cost} = \frac{3}{4}\frac{\Delta R}{R}$$

and for the spools, assume

$$\frac{\Delta cost}{cost} = \frac{3}{8}\frac{\Delta R}{R}.$$

Then these assumptions lead us to the results shown in

Relative to a 5 cm dipole and a 4 cm quad, the 4.8 cm dipole and quad would be approximately cost and aperture neutral (with a small aperture benefit). The 4.8 cm diameter is desirable over the 4 cm quad because it permits a larger diameter smooth beam pipe with lower impedances. The aperture as a function of injection energy is given in Table 6 for the average of two simulation assumptions.

Table 5 (given in relative technical cost units).

Table 5:

	$\Delta cu/\sigma$	cu(base line)
for bends	15	410
for quad/spool/corrector	10	47+28+09

Table 6:

E_{inj} (TeV)	Aperture	10σ beam (mm)	Aperture/σ
3	4.7	3.1	15
2	4.2	3.8	11
1.8	4.0	4.0	10
1.5	3.6	4.4	8
1.0	2.25	5.3	4.2

The result is an almost linear increase in the number of σ's with injection energy, or about 1σ per 0.2 TeV of energy increase. Below 1.5 TeV the aperture from simulation results drops rapidly to about 2 to 2.5 mm at 1 TeV. Presumably, this could be understood and compensated to some extent by mid-cell correctors. However, the drift in persistent currents will cause more and more severe problems at lower energy. These are not part of the simulation.

Using 1σ per 0.2 TeV, a differential cost and figure of merit for increased energy can be estimated. HEB cost, including civil construction and beam lines is about 114cu for 2 TeV so injection energy gives $11\text{cu}/\sigma$ aperture increase or decrease.

Injection at 1 TeV with conventional warm magnets has been suggested. An argument being that injection time could be substantially reduced with an

associated increase in aperture. Ignoring the fact that a 1 TeV conventional ring would not fit on site and the bi-polar injection would be required of a conventional iron magnet system, we can look at some of the other features.

The present 200 GeV MEB has a cycle time of 4.5 sec, whereas the HEB has a collider fill time of 72 min. Assuming a 1 TeV MEB has a 4 times longer cycle time and needs 16 cycles to fill the collider, gives 290 sec or about 5 minutes for a reduction factor of .07 compared to the previous filling time. The associated increase in dynamic aperture is $.07^{-.065} = 1.19$. However the beam σ is $\sqrt{2}$ larger, so Aperture/σ is 0.84 of the previous case. This does not yet take into account the shrinking dynamic aperture with energy to 2.25 mm, resulting in an aperture acceptance of 5σ (or 1/2 of our 10σ requirement).

The cost of such an injector can be scaled from the MEB, leaving out beam line components but including conventional construction. The cost of the MEB is ~36cu. We would need to scale by 4.5 to about 162cu for a 1 TeV warm HEB. This is to compare with the HEB cost without beam lines of 108cu. Even if one assumed one didn't need the present MEB, the cost would be about 17cu more for a 1 TeV instead of a 2 TeV injection complex.

What is at play here is that conventional and superconducting accelerators cost approximately the same per linear foot, with typically superconducting accelerators being 10-20% more expensive.

In the light of trying to understand the cost optimization of the Collider and to find a cost neutral way to increase the quad/spool aperture to 5 cm, a tabulation of the effects of cell length and phase advance is appropriate. Assuming that about 20% decrease in integrated quad strength is needed for a cost neutral change, the impact can be evaluated.

If this were taken up by decreasing the phase advance to 71° but leaving 90 meter spacing, the β the spot size σ hardly changed. On the other hand, the dispersion function and the dispersion spot size would increase by 1.5 times. The 71° phase advance has the disadvantage of not canceling dispersion every 2, 6, etc. cells.

If the cell length were changed but 90° per cell retained, then a 10% increase in cell length to 100 meters would decrease the quad strength by 10% and the number of cells by 10% giving a 20% net savings. The β would be increased by 10% and the dispersion by $(1.1)^2$ or 20%.

At most, the betatron spot has increased 5% so that if dynamic aperture were unchanged, one would be forfeiting on the order of less than 1/2 σ by this change.

Simulations give a decrease in aperture of about 2 σ in changing the phase advance from the 1/2 cell length 90 to 70 degrees or in changing from 90 meters to 100 meters.

This reduction would only be partially made up by an increase at the quadrupole aperture to 5 cm. equivalently we are losing on the order of 2σ

of aperture for a savings of about 9 cu's. Moving in the other direction larger phase advance gives no improvement. Shorter 1/2 cell length (80 m) gives an increase of a little more than 1 σ.

There are a number of trade-offs that could, in principal, be considered in order to accommodate larger quad coil size — e.g., reducing the dipole coil diameter, increasing the cell length, decreasing phase advance or injection energy. Approximate cost per differential spot σ can be estimated for the various choices and is displayed in Table 7.

Neither increased cell length nor reduced phase advance seem to be reasonable alternatives at this point in the project as they disrupt too many other areas of the base line. A similar statement is probably equally true for the Collider bend coil diameter and HEB circumference.

Table 7:

	Δ cu/σ
bend coil diameter	14cu
quad spool coil diameter	10cu
injection energy	11cu
phase advance, cell length	5cu *

* Loss in effective aperture only

The choice of parameters seems reasonably optimized within the accuracy of the approximation and indicates that, if anything, higher injection energy is more cost effective than coil diameter.

3 High Energy Booster

It would be highly desirable if the HEB could use (with minor modification) the 5 cm magnets developed for the Collider. Simulations of dynamic aperture for the HEB are on-going. The needed aperture for the present 200 MeV injection energy and 38 m half cell with two 15 m dipoles is 7.1 mm for 10σ of a 0.8π emittance beam. This emittance allows for 0.2π dilution in processes associated with HEB and Collider acceleration and transfer. The potential test beam option for the HEB specifies 4π emittance (95% beam = 4.6 mm). The 10σ aperture design is not required for this mode of operation; however, it is clear that much less than 7 mm aperture might make for unacceptable losses in fixed target operation.

Parameter fits developed for the Collider simulations can be used for a zero order estimate of the HEB aperture. HEB injection time is about 12 sec or 3×10^5 HEB turns. In some approximate sense, one might expect this to be

equivalent to looking at the Collider aperture for 3.8×10^4 turns:

$$A_{HEB} \approx A_{Collider}(@10^7)\left(\frac{n_H}{n_C}\right)^{-.065} = 1.4A_{Collider}.$$

Using the Collider aperture of 4.6 mm for 5 cm quads and bends leads to an expected HEB aperture of 6.4 mm. This is to be compared with an actual HEB simulation at $\Delta p/p = 5 \times 10^{-4}$ which gives a result of 5.8 mm (and 6.1 mm for $\Delta p/p = 7.5 \times 10^{-4}$). Thus we see that the simulated aperture does not comfortably fit the design requirement. However, the required $5\sigma_p/p$ for the HEB is 2.5×10^{-4} and the design calls for use of 2 $\frac{1}{2}\mu$ filament wire. These effects together sufficiently boost the aperture. Simulation of a 6 cm coil for the HEB gives 10 mm of aperture, a substantial increase over the 5 cm coil. At one time it was felt that this aperture might be necessary as well for cooling to remove eddy current AC losses from the fast cycling HEB. Further investigation of the cooling indicates it is adequate for 5 cm.

Results of simulations are given in Table 8a. There is a dependance on $\Delta p/p$. The 5σ $\Delta p/p$ for baseline Collider operation is 2.5×10^{-4}. The potential for higher intensity and test beams make it desirable to consider greater $\Delta p/p$ as well, and 7.5×10^{-4} has been used in much of the analysis.

Source of the options considered are

1. base line (as function of $\Delta p/p$)
2. setting average b_2, b_4, b_6 to values consistent with $2.5\mu m$ filament diameter (as function of $\Delta p/p$)
3. shorter half-cell length – 32.5 m instead of 38 m
4. 240 GeV instead of 200 GeV (as function of $\Delta p/p$) injection
5. both (as function of $\Delta p/p$)
6. 6 cm bend coil diameter

Also included in the calculations are sorting on b_2 and setting systematic b_2 b_3, b_4, b_6 to zero.

1. setting systematic b_2, b_3, b_4, b_6 to zero
2. setting systematic b_3 to zero

Sorting on b_2 might require cold measurements of all magnets. Setting systematic b_2, b_4,and b_6 to zero is modeled from the idea that if nickel filament were incorporated in the strand in the proper proportion, it could compensate for the persistent current effects. It could not, however, compensate for the drift in persistent currents. The use of $2.5\mu m$ filaments instead of $6\mu m$ on which the

multipole set is based would reduce the systematic persistent current multipoles by 2.5/6 as well as reduce the cooling requirements to about 2/3 of that required for $6\mu m$ coils.

It is clear that going to a 6 cm diameter coil completely satisfies the dynamic aperture requirements with comfortable margin and gives about a 5σ (about 50%) increase in dynamic aperture. Going to a shorter cell or higher energy injection each gain about 10% to 20% (1 to 2σ) and the combination of both yields 20% to 50%. The improvement is more pronounced at $\Delta p/p = 5 \times 10^{-4}$ and below. It is less obvious at 7.5×10^{-4}.

The "sorting" of b_2 and the reduction of systematics seem to have a more positive effect (1σ) relative to the base line cell length and less effect when added to the shorter cell simulations. All in all, there is enough scatter in the results to restrain one from putting too fine an interpretation on them.

As in the collider, very approximate cost benefit implications can be attempted. For the coil diameter, using

$$\frac{\Delta cost}{cost} = \frac{3}{4}\frac{\Delta R}{R} = .15$$

for the dipole, quad, and correctors/spool gives about 1.7cu/σ (6 cm = cost increase of 9.4cu). Actual estimates of the dipole cost indicate 10% increment is more appropriate.

The cell length cost can be approximated by linear scaling of the total quad/spool integral strength increase of (38/32.5):

$$\frac{\Delta cost}{cost} = \frac{3}{4}\frac{\Delta L}{L} + 1\frac{\Delta N}{N} \approx 0.30$$

where N is the number of components. For the quad/spool correctors, this gives about 3.4cu/ σ (increase of 6.2cu) assuming about a 2σ improvement.

Higher energy injection from the MEB costs about 8.8cu/40GeV if we scale the total MEB and beam line costs. Again, assuming about a 2σ improvement, this gives about 4.2cu/ σ.

Here, if the magnet field in the MEB could be pushed effectively without an increase in the MEB circumference, then the cost would be substantially less. Operation of the MEB above 2 T (from a nominal of 1.75 T) seems unlikely and would only yield an increase of about 25 GeV te 30 GeV.

Smaller filament wires, etc., have of the order of 5% effect on cost of the magnets with a potential cost/benefit of 2.5cu σ if it could be realized.

Sorting on b_2 might require cold measurements resulting in about 1.4cu σ.

A cost/benefit summary (very approximate) is shown in Table 8. The reader is again warned fo the debateably nature of the cost analysis.

A trade-off which from the above would seem attractive would be to go to the 6 cm coil and reduce the injection energy by 40 to 50 GeV. This would be approximately cost neutral and increase the aperture. Trade off with longer cell

Table 8: HEB Differentials

	cu/σ
coil diameter	1.7
cell length	3.4
injection energy	4.2 (less if no circumference change)
filaments	2.5
sorting	1.4

length could also be contemplated. In either case, further simulations would be required as the changes would be substantial.

In reality, lower injection energy is not feasible because of the test beams requirement.

A 6 cm coil for the HEB could be approximately cost neutral if the HEB energy were reduced to 1.8 TeV and if 6μm filament wire were used. This would appear very attractive were it not felt that there is substantial risk in undertaking the development of yet another style of superconducting magnet and for the loss of about 1σ of collider aperture.

In summary, the 6 cm coil has been dropped from consideration. The 5 cm coil with $2\frac{1}{2}\mu$ filaments meets requirements and gives about 1σ more aperture than a 5 cm coil with 6μ filaments. Reducing the half cell length from 38 m to 32.5 m increases the aperture about 1.5 σ over the $2\frac{1}{2}\mu$ filament, 38 m case.

The cost of this option of reducing the cell length needs to be looked at in more detail. It is in all likelihood the most practical and needs serious evaluation. Possibly it can be done more economically than indicated and that some savings can be obtained by deciding to use 6μm wire. Here again, there is the feeling that 2.5 μm filaments or nickel wire have sufficient development risk so that counting on them as part of the base design may be impractical.

In comparing the cost trade-off numbers for the Collider and HEB, it appears that for the Collider it is more economical to go to higher energy and smaller coil diameter, whereas for the HEB the opposite is indicated. This is probably a reflection of the fact that the Collider is two rings being fed by one superconducting injector. The HEB is only one ring and it is fed by a conventional warm injector which is much more expensive per unit energy.

A final comment about design to cost and optimization of that design. Such optimization can be done only if one is willing to go back and open areas of design which have already been frozen (e.g. Collider coil aperture — 4.8 mm vs. 5 mm) or to take on development risks (e.g. 6 cm HEB). The former process is extremely destructive to forward progress on the project and probably is not cost effective. The latter is a balancing of risk and schedule vs. potential long-term benefit.

4 The LEB Peak Energy, Ring Circumference and the MEB Injection Energy

The choice of LEB circumference (and injection energy) determines the space charge tune shift of that accelerator and sets the brightness scale of the whole accelerator chain. Thus, the LEB circumference is a parameter which must undergo considerable technical scrutiny through cost effectiveness is not an important criterion. In looking at this parameter it is important to keep in mind that the $\Delta\nu_s c$ scales linearly with radius (R) and that small reduction is in R at the penalty of forcing marginal space allocation for engineering equipment (e.g. rf systems, magnet ends etc.) is not prudent. Big reduction like a charge in radius to 2/3 its present value begins to have significant impact. Of equal importance is the consideration that the LEB injection energy is upgradeable and tunnel space is provided between the Linac and LEB for a linac upgrade to 1 Gev cup (KE) from 600 MeV. Alternatively or a small prebooster could be added at a later time. The 1 Gev linac reduces LEB space charge by a factor of 1.75. A prebooster could in principal reduce it even more.

In setting LEB to MEB parameters it should be assured that the MEB will not become the performance bottleneck of the accelerator chain. In the LEB, peak energy, fast cycling (10Hz resonant excitation) and avoidance of transition crossing are factors. In the MEB space charge tune shift, emittance dilution from beam-gas multiple scattering and injection field quality must be considered. (The latter is not considered to be a limitation within any feasible range of injection energy.)

In both the LEB and MEB, transverse emittance growth is the parameter that is driving the design choices, and our understanding of the process and what is important is limited. Experience from operating accelerators is hard to extrapolate because of the small emittance and growth required. In particular the emittance growth with space charge tune shift as a function of dwell time at injection is not completely understood (at least by us). A fast cycling LEB has been chosen to minimize the time spent at injection in both the LEB and MEB and to minimize the growth from space charges as well as gas scattering (MEB) (This choice also allows for reasonable test beam fixed target capability as well).

The 10Hz operation needs sufficient space for rf cavities. Transition has been avoided in the LEB because of the experience with the FNAL booster and longitudinal instabilities observed there. It is not known to what extent these might also effect transverse emittance but it is recognized that precise beam manipulations at transition can be tricky in a fast cycling accelerator. The avoidance of transition in the LEB makes for a non conventional lattice and possibly not as efficient utilization of space as might otherwise be achieved.

Table 9a – tabulates the approximate circumference penalty associated with

fast cycling, transition, and the difference in peak momentum of 10 to 12 GeV/c.

Table 9: Tune Shifts LEB and MEB as Function of LEB Circumference and Energy

LEB Circumference/p	LEB	LEB/1.75	MEB Inj./1.75
570/12 Gev/c	0.6	0.34	0.08/014
475/10 Gev/c	0.5	0.28	0.11/0.20
380/8 Gev/c	0.4	0.23	0.18/0.31
Note	1	2/3	4/5

1) Nominal intensity, 0.6 GeV or 1.75 nominal at 1 GeV
2) Nominal intensity 1.0 GeV LEB
3) Nominal intensity MEB at injection
4) 1.75 brightness MEB – at injection.

In the LEB space charge the shift is estimated to be 0.6 at 0.4 π mm–mrad emittance and 600 Gev (KE)injection. This estimate is controversial as it depends strongly on the bunching factor assumed. The typical range in $\Delta\nu$ is 0.4 to 0.6 consistent analysis leads to the same sort of value for the FNAL Booster operation. This is reduced by 1.75 at one GeV (KE).

The MEB with 12 Gev/c injection has a space change tune shift of 0.08 during the injection dwell. This will increase during the start of ramps to approximately 0.12 depending on ramp conditions. These numbers appear reasonably small but still may be difficult to fit within major resonant lines. Low energy dwell times are fractions of a second, not msecs as in the LEB.

With an LEB upgrade to increased N/ϵ by 1.75 the MEB numbers for injection becomes 0.14. One can then ask what happens at lower injection energy (linearly smaller radius LEB) to the tune shifts in both rings. (Table 9b) What is at play here is that the LEB tune shift gets smaller linearly with energy (R) and the MEB tune shift increases inverely with the energy squared. At $8Gev/c$ the $\Delta\nu$ is almost equal in the two rings under the condition of upgraded linac energy (0.4 to 0.31). Considering the relative dwell time of the two accelerators this would seem to be an optimum condition.

Emittance growth in the MEB from beam gas multiple scattering goes like $d\epsilon \propto \frac{Pt}{\gamma}$, where P is pressure ($5 \times 10^{-8}$nominal) and t is dwell time.

For the nominal design (12 Gev/c, 5×10^{-8}torr, 1/2 sec injection time) this gives $\Delta\epsilon = 0.077$ mm-mr or 7 % of the emittance growth budget for the MEB of 0.1 mm-mr. This is well within a possible allotment of 0.02 mm-mmr for this contribution. Injection energy is not a serious limitation here. However a decrease in LEB cycletime to say 1 Hz would require careful investigation of the

MEB achievable vacuum. The criteria to use would be beam pipe bake before magnet assembly but without insituo bake. Experience would indicate factors of at least 2 below $5x10^{-8}$ may be achievable. Larger factors have been reported serious investigation would be necessary before changing the nominal pressure to be a lower value. .

The choices of LEB energy, cycle rate, transition gamma, lattice and resulting circumference have been made largely on the basis of experience. The allowance for an LEB injection energy increase is a fundamental part of this choice. A smaller circumference 10 Gev LEB is potentially as satisfactory a choice, and may need to be revisited if significant circumference redution could be realized (ie $\sim$ 475m)

5 Medium Energy Booster

5.1 Choice of Peak Momentum

During the site specific design development, the choice of 200 Gev/c for the MEB was somewhat arbitary and was based on the need to raise the injection energy into the now 2Tev HEB and on the requirements of the test beams for highest possible lepton energies. The 200 Gev/c MEB was part of the June 1990 cost estimate.

Since the review, analysis of the HEB injection aperture has undergone optimigation studies. One solution purosed was to further increase the MEB peak momentum. Two approaches to higher momentum in the MEB are herein addressed. The first is to increase the circumference. This solution in technically sound. The only anticipated implication on machine performance is that of space charge tune shift at injection. This issue will be discussed later with respect to the arguments of the choice of injection parameters. The increased cost of the MEB is expected to scale with the increase in circumference, and therefore with the final momentum. Thus the machine would cost:

$$36cu \times (P/200)$$

where P is the choice of top momentum. It is to be noted that considerable work has been done in siting the injector machines, and civil construction design work is proceeding on the linac. Therefore, the position has been taken that a change to the circumference of the MEB is not an option.

The second approach to higher momentum in the MEB is to increase the strength of all magnetic elements. In addressing this idea, it should first be noted that there is no excess room in the MEB lattice to make devices stronger by increasing their length. The MEB at a peak momentum of 200 GeV/c and

a circumference of 3960 meters is tight for free space. All the drift spaces have been made as short as possible. The space for high momentum extraction is 25 meters. A shorter straight region would complicate extraction. Furthermore, three high momentum extraction locations are needed, and to retain symmetry the ring has six. Space has been retained in the lattice for the possible inclusion of γ_t jump quadrupoles, and the necessary inclusion of slow extraction devices.

The only other way to increase the strength of the elements is to increase their magnetic strength. Clearly this cannot be done without limit. The magnetic strength of the main dipoles is 1.75 T and that of the quadrupoles is 23.8 T/m at 200 GeV; the strength scales directly with momentum.

The chromaticity sextupoles, which are already strong devices, will also have to become somewhat stronger. It is not possible to quantify the increase since it is dependent on the saturation characteristics of the dipole, and at present this information is not known. If the quadrupoles are made appreciably stronger, they will require more iron and a larger profile than presently specified. This will introduce a complexity into the extraction system since the departing beamline will first have to avoid a quadrupole.

5.2 Choice of Injection Momentum

The present choice for the injection momentum is 12 GeV/c. Any motivation for a change to this parameter is from the LEB, in an attempt to alleviate problems there. Arguments in behalf of the MEB to retain the 12 GeV/c parameter must address technical issues associated with the ability of the MEB to meet its design requirements. Specifically, this choice is not too dependent on cost issues, but really rests on technical arguments. Clearly, from an MEB point of view, higher injection momentum are better. Therefore each issue must be questioned based on what risks are incurred by lowering the injection momentum below 12 GeV/c. The following are the issues.

5.2.1 Emittance growth due to beam gas scattering

The model for emittance growth is: [8,9]

$$< d\epsilon/dt > /\pi = constant \quad \times \quad vacuum \;\; pressure/\gamma.$$

For the MEB at 12 GeV/c, and at the design vacuum pressure of 5×10^{-8} torr, this is

$$< d\epsilon/dt > /\pi = .0143 \;\; mm - mrad/sec.$$

The MEB dwell time for the first LEB batch is about .5 sec., so that it will experience growth of 0.0072 mm-mrad. This is 7% of the MEB emittance growth budget, and is not considered a problem. A reduction in the MEB injection momentum to 10 GeV/c would increase this to 9%. This also is not a problem.

Note however that a reduction of the LEB cycle time by a factor of 10 (as has been suggested) would have an impact, and lead to a more stringent vacuum requirement in the MEB.

5.2.2 Transverse emittance growth due to space charge tune shift

It is a straight forward calculation to derive the space charge tune shift. It is more difficult to determine the subsequent emittance growth. With the standard collider parameters, the calculated space charge tune shift at injection is 0.077. This is consistent with what has been achieved in other machines in the momentum range of the MEB. Simulation deriving emittance growth from space charge tune shift are still focusing on the LEB problem. Results for the MEB are anticipated during the summer of 1991. Simply lowering the injection momentum to 10 GeV/c, while leaving other parameters the same, would increase the space charge tune shift parameter to .11. Of all the arguments supporting the 12 GeV/c injection momentum, this is the strongest. However, as pointed out above, the real problem, emittance growth cannot be strongly tied to the tune shift parameter, so no claim can be made, as of yet, as to what injection momentum is acceptable, and what is not.

5.2.3 Dynamic Aperture

The dynamic aperture varies as a function of injection momentum through two mechanisms. Firstly, the beam size goes as the inverse of the square root of gamma. Secondly, the field quality deteriorates as the injection momentum goes down. The present design of the MEB anticipates a good dynamic aperture at 12 GeV/c. While no explicit MEB tracking has yet been done, tracking studies performed on the Fermilab Main Injector indicate a dynamic aperture of about 17.5 mm. (these tracking studies were done independent of beam momentum, that is, the inverse square root of momentum was not yet applied to these results, and the field level at injection to the MI is the same as the field level of the MEB at injection although the momenta are different.) This corresponds to 10 sigma for collider operation and 4 sigma for test beam operation. If the injection momentum of the MEB was to be lowered to 10 GeV/c, the sigma numbers would become 9 and 3.6 respectively, just from beam size considerations. The question of magnetic field quality, and its impact, is harder to assess. Field nonlinearity, arising from remanent effects is not easy to calculate. Limits on multipoles can be specified so that the sigma parameters are essentially uneffected over the injection momenta range of 10 GeV/c to 12 GeV/c. However the results will ultimately depend on the quality of the steel that is obtained. These specs are being written very carefully. The argument then, is that the steel will be good enough so that it won't matter to the field quality what the injection momentum is if it is in the range of 10 GeV/c to 12 GeV/c is used. However, in the absence

of specific numbers, the higher field is preferable.

The conclusions with respect to the injection momentum is that 12 GeV/c is preferred by the MEB. All of the arguments are soft, the strongest being that related to space charge. The MEB specs will be written in such a way that operation at 10 GeV/c is possible if needed as a fall back by LEB limitations.

5.3 Transition Crossing

The arguments for choosing a lattice which crosses transition have been given before, and basically involve complexity, an increase in needed circumference, and cost. Furthermore, at the time decisions were being made, a proposal for crossing transition, using a scheme in which the non-wanted longitudinal focusing forces are removed, was suggested. It is this scheme that we are planning on using. Simulations are being done here, and at Fermilab. Again, the main concern for the MEB is that the tight bunching, which normally occurs as transition is encountered, will produce transverse emittance growth. The varying factor in the space charge tune shift equation (the ratio of bunching factor to $1/\gamma^*2$) is seen in the simulations to be the same at the onset of the non-focusing scheme as it is at injection, and it decreases after that. This scheme continues to receive study. It is noted that there are engineering complexities in the rf system associated with the amplitude and phase control of additional cavities operating at harmonic frequencies. As a contingency, space has been reserved in the lattice, at locations of focusing quadrupoles, for γ_t jump quadrupoles.

6 Low Energy Booster

6.1 Introduction

The Low Energy Booster **(LEB)** is to be the first synchrotron in the injection system. The general design specifications for the **LEB** are given in Table 10 and 11. Detail information is provided in [11,12,13,14,15]

The basic lattice design constraints were a small circumference to minimize space charge effects, adequate azimuthal space for the required hardware, and sufficiently large γ_t to avoid crossing transition and to provide an adequate slip factor at extraction to support cogging procedures.

Several alternative lattices were explored in light of these specifications and those given in Table 10. A more detailed discussion of the design philosophy and concepts involved in these considerations and tracking evaluations are given in [13,14]. The basic lattice parameters are given in Table 11.

Table 10: **LEB** Design Parameters

Parameter	Value
Injection Momentum (GeV/c)	1.22
Extraction Momentum (GeV/c)	12.0
Repetition Rate (Hz)	10
Circumference (m)	570
Harmonic Number	114
ϵ^*_{rms} (π mm-mrad)	0.6
Particles/bunch	1×10^{10}

Table 11: **LEB** Lattice Parameters

Parameter	Nominal Value	Range
ν_x	11.65	10.85 - 11.85
ν_y	11.60	10.8 - 11.8
χ_x (natural/corrected)	-15.7/0	-14.0 - -16.5/0
χ_y (natural/corrected)	-17.7/0	-15.0 - -18.5/0
γ_t	22.1	24.4 - 21.9

Although the beam intensity requirement for the **LEB** is relatively modest compared to existing machines, the required small beam emittance results in a significant tune depression. In terms of the Laslett tune shift, the tune depression is $\approx$0.6 at an injection momentum of 1.22 GeV/c. Therefore, the effects of space charge are considered a major constraint with respect to the beam dynamics. Certainly a smaller space charge induced tune shift is preferable. However, the maximum allowable tune shift is not a well defined number. Experimental results of existing machines indicate that a tune shift of even more than 0.5 may be acceptable. Machine parameters such as resonance strengths, superperiodicity, or operating transverse and synchrotron tunes all have a bearing on the resultant acceptable tune depression.

To explore the relevant parameter space, a code continues to be developed which employs multi-particle tracking with the transverse dynamics of the thin lens code TEAPOT, the space charge force introduced as kicks. Synchrotron oscillations and acceleration are included. Emittance evolution as well as the particle distribution are simulated as a function of time.[15].

6.2 Parameter Evaluations

The **LEB** basic design parameters were chosen after significant considerations as explained below. In all cases, technical performance as opposed to cost was the overriding issue commensurate with the total cost of the **LEB** being only 1/2 % of the project cost.

6.2.1 Injection Momentum

The baseline injection momentum (1.22 GeV/c) was chosen to be compatible with FNAL Booster experimental data which imply a maximum acceptable tune shift value of ≈0.6 being a threshold below which there is little emittance dilution. However, because the FNAL data would be statistically consistent with a significantly lower threshold tune shift, because the simple scaling implied by the Laslett tune shift formula may not be sufficiently valid in light of the small **LEB** emittance growth budget ($\Delta\epsilon_{total} \approx 0.2\ \pi$ mm mrad), and because higher intensities may be desirable in the future, the Linac design is compatible with an increase in the injection momentum to 1.7 GeV/c which provides (assuming Laslett scaling) a tune shift reduction to $\Delta\nu = 0.34$ for the same emittance and intensity conditions. The rf frequency range (47.5 - 59.8 MHz) necessary to support an injection momentum of 1.22 Gev/c has been accomplished at FNAL and is therefore, achievable.

6.2.2 Extraction Momentum

The extraction momentum of 12 GeV/c was chosen primarily on technical **MEB** performance issues. Based upon detailed lattice hardware evaluations, it was found that an extraction momentum of 12 GeV/c required a circumference of 570 m and that an extraction momentum of 10 GeV/c required a circumference of 540 m If a smaller circumference could be realized then 10 Gev/c would become desireable. .

In favor of a 540 m, 10 GeV/c **LEB** were a reduction in cost due to reduced integral dipole length (≈17%), and reduced RF voltage requirement (≈15%).

Against a 540 m, 10 GeV/c **LEB** with respect to the **LEB** performance was the potential increase in space charge effects (≈12%) due to a lower average ramp rate. The **MEB** would have, with the lower **LEB** extraction momentum, a potential decrease in dynamic aperture due to remnant fields, an increase in the space charge tune shift (≈45%), and an increase in emittance dilution due to multiple scattering from residual gas (≈20%). In addition, there would be a larger frequency range (≈45%) required of the **MEB** rf system.

In conclusion, it was felt that the overall system (**LEB & MEB**) performance would be enhanced with a higher design value for the **LEB** extraction momentum more than offsetting the possible slight cost savings due to the reduced rf and dipole requirements. This solution also provides a technical contingency.

6.2.3 Lattice Design

The choice of lattice designs revolved primarily around the issue of γ_t. The value of γ_t was chosen to avoid crossing transition, i.e., $\gamma_t \geq 12.8$. In a fast cycling machine (10 Hz), where the transverse emittance (at intensity) is the single most important parameter, the penalty of crossing transition was felt to be unnecessary since it could be avoided by appropriate choice of lattice. Although schemes exist, in principle, to mitigate the bunch compression at transition; to assume that they could adequately be implemented in a fast cycling machine represents a significant technical risk. In lieu of these schemes, emittance dilution of some magnitude is unavoidable.

A further criterion with respect to γ_t was to have an adequate value of the slip factor [define] at extraction to support possible **LEB** to **MEB** cogging scenarios. Based upon these analyses a $\gamma_t \geq$20 was found to be desirable. A standard FODO lattice results in a value of $\gamma_t \approx \nu$. The SCDR **LEB** design utilized a high tune to achieve a value of $\gamma_t \approx$14.5 with a circumference of 540 m. To expand the SCDR concept to a value of $\gamma_t \approx$20 would have required a significant increase in circumference. (The SCDR design could not have been constructed within a circumference of 540 m because of insufficient free space allocation).

However by creating an oscillation around the ring of the dispersion function, the the value of γ_t is increased significantly above the tune. Two such designs were evaluated and found to have adequate dynamic aperture and acceptable sensitivity with respect to perturbations (mispowering, multipoles, and misalignment).

Therefore, since a lattice design exists which provides the appropriate values of γ_t and circumference, and has adequate dynamic aperture and acceptable error sensity, it has been adopted as the reference design.

6.2.4 Ramp Rate

Several possible acceleration ramp profiles were explored. These included both resonant and linear systems. The resonant power system cost increased as the frequency decreased with the inverse true of the linear system. The cost maximum of both was at $\approx$5 Hz. The required rf, and therefore the cost, scale with frequency.

Because the effects of space charge are likely to be exacerbated by a slower cycle rate, because the emittance dilution due to gas scattering in the **MEB** would be increased (or require an improved and more costly vacuum system) with slower cycle rate, and because it is always possible to run a machine at a slower rate than the design value, the 10 Hz resonant cycle was chosen.

In order to provide improved diagnostic capability for commissioning, and to have the option of a linear ramp, the circuit chosen allows, at the expense of several hours of labor, the ability to run the **LEB** with a linear ramp. The

initial power supplies required for the 10 Hz system are compatible with a 0.3 Hz linear ramp. Implementation of additional power supplies allows the possibility of higher linear ramp rates.

The magnets were specified compatible with the 10 Hz ramp rate. This resulted in a peak field value of 1.3 T for the dipoles and a maximum gradient of 14.9 T/m for the quadrupoles. The dipoles and quadrupoles will be in a single resonant circuit. The laminations of the dipole and quadrupole have been carefully designed to ensure that there is good tracking between them during the ramp, and trim quadrupoles have been specified to provide a full integer tune variation, to correct for tracking errors, and to reduce the half-integer resonance stop band.

7 Linac

The linac injector for the LEB provides a 600 MeV, 25 mA H^- beam at a 10 Hz pulse rate with normalized rms transverse emittances $< 0.4\pi$ mm-mrad in both planes. The pulse length is $\sim 8\mu$sec for three-turn injection of $\sim 10^{12}$ protons into the LEB in Collider-fill mode, and $\sim 35\mu$sec for 16-turn injection of 5×10^{12} protons in test-beam mode. The design of the linac is conventional, beginning with a 35 kV ion source and LEBT, followed by an RFQ in which the energy is increased to 2.5 MeV. The 2.2 m long RFQ operates at 427.6 MHz, and has peak surface fields of 36 MV/m, which corresponds to 1.8 times the Kilpatrick "limit." Improved performance is achieved by increasing the vane voltage slightly as the particle energy is increased.

The RFQ is followed by a drift-tube linac, also operating at 427.6 MHz, which increases the proton energy to 70 MeV. Higher output energies were considered, but the desire to minimize costs provided an incentive to switch to the less expensive coupled-cavity structure as early as possible. Peak surface fields in the DTL are held to 28 MV/m, or 1.4 times the Kilpatrick limit. The reduction in field, relative to the RFQ, is held to be necessary in view of the 24 m length of the DTL, so that the relative probability of sparking is nearly equal in the two devices. The 4-tank DTL will use permanent magnet quadrupoles in a FODO array, and post stabilizers. Each tank will have its own 4 MW klystron.

A side-coupled linac, operating at 1282.2 MHz, the third harmonic of the RFQ/DTL frequency, complete the acceleration to 600 MeV. This portion consists of 60 coupled-cavity sections, each with 20 or 22 accelerating cavities, connected into 10 modules of 6 sections each. The sections in each module are connected with bridge couplers, and each module is powered by a 20 MW klystron. The CCL portion of the linac is 111.6 m long, and the peak surface field of 32 MV/m is equal to the Kilpatrick limit at this frequency to ensure reliable spark-free operation of this long system.

The linac operating frequencies were chosen to be the 9-*th* harmonic of the

LEB rf injection frequency. Thus, the option for bunch-to-bucket filling, or "painting" is preserved, even though initial operation scenarios assume the use of adiabatic capture. No sufficiently persuasive case has been made to date that painting schemes can contribute to reduced space-charge tune spread in the LEB, without leading to unacceptably large transverse emittances. In addition, adiabatic capture is a process which is well established and understood.

The LEB design is still troubled with the effects of space charge at injection. In anticipation of this, space has been reserved in the linac building designs for an upgrade of the energy to 1000 MeV, simply by installing additional CCL modules. Thus, the decision to upgrade the linac energy and improve operation of the LEB can be taken at any time. The additional costs associated with this upgrade are estimated to be $\sim$ \$15 M.

8 Summary and Conclusions

Major parameters of the SSC injection chain have been finalized through minor adjustments can still be encorporated if sufficiently justified. An attempt has been made in this paper to describe the complicated interplay of parameters and the various trade-off considerations that enter into parameter choices of the SSC. Particular focus has been given to the series of accelerators through injection to the Collider. In some areas, such as LEB energy, technical uncertainties drive the choice of parameters. Other areas lend themselves in principal to cost optimization. Realistically, however, in a project such optimization often cannot be carried out as parameters which have already been frozen should not be reopened if progress is to be made. A study such as this can support the position that choices already made are rational, but is unlikely to lead to fundamental change unless specific single changes can take place at some cost penality.

9 Acknowledgements

In assembling this material, we are playing the roles of *rapporteurs*; the generation of text has been done by others (who may also be playing the same role, of course). For this paper, our principal sources of words have been Helen Edwards and Bob Palmer of the Project Management Office, and our associates Alex Chao, Warren Funk, Rod Gerig, Dave Johnson, Ken Kauffmann, and Richard York.

References

[1] "Conceptual Design of the Superconducting Super Collider," ed. J. D. Jackson, SSC Report SSC-SR-2020, Berkeley, March 1986.

[2] R. Gerig, et al, "Simulations of the Fermilab Main Ring," Proc. of 1987 IEEE PAC, No. 87CH2387-9, March, 1987.

[3] R. Gerig, et al., "Improvements to the Fermilab Main Ring," European Accelerator Conference, Rome, 1988.

[4] D. Edwards and M. Syphers, "Selection of Basic Parameters for the Collider Rings," SSC Report SSCL-297, Dallas, June 1990.

[5] T. Garavaglia, K. Kauffman, and R. Stiening, SSCL-265, SSCLN-739.

[6] D. Ritson, SSCL-305.

[7] R. Palmer, K. Kauffman, private communication.

[8] R. Gerig, "Main Ring Dynamic Aperture Studies," FNAL internal report EXP—164, January, 1989.

[9] M. Syphers, "Beam-Gas Scattering Lifetimes in the Fermilab Main Ring," FN-484, Fermilab, 1988.

[10] R.C. York, *et al.* "The Superconducting Super Collider Low Energy Booster: A Status Report ", Proceedings IEEE PAC - 1991

[11] N.K. Mahale, *et al.* "Debunching and Capture Effects in the SSC Low Energy Booster", Proceedings IEEE PAC - 1991

[12] N.K. Mahale, *et al.* "Longitudinal Matching between LEB and MEB for the SSC", Proceedings IEEE PAC - 1991

[13] E.D. Courant *et al.* "Low Momentum Compaction Lattice Study for the SSC Low Energy Booster", Proceedings IEEE PAC - 1991

[14] F. Pilat, *et al.* "Dynamic Aperture and Performance of the SSC Low Energy Booster Lattice ", Proceedings IEEE PAC - 1991.

[15] S. Machida, *et al.* "Space Charge Effects in the SSC Low Energy Booster", Proceedings IEEE PAC - 1991.

Computing

K. Rich

SSCL COMPUTING ENVIRONMENT

General Laboratory Computing

Specific Project Computing

Specific Physics Computing

SSCL KR/GL 10/14/91

GENERAL LABORATORY COMPUTING

People doing business applications

Word processing, spreadsheets, graphics, E-Mail, etc...

SSCL KR/GL 10/14/91

SPECIFIC PROJECT COMPUTING

Construction of the collider complex

Simulation/controls, CAD/CAE. etc...

Operation of the collider complex

SSCL KR/GL 10/14/91

SPECIFIC PHYSICS COMPUTING

Construction of detectors by collaborations

Simulation/controls, CAD/CAE, etc...

Operation of detectors by collaborations

SSCL KR/GL 10/14/91

OPERATION OF DETECTORS BY COLLABORATIONS

Online Data Acquisition	Offline Data Analysis
5,000	20,000 GB per day per detector
50,000	200,000 MIPs per detector
15,000	60,000 MFLOPs per detector

SSCL KR/GL 10/14/91

THE CHALLENGES FOR THE COMPUTING DIVISION

The data is huge and the data rates are fast

The amount of compute power is staggering

Some of the above numbers are probably low

SSCL KR/GL 10/14/91

THE IMPLICATIONS FOR SSCL PHYSICS COMPUTING

Performance ⇒
RISC ⇒
Unix ⇒
Commitment ⇒
Work

SSCL KR/GL 10/14/91

SSCL UNIX COMPUTING

Distributed Administration
NFS -> AFS
YP -> Kerberos
Telnet -> Xwindows
News!
Mail!
Native Unix Tools
- Make
- RCS, etc.
- GNU
- etc.

SSCL KR/GL 10/14/91

AFS (why)

Performance (caching)
Security (world-wide)
Uniform Naming

SSCL KR/GL 10/14/91

Conventional Construction

J. Ives

Conventional Construction Presentation
Jon R. Ives Associate Director, SSCL

Captions for Slides used during Presentation

1. Title Slide

2. Locations map for Super Collider Ring in Ellis County

3. West Complex, showing N-15 Service Area, Injector Complex, two Interaction Regions (IR1 and IR4), and Campus Facilities

4. Artist's rendering of layout of N-15 service area, site of initial major construction activity

5. Aerial photo of N-15 site, showing intense construction activity

6. Magnet Development Laboratory, a 100,000 square foot building for magnet R&D and production of over 100 SSCL specialized, low-volume magnets. Facility completed and turned over to SSCL mid-October 1991.

7. Inside shot of Magnet Development Laboratory high bay area where magnets will be built

8. Inside shot of Magnet Development Laboratory Machine Shop, turned over to SSCL mid-May 1991. Production equipment installed and in operation.

9. Accelerator System String Test Facility. Note curve in 200 meter long string test facility to emulate the collider tunnel geometry.

10. Inside shot of string test facility, showing installed HVAC distribution ducts and sprinkler system for fire protection. Building turned over to SSCL on October 14th.

11. Photo taken in July 91 showing extensive sub-slab conduits installed for signal cables used to control cryogenic compressors for N-15.

12. Photo showing current status of construction of the N-15 cryogenic compressor building. Note long grey areas -- these are grates covering large pipe trenches below, which will enable a very "clean" cryogenic installation with all piping below the operating floor

13. Photo from earlier in the summer showing construction of concrete formwork for the 27-foot deep cold boxes in the N-15 refrigerator/service building.

14. Current photo of construction status of the refrigerator/service building. Note the three cold box locations in the floor for Accelerator System String Test, Magnet Test Lab, and the N-15 collider cryogenic service.

15. Drill rig for exploratory shaft at the site of Interaction Region Four. Shaft to be drilled primarily to obtain key geotechnical data to be used for design of IR underground halls and collider tunnel, but will also be a useful piece of construction incorporated into the IR hall design.

16. Another photo of drill rig and supporting mobile crane. This specialized rig was created by a small business contractor, A. H. Beck, by modifying an oil-drilling rig. Note American flag at top of rig.

17. Diagram illustrating sequence of operations and current progress. Initial step is drilling a 28" pilot hole, currently developed to a depth of 201 feet. Excellent vertical control -- only 1/4" off vertical. Second step is to ream out the pilot hole with an 8-foot diameter augur. The 8-foot hole is down to 160' depth. The hole is then enlarged to the full diameter of 16.5 feet, using cutting bit and scraper extension arms on the 8-foot diameter bucket. The 16.5-foot diameter hole is currently at a depth of 98 feet. In the final step, reinforcing and shotcrete are applied to the sidewalls of the shaft. When fully developed, the shaft will go to a depth of 265 feet, well into the Eagle Ford Shale which underlies the Austin Chalk. A horizontal adit will be developed at the intersection of the Austin Chalk with the Eagle Ford Shale. Extensive tests and instrumentation will be installed to better define the geomechanical properties of the Eagle Ford Shale for use in design, particularly for the foundations of the experimental halls.

18..Shot of top of shaft, showing steel formwork for concrete collar surrounding the shaft. The orange object is the man cage used to lower workers for application of the shotcrete to the shaft sidewalls.

19. The augur used for reaming the pilot hole to a diameter of eight feet. Note 27-inch diamter kelly bar which applies the enormous downward pressure and rotational torque necessary for cutting the rock.

20. The eight-foot diameter bucket used for removing spoil generated by enlarging the hole from eight to 16.5 feet.

21. Fitting the bucket with extension arms to cut the 16.5-foot diameter. The bucket is fitted with alternating cutting arms and scraper arms to both loosen the material and sweep it into the bucket for removal.

22. Fitting the bucket with its scraper arms to sweep the loosened material into the bucket.

23. Preview of "coming attractions" in construction. The items with green dots are all actively under design.

24.. Some of the current challenges we're working on:

Timely definition of the requirements for conventional construction is a constant challenge. To maintain schedule, the conventional facilities have to be "first out of the chute," which means that we need to extract facilities requirements from the users while their own designs for accelerator or detector components are still on-going. Makes for interesting "dynamics. . . ."

The geology also presents a bit of a challenge. About half the collider tunnel is in Austin Chalk, an excellent tunneling medium. The rest of it, however, is in Eagle Ford Shale (on the west) or Taylor Marl (on the east) which are much weaker and less stable. The foundations of the experimental halls on the west present a particular challenge. To minimize our involvement with Eagle Ford Shale, we are looking into some final adjustment of the ring elevation which appears to have promise for reducing both cost and risk in experimental hall and collider construction.

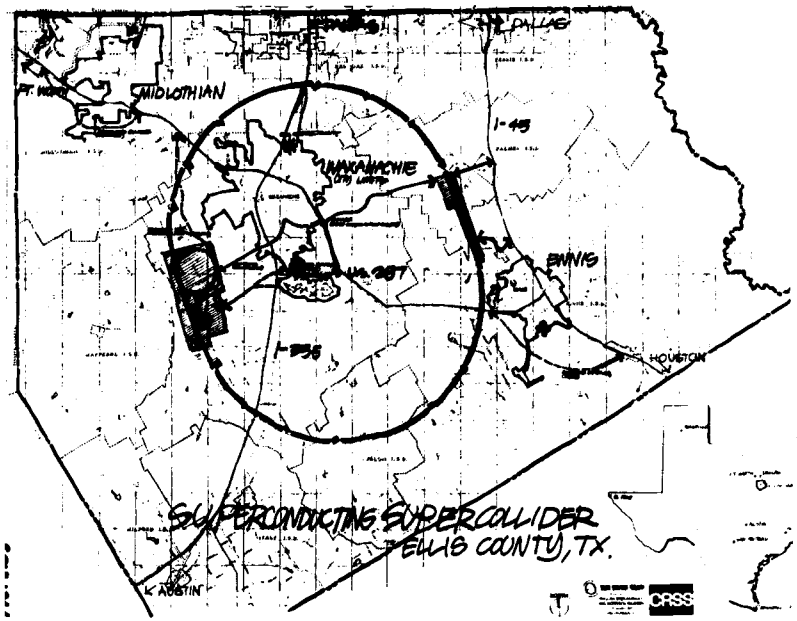
Infrastructure is also a bit of a challenge, making sure that utilities and roads are developed in a timely manner to support the schedules for the principal facilities

25.. Closing. I hope I have been able to convey, especially through these construction progress photos, that we have made the transition from "paper project" to a <u>real</u> one. When you come visit us you'll definitely need your hardhat!

Conventional Construction

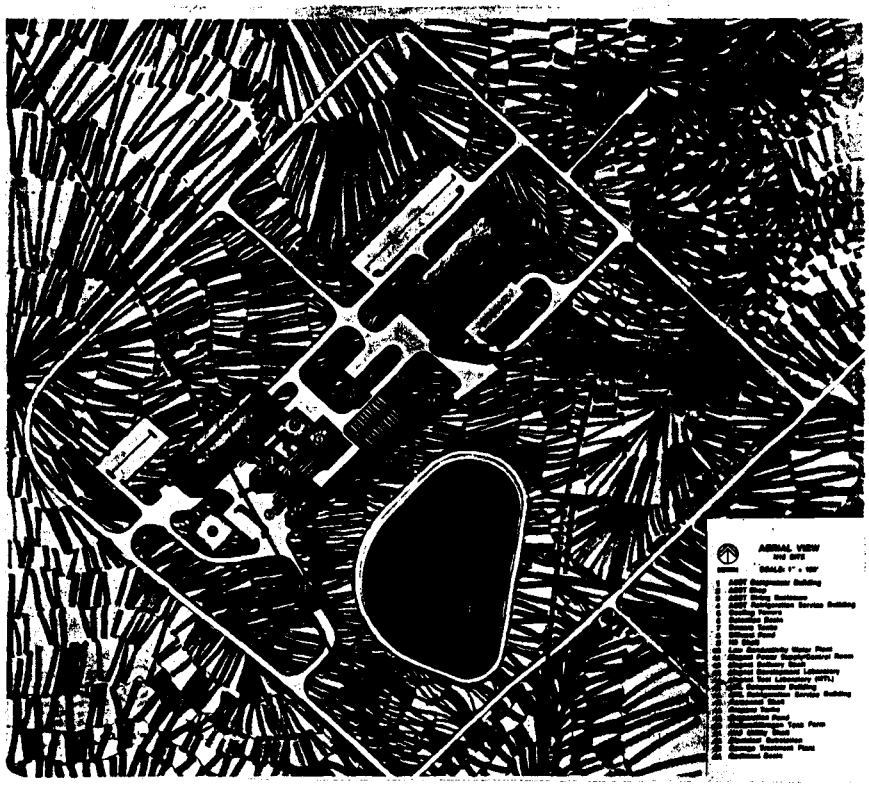
Status

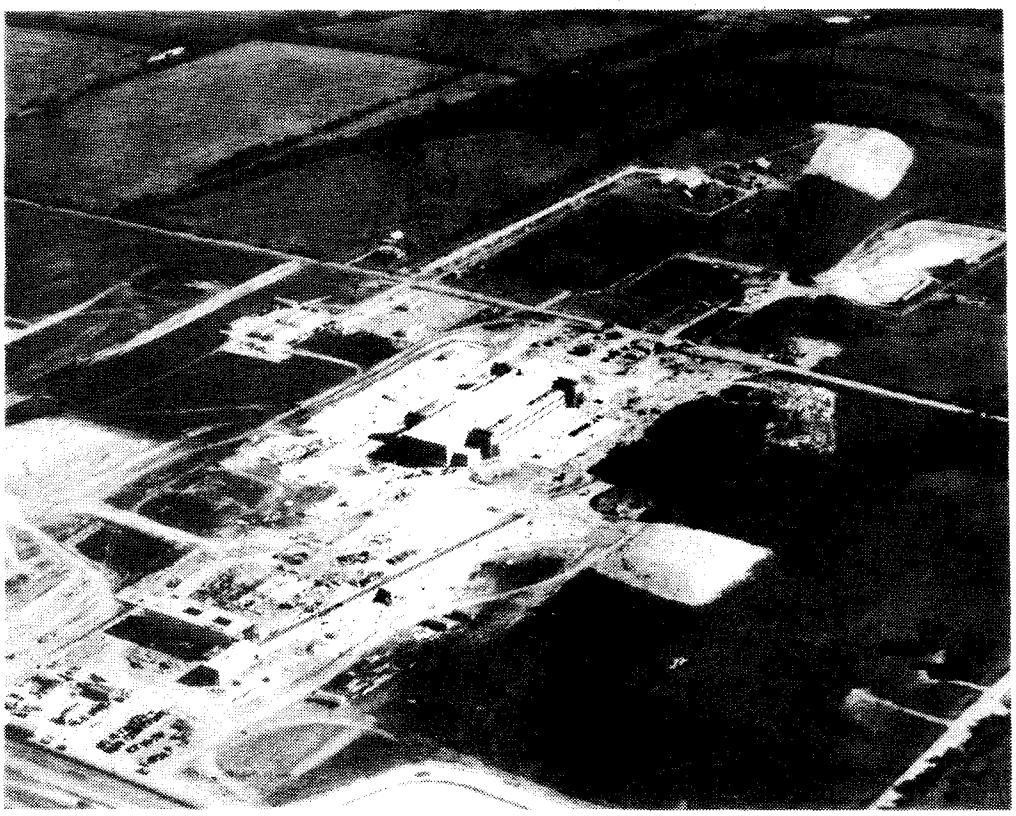
Challenges



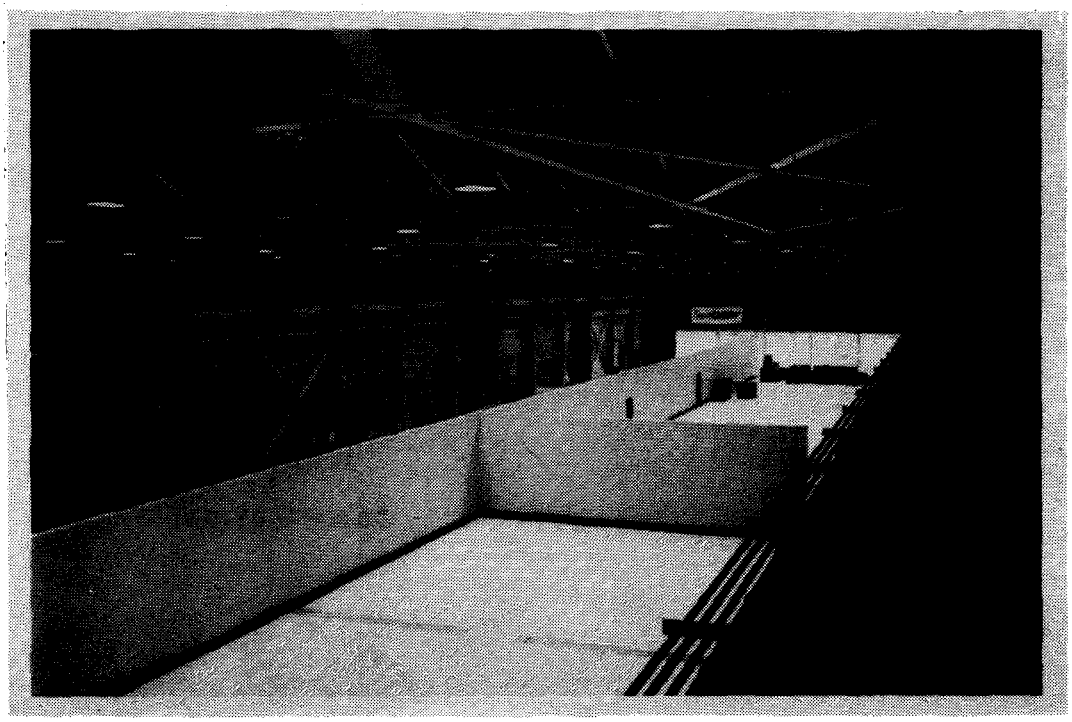
Jon Ives
Oct 14, '91

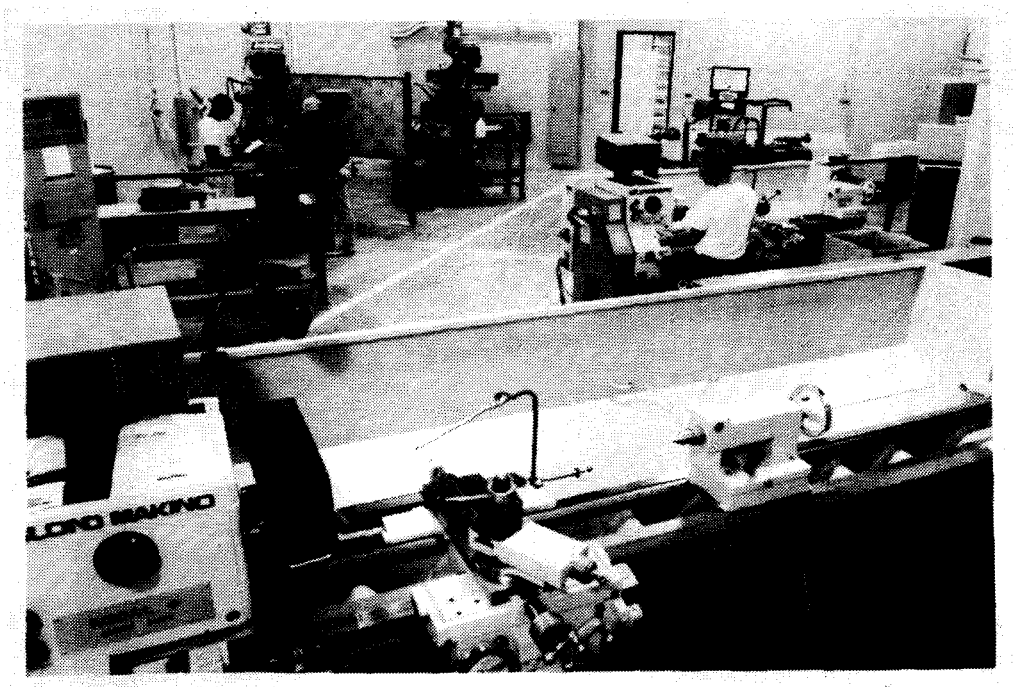

WEST COMPLEX LONG RANGE
ILLUSTRATIVE MASTER PLAN
SUPERCONDUCTING SUPER COLLIDER
CRSS







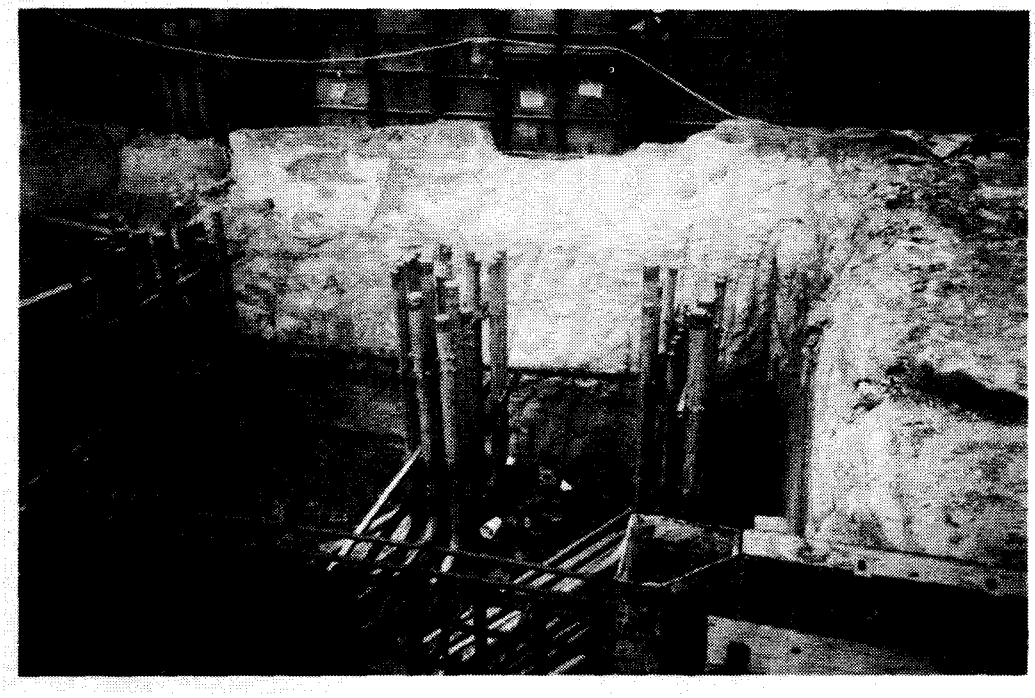




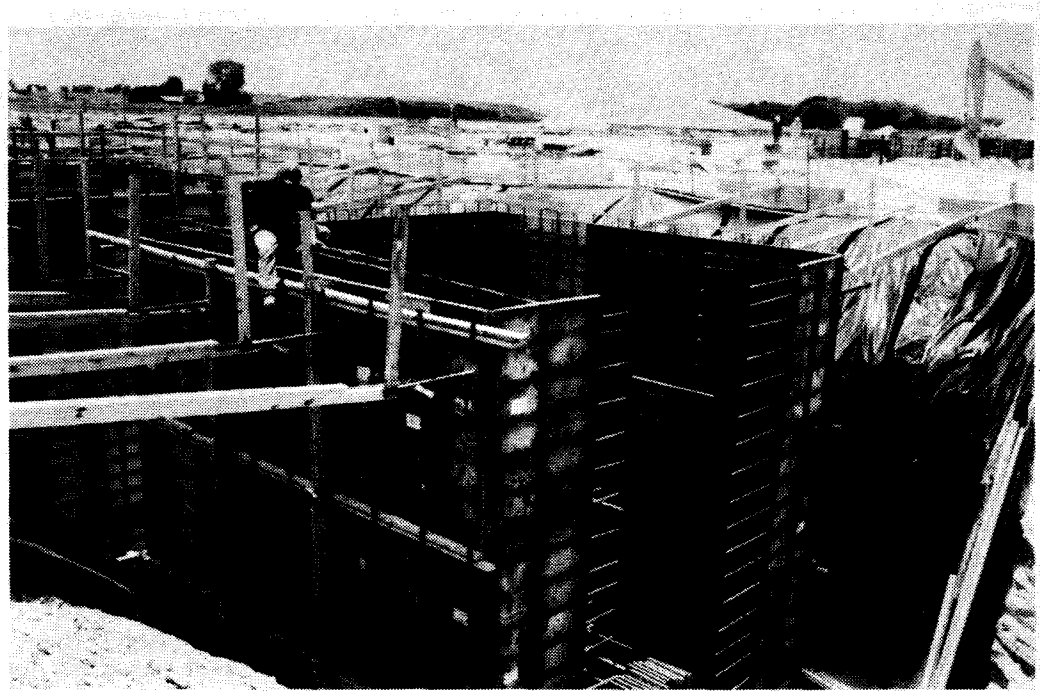
Magnet Development Laboratory
Machine Shop
October 1991

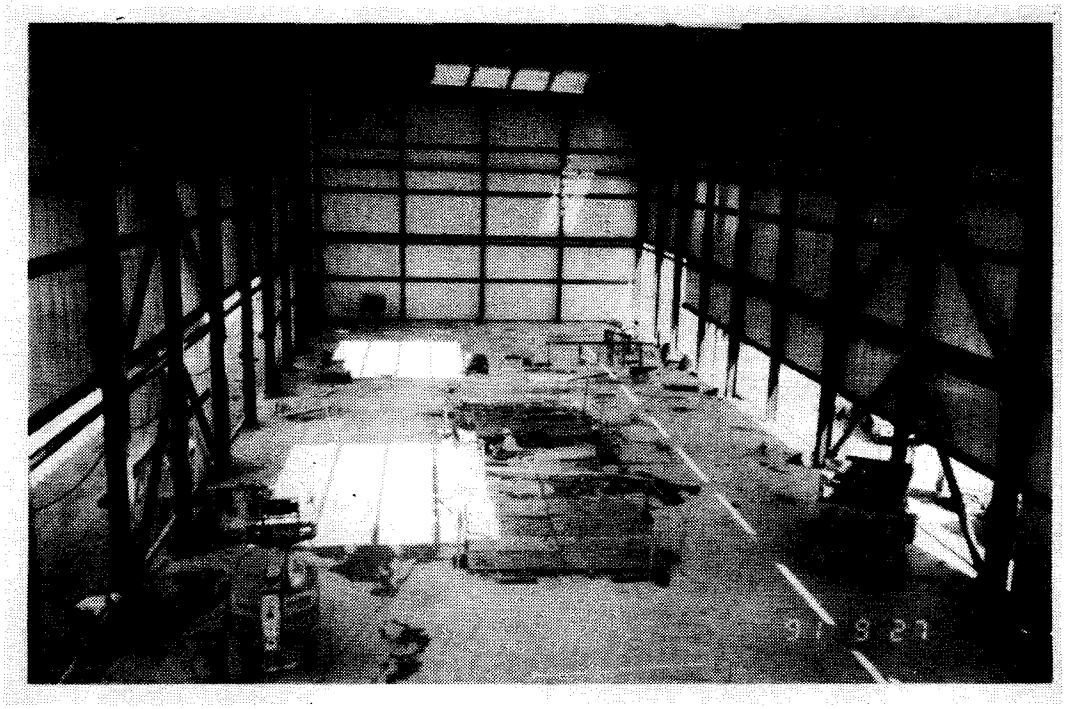


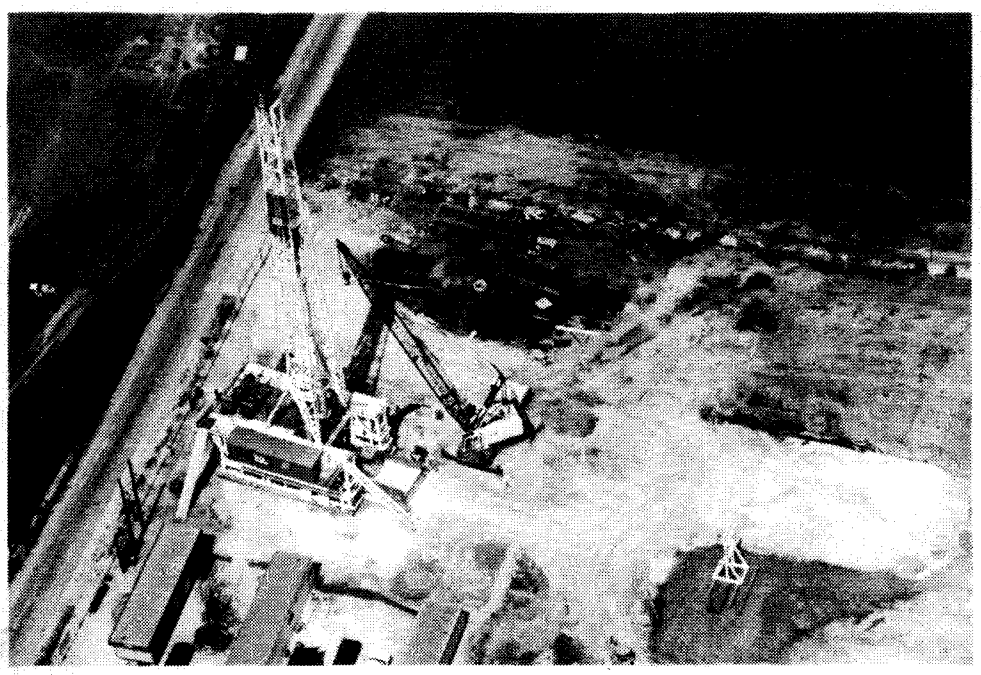




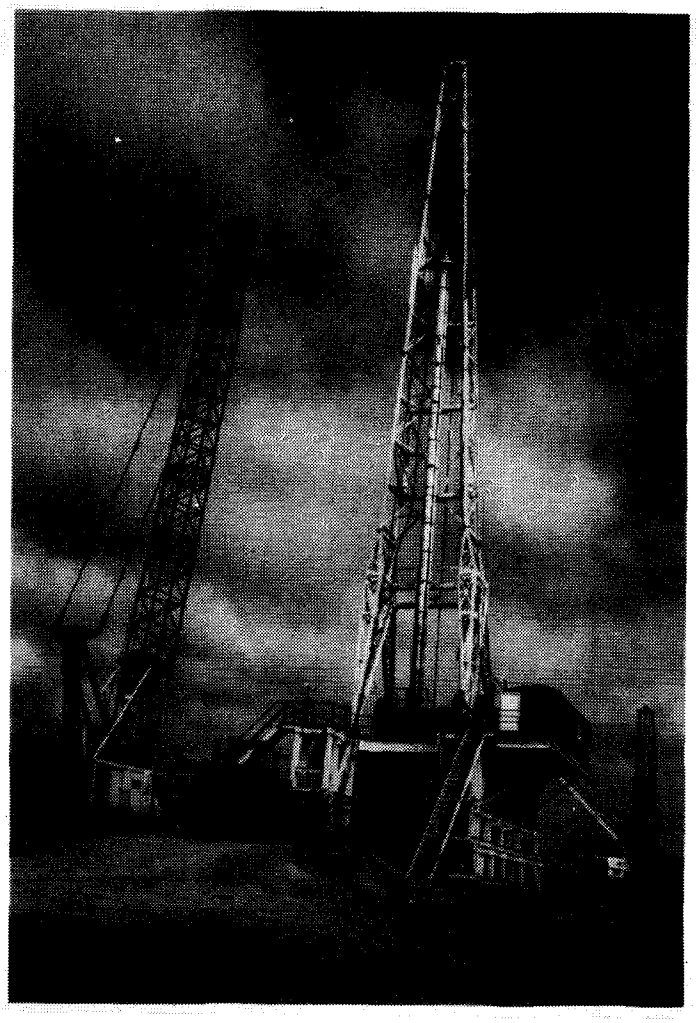


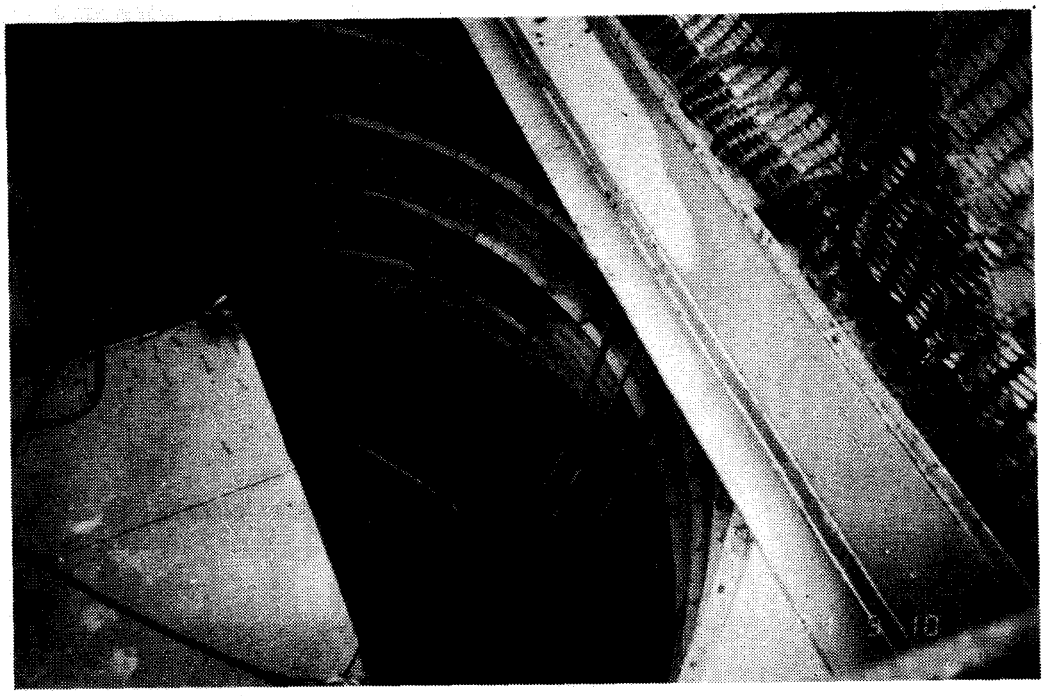


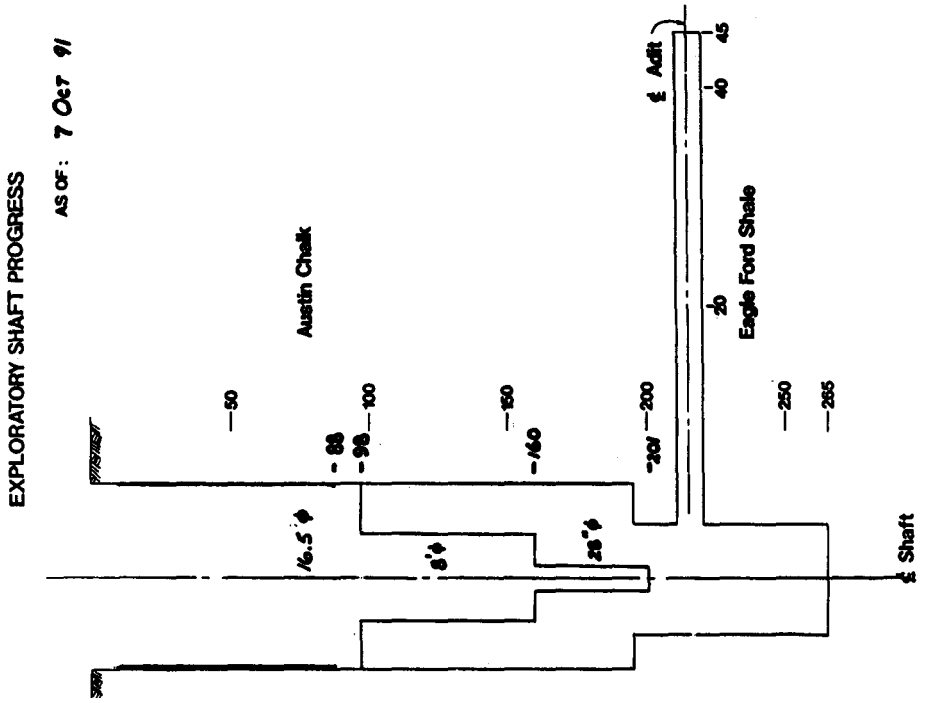


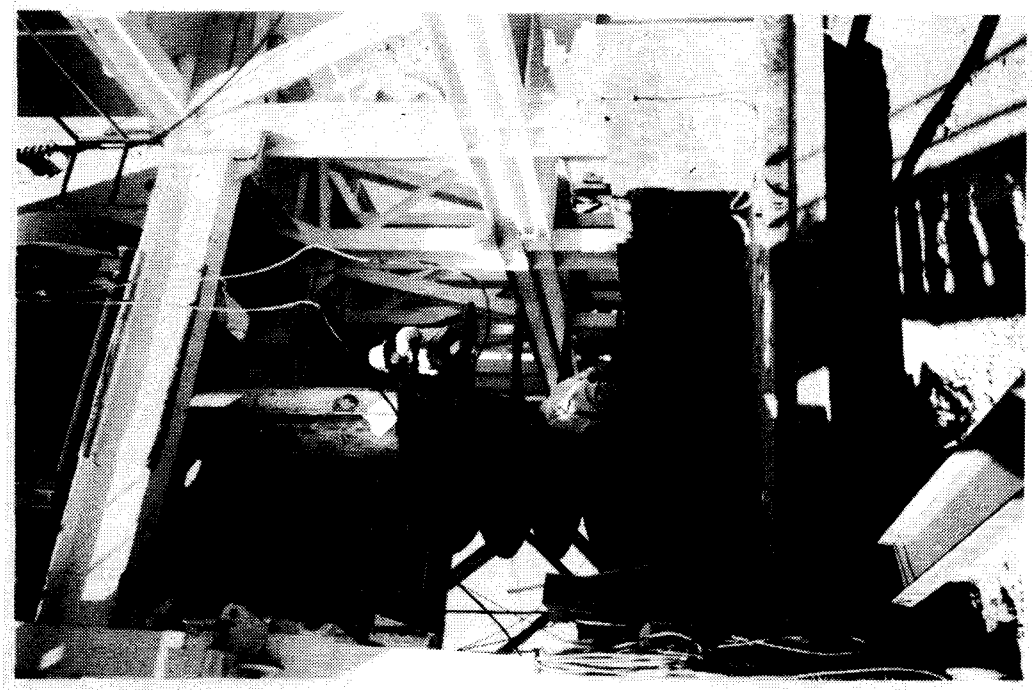


Exploratory Shaft Site
Drilling Operations
October 1991

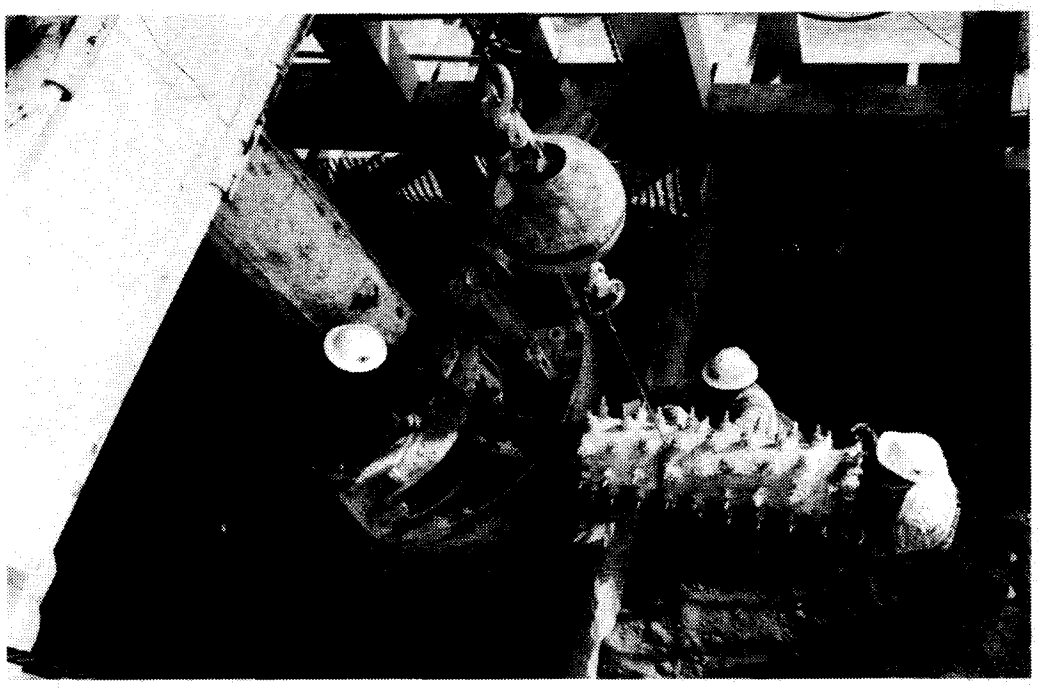


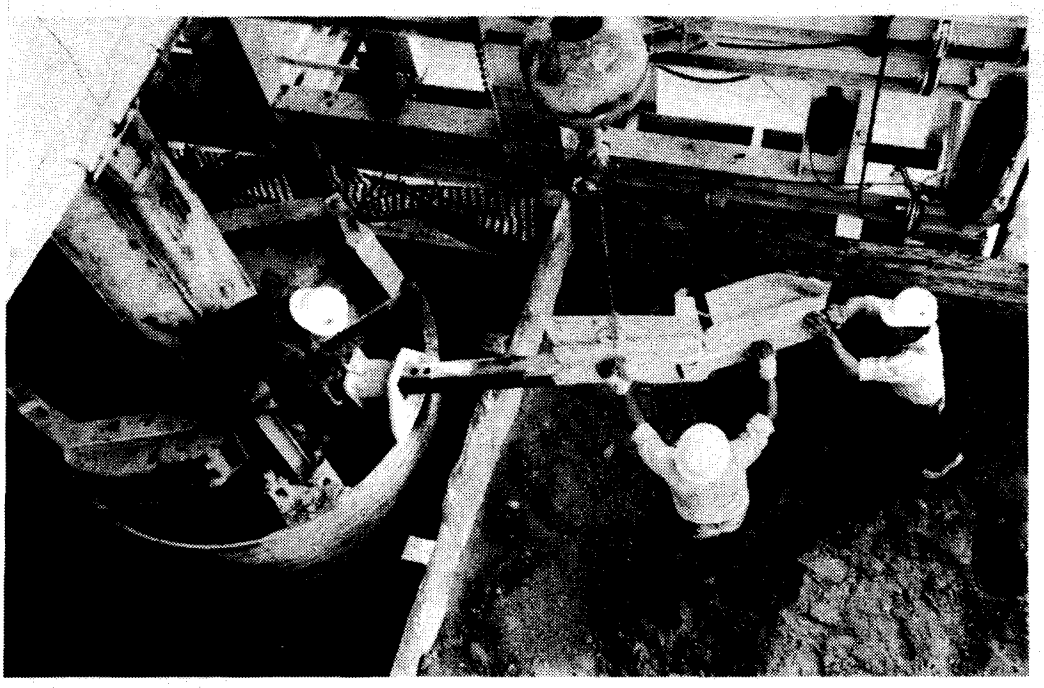


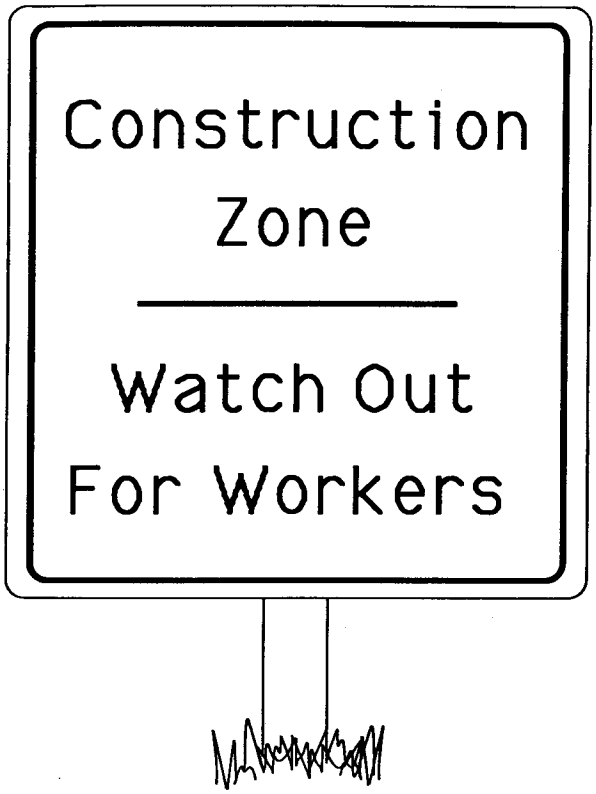

EXPLORATORY SHAFT PROGRESS
AS OF: 7 Oct 91
Austin Chalk
Eagle Ford Shale
℄ Adit
℄ Shaft
50
88
98
100
150
160
200
207
250
255
45
40
20
16.5 ϕ
8 ϕ
25 ϕ










Construction
Zone
Watch Out
For Workers

SSC Physics Signatures

F. Paige

SSC PHYSICS SIGNATURES

Frank E. Paige

Physics Department
Brookhaven National Laboratory
Upton, NY 11973
and

Physics Research Division*
Superconducting Super Collider Laboratory
2550 Beckleymeade Avenue
Dallas, TX 75237

ABSTRACT

The main goals of the SSC physics program are to discover the origins of electroweak symmetry breaking and of quark and lepton masses, and more generally to search for any particles at the TeV mass scale. Signatures for this physics are reviewed.

1. Introduction

The main goals of SSC physics program are to discover the origin of electroweak symmetry breaking, to discover the origin of quark and lepton masses (which might or might not be the same), and to search for new particles at the TeV mass scale. These are the goals of the large detectors, the Solenoidal Detector Collaboration (SDC)[1,2] and Gammas-Electrons-Muons (GEM),[3,4] now being considered for approval. While only high-mass physics is discussed here, one should not forget that the SSC can do many other things. Expressions of Interest have been received to study B physics, using both the collider and external beams;[5,6,7] to study diffractive physics, both of the traditional low-p_T type and at moderately high p_T.[8,9] All of these are potentially interesting. One should also not forget that much of the high-mass physics discussed here might be done at the proposed Large Hadron Collider at CERN.

2. Physics Prospects

The standard model is in very good agreement with almost all existing data. For example, one can compare various determinations of $\sin^2\theta_W$:[10]

$$\begin{aligned} \sin^2\theta_W &= 0.2300 \pm 0.0030 \pm 0.0050 \qquad (\nu_\mu N) \\ &= 0.2325 \pm 0.0010 \pm 0.0006 \qquad (\nu_\mu e) \\ &= 0.2310 \pm 0.0070 \qquad (\text{LEP}) \end{aligned}$$

* Current address.

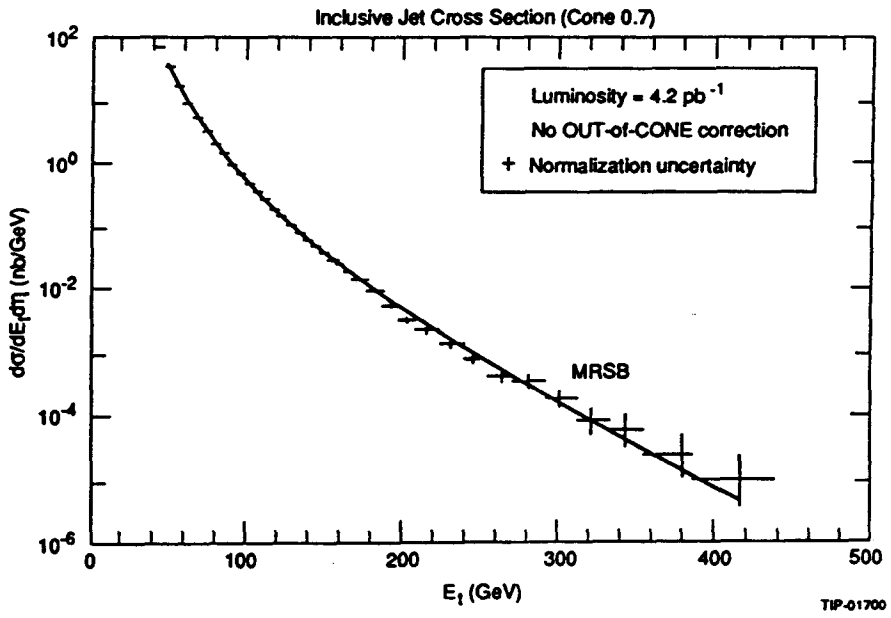


Figure 2.1: CDF jet cross section and perturbative QCD prediction.

The agreement of these values indicates that the standard model works well over the entire range of observed Q^2 values. QCD also agrees with all existing data, although it is less precise. A good example is provided by the jet cross section observed at the Tevatron,[11] Fig. 2.1, which agrees to better than a factor of two with the theoretical calculation over seven orders of magnitude.

The only missing particles of the standard model are the t quark and the Higgs boson. The t mass can be bounded by considering radiative corrections to the $W^{\pm}$ and Z^0 masses, while the H mass is bounded by direct searches at LEP:[12,13,14,15]

$$m_t = 130 \pm 40\,\text{GeV}$$
$$m_H > 48\,\text{GeV}$$

Lattice studies of the Higgs sector suggest an upper limit on the Higgs mass,[19]

$$m_H < 650\text{–}800\,\text{GeV}$$

if there is no new physics for $M \lesssim 1\,\text{TeV}$. This is a bit lower than but similar to bounds determined by unitarity constraints. Given these results, one expects any new physics to be at high mass and/or weakly coupled to ordinary matter.

It is possible to bound any new physics by its loop corrections to the W and Z propagators:[21]

$$\frac{\Pi_W\left(m_W^2\right) - \Pi_W(0)}{m_W^2} = \frac{\alpha\left(m_W^2\right)}{4\sin^2\theta_W\left(m_Z\right)} S_W$$

$$\frac{\Pi_Z(m_Z^2) - \Pi_Z(0)}{m_Z^2} = \frac{\alpha(m_Z^2)}{\sin^2 2\theta_W} S_Z$$
$$\frac{\Pi_W(0)}{m_W^2} - \frac{\Pi_Z(0)}{m_Z^2} = \alpha(m_Z^2)\, T$$

with $S = S_W \approx S_Z$.[21] Present data give[22]

$$T = -0.06 \pm 0.23$$
$$S = -2.2 \pm 1.3$$

This is already sufficient to constrain, for example, some technicolor models, and the bounds will improve with future experiments.

The main problem of the standard model is with the Higgs mechanism used to produce electroweak symmetry breaking and fermion masses. It is responsible for most of the 19 arbitrary parameters in the model. It is also responsible for the naturalness problem: radiative corrections give contributions to the Higgs mass of order the heaviest mass in the theory, e.g., the Planck mass. Despite these problems, the Higgs mechanism does determine the mass scale for electroweak symmetry breaking,

$$v = 246\,\text{GeV}.$$

Any new physics related to electroweak symmetry breaking must occur at $M \sim v$, or more generally at $M \lesssim 1\,\text{TeV}$.

There have been only a few general ideas for explaining electroweak symmetry breaking:

- The standard model Higgs boson;
- Multiple elementary Higgs bosons, which complicate the standard model but do not solve any of its problems;
- A $t\bar{t}$ bound state effective Higgs, which is possible only because the top is heavy;
- Technicolor models, which replace the Higgs with bound states of new heavy fermions;
- Supersymmetry, which provides a natural framework for elementary scalars;
- Composite fermions which somehow generate dynamical masses.

In addition to particles directly related to electroweak symmetry breaking, the SSC can also look for other possible new particles, including new quarks, possible including the t quark, and new W' and Z' bosons. Almost all of these ideas have been discussed at least since 1984,[23] although the models have been greatly elaborated since then.

Lists of possible new physics like this form the basis for the "physics benchmarks" used to test SSC detectors.[24] Almost all of these possibilities could be discovered by the detectors proposed for the SSC. But while these benchmarks represent plausible discoveries, they are much more useful as guides to the design of detectors than the intrinsic plausibility of the underlying models might

indicate. They also reflect the fact that any new particle must decay either into quanta of the standard model or into particles which are weakly coupled to ordinary matter and so produce missing energy. If a detector can detect all of these, it probably can also detect something quite unanticipated.

3. General Requirements

New particle must be either stable or decay into the quanta of the standard model — jets (quarks and gluons), leptons (e, μ, and τ), prompt photons, W and Z bosons — or decay into new particles which are undiscovered because they are weakly coupled to ordinary matter. Particles associated with electroweak symmetry breaking in particular tend to couple to heavy quarks, so tagging of b and other heavy quarks is useful. For the mass scales not observable at LEP or the Tevatron and so of interest at the SSC, the typical kinematic values of interest are:

$$\begin{aligned} p_T &\gtrsim 15\,\text{GeV}, \ |\eta| \lesssim 3 \quad \text{for leptons} \\ p_T &\gtrsim 25\,\text{GeV}, \ |\eta| \lesssim 3 \quad \text{for jets} \\ p_T &\gtrsim 50\,\text{GeV}, \ |\eta| \lesssim 5.5 \quad \text{for } p_{T,\,\text{miss}} \end{aligned}$$

New particles are typically produced with $p_T \lesssim m$ and decay into several different quanta. Hence it is important to detect all the quanta of the standard model over a large $\Delta\Omega$, leading to large detectors. Within this general framework there are two different and complementary approaches. One approach, exemplified by SDC, emphasizes tracking, giving more detailed information about the events and redundancy between tracking and calorimetry. The other approach, exemplified by L*, E/T, and GEM, emphasizes calorimetry, allowing better calorimetry and better performance at high luminosity because of less dependence on central tracking.

4. Top

The top quark is the one new particle which must exist, since it is by definition the partner of the b, which is known to be in a weak isospin doublet. Direct searches for the t in $p\bar{p}$ collisions have established a lower bound[15]

$$m_t > 89\,\text{GeV},$$

assuming standard model production[16] and decays. Otherwise the only bound is from LEP and is about $m_Z/2$. The mass inferred from radiative corrections, $m_t = 130 \pm 40\,\text{GeV}$, will probably allow discovery at the Tevatron if the proposed upgrades are made. If not, then the top can be trivially discovered at the SSC by the process

$$gg \to t\bar{t} \to e^{\pm}\mu^{\mp}X,$$

even if the t mass is much larger than expected.

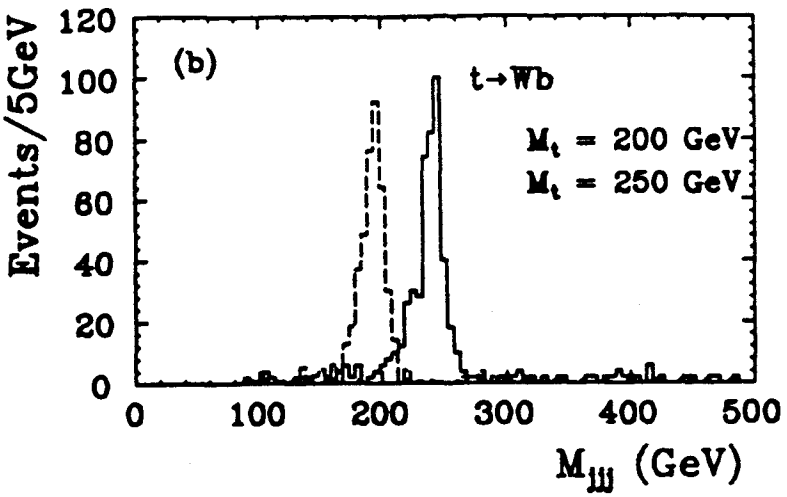


Figure 4.1: $t \to Wb$ jet mass distribution using a $b \to \mu^- \mu^+ X$ tag. (L*)

4.1. Mass

Even if the top is discovered at the Tevatron, detailed measurements will need the SSC. The top mass is clearly a basic phenomenological parameter, especially since the fact that the t is so heavy suggests that it may play unique dynamical role. The simplest way to measure m_t is to measure the top production cross section. Since

$$\sigma \approx 10\,\text{nb} \quad \text{for} \quad m_t = 140\,\text{GeV},$$

the statistical error will be negligible. The theoretical uncertainty from the gluon distribution, higher order QCD corrections, and trigger acceptance is probably about 50%, giving a determination of m_t to about 10%, assuming the standard model for its production and decay.

A direct measurement of the mass can be made by reconstructing the $W \to q\bar{q}'$ and Wb masses with a single lepton trigger:

$$t + \bar{t} \to \ell^+ \nu b + q\bar{q}'\bar{b}$$

This is an example of jet spectroscopy. To reduce the combinatorial background, SDC[2] proposes to tag b jets with their vertex detector. L* requires two non-isolated muons to tag the b jet, giving a clean sample, albeit with low efficiency. The resulting simulated W and top masses are shown in Fig. 4.1. Based on the difference between the input and reconstructed masses, the error on the m_t is a few GeV.[17] The W mass provides a check on the accuracy of jet measurements.

In addition to these methods, GEM[4] suggests selecting events containing a lepton and a jet with $|\vec{p}_{T,\ell} + \vec{p}_{T,\text{jet}}| > 300\,\text{GeV}$. Then the highest p_T recoil jet

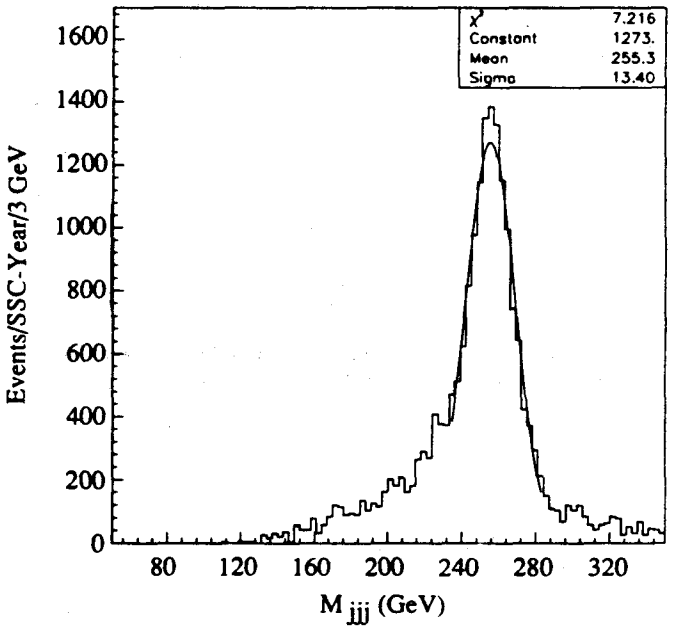


Figure 4.2: $t \to Wb$ jet mass using a large $p_{T,t}$ selection. (GEM)

with two other jets in a cone $\Delta R = 1.0$ is selected, with little additional energy in a larger cone $\Delta R = 1.3$, and the three-jet mass is reconstructed. The result, Fig. 4.2, shows a background which is smaller than that found by SDC and comparable to that found by L* with a double muon tag.

Finally, it is possible to use the high statistics available at the SSC to find mean of a kinematic distribution, e.g.

$$\begin{aligned} M(\ell_1\ell_2): &\quad t + \bar{t} \to \ell_1\nu b + \ell_2\nu\bar{b} \\ M(\ell_1 b): &\quad t \to \ell_1\nu b \\ M(\ell_1\ell_3): &\quad t \to \ell_1\nu b,\ b \to \ell_3 X. \end{aligned}$$

These distributions may be easier to measure precisely, although the connection to m_t is more indirect.

The high statistics available at the SSC allow many possible analyses, allowing checks of systematics and possibly providing the first hint of something nonstandard about top physics.

4.2. Decays

Top decays are not very interesting in standard model. It is important to verify that $t \to Wb$ is dominant to be certain that a new quark is in fact the top. This can be done using b-tagging with a vertex detector and/or with nonisolated muons. It is possible that a b' could be lighter than the t, so one needs to do

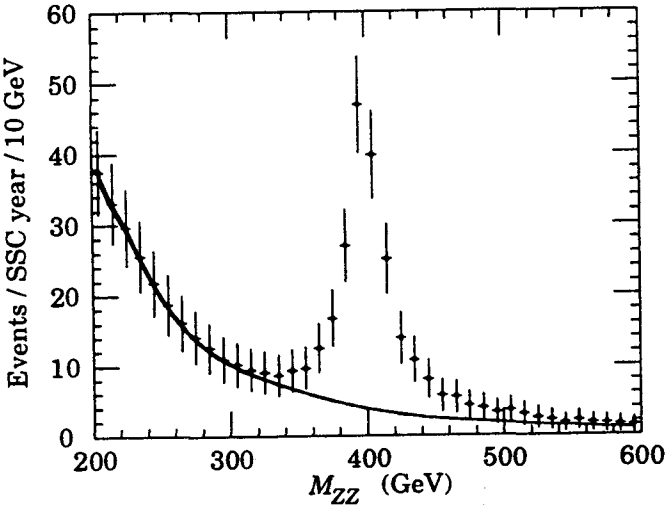


Figure 5.1: $H \to Z^0Z^0 \to \ell^+\ell^-\ell^+\ell^-$ signal and Z^0Z^0 continuum background for $m_H = 400\,\text{GeV}$. (SDC)

the tagging well enough to distinguish $b' \to Wc$ from $t \to Wb$. It would be nice also to measure the Cabibbo suppressed decay $t \to Ws$, but there seems to be no good way to identify s quark jets sufficiently well.

Nonstandard decays of the t are of course possible. If there exists a charged Higgs boson H^+ lighter than t, then a substantial branching ratio for $t \to H^+b$ is expected, with $H^+ \to c\bar{s}$ or $H^+ \to \tau^+\nu$.[26] In either case one can trigger on one t or $\bar{t}$ decaying through Wb to a lepton. For $H^+ \to c\bar{s}$, one would reconstruct the jet masses as for the $t \to Wb \to jjj$ decay, imposing in addition a veto $M_{jj} \neq M_W$. This gives a few percent meausrement of the H^+ mass provided that the combined brancing ratio is greater than about 1%. If $H^+ \to \tau^+\nu$ dominates, one must test $e/\mu/\tau$ universality by measuring the ratio of one-prong jets to leptons. The τ misidentification seems small even without detecting the τ vertex, and the sensitivity for the combined branching ratio is also of order 1%.

Other plausible nonstandard decays include $t \to Z^0c$, which could be large if there were a fourth generation of quarks strongly mixed with the t, and the supersymmetric mode $t \to \tilde{t}\tilde{\chi}_1^0$. These modes do not seem to put any particular constraints on the detectors.

5. Higgs

The Higgs boson is the most unsatisfactory part of the standard model. It is responsible for most of the 19 arbitrary parameters in the theory. Furthermore, a low Higgs mass is unnatural[18] in the presence of high mass scales, and at least one such scale, the Planck mass, must be present in any theory which

incorporates gravity. Nevertheless, being able to detect the standard Higgs boson is an important benchmark for any SSC detector both for its own sake and for what it indicates about the ability to study WW physics. The masses of interest range from about 80 GeV, the upper limit which would be observable at LEP-200, to a theoretical upper limit $m_H \geq 650$–$800\,\mathrm{GeV}$ determined by lattice studies of the gauge-Higgs theory.[19] This is a refinement of the old limit from perturbative unitarity.[20]

Since the top is heavy, it is possible[27] to replace the Higgs boson with a $t\bar{t}$ bound state made by some unknown new dynamics at a scale $\Lambda \sim 10^{15}\,\mathrm{GeV}$. At this new scale, $m_H = 2m_t$, but the renormalizaton group then implies $m_H \approx m_t$. This picture gives essentially the standard model up to masses of order Λ with a relatively light Higgs boson.

The search for the Higgs boson naturally divides into the heavy mass region, $m_H > 2m_Z$, where the dominant decays $H \to W^+W^-$ and $H \to Z^0Z^0$ can be used, and the intermediate mass region, $80\,\mathrm{GeV} < m_H < 2m_Z$, where backgrounds overwhelm the dominant $H \to b\bar{b}$ and rare decays such as $H \to \gamma\gamma$ and $H \to ZZ^*$ must be used.[28]

5.1. Heavy Higgs

For $m_H > 2m_Z$, $\Gamma_H(W^+W^-) \approx 2\gamma_H(Z^0Z^0)$. Since the W^+W^- mode has a large background from $t\bar{t}$ events and is harder to reconstruct, it is natural to concentrate on the Z^0Z^0 mode.

$H \to Z^0Z^0 \to \ell^+\ell^-\ell^+\ell^-$, where $\ell = e$, μ, has been beaten to death.[29] If the $Z^0 \to \ell^+\ell^-$ mass resolution is comparable to the Z^0 width, then only known background is the Z^0Z^0 continuum. The only problem with this mode is that the statistics become small for $m_H \gtrsim 600\,\mathrm{GeV}$; see Fig. 5.1. For higher masses one must either rely on $\mathcal{L} \sim 10^{34}\,\mathrm{cm}^{-2}\mathrm{s}^{-1}$ or use Z^0 decay modes with larger branching ratios but more backgrounds.

$H \to Z^0Z^0 \to \ell^+\ell^-\tau^+\tau^-$ has a rate equal to the 4ℓ rate. If the τ mass is ignored, then one has a 1-constraint fit, using the two components of $\vec{p}_{T,\,\mathrm{miss}}$ plus the Z^0 mass to determine two sums of missing neutrino energies. The backgrounds are probably small, especially if one uses a vertex detector or requires at least one of the τ's to decay leptonically. Unfortunately, no thorough background study has been done, although the backgrounds seem to be small.[31]

$H \to Z^0Z^0 \to \ell^+\ell^-\nu\bar{\nu}$ gives six times the 4ℓ rate.[30] There is a large background from $Z^0 +$ jets, where the jets are somehow missed. This can be rejected with a perfect detector covering $|\eta| \lesssim 5.5$.[32] A realistic estimate of the background requires a full detector simulation. The simulations which have been done are not complete, but they have used full GEANT simulations to examine the effect of the calorimeter edges at $\eta \approx 3$ and the transverse shower spreading in the forward calorimeter.[33] It seems that these are not fatal and that sufficient background rejection can be obtained with coverage of $\eta \lesssim 5$.

$H \to Z^0Z^0 \to \ell^+\ell^- q\bar{q}$ has a large branching ratio but also a large background from $Z^0 +$ jets. Several studies of the analogous $H \to W^+W^-$ mode with one hadronic decay were made assuming light t quarks but were inclusive.

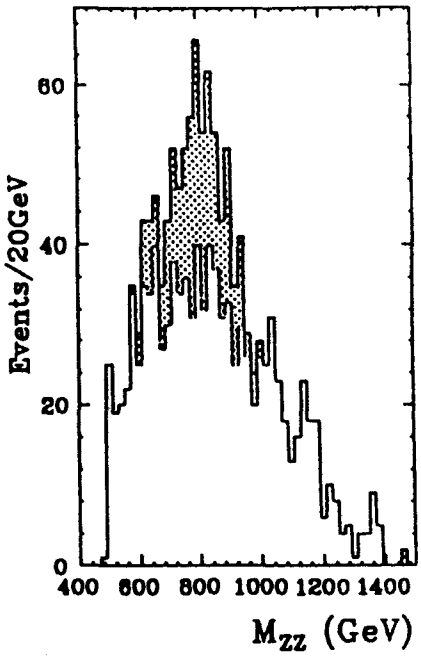


Figure 5.2: $H \rightarrow Z^0Z^0 \rightarrow \ell^+\ell^- q\bar{q}$ mass distribution from 800 GeV Higgs and background. (L*)

Given the large additional background from $t\bar{t}$, this channel looks difficult. The first successful analysis of the Z^0Z^0 mode with one hadronic decay was made by L*,[25] using the following cuts for $m_H = 800\,\text{GeV}$:

$p_{T,Z} > 240\,\text{GeV}$

2 jets in $\Delta\phi = \pm 50°$ from Z^0.

This gave 210 events on a background of 640, which is statistically significant, although the signal and background peak in the same place; see Fig. 5.2.

For an 800 GeV Higgs, about half the cross section comes from WW fusion. Since the W bosons are radiated from valence quarks, these events generally have jets with $p_T \sim m_W$ at large η. An EMPACT/TEXAS analysis[31] and later a GEM analysis[4] found an improvement in the signal/background by requiring jet with $p_T > 50\,\text{GeV}$ and $\eta > 3$; the latest GEM analysis is shown in Fig. 5.3. Even if forward jet tagging is not essential for observing the signal, it is an important confirmation of the production dynamics.

One might also use cuts or the shape of the recoil jets and cuts on the multiplicity of the associated event.[34] The usefulness of these, especially of the multiplicity cut, depend on a detailed understanding of the event structure.

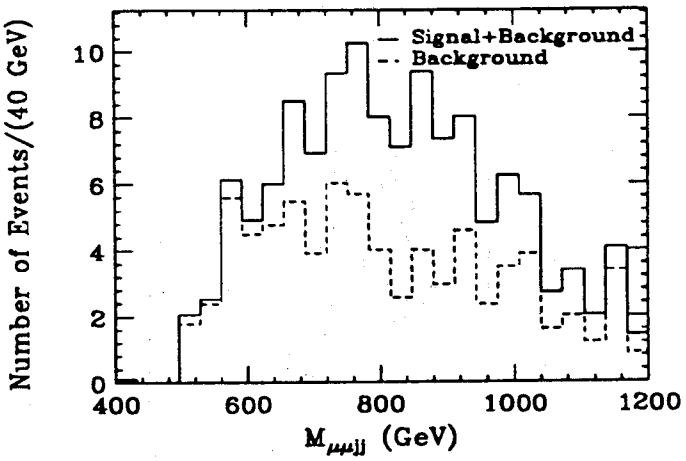


Figure 5.3: $H \to Z^0Z^0 \to \ell^+\ell^- q\bar{q}$ mass distribution from 800 GeV Higgs and background with forward jet tagging. (GEM)

5.2. Intermediate Mass Higgs

For $m_H < 2m_Z$ the dominant decays are $H \to b\bar{b}$ and $H \to \tau^+\tau^-$. Both suffer from large backgrounds, and the $\tau^+\tau^-$ decay cannot be reconstructed except for $m_{T,H} \gtrsim m_H$. Hence one is forced[26] to rely on the rare decays $H \to \gamma\gamma$ and $H \to ZZ^*$.

$H \to \gamma\gamma$ has a branching ratio of order 10^{-3}. The irreducible background comes from the QCD processes $q\bar{q} \to \gamma\gamma$ and $gg \to \gamma\gamma$. Since the Higgs is narrow in this mass range, this irreducible background can be rejected if $\Delta M_{\gamma\gamma}/M_{\gamma\gamma} \lesssim 1\%$. This requires a high resolution electromagnetic calorimeter and determination of the event vertex, either by directional information from the calorimeter or by finding the z-vertex using charged particle tracks. If multiple interactions occur in the same bunch crossing, the most probable vertex can be determined by selecting the one with the highest multiplicity of tracks.[25]

There is also a large potential background from QCD jets which fragment into hard leading π^0's and so give electromagnetic energy. The required γ/jet rejection is about 10^{-4}. It appears possible to achieve this using a combination of calorimetric and tracking isolation cuts and perhaps information from a preshower detector in front of the calorimeter.[4] A large part of the rejection must be achieved at the trigger level to make the trigger manageable.

The $H \to \gamma\gamma$ signal/background might be improved by looking for associated Higgs production. Kleiss and Stirling[35] proposed to look for $q\bar{q}' \to WH$ production. The real background in this channel is small, but only about 6 events/yr are produced. An alternative is to look for $gg \to Ht\bar{t} \to \gamma\gamma\ell\nu X$, giving about 50 events/yr.[36] The backgrounds from $t\bar{t}\gamma\gamma$ have been calculated and are manageable but not negligible.[37] There are also potential backgrounds from jets

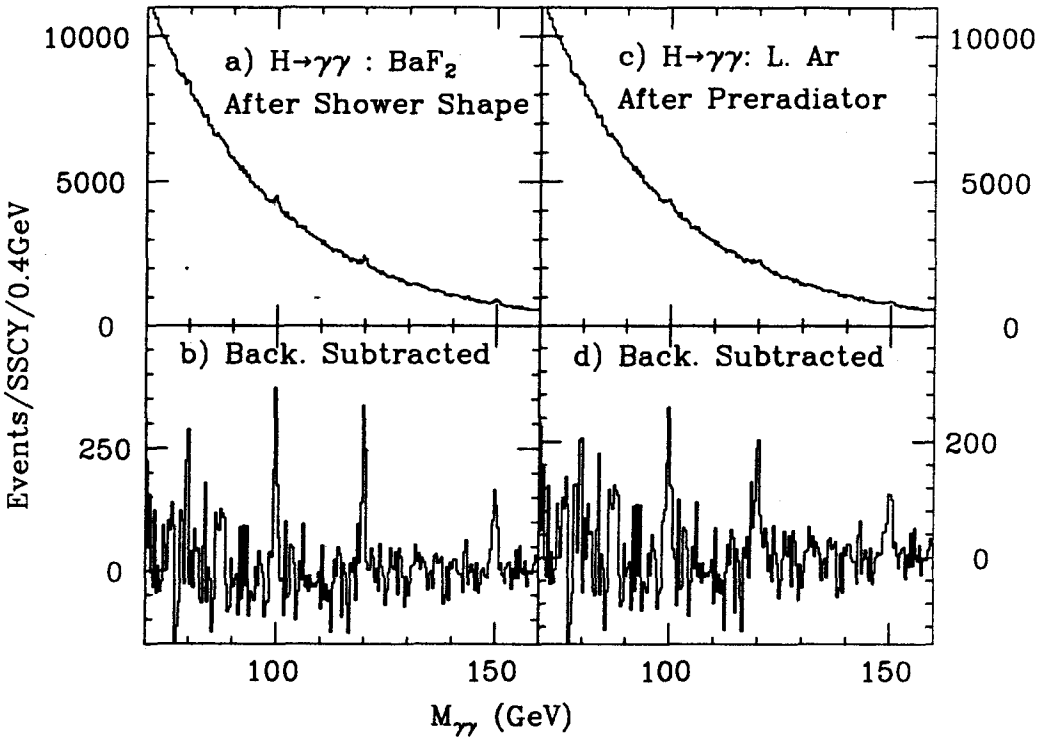


Figure 5.4: $H \to \gamma\gamma$ and backgrounds from real $\gamma\gamma$ events and from jets for two different calorimeters. (GEM)

giving π^0's which are also not negligible. Whatever the true background situation, it is clear that such tagged processes will at best give a small number of events.

For $140\,\mathrm{GeV} \lesssim m_H < 2m_Z$, the rare decay $H \to Z^0 Z^{0*} \to \ell^+\ell^-\ell^+\ell^-$ has an observable branching ratio. Backgrounds come from $Z^0\gamma^*$, $Z^0 b\bar{b}$ and $Z^0 t\bar{t}$ production. Since the Higgs is narrow in this mass range, the backgrounds can be minimized by good mass resolution. The estimated signal and background[2] are shown in Fig. 5.5. To detect this signal, it is essential to have an efficient $Z \to \ell^+\ell^-$ trigger and to detect low-p_T leptons.

For $2m_W < m_H < 2m_Z$, the $H \to ZZ^*$ branching ratio becomes small because of $H \to W^+W^-$ decays. In this mass range it may be possible to confirm a $H \to ZZ^*$ signal by detecting $H \to W^+W^- \to e^\pm\mu^\mp X$. The signal for $M_{\ell\ell} \sim m_H/2$ is about equal to the background from continuum W^+W^- pair production. To veto the very large background from $t\bar{t}$ production, it is essential to detect extra jets very efficiently. It is unclear whether this is possible; a realistic study is needed.

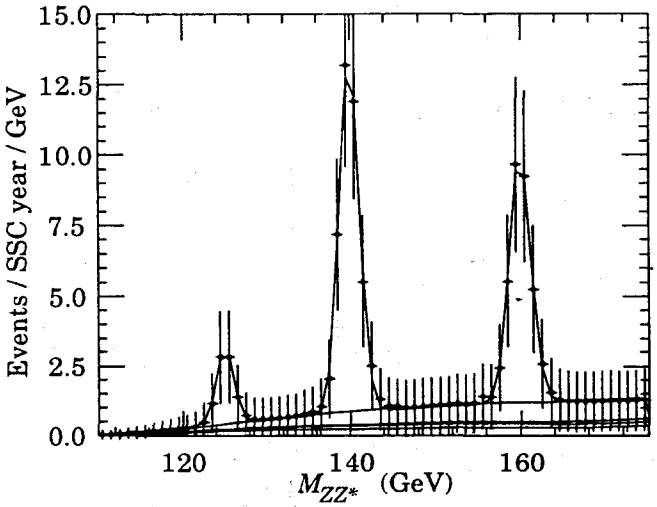


Figure 5.5: $H \to ZZ^* \to \ell^+\ell^-\ell^+\ell^-$ signal and cumulative backgrounds. (SDC)

5.3. Nonstandard Higgs

Nonstandard Higgs bosons are not very unlikely: supersymmetry provides the only known natural framework for elementary scalars, and it requires at least two Higgs doublets and hence both charged and several neutral Higgs bosons.[38]

A possible signature for charged Higgs $H^\pm$ is $gb \to H^-t$, $H^- \to W^-h^0$. A similar possible signature for the $CP = -1$ neutral Higgs A is $gg \to A^0$, $A^0 \to Z^0h^0$. In both cases, the light h^0 mass is presumably known, but b jet tagging is probably necessary to reject the background. More work on signatures of this sort should be done.

6. Technicolor

In technicolor models,[39] elementary Higgs bosons are replaced by bound states of technifermions made by new technicolor interactions which become strong at the 1 TeV scale. Such models explain the $W^\pm$ and Z^0 masses, but they do not generate fermion masses unless extended technicolor interactions are introduced. These potentially give flavor-changing neutral currents much larger than the experimental bounds. In "walking" technicolor models,[40] the couplings run slowly between the technicolor and extended technicolor scales, resulting in much smaller flavor-changing neutral currents.

The minimal technicolor model gives only a QCD-like spectrum at the 1 TeV mass scale, with the longitudinal $W^\pm$ and Z^0 playing the role of pions. This is difficult to detect even at the SSC. One must look for, e.g., $\rho_{TC}^\pm \to W^\pm Z^0$, which is produced by WW fusion and by $W - \rho_{TC}$ mixing. The experimental cross section with leptonic $W^\pm$ and Z^0 decays is tiny,[41] as shown in Fig. 6.1.

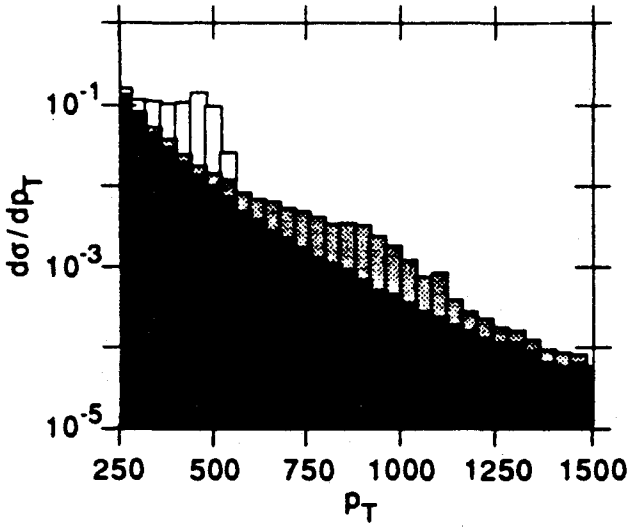


Figure 6.1: p_T, Z distribution for $\rho_{TC}^{\pm} \to W^{\pm}Z^0$ and standard model backgrounds with leptonic decays. Ref. 41

One might also look for mixed leptonic-hadronic decays like those considered for the standard model Higgs, but no careful study has been done.

In the minimal model one can also look for $\omega_{TC} \to Z^0\gamma$.[2] This gives a better signature, but the rates are still tiny,[2] as shown in Fig. 6.2. This process does illustrate the importance of identifying isolated single photons.

Fortunately, realistic technicolor models[42] have much more structure and are easier to detect. Typical ingredients of such models include:

- o More technifermions, some with $SU(3)$ color.
- o "Walking" couplings above Λ_{TC}. May change masses and decays.
- o Perhaps multiple mass scales.
- o Pseudo-Goldstone bosons.

The Pseudo-Goldstone bosons in particular give promising signatures. For example, a color-3 leptoquark P_3 is produced with a cross section about 15% that of a quark of the same mass. It probably decays dominantly into τb, which can be reconstructed in principle using $\vec{p}_{T,\,\mathrm{miss}}$ to determine two sums of missing neutrino energies. It may also be possible to look for one $P_3 \to \mu b$ decay, since it is likely that

$$\frac{\Gamma(\mu b)}{\Gamma(\tau b)} \sim \left(\frac{m_\mu}{m_\tau}\right)^2 \sin^2\theta.$$

This would give a much better signature. A good background study is needed.

Another possible technicolor signature is $P_8 \to t\bar{t}$. This was studied[43] for $m_t = 20\,\mathrm{GeV}$ but has not been reconsidered since it was learned that the top is heavy. Again, a realistic study is needed.

Finally, technicolor models might also give narrow colored resonances ρ_{TC}^8 decaying into leptoquarks or jets.[44] Such signatures are model dependent but

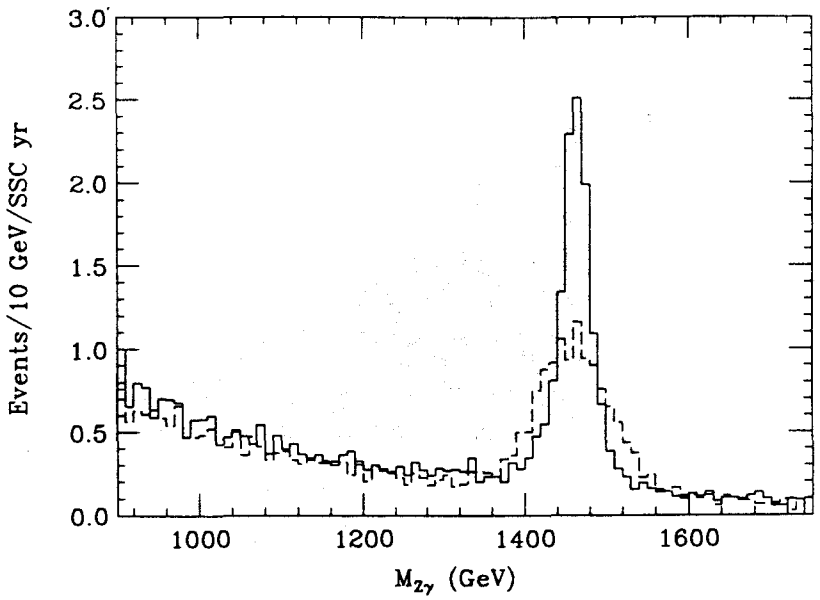


Figure 6.2: $\omega_{TC} \to Z^0\gamma$ cross section and standard model backgrounds.

indicate the importance of having detectors able to look at the full range of possible signatures.

7. Supersymmetry

Supersymmetry at the 1 TeV scale would solve the naturalness problem of the standard model. In addition, supersymmetry provides a plausible example of a model with with complex signatures and with calculable production and decay rates.

The minimal supersymmetric extension of the standard model[38] has a conserved R parity, with $R = 1$ for all ordinary particles and $R = -1$ for their supersymmetric partners. It requires two Higgs doublets, implying three neutral and a pair of charged Higgs bosons plus supersymmetric partners for all the ordinary particles. The color singlet superparticles are:

$$\tilde{\gamma},\ \tilde{Z},\ \tilde{h}^0,\ \tilde{H}^0 \Rightarrow \tilde{\chi}_i^0$$
$$\tilde{W}^{\pm},\ \tilde{H}^{\pm} \Rightarrow \tilde{\chi}_i^{\pm}$$

R-parity requires that supersymmetric particles be produced in pairs and decay to the lightest supersymmetric particle χ_1^0, which is weakly interacting and so escapes, producing missing energy. Heavier $\tilde{\chi}$'s decay to lighter ones, giving complex cascade decays.[45]

There are significant limits on the minimal supersymmetric model from LEP, although these are complicated by t-quark loop corrections.[46] The present values of the $W^{\pm}$ and Z^0 masses are inconsistent with the assumption of grand unification of the couplings but can be made consistent[47] by introducing supersymmetric particles with $m \sim 1\,\mathrm{TeV}$. Unfortunately, the results of this analysis are extremely sensitive to detailed assumptions about the standard model and the boundary conditions at the unification scale, so the conclusions about supersymmetry are inclusive even if one accepts the assumption of grand unification.

Recent analyses have concentrated on gluinos, since their decays are most affected by the cascade decays characteristic of the minimal supersymmetric model. A "typical" 750 GeV gluino event is

$$g + g \to \tilde{g} + \tilde{g}$$

$$\begin{array}{ll} \tilde{g}_1 \to \tilde{\chi}_4^0 q\bar{q} & \tilde{g}_2 \to \tilde{\chi}_2^+ q\bar{q}' \\ \tilde{\chi}_4^0 \to \tilde{\chi}_1^+ W^- & \tilde{\chi}_2^+ \to \tilde{\chi}_2^0 W^+ \\ \tilde{\chi}_1^+ \to \tilde{\chi}_1^0 \ell^+ \nu & \tilde{\chi}_2^0 \to \tilde{\chi}_1^0 h^0 \end{array}$$

This event, for which all the branching ratios are not small, contains seven undiscovered particles. Obviously, such a rich theory gives many possible experimental signatures.

7.1. Missing p_T

Since the lightest supersymmetric particle $\tilde{\chi}_1^0$ is weakly interacting and escapes any detector, the basic signature for supersymmetry is missing energy. The physics backgrounds are neutrinos from c, b, t quarks and from $W^{\pm}$ and Z^0 produced at large p_T by QCD processes. These backgrounds are less than the signal[48,4] after cuts designed to select heavy particle production with $p_T \lesssim m$; see Fig. 7.1. Detector effects such as the transition between the endcap and forward calorimeters at $\eta \approx 3$ and the resolution $\Delta p_T/p_T \lesssim 10\%$ in the forward calorimeter do not overwhelm the signature. Therefore, while the $\not{E}_T$ signature clearly depends on the global performance of the detector, it appears to be possible to detect.

7.2. Like-sign Dileptons

Since the gluino is a Majorana fermion, it decays equally into $\ell^+ X$ and $\ell^- \bar{X}$, giving substantial rates for like-sign dileptons. The backgrounds for isolated like-sign dileptons come from $t\bar{t}$ events in which a b quark happens to give an isolated lepton, from $W^{\pm}W^{\pm}$ events, and from various other small cross sections. All of these have been shown to be small compared to the gluino signal.[49] Hence the like-sign dilepton signature can be used to identify the Majorana fermion gluino characteristic of the minimal supersymmetric model. To detect this signal, it is useful to measure the signs of electrons as well as muons.

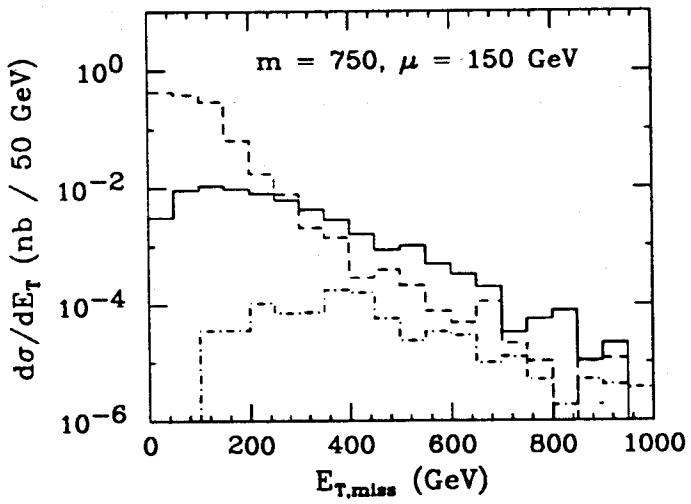


Figure 7.1: SUSY signatures and backgrounds. Solid: gluino, $m = 750\,\text{GeV}$. Dashed: Heavy quark background. Dotted: $Z \to \nu\bar{\nu}$ background. (EMPACT/TEXAS)

The minimal supersymmetric model also predicts a variety of multilepton signatures and $Z^0 \to \ell^+\ell^-$ plus lepton signatures, all associated with missing transverse energy.[49]

It therefore appears that supersymmetry at the 1 TeV mass scale can be detected at the SSC. The open questions relate mainly to the question of determining all the parameters of the supersymmetric model, including the masses of the χ_i states appearing in gluino decays. To do this, it it minimally necessary to reconstruct all the standard model states appearing in the cascade decays, including in particular $W \to q\bar{q}'$. This seems to be possible but requires good lepton identification and hadron resolution in complex events.

8. Quark/Lepton Substructure

Given the layers of structure observed previously, it is natural to conjecture that quarks and leptons might be composites of more elementary constituents bound by a new interaction at some mass scale Λ. The masses and mixings would then be generated by the new dynamics, and one would have unknown new effects at the scale Λ. The dominant consequence for $Q^2 \ll \Lambda^2$ is new four-fermion interactions between interactions sharing constituents:[50]

$$\mathcal{L}_I = \frac{4\pi}{\Lambda^2}\, \bar{f}\Gamma f\, \bar{f}\Gamma f$$

(The normalization is conventional and corresponds to a strong coupling at Λ.)

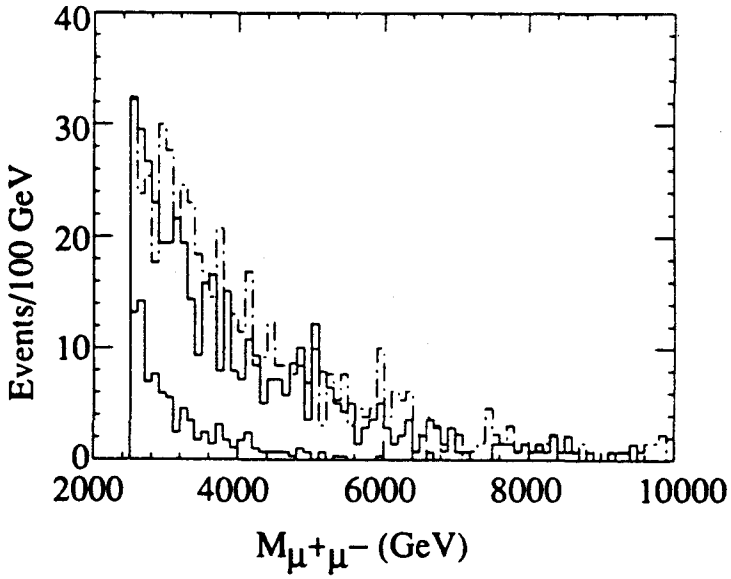


Figure 8.1: Drell-Yan cross section for standard model and for a compositeness interaction at $\Lambda = 20\,\text{TeV}$. (GEM)

Such interactions must minimally occur between identical quarks and leptons. Previous studies[23] have found that the jet cross section is sensitive to a scale $\Lambda \approx 20\,\text{TeV}$, compared to present bounds of order 1 TeV.

If the picture is to be at all attractive, then different fermions must share constituents. Hence one might expect four-fermion interactions in processes like $q\bar{q} \to \mu^+\mu^-$, even though these are model dependent. This measurement particularly benefits from higher luminosity, since the Drell-Yan cross section is small and lepton identification remains feasible. Fig. 8.1 shows the expected number of events per year at $\mathcal{L} = 10^{34}\,\text{cm}^{-2}\text{s}^{-1}$ for $\Lambda = 20\,\text{TeV}$.[4] Clearly, the sensitivity of the search is considerably better than this.

If compositeness were observed, it would be important to measure the $\mu^+\mu^-$ angular distribution, since this depends on the underlying dynamics. Fig. 8.2 shows the angular distribution for two possible models, one with helicity conservation and the other with an S-wave interaction.[4] Measuring this needs many events and emphasizes the gain from high luminosity.

9. Conclusion

The SSC will open up a qualitatively new mass scale. At this scale, we can plausibly expect to learn the origin of electroweak symmetry breaking, and we may also understand the origin of fermion masses. These are fundamental issues in particle physics, and ones on which little progress has been made since the SSC was first discussed in 1982.

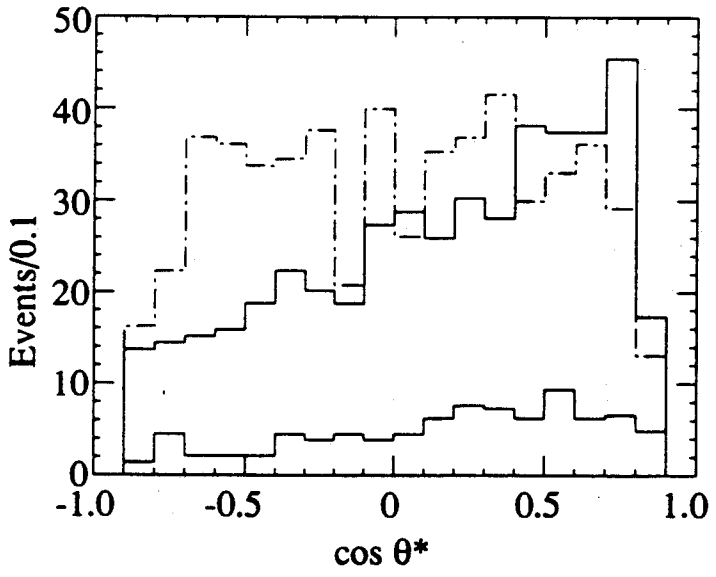


Figure 8.2: Drell-Yan angular distributions for standard model and for two different compositeness interactions at $\Lambda = 20\,\mathrm{TeV}$. (GEM)

We do not know what the new physics may be. There are many possibilities, and it would be a surprise, perhaps even a disappointment, if any of the ones which have been discussed turned out to be the truth. But we do know that *any* new particle must either be stable, or decay into the quanta of the standard model, or decay into an unknown and therefore weakly interacting particle, giving missing energy. This means that we have some reasonable basis for designing detectors for the SSC and some hope that if those detectors can observe various hypothetical signatures, they can also detect what is actually there.

This work was supported in part by the U.S. Department of Energy under contract numbers DE-AC02-76CH00016 and DE-AC02-89ER40486.

References

1. SDC Collaboration, G.H. Trilling, et al., *Solenoidal Detector Collaboration Expression of Interest*, (July, 1990).
2. SDC Collaboration, G.H. Trilling et al., *Solenoidal Detector Collaboration Letter of Intent*, (November, 1990).
3. GEM Collaboration, B. Barrish, W. Willis, et al., *Gammas-Electrons-Muons Collaboration Expression of Interest*, (July, 1991).
4. GEM Collaboration, B. Barrish, W. Willis, et al., *Gammas-Electrons-Muons Collaboration Letter of Intent*, in preparation.

5. BCD Collaboration, N.S. Lockyer, K.T. McDonald, et al. *Bottom Collider Detector Expression of Interest*, (July, 1990).
6. SFT Collaboration, B. Cox, et al. *Super Fixed Target Beauty Facility Expression of Interest*, (July, 1990).
7. P. Schlein, *Forward Collider Detector to measure CP-violation in B Decays*, ().
8. J. Orear, et al., *Low-p_T Physics Expression of Interest*, (July, 1990).
9. J.D. Bjorken, *Full Acceptance Detector Expression of Interest*, ().
10. W.J. Marciano, BNL-45999 (1991).
11. CDF Collaboration, FERMILAB-PUB-91-231-E (1991).
12. ALEPH Collaboration, Phys. Lett. B246, 306 (1990).
13. L3 Collaboration, Phys .Lett. B248, 203 (1990).
14. OPAL Collaboration, CERN-PPE-90-150 (1990).
15. CDF Collaboration, Phys. Rev. D43, 664 (1991).
16. P. Nason, S. Dawson, and R.K. Ellis, Nucl. Phys. B303, 607 (1988).
17. R.M. Barnett, et al., "Report of the Subgroup on the Top Quark," these proceedings, ANL-HEP-90-98 (1990).
18. S.L. Glashow, S. Weinberg, Phys. Rev. D15, 1958 (1977).
19. J. Kuti, L. Lin, and Y. Shen, Phys. Rev. Lett. 61, 678 (1988).
20. B.W. Lee, C. Quigg, and H.B. Thacker, Phys. Rev. Lett. 38 883 (1977).
21. M. Peskin and T. Takeuchi, Phys. Rev. Lett. 65, 964 (1990).
22. W.J. Marciano and J.L. Rosner, Phys. Rev. Lett. 65, 2963 (1990).
23. E. Eichten, I. Hinchliffe, K. Lane, and C. Quigg, Rev. Mod. Phys. 56, 579 (1984).
24. R. Palmer, J. Peoples, et al., *Proc. 1982 DPF Summer Study on Elementary Particle Physics and Future Facilities* (Snowmass, 1982), p. 90.
25. L* Collaboration, Letter of Intent, (Nov., 1990).
26. J.F. Gunion, H.E. Haber, G.L. Kane, and S. Dawson, *The Higgs Hunter's Guide*, ISBN 0-201-50935-0 (1990).
27. W.A. Bardeen, C.T. Hill, and M. Lindner, Phys. Rev. D41, 1647 (1990).
28. J.F. Gunion, G.L. Kane, and J. Wudka, Nucl. Phys. B299, 231 (1988).
29. R.N. Cahn, M. Chanowitz, M. Golden, M.J. Herrero, I. Hinchliffe, E.M. Wang, F.E. Paige, J.F. Gunion, and M.G.D. Gilchriese, in *Workshop on Experiments, Detectors, and Experimental Areas for the SSC*, (Berkeley, CA, 1987), p. 20.
30. R.N. Cahn and M.S. Chanowitz, Phys. Rev. Lett. 56, 1327 (1986).
31. EMPACT Collaboration, M. Marx, et al., *EMPACT Collaboration Letter of Intent*, (November, 1990).
32. F.E. Paige and E.M. Wang, in *SSC Workshop on Calorimetry: The Superconducting Super Collider*, (Tuscaloosa, AL, 1989), p. 99.

33. G. Forden, private communication.
34. J.F. Gunion, G.L. Kane, H.F.W. Sadrozinski, A. Seiden, A.J. Weinstein, and C.P. Yuan, Phys. Rev. D40, 2223 (1989).
35. R. Kleiss and W.J. Stirling, Phys. Lett. 200B, 193 (1988).
36. W.J. Marciano and F.E. Paige, Phys. Rev. Lett. 66, 2433 (1991).
37. R. Zhu, private communication.
38. H.E. Haber and G.L. Kane, Phys. Rept. 117, 75, (1985), and references therein.
39. S. Weinberg, Phys. Rev. D13, 974 (1976);
S. Weinberg, Phys. Rev. D19, 1277 (1979);
L. Susskind, Phys. Rev. D20, 2619 (1979)..
40. T.W. Appelquist, D. Karabali, and L.C.R. Wijewardhana, Phys. Rev. Lett. 57, 957 (1986);
T. Appelquist, L.C.R. Wijewardhana, Phys. Rev. D36, 568 (1987).
41. J. Bagger, T. Han, and R. Rosenfeld, FERMILAB-CONF-90-253-T (1990).
42. For a review see S. Dimopoulos, S. Raby, and G.L. Kane, Nucl. Phys. B182, 77 (1981).
43. C. Baltay and H. Gordon, in *Proc. 1982 DPF Summer Study on Elementary Particle Physics and Future Facilities* (Snowmass, 1982), p. 500.
44. K. Lane, M.V. Ramana BUHEP-91-6, (April 1991).
45. By H. Baer, X. Tata, J. Woodside, Phys. Rev. D42, 1568 (1990).
46. H. Baer, M, Drees, X. Tata, Phys. Rev. D41, 3414 (1990).
47. U. Amaldi, W. de Boer, Hermann Furstenau, Phys.Lett. B260, 447 (1991).
48. R.M. Barnett, J. Freeman, R. Raja, J.F. Gunion, H.E. Haber, R. Hollebeek, F.E. Paige, and A.P. White, in *Proc. of 1988 Snowmass Summer Study on High Energy Physics in the 1990's* (Snowmass, CO, 1988), p. 226.
49. H. Baer, X. Tata, J. Woodside, FSU-HEP-910731 (July, 1991).
50. E. Eichten, K. Lane, E. Peskin, Phys. Rev. Lett 50, 811 (1983).

The GEM Detector for the SSC

B. Barish

The GEM Detector for SSC

Barry C. Barish
California Institute of Technology
Lauritsen Laboratory
Pasadena, CA 91125

Abstract

This paper describes the present status of the detector concept for GEM. The GEM collaboration formed in June 1991 and has rapidly evolved the scope, goals and many of the chosen technologies. The aim of GEM is to build a powerful detector with broad abilities, but in particular, to emphasize precision measurements of gammas, electrons, and muons (hence the name GEM). The detector is based upon a large superconducting magnet totally surrounding both the calorimetry and muon systems, thus eliminating intervening materials and thereby allowing precision measurements.

1.0 Introduction

The GEM collaboration formed in June 1991 with the express purpose of developing a major detector for SSC complementary to SDC. In particular, the collaboration quickly agreed to emphasize high P_T physics and build directly on the excellent work that had been done for EMPACT/TEXAS and L*. In July, we submitted an EOI outlining the general concepts for GEM and the technological options under consideration. We proceeded over the next months to refine the goals of the experiment and to either determine the technologies for each subsystem or, at least, to reduce the choice to a couple technologies for study in our R&D program over the coming year.

Our primary and most important decision has been to base the experiment upon the idea espoused in L* to place the magnet coils outside all detector elements. This allows building a calorimeter system limited only by its inherent resolutions, since almost all intervening materials have been removed. In addition, the muon momentum and direction are measured in air in a shielded area, following the calorimeter, allowing both high precision and a robust system at high luminosities.

The main physics goals of GEM are high P_T physics directed at the signatures for the Higg's sector and the new physics beyond the standard model. There are many ideas for this new physics, as illustrated in Table 1. One notable feature of this table is that, for the most part, it has remained unchanged over the past 5 years or so. This emphasizes that, despite the impressive results on the Z^0 from LEP, hadron collider results from CERN and Fermilab, searches for rare kaon decay modes, proton decay limits, etc., we have made very little progress toward revealing the underlying physics beyond the standard model. This means that the motivation for the SSC is even stronger than when it was proposed, since going to high enough energy (rather than precision experiments or rare decays) appears to be the means to discover this physics. The other notable feature of this table is that the common signatures for this physics are leptons, jets and missing E_T. In GEM, our design goals have been to emphasize identification of these signatures and making precision measurements in order to determine the parameters, reduce background, etc.

In this paper, I will briefly describe the design and technologies for GEM, as we now see them, and the reasons for the choices. More detailed descriptions can be found in the GEM LOI and internal notes. I will also describe the principle aims of our R&D and Engineering programs over the coming year, leading toward a technical design report (TDR) for GEM. Finally, I will demonstrate the abilities of GEM for a few key physics topics.

The design philosophy for GEM is to "design to cost" and we are following the SSC PAC guideline that the major detectors should not exceed \$500M in this design. In this context we are designing, costing, redesigning etc. in order to evolve our design at the target cost. The GEM collaboration is growing rapidly, presently over 650 collaborators from 85 institutions in 15 countries. It is still too early to determine the total resources available to us or how we will divide the responsibilities.

Table 1. Physics and Signatures for SSC

Physics	Signatures
Standard H^0	$\gamma\gamma, ZZ^* \to l^+l^-l^+l^-$
	$ZZ \to l^+l^-l^+l^-, l^+l^-jj, l^+l^-\nu\nu$
Extended $H^0, h^0, H^\pm$	Same as above
	Heavy $f\bar{f} \Rightarrow$ flavor tags, isolated $l^\pm$,
	$W^\pm \to jj$, etc.
Heavy $Q\overline{Q}$	$W^\pm q \to$ jets + isolated $l^\pm$
W', Z (mass, width, asymmetry)	$l^\pm + E_T, l^+l^-$, dijets
Strong VV scattering	$WW, WZ, ZZ \to l^\pm$ + jets
Technicolor	$P_T \to$ dijets, $WZ(\to l^\pm$jets$), \pi_T \pi_T$
	$\pi_T \to$ heavy $f\bar{f}$, dijets
Supersymmetry	multi-isolated $l^\pm$, jets, E_T
q Substructure	high-mass dijets
q/l Substructure	high-mass dileptons, E_T
None of the Above!	All of the above!

2.0 The GEM Magnet

The design of GEM is based on a very large superconducting solenoid with field shaping iron poles that surround both the calorimeter and muon system. This allows the design of a robust high resolution muon system having 5% momentum resolution for 500GeV at 90 degrees with no vertex constraint. In addition, by having no intervening material in front of the calorimeters, precision electromagnetic colorimetry is possible.

The GEM magnet design is not yet optimized for field, radius or length, but presently we are considering a nominal field of $\sim 0.8T$, a diameter of $\sim$ 18m, and a length of $\sim$ 30m. A cut-away view of the magnet, showing the coil assembly, shaping iron end-poles and the central membrane that will hold the detector elements is shown in Figure 1. The magnet has a stored energy of $\sim$ 2 GJ; an operating current of $\sim$ 50KA, discharge time of $\sim$ 2 hours and in an emergency $\sim$ 5 minutes. The GEM design team is from Lawrence Livermore National Laboratory and MIT Plasma Fusion Center.

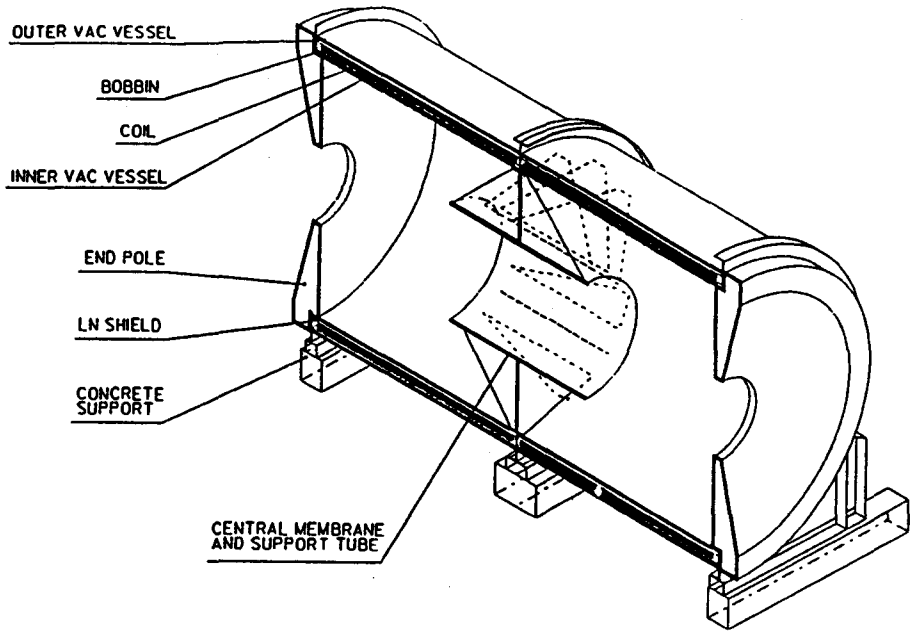
Different conductor designs are presently being considered, but all involve standard niobium-titanium conductor with either copper or aluminum stabilizer. Different liquid helium cooling schemes and manufacturing techniques are being considered. The iron magnet poles are used for field shaping and not for flux return. Designs for a conical snout flux concentration that will improve the resolutions in the forward direction are being considered and I discuss the potential gain in the next section.

One important consideration in this magnet design is the fringe field, both in the experimental hall and at the earth's surface above the detector. The reason we have chosen such a design is the very large cost saving $\sim \$100M$ realized by eliminating the flux return, and the fact that there is considerable experience working around such fringe fields at other magnet facilites (MRI installation, plasma fusion facilities, FNAL IS' Bubble Chamber, etc.). At the earth's surface, if necessary, a plate of $\sim$15cm thickness will be installed

to contain this fringe field. Although special attention to this fringe field is necessary, there are no major envisioned problems for the operation of GEM.

The GEM magnet is not particularly difficult technically, in terms of pushing the state of the art, however, due to its size, it must be constructed at the site, and because it is a critical path item in the GEM construction, a very rapid scheme for manufacturing, assembling and testing is required. The scheduled completion during 1996 requires early availability of surface facilities, where the coils will be wound, and the experimental hall, where the magent will be assembled.

Figure 1. GEM Magnet



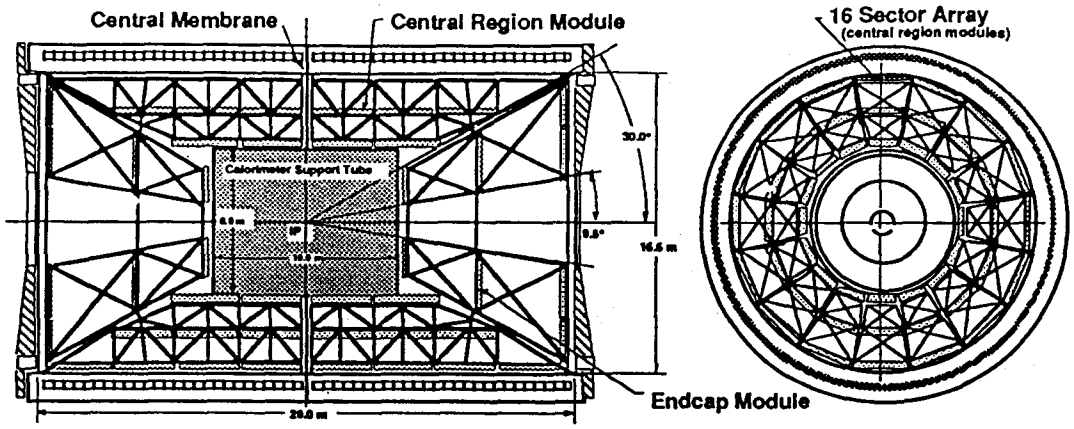
3.0 The GEM Muon System

Muons provide signatures at the SSC for a wide range of important physics, including Higgs production, supersymmetry, new heavy Z bosons, etc. To reach this physics the GEM muon system is designed both for accuracy (eg. $\frac{\Delta P}{P} = 5\%$ for 500 GeV at 90°) and to be robust to the highest luminosities (eg $L{\sim}10^{34}cm^{-2}s^{-1}$) attainable at the SSC.

3.1 Muon System Design Considerations

Muons are identified by penetration through the calorimeter system, also providing a region with low enough rates to enable triggering and momentum measurements, since all measurements are in this well shielded region. Figure 2 shows an overview of the GEM muon system. Muon momentum is measured using the sagitta method in three superlayers between the calorimeter and the magnet. The sagitta is given by the expression, $S = 0.3\ BL^2/8p$ for 90°, where L = path length of the measurement in meters, B = magnetic field in Tesla, and p = momentum in GeV/c. Since the resolution varies with L^2 it is important to make a large radius for the magnet. Such a magnet has been described in Sec. 2.0, where we have made both a large radius ($\sim$ 9 meters) and a strong field ($\sim$ 0.8 - 1.0 T), using a single layer superconducting coil.

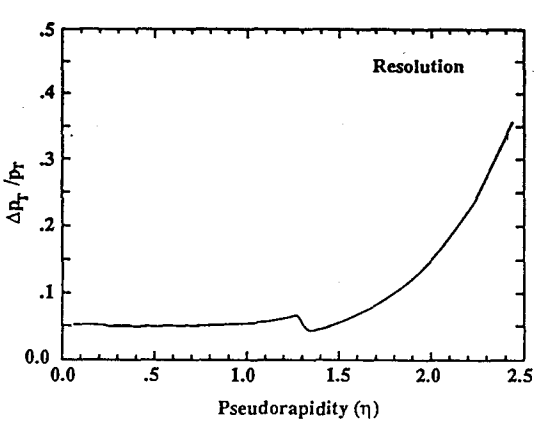
Figure 2. The GEM Muon System

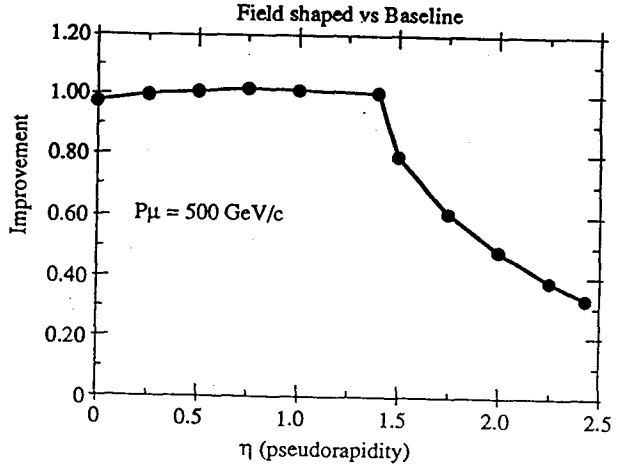


In terms of the measurements of the muon momentum, the resulution is given by, $dp/p = [(ap)^2 + b^2]^{\frac{1}{2}}$, where the first term a, which is a function of muon angle, is determined by the spatial measurement errors (both inherent and alignment). The second term is due to multiple scattering in the middle layer. In practice, at high energies (eg. hundreds of GeV) the first term $(ap)^2$ dominates, while at low energies (eg. below 100 GeV) the second term dominates. It is therefore crucial in the muon system to strive for both high accuracy in position measurements and minimum scattering material. Our studies, based on studying the effects on our resolution for Higg decay (eg. $H \rightarrow 4\mu$), indicate that the middle layer must be $< 10\%$ of a radiation length in order to not degrade the system. For high momentum, the most demanding problem is sign selection for each muon for example from Z^1 decay at the heaviest mass accessible at SSC ($\sim 6TeV/c^2$). This requirement demands single layer resolutions $\sim 100\mu m$ and alignment between superlayers to $\leq 50\mu m$.

Figure 3a shows the design momentum resolution versus polar angle resulting from this muon system and the baseline magnet. In our basic design there are several means of improving the final momentum resolution. The most important of these is obtained by shaping the field in the forward direction by inserting a conical iron field concentrator. Such a field concentrator is now under design and we expect to incorporate it in our final design for GEM. The fractional improvement in momentum resolution that can be expected is shown in Figure 3b.

Figure 3a and Figure 3b. Resolution of Baseline Muon System (a) and Field Shaping Improvement (b).





Another consideration that affects the design of the muon system is chamber occupancy. To keep the rates in the muon region at levels that can be handled, we are presently planning to use a barrel calorimeter of 12λ and an endcap calorimeter of 14λ. Further studies, including beam test results, will be needed to make a final determination of this thickness. Our estimates of rates in the muon system using this arrangement are $< 1 Hz/cm^2$ in the barrel region, while it is $\sim 10^2 Hz/cm^2$ in the inner layer of the forward direction.

3.2 GEM Muon Technologies

The very different demands in the barrel region (large area, precision, low rates) and the end caps (small area, high rates) have suggested different technological solutions. In the barrel region, pressurized drift tubes (PDT) or limited streamer drift tubes (LSDT), seem to meet our requirements. We plan a vigorous R&D program over the coming year to select which of these options is best suited. Neither offer a natural solution for Level 1 triggering on muons, so another technology is required. At present, resistive plate chambers (RPC) are being investigated for providing the beam crossing trigger. In the forward direction, our proposed technology is cathode strip chambers (CSC) which, operating in the proportional mode, will provide both the measurements and the trigger.

For the barrel region, PDT's make an attractive solution. Aligned parallel to the magnetic field and using the fact that the resolution improves as $1/\sqrt{p}$, (p = pressure), the required resolution, robustness, and cost should be attainable. The GEM design uses 3cm Aluminum tubes with $300\mu m$ wall thickness. The difficult engineering problem is to obtain the necessary alignment accuracy. We believe this can be achieved with precision machined end assemblies.

The second option we are investigating for the barrel region is LSDT's. The positioning of the wires will be achieved by accurately machined insulating bridges, which are held against a reference point on the outside of the chamber. The wires will be operated in the limited streamer mode giving large, fast pulses for good drift time measurements. Strips can be used to obtain measurement of the position along the wire, an advantage of this technique.

Neither of the above options provides a natural Level 1 trigger. For this difficult problem, the present effort is to develop a trigger based on RPC's. These chambers, made of bakelight or resistive glass, use an electric field of ~40KV/cm between parallel electrode plates. The readout, by means of pick-up strips insulated from the field electrodes, are fast enough to tag the beam crossing. R&D to determine the viability of employing RPC's for the trigger is underway.

A vigorous R&D and Engineering program is being undertaken during 1992 to determine the final technologies, design and costs. This will include a direct comparison of the performance of different technologies in a cosmic ray test station being assembled at SSC laboratory. I expect their will be considerable evolution in our ideas and design over the coming year, before determining the final muon system.

4.0 The GEM Calorimeter System

One of the primary goals of GEM is to obtain the best electromagnetic calorimeter resolution that can be practically obtained, combined with good resolution for hadron jets and missing E_T. This is motivated by a wide range of physics goals, including the search for the Higgs particle. For the difficult mass region between 80 and 180 GeV, the primary signature is the decay, $H \rightarrow \gamma\gamma$. This is very challenging, due to the large QCD background, and requires both precision resolution and good background rejection. Since the GEM design has the magnet coil outside the calorimeters, there is little intervening material between the interaction point and the electromagnetic calorimeter. This provides the opportunity to do the precision calorimetry necessary for our physics goals.

The resolution of a calorimeter can be expressed as: $\sigma/E = a\%/\sqrt{E} \oplus b\%$, where a is the stochastic term in the resolution, and b is the systematic term. For the crucial $H \rightarrow \gamma\gamma$ search, the importance of a and b is shown in Table 2, where the entrees are the relative time for discovery.

Table 2. Effect of Energy Resolution: Time for $H \rightarrow \gamma\gamma$ discovery, as a function of a and b.

a =	2.0	5.0	7.5	10	15
b = .25	0.63	1.2	1.7	2.2	3.3
b = 0.5	1.0	1.4	1.8	2.3	3.4
b = .75	1.4	1.7	2.1	2.6	3.6
b = 1.0	1.8	2.1	2.4	2.9	3.7

We are considering two different approaches to obtaining the necessary resolution. The first approach is to use a BaF_2 crystal calorimeter, which has the feature of providing a very small stochastic term ($\sim 2\%/\sqrt{E}$), high speed and hermiticity. On the other hand, there is much more uncertainty about controlling the systematic term at the necessary level, particularly due to questions of radiation hardness, but also due to calibration and monitoring problems in this large system. In addition, there is no longitudinal segmentation in this system, a disadvantage for background rejection. The second approach is Liquid Argon/Krypton Accordion calorimeter, which can provide good and demonstrated ability for the systematic term, but it is uncertain whether the necessary accuracy for the stochastic term can be obtained.

We are undertaking a vigorous study of both approaches including a program to make radiation hard crystals and to do beam tests on a prototype matrix for BaF_2; and to study the systematic terms extensive engineering to determine realistic thicknesses, hermeticity, etc. and also a beam test program to study resolution questions for Liquid Argon/Krypton. We expect to make a decision between these two options by Fall '92.

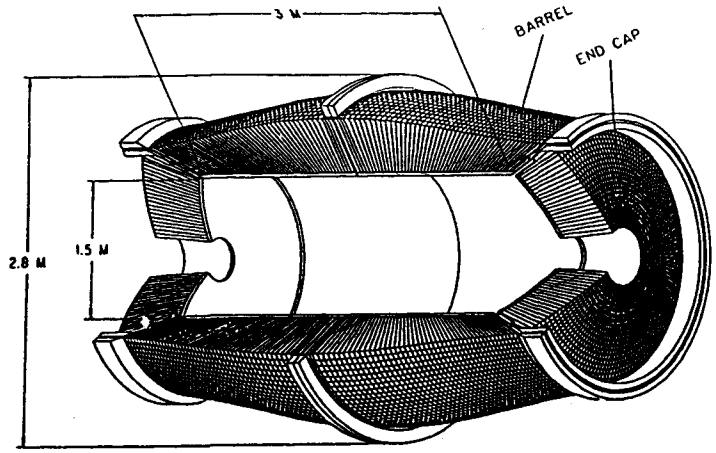
4.1 BaF_2 + Scintillating Fiber Hadron Calorimeter

The conceptual design of the BaF_2 option is shown in Figure 4. The array consists of 15024 crystals (each made from two 25cm pieces) which are housed in a carbon fiber-epoxy structure. The crystals are read out using Hamamatsu UV-selective R4406 phototriodes, which suppress the slow component and operate in $\sim$1 Tesla B-field, as required.

An initial test matrix (7 x 7 crystals) has been developed for beam tests at Fermilab. Results from this test are expected in early 1992. A tentative plan for a second set of beam tests at CERN, using an improved matrix and followed by a scintillating fiber test hadron calorimeter later in 1992 is under consideration.

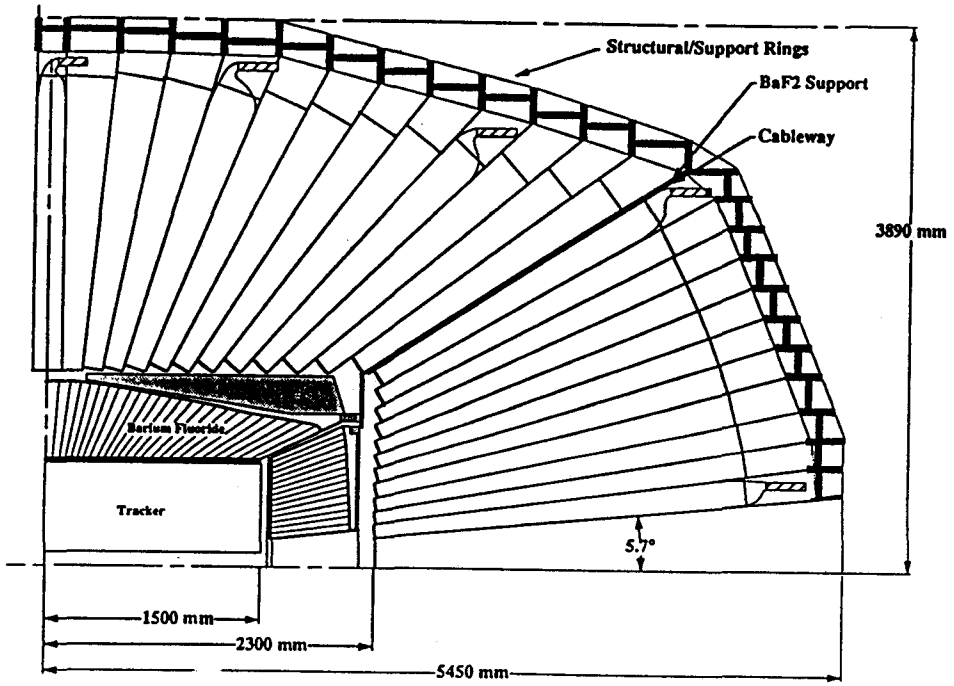
A major issue for the BaF_2 option is whether manufacturable crystals of the necessary radiation hardness can be developed in the time frame necessary to proceed with this option. We have assembled a 'panel of experts' on radiation damage, crystal, technology and other relevant expertise to advise us on whether and how to proceed with this development. We expect their recommendations in February 1992.

Figure 4. BaF_2 Array



For the BaF_2 option we have decided to develope a Spaghetti Fiber Hadron Calorimeter to follow the BaF_2. This choice offers hermeticity, projective geometry and "effective compensation". The combined calorimeters are shown in Figure 5. The spaghetti modules will employ 3mm diameter fibers cast within an absorber matrix of lead and lead/bismuth alloy. Calculations using GEANT indicate that despite the e/h ~ 2 of BaF_2, it is possible to improve the hadron resolution by making e/h ~ 1 in the hadronic calorimeter. Since the e/h can be adjusted in the spaghetti calorimeter design, we are pursuing this both in calculations and in our plans for a beam test behind BaF_2.

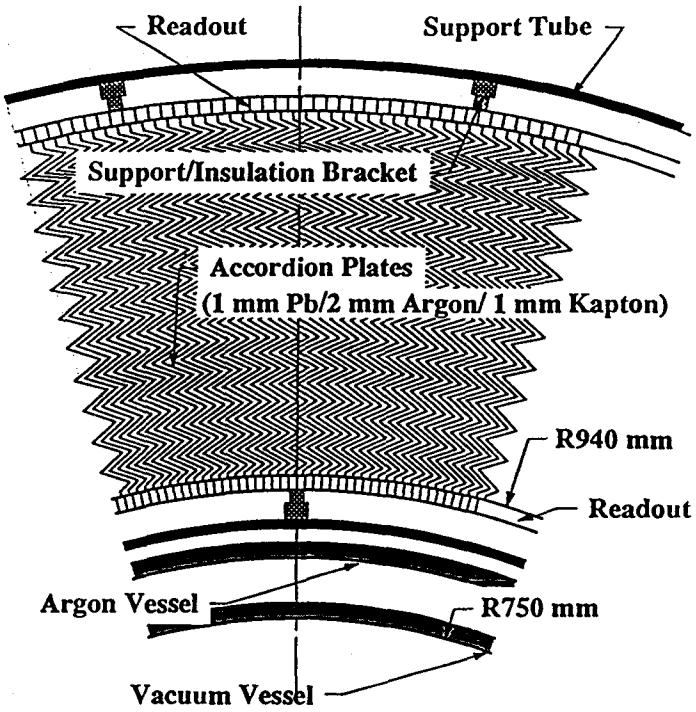
Figure 5. The GEM BaF_2 + Hadron Spaghetti Option.



4.2 Liquid Argon/Krypton Accordian Calorimeter

Liquid Argon is an attractive option for our calorimetry system due to its radiation resistence, uniformity and ease of calibration. In addition, for liquid-argon calorimeters, there exists extensive experience with large systems. A recent development of the so-called accordian geometry appears very attractive for our application in GEM (Figure 6). It allows good hermeticity, and faster readout due to lower inductance and capacitance.

Figure 6. Liquid Argon Hadron Calorimeter EM Accordion Plates

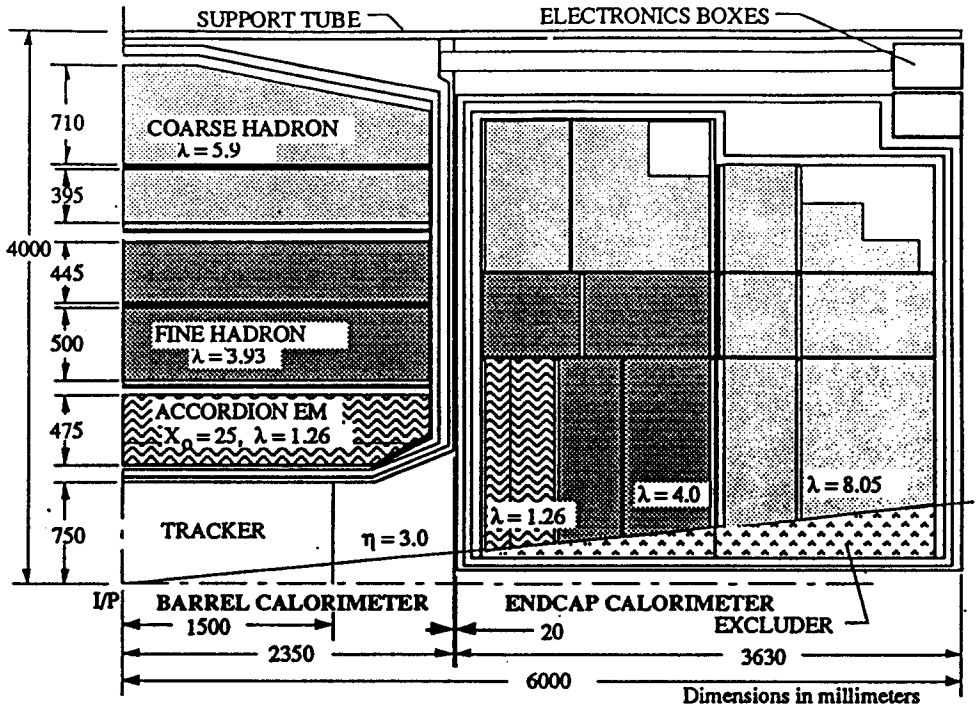


Results from a test calorimeter at CERN have been quite impressive giving electron energy resolution of $(10.1\pm0.4\%)/\sqrt{E}\oplus 0.2\pm0.2\%$; linearity of 1% from 30 - 200 GeV; position resolution of $4.4\text{mm}/\sqrt{E}$; and angular resolution of 6.1 mrad at 120 GeV using the longitudinal information.

The primary goal of the R&D program during 1992 will be to attempt to improve the resolution of this technique to the level $(7\%/\sqrt{E})$, which we have established as our design goal for GEM. We are approaching this problem in two ways. The first approach is to improve the sampling by using 1mm (instead of 2mm) absorber plates. A GEANT simulation indicates this will give the required resolution, however the mechanical problems of forming a calorimeter with these thin plates must be solved and a beam test performed to determine the resolution. The second approach, is to replace Argon with Krypton using standard 2mm plates. This, also, should improve the resolution to the design value.

Our present plan in this option is to use an integrated calorimeter, that is to make a liquid argon hadronic section to follow the Liquid Argon/Krypton electromagnetic calorimeter. However, we may still consider options using a scintillator based hadron calorimeter. For the liquid argon hadron calorimeter a plate geometry will be used with longitudinal sampling (four sections), having fine and course sections as shown in Figure 7.

Figure 7. Liquid Argon/Krypton Calorimeter Arrangement.



Forward Calorimetry

GEM forward calorimetry is less well developed at this time. The goal is to measure P_T of particles near the beam pipe, thereby determining missing P_T due to neutrinos. These signatures will be sought for missing P_T of 100 GeV/c or greater.

The forward calorimeter must be integrated with the beam pipe, end cap calorimeter, muon chambers and magnet flux concentrator. We are studying configurations for the forward calorimeter integrated with these other systems. Preliminary work indicates that we can obtain the required resolution at 6.5m from the interaction point. Therefore, we are considering designs integrated or near the end cap calorimeters. Technologies under consideration for this calorimeter include liquid Argon/Tungsten Plate, High Pressure Gas Tubes and Liquid Scintillator Spaghetti.

5.0 The GEM Central Tracker

The main goal of the central tracker is to support the primary objectives of GEM, namely detection of gammas, electrons and muons at high P_T. In order to obtain our physics goals this leads to the following requirements:

1) Identification of the primary event vertex in order to reduce pileup problems.
2) Separation of electrons and gammas by identifying whether a charged track accompanies an electromagnetic shower.
3) Provide track information for isolation cuts.
4) E vs p comparision for electron-hadron separation.
5) Comparison of P_μ (central) with P_μ (outside) for background rejection.
6) Determination of the electron sign to 400 GeV/c.

It is also our aim that these capabilities survive to luminosity of $10^{34}cm^{-2}s$, if possible. In addition, we plan to incorporate as much as is practical and affordable other features like: full event reconstruction of charged tracks; secondary vertex finding; and low momenta tracking. Table 3 gives the design parameters for our tracker.

Table 3

Design Parameters for GEM Central Tracking

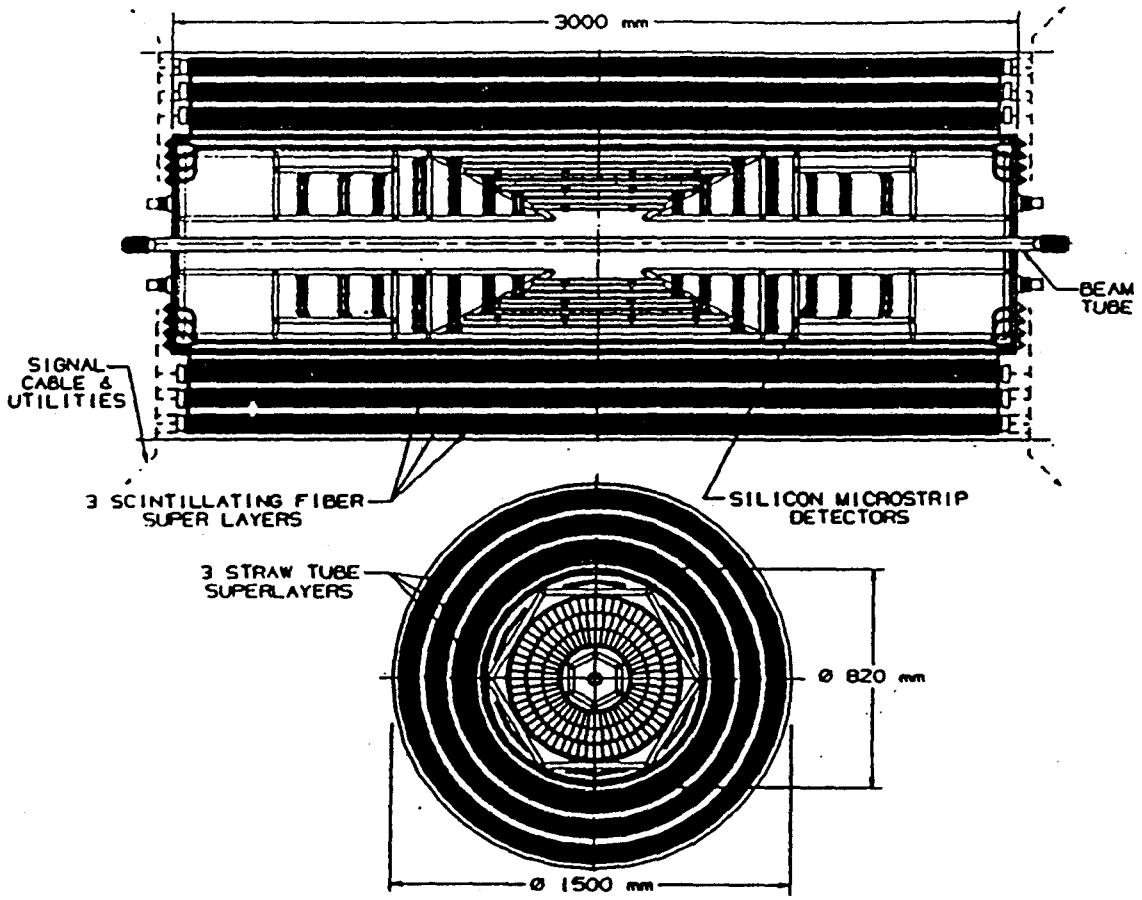
Outer Radius	70 cm
Length	±150 cm
Rapidity Coverage	$\|\eta\| \leq 2.5$
Magnetic Field	0.8T
Occupancy	
at $\mathcal{L}= 10^{33}\ cm^{-2}s^{-1}$	$\leq 1\%$
at $\mathcal{L}= 10^{34}\ cm^{-2}s^{-1}$	$\sim 3\%$
2σ charge separation	$p \lesssim 400$ GeV/c
Momentum Resolution at 90°	
at high momenta	$\Delta p/p^2 \sim (1 \text{ to } 3) \times 10^{-3}$
(measurement limited)	$(GeV/c)^{-1}$
at low momenta (multiple scattering limited)	$\Delta p/p \sim 2$ to 4%
Vertex Resolution	
along beam direction	$\delta z \sim 1$ mm
impact parameter	$\delta b \sim 20\ \mu$m above 10 GeV/c

The baseline GEM central tracker consists of an inner section which is a silicon tracker and an outer section with both straw tubes and scintillating fibers. It is shown in Figure 8.

The silicon section consists of six layers, each having back to back single sided silicon sensors with a 5 mrad stereo angle. The pairs give space points with resolution of 10μm in r-ϕ and 3mm in r-ϕ and 300μm r-z accuracy. This inner tracker section is 2.5m long and extends to 40cm radius. The straw/fiber section consists of three superlayers, each providing a track stub measurement with 25μm r-z accuracy.

At this moment, we are seriously considering an alternative to this baseline tracker that will better match the GEM goals described above (Table 3). In particular, the calculated occupancy in the baseline straw system is 10%, luminosity $\sim 10^{33} cm^{-2} s^{-1}$ which is certainly an underestimate. This means that the baseline tracker has no possibility at yet higher luminosity and even has problems at standard luminosity.

Figure 8. Baseline Central Tracker



This occupany problem has motivated us to consider, instead, an outer tracker consisting of Interpolating Pad Chambers (IPC), which, because they measure space points will have much lower occupancy, even at luminosity of $10^{34} cm^{-2} s^{-1}$. Similar pad chambers have been used in E-814 at the AGS.

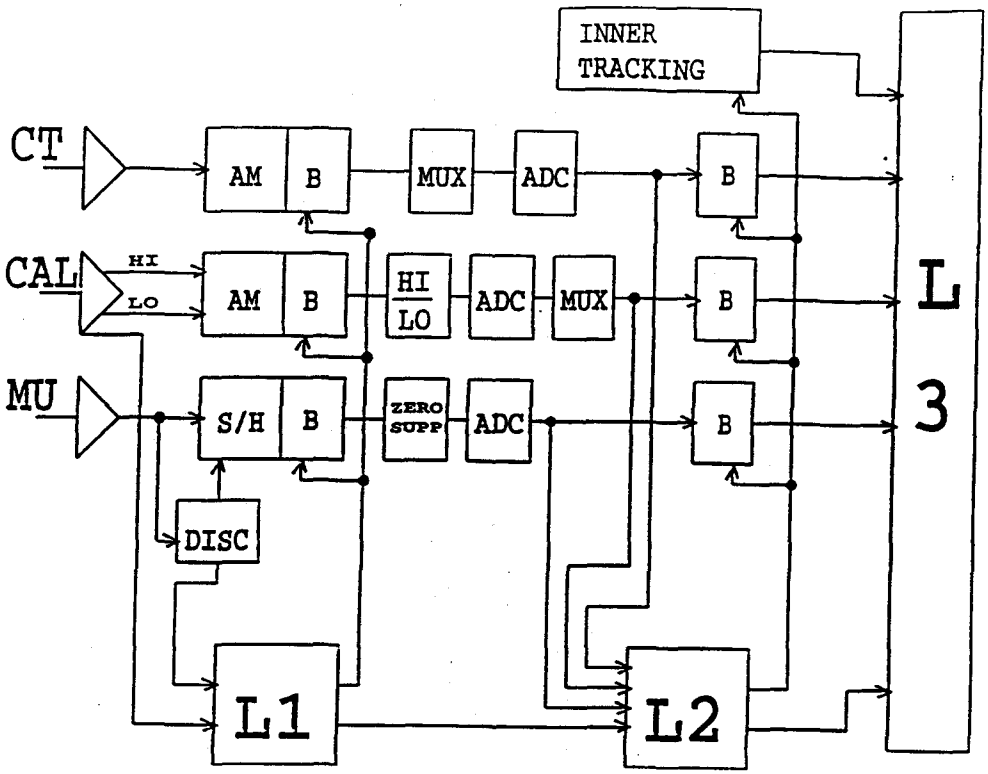
Our present pad chamber system is very preliminary and still requires a detailed mechanical and electrical design, as well as realistic simulation studies. However, our present thinking is to employ three such layers of pads of three chambers each of uniform $\Delta y \times \Delta \phi = 0.001$ in all parts of the tracker. This gives 300,000 pads total. A preliminary analysis of the readout, multiplexing and perchannel costs are encouraging.

Further work is proceeding, especially on both mechanical alignment and whether the total amount of material can be kept at a tolerable level from the standpoint of both multiple scattering and secondary interactions. We are not yet far enough advanced to consider changing from our baseline tracker, but expect to evaluate whether to adopt this option in early 1992.

6.0 The GEM Trigger and Data Acquisition System

The trigger and data acquizition for GEM follows the usual three-level approach shown in Figure 9, with rates summarized in Table 4.

Figure 9. The GEM three-level trigger arrangement.



The level 1 trigger, a synchronous, pipelined system, is based on a reduced set of calorimeter and muon signals - (eg. calorimeter tower sums digitized and compared with pre-set thresholds, muon trigger primitives from hit patterns, etc.). A trigger 1 decision will be determined for each beam crossing.

Table 4.

Design goals for the GEM Trigger/DAQ System. Output rates are for operation at $\mathcal{L} = 10^{33}$ cm^{-2}s^{-1}

GEM Trigger/DAQ Design Goals				
Lvl.	Max Av. Rate In	Rate Out	Latency	Comments
1	62 MHz	10 kHz	3 μs	Synchronous, Pipelined
2	100 kHz	300 Hz	100 μs	Asynchronous, Monotonic
3	3 kHz	10 Hz	—	CPU Ranch

The level 2 trigger, asynchronous and pipelined, will use digitized data for more refined triggering strategies. For example, in the case of muons a momentum determination will be possible. Level 3 will be carried out by a set of processors using data from the entire detector.

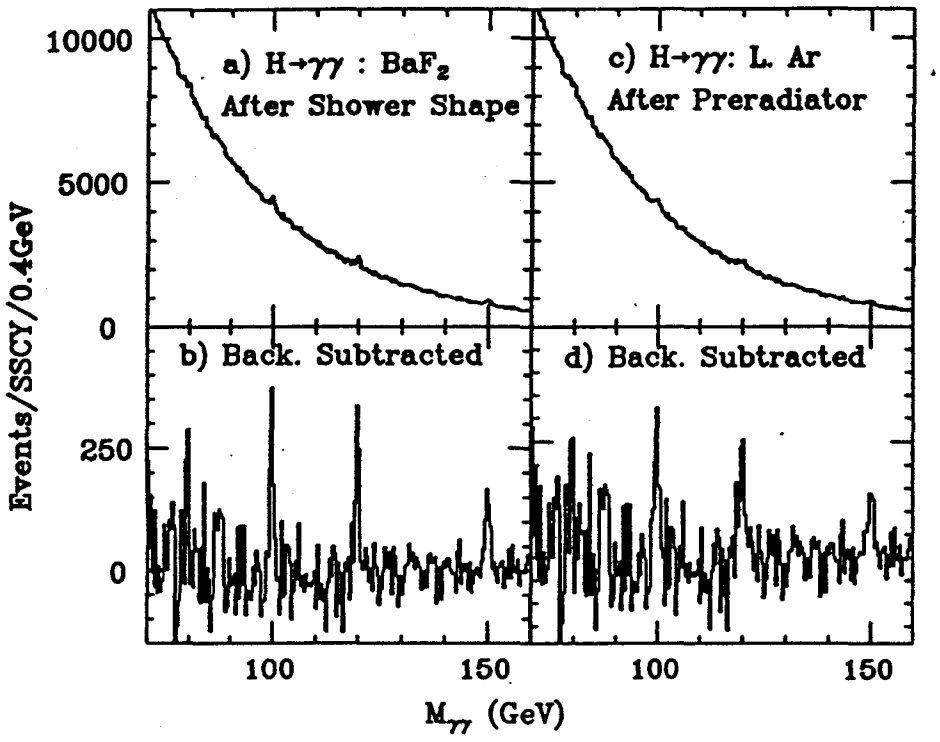
7.0 The GEM Physics Performance

I will only briefly describe some physics with GEM. A more detailed presentation is available in the GEM LOI. In general, we have designed the detector to discover and study electroweak symmetry breaking, the origin of flavor and other physics requiring high precision measurements of gammas, electrons and muons. In addition, we have concentrated on physics requiring high luminosity ($L \approx 10^{34} cm^{-2} s^{-1}$) and signatures from missing E_T.

In this brief report, I will only address the question of discovering the Higgs boson, perhaps the strongest motivation for the SSC and a good illustration of the power of the GEM detector.

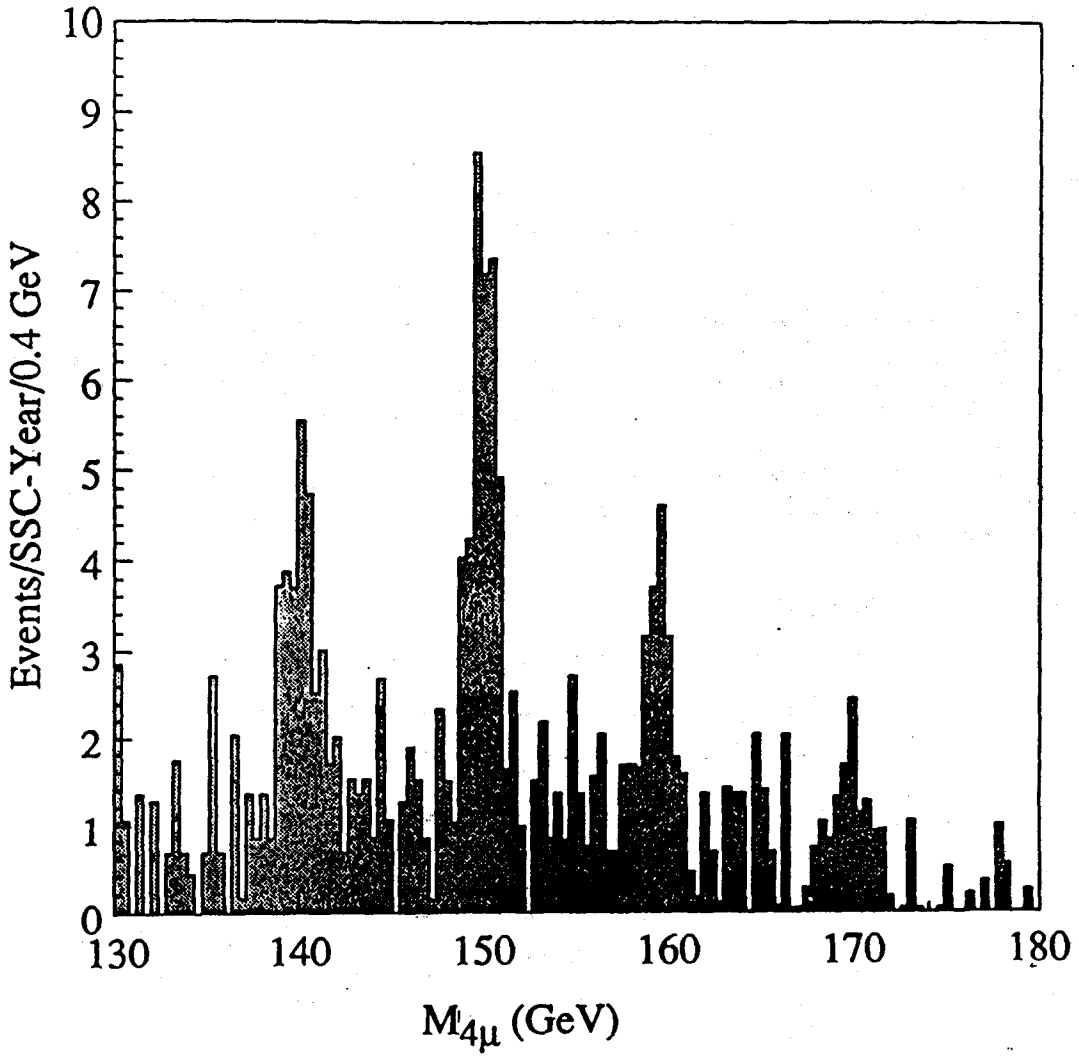
The most difficult region to observe the Higgs is if the mass is below the mass of twice the Z°. In this region, 80 - 180 GeV the most attractive reaction to pursue appears to be to detect the decay $H \rightarrow \gamma\gamma$. However, because of the large QCD background, this requires both precision calorimetry and good background rejection. Therefore, it makes a good flagship to evaluate the performance. Figure 10 shows the ability of GEM to detect this decay mode for several different masses in this range and for both calorimetry options. The upper graphs include the QCD background, and the lower illustrate the signal for various Higgs masses after backgound subtraction.

Figure 10. Higgs $H \rightarrow 2\gamma$ in GEM.



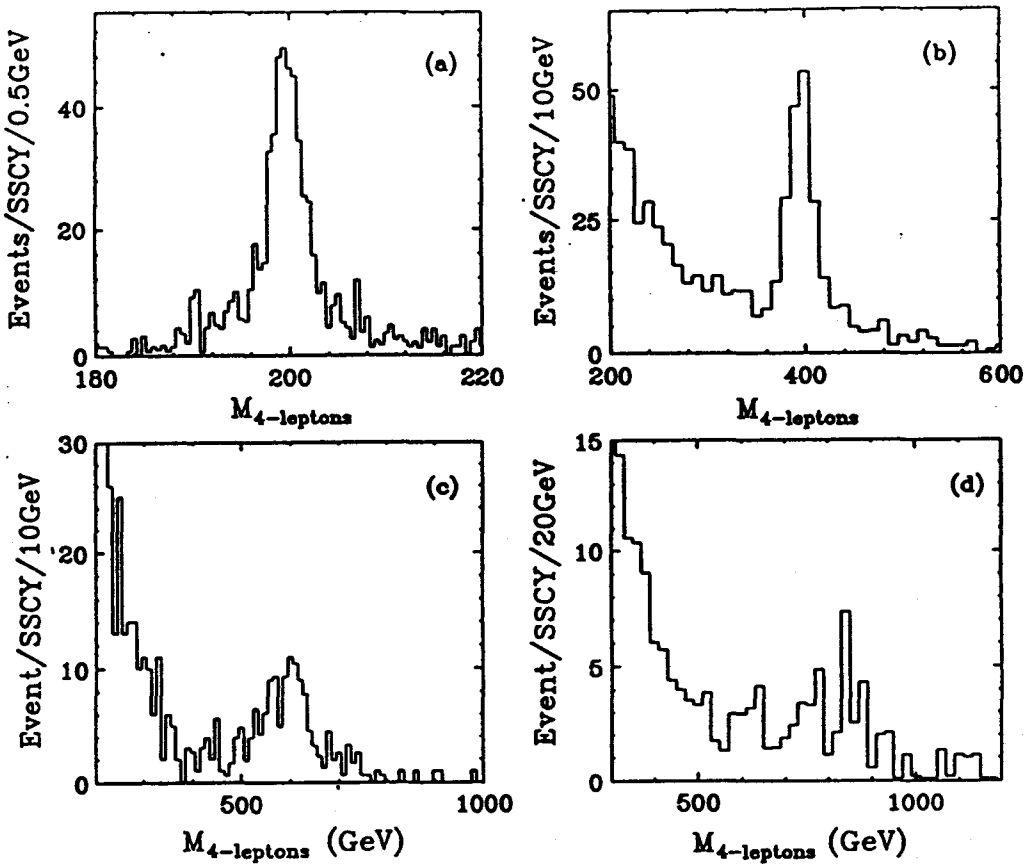
Near the mass of 2Z's (~ 140 - 180 GeV) the best decay mode becomes $H \rightarrow ZZ^* \rightarrow$ 4 leptons. Figure 11 shows this signal in the GEM detector for $H \rightarrow \mu^+\mu^-\mu^+\mu^-$. Of course, the Higgs can also be detected in the modes $H \rightarrow ZZ^* \rightarrow e^+e^-\mu^+\mu^-$ or $H \rightarrow e^+e^-e^+e^-$. GEM, because of its excellent electromagnetic calorimetry has good signals in all these channels.

Figure 11. Higgs $H \rightarrow ZZ^* \rightarrow \mu^+\mu^-\mu^+\mu^-$.



For the Higgs from 200 - 800 GeV, the signal is very clean and easy to detect in any SSC detector, except for the highest energy where the rate is low and the Higgs has become broad. Figure 12 shows the detection of the Higgs in this region for GEM, including backgrounds. At the highest energy $\sim$ 800 GeV, where the rates are low, it is necessary to either run at higher luminosities (eg. $L \sim 10^{34} cm^{-2} s^{-1}$ to obtain more statistics or to also measure the mode H $\rightarrow l^+l^-jj$.

Figure 12



8.0 Conclusions

In the six months since the GEM detector collaboration was formed, we have made good progress in defining the concept for GEM and the technologies we will employ. Some final technological choices (eg. e-m calorimetry, barrel muon tracking and forward calorimetry) will take further R&D over the coming year.

We feel confident from the work we have done that a powerful detector with excellent discovery potential and complementary to SDC can be built on time and within the PAC guideline of $500M. It will take a lot of hard work and good discipline, but we are prepared to do that!

SDC

T. Kondo

S D C

*S*olenoid *D*etector *C*ollaboration

1991.10.15

T.Kondo (KEK)

1991 Symposium on the
Superconducting Super Collider Laboratory
at Corpus Christi, Texas
October 13-17, 1991

SDC MANAGEMENT

Spokesperson:	G. Trilling (LBL)
Deputy Spokespersons:	G. Bellettini (Pisa)
	D. Green (Fermilab)
	T. Kondo (KEK)
Technical Manager:	M. Gilchriese (LBL)
Chairman, Institutional Board:	T. Kirk (ANL)

SDC Executive Board

R. Amendolia (Pisa)	J. Elias (Fermilab)
S. Errede (Illinois)	G. Feldman (Harvard)
E. Gabathuler (Liverpool)	K. Kondo (Tsukuba)
A. Maki (KEK)	S. Mori (Tsukuba)
Y. Nagashima (Osaka)	T. Ohsugi (Hiroshima)
R. Orr (Toronto)	L. Price (ANL)
R. Ruchti (Notre Dame)	A. Seiden (U.C.S.C.)
J. Siegrist (SSCL)	M. Strovink (LBL)
R. Thun (Michigan)	



SDC Technical Board

K. Amako (KEK)
G. Bellettini (Pisa)
D. Bintinger (SSCL)
M. Edwards (RAL)
J. Elias (Fermilab)
W. Ford (Colorado)
I. Gaines (Fermilab)
D. Green (Fermilab)
R. Kephart (Fermilab)
A. Lankford (U.C.I.)
S. Mori (Tsukuba)
L. Price (ANL)
A. Seiden (U.C.S.C.)
W. Smith (Wisconsin)
G. Trilling (LBL)
H. Williams (Pennsylvania)
A. D. Baden (Maryland)
J. Bensinger (Brandeis)
M. Campbell (Michigan)
K. Einsweiler (LBL)
G. Feldman (Harvard)
W. Frisken (York)
M. Gilchriese (LBL)
R. Hubbard (Saclay)
T. Kondo (KEK)
A. Maki (KEK)
T. Ohsugi (Hiroshima)
J. Proudfoot (ANL)
J. Siegrist (SSCL)
R. Thun (Michigan)
Y. Watase (KEK)



COLLABORATION INSTITUTIONAL MEMBERSHIP

U.S.A.	49 institutions including 6 national labs
Canada	6 institutions including 1 national lab
China	2 institutions
Japan	17 institutions including 1 national lab
Western Europe	7 institutions including 2 national labs
U.S.S.R.	7 institutions including 1 international lab
Eastern Europe	4 institutions
Israel	1 institution

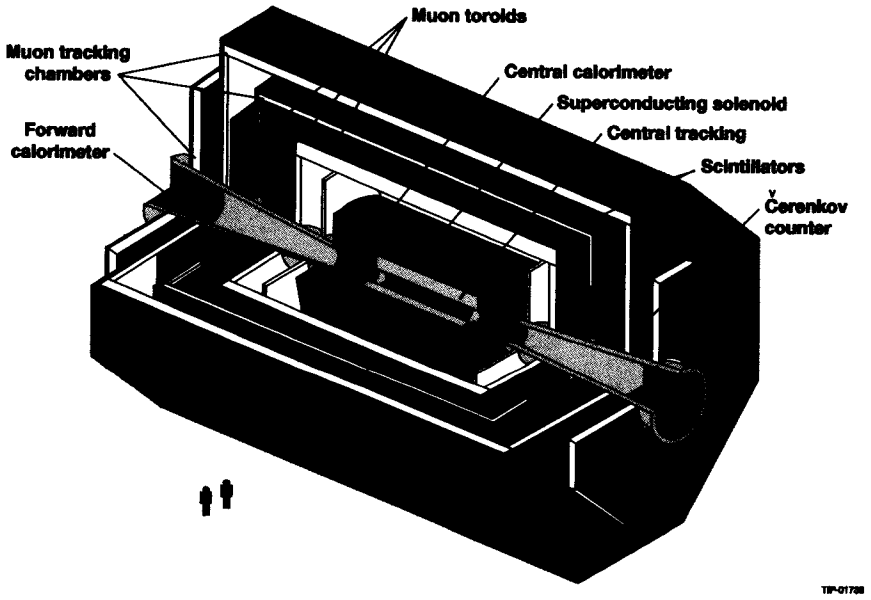


SDC Detector Concepts

- **a general purpose detector with**

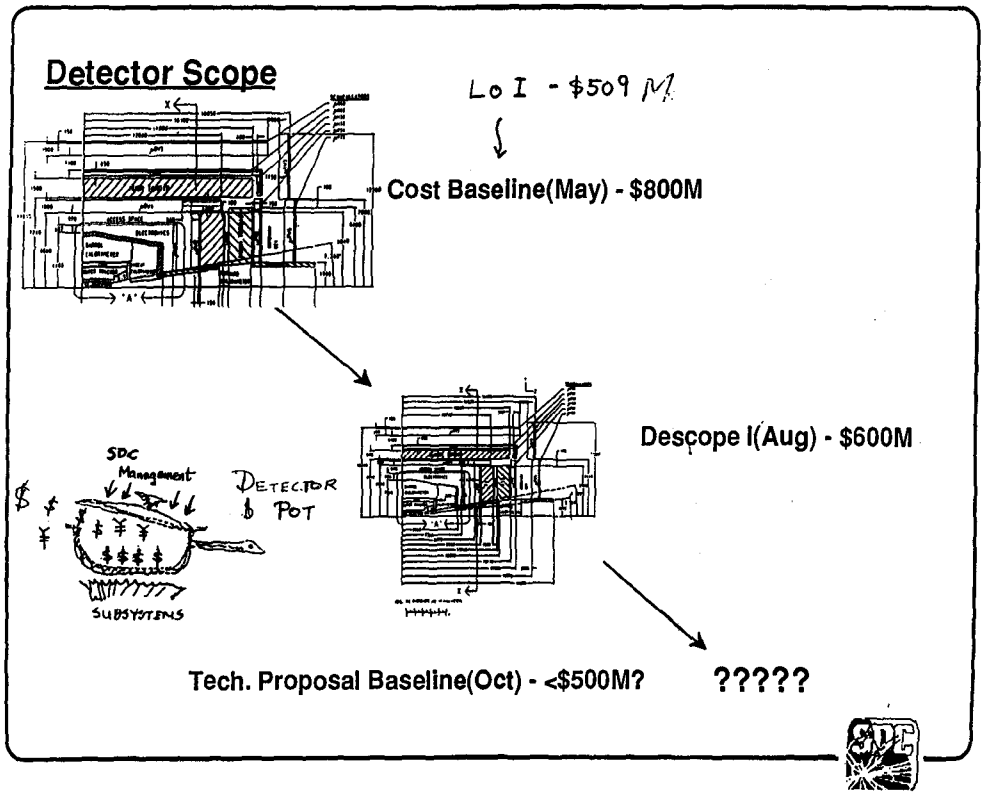
  solenoid field
  central tracking
  hermetic calorimeter
  e, μ identification and measurement
  vertex detection

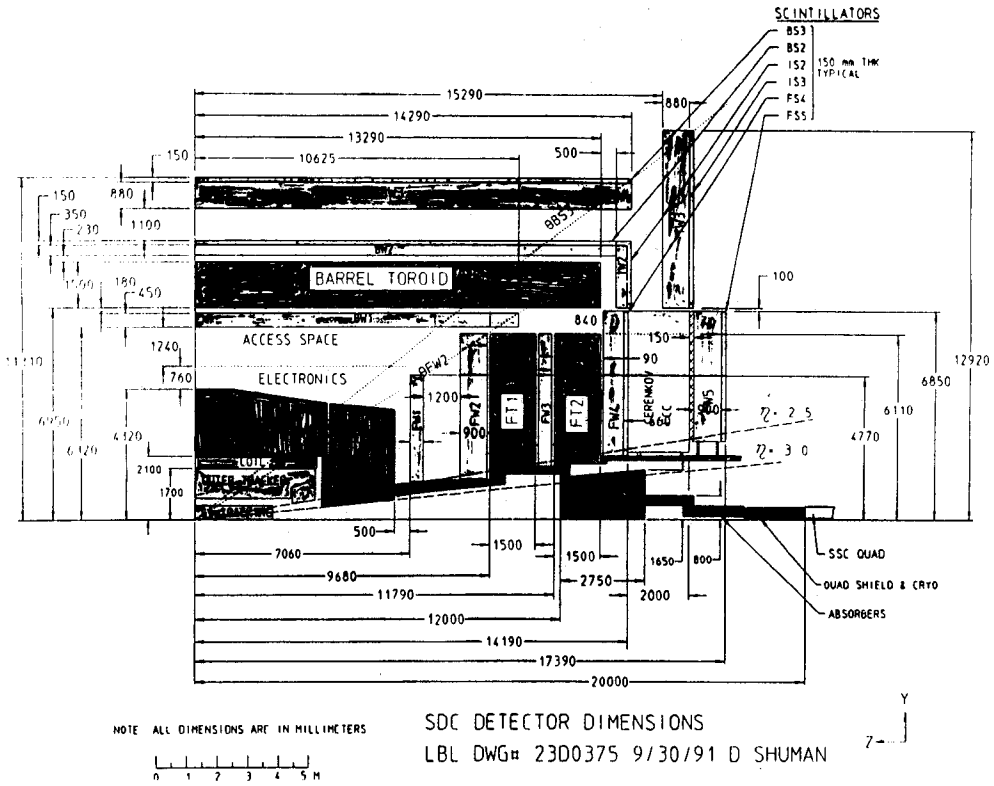
- **fully functional at 10^{33} $cm^{-2}s^{-1}$**
  reduced functionality at higher luminosity



SDC meetings

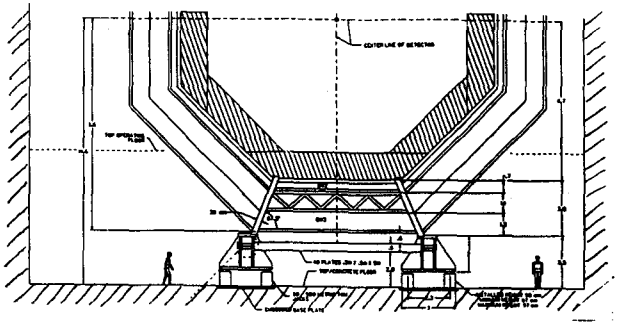
1989	**9**	**Fermilab**	**solenoid detector**
	11	**ANL**	
	12	**Fermilab**	**SDC formation**
1990	**1**	**LBL**	**(calorimeter)**
	3	**SSCL**	
	5	**SSCL**	
	7	**Snowmass**	
	8	**Fermilab**	
	9	**SSCL**	
	11	**LBL**	
1991	**1**	**SSCL**	
	2	**ORNL**	**(tracking wksp)**
	3	**ANL**	
	5	**KEK**	
	6	**SSCL**	
	8	**LBL**	
	9	**ORNL**	
	11	**SSCL**	
1992	**1**	**Pisa**	
	2	**SSCL**	
	4	**Fermilab**	
	5/6	**KEK**	

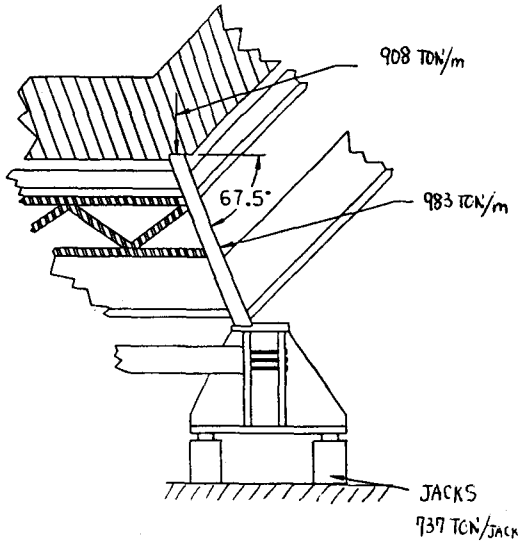


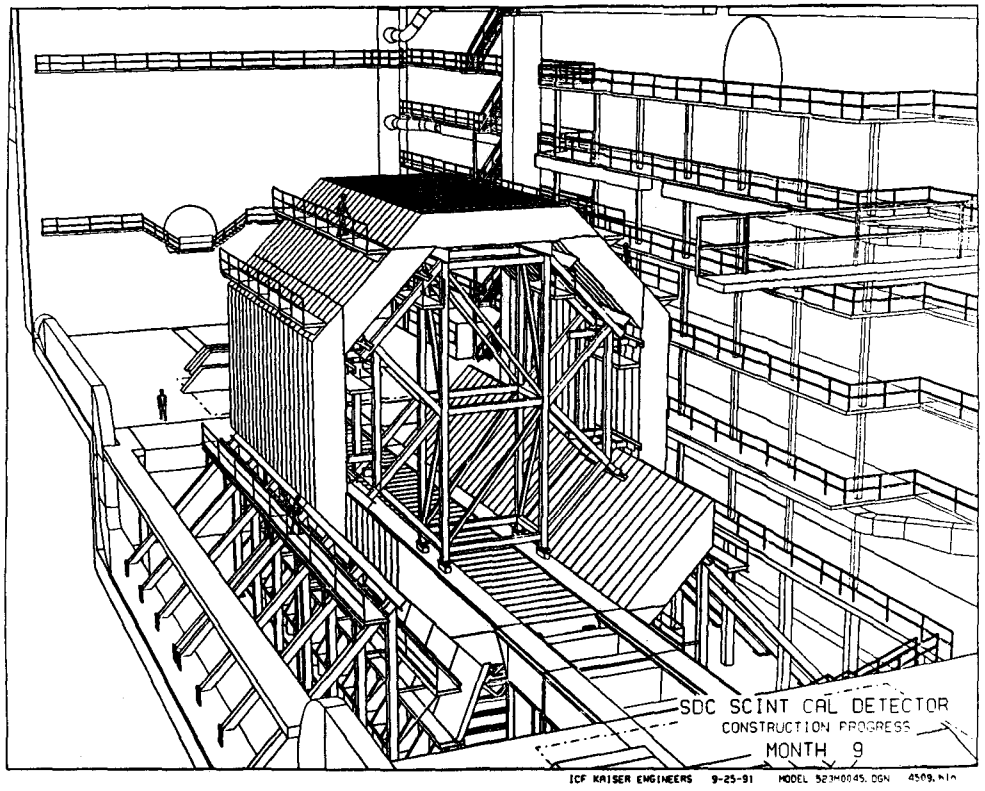


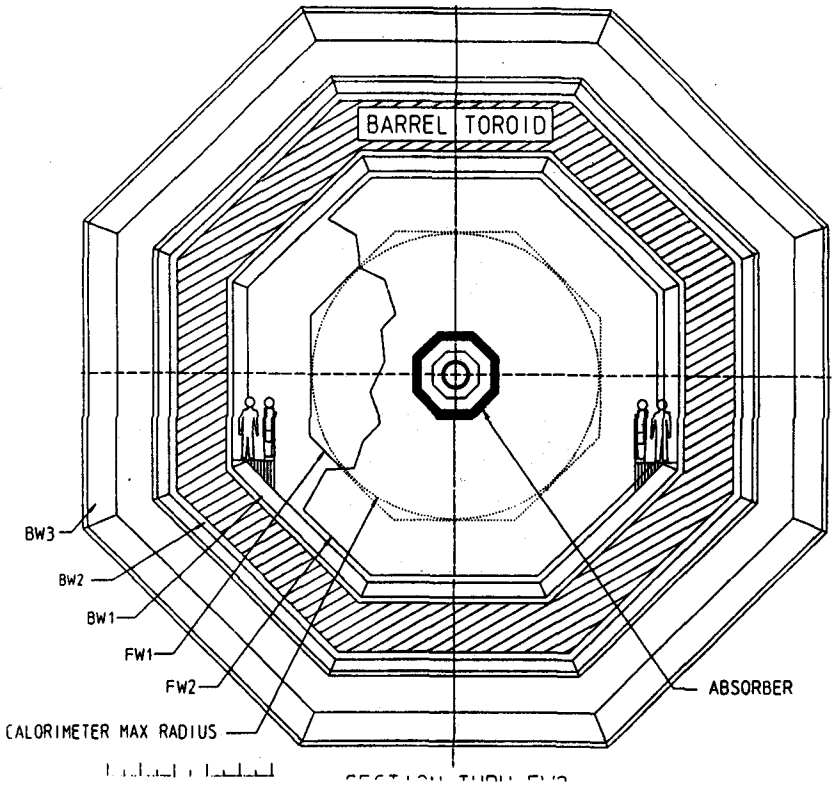
Progress on Detector Integration

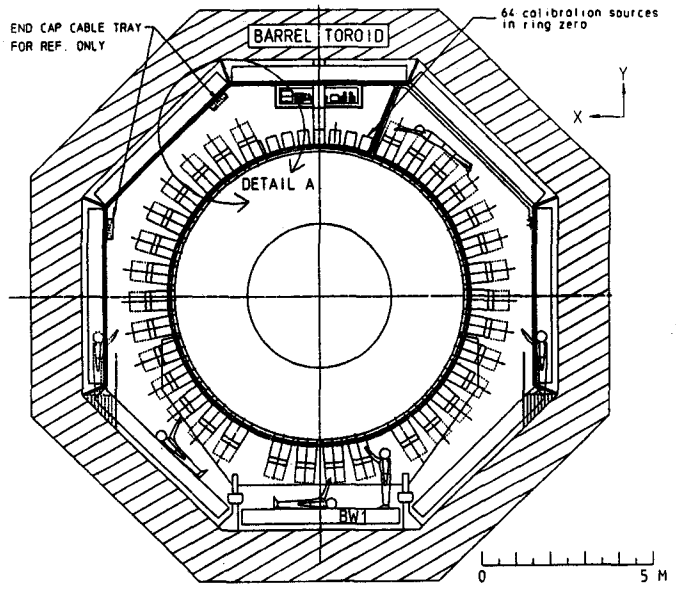
- **Radius of tracking volume is fixed to 170 cm.**
- **Access capability to the calorimeter and on-detector electronics without moving any heavy objects is maintained.**
- **Utilities (cryogenics, cables, cooling water,.....) are taken into account.**
- **Construction scheme of the muon iron toroids is fixed including toroid supports.**
- **Installation procedures are examined in detail.**
- **Hall parameters are being fixed.**




908 TON/m
67.5°
983 TON/m
JACKS
937 TON/JACK

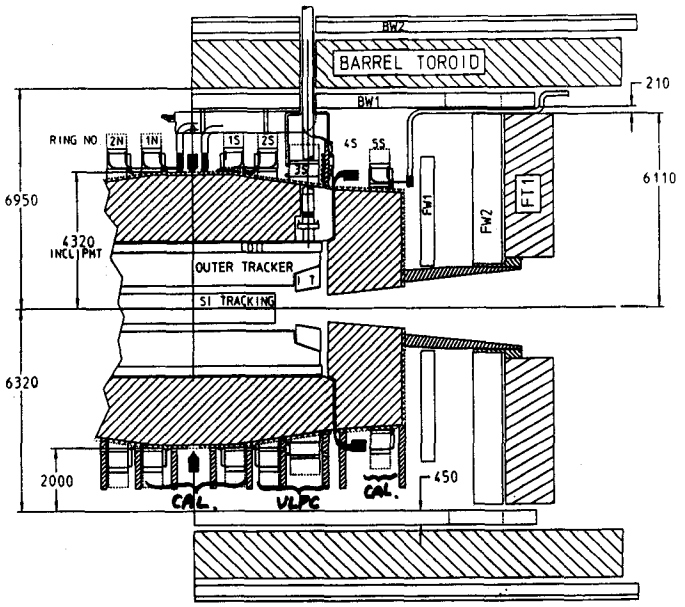

SDC SCINT CAL DETECTOR
CONSTRUCTION PROGRESS
MONTH 9
ICF KAISER ENGINEERS 9-25-91 MODEL 923M0045.DGN 4509.A1A





RINGS 1 AND 2 32 crates

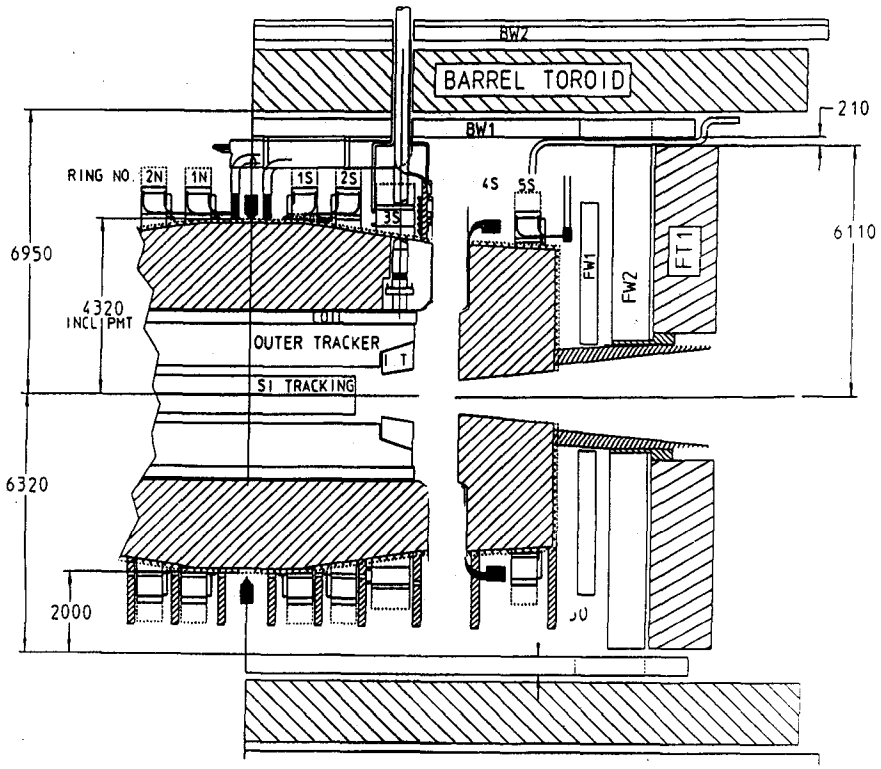
SDC CALORIMETER/TRACKER
CRATE ARRANGEMENT WITH VLPCs. MAX CRYDSTACK OPENING
10/8/91 LBL DWG NO. 23D0345 Y MINAMIHARA
filename:~mhara/hoff/ecl_crate_lo_10_4_91



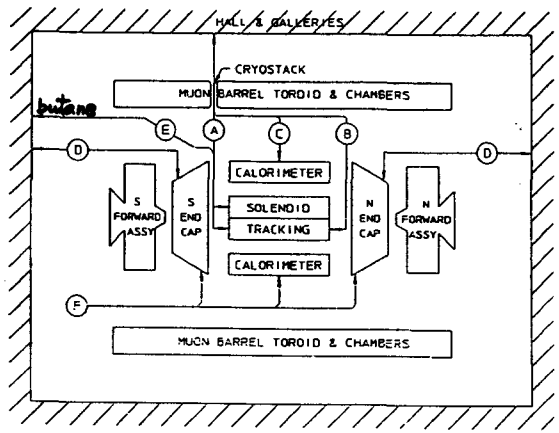
SECTION SHOWING OCTANT 1 CABLEWAY

SDC CALORIMETER/TRACKER
CRATE ARRANGEMENT WITH VLPCs, MAX CRYOSTACK OPENING
10/8/91 LBL DWG NO. 23D0345 Y.MINAMIHARA
filename -mhoro/hoff/sci_crate_lo_10_4_91

0 5 M
NOTE: ALL DIMENSIONS ARE IN MILLIMETERS



CABLE & PIPING ROUTES



A1: SCHEMATIC DIAGRAM OF CABLE & PIPING ROUTES
(with maximum use of the cryostack)

Route	Via Octant	Description of services
A	.....1. cryostack	.....Solenoid, all services.
		Silicon tracker, all except butane pipe (see E).
		Straw or Fiber tracker, all services.
		Gas microstrip, all services.
B	.....1. cryostack	..... Same as A except no solenoid services.
C	.....1. cryostack	.....Calorimeter and internal crate services, except cooling water (see F
D	.....7. South	.....South endcap, all services except cooling water (see F).
	8. North	.....North endcap, all services except cooling water (see F).
E	.....7. South	.....Butane for silicon tracker.
F	.....3. South	.....Cooling water for all crates

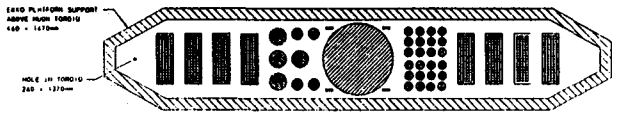


FIGURE 1 - MINIMUM UTILITIES VIA THE CRYO STACK

SDC DETECTOR
CRYO STACK SECTION
9/24/91 T. NISHIHARA

NOTE: ALL DIMENSIONS ARE IN MILLIMETERS

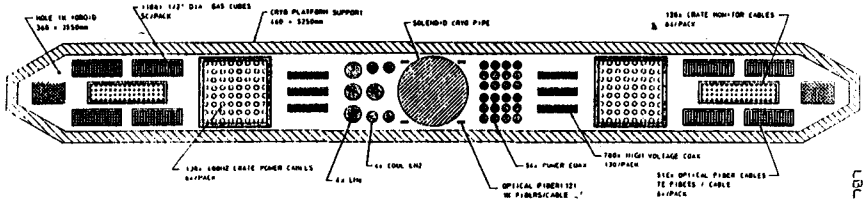
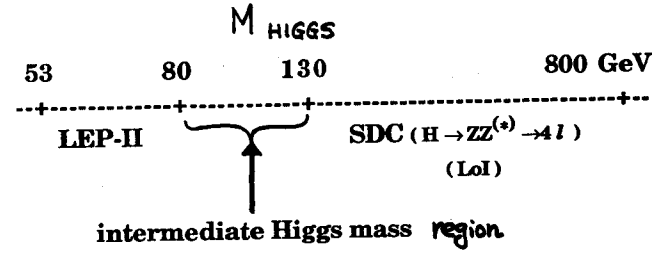


FIGURE 2 - ALL CALORIMETER BARREL & CRACKER UTILITIES VIA THE CRYO STACK

A3

Q1 : How good the EM Cal should be?

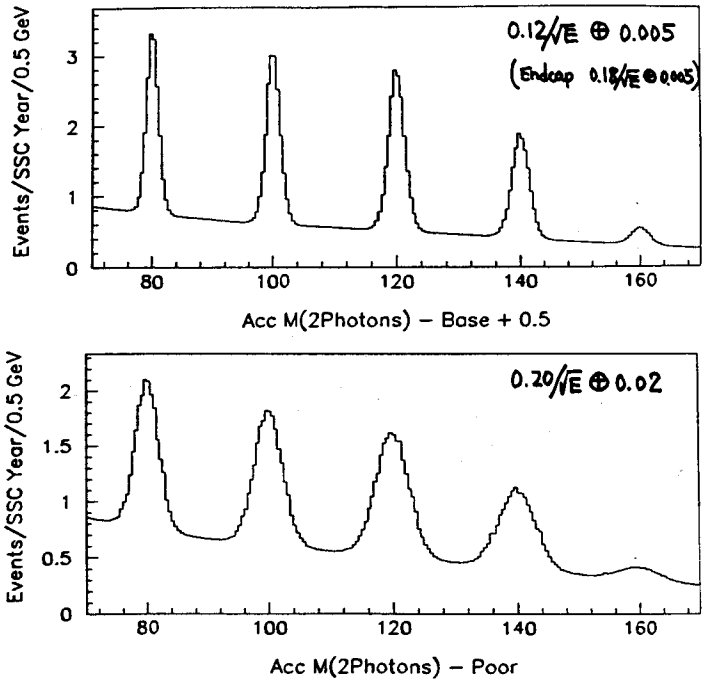
A1 : Look for Associated Higgs Production at 80<M_{Higgs}<140 GeV



- **$H \to \gamma\gamma$ is difficult in SDC**
  - **huge QCD background ($q\bar{q} \to \gamma\gamma$, $gg \to \gamma\gamma$)**
  - **huge π^0 production**

- **W+H, $H \to \gamma\gamma$**
  - **10^{41} cm^{-2} will make the peak clear (LoI)**

- **$gg \to t\bar{t}$ + H, $H \to \gamma\gamma$**
  - **cross sections ~ 5 x (W+H)**
  - **requires isolated leptons + 2 photons**



Conclusion :

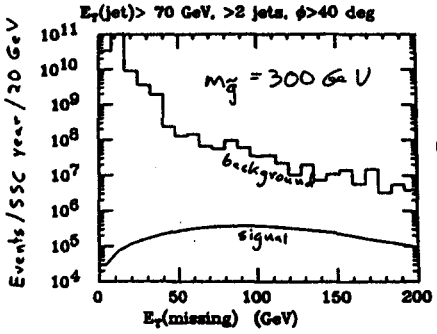
important to have a good EM calorimeter

good : $\frac{10\%}{\sqrt{E}}$ ● **0.25 %**

poor : $\frac{20\%}{\sqrt{E}}$ ● **2%**

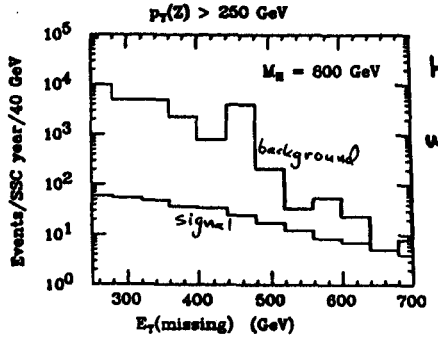
Q2 : Is Forward Calorimeter can be Delayed?

$(3<|\eta|<5)$



$\tilde{q}$ search

without FC



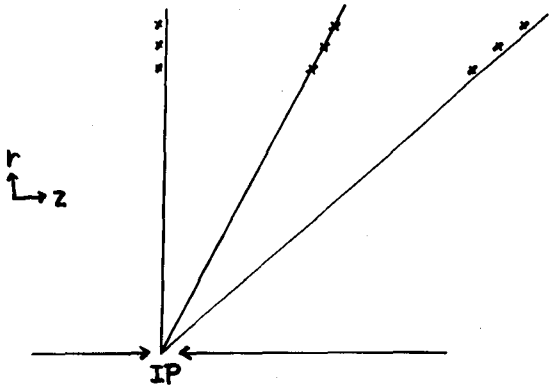
$H \to ZZ \to \ell\bar{\ell}\nu\bar{\nu}$

without FC

A2 : No !

Parameter	Requirement	Model A	Model B
EM allowed cracks	< 5 – 10%	~ 0	1.5%
holes $/\eta/ < \eta max$		1.5%	1.5%
Total electron acceptance	> .9	> 98%	> 97%
Energy Resolution			
EM stochastic term	14-20%/$\sqrt{E_T}$	12	13.5
EM constant term	< 1 – 2%	ok	ok
HAD stochastic term	50-75%/$\sqrt{E_T}$	65	60
HAD constant term	< 4%	< 4	2
Time stability	< 1% after correction	ok	ok
e/h response	< 1.3	< 1.2	1.0-1.05
Spatial uniformity			
EM	< 5% loss	< 2%	< 2%
HAD		< 5%	< 5%
Dynamic range			
EM	20 MeV-2 TeV	30 MeV	30 MeV
HAD	50 MeV-5 TeV	60 MeV	60 MeV
Time resolution			
EM	$\sigma \sim 5nsec, E_T > 15$	< 2nsec	< 2 nsec
HAD	$\sigma \sim 5nsec, E_T > 100$	< 2nsec	< 2 nsec
Signal peaking time	< 200 nsec	~ 10nsec	~ 10 nsec
Baseline rest.	100 nsec < τ < 6μ sec	~ 30nsec	~ 30 nsec
Noise	< 5 GeV, Δ R=.3	0	0
Pileup	< 5 GeV, Δ R=.3	ok	ok

Table 1: Critical Performance Requirements



FOR μ-ON TRIGGER,
SENSE WIRES LINE UP
TO I.P.

SDC Muon System

- **Primary functions :**

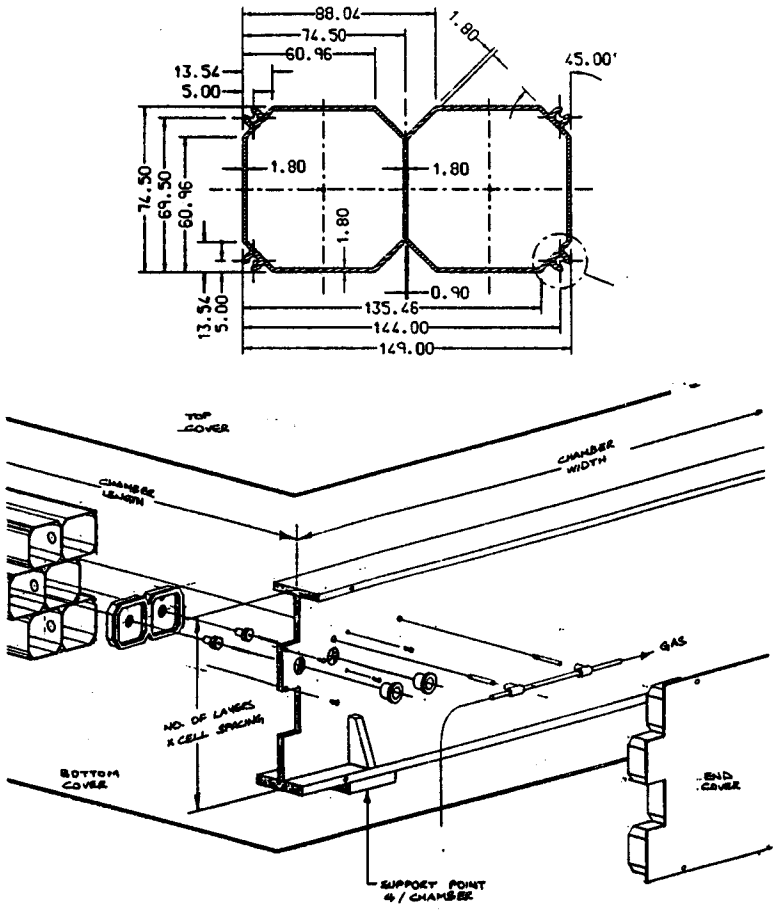
  muon trigger
  muon ID
  Pt measurement
  barrel : redundant measurement
  forward : primary measurement

- **Minimal configuration for the barrel**

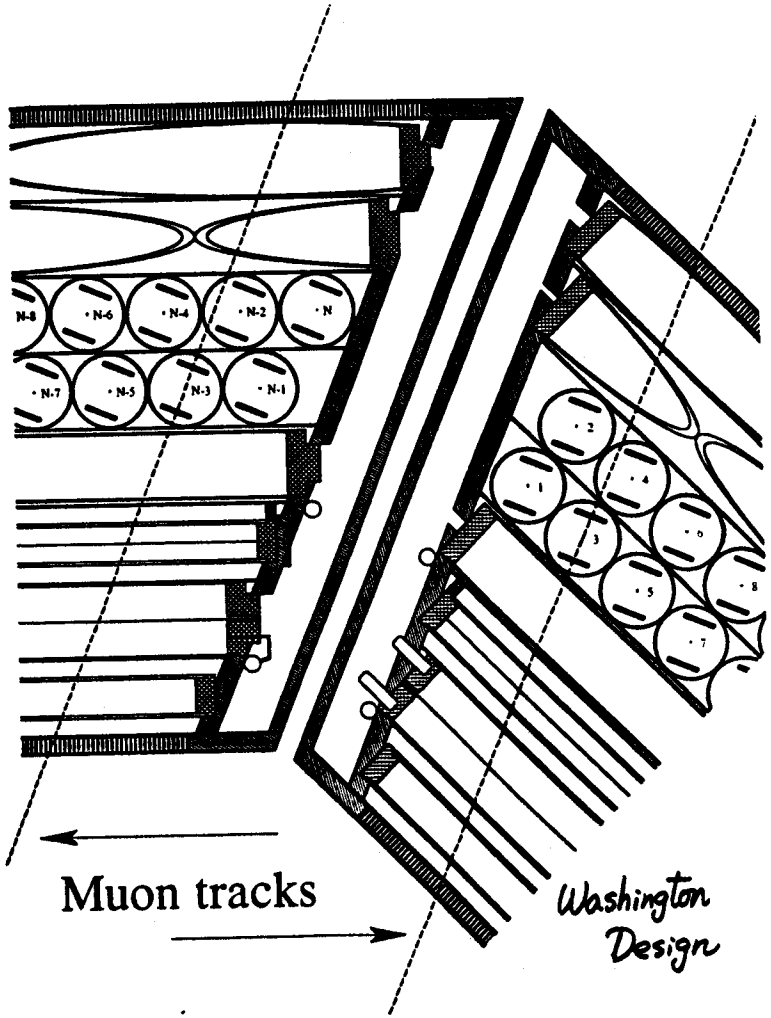
	r	
BW1	6.54 m	4 θ chamber
Toroid	7.70 m	iron (1.5 m thick)
BW2	8.86 m	4 θ chamber
SC1	9.10 m	trigger scintillator
BW3	10.8 m	4 θ chamber
		4 ϕ chamber
		2 s chamber
SC2	11.2 m	trigger scintillator

- **Barrel tracking chamber : 4 designs**

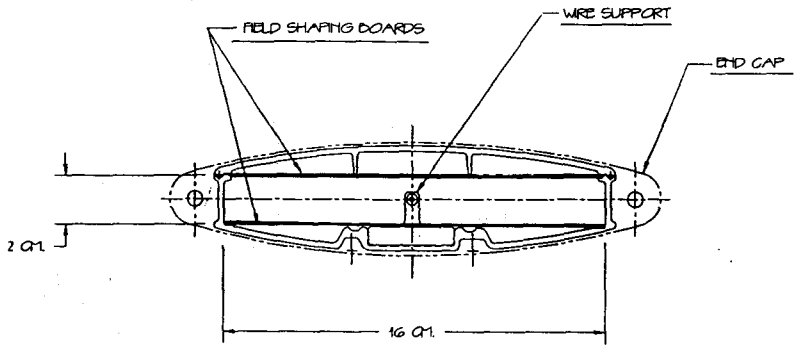
Boston design	oval tube
Wisconsin design	octagonal tube
Washington design	round tube
KEK design	slanted jet chamber



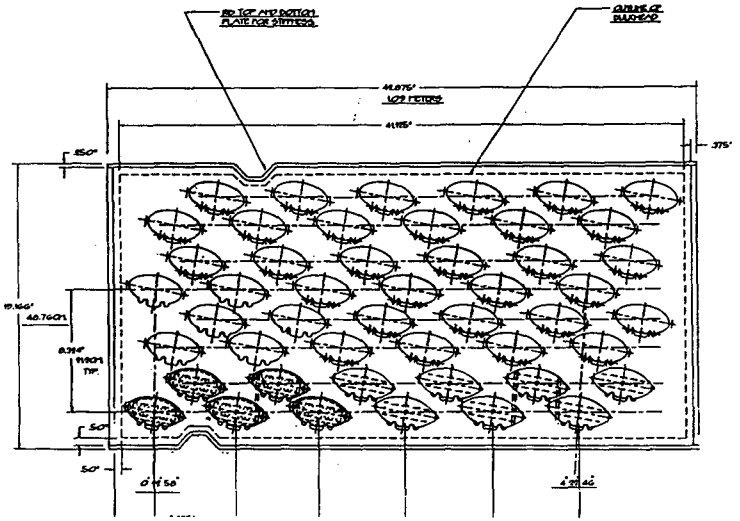
Wisconsin Design



Washington Design



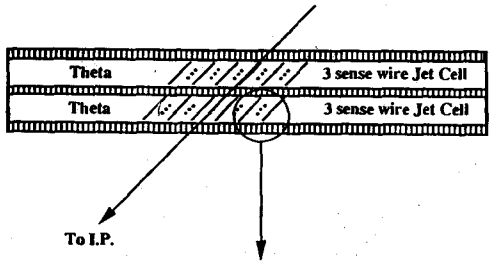
Boston Design



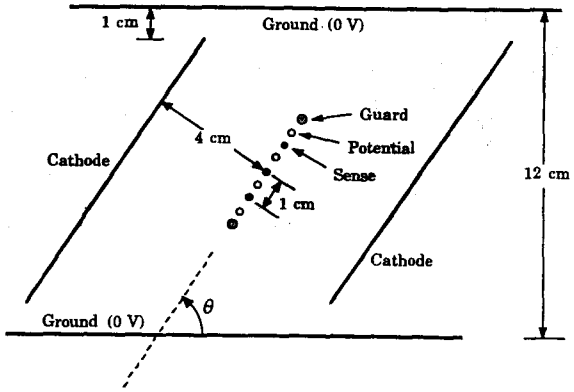
Slanted Jet cell partitioned with stiff cathode plates placed in a rigid box frame

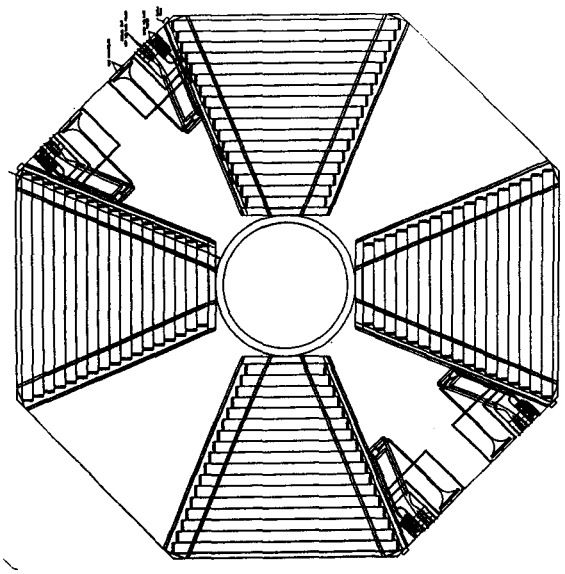
KEK Design

Jet Cell Chamber Module

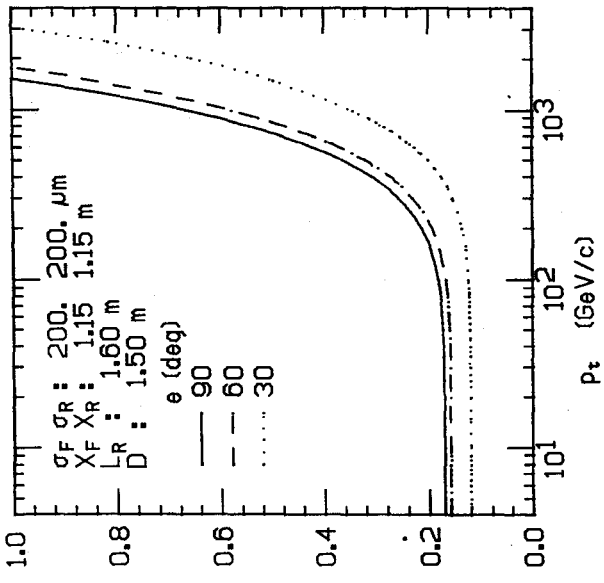


Cell Structure





FORWARD MUON CHAMBERS



SDC Central Calorimetry

- **Calorimeter Technology Selection:**

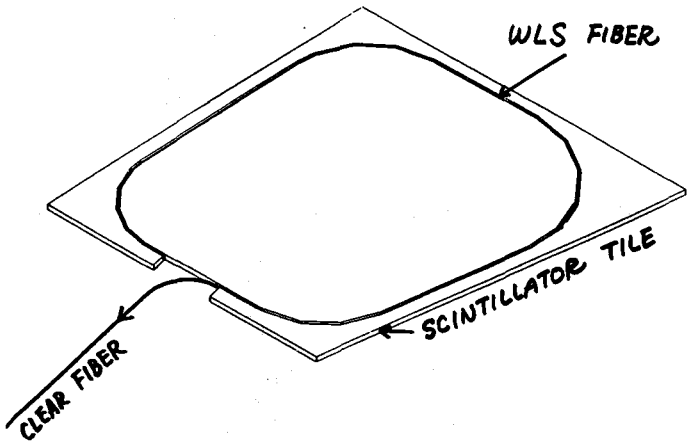
4 technological options (TF, SP, LA, WL)

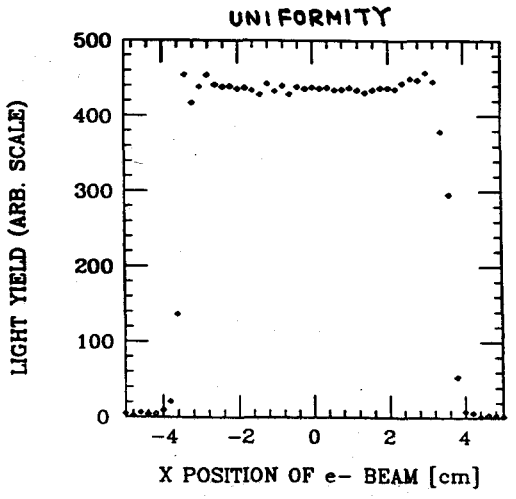
Nov. 1990

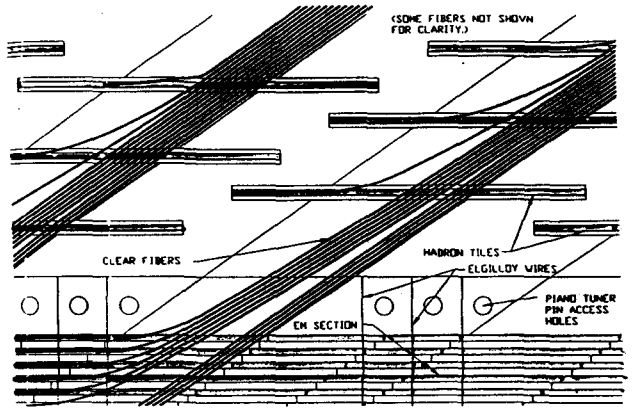
2 options (TF, LA) —Sep.1991→ **Scintillation tiles with fiber readout**

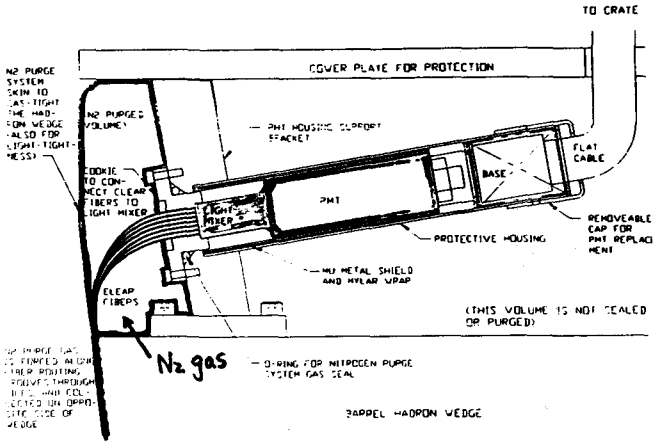
The final selection was done by comparing ;

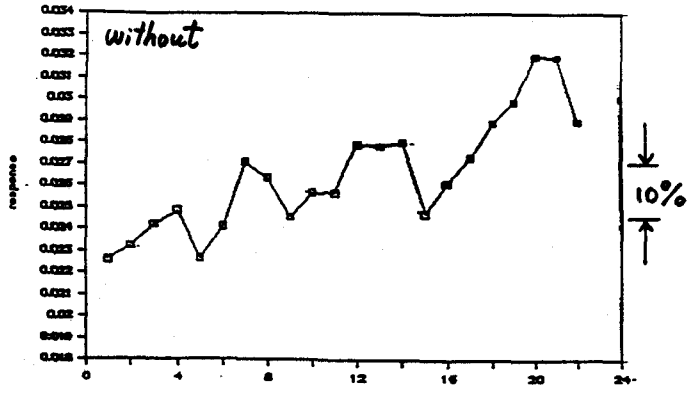
electron acceptance	**e-ID, γ-ID, isolation**
EM resolution- stochastic	**hadronic resolution-stochastic**
EM constant term	**hadronic constant term, e/h**
hadronic transverse segmentation	**missing Et measurement**
schedule	**magnetic field uniformity**
integration	**safety**
impact on electronics,DAQ,trigger	**muon system performance**
neutron albedo in cavity	**flexibility, upgrade**
high *L* performance	**maturity of design**
radiation resistance	**ease of calibration**
cost (including impact on other systems)	

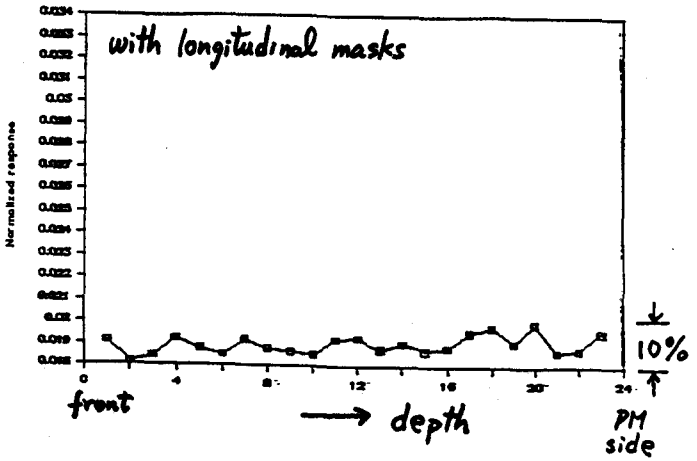





(SOME FIBERS NOT SHOWN FOR CLARITY.)
CLEAR FIBERS
HADRON TILES
ELGILLOY WIRES
PIANO TUNER PIN ACCESS HOLES
CM SECTION


TO CRATE
COVER PLATE FOR PROTECTION
N2 PURGE SYSTEM SKIN TO GAS-TIGHT THE HADRON WEDGE (ALSO FOR LIGHT-TIGHTNESS)
N2 PURGED VOLUME
PMT HOUSING SUPPORT BRACKET
FLAT CABLE
BASE
COOKIE TO CONNECT CLEAR FIBERS TO LIGHT MIXER
LIGHT MIXER
PMT
REMOVEABLE CAP FOR PMT REPLACEMENT
PROTECTIVE HOUSING
MU METAL SHIELD AND MYLAR WRAP
CLEAR FIBERS
(THIS VOLUME IS NOT SEALED OR PURGED)
N2 gas
O-RING FOR NITROGEN PURGE SYSTEM GAS SEAL
BARREL HADRON WEDGE


without
response
10%


with longitudinal masks
Normalized response
10%
front
depth
PM side

- **Three options for absorber configuration**

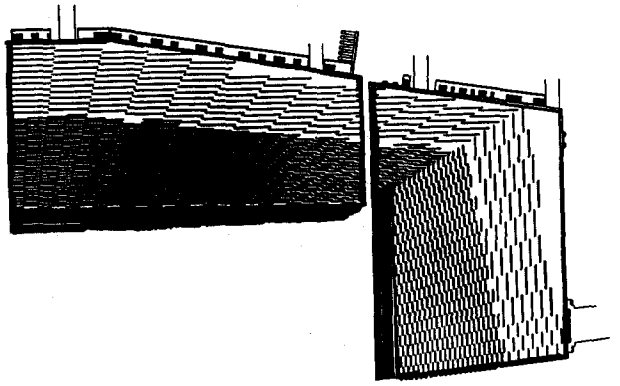
		EM	HAC1	HAC2
model A :		lead	iron	iron
model B :		lead	lead	iron
model M:	barrel	lead	lead	iron
	endcap	lead	iron	iron

- **Rad damage tests at Tsukuba, Beijin, and Orsay**

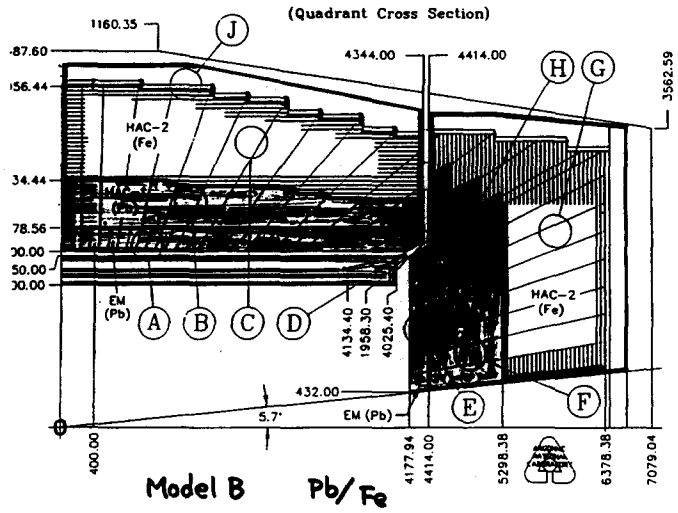
  - 3 experiments agree
  - electron shower induced damage ~ ^{60}Co induced damage
  - damage is uniform over a tile
  - ~40% degradation at 1 Mrad

- **Strategy for radiation induced degradation**

  - development of radiation resistant scintillators/shifters
  - longitudinal division in the EM section and correction
  - adjustment of longitudinal masks
  - replacement of part of the endcap EM calorimeter



Model A HAC1/HAC1 = Fe/Fe



Model B Pb/Fe

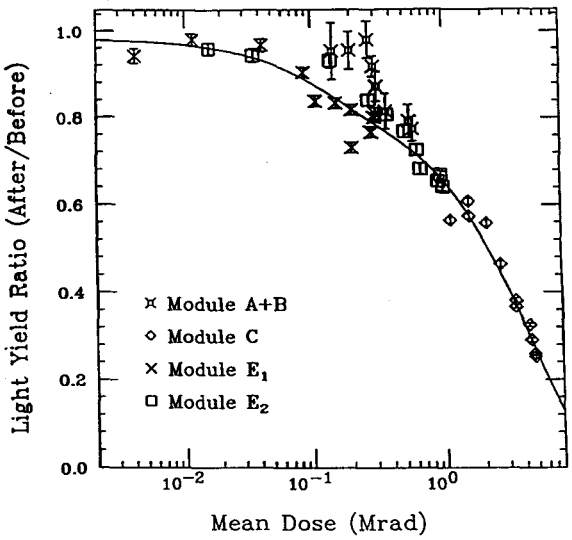


Figure 16: The 2.5-GeV electron shower induced damage as a function of the mean dose, measured with electron beam (in square-crosses) and with a ^{106}Ru source (in squares, diamonds and crosses). The curve is a fit given by Eq. (2).

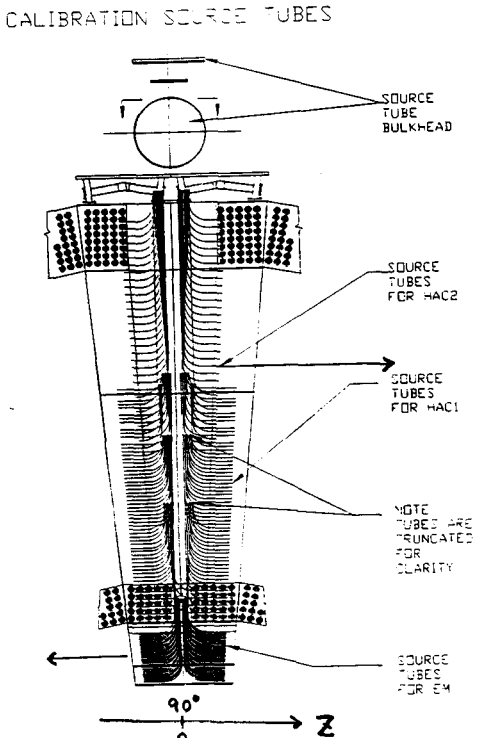
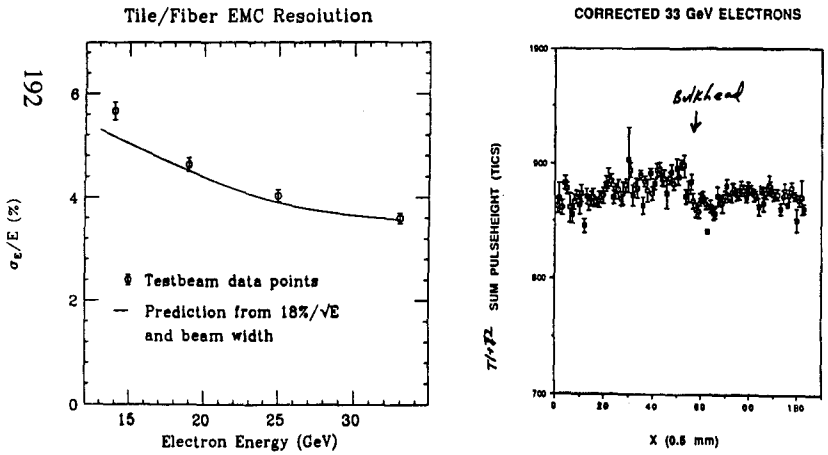


Figure 9.2 Layout of the source tubes for a single barrel wedge. Two basic tyubes fan out to the 2 towers of the wedge. Each tile in the wedge is scanned transversely.

- **Test beam results on tile-fiber calorimeter**

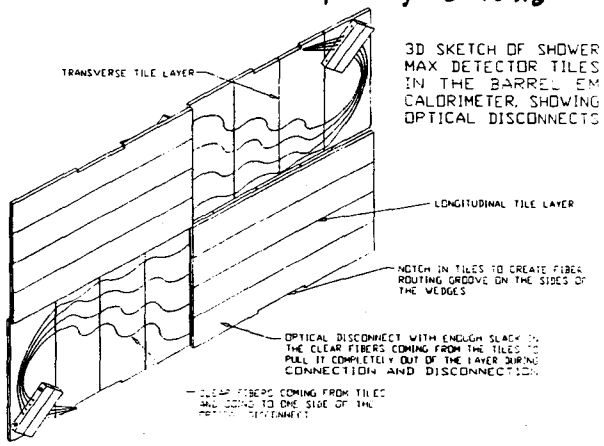
MP : **cast-Pb EM calorimeter by ANL/WSTC group**

MT : **Hanging file calorimeter to perform basic tests (material, thickness, sampling, gate times, e/h, ...)**



Shower Max Detector

at the depth of $6 \sim 10 X_0$



SDC Superconducting Solenoid

Specifications:	**central field**	**2 Tesla**
	inner radius, length	**1.75 m, 8 m**
Basic design :	**type**	**indirect cooling**
	transparency ($\eta = 0$)	**~ 1.2 X_0**
	nominal current	**8000 A**
	stored energy	**133 MJ**
	E/M (energy/cold mass)	**7.4 kJ/kg**
	cold mass, total weight	**18 tons, 23 tons**
	radial magnetic pressure	**1.6 MN/m^2**
	axial compressive force	**18 MN**
	conductor size	**4.37 x 43.7 mm^2**
Prototype coil : (1991~1993)	**joint work by KEK and Fermilab**	
	study of	**fabrication technique,**
		quench behavior,
		mechanical rigidity to axial force,
		vacuum vessel (isogrid/honeycomb)



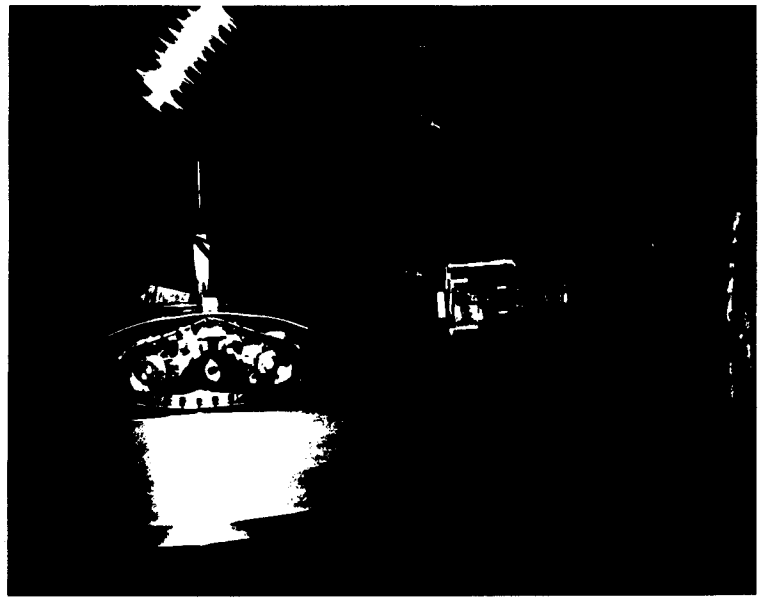
図１．１２　ＳＤＣ用アルミ安定化超伝導線断面

CROSS SECTION OF THE SDC SUPERCONDUCTOR

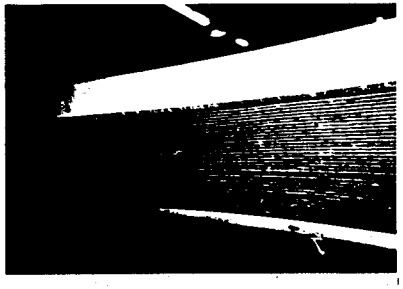


図１．１３　ＳＤＣ用アルミ安定化超伝導線断面拡大

ENLARGED NbTi/Cu_4 CABLE

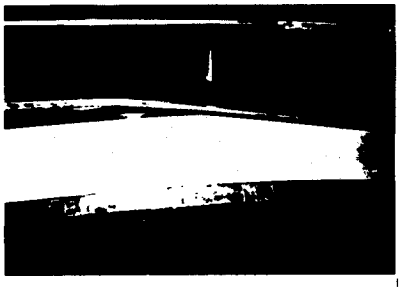


SDC-4



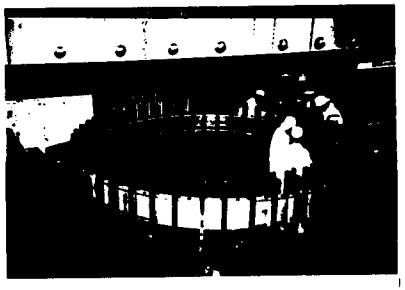
7
導体接続部

CONDUCTOR
WELDING-JOINT



8
同上テーピング

INSULATION AFTER
WELDING JOINT



9
プレス治具

CURE・FIXTURE

SDC tracking system has been descoped significantly from LoI in order

to reduce cost
to reduce total amount of material

Tracking radius is fixed to 1.7m

Present considerations on technology:

R < 50 cm : 7~8 layers of silicon strips
R > 70 cm : 4~5 superlayers of straws or fibers
intermediate angle region : gas microstrips

Simulation studies for pattern recognition started

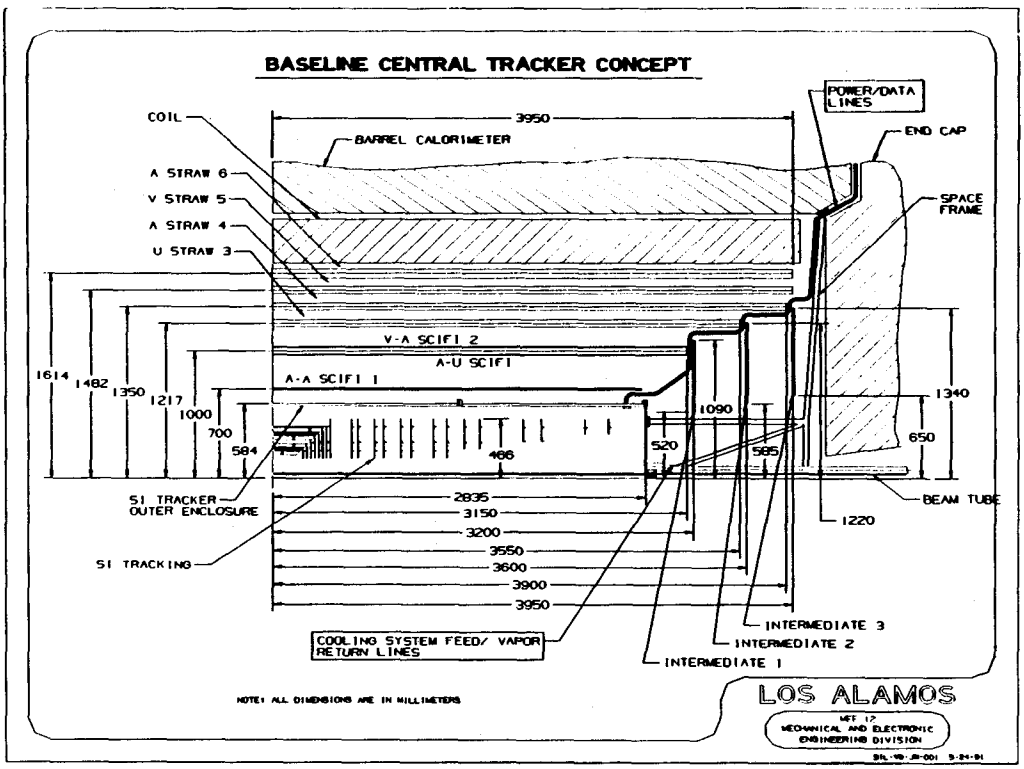
SDC Tracking System

Goals

- **Momentum measurement for $|\eta|<2.5$**
- **Level 1 or 2 trigger capability for p_t >10GeV/c**
- **Pattern recognition capability in jets up to 1 TeV/c**
- **b tagging capability**
- **Functionality of part of the system at $L>>10^{33}cm^{-2}s^{-1}$**

Specifically

- **efficiency of leptons of $H\rightarrow 4l$: >90% at 10^{33}, >75% at $4x10^{33}$**
- **$\sigma_{pt}/p_t^2 < 0.2$ (TeV^{-1}) for $|\eta|<1.8$**
- **e-ID > 85%, μ-ID >90% for p_t >10GeV/c**
- **b single tagging efficiency > 30%**
- **$\sigma_{pt}/p_t^2 < 10$ for L1 trigger, < 2.5 for L2 trigger**
- **$\sigma_{r\text{-}\phi} < 2.5$ mm at the calorimeter entrance**



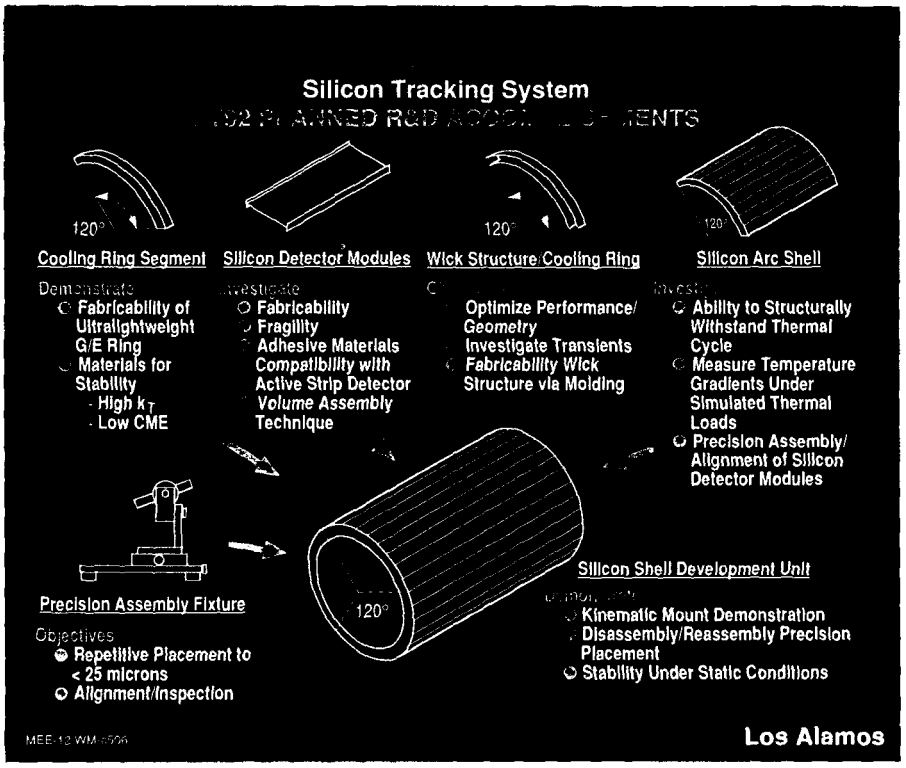
SDC Silicon Tracking System

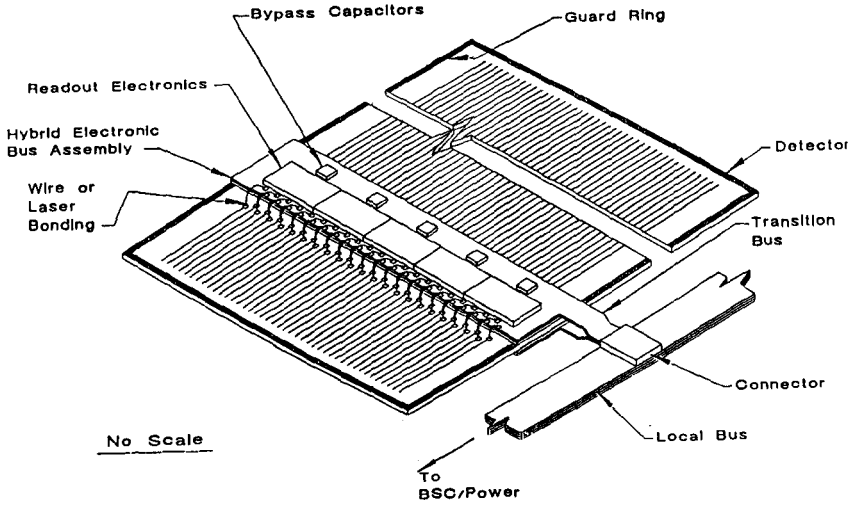
- **Silicon (and pixel) is the only choice at R<50cm**
  low occupancy, high precision,
  good two track separation.....

- **Many new technological challenges !**

silicon detector area :	**16 m^2**
readout channels :	**6 x 10^6 channels**
readout :	**while input is active**
electronics on silicon :	**< 1 mW/ch (BJT+CMOS)**
cooling :	**butane evaporation**
detector :	**double sided**
radiation level :	**~ 5 Mrad**

Present progress indicates promising future.


Silicon Tracking System
120°
Cooling Ring Segment
Demonstrate
Fabricability of Ultralightweight G/E Ring
Materials for Stability
High k_T
Low CME
Silicon Detector Modules
Investigate
Fabricability
Fragility
Adhesive Materials Compatibility with Active Strip Detector
Volume Assembly Technique
120°
Wick Structure/Cooling Ring
Optimize Performance/ Geometry
Investigate Transients
Fabricability Wick Structure via Molding
Silicon Arc Shell
Ability to Structurally Withstand Thermal Cycle
Measure Temperature Gradients Under Simulated Thermal Loads
Precision Assembly/ Alignment of Silicon Detector Modules
Precision Assembly Fixture
Objectives
Repetitive Placement to < 25 microns
Alignment/Inspection
120°
Silicon Shell Development Unit
Kinematic Mount Demonstration
Disassembly/Reassembly Precision Placement
Stability Under Static Conditions
Los Alamos


Bypass Capacitors
Guard Ring
Readout Electronics
Hybrid Electronic Bus Assembly
Wire or Laser Bonding
Detector
Transition Bus
Connector
Local Bus
No Scale
To BSC/Power

Straw Tube Tracking

- 5 superlayers (A, S+, A, S-,A), 135,456 straws
- Straw R&D : attenuation length > 5m
  radiation effects → >10 years at 10^{33}
  rate study, gas study,
  cathode material, termination.....
  σ=120μm with 2.7m long straws
- wire positioning : 25μm achieved
  module construction underway
- space frame design
- readout : A/S/D, TMC tested successfully

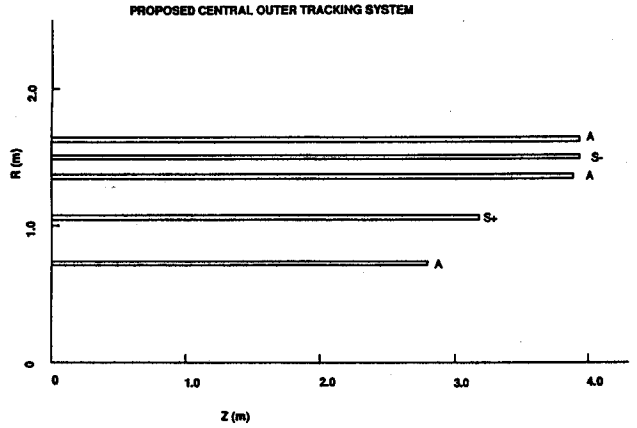
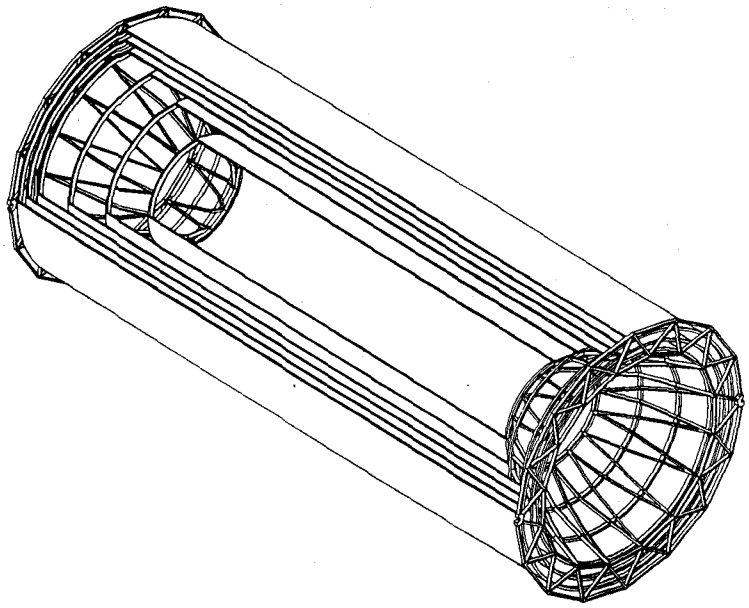


Table. Central Outer Tracker Design

Superlayer	Radius (m)	Straws/Layer	Modules	Layers/Super layer	z_{max} (m)	Stereo Angle (°)
1	0.708	1112	84	6	2.80	0
2	1.04	1640	124	6	3.20	+3
3	1.35	2120	160	8 (trigger)	3.90	0
4	1.48	2328	176	6	3.95	-3
5	1.61	2536	192	8 (trigger)	3.95	0

total straws ~135K

CENTRAL TRACKER SUPPORT STRUCTURE

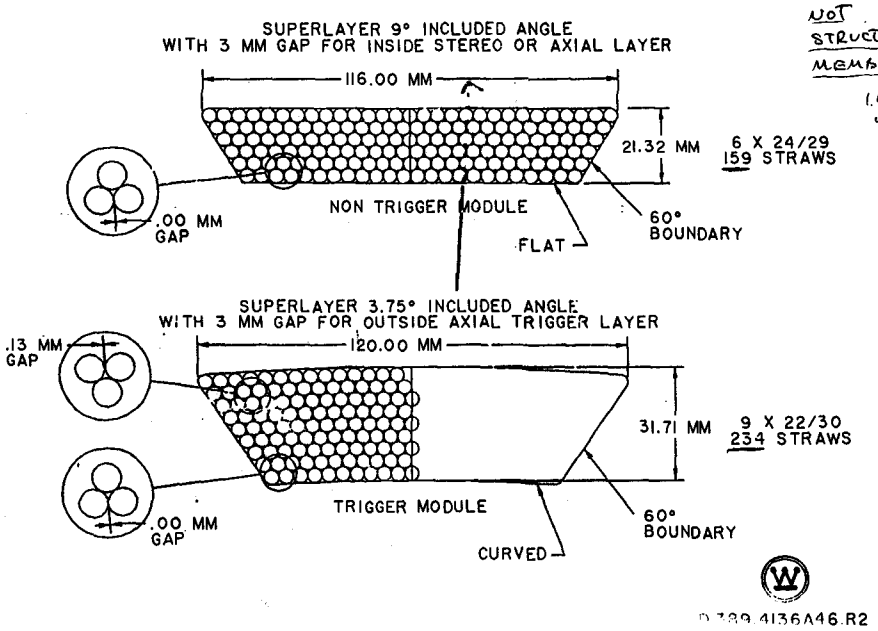


WESTINGHOUSE STC

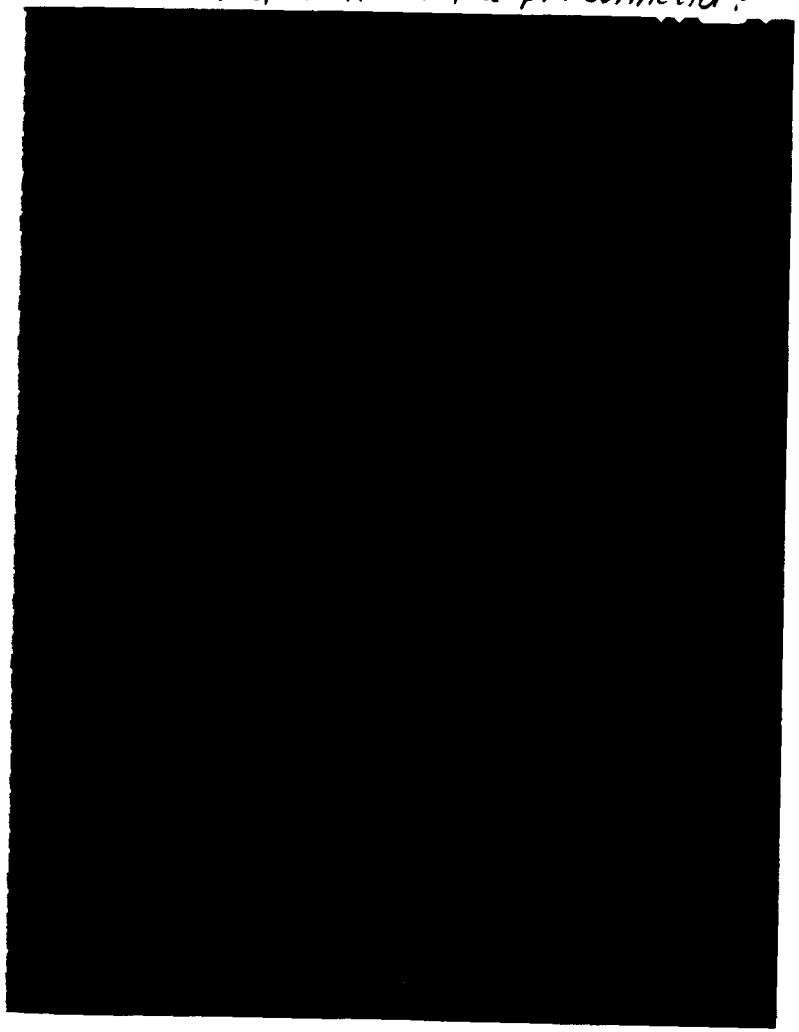
MODULAR CENTRAL TRACKING
SUPERLAYER MODULES
POST L01

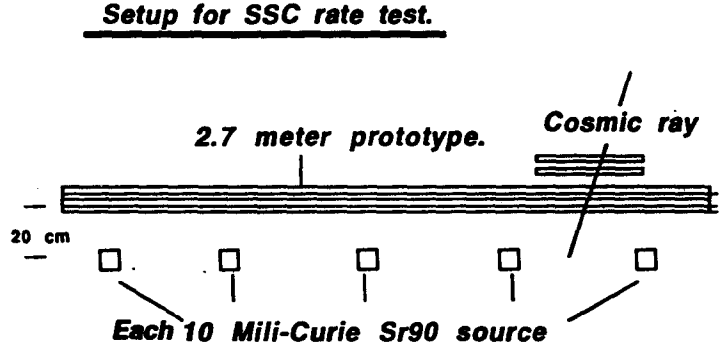
STRAWS ARE NOT STRUCTURAL MEMBERS

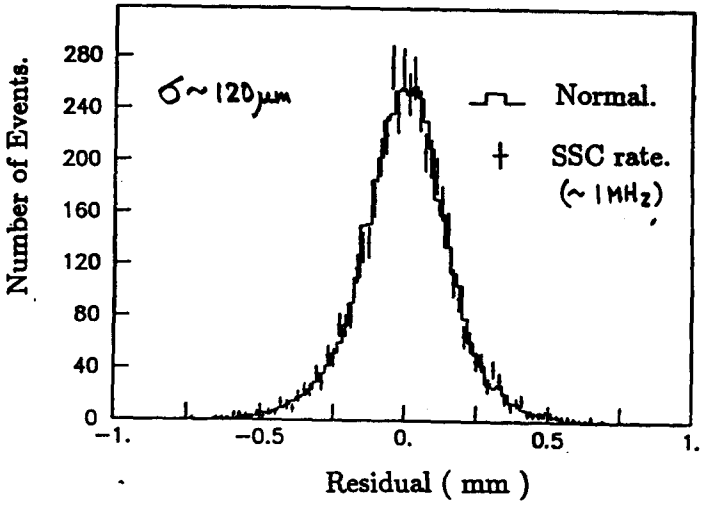
1.4 mils wall



D 789 4136A46.R2


close up of hands & a pin connector?

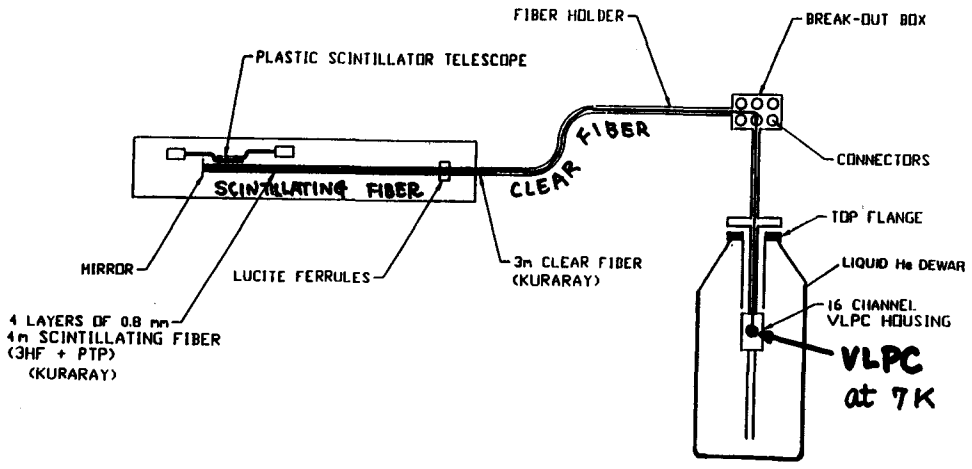

Setup for SSC rate test.
2.7 meter prototype.
Cosmic ray
20 cm
Each 10 Mili-Curie Sr90 source

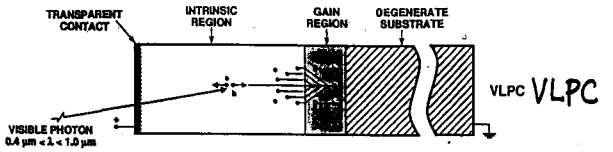

σ ~ 120μm
Normal.
SSC rate.
(~ 1MHz)
Number of Events.
280
240
200
160
120
80
40
0
−1.
−0.5
0.
0.5
1.
Residual (mm)

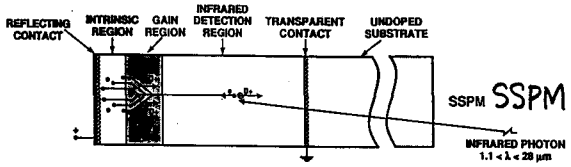
Scintillating-fiber Tracking

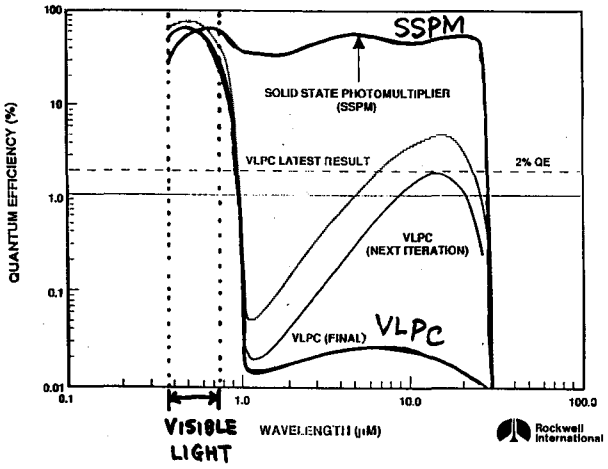
- **Fibers : polystyrene, diameter~830 μm**
  fiber ribbons are comercially made
- **SDC design : 4 superlayers, 610K fibers**
  1/4 offsetting for better resolution
  readout and trigger design exist
- **VLPC (visible light photon counter)**
  developed at Rockwell Intern. Scien.Center
  Q.E. ~ 85 % for visible light
  must be kept at 7K
  cassette readout units
- **Cosmic ray test**
  4m scintillating fiber + 3m clear fiber
  ~ 6 photoelectrons

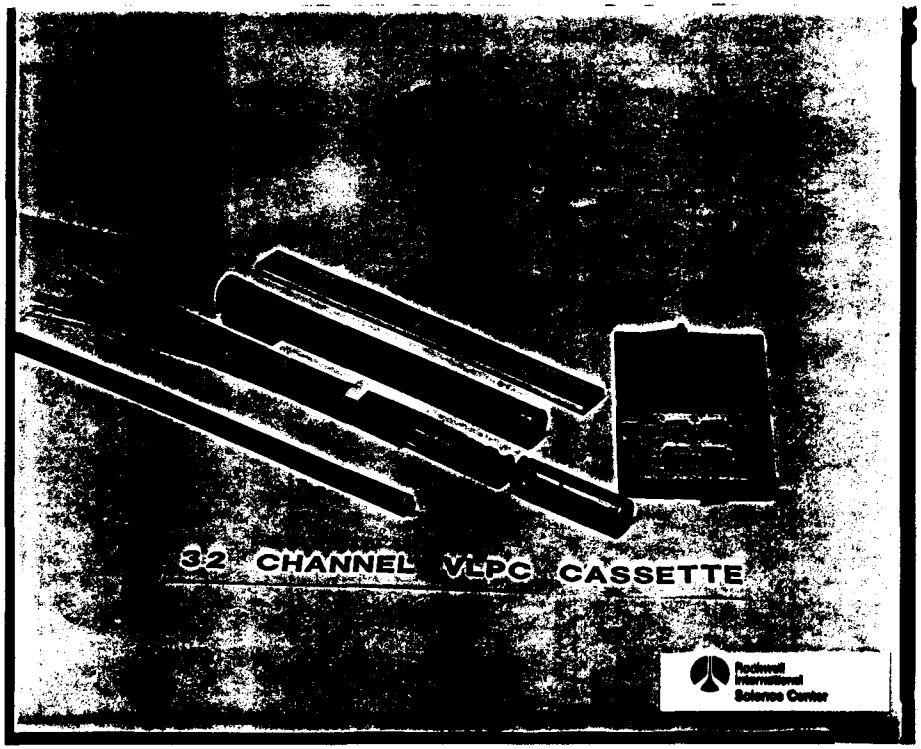
M.Atac, J.Park, D.Chrisman
U C L A
H. Fenker, K.Morgan
S S C L

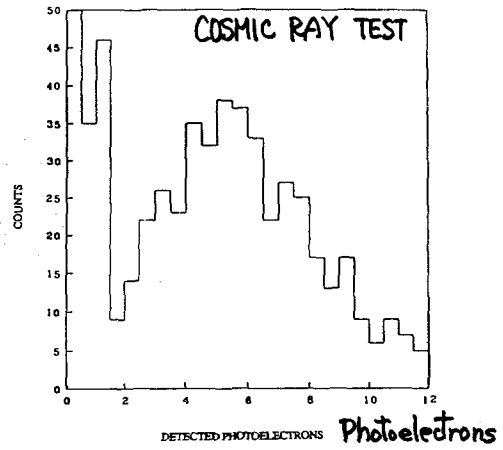


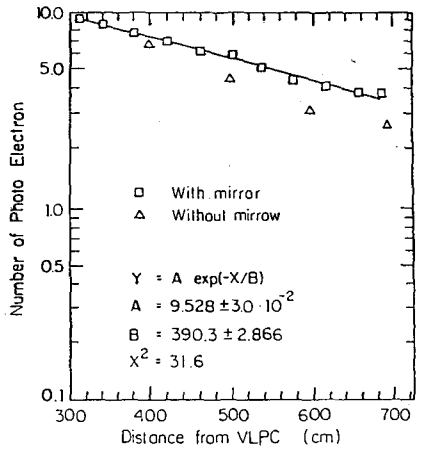

TRANSPARENT CONTACT
INTRINSIC REGION
GAIN REGION
DEGENERATE SUBSTRATE
VLPC VLPC
VISIBLE PHOTON
0.4 μm < λ < 1.0 μm


REFLECTING CONTACT
INTRINSIC REGION
GAIN REGION
INFRARED DETECTION REGION
TRANSPARENT CONTACT
UNDOPED SUBSTRATE
SSPM SSPM
INFRARED PHOTON
1.1 < λ < 28 μm

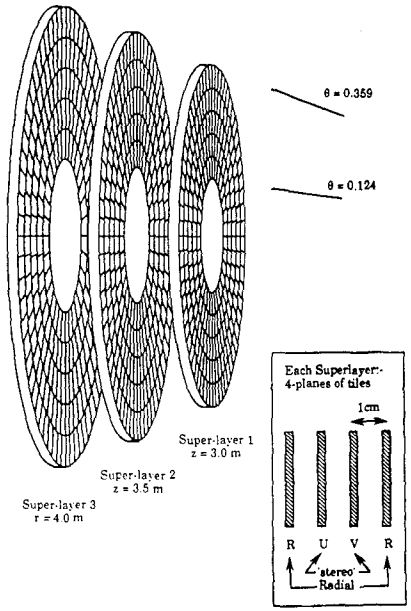

QUANTUM EFFICIENCY (%)
100
10
1.0
0.1
0.01
SSPM
SOLID STATE PHOTOMULTIPLIER (SSPM)
VLPC LATEST RESULT
2% QE
VLPC (NEXT ITERATION)
VLPC (FINAL)
VLPC
0.1
1.0
10.0
100.0
VISIBLE LIGHT
WAVELENGTH (μM)
Rockwell International


32 CHANNEL VLPC CASSETTE
Rockwell International Science Center

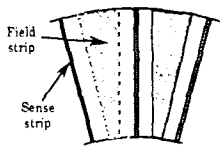


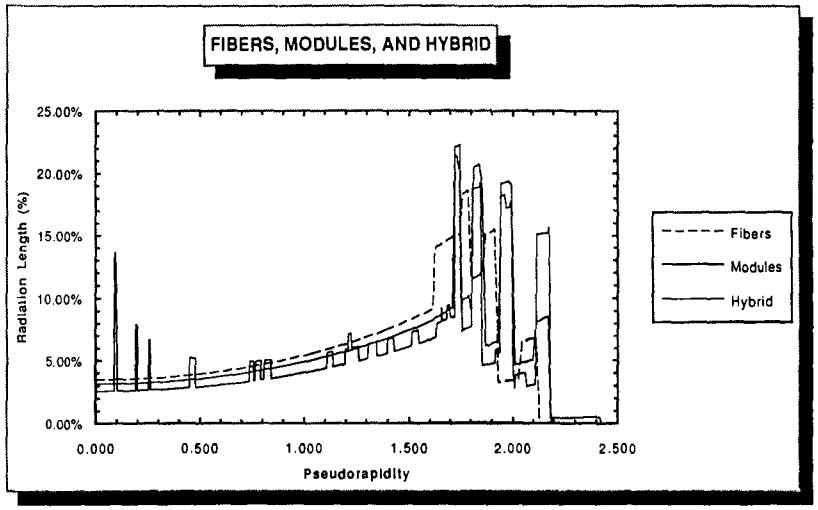


SDC Intermediate-angle Tracking



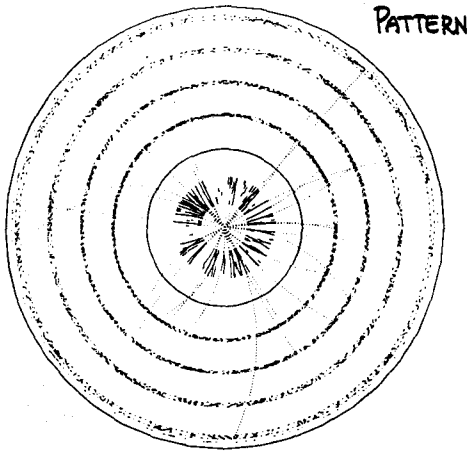
Gas micro-strip detector is being considered to be a good candidate that meets requirements in this region.

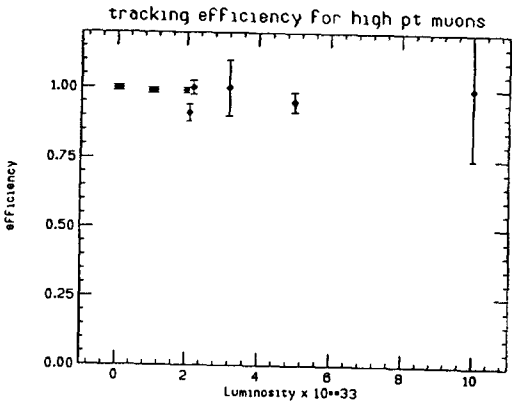




ornl
RML
9/27/91

PATTERN RECOGNITION





SDC Front-End Electronics

- **VLSI chips under development for SDC:**

  Switched capacitor array (SCA) at LBL : tested

  Phototube splitter/integrator digitizer at Fermilab

  Drift chamber readout (A/S/D, TVC/AMU) at Penn

  Drift chamber time digitizer (TMC) at KEK : tested

  Readout of silicon strips at LBL, KEK, Santa Curz

  etc

- **Level-1 buffer depth is estimated to be 3.4 ~ 3.9 μs.**

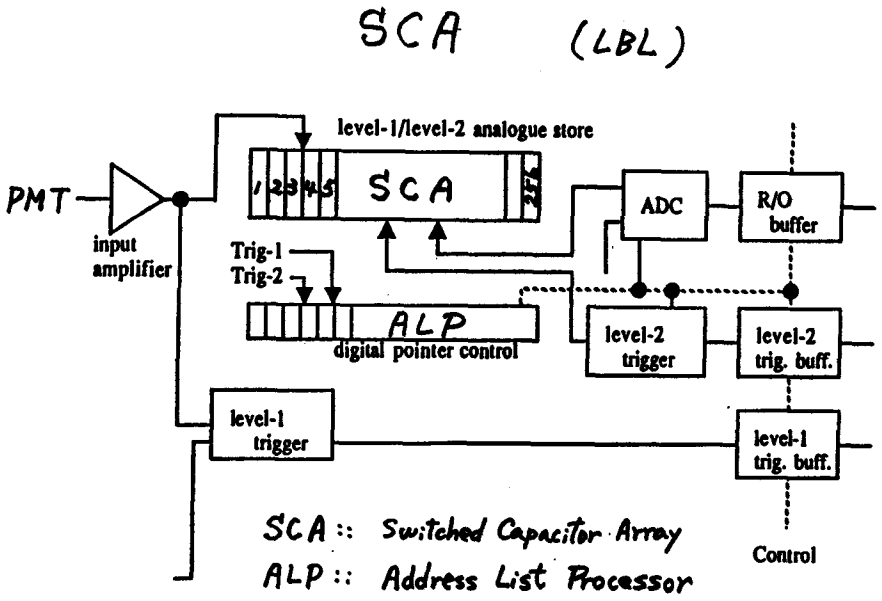
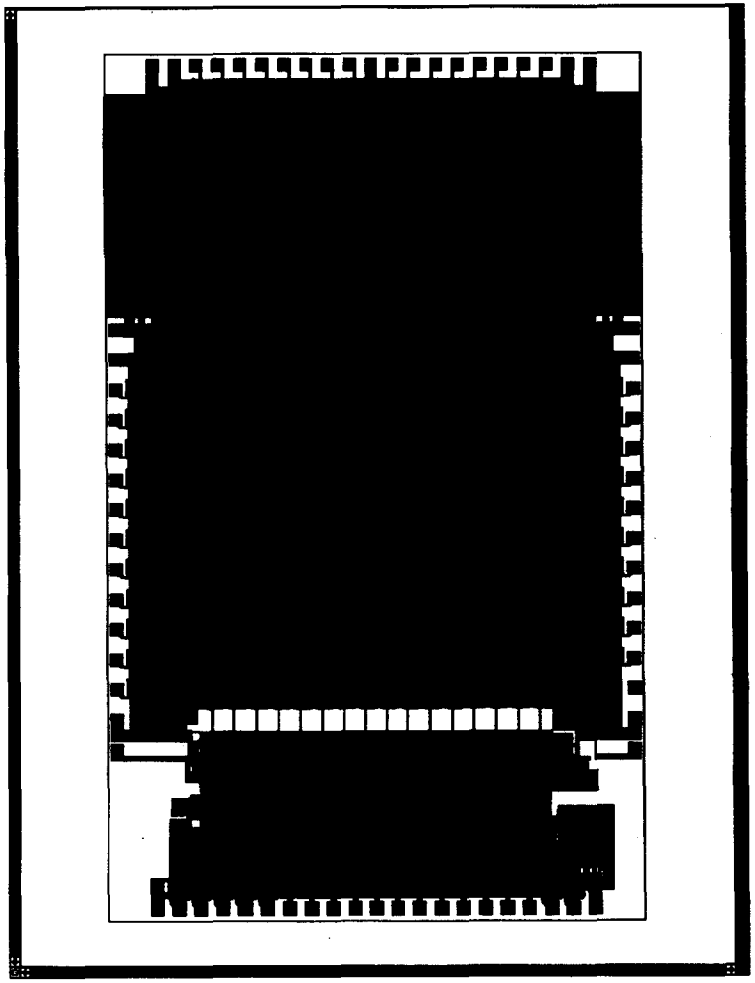


Fig. 1.3. Single Analog Store, Pointer-Address Architecture.



This corresponds to a total dynamic range of 1:5500 or 12.4 bits. The measured parameters of the SCA are summarized in Table 3.2.

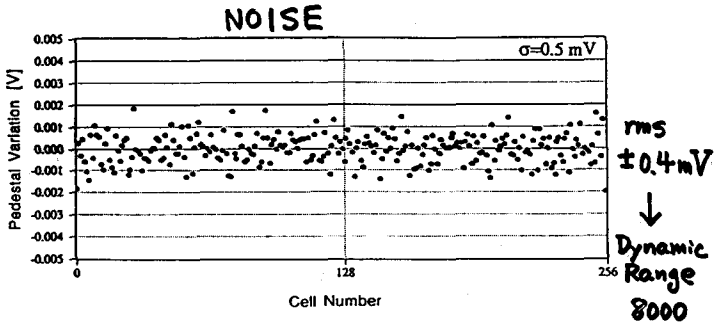


Fig. 3.6. Cell-to-cell pedestal variation as a function of cell number across a single channel. The small pedestal variation will permit large dynamic range operation of the circuit without corrections.

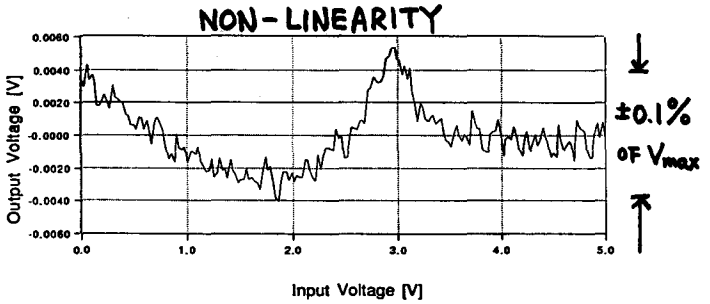
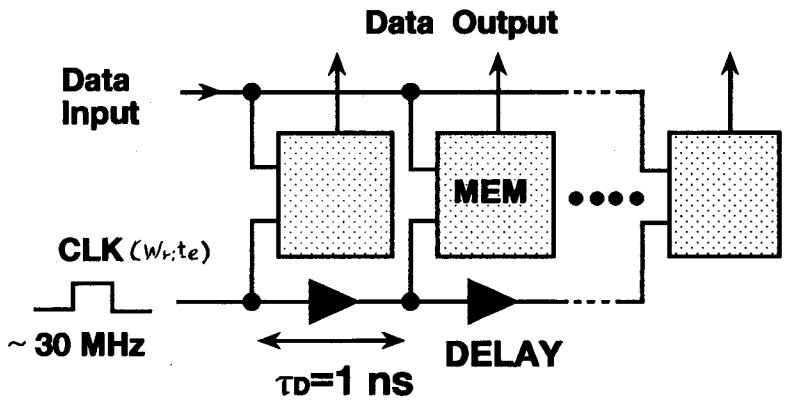


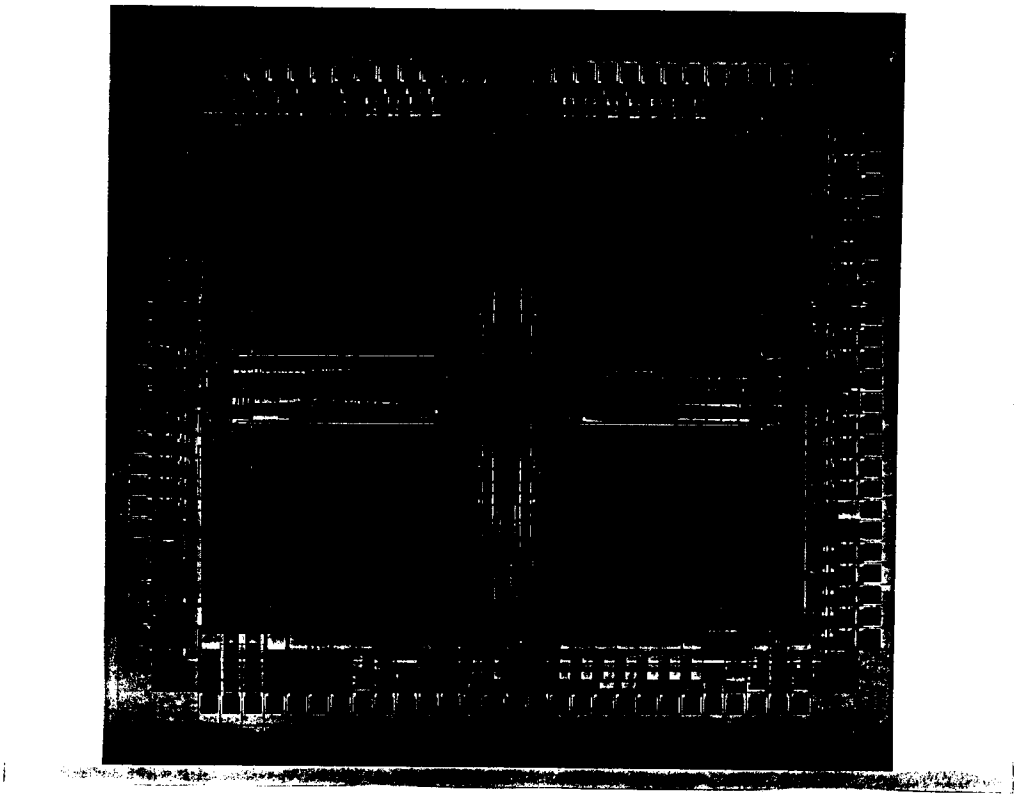
Fig. 3.7. Non-linearity of the 1.2 μm CMOS 256 cells per channel switched capacitor array. Shown is the deviation from a best fit line.

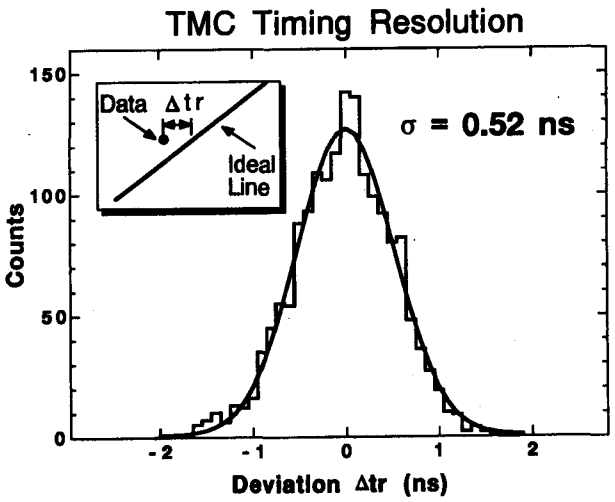
What is a Time Memory Cell (TMC) ?

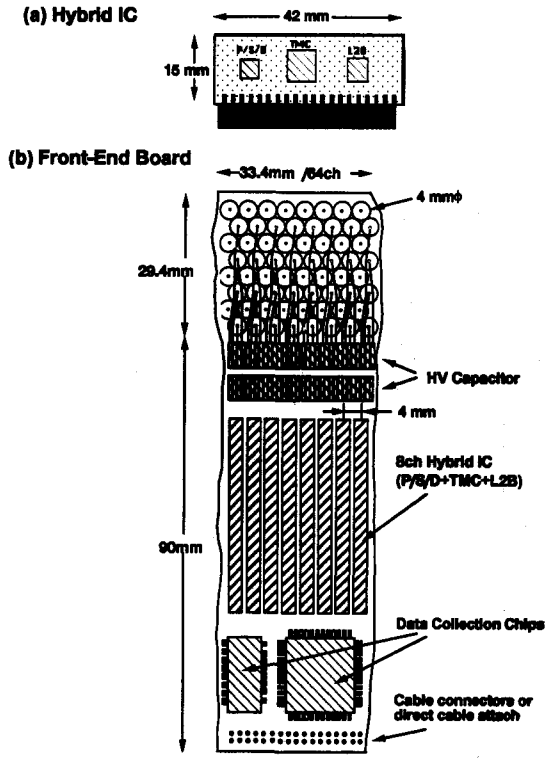


- Input : Timing Information
- Store /Output : Digital Data as Bit Position

⇨ Time-to-Digital Converter and Drift Time の記録

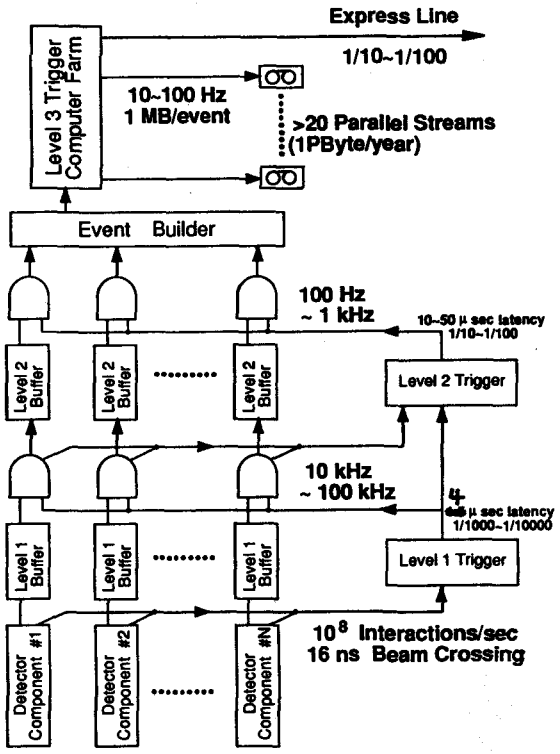






Front-End Electronics Mounting Example

Trigger and Dataflow



SDC Trigger

Level 1

Calorimeter : E_t**-sum,** E_t**, isolated-e, jet**
Tracking : stiff (P_t **> 5GeV) track segments**
Muons : stiff (P_t **>10GeV) muon tracks**

Level 2

Calorimeter : Ejet by clustering
more E_e **and isolation calculation**
match Shower Max with tracking
Tracking : P_t **calculation**
link to calorimeter and muon systems
link Silicon with outer tracker
Muons : P_t **calculation and link to tracking**

Level 3

full reconstruction of events
correlated total E_t **and** E_t**jet**
invariant mass from leptons and jets

e Trigger rate (level 1)

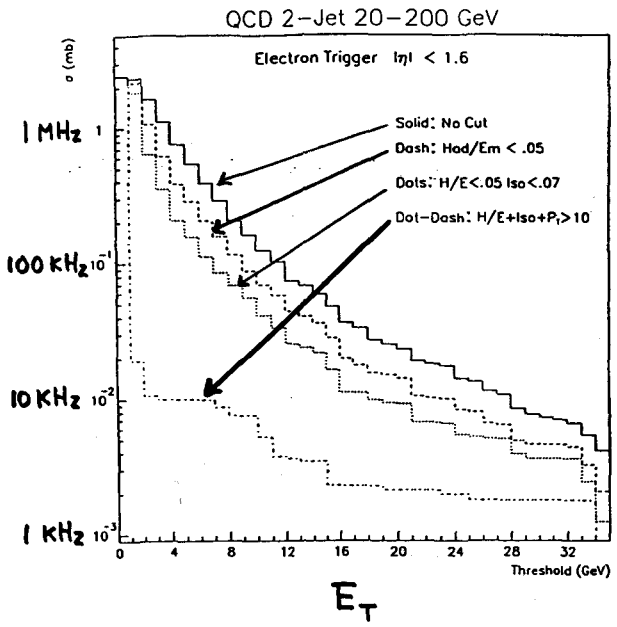


Figure 3: The level 1 inclusive electron trigger rate in the barrel calorimeter versus the E_T threshold for no cut (solid), Had/Em cut (dashed), Had/Em and isolation (dot), and finally adding the requirement of a track match in ϕ with the tower (dot-dash).

SDC Data Acquisition

CHANNEL COUNT	**Calorimeter:**	**~ 4 x 10^4 phototubes**
	Shower max:	**~ 4 x 10^4 channels**
	Silicon:	**~ 6 x 10^6 channels**
	Straw tubes:	**~ 1.3 x 10^5 channels**
	Scinti-fibers:	**~ 6.1 x 10^5 channels**
	Muon chamber:	**~ 1 x 10^5 channels**
EVENT SIZE		**~ 1 MByte**
DAQ RATE (after L2 trigger)		**~ 1 kHz (10kHz capacity)**
TOTAL TRANSFER RATE		**~ 1 GByte/s (10 GByte/s capacity)**
DATA STORAGE SIZE		**~ 1 PByte/year**

Critical Issues in SSC/SDC Computing

Hardware

- Huge event rate
- CPU power
- Data storage and retrieval

Software

- Program development by > 100 physicists (?)
- Program development in regionally wide spread areas
- Software life of more than 20 years

SDC Computing and Software

CPU

Level-3 farm :	**10^5 MIPS**
2nd-pass reconstruction:	**10^5 MIPS**
Simulation facility :	**2×10^5 MIPS**
Workstations :	**100people x 100MIPS**

Data Storage

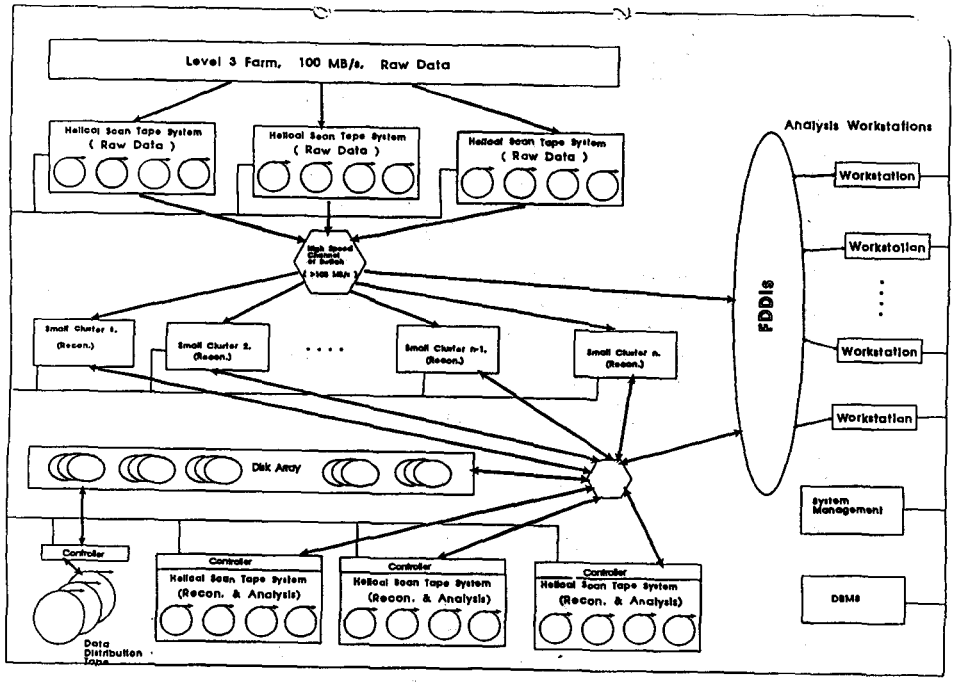
Fast storage :	**10 TB**
Medium speed storage :	**100 TB**
Long term storage :	**2 PB/year**

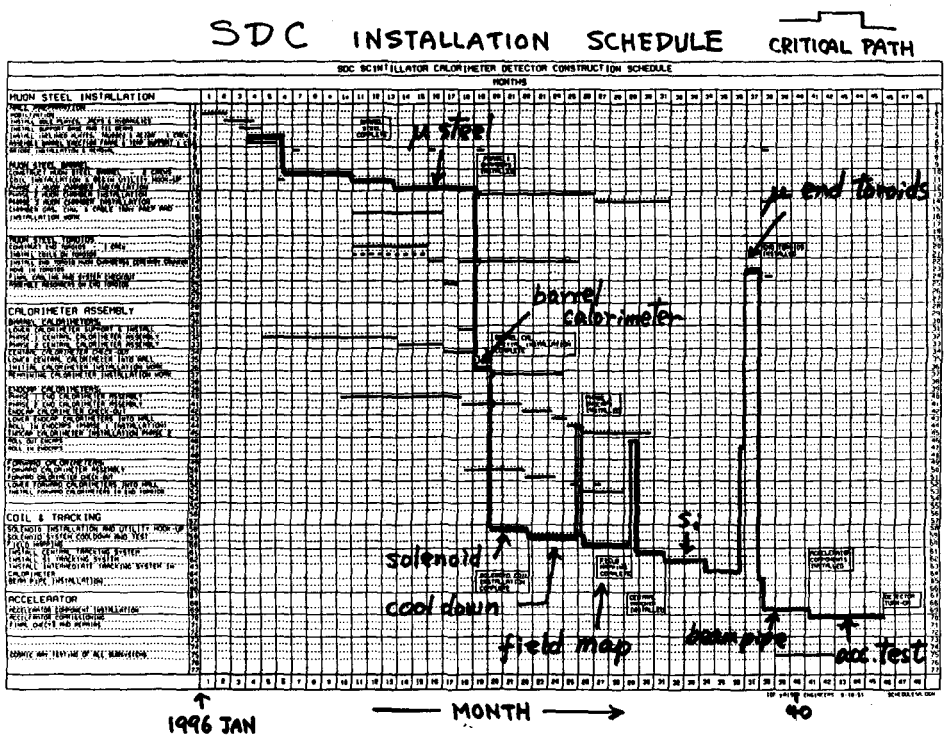
Computing Model

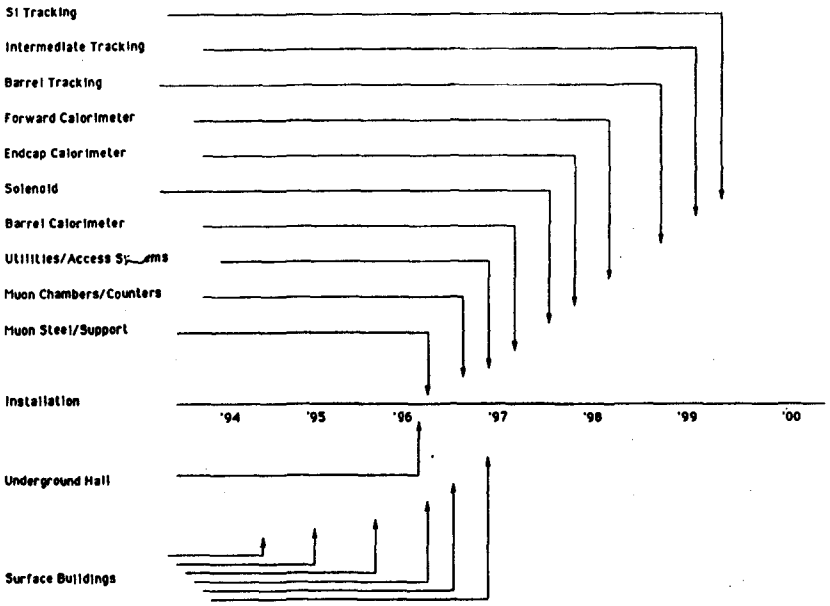
Centralized at SSCL or
Distributed :
SSCL + ~6 regional centers

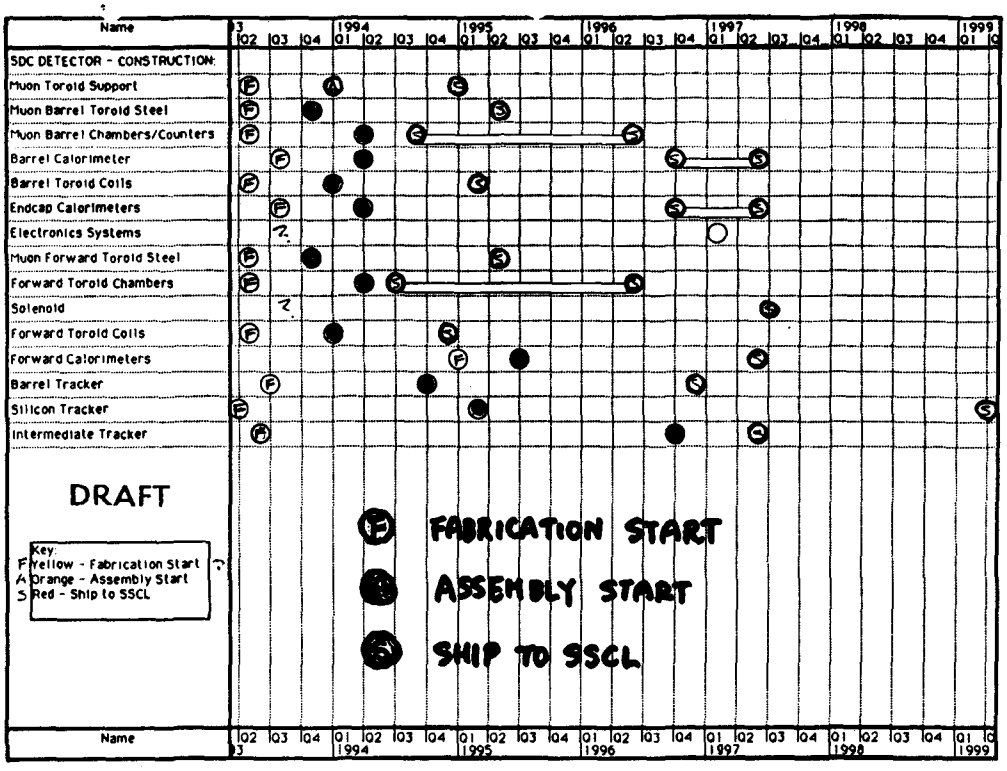
Network

Dedicated 1Gbps (SSCL ⟷ regional center)
Dedicated 100Mbps (regional center⟷ institute)


Level 3 Farm, 100 MB/s, Raw Data
Helical Scan Tape System (Raw Data)
Helical Scan Tape System (Raw Data)
Helical Scan Tape System (Raw Data)
Analysis Workstations
Workstation
Workstation
Workstation
Workstation
FDDIs
Small Cluster 1. (Recon.)
Small Cluster 2. (Recon.)
Small Cluster n-1. (Recon.)
Small Cluster n. (Recon.)
Disk Array
System Management
DBMS
Controller
Controller
Helical Scan Tape System (Recon. & Analysis)
Controller
Helical Scan Tape System (Recon. & Analysis)
Controller
Helical Scan Tape System (Recon. & Analysis)
Data Distribution Tape


SDC INSTALLATION SCHEDULE
CRITICAL PATH
SDC SCINTILLATOR CALORIMETER DETECTOR CONSTRUCTION SCHEDULE
MONTHS
MUON STEEL INSTALLATION
CALORIMETER ASSEMBLY
COIL & TRACKING
ACCELERATOR
fe steel
fe end toroids
barrel calorimeter
solenoid cool down
field map
beam pipe
acc. test
1996 JAN
MONTH
40


SI Tracking
Intermediate Tracking
Barrel Tracking
Forward Calorimeter
Endcap Calorimeter
Solenoid
Barrel Calorimeter
Utilities/Access Systems
Muon Chambers/Counters
Muon Steel/Support
Installation
'94
'95
'96
'97
'98
'99
'00
Underground Hall
Surface Buildings


Name
SDC DETECTOR - CONSTRUCTION
Muon Toroid Support
Muon Barrel Toroid Steel
Muon Barrel Chambers/Counters
Barrel Calorimeter
Barrel Toroid Coils
Endcap Calorimeters
Electronics Systems
Muon Forward Toroid Steel
Forward Toroid Chambers
Solenoid
Forward Toroid Coils
Forward Calorimeters
Barrel Tracker
Silicon Tracker
Intermediate Tracker
DRAFT
Key:
F Yellow - Fabrication Start
A Orange - Assembly Start
S Red - Ship to SSCL
FABRICATION START
ASSEMBLY START
SHIP TO SSCL

Technical Proposal Schedule

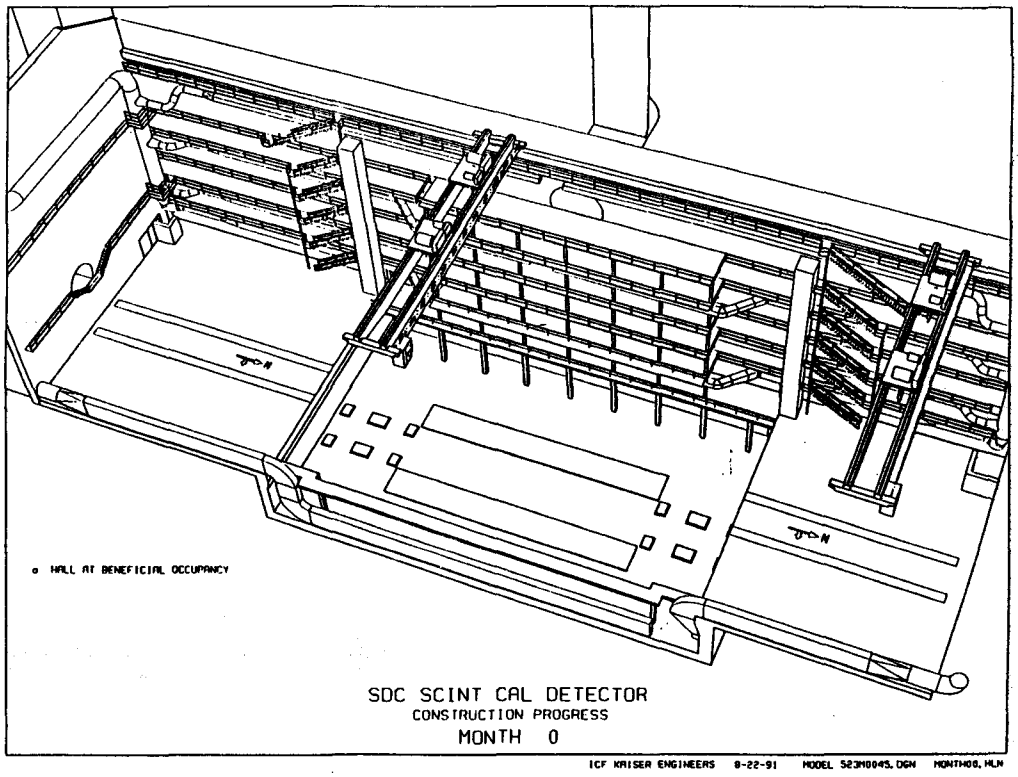
October 1	Assign coordinating editors
November 13	Detailed outline + final writing assignments and/or draft text
December 13	Zeroth draft submitted to chapter editors(and overall editors for comments)
January 3	Submit first draft to overall editors
January 31	Submit second draft to overall editors
February 21	Deliver final draft to SSCL for duplication of 150 copies
February 26-29	Review of final draft by collaboration and editors
March 23	Final printout of text with figures
March 25	Assemble, print and bind 40 copies
April 1	Submit 40 copies to SSCL

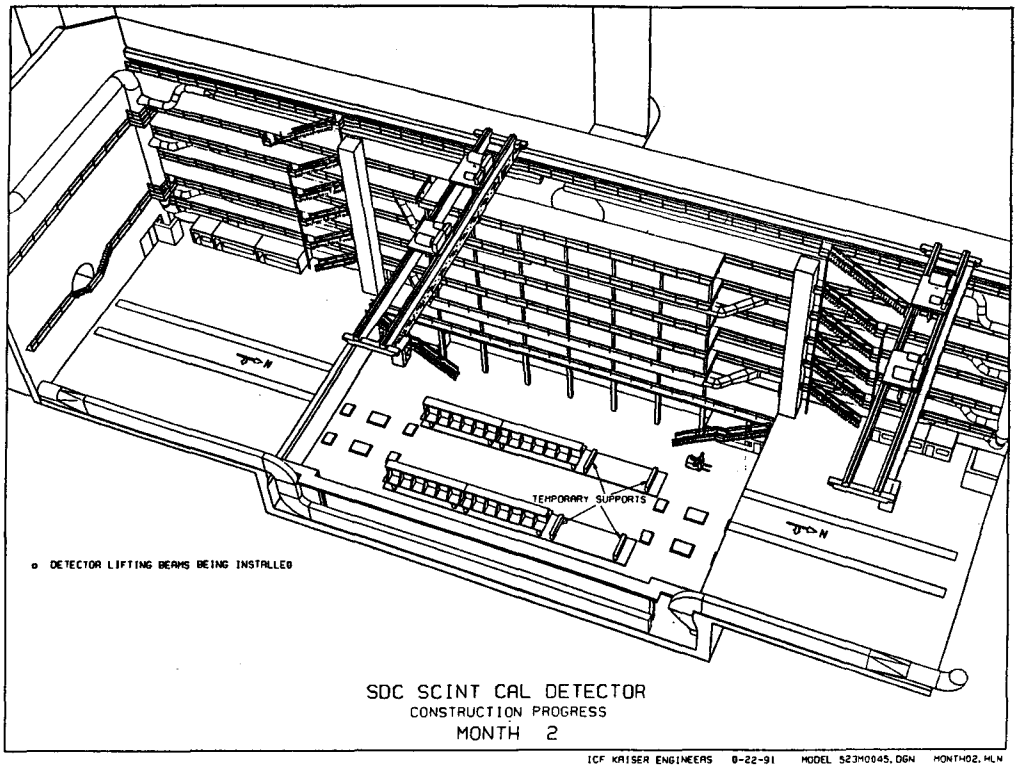


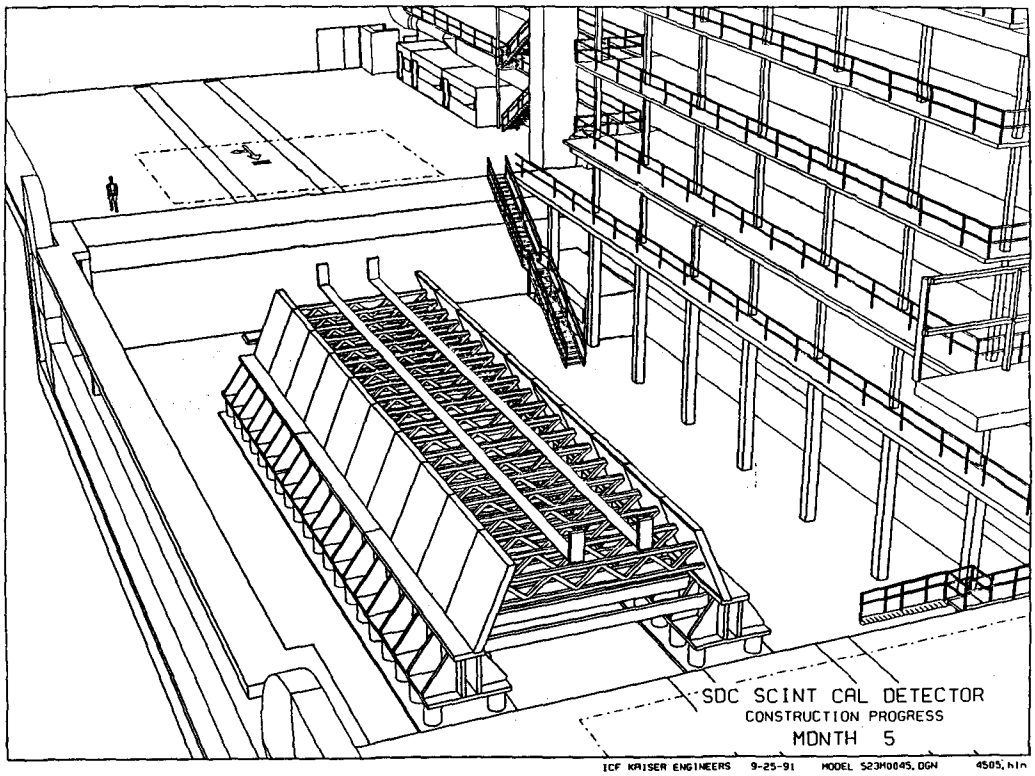
INTERESTS OF NON-U.S. SDC GROUPS

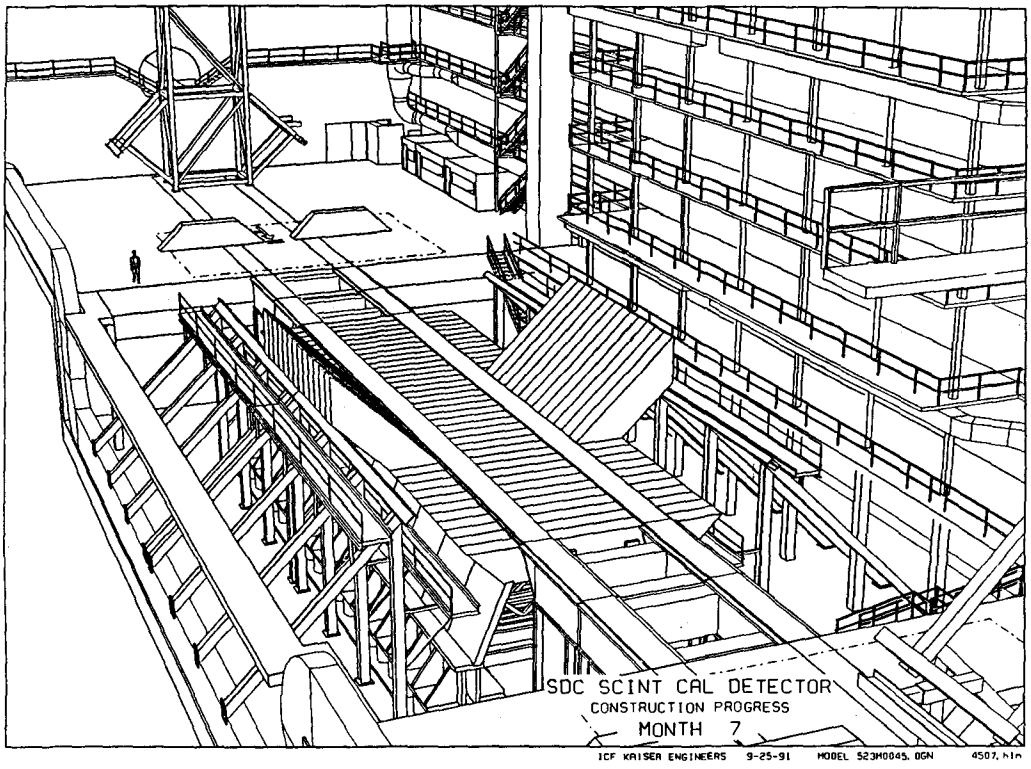
JAPAN	silicon detectors wire chamber readout system calorimeter tile-fiber assemblies muon chambers, counters, readout solenoid magnet liquid argon calorimetry aspects of DAQ/trigger/electronics computing/software for SDC
USSR	muon counters muon toroids scintillator for calorimetry forward calorimetry silicon detectors
CANADA	front-end electronics forward calorimetry intermediate-angle outer tracker

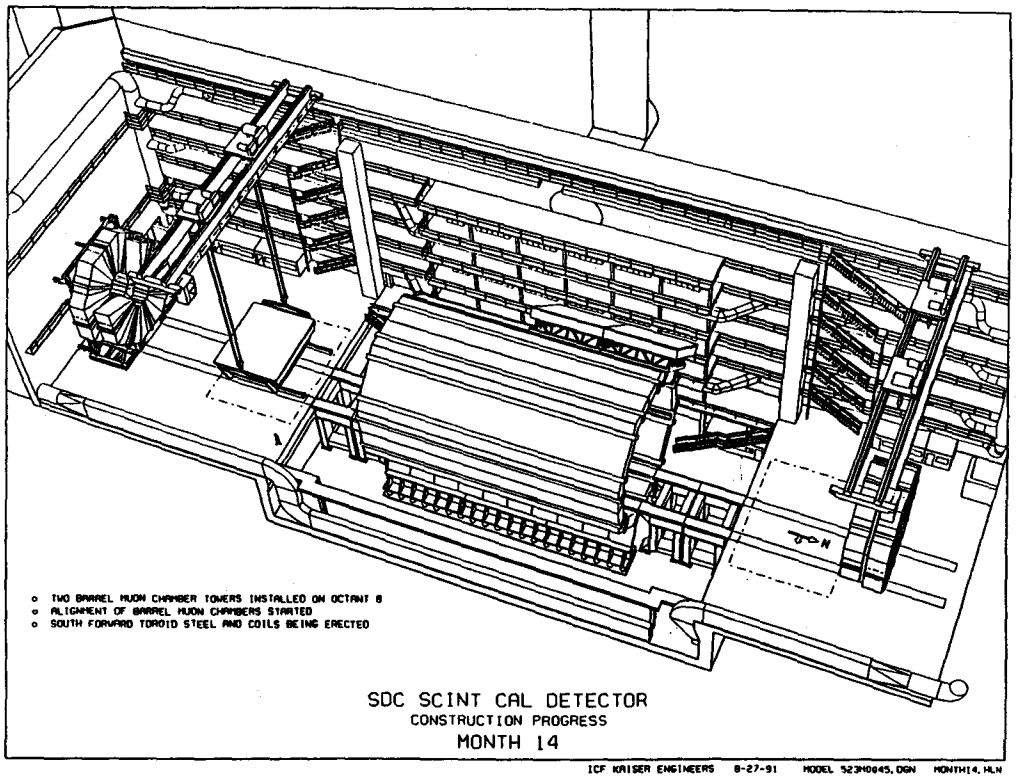


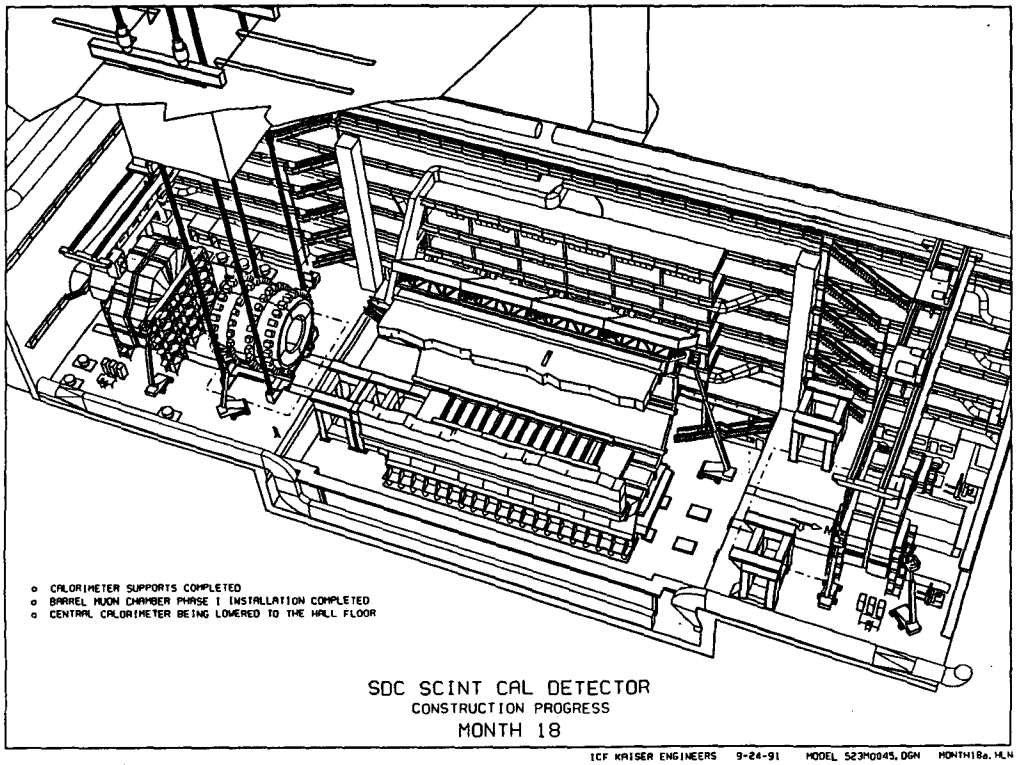

o HALL AT BENEFICIAL OCCUPANCY
SDC SCINT CAL DETECTOR
CONSTRUCTION PROGRESS
MONTH 0
ICF KAISER ENGINEERS 8-22-91 MODEL 523M0045.DGN MONTH00.MLN

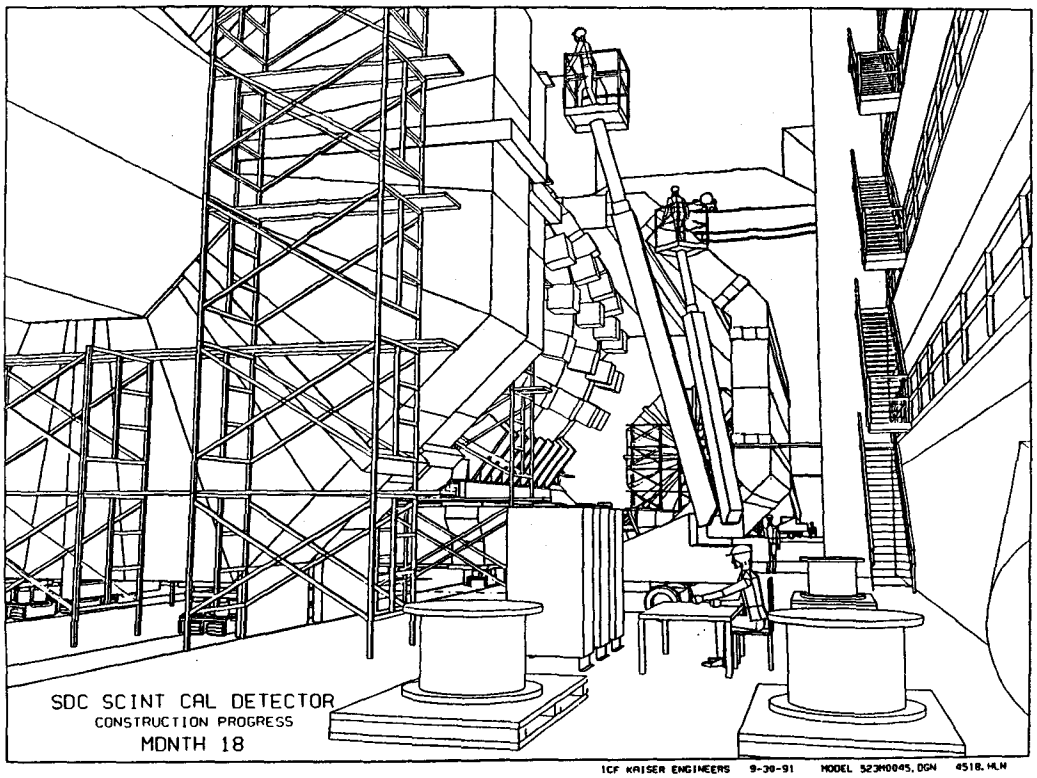

TEMPORARY SUPPORTS
o DETECTOR LIFTING BEAMS BEING INSTALLED
SDC SCINT CAL DETECTOR
CONSTRUCTION PROGRESS
MONTH 2
ICF KAISER ENGINEERS 8-22-91 MODEL 523M0045.DGN MONTH02.MLN

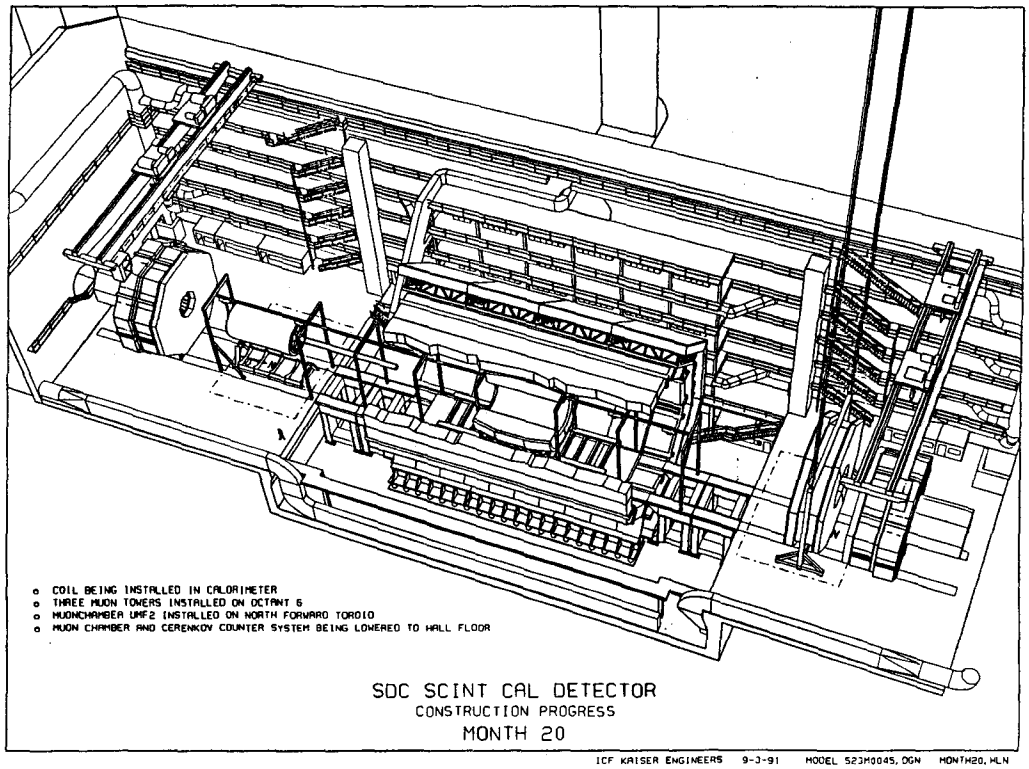

SDC SCINT CAL DETECTOR
CONSTRUCTION PROGRESS
MONTH 5
ICF KAISER ENGINEERS 9-25-91 MODEL 523M0045.DGN 4505.hln

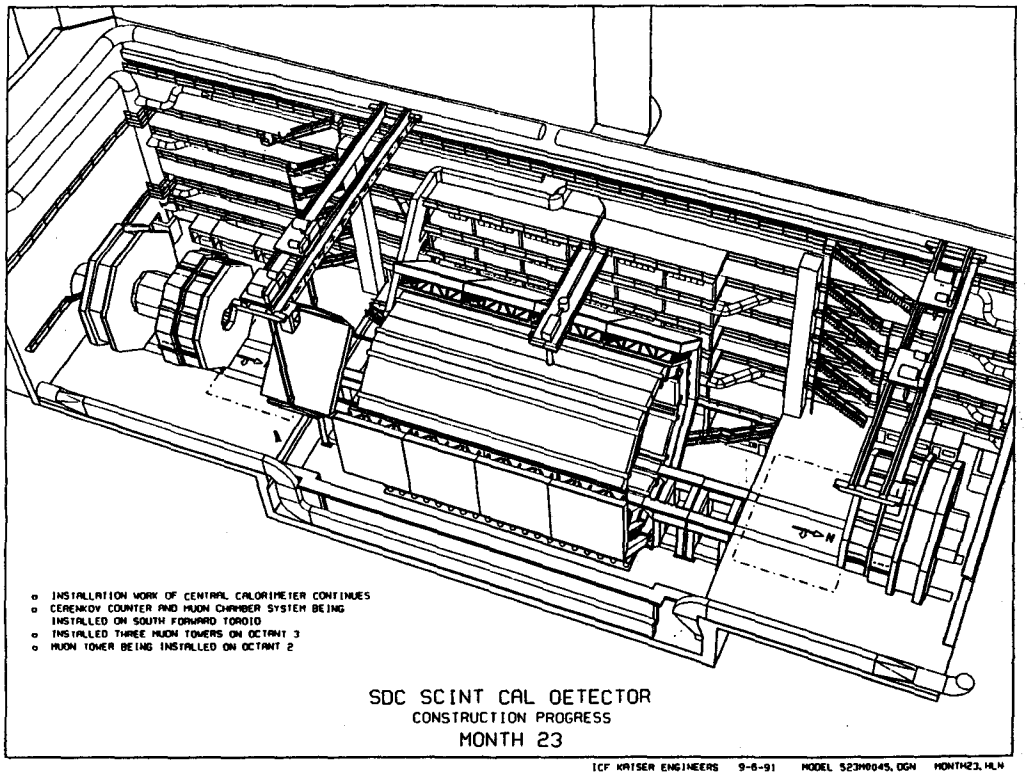

SDC SCINT CAL DETECTOR
CONSTRUCTION PROGRESS
MONTH 7
ICF KAISER ENGINEERS 9-25-91 MODEL 523M0045.DGN 4507.hln

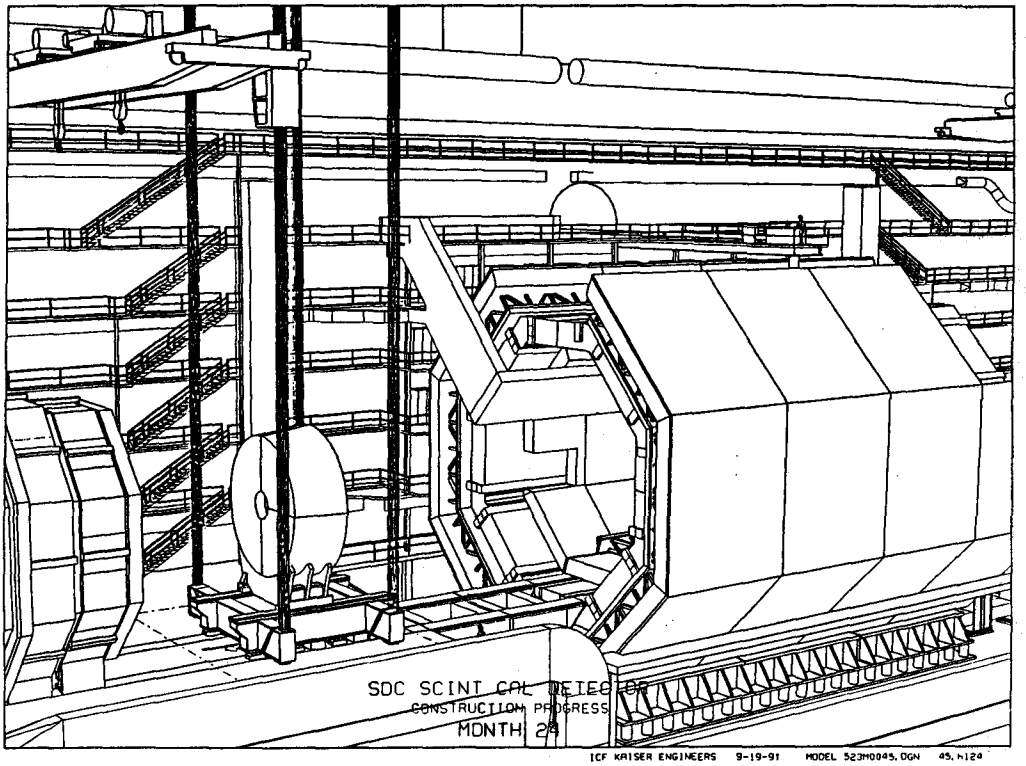

o TWO BARREL MUON CHAMBER TOWERS INSTALLED ON OCTANT 8
o ALIGNMENT OF BARREL MUON CHAMBERS STARTED
o SOUTH FORWARD TOROID STEEL AND COILS BEING ERECTED
SDC SCINT CAL DETECTOR
CONSTRUCTION PROGRESS
MONTH 14
ICF KAISER ENGINEERS 8-27-91 MODEL 523M0045.DGN MONTH14.HLN

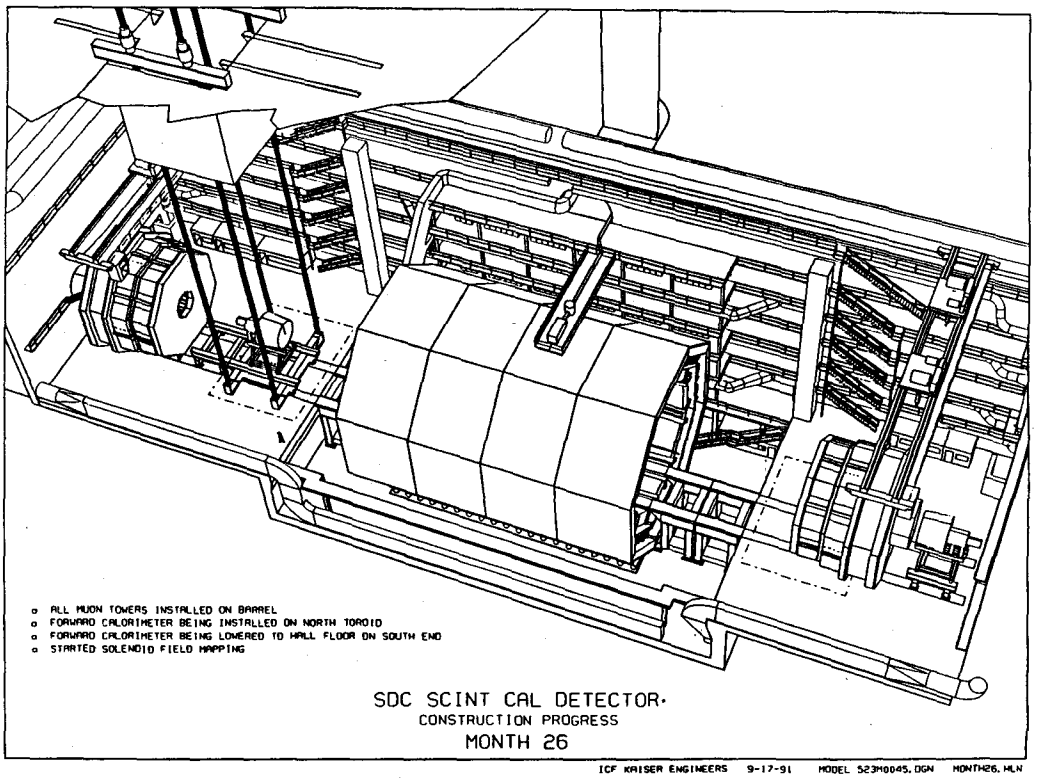

o CALORIMETER SUPPORTS COMPLETED
o BARREL MUON CHAMBER PHASE I INSTALLATION COMPLETED
o CENTRAL CALORIMETER BEING LOWERED TO THE HALL FLOOR
SDC SCINT CAL DETECTOR
CONSTRUCTION PROGRESS
MONTH 18
ICF KAISER ENGINEERS 9-24-91 MODEL 523M0045.DGN MONTH18a.HLN

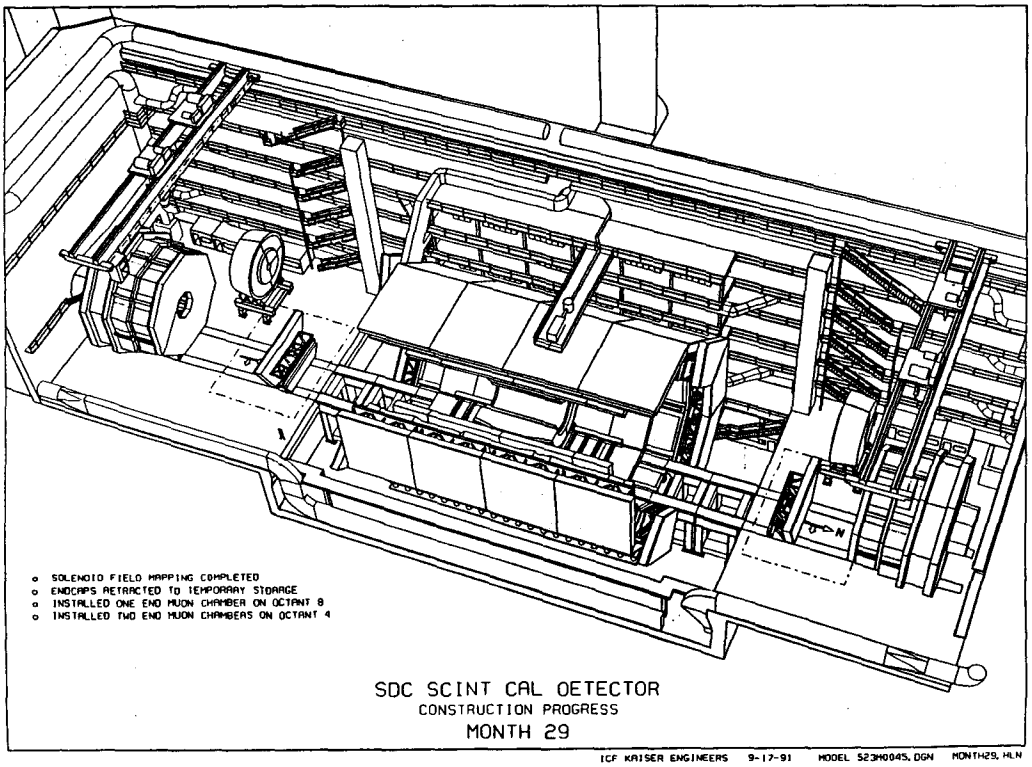

SDC SCINT CAL DETECTOR
CONSTRUCTION PROGRESS
MONTH 18
ICF KAISER ENGINEERS 9-30-91 MODEL 523M0045.DGN 4518.HLN

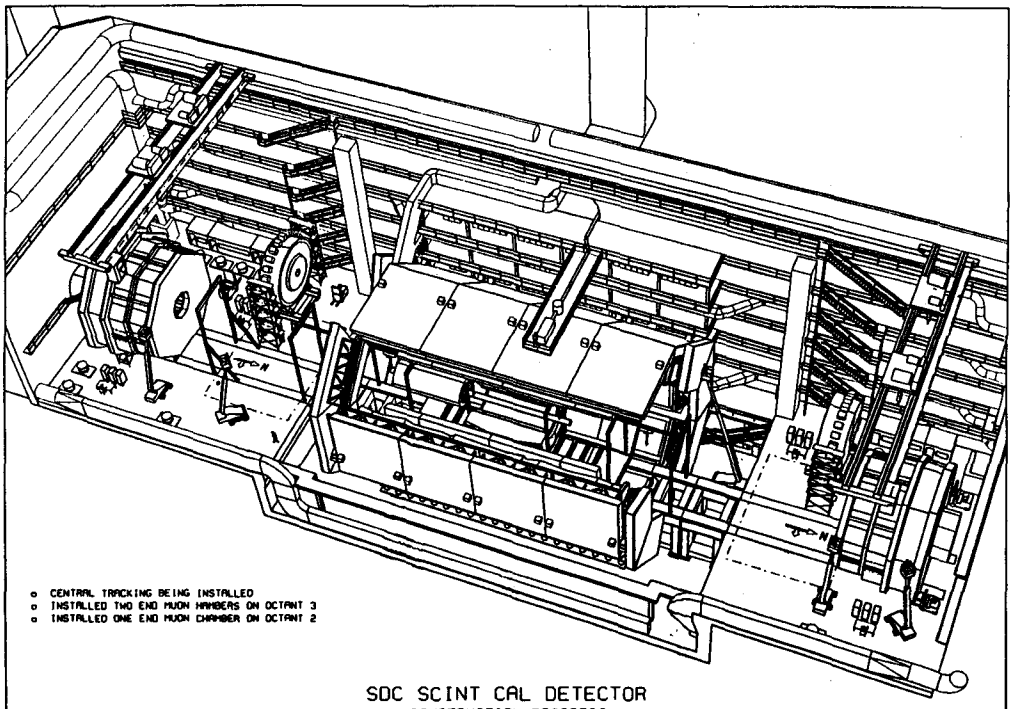

o COIL BEING INSTALLED IN CALORIMETER
o THREE MUON TOWERS INSTALLED ON OCTANT 6
o MUONCHAMBER UMF2 INSTALLED ON NORTH FORWARD TOROID
o MUON CHAMBER AND CERENKOV COUNTER SYSTEM BEING LOWERED TO HALL FLOOR
SDC SCINT CAL DETECTOR
CONSTRUCTION PROGRESS
MONTH 20
ICF KAISER ENGINEERS 9-3-91 MODEL 523M0045.DGN MONTH20.HLN


o INSTALLATION WORK OF CENTRAL CALORIMETER CONTINUES
o CERENKOV COUNTER AND MUON CHAMBER SYSTEM BEING INSTALLED ON SOUTH FORWARD TOROID
o INSTALLED THREE MUON TOWERS ON OCTANT 3
o MUON TOWER BEING INSTALLED ON OCTANT 2
SDC SCINT CAL OETECTOR
CONSTRUCTION PROGRESS
MONTH 23
ICF KAISER ENGINEERS 9-6-91 MODEL 523M0045.DGN MONTH23.HLN


SDC SCINT CAL DETECTOR
CONSTRUCTION PROGRESS
MONTH 24
ICF KAISER ENGINEERS 9-19-91 MODEL 523M0045.DGN 45.H124

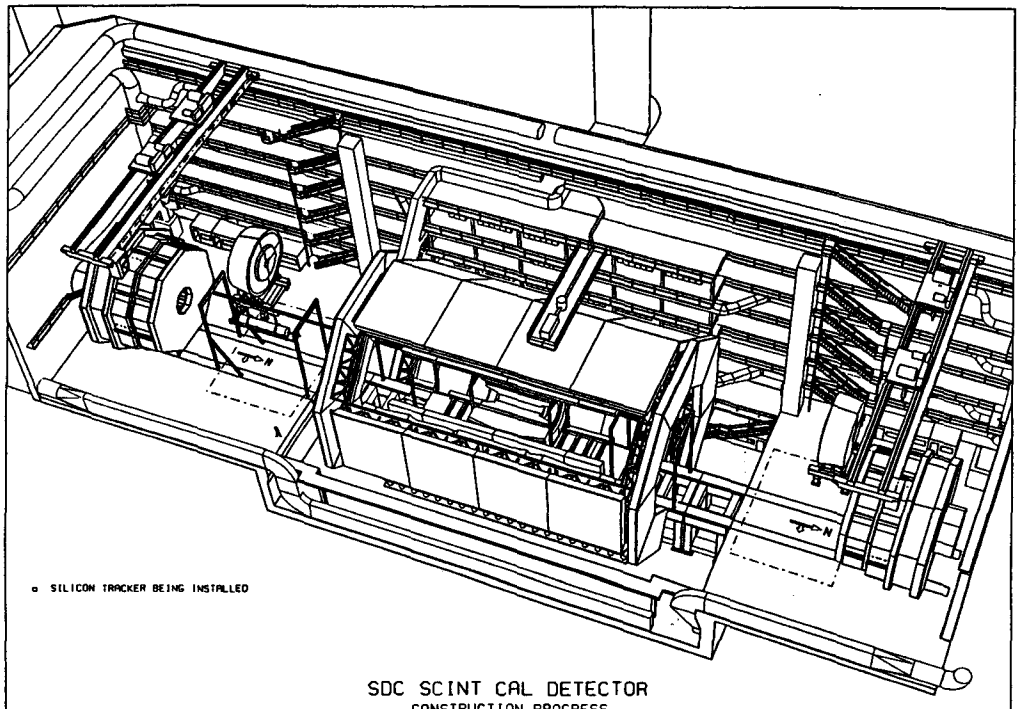

o ALL MUON TOWERS INSTALLED ON BARREL
o FORWARD CALORIMETER BEING INSTALLED ON NORTH TOROID
o FORWARD CALORIMETER BEING LOWERED TO HALL FLOOR ON SOUTH END
o STARTED SOLENOID FIELD MAPPING
SDC SCINT CAL DETECTOR·
CONSTRUCTION PROGRESS
MONTH 26
ICF KAISER ENGINEERS 9-17-91 MODEL 523M0045.DGN MONTH26.MLN


o SOLENOID FIELD MAPPING COMPLETED
o ENDCAPS RETRACTED TO TEMPORARY STORAGE
o INSTALLED ONE END MUON CHAMBER ON OCTANT 8
o INSTALLED TWO END MUON CHAMBERS ON OCTANT 4
SDC SCINT CAL OETECTOR
CONSTRUCTION PROGRESS
MONTH 29
ICF KAISER ENGINEERS 9-17-91 MODEL 523M0045.DGN MONTH29.MLN



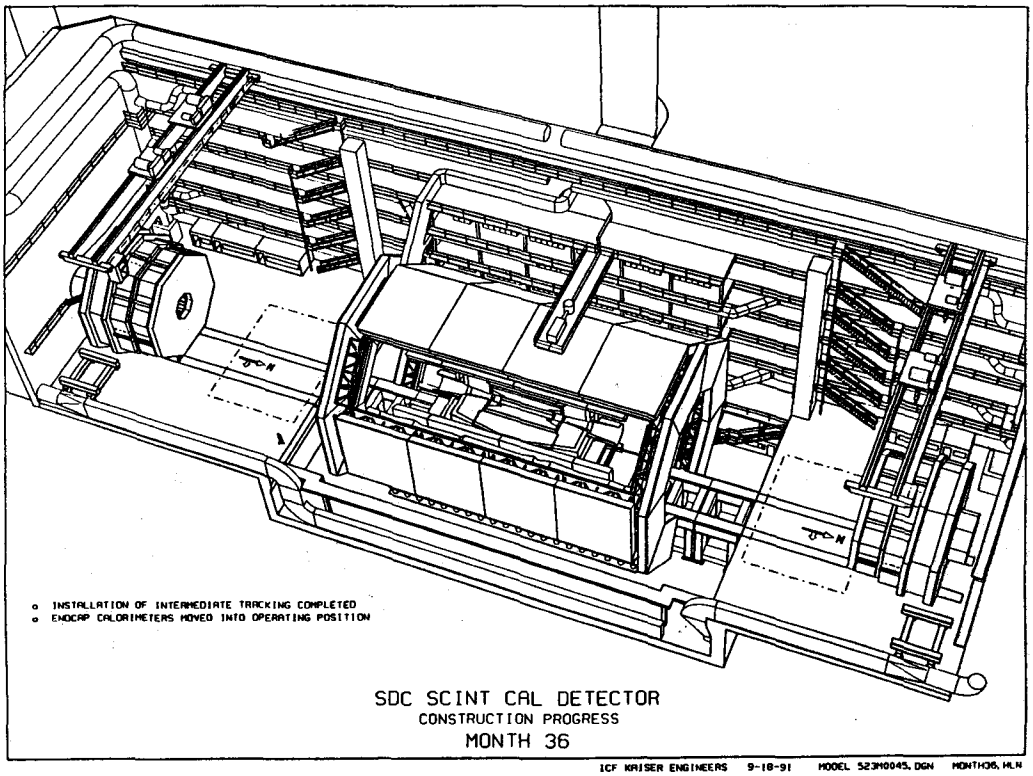
SDC SCINT CAL DETECTOR
CONSTRUCTION PROGRESS
MONTH 30

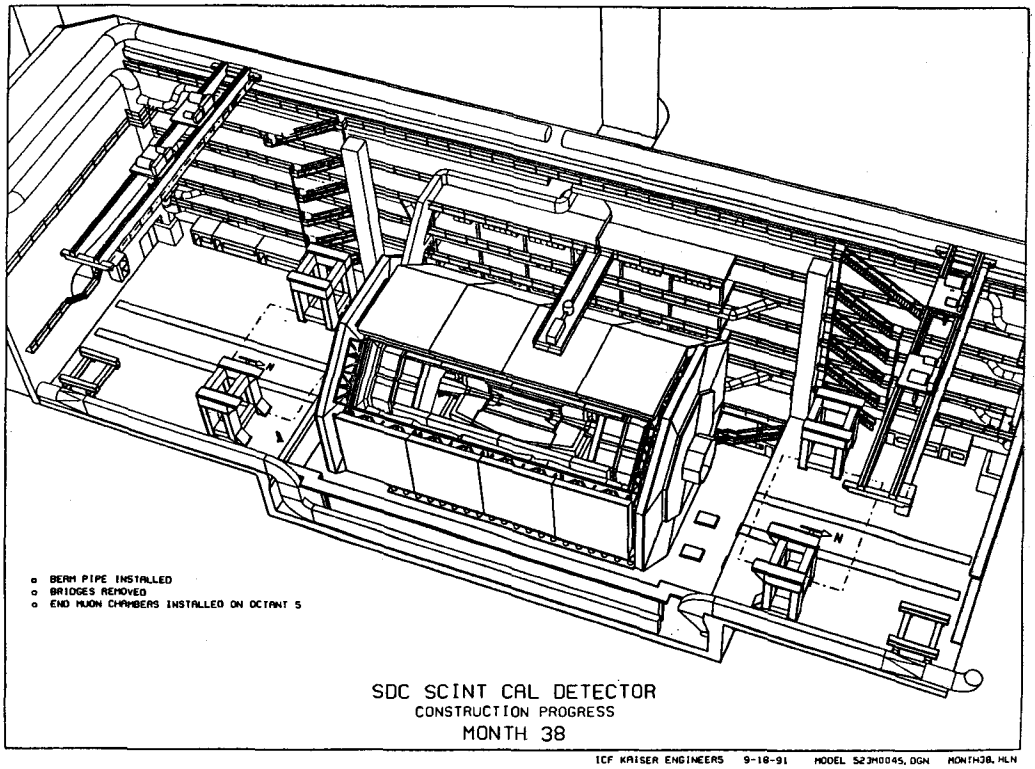
ICF KAISER ENGINEERS 9-30-91 MODEL 523M0845.DGN MONTH30.MLN

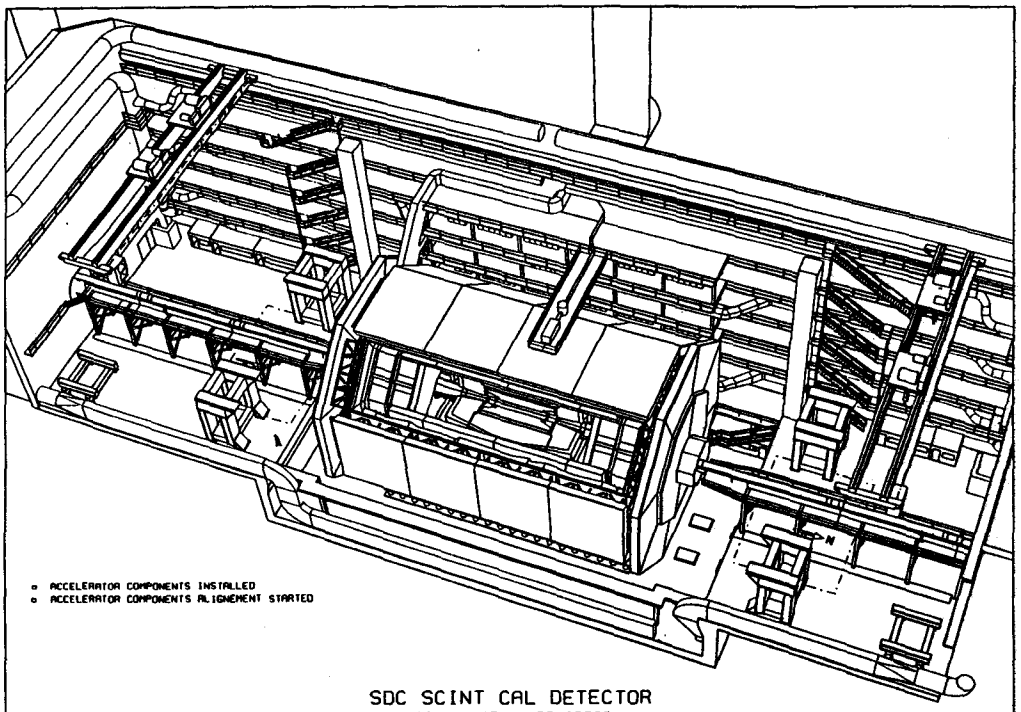


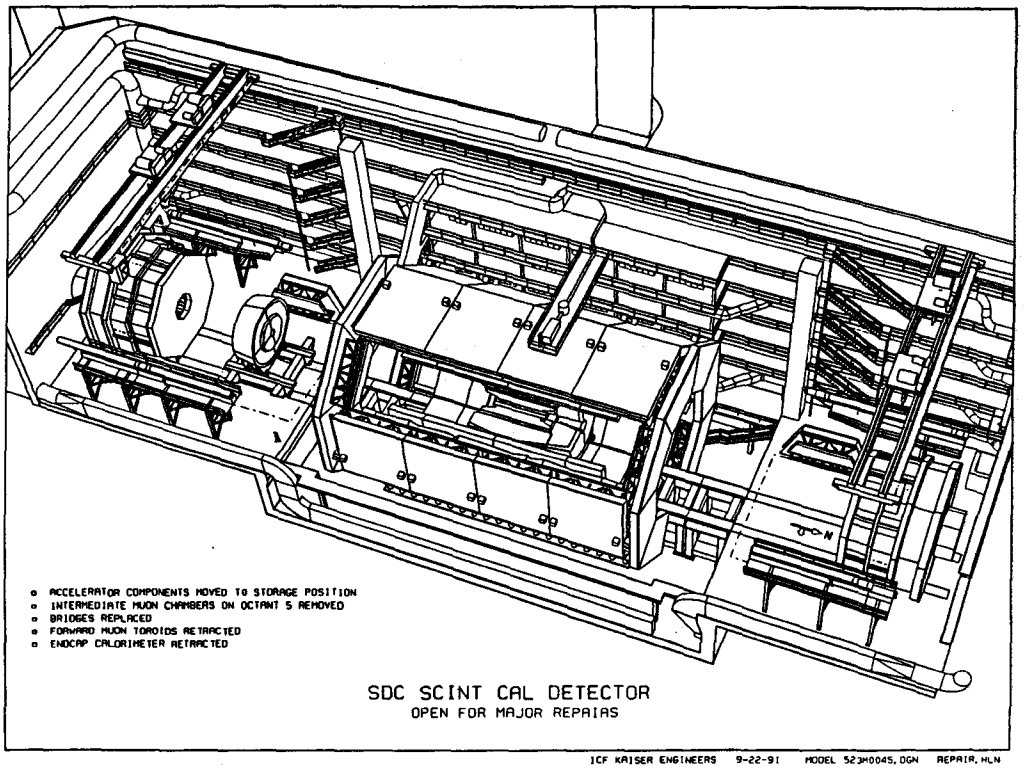
SDC SCINT CAL DETECTOR
CONSTRUCTION PROGRESS
MONTH 32

ICF KAISER ENGINEERS 9-18-91 MODEL 523M0845.DGN MONTH32.MLN


o INSTALLATION OF INTERMEDIATE TRACKING COMPLETED
o ENDCAP CALORIMETERS MOVED INTO OPERATING POSITION
SDC SCINT CAL DETECTOR
CONSTRUCTION PROGRESS
MONTH 36
ICF KAISER ENGINEERS 9-18-91 MODEL 523M0045.DGN MONTH36.MLN


o BEAM PIPE INSTALLED
o BRIDGES REMOVED
o END MUON CHAMBERS INSTALLED ON OCTANT 5
SDC SCINT CAL DETECTOR
CONSTRUCTION PROGRESS
MONTH 38
ICF KAISER ENGINEERS 9-18-91 MODEL 523M0045.DGN MONTH38.MLN


ACCELERATOR COMPONENTS INSTALLED
ACCELERATOR COMPONENTS ALIGNEMENT STARTED
SDC SCINT CAL DETECTOR
CONSTRUCTION PROGRESS
MONTH 40
ICF KAISER ENGINEERS 9-18-91 MODEL 523M0045.DGN MONTH40.HLN


ACCELERATOR COMPONENTS MOVED TO STORAGE POSITION
INTERMEDIATE MUON CHAMBERS ON OCTANT 5 REMOVED
BRIDGES REPLACED
FORWARD MUON TOROIDS RETRACTED
ENDCAP CALORIMETER RETRACTED
SDC SCINT CAL DETECTOR
OPEN FOR MAJOR REPAIRS
ICF KAISER ENGINEERS 9-22-91 MODEL 523M0045.DGN REPAIR.HLN

Summary

- **SDC is an international collaboration of about 700 physicists from a dozen countries.**
- **SDC detector is a general purpose magnetic detector optimized for high p_t physics at the design luminosity with capability at higher luminosity.**
- **Calorimeter technology is selected. Tracking radius is fixed.**
- **Works on integration, cost and schedule have proceeded very well.**
- **SDC detector design is progressively put into definite shape toward the submission of Technical Proposal due on April 1, 1992.**

INTERESTS OF NON-U.S. SDC GROUPS
(continued)

FRANCE	shower-max system for e ID read-out electronics for SM level 2 trigger
GREAT BRITAIN	intermediate-angle outer tracker DAQ/trigger for silicon system
ITALY	silicon detector tile-fiber assemblies for calorimetry trigger and control electronics fiber tracker and/or muon system
PRC	EM module radiation damage studies

Optimistic estimate of non-U.S. SDC level: $290M
Reasonable goal: $200M. (Actual could well be less.)



B Physics at the SSC

S. Stone

B Physics at the SSC

Sheldon Stone
Department of Physics
Syracuse University
Syracuse, N. Y. 13244-1130, USA

Abstract

Ideas for both fixed target and collider experiments at the SSC are examined in terms of their potential to measure CP violation in the B system. Detector configurations are briefly described. Triggering and flavor tagging strategies are discussed. Collider experiments are shown to be able to make interesting physics measurements, including CP violation. They have an inherent advantage in rate over fixed target experiments which need to run at an $\approx$25 times larger interaction rate to be competitive.

1.0 Introduction

Currently, a few hundred B mesons have been fully reconstructed in many decay modes using e^+e^- colliders operating at the peak of the $\Upsilon(4S)$ resonance.[1] A few dozen have been reconstructed at the Tevatron in the modes ψK^- and ψK^{*0}.[2] In addition, we have learned that the b-lifetime is 1.3 ps, the semileptonic branching ratio is 11% and the the CKM matrix element V_{cb} =0.041$\pm$0.002$\pm$0.004, while the value for the ratio $|V_{ub}|/|V_{cb}|$ is $\approx$0.1.[1] The observation by the ARGUS group[3] that the mixing probability in the $B^0-\overline{B}^0$ system is 20% had the important implication that CP violating effects may be within experimental reach in the next generation of b experiments.

Much as searches for TeV scale phenomena are for either further understanding of the standard model, e. g. Higgs particles, or probes beyond the standard model, e. g. supersymmetric particles, measurements of CP violation in B decays

function both for finding standard model parameters, and as probes beyond the standard model particularly if they are not consistent with measurements from other systems. The triangle which can be derived from the unitarity constraint of the CKM matrix is shown in Fig. 1. Measurements of CP violation in neutral B meson decays can, in principle, determine all three of these angles.[4] CP violation measurements in charged B decays can also be used to test for "direct CP violation", i. e. CP violation that occurs through the decay rather than through the mass matrix, in analogue with ϵ'/ϵ experiments in the kaon system. We also would like to measure mixing in the B_s system and find rare B decays in so called "Penguin" modes such as $K\pi$, $K^*\gamma$, and $K\mu^+\mu^-$.

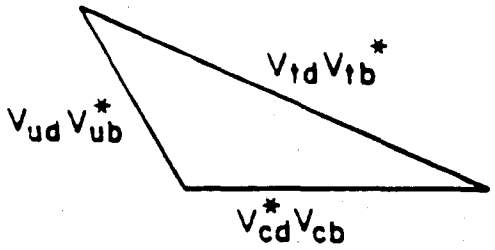


Fig. 1 The unitarity triangle illustrating the a relation among quark mixing matrix elements implied by unitarity of the CKM matrix. The angles can be determined by measuring CP violation in B decays.

In the next couple of years it is possible that some of these rare decays will be found. CP violation using the ψK_s will be found if an e^+e^- b-factory is constructed. There are prospects for measuring B_s mixing at LEP or the Tevatron but it is no means certain that this will be accomplished. The potential for B physics experiments proposed for the SSC will be discussed in this paper.

2.0 The SSC as a producer of B's

The SSC can be used to produce B's either in the collider or by interacting one 20 TeV proton beam with a fixed target. The cross-sections for $b\bar{b}$ production are very different in these two modes. The b-quark production diagrams are shown in Fig. 2. The relative size of the α^2 and α^3 terms is not well known and is expected to vary with energy.[5] Fig. 3 shows Berger's[6] predictions, including the α^3 term, for $p\bar{p}$ collisions as a function of center-of-mass energy. It is assumed that $b\bar{b}$ production in pp collisions is quite similar as suggested by Altarelli et al.[7] Also shown is the measured cross-section point from the UA1 collaboration.[8] The α^3 term is approximately 1.3 times as large as the α^2 term at UA1 energies

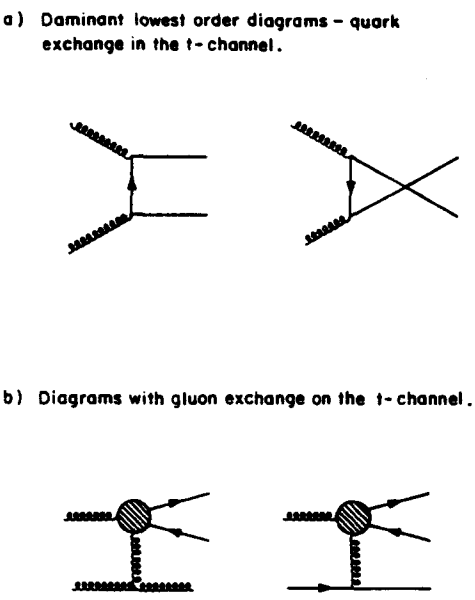


Fig. 2 Diagrams for $b\bar{b}$ production, (a) is for order α^2 with quark exchange, while (b) is for order α^3 with gluon exchange. From Ref. 5.

and its inclusion is necessary to obtain the good agreement with the data. The predicted cross-sections have large errors. At the fixed target center-of-mass energy of 194 GeV the uncertainty is smaller and an estimates of 2 ± 1 μb will be used. The collider center-of-mass energy is far above any experimental information and is a large theoretical extrapolation. The lowest order calcuation gives a value of 400 μb.[9] It may be an underestimate since the α^3 terms are not included. Preliminary CDF cross-sections, in limited η and p_t ranges, are factors of $\approx$5 larger than the lowest order calculation.[2] The dominant uncertainty at high energy results from the unknown gluon distribution functions at small scaled momenta, leading to an error of $\pm$300 μb on the lowest order calculation. If the higher order term stays 1.5 times as large as the lowest order the cross section would be 1 mb at the collider. These considerations lead to the use of the value $400^{+1300}_{-\ 300}$ μb for the collider modes cross-section.

Other important considerations are the production ratios of $b\bar{b}$ to total and charm to $b\bar{b}$. The former is important because it sets the scale for how effective the event trigger must be in discriminating against most events (often called "minimum bias events"), while the latter is important because charm events have important similarities to beauty events, in that they produce leptons and have life-

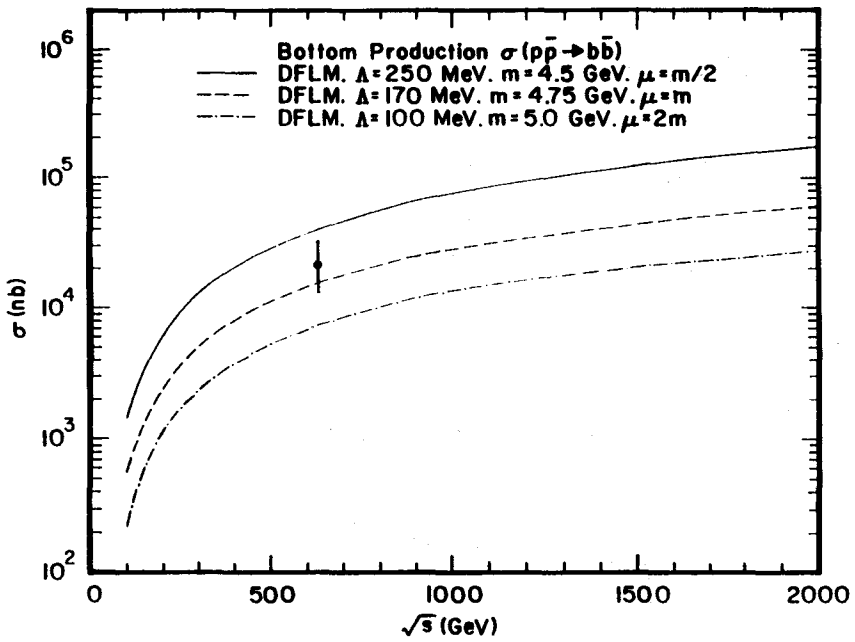


Fig. 3 Predicted cross-section for $b\bar{b}$ through order α^3, for different choices of the QCD scale parameter Λ, m_b and factorization scale μ. From ref. 5.

times comparable to beauty hadrons, therefore having topologies that also include detached vertices. The average predicted $c\bar{c}/b\bar{b}$ ratios given in Table 1 and shown as functions of rapidity and transverse momentum in Figs. 4 and 5.[10] It can be seen that the ratio changes by large factors in different rapidity and transverse momentum regions.

Table 1: SSC $b\bar{b}$ cross-sections and ratios

	Collider	Fixed Target
$\sqrt{s}$	40 TeV	194 GeV
$\sigma(b\bar{b})$	400^{+1300}_{-300} μb	2 ± 1 μb
$c\bar{c}$:$b\bar{b}$	10:1	100:1
$\frac{b\bar{b}}{\text{total}}$ *	$\frac{1}{60} - \frac{1}{250} - \frac{1}{1000}$	$\frac{1}{4200} - \frac{1}{6250} - \frac{1}{12500}$

* for A=1 in collider and A=184 for fixed target

Since the $b\bar{b}$ and total cross-sections have different dependencies on the atomic

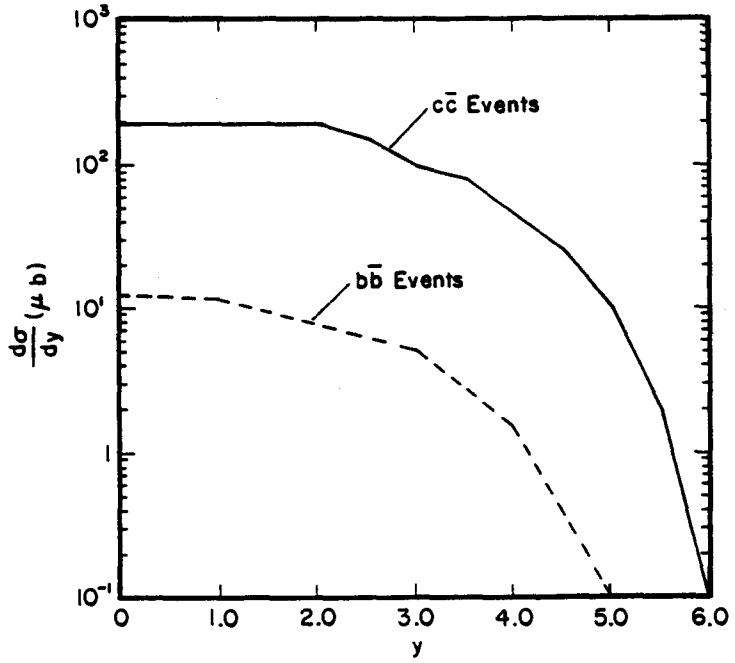


Fig. 4 Predicted rapidity distributions for $c\bar{c}$ and $b\bar{b}$ production at $\sqrt{s}$=1.8 TeV.

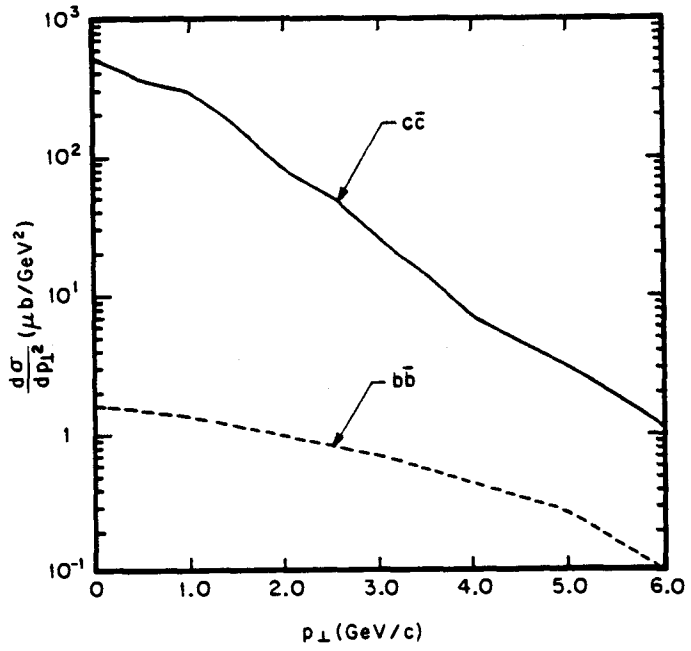


Fig. 5 Predicted transverse momentum distributions for $c\bar{c}$ and $b\bar{b}$ production at $\sqrt{s}$=1.8 TeV.

number A, it is possible, in the fixed target mode, to enhance the ratio of $b\bar{b}$ to total cross-section by using a large A target. The ratio $\frac{b\bar{b}}{\text{total}}$ varies as $\approx A^{\frac{1}{3}}$ For example, use of tungsten would enhance $\frac{b\bar{b}}{total}$ by a factor of 4, but with an increase in the average multiplicity of minimum bias events. In what follows a tungsten target is assumed.

The relative size of the first order and α^3 terms in the perturbative expansion of the cross-section calculation also affects the correlations in azimuthal angle and rapidity (η)[11] of the b and the $\bar{b}$. It is generally thought that the b and $\bar{b}$ are produced within two units of rapidity of each other. Production is at low p_t, with $p_t \approx m_b$ and widely spread in η. These two characteristics lead to sharply peaked angular distributions (see Fig. 6).

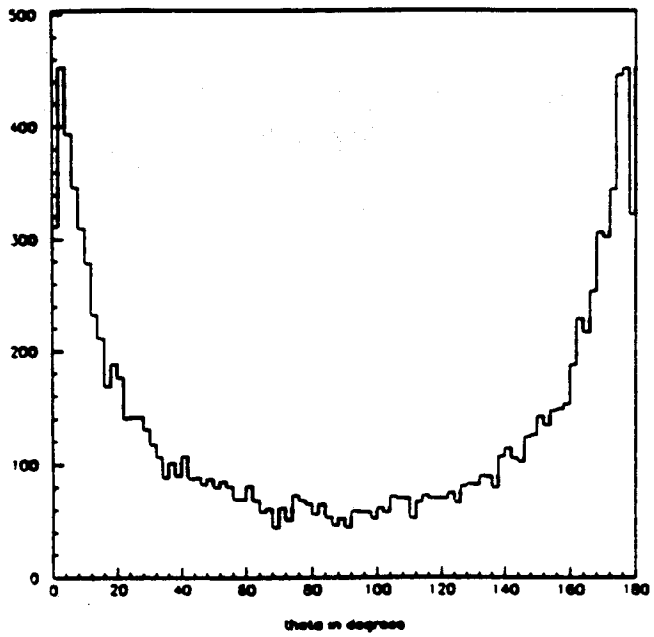
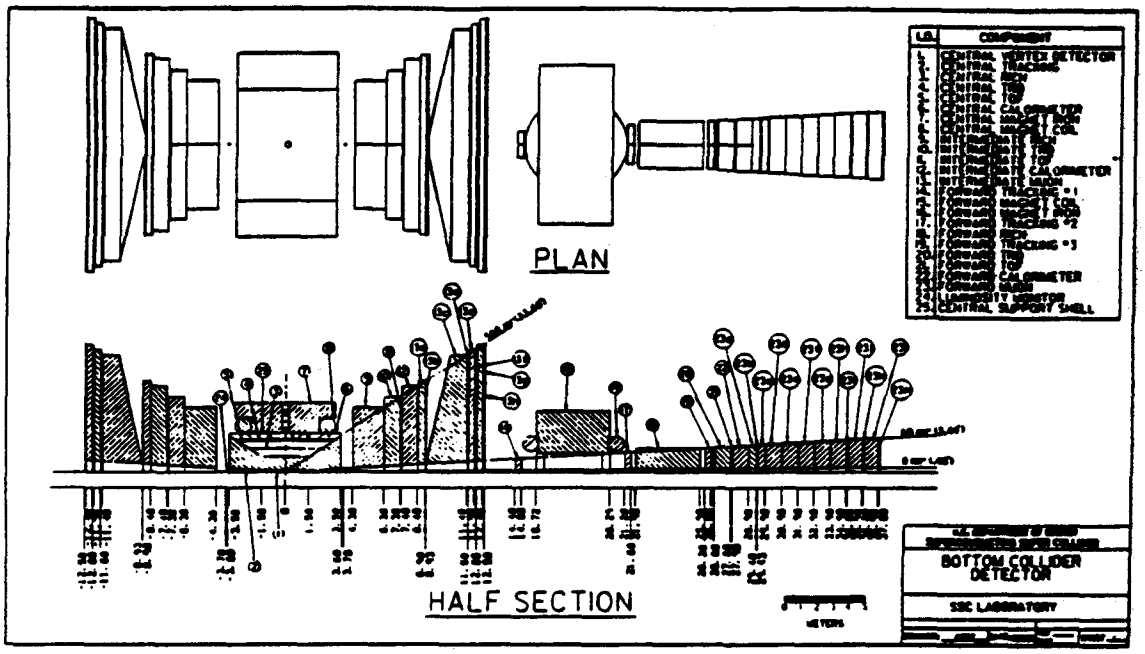


Fig. 6 Polar angular distribution (in degrees) for tracks from b events (from BCD).

3.0 Proposed Detector Configurations

Four EOI's have been submitted to SSC, two for fixed target experiments and two for collider experiments. All of the detectors proposed for fixed target or collider B experiments have a set of common elements. Closest to the interaction point is a silicon vertex detector followed by charged particle tracking with magnetic momentum analysis. Each of them has charged particle identification using

one form or another of ring imaging Cherenkov counters. These are followed by comparatively poor resolution electromagnetic shower counters, mostly to identify electrons. All have (or should have) iron for muon identification. The reasons for this commonality are easy to understand: the silicon is used to find separate decay vertices for the B's, the magnet is for good mass resolution, the Cherenkov's provide particle identification information useful for B flavor tagging and exclusive B reconstruction, while the shower counter and muon detector provide lepton identification necessary in the trigger and useful for flavor tagging.



Plan and section views of the BCD. Central Detector: 1: silicon vertex detector, 2: straw-tube tracking system, 3: RICH counter, 4: transition radiation detector, 5: time-of-flight system, 6: electromagnetic calorimeter, 7: magnet yoke, 8: superconducting coil. Intermediate Detector: 9: RICH counter, 10: TRD, 11: time-of-flight, 12 E-M calorimeter, 13: Muon system. Forward Detector: 14, 17, 19: tracking, 15: superconducting coil, 16: magnet yoke, 18: RICH counter, 20: TRD, 21: time-of-flight, 22: E-M calorimeter, 23 muon system, 24: luminosity monitor, 25: central support shell.

Fig. 7 View of the BCD detector.

The BCD group[12] proposes a collider detector which emphasizes the central region but also tries to get as large an η coverage as possible. A schematic view is

shown in Fig. 7. This group is now trying to downsize their proposal, which they had originally estimated to cost \$200 million, to \$50 million. They are performing R&D on silicon vertex detectors, straw-tube tracking, hadron identification, trigger and data acquisition.

The other collider detector proposal adopts a very different approach. Two forward arm spectrometers are proposed,[13] covering the region $5.5 > \eta > 1.2$, with each spectrometer consisting of three separate mini-spectrometers as shown in Fig. 8. One key element in this proposal is to have the silicon vertex detector inside the beam pipe vacuum, allowing for high accuracy vertex determination. The momentum distribution of B's produced at the LHC (SSC spectra are similar) within the detector acceptance is high enough (see Fig. 9) to provide easily detectable separations between B decay vertices and the main event vertex.

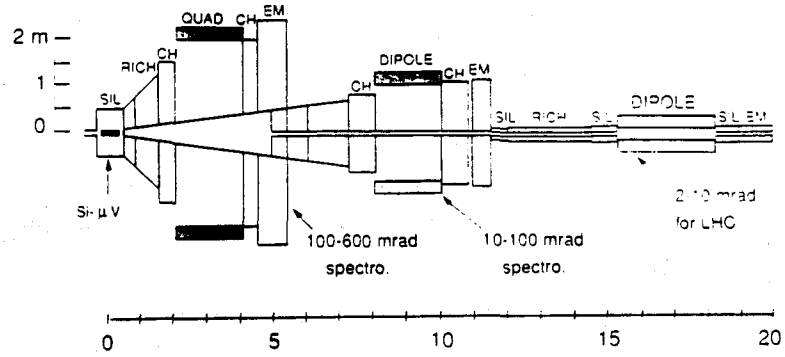


Fig. 8 Layout of one arm of the Forward Beauty Spectrometer, FBC.

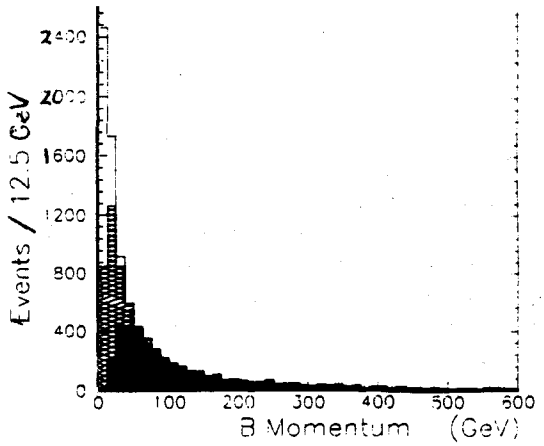


Fig. 9 Momentum distributions of B mesons at LHC as generated in lowest order QCD using PYTHIA. Unshaded are all events, shaded are those with laboratory angle <600 mr and solid are those events which have all tracks contained within 600 mr. The B flight path is $\approx$7.5 mm per GeV/c.

There are two concepts for fixed target experiments; one uses an internal gas jet target (IGT),[14] while the other uses an extracted 20 TeV beam from a bent crystal channel (SFT).[15] Apparently, both methods are feasible but the effects on the stored beam have not yet been evaluated. It will be assumed that there are no "show stoppers" in this regard. For the fixed target experiments a particle moving at 90° with respect to the beam axis in the center-of-mass system appears at 10 mr in the laboratory. As a consequence particles will be collimated in an extremely narrow cone around the beam axis. This requires these experiments to do a excellent job of tracking and pattern recognition down to very small angles.

The IGT detector is shown in Fig. 10. The SFT external beam experiment is shown in Fig. 11. This experiment has a target of 10% of an interaction length thickness composed of Be foils interspersed between silicon strip detectors.

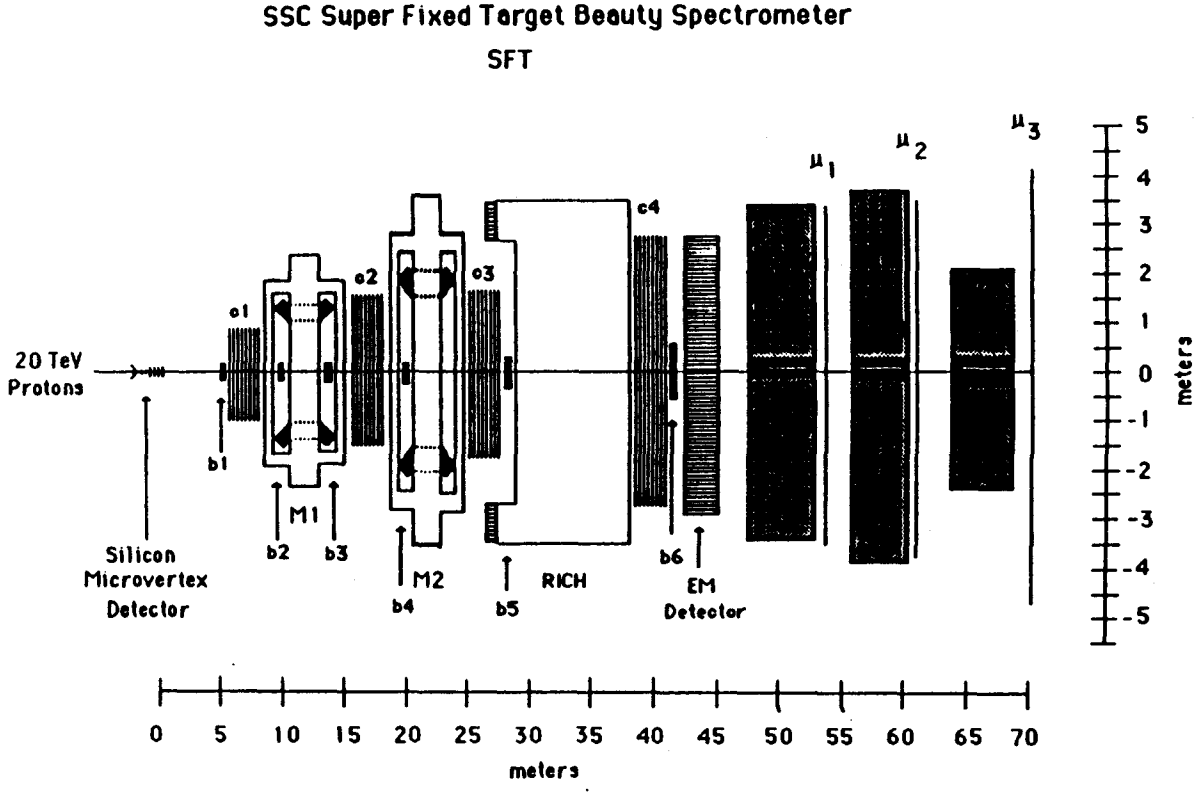


Fig. 11 View of external beam experiment, SFT

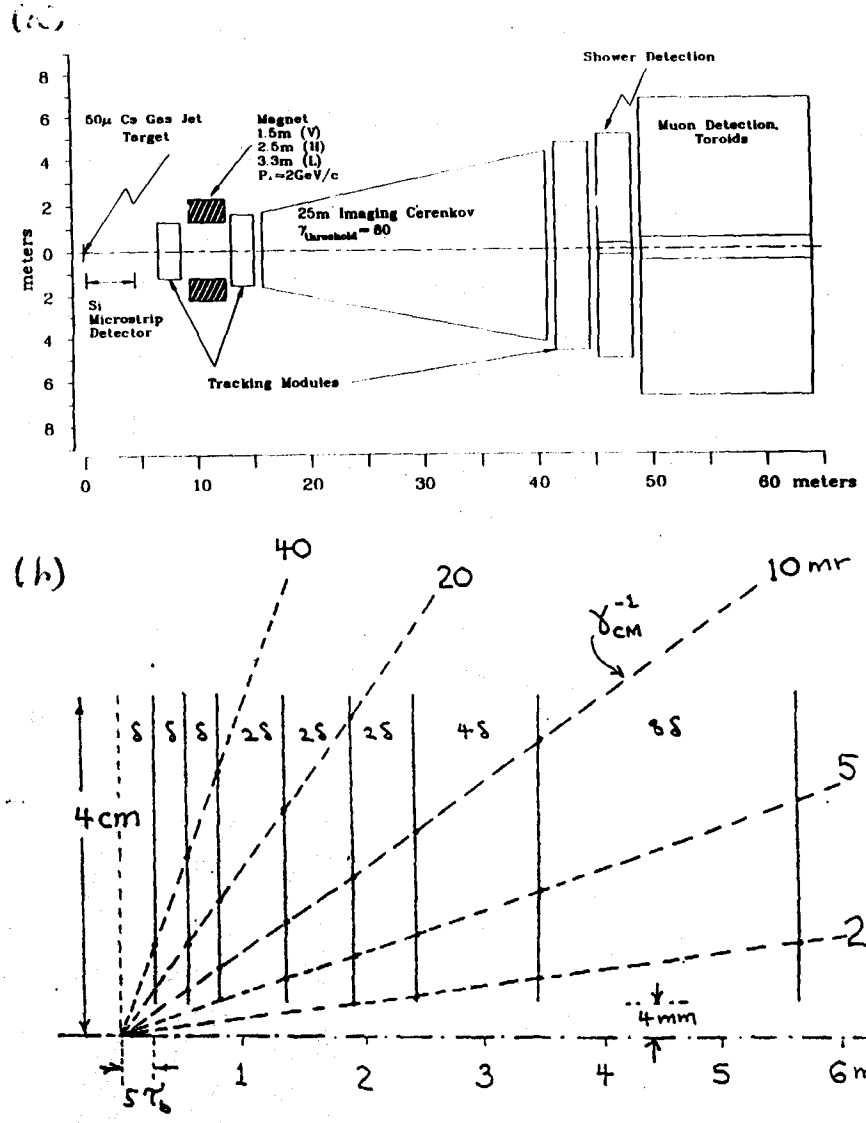


Fig. 10 View of Internal Gas Jet target experiment (a) overall, (b) silicon vertex detector.

4.0 Constraints

There are various experimental limitations which must be respected by all configurations. The effects of radiation damage must be considered for all elements. The silicon detectors detectors for the FBC and IGT experiments are particularly vulnerable since they are inside the beam pipe. The primary interaction rate is also limited by the response of the different detector elements. For example, the silicon shaping time has to be $\approx$20 ns to have single beam bucket resolution. At 10^7

interactions/sec, 10% of the events have more than one interactions. This makes it particularly difficult to implement certain event triggers, such as the detached vertex trigger. Therefore, for purposes of this talk, a rate if 10^6 interactions/sec will be considered as a conservative albeit achievable upper bound.

The rate at which data can be archived, that this written to tape or other medium, also presents a serious limit. Right now the maximum achieved rate is 10 megabytes/sec (MB/sec). In the future it may be that 100MB/sec is achievable. For a 100 kilobyte sized event (typical CDF event size), one can collect 100 events/sec now, which might rise to 1000 events/sec. Note, that if one wants to collect 10^9 $b\bar{b}$ events in a year (10^7 sec), one is saturating the data stream with real events at a 100 event/sec storage rate.

The forward direction is where most of the B decay tracks are. For BCD this is a severe limitation because the silicon is placed outside of the beam pipe and starts 1.25 cm from the beam line. A particle at 10 mr experiences 100 times the beam pipe thickness and is likely to scatter or interact. BCD has thought of schemes of flaring the beam pipe but this leads to regions within the acceptance where particles cross a practically infinitely thick section. The acceptance is limited to <2 mr for FBC because of the hole down the beam pipe and to >600 mr because of the size of the spectrometer. As the beam pipe is outside the silicon detectors, particles will not undergo appreciable multiple scattering or have a significant hadronic interaction probability before crossing these devices, however the beam pipe must be somewhere and it will cause interactions of some of the secondary particles. The limitations in forward acceptance for the fixed target experiments are more severe because the center of mass is folded so far forward. (Recall a particle at 90° in the center-of-mass is at 10 mr in the laboratory.) The IGT spectrometer is limited to > 2 mr because of the beam hole and SFT has similar limitations.

5.0 Triggering

5.1 Strategies

We have seen that we need to reduce the event rate to 100-1000 Hz. Three strategies to achieve this goal have been discussed in various ways by the different EOI's.

1. Use the decay $B \to \psi X$, with the subsequent decay of the $\psi \to \ell^+\ell^-$. The efficiency of this trigger, ϵ_ψ, can be estimated as:

$$\epsilon_\psi = 2 \cdot B(B \to \psi X) \cdot B(\psi \to \ell^+\ell^-) \cdot \epsilon_a,$$

where ϵ_a is the ψ reconstruction efficiency of the apparatus. This will differ among

the experiments and 1/4 appears to be a "reasonable" estimate. Using $B(B \rightarrow \psi X) = 1.2\%$ and $B(\psi \rightarrow \ell^+\ell^-) = 14\%$, results in $\epsilon_\psi = 8 \times 10^{-4}$.

2. Use the semileptonic decay $B \rightarrow X\ell\nu$. Perhaps this is restricted to the case where the lepton is a muon because of the background in the electron sample from $\gamma \rightarrow e^+e^-$, Dalitz decays of the π^0, etc. The efficiency of this trigger is:

$$\epsilon_\mu = 2 \cdot B(B \rightarrow X\mu\nu) \cdot \epsilon_a \cdot \epsilon_p = 3 \times 10^{-2},$$

where ϵ_p ($\approx$1/2) is the efficiency for the momentum and p_t used to preferentially select muons from b decays instead of those from charm decays and B($B \rightarrow X\mu\nu$) is taken as 11%.[16]

3. Use detached vertices. In principle this can have a large efficiency, especially if the B momentum is large. A reasonable expectation may be ϵ_v=0.7, but it also has good efficiency for charm.

There have also been some suggestions in fixed target experiments to use additional hadrons with p_t >1-1.5 GeV to enhance the trigger, but this suggestion will not be pursued further in this paper.[17]

5.2 Trigger Rates

It is difficult to evaluate the rates of the different triggers without a detailed Monte Carlo study and it would be useful to be able to compare such a study with some data even if taken at lower energies. Nevertheless, it is possible to make some general comments. First of all the needed rejections are quite large. To get a data sample which is an equal amount of B signal and background the trigger rejections must be $250 \times 1/\epsilon$ against minimum bias events at the collider and approximately a factor of 25 better at the fixed target. Furthermore the needed rejection factor against charm at the collider is $10 \times 1/\epsilon$, depending on the η region (see Fig. 4) and $\approx$10 times higher for fixed target.

The rejection and efficiencies of the different triggers are intimately tied to the detector geometry. The best situation for detached vertex triggering is in the IGT geometry because the main event vertex is approximately a point source. (The actual size is $\approx 50\mu m^3$.) The next best situation is a line source as present in the two collider experiments (BCD and FBC). The worst situation is a volume source which we will see is the situation for SFT.

To achieve maximum signal to background it may be essential to combine triggers. For example, the high p_t muon trigger can be combined with a detached vertex trigger to reduce the background from both minimum bias and charm events.

Let us see how many tagged fully reconstructed B meson decays can be accumulated at the SSC under some specific trigger scenarios. In the first case, the ψ trigger discussed above is used. We assume that the background in this trigger is negligible. (If needed, we could add in the detached vertex requirement in without a substantial loss of efficiency.) Defining a year as 10^7 seconds, the number of $B \to \psi X$ events accumulated in a collider experiment running at a luminosity of $10^{31}\text{cm}^{-2}\text{sec}^{-1}$ is given by:

$$\#\text{ of events} = \mathcal{L} \cdot \#\text{ of sec} \cdot \sigma_{b\bar{b}} \cdot \epsilon_{\psi} = 10^{31} \cdot 10^{7} \cdot 400\mu b \cdot 8 \times 10^{-4} = 3.2 \times 10^{7}.$$

For the fixed target at 10^6 interactions per second on tungsten:

$$\#\text{ of events} = \text{int/sec} \cdot \#\text{ of sec} \cdot b\bar{b}/tot \cdot \epsilon_{\psi} = 10^{6} \cdot 10^{7} \cdot (1/6250) \cdot 8 \times 10^{-4} = 1.3 \times 10^{6}.$$

Thus the number of $b\bar{b}$ is 25 times larger for the collider than the fixed target for the cross-section assumptions given in Table 1 and equal trigger, geometric and track reconstruction efficiencies. These capabilities depend strongly on actual detector configurations.

The fraction of ψK_s events in this data sample (collider) is given by:

$$\frac{\psi K_s}{\psi X} = \frac{B^0}{b} \cdot \frac{B(B^0 \to \psi K_s)}{B(B \to \psi X)} \cdot B(K_s \to \pi^+\pi^-)\epsilon_{K_s} = \frac{1}{4} \cdot \frac{1}{33} \cdot \frac{2}{3} \cdot \frac{1}{3} = 1.7 \times 10^{-3},$$

where $\frac{B^0}{b}$ is the fraction of B^0 events guessed to be 1/4 and ϵ_{K_s} is the efficiency for finding the K_s, guessed as 1/3. Thus, the number of flavor tagged ψK_s events per year in the collider mode is $5.4 \times 10^4 \cdot \epsilon_{tag}$. The tagging efficiency, ϵ_{tag}, must be evaluated for each experiment and will be discussed later. A reasonable tagging efficiency is 10%. Thus we can expect 5400 tagged ψK_s events per year which can be favorably compared to the $\approx$500 expected in an e^+e^- b factory.[18] The ψK_s events can be used to measure one of the three angles describing CP violation in the B system. Can we use the events from this trigger for anything else? Let us consider B_s mixing. Unfortunately the decay $B_s \to \psi\phi$ cannot be used to measure B_s mixing because in is not flavor specific.[19] However the Cabibbo suppressed B_s decay $\psi K^-\pi^+$ does discriminate between B_s and $\overline{B}_s$ and can be used. The decay diagram is shown in Fig. 12. The branching ratio is estimated as $B(\overline{B}_s \to \psi K^-\pi^+) = sin^2\theta_C \cdot B(\overline{B}^0 \to \psi K^-\pi^+) = 10^{-4}$. Thus, in one year a sample of the order of 100 events should be collected but the background levels need to be estimated. Another possible use of this sample is to provide a flavor tag by fully reconstructing final states such as ψK^-, $\psi K^-\pi^+$, etc.. The number of ψK^- events alone is 4.2×10^5 per year. This could also be useful for measuring B_s mixing but

again detailed studies need to be performed to evaluate the detector efficiency for reconstructing B_s decays such as $D_s\pi^-$ and how large the backgrounds are. Thus the ψ trigger has important but limited uses.

The next example, which appears very promising, involves a combination of the high p_t and detached vertex triggers. These two criteria need to be used simultaneously in order to discriminate both against minimum bias and charm events. The efficiency of this combination will be taken as 2%; however it is possible that the background rate would require more stringent vertex or p_t cuts and thus the efficiency could go down. Using this assumption, we have 8×10^8 events in the collider mode per year. These events are also flavor tagged by the muon in the trigger. It is possible that some of these are wrong sign coming either from background or the decay chain $b \rightarrow c \rightarrow \mu$. The size of this effect must be evaluated. However, for purposes of the present discussion, it will be ignored. Interesting final states will need to be selected out of this flavor tagged sample. For example, the number of $B^0 \rightarrow \pi^+\pi^-$ with positive versus negative lepton tags, provides a measure of a CP violating angle different than the one provided by $B^0 \rightarrow \psi K_s$. The number of flavor tagged $B^0 \rightarrow \pi^+\pi^-$ depends on the product of the branching ratio, taken as 2×10^{-5}, and the detection efficiency, which includes solid angle, vertex cuts and track reconstruction efficiencies. This must be evaluated in a full Monte Carlo simulation including background. Assuming that at least a 10% efficiency can be achieved, implies 400 flavor tagged events/year. This is a significant number provided that the wrong flavor tags are not large. Clearly this estimate applies to any channel with an equivalent product of branching ratio times reconstruction efficiency. The corresponding numbers of events in the fixed target mode would be 25 times smaller, only 16 events, and would probably contain a larger background fraction.

6.0 Flavor Tagging

Measurements of CP violation require that the flavor tags used be not contaminated by much wrong sign background. The number of reconstructed events required is proportional to the square of the observed asymmetry (A_{obs}) and $A^2_{obs} \propto (1-2\omega)^2 A^2_{sym}$, where ω is the fraction of wrong sign tags and A_{sym} is the real asymmetry.

Different triggers require different tagging strategies. The ψ trigger and the detached vertex trigger generally require an independent tag, while for the high p_t muon trigger the muon itself is the tag.

There are several possible tagging strategies besides a high p_t lepton from a detached vertex. For instance, one could consider a charged kaon from a detached

vertex. This tag has good efficiency but a rather large inherent wrong sign content. Overall, useful rate is provided. Another tagging strategy that has been mentioned is to merely count the charge balance at a secondary vertex and so be able to identify B^+ or B^- decays. Although this tag can have, in principle, a high rate, the fraction of wrong sign tags may be considerable and thus a detailed study with a realistic simulation of tracking strategy is needed to support its use.

7.0 Tradeoffs Among Possible Systems

7.1 Fixed Target

Extracted beams and internal gas jet targets for fixed target experiments are possible and are quite adequate to generate large interaction rates. The important, as yet, unanswered question is how they interact with the stored beams. The fixed target has some advantage over the collider in that the average multiplicity is about a factor of 2-3 less when using a tungsten target. It appears to be difficult to run at more than a 1MHz interaction rate. The external target experiment (SFT) can't possibly run with 10^8 protons/sec (required for 10MHz rate) using a pencil beam due to radiation damage and multiple interaction problems. Perhaps a pencil beam is not viable even with 10^7 protons/sec. Thus they must spread the beam over the target and this leads to triggering problems. They also have a large problem with hadrons from the primary proton nucleus interaction making secondary interactions in the target which look like detached vertices. For a 10% interaction length target and an average charged multiplicity of 40, on the average two charged tracks also interact in the target.

The internal gas jet target experiment (IGT) has an advantage of triggering on a point source. With a 1MHz interaction rate they can accumulate more than 10^7 tagged $b\bar{b}$'s/year. There remains an important question of how close the silicon can be to the beam and still survive. The current configuration has the silicon at 4mm from the beam line but it is retracted during injection. Both of these experiments need to show that the tracking system is sufficiently robust to measure tracks down to 2 mr with high efficiency and good resolution. Another negative aspect of the fixed target experiments is that they must show that they can run at 10^7 interactions/sec in order to accumulate sufficient numbers of B's.

7.2 Collider

The quasi-hermetic collider detector, BCD, looks very complex, costly and sacrifices acceptance at large η, where $B's$ are fastest, largely due to keeping the silicon outside the beam pipe. The forward B spectrometer (FBC) proposes two

arms, but as the gain in solid angle is only a factor of two over one arm, a single arm implementation would be sufficient. The $B's$ are moving fast in the forward direction which is an advantage over BCD but they are not as forward as in fixed target where everything tends to follow the beam.

It is tempting to think that a single detector could be used for both internal gas jet target and collider running, but practical considerations usually do not allow the implementation of such fanciful dreams.

8.0 Conclusions

There are many conceptual issues which need to be addressed. Some group have started this process. These include justifications of trigger strategies, tracking efficiencies, tagging efficiencies, including the level of wrong sign tags, mass resolutions and backgrounds in the B samples.

Similarly, there are serious hardware issues such as silicon vertex detectors, tracking chambers, RICH, trigger and data acquisition.

The factor of $\approx$25 higher effective b rate for the same total interaction rate favors the collider experiments. The fixed target experiments would need to be able to run at 10 times the interaction rate of the collider to be competitive. There is great potential for B physics at the SSC. Pessimistic assumptions have been used to derive rates which are quite sizeable, especially in the collider. Part of the pessimism is based on the lack of results from experiments doing this kind of physics at hadron machines. It is likely that a long term experimental program at the SSC will develop techniques which would far exceed these estimates.

9.0 Acknowledgements

I benefited greatly from discussions with Marina Artuso, Alex Chao, G. Carboni, Jim Patrick, Jerry Rosen, Peter Schlein and Mike Syphers. This work was supported by the National Science Foundation through a grant to Syracuse University.

REFERENCES

1. K. Berkelman and S. Stone, "B Meson Decays", to be published in Annual Review of Nuclear and Particle Science, Dec. 1991.
2. P. Tipton, talk given at *Future Directions in B Physics* conference, Ohio State Univ., Columbus, Ohio (1991).
3. H. Albrecht et al. Phys. Lett. B **192**, 245 (1987); for a review of all current data see H. Schröder, "$B\overline{B}$ Mixing", to be published in *B Decays*, ed. by S. Stone, World Scientific (Singapore).
4. I.I. Bigi, V.A. Khoze, N.G. Uraltsev and A.I. Sanda, in *CP Violation*, ed. by C. Jarlskog, World Scientific (Singapore) 1988.
5. For a recent calculation see M.L. Mangano, P. Nason and G. Ridolfi, "Heavy Quark Correlations in Hadron Collisions at Next-to-leading order", Pisa preprint, IFUP-TH 32/91, UPRF 91-308 (1991).
6. E. Berger, in *CP Violation and Beauty Factories and Related Issues in Physics,* Ann. of The N. Y. Academy of Sci. Vol. **619**, 119(1991).
7. G. Altarelli et al. Nucl. Phys. B **308**, 724 (1988).
8. C. Albajar et al. Phys. Lett. B **256**, 121 (1991); errata, ibid. 262, 497(1991). See also N. Ellis and A. Kernan, Phys. Reports, **195**, (No. 2 & 3), 1(1990).
9. K.J. Foley et al., in "Experiments, Detectors and Experimental Areas for the Supercollider., ed. by R. Donaldson and M.G.D. Gilchriese, World Scientific, Singapore, 701 (1988).
10. These figures are from calculations of Artuso based on ref. 6, see M. Artuso, "Experimental Facilities for b-Quark Physics", to be published in *B Decays*, ed. by S. Stone, World Scientific (Singapore).
11. Rapidity $y = tanh^{-1}(p_z/E)$ and pseudo-rapidity $\eta = -ln(tan(\theta/2))$ are taken as equal at these high energies.
12. The BCD Collaboration, SSC Proposal SSC-0240-mc (1989).
13. The detector is described in S. Erhan et al."Collider Beauty Physics at LHC", CERN-PPE/91-10 (1991).
14. J. Rosen SSC Expression of Interest EOI0013 (1990).
15. B. Cox et al., SSC Expression of Interest EOI0014 (1990).
16. S. Stone, "Semileptonic *B* Decays - Experimental", Syracuse preprint HEPSY 4-91 (1991), to be published in *B Decays*, ed. by S. Stone, World Scientific (Singapore).
17. G. Carboni private communication.

Special Purpose Detectors

R. Stefanski

Special Purpose Detectors

Ray Stefanski

SSC Laboratory Physics Research Division

EOIs Mentioned in this Talk

EOI - 1	Krisch	Spin - Spin Effects @ 2 & 20 TeV
EOI - 2	Orear	Low Pt Physics
EOI - 4	Sobel	Neutrino Oscillations @ 200 GeV
EOI - 8	Lockyer	BCD
EOI - 9	Kagan	Compact Diamond-Based Detector
EOI -13	Rosen	Internal Target Beauty Physics
EOI -14	Cox	SFT
EOI -15	Giacommelli	Magnetic Monopoles
EOI -17	Bryant	Relativistic Atomic Physics
EOI -19	Bjorken	Low and Intermediate Mass Detector

Funding for Small and Special Purpose Detectors (FY90 $)

R&D for Detectors	$ 40M
Two General Purpose Detectors	550M
Special Purpose Detectors	75M
Detector Related Computing	87M
Total	$ 752M

Experimental Facilities (halls and infrastructure) $179M

Test Beams @ 200 GeV also provided for in addition to the above.

R. Stefanski 10/15/91

SSC Laboratory Physics Research Division

EOI-1 Spin

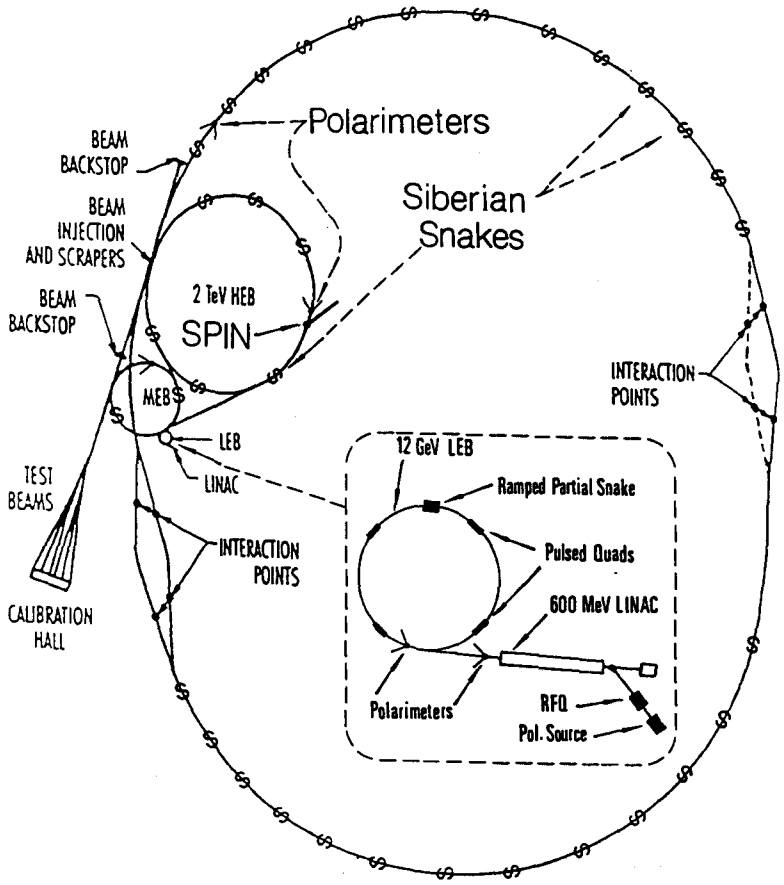
Two EOIs submitted:

1. Spin-Spin Physics at 20 TeV
2. Spin-Spin Physics at 2 TeV

SSCL accelerator physicists have produced lattice designs that permit future upgrades which could allow polarized beam operations.

Polarization experiments will be considered as part of future calls for proposals.

R. Stefanski 10/15/91



General Comments and Suggested Timetable

Call for Proposals should come with a deadline of late '93 or early '94.

Workshops should be organized to focus efforts toward submittal of proposals on this timetable.

Current SSCL work is focused on

- Understanding the Impact of these experiments upon SSCL facilities and schedules.
- Avoiding the inadvertent foreclosure of experiments by accelerator design decisions which have to be made before decisions on future experiments.
- Planning the scope and schedule for this aspect of the SSC experimental program.

R. Stefanski 10/15/91

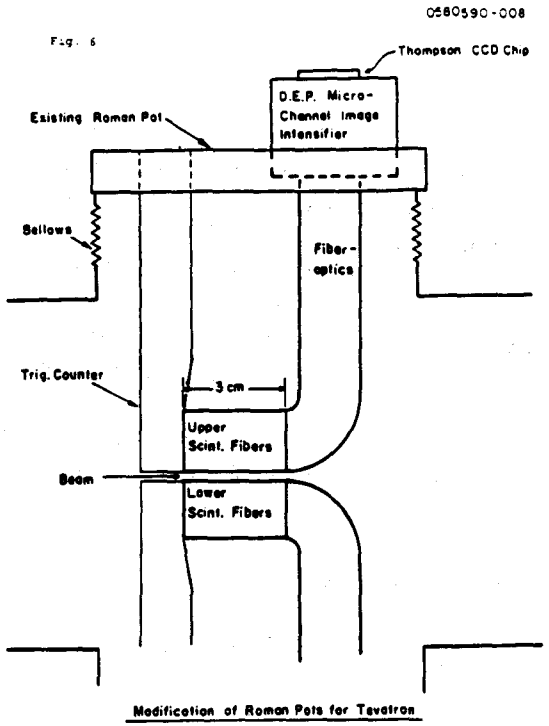
EOI-2

The physics goals are supported by the PAC although no action is needed at this time.

Project Status:

- Will develop Scintillating Fiber Detector
- Work will also progress on an Imaging Silicon Drift Detector
- Some of these tests will be part of E-710 (FNAL)

R. Stefanski 10/15/91



Modification of Roman Pots for Tevatron

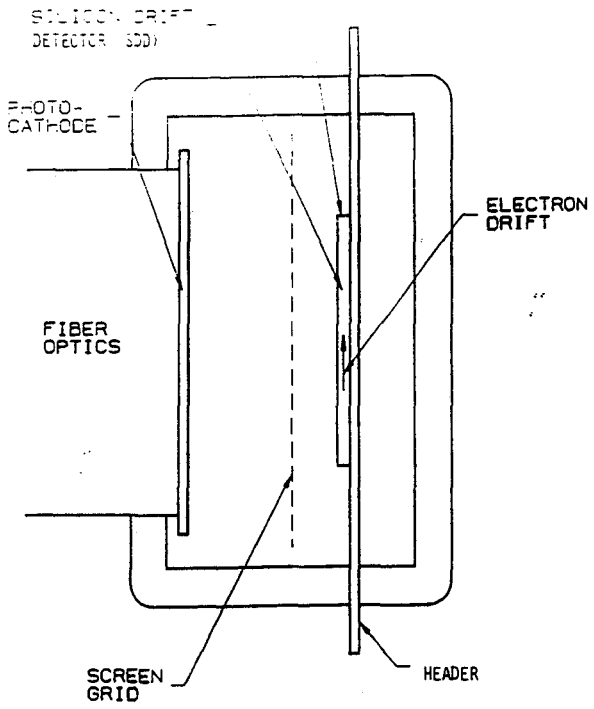


Figure 1: SDD Potted in Proximity Focused Tube

Experimental Facilities on the East Campus

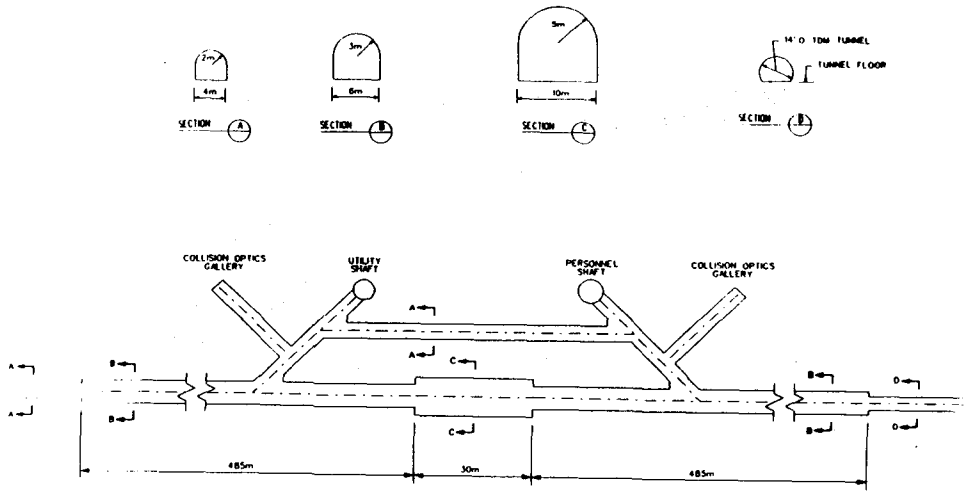
- **Experimental Hall requirements must be established by January 1992.**
- **Facilities for Special Purpose detectors must be designed before proposals are called for.**
- **To encourage the development of a diverse program of physics, the Laboratory will attempt to proceed with "generic" facilities for special purpose detectors.**
- **One IR may have only an access shaft for very small experiments (like EOI-2)**
- **One IR may contain a 6 m diameter tunnel of approximately 1000 m in length for forward physics (like EOI-19). This facility would also have a somewhat enlarged center section of 10-12m by 40 m in length. (for detectors like P-845 or EOI-9.) It may also be possibl to extract from this area.**
- **The SSCL is currently studying these options to find some optimal approach. (It will not cover all possibilities!)**

R. Stefanski 10/15/91

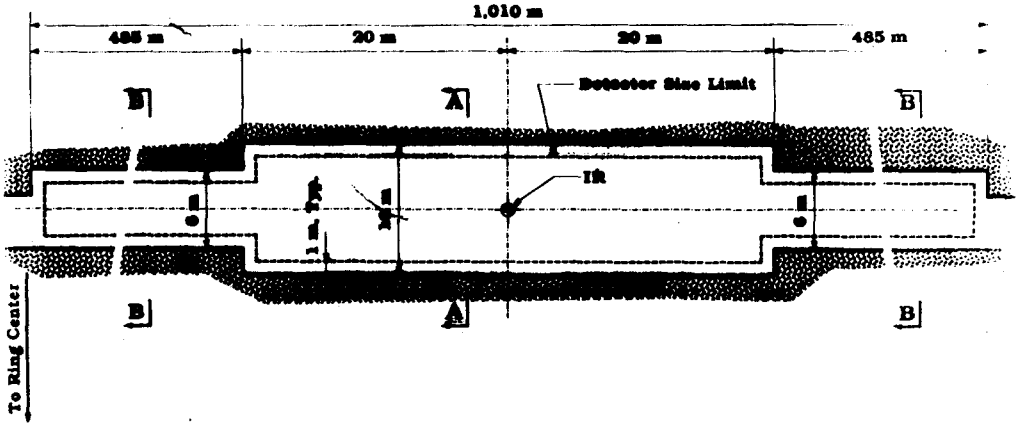
B Physics at the SSC

- **"The SSC has special capabilities for B-physics. Both the fixed target and collider modes have the potential of going well beyond other accelerator facilities."**
- **Substantial progress continues at Fermilab, CERN and in resolving the B-factory options.**
- **The SSCL should hold a workshop in late 1992, to examine in depth the strategy for B physics at the SSC. "The workshop should address the basic questions of whether the collider or fixed target approach is optimal for the initial program and of the appropriate design of a B physics experiment."**
- **An important constraint in choosing among designs will be the funds available for such an effort.**

R. Stefanski 10/15/91



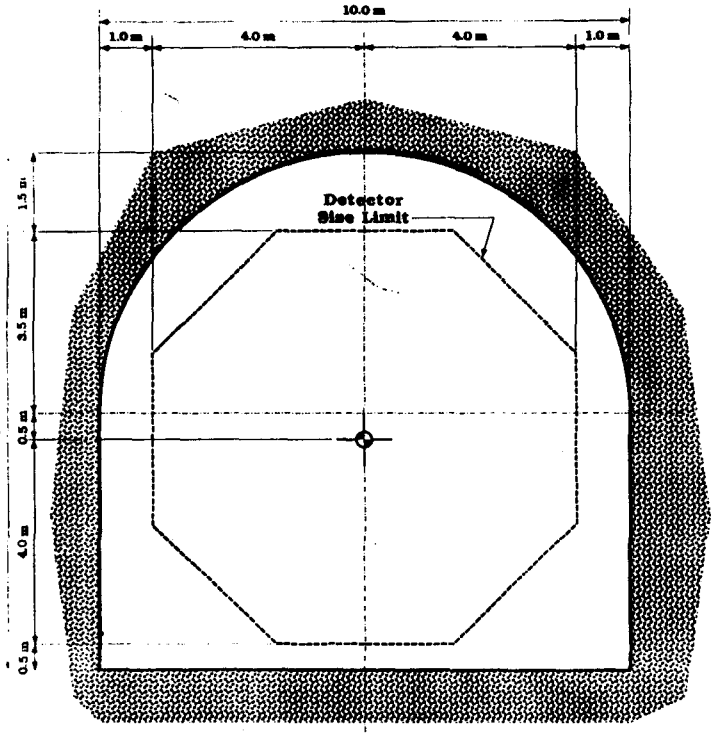
Potential East Cluster Layout



Scale ~ 1:800

Interaction Hall Plan

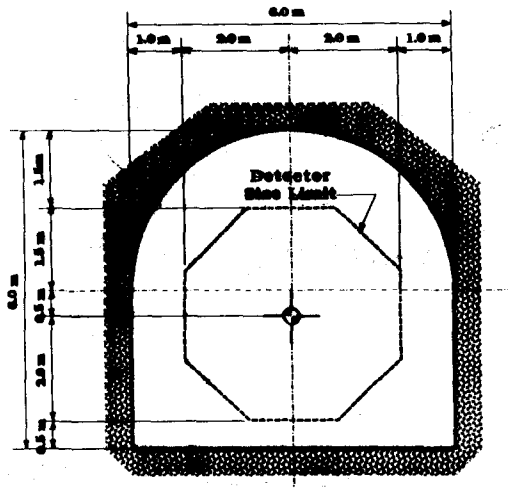
1



Scale ~ 1:75

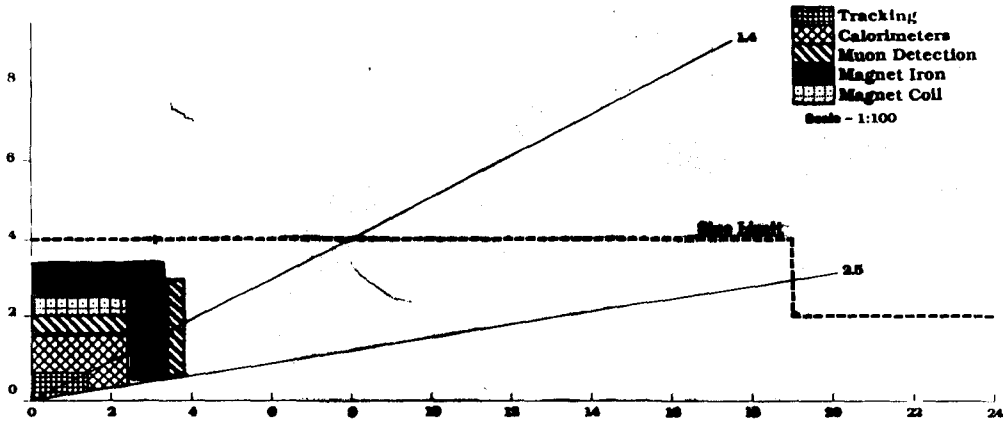
SECTION A - A

2



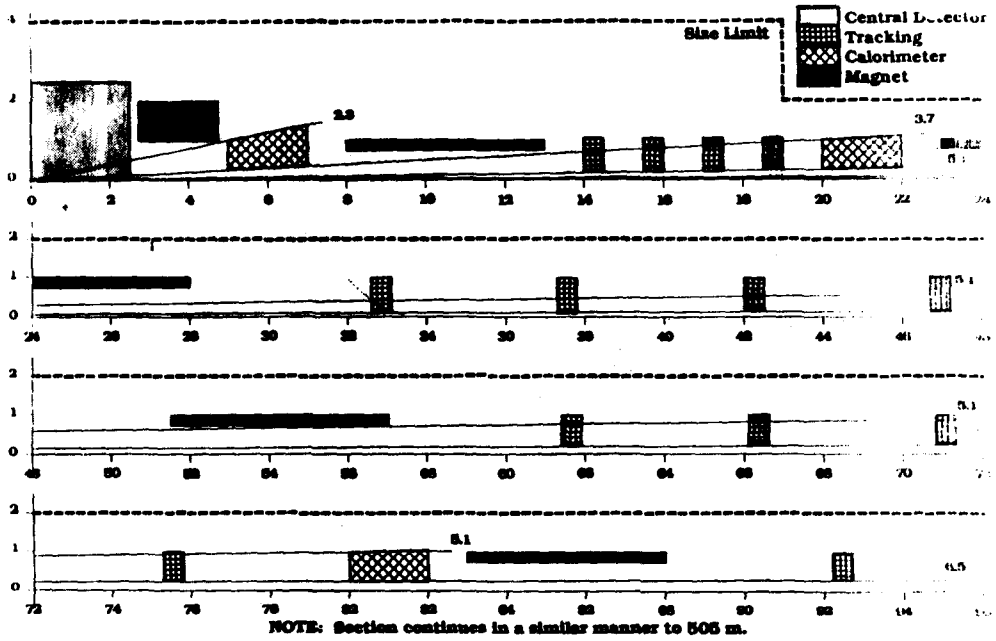
SECTION B - B

Scale - 1/75



Quarter Section
SSC-EOI-0009

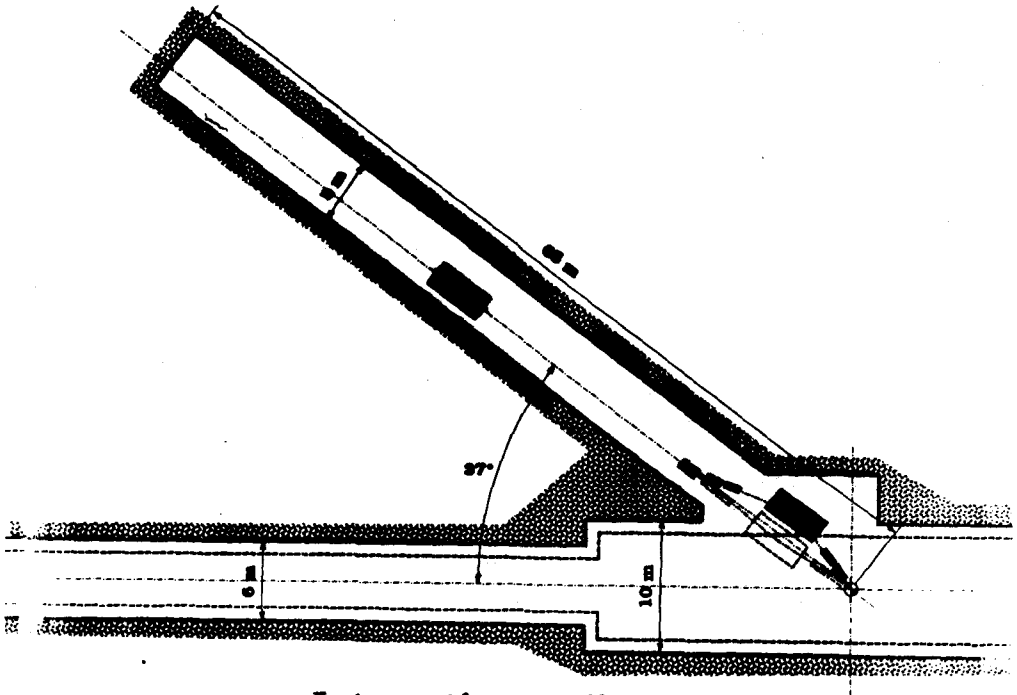
6



Scale - 1:100

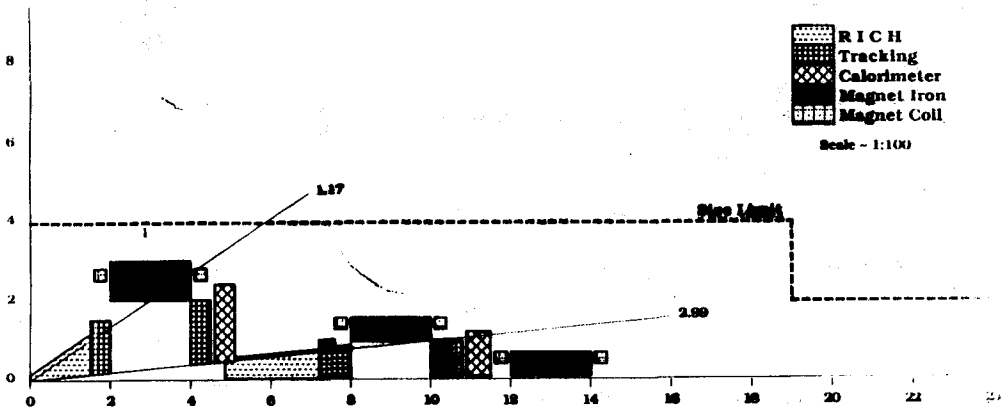
Quarter Section
SSC-EOI-0019

10

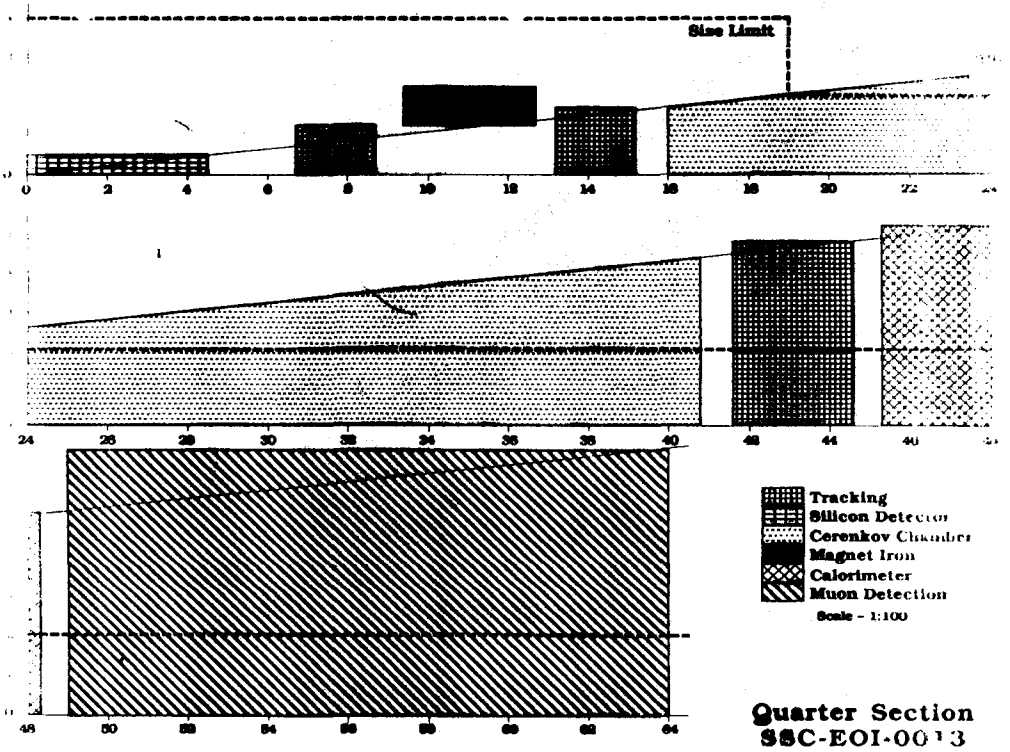


Scale - 1:300 **Interaction Hall Plan**
SSC-EOI-0001

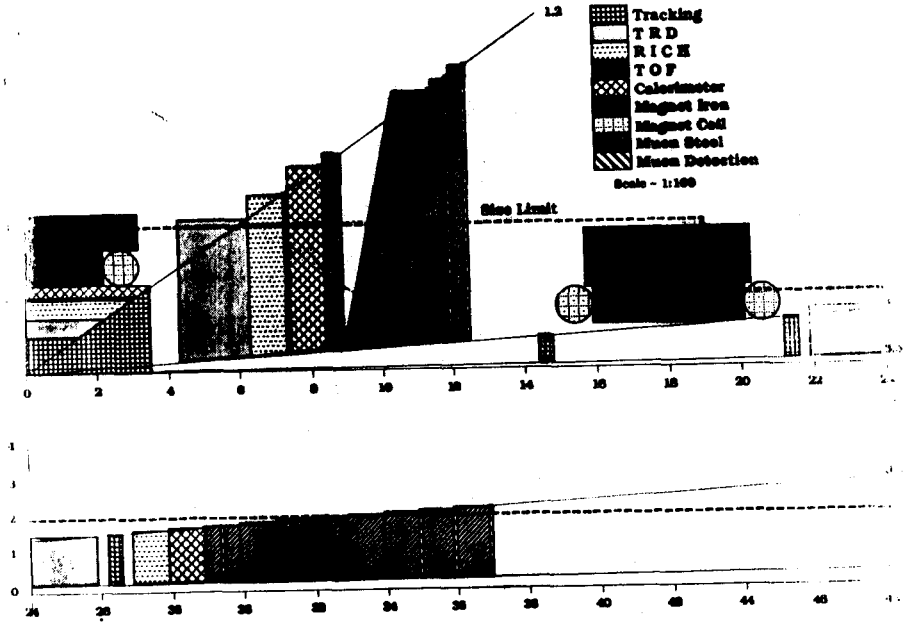
11



Quarter Section
SSC-EOI-(FNAL-P845) 13



Quarter Section
SSC-EOI-0013



Quarter Section
SSC-EOI-0008

257

Appendix I Physics Goals and Motivation

The goal of the DiAMAS collaboration is to perfect high speed, radiation resistant diamond detectors capable of operating at the highest possible SSC luminosities. The critical path of the entire project (SSCL and TNRL funds) leads to a prototype detector module that demonstrates proof of concept. During the first year grant period the collaboration will focus its efforts on:

Task 1: **Material and Device Classification and Characterization studies.** The material study will consist of measurements of the structural and electronic properties of diamond films, growth processes, and surface contact technology. Of particular importance is the study of crystalline defects and impurities and their effects on the electronic properties of the diamond samples. The device studies consist of measurements of the electronic properties (capacitance vs voltage, leakage current vs voltage, and resistivity) of sample detectors. These studies will provide the base parameters for the design of larger diamond detectors.

Task 2: **Photoconductivity measurements.** These measurements will consist in charge collection studies on diamond during exposure to short pulse laser light and synchrotron radiation, leading to determination of electron and hole mobility and lifetimes. These tests measure *surface properties* and are necessary for determination of the overall quality of a diamond sample.

Task 3: **Beam tests.** These tests will consist of exposing diamond samples and detector prototypes to test beams at KEK (Japan), Fermilab (US), and Triumf (Canada) to measure the ionization and collection of charge produced by showering and minimum ionizing particles. The collection region of the diamond will be determined, providing electron and hole mobility and lifetime measurements under high energy laboratory conditions. These tests measure the *bulk properties* of the diamond samples.

Task 4: **Relationship between bulk and surface properties.** Beam test data and photoconductivity data must be correlated to close a feedback loop between materials science and high energy physics elements of the project. With this relationship understood, the industrial feedback loop for tuning electronic parameters can proceed from a strong base in the second year of the project.

Task 5: **Prototype detectors.** In the latter stages of the first year, depending on the results of the beam tests, prototype detectors will be designed and constructed. These devices will be tested in a beam and the results compared to a Monte Carlo simulation demonstrating the proof of concept of diamond as a detector for measuring energy deposited by a charged particle. This design and construction task should lead to estimates of the eventual cost of a full scale SSC detector or detector sub-system.

DIAMAS R&D

Diamond Detectors

- Obtained "off-the-shelf" samples of diamond sheets. Learned to make ohmic contacts on diamond.
- Measure electrical properties of diamond including carrier lifetimes and mobilities in natural diamond.
- Carrier lifetimes and mobilities will be measured in CVD. (Diamond produced by Chemical Vapor Deposition techniques.)
- Beam tests were carried out at KEK and TRIUMF.
- This constitutes the first demonstration that CVD diamond can detect charged particle minimum ionizing radiation and handle large rates.

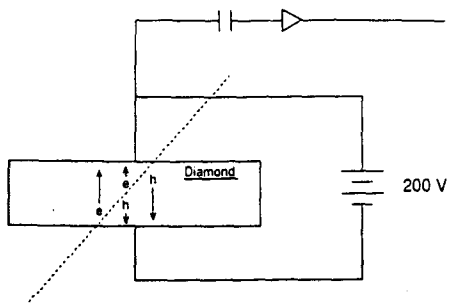


Figure 1

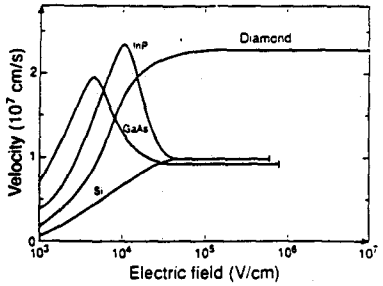


Figure 2

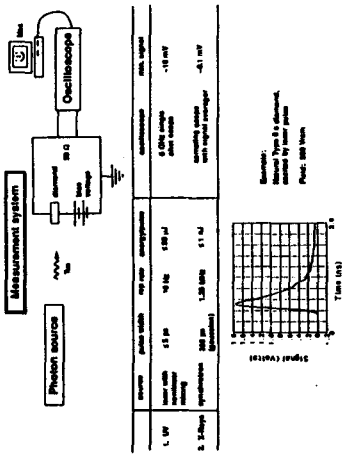


Figure 5

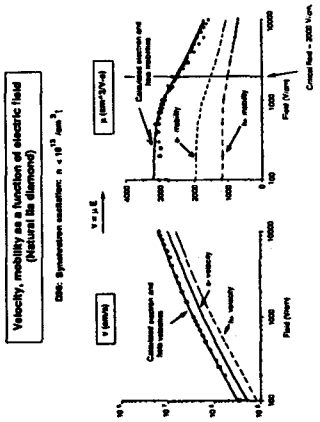


Figure 6

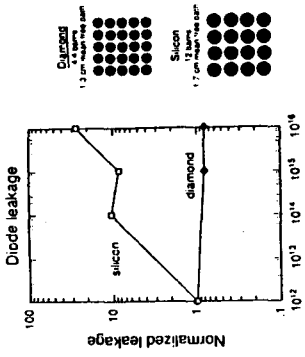


Figure 3

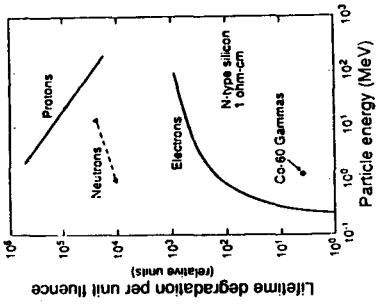


Figure 4

DIAMAS R&D Goals for FY92

- Continue systematic structural and electrical studies of diamond.
- Initiate impurity/defect study
- Initiate growth process studies including high growth rate techniques.
- Specify desired structural and electrical characteristics of detectors.
- Initiate radiation hardness studies.
- Produce 500 cm^2 of CVD diamond for use in detectors.
- Continue production of prototype calorimeters.
- Construct and test a prototype electromagnetic calorimeter.
- Construct a prototype tracker.
- Study cost of large scale production of detector grade diamond.
- Design first large scale calorimeter and tracking devices.

R. Stefanski 10/15/91

Appendix I Physics Goals and Motivation

Hadron identification is an important part of any experiment to explore B physics at the SSC. The ring imaging Cerenkov detector offers such a technology for $\pi/K/p$ identification over a momentum range from 0.3 to 300 GeV/c. The high interaction rate at the SSC places a challenge on this technology to exceed the performance recently demonstrated by the SLD and Delphi groups at e^+e^- colliders.

Two detector technologies are emerging that may prove capable of detecting UV Cerenkov photons over large areas with 16-ns time resolution. The first is the multistep avalanche chamber (MSAC) operating with low-pressure, hot (80°C) photosensitive TMAE gas. Two amplification stages would be separated by a gate to allow high-rate operation.

We propose to pursue an alternative based on a solid UV photocathode (CsI with adsorbed TMAE) and a single-step low-pressure avalanche chamber. Because all photoelectrons are produced in the thin photocathode and all drift the same small distance to the anode, submanosecond timing resolution is possible. The low-pressure chamber can operate with gains of order 10^6 and with essentially no background from ionization by passing charged particles.

The initial goal of the R&D program is to design, build, and test, on the bench and in a beam, a prototype low-pressure, solid photocathode, UV photon detector module for fast Ring Imaging Cerenkov (RICH) detectors. The ultimate goal is a system of standard detector modules that can be manufactured inexpensively by industry and assembled like tiles into large-area detectors for 4π collider experiments as well as fixed-target RICH detectors. Other applications of fast, cheap, position-sensitive UV-photon detectors are readily imagined: detection of Cerenkov light from cosmic-ray air showers, detection of photons in BaF_2 calorimeters, detection of x-ray-to-UV-shifted photons in Xe TRD's, etc.

BCD R&D

CsI-TMAE Photocathodes

- Readout system for a fast Ring Imaging Cerenkov Detector (RICH) or TOF Detector when coupled to a solid Cerenkov radiator
- Operates with 20 Torr methane or 15 Torr Butane
- Insensitive to magnetic fields
- SVX chip used with pad readout.
- QE between 20 to 35%
- S/N ≤ 10,000:1 for RICH. Integration time of 400 ns.
- S/N 4:1 for TOF with fast pulse readout. Time resolution of 70 ps.
- Absorbed TMAE helps QE by about 1.5

R. Stefanski 10/15/91

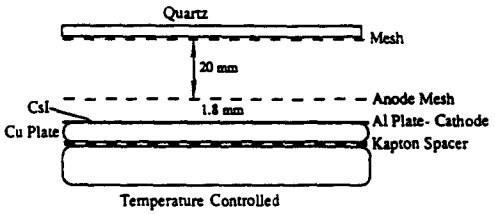


Figure 1. Parallel plate avalanche chamber with solid photocathode.

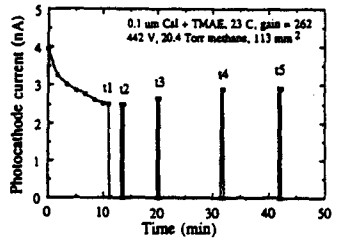


Figure 2. Current of a CsI-TMAE photocathode as a function of time for a typical measurement. The gas gain is 262 and the pressure is 20.4 Torr of methane. The UV light is interrupted at time t1, and reestablished for a moment at times t_2-t_5.

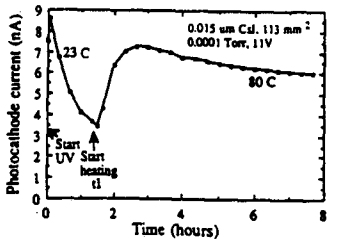


Figure 3. Current as a function of time for a CsI photocathode. At time t_1 the photocathode is heated to 80 °C.

Progress Report and Renewal Request for R&D on

A Silicon Vertex Detector with Interleaved Disks and Barrels

(Submitted to the Superconducting Super Collider Laboratory)

D. Gunter and I. Husein
Department of Mathematics, Physics, and Industrial Technology, Langston University, Langston, OK 73050

P. Gutierrez, G.R. Kalbfleisch,[1] J.F. Kuehler, and M.L. Wood
Department of Physics and Astronomy, University of Oklahoma, Norman, OK 73019

W.S. Anderson, J.G. Heinrich, C. Lu, and K.T. McDonald
Joseph Henry Laboratories, Princeton University, Princeton, NJ 08544

(September 15, 1991)

Summary

For a B-physics experiment at a hadron collider, the large angular range of the B-decay products leads to the requirement of a silicon vertex detector with interleaved disk and barrel detectors. As no present or approved collider experiment uses this geometry we have undertaken an R&D program to demonstrate its viability. We report on progress on mechanical modelling, development of custom VLSI readout chips, bench and beam tests of silicon detectors, and on simulations of system performance. We propose a two-year continuation of this program to produce two hexagonal modules of fully instrumented silicon detectors. For this we seek a budget of **$287k** at U. Oklahoma and **$135k** at Princeton U., with 50% of the funding in each of FY92 and FY93.

[1]Contactperson



SSC Laboratory **Physics Research Division**

EOI-14 Super Fixed Target B Physics Facility

The extraction of beam from the SSC using channeling techniques is of general interest as it might ultimately be useful for test beams or fixed target experiments. Thus continued interaction with the SSCL staff on extraction of beams using crystal channeling seems appropriate as long as it does not adversely affect other high priority work at the Laboratory. One element of the submitted R&D plan is a test of extraction using channeling at Fermilab. Because of the general interest, SSCL could consider contributing to the cost of the hardware to carry out this test.

R. Stefanski 10/15/91

Report of the Users Organization for the SSC

D. Cassel

Report of the Users Organization for the SSC

David G. Cassel
Newman Laboratory, Cornell University, Ithaca, NY 14853

Abstract

At this conference I presented a brief report of the activities during the past year of the Executive Committee of the Users Organization for the SSC. Since this report coincided with my retirement from the Executive Committee, I have taken the opportunity of contributing an article to the proceedings to expand my comments into a brief history of the Users Organization, including some of my personal recollections.

The Users Organization for the SSC (UOSSC) is unique among the users organizations of the national laboratories because it existed before the laboratory itself was established. I became aware of the need for a users organization for the SSC at the workshop titled, *Physics of the Superconducting Supercollider*, held in the summer of 1986 at Snowmass, Colorado. This workshop was organized by the Division of Particles and Fields (DPF) of the American Physical Society, chaired by Lee Pondrom.

I recall this workshop as an optimistic and exhilarating point in the history of the SSC. The Central Design Group led by Maury Tigner had just finished the 700-page Conceptual Design Report. This meant that it began to look like a 20 TeV $\times$ 20 TeV pp collider could be built and a set of realistic accelerator parameters was available. Therefore, we could begin to design experiments with some confidence that we were addressing realistic rate and background conditions. The anticipated rates and backgrounds were frightening and the detector volumes required for even modest resolution for particles with TeV energies were staggering. We responded naturally to these difficulties by accepting them as challenges to our ingenuity. The experience gained at a number of previous workshops, especially the one at Snowmass in 1984, helped us to identify many of the most important issues and to focus our efforts at imagining innovative detectors that began to look realistic.

Although smaller groups of individuals with similar interests were beginning to crystalize around different concepts for SSC detectors, the large collaborations that now dominate the SSC experimental program were not in sight. Hence, many individuals felt a need for an organization to represent the interests of potential users of the SSC. This concern took the form of the widespread interest in establishing a Users organization for the SSC. This concern was voiced publicly in a "Town Meeting" held during the workshop. The DPF responded by taking the initiative to organize a users group. Under DPF auspices an Executive Committee (EC) was elected, with Lee Pondrom and Tom Kirk as the first chairman and secretary, respectively. All past and present members and officers of the EC are listed in a table at the end of this report.

The first EC meeting was held at Berkeley in November, 1987. The constitution proposed by the EC was overwhelmingly endorsed by over 1,000 UOSSC members in early 1988. This short constitution specifies the qualification for membership in the UOSSC, defines the functions of the EC and the procedures for its election, and mandates an Annual Meeting of the Users. EC members serve for three years; after one year in the EC as "elect", officers serve for two years. Funds for the operation of the UOSSC are provided by the Universities Research Association (URA), which manages Fermilab and the SSC, and at that time managed the Central Design Group. Originally the UOSSC office was located at the University of Wisconsin, which provided most of the administrative support.

I was elected to the EC in the summer of 1988 and I attended my first EC meeting in August. It was held at the DPF Conference at the University of Connecticut at Storrs, which was also the site of the first Annual Meeting of the UOSSC. A week before this meeting the Department of Energy (DoE) announced that it would seek a contract with an organization in the private sector for the management of the SSC Laboratory. We were aware that the URA planned to submit a proposal for management of the laboratory and that the URA would establish a search committee to select the director. We felt that the URA was the appropriate body to manage the project, and that it was important the the users community have a voice in the selection of the director. Therefore, we nominated a colleague for membership on the search committee and he was included on the committee. This was the first of a number of instances in which we have nominated individuals for membership on important SSC-related committees, whether or not we were invited to make such nominations. Apparently our advice has been useful because each committee has included at least one person whom we nominated.

We decided that our next meeting in December should be held "on site", wherever that would be. We acted on rumors that Ellis County would be the site and scheduled our meeting at the Holiday Inn in Desoto, TX. A few protocol problems developed because the designation of the site was not final, but we were warmly received by local community leaders. We also met the local member of the House of Representatives, Joe Barton, at a Texas barbecue in his home town, Ennis. We were pleased to learn much support there was for the SSC in Ellis county, and how committed community leaders were to the success of the project! We were also pleased to learn that Roy Schwitters had just agreed to direct the project. We continued our new tradition of freely providing advice by offering suggestions to Roy on how he should initiate the experimental program and on the necessity to develop laboratory computer facilities at an early date. We were gratified with the response to our suggestions.

During the next year, 1989, the Laboratory began to take shape in Dallas and Phyllis Hale was hired to be the Head of the Users Office. Those of us who knew her from her analogous position at Fermilab were pleased that she joined the laboratory and brought her experience and well-known interest in the concerns of users to the laboratory. When Lee Pondrom retired from the chairmanship of the EC, the UOSSC office was transferred to Phyllis at the Laboratory.

The EC represented users at a number of meetings, during this period, including the HEPAP Subpanel meeting at Hilton Head, SC. We joined in planning the October *Conference on Supercollider Physics and Experiments* in Dallas and included the UOSSC

Annual Meeting in the program. This consisted of a session where groups preparing Expressions of Interest presented their plans. This was the first opportunity for the HEP community at large to hear the plans of nearly all groups designing SSC detectors.

As the site-specific cost estimate for the SSC was nearing completion near the end of 1989 it became clear that the facility would be more expensive than earlier estimates for a generic site. In addition, experience with persistent currents at the Tevetron drove the design to a higher energy High Energy Booster and a larger dipole magnet aperture. This meant that the Laboratory had to choose between lowering the energy substantially to save money or maintaining 20 TeV at a larger cost in dollars and more difficulty in obtaining funding. As this problem became known the EC received clear signals that the HEP community strongly supported 20 TeV. Three members of the EC, Alex Chao, Gordon Kane, and I, served on on an *Ad Hoc Committee on SSC Physics* to consider the how lower energy would impact the physics program. The committee concluded that it may not always be possible to achieve the same physics reach with lower energy and higher luminosity, especially given the difficulty of imagining practical general purpose detectors at luminosities substantially above the CDR design value, 10^{33} cm^{-2} s^{-1}. In its December meeting in Dallas the EC strongly endorsed this conclusion and wrote a letter urging Roy Schwitters to do everything possible to maintain the 20 TeV design goal. After also receiving support for 20 TeV from many other members of the HEP community, including a HEPAP Subpanel headed by Sidney Drell, Roy Schwitters decided to stick to this energy. There was one useful result of the tremendous effort expended on thinking about an SSC with lower energy and higher luminosity; many of us started to think seriously about the accelerator and detector consequences of possible future upgrades to luminosities of 10^{34} cm^{-2} s^{-1} or more.

The EC and I participated in organizing a number of other meetings at this time. Sessions on SSC physics were organized for the 1990 DPF Conference held at Rice University. We organized a Town Meeting for SSC users when the HEPAP Subpanel on the U.S. High Energy Physics Research Program for the 1990's met at the Laboratory. This was mostly devoted to presentations by proponents of the major Expressions of Intent that were active at that time. The 1990 Annual Meeting was held at the Snowmass workshop that summer; the principal program was an opportunity for the HEP community to hear from proponents of all of the Expressions of Interest being considered by the Laboratory PAC.

The EC has fallen into a pattern of holding 4 meetings per year. Two were "on-site" at the Laboratory, one was held at the SSC conference held in Texas each fall, and one at the American Physical Society meeting in Washington. The latter choice provides an opportunity for the EC to become better acquainted with the personnel and operations of the URA. After the 1990 Snowmass workshop, Roy Schwitters and the EC agreed to include the UOSSC Annual Meeting in the program of the fall SSC conferences. This report to the Corpus Christi conference is part of the Annual Meeting.

Opportunities to represent the user community in meetings continue to be a responsibility of the EC chairman. In the Atlanta Conference on the SSC I had to opportunity to speak to a group that included many more people from industry than my normal audience. I took this opportunity to describe the importance of university groups in the SSC effort. My concern is that the university groups may become invisible to the public

at large because most emphasis in the press is focused on the Laboratory or the large collaborations. Seldom does the public hear how essential university groups are in the total SSC picture.

Keeping members of the HEP community informed on the progress of the SSC in Washington has been a concern of the EC. The EC and the DPF Executive Committee agreed that it is important to have some individual(s) take responsibility for keeping the community informed on actions in Washington that affect the SSC, HEP, and physics in general. Lee Pondrom and Gordon Kane shared this responsibility for one year, Gordon carried it out by himself for two years, and now Aihud Pevsner is responsible.

Plans for user facilities at the Laboratory has been a major concern of mine that has been shared by many users. This interest reached a peak in the 1989 fall meeting in Dallas where many users offered to share their experience at other laboratories and to work with laboratory planners to help devise the most attractive and useful facilities. Jean Slaughter and Tom Devlin worked together to harness this interest. Only recently has laboratory planning matured to the point where it is useful to have substantial interaction between laboratory planners and the user community. In the April EC meeting in Washington this year Jim Sanford described the working concepts for laboratory facilities. We reacted very favorably to these ideas and invited Jim to make a similar presentation in the UOSSC Annual Meeting at this conference. We hope that this will rekindle user interest and that we will be able to develop a fruitful relationship between members of the user community and laboratory planners.

My three years on the EC have been exciting and sometimes hectic or frustrating. We have frequently offered our advice on policy matters to various organizations connected with the SSC. It has been satisfying to see that our advice has often had a positive effect. I am confident that the EC, with Bob Adair as Chairman, will be a useful and constructive voice for users in the future.

It is impossible to properly acknowledge all of the people who have made significant contributions to the work of the EC during my tenure as Chairman. However, I do wish to especially thank Roy Schwitters and other members of the Laboratory directorate, Phyllis Hale, URA President John Toll, and my fellow members of the UOSSC EC. Their support has been essential for all of the things we have accomplished.

UOSSC Executive Committee Membership

Current – October 1991

R. Adair	Yale	Chairman
L. Price	Argonne	Secretary
R. Kephart	Fermilab	Secretary–Elect
R. Cahn	LBL	
R. Cashmore	Oxford	
A. Chao	SSC	
T. Devlin	Rutgers	
D. Green	Fermilab	
R. Hubbard	CEN Saclay	
A. Kernan	UC Riverside	
K. Morgan	SSC	
Y. Unno	KEK	

Retired – 1991

D. Cassel	Cornell	Chairman
M. Abolins	Michigan State	
P. Grannis	Stony Brook	
G. Kane	Michigan U	

Retired – 1990

T. Kirk	Argonne	Secretary
G. Barbiellini	CERN	
G. Hanson	Indianna	
T. Kondo	KEK	

Retired – 1989

L. Pondrom	Wisconsin	Chairman
F. Sciulli	Columbia	
M. Witherell	Santa Barbara	

Retired – 1988

A. Bodek	Rochester
R. Orr	Toronto
J. Peoples	Fermilab
G. Wolf	DESY

Highlights of the SSC Site Development Plan

J. Sanford

Highlights of the SSC Site Development Plan

James R. Sanford
Superconducting Super Collider Laboratory, Dallas, TX 75237

This paper summarizes highlights of the Site Development Plan for the Superconducting Super Collider Laboratory. The Plan, sometimes called a Master Plan, was prepared by the architectural and engineering firm for the Laboratory: Parsons Brinckerhoff/Morrison Knudsen (PB/MK) working in association with CRSS. Their task was to interpret the SSC project needs in the context of the Ellis County, Texas site. The team effort was under the direction of Lewis May from CRSS, guided by Robert Sims from the SSC Laboratory.

After examining the physical features of the many individual sites around the 54-mile ring as well as the technical requirements for the project as described in the Site-specific Conceptual Design Report, the CRSS team held a series of meetings with people at the Laboratory. One was the Community Group set up by the Director and the other, the Citizens Advisory Committee from Ellis County. In addition to guidance from laboratory personnel, each group provided advice and site-specific information to the CRSS planning team.

One of the first tasks was to place the SSC in the context of the Dallas - Fort Worth metropolitan area as well as within Ellis County (Figures 1 and 2). Here the objective was to study the access to the site via major and minor highways with particular emphasis on the roads to the DFW airport. Within the county, the ability to connect from the west to east land complexes of the project was of vital concern.

From the information about the technical needs of the SSC and the site surveys, CRSS prepared a land use analysis. This was a documented report that described the surface and infrastructure features of the land and services available on the west and east sides of the Collider ring, as well as at the remote service areas. From this beginning, it was possible to overlay the major scientific components of the accelerators and experimental areas. Figure 3 illustrates the results of this analysis for the 7355 acres on the west complex; a similar analysis was undertaken for the east complex and will be described later in this paper.

Within the overall boundaries of the two main and sixteen secondary sites, the planners were able to evaluate the land features including topography, soils types, access, etc. This led to a plan that zoned the various pieces of land according to their primary Laboratory purpose (Figure 4). From such a study, the planners were able to identify the zones (Figure 5) within the west complex that are favored for surface facilities development. A similar analysis was done for the east complex.

In conjunction with the land use study the infrastructure capabilities were documented and analyzed. As an example, Figure 6 indicates the sources of raw and processed water that overlay the various SSC sites. Similar diagrams were created for electrical power, natural gas, and other utilities. An examination of the overall pattern of utility sources and

distribution systems was undertaken. This study was done in conjunction with the technical areas where the services are needed in order to minimize the costs for the new distribution systems. These studies led to the determination of two utility corridors for bringing services into and through the west complex site. These are shown in Figure 7.

With the technical and infrastructure requirements satisfied, attention turned to the campus facilities. In the process of siting the central Laboratory facilities, the road network was examined. Attention was given to the needs of the surrounding populace as well as those of Laboratory personnel. These considerations led to the designation of some roads as primary offsite for general purpose use and others for onsite traffic and maintenance purposes (see Figure 8). Primary access to the west Laboratory site would be from Rt. 66 initially, but later from FM 1493. To enhance access to the site during the research phase of the project, a north/south road connecting with US 287, as shown in Figure 9, is recommended.

In parallel with the previously described considerations, the natural features of the land were catalogued and mapped. As shown in Figure 10, an examination of the land suggested that designated areas be maintained as open prairie and for preservation of the any significant, man-made features. A listing of the various Laboratory features for the west complex are summarized on Figure 11. Attention should be given to the special opportunity and campus areas shown in the illustration. The campus is designed to support the core activities of the Laboratory including the operation, maintenance, and improvement of the accelerators and experimental areas. Activities that support and enhance the broader functions of the Laboratory are found in the special opportunity areas.

The campus and special opportunity areas are shown in Figure 12 in a representative manner only. The essential features of the campus are shown in four (later six) buildings enclosing 420,800 square feet of interior space. The campus buildings are placed in close proximity to the injector accelerators, two of the experimental areas, and the test beam facilities. Near to the campus are found the buildings that are in the special opportunity region on the west complex. These support the education, visitor, and research user needs at the laboratory. The buildings are clustered in a region somewhat separate from the campus, yet close enough to facilitate close interaction of the people involved.

The east complex, consisting of 1861 acres, is located near I 45, nearly 16 miles from the west complex. This area, like the west area, has the potential for four experimental areas with some greater growth possibilities due to the utility region on the lower part of the east side. Figure 13 illustrates the scientific features and constraints on the east side, leading to the development regions displayed in Figure 14. When zoned, the overall land use is illustrated in Figure 15, with the acreage tabulated on the Figure. The east/west and north/south utility corridors are diagrammed in Figure 16 where the pathways are adjusted to take advantage of the source and distribution networks on the east side.

There are many fewer roads on the east side. FM 878 touches the north boundary of the site, while FM 879 is near the southern portion. Only FM878 connects to I 45 for the movement to and from the east complex. It is fortunate that the east experimental areas are near to this access road. As shown in Figure 17, new, or improved north/south roads will

be needed to connect the research zones in the area. With such roads, access to the area can be achieved from either of the primary roads, as can be seen in Figure 18. Because of the smaller surface area, there are fewer natural features on the east side (Figure 19), yet care will be taken to preserve natural and historic features. The specific laboratory features of the area are identified in Figure 20.

Considerable attention was given to the sixteen remote sites that are the service areas around the collider ring. Figure 21 shows the location of the areas and the access roads that have been designated for entry. Studies concentrated on each area with respect to land forms, soils analyses, slopes, interference with man-made features, etc. Figure 22 illustrates the results from one such study site. The Site Development Plan documented the conclusions for all the N and S sites and guided the shape and acquisition of the land by the Texas National Research Laboratory Commission. Six potential large shaft locations for the delivery of magnets to the underground tunnel were identified in the study, as illustrated in Figure 23. Those sites were examined in the same manner as the service areas and the results used in the land procurement.

The initial objectives of the Master Plan were realized through the working out of detailed studies for each site. The overall placing and configuration of the SSC Laboratory facilities have been considered. There is much more work to be done before this project can be considered complete. The next steps require advancing the design definition of the accelerator and experimental facilities by PB/MK as part of the Title I and II design process. It is then hoped that the Master Plan can be updated with more definite and current information.

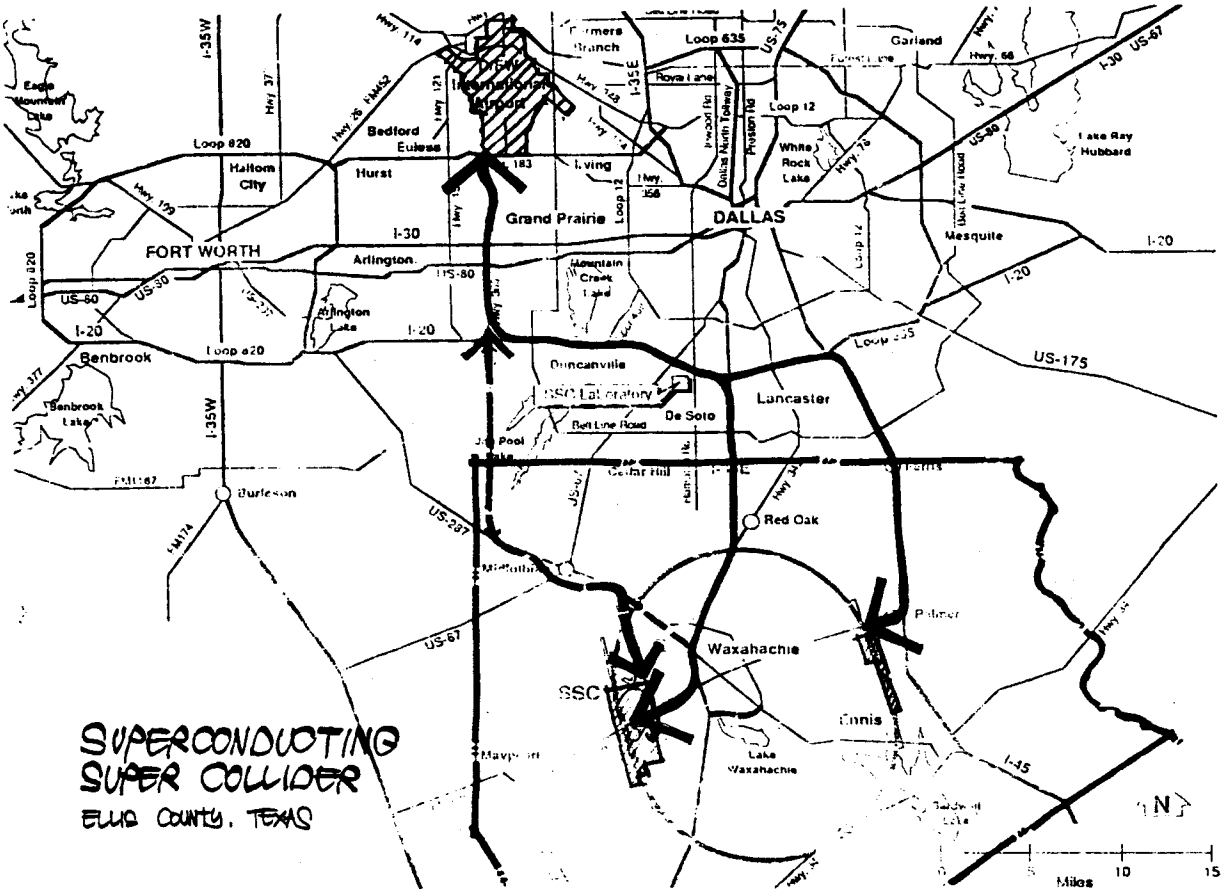

SUPERCONDUCTING
SUPER COLLIDER
ELLIS COUNTY, TEXAS
SSC
SSC Laboratory
FORT WORTH
DALLAS
Grand Prairie
Arlington
Benbrook
Duncanville
Lancaster
De Soto
Red Oak
Waxahachie
Ennis
Palmer
Burleson
Bedford
Euless
Hurst
Haltom City
Garland
Mesquite
Irving
Farmers Branch
Royal Lane
White Rock Lake
Lake Ray Hubbard
Mountain Creek Lake
Arlington Lake
Benbrook Lake
Lake Waxahachie
Cedar Hill
Bell Line Road
Loop 820
Loop 635
Loop 12
Loop 14
I-35W
I-35E
I-30
I-20
I-45
US-67
US-287
US-175
US-80
US-75
US-30
US-60
Miles
10
15
N

Figure 1.

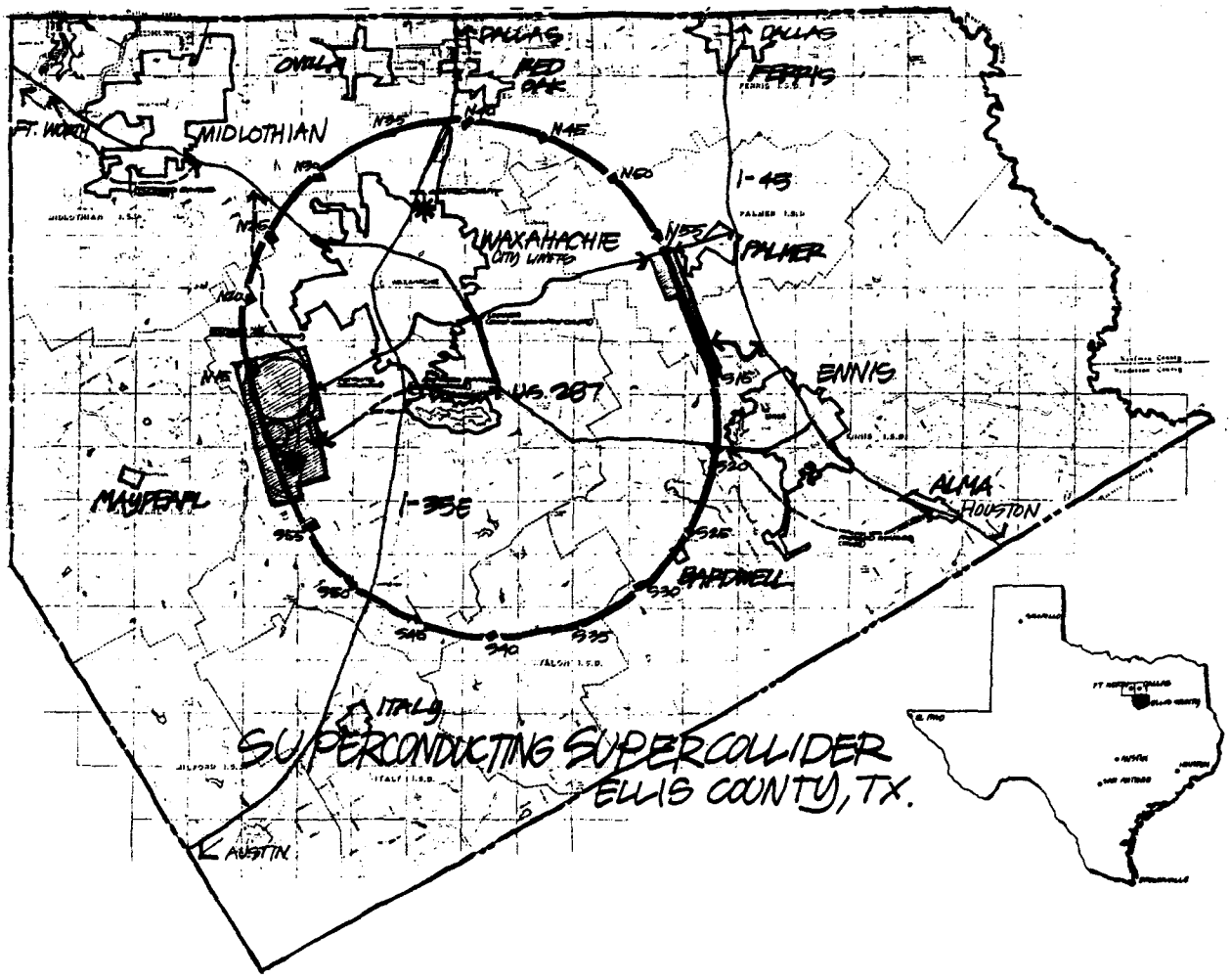

DALLAS
OVILLA
RED OAK
DALLAS
FERRIS
FT. WORTH
MIDLOTHIAN
I-45
WAXAHACHIE
CITY LIMITS
PALMER
ENNIS
US 287
ALMA
HOUSTON
MAYPEARL
I-35E
BARDWELL
ITALY
SUPERCONDUCTING SUPERCOLLIDER
ELLIS COUNTY, TX.
AUSTIN

Figure 2.

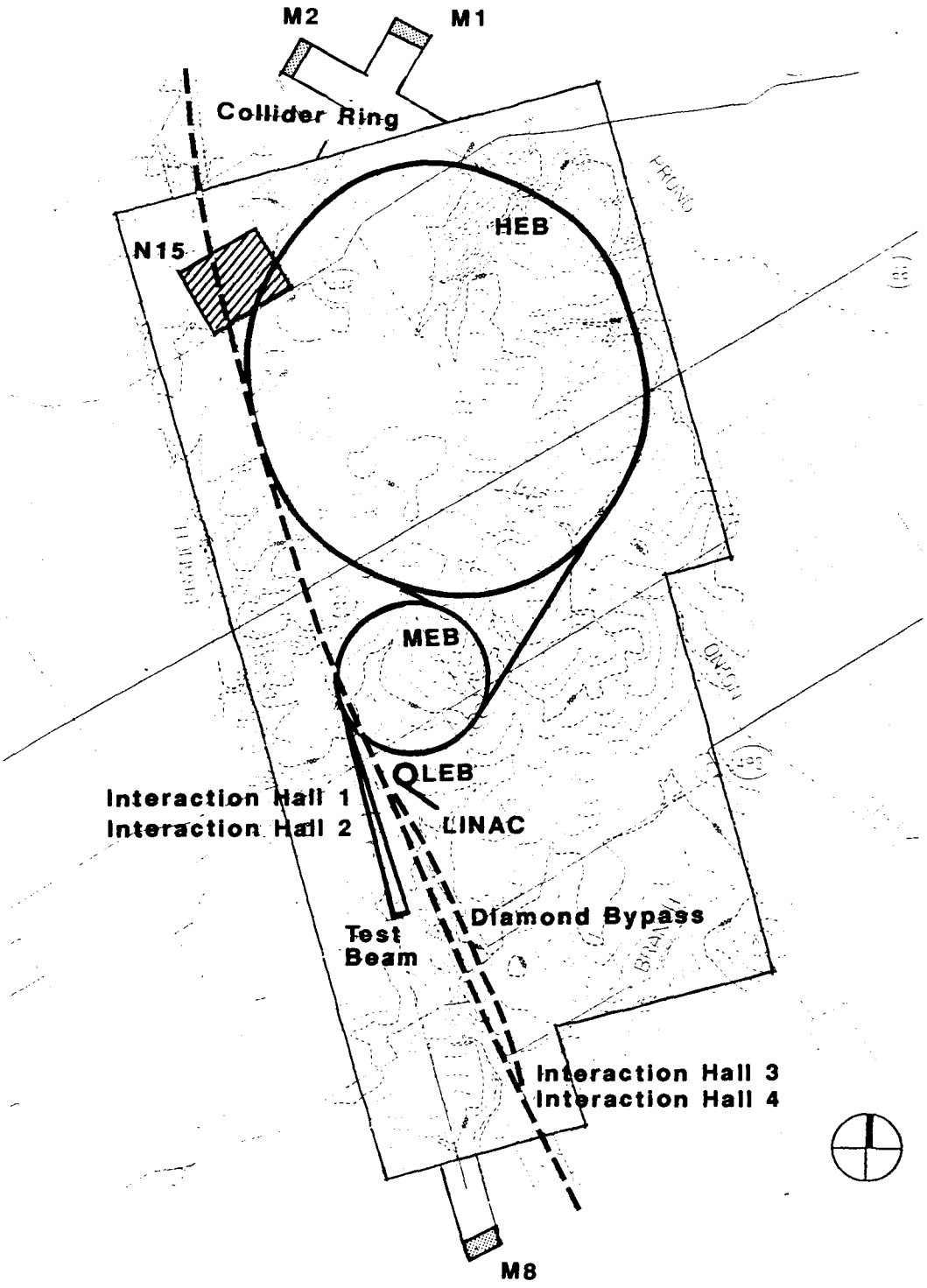

M2
M1
Collider Ring
N15
HEB
MEB
LEB
LINAC
Interaction Hall 1
Interaction Hall 2
Test
Beam
Diamond Bypass
Interaction Hall 3
Interaction Hall 4
M8

Figure 3.

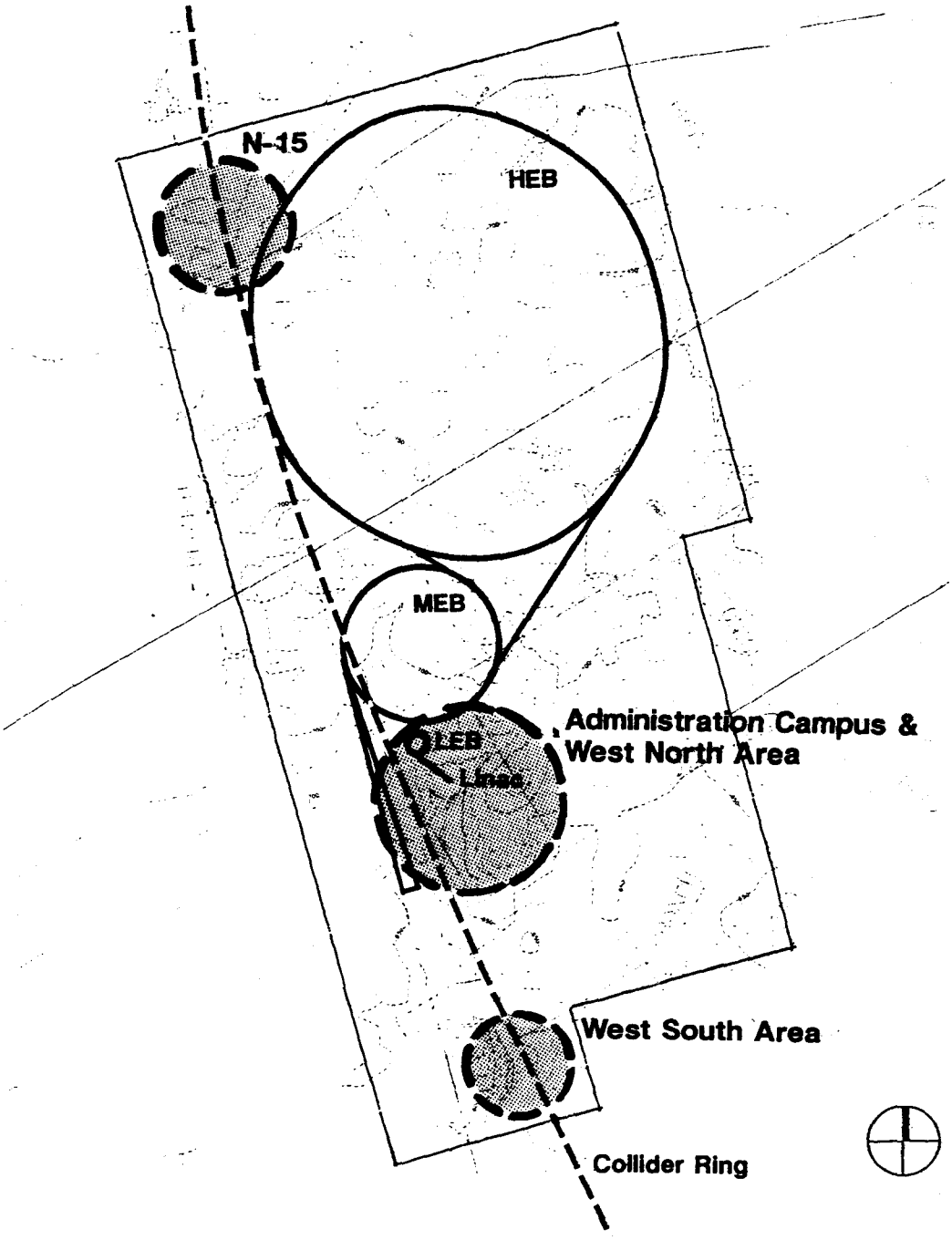

N-15
HEB
MEB
LEB
Linac
Administration Campus &
West North Area
West South Area
Collider Ring

Figure 4.

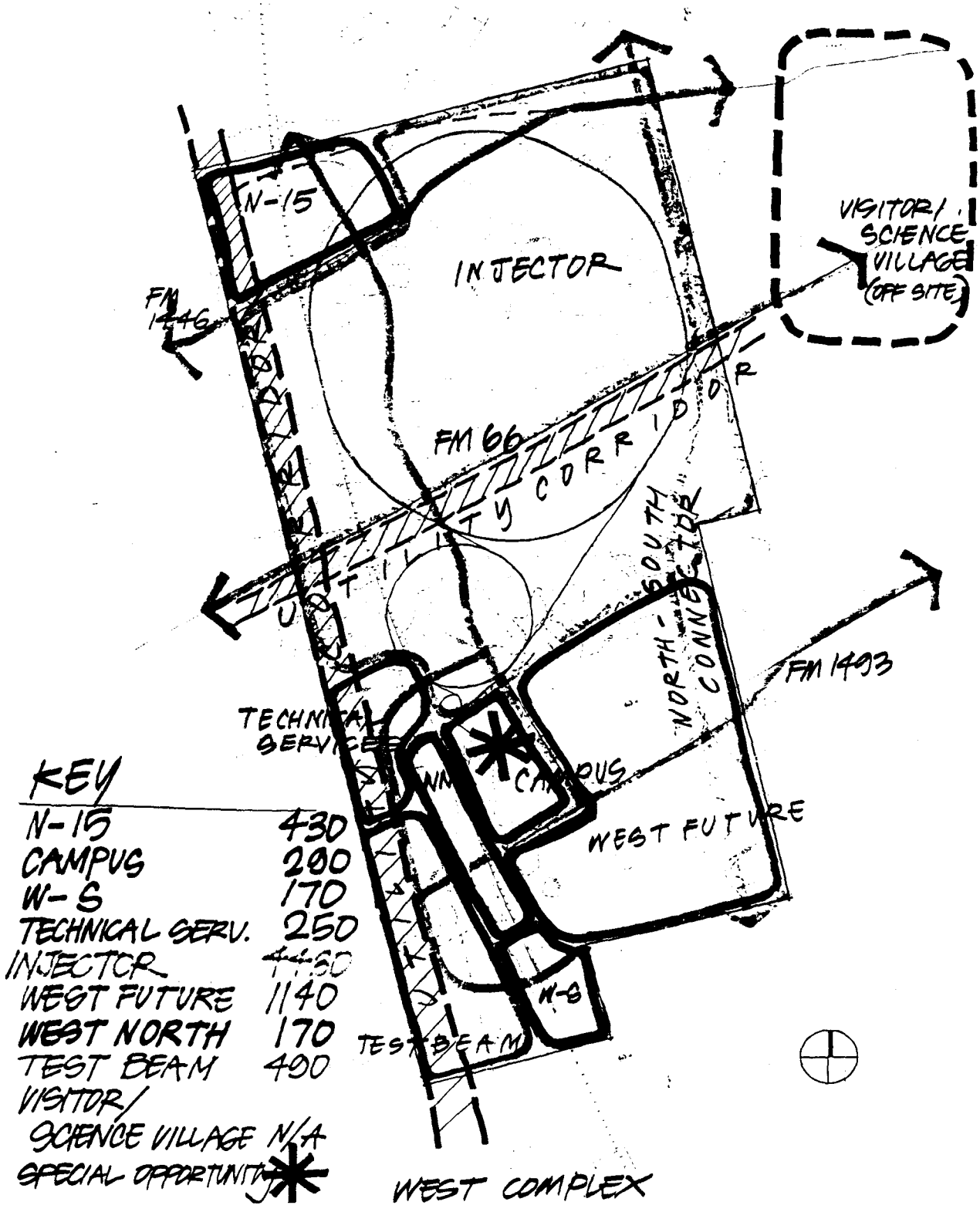
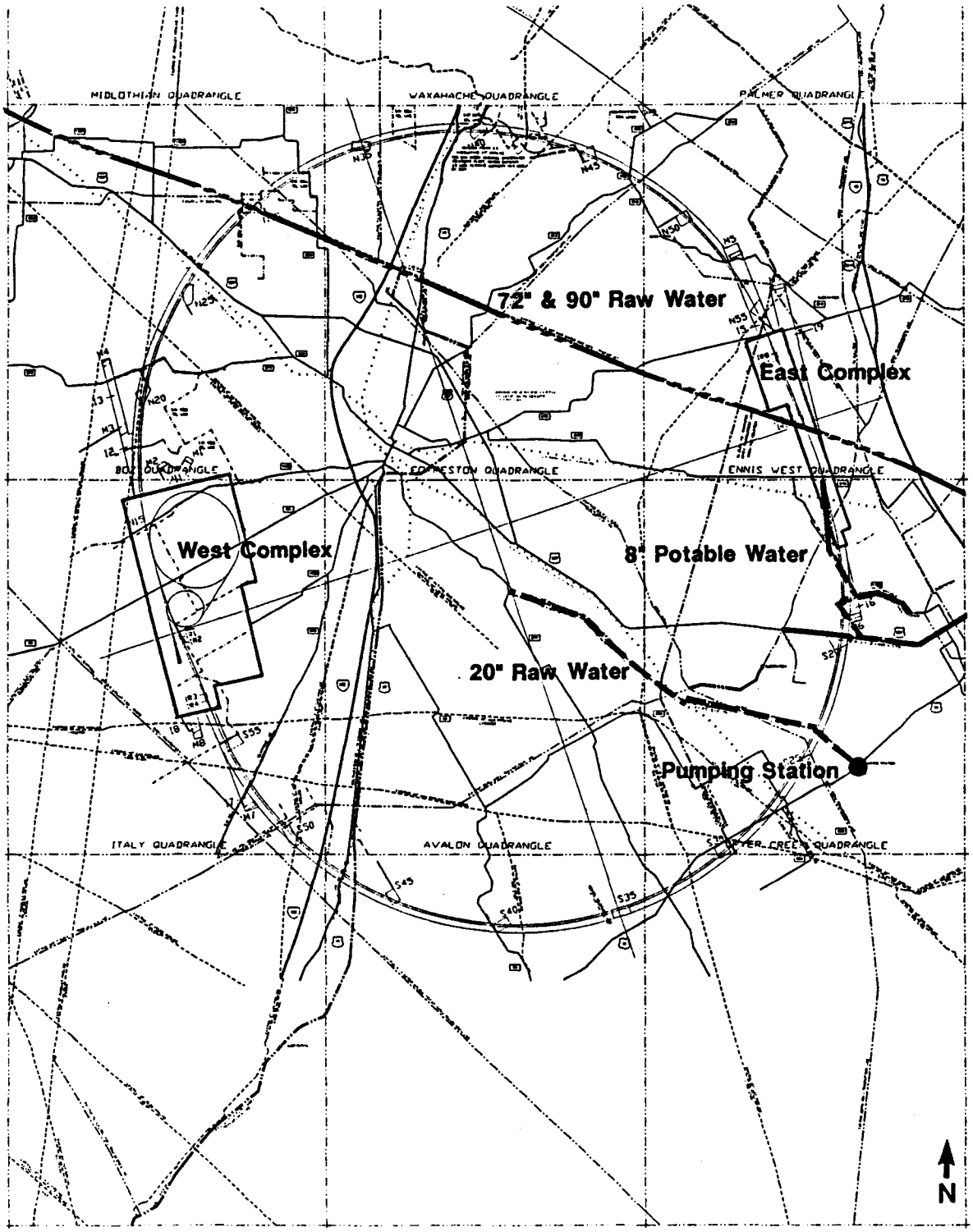

N-15
INJECTOR
VISITOR/
SCIENCE
VILLAGE
(OFF SITE)
FM
1446
FM 66
UTILITY CORRIDOR
NORTH-SOUTH CONNECTOR
FM 1493
TECHNICAL
SERVICES
CAMPUS
WEST FUTURE
W-S
TEST BEAM
WEST COMPLEX
KEY
N-15 430
CAMPUS 200
W-S 170
TECHNICAL SERV. 250
INJECTOR 450
WEST FUTURE 1140
WEST NORTH 170
TEST BEAM 490
VISITOR/
SCIENCE VILLAGE N/A
SPECIAL OPPORTUNITY *

Figure 5.



Tarrant County Water Control and Improvement District No. 1 Pipeline

Ellis County Water Control and Improvement District No. 1 Pipeline

City of Ennis Pipeline

Figure 6.

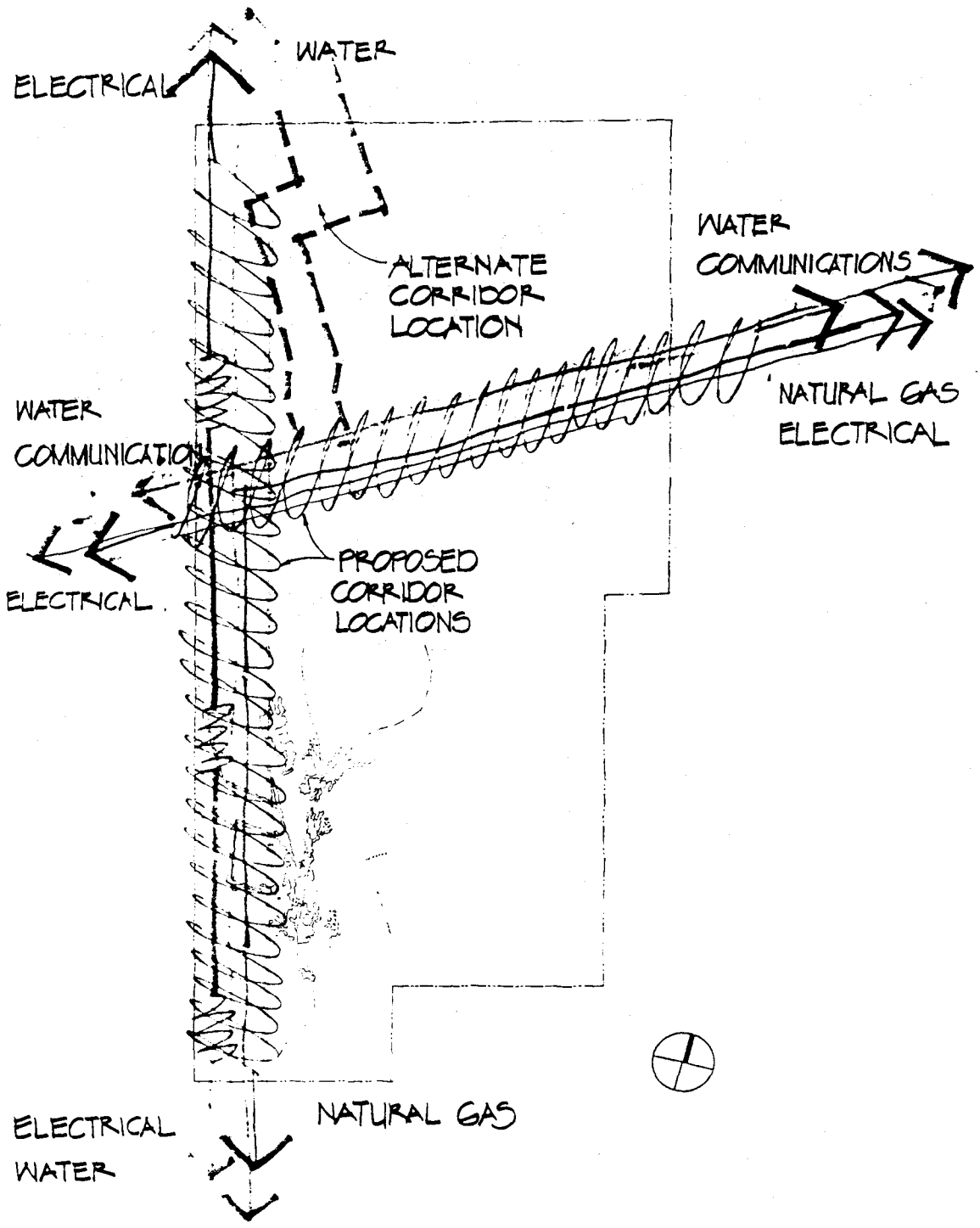

ELECTRICAL
WATER
ALTERNATE CORRIDOR LOCATION
WATER
COMMUNICATIONS
NATURAL GAS
ELECTRICAL
WATER
COMMUNICATION
ELECTRICAL
PROPOSED CORRIDOR LOCATIONS
NATURAL GAS
ELECTRICAL
WATER

Figure 7.

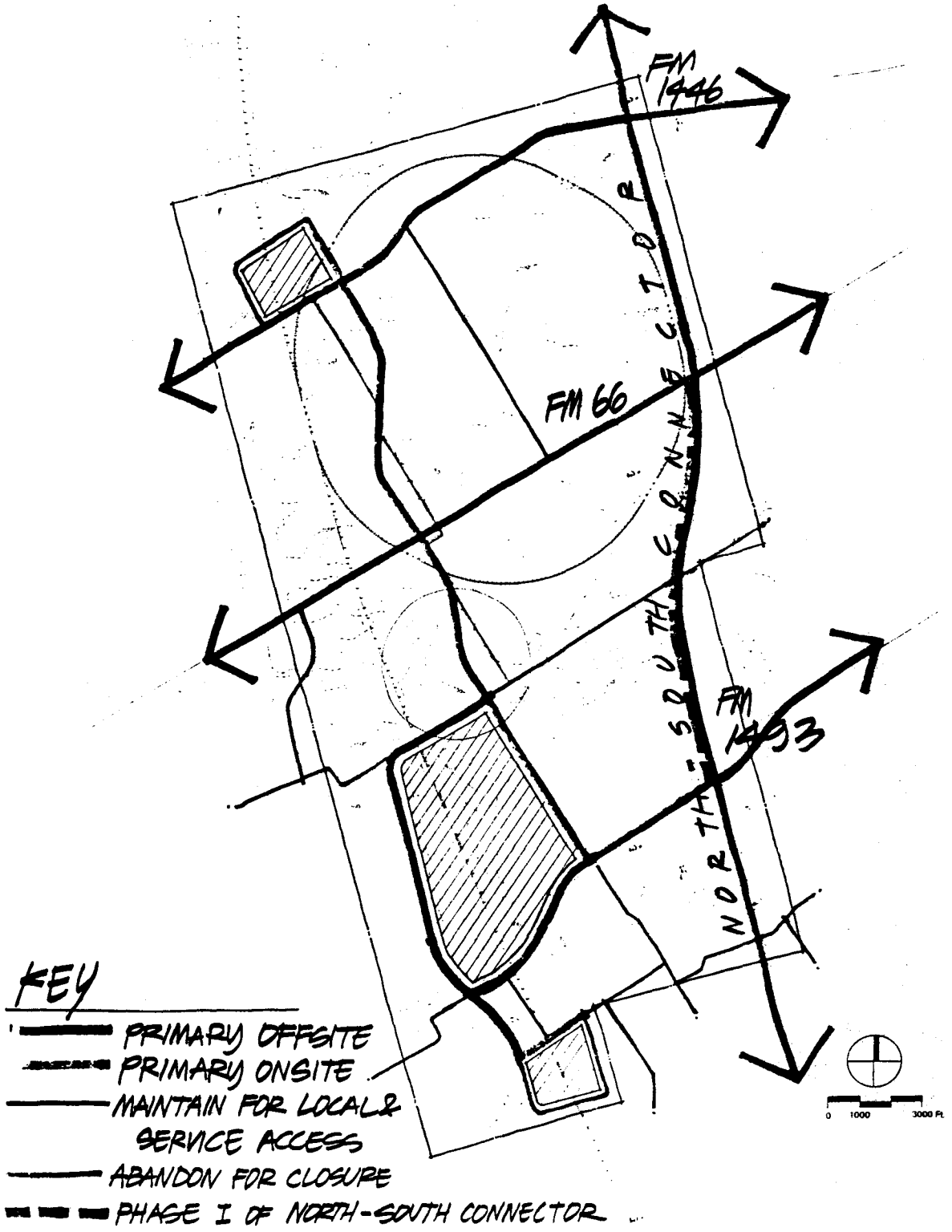

FM 1946
FM 66
FM 1393
NORTH - SOUTH CONNECTOR
KEY
PRIMARY OFFSITE
PRIMARY ONSITE
MAINTAIN FOR LOCAL & SERVICE ACCESS
ABANDON FOR CLOSURE
PHASE I OF NORTH-SOUTH CONNECTOR
0
1000
3000 Ft.

Figure 8

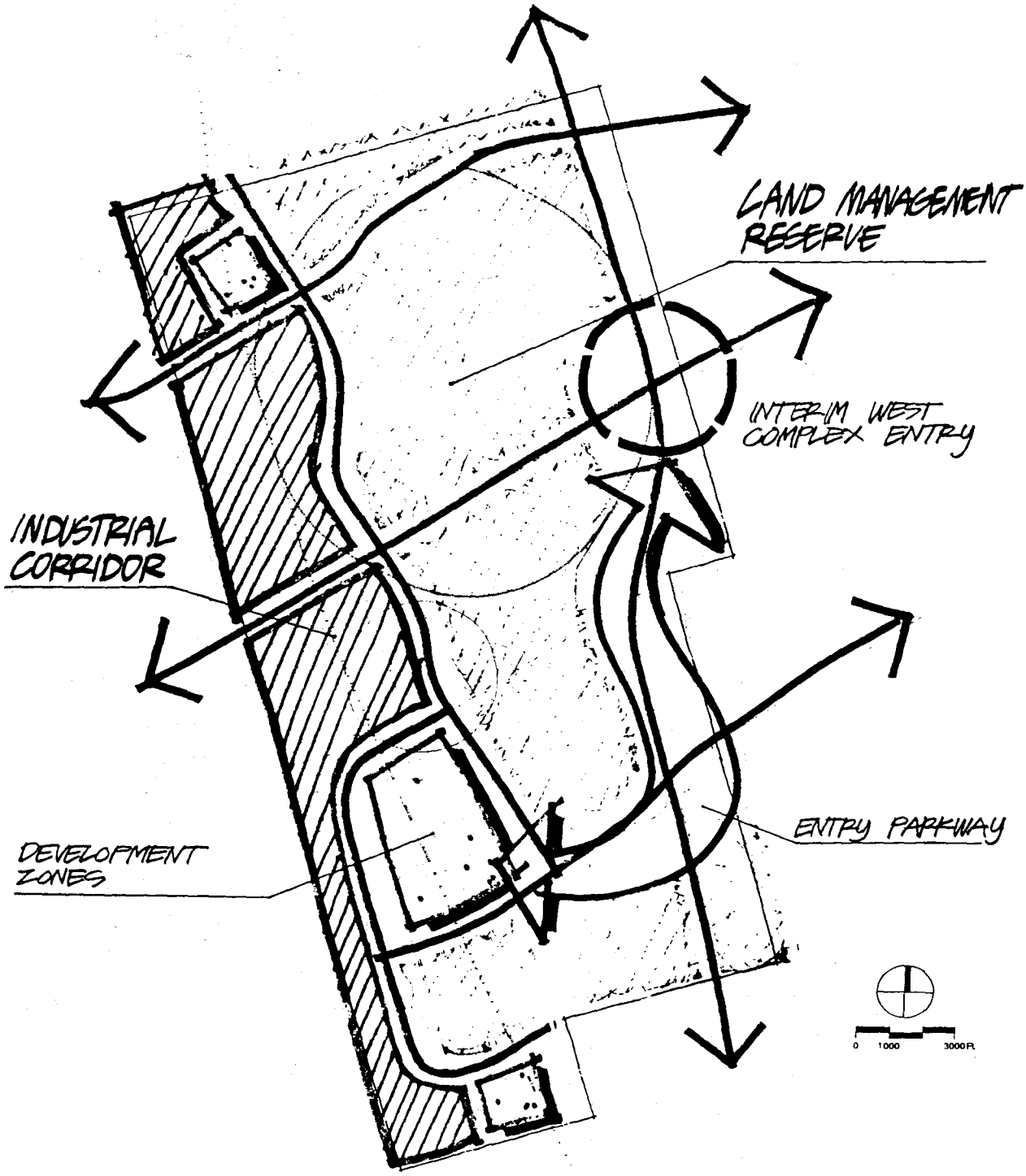

LAND MANAGEMENT RESERVE
INTERIM WEST COMPLEX ENTRY
INDUSTRIAL CORRIDOR
ENTRY PARKWAY
DEVELOPMENT ZONES
0 1000 3000 ft

Figure 9.

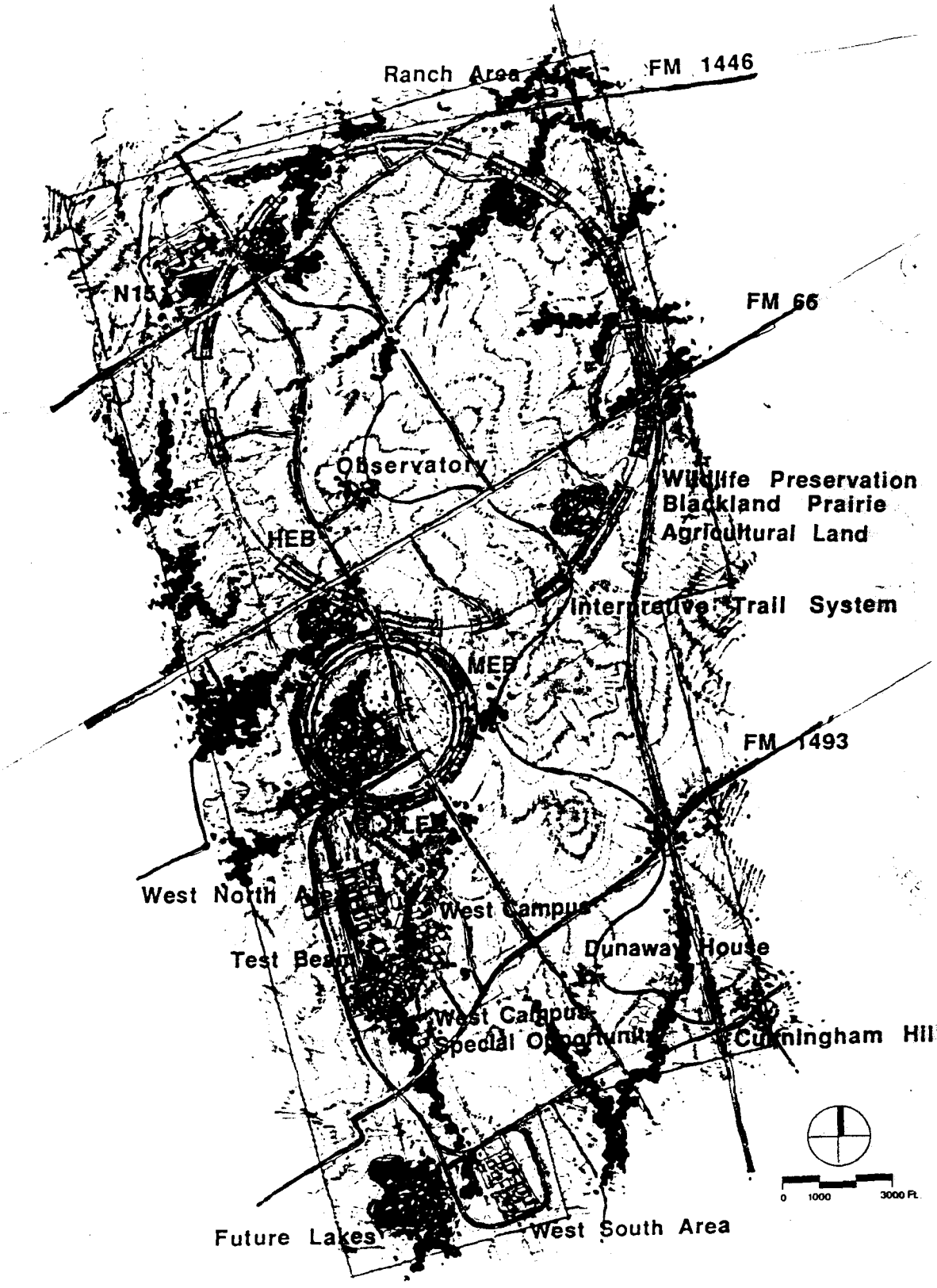

Ranch Area
FM 1446
N15
FM 66
Observatory
Wildlife Preservation
Blackland Prairie
Agricultural Land
HEB
Interpretive Trail System
MEB
FM 1493
West North Area
West Campus
Test Bed
Dunaway House
West Campus
Special Opportunity
Cunningham Hill
Future Lakes
West South Area
0 1000 3000 Ft.

Figure 10.

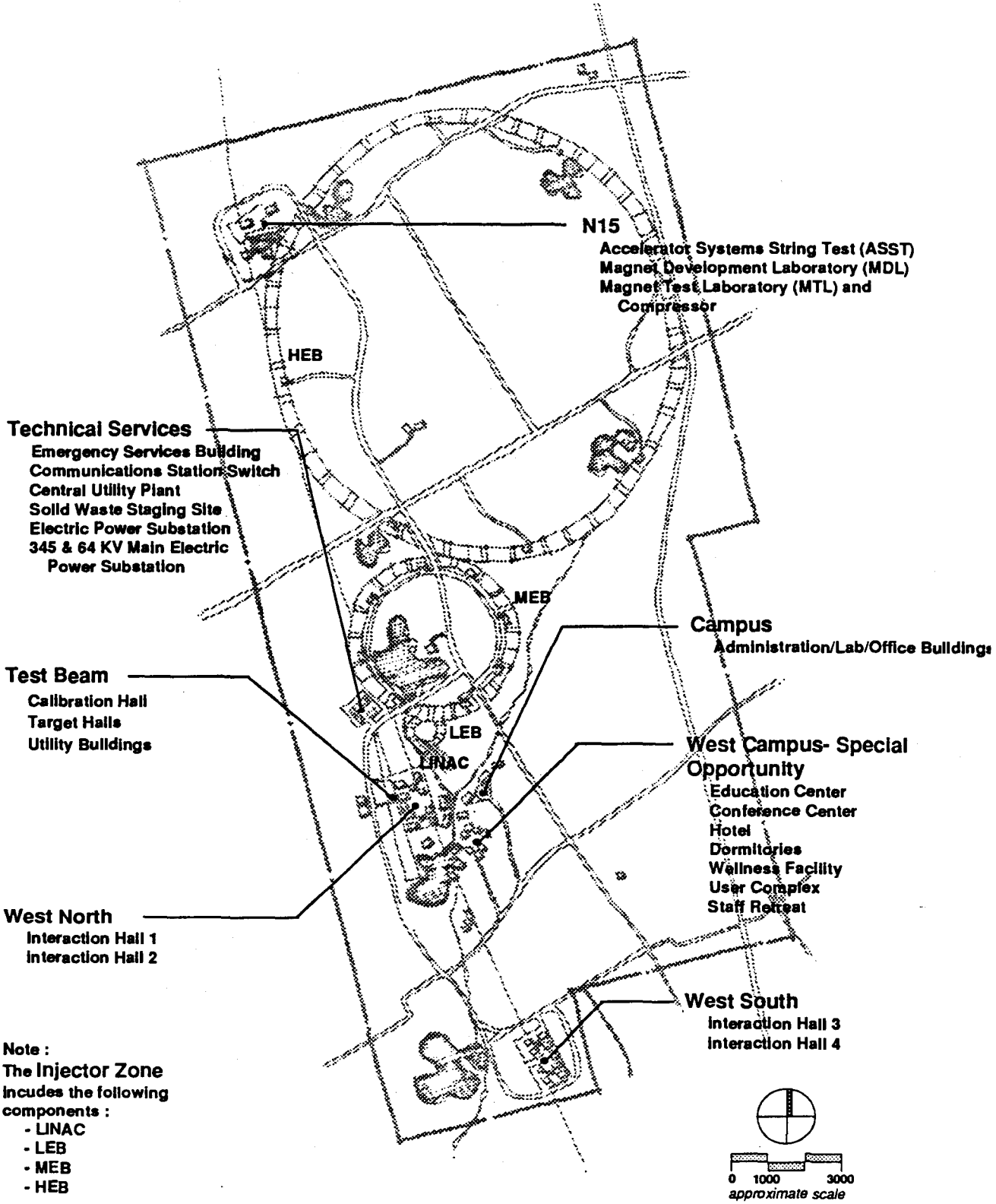

N15
Accelerator Systems String Test (ASST)
Magnet Development Laboratory (MDL)
Magnet Test Laboratory (MTL) and
Compressor
HEB
Technical Services
Emergency Services Building
Communications Station Switch
Central Utility Plant
Solid Waste Staging Site
Electric Power Substation
345 & 64 KV Main Electric
Power Substation
MEB
Campus
Administration/Lab/Office Buildings
Test Beam
Calibration Hall
Target Halls
Utility Buildings
LEB
LINAC
West Campus- Special
Opportunity
Education Center
Conference Center
Hotel
Dormitories
Wellness Facility
User Complex
Staff Retreat
West North
Interaction Hall 1
Interaction Hall 2
West South
Interaction Hall 3
Interaction Hall 4
Note :
The Injector Zone
incudes the following
components :
- LINAC
- LEB
- MEB
- HEB
0 1000 3000
approximate scale

Figure 11.

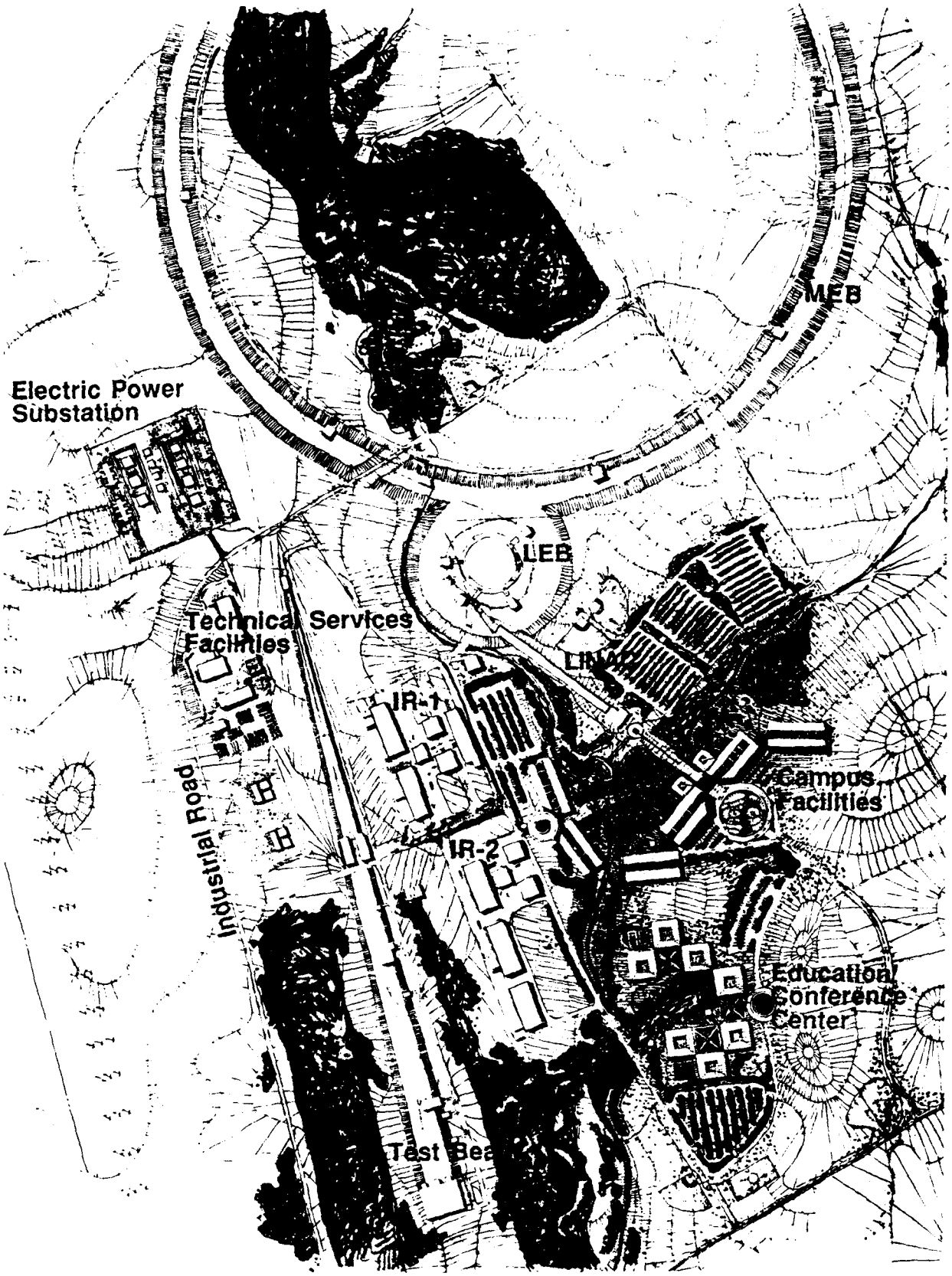

MEB
Electric Power
Substation
LEB
Technical Services
Facilities
IR-1
Industrial Road
IR-2
Campus
Facilities
Education/
Conference
Center

Figure 12.

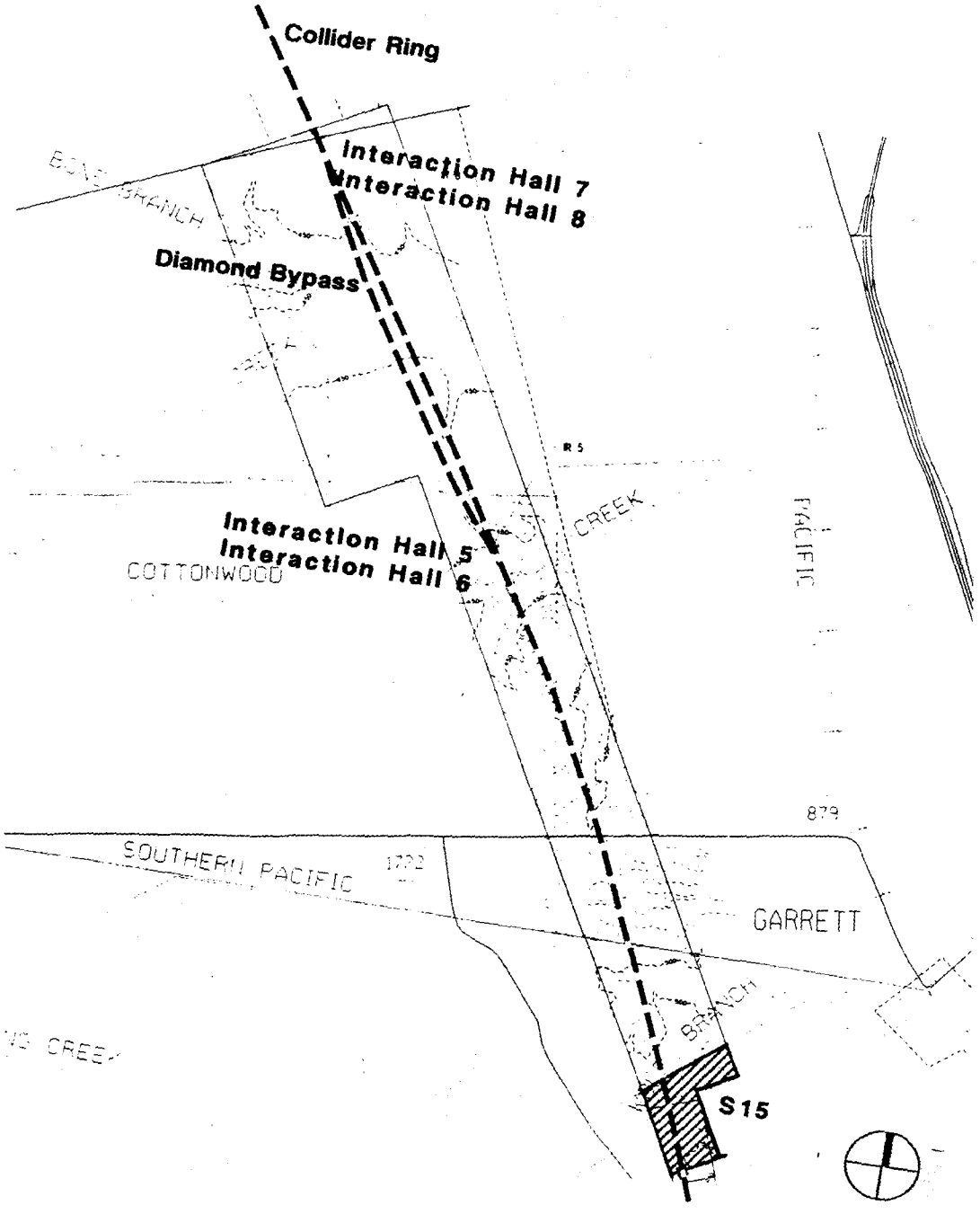

Collider Ring
Interaction Hall 7
Interaction Hall 8
Diamond Bypass
Interaction Hall 5
Interaction Hall 6
COTTONWOOD
CREEK
PACIFIC
R 5
879
SOUTHERN PACIFIC
1722
GARRETT
BRANCH
S15

Figure 14.

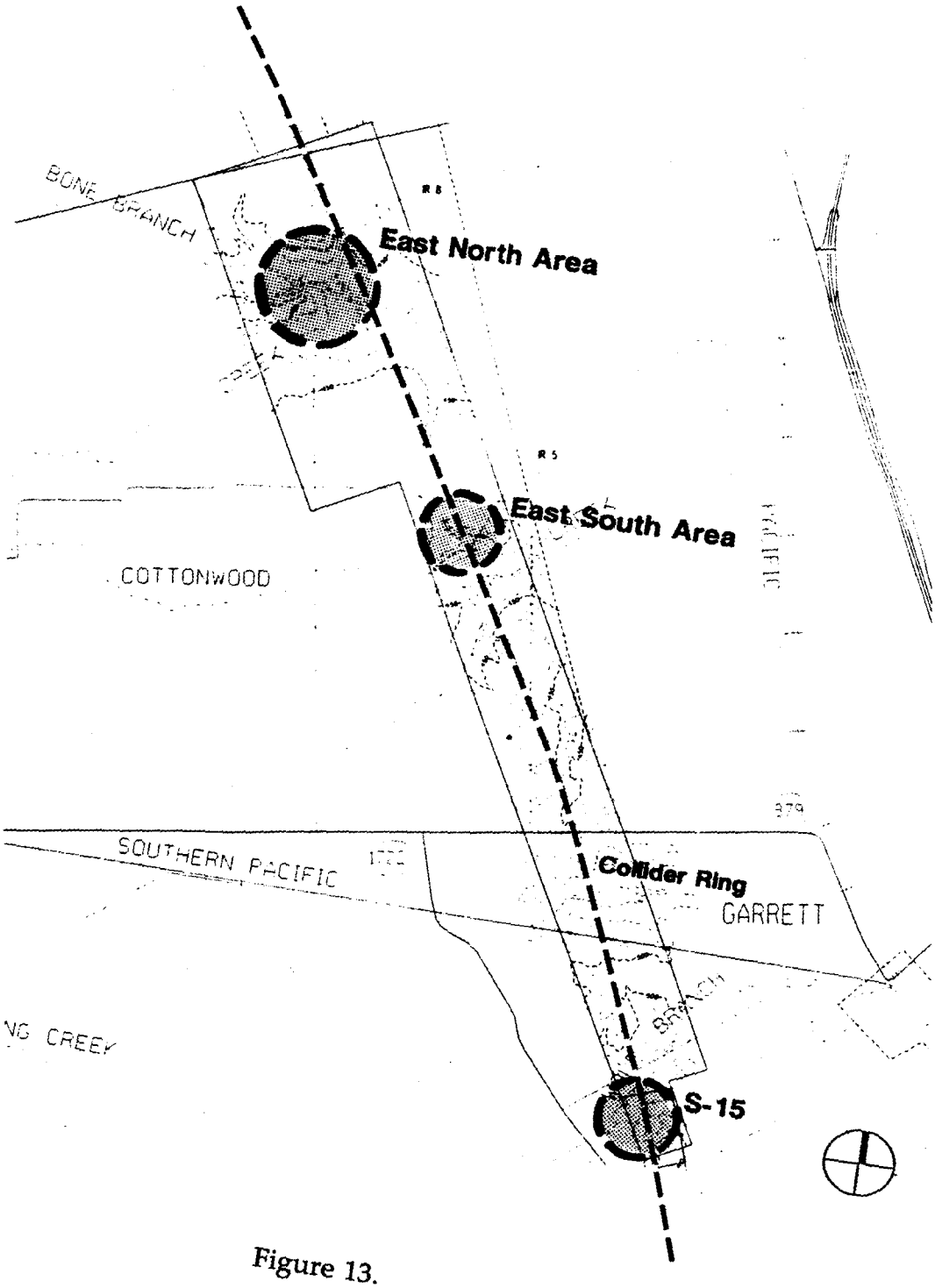

BONE BRANCH
East North Area
East South Area
COTTONWOOD
SOUTHERN PACIFIC
Collider Ring
GARRETT
S-15

Figure 13.

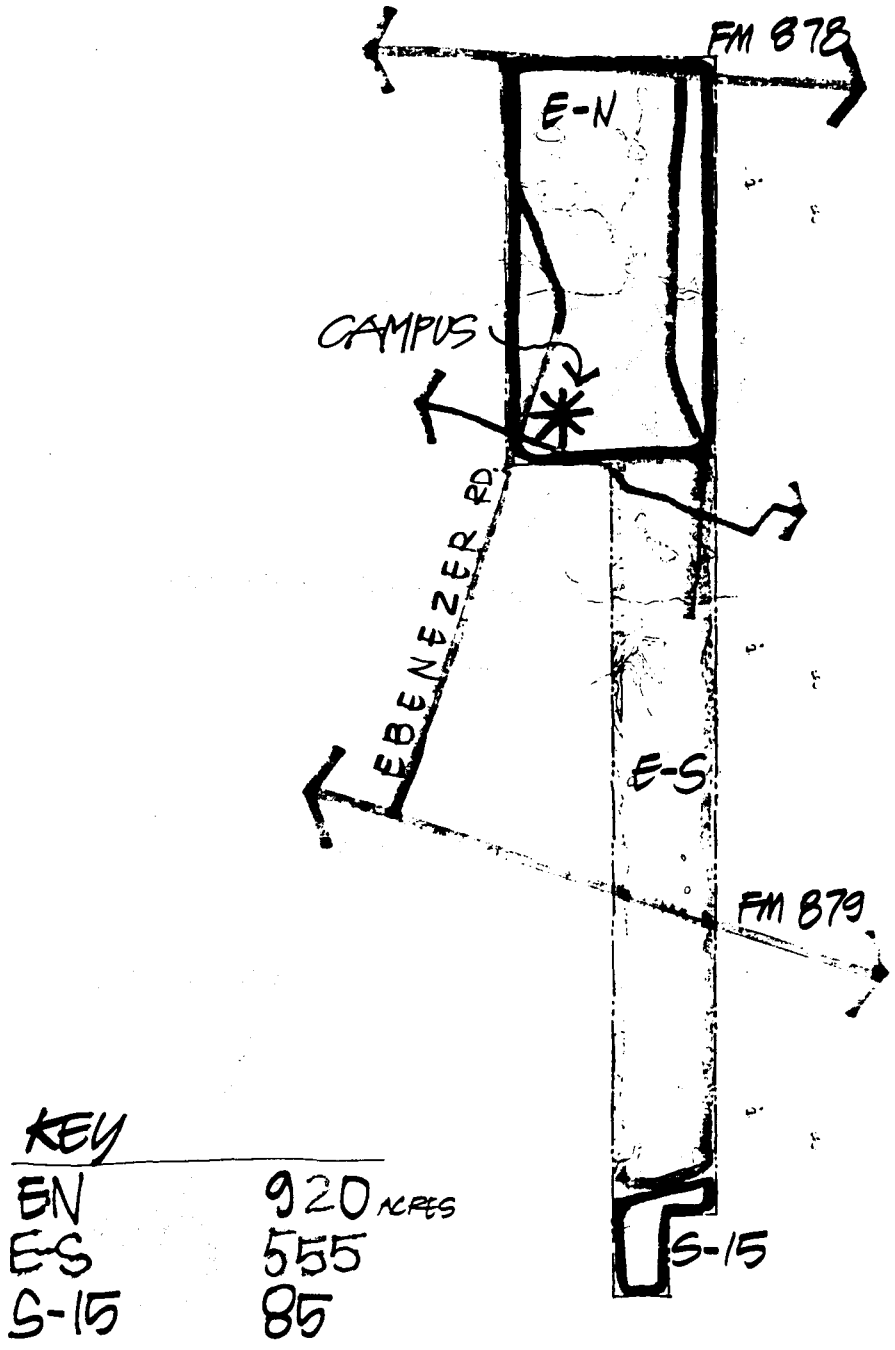

FM 878
E-N
CAMPUS
EBENEZER RD
E-S
FM 879
S-15
KEY
EN 920 ACRES
E-S 555
S-15 85

Figure 15.

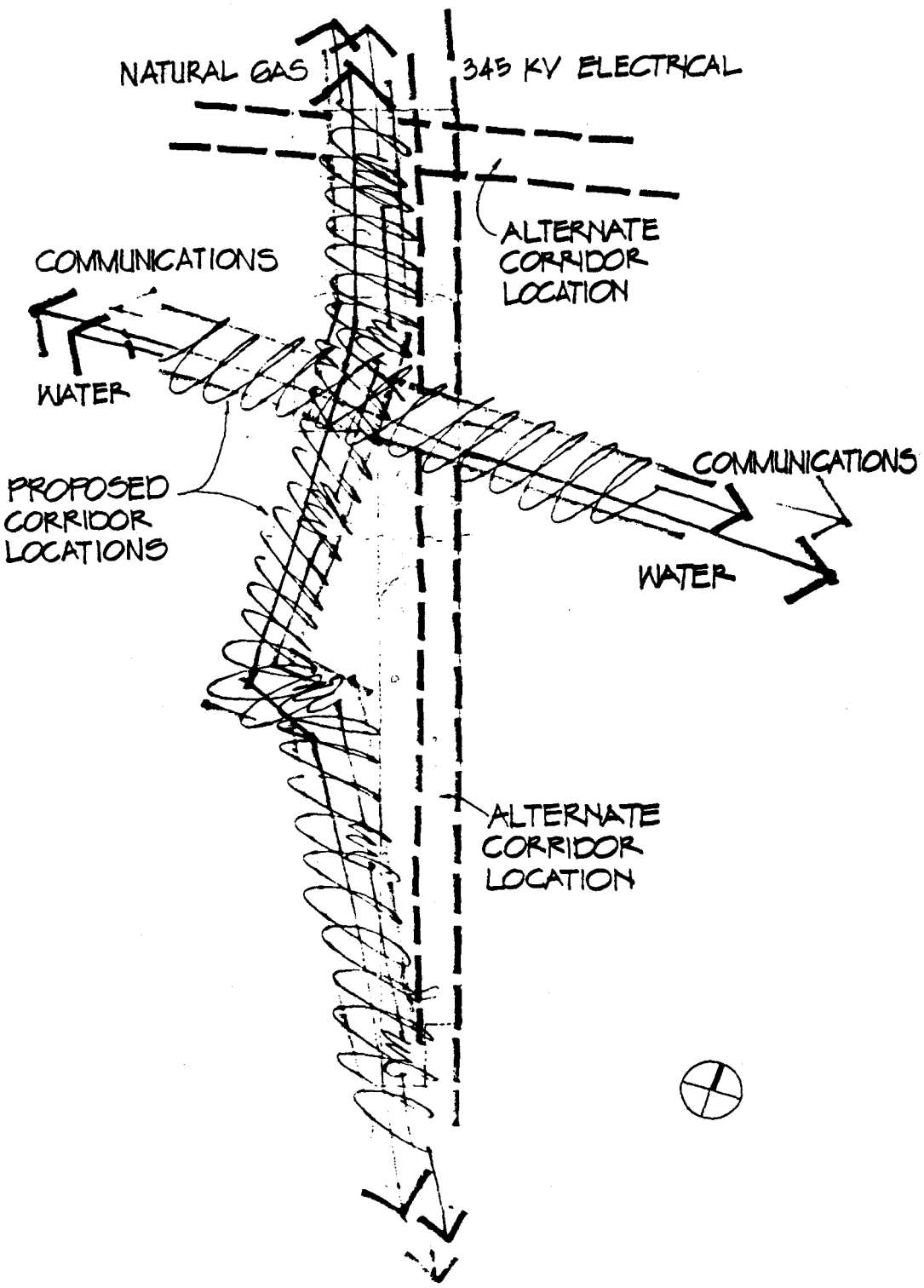

NATURAL GAS
345 KV ELECTRICAL
ALTERNATE CORRIDOR LOCATION
COMMUNICATIONS
WATER
PROPOSED CORRIDOR LOCATIONS
COMMUNICATIONS
WATER
ALTERNATE CORRIDOR LOCATION

Figure 16.

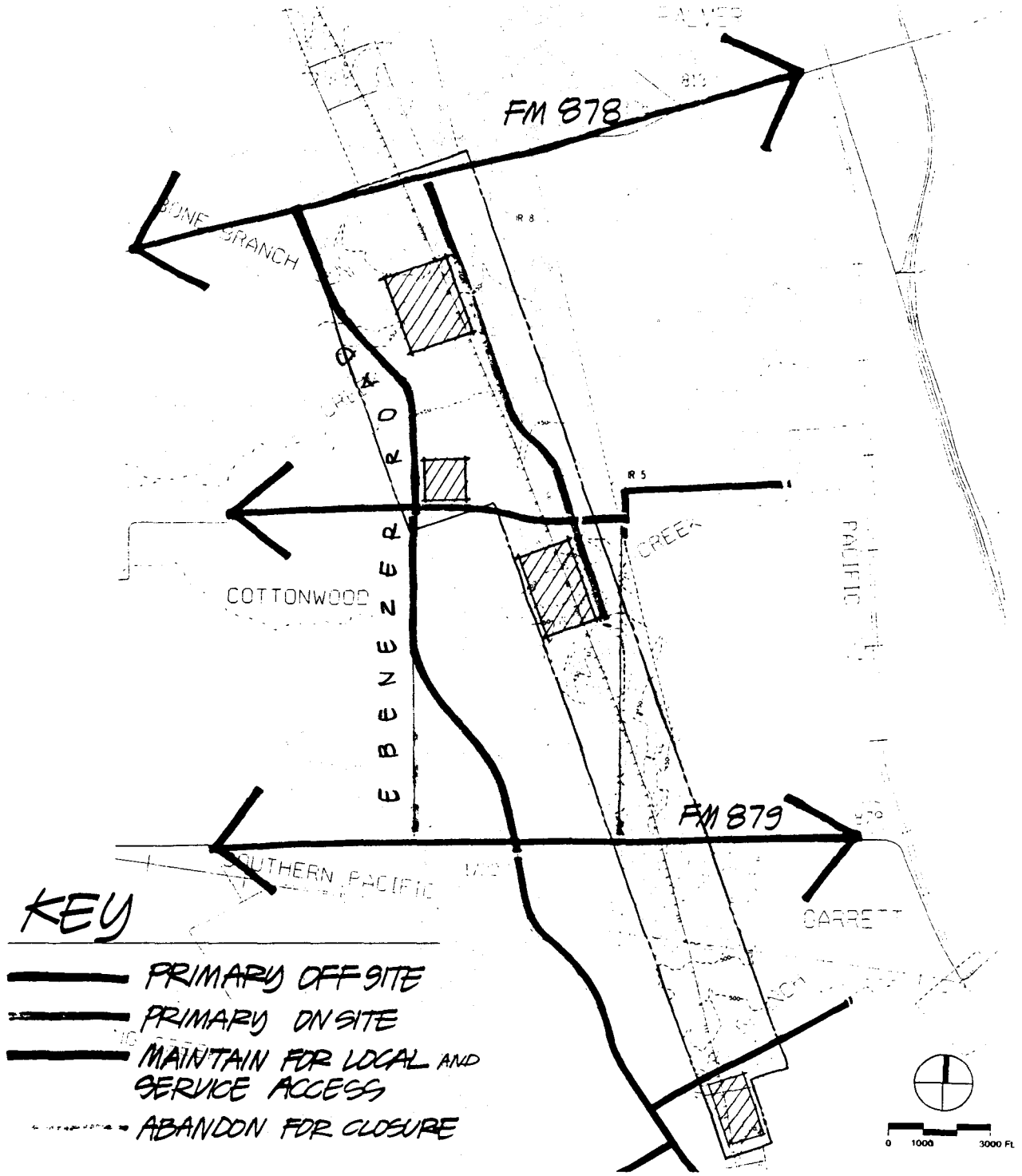

FM 878
BONE BRANCH
EBENEZER ROAD
COTTONWOOD
CREEK
PACIFIC
FM 879
SOUTHERN PACIFIC
CARRETT
KEY
PRIMARY OFF-SITE
PRIMARY ON-SITE
MAINTAIN FOR LOCAL AND SERVICE ACCESS
ABANDON FOR CLOSURE
0 1000 3000 FT

Figure 17.

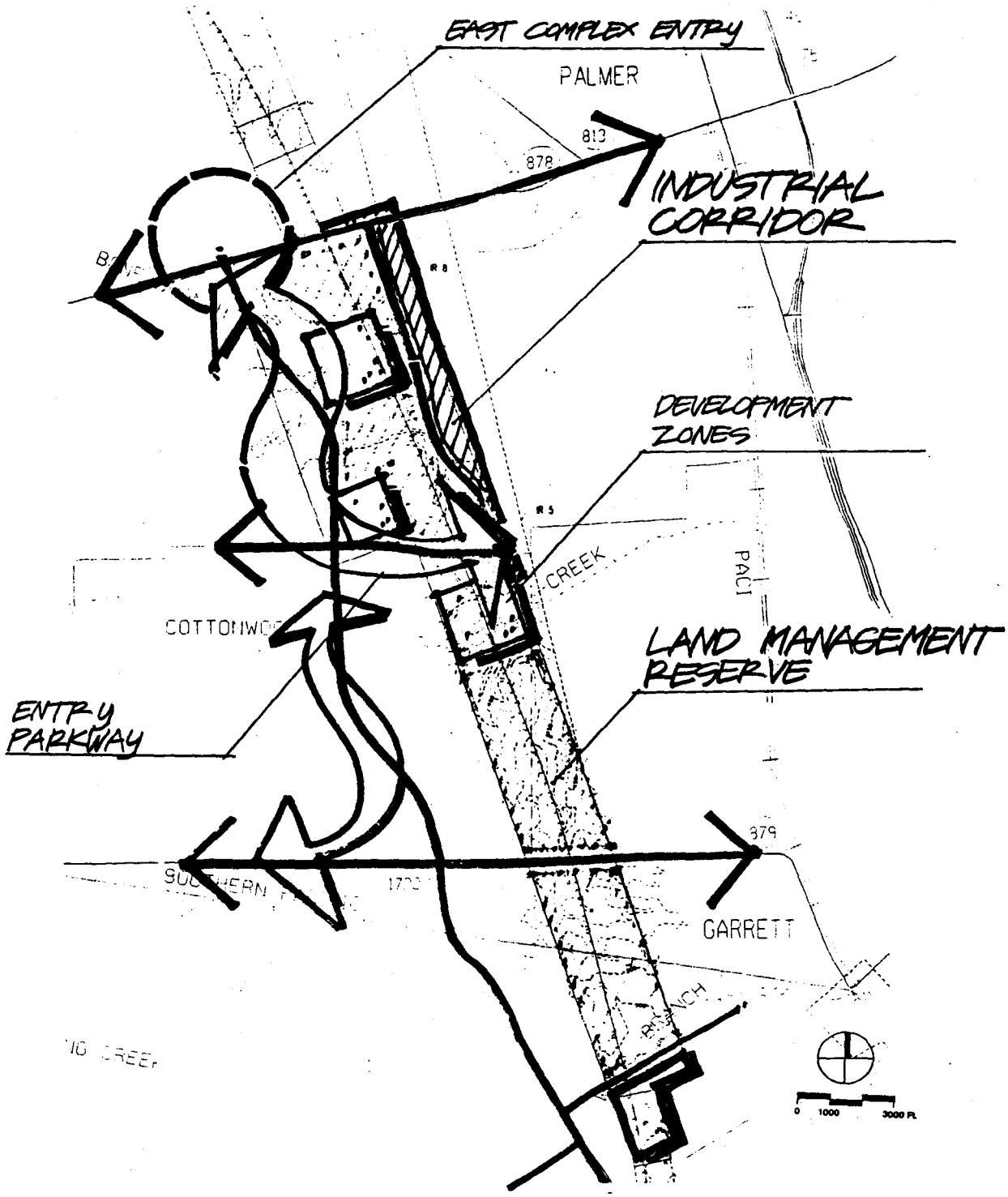

EAST COMPLEX ENTRY
PALMER
813
878
INDUSTRIAL CORRIDOR
DEVELOPMENT ZONES
CREEK
LAND MANAGEMENT RESERVE
ENTRY PARKWAY
879
GARRETT
0 1000 3000 FT

Figure 18.

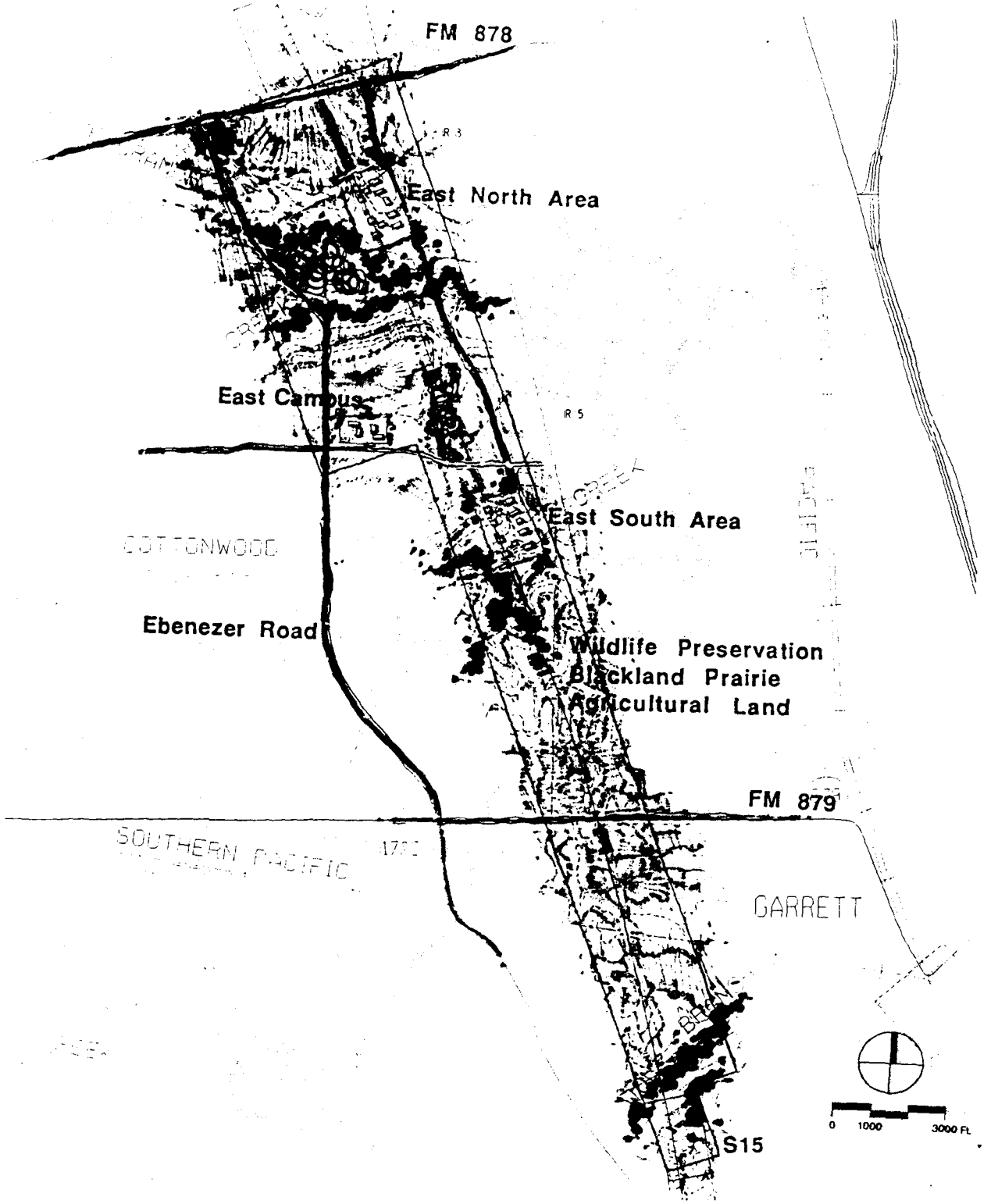

FM 878
East North Area
East Campus
East South Area
COTTONWOOD
Ebenezer Road
Wildlife Preservation
Blackland Prairie
Agricultural Land
FM 879
SOUTHERN PACIFIC
GARRETT
S15
0 1000 3000 FT

Figure 19.

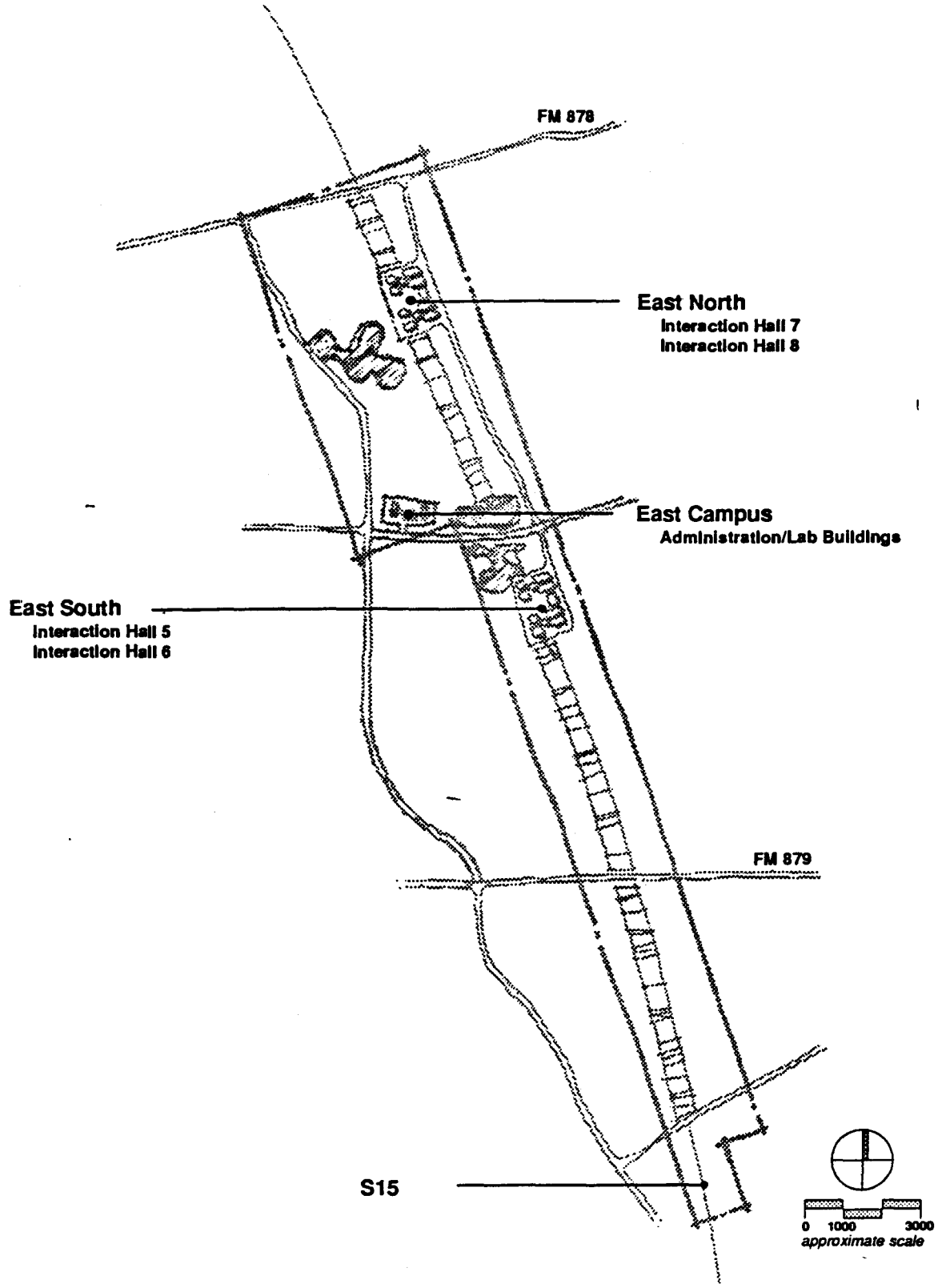

FM 878
East North
Interaction Hall 7
Interaction Hall 8
East Campus
Administration/Lab Buildings
East South
Interaction Hall 5
Interaction Hall 6
FM 879
S15
0 1000 3000
approximate scale

Figure 20.

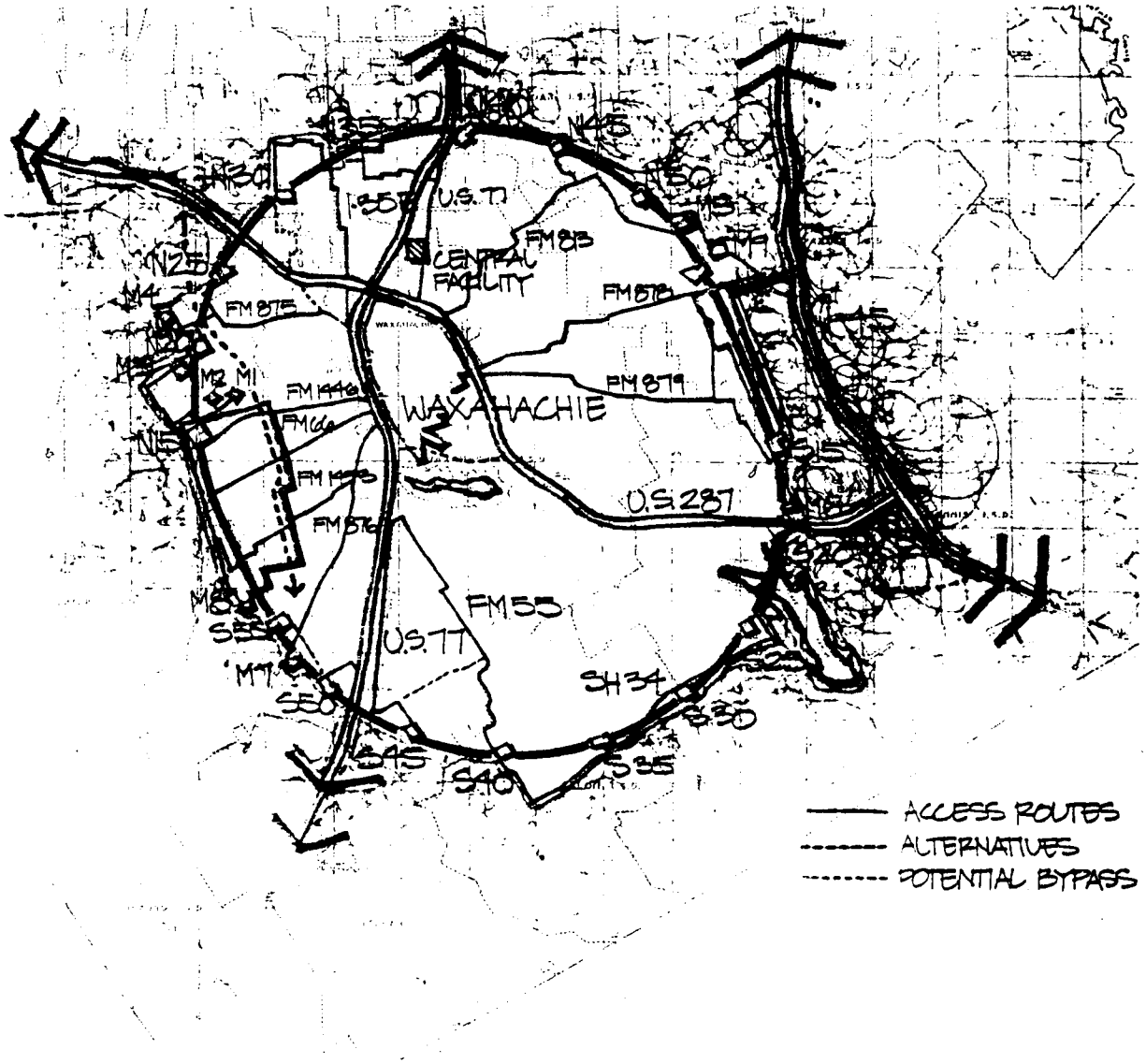

I-35E
U.S. 77
FM 85
CENTRAL FACILITY
FM 875
FM 879
WAXAHACHIE
FM 66
U.S. 287
FM 55
U.S. 77
SH 34
ACCESS ROUTES
ALTERNATIVES
POTENTIAL BYPASS

Figure 21.

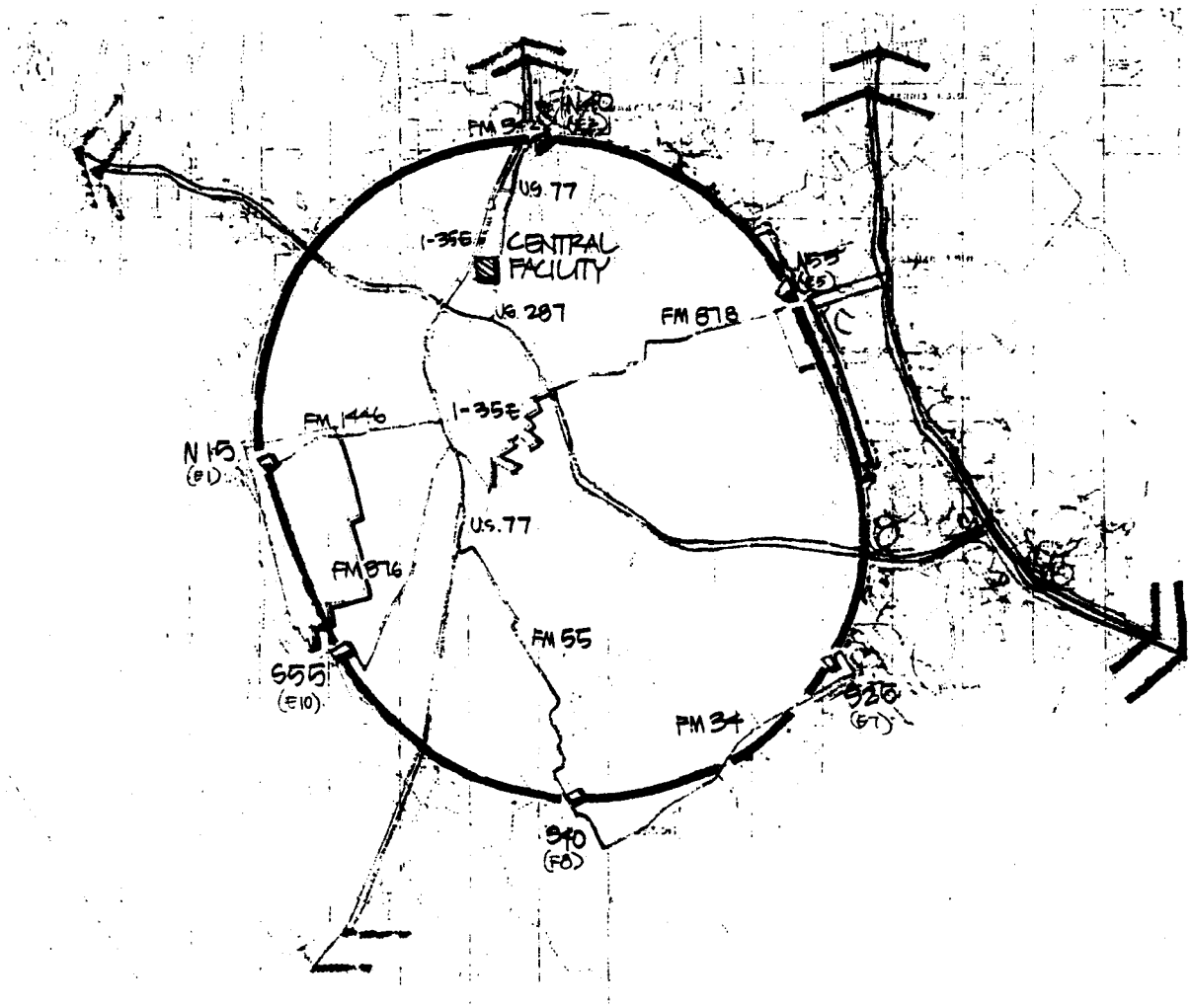


Figure 22.

Figure 4.05 Magnet Delivery Routes for Discussion

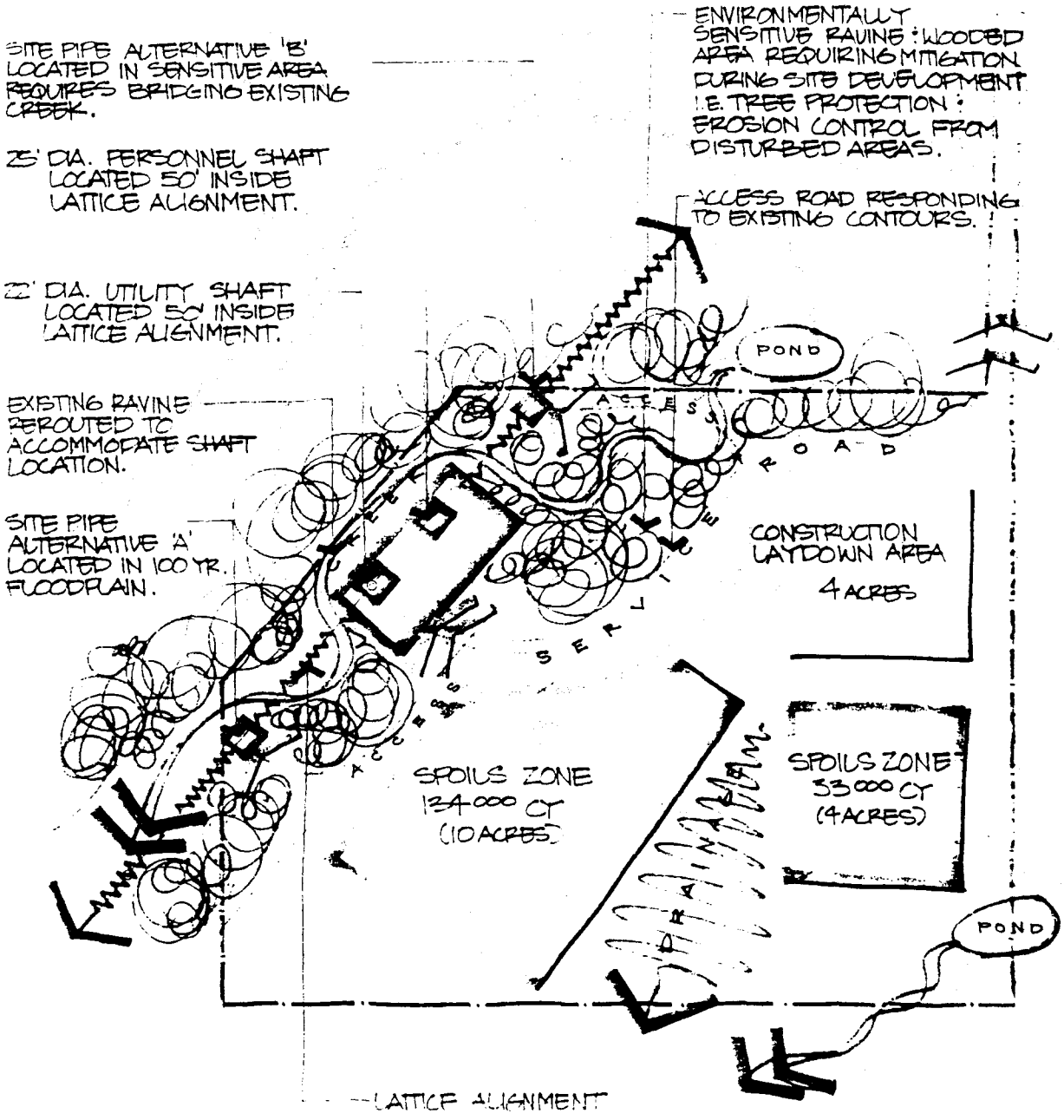

SITE PIPE ALTERNATIVE 'B' LOCATED IN SENSITIVE AREA REQUIRES BRIDGING EXISTING CREEK.
25' DIA. PERSONNEL SHAFT LOCATED 50' INSIDE LATTICE ALIGNMENT.
22' DIA. UTILITY SHAFT LOCATED 50' INSIDE LATTICE ALIGNMENT.
EXISTING RAVINE REROUTED TO ACCOMMODATE SHAFT LOCATION.
SITE PIPE ALTERNATIVE 'A' LOCATED IN 100 YR. FLOODPLAIN.
ENVIRONMENTALLY SENSITIVE RAVINE: WOODED AREA REQUIRING MITIGATION DURING SITE DEVELOPMENT I.E. TREE PROTECTION: EROSION CONTROL FROM DISTURBED AREAS.
ACCESS ROAD RESPONDING TO EXISTING CONTOURS.
POND
ACCESS ROAD
CONSTRUCTION LAYDOWN AREA 4 ACRES
SPOILS ZONE 134000 CY (10 ACRES)
SPOILS ZONE 53000 CY (4 ACRES)
POND
LATTICE ALIGNMENT

Figure 23.

Draft Site Development Plan - as Revised

1. Executive Summary

2. General Site Information
   - 2.1. SSC Background
   - 2.2. Regional Overview
   - 2.3. Specific Locale Data
   - 2.4. Regional Public Transportation
   - 2.5. Regional Utilities and Infrastructure
   - 2.6. Geology/Topography
   - 2.7. Meteorology

3. Long Range Master Plan
   - 3.1. Long-range Master Plan Overview
   - 3.2. Site-specific Scientific Components
   - 3.3. Development Zones
   - 3.4. Land Use Zoning
   - 3.5. Long-range Transportation
   - 3.6. Utility Corridors
   - 3.7. Future Needs
   - 3.8. Long Range Master Plan

4. Site Development Plan
   - 4.1. Facility Needs
   - 4.2. 1999 Baseline Plans
   - 4.3. Land - 1999 Site Development Plan
   - 4.4. Buildings and Structures in Progress
   - 4.5. Utilities and Infrastructure
   - 4.6. Collider Ring Service Area Access
   - 4.7. Environmental Issues
   - 4.8. Security
   - 4.9. Safety
   - 4.10. Cost

5. Existing Conditions
   - 5.1. Existing Land Use
   - 5.2. Mission and Program
   - 5.3. Population
   - 5.4. Operations
   - 5.5. Existing Infrastructure
   - 5.6. Physical Site Characteristics

6. Master Planning Analysis
   - 6.1. Methodology
   - 6.2. Goals
   - 6.3. Evaluation
   - 6.4. Site Adequacy Studies
   - 6.5. Development of Master Plan
   - 6.6. West Complex/Campus Prel. Planning Alternatives
   - 6.7. East Complex Prel. Planning Alternatives

Appendices

Example Special Opportunities

Users

- Offices & Work Spaces
- Computer Facilities

Visitors

- Exhibit Space
- Tour Facilities

Education

- Auditorium & Meeting Rooms
- Training Facilities

Amenities

- Housing - short & long
- Food Service - after hours

Community

- Recreation
- Day Care

Calorimetry Subsystem R&D

J. Brau

Calorimetry Subsystem R&D

Barium Fluoride

Scintillating Fiber

Liquid Argon

Liquid Krypton, Xenon

Silicon

Corpus Christi - J.E. Brau - Oct. 16. 1991

THE BaF_2 COLLABORATION

G. Gratta, M. Grossvald, D. Kirkby, W. Lu, R. Mount,
H. Newman, S. Shevchenko, X. Shi, R.Y. Zhu, Z. Y. Wei
California Institute of Technology, *Pasadena, California, U.S.A.*

D. Anzer, J. Branson, H. Kobrak, R. Swanson
University of California, *San Diego, California, U.S.A.*

P. Denes, M. Ito, D. Marlow, P. Pirous, B. Sadoghi, D. Stickland
Princeton University, *Princeton, New Jersey, U.S.A.*

A. Engler, T. Ferguson, R. Kramer, R. Sutton, H. Vogel
Carnegie Mellon University, *Pittsburgh, Pennsylvania, U.S.A.*

J.A. Kierstead, P.W. Levy, C.L. Woody, S. Stoll
Brookhaven National Laboratory, *Upton, New York, U.S.A.*

M. Bauer, C. Britton, H. Cohn, J. Moore, F. Plasil, K. Read,
M. Ramish, A. Wintenberg
Oak Ridge National Laboratory, *Oak Ridge, Tennessee, U.S.A.*

D. Brown, A. Bowman, D. Lee, G. Sanders
Los Alamos National Laboratory, *Los Alamos, New Mexico, U.S.A.*

X.L. Fang, P.X. Gu, J.K. Guo, C.F. He, G.Q. He, S.K. Hua, H.J. Li,
J.L. Li, P.J. Li, Q.Z. Li, Z.L. Pan, D.Z. Shao, G.S. Shen, R.W. Shi,
W.T. Su, X.X. Wang, Y.Y. Xia, L. Xu, Z.L. Xue, D.S. Yan, Z.W. Yin,
X.L. Yuan, Y.F. Zhang, G.M. Zhao, Y.L. Zhao, W.Z. Zheng
B.M. Zhou
Shanghai Institute of Ceramics, *Shanghai, China*

G. Chen, Z.Z. Dai, X.Y. Deng, Y.L. Fang, J. Hu, Y.C. Gao, T.Z. Li,
G.T. Liu, Z.Q. Liu, S.Q. Mao, S.X. Ren, Z.L. Su, Y.T. Wang, Ou Wen,
H. Xiao, H.Z. Yang, F.C. Zhang, F.Y. Zhang, J.Q. Zhang, Q. Zhang,
Y.N. Zhang,
Beijing Glass Research Institute, *Beijing, China*

H.S. Chen, S.Q. Gao, J.T. He, B.N. Jin, P. Kong, Q. Liu, Y.Y. Shao,
H.S. Sun, X.W. Tang, G.Y. Zhu, Y.C. Zhu
Institute of High Energy Physics, *Beijing, China*

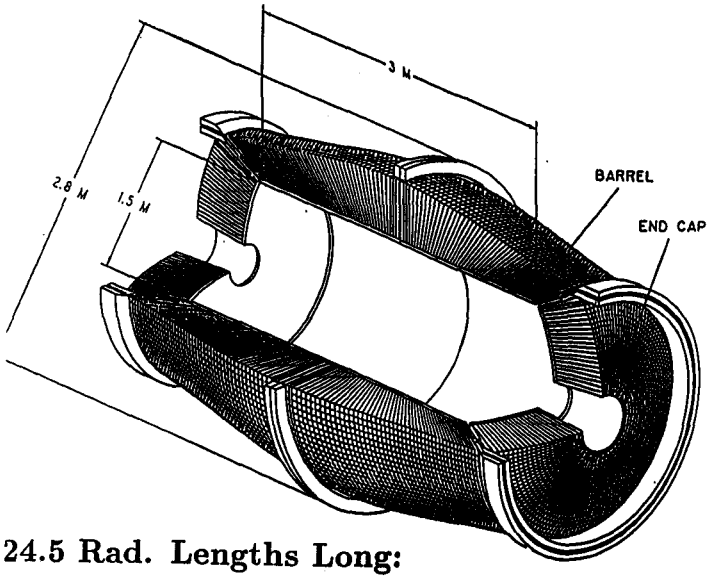
T. Asin, S. Banerjee, S. Ganguli, S. Gupta, A. Gurtu,
P. K. Malhotra, R. Raghavan, K. Sudhakar, S. Tonwar
Tata Institute of Fundamental Research, *Bombay, India*

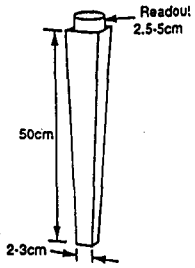
Z.F. Gong, Z.M. Wang, Z.Z. Xu
University of Science and Technology, *Hefei, China*

L.Y. Chen, J. Du, M. Gu, J. Wang, L.M. Wang, X. Wu,
K.H. Xiong, W.H. Zhang
Tongji University, *Shanghai, China*

Contact Person:
Harvey B. Newman
Caltech

BARIUM FLUORIDE
PRECISION EM CALORIMETER





- $\Delta\eta \approx \Delta\varphi \approx 0.04$
- $|\eta| \leq 2.5$
- Gate in One Beam Cross

24.5 Rad. Lengths Long:

- Total 16,060 Crystals,
  - 10.3 m^3, 50.2 Tons

• BaF_2 CRYSTAL PRODUCTION at SIC and BGRI

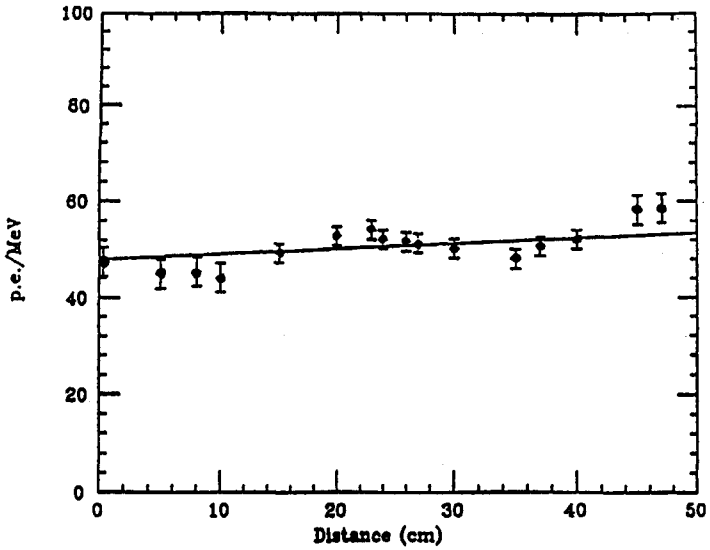
- First 7×7 Pre-Production Prototype Completed (Now at FNAL).
- Medium Scale Production Facility Funded By China:
  - 140 Pieces/Month By 12/91*
- MOU BETWEEN SIC, BGRI and CALTECH, May 29, 1991 at Shanghai:
  - MASS PRODUCED RAD HARD CRYSTAL PRICE FIXED AT $ 2.5/CC
  - 9×9 Full-Size Prototype Price At $ 3.5/cc
  - BGRI Demonstration of 35 cm Crystal Pieces

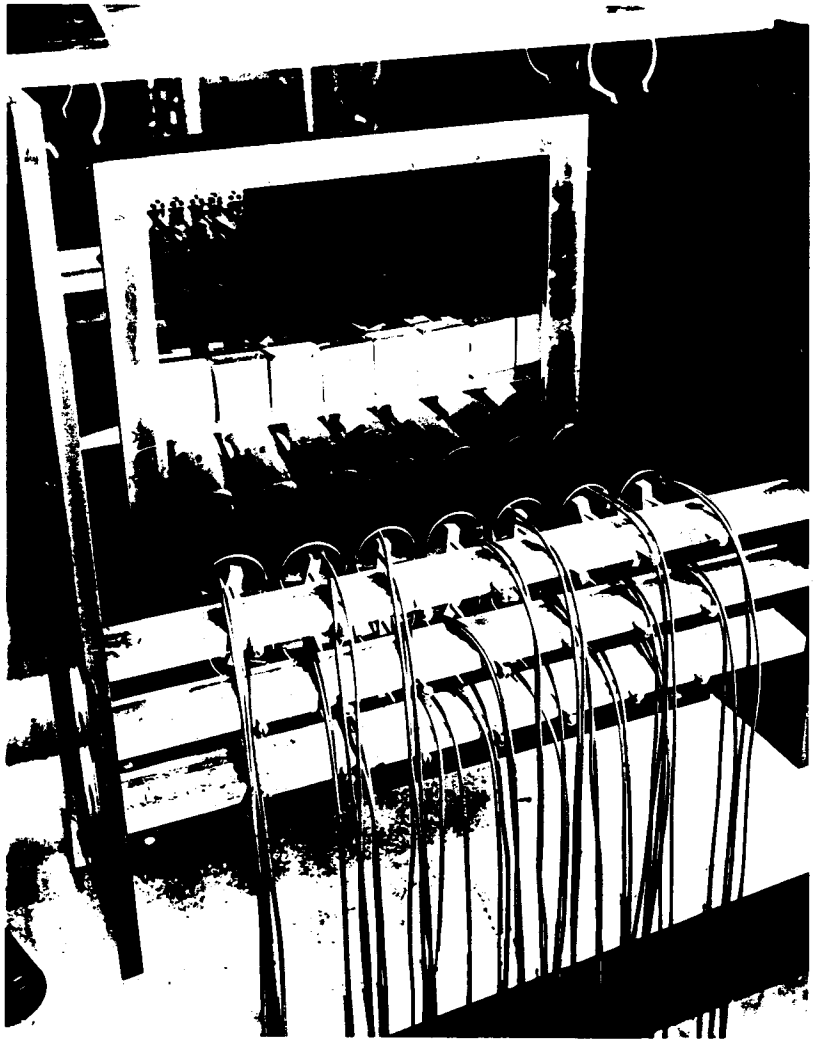
- * 18% of FULL PRODUCTION: 800 CRYSTAL PIECES/MONTH
- 32,120 PIECES REQUIRED



→ COMPLETION of 49 CRYSTAL PAIRS
at Caltech

Photoelectrons/MeV For 50 cm BaF_2 Crystal-Pair Measured With Cs^{137} Source: $\delta = 6.8\%$.

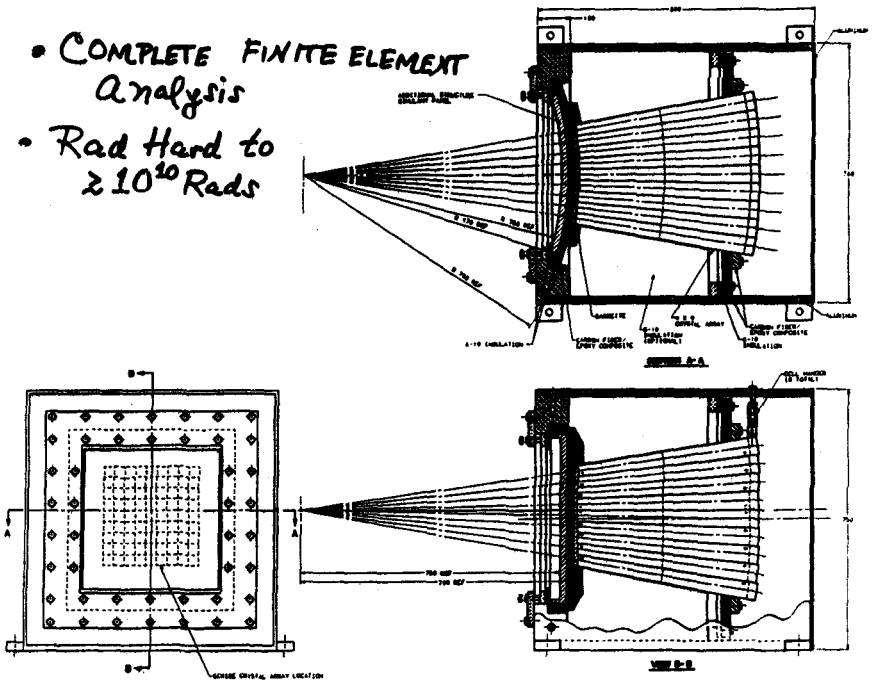




FIRST ROUND TEST:
7×7 ARRAY (9/91 - 12/91)

- **ELECTRON RESOLUTION**
  To Demonstrate $\sigma_E/E = (2.0/\sqrt{E} \oplus 0.5)\%$
  With Electrons from 10 GeV to $\geq$ 100 GeV
  - Calibrate the gain for each crystal + phototube.
  - Scan the beam across the central crystal to establish the (position corrected) uniformity of response.
  - Check the stability of a period of weeks.
  - Compare to GEANT predictions for resolution, energy sharing distributions, and position reconstruction accuracy as a function of the impact point.
- **PION RESPONSE**
  From 10 GeV to $\geq$ 100 GeV
  - Using data taken at the same time as for the electrons above.
- **ELECTRON-PION SEPARATION**
  Note: because of the limited transverse size of the first round crystal array, we will be able to test our electron selection criteria, but we will not have a complete test of e/π separation.
  - Test (Sum of 25)/(Sum of 49)
    Note: This is like (Sum of 9)/(Sum of 25) with the final crystal sizes.
  - E (electromagnetic energy) versus p (Momentum),
    using the drift chamber spectrometer.
  - Possibly: Veto on the energy in the backup calorimeter.
    Note: This may or may not be possible given the thickness of the calorimeter plates. A better HCAL module is needed.
- **MIPs CALIBRATION TEST**
  - Calibrate the crystals using minimum ionizing particles (MIPs) going along the long axis of a crystal. The mean energy for a MIP is expected to be 330 MeV.

- **ELECTRONICS DEVELOPMENT**
  - Test the resolution without a large electronic-noise contribution (with Rb-Te PMT's).
  - Isolate the contribution of noise using vacuum phototriodes and a first-round preamp and shaper matched to standard FASTBUS ADC's.
  - Develop mounting, shielding and grounding techniques to reach an acceptable noise level.
  - Possibly: Test a second-round of preamps and shapers with a shaping time $\sim$ 10 nsec or less, lower noise, and higher rate capability, used together with custom ADC's.
  - Test a Switched Capacitor Array readout module.



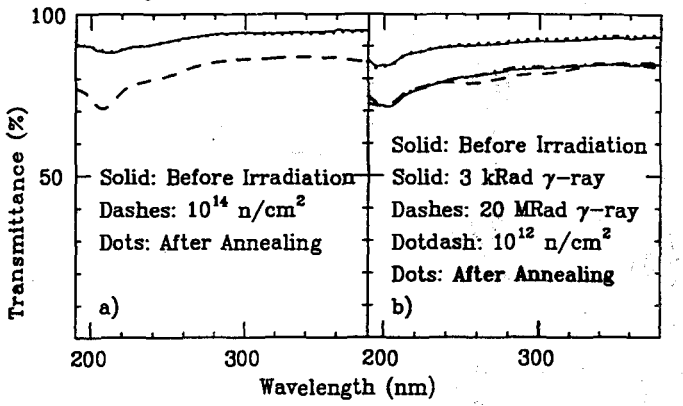
BoF2 EMC PROTOTYPE - 9 X 9 ASSEMBLY

BaF_2 CRYSTAL PRODUCTION and RADIATION RESISTANCE

- Studies of Critical Impurities and Radiation Hardness
  - at SIC, BGRI, IHEP (Beijing)
- Purify Raw Materials:
  - Eliminate Selected Metals (Ce, Pb, Co) To < 1 ppm
  - Specifically Eliminate O_2, OH^- During Pre-Treatment and Growth
- **EXPERT REVIEW PANEL**

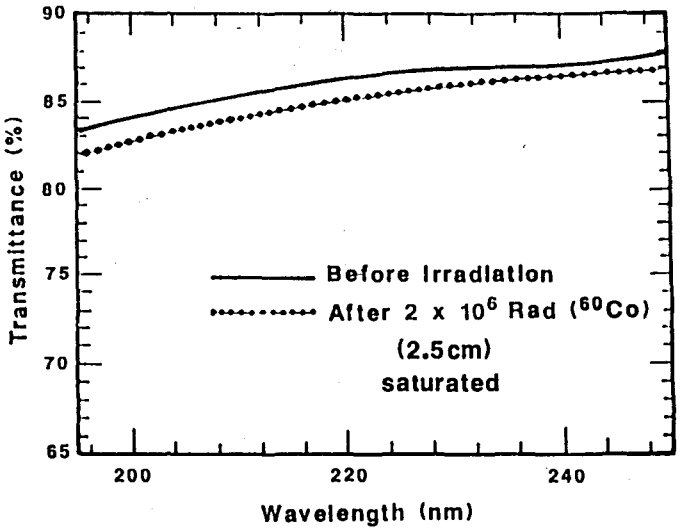
BaF_2 Transmission Before and After Irradiation:

- (a) Recovery from Neutron Damage
- (b) Typical Saturation Effect :
  - Same for γ, NEUTRONS
  - NO ANNEALING at ROOM TEMPERATURE



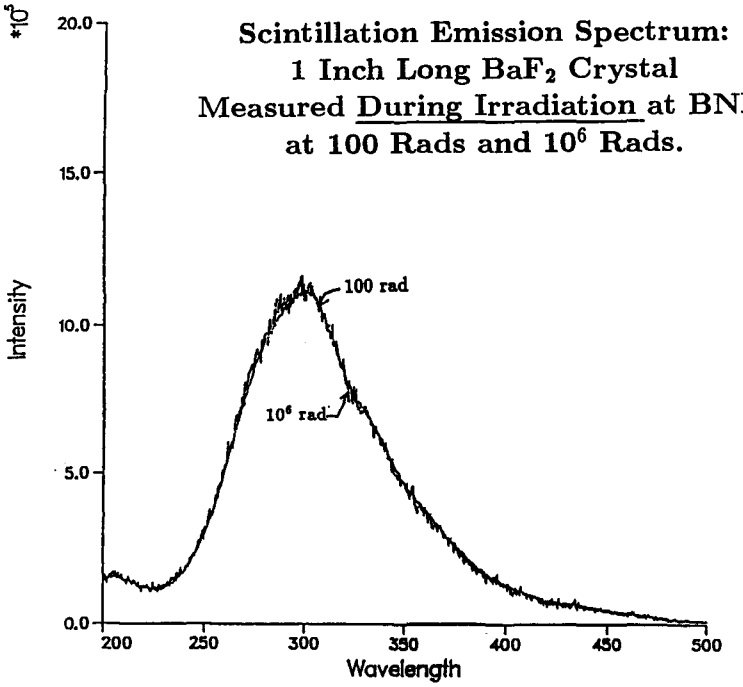
- UC IRVINE REACTOR : NEUTRONS , JPL : Co^{60} γ RAYS

R&D RESULTS
BaF_2 Radiation Resistance



At 200nm effect equals to 1%

This implies a 20% effect for 50cm (acceptable)



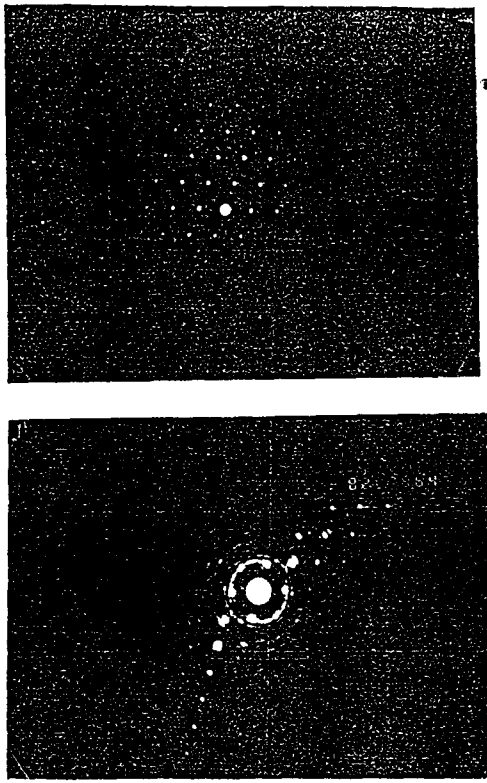


Fig.12 Electron diffraction patterns of BaF_2 crystal

(a) Just start bombardment of electron beam on crystals
(b) After certain time of bombardment of electron beam, pattern shows appearance of BaO rings

PRESENT UNDERSTANDING OF RADIATION DAMAGE MECHANISMS IN BaF_2

Important role for cationic impurities, eg. Pb, Ce
Oxygen absorption contributes

Therefore:
Use higher purity crystals
Control pretreatment to remove oxygen

GEM is establishing an EXPERT PANEL
- Assess prospects for solution
- Advise further R+D effort

The Engineering and Testing of a Fiber Calorimeter Prototype For the Second Detector

The SSCintCal Collaboration

R. Carey, T. Coan, S.T. Dye, E. Hazen, D. Higby, S. Klein,
J.P. Miller, B.L. Roberts, J. Stone, L. Sulak, W. Worstell
Boston University, Boston, MA 02215

C. Lane
Drexel University, Philadelphia, PA 19104

D.R. Winn
Fairfield University, Fairfield, CT 06430

R. McNeil
Louisiana State University, Baton Rouge, LA 70803

C. Bromberg, J. Huston, R. Miller
Michigan University, East Lansing, MI 48824

T. Kamon, R. Webb
Texas A&M University, College Station, TX 77843

D. Acosta, J. Branson, B. Ong, H. Paar, M. Sivertz, D.Thomas
University of California–San Diego, La Jolla, CA 92093

with Government and National Laboratory Affiliates

F. Ayer, C. Elder, D. Sullivan
C.S. Draper Laboratory, Cambridge, MA 02138

A. Para
Fermi National Accelerator Laboratory, Batavia, IL 60510

R. Bionta
Lawrence Livermore Laboratory, Livermore, CA 94551

September 15, 1991

PROGRESS IN SCINTILLATING FIBER CALORIMETRY

1. **CERN beam tests to 150 GeV demonstrate improved EM resolution consistent with EGS and decreased constant term (0.4%) with smaller diameter fibers (0.5mm) and projective geometry (see Figure).**

   EGS scaling of JETSET results from compensating fraction (20%) to high sampling fraction (50%) implies $4\%/\sqrt{E}$.

   Test modules under construction. (SPACAL/US)

2. **New fabrication technique (low temperature casting) fully developed for projective hadronic calorimeter towers.**

   Four 1-tonne towers (0.1 eta x 0.1 phi) being cast for FNAL beam tests in November 1991. (SSCintCal)

   GEM EoI Hadron Calorimeter Baseline Option.

3. **High-sampling EM calorimeter operating in JETSET experiment at CERN demonstrates $6\%/\sqrt{E}$ in calibration runs for 300 modules (3% of GEM baseline).**

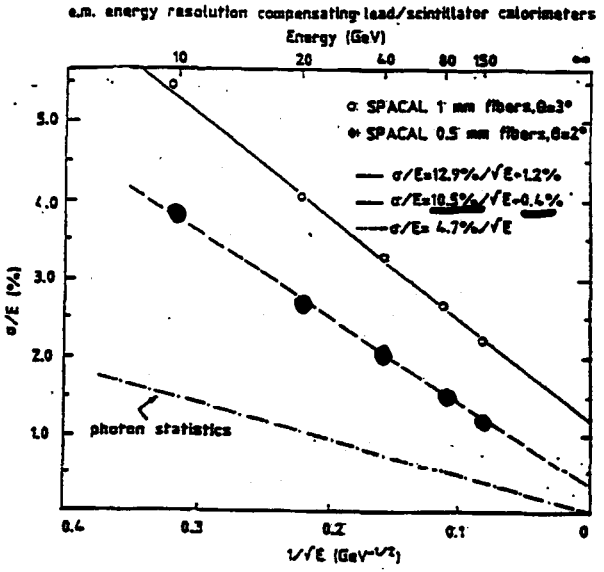
   Operational for one year.

   9 modules 24 X_0 long now in test beam at FNAL to measure constant term.

   GEM EoI Electromagnetic Baseline Option.

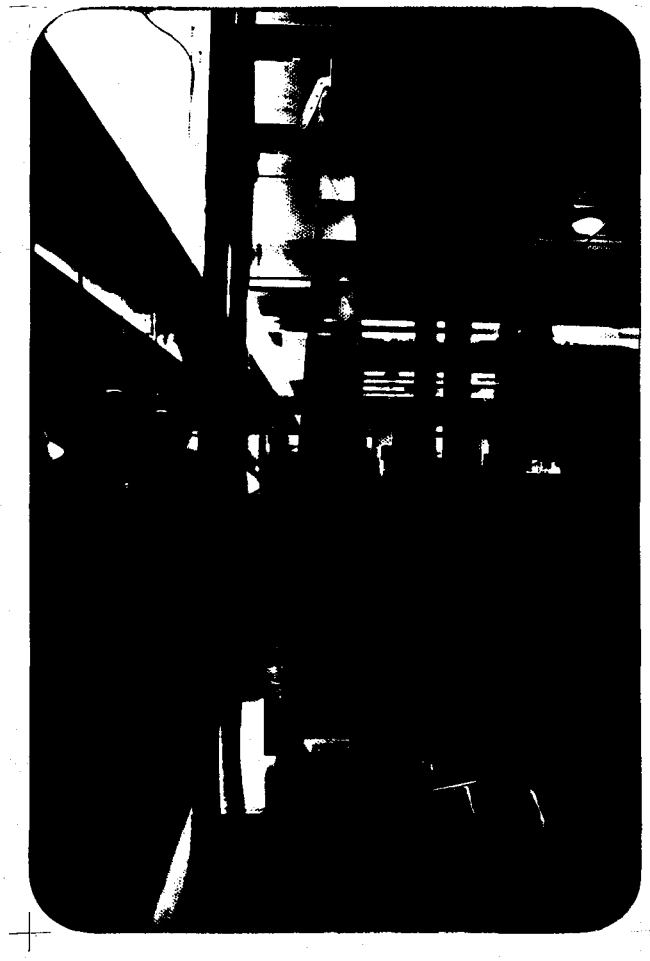
4. **Progress in development of radiation-hard scintillating fibers and assessment of radiation damage consequences for detector performance.**

   Safe for 3 years at 10^{34} at eta=2.5



0.5mm fibers - 20%

UCSD group now building module
with 0.5mm - 50% (expect 4-5%/√E)



SSCintCal 1: Scintillating fiber preform fully strung and ready to be cast with eutectic lead. This is the baseline prototype for the GEM hadronic calorimeter (fiber option).

PAAR et al

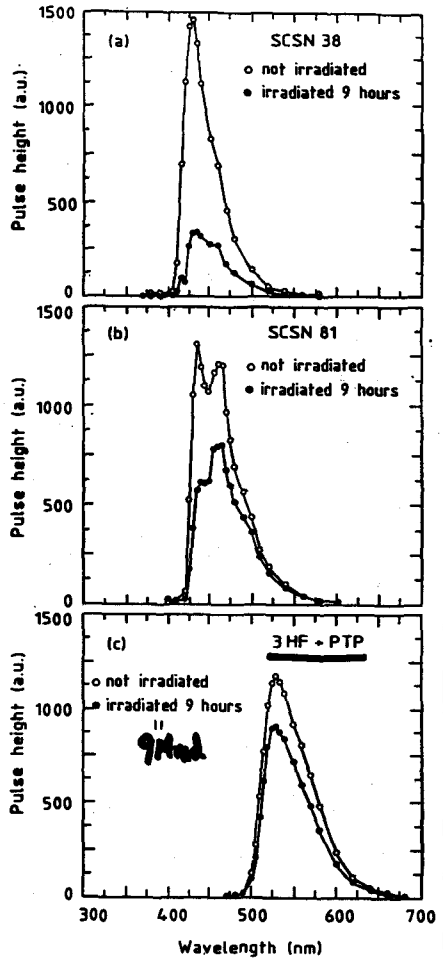


Fig. 4

Co^{60}

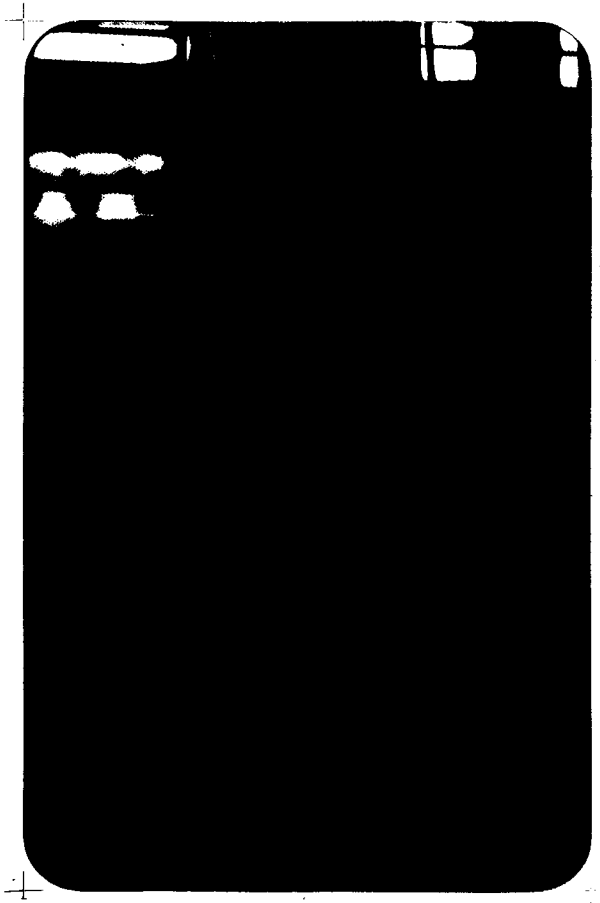
Also:
n to 1.2×10^{13} n/cm²
10% light loss
↓
0.5% constant term w/o annealing

SSC Int Cal Dichroic Towers

2 laminated, chromatically separated EM/Hadron signals being tested at FNAL

28 cm EM green
180 cm hadronic blue

fiber welding machine developed (10 sec/joint)



SSCintCal 2: Close up of scintillating fiber projective tower with its internal stainless steel support structure (the ladder and cross struts) and the spacers that maintain the tolerance of the scintillating fibers. This preform was strung by hand; the design of a simple pick-and-place machine and automatic fiber inserter have been made by Draper Lab and Bicron, resp.



SSCintCal 3: View of the precision mold (on the right) for the GEM hadronic calorimeter

HADRONIC SPACAL MODULES

2 2m laminated, projective towers constructed in U.S. and tested w/ SPACAL this summer

ANALYSIS IN PROGRESS

SSC Liquid Argon Collaboration

R. Steiner
Adelphi University

G.Forden, J. Rutherfoord, M. Shupe, T. Bowen, A.Nelson
The University of Arizona

H.A.Gordon, E. Kistenev, P. Kroon, H. Ma, D. Makowiecki,
V. Radeka, D. Rahm, S. Rescia, H. Themann(SUNY-Stony Brook
Brookhaven National Laboratory

J. Womersley.
Florida State University

S. DeBoer, J. Hauptman, M. Pang, A. Zinchenko
Iowa State University

S. Inaba, H. Iwasaki, N. Kanematsu, T. Kondo, Y. Sakai, Y. Unno
KEK, National Laboratory for High Energy Physics

K. Kaneyuki, L. Soso, Y. Watanabe
Tokyo Institute of Technology

G.S. Abrams, D.E.Groom, C. Hearty, M. Levi
The Lawrence Berkeley Laboratory

R. Black, C. Chang, H. Deng, J. Goodman, D. Fong, N. Hadley, G. Long
The University of Maryland

T. Adams, N. DiGiacomo, L. Mason
Martin Marietta Astronautics

R. Richards, H. Weerts
Michigan State University

L. Cremaldi, B. Moore, J. Reidy
The University of Mississippi

R.G. Alsmiller, P. Fu, T.A. Gabriel
Oak Ridge National Laboratory

F. Lobkowicz, J. Ftacnik, I. Horvath, G. Diloretto
The University of Rochester

J.Siegrist, M. Turcotte, L. Villasenor, J. Yarba
The SSC Laboratory

T. Handler
The University of Tennessee

T. Burnett, V. Cook, J. Eisenberg, D. Forbush, P. Mockett, R.W. Williams
The University of Washington

GORDON

Liquid Argon Calorimetry

- Mature Technology
  Much Experience with large Systems
- Unit Gain - Linear Response
- Relatively Easy to Calibrate - Good Energy Resolution
- Radiation Hard
- Easy to Segment

However ...

Drift Velocity ~ 5mm/μsec

⇒ 400 ns to drift 2mm = reasonable gap

* Can Collect 44% of charge in 100ns

Signal to Noise worse, OK if total charge large

Use "leading edge" to determine when incident particle arrived.

$\tau_{RT} \ll \tau_{integration}$

GORDON

- Build LA Calorimeter with Fast Time Shaping
  50ns, 100ns, ~125ns, 200ns
- Measure Resolution, σ/E, pile up

Electronics based on HELIOS design

12 mm thick lead plates
not Uranium, compensation

LAC 1m × 1m × 7.5λ
3 modules each 1m × 1m × 2.5λ

unit cell: 12 mm lead, 2 mm argon, readout board, 2 mm argon

Readout board: 3 Layers; 2 HV outer, signal inner

Readout Strips on Signal board: 2.5 cm × 1 meter
X and Y strips interleaved

Readout Channel: 16 strips ganged in depth

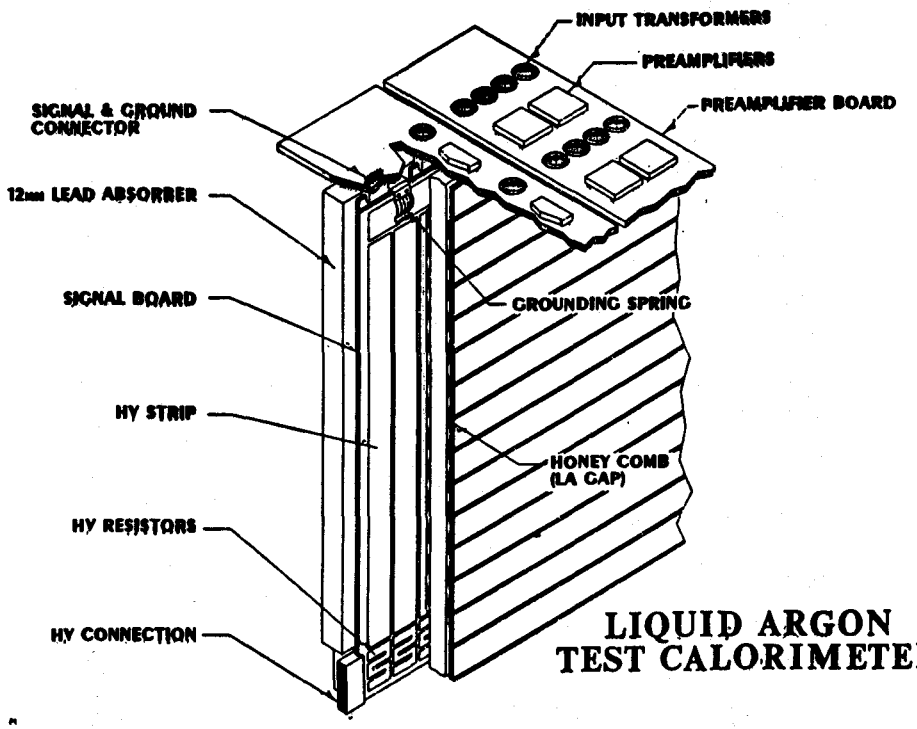
Total Channels = $40 \times 2 \times 3$

$\frac{100}{2.5}$ X+Y 3 modules

LIQUID ARGON CALORIMETRY

CHARACTERISTIC	HELIOS	LAC
ABSORBER	3.4mm ^{238}U	12mm Pb
ABSORBTION LENGTH	4.5λ	7.5λ
SIZE	120cm x 120cm	100cm x 100cm
LA GAP	2.5mm	2.0mm
READOUT	(48) 2.5cm STRIP	(40)2.5cm STRIP
SAMPLING RATIO	12%	5%
NUMBER OF CELLS	10	16
TRANSFORMER RATIO	1:1	12.5:1
FEEDBACK CAPACITOR	5Pf	5Pf
SHAPING TIME	135 Nsec	50,100,190Nsec
mv/GEV	1.8mv/GEV	1mv/GEV
CHARGE TRANSFER TIME	~35Nsec	~25Nsec

GORDON

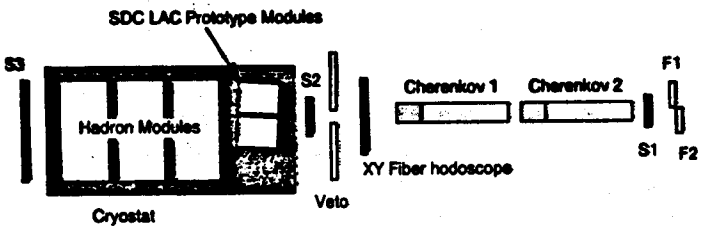


LIQUID ARGON TEST CALORIMETER

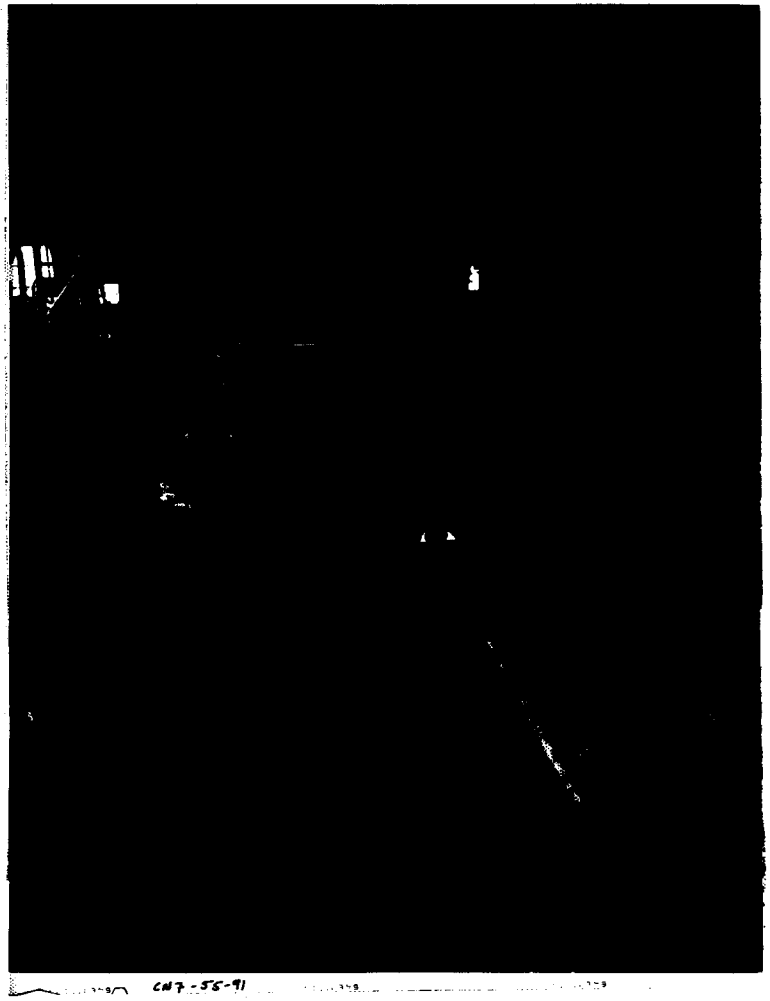
GORDON

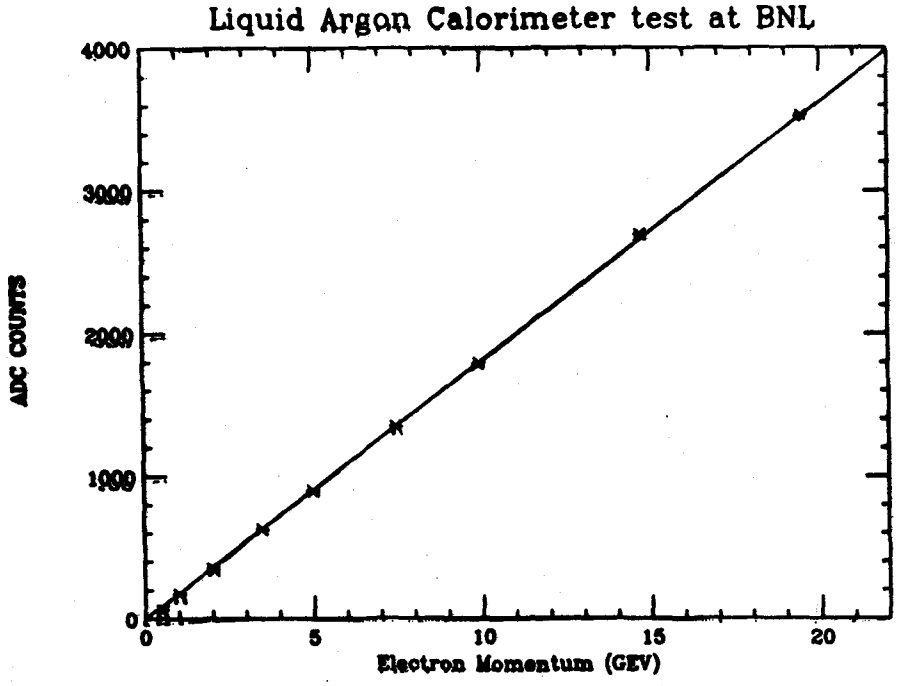
Test Beam

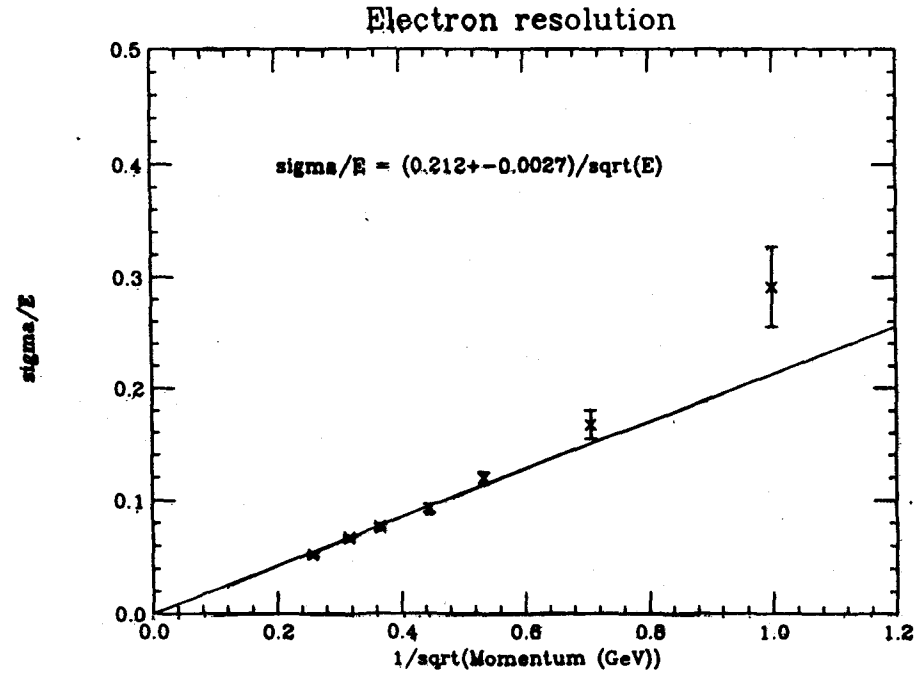
- Secondary Beam 24 GeV Protons on 1λ target
- π^-, e^- from 500 MeV/c to 20 GeV/c
- maximum intensity 2×10^6 particles per 1 second spill
- Č Particle ID, TOF,
- 1 mm Fiber Hodoscope for particle position



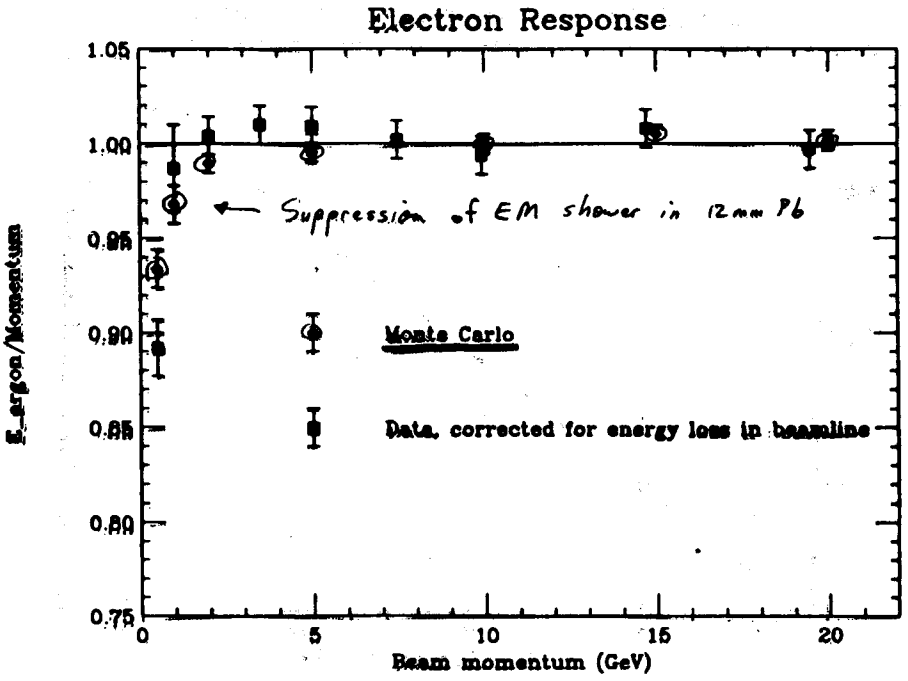
Schematic view of the BNL Spring '91 test



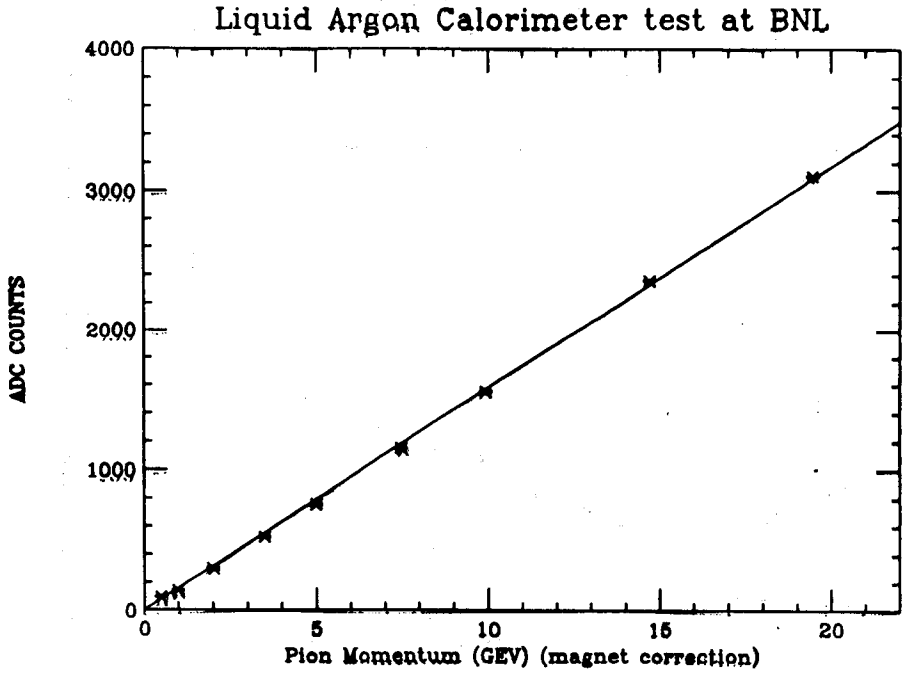

Liquid Argon Calorimeter test at BNL
ADC COUNTS
Electron Momentum (GEV)
0
1000
2000
3000
4000
0
5
10
15
20


Electron resolution
sigma/E = (0.212+-0.0027)/sqrt(E)
sigma/E
1/sqrt(Momentum (GeV))
0.0
0.1
0.2
0.3
0.4
0.5
0.0
0.2
0.4
0.6
0.8
1.0
1.2

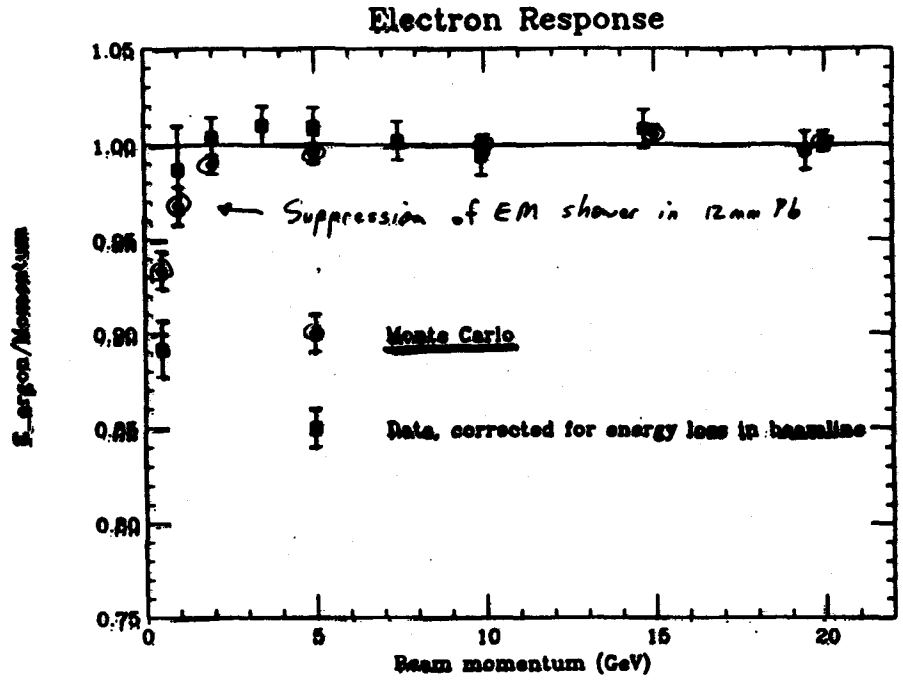
GORDON



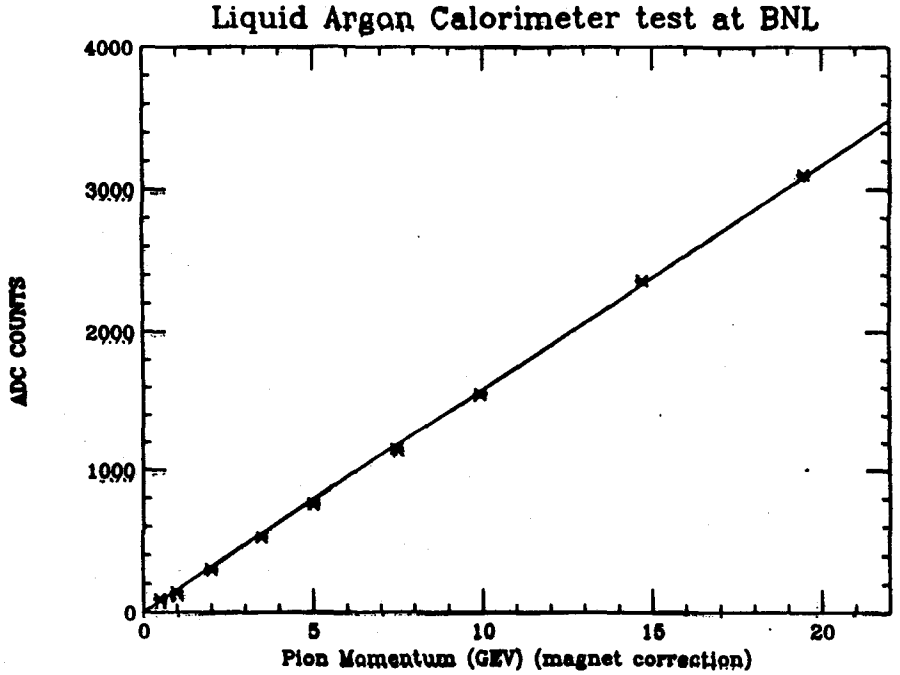
GORDON



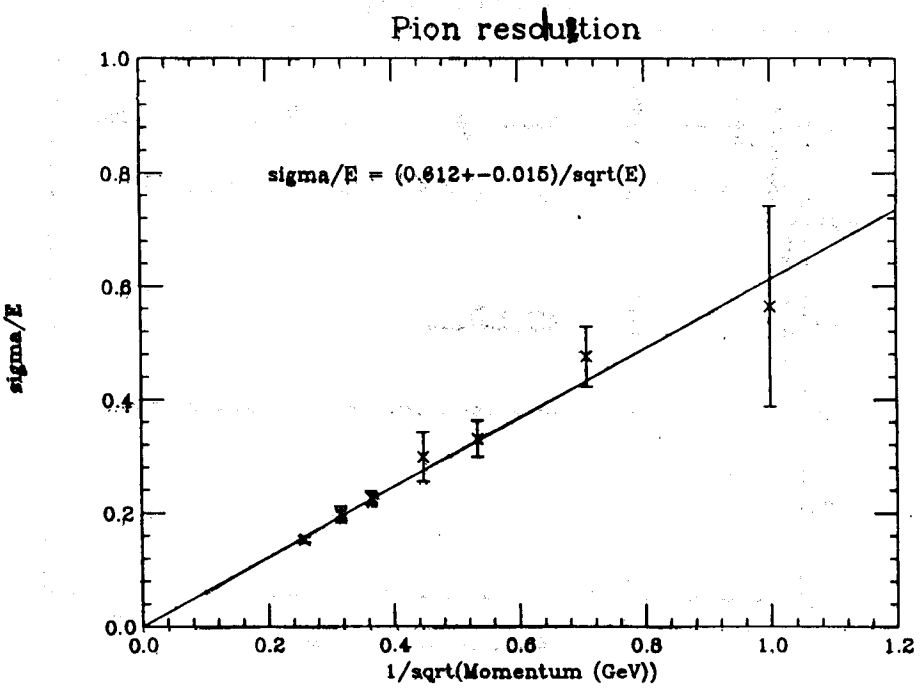
GORDON

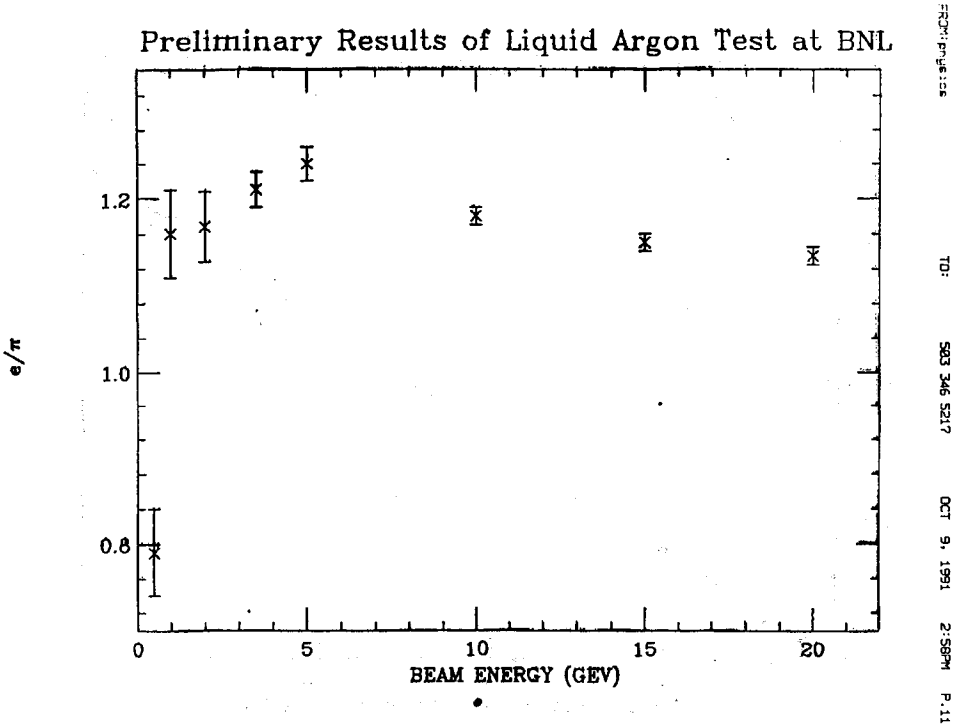


GORDON



GORDON





FROM:Physics TO: 583 346 5217 OCT 9, 1991 2:58PM P.11

Preliminary Results

- Response Linear for All Shaping Times - See $\frac{e}{\pi}$
- $\frac{e}{\pi}$ vs Momentum - Same within errors for all shaping times

$\frac{e}{\pi} = 1.17$ at 20 GeV

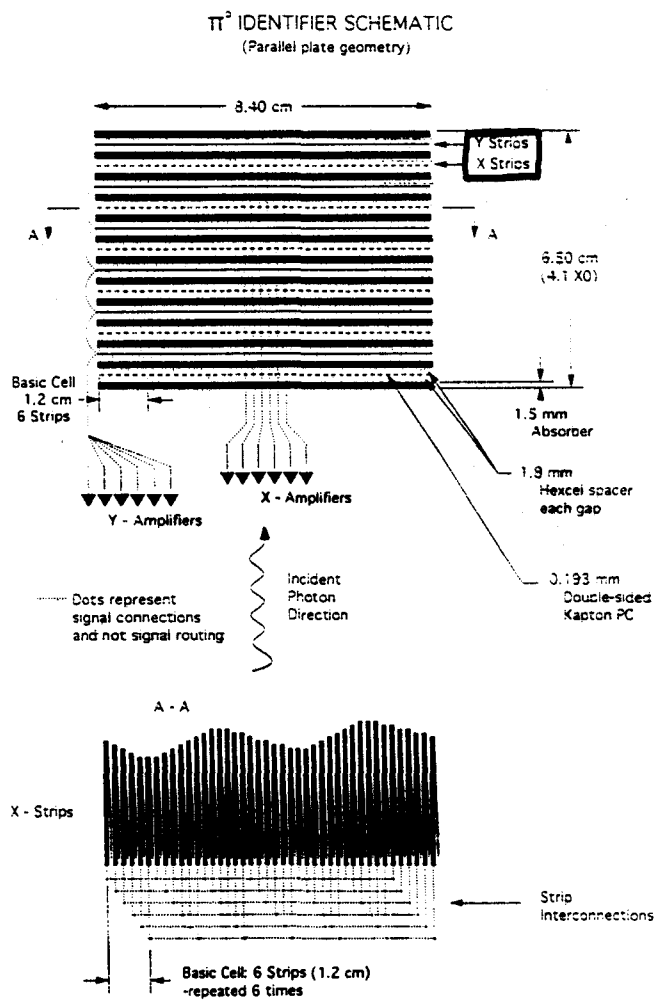
- Resolution

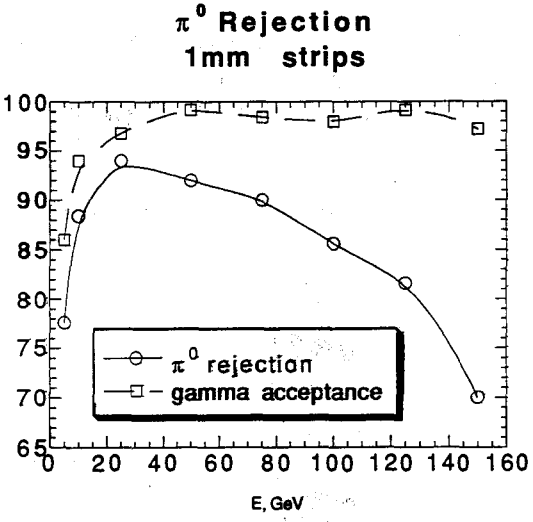
Sampling term e $\frac{21 \pm 3 (\text{[redacted]})\%}{\sqrt{E(\text{GeV})}}$

π $\frac{61 \pm 1.5 (\text{[redacted]})\%}{\sqrt{E(\text{GeV})}}$

Agrees with EGS and CALOR89

- Noise ~ 100 MeV for each of 240 channels for the digital output shaping time ~125 ns
  ⇔ inversely proportional to shaping time
- Timing Resolution - 4 ns for 20 GeV Pion





Scintillating LXe/LKr EM Calorimeter

M. Chen, S. S. Gau, D. Pelly, S. Shei, S. Shotkin,
L. Cai K. Sumorok, X.J. Yan, X. Zhang
Laboratory for Nuclear Science, MIT, Cambridge, MA, USA

D. Akyuz, E. Chen, M.P.J. Gaudreau, M. Li, D.B. Montgomery, J.D. Sullivan
Plasma Fusion Center, MIT, Cambridge, MA USA

E. Aprile, R. Mukherjee, M. Moulsen
Dept. of Physics, Columbia University, New York, NY, USA

V. Cook, P. Mockett
Dept. of Physics, University of Washington, Seattle, WA, USA

A. Bolozdynya, V. Tchernyshev, P. Goritchev, V. Khovansky, A. Koutchenkov
A. Kovalenko, V. Lebedenko, V. Vinogradov, L. Gusev
ITEP, Moscow, USSR

R.N. Krasnokutsky, R.S. Shuvalov, N.N. Fedyakin, V.V. Sushkov
IHEP, Serpuchov, USSR

T. Doke, J. Kikuchi, A. Hitachi, T. Kashiwagi,
H. Ichinose
Science and Eng. Res. Lab., Waseda University, Tokyo 162, Japan

K. Masuda , E. Shibamura
Saitama College of Health, Saitama 338, Japan

M. Suzuki, T. Takahashi
Riken, Saitama 351, Japan

H.L. Ding
Institute of Atomic Energy, Beijing, China

Liquid Xenon/krypton EM Calorimeters

Status of LKr/LXe R&D projects:

- **Construct and test**
  1x1 and 7x7 homogeneous LXe/Kr detectors (Fig. 1)
  to achieve high energy resolution
  with α calibration in situ;
- **Design a pointing ionization sampling calorimeter,**
  (LKr-Accordion, Fig. 2a),
  with an additional homogeneous pre-radiator
  (SandI, Fig. 2b)
  to improve
  - **energy resolution,**
  - photon vertex determination
  - and γ versus π^o separation
- **Liquid xenon SPACAL (Fig. 3):**
  LXe scintillation light
  has total internal reflection against MgF_2
  —> replace fibres in a SPACAL with LXe capillaries
  A LXe SPACAL has better resolution,
  since LXe
  - **radiation hard,**
  - **short radiation length,**
  - **lower critical energy,**
  - **better "fibre" to "fibre" uniformity.**

CMS

Liquid Xenon/krypton EM Calorimeters

Liquid xenon (or krypton) is:

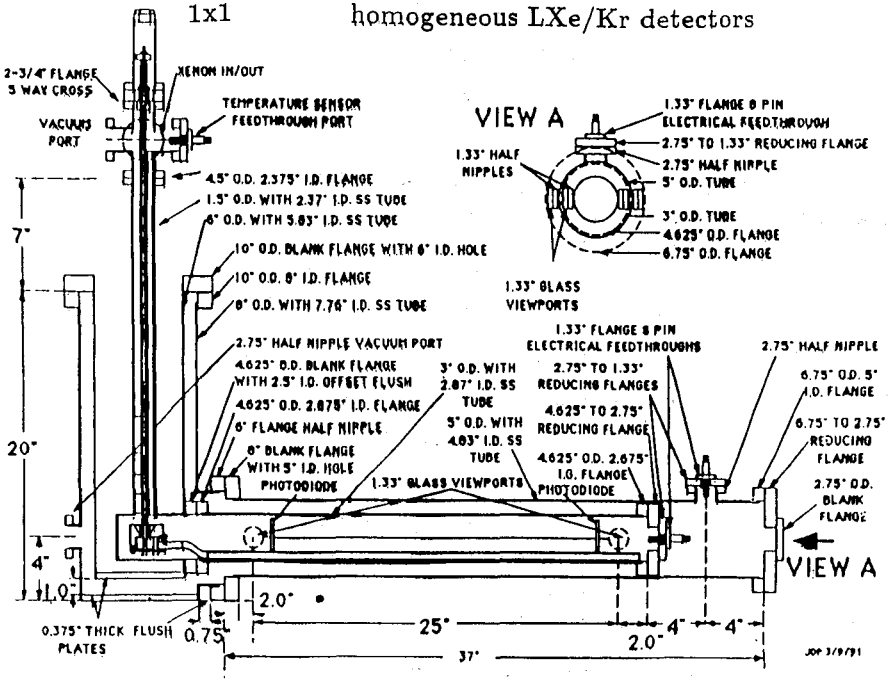
- **Fast: 2 ns for α and 20 ns for γ,**
- **Intense light as well as ionization:**
  4-7 10^7 γ/GeV,
- **Radiation hard,**
- **Homogeneous and good optical contact,**
- **Low critical energy.**

Major difficulty: uniformity for long cells
Most liquids have no total internal reflections.

CHEN

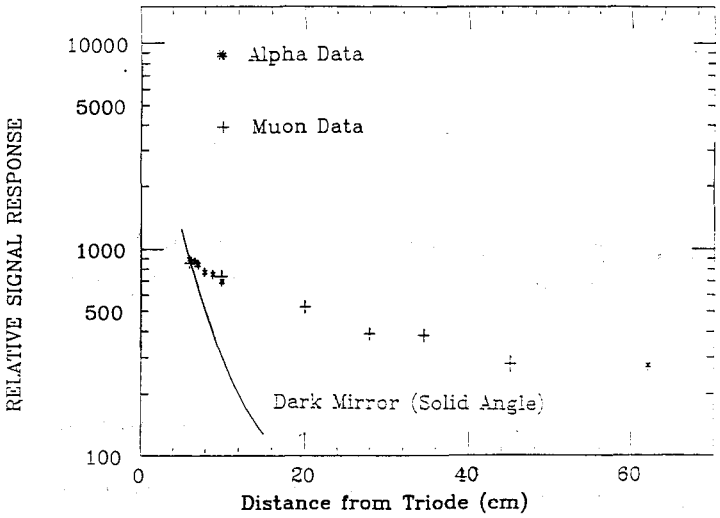
MIT CHAMBER II

1x1 homogeneous LXe/Kr detectors



Observation of
total internal reflections of xenon scintillation light
against black walls coated with MgF_2.

PRELIMINARY TEST RESULTS OF FULL SIZE LXe CELL



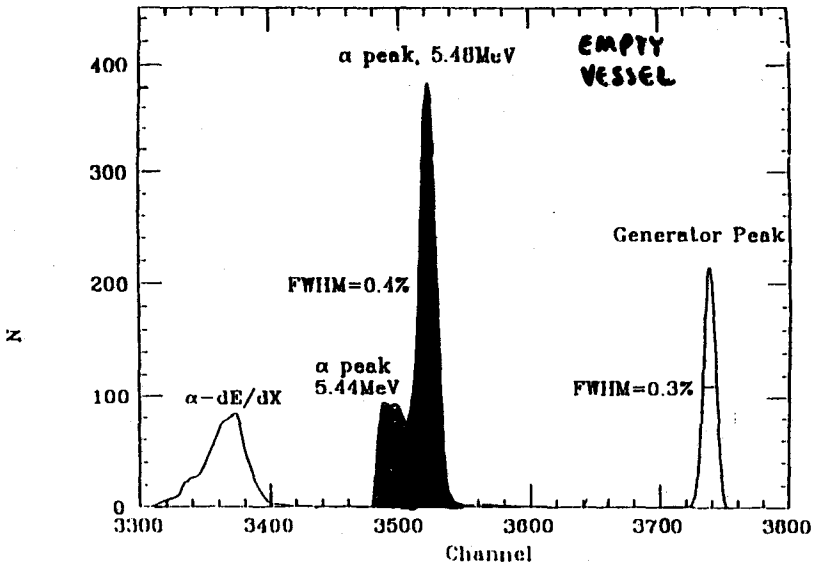
Future improvements:

- Better vacuum: 10^{-5} to 10^{-8} torr,
- Molecular sieve from 1.3 to 0.4 nm for gas,
- Hamamatsu UV-diodes,
- Coated with Al under MgF_2.

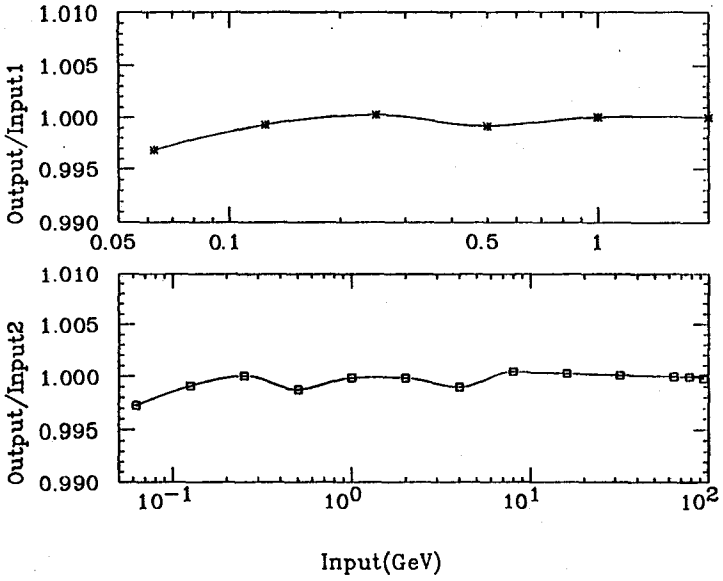
Calibration

$$\delta E/E = (A/\sqrt{E} + B + C)\%$$

- C depends on in situ calibration,
  e.g., LXe gets 0.2% per α.

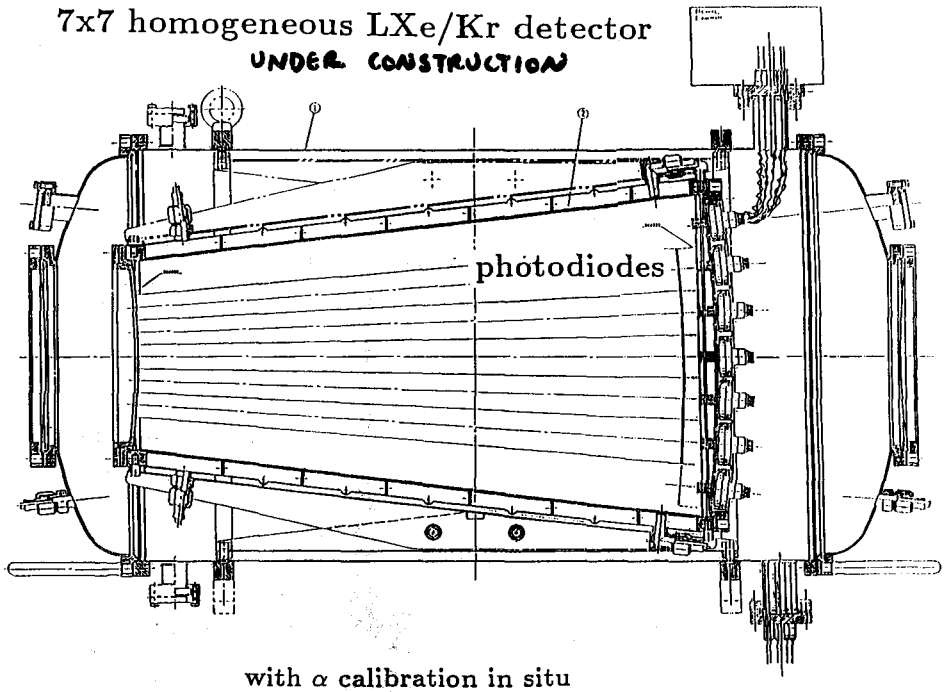


4. Our amplifier/diodes are linear to 10^{-3} from 1 to 100,000 MeV and will be further improved to reach higher energies. So the calibration of α in liquid and vacuum α can be extrapolated to 100 GeV for now.



7x7 homogeneous LXe/Kr detector

UNDER CONSTRUCTION

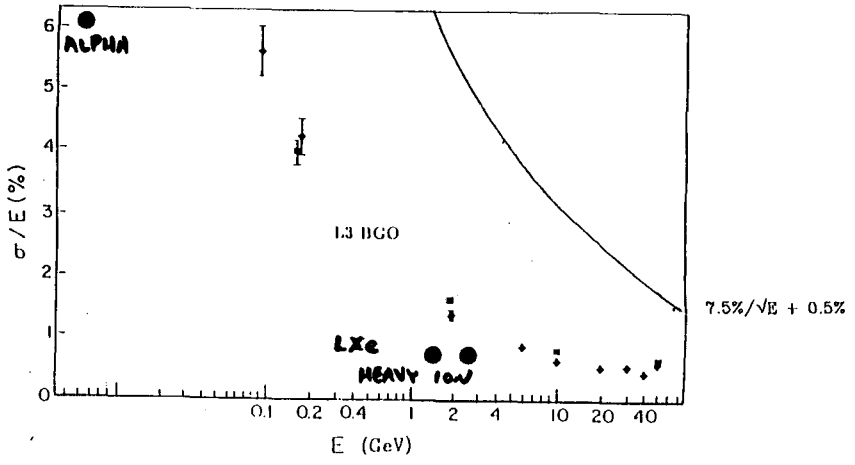


with α calibration in situ

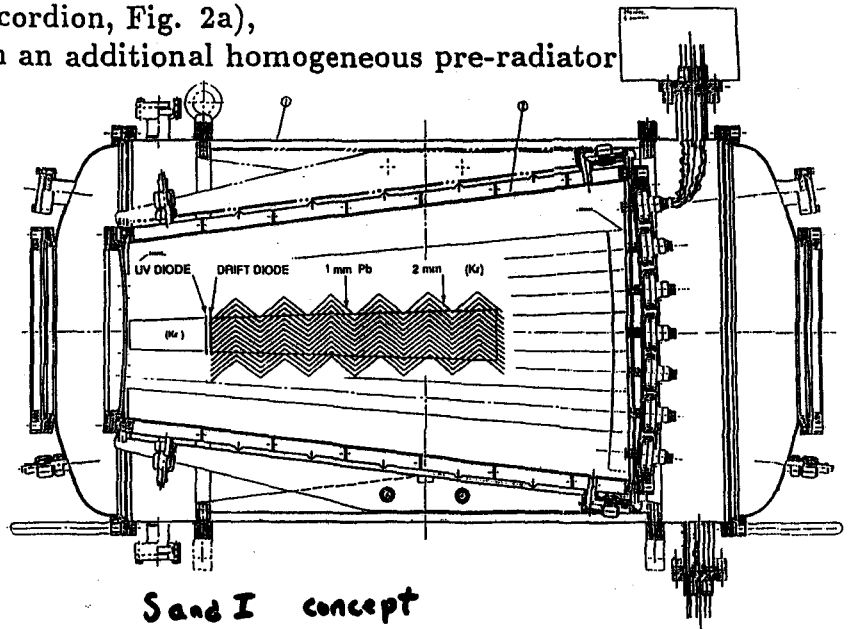
Energy Resolution

$$\delta E/E = (A/\sqrt{E} + B + C)\%$$

- A < 1 for LXe;
  = 1.3 for BGO; and
  = 6–10 for Fibre or LAr.
- B depends on systematics, e.g., BGO achieved 0.5.



a pointing ionization sampling calorimeter,
(Accordion, Fig. 2a),
with an additional homogeneous pre-radiator



S and I concept
- homogeneous Scintillating front end (few X_0)
- accordion Ionization back end

LXe SPACAL (Macaroni)

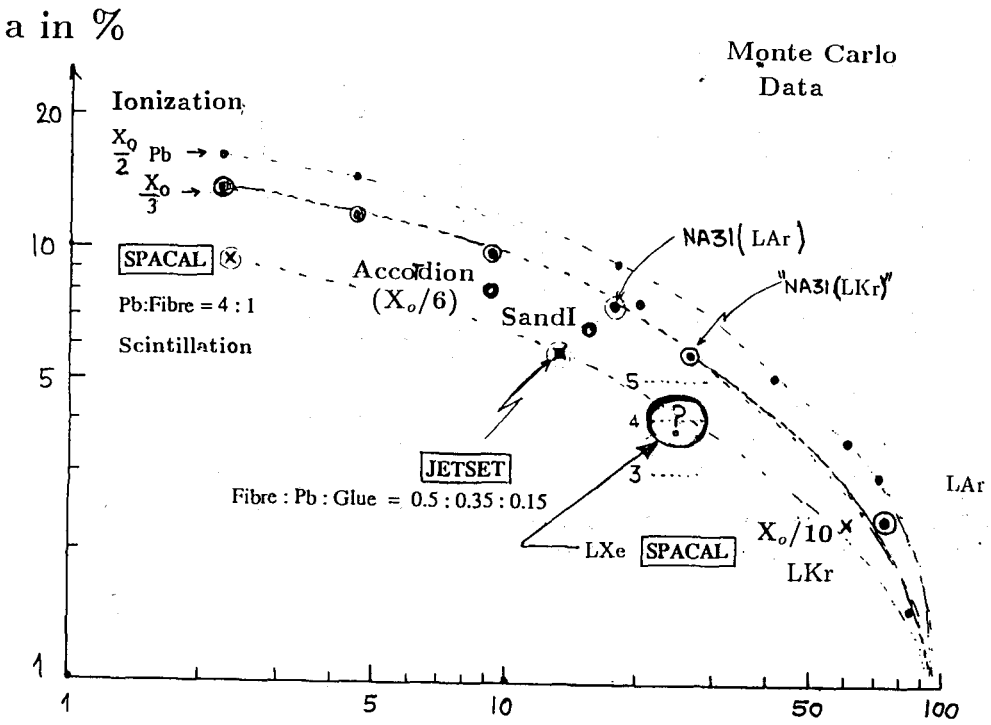
Having observed Total Internal Reflection in LXe against MgF_2, we (also Virdee of CMS, CERN), are developing a calorimeter with Pb:LXe=1:1, using small kapton capillaries coated with MgF_2.

- **Radiation length: 1cm,**
- **25% of energy deposited in LXe,**
- **SSC EM calorimeter: 3 m^3 of LXe (8 M$),**
- **Expected resolution: $4\%/\sqrt{E} + 0.5\%$.**

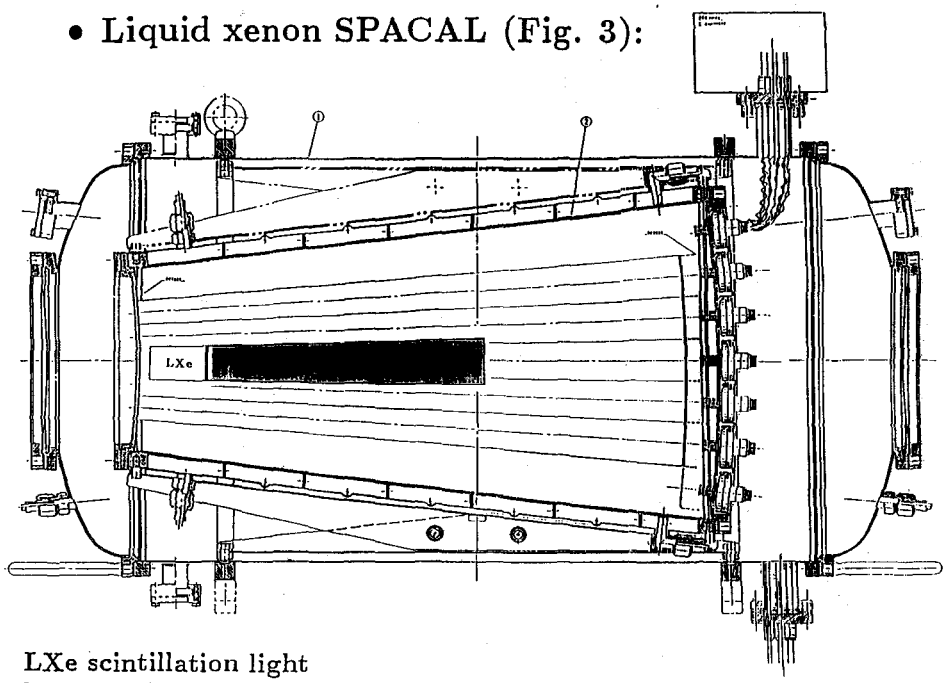
We are measuring at MIT the uniformity in a 26 cm long LXe capillary.

LXe SPACAL (compared with fiber) is:

- **radiation hard,**
- **shorter radiation length: no γ sneak-thru ,**
- **lower critical energy,**
- **better "fibre" to "fibre" uniformity and optical contact.**



- **Liquid xenon SPACAL (Fig. 3):**



LXe scintillation light
has total internal reflection against MgF_2
—> replace fibres in a SPACAL with LXe capillaries

SUMMARY: NOBLE LIQUID PROTOTYPE DETECTOR R&D STATUS

- Fast UV-diodes and matching amplifiers have been tested in LXe/LKr with beams, and being mass produced.
- The effective quantum efficiency of the diodes > 50%; the peaking time of the diode/amplifier < 10 ns.
- LXe/LKr have large output (10^7 photoelectrons/GeV); this large photon yield permits easy calibration with 5.5 MeV α's with a precision of $\delta p/p = 0.2\%$ per α particle and is stable to 10^{-3}.
- $\sigma(E)/E < 0.5\%$ at $E > 2.5$ GeV with heavy ions.
- Total internal reflection in LXe against MaF_2 walls has been seen experimentally.
- A conical 7×7 LXe/LKr detector are being put together for cosmic ray tests.
- The purification and storage system is completed.
- Conceptual design of a LKr Accordion with a preradiator has been developed.
- Uniformity of a liquid xenon capillary for a LXe-SPACAL calorimeter is being measured.

SILICON ELECTROMAGNETIC CALORIMETER COLLABORATION

H. W. Kraner, Zheng Li, V. Radeka
Brookhaven National Laboratory, Upton, LI, NY 11973

Mark Clemen, J. S. Russ
Carnegie Mellon University, Pittsburgh, PA 15213

E. Fretwurst, G. Lindstroem, R. Wunsdorf
Institut für Physik, Universität Hamburg, Hamburg, FRG

John Walter
InnoSpec, Inc., P.O. Box 847, Oak Ridge, TN 37831

A. Arodzero, G. Bashindzhagyan, P. Ermolov, Y. Fleyak, M. Merkin, A. Voronin, S. Zotkin
Moscow State University, Moscow, USSR

G. T. Alley, M. Bauer, C. L. Britton, H. R. Brashear, H. O. Cohn, T. A. Gabriel, F. Plasil, M. Rennich, R. Todd
Oak Ridge National Laboratory, Oak Ridge, TN 37831

J. E. Brau, R. Frey, K. Furuno
University of Oregon, Eugene, OR 97403

S. Berridge, W. M. Bugg*, Y.-C. Du, T. Handler, I. Tweybak
University of Tennessee, Knoxville, TN 37996

*Spokesman

SILICON EM CALORIMETER COLLABORATION

SSC SUBSYSTEM R&D - FY91

LINDSTROM

I. RADIATION DAMAGE STUDIES

- USEABLE UP TO 10^{14} n/cm^2
- PAD DETECTORS NUERT AT ~ 2×10^{12} n/cm^2
- HIGHLY NON-UNIFORM DAMAGE
  (EFFECT OF IMPURITY NON-UNIFORMITIES APPLIFIED — NOT A PROBEM FOR TRADITIONAL PAD DETECTORS)

II. PROTOTYPES NEAR COMPLETION (BEAM TEST IN DECEMBER)

- 28 X_0 EM Calorimeter FAST electronics
- Pre-radiator with pads and 1mm strips

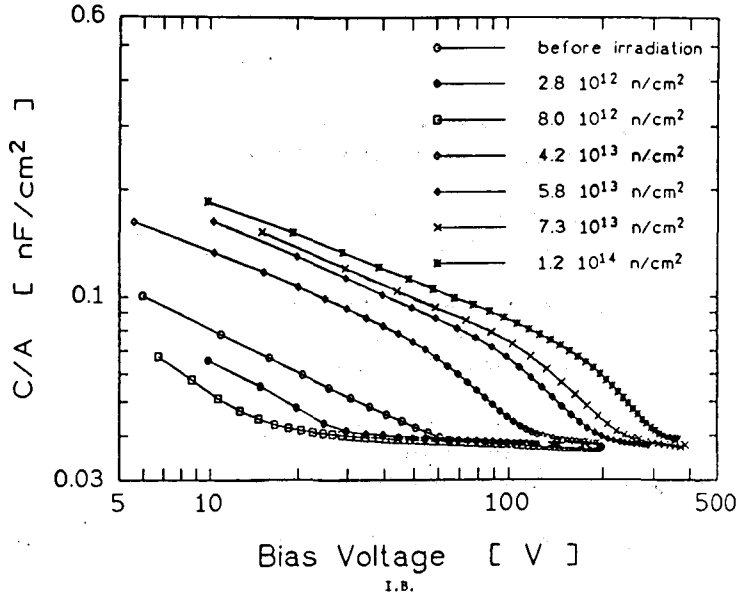


Fig. 4. C/V characteristics measured at 10 kHz immediately after irradiation by various neutron fluences up to $1.2\cdot10^{14}$ n/cm^2.

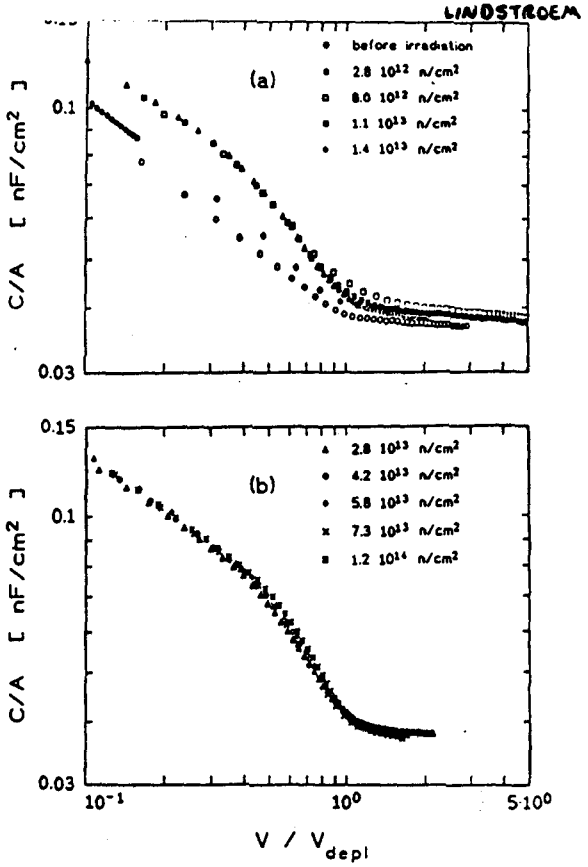


Fig. 5. Same data as in fig. 4 but plotted as function of the bias voltage normalized to total depletion.

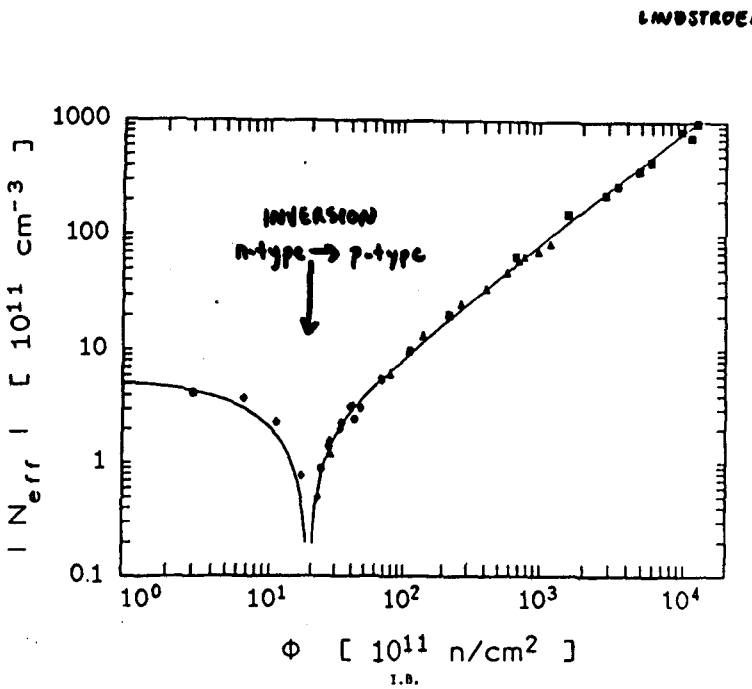


Fig. 7. Absolute value of the effective impurity concentration versus fluence up to 10^{13} n/cm^2. The solid curve represents a fit according to eq. (21.

WALTER

Neutron Damage Induced Changes in the Compensation (Resistivity) of Silicon
$(N_d)_0=2.3\times10^{12}$, $(N_a)_0=1.3\times10^{12}$, $N_0=1\times10^{12}$

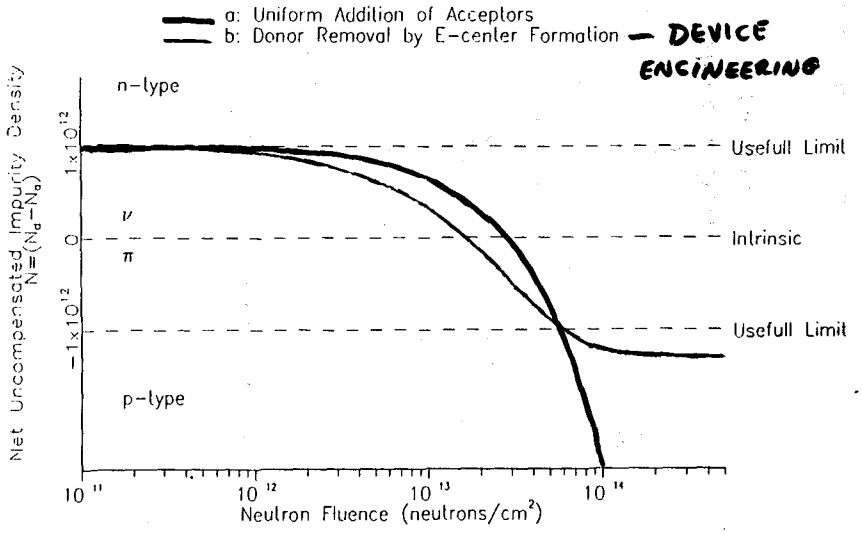


FIGURE 1
I.A.

WALTER

Neutron Damage Induced Changes in the Compensation (Resistivity) of Silicon
$(N_d)_0=2.3\times10^{12}$, $(N_a)_0=1.3\times10^{12}$, $N_0=1\times10^{12}$
Donor Removal by E-center Formation

$\tau = 1.5 \times 10^4$ min.

DEVICE ENGINEERING

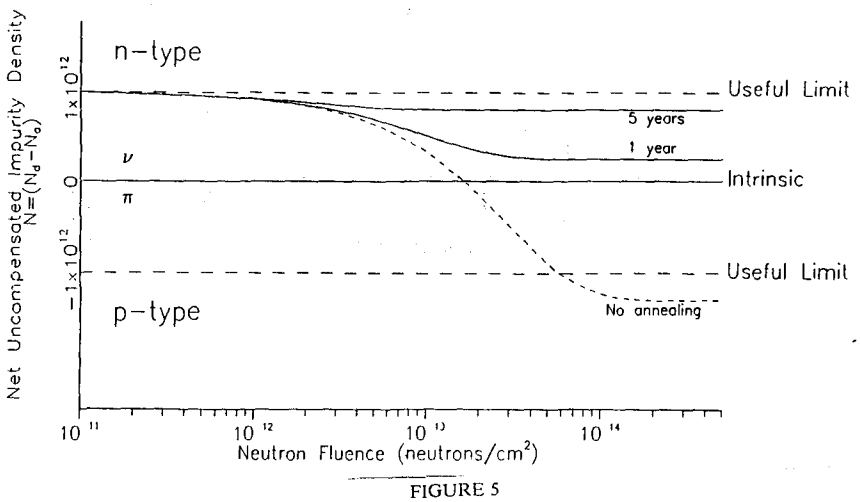
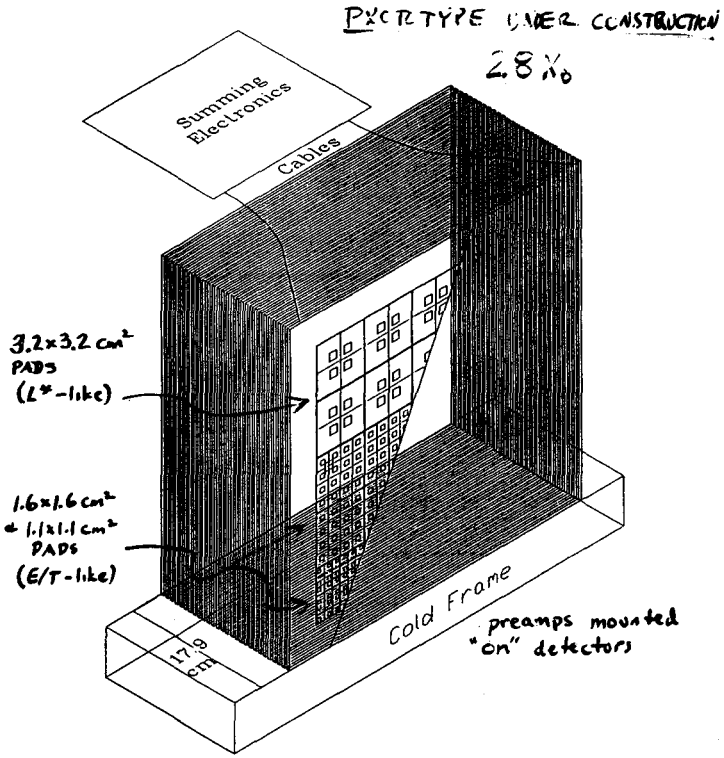


FIGURE 5
I.A.



Oblique Block Cutaway of SECC Calorimeter

SCB 7/01/91

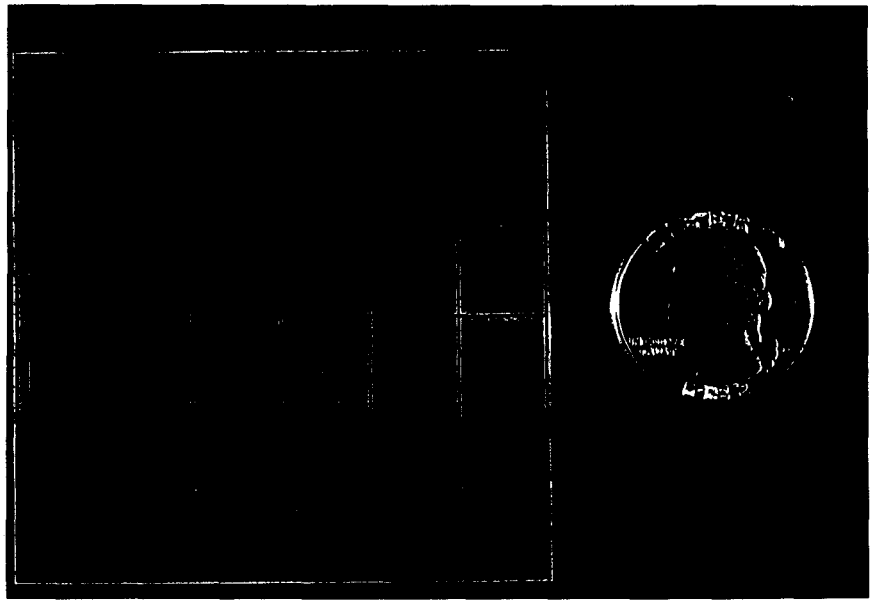


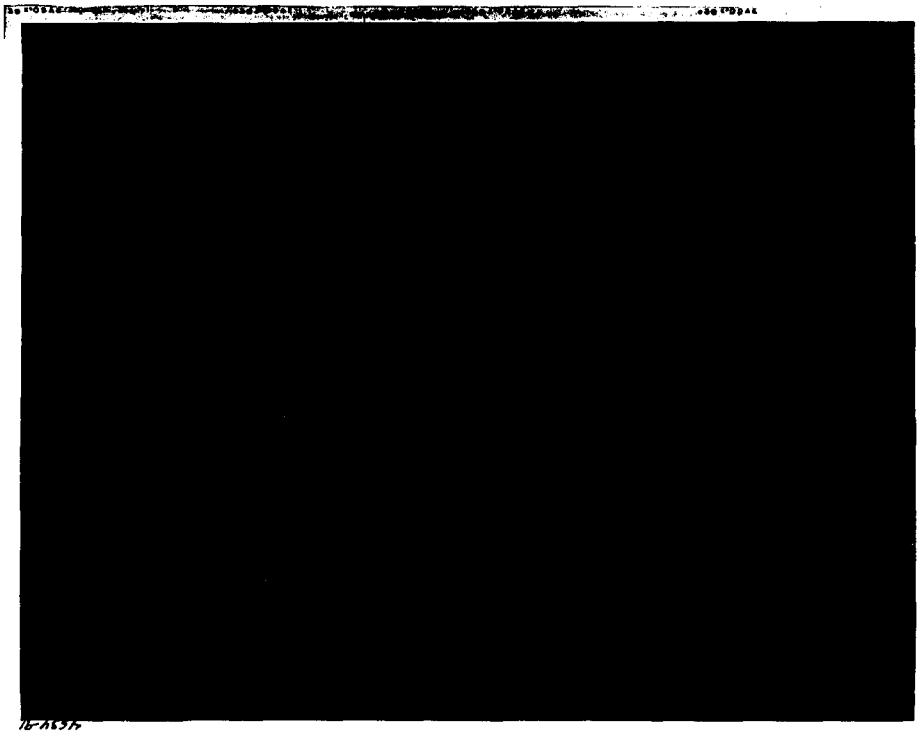
Figure IV.1

Simulation Results for the Charge-Sensitive Bipolar Preamplifiers using Harris' VHF Process.

Preamp Type / Detector Size	Folded Cascode 1x1	Folded Cascode 2x2	Folded Cascode 3x3	Current Feedback 1x1	Current Feedback 2x2	Differential 3x3	Differential 4x4
C_d (pF)	27	108	243	27	108	243	432
ENC_e	4152	5001 (6167)	7868	7619	9023 (7971)	13,750	19,200
P_d (mW)	18.2	19.5 (17.4)	19	15	15 (15.3)	23.5	23.5
t_r (ns)	3.5	3.3	5.4	2.4	6.7	5.6	4.2
Ext. Cap. ?	NO	NO	NO	YES	YES	YES	YES

Cd is detector capacitance for 400 um thick silicon; ENCe (equivalent noise charge) is given in rms electrons at -20C for CR-RC peaking time of 50 ns; Pd (power dissipation) is given for +/-5 V supplies; tr (rise time) given for 10 mV output signal.

ornl



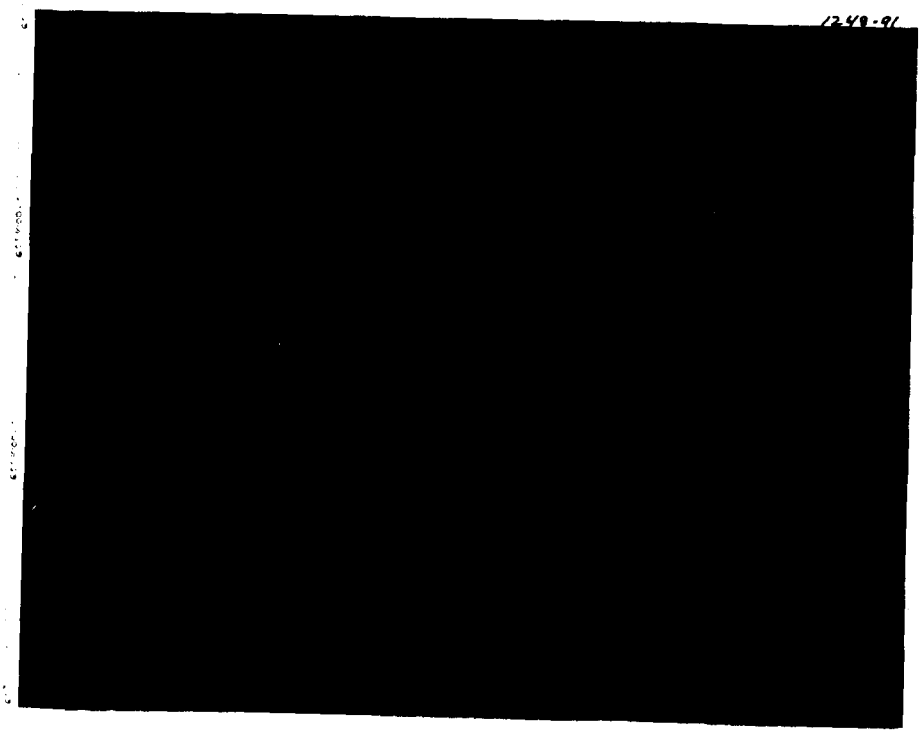
Design Topologies vs. Detector Size

(Detector thickness = 400μ, sizes in cm²)

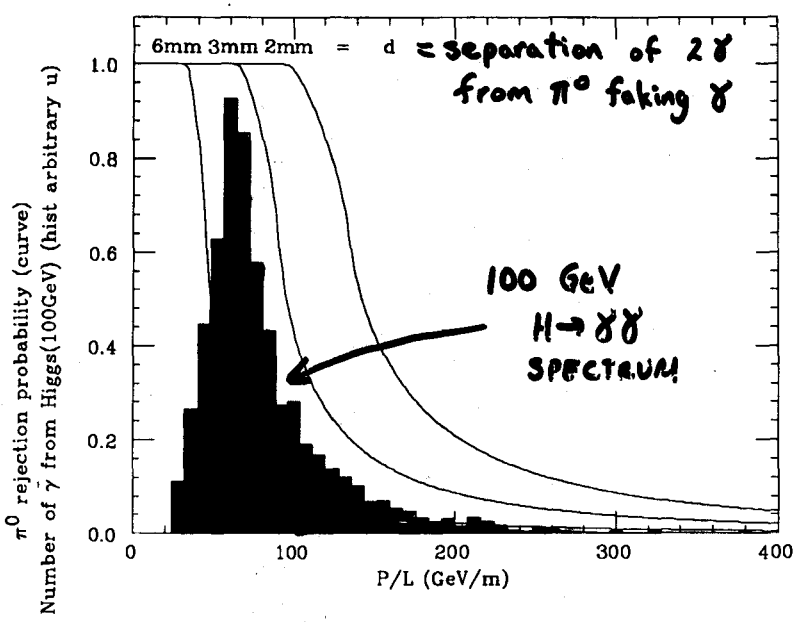
Detector size	1x1	2x2	3x3	4x4
Detector cap.	27 pF	108 pF	243 pF	432 pF
Folded cas.	FC1x1	FC2x2	FC3x3	
Current feed.	CF1x1	CF2x2		
Differential			DF3x3	DF4x4

ornl

Gary Alley



GEM PRERADIATOR



CONCLUSION

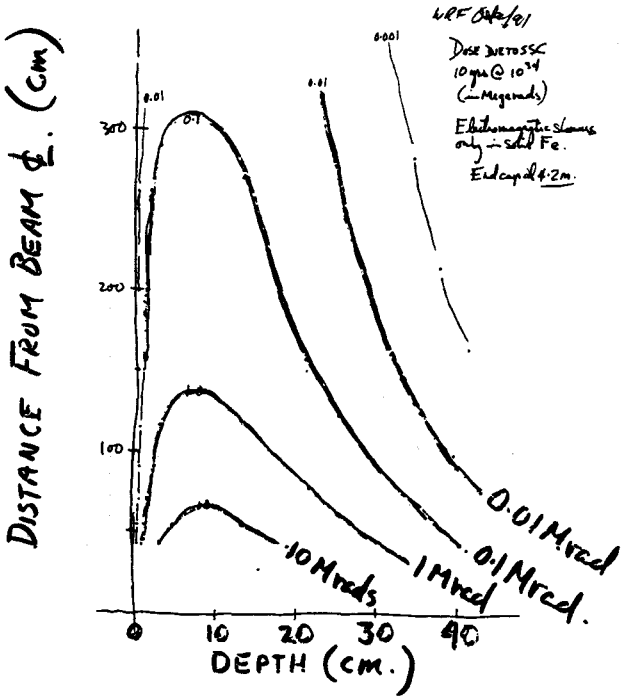
THIS PAST YEAR HAS SEEN GOOD PROGRESS ON THESE TECHNOLOGIES

WORK ON THESE IS NOW BEING APPLIED TO THE GEM DETECTOR

Calorimetry II

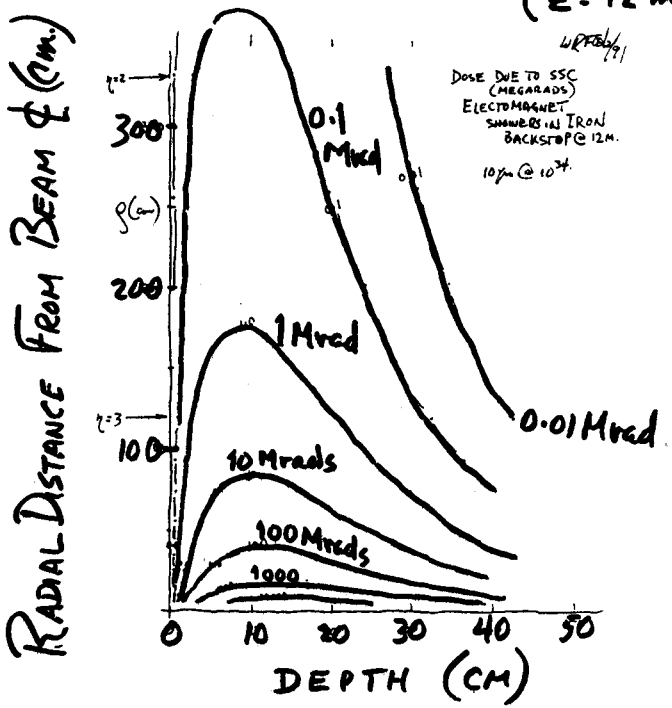
W. R. Frisken

Dose Contours in (Fe) Endcap CAL ($z = 4.2$ m)



10 yrs with $\mathcal{L} = 10^{34}$

Dose Contours in (Fe) Forward CAL ($z = 12$ m)



10 yrs with $\mathcal{L} = 10^{34}$

LIQUID SCINTILLATOR

1. Liquid Tiles Reidy et al (show cover page)

Chemical compatibility of components

Radiation Resistance of Components

Clear ig Fibers } tests at very high rate, anneal >>>5-10 Mrad ok? need to study rate dependence

WLS Fibers }

Reflector — Paint (TiO_2/polyureth) ok to 9Mrad

Light Yield

Component studies } >>>>>optimization

LTRANS mc code }

SINGLE CELL TESTS

Calibration and Monitoring

2. Liquid SPACAL White/Huson, Texas A/M

A Research and Development Proposal

submitted by

E. Ables, P. Armatis, R. Bionta, H. Britt O. Clamp, C. Cochran, G. Graham, M. Lowry, D. Masquelier, K. Skulina, C. Wuest
Lawrence Livermore National Laboratory, Livermore, California,USA

L.Bolen, L.Cremaldi, S.Harper, B.Moore, B.Quinn, J.Reidy (co-spokesman and contact person), J.Zhou
University of Mississippi, University, Mississippi, USA

L.Croft, R.Piercey,
Mississippi State University, Mississippi State, Mississippi, USA

M.L.Bauer, B.L.Bishop, H.O.Cohn, T.A.Gabriel, A.Gordeev, Yu.Kamyshkov (co-spokesman), R.A.Lillie, F.Plasil, K.Read, M.J.Rennich, A.Savin, K.Shmakov, B.H.Singeltary, A.Smirnov, E.Tarkovsky, R.A.Todd, K.G.Young,
Oak Ridge National Laboratory, Oak Ridge, Tennessee, USA

S.C.Berridge, W.M.Bugg, T.Handler, M.Pisharody,
University of Tennessee, Knoxville, Tennessee, USA

T.Aziz, S.Banerjee, S.R.Chendvankar, S.N.Ganguli, P.K.Malhotra, K.Mazumdar, R.Raghavan, K.Shankar, K.Sudhakar, S.C.Tonwar
Tata Institute of Fundamental Research, Bombay, India

A.Arefiev, S.Burov, N.Bystrov, Yu.Galaktionov, Yu.Gorodkov, A.Malinin, A.Nikitin, V.Markizov, V.Plyaskin, V.Pojidaev, A.Rozjkov, E.Shoumilov, V.Shoutko, V.Tchudakov, O.Zeldovich
Institute for Theoretical and Experimental Physics, ITEP, Moscow, USSR

A.Kozelov, A.Lebedev, S.Medved, E.Slobodyuk, A.Vasiliev.
Institute for High Energy Physics, Serpukhov, USSR

TABLE 1

Major Advantages of Liquid Scintillator calorimetry in SSC environment

- High operation speed;
- No radiation damage problem for liquid scintillator since it can be easily exchanged;
- High radiation resistance of WLS and clear transport fibers;
- Detector flexibility permits fine segmentation both tansversaly and longitudinaly;
- Good energy resolution (e/h=1) as in well understood high performance plastic scintillator calorimeters;
- Simple mechanical modular design which ensures good uniformity and hermeticity and allows beam calibration of each module prior to installation in the experiment;
- Easy performance monitoring (with radioactive source per each readout channel);
- Good signal/noise ratio (1 mip ~ 30 photoelectrons per readout channel in PMT);
- Low cost technology suitable for mass production.

BUT NEEDS SYSTEM TESTS.

TABLE 6

Physical Properties of BC-517PKO Liquid Scintillator

Light Output:	35% anthracene
Mean Free Path (400-500 nm):	> 6 meters
Decay Time (approx.):	2.2 nsec
Wavelength of Maximum Emission:	425 nm
Refractive Index:	1.47
Specific Gravity:	0.85 g/cm^3
Flash Point (T.O.F):	115°C

Liquid Tiles Light Yield

Component studies:

- Improved scintillator BC-517PKO >>>>>>>see table 6
- Reflectance of TiO_2 paint >>>>>>>see figures 3, 4, 5
- wls fibers. testing comm fibers..>>>figs 6,7,8,9 table 7

  fiber development...absorb heavily.
- Fiber joints good results.>>>>>>show fig 16

LTRANS mc code: THE KEY.....

Cell Design.....show fig 10

Light yield >>>>>>show fig 15

Uniformity >>>>>>show fig 13, tables 10a,b

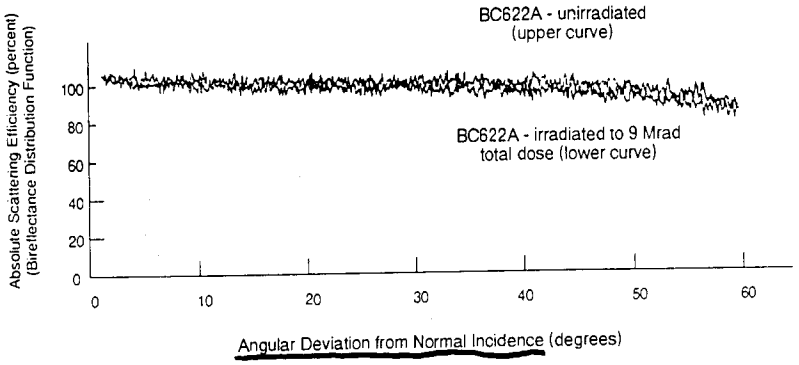


Fig.3. Measurement of Bicron BC622A reflecting paint for radiation damage. A sample was irradiated to 9 Mrad total dose over an 8 hour period using the LLNL Co^{60} source. The measurement of the diffuse scattering efficiency as a function of laser illumination angle from the irradiated sample is shown along with a similar mea- surement from an unirradiated sample. Zero degrees corresponds to scattering directly back in the direction of the source, 90 degrees corresponds to scattering parallel to the surface of the sample. There is no significant difference between the two samples.

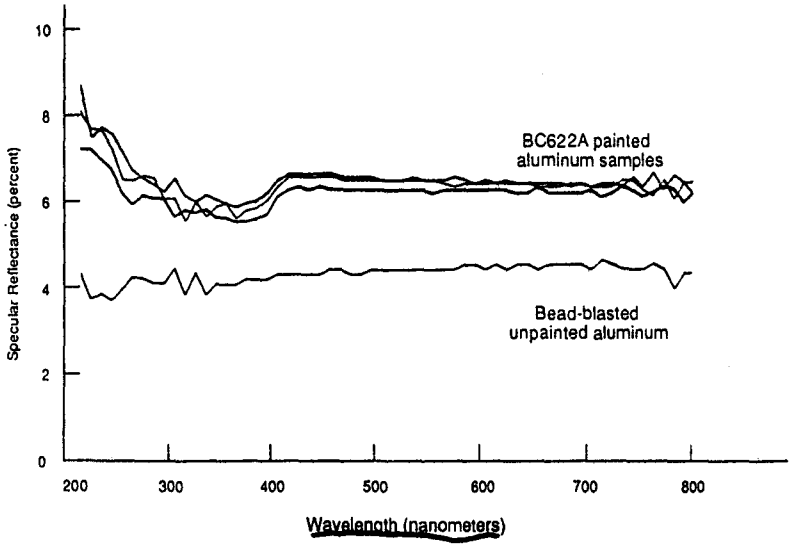


Fig.4. Measurement of the near-normal specular reflectance of Bicron BC622A paint as a function of wavelength. Three painted samples are compared along with an unpainted bead-blasted alu- minum sample.

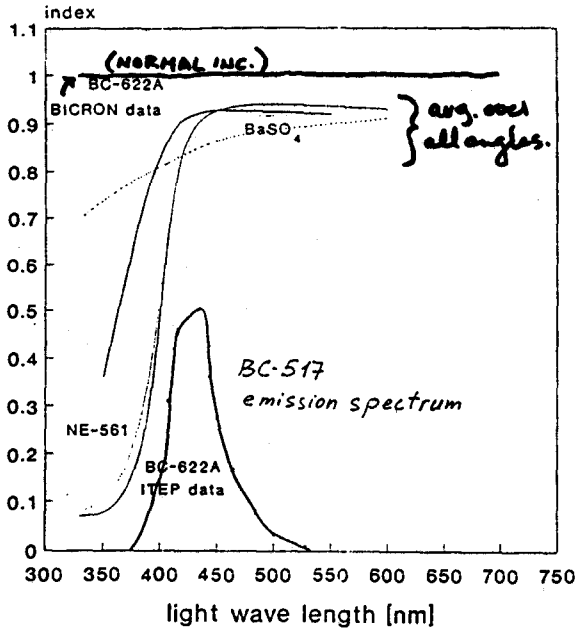


Fig.5. Results of measurements at MRIOPM for diffusive paint reflection coefficient.

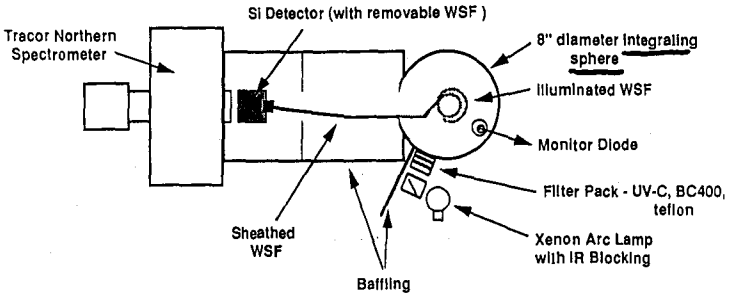


Fig.6. Schematic representation of the integrating sphere containing a coiled length of waveshifting fiber optic. The sphere is illuminated using a tailored spectrum approximating the emission of the liquid scintillator. Spectrally resolved and integrated measure- ments of the waveshifting fiber or integrating sphere are accom- plished with silicon diodes or spectrophotometers by either connect- ing or disconnecting the fiber from the photodetectors.

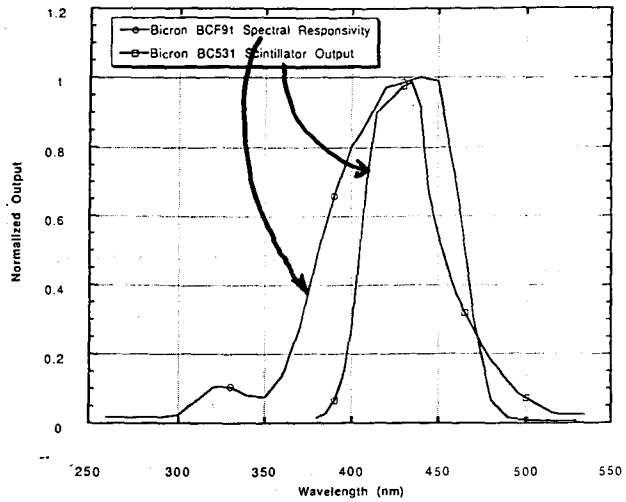


Fig.7. Result of the measurement of the waveshifting fiber output (emission) as a function of incident light wavelength (excitation). Also shown in the figure is the spectrum of output light from the Bicron liquid scintillator. The waveshifting fiber is seen to be well matched to the liquid scintillator out to about 480 nm where its response drops to nearly zero.

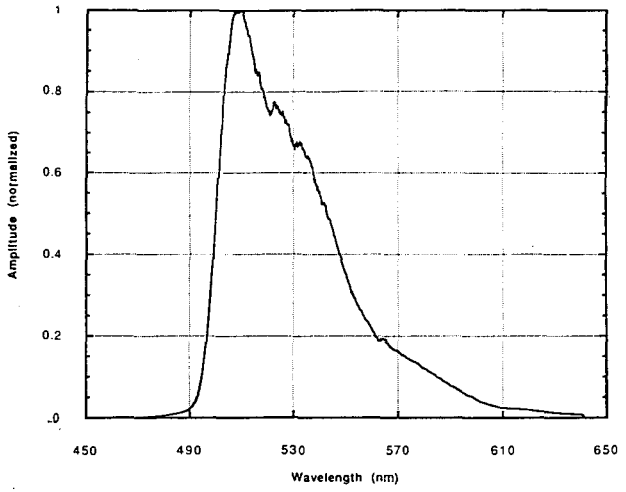


Fig.8. Spectrum of light emitted from the end of WLS fiber measured with integrating sphere and spectrometer.

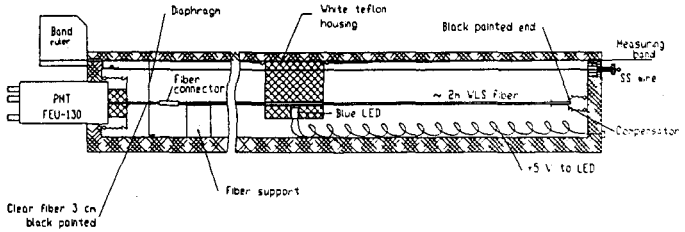


Fig.9. Schematic view of the setup for WLS fiber attenuation length measurements.

TABLE 7

WLS Fiber transmission measurement two exponent fit results.

WLSF	Dye concentration (ppm)	Light yield (a.u.)	Fraction of short absorption	Short absorption length (cm)	Long absorption length (cm)	χ^2/DOF
Bicron						
BCF91 #1[1]	200	484	0.42	38.1	130	36
BCF91 #2	200	393	0.52	21.6	132	7.4
BCF91A #1	200	475	0.47	33.8	290	1.5
BCF91A #2	200	461	0.48	31.2	287	1.7
BCF9926	100	416	0.33	32.9	185	2.1
BCF9927	300	509	0.49	28.5	162	1.5
BCF9928	400	513	0.33	21.0	159	3.3
Kuraray						
Y7	60	412	0.35	26.8	215	5.9
Y7[2]	60	416	0.37	27.8	216	2.4
Y7	100	593	0.47	22.0	157	5.7
Y7	150	565	0.57	33.4	183	2.6
Y7[3]	150	584	0.53	30.9	155	3.2
Y8	100	333	0.40	18.7	241	2.1
Y8	150	350	0.42	25.6	218	1.3
Y8	250	380	0.43	27.5	208	1.7
Y9	30	409	0.33	22.6	140	1.0
Y9	60	456	0.41	26.7	113	1.4
Y9	120	538	0.50	17.8	63	1.3

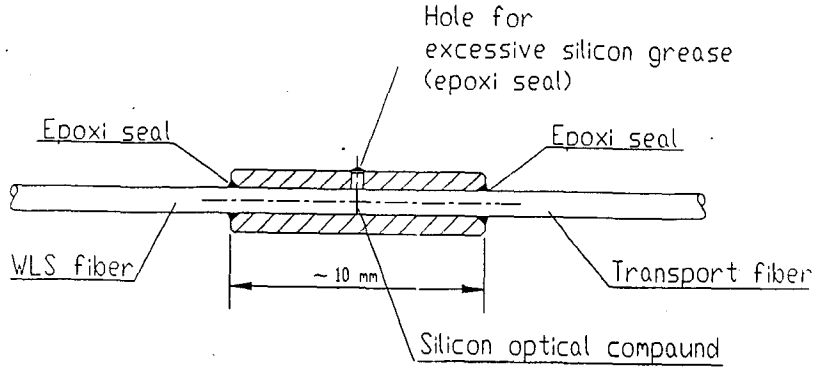


Fig.16. Fiber splicing schematic view.

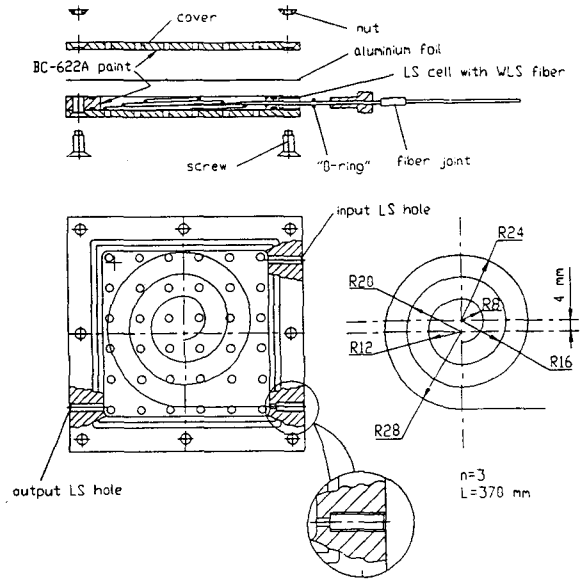


Fig.10. Schematic view of LS cell prototype.

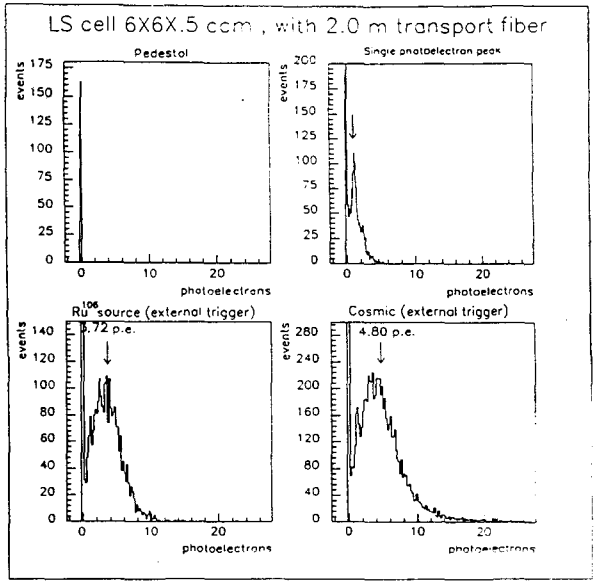


Fig.15. Cell prototype light yield measurement results.

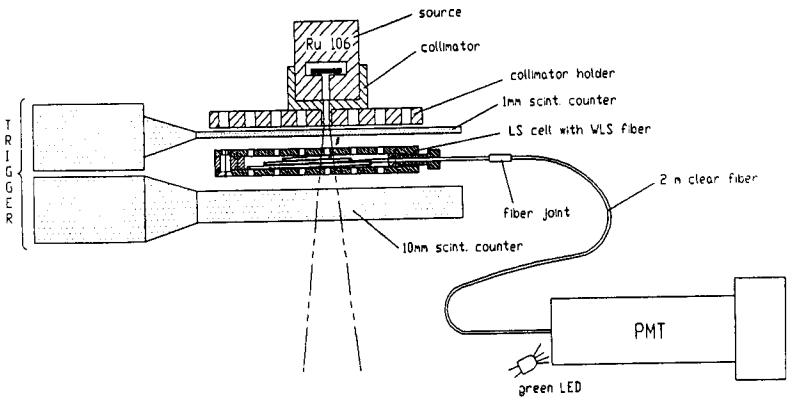


Fig.13. Schematic view of cell test setup.

TABLE 10a

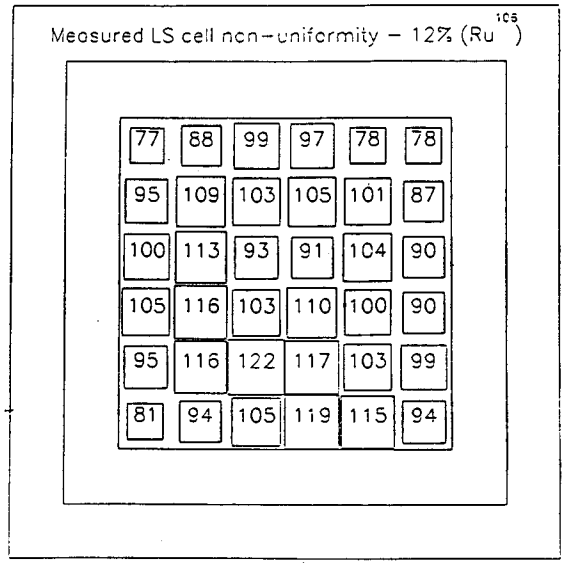
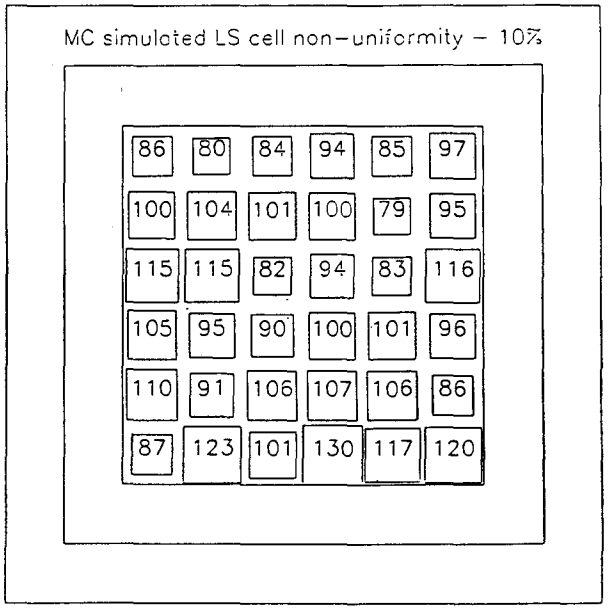


TABLE 10b



Liquid Scintillator Calorimetry Collaboration
FY 1991 Progress Report for
SSC R&D Proposal # 257

James T. White and F. Russel Huson
Texas A&M University
College Station Texas, 77843

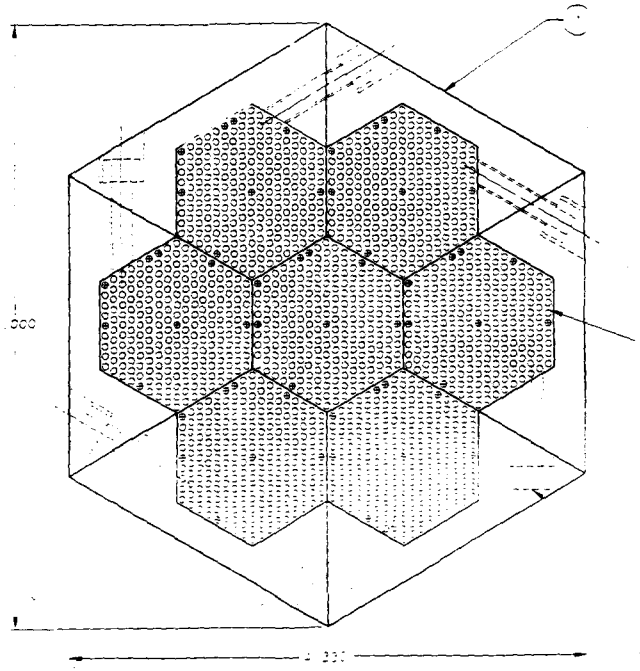
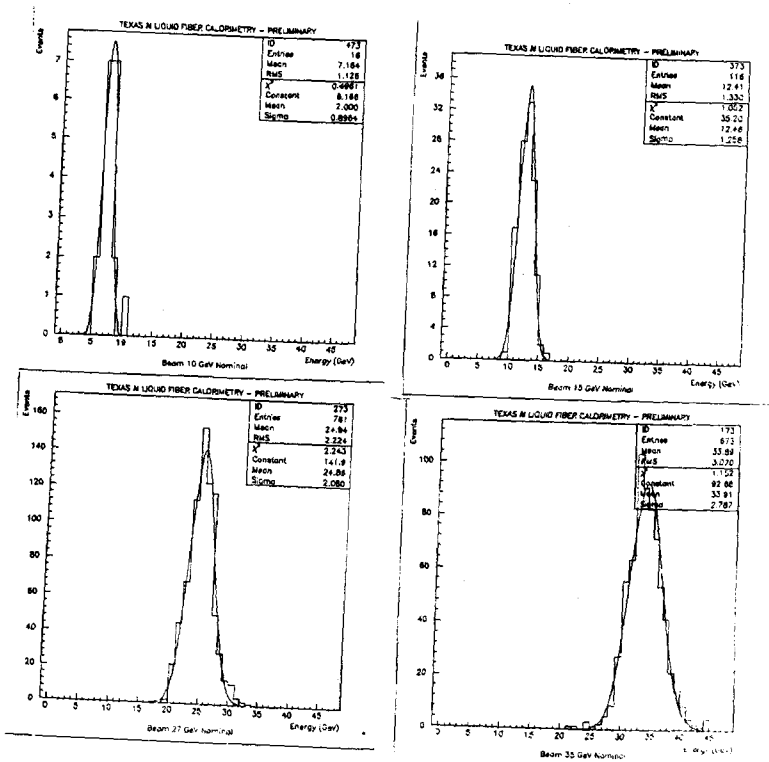
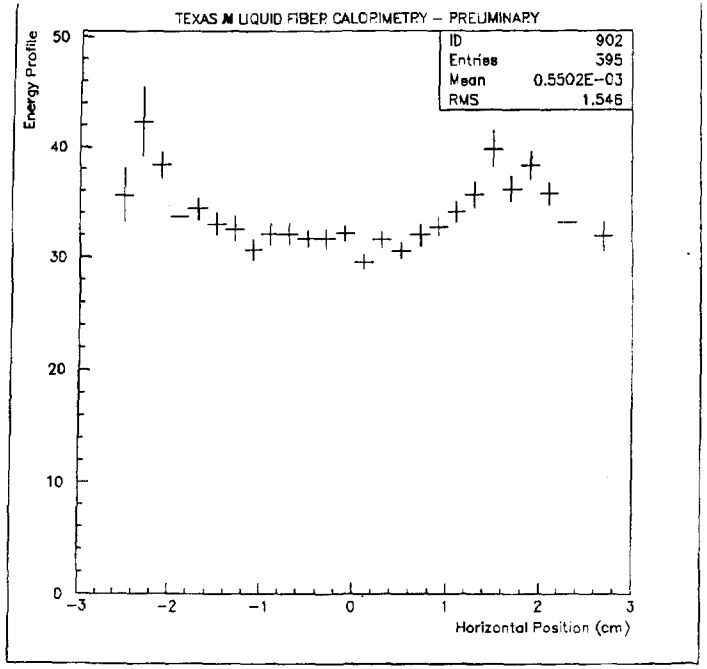


Figure 2


TEXAS M LIQUID FIBER CALORIMETRY – PRELIMINARY
Beam 10 GeV Nominal
Energy (GeV)
TEXAS M LIQUID FIBER CALORIMETRY – PRELIMINARY
Beam 15 GeV Nominal
TEXAS M LIQUID FIBER CALORIMETRY – PRELIMINARY
TEXAS M LIQUID FIBER CALORIMETRY – PRELIMINARY



LBL-Group A Physics Note 973

WARM LIQUID CALORIMETRY LARGE SUBSYSTEM R&D PROGRESS REPORT

WALIC

FASTMS

September 1, 1990

J. Busenitz, D. DiBitonto, M. Timko
University of Alabama

B. Aubert, J. Colas, P. Ghez, J. -C. Lacotte, J. -C. Lemarec, and P. Petitpas
Laboratoire d'Annecy-le-Vieux de Physique des Particules

J. Bensinger
Brandeis University

A. Ciocio, M. Hoff, J. Kadyk, P. Limon, M. Pripstein*,
M. Sttovink, W. Thur, T. Weber, W. A. Wenzel
University of California, Berkeley and Lawrence Berkeley Laboratory

L. Dobrzynski, D. Kryn, J.P. Mendiburu, and P. Salin
Laboratoire de Physique Corpusculaire du Collège de France

J. Womersley
Florida State University

G. Brandenburg, A. Daw(st), S. Geer, J. Oliver, and E. Sadowski
Harvard University

R. Kikuchi
Kyoto University

K. Miyano
Niigata University

M. Gregory(st), R. Hollebeek, M. Newcomer, and Cen Yi(st)
University of Pennsylvania

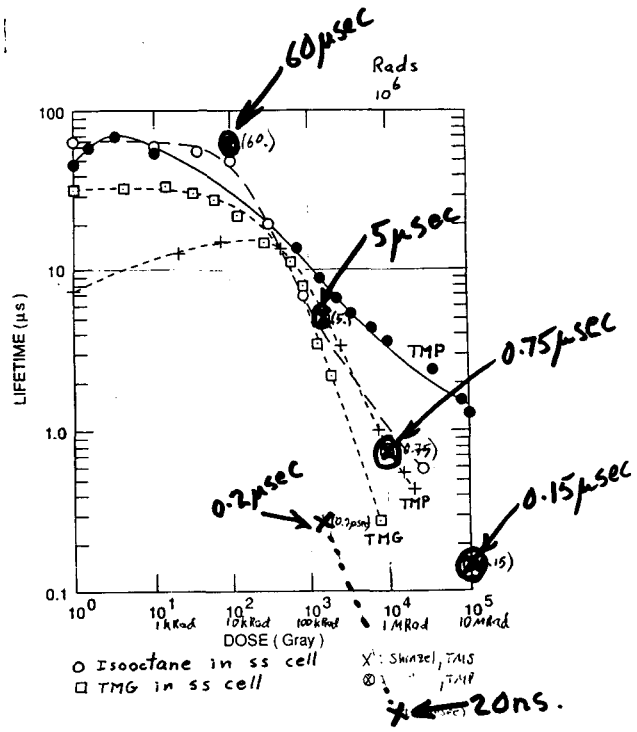
Ph. Lavocat, B. Mansoulié, S. Palanque, and J. Teiger
CEN Saclay

K. Matsuda
Saitama College of Health

K. Abe, K. Hasegawa, F. Suekane, H. Yuta
Tohoku University

M. Higuchi, Y. Hoshi
Tohoku Gakuin University

* Contact person
(st) student



CERN: { ⊗ Schinzel TMP
x " TMS

NEW measurements for TMP fall right on the curve. — OK at 10 Mrad.

WARM LIQUID IONIZATION CALORIMETRY
(WALIC)

- LARGE INTERNATIONAL COLLABORATION >>>>>SHOW LIST>>>
- WORKING SINCE 1985 SEE FORT WORTH PROCEEDINGS
- CRITICAL (and other important) ISSUES
  - -TEST PROOF OF PRINCIPLE MODULE (PISCINE)
  - -MATERIALS COMPATIBILITY
  - -SPEED-OF-RESPONSE/SIGNAL-TO-NOISE
  - -e/h
  - -PURIFICATION, CLEANLINESS, LONG TERM STABILITY
  - -RADIATION RESISTANCE
  - -ENGINEERING OF A REAL CALORIMETER SYSTEM

A SEARCH FOR MATERIALS COMPATIBLE WITH WARM LIQUIDS

B. Aubert[2], A. Ciocio[3], J. Colas[2], L. Dobrynski[1], P. Ghez[2], P. Guillouet[1], J. Kadyk[3], D. Kryn[1], P. Lebasque[1], P. Limon[3], D. Marchand[1], B. Mansoulié[4], J.P. Mendiburu[1], S. Ochsenbein[5], M. Pripstein[3], G. Przybylski[3], P. Salin[1], G. Sajot[1], M. Strovink[3], J. Teiger[4], W. Thur[3], T. Weber[3], W. Wenzel[3]

WALIC Collaboration*)

1) Collège de France, Paris, France
2) LAPP, Annecy, France
3) LBL, Berkeley, USA
4) CEA, Saclay, France
5) PSI, Villigen, Switzerland

Abstract

This paper reports on the search undertaken since 1987 by a part of the WALIC collaboration to find new materials for the construction of ionizing detectors filled with room-temperature liquid hydrocarbons, tetramethylsilane and tetramethylpentane. We have found that several metals, glasses, plastics and glues, very promising for their mechanical, electrical, and radiation hardness properties, can be put into contact with these liquids without observing, during the drift time, any significant decrease in the lifetime of the electrons created by ionization.

(Submitted to Nucl. Instrum. Methods A)

*) The WALIC (for WArm-LIquid Calorimetry) Collaboration is composed of the following laboratories: CEA (Saclay), Collège de France (Paris), LBL (Berkeley), LAPP (Annecy).

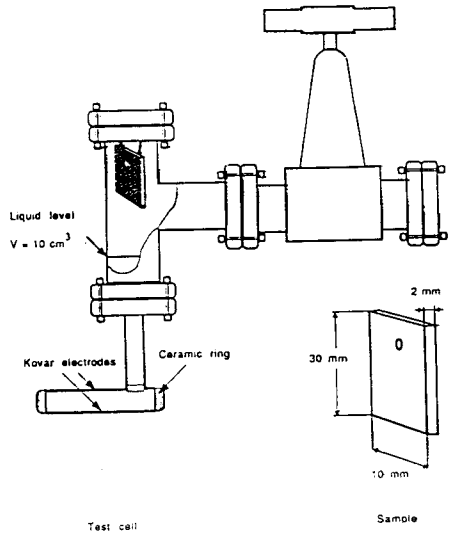


Figure 2

Table 1: Compatibility of metals

Material*)	Contact time	Lifetime (errors) (μs)	Drift voltage (V)
Copper (1)	5 min	42.0 (−6.8,+7.8)	20 and 40
	2.5 h	49.4 (−6.4,+7.3)	20 and 40
	8 d	40.6 (−6.0,+6.0)	40
	21 d	88.0 (−5.0,+5.0)	20 and 70
Lead 1 (2)	0	2.1 (±0.4)	
	6 h	3.8 (±8)	
	28 h	5.9 (±1.2)	
	1.5 d	9.3 (±1.9)	
	6 d	27 (±5.4)	
	29 d	33 (±6.6)	
Lead 2 (1)	0	41.7 (−10.8,+19.5)	70
	1 h	45.7 (−7.6,+10.7)	70
	13 d	49.5 (−7.8,+10.8)	70
	27 d	45.5 (−6.0,+7.8)	70
Lead 3 (1) (see text)	0	48.1 (−12.,+24.9)	103
	15 min	38.7 (−8.6,+14.5)	103
	3 d	61.7 (−14. 6,+25.6)	70
	10 d	63.7 (−17.4,+34.6)	70
	17 d	54.5 (−10.6,+16.4)	70
	44 d	76.7 (−17.3,+29.6)	70
	61 d	111.4 (−11.0,+13.4)	40
Tungsten (1)	0	54.5 (−15.8,+27.9)	30 and 50
	2 h	54.6 (−11.2,+16.7)	40 and 70
	3 d	96.1 (−17.1,+23.6)	20
	10 d	243 (−53,+83)	10
	21 d	383 (−75,+114)	10
	33 d	381 (−90,+155)	5 and 10
Aluminium (2)	0	9.6 (±1.9)	
	5 h	9.6 (±1.9)	
	61 d	7.2 (±1.5)	
	120 d	9.5 (±1.9)	
	270 d	8.5 (±1.7)	
	360 d	7.7 (±1.5)	

*) Materials marked (1) have been measured with TMS at the Collège de France, whilst those marked (2) have been measured with TMP at LBL.

Table 2: Compatibility of insulating materials

Material*)	Contact time	Lifetime (errors) (μs)	Drift voltage (V)
Teflon	0	100	12
	2 min	0	1500
PEEK	0	14.7 (−2.2,+3)	800 and 1000
	5 min	6.1 (−1.8,+2)	1000
	49 h	19.9 (−4.5,+8)	1000
	14 d	15.6 (−3,+4.7)	500 and 600
	31 d	7.2 (−2.8,+8.0)	300 and 250
Vectra (metallized)	0	18.9 (−4,+6.3)	100.7
	5 min	18.5 (−5.3,+11.6)	131.3
	2 h	27.1 (−12.0,+15.4)	116.5
	7 d	25.2 (−6.1,+9.7)	70
	16 d	23.9 (−3.5,+4.5)	143
	37 d	28.1 (−4.9,+6.6)	50
	55 d	27.7 (−6.7,+10.9)	70
Zerodur	0	40.1 (−6.0,+8.3)	100
	1 h	29.4 (−7.5,+13.4)	100
	11 d	32.8 (−6.8,+10.7)	100
	28 d	45.2 (−9.7,+16.0)	70
	46 d	55.5 (−15.5,+23.7)	70
Suprax	0	117.6 (−26.0,+43.4)	35 and 70
	1 h	78.4 (−22.0,+45.8)	70
	15 d	64.1 (−8.9,+11.8)	70
	35 d	74.4 (−11.5,+16.1)	70
Kerimid 500	0	14.9 (−2.2,+2.9)	70, 105, 150.4
	15 min	16.2 (−3.0,+4.5)	151.7
	8 d	17.3 (−2.9,+4.1)	151.5
	17 d	6.8 (−1.5,+2)	153.4
	28 d	15.4 (−3.,+4.4)	153.5
	41 d	18.4 (−4.3,+7.4)	153

*) All materials have been measured with TMS at the Collège de France.

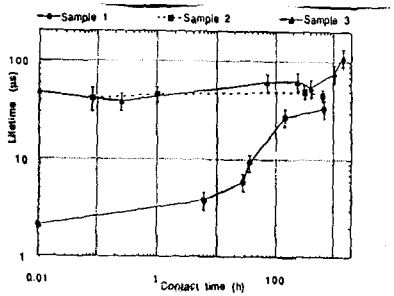


Figure 5a

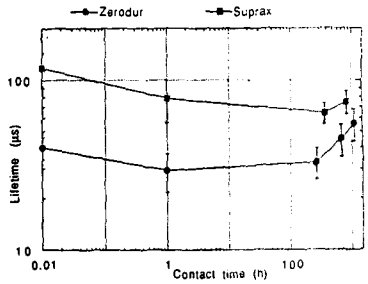


Figure 6a

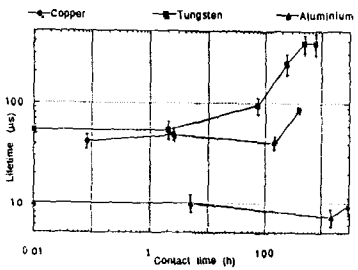


Figure 5b

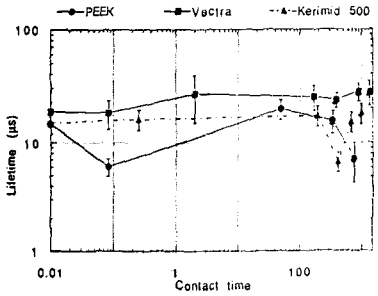


Figure 6b

METALS ARE "GETTERS".

LAPP-EXP/91-xx
17 September 1991

COMPENSATION STUDIES OF A LEAD/TMP CALORIMETER

The WALIC collaboration

B. Aubert[1], A. Ciocio[3], J. Colas[1], L. Dobrzynski[4], P. Ghez[1], J. Kadyk[3], R. Kikuchi[2], D. Kryn[4], J.C. Lacotte[1], P. Lavocat[5], B. Mansoulie[5], J.P. Mendiburu[4], M. Pripstein[3], G. Sajot[4], P. Salin[4], M. Strovink[3], J. Teiger[5], W. Thur[3], M. Timko[6], T. Weber[3], W.A. Wenzel[3]

Annecy (LAPP)[1] - Kyoto (KU)[2] - LBL (Berkeley)[3] - Paris (College de France)[4] - Saclay (CEN)[5] - Tuscaloosa (U of A)[6]

Abstract

We present results from a fully modular Lead/TMP calorimeter. In electromagnetic configuration, we have measured the response of 2.5 to 150 GeV/c electrons. The e/π fraction has been determined with electron and pion beams from 5 to 50 GeV/c in hadronic configurations. The modularity of the calorimeter has permitted us to study the compensation for various sampling fractions and various amount of hydrogen traversed by the showers. A detailed comparison to a Monte Carlo simulation of all the results is presented.

(submitted to Nuclear Instruments and Methods)

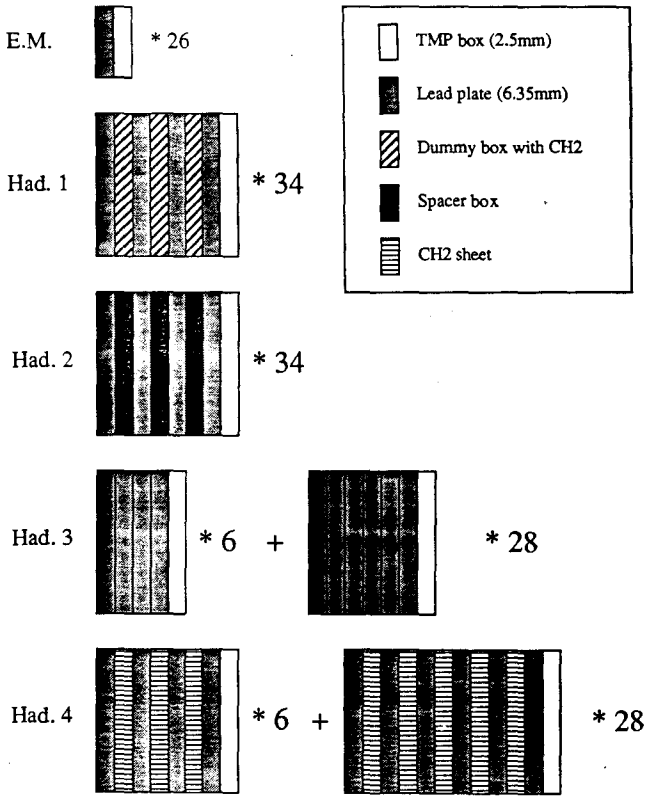


Figure 1

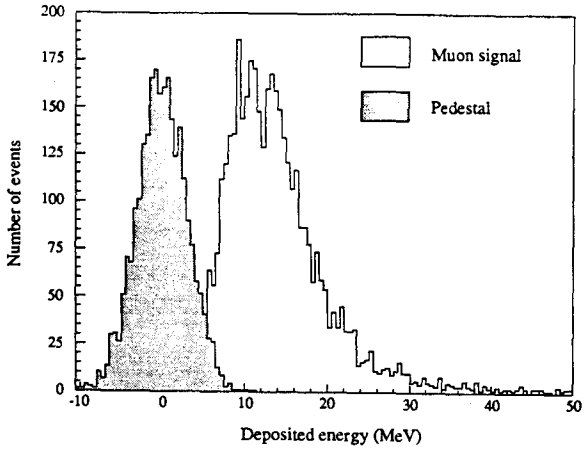


Figure 2.a

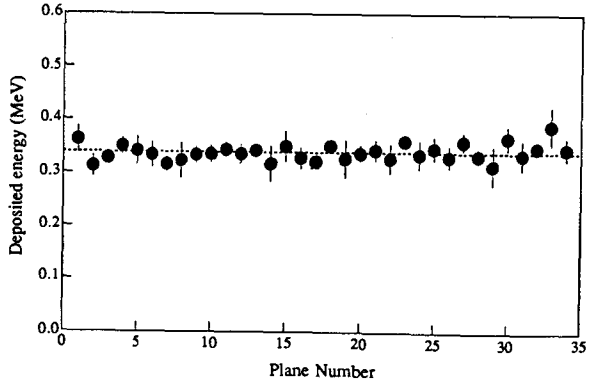


Figure 2.b

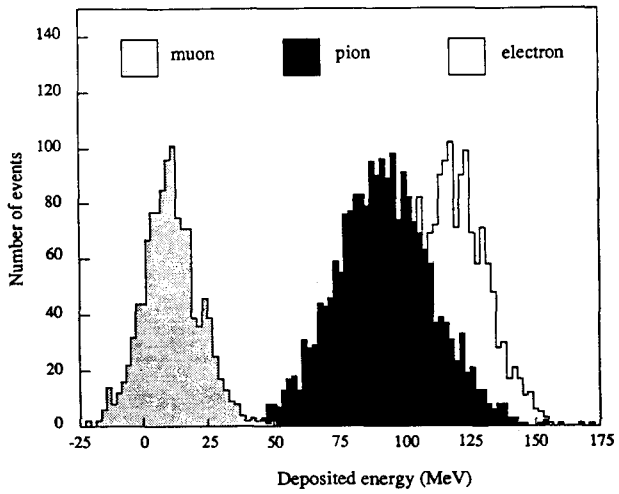
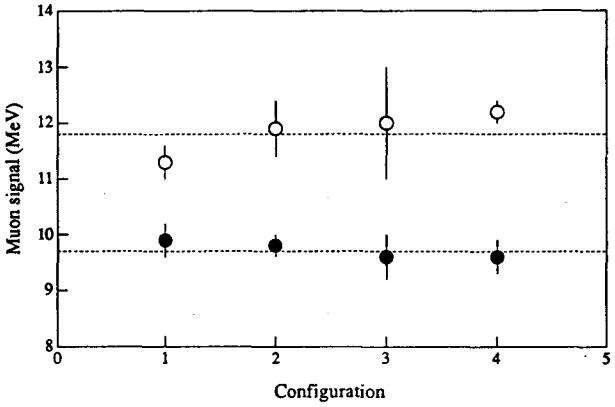


Figure 4.a



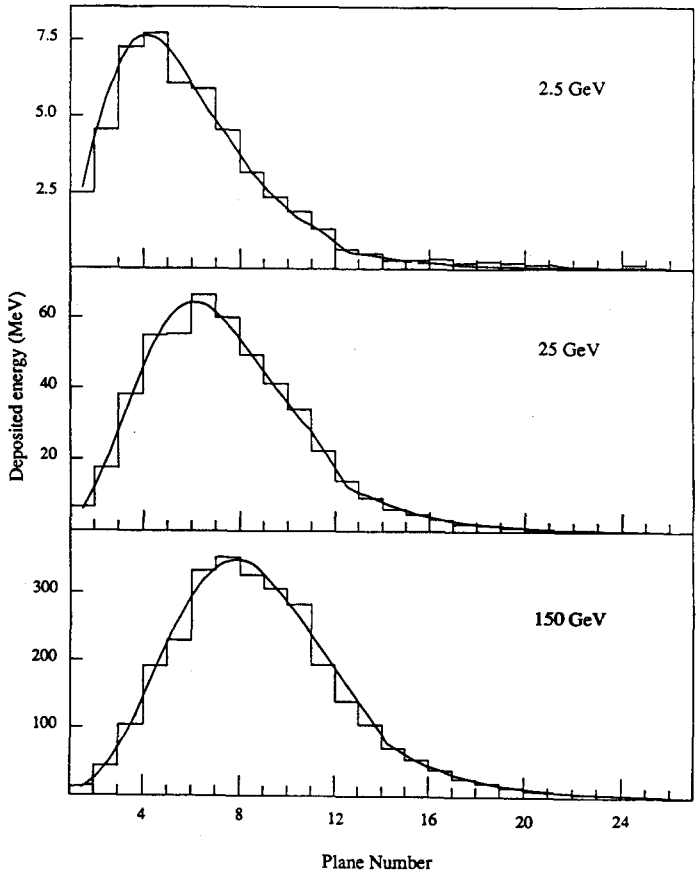


Figure 6

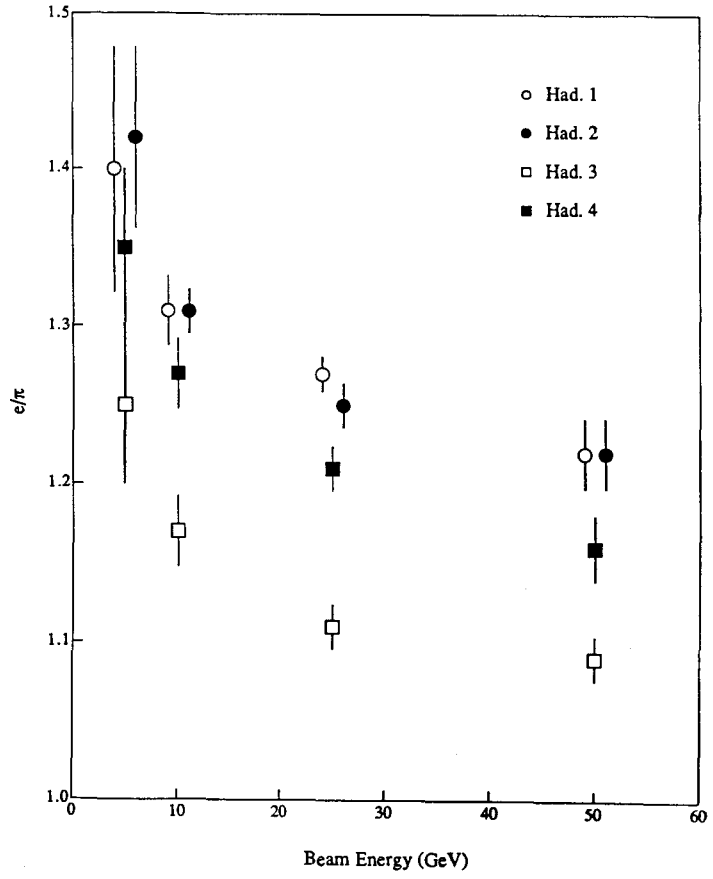


Figure 5

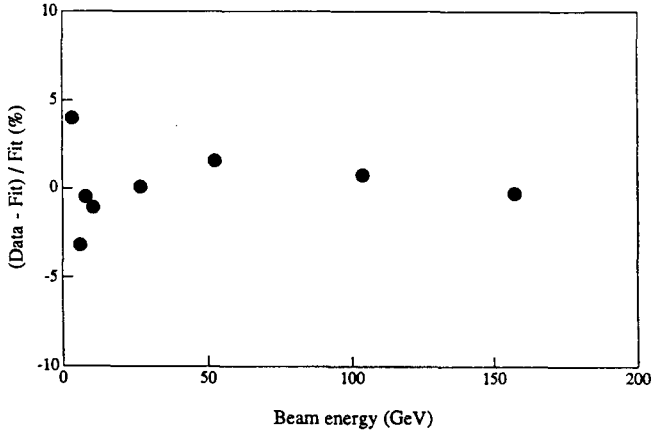


Figure 3.a

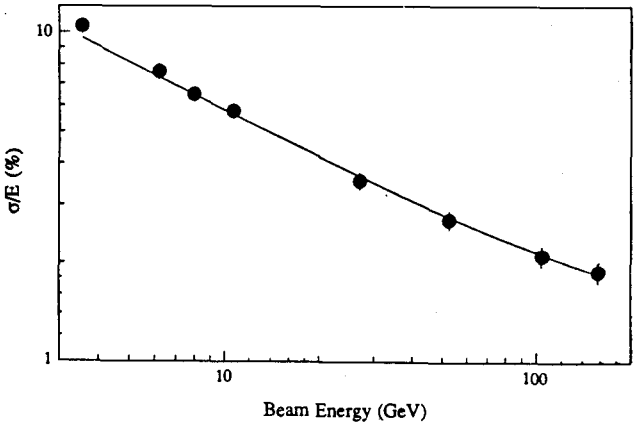


Figure 3.b

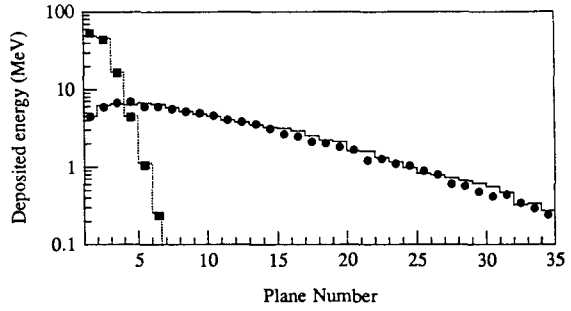
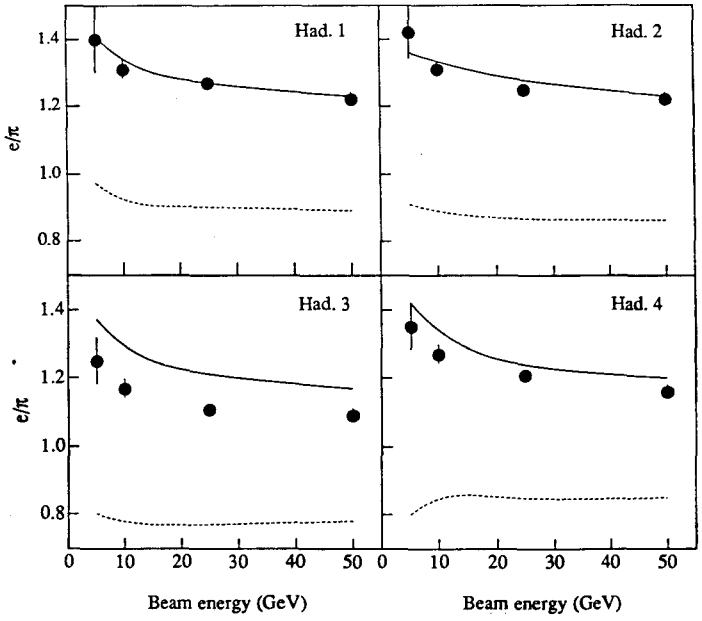


Figure 7.a



Tables

Density (g/cm^3)	0.72
dE/dx (MeV/cm)	1.48
G_{fi} (ion pairs/100 eV at 15kV/cm)	1.37
Mobility (cm^2/V s)	30.0
Flash point (°C)	7.0
Boiling point (°C)	122.0
Dielectric constant	1.98

Table 1: Properties of TMP

Config.	Ebeam (GeV)	e/π
1	5	1.40±0.08
1	10	1.31±0.02
1	25	1.27±0.01
1	50	1.22±0.02
2	5	1.42±0.06
2	10	1.31±0.01
2	25	1.25±0.01
2	50	1.22±0.02
3	5	1.25±0.05
3	10	1.17±0.02
3	25	1.11±0.01
3	50	1.09±0.01
4	5	1.35±0.05
4	10	1.27±0.02
4	25	1.21±0.01
4	50	1.16±0.02

Table 2: e/π response for the 4 hadronic configurations

Beam energy (GeV)	e/π	e/π wide module
5	1.41	1.30
10	1.32	1.22
25	1.26	1.17
50	1.23	1.16

Table 3: Simulated e/π as a function of the beam energy for configuration 1.

Electric field (kV/cm)	k_B (cm/MeV)	e/π
6.7	0.127	1.31
20.0	0.100	1.04
40.0	0.086	0.95

Table 4: Simulated e/π as a function of the electric field (25 GeV, configuration 1)

CONCLUSIONS FROM WALIC e/π TESTS

1. e/π varies between 1.1 and 1.4 (beam E, det configuration)
2. simulation correctly reproduces the data

   and so.....
3. e/π very sensitive to value of Birk's constant
4. in these tests, lateral shower leakage increases e/π by 7%

IRON IS NEXT.....

WARM LIQUID IONIZATION CALORIMETRY (FASTMS)

1. GaAs FRONT END ELECTRONICS (with Honeywell Corp.)

   (SHOW EXTRA TRANSPARENCIES>>>>>>>>>>>>>)
2. PURIFICATION

   -setting up surface cleaning facility
3. ACTIVATION, RADIOLYSIS, FLAMABILITY OF TMS

   -beam tests at BNL in January '92
4. ENGINEERING AND SURFACE PREPARATION

   Aachen studying encapsulation, and purity survival, particularly after irradiation.
5. SIMULATION

   CALOR on Apollo DN 10000.

#243

Progress Report
to the
SSC Laboratory
from the
FASTMS Collaboration

DoE Grant No.: DE-FG05-84ER40141, Task B

Reporing period
June 1, 1991, to September 1, 1991

Prepared by
D. DiBitonto

Department of Physics and Astronomy
The University of Alabama
Tuscaloosa, Alabama 35487

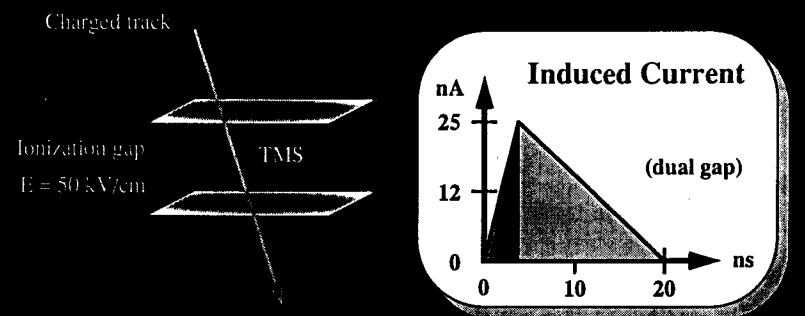
Submitted by

Office for Sponsored Programs
The University of Alabama
Tuscaloosa, Alabama 35487

September 1991

SSC Sponsored Research

Ionization Current Profile



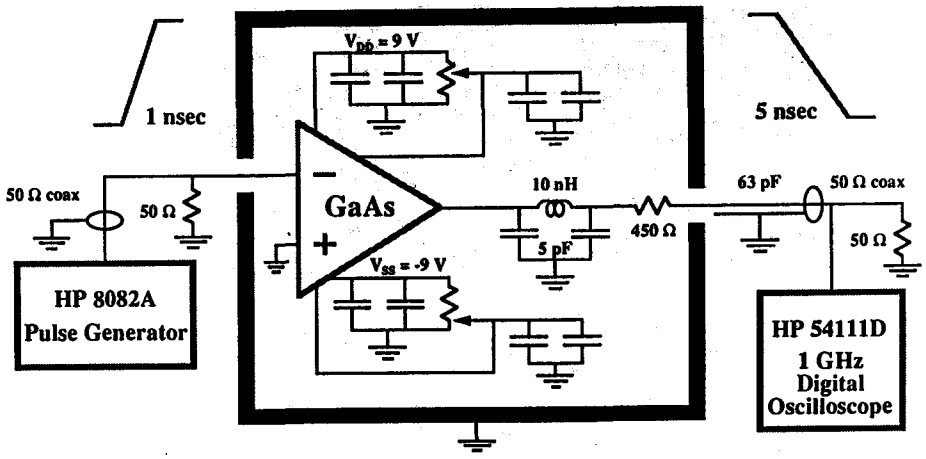
SSC Sponsored Research

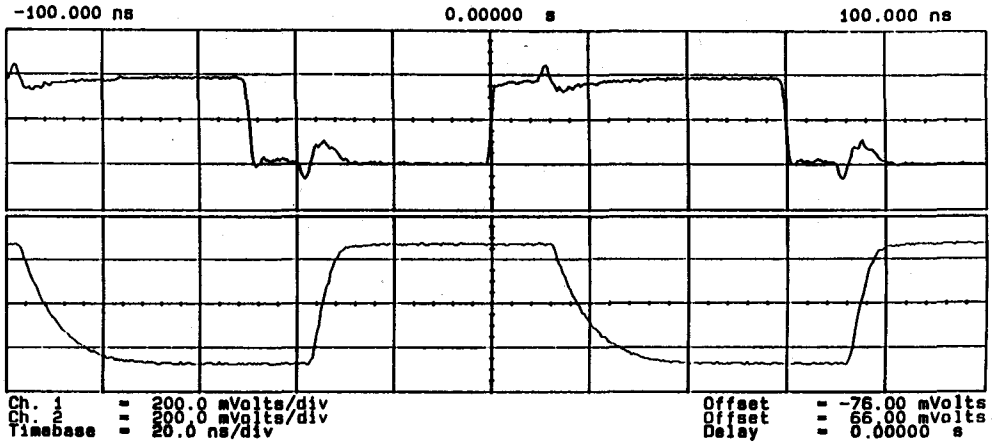
GaAs Front-end Electronics

- Speed: < 5 nsec risetime
- Sensitivity: <10 nA input referred noise
- Radiation Hardness: > 1000 Mrad, 10**16 n/cm2
- Linear Dynamic Range: 1:1000

Honeywell Systems Research Corp.

D. DiBitonto, Univ. of Alabama


1 nsec
5 nsec
V_{pp} = 9 V
V_{ss} = -9 V
GaAs
50 Ω coax
50 Ω
10 nH
5 pF
450 Ω
63 pF
50 Ω coax
50 Ω
HP 8082A
Pulse Generator
HP 54111D
1 GHz
Digital
Oscilloscope


-100.000 ns
0.00000 s
100.000 ns
Ch. 1 = 200.0 mVolts/div
Ch. 2 = 200.0 mVolts/div
Timebase = 20.0 ns/div
Offset = -76.00 mVolts
Offset = 66.00 mVolts
Delay = 0.00000 s

#250

PRESHOWER/SHOWER MAX

TASKS:

1. PROVIDE PRESHOWER TEST MODULE TO PRECEDE COMPOSITE ANL(em)/FNAL(hac) TEST CALORIMETER.
   - -SEE EXTRA TRANSPARENCIES>>>>>>>>>>>>>>>
   - -READY IN TEST BEAM
2. PROVIDE SHOWER MAX (SCINT.TILE) DETECTOR FOR ANL(em)
3. EVALUATE APD'S (LINEAR MODE) FOR PS/SM DETECTORS
   - -LINEAR, NEED TEMPERATURE COMPENSATION
   - -SEE EXTRA TRANSPARENCIES>>>>>>>>>>>>>>>
4. EVALUATE MULTI CHANNEL PM TUBES FOR PS/SM DETECTORS
5. DESIGN/DEVELOP PIXEL TUBE FOR PS/SM READOUT
6. DEVELOP SIMULATION SOFTWARE FOR PS/SM AT SSC

- -SDC π^0/gamma SEPARATION BY FIBER PRESHOWER DETECTOR
- -SDC TRACKING MATERIAL STUDIES (CONFUSION OF TRACK TO SH.MAX CLUSTER MATCHING FOR BREMMING ELECTRONS)

SEE EXTRA TRANSPARENCIES>>>>>>>>>>>>>>>>>>>>>>>>

- -GEM PRESHOWER STUDIES (PRESHOWER DETECTOR DESIGNED TO COMPLEMENT A SPACAL CALORIMETER)

250
31400

STATUS REPORT AND PROPOSAL FOR THE PRE-SHOWER AND SHOWER-MAXIMUM DETECTOR SUBSYSTEM

G. Alverson, M. Glaubman, A. Grimes,
I. Leedom, S. Reucroft, T. Yasuda
Northeastern University, Boston, USA.

A. Bhatti, P. Melese, R. Rusack *, Z. Wu.
The Rockefeller University, New York, USA.

P. Bouamy, J. Ernwein, J.R. Hubbard, P. Le Du, G. Villet
CEN Saclay, France

H. Fenker, K. Morgan, T. Regan
SSC Laboratory, Dallas, Texas, USA.

J. Grunhaus, S. Kananov, C. Milstene
Tel Aviv University, Tel Aviv, Israel

C. Rosenfeld, A. Wang, M. Zheng
University of South Carolina, Columbia, USA.

P. Cushman ‡ S. Hou, V. Singh, J. Slaughter
Yale University, New Haven, USA.

*Co-spokesperson: 212-570-8827, ROCKUP::RUSACK
‡Co-spokesperson: 203-432-3806, YALPH1::PRISCA

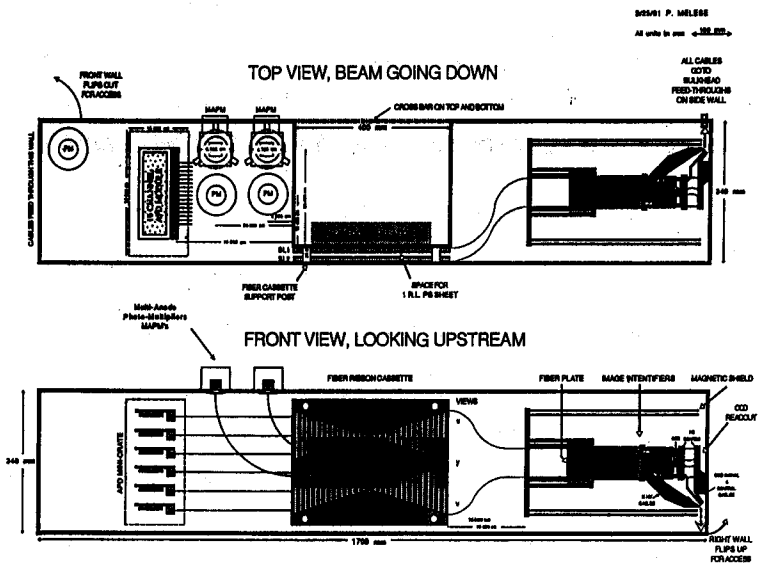


FIGURE 1. SDC PROTOTYPE PRESHOWER DETECTOR

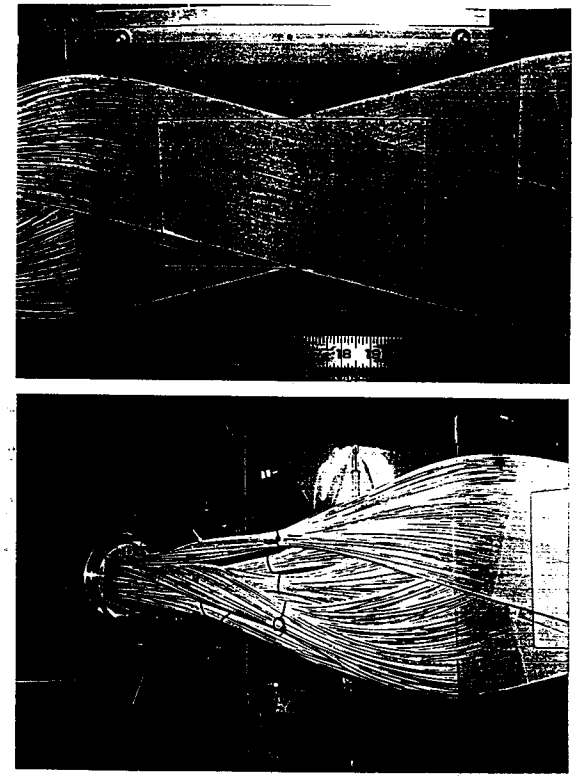


Figure 2: Pictures of SDC Prototype Preshower Detector:
top - shows fiber ribbons at stereo angles;
bottom - shows fiber ends going into II/CCD plate

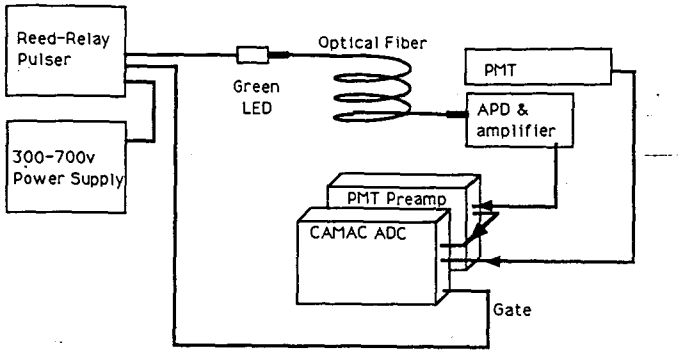


Fig. 9. Block diagram of experimental arrangement for initial APD studies.

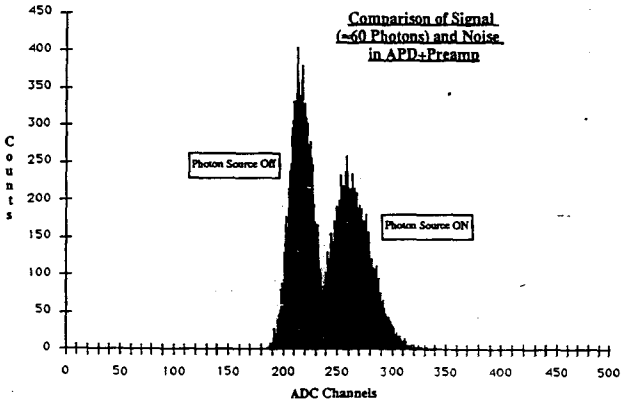


Fig. 10. Early test results of an APD operating in linear mode and exposed to about 60 green (565nm) photons. The electronic noise apparent in this figure was later reduced.

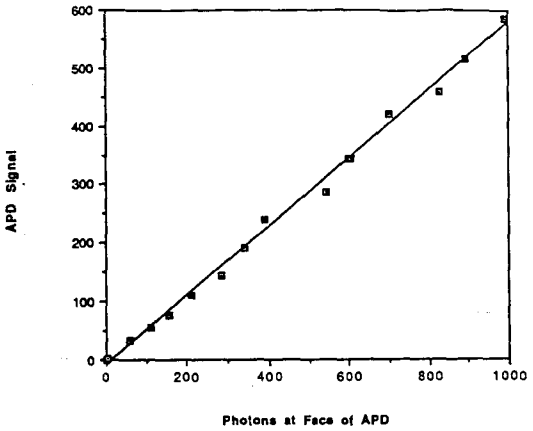


Fig. 11. Response of an avalanche photodiode to varying amounts of incident light. The scatter of the data above and below the straight line was reduced by stabilizing the temperature of the APD.

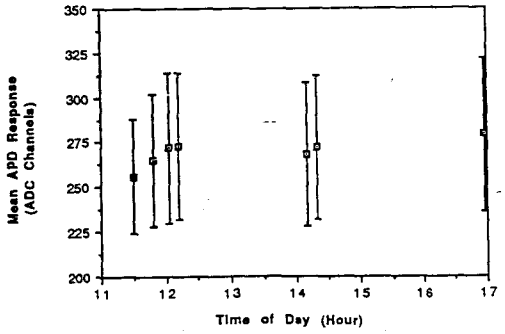


Fig. 12. Variation of APD response with time of day. Thermal stabilization of the APD eliminated this variation. Note that error bars indicate the statistical spread in the signals. The error on the mean is of order one ADC count.

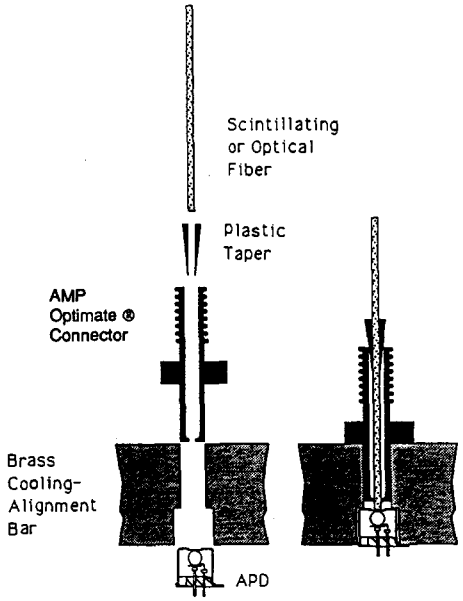


Fig. 17. Optical Alignment Procedure. The APD is mounted in a thermally stabilized brass bar.

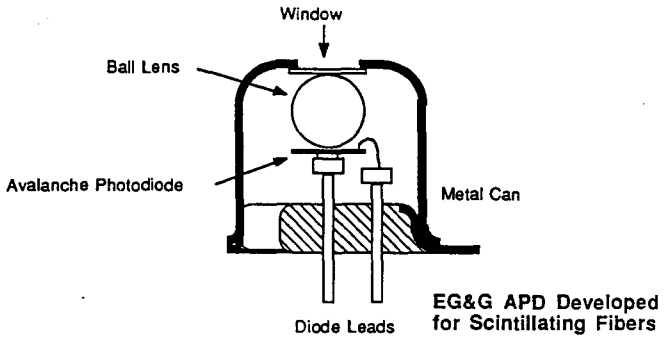


Fig. 18: Cross section of the Avalanche Photodiode developed by EG&G Optoelectronics for use with 1mm dia. fibers. The APD itself is only 0.5mm wide.

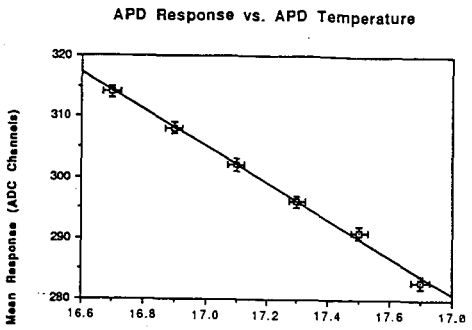


Fig.20. Variation in Avalanche Photodiode response as a function of temperature. The data were taken by monitoring the system for an extended period of time while the temperature went through its normal cycle. The line represents a least-squares fit.

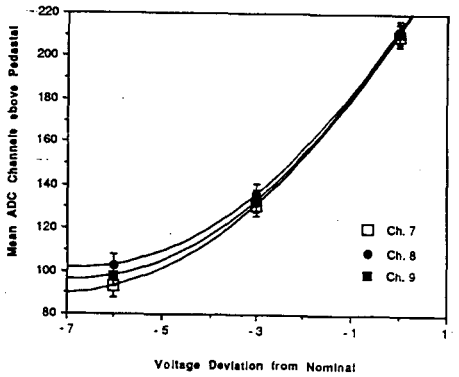


Fig. 21. The gain variation of three channels of APD as the global bias voltage supply is varied. The lines are the results of quadratic fits to the data. The error bars represent errors on the means of the distributions.

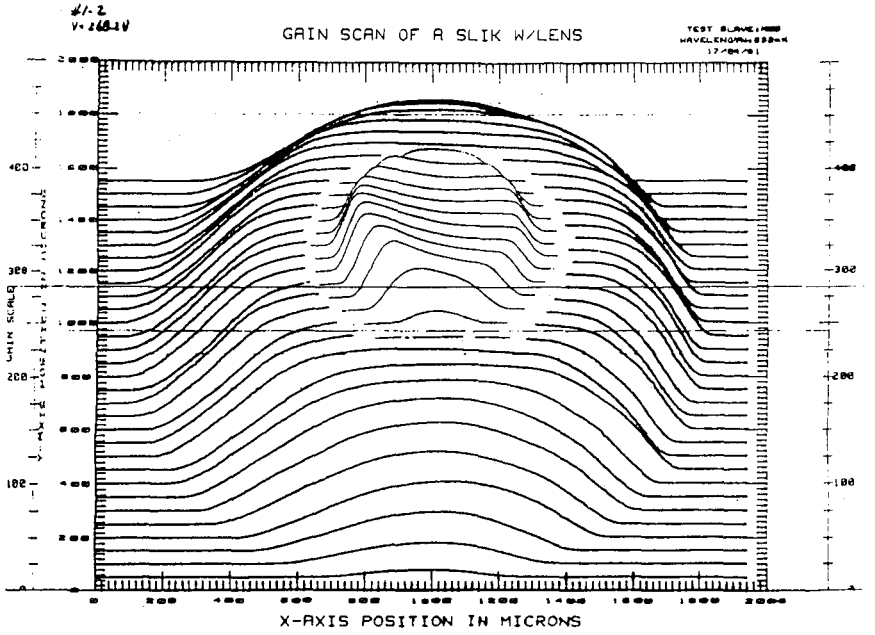


Fig. 19. Map of the response of the APD - Ball Lens assembly. Although the APD itself has diameter only 0.5mm, the lens collects light over about a 1.2 mm.

SDC
Cluster matching M.C. — Wu, Rusack.

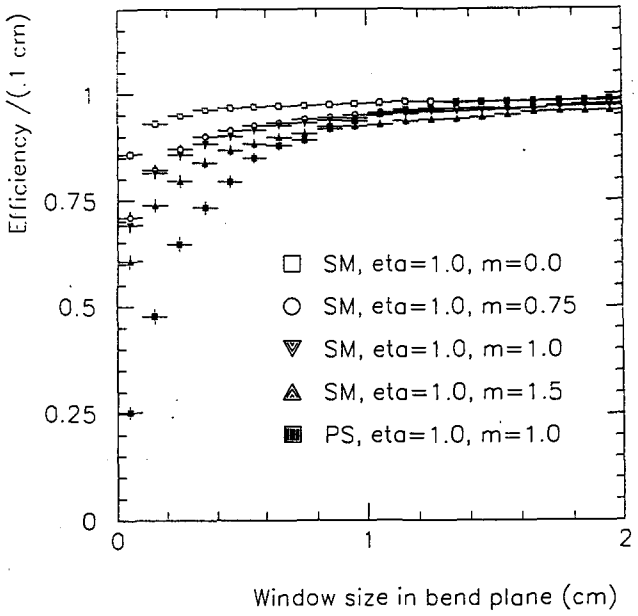


Figure 3: Efficiency of finding a shower as a function of the window size in bend plane for different amount of tracking materials at $\eta = 1.0$

Wu/Rusack.

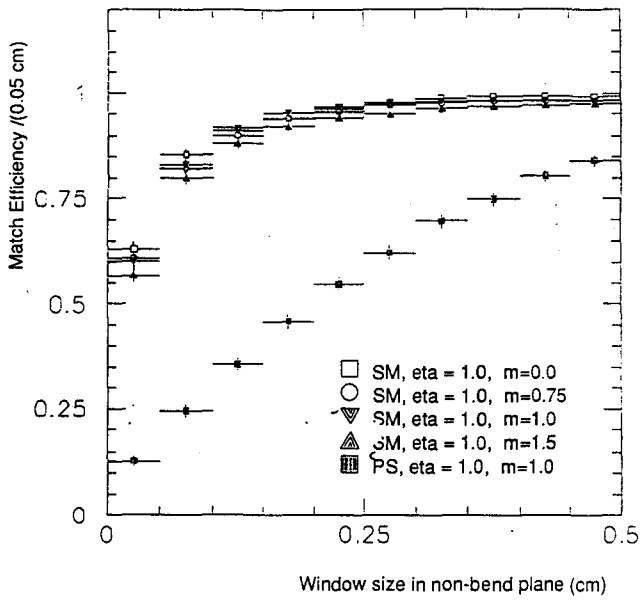


Figure 4: Efficiency of finding a shower as a function of the window size in non-bend plane for different amount of tracking materials at $\eta = 1.0$

RADIATION DAMAGE IN SCINTILLATORS AND FIBERS

University of Florida, J. K. Walker

The role of T_g, the glass temperature

"LOW T_g THERMOPLASTICS", THAT IS WITH T_g = 40 - 50 C,

- GOOD MECHANICAL PROPERTIES (RIDGID, NOT "RUBBERY")
- SHOW RAPID RELAXATION OF RADIATION INDUCED STRESS.

EG PMMA → PEMA (ETHYL METHYL)

→ PiBMA (isoBUTYL METHYL) etc.

THE HEAVIER THE SUBSTITUTION RADICAL, THE LOWER THE T_g.

OTHER APPROACHES INCLUDE

- COPOLYMERIZATION WITH LOWER T_g POLYMERS,
- BLENDING HIGH AND LOW T_g POLYMERS (POST POLYMERZATION)
- SIMPLY ADDING A PLASTICIZER TO REDUCE T_g (TEMPORARY??)

OTHER ACTIVITIES:

- PLATE CASTING, MOLDING (COMPRESS(ON, INJECTION)
- FIBER SPINNING, INCLUDING BICOMPONENT (CLAD) FIBERS

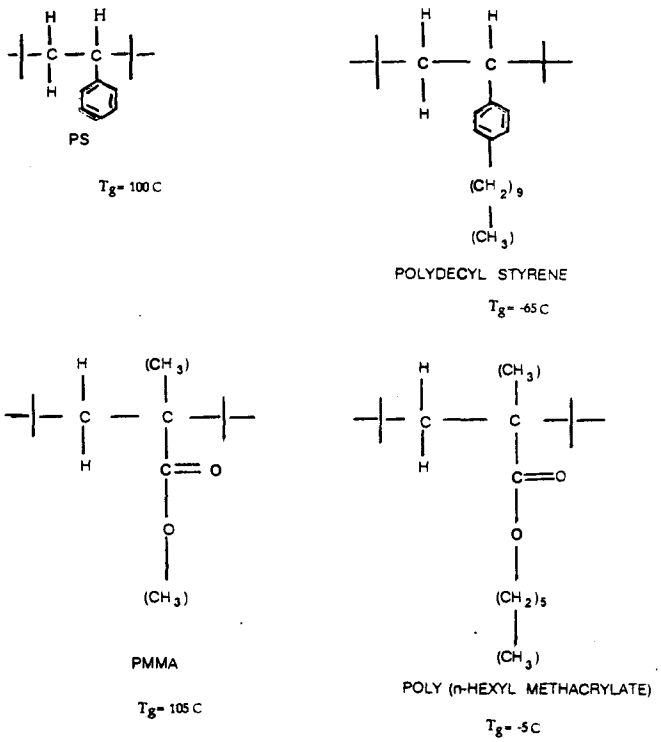


FIGURE 5.

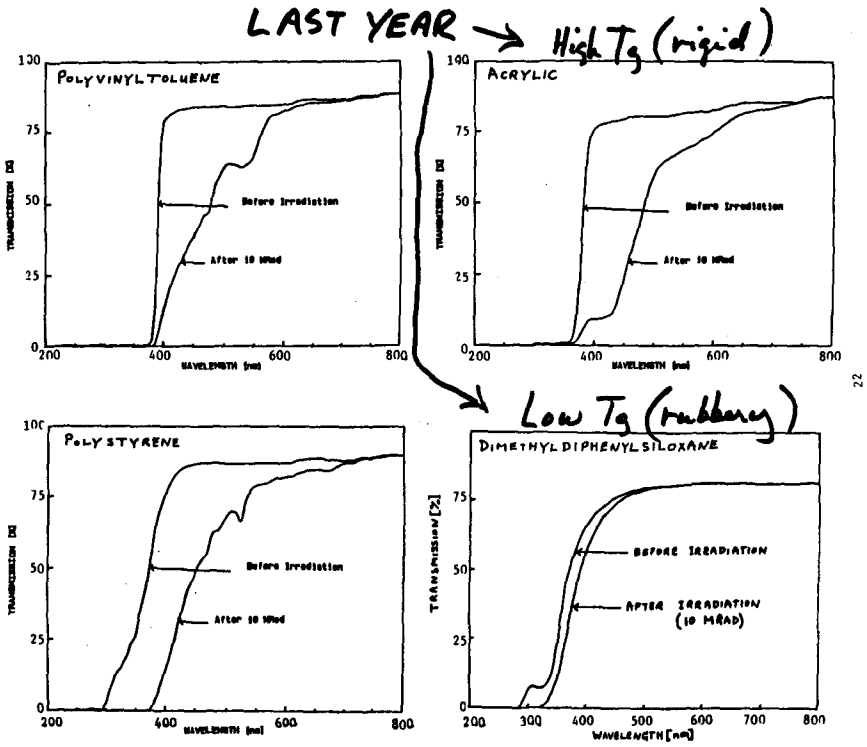
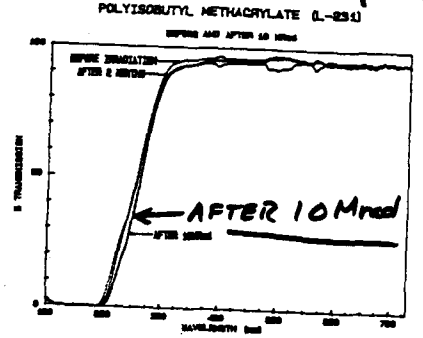


FIGURE 1

22

NEW: PiBMA is mechanically "rigid"

PiBMA



PMMA

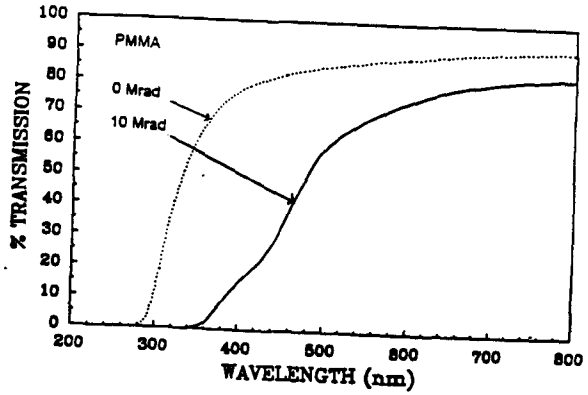
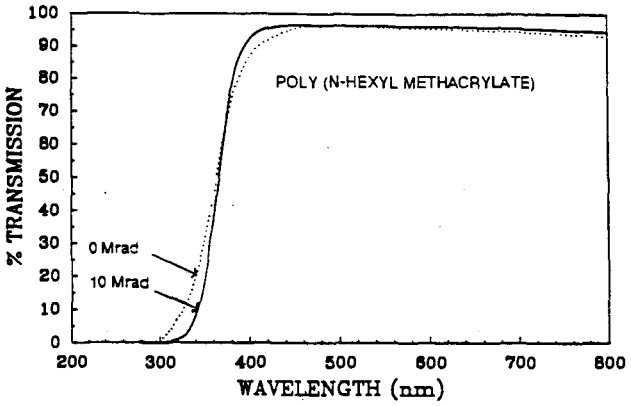


FIGURE 9

30



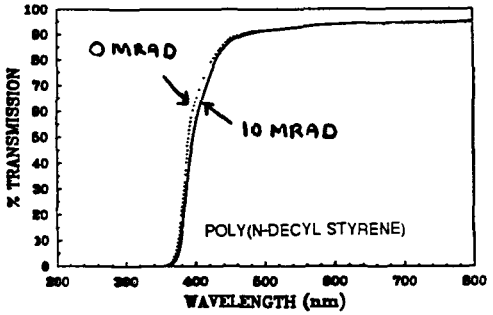


FIGURE 6.

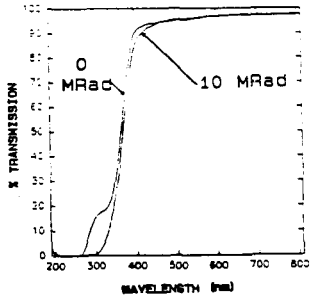


FIGURE 11. PHFBM CLADDING MATERIAL

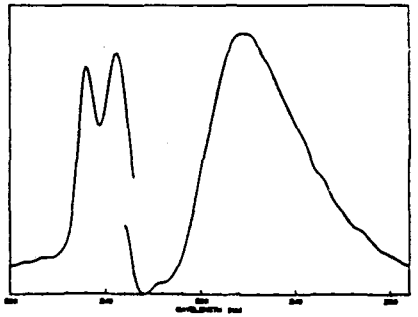


FIGURE 12. ABSORPTION - EMISSION OF PS

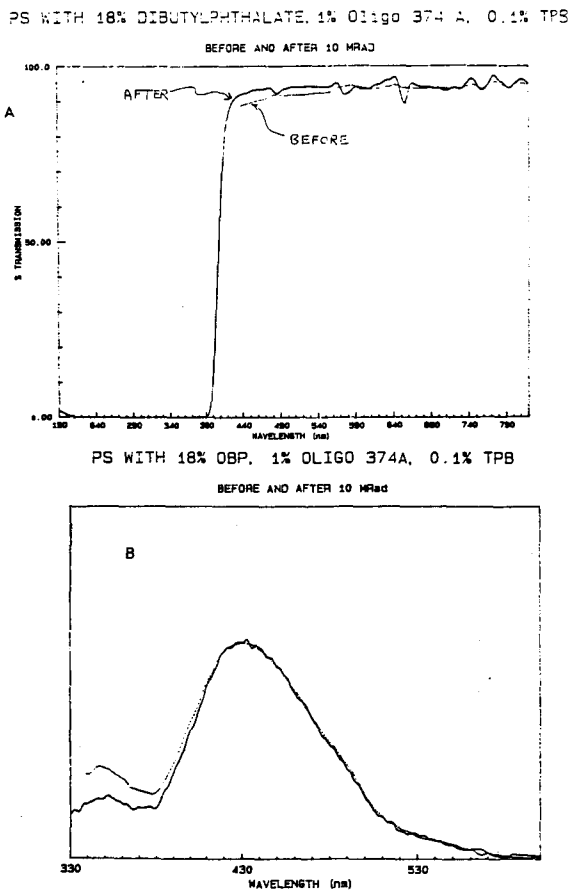
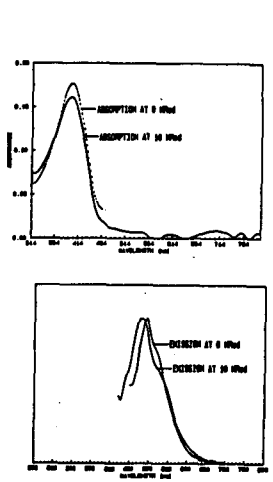
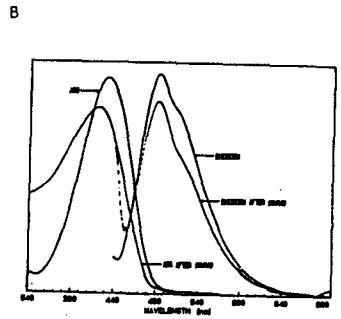


FIGURE 17



Absorption and emission spectra of Coumarin 545 in PMMA, before and after irradiation in air.



Absorption and emission spectra of Fluorol 7GA in PMMA, before and after irradiation in air.

FIGURE 16.

CONCLUSIONS

1. RAD HARD, HEAT PROCESSIBLE POLYMERS
   - •PLASTICISED POLYSTYRENE
   - •POLY IsoBUTYLMETHACRYLATE
   - •PhFBM (low refractive index....cladding material)
2. RAD HARD FLUORS
   - •PRIMARY FLUOR — oligo 374A
   - •SECONDARY FLUOR — TPB
   - •WAVELENGTH SHIFTERS — Coumarin 545; Fluorol 7GA

#255

THE COMPENSATING SCINTILLATOR PLATE CALORIMETER SUBSYSTEM COLLABORATION FY91 REPORT TO THE SUPERCONDUCTING SUPERCOLLIDER LABORATORY[1]

H. B. Crawley, W. T. Meyer, E. I. Rosenberg
Ames Laboratory, Iowa State University

R. E. Blair, R. Hagstrom, P. Job, T. Kirk, L. Nodulman, L. Price,
J. Proudfroot(PI), H. Spinka, R. Talaga, H.-J. Trost,
D. Underwood, R. G. Wagner, A. B Wicklund, J. Dawson, T. Eckenberg,
D. Morgan, N. Hill, J. Nasiatka, E. Petereit
Argonne National Laboratory

C. Hurlbut
Bicron Corperation

L. Bartoszek, A. Baumbaugh, M. Binkley, A. Bross, A. Byon, D. Finlay,
G. W. Foster(PI), J. Freeman, D. Green, D. Kim, R. Vidal,
W. Wu, R. Yarema, J. Hoff, T. Zimmerman
Fermi National Accelerator Laboratory

V. Hagopian, K. Johnson, P. Rulon, H. Wahl, J. Xu, J. Thomaston,
K. Bertoldi, K. Hu
Florida State University

D. E. Groom
Lawrence Berkely Laboratory

A. Fazely, R. Imlay, R. McNeil, W. Metcalf
Lousiana State University

C. Bromberg, J. Huston, R. Miller, R. Richards
Michigan State University

R. Gustafson
University of Michigan

L. Bolen, L. Cremaldi, B. Moore, J. Reidy
University of Mississippi

R. G. Alsmiller, Jr., C. Y. Fu, T. Gabriel
Oak Ridge National Laboratory

V. E. Barnes, A. F. Garfinkel, A. T. Laasenen, J. Tonnison
Purdue University

A. Bodek, H. Budd, P. de Barbero, W. Sakumoto, R. Walker, H. W. Zheng,
S. Ohlsen, T. Haelen
University of Rochester

A. Bhatti, T. Chapin, N. Giokaris, K. Goulianos, P. Melese,
R. Rusack, S. White
Rockefeller University

T. Handler
University of Tennessee

B. Lu, L. Mo, L. E. Piilonen, T. Nunamaker
Virginia Polytechnic Institute

M. Burke, C. Einholf, D. T. Hackworth, T. Horduhay, D. Marshik,
D. Scherbarth, R. Swensrud
Science and Technology Center, Westinhouse Electric Company

D. Carlsmith, C. Foudas, D. Loveless, D. Reeder, W. H. Smith,
M. Jaworski, J. Lackey, P. Robb
University of Wisconsin

[1]We gratefully acknowledge the efforts of the following individuals in carrying out the MP Testbeam Program: D. Lopiano, D. Hill, D. Grosnick, *Argonne Nat. Lab.*, A. T. M. Wang, J. Wilson, *U. of South Carolina*, P. Cushman, S. Hou, C. Ishida, Yale U., M. Hulbert, D. Ruuska, I. Leedom, *Northeastern U.*, H. Fenker, K. Morgan *S. S. C. L.*

CENTRAL CALORIMETER CONCEPTUAL DESIGN REPORT

The Solenoidal Detector Tile/Fiber Collaboration*

September 4, 1991

* *written and edited by* L. Bartoszek, A. Byon-Wagner, G. W. Foster, J. Freeman, D. Green, S. Gourlay, R. Wands *Fermi National Accelerator Laboratory*, V. Guarino, N. Hill, T. B. W. Kirk, L. E. Price, J. Proudfoot, L. Nodulman, A. B. Wicklund *Argonne National Laboratory*, V. E. Barnes *Purdue University*

CONTENTS

- INTRODUCTION
- PHYSICS REQUIREMENTS AND PERFORMANCE
- MODEL A TILE/FIBER DESIGN
- MODEL B TILE/FIBER DESIGN
- MAGNETIC FLUX RETURN
- OPTICAL SYSTEM
- PHOTON DETECTOR AND ASSOCIATED ELECTRONICS
- RADIATION HARDNESS OF TILE/FIBER CALORIMETRY
- CALIBRATION
- SHOWER MAXIMUM DETECTOR
- PROTOTYPE AND TEST BEAM PROGRAM
- RISK ASSESSMENT
- COST AND SCHEDULE
- SAFETY
- FUTURE PLANS AND SCHEDULE FOR DECISIONS

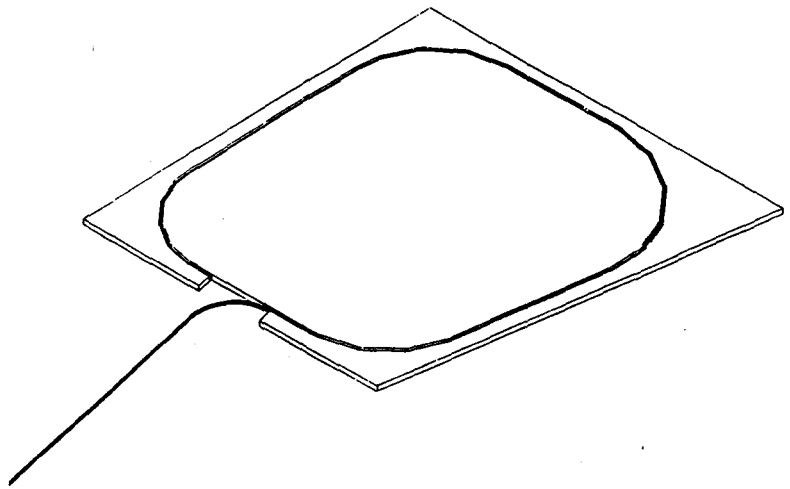


Figure 6.1 Sketch of Sigma Tile fiber route

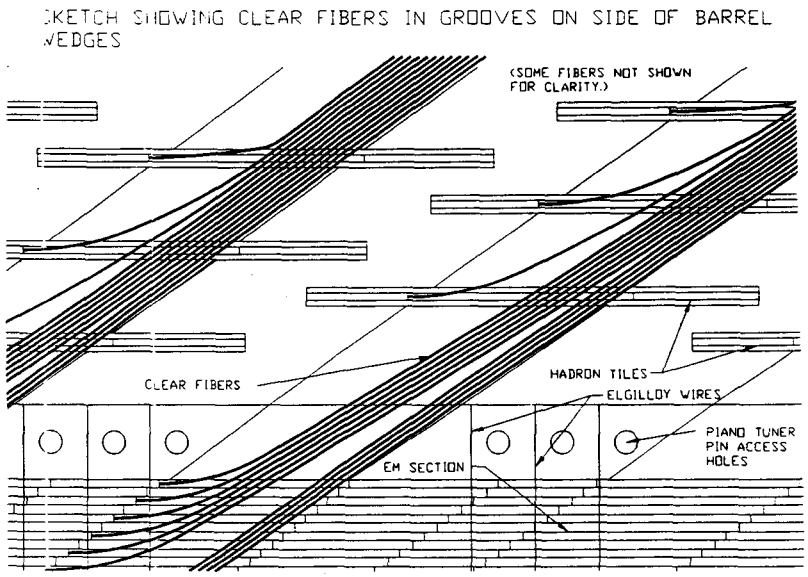


Figure 3.7 - Side view of the Barrel EM calorimeter, showing fiber routing pattern and "piano wires" for stack compression.

SEVERAL RADDAM. TEST CALORIMETERS.
TESTED @ Beijing, KEK, Saclay ...

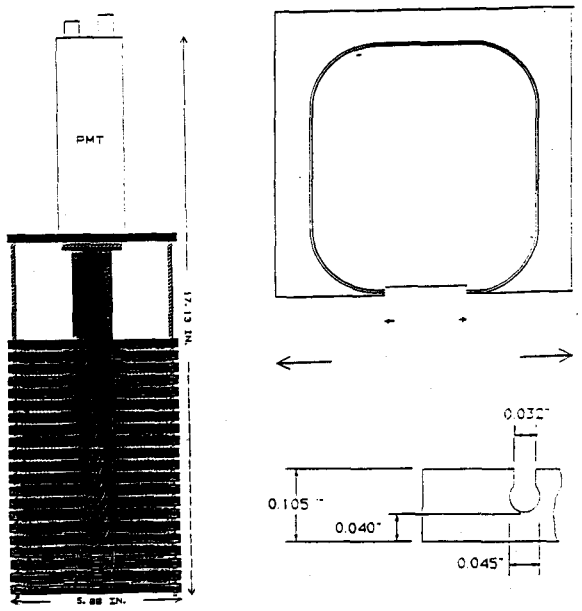


Figure 8.2 Radiation hardness test beam module.

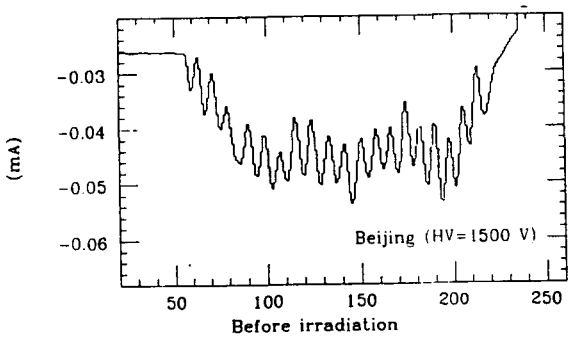


Figure 8.3 longitudinal source scan of a Beijing module.

NOTE: LATERAL UNIFORMITY SURVIVES AS RAD DAM PROGRESSES (ESSENTIAL TO SDC STRATEGY)

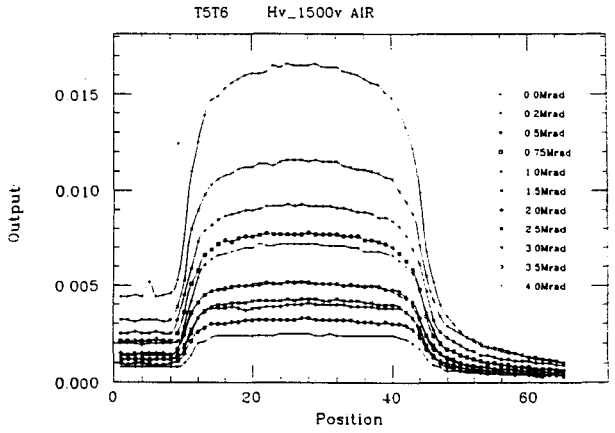


Figure 8.4 Transverse source scan of a Beijing module. The module was rapidly irradiated with an accumulated dose of 4 Mrad. Note that the Cs source "size" makes short wavelength structure invisible. The induced nonuniformity is seen to be small.

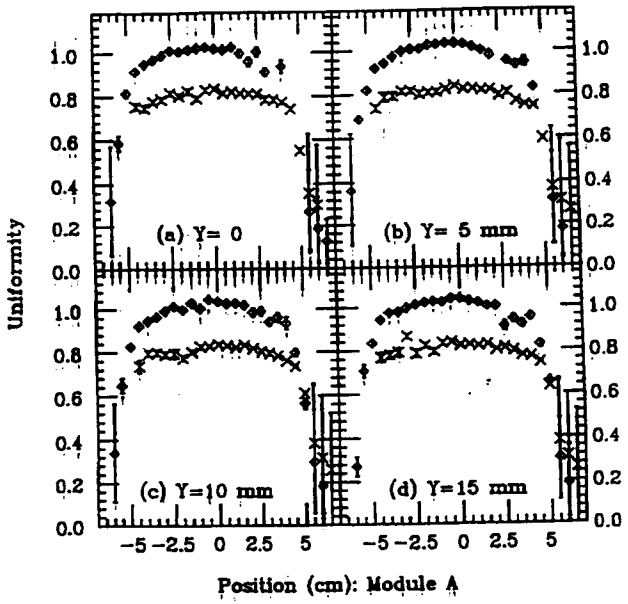


Figure 8.5 Transverse scan using an electron beam for the KEK tests. Data are shown for various strips traversing the tile both before and after 1 Mrad. applied dose.

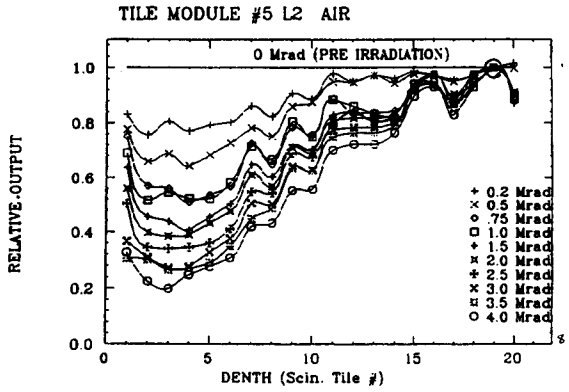


Figure 8.6 Damage profile from source tube scans immediately after irradiation. The data is normalized to no damage at depth t=19.

SDC STRATEGY:

1. Barrel Calorimeter ok (SCSN 81, for example)
2. Parts of Endcap Calorimeter will be replaced every few years.
3. Develop systems that are more radhard.
   ↳ to longer wavelength → green.

lateral uniformity preserved during damage.

- Monitor light loss
- Adjust weighting of the 2 longitudinal E.M. compartments.
- Change the neutral density filters at the phototubes → this gives a tile-by-tile adjustment. (but EATS PHOTONS!).

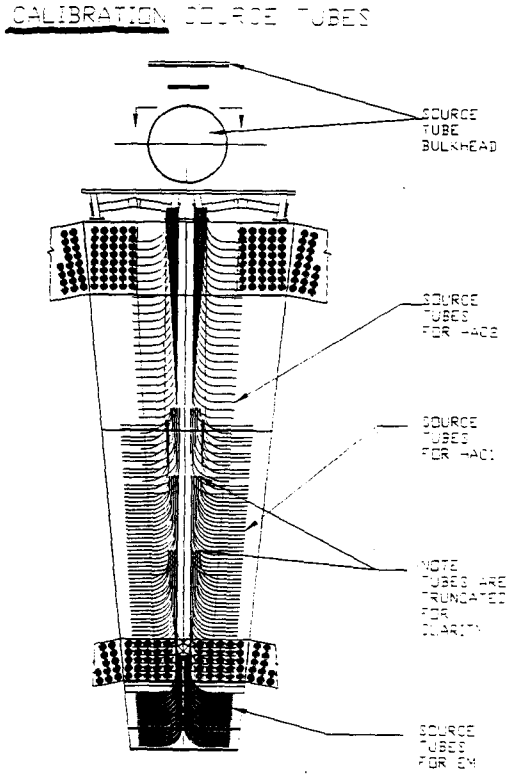


Figure 9.2 Layout of the source tubes for a single barrel wedge. Two basic tyubes fan out to the 2 towers of the wedge. Each tile in the wedge is scanned transversely.

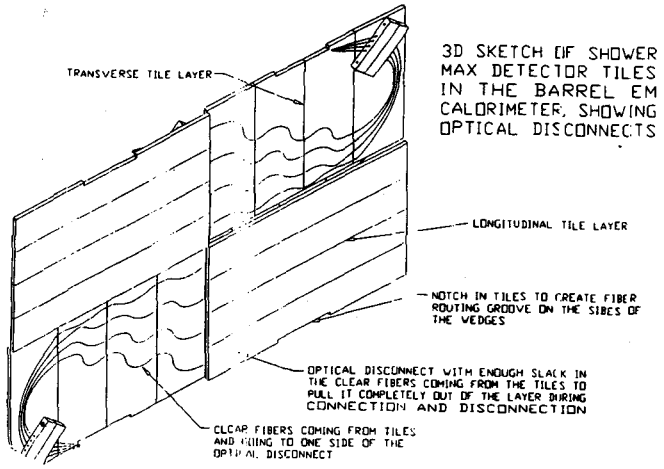


Figure 10.2 Three dimensional sketch of the barrel SM detector. The crossed arrays are spliced to clear fibers going to optical disconnects.

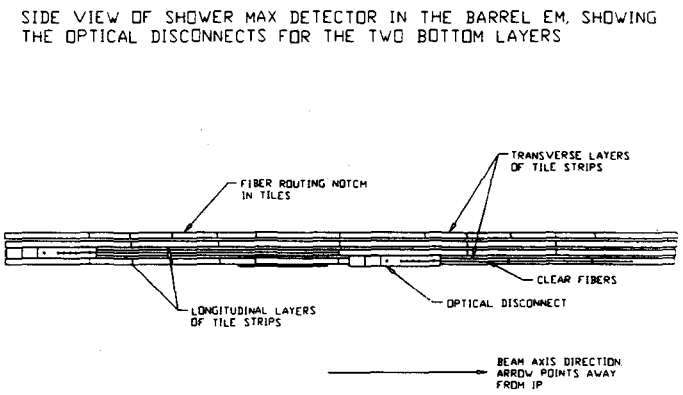


Figure 10.1 Side view of the Shower Maximum detector for the barrel . The crossed hodoscopic planes are evident, along with the optical disconnects.

The NOMAD Fiber-Based Electromagnetic Calorimeter Prototype

TEST BEAM RESULTS FROM CERN.

The NOMAD Collaboration
(Neutrino Oscillations with a MAgnetic Detector)
WA96 at CERN, approved September 1991
LPC (Algiers), Boston U., CERN, Dubna, Paris College de France,
Paris Univ. VI and VII, Michigan, Saclay, Zagreb

Final calorimeter will be 3 x 3 m^2 -- 100 times prototype size
Total of 36,000 10 x 10 cm^2 tiles.
Experiment will run in 1994.

Prototype Description and Test Beam Results

Construction (see Figs. 1,2)

* Lead/scintillator interleaved sandwich.
* 9 towers, 10 x 10 cm^2 transverse cross section.
* 40 planes of 3 mm thick lead, 40 planes 10 mm thick NE110 scintillator.
* Individual tiles read out by single embedded 2 mm diameter Y-7 (Kyowa, Japan) wavelength-shifting fiber, polystyrene base, running diagonally in tile surface (see Fig. 2), alternating from layer to layer.
* WLS fibers are fused to 2 mm diameter clear fibers, polystyrene base (see Fig. 2).
* The 40 clear fibers from each tower are 4 m long and are coupled to 1 inch diameter photomultiplier tubes.

"Coat-hangar" construction of prototype allows insertion of different thicknesses of lead radiator.

Test Beam Results (see Figs. 3, 4, 5, 6)

* CERN X5 beam in West Area; electrons and pions, energies ranging from 3 to 100 GeV, August - September, 1991.

* In plots which follow, total energy is sum of 9 tower energies, normalized with 50 GeV electron beam in center of each tower.

Fig. 3: Energy Resulution vs. Energy shows $\sigma(E)/E = 0.65\% + 8.96\% / \sqrt{E}$
over electron beam energies from 3 to 90 GeV.

Fig. 4: Deviations from linear response are less than 1.5% for energies from 10 to 90 GeV.

Fig. 5: Fine uniformity scan around face of central tower, with corresponding scan positions shown. Plot shows deviation from response at center of central tower. Maximum nonuniformity < 7%, near edges of scintillator tiles.

Fig. 6: Fine uniformity scan moving horizontally across vertical crack between two towers. Delay-wire chambers in beam determine incident position to 200 μm. Note supressed zero on vertical scale. We see 10% loss of signal at crack due to 1.) lower light collection at tile edges and 2.) loss of particles in crack (approx. 0.5 mm wide).

Studies with preradiator performed, data to be analyzed.
Hadron rejection studied with pions, data to be analyzed.

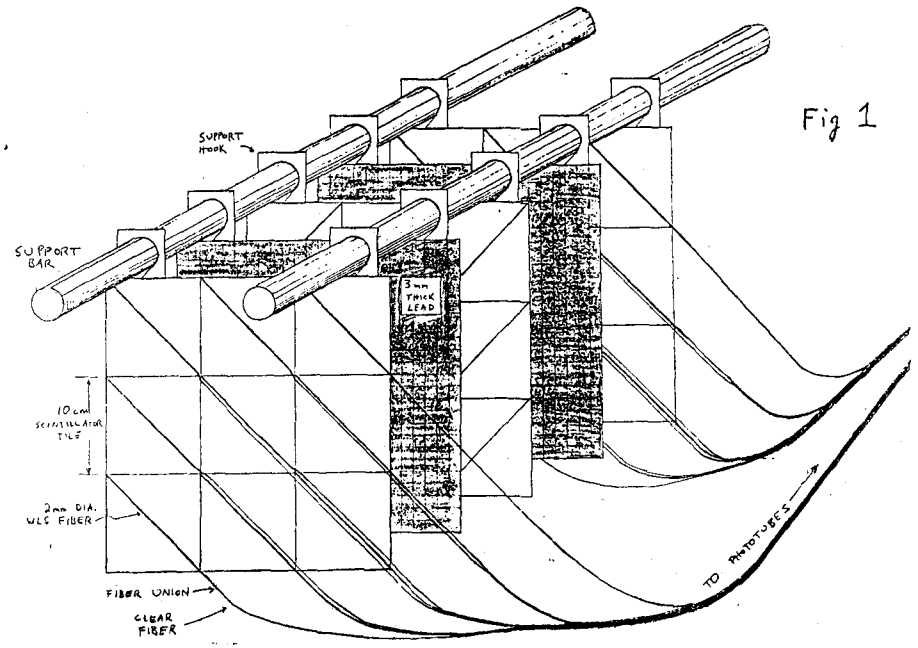
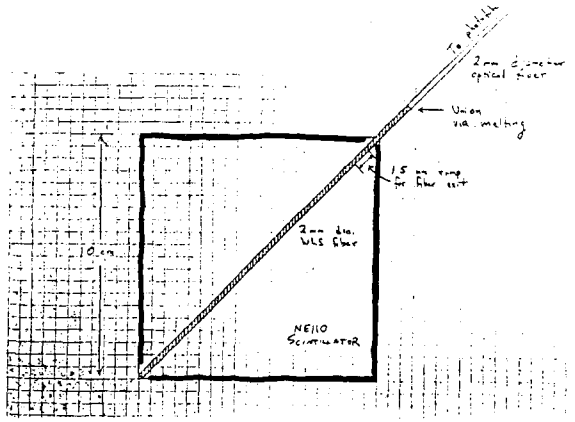

SUPPORT HOOK
SUPPORT BAR
3 mm THICK LEAD
10 cm SCINTILLATOR TILE
2 mm DIA. WLS FIBER
FIBER UNION
CLEAR FIBER
TO PHOTOTUBES

Fig 1


2 mm diameter optical fiber
Union via melting
2 mm dia. WLS fiber
10 cm
NE110 SCINTILLATOR

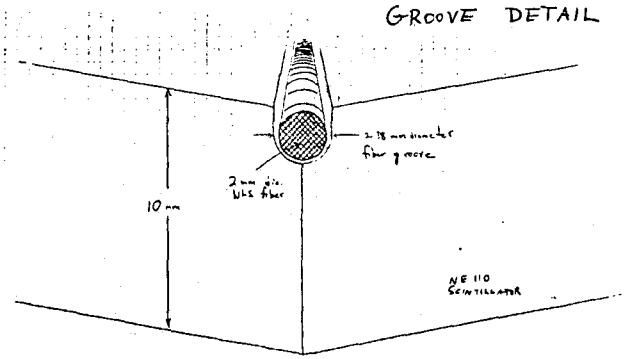

GROOVE DETAIL
2 mm dia. WLS fiber
10 mm
NE 110 SCINTILLATOR

Fig. 2

3mm Pb 9%/√E

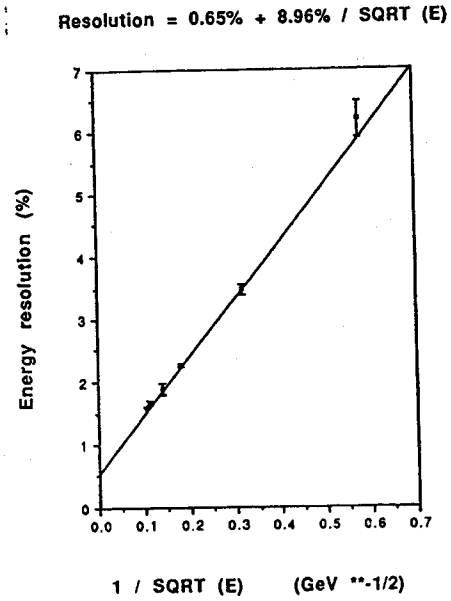


Fig. 3

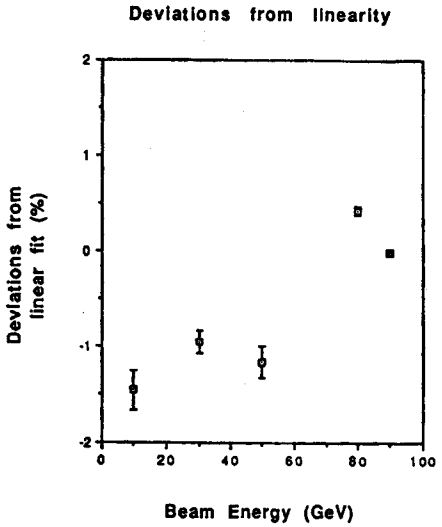
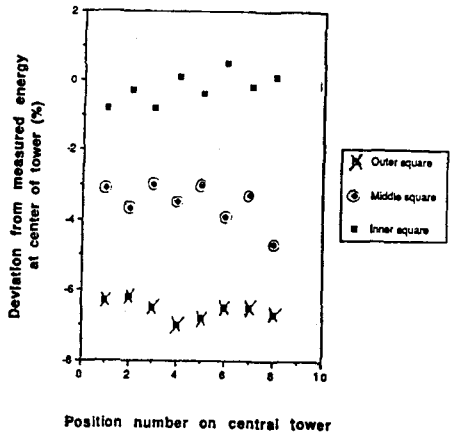


Fig. 4


Deviation from measured energy at center of tower (%)
Position number on central tower
Outer square
Middle square
Inner square

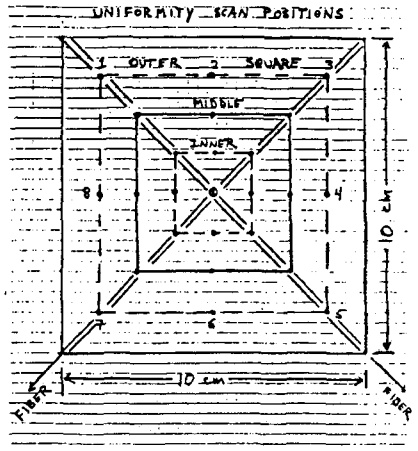

UNIFORMITY SCAN POSITIONS
OUTER
SQUARE
MIDDLE
INNER
10 cm
10 cm
FIBER
FIBER

Fig. 5

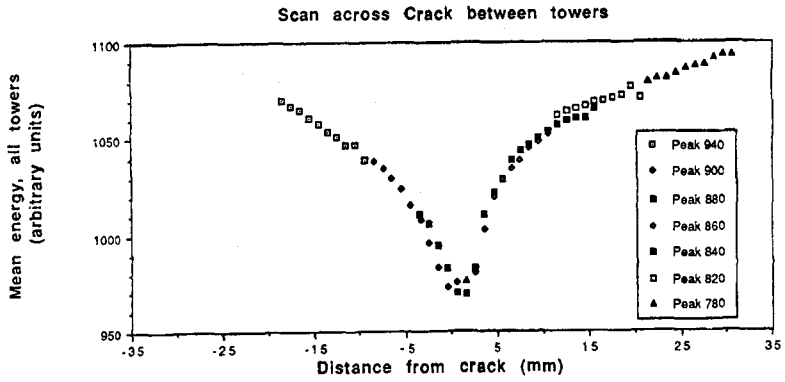

Scan across Crack between towers
Mean energy, all towers (arbitrary units)
Distance from crack (mm)
Peak 940
Peak 900
Peak 880
Peak 860
Peak 840
Peak 820
Peak 780

Fig. 6.

CALORIMETRY II

Presented by Bill Frisken, LBL/York U.

Corpus Christi, Oct. 16/1991

OUTLINE:

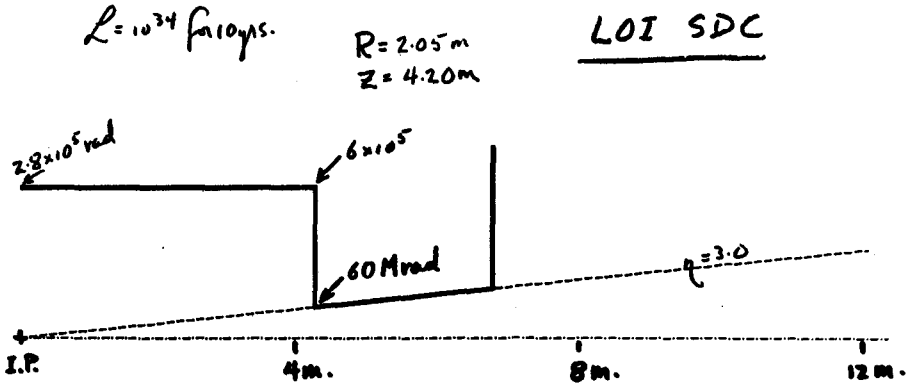
1. INTRODUCTORY REMARKS: THE SSC ENVIRONMENT

2. LIQUID SCINTILLATOR
   - #247 REIDY/KAMISHKOV
   - #257 WHITE/HUSON

3. WARM LIQUID IONIZATION
   - #225 WALIC
   - #243 FASTMS

4. PRESHOWER/SHOWERMAX #250 CUSHMAN/RUSACK

5. PLASTIC SCINTILLATOR
   - #249. RADIATION DAMAGE TO TILES, FIBERS. WALKER
   - #235. COMPENSATING TILE/FIBER. FOSTER/PROUDFOOT
   - TEST DATA FROM "NOMAD" PROTOTYPE. Greg SNOW



Research and Development for Supercollider Calorimetry: The European Scene

C. Fabjan

Research and Development for Supercollider Calorimetry: The European Scene

C.W. Fabjan
CERN, Geneva, Switzerland

1. Introduction

At present, most of the European R&D effort on calorimetry for Large Hadron Collider (LHC) experiments is being carried out in a vigorous programme coordinated through the 'Detector R&D Committee' (DRDC). In addition, the Lepton Asymmetry Analyses (LAA) project is supporting a major programme on fibre calorimetry. Progress achieved during the past year will be summarized in this note. Several, more modest, national efforts have been initiated recently, such as an exploratory study on 'forward' ($\eta > 3$) calorimetry concepts pursued at ITEP Moscow and IHEP Serpukhov. These efforts, too recent to have yet produced results, will not be further discussed here.

The information available will be presented in three sections. In Section 2, test results will be discussed to demonstrate the potential suitability of a number of calorimeter concepts, including both new results on homogeneous electromagnetic (e.m.) devices and data on sampling detectors, suitable for e.m. and hadronic calorimetry. In Section 3, some new information related to the signal processing from calorimeters is presented. A few comments on the status of the work on subsystems and the program for the design of a complete calorimeter will be sketched in Section 4.

2. Performance of Calorimeter Concepts

2.1 Homogeneous Electromagnetic Calorimeters

Very–high–performance e.m. calorimetry is being pursued by three collaborations. The 'Crystal Clear' group (RD18) has launched a very systematic search for and study of scintillating crystals [1]. The properties of interesting candidate crystals are tabulated in Table 1. The 'ideal' crystal has a very short radiation length and Moliere radius, a fast ($\tau_{decay} \leq 30$ ns) fluorescent component, is made from low–cost raw materials, and is easily grown [2]. One promising candidate is CeF_3 [3], which has recently been shown to tolerate a radiation of more than 1000 Gy,

Table 1: Characteristics of Crystals [1]

Crystal	Density ($g\,cm^{-3}$)	Radiation length (cm)	Moliere radius (cm)	Decay time (ns)	Peak emission (nm)
BGO	7.13	1.11	2.33	300	480
BaF_2	4.89	2.06	3.39	0.6, 620	210, 310
CeF_3	6.16	1.68	2.63	5, 20	300, 340
YAP: Ce	5.35	2.83	2.82	35	390
GSO: 0.5% Ce	6.71	1.39	2.42	55	435
GSO: 2.5% Ce	6.71	1.39	2.42	31	450
ThF_4	6.32	1.18	2.71	≤ 25	315, 330, 450
$BaLiF_3$	5.24	2.13	3.13	≤ 25	435
$LiYbF_4$	6.09	1.56	2.70	≤ 25	≈ 450
PbF_2	7.77	0.93	2.21	Not (yet) scintillating	

provided the impurity levels can be sufficiently reduced. Another crystal with 'clear' potential is PbF_2; luminescence has not yet been observed but crystals are being grown where the high degree of the lattice symmetry will be broken, an arrangement which is considered more favourable for scintillation.

The alternate route towards superb e.m. calorimetry explores 'Noble Liquids'. The LAA/RD14 Collaboration is concentrating on an evaluation of the fundamental properties of liquid xenon (LXe) [4]. Some of the measurements are given in Table 2.

Table 2: Results on LXe Calorimetry [4]

Measurement	Energy resolution σ/E (ionization)	Angular resolution (5 longitudinal segments)	Light (charge) output
Result	$\frac{0.004}{\sqrt{E}} \oplus 0.004$	$\sigma_\theta = 1.4$ mrad (10 GeV) $\sigma_\theta = 1$ mrad (25 GeV)	W = 35 eV/photon (fast + slow components) W' = 14 eV/electron

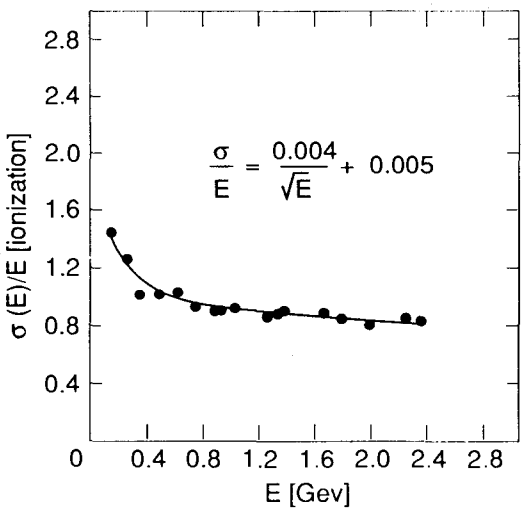


Fig 1 Energy resolution observed in a homogeneous LKr e.m. calorimeter. Note that the deposited energy was delivered with short pulses of 100 keV electrons of different intensities. The values for the energy resolution should therefore be considered as lower limits. Very similar results are expected for LXe [5].

The measured energy resolution is shown in Fig. 1. The (anti)correlation between the produced charge and scintillation light has also been measured: it can be parametrized as [5]

$$E = K \cdot (Q + \alpha\, Sc).$$

Interesting information is starting to become available from the NA48 Collaboration [6]. This group is preparing a very–high–statistics CP–violation experiment at the CERN SPS, requiring the precision measurement of neutral and charged pions. A liquid krypton (LKr) homogeneous calorimeter has been chosen as the device for the $\pi^o \rightarrow \gamma\gamma$ spectroscopy. The design specifications are given in Table 3 [7]. It is seen that, in many respects, this calorimeter (termination scheduled for 1993) meets LHC/SSC specifications. A conceptual view of the electrode arrangement is shown in Fig. 2a; the expected energy resolution is presented in Fig. 2b.

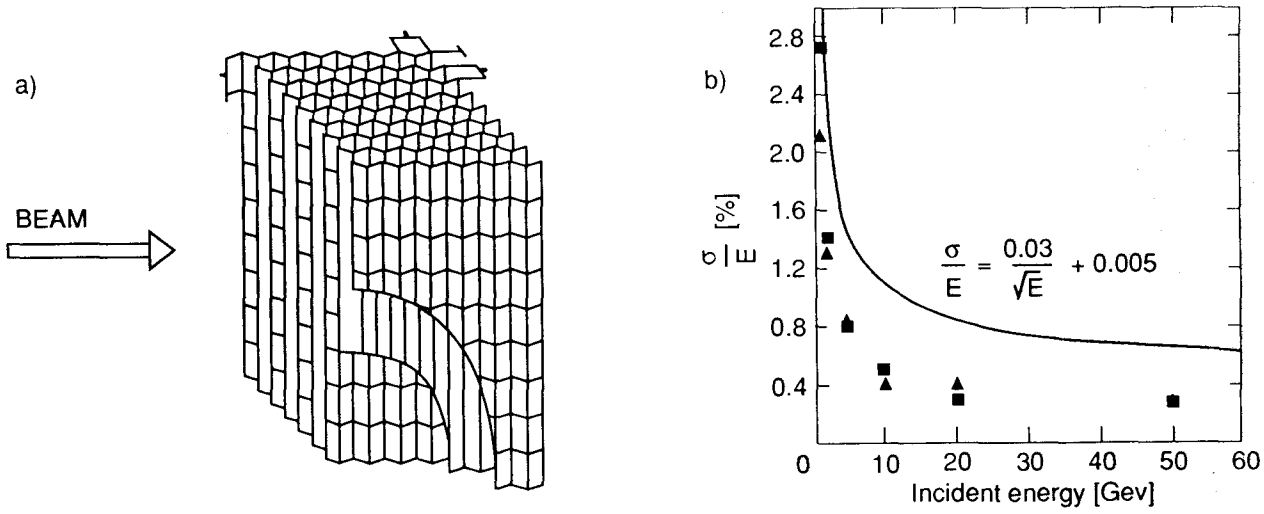


Fig 2 a) Schematic view of the electrode arrangement for the NA48 LKr calorimeter. The electrodes are made from 125 μm thick Kapton with deposited Cu–electrodes. They may be arranged in an accordion–like shape to suppress 'channelling';
b) estimated energy resolution.

Table 3: Design Specifications of the NA48 LKr e.m. Calorimeter [7]

Specification	Expected energy resolution σ/E	Tower size (cm x cm)	Number of towers	Signal–shaping time	Signal digitization frequency
Value	$\frac{0.03}{\sqrt{E}} \oplus 0.005$	2 x 2	11000	τ_{peak} = 100 ns	40 MHz

2.2 Sampling Calorimeters

Whilst homogeneous e.m. calorimetry offers undisputed advantages for the precision measurement of e.m. showers, high quality e.m. sampling calorimetry is arguably an acceptable alternative [8]. A key to success is both a reasonably small sampling term, $(\sigma_{sample}/E) \leq (0.1/\sqrt{E})$, combined with excellent control over the 'constant' terms $(\sigma_{const}/E) \leq 0.002$.

In Europe, two techniques are being pursued. One is based on scintillating fibres [9, 10], the other (RD3) on LAr [11]. Both concepts work well, because – not too surprisingly – the performance of a sampling calorimeter is rather insensitive to the direction of the readout sensor: a scintillating fibre or a LAr gap oriented almost parallel to the incident particle will perform almost as well as a device with the readout sensors oriented perpendicularly [12]. The two groups perfecting the scintillating fibre technique have already obtained a number of impressive results. The most significant one concerns the demonstration that these techniques permit the construction of almost perfectly compensating hadron calorimeters: fibres embedded in a lead matrix with the ratio of the volume of lead/fibres = 4/1 will 'compensate' over a large range of particle energies. Recent work of the two groups concentrated on performance and design aspects relevant for an LHC/SSC calorimeter:

- construction and performance of calorimeters with projective geometry;
- electron/pion discrimination;
- longitudinal segmentation.

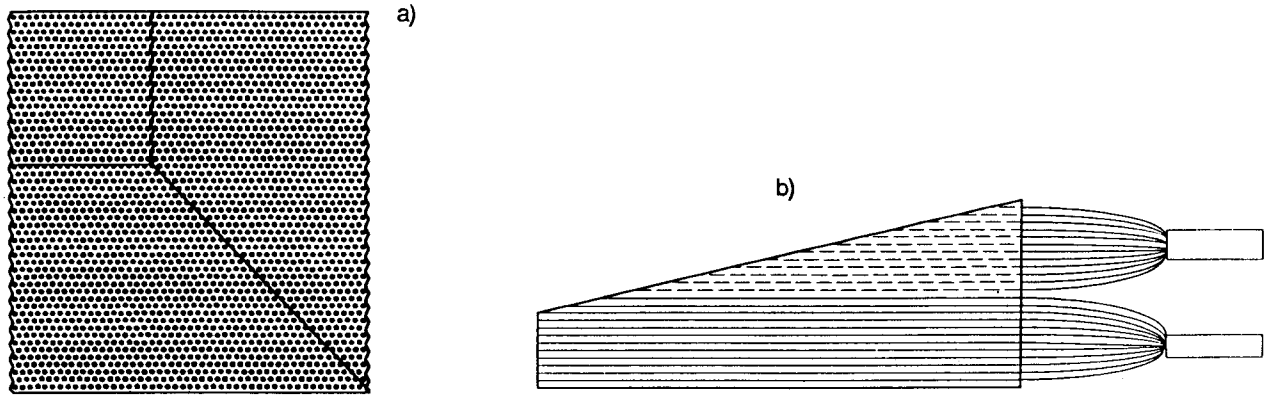


Fig 3 Schematic view of a scintillating fibre calorimeter with projective tower geometry. The entrance face is 4 x 4 cm^2 and the output face is 10 x 10 cm^2 (Fig. 3a). The total length of each module is close to 2 m (Fig. 3b) [10].

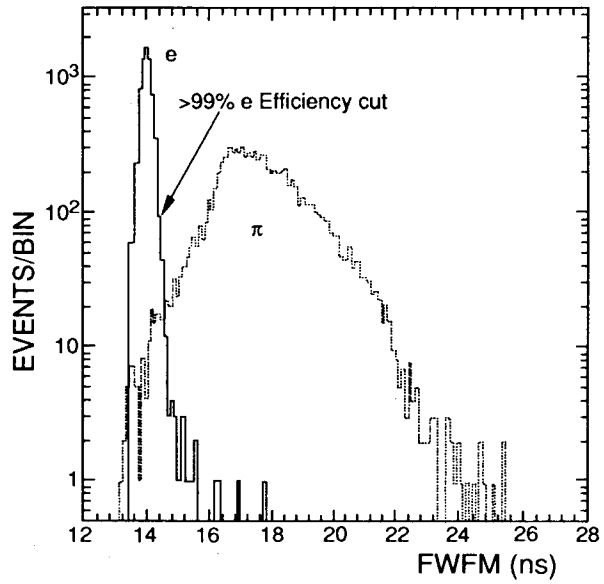


Fig 4 Time distribution (measured at one fifth of maximum) of shower lengths induced by electrons and pions. A π–discrimination of approximately 10^3 can be achieved by accepting showers with a duration of less than 15 ns.

The example for a tower arrangement with projective geometry is shown in Fig. 3. Electron/pion separation may be achieved in the conventional manner through longitudinal subdivision; alternatively [12,13], the time structure of the showers, which is quite different for e.m. and hadronic showers, may be used in a sensitive way (Fig. 4). Rejections of pions of the order of ~ 10^3 have been obtained with either of these two approaches.

It should be noted that the e.m. and the hadronic segments do not 'naturally' have the same structure, thus indicating a rather fundamental reason for a change of the fibre/metal matrix dimensions behind the e.m. calorimeter. In the e.m. part, a fibre diameter of 1 mm and a 'compensating' filling factor Pb/scintillator = 4/1 will result in a rather modest performance:

$$\frac{\sigma}{E} \approx \frac{0.15}{\sqrt{E}} + \text{constant term.}$$

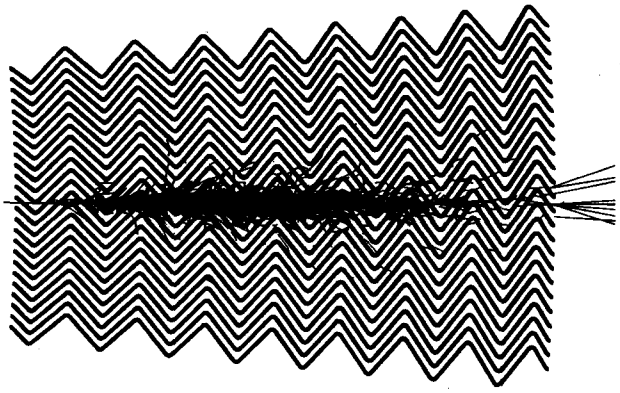


Fig 5 Schematic concept of the 'accordion' sampling geometry. A Monte Carlo view of a 40 GeV e.m. shower is also shown [11].

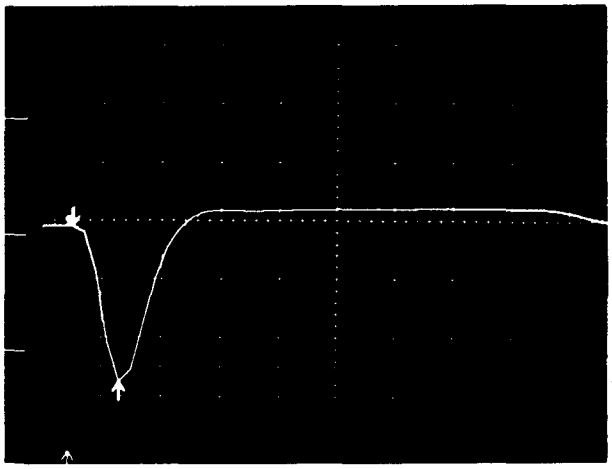


Fig 6 Oscilloscope trace of the shaper output, showing the pulse generated by a 60 GeV electron. The pulse peaks after $\tau_{peak} = 38$ ns; a long opposite–polarity signal persists during the duration of the drift ($\tau_{drift} = 400$ ns). The abscissa is in units of 50 ns per square, the ordinate is 50 mV per square [14].

This can only be alleviated by using smaller–diameter fibres (impractical) or choosing a finer (non–compensating) sampling, e.g. Pb/scintillator = 2/1. Encouraging progress has been made on improving the radiation hardness of the fibres. Both the scintillating matrix and the cladding of the fibres are being improved. A 20% reduction in the light output occurs after a radiation level of 10^4 Gy, probably adequate for operation at small rapidities (10^4 Gy correspond to $L \approx 10^{42}$ cm^{-2} at $\eta = 0$ and radius $r \approx 1$ m).

In 1991, the RD3 Collaboration tested the LAr/Pb 'accordion' concept with fast ($\tau_{peaking} = 38$ ns) electronics. The basic structure is indicated in Fig. 5; a record of the pulse shape induced by an electron is shown in Fig. 6. The pulse peaks after 38 ns; equal area shaping is used such that the opposite polarity pulse extends for the full drift time, $\tau_D = 400$ ns. The uniformity of this somewhat unusual electrode structure has been extensively measured. In Fig. 7, the results for scans across the accordion fold are shown together with the corresponding GEANT 3.14 simulation. Small variations are observed, and reasonably well reproduced by the simulation. The r.m.s. non uniformities are seen to be $\sigma_{nonuniform} \leq 0.5\%$.

The energy resolution is shown in Fig. 8 and compared with the 1990 test results obtained with the much slower shaping of $\tau_{peaking} = 140$ ns. Both tests give identical energy resolution (correcting for the much larger electronic noise): this demonstrates that fast LAr calorimetry can be mastered and the expected performance can be obtained.

The spatial resolution, σ_x, has also been measured with fast shaping. It can be parametrized in the form :

$$\sigma_x \approx \frac{3.6 \pm 0.2}{\sqrt{E}} + (0.012 \pm 0.027)\ \text{mm}$$

The angular resolution, using only the two centre–of–gravity determinations in the two longitudinal segments, was also determined. The two segments were chosen to be 12 X_o each, not optimal for a calorimeter direction measurement of the e.m. shower. The result is found to be:

$$\sigma_\theta = 75\ \text{mrad}/\sqrt{E} \text{ for } E \geq 30\ \text{GeV}.$$

This internal angular resolution is close to adequate for invariant mass determinations, e.g. $H \rightarrow \gamma\gamma$.

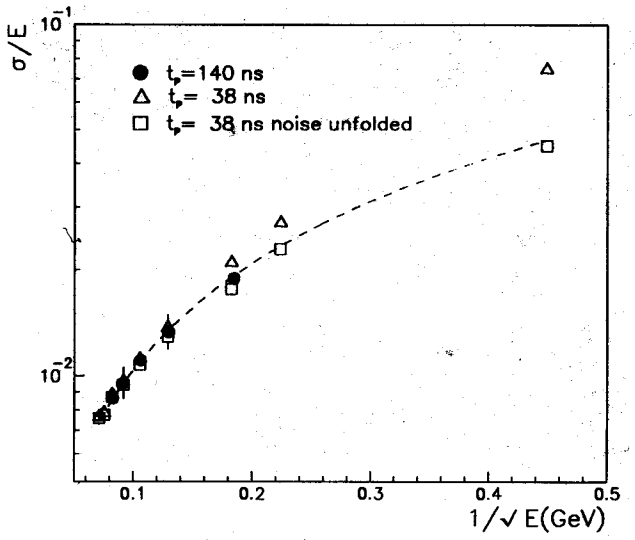


Fig 7 High–statistics scan across one cell of the 'accordion'. Shown are the Monte Carlo evaluation (open circles) and the measurements (crosses). The close agreement indicates that existing MC tools (EGS 4) are adequate for a detailed performance evaluation of even very intricate geometries [14].

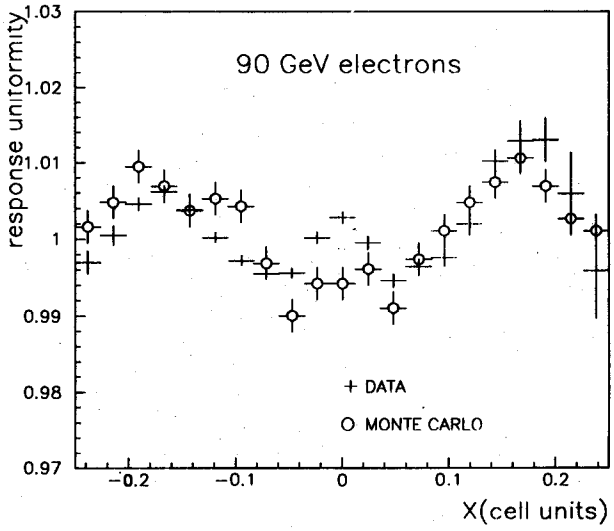


Fig 8 Measured energy resolution using fast shaping (open triangles). The resolution can be parametrized in the form $(\sigma/E) = (a/\sqrt{E} \oplus b \oplus c)$; a = 10.1 ± 0.2%, b = 0.2 ± 0.08%; c = 299 ±10 MeV. The electronic noise term c of 299 MeV represents the sum of 18 channels (a matrix of 3 x 3 channels, with twofold longitudinal segmentation). The energy resolution with the electronic noise unfolded (open squares) agrees very well with the one measured with the same calorimeter in 1990 (filled circles), but has slower shaping (τ_{peak} = 140 ns).

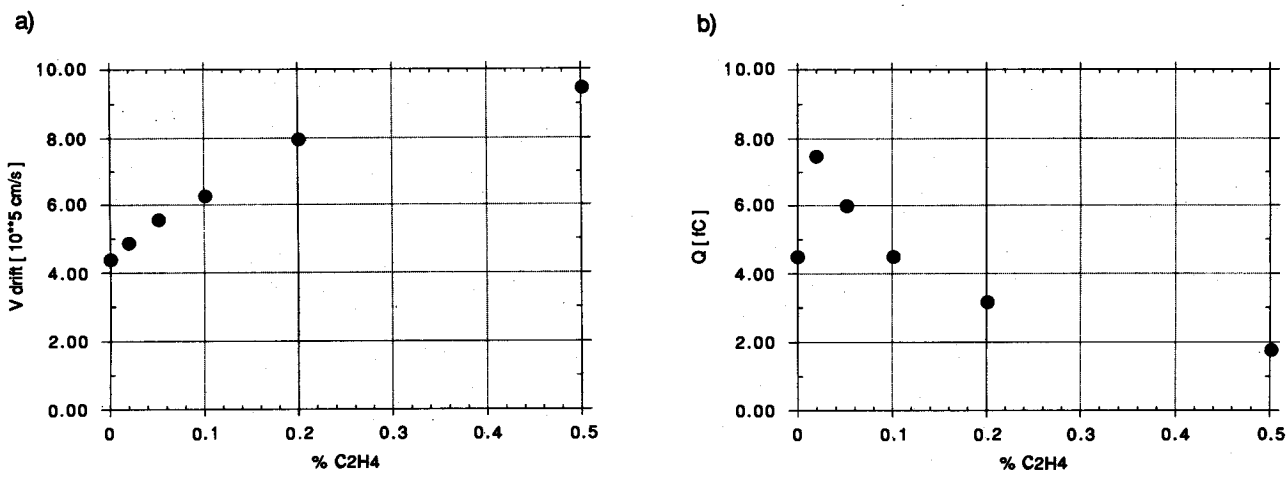


Fig 9 a) Drift velocity at E = 10 kV/cm in LAr as a function of C_2H_4 concentration. An addition of 0.5% C_2H_4 results in a doubling of the drift velocity compared with undoped LAr.
b) Charge registered from α particles (^{241}Am) as a function of C_2H_4 concentration. An increase is observed at low concentrations owing to the photosensitivity of C_2H_4 [16].

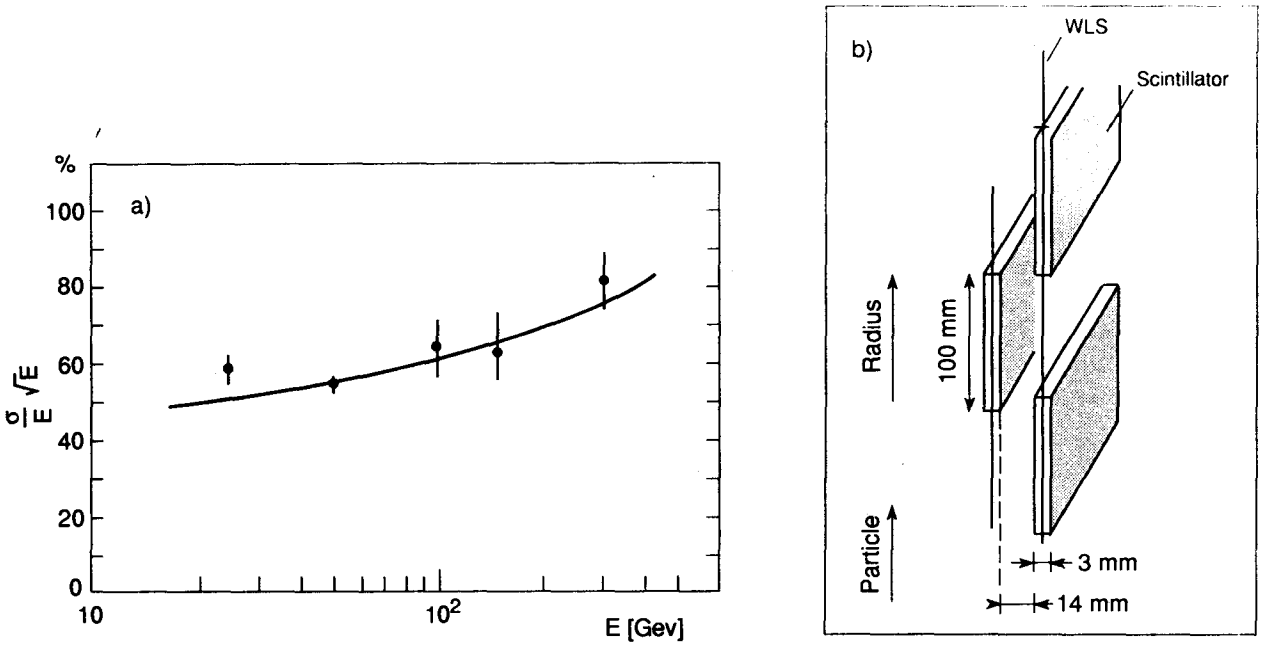


Fig 10 a) Monte Carlo evaluation for the jet resolution of the 'radial–tile' sampling calorimeter;
b) Schematic view of the geometry of the tiles and Fe absorber [17].

In a separate R&D programme, the possibility of using dopants to improve certain parameters of LAr was studied [15]. Some results are shown in Fig. 9. Ethylene was measured as it combines photosensitivity at low concentrations while cooling the drift electrons sufficiently, resulting in increased drift speed. Unfortunately, neither ethylene nor other dopants studied, such as TMAE result in a simultaneous useful increase in charge and drift velocity. Considering the problem associated with the radiolysis of these dopants in the intense radiation field at the LHC/SSC, their use does not appear to be very attractive [16].

The principle of 'directional insensitivity of the readout sensors' is also the basis of a novel concept for a hadronic scintillator tile calorimeter [17]. The tiles are no longer arranged in the 'conventional' cylindrical geometry, surrounding the colliding beams coaxially, but rather in a radial direction (Fig. 10a). This topology avoids the complication of bending the readout fibres, typical of the 'conventional' approach. The energy resolution for jets has been estimated, for a Fe/scintillator tile device behind a 1 λ e.m. calorimeter (Fig. 10b):

$$\frac{\sigma}{E}(\text{jets}) \approx \frac{0.46}{\sqrt{E}} \oplus 0.02 \; ;$$

it is very similar to that expected for a conventional tile calorimeter with the same sampling fraction. The potential advantages that this topology may offer for a full–size calorimeter, are being studied at present.

3. Signal Processing

The RD16 Collaboration has embarked on an ambitious generic signal–processing project for calorimeters [18]. The functional diagram of the ASICs under study is seen in Fig. 11. The group observes that the required dynamic range for e.m. calorimetry, approximately 15 bits, can be compressed, without any loss in performance, into ~ 10 bits, if a non–linear response function of the analog front end is implemented. The complete signal–processing chain will be assembled from several ASICs, using multichip connection techniques. The group intends to finish the simulation of the various building blocks by early 1992; first prototypes are expected to be available in early 1993.

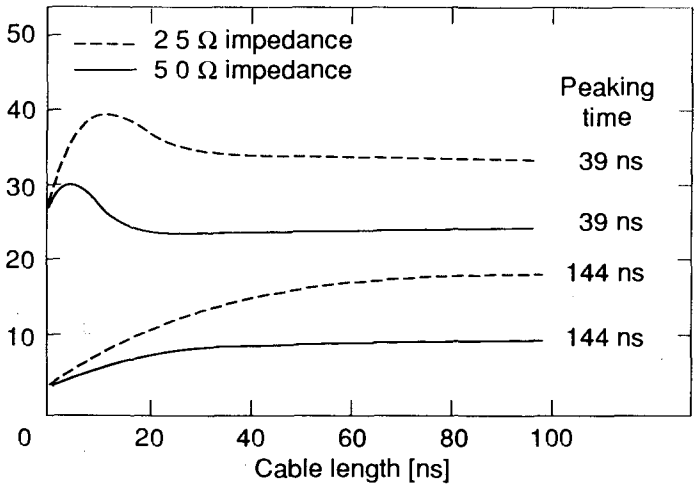


Fig 11 Block diagram of the ASIC under development for calorimeter front ends [18].

The RD3 Accordion Collaboration has tested several readout possibilities suitable for fast LAr calorimetry; they are summarized in Table 4. Besides the development of low–noise, low–power preamplifiers, both in Si and in GaAs technologies, two 'minimal' solutions were tried. The 'one–transistor' operates on the readout electrodes in the LAr and drives the coaxial cable. In principle, it is even possible to do away altogether with active components, provided the characteristic signal–shaping time is much shorter than the cable transit time (Fig. 12). Apart from a slight noise penalty, there are two additional drawbacks to this method:

i) The noise level only remains acceptably low if the cable resistivity does not become a dominating noise source. This imposes a minimum size on the conductor diameter (skin effects!) making these transmission lines rather bulky.
ii) This arrangement is more sensitive to pick–up noise. Even a relatively small level may be unacceptable, as it destroys the quality of energy sums used for trigger decisions.

These various readout methods will be pursued by the RD3 Collaboration. The zero–transistor scheme could possibly be of considerable use for the particularly ferocious radiation environment of small–angle calorimetry [20].

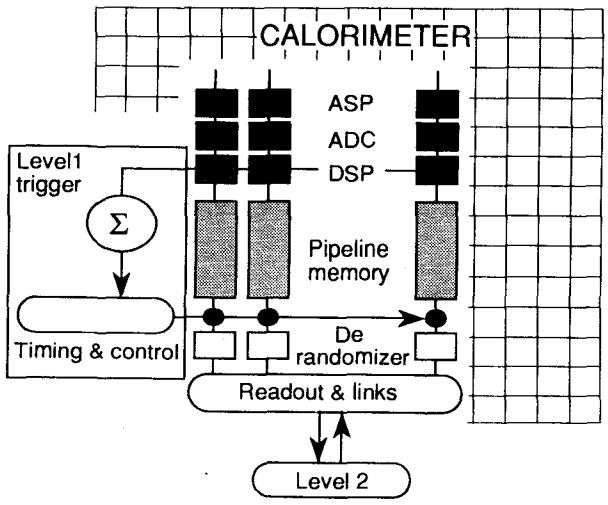


Fig 12 The increase of electronic noise observed if the preamplifier and signal electrodes are separated by a coaxial transmission line of a certain length, given on the abscissa in nanoseconds [20].

Progress has been reported on novel light detectors. The RD14 group has constructed photodiodes, using a CsI photocathode. Quantum efficiencies Q.E. ~ 1 have been measured for light in the range 180 to 300 nm. Such devices, which are operated in 1 atm of CH_4, have a much lower capacitance than Si photodiodes, and would be used for example in LXe e.m. calorimetry [5].

Table 4: Front–end readout options tested by the RD3 Collaboration [14]

a) Front–ends evaluated (during the 1991 beam tests)

- Si preamplifiers (cold)
- GaAs preamplifiers (cold)
- one transistor (cold)
- zero transistor (preamplifier after ~ 6 m cable)

b) Preamplifier characteristics

Lab.	Type	C_{in} (pF)	T_r (ns)	R_{in} (Ω)	P_d (mW)
BNL	Si	~ 100	16	13	70
Milano	GaAs	~ 80	≤ 10	< 10	55

The LAA fibre calorimeter group has tested a 'hybrid photodiode' [19], Fig. 13. Photoelectrons, emitted from a photocathode, are accelerated to approximately ~ 10 keV and detected by a conventional silicon solid–state detector. The advantages of this device are said to be:

- fast and linear response; the measurements indicate linearity up to ~ 5 x 10^6 photoelectrons;
- relatively–good long–term stability;
- adequate lifetime: ~ 5 x 10^{19} photoelectrons have been recorded with a tolerable loss in efficiency.

An improved version using proximity–focussing to render the diodes insensitive to magnetic fields is under development. A similar development is also being carried out by the RD1 Collaboration.

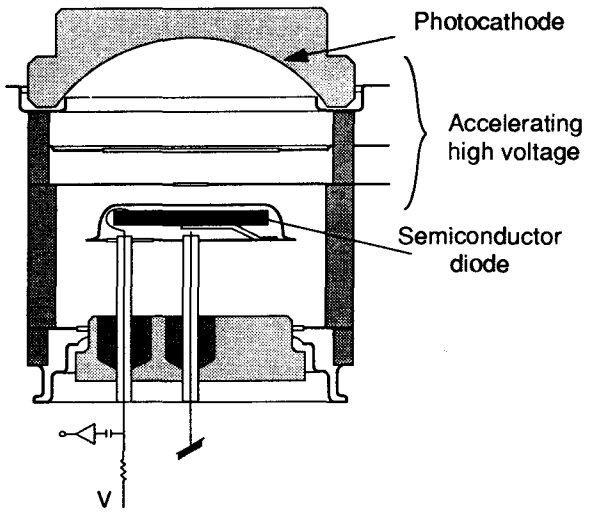


Fig 13 Schematic structure of the hybrid photodiode tested by the LAA Collaboration [19].

4. Emerging Calorimeter Systems

Scintillating fibre calorimeters: in Section 2, we indicated certain advantages for a different structure of e.m. and hadronic fibre calorimeters. Two possibilities are being considered:

- One is to provide a mechanical separation; the photon detectors of the e.m. section are placed directly on the e.m. calorimeter.
- alternatively, the fibres of the e.m. calorimeter are combined and 'mixed' in an optical mixer, e.g. a piece of plastic tapered light guide of square or hexagonal cross–section; a certain fraction, approximately 20%, of this light is subsequently transported by clear fibres, traversing channels in the hadronic section. The resulting loss in light from the e.m. calorimeter and the reduced sampling in the hadronic part appear to be acceptable. Tests carried out on such a structure [21] indicate that the showering in the mixer may not introduce excessive spurious signals.

The RD3 Accordion Collaboration is preparing a major subsystems test of a large e.m. and hadronic accordion calorimeter for 1992 [20]. Emphasis is placed on construction techniques, which could also be used in an LHC/SSC barrel calorimeter. The e.m. calorimeter uses accordions folds coaxial with the beam. A constant sampling fraction radially is achieved by increasing the fold angle from 85° to 110° with increasing radius. The hadronic part is again an accordion, using 10 mm thick stainless steel plates. The 'electrostatic transformer' [23] is used with transformer ratios of 1:3 and 1:4 to reduce the detector capacitance. A fourfold longitudinal segmentation is planned in order to permit longitudinal weighting.

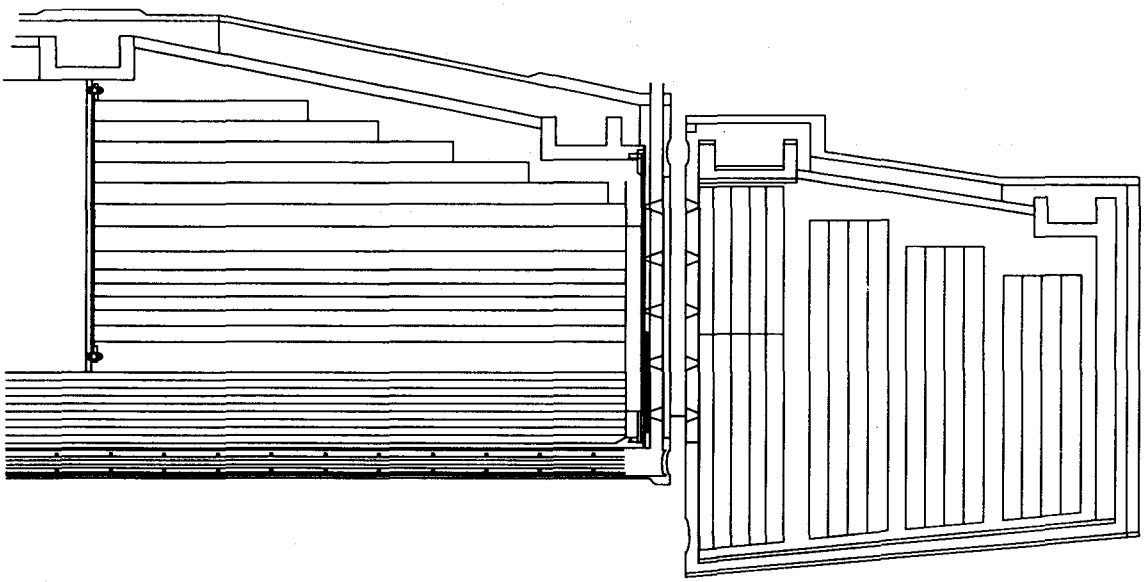


Fig 14 Engineering prestudy of the transition between a LAr barrel calorimeter and the end–cap calorimeter. Material in the warm, outer vacuum tank is minimized by supporting the walls off the cold, moving calorimeter section [22] with spaces.

Considerable effort is also being directed towards cryostat concepts, the integration of a superconducting solenoid, and the notoriously difficult transition between the 'barrel' and the 'end–caps'. Figure 14 shows a concept in which cold, load–bearing disks support the absorber structures. The warm, thin, outer shell is supported by this cold structure and is allowed to follow the thermal contraction of the cold mass. This technique is similar to the one previously used for the NA31 calorimeter [24].

5. Acknowledgements

The assistance of many colleagues who explained their results to me, prior to publication, is gratefully acknowledged.

6. References

1. A. Hervé et al. (RD18 Collaboration), R&D proposal for the study of new, fast and radiation hard scintillators for calorimetry at LHC, CERN/DRDC P27/91–15 (1991).

2. P. Lecoq et al., Progress and prospects in the development of new scintillators for future high energy physics experiments, preprint CERN–PPE/91–124, to be published in Nucl. Instrum. Methods.

3. W.W. Moses and S.E. Derenzo, IEEE Trans. Nucl. Sci. NS–36 (1989) 137.
D.F. Anderson, Nucl. Instrum. Methods A287 (1990) 660.

4. J. Seguinot et al., A totally active liquid xenon or krypton electromagnetic calorimeter for high luminosity hadron colliders, CERN–LAA/PC/90–24;
J. Seguinot et al. (RD14 Collaboration), Detector R&D proposal: Liquid xenon (krypton) calorimetry, CERN/DRDC/90–70.

5. T. Ypsilántis, private communication.

6. G.D. Barr et al. (NA48 Collaboration), Proposal for a precision measurement of ε'/ε in CP violating $K^0 \to 2\pi$ decays, CERN/SPSC/90–22/P253.

7. P. Buchholz, the NA48 Liquid krypton calorimeter, Conf. on liquid noble gas detectors and their applications, Stockholm, T. Lindblad et al. ed. (to be published).

8. J. Colas et al., Calorimetry at the LHC, CERN 90–10, Vol. 1, p. 370.

9. B. Bencheikh et al., 'First results on the spaghetti calorimeter projective prototype', CERN/LAA/HC/91–022 (1991), presented at the 5th Pisa Conference on Advanced Detectors, la Biodola, Italy, May 26–31, 1991, to be published in Nucl. Instrum. and Methods.

10. D. Acosta et al. (RD1 Collaboration), Scintillating fibre calorimetry at the LHC, CERN/DRDC/90–23.

11. B. Aubert et al., (RD3 Collaboration), Liquid argon calorimetry with LHC performance specifications, CERN/DRDC/90–31 (1990).
B. Aubert et al., Performance of a liquid argon electromagnetic calorimeter with an 'accordion' geometry, preprint CERN–PPE/91–73; to be published in Nuclear Instrum. Methods.

12. D. Acosta et al., Electron, pion and multiparticle detection with a lead/scintillating–fibre calorimeter, preprint CERN–PPE/91–85; Submitted to Nucl. Instrum. Methods.

13. A. Contin, private communication. (see also: D. Acosta et al., 'Electron–pion discrimination with a scintillating fibre calorimeter', preprint CERN–PPE/90–172 (1990)).

14. B. Aubert et al. (RD3 collaboration), private communication.

15. P. Cennini et al. (RD4 collaboration), Study of liquid argon dopants for LHC hadron calorimetry, CERN/DRDC/90–34 (1990).

16. V. Vuillemin et al., CERN–PPE/91–171, to be published in Nucl. Instrum. Methods.

17. O. Gildermeister, private communication.

18. B. Lofstedt et al. (RD16 Collaboration), A digital frontend and readout microsystem for calorimetry at LHC, CERN/DRDC/90–74.

19. R. De Salvo et al., First results on the hybrid photodiode tube, preprint CERN–PPE/91–142, submitted to Nucl. Instrum. and Methods.

20. C. de la Taille et al., presented at the 2nd International Conf. on Calorimetry in High Energy Physics, Capri Oct. 1991.
B. Chase et al., to be submitted to Nucl. Instrum. Methods.

21. J.M. Gaillard (RD1 Collaboration), private communication.

22. B. Aubert et al. (RD3 collaboration), Hadronic and electromagnetic liquid argon LHC prototype calorimeter with pointing geometry, CERN/DRDC/92–21.

23. J. Colas et al., Nucl. Instrum. Methods A294 (1990) 583.

24. M. Burkhardt et al., Nucl. Instrum. Methods A268 (1988) 116.

SSC Tracking Detectors Using Straw Tube Drift Chambers and Scintillating Fibers

A. Goshaw

SSC Tracking Detectors using Straw Tube Drift Chambers and Scintillating Fibers

A. T. Goshaw
Duke University

1991 Symposium on The Superconducting Super Collider
Corpus Christi, Texas

October 16, 1991

Subsystem Collaborations

Transition Radiation Detector Collaboration (209)
AT&T Bell Laboratories
Boston University
Brookhaven National Laboratory
Columbia University
Moscow Physical Engineering Institute
Lebedev Institute of Physics

Fiber Tracking Collaboration (222)
University of California at Los Angeles
Fermilab
University of Illinois at Chicago
Indiana University at Indianapolis
Massachusetts College of Pharmacy and Applied Health Sciences
Northeastern University
University of Notre Dame
Oak Ridge National Laboratory
Pennsylvania State University
Philadelphia College of Pharmacy and Science
Purdue University
Rice University
University of Texas at Dallas
Tsukuba University

Compact Central Tracker Collaboration (244)

Boston University
Indiana University
Los Alamos National Laboratory

Central and Forward Tracking Collaboration (223)
Indiana University
University of Colorado
University of Pennsylvania
KEK National Laboratory
Lawrence Berkeley Laboratory
University of California, Berkeley
University of Michigan
Rutherford Appleton Laboratory
University of Liverpool
University of Glasgow
Westinghouse Science and Technology Center
Oak Ridge National Laboratory
Los Alamos National Laboratory
Stanford Linear Accelerator Center

Precision Straw Tube Tracking (223)
Princeton University

Hybrid Central Tracking Chamber Collaboration (234)
Continuous Electron Beam Accelerator Facility
Duke University
EG&G, Canada
Florida State University
KEK National Laboratory
North Carolina State University
Northeastern University
Oak Ridge National Laboratory
Quantum Research Services
Supercomputer Computations Research Institute
TRIUMF
University of Pennsylvania

SSC Subsystem Research to be Reviewed (concentrating on new results)

Straw Tube Drift Chambers

Subsystem	Detector Affiliation	Code for this Talk
Transition Radiation	GEM	TRD
Central and Forward Tracking	SDC	Wire
Precision Straw Tube Tracking	B Physics	Precision
Hybrid Central Tracking	SDC	Hybrid
Compact Central Tracker	GEM	Compact

Scintillating Fibers

Fiber Tracking	SDC	Fibers
Hybrid Central Tracker	SDC	Hybrid

Goals of Talk

* review status of recent straw tube and scintillating fiber R&D work
* evaluate their suitability for use in an SSC tracking detector
* discuss additional R&D required

Omissions from Talk

* readout electronics (except photodetection) [see electronics talks latter today]
* Monte Carlo simulations of tracking detectors
* specific tracking detector designs

Outline

1.0 Straw tube drift chambers

* mechanical construction
* gas selection
* performance evaluation
* candidate for SSC use
* further R&D required

2.0 Scintillating fibers

* mechanical construction
* scintillator selection
* performance characteristics
* candidate for SSC use
* further R&D required

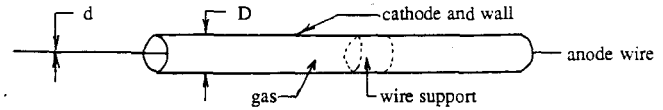
3.0 Superlayer construction

* general concept
* straw tube superlayers
* scintillating fiber superlayers

4.0 Summary

* performance comparisons
* R&D priorities for FY92

Straw Tube Drift Cells



anode wire: gold plated tungsten

d = 20 to 50 μm under consideration

favored: d = 25 μm ==> R = 110 Ω/m

comment: Choice influenced by radiation hardness studies, electrostatic stability requirements, gas gain considerations, and mechanical strength of wire. This determines the attenuation loss.

straw tube: D = 4 to 7 mm under study

wall thickness 20 to 40 μm of mylar or kapton or polycarbonate

cathode 0.1 to 10 μm of aluminum or copper

favored: D = 4 mm

wall ~ 38 μm of mylar or kapton

cathode ~ 0.15 μm of copper ==> R = 20 Ω/m

comment: Choice influenced by radiation hardness studies, occupancy limitations and mechanical fabrication requirements.

Attenuation Length of Signals in Straw Tube Drift Cells

Attenuation lengths of straw tube drift cells have been measured by the Hybrid (Duke) and Wire (Indiana) Subsystem Groups.

These are fixed by the properties of the anode wire and the cathode structure.

straw tube cell	Attenuation Length (cm)	
25.4 μm wire 0.25 μm Al cathode	380	(Indiana)
51.0 μm wire 0.25 μm Al cathode	710	(Indiana)
25.4 μm wire 0.15 μm Cu cathode	510	(Duke)

(errors < 10 %)

Measured and calculated values agree well.

===>

Pulse Attenuation in Straw Tubes

$V=V_0\exp(-\alpha z)$ where $\alpha=R_l/2Z_0$

z is the length along the tube
α is the attenuation constant
R_l is the sum of the of the cathode and the anode resistance per unit length
Z_0 is the characteristic impedance.

Z_0=304 ohms for a 25.4 μm wire in a 4 mm tube
=279 " " " 38.0 " " " " " " "
=262 " " " 51.0 " " " " " " "

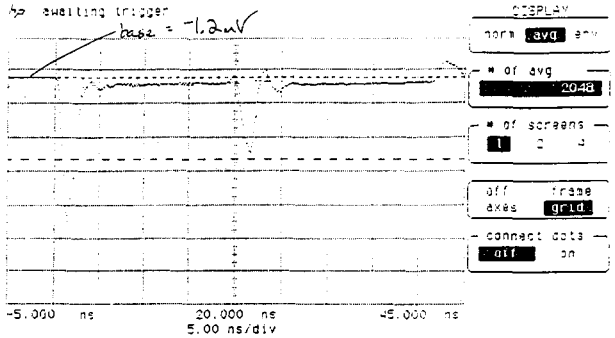
Resistance of 25.4 μm gold plated tungsten wire is 116±4 ohms/meter.

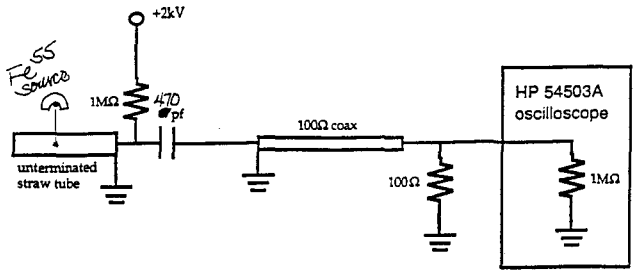
Resistance of 51. μm gold plated molybdenum wire is 30±1 ohms/meter

Resistivity of 0.2-0.25 μm aluminum coating is about 0.3 ohms/square

Resistivity of 0.15 μm copper coating is about 0.12 ohms/square

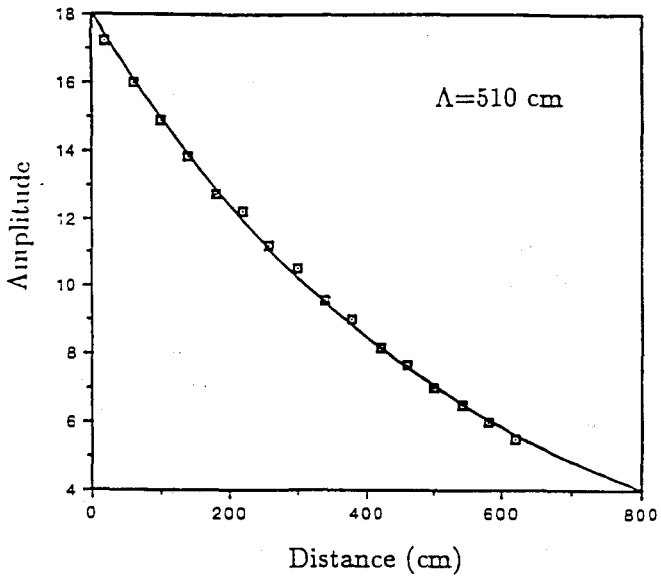
WIRE (Indiana)





HYBRID (Duke)

Measurement of attenuation length in a 7 meter long straw tube



Radiation Length of Straw Tube Drift Cells

The radiation length of a straw tube averaged over the diameter of the tube and at normal incidence is:

$$\langle t \rangle = (5.0 + 1.0) * 10^{**-4}\ X_0$$

assuming the "favored" straw tube construction described previously.

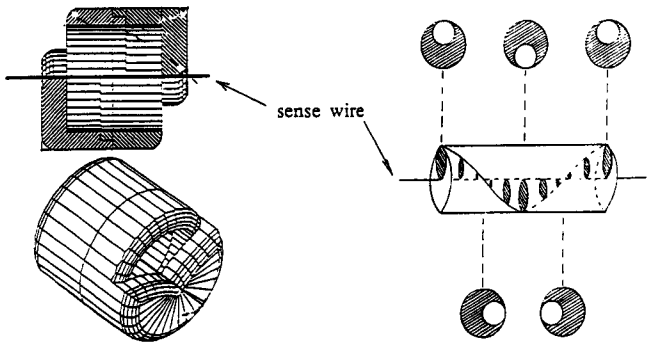
==> a 8 deep superlayer has a thickness of ~0.4% X0
(plus structural supports and electronics).

Wire Supports

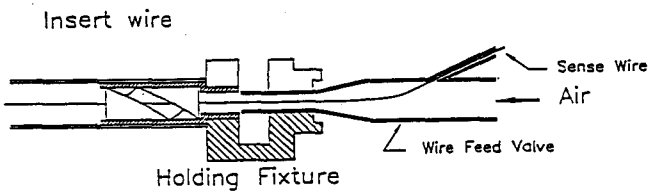
* accurately position sense wire
* allow gas flow through tube
* allow stringing of sense wire after tube is assembled

WIRE
(Indiana and Colorado)

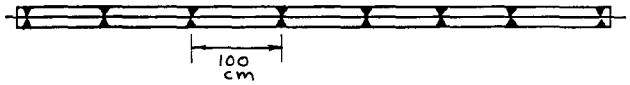
HYBRID
(Duke)



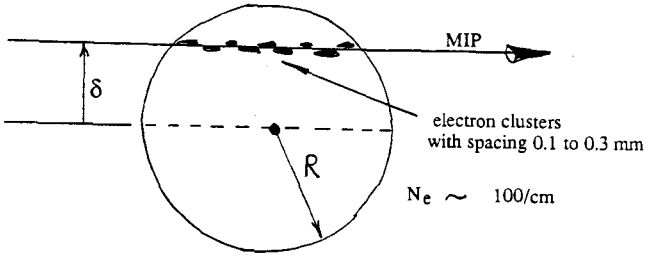
Stringing Sense Wire in Assembled Straw Tubes



7 Meter Long straw Tubes with 8 wire supports.



Drift Gas



Geometry: $N_e(\delta) = N_e(0)\sqrt{1 - (\delta/R)^2}$

Gas Selection Controls:

* drift velocity ⟹ occupancy
* gas gain ⟹ operating voltage
* dispersion of drift electrons ⟹ resolution
* electron attachment ⟹ efficiency
* radiation damage effects ⟹ lifetime

Groups Studying Gases

COMPACT (Boston U.):
precision measurements of drift velocity and Lorentz angle

HYBRID (Duke,TRIUMF):
study effects of gases on wire and cathode aging;
mesure drift cell resolution

PRECISION (Princeton):
detailed studies of avalanche characteristics with the aim of finding limitations on measurement precision

WIRE (Indiana, SLAC):
study effects of gases on wire and cathode aging;
measure drift cell resolution

TRD
study detection of transition radiation using xenon/CO_2

Many interesting results.

Present some associated with the gas mixture CF4: isobutane (80:20)

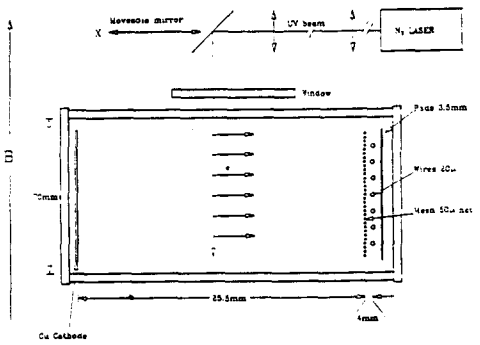
$\Longrightarrow$ ~ 4 electron clusters/ mm

$\Longrightarrow$ ~ 3 electrons/ cluster

$\Longrightarrow$ $Ne(\delta) = 49\sqrt{1 - (\delta/R)^2}$

COMPACT
(Boston University)

Measurement of drift velocity.



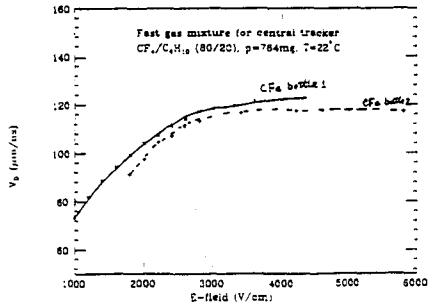


Figure 5 CF_4 – isobutan (80-20) mixture drift velocity measurements: solid line and dash line were measured using different CF_4 gas bottles.

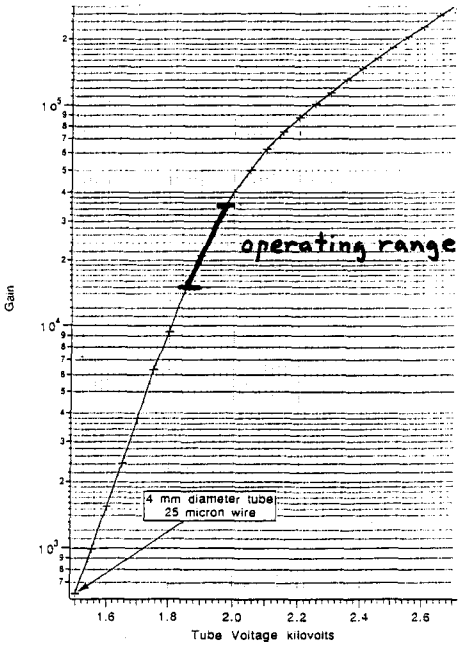
WIRE
(Indiana)

Gas gain versus tube voltage

CF4/isobutane 80:20

wire d =25 μm

tube D = 4 mm



Precision Straw Tube Tracking

Princeton U.

- Work in progress: gain and attachment coefficients.

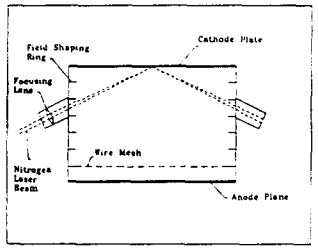


Figure 22: Set-up to measure $\alpha - \eta$.

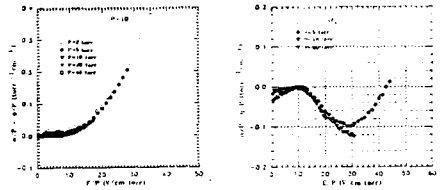


Figure 23: Preliminary measurements of the gas coefficients $(\alpha - \eta)/P$ as a function of E/P for (a) P-10, and (b) CF_4.

- New studies of attachment, and of drift velocity.

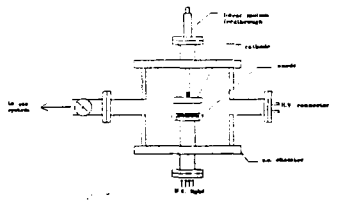
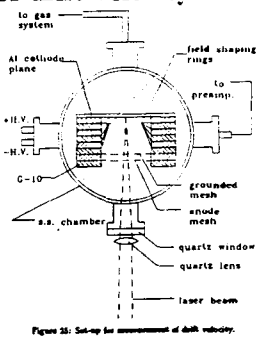


Figure 24: Set-up to measure a second function of the gas coefficients α and η.

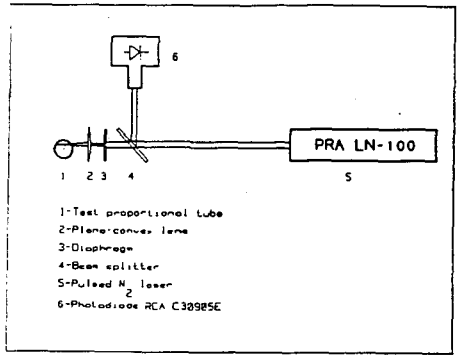


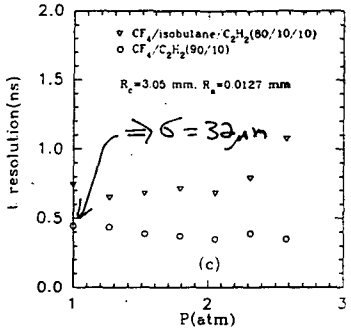
- ⇒ complete characterization of drift, gain, attachment, and diffusion.

Precision Straw Tube Tracking

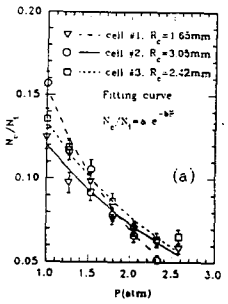
Princeton U.

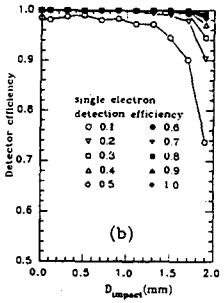
• Characterization of single-electron avalanches.

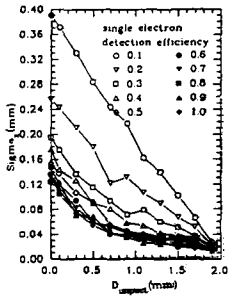




• Electron attachment in CF_4 gas mixtures.







WIRE (SLAC)

Study of accelerated chamber aging using

CF4/isobutane 80:20

wire d = 38 μm

tube D = 4 mm

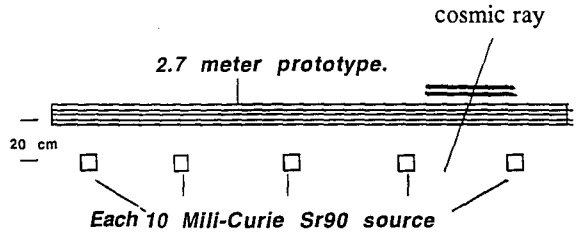
Table 1. Accelerated Aging Test Results

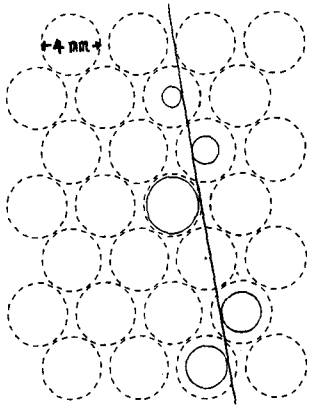
Gas	Gain Loss, R (%/(C/cm))	Linear Charge Transfer (C/cm)	Materials: Wall/Cathode	Comments
CF_4/Isobutane (80/20)	3	0.5	Mylar/Al	Discharges quenched by H_2O (Fig. 1)
"	6	1.0	Kapton/Al	gain=1.5×10^5
"	200	0.06	polycarbonate/Al	Rapid gain loss and discharges; gain=1.5×10^5
"	<1	0.5	Al/Au	Very stable, Sr^{90} (Fig. 1)
"	2	0.2	Al/Ni	Sr^{90}
"	10	0.2	Al/Cu	Sr^{90}
"	9	0.1	polycarbonate/Al	gain=1.5×10^5
"	4	0.4	Kapton.Al	gain=1.5×10^5
"	9	0.2	Mylar/Al	gain=1.5×10^5
+1000 ppm H_2O	5	0.4	Mylar/Al	Same as above, with H_2O added.

One C/ cm of integrated charge corresponds to 50 -100 years of operation of a straw tube at R = 70 cm from the beam with luminosity = 10^{33} cm^{-2} s^{-1}.

HYBRID
(Duke)

Measurement of the resolution of straw tube drift cells in a 2.7m long superlayer with simulated SSC background rates.





singles rate 1-2 MHz

current draw ~ 5 μA/wire

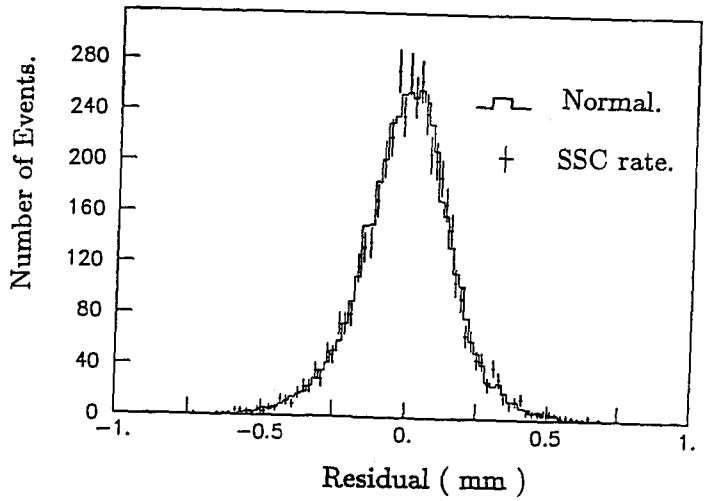
gain ~ 10^5

HYBRID
(Duke)

High rate test of straw tube position resolution.

==> σ = 120 μm / straw tube

==> $\sigma/\sqrt{8}$ = 42 μm / 8 deep superlayer



SUMMARY
Straw Tube Drift Chambers

Candidate for SSC Detectors

* anode wire = 25 μm gold plated tungsten
* straw tube = ~ 38 μm mylar or kapton
* cathode = ~ 0.15 μm copper
* gas = CF4/isobutane 80:20
* wire support problem solved

==> expected superlayer position resolution of ~ 40 μm

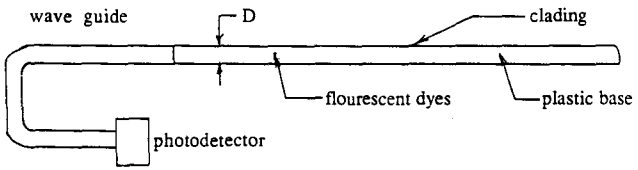
SUMMARY
Straw Tube Drift Chambers
(continued)

Further R&D Needed

Major:
* on-chamber, high density, frontend electronics with required cooling
* colinear coupling of electronics to straw tubes with provision for removing electronics
* straw tube resolution measurements with gas gains ~ $2*10^4$
* superlayer support structure

Minor:
* superlayer fabrication technique
* optimization of drift gas mixture
* further radiation hardness evaluation

Scintillating Fibers



fiber: D = 500 to 1500 μm (830 μm currently favored)

clading: t = 15 to 30 μm acrylic PMMA (n = 1.49)

plastic base: polystyrene (n = 1.59)

flourescent dyes: many under study

standard: p-terphenyl (PTP) plus dimethyl POPOP

comment: radiation damage considerations favor wave shifts to the green

favored: PTP plus 3-hydroxyflavone (3HF)

==> radiation hard to ~ 10 Mrad
==> λ_{peak} ~ 530 nm

photodetectors: solid state photomultiplier (SSPM)
--> visual light photon counter (VLPC)
avalanche photodiode (APD)

FIBER Subsystem

radiation hardness of polystyrene/PTP/3HF

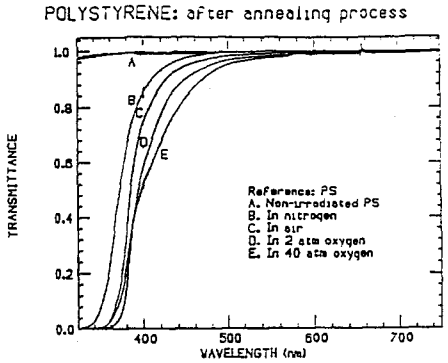


Figure 16. Transmission in polystyrene under various conditions during irradiation.

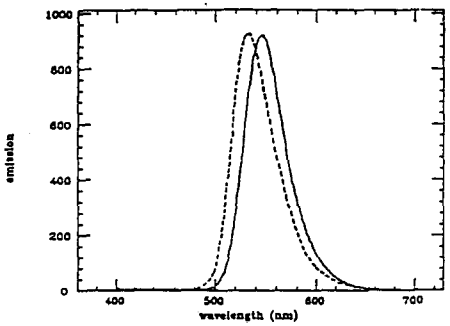
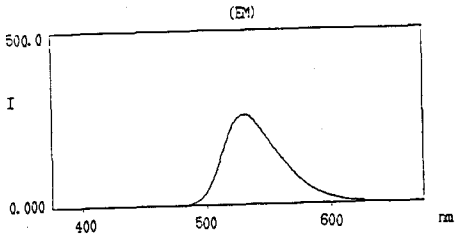


Figure 17. Emission of polystyrene/PTP/3HF scintillator.

Fluorescence emission (for 3-HF (dashed curve) and a variant BC447 (solid curve) which has red-shifted emission. The new dye appears as a strong yellow, whereas 3-HF appears yellow-green.

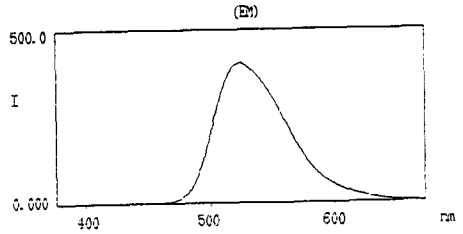
FIBER
(Massachusetts College of Pharmacy and Applied Health Sciences)

improved flourescent emmision in the green



3HF

Figure 1a. Fluorescence emission of 3HF.



newly developed dye

Figure 1b. Fluorescence emission of the new MCPAHS dye.

FIBER
(UCLA, Notre Dame)

Splicing fibers to wave guides:
developing a quick disconnect coupler using optical greases
(essential for fabrication of many-channel systems)

FIBER
(UCLA,Fermilab,Purdue,Notre Dame, UT Dallas)
HYBRID
(Northeastern)

Ribbon manufacture:
high quality fiber ribbons are available from Bicron and Kurray
==> $\sigma_D / D \sim 1\%$
==> fiber center to center registration with $\sigma \sim 25\ \mu m$

FIBER
(UCLA,SSCL,Rockwell,Purdue,UT Dallas)
HYBRID
(Northeastern, EG&G,Quantum Research Services)

Photodetectors:
SSPM ---> VLPC development ==>
APD development ==>

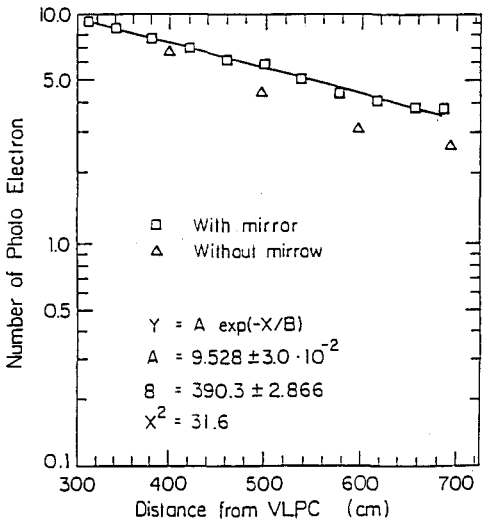
FIBER
(Fermilab, UCLA)

fiber diameter = 830 μm, length = 4 m

scintillator = polystyrene/PTP/3HF

3 m light guide with VLPC readout

==> attenuation length of 390 cm

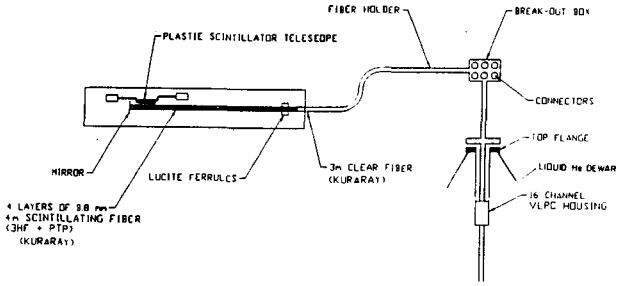


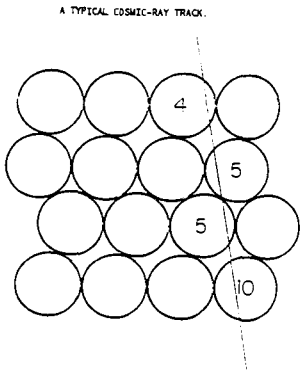
Detected number of photons as a function of source positions from the VLPC are indicated with and without a mirror at the end of the scintillating fiber.

FIBER
(SSCL,UCLA)

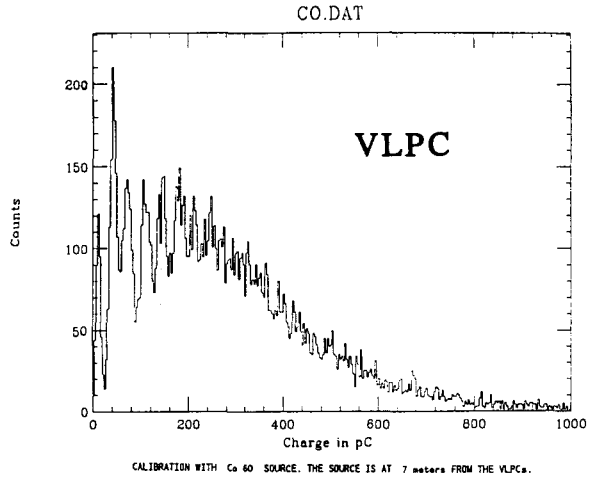
VLPC

M.Atac, J.Park, D.Chrisman
U C L A
M. Fenker, K.Morgan
S S C L

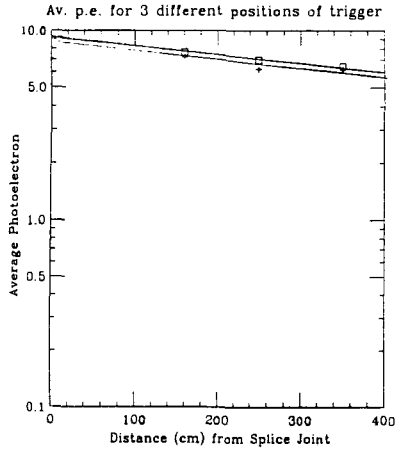




FIBER
(SSCL,UCLA)



CALIBRATION WITH Co 60 SOURCE. THE SOURCE IS AT 7 meters FROM THE VLPCs.



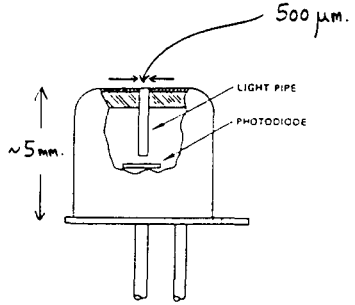
Triggered by 1st & 4th Layers

Layer 2 triggered by 1 p.e. □
Layer 3 triggered by 1 p.e. +

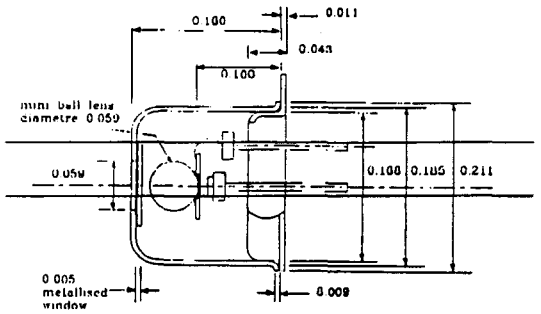
NUMBER OF PHOTOELECTRONS AS A FUNCTION OF DISTANCE FROM THE SPLICED JOINT. THERE IS 3 meters OF CLEAR FIBERS BETWEEN THE JOINTS AND THE VLPCs. COSMIC-RAY TRACKS WERE USED FOR THE PLOT. ATTENUATION LENGHT IS ABOUT 5 meters.

HYBRID
(Northeastern, EG&G, Quantum Research Services)

APD



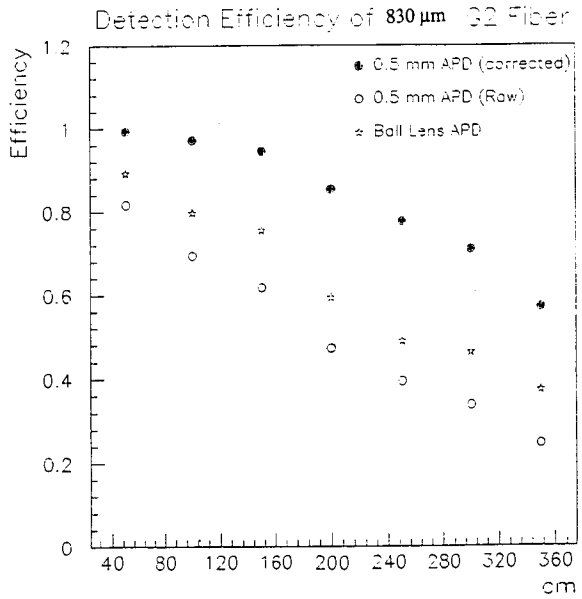
Ball lens for focusing onto APD



HYBRID
(Northeastern, EG&G, Quantum Research Services)

APD

* deadtime ~ 120 ns in Geiger mode
* currently doing tests in sub-Geiger mode
* advantage is operation at room temperature



SUMMARY
Scintillating Fibers

Candidate for SSC Detectors

* diameter 830 μm (or larger)
* clading thickness ~ 20 μm of acrylic PMMA
* scintillator composition = polystyrene/PTP/3HF
* VLPC photodetection
* single fiber resolution = $D/\sqrt{12}$ = 240 μm
* possibility of 1/4 D stagger in fiber superlayers to improve resolution faster than $1/\sqrt{N_{layers}}$ ==>

SUMMARY
Scintillating Fibers
(continued)

Future R&D Needed

Major:
* critical evaluation of VLPC's and APD's by several groups; development of appropriate preamps
* obtain firm cost estimates for VLPC's and APD's
* mechanical fabrication of fiber superlayers with 1/4 D stagger
* fiber-waveguide and waveguide VLPC/APD coupling
* superlayer support structure

Minor:
* optimization of flourescent dyes
* cladings with lower index of refraction
* continued radiation hardness studies

Barrel Superlayer Construction with Straw Tubes and Scintillating Fibers

Support structure common to straws and fibers

* uses continuous stable base cylinders spanning the tracking volume
* cylinder thickness on the order of 0.25% X_0
* design and assembly concepts being developed but no detailed structural analysis
* this is an area that requires major R&D work

Straw tube superlayer construction

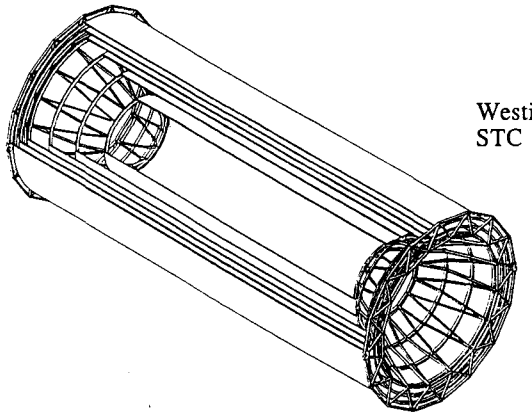
* small superlayer prototypes have been constructed
* advanced R&D work on 3 options for placing straws into superlayers
* techniques for surveying sense wire positions have been developed

Scintillating fiber superlayers

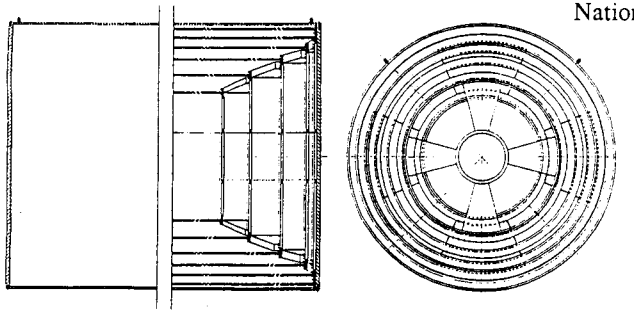
* a concept exists but no prototypes have been constructed
* this is an area that requires major R&D work

Superlayer Support Structure for SDC Barrel Tracker

(length = 8 m radius = 1.6 m)



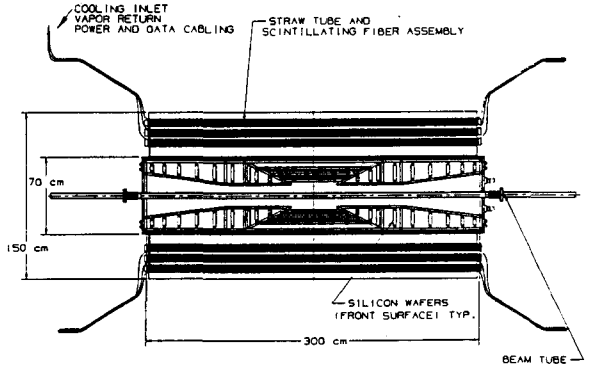
Westinghouse
STC



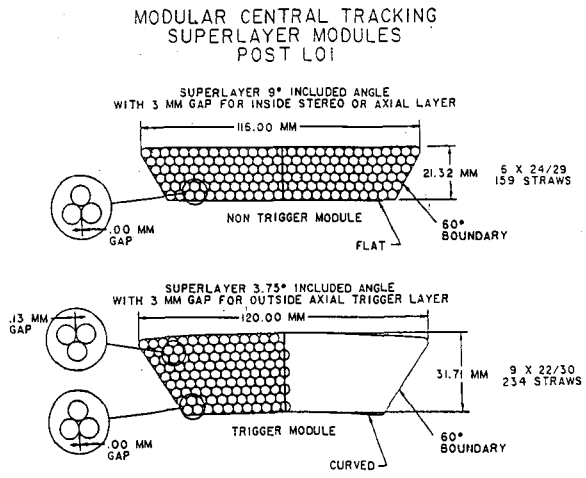
Oak Ridge
National Lab

Superlayer Support Structure for GEM Barrel Tracker

(length = 3m radius = 0.75 m)

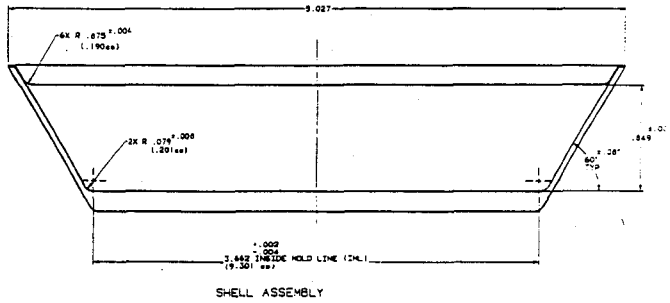


WIRE
(Indiana,ORNL,WSTC)



WIRE
(Indiana,ORNL,WSTC)

Module construction



Material in 6 layers of straws= 0.23% X_0

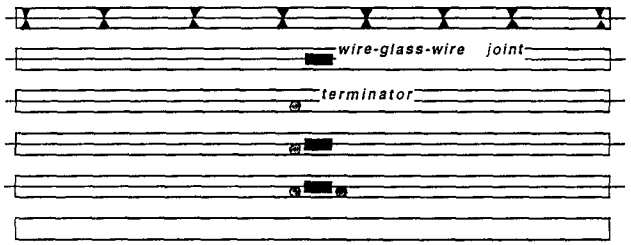
Material in lid and base (averaged over sides)= 0.301% X_0 (3 layers-0.0015 ", IG31 foam)

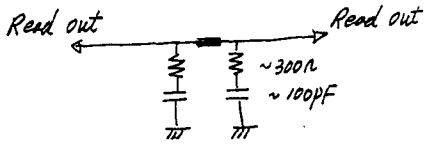
Total material = 0.53 %X_0

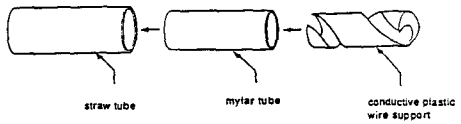
HYBRID
(Duke,ORNL)

Construction of a straw tube superlayer from full length length straws placed directly on a stable base support cylinder.

7 Meter Long straw Tubes with 8 wire supports.

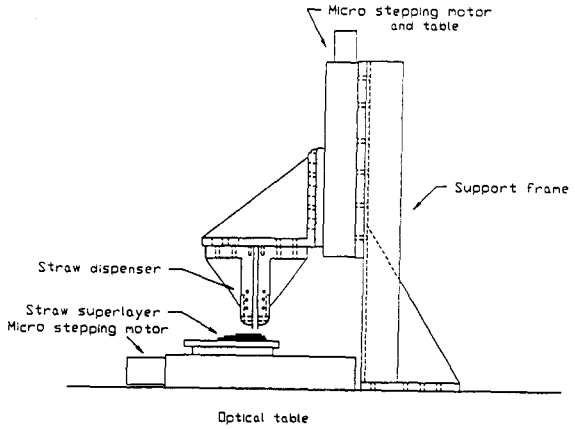




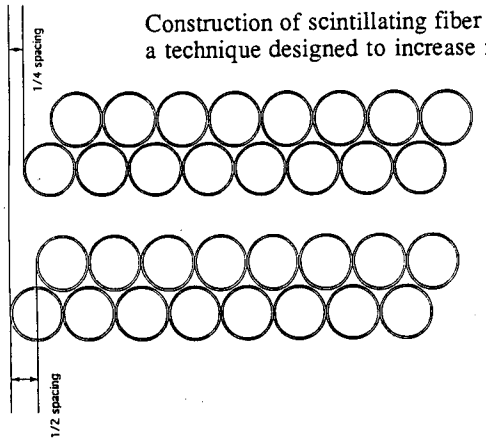


HYBRID
(Duke,ORNL)

Transverse cross section of a 3 meter long semiautomatic straw tube placement machine.



FIBER
Subgroup



Construction of scintillating fiber superlayers using a technique designed to increase measurement precision.

TABLE 1. SCIFI SUPERLAYER PERFORMANCE

Gap, Clad: (microns)	dx/dy range	Avg PE	Eff. 1 PE	RMS (um)	n out of n	n-1 out of n	n-2 out of n	< n-2 of 4	S.L. Eff.
Four Layer Configurations (775/8/sqrt(12) = 28 um):									
25, 22.5	.001	3	80%	61	24.9%	54.5%	18.2%	2.3%	93.0%
25, 22.5	.100	3	80%	75	28.0%	49.4%	20.1%	2.5%	93.3%
25, 22.5	.200	3	80%	88	30.2%	45.6%	21.1%	3.1%	93.2%
25, 22.5	1.000	3	80%	127	49.6%	36.5%	12.3%	1.6%	94.8%
25, 22.5	.001	4	80%	50	36.1%	55.1%	8.4%	0.4%	97.8%
25, 22.5	.100	4	80%	65	39.9%	48.6%	10.9%	0.7%	97.7%
25, 22.5	.200	4	80%	75	42.4%	44.2%	12.5%	0.9%	97.7%
25, 22.5	1.000	4	80%	117	64.9%	28.6%	5.9%	0.6%	98.1%
25, 22.5	.001	4	100%	45	42.8%	52.5%	4.6%	0.1%	99.0%
25, 22.5	.100	4	100%	59	46.3%	46.4%	7.2%	0.2%	99.0%
25, 22.5	.200	4	100%	69	48.9%	41.7%	9.1%	0.4%	98.9%
25, 22.5	1.000	4	100%	111	72.4%	23.6%	3.9%	0.2%	99.1%
25, 22.5	.001	10	100%	31	60.2%	39.8%	0.0%	0.0%	100.%
25, 22.5	.100	10	100%	47	62.2%	36.2%	1.7%	0.0%	100.%
25, 22.5	.200	10	100%	60	66.1%	30.5%	3.4%	0.0%	100.%
25, 22.5	1.000	10	100%	103	87.9%	11.1%	1.0%	0.0%	100.%

Summary of Prospects for Using Straw Tubes and Scintillating Fibers in SSC Detectors

Performance Comparison

	straws	fibers
σ(point)/ element	~ 120 μm	~ 240 μm
σ(point)/superlayer	~ 50 μm	~ 50 μm
attenuation length	~ 5 m	~ 4 to 5 m
occupancy @ 10^{33} $cm^{-2}s^{-1}$ <	~ 10%	~ 1 %
2 track resolution/element	~ 4 mm	~ 1 mm
trigger	yes	yes
stereo	harder	easier
cost	less	more
risk	lower	higher ==>

Scintillating Fiber R&D Priorities in FY92

(R&D)^0 * most single-fiber mechanical problems solved

(R&D)^0 * a suitable scintillator has been found (polystyrene/PTP/3HF) (searches for better scintillators should continue)

(R&D)^0 * radiation hardness is probably acceptable

(R&D)^1 * optical coupling to wave guides and photodetectors needs work

(R&D)^2 * superlayer construction techniques in a primitive stage

(R&D)^2 * need evaluation of VLPC/APD - preamp readout on a large scale by several groups

$ * need to obtain firm cost estimates for photodetectors and preamps

Straw Tube R&D Priorities in FY92

(R&D)^0 * most single-cell mechanical problems solved

(R&D)^0 * a suitable gas has been found (CF_4/isobutane) (searches for better gases should continue)

(R&D)^0 * radiation hardness is probably acceptable

(R&D)^1 * superlayer construction design and fabrication is in an advanced stage

(R&D)^2 * need proof-of-principle of readout with high density, colinear analog and digital electronics

==> evaluation of noise, cross talk and resolution with gas gain ~ $2*10^4$ for few hundred channels

Mechanical Support Structure R&D Priorities in FY92

$(R\&D)^2$ * design and assemby concepts for large superlayer support structures are in a primitive stage

$(R\&D)^2$ * element placement precision and stability are not known well

$(R\&D)^2$ * large volume alignment and survey techniques need to be developed

CONCLUSIONS

* Enormous progress has been made over the past two years in the development of straw tube drift cells and scintillating fibers.

* No "drop-dead" problems have been found.

* R&D in FY92 will move from single element studies to system considerations

* Proof-of-principle questions remain for both straws and fibers. R&D planned for FY92 should be able to address the remaining issues.

High Precision Tracking: Silicon Detectors, Gas Microstrips

A. Seiden

High Precision Tracking: Silicon Detectors, Gas Microstrips

A. Seiden
Santa Cruz Institute for Particle Physics
University of California, Santa Cruz, CA 95064

Abstract

The last three years have witnessed great progress in the area of high precision tracking. These devices, various types of silicon detectors and gas microstrip detectors, will allow very precise position measurement, very fine two particle separation and fast signal timing. R&D in the areas of maximally radiation-hard detectors; fast, low-power, radiation-hard electronics; high precision, light, support and cooling structures has produced concrete solutions to many of the challenging problems posed by detection at the SSC.

1. Introduction

The development of high precision tracking devices will allow SSC detectors to meet the challenge of the very high rates and particle densities at the SSC. As an example, Fig. 1 shows, in quarter section, the LOI design of the SDC detector.[1] Nearest the beam-pipe are two layers of pixel silicon detectors. Covering the region out to 50 cm in radius and ± 250 cm along the beam are silicon strip detectors arranged in cylindrical layers near the beam and annular disks in the forward regions. In the very forward direction three annular disks made of gas microstrips would provide a good match to occupancies and the forward geometry. In the central region from radii of 70 cm to 170 cm, superlayers of devices of lower segmentation, when coupled with the precise inner measurements, provide excellent momentum measurement and triggering capability.

The capabilities of such a tracking system are outlined in Table 1. The achievement of items (1), (2), (3), (4), and (6) depends critically on the presence of the high precision tracking elements.

To arrive at detectors well matched to the challenging SSC environment has necessitated R&D focussed on the following areas:

1. The development of maximally radiation-hard detectors.
2. Low-power, low-noise, radiation-hard electronics.
3. Low-mass, ultra-stable, mechanical structures.
4. Low-mass, vibration-free, cooling systems.

We discuss below some of the work in these areas.

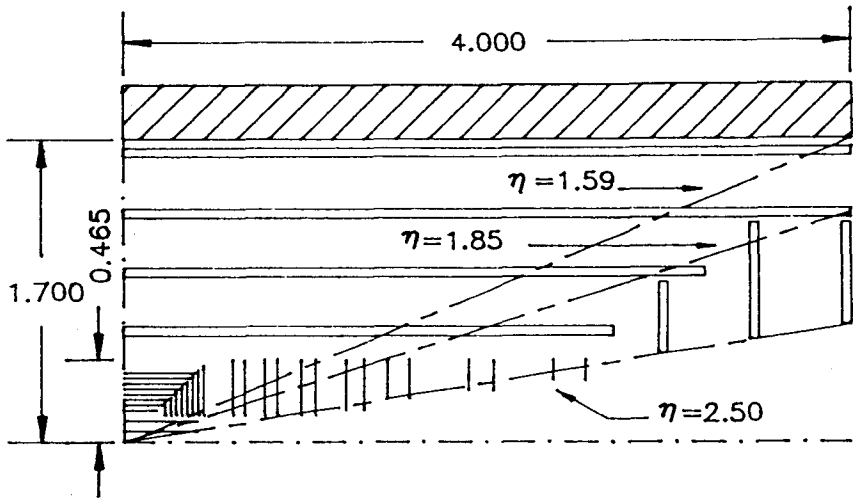


Fig. 1 SDC LOI detector. Inner two layers are silicon pixel detectors, following by a large array of silicon strip detectors. At forward rapidities three detector stations of gas microstrips complete the coverage. Dimensions are in meters, B field is 2 Tesla.

Table 1. Special Capabilities of a Mixed Tracking System

(1) Measurement of dE/dx in a few inner layers: to search for oddly ionizing particles and to reject overlapping electron-positron pairs coming from photon conversions.

(2) Vertexing: look for long-lived particles and special events yielding B's or τ's in the final state. Especially important in studying the top quark and looking for unusual top decays. Assignment of leptons among vertices. For multiple events in a time bucket, allows assignment of tracks to each event.

(3) Momentum resolution $\sigma_{P_\perp}/P_\perp \sim 10\%P_\perp$ (TeV): allows good mass reconstruction of narrow objects, e.g., Z^0, H^0 near 200 GeV, Higgs in multi-Higgs models.

(4) Very good efficiency over $|\eta| \leq 2.5$ to reconstruct high $P_\perp$ isolated tracks, e.g., for the four charged leptons in H^0 decay.

(5) Very good lepton identification for the overall detector: for e by matching with the calorimeter, for μ by matching with the outer muon identifier.

(6) Track reconstruction in high $P_\perp$ jets: measurement of multiplicity and most tracks in events with $P_\perp$ up to 1 TeV. This could be important in understanding jet parentage and allows reconstruction of leptons in jet environments.

(7) Tracking directly in front of the calorimetry for excellent matching between devices and triggering.

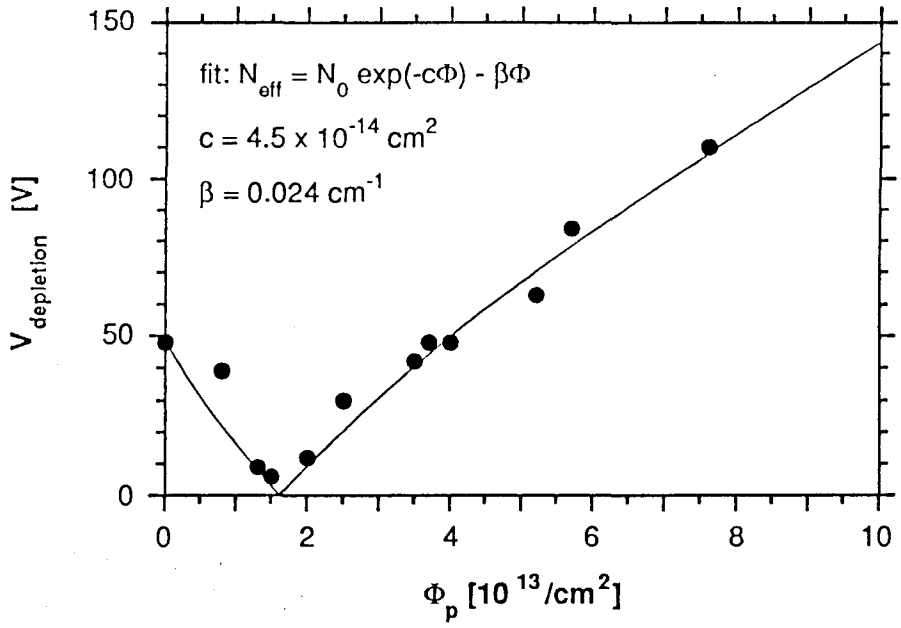


Fig. 2 Depletion voltage vs. proton fluence for SI detectors. Type inversion occurs at $\Phi = 1.5 \cdot 10^{13}/\text{cm}^2$. The line is the best fit according to eq. (1).

2. Radiation Effects in Silicon Detectors

There are three primary bulk radiation effects in silicon detectors. The first is the generation of leakage current. This is not too serious a problem provided the detectors are run near $0°C$, rather than at room temperature. As an example, for a fluence of 10^{14} particles/cm^2 at the SSC, which is a limiting fluence discussed below, a strip of dimensions: 12 cm long $\times$ 50 μm pitch $\times$ 300 μm thickness would suffer a leakage current of 0.5 μAmp at $0°C$. This would give a 350 e^- shot noise contribution for 20 nsec rise-time electronics. This is small compared to a typical signal which contains 25,000 e^-.

The second radiation effect is the change in doping concentration through the removal of initial donors and creation of acceptors for n-type, high resistivity, silicon. The physical effect for a depleted detector is that the silicon which initially contains fixed positive charges spread throughout the volume ends up, after significant radiation, with fixed negative charges. These affect the electric field profile within the detector necessitating voltage changes on the electrodes to achieve fast charge collection.

We can describe the doping concentration by the following formula:

$$N = N_o e^{-c\Phi} - \beta\Phi \qquad (1)$$

where: N_o = initial donor concentration, c characterizes donor removal, β characterizes acceptor creation, Φ is the fluence of a given particle.

Some data on these phenomena are shown in Figs. 2 and 3, from Refs. 2 and 3, respectively. The first set of data are from irradiation by protons of momentum

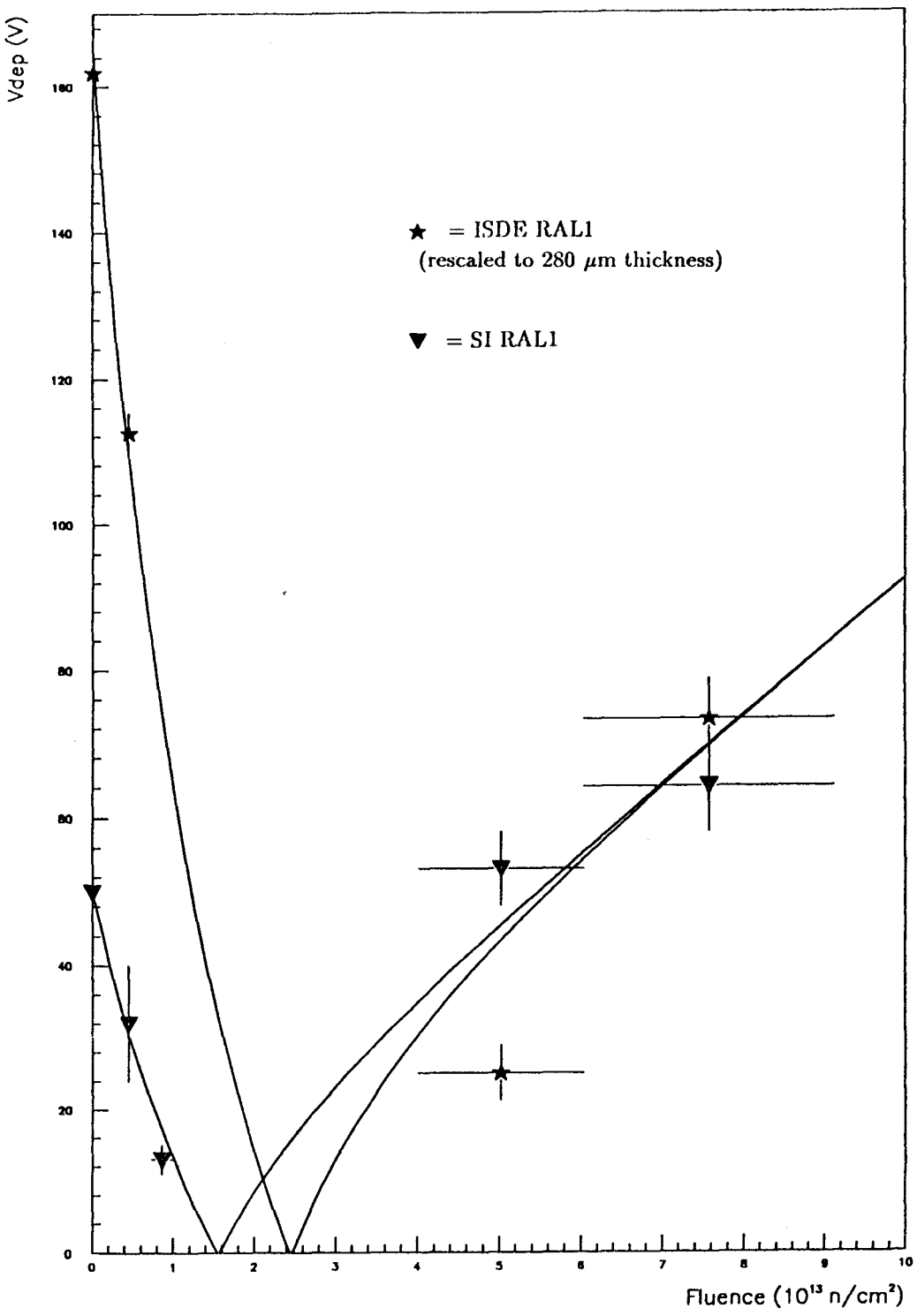


Fig. 3 Depletion voltage vs. neutron fluence for SI and ISDE detectors. Note ISDE detectors start off with much larger donor concentration but both follow same type of curve, given by eq. (1).

800 MeV (damage expected is about twice that of typical pions at the SSC) and the second uses 1 MeV neutrons. The neutron data contain results from two detectors with very different initial doping concentration which nevertheless follow eq. (1), above.

If we assume, based on experience, that detector voltage breakdown will limit the voltage to about 150 volts, then the detector fluence lifetime is about 10^{14} particles/cm^2. This corresponds to a running period of 20 years at the standard SSC luminosity for a detector at a radius of 15 cm.[4]

Figure 4(a) and (b) shows the effect of the changing depletion voltage for the β spectrum observed in a silicon detector.[5]. The two detectors had been irradiated by 1 MeV neutrons, with the fluences equal to 1.7 $\times 10^{12}$/cm^2 (very lightly irradiated) and 6 $\times 10^{13}$/cm^2 (heavily irradiated), respectively. The charge was measured using a 40 nsec gate on an ADC, thus it measures not only the total charge but how prompt the collection is. The lightly irradiated detector requires 60 volts for nearly full prompt collection, while the irradiated detector requires about 100 volts. Once the voltage is adjusted, the heavily irradiated detector shows essentially full prompt charge collection

The third bulk affect in the silicon is the trapping of drifting charges by deflects. This appears to not be a large effect for fluences below 10^{14} particles/cm^2. This phenomenon, for holes and electrons, needs more quantitative study particularly in the fluence range:

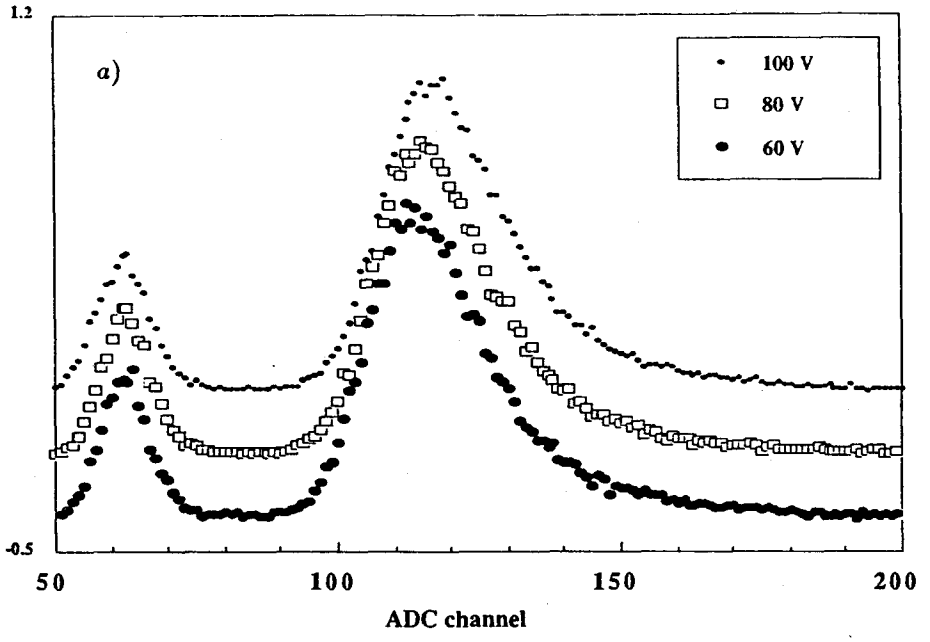
$$5 \times 10^{13}/\text{cm}^2 \leq \Phi \leq 5 \times 10^{14}/\text{cm}^2 \ .$$

3. Front-end Electronics

Fast front-end electronics are a challenging area for silicon detectors at the SSC. Key issues are pitch, speed, radiation hardness and signal-to-noise. Radiation hardness measurements have been presented a year ago,[6] implying the suitability of junction bipolar transistors for analog functions and radiation-hard CMOS for digital circuits at the 3 megarad-level characteristic of 10^{14} particles/cm^2 fluence. New data on analog applications of radiation-hard CMOS are available this year.[7]

A major milestone is the production of a first prototype preamplifier-discriminator meeting the 1 milliwatt per channel SSC goal.[8] This was done using the orbit foundry through MOSIS. We expect, in the next year, to have other examples of such amplifiers from Tektronix, AT&T, HP and possibly NTT in Japan, all using a better optimized bipolar process.

The circuit diagram is shown in Fig. 5; a comparison of simulated and measured analog and comparator pulses are shown in Fig. 6(a) and (b). Table 2 gives a list of some of the circuit's performance properties and the goal for the final SSC circuit.



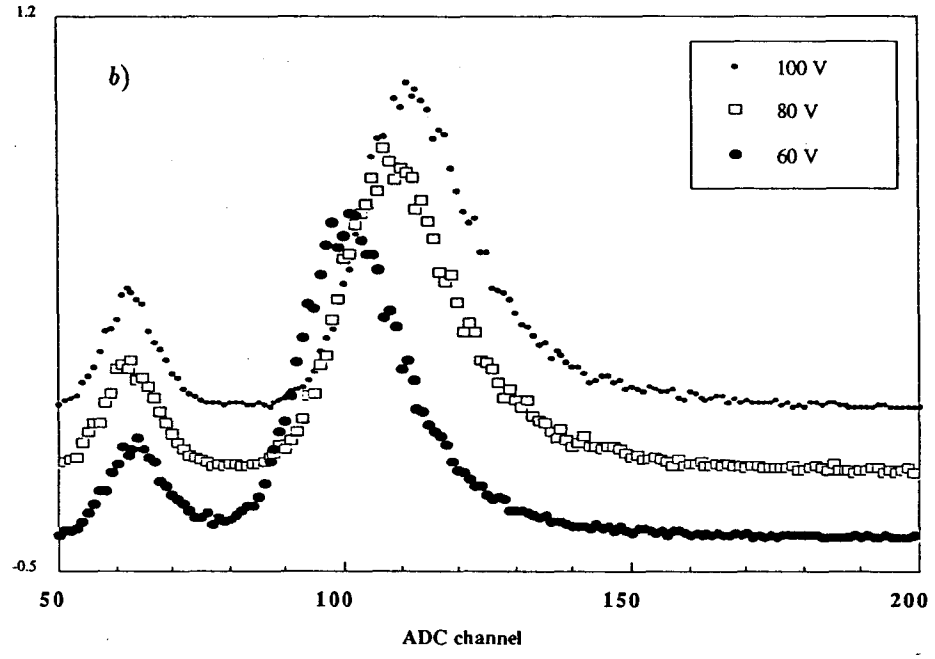


Fig. 4 Beta spectrum from irradiated diode. (a) Fluence = 1.7×10^{12} n/cm^2. (b) Fluence = 6.0×10^{13} n/cm^2.

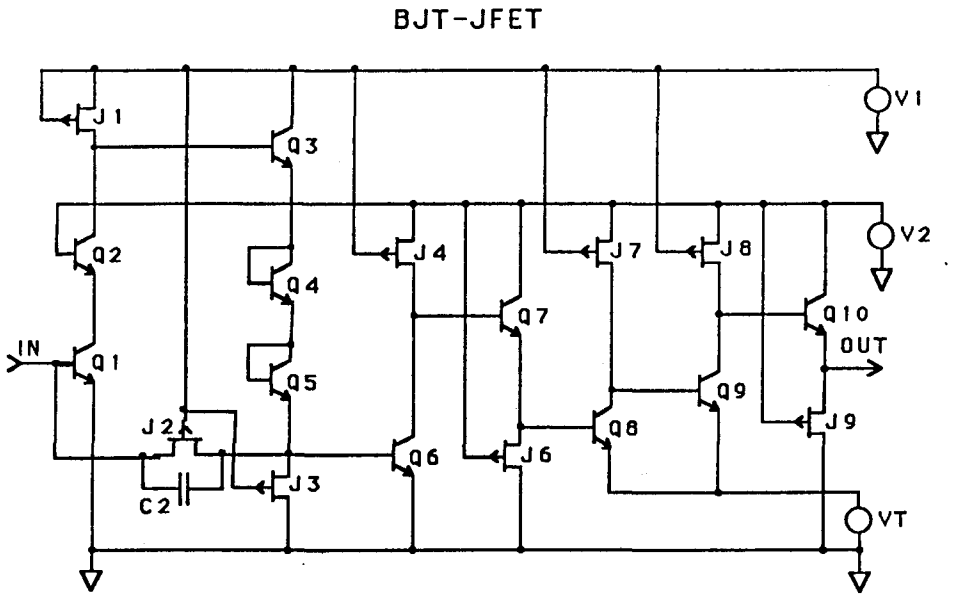


Fig. 5 Circuit diagram of the single channel of BJT-JFET front end.

Table 2. Front-end Performance

Orbit Chip		Final SSC Chip
Power:	Preamp 0.65 mW	OK
	Discriminator 0.23 mW	OK
Risetime:	25 nsec	20 nsec
Signal-to-noise:	12/1	20/1
Time-Walk, 2 fC–8 fC:	15 nsec	7.5 nsec

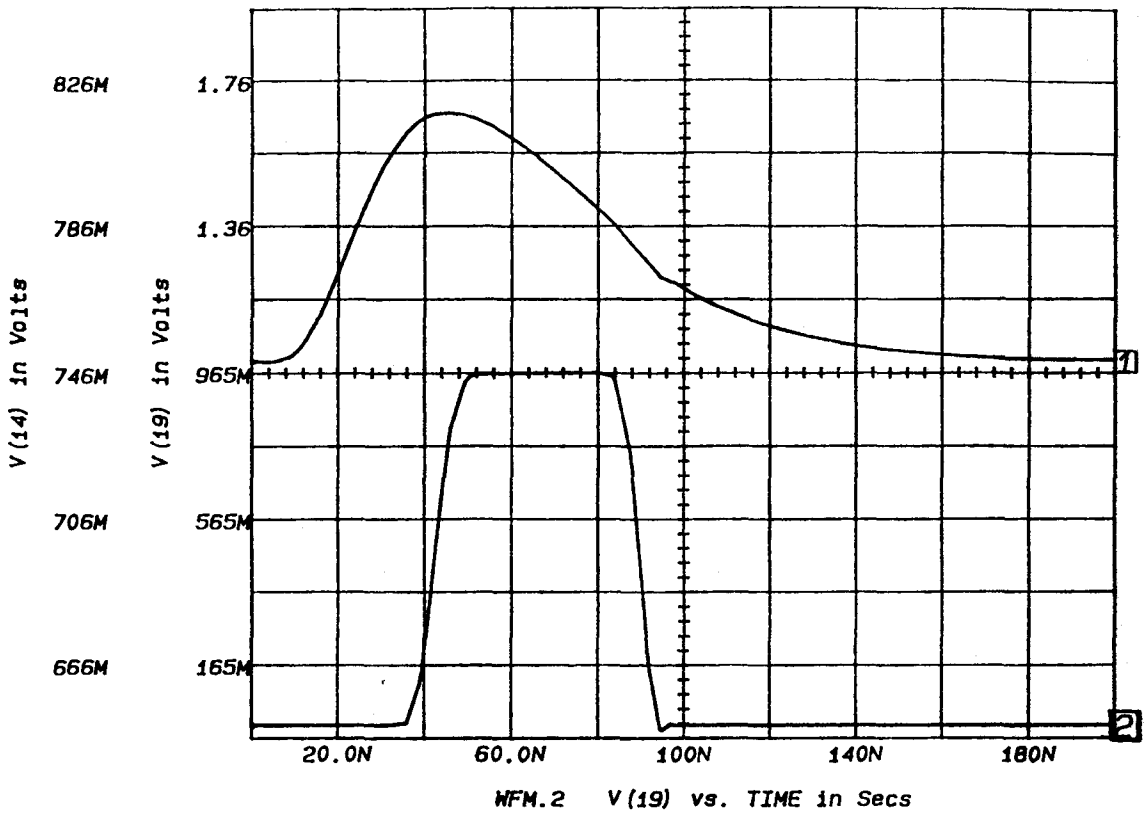


Fig. 6 (a). Simulated output waveforms of BJT-JFET circuit for a minimum ionizing particle and detector capacitance of 10 pF; 1-V(14) preamplifier output, 2-V(19) discriminator output.

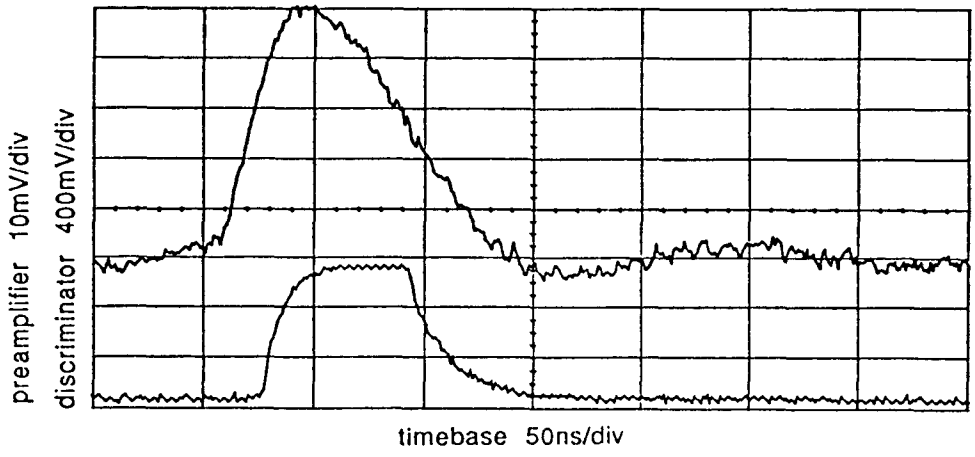


Fig. 6 (b). Records of the output signals from the BJT-JFET circuit for input charge of 4 fC and input capacitance of 10 pF; (a) preamplifier output, (b) discriminator output.

4. Mechanical Considerations

The silicon detector's pitch has been chosen to allow position measurement with an accuracy in the 10–15 μm range per double-sided detector. To avoid degrading the detector performance, it is important that the mechanical system which holds the detectors provide position stability of about 5 μm, as discussed below. In addition, the amount of material that can be tolerated in the support structure is, at most, a few per cent of a radiation length.

Fig. 7 shows a picture of the suggested support framework planned for the detectors. The detailed design has been done by a group at the Los Alamos National Laboratory.[9] The central detector wafers are stiffened by edge-bonded carbon fiber strips as shown in Fig. 8. These units are supported on cylinders which can hold up to 4 layers and which are in turn held on a large frame which also supports the forward planes. Figure 9 shows the units from which the frame is made. Figure 10 shows the frame in more detail. It is made of cylindrical tubes which connect together. To provide adequate positional stability, the material for the detector framework has to be chosen to avoid creep as well as dimensional change under radiation. It must be built in such a way as to avoid putting stresses on the brittle silicon detectors as temperatures change.

A highly desirable property for the frame would be a negligible coefficient of thermal expansion. This can be achieved by the use of graphite–metal matrix composite materials, which also have adequate strength and reasonably good thermal conductivity. Figure 11 shows the coefficient of thermal expansion versus the composition of the material. A value of zero with mostly graphite, which has a large radiation length, is possible.

Figure 12 shows the material intersected by a particle for the space frame support as a function of azimuth at a 30° production angle, which is chosen as an example. Shown in the figure is an all beryllium support (best material from a radiation-length point of view, but not best thermal properties) as well as the metal matrix material. The flat baseline is the material from the beampipe and outer detector enclosure. The average number of radiation lengths is less than 1.5%.

An end view of the barrel detector is shown in Fig. 13. The paired detectors, tilted to compensate for the magnetic fields influence on charge collection in the silicon, and the three support cylinders needed for 10 silicon layers are shown. The most likely material for the cylinders are thin carbon fiber skins sandwiching a corrugated ribbon filler. The silicon pairs and servicing rings which carry coolant and cables are shown in Fig. 14.

The plan for the cooling of the detector electronics involves evaporative cooling using heat pipes. Such a system is extremely efficient, involves small fluid flows, and will equilibrate the temperature globally. The elements involved in such a system are:

(a) Reservoir to provide fluid, which requires a few cm diameter input line.

(b) Arteries to feed fluid to circuits.

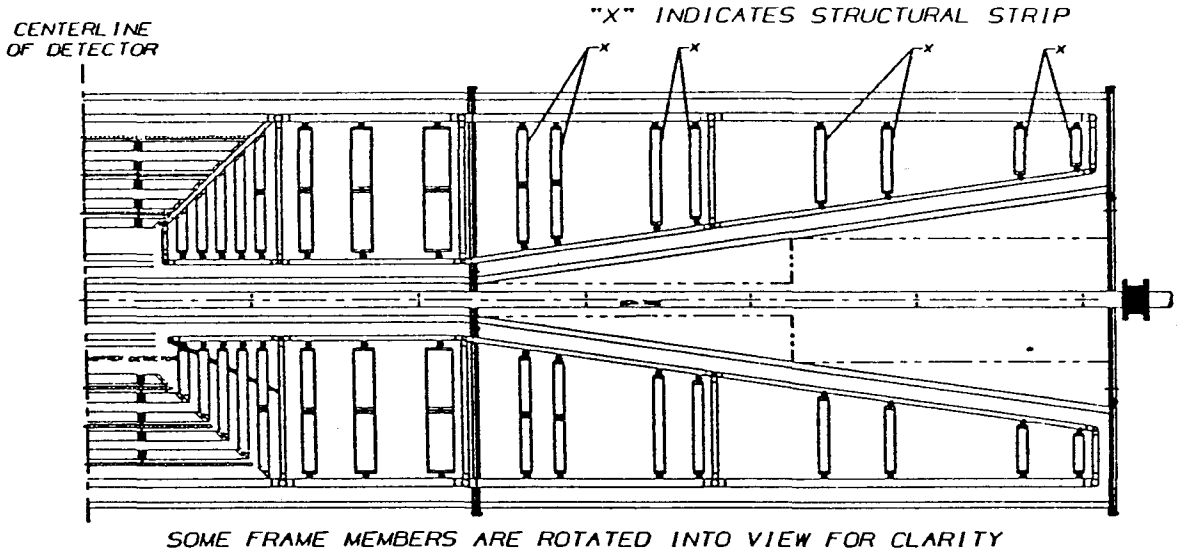


Fig. 7 Schematic drawing of silicon detectors and support members.

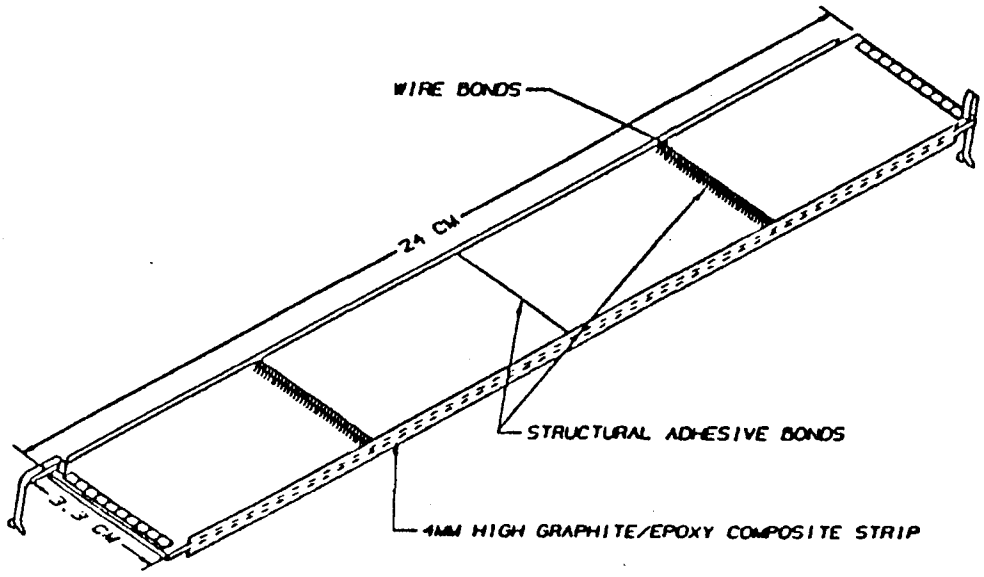


Fig. 8 Silicon wafer assembly with wire and adhesive bonds and graphite/epoxy composite edge-strip reinforcement.

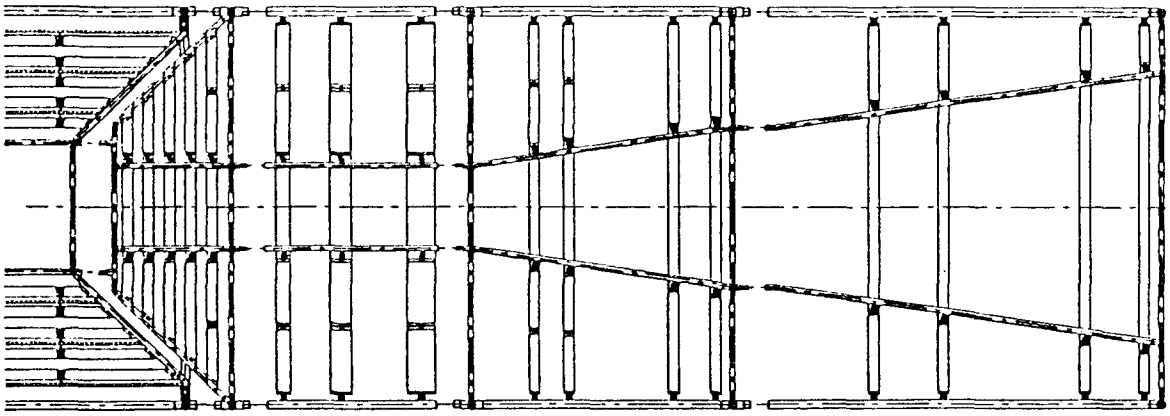


Fig. 9 Schematic drawing of pieces from which the detector is assembled.

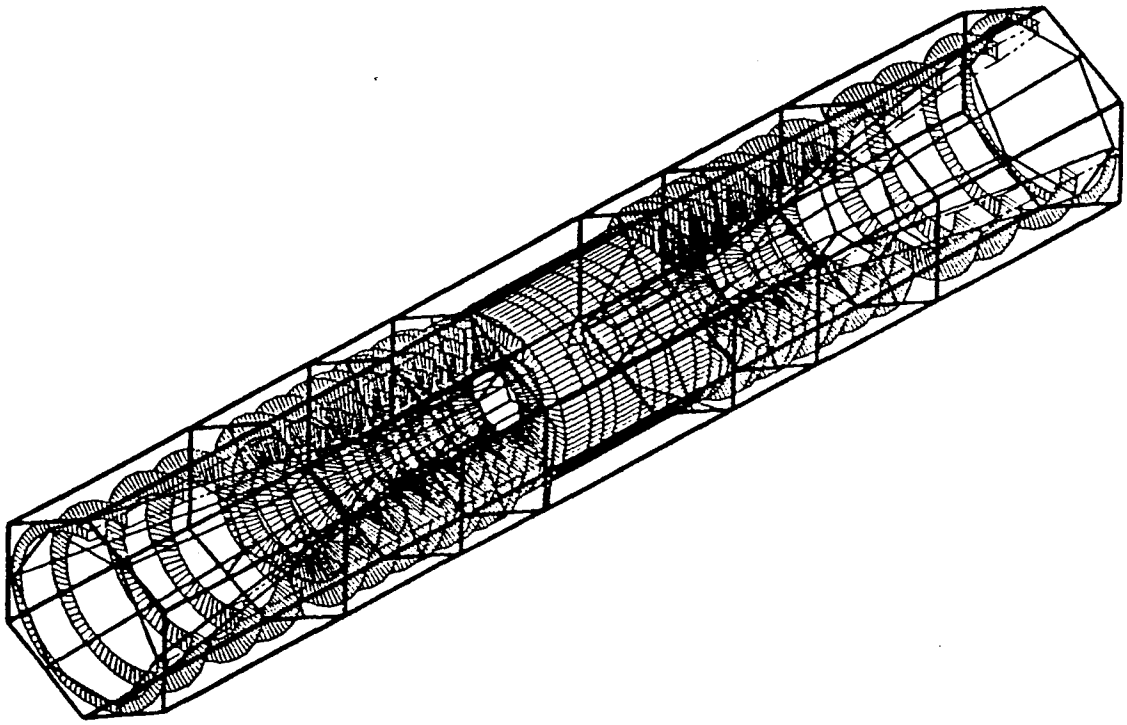


Fig. 10 Three-dimensional picture of framework for detectors.

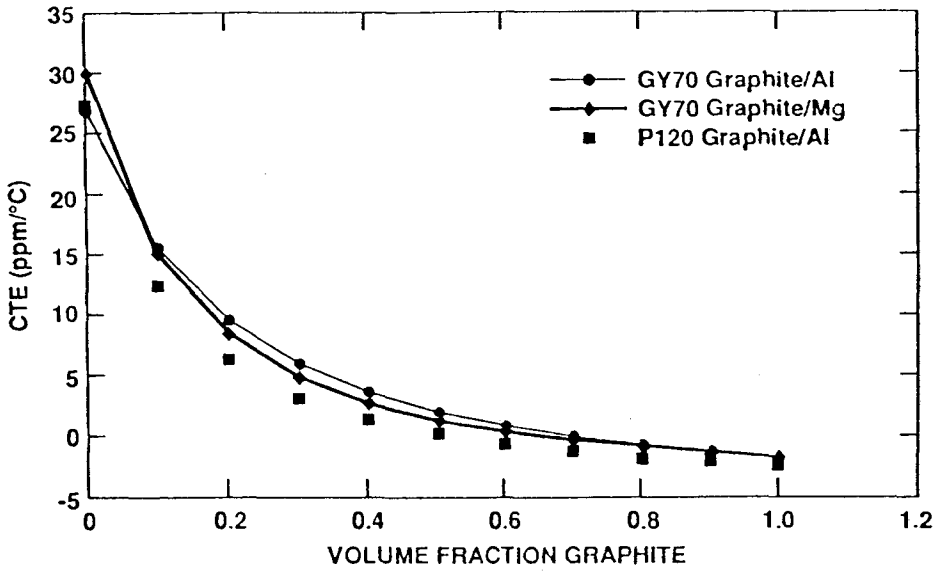


Fig. 11 Isotropic thermal expansion coefficient vs. metal matrix composition.

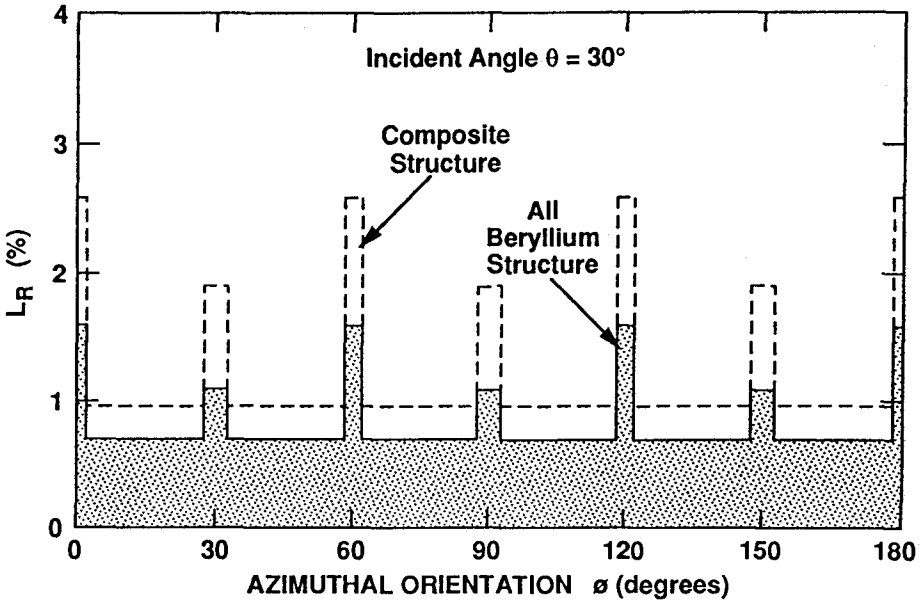


Fig. 12 Per cent radiation lengths, as a function of azimuthal angle, crossed by a particle emanating from the origin at 30° to the beam.

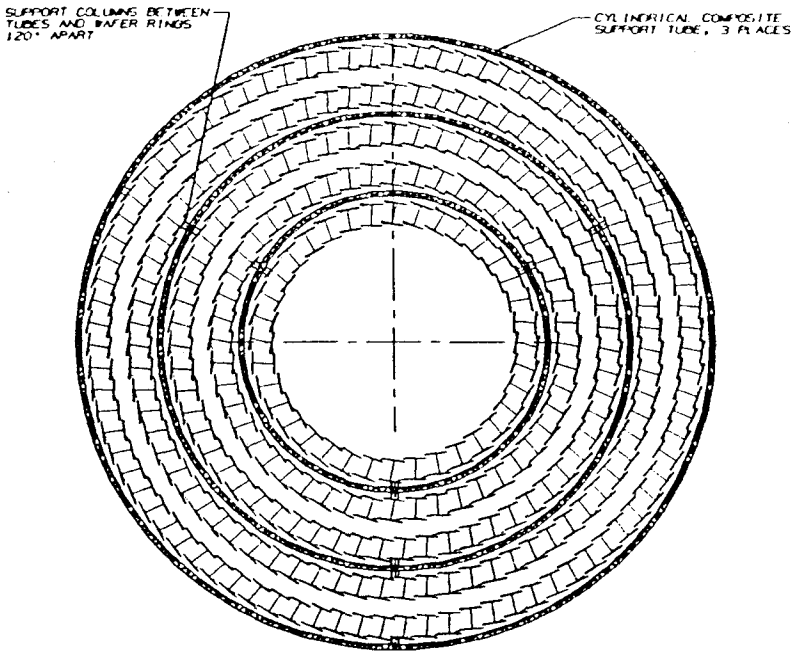


Fig. 13 End view of barrel detector.

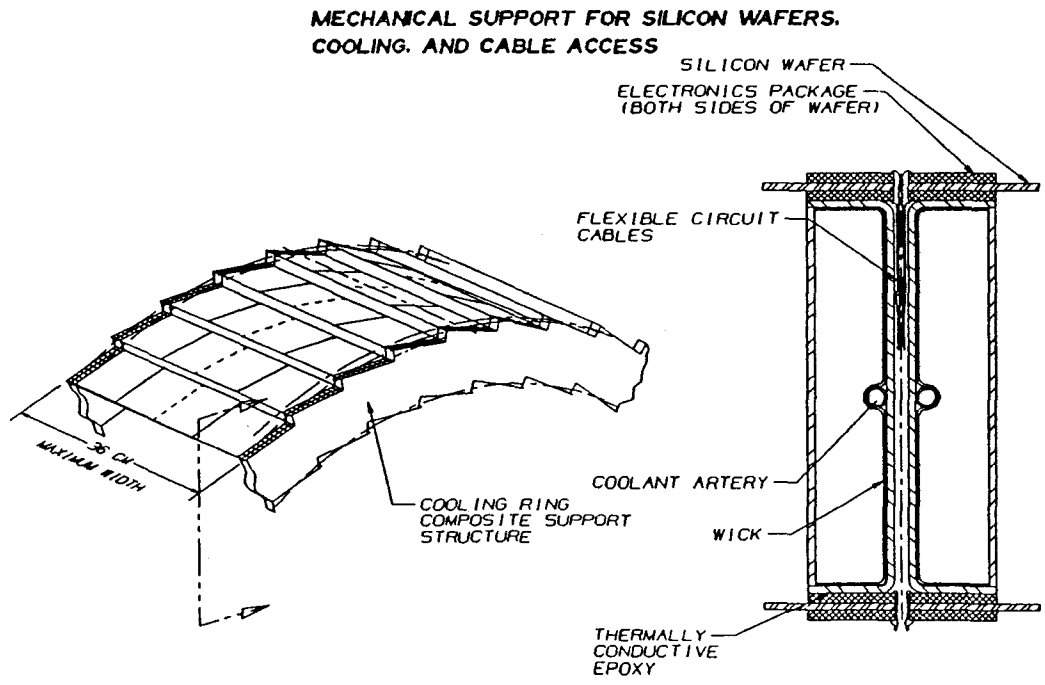


Fig. 14 Silicon paired layers and end cooling rings. Design assumes double-sided detectors with end readout.

(*c*) Wick structure to take heat from the electronics. This is a set of capillaries which soak up the liquid. This is self-regulating—the amount of heat drives the absorption rate of liquid by the wick. The temperature is set by the liquid evaporation temperature.

(*d*) The vapor can fill the detector cavity (if it is non-reactive) or can be returned along sealed paths.

(*e*) Outside the detector volume a condenser turns the vapor back to liquid.

(*f*) Our present choice of cooling fluid is a hydrocarbon. This allows a range of temperature choices, however has the disadvantage of involving a flammable substance. At present we plan to run at 0° C temperature.

A first wick and cooling ring prototype has been tested with butane as the coolant. The wick material is polystyrene and it has successfully demonstrated the removal of heat for hours by a fully passive system (i.e., without pumps). To achieve the full benefit of such a system it is critical that the resistance to heat flow between the heat source and wick be minimized. This will require, in the coming year, a careful selection of glues and design optimization of the cooling ring itself.

The stability goals for the strip elements have been chosen to be:

5 μm in the circumferential position

80 μm in the radial position

250 μm in the longitudinal position

The edge bonded wafers will sag less than 50 μm at the center which is compatible with the 80 μm goal above. The goal for circumferential placement is 25 μm, with mapping of this coordinate to the 5 μm level.

The large sub-assemblies (the cylinders or forward disk arrays) are meant to be constructed within the radial and longitudinal tolerances and then mapped to achieve the circumferential accuracy listed above. These large sub-assemblies then have to be aligned relative to each other. Beam particles in events will provide a final measurement and monitor for the alignment and stability.

5. Pixel Detectors

Pixel detectors are an attractive choice for the inner layers of an SSC tracking system. Two major directions are being pursued. The first involves separate detectors with matching chips which are bump bonded together.[10] Initial electronics for a 50 μm by 150 μm pixel cell has been developed by Hughes. An advanced pixel cell has also been designed at LBL. The second method involves the fabrication of detectors and electronics integrated on the same wafer. First results from such a detector, developed by the University of Hawaii and the Stanford Center for Integrated Systems, are now available.[11]

Figure 15 shows a block diagram of the LBL advanced pixel cell, which features DC stabilization, signal filtering, analog sampling, neighbor logic and discriminator

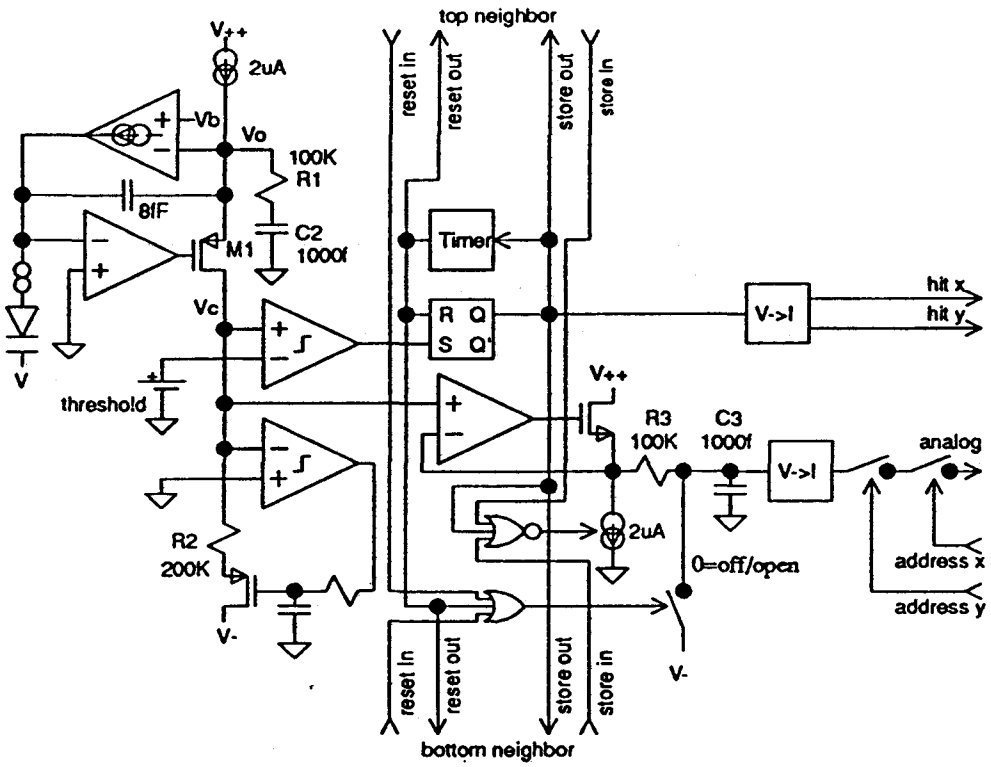


Fig. 15 A block diagram of the LBL advanced pixel cell, illustrating DC stabilization, signal filtering, analog sampling, neighbor logic and autoreset.

autoreset. One of the more difficult issues is achieving single time bucket discriminator timing at very low power. Figure 16 shows the time slewing for the LBL discriminator. One interesting suggestion[10] is to measure the time-over threshold, t_1 and t_2 in Fig. 17, and use the two times to reconstruct the total charge and bucket timing. This would require only logic cells for recording discriminated signals rather than charge storage elements allowing for a smaller pixel cell.

Figure 18 shows the schematic for the monolithically integrated pixel detector. Figure 19 shows the signal seen in such a detector. After pedestal subtractions the signal-to-noise is greater than 100 to 1.

Figure 20 shows what a pixel ladder, compatible with the strip system cooling and mechanics might look like. Such ladders could be placed to form a cylindrical array with little or no dead area.

6. Silicon Drift Detectors

The final type of silicon detector under development is the silicon drift detector. In this arrangement all of the electronics is located at the edge of the silicon wafer. The electric field in the detector is arranged to cause the electrons to drift to the edge. Two-dimensional position information is then given by the channel collecting

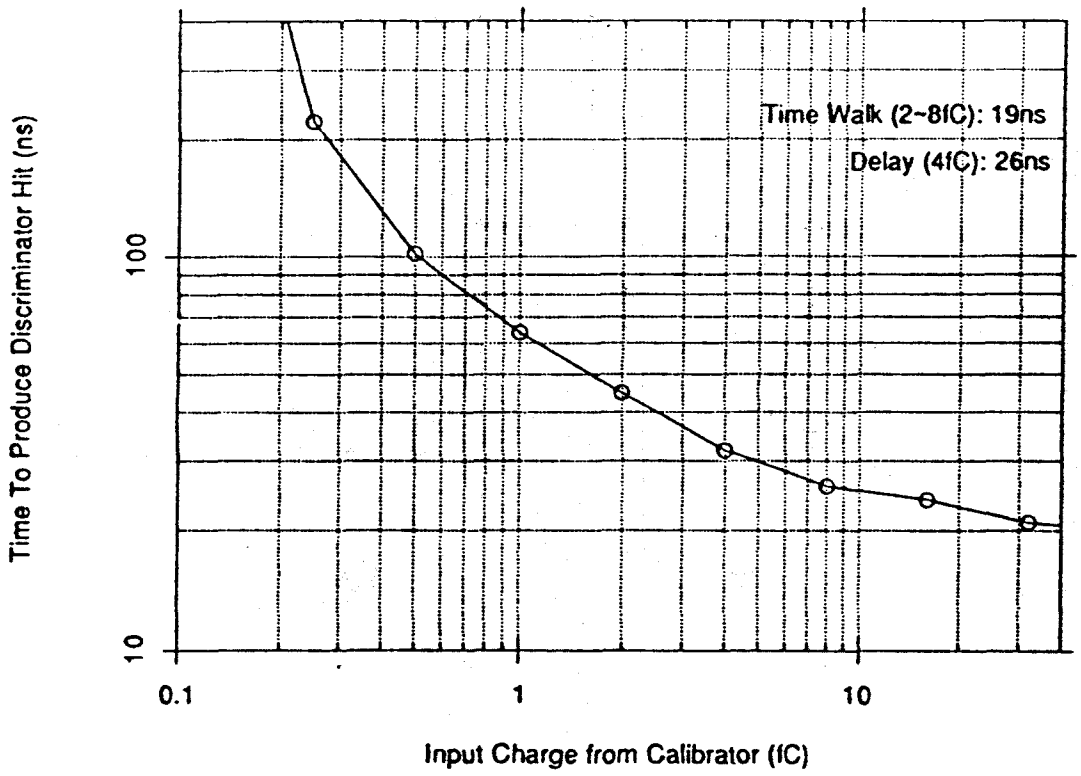


Fig. 16. A measurement of the time-walk for a wide range of input charges and a threshold of 1000 electrons (1/6 fC).

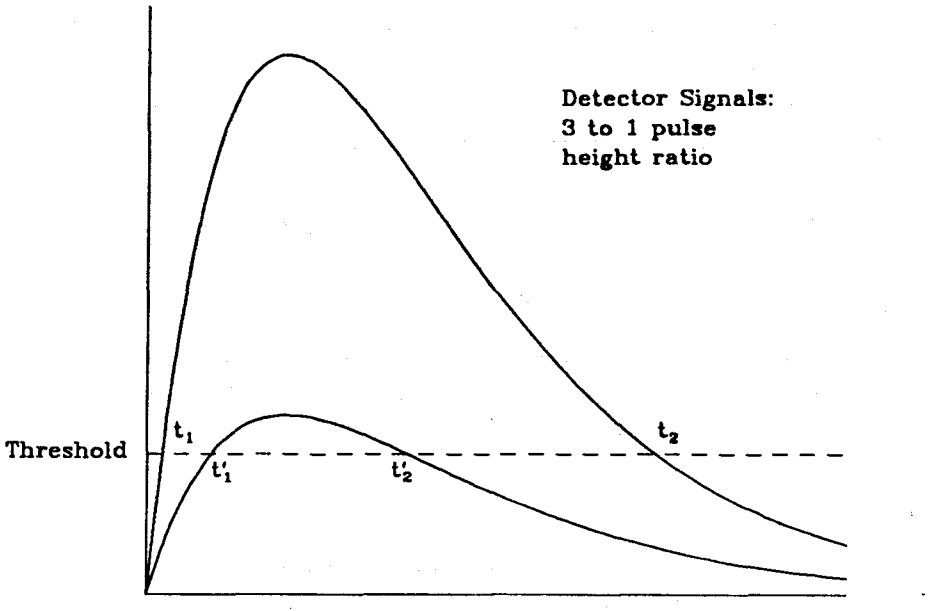


Fig. 17. Use of t_1 and t_2 as determined by discriminator to get total charge collected and bucket time association.

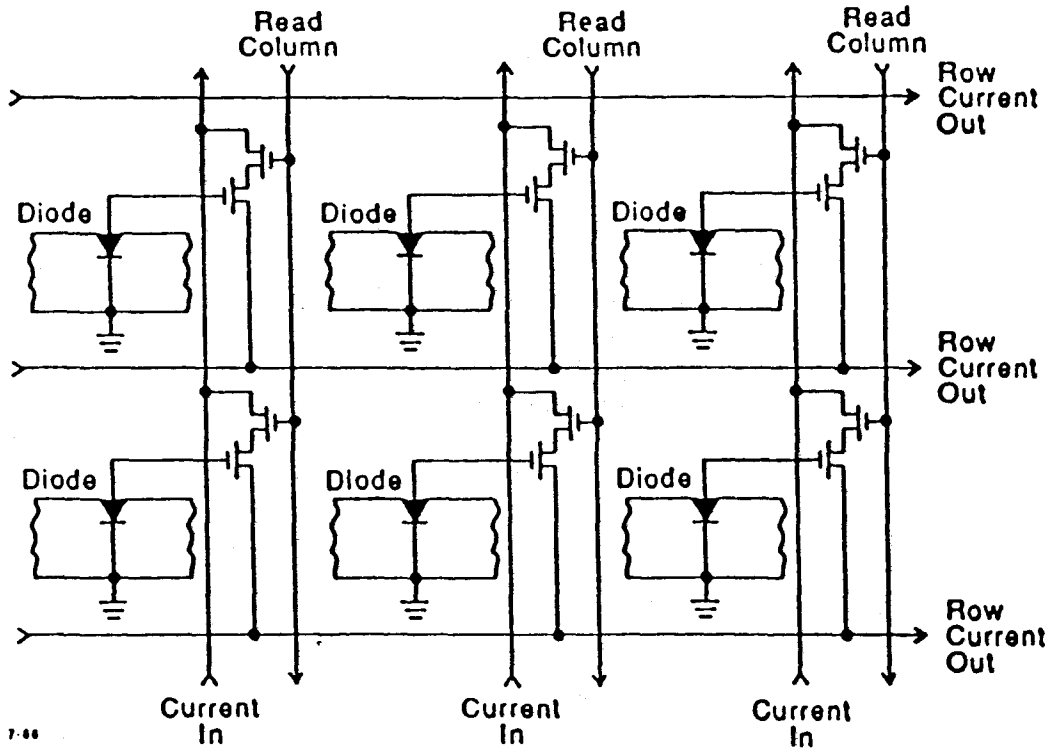


Fig. 18. Schematic for monolithically integrated pixel detector.

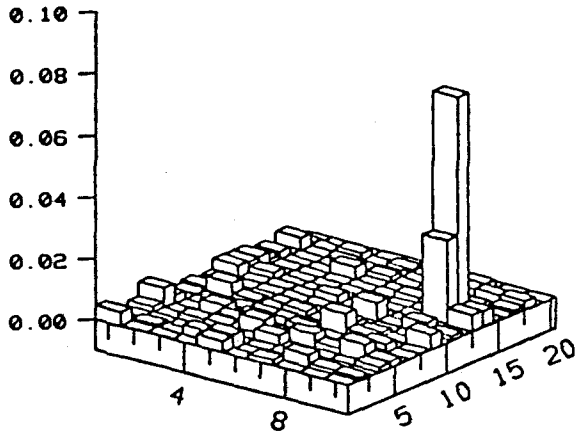


Fig. 19. Signals for a pixel device with one passing particle.

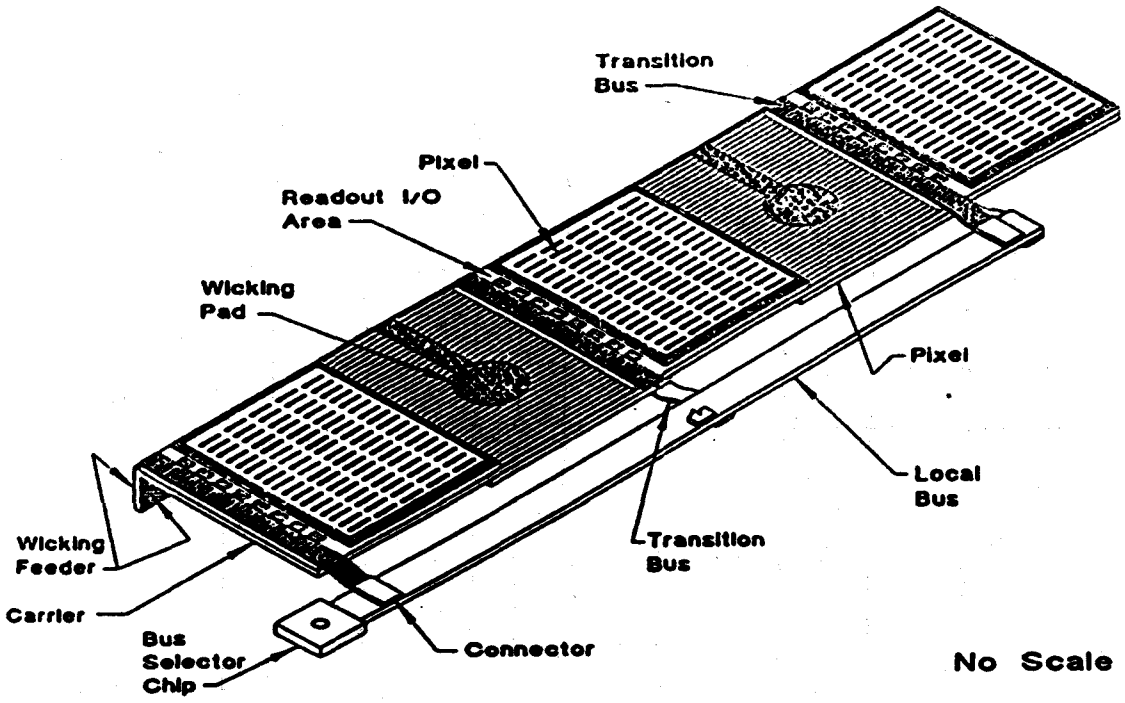


Fig. 20. The pixel/carrier subassembly illustrating the evaporative cooling concept.

the charge and the drift time. To unravel the drift-time from the time-bucket of the event, it is necessary to use paired detectors with electronics on opposite ends.

Since the position accuracy is dependent on the mobility and field, a careful understanding of these quantities is needed. Initial measurement[12] of the electron mobility (related to the velocity) and the Hall mobility (related to the Lorentz Angle) is given in Fig. 21. This type of detector is potentially the most sensitive to radiation damage since the time determination depends on the details of the electric field within the silicon. A quantitative understanding of this issue still doesn't exist.

7. Gas Microstrips

This is a recent development which aims at the replacement of a multi-wire proportional chamber by metal lines on a dielectric substrate.[13] This allows the reduction of the anode pitch to 300 μm or less, allowing good resolution and very low occupancy when compared to typical devices with wires.

Some of the special R&D issues relevant for use of this technology at the SSC are as follows:[14]

1. It would be advantageous to replace the glass-substrate on which the metal lines are placed by a less fragile, thinner material.
2. Charging of the substrate by positive ions is a potential problem for high rate stable operation.

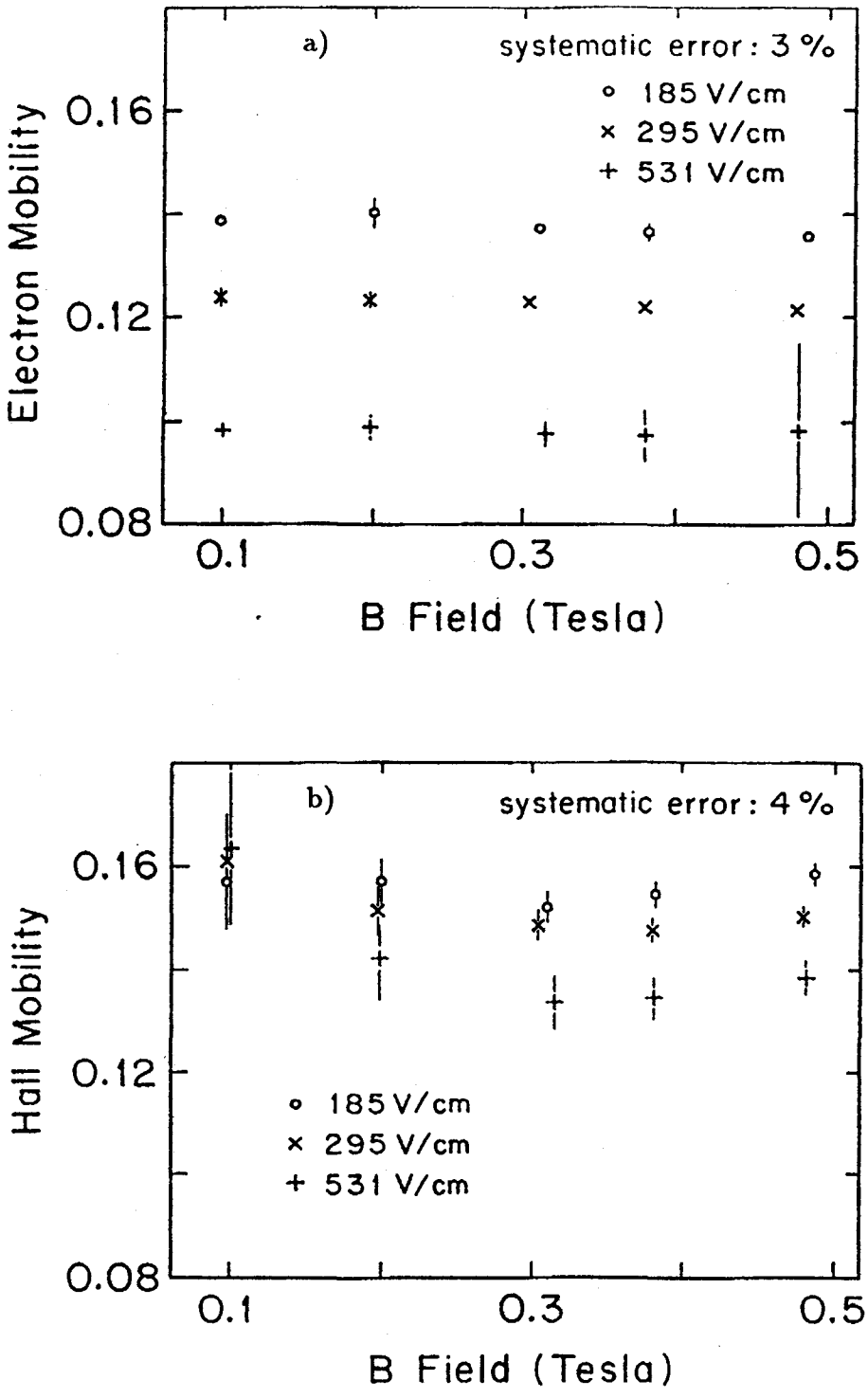


Fig. 21. a) Electron mobility vs. magnetic field at a constant temperature; b) Hall mobility as a function of the magnetic field at a constant temperature.

3 One would like to be able to reduce the pitch for higher precision. This is limited by surface breakdown.

4. Because of ionization statistics in the chamber gas it is difficult to get 100% efficiency and single bucket response time.

Figure 22 shows a typical planar gas microstrip chamber. Figure 23 shows a chamber made on a silicon substrate.[14] Through the use of trenching the field is reduced between the metal electrodes allowing for a reduction in pitch to 75 μm. This allows more precise position measurement but still uses a substrate which is difficult to make in large dimensions.

The use of insulating substrates presents a problem because of charging. The insulation would be adequate and the ions removed if a substrate with surface resistivity of $10^{13}\Omega$/square could be found. The use of heterogeneous mixtures (conductive regions in an insulator) does not work very well because of non-ohnic resistive properties and internal micro-discharges. Both homogeneous glasses and plastics have now been found with resistivity in the correct range. These will be undergoing extensive tests in the near future.

Figure 24 shows an arrangement of gas microstrip detectors which could be used to cover forward rapidities in the SDC detector. The detector has three stations, each providing four measurements. Half the measurements directly measure the bending coordinate ϕ, the other half are small angle stereo. The individual gas microstrip detectors are wedge shaped. These three stations provide a stiff track first level trigger as well as precision position measurement for forward going tracks.

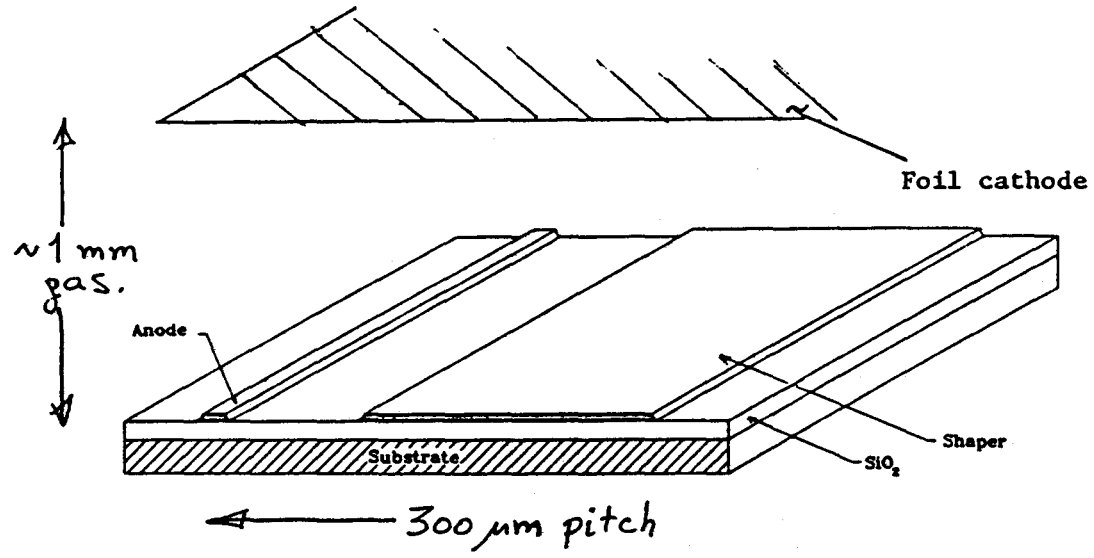


Fig. 22. Typical planar gas microstrip chamber showing anode, field shaping electrodes and 1 mm gas gap.

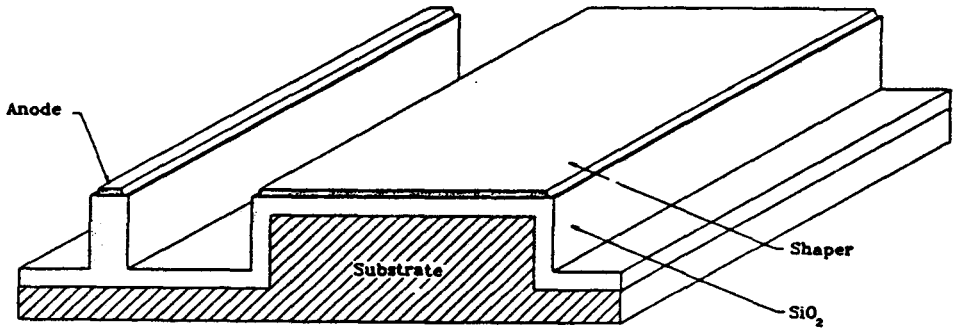


Fig. 23. Gas microstrip chamber with trench near anode to reduce electric field in substrate.

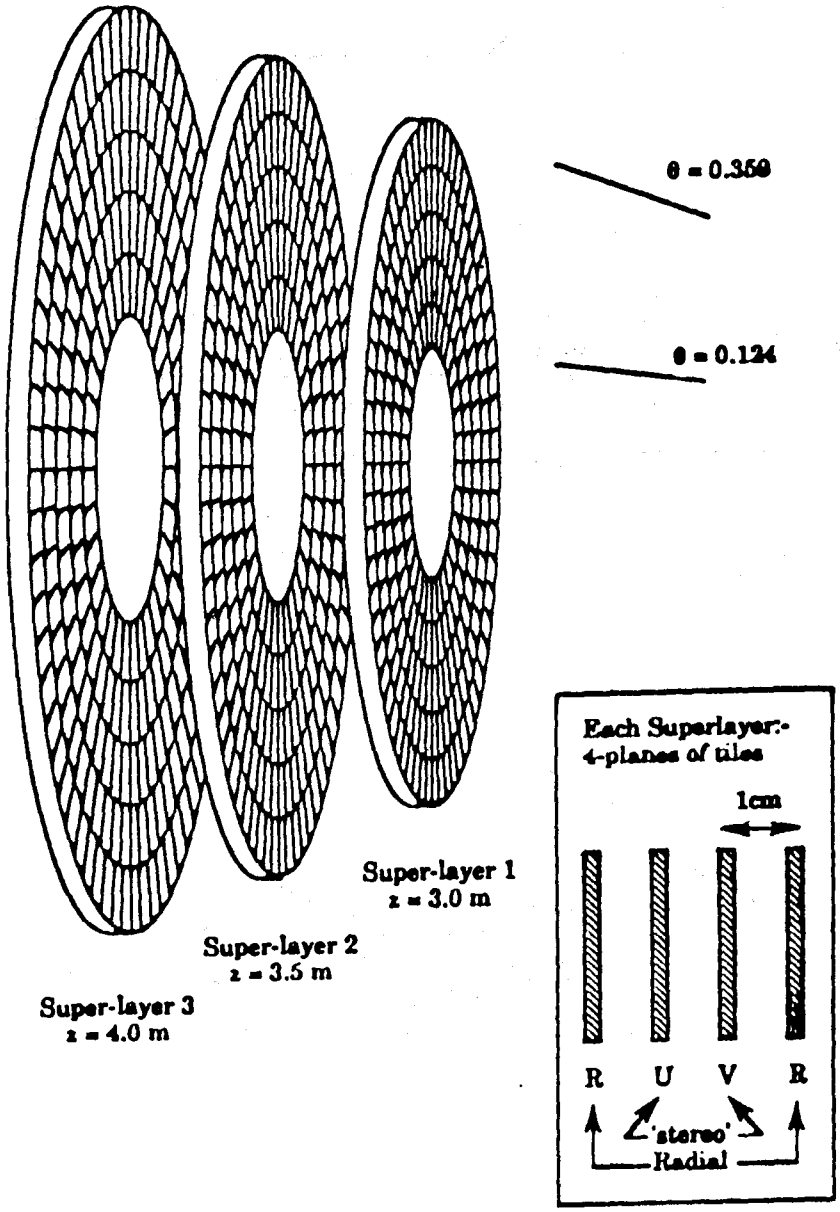


Fig. 24. Three superlayer gas microstrip disk arrays proposed for the SDC. Each superlayer contains, shown in inset, two layers which measure the ϕ angle (radial strips), and two stereo layers.

REFERENCES

1. G.H. Trilling *et al.*, Letter of Intent by the Solenoidal Detector Collaboration to construct and operate a detector at the Superconducting Super Collider, SDC-90-000151 (November 30, 1990).
2. D. Pitzl *et al.*, Type Inversion in Silicon Detectors, SCIPP Preprint 91/05 (1991).
3. P. Giubellino *et al.*, SCIPP 91/22, presented at the 5th Pisa Meeting on Advanced Detectors, Isola d'Elba, La Biodola, May 26–31, 1991.
4. J. Hylen *et al.*, Silicon Tracking Conceptual Design Report, SCIPP Preprint 90/24 (1990).
5. G. Hall and S. Sotthibandhu, Imperial College Internal Note IC/HEP/91/1 (1991).
6. H.F.-W. Sadrozinski *et al.*, presented at the 2nd London Conference on Position Sensitive Detectors, London, September 4–7, 1990, SCIPP Preprint 90/34 (1990).
7. W. Dabrowski *et al.*, presented at the IEEE Nuclear Science Symposium, Santa Fe, NM, November 5–9, 1991, SCIPP Preprint 91/24.
8. W. Dabrowski, H.F.-W. Sadrozinski and J. DeWitt, SCIPP Preprint 91/31 (October 1991), submitted to *Nucl. Instrum. & Methods A.*
9. W.O. Miller *et al.*, Superconducting Super Collider Silicon Tracking Subsystem Research and Development, LA-12029 (December, 1990).
10. E. Arens *et al.*, SSC Subsystem R&D Program, Progress Report of the Collaboration for Development of Pixel Vertex Detector Technology, September 1991.
11. Sherwood Parker, private communication, 1991.
12. W. Chen *et al.*, SSC Detector Subsystem R&D Interim Report on Silicon Drift Devices for Tracking and Vertex Detection, September 1991.
13. A. Oed, *Nucl. Instrum. & Methods* **A263**, 351 (1988); F. Angelini *et al.*, presented at IEEE Symposium on Nuclear Science, Arlington, VA (1990).
14. P. McIntyre, Gas Microstrip Chambers, SSC Subsystem R&D Program FY 1991 Progress Report, Texas A&M University (1991).

Tracking III

H. J. Hilke

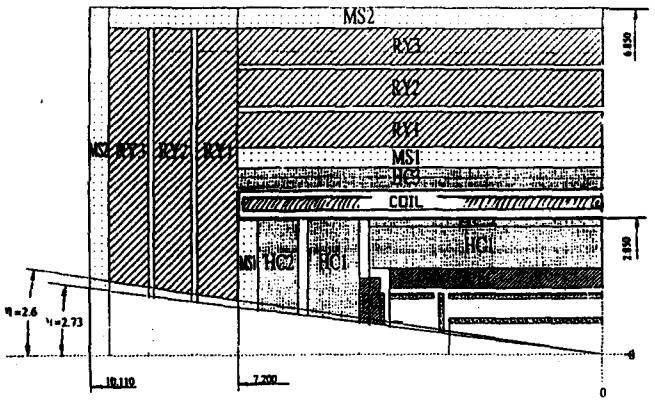


Figure 1. Compact Superconducting Solenoid. 4T

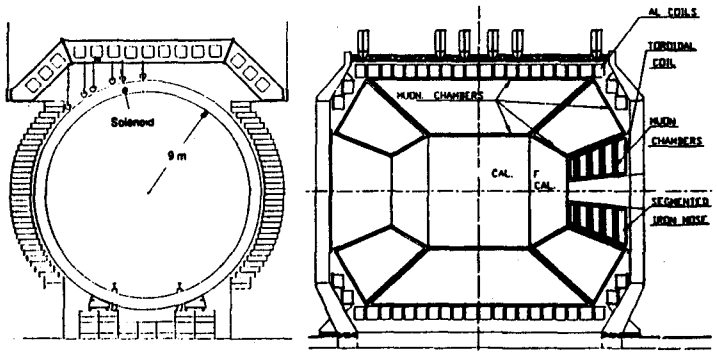
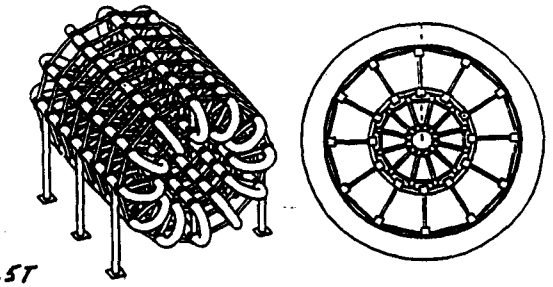
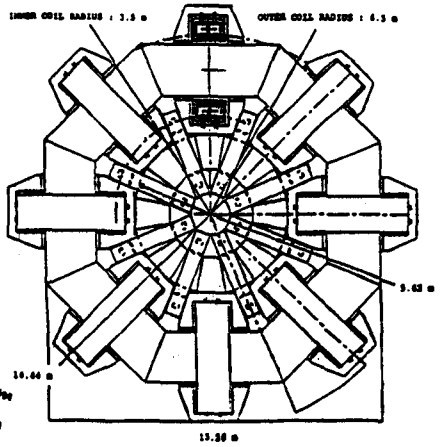


Figure 2. Large Field-Shaped Solenoid. 0.5T



1.5T
Ø : 20m
L : 26m

Figure 3. Superconducting Air- Core Toroid.



3.5T
Ø₀ : 12.8 m
L : 20 m

Figure 4. Superconducting Iron-Core Toroid.

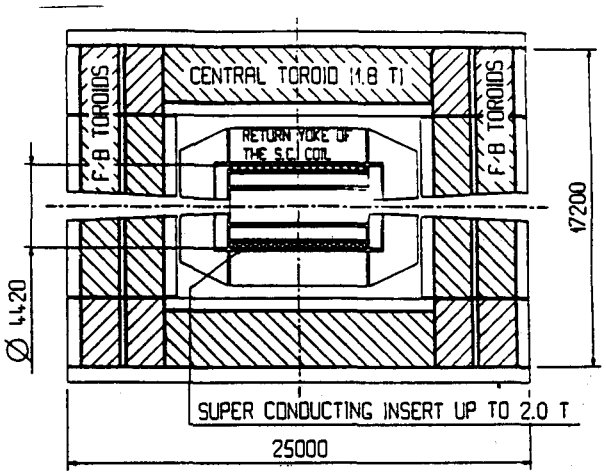


Figure 5. Warm Iron-Core Toroid with Central Superconducting Solenoid.

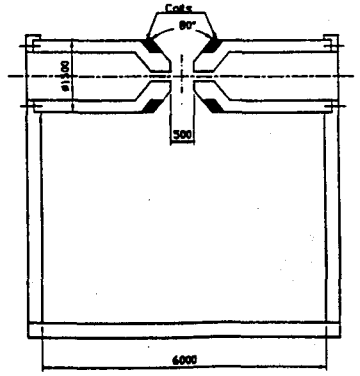


Figure 6. Open Axial-Field Magnet for Heavy Ion Experiment.

II MUON DETECTION

'COMPACT MUON SOLENOID DET.' (CMS)
(RD5)

(Aachen - Budapest - CERN - SEFT - CIEMAT - NIKHEF - Padova - Roma - UCLA - Riverside - Vienna - Warsaw)

SYSTEM TEST OF VARIOUS ELEMENTS:

- MUON RECONSTRUCTION + MOMENTUM MEAS. (EFFECTS OF 'CATASTROPHIC ΔE + δ-Electrons)
- TRIGGER: EFFICIENCY + REJECTION AGAINST h-PUNCH-THROUGH + DECAY MUONS
- EVALUATION OF TRACKING DET.:
  - * RESISTIVE PLATE CHAMBERS (RPCs) (Mainly for trigger)
  - * HONEYCOMB CHAMBERS
  - MICRO-STRIP GAS CHAMBERS
  - Si - TRACKERS

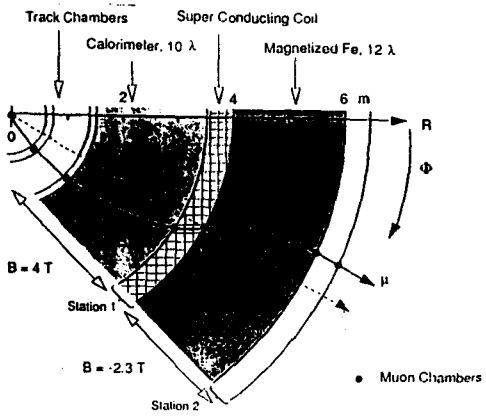


Figure 7. Principle of Compact Muon Solenoid Detector.

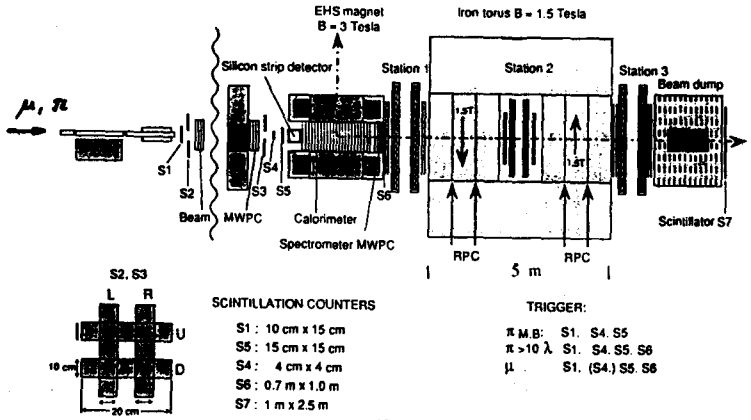
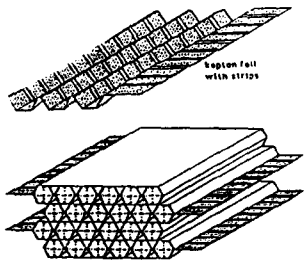


Figure 8. Test Beam Set-up for RD5.

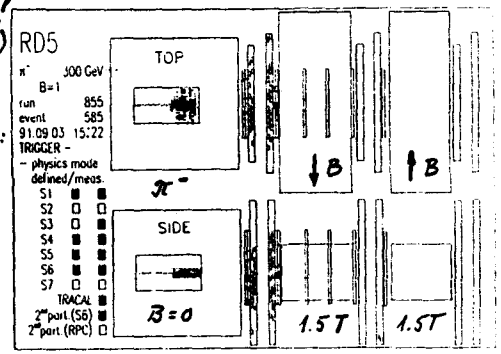
JM: BEAM DATA TAKEN WITH:

- B_1 (CAL.) = 0 ; B_2 = 1.5T
- CALORIMETER : 4/8 cm Fe samples + Honeycomb Chambers (25x) 0.7 × 1.2 m²
- Resistive Plate Chambers 2 × 2 m²

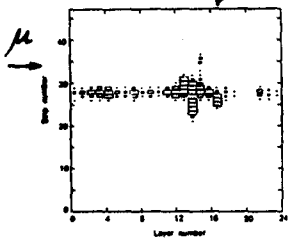
Prelim. : No drop in ε for 2 kHz/cm²! (lower res. plates)

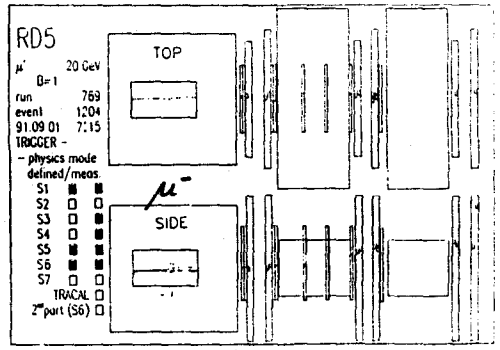


EVENT DISPLAYS:



'CATASTROPHIC ENERGY LOSS'

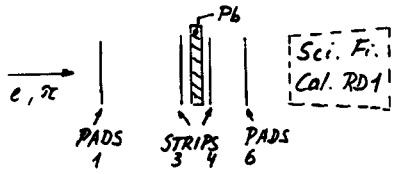




HONEYCOMB CH. IN CALOR.

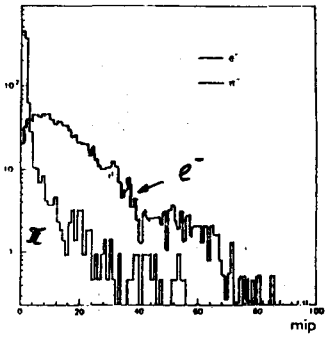
↳ PROTOTYPE (0.6 × 0.8 m²) gave σ_x = 70 μm

'91 TESTS



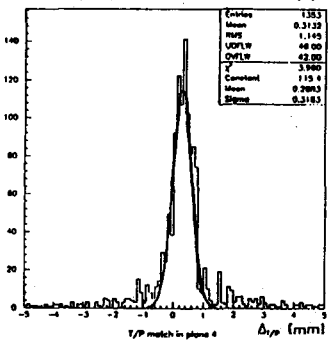
- PRELIM. RESULTS:

PH in Plane 4



MATCH TRACK w. PRE-SHOWER

Match (1-3) with PH Maximum(4)



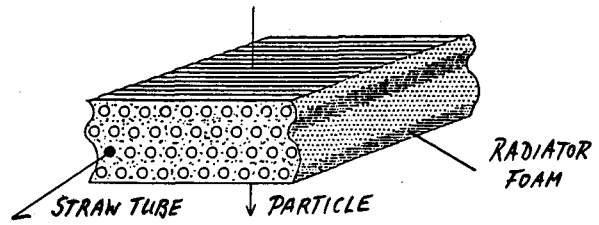
↳ FWHM/2.35 = few 100 μm.

- RADIATION TESTS : 20°, -20°, -170°C
  ANNEALING AT +20°C SEEMS NECESSARY!
- ELECTRONICS : NEW 32 ch. CHIP BEING TESTED, INCL. PIPELINE + SOME LOGIC

III.2. TRACKING TRD DET. (RD6)

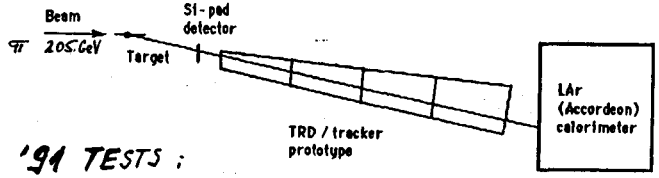
(Boston - BNL - CERN - Glasgow - Dubna - Lebedev Moscow - Leningrad - Lund - Moscow PEI - RAL)

4 mm Ø STRAW TUBES INSIDE POLYETHYLENE FOAM (= TRANSITION RADIATOR)



BEFORE : Xe / CO_2 50/50%
NOW : Xe / CF_4 / CO_2 70/10/20 %

TEST BEAM SET-UP

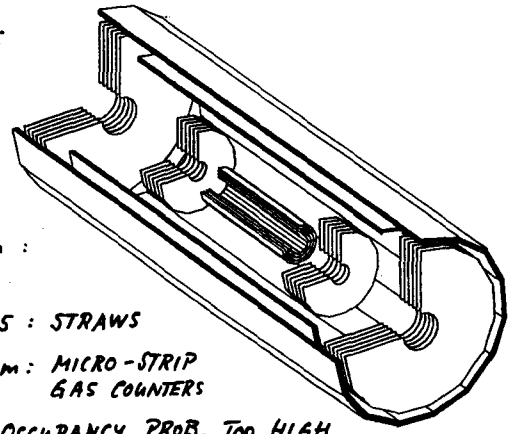


'91 TESTS :

- 1000 STRAWS ; 48 / TRACK ('90 : 2 = 192 STRAWS)
- NEW GAS
- B = 0

INNER TRACKERS

2 OPTIONS STUDIED :

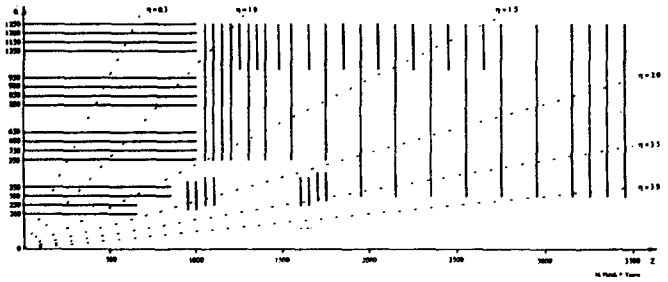


(a)

- $R = 0.15 - 0.3\,m$: SILICON
- $R = 1.15 - 1.45$: STRAWS
- $z = 1.7$; $3.7\,m$: MICRO-STRIP GAS COUNTERS

STRAWS : OCCUPANCY PROB. TOO HIGH (10% at 1.1 m , $\mathcal{L} = 2 \times 10^{34}$)

(b)



$R = 0.2 - 0.3\,m$: SILICON

$R = 0.5 - 1.2\,m$ + FORWARD : MICRO-STRIP GAS C.

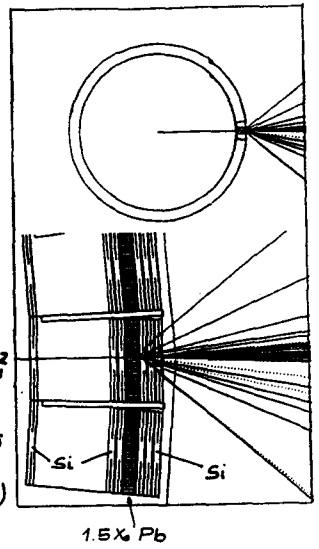
III ELECTRON IDENTIFICATION

1. SILICON TRACKING + PRE-SHOWER DET. (SITP)

(Cambridge, Oxford, RAL, Dortmund, Hamburg, Oslo, Perugia, Australia, Saclay, CERN, Geneva.) (RD2)

Aim

- **Provide track vector preceding calorimeter**
- +
- **Preshower information for rejection of backgrounds to electron identification**

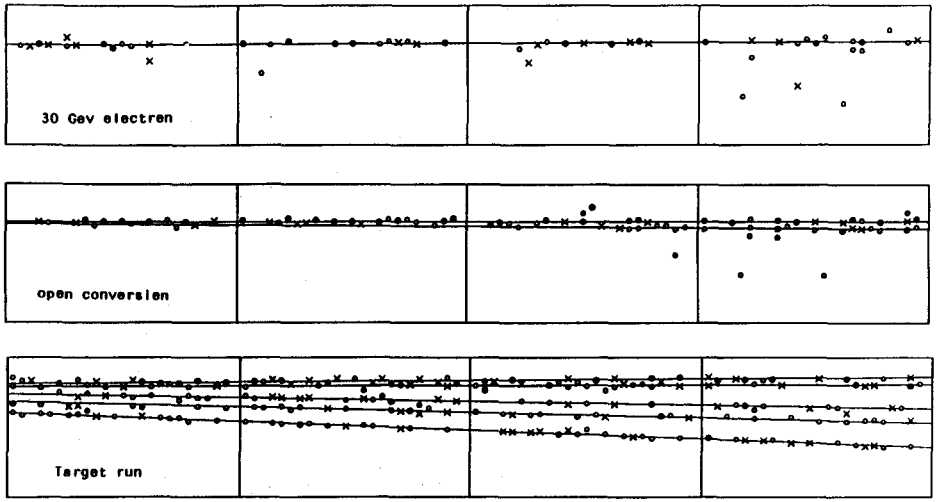


PADS $3 \times 3\,mm^2$

+ STRIPS $0.4 \times 24\,mm^2$

EACH PLANE = 4 COUNTERS WITH OVERLAP (i.e. 4×64 channels)

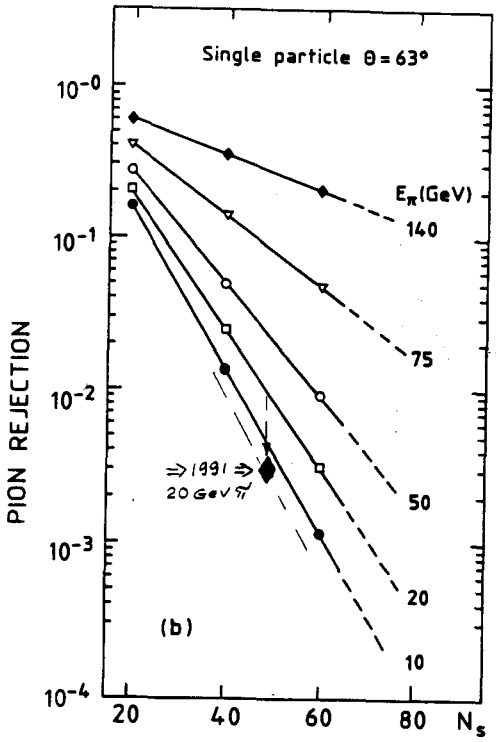
RD-6 TRD Event Display



3 THRESHOLDS :

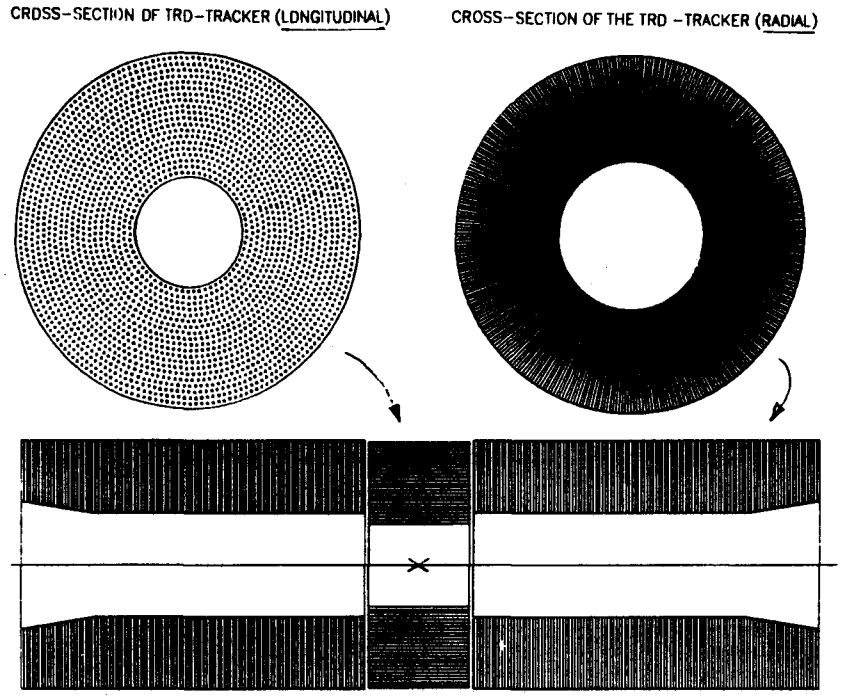
o - '1 MIP' : 0.2 - 1.5 KeV
x - 'DOUBLE HIT' : 1.5 - 5 "
● - TR-CLUSTER: > 5 KeV

LINES ≡ RECONSTRUCTED TRACKS



'90 DATA , except
◆ FROM '91 : IMPROVEMENT DUE TO NEW GAS MIXT.

POSSIBLE LAYOUT FOR LHC

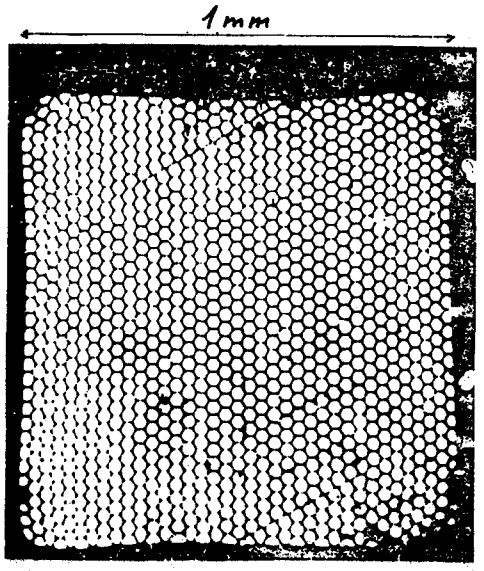


IV SCINTILLATING FIBRES

1. THIN FIBRES (30 μm) (RD7/LAA)

(CERN - DEP Rodenstock, Karlsruhe - Kuraray - L.G.E. Toulouse - L.I.M. Toulouse - Zeuthen)

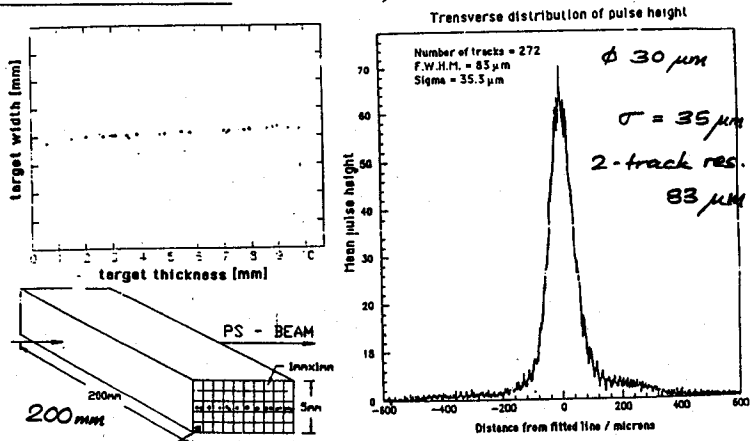
- NEW DOPANTS (PMP : Abs/Em = 300/420nm)
  ↳ NO CROSSTALK BETWEEN FIBRES



FUSED - COHERENT FIBRE BUNDLE (Kuraray)

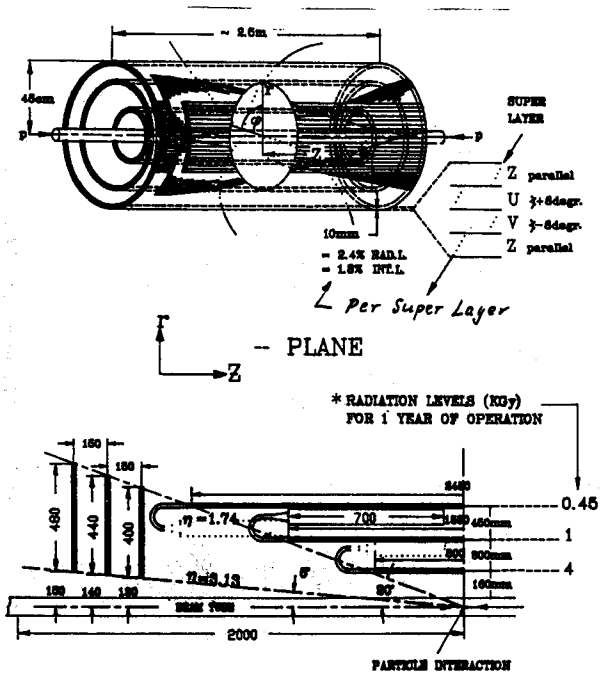
900 FIBRES, $\phi = 30\,\mu m$

TEST BEAM RESULT (5 GeV π^-)



• INVESTIGATING BETTER PMP MIXTURES.

POSSIBLE LAYOUT FOR LHC FIBRE TRACKER.

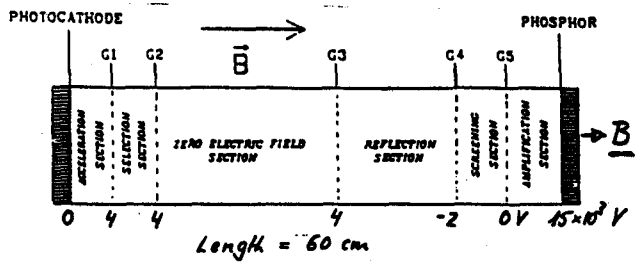


* INTEGRATED LUMINOSITY ($L = 10^{33}\ cm^{-2}\ s^{-1}$):
$\int Ldt = 10^{40}\ cm^{-2} = 0.1$ INVERSED FEMTOBARNS
FOR 8 TeV + 8 TeV

READ-OUT OF THIN FIBRES

GATABLE DELAY TUBE (1 μs) (LAA)

- PIPELINE FOR OPT. IMAGES (FOR 1. LEVEL TRIGGER)



- Measured: Space Resol. = 25 μm for $B \geq 0.7$ T
- CAN IMAGE $\leq 10^6$ FIBRES
- READ-OUT B :
  - Proximity Focussed Image Intensifiers → CCD
  - Electron Bombarded CCD instead of Phosphor
  - Electron " Si-Pixel-Det. " "
    (being investigated)
- Tubes a few % X_0 thick.
- TRIGGER : OFF : e^-

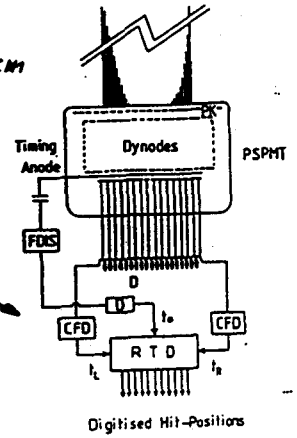
  ON : → by -200V on G1
- TIME RESOLUTION : ~ 10 ns

2. READ-OUT OF 'THICK' FIBRES (0.5-1mm)

POSITION SENSITIVE PHOTOMULTIPLIERS (RD17)

(CERN - FNAL - IHEP - INFN - IOWA - LAPP - Kyoto - Osaka)

- FAST : $\Delta t < 1$ ns → $\Delta z < 20$ cm
  Pulsewidth ~ 10 ns
- HIT DIGITIZATION IN REAL TIME



RD for '91 :

- UPGRADED PSPM's with
  Smaller dynodes, anodes
  ↳ fabricated, but not yet mounted
- PROTOTYPE SYSTEM, incl.
  Fibre Plane + Real Time Digitizer

V SEMICONDUCTOR DETECTORS

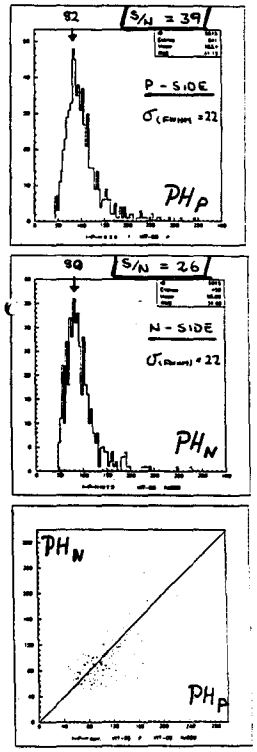
1. Si - STRIP DETECTORS (RD 20)

(CERN - Cracow - Helsinki - IC - Oslo - RAL - SI - Strasbourg - Turin - Yale - Liverpool - Marseille)

GOAL : DOUBLE-SIDED DET. FOR HIGH RATES + ∫DOSE

PROGRAM:

- MONOLITHIC ELECTRONICS:
  PREAMPS : SHAPING = 45 ns → GOOD S/N → TOLERANCE TO ΔPH
  + AN. PIPELINE + PROC.
- MECHANICS + COOLING FOR BIG SYSTEM ↳ HE-Gas : -20°C
- DETECTORS
  DOUBLE-SIDED DET. WORK WELL :
  e.g. DELPHI 2. STAGE :
  Excellent S/N → $\sigma_p = 7\,\mu m$
  $\sigma_N = 8\,\mu m$



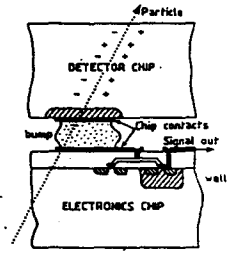
CONCENTRATE ON RAD. HARDNESS:
Proceed in 3 stages
1. Test different options on p-side
2. " " " " n-side
3. Final design p+n (in ~ 1y!)

2. Si - PIXEL DETECTOR (RD 19)

(1. Version : LAA)

1. STEP : HYBRID VERSION

- BUMP-BONDING OF DET. TO ELECTRONICS
- 16 × 64 PIXELS:
  $75 \times 300\,\mu m^2$
  BINARY R.O. : WORKS!
  → Ω - EXPER. < 1. Nov. '91.
  Noise < 60 e⁻ ; ΔTHRESHOLD ~ 500 e⁻.



- MID '92 : BUILD UP
  $5 \times 5\,cm^2$ MOSAIC.

2. STEP : MONOLITHIC VERSION IN SOI

- DETECTOR SAMPLES (cm^2) LOOK ACCEPTABLE
  (SIMOX - SOI) [IMEC - PISA - SOI]
- DEVELOPMENT CONTINUES WITH IMEC.

3. GaAs DETECTORS (RD8 / LAA)

(Bologna - CERN - Florence - Glasgow - Lancaster - Modena - RAL - Sheffield)

ADVANTAGES OF GaAs:

- RADIATION HARDNESS
- HIGH SPEED

DISADVANTAGES ?

- POOR MATERIAL
  → high dark current, low collection efficiency.
- HIGH PRODUCTION COSTS
- LIMITED WAFER SIZE

} SO FAR!

RECENTLY GOOD PROGRESS:

- SMALL DIODE SAMPLES (ϕ = 1mm, Aachen) show:
  - Noise < 10^3 e^-
  - Collection Efficiency ~ Si !
- 4 inch WAFERS BECOME AVAILABLE

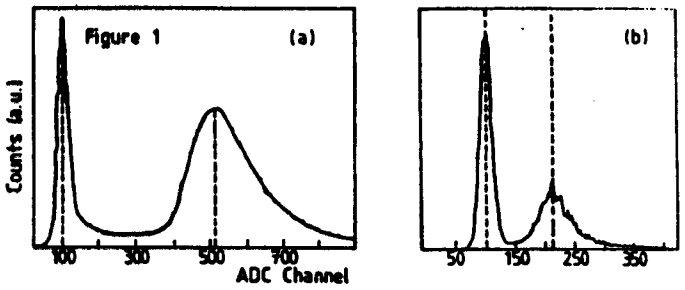
(MORE DETAILS AT IEEE CONF., SANTA FE, A. SMITH

RESULTS ("OLD" GaAs)

1. RADIATION HARDNESS

SINGLE SCHOTTKY DIODE, Ru^{106} SPECTRUM

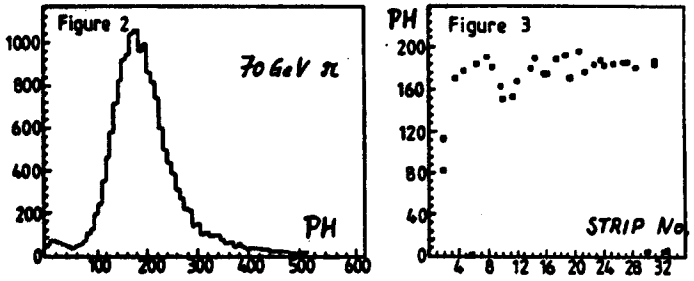
BEFORE EXPOSURE AFTER 7×10^{14} n/cm² (ISIS)



AFTER 1×10^{14} n/cm² : ΔPH ~ -20% ONLY!

2. DETECTOR WITH 64 STRIPS

(SITP MASK ; 600 μm thick ; AMPLEX PREAMP)



S/N ~ 8

(WITH NEW GaAs BIG IMPROVEMENT EXPECTED!)

VI EXAMPLES OF OTHER R&D PROJECTS

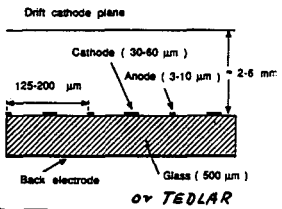
1. RADIATION HARDNESS OF GASEOUS DET. (RD 10)

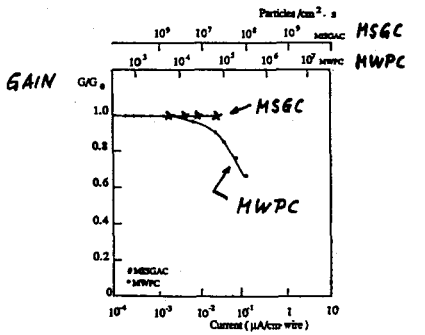
SYSTEM FOR PRECISE, SYSTEMATIC STUDIES
BEING SET-UP AT CERN.

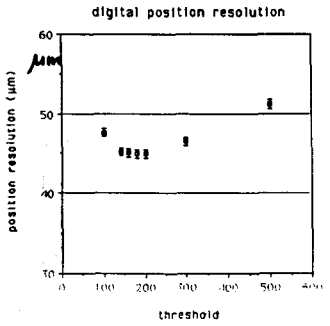
2. MICRO-STRIP GAS COUNTERS

(NIKHEF - PISA - CERN)

- FAST : $\sigma_t \sim 15$ ns
- PRECISE : $\sigma_x = 30\,\mu m$ (analog R.O.)
  $= 45\,\mu m$ (digital R.O.)
- RATE CAPABILITY $> 10^7$ Hz/cm^2







3. CsJ - PHOTOCATHODES

+ ADSORBED FERROETHYLENE : $\varepsilon = 20\%$ @ 190nm
or + " TMAE $\varepsilon = 38\%$ "

APPLIC. : FAST-RICH , FAST E.M. CAL.

Electronics I

J. Dorenbosch

DORENBOSCH

R&D: Triggers and Data Acquisition

Triggers and Data Acquisition
- The Project: Event Reduction, Monitoring and Readout
- The Progress: Physics and Detector Simulation
- The Progress: Muon hit rate simulations
- The Physics: Muon trigger rates and Thresholds

Level 1 trigger
- The Project: Straw Tube tracker
- The Progress: Synchronizer Prototype
- The Physics: Electron Trigger

Level 2 trigger
- The Project: Neural Net Trigger
- The Project: Neural Net Trigger
- The Progress: Tests in CDF
- The Physics: B Physics at the Fermilab Collider

Level 3 trigger
- The project: R&D of a parallel Computing farm

Data Acquisition
- The Project: Data Collection Circuits
- The Progress: Data Collection Chip Simulation
- The Physics: Data Taking Efficiency

Data Transport
- The Project: Optical Modulators
- The Progress: Mach-Zender measurements
- The Physics: Tracking Readout

Event Builders
- The Project: Barrel switch
- The Progress: 8 X 8 Prototype completed
- The Physics: Throughput

Triggers and Data Acquisition

The Project: Event Reduction, Monitoring and Readout

The trigger and data acquisition must capture the most interesting events

A good understanding is obtained about many of the components and methods that are needed to do this.

What needs more attention is the definition of a coherent trigger strategy:

- What algorithms can be used?
- What data is needed by these algorithms?
- What reduction is obtained?
- How does reduction improve using more detailed data?
- How can algorithms be implemented at different levels
- What algorithms can be combined at each level?
- What are the resulting trigger rates?
- What is the approximate cost of each strategy?
- How can the trigger and Data Acquisition be optimized?

A better understanding is needed before a global optimization can be made.

The Progress: Physics and Detector Simulation

Extensive detailed simulations are now under way address these questions.

Example: the GEM collaboration[1] studies the hit rates in the muon chambers:

- prompt μ's
- pion and K decay in front of calorimeter
- punch through
- μ interactions in the calorimeter
- μ energy loss, etc.

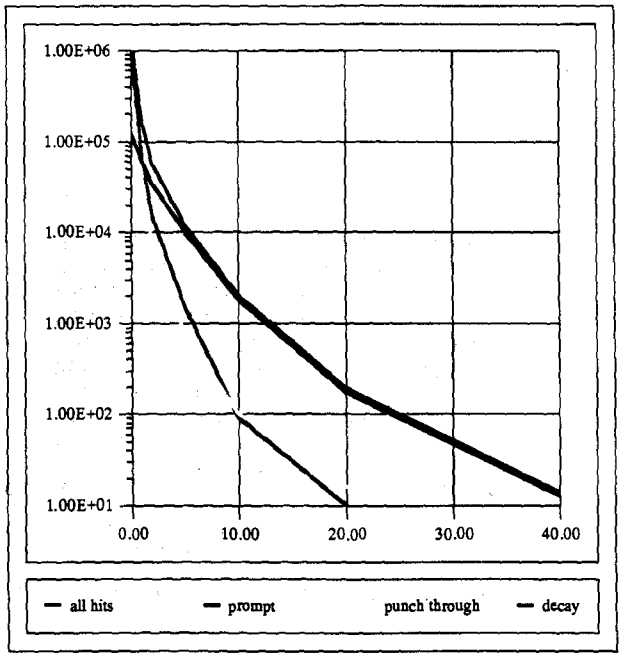
To do a full optimization one needs to know more:

- rates and threshold curves using low resolution drift times or subset of chambers
- same for full resolution
- implementation possibilities
- interaction with detector layout (connectivity)

[1] M. Seman et al., Nevis Lab

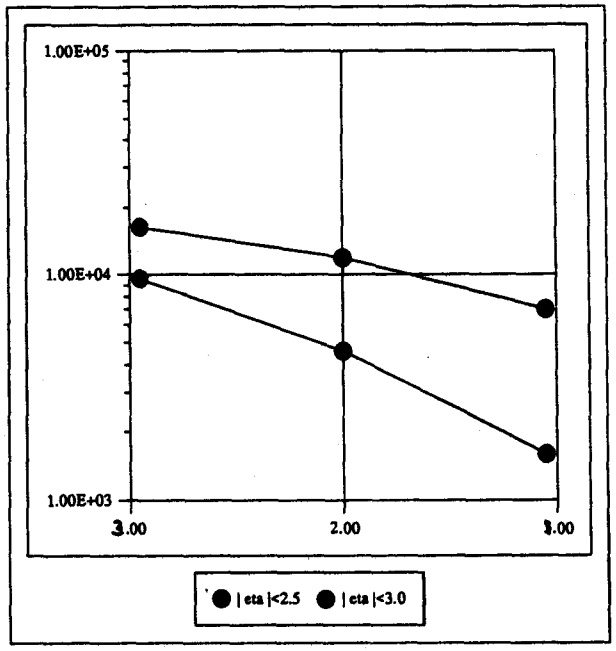
The Progress: Muon hit rate simulations

Hit rate in layer 1 of μ chamber (Hz)
Loopers included
(GEM preliminary)



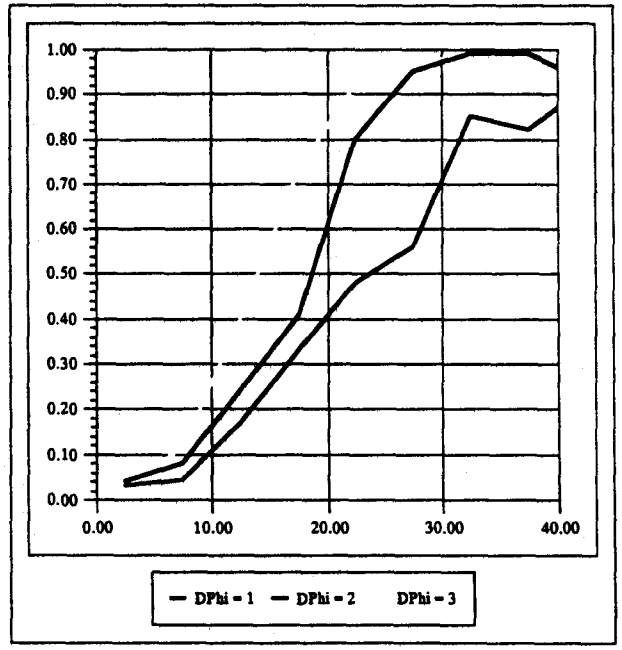
The Physics: Muon trigger rates and Thresholds

Muon trigger rate for different eta ranges
using 1, 2 or 3 Phi bins in trigger
(GEM preliminary)



Muon Thresholds

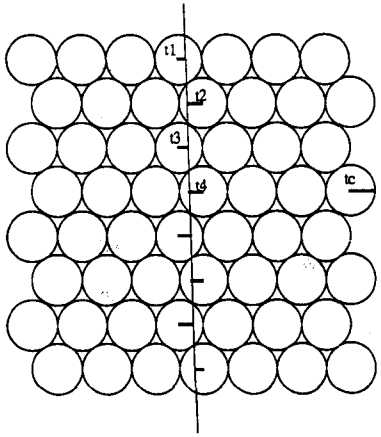
Muon trigger thresholds
using 1, 2 or 3 Phi bins in trigger
(GEM preliminary)



Level 1 trigger

The Project: Straw Tube tracker[2]

- Recognize track
- Determine bunch crossing
- Measure track angle
- Select steep tracks

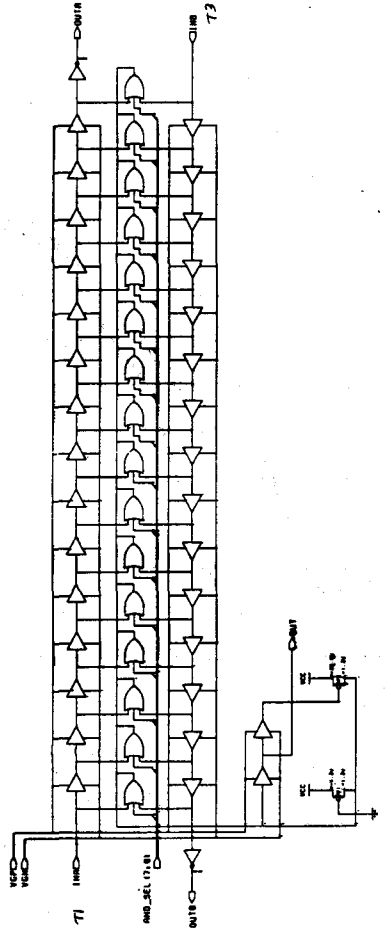


$t1 + t2 = tc$

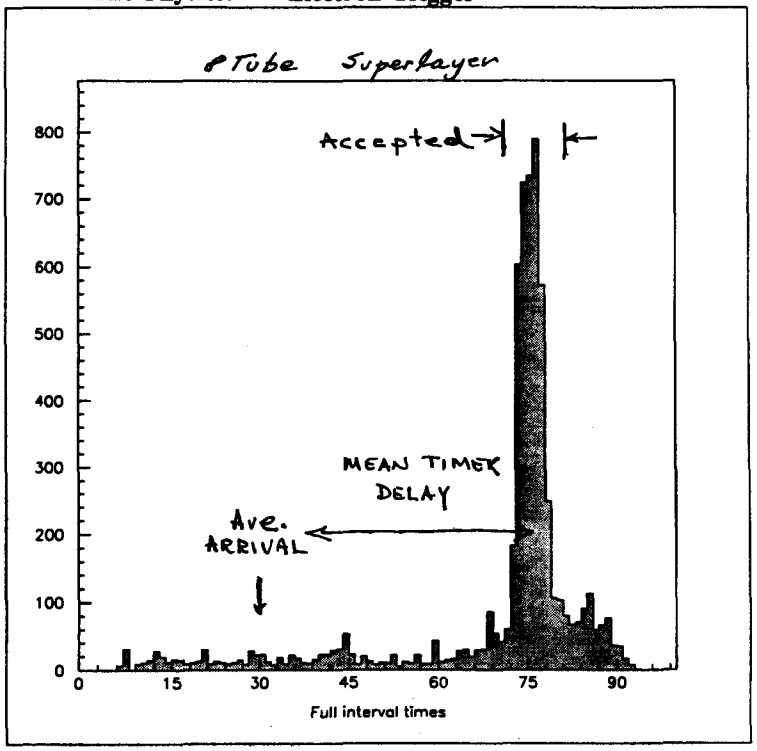
$t1 - t3 \propto \alpha$

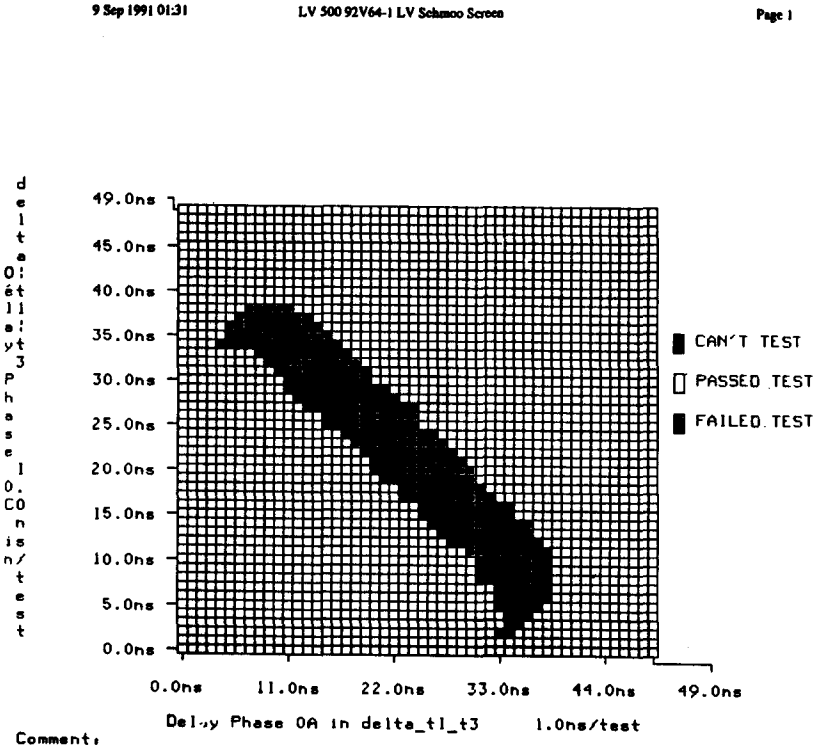
[2] J. Chapman et al., University of Michigan

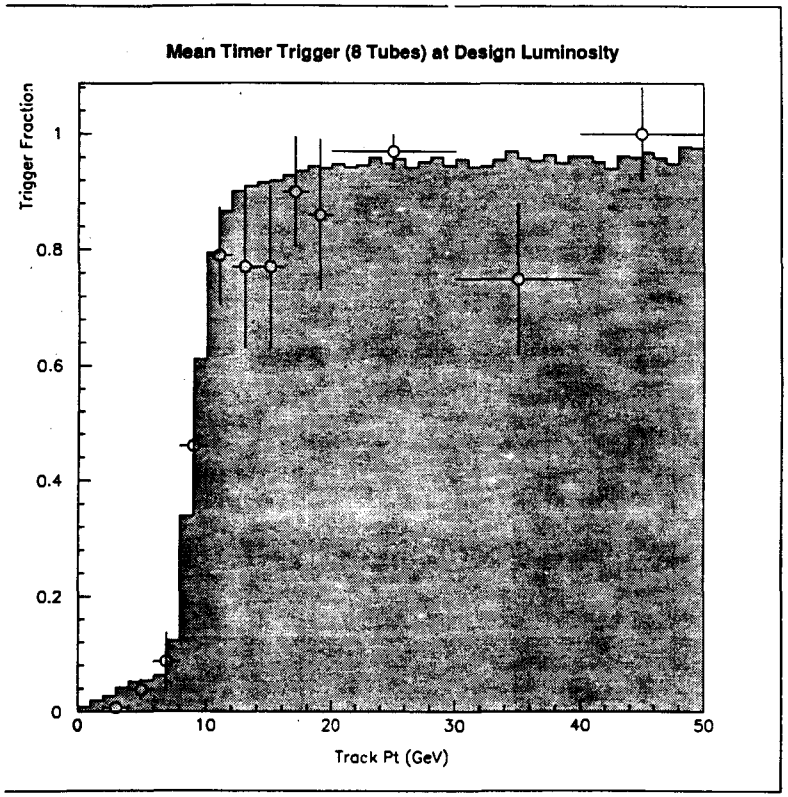
The Progress: Synchronizer Prototype



The Physics: Electron Trigger







Level 2 trigger

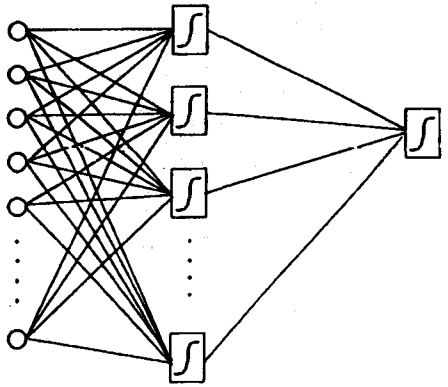
The Project: Neural Net Trigger[3]

Neural Nets may be useful for Pattern Recognition in second level triggers:

- Possible to implement complex algorithms
- Good connectivity
- Programmable

There is little experience using these chips in H E P experiments

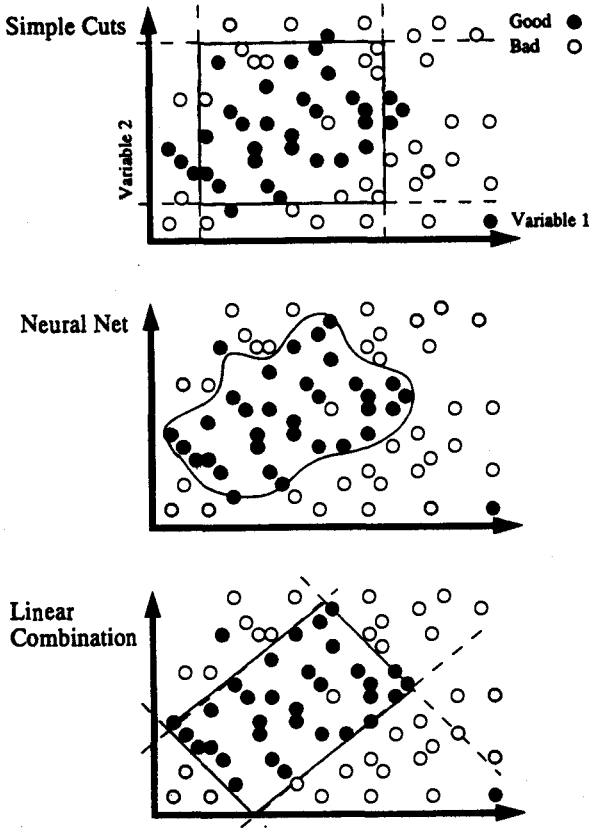
- Implement a neural net trigger in a Collider Experiment, CDF
- Trigger on B -> evX + jet



Layer 0: Signal Inputs x_i — Layer 1: Hidden Nodes f_j — Layer 2: Output Node g_k

M. Campbell et al., University of Michigan

The Project: Neural Net Trigger



The Progress: Tests in CDF

Installed extension to the CDF second level calorimeter trigger

- Start with electromagnetic cluster in calorimeter
- Zoom in on the area around the electron candidate
- Feed 5*5 e.m. and 5*5 hadronic energies to neural net trigger
- One ETANN chip does it all (+ 10 Fastbus boards)

- Will see real data in the upcoming collider run

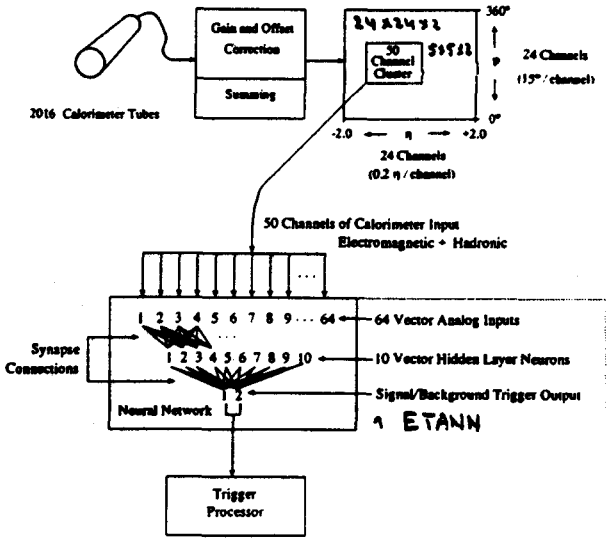


Figure 1. Schematic diagram of neural net trigger

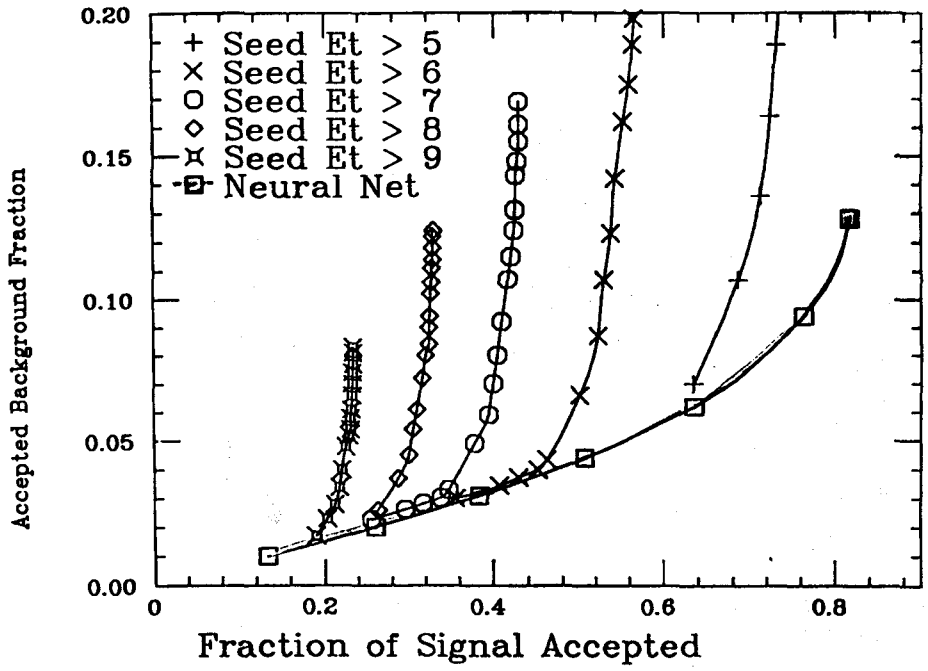


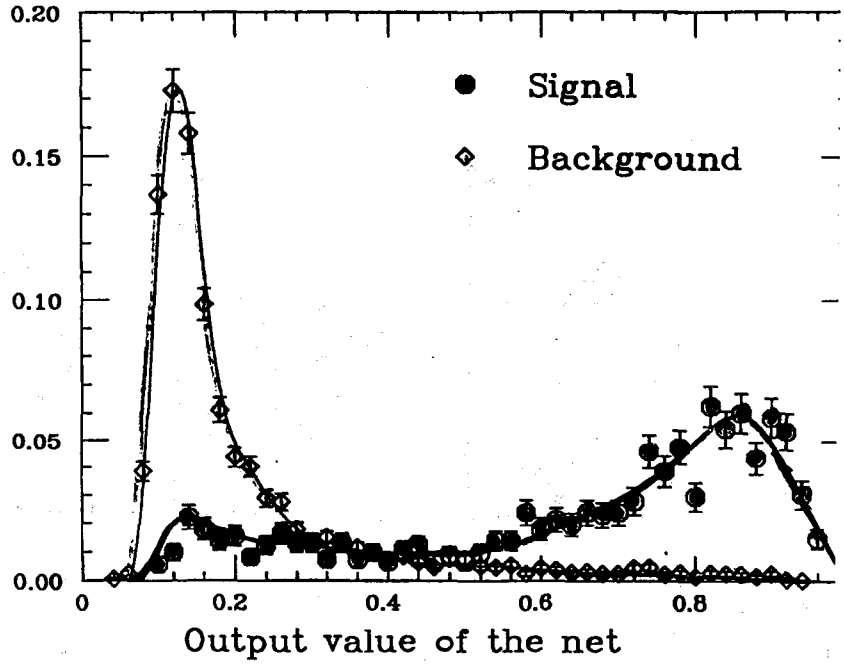
Fig. 4

The Progress. The Project. The Physics Corpus Christy. Oct 91 m 13

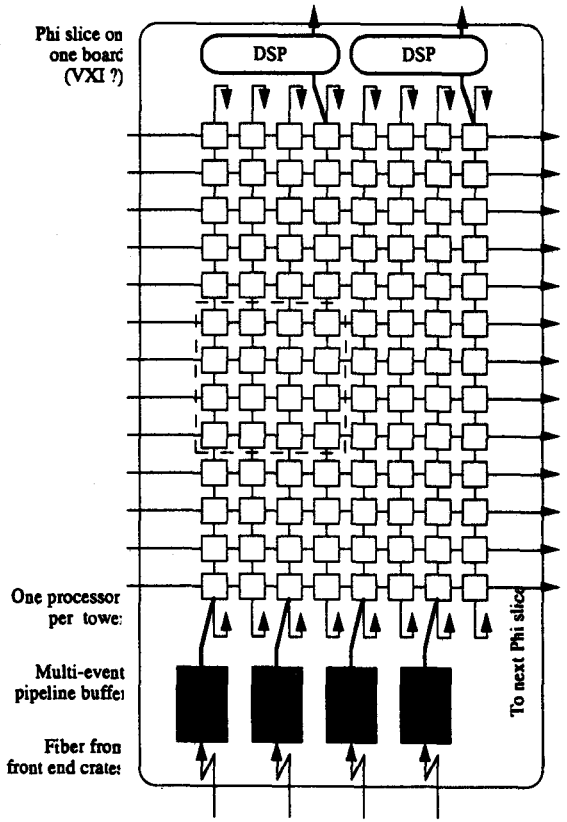
The Physics: B Physics at the Fermilab Collider

Monte Carlo studies of improved yield of B events

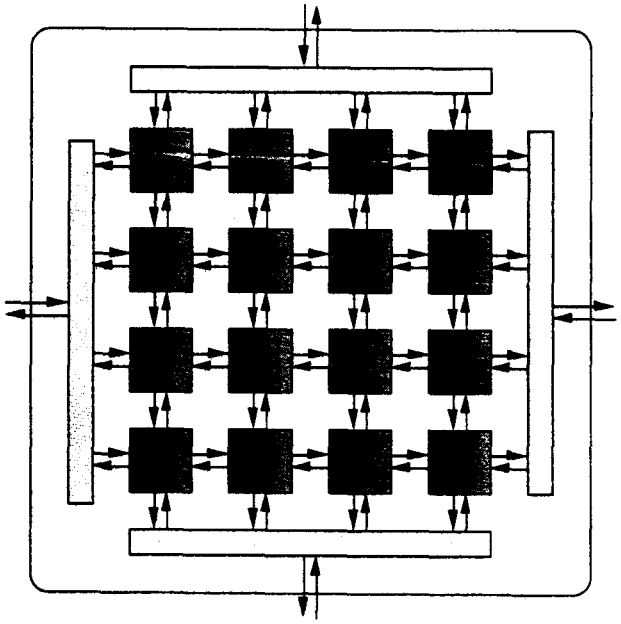
Applications at SSC



Calorimeter trigger using graphics processors



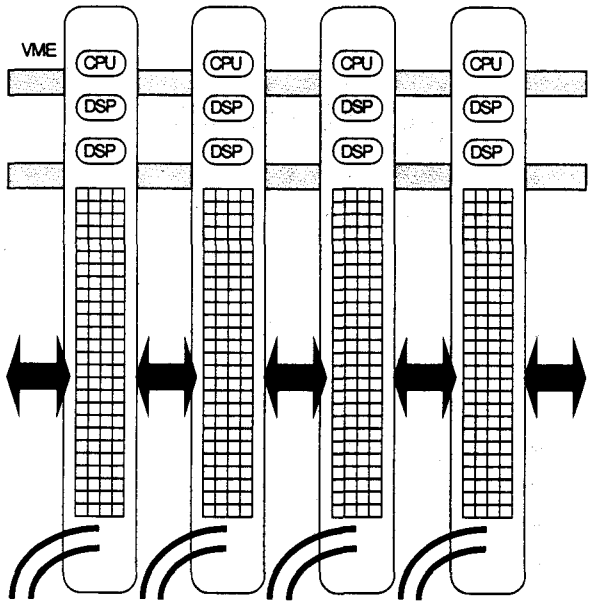
Trigger Chip[5]



Commercial Graphics Multi Processor Chip are expected in the mid 90's

[5] D. Crosetto et al., SSCL

Trigger Crate



Phase 1 data enters on fibers (8 μs)
Phase 2 processors find electrons, jets, and missing Et (8 μs)
Phase 3 DSP / CPU combines results with tracking (8 μs)
Phase 4 (For accepted events only) Data Collection on VME

Level 3 trigger

The project: **R&D of a parallel Computing farm**[6]

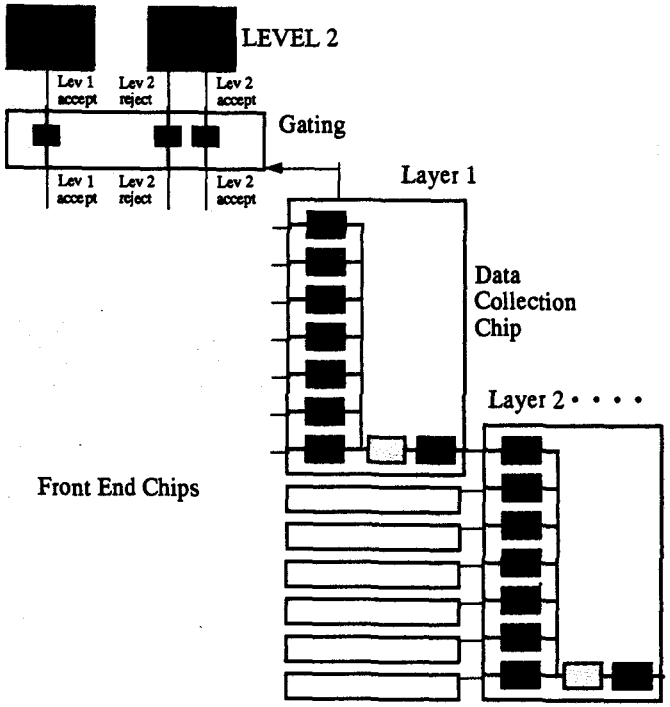
Will be discussed by Ken McFarlane (Computing).

More intense R&D is needed on:
- trigger strategies,
- algorithms and
- implementations

[6] N. Lockyer, University of Pennsylvania

Data Acquisition

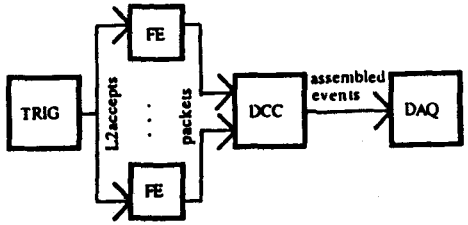
The Project: Data Collection Circuits

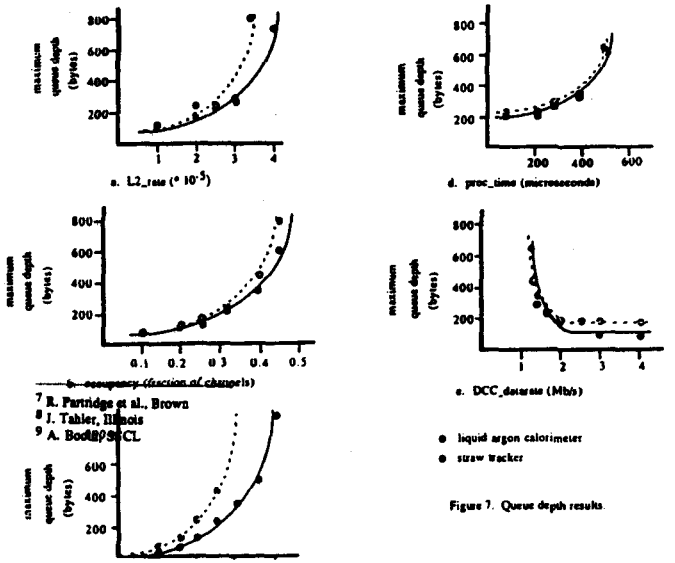


The Progress: Data Collection Chip Simulation

This work is done in different places[7,8,9]

The work at Illinois concentrates on a single DCC





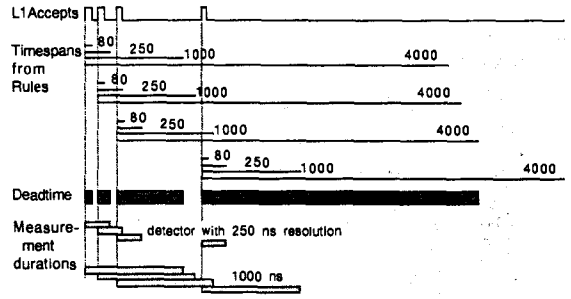
[7] R. Partridge et al., Brown
[8] J. Tahler, Illinois
[9] A. Bodek, BNL

- liquid argon calorimeter
- straw tracker

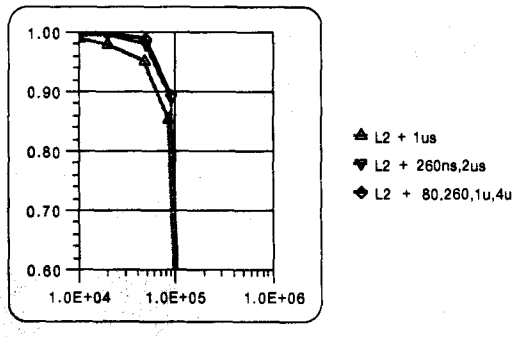
Figure 7. Queue depth results.

The Physics: Data Taking Efficiency

One can define very sophisticated protocols to control the DAQ:



But sometimes it does not make a lot of difference:



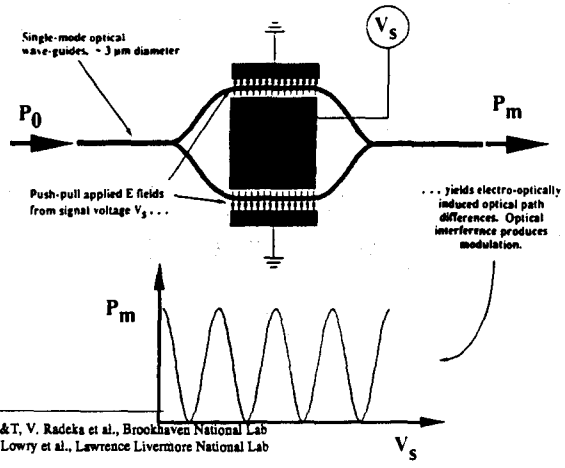
Data Transport

The Project: Optical Modulators

Optical modulators may bring signals out of the detector without amplifiers

Two groups have been testing Optical modulators[10, 11]

- sensitivity
- noise
- linearity
- temperature stability
- phase trimming at fabrication time
- rad hardness



[10] AT&T, V. Radeka et al., Brookhaven National Lab
[11] M. Lowry et al., Lawrence Livermore National Lab

The Progress: Mach-Zender measurements

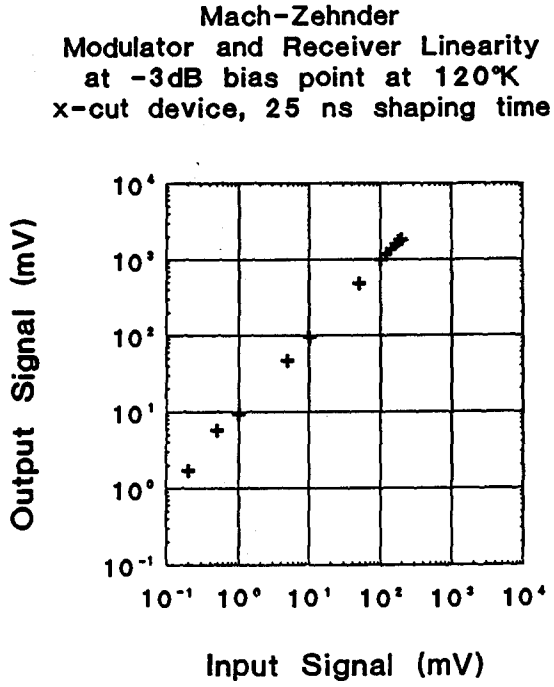


Fig. 12

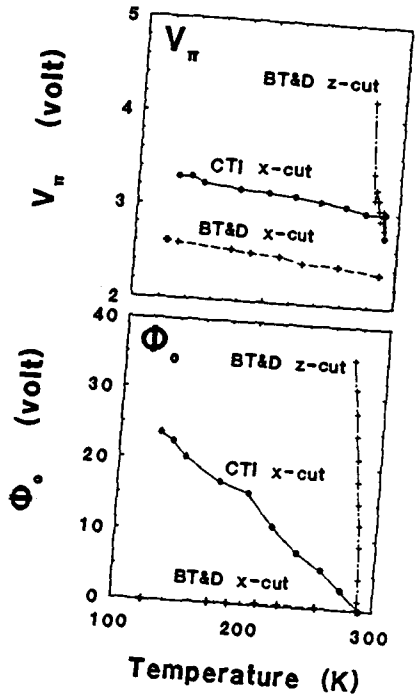


Fig. 13

The Physics: Tracking Readout

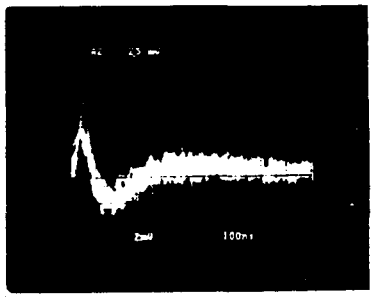
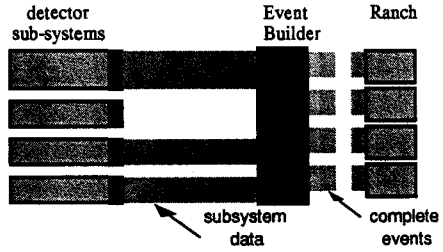


Figure 4. Oscilloscope picture of the output of the optical receiver for cobalt-60 gamma ray interactions in the drift chamber. The vertical axis is 2 mV/division and the horizontal axis is 100 ns/division. The exposure was for 1/4 second. The bandwidth of the signal is given by the RC time constant of the modulator's internal capacitance and the chosen termination resistor and has not been optimized.

Event Builders

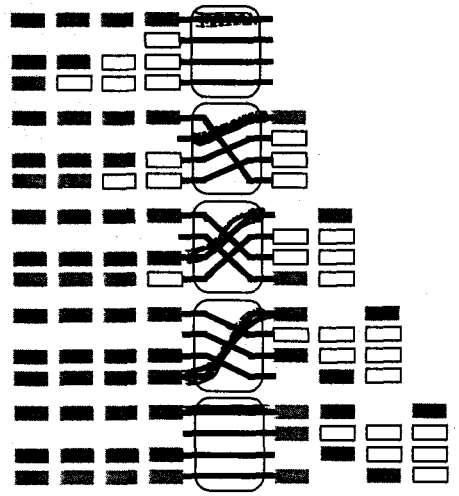
The Project: Barrel switch[12]

An event builder combines the data from the detector subsystems into complete events

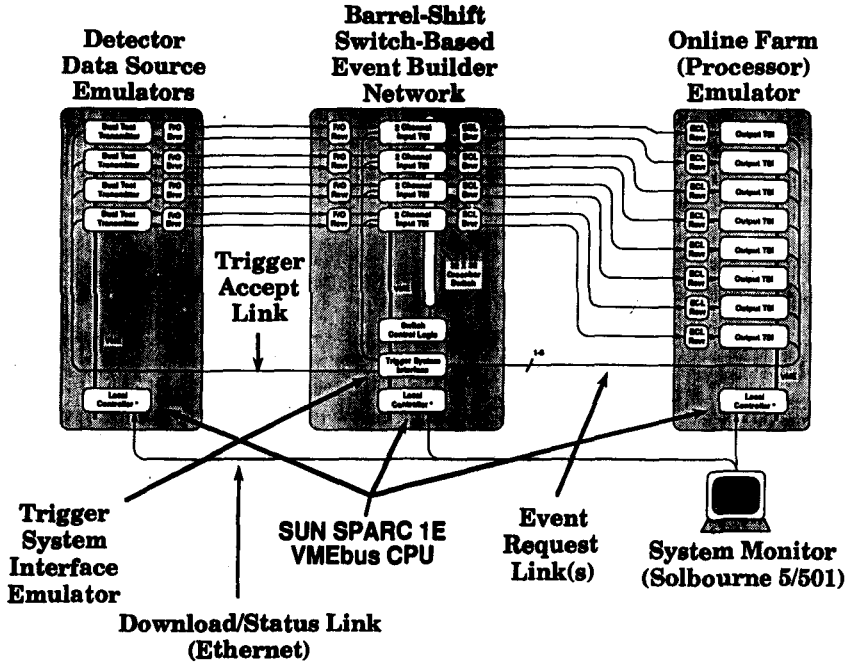


[12] FermiLab

Barrel Switch Operation



The Progress: 8 X 8 Prototype completed

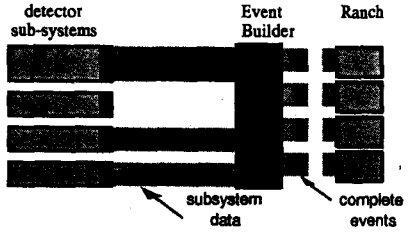


The Physics: Throughput

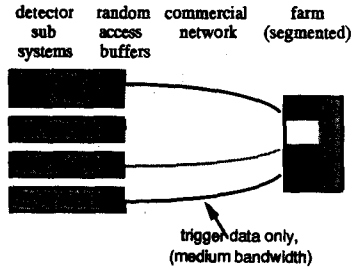


Alternatives to event builders[13]

Traditional architecture:
Event builder sends all events to the Ranch for further processing



Alternative:
Farm only reads the data needed for triggering

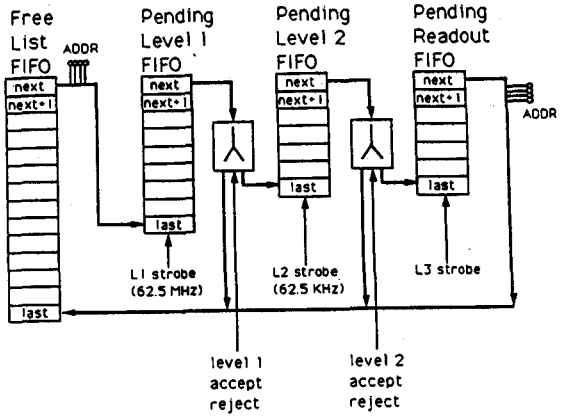


Another Alternative:
Dual port memory event builders are under extensive study[14]

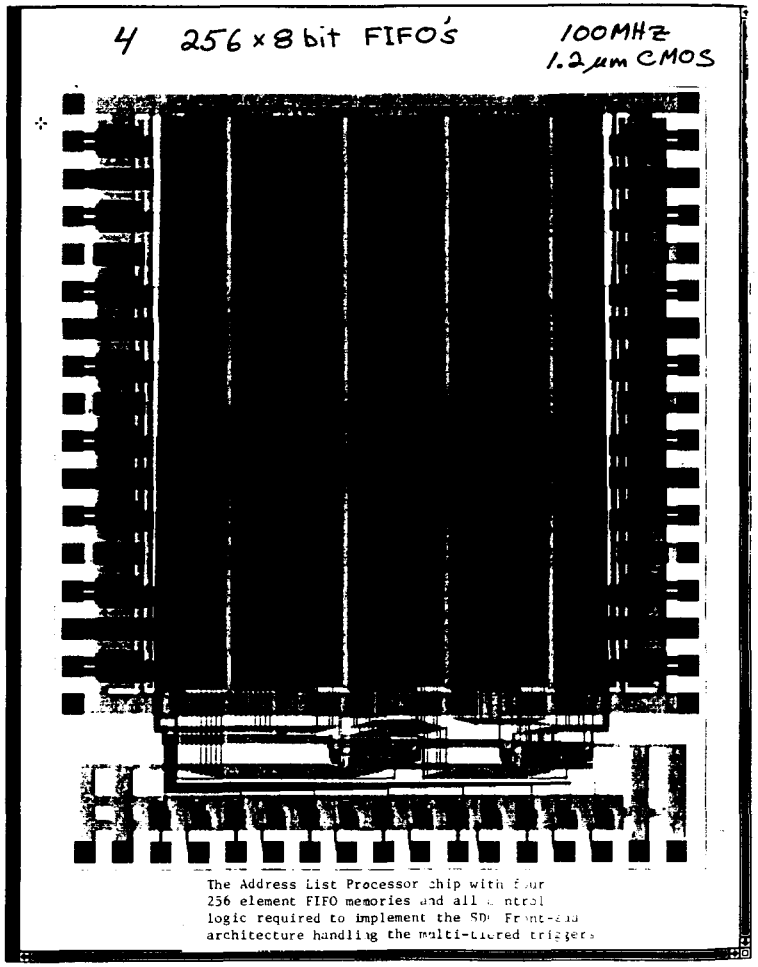
[13] J. Dorenbosch et al., SSCL
[14] R. Partridge et al., Brown

Address List Processor for SCA

* One storage array of capacitors
* Simulate multiple "virtual" pipelines with address lists in FIFO's



* FIFO's have internal fall-through rate of > 300 MHz
* Total through-put rate ≈ 100 MHz
* Four 256 word x 8 bit FIFO's on single die (1.2 micron)



The Address List Processor chip with four 256 element FIFO memories and all control logic required to implement the SDC Front-end architecture handling the multi-tiered triggers

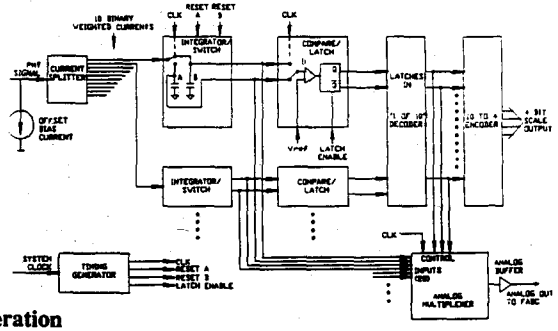
60MHz Flash ADC with 18-bit Dynamic Range

EN4L

Specifications

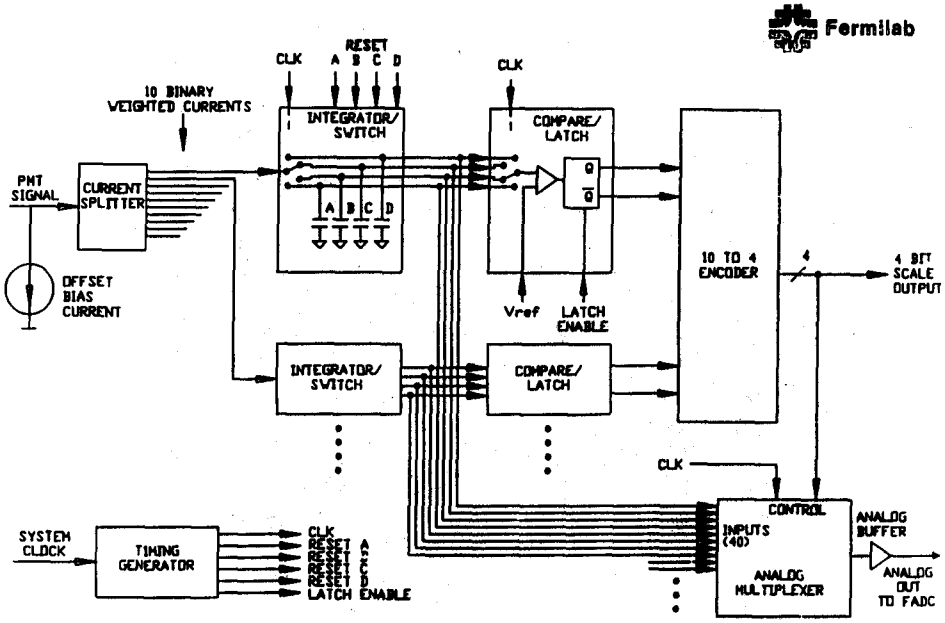
* 18 bit dynamic range => "floating point ADC"
* Accuracy - 8 bits
* 60 MHz conversion rate
* Gated Integrator provides charge sampling

Schematic



Operation

* Input current divided into 10 binary-weighted currents
* Each current integrated onto capacitor every 16 nsec
* Capac with V_{out} between 0.5 & 1 full scale -> 8 bit FADC



PHOTOMULTIPLIER TUBE GATED INTEGRATOR/DIGITIZER CHIP

Front End Electronics for SSC/LHC Detectors

H. H. Williams

Front End Electronis for SSC/LHC Detectors

H. H. Williams
Univ of Pennsylvania

Calorimeter Readout
- switched Capacitor
- Flash ADC
- Signal Processing for Ionization Calor.

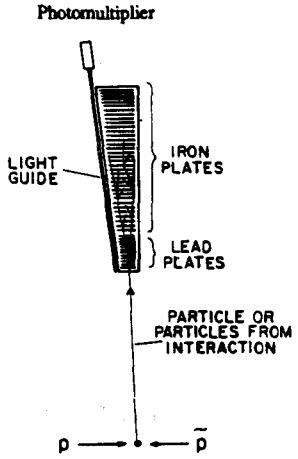
Wire Chamber Electronics
- Preamp/Shaper/Comparator
- Time Measurement

Scintillating Fiber Readout

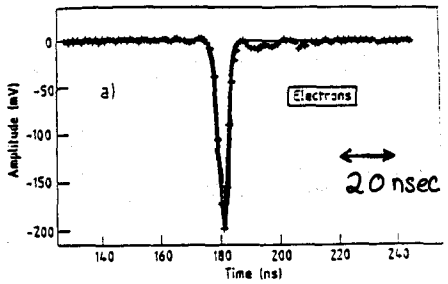
Radiation Hard CMOS
- Noise
- Threshold Shift
- g_m

Calorimeter Detectors

* Scintillator-Lead/Iron Sandwich
* Photomultiplier Readout
* Measure Total Energy
* Risetime of few nsec
* $C_d \approx 3\text{-}5$ pF



Typical Time Response



Calorimeter Readout - Specifications

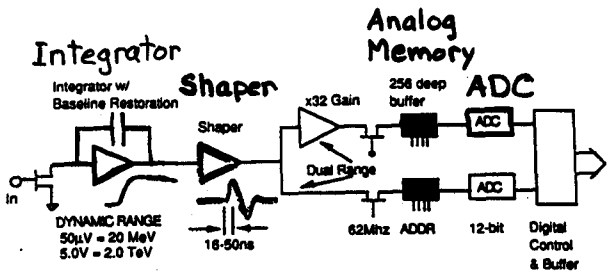
Preamplifier

* Charge integration
* Bandwidth ≈ 200 MHz
* Detectable Charge 1 fC -> 100 pC
* Input referred noise ≈ 2 nV/Hz$^{1/2}$

System (Switched Capacitor) LBL

* 64 - 128 readout channels/ VME card
  - Preamplifier
  - Buffer/Shaping Amplifier
  - 60 MHz Dual Port Analog Memory (switched capacitor) (256 storage locations)
  - ADC, control logic for Analog Memory, DSP
* 17 bit dynamic range
  - Two 12 bit systems offset by x32 in gain
* Linearity ≈ 0.3% - 0.5% of reading
* Power Dissipation ≈ 500 mW per channel

Calorimeter Readout - Schematic

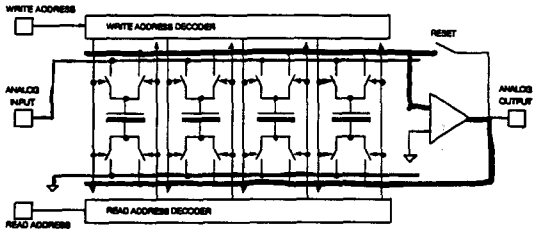


* Key Elements are
  - Dual Port Analog Memory
  - 12 bit ADC (Wilkinson Current run-down) per channel
  - Address List Processor for Analog Memory

Calorimeter Dual Port Analog Memory

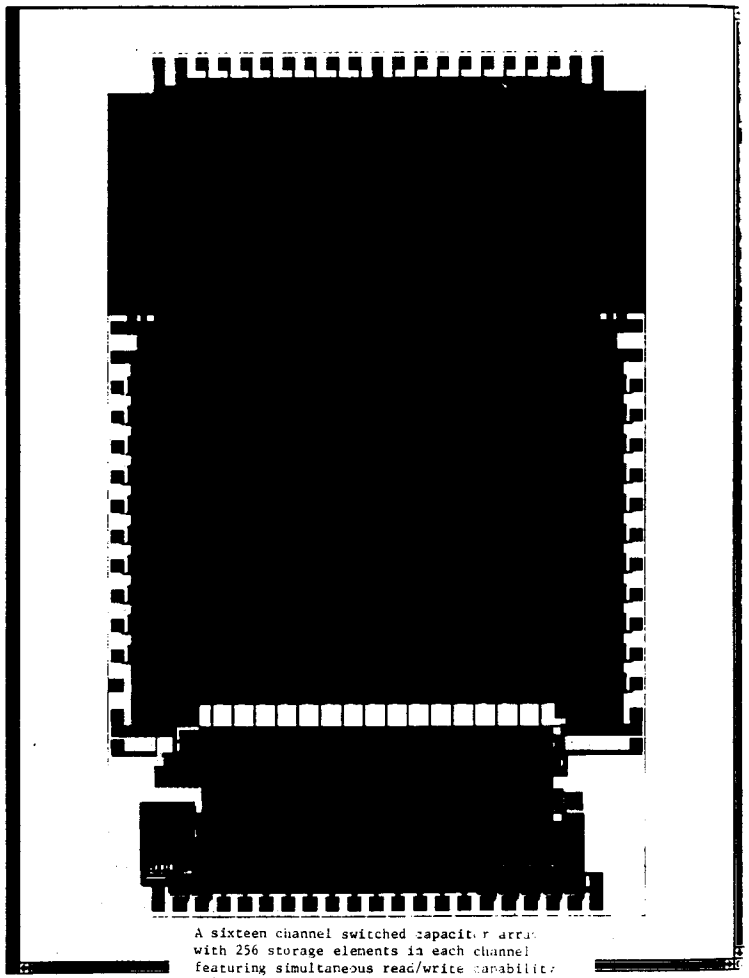
(Switched Capacitor Array - SCA)

* Use PMOS/NMOS switches for rail-to-rail range
* Voltage sampling so no reset needed
* Rail-to-rail operational amplifier for readout



SCA Performance

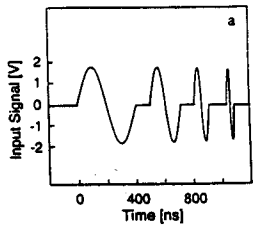
SCA Parameters	Achieved Performance
No. channels/chip	16
No. of elements/channel	256
Power/channel	10mW
Non-linearity	± 0.1% (≈ 0.5% of reading)
Pedestal variation	0.5 mV rms
Charging time constant	1.5 ns
Channel dynamic range	5000
Maximum sample rate	90 MHz
Maximum readout rate	200 KHz
Noise floor	0.7 mV rms
Input voltage range	0.2–4.8 Volts
Capacitor droop rate	0.1 mV/msec
Output Settling Time	1.2 μsec (to 0.02%)



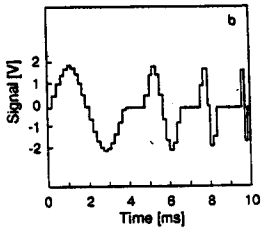
A sixteen channel switched capacitor array with 256 storage elements in each channel featuring simultaneous read/write capability and an on chip sixteen channel 12-bit ADC

Waveform Sampling with SCA

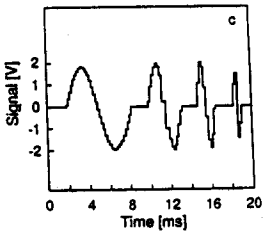
Input: 400, 200, 100, 40 nsec sinewave

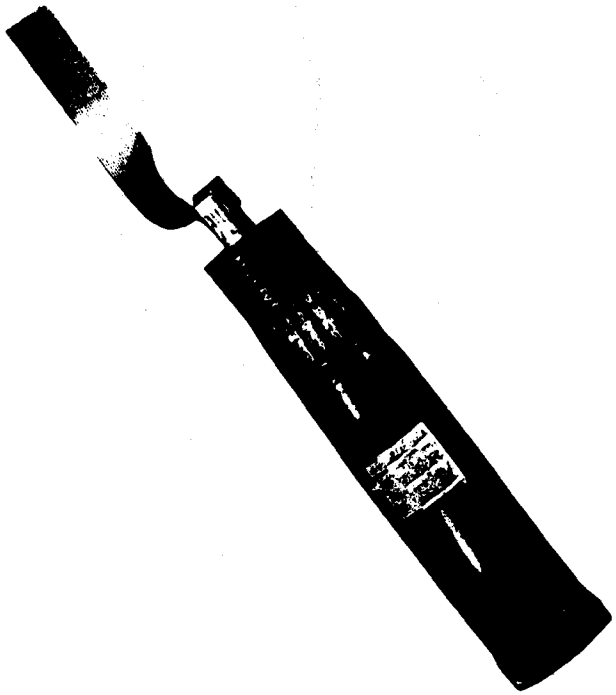


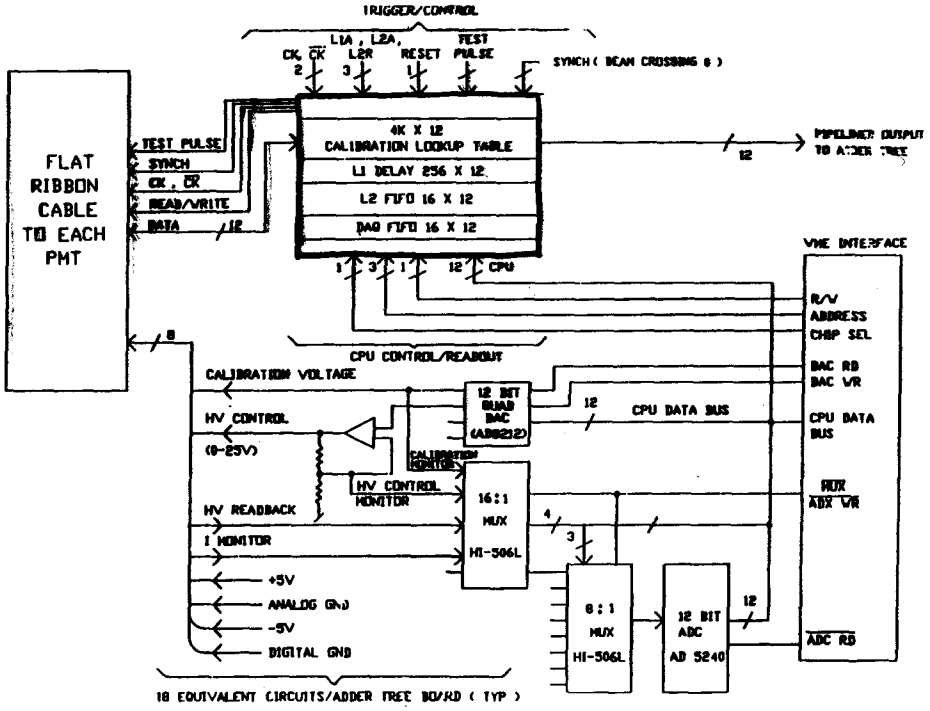
Output: 50 MHz Sampling



Output: 90 MHz Sampling






TRIGGER/CONTROL
L1A , L2A,
CK, CK
L2R
RESET
TEST PULSE
SYNCH (BEAM CROSSING #)
FLAT RIBBON CABLE TO EACH PMT
TEST PULSE
SYNCH
CK , CK
READ/WRITE
DATA
12
4K X 12 CALIBRATION LOOKUP TABLE
L1 DELAY 256 X 12
L2 FIFO 16 X 12
DAQ FIFO 16 X 12
12
PIPELINED OUTPUT TO ADDER TREE
CPU
VME INTERFACE
R/W
ADDRESS
CHIP SEL
CPU CONTROL/READOUT
CALIBRATION VOLTAGE
12 BIT QUAD DAC (AD8212)
BAC RD
BAC WR
CPU DATA BUS
CPU DATA BUS
HV CONTROL
(0-25V)
HV CONTROL MONITOR
HV READBACK
I MONITOR
16:1 MUX HI-506L
MUX ADR WR
+5V
ANALOG GND
-5V
DIGITAL GND
8:1 MUX HI-506L
12 BIT ADC AD 5240
ADC RD
18 EQUIVALENT CIRCUITS/ADDER TREE BOARD (TYP)

Radiation Hard Monolithic JFET Preamplifiers

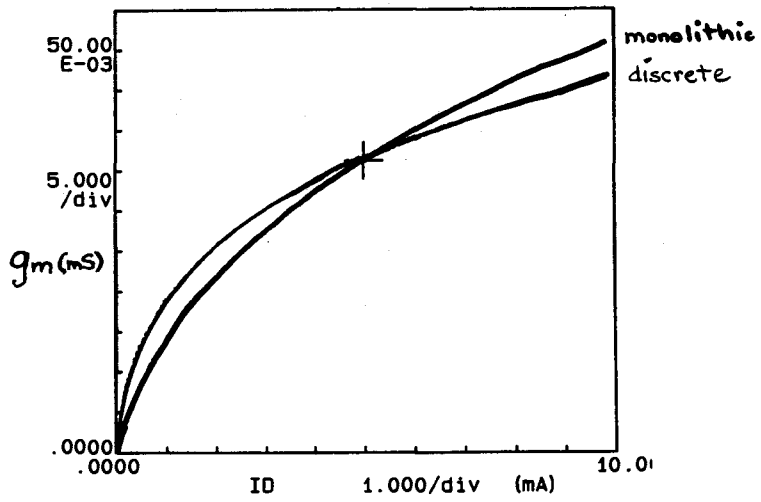
BNL - Pavia ...

Requirements

- **Integrated preamplifier for density, cost, reliabil.**
- **Same excellent noise performance as discretes**
- **Radiation hardness**
- **Full dielectric isolation for circuit flexibility**

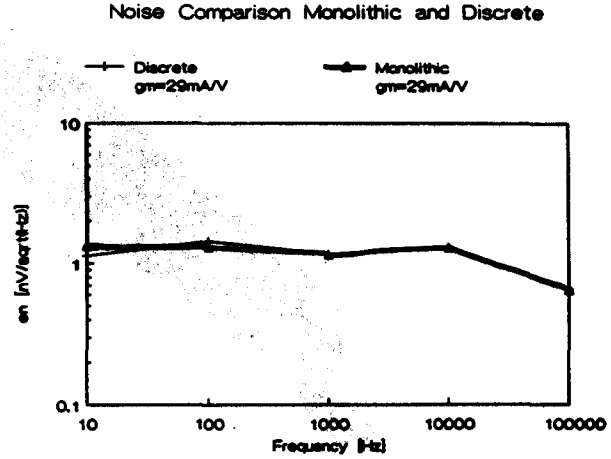
Accomplishments

- **Characteristics for discrete and monolithic nearly identical**



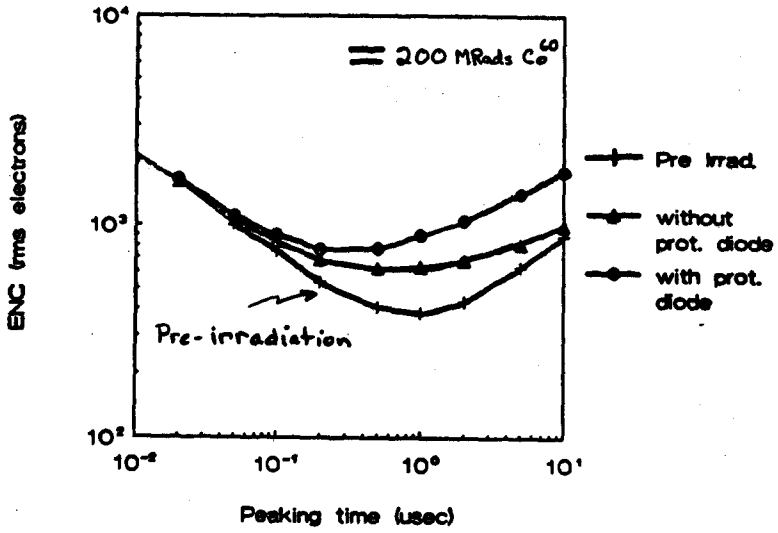
Monolithic JFET Devices - Noise

- **Noise performance of discrete and monolithic devices nearly identical**



Radiation Hardness of Discrete JFET's

* ≈ 25% increase in noise after 10^{14} n/cm^2 (short shaping times)
* No increase in noise after 200 MRads (short shaping times)



Fast Pulse Shaping for Liquid Ionization Calorimeters

Requirements

* Optimal pulse shaping for minimal noise and pileup
* Integrated circuit for low cost, reliability
* Shaping is precise and predictable
* Large dynamic range and excellent linearity

Challenges

* Adapt for process variations
* Maintain excellent linearity

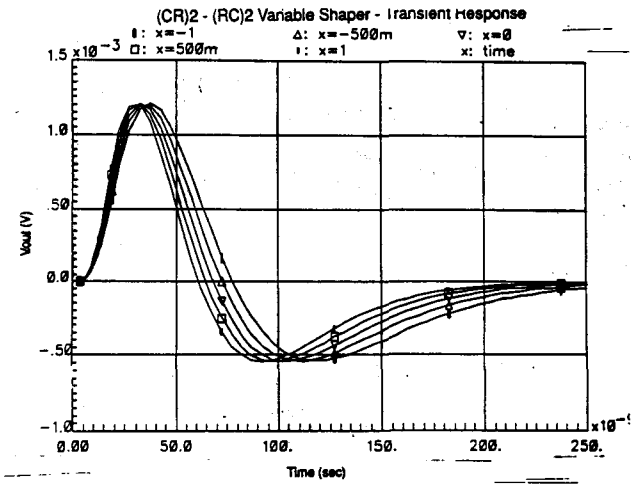
Status

* Several detailed designs from BNL and Harvard
* Fabrication soon in complentary Bipolar/BICMOS

Fast Pulse Shaping -

* **Simulation of variable pulse shaping circuit**

BNL-
Harvard



Time (nsec)

Wire Chamber Readout

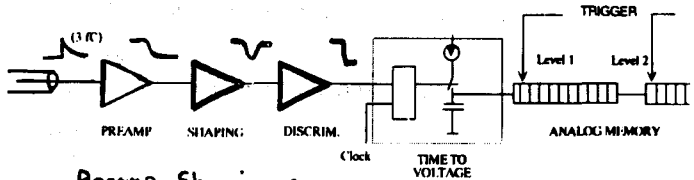
Detector

* Miniature proportional tube (wire in center of 4 mm "straw")
* $C_d \approx 30$ pF $Z_o \approx 250$ ohms
* Goal is to measure **time** of pulses

Specifications

* Minimum Detectable Charge	≈ 1 fC
* Time resolution	< 0.5 nsec
* Double Pulse Resolution	< 20 - 30 nsec
* Analog Storage Time	3 - 4 microsec
* Power Dissipation	< 15 - 25 mW

Schematic Diagram



Preamp Shaping Comp. Amp.

Time Measurement

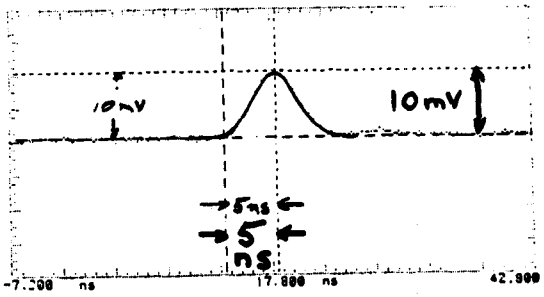
Preamp/Shaper/Comparator (Penn)

Design Features

* Bipolar for speed, low noise, comparator offset
* Common emitter preamplifer stage
* Four stages integration for semi-gaussian shaping
* Fully differential for noise/crosstalk immunity
* Prototypes fabricated in AT&T complementary bipolar proc.

Impulse Response

* Response to "delta function" (≈ 300psec) charge injection



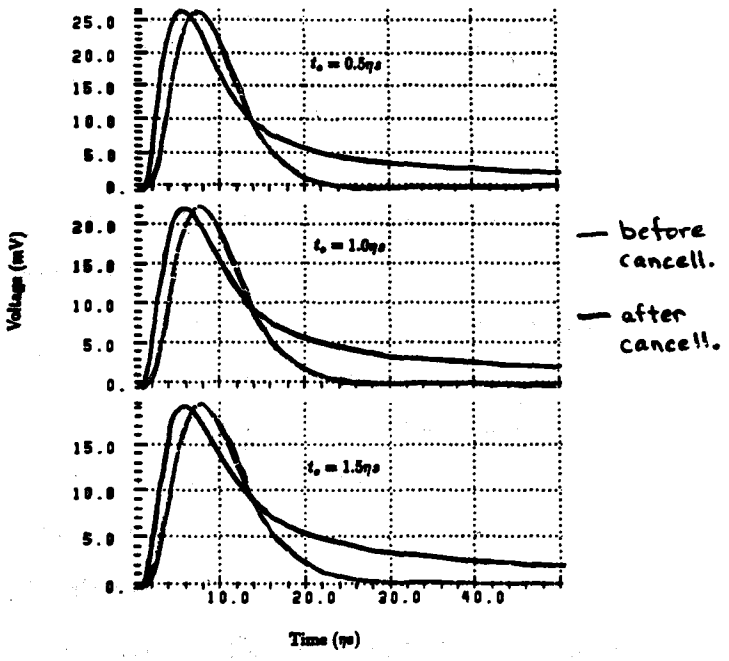
* Circuit works satisfactorily for radiation doses > 5 MRads

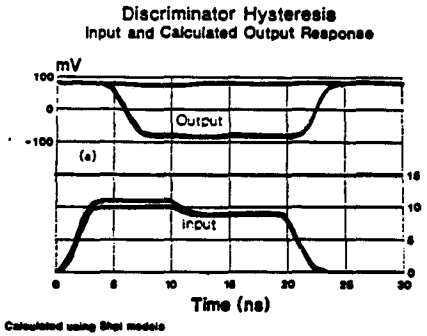
Preamp/Shaper/Discriminator - Status

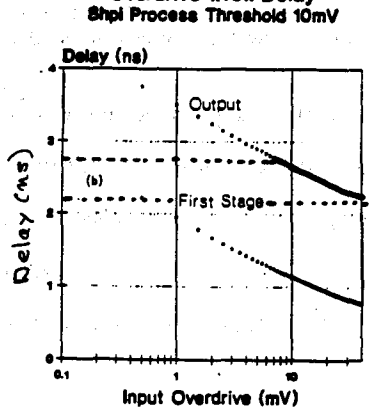
* **≈ 4000 single channel devices fabricated**
* **600 packaged**
* **Yield after packaging ≈ 90% (center of wafer_**
* **< 5% in gain and noise after 5 MRads Co^{60}**
* **Simulations of tail-cancellation & discriminator look good** Trans.
* **8 channel preamp/shaper/disc laid out in Tektronix SHPi process**

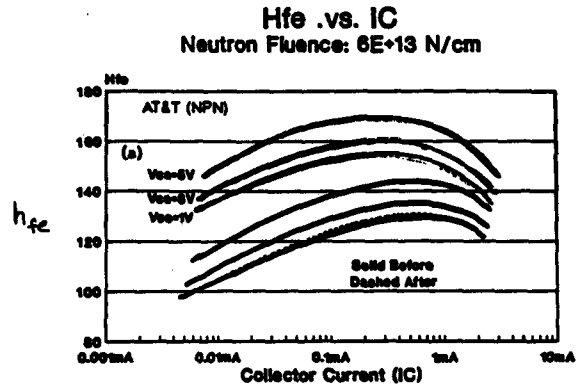
Tail Cancellation of $1/t_0$ tail

* Cancel tail due to heavy ion motion
* Insensitive to exact value of t_0
* Insensitive to process variations









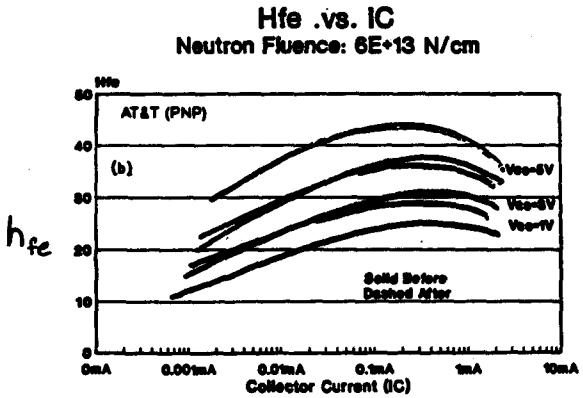


Figure 7. The current gain, h_{fe}, of transistors in the AT&T CBIC U process as a function of collector current, I_c, before and after neutron irradiation with a fluence of 6 10^{13}n/cm^2. (a) NPN transistor (b) PNP transistor.

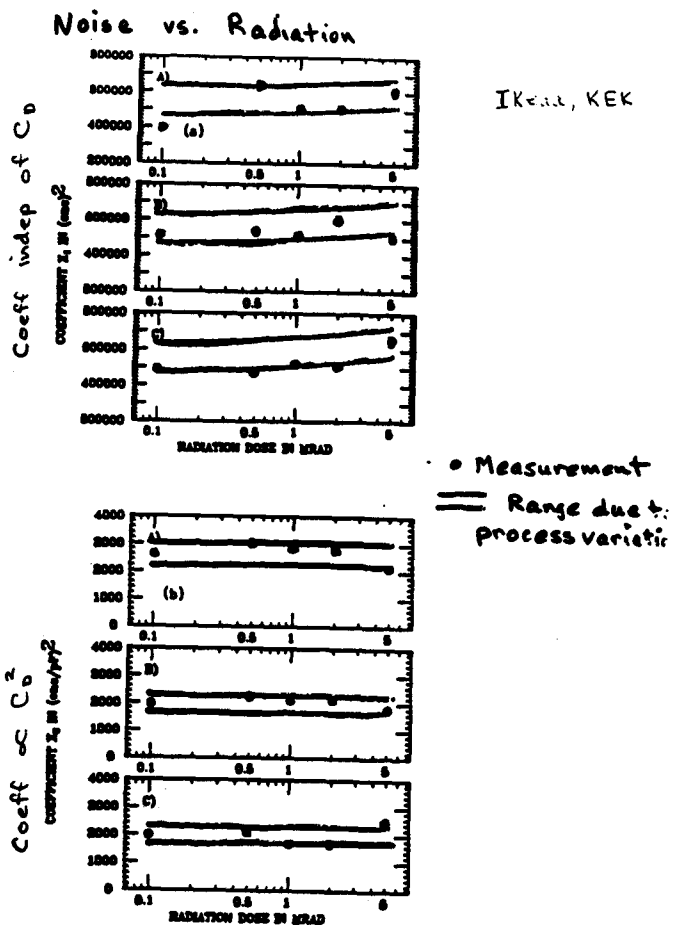
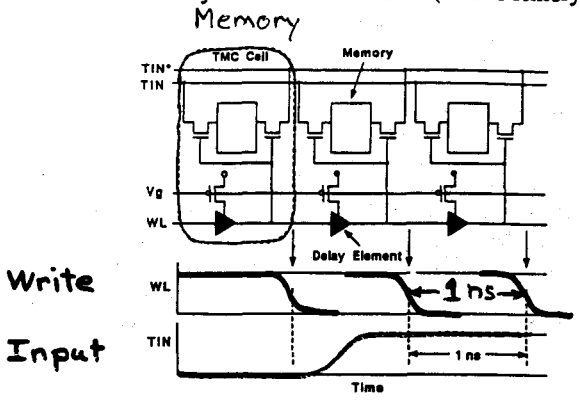


Figure 10. The change in the noise (ENC^2) for NTT bipolar transistors as a function of Co^{60} irradiation. The top three plots show the coefficient of noise which is independent of the source capacitance, for three different devices. The bottom three plots show the coefficient of noise which is proportional to the detector capacitance squared.

TMC - CMOS Time to Digital Converter

KEK (Arai)

* Use memory for time measurement (Time Memory Cell)



* Operation

- Pulse appears simultaneously at **Data In** of 32 memory cells
- **Write** propagates down inverter chain, 1nsec/inverter
- Pattern of 0's & 1's written determines time

* Write Pulse is 32 MHz clock

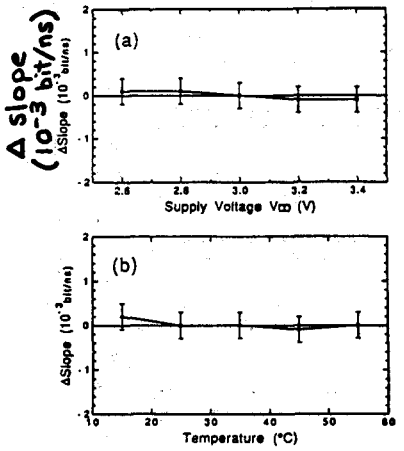
* Fabricated in 0.8 micron NTT BICMOS (only CMOS used)

* 4 kbit memory on chip, 5.0 x 5.6 mm
  - 4 ch of 1 kbit (1 microsecond)
  - 2 ch of 2kbit (2 microsecond)
  - 1 ch of 4 kbit (4 microsecond)

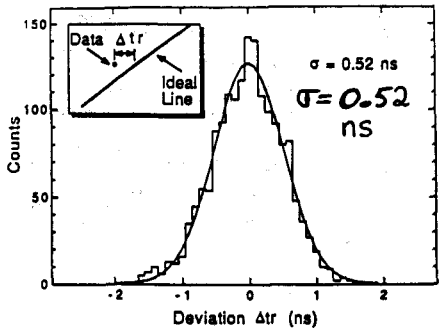
* Power Dissipation ≈ 7 mW/ch

Time Memory Cell (cont)

* Use 32 MHz clock and feedback to stabilize inverter delay



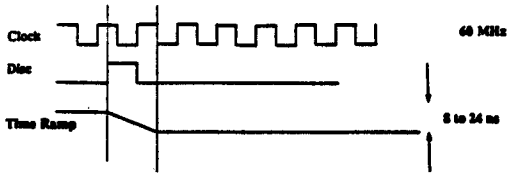
* Measured time resolution



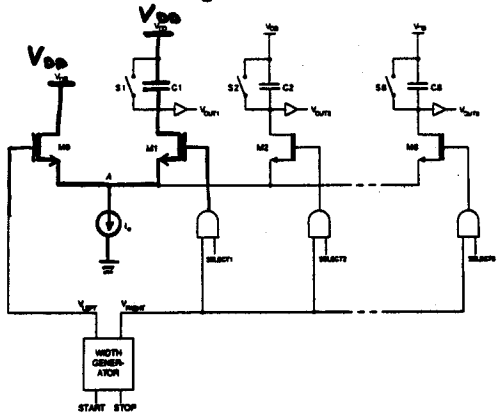
Time-to-Voltage Converter & Analog Memory (TVCAMU)

Penn-Leuven

* Time to voltage conversion for "local time" (8 - 24 nsec)
* Count clock pulses for long time scale (many microseconds)



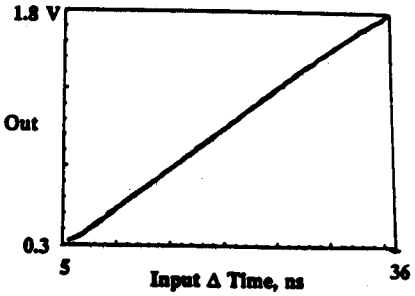
Schematic for time-to-voltage conversion



* Repetition of right-hand-side of transistor pair allows
  - Multihit capability
  - Analog memory

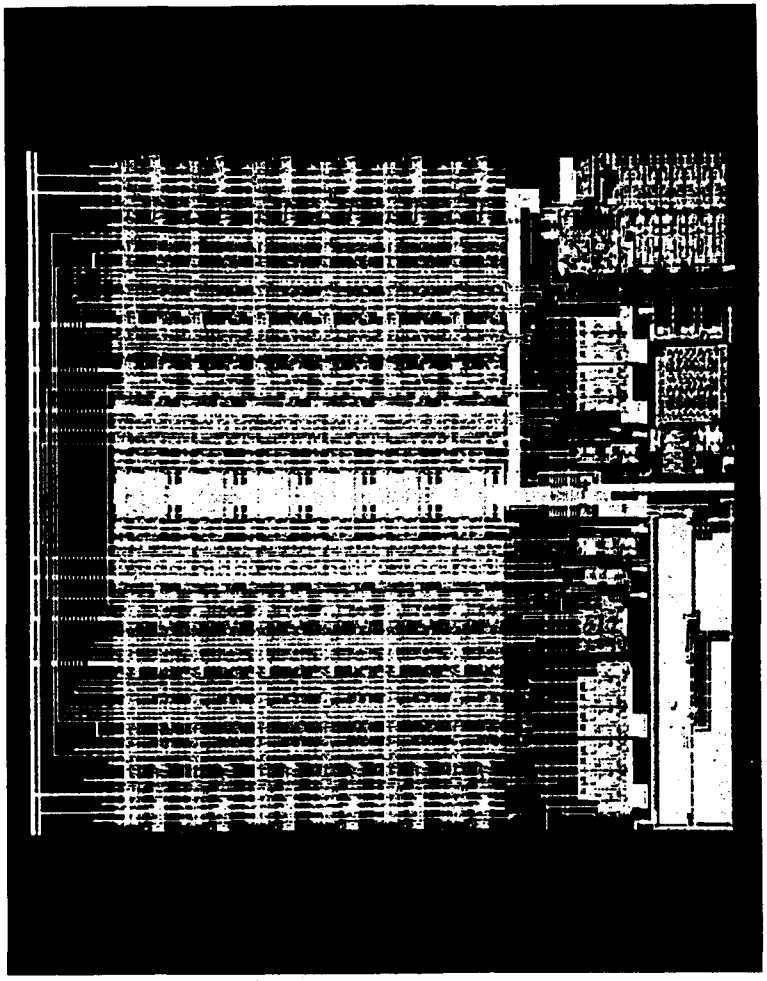
Time-to-Voltage Converter (cont)

Output Voltage vs
Input Time Difference
(8 responses superimposed)



* Fabricated in 1.6 micron CMOS
* Time resolution < 100 psec

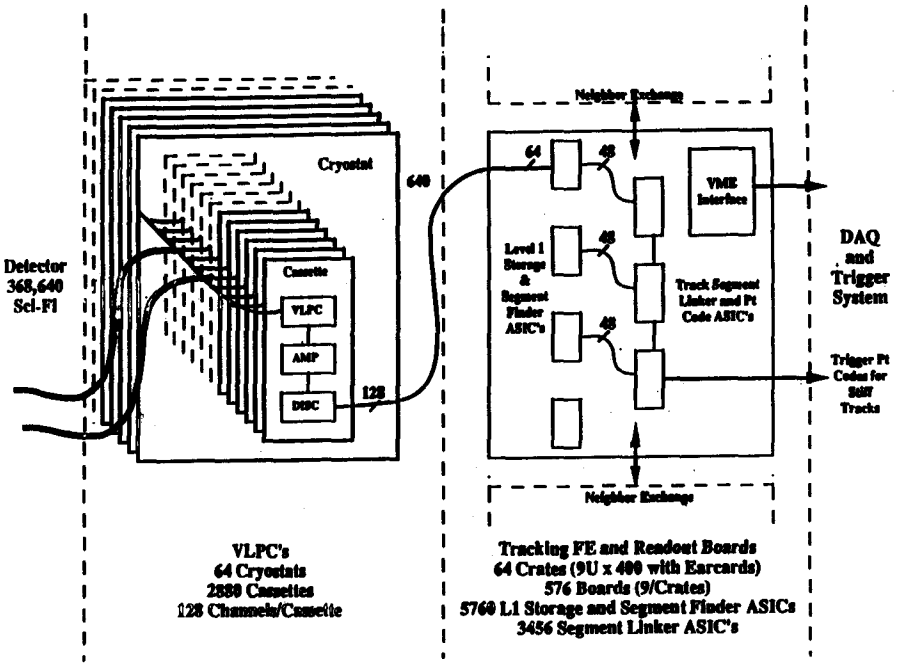
Chip Includes Level 1 - Level 2 storage
Interface to trigger
ADC
etc



TVCAMU - Status

- **All subcircuits simulated to > 60 MHz**
- **Basic TVC and Level 1 - Level 2 Transfer tested**
- **Comparison of extracted and schematic netlist**
- **SPICE simulation on full 10,000 transistor circuit, from extraction of layout (1 usec/day)** ← Brute force solution to mixed analog/digital simul. problem
  - **Time-to-voltage conversion**
  - **Level 1 & Level 2 storage**
  - **ADC conversion**

SDC Barrel Fiber Tracker Block Diagram



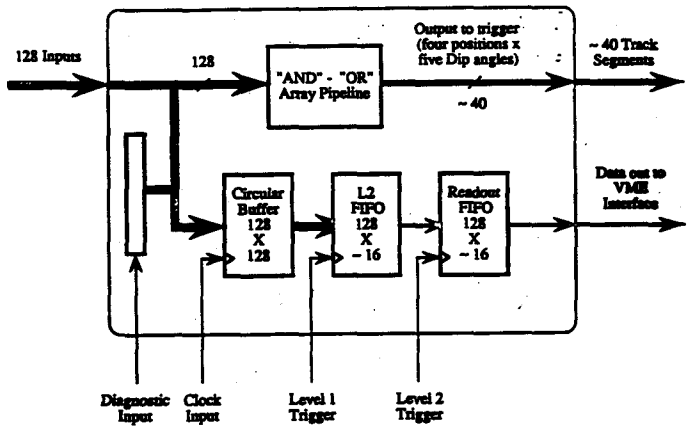
SDC
Tracking/Trigger ASIC 1

(7.0K Required)

Stores all "Hit" information locally while trigger is formed

Provides serial readout of selected events

Provides "Track Segments" for trigger



(ASIC 2 is similar for segment linking, 3.5K required)

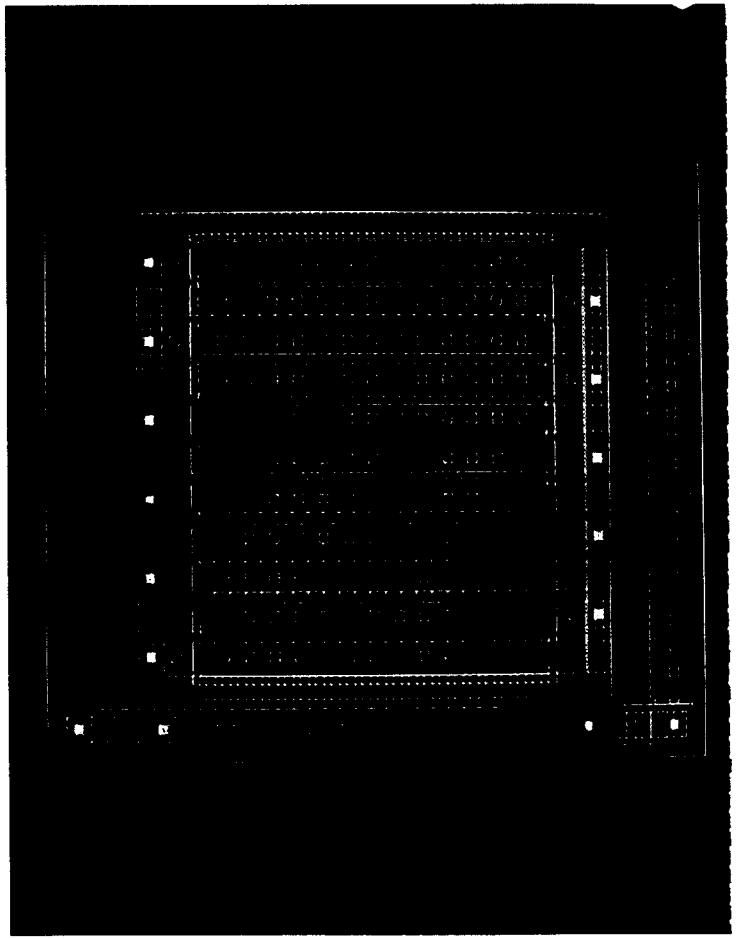
Radiation Hard CMOS

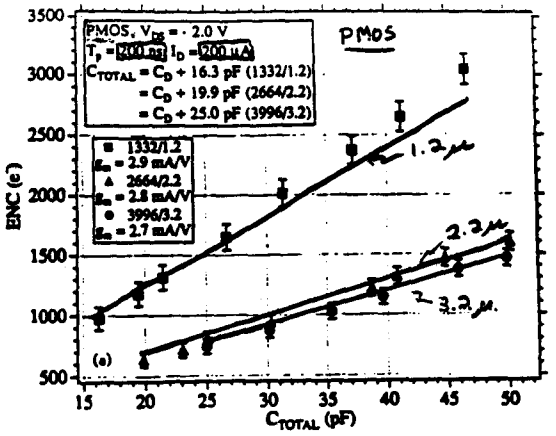
Digital Circuits

- **Reasonably straight forward to > 10 MRads**

Analog Circuits (Requirements)

- **Small and reproducible threshold voltage shifts**
- **Small changes in transconductance and output conductance**
- **Noise independent of radiation**
- **Current matching independent of radiation**
- **Low leakage currents**





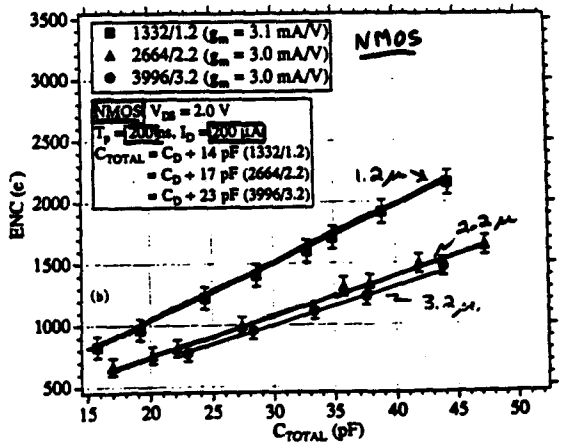
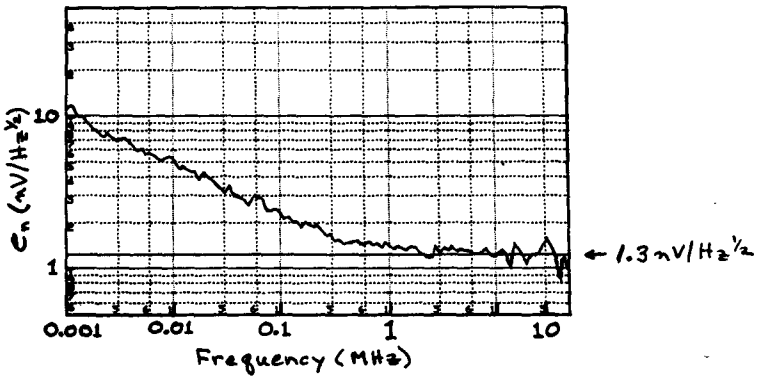


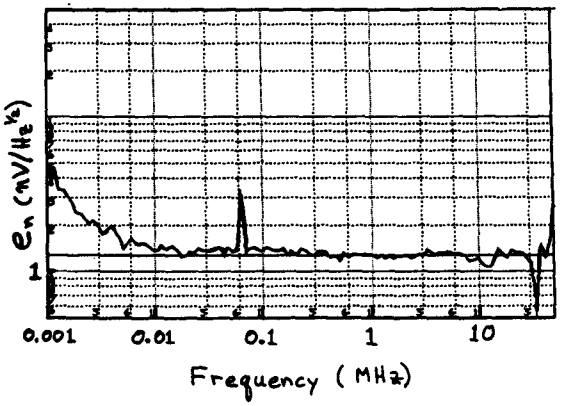
Figure 17. Equivalent noise charge as a function of capacitance for transistors of different channel lengths but the same w/l ratio. The source-bulk voltage V_{bs} = 0. (a) PMOS. (b) NMOS.

Rad Hard CMOS - Noise

* **Noise power spectrum - NMOS**

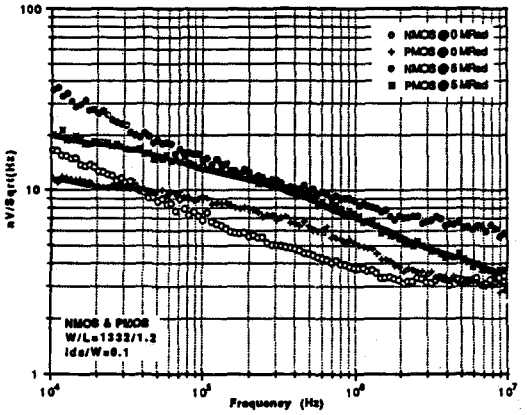


* **Noise power spectrum - PMOS**



Noise Power Spectrum
vs.
Radiation

Santa Cruz
- LBL

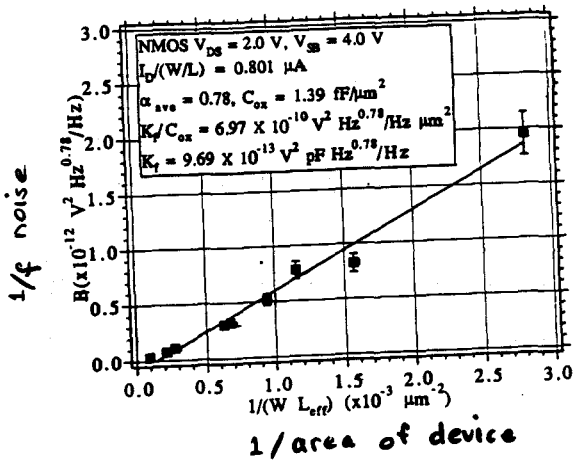


— PMOS 5 MRads

— PMOS 0 MRads

Rad Hard CMOS - 1/f

* 1/f scaling with area



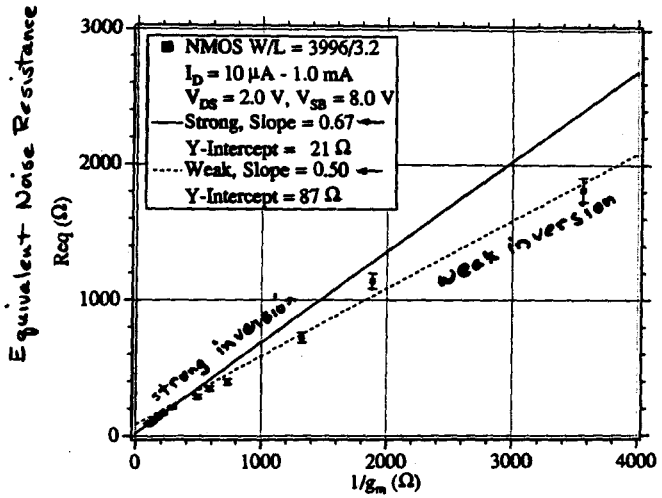
1/f noise

1/area of device

Rad Hard CMOS - Thermal Noise

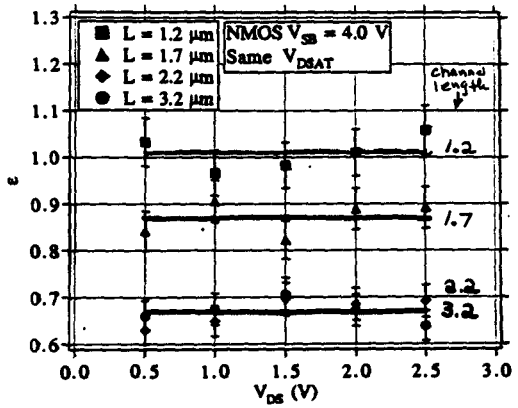
Determination of coefficient of $1/g_m$

* **Minimize gate resistance, R_g (≈ 7 ohms)**
* **Minimize bulk resistance, R_b (≈ 10 ohms)**
* **Plot noise versus $1/g_m$**
* **Span strong inversion to deep weak inversion**



Rad Hard CMOS - Thermal Noise

Dependence on channel length

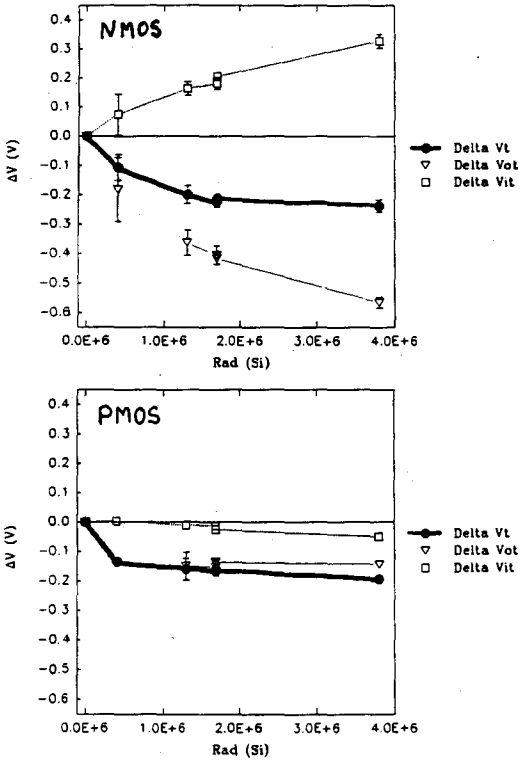


Intermediate Conclusions

* **nearly ideal theoretical result for L > 2.0 microns**
* **Significant increase for shorter channel lenghts**
* **Increase not due to conv. "hot electron" effects**
* **May be due to "warm" electrons**

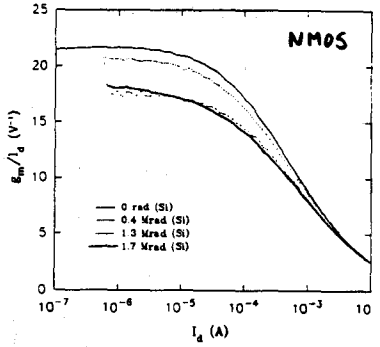
Rad Hard CMOS - Threshold Voltage Shifts & Matching

* **Threshold Voltage shifts 150 - 200mV (2 MRads)**
* **Devices track one another very well (if same bias)**
* **Slow change after 1 MRad**

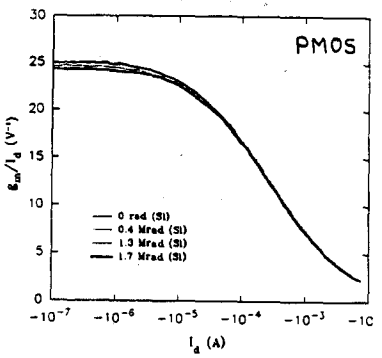


Rad Hard CMOS - Transconductance

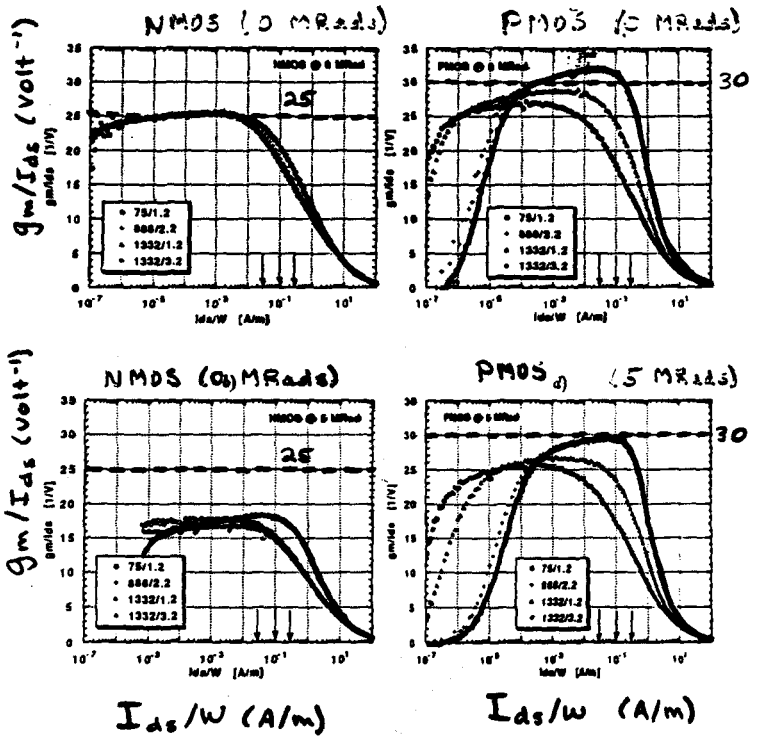
* **g_m decreases by ≈ 25% for NMOS (1.7 MRads)**



* **g_m nearly unchanged for PMOS (1.7 & 5 MRads)**



Gm/Ids versus Radiation



Signal Processing, Trigger and DAQ R&D at CERN

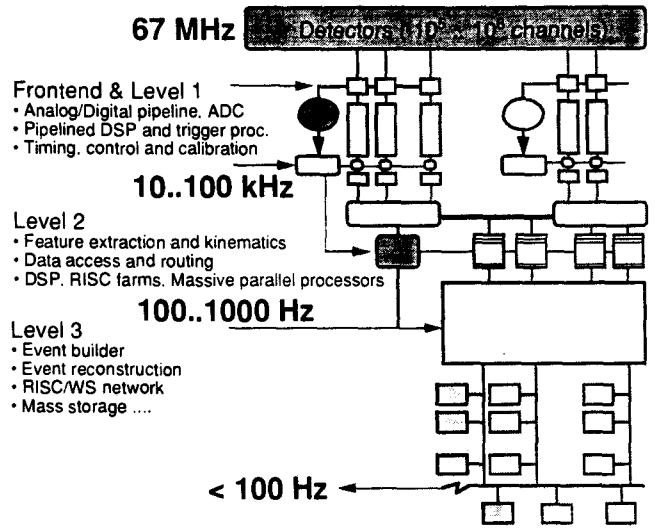
S. Cittolin

Signal Processing, Trigger and DAQ R&D at CERN

S. Cittolin/CERN-ECP. C. Christi Oct. 91

- DRDC projects
- Front-end
- Trigger level 1
- Optoelectronics
- Trigger level 2
- DAQ and computing
- Future

LHC Data Acquisition



Current R&D :

Subsystem developments (applied to detector R&D):

- Select technologies and acquire expertise
- Develop concepts and implement prototypes
- Develop industry partnerships

R&D Projects and Proposals

Frontend

RD-2 Proposal to study a **tracking/preshower detector** for the LHC. (CERN, Cambridge, Dortmund, Haqmburg, Melbourne, Olso, Oxford, INFN Perugia, RAL, Sydney)

RD-19 Development of hybrid and monolithic silicon **micropattern detectors**. (CERN, CDF, EPFL, INFN, IMEC, CPPM)

RD-20 Development of high resolution **Si strip detectors** for experiments at high luminosity at LHC (CERN, INP Cracow, Helsinki, Norway, RAL, LEPSI, INFN Turin, Yale)

RD-9 A demonstrator analog signal processing circuit in a **radiation hard SOI-CMOS** technology. (CERN, TMS)

RD-16 **A digital front-end** and readout microsystem for calorimetry at LHC. (CERN, Linkoping, INFN, Stockholm)

RD-12 Readout system **test benches.**(CERN, LAPP, INFN, Helsinki, Tampere)

MEC2 **A micropipelined first level** storage buffer with data recalibration and selective zero suppression.

RD-xx **Optoelectronic** analog signal transfer for LHC detectors.(CERN, Birmingham, EPFL, Imperial College, Oxford, GEC-Marconi)

Second level trigger

RD-11 Embedded **architecture for second-level** triggering in LHC experiments (EAST). (CERN, NIKEF, Bucharest, Budapest, Cracow, EPFL, INFN, London, Uthrech, Zeuthen)

MPPC Massive **Parallel Processing** Collaboration. (CERN, ASPEX, Saclay, IN2P3)

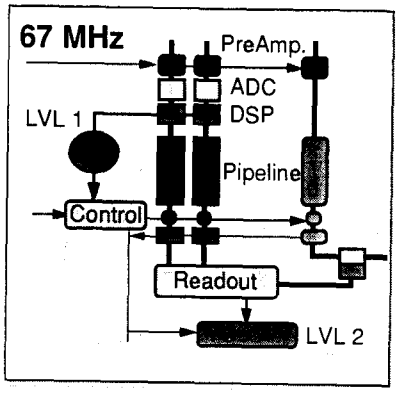
Data acquisition & computing

RD-13 A scalable **data taking system** at a test beam for LHC (CERN, INFN Pavia, Rome, LBF, Saclay)

GP-MIMD **GP-MIMD** project ((EC-Esprit, INMOS, MEIKO, PATSYS, TELMAT, CERN European universities)

RD-xx Applications of **Scalable Coherent Interface (SCI)**

Frontend



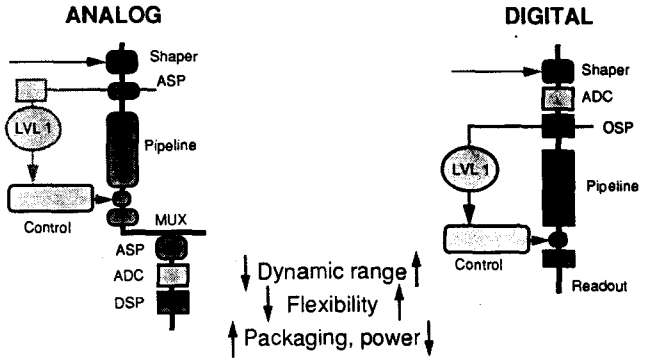
Functional blocks in FE (the main challenges):

- Preamp and pulse shaping
- Analog to Digital Conversion.
- Digital Signal Processing
- Pipelined readout structures
  (Analog delays / Digital pipelines, µpipelined architectures)
- Systolic trigger and data flow processor systems
- Event tagging. Timing and Control.

More FE challenges:

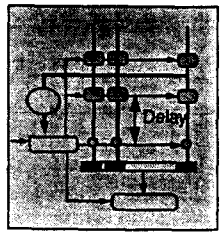
- Power, radhard, cabling, packaging, cooling
- Data access and Calibration

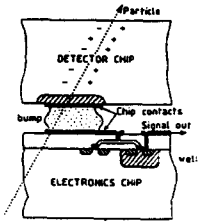
Analog / Digital frontend



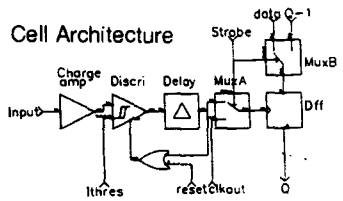
Low dynamic range (≈8bits)	Large dynamic range (15bits)
Low resolution (<8bits)	High resolution (10-11bits)
No. of channels 10^5.. 10^7	No. of channels ≤ 10^5
RD-19 Micropattern detector	RD-16 Spacal, FERMI
RD-2 Preshower. SITP	RD-12 Accordion.
RD-20 Strip detectors. APSP	NA48 Liquid Krypton. MEC2

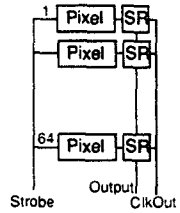
Micropattern Detector (RD19)





Cell Architecture





Hybrid approach.

Bump-bonded detector and readout electronics
- LAA readout chip (1984)
- OMEGA (heavy -ion) readout chip (1991)
  - Matrix of 16•64 pixel of 75μm•300μm. ≈ 20μW/channel
  - Threshold 4000 e^- ± 1000 e^-. Noise ≈ 60 e^-
  - Minimum strobe width ≈ 200 ns. Maximum delay ≈ 1μs
  - 16 bit serial readout at 5 MHz
  - Detector and electronics bonding

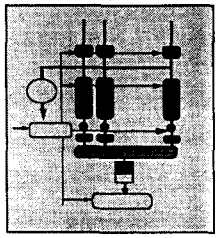
Monolithic approach

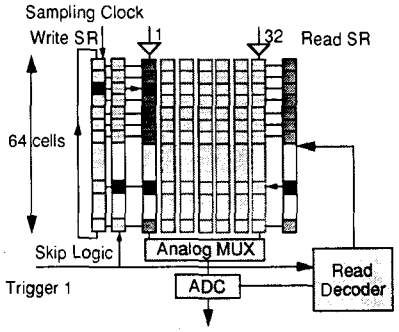
SOI on high resistivity substrate
- In technology development phase at INEC

Silicon Tracker Preshower SITP (RD2)

HARP (Hierarchical Analog Readout Pipeline Processor)

SI tracker preshower

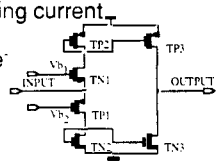




ICON :

very fast low power charge preamplifier using current conveyor principle

- 15-20 ns peaking time. Noise < 2500 e⁻

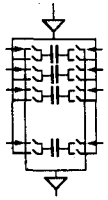


SAPE :

4 / 32 / 128 channels pipeline. 66MHz

64 storage elements using switched capacitor techniques with sparse data scan

- 1.2 CMOS (SOI-CMOS). 5 - 10 mW /channel
- ≈ 400 µV output noise. 4V dynamic range
- 40 mV/MIP gain (ICON). 1 MIP = 25000 e⁻
- < 1% internal crosstalk



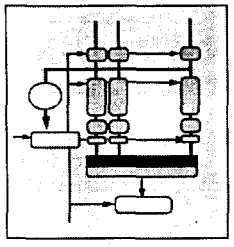
- Readout test with preshower detector
- Readout decoder VLSI design
- More cells & channels per chip

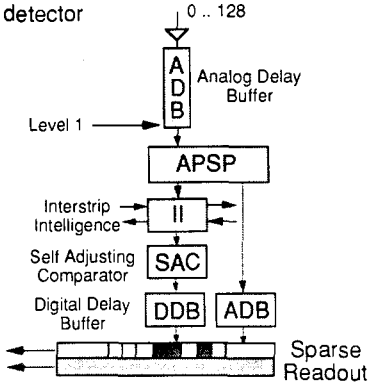
SI Strip detector. APSP RD20

Analog Pulse Shaping Processor

RD-20 Development of high resolution **Si strip detectors** for experiments at high luminosity at LHC

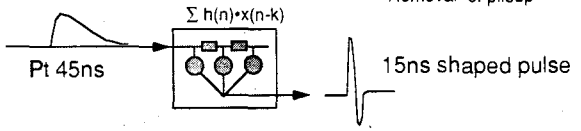
Silicon tracker / vertex detector





APSP. Analog deconvoluter:

- Recovery of timing information
- Removal of pileup



- Off-line analysis. Deconvoluter study
- Multi-channel VLSI chip

Radhard Technology (RD9)

Project's goal.
Assess the SOI-CMOS radiation hard technology from Thompson Military Spatial TMS (S013HD) up to

10Mrad and 10^{14}n/cm^2 for analog applications

in particle physics. SOI technology is faster than BULK technology. Parasitic capacitances of MOS transistor, on SOMIX silicon wafer, are reduced.

Fast digital processor, RAM and 8 bit 25MHz FADC have been hardened up to 100 Mrad.

Project status.

- Prerad measurement of SOI transistors (august 91). Results are beeing analyzed.
- Preliminary noise measurement on small structures indicates a corner noise frequency at 10Mrad exposition :
  n-channel device : prerad ≤ 100KHz post rad ≤400KHz
  p-channel device : prerad ≤ 10KHz post rad ≤100KHz

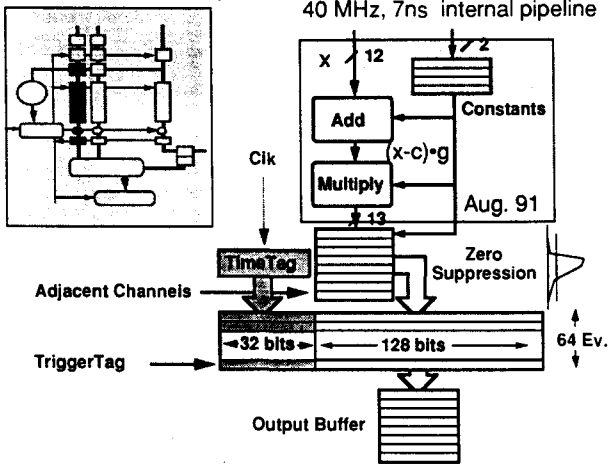
- Large transistors for accurate noise measurement are processed and will be available end 91
- Neutron irradiation is now starting at CERN, and gamma C_o^{60} irradiatiation at Saclay. Result in November 91
- SPICE model of this technology is under study. The analog model is still a problem because of the complexity of the SOIMOS transistor.
- Preparation of analog demonstrator (amplifier, comparator, analog memory). 1992

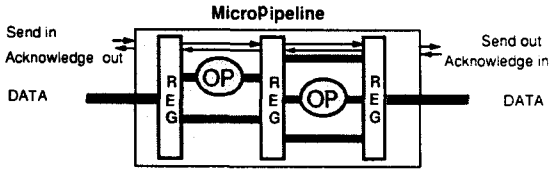
MEC2 μpipeline

Micropipelined Equalizator Corrector and first level storage buffer (CERN/ECP-MIC)

Liquid Krypton (NA48)

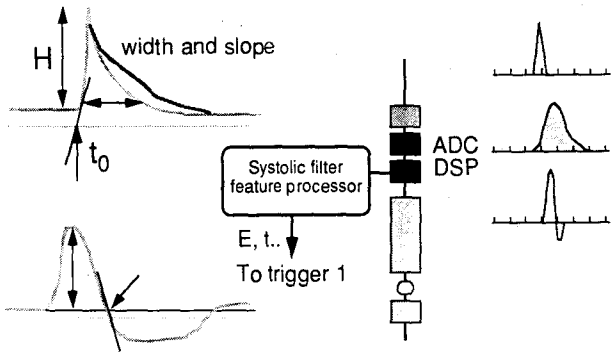
1.2μ CMOS.
40 MHz, 7ns internal pipeline





Digital Signal Processing

The signals generated by an LHC calorimeter cell will be diffused over more than one bunch crossing. A digital channel with programmable filter capability is needed to extract the physical information and to associate events within bunch crossings.
In addition, for those detectors where the particle (e/π) can be identified by the signal shape in a single channel, the digital analysis can be the first step of the trigger process.

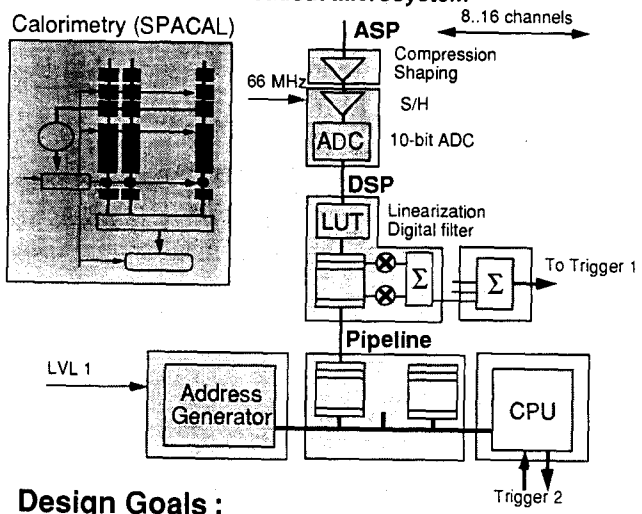


Apart from considerations of power consumption, electronics packaging and radiation hardness, it seems very attractive to go digital immediately after the preamplifiers, complementing the analog shaping with a **pipelined digital signal processor**.

Basic filter operation : $\sum X_i \cdot W_i$

FERMI. (RD16)

FrontEnd Readout Microsystem



Design Goals :

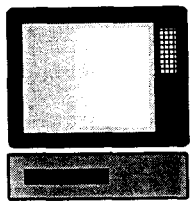
- CMOS 1μm
- 15 bit (compressed) dynamic range
- Pipelined ADC. 10 bit resolution
- Digital Signal Processing. Time tagging, Level 1 Sums
- Data storage during LVL1 & LVL2 latency
- Fault tolerance & reconfigurability
- Si-on-Si Microsystem architecture

and . . . .

- Power, radhard, connectivity, packaging, cooling
- Data transfer (bandwidth), calibration

Industry

In the last 20 years, the requirements of telecommunications and in particular of television have strongly contributed to the development of IC technology (CMOS, BiCMOS) and mass production by industry. Together with other fields, high energy physics experiments have exploited these developments extensively.



Flash ADC
Analog memory
Helical scan recording
Image processing
Data compression
Data communication

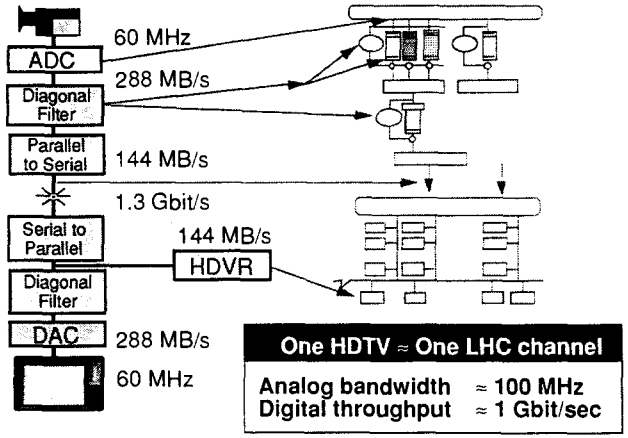
In recent years the world television industry has undertaken a new challenge :

High Definition TeleVision (HDTV).

This represents a tremendous effort of research and development in the field of CMOS technology.
In Europe it is organized under the EUREKA projects.

HDTV chain/LHC

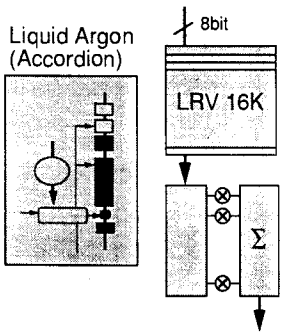
- **Digital** - ADC (144, 27 MHz, 10 bits)
- **Data compression**
- **Multi-standards**
- **High quality pictures**
  - Digital signal processor
  - Memory delays
  - Pipeline and data driven architectures
- **Transmission**
  - High speed (2 GB/s) optical links
- **Mass storage**
  - Parallel to serial converter
  - High speed (100 MB/s) recorders



Digital Pipe & Filter. (RD11-LAPP)

HDTV digital pipeline Test Bench.

IC prototypes designed and developed by CNET (Centre National d'Etudes des Telecommunications) in Grenoble in the framework of the HDTV project



LRV 16K.
Memory delay line.
2048 Bytes 72MHz FIFO

MULAC8.
Transversal filter processor.
94MHz Systolic array of 8 multiplier/adder for real time digital image processing and filtering.
XOUT(30bits) = $\sum$ XIN(i)•W(i)
[10bit•12bit, i=1-8]

- CNET chips integration in a test bench

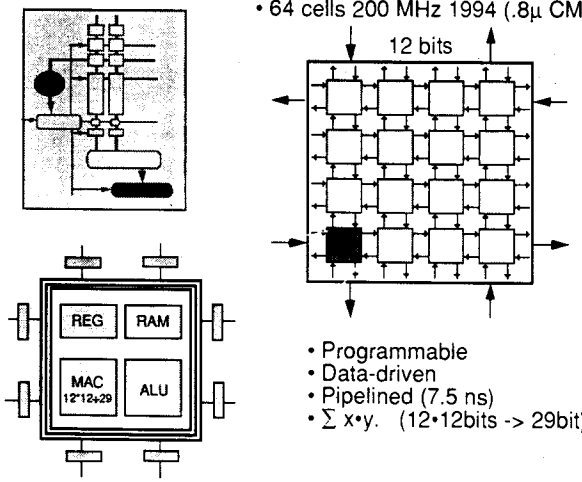
- Design of a two step FADC with 15bits dynamic range
- Study of a digital filter for liquid Argon calorimeter (Accordion)
- CNET collaboration for the design of 16-bit pipelined digital filter(1992).

VSP test bench (RD11,RD12)

DAVIS. Data Driven Video Signal Processor

(ITT-Intermetal)

- 16 cells 125 MHz 1991 (1.2µ CMOS)
- 64 cells 200 MHz 1994 (.8µ CMOS)

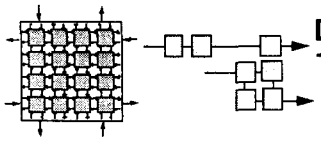


- Programmable
- Data-driven
- Pipelined (7.5 ns)
- $\sum$ x•y. (12•12bits -> 29bit)

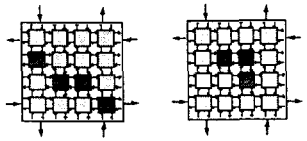
- Software simulation of data driven systems :
  - Pulse feature extraction : Zero-crossing, Max Minimum, Area...
  - Computational algorithms : Least square fit, Spline....
  - Digital Filters
  - Clustering and total energy
  - Tracking
  - Image processing functions
- Prototype integration in a frontend test bench

DAVIS

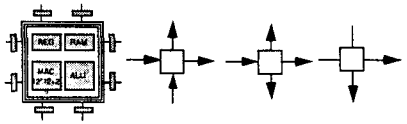
12bits • 4 I/O ports 125MHz 16 cells (200 MHz 64 cells 1994)



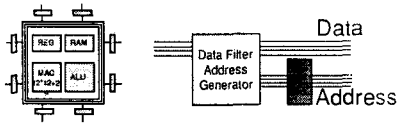
Data Driven processor
1D-2D Digital filters



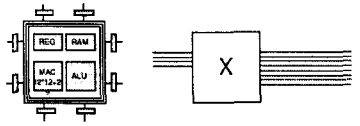
Contiguity Machine
7.5 ns cycle



Bus switch
750 MByte/s peak



DMA Controller
375 MByte/s



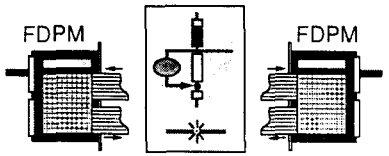
Intelligent
LookUp Table

Readout System Test Benches. RD12

Develop and exploit multipurpose **Personal Computer-based Test Benches** to support the evaluation and design of the basic elements required for digital front-end readout and data transmission systems for an LHC experiment.

They will support components such as **fast ADCs, hybrid fibre-optic transceivers, and the prototype VLSI systolic array and data-flow processors** currently being developed in national research laboratories and by the emerging European HDTV industry.

Test benches

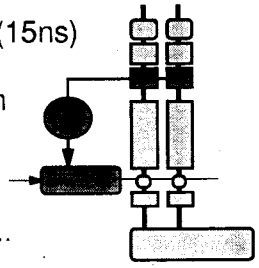


Fast Dual Port Memory
• 133 MHz. 24 bit. CMOS
• Programmable Memory Control. VLSI sequencer (Padova)

- Hybrid fibre-optic transreceivers (Helsinki)
- Timing distribution
- Digital pipelines (MEC2. HDTV. FERMI)
- Data flow processors
- ADC (RD12. RD16)
- Neural Nets track finders
- Crossbar switches

First level trigger

- Pipelined processors (15ns)
- ≤ 1μs latency
- $10^3..10^4$ rate reduction
- Local / global



- Engineering.
  Data transport, power..

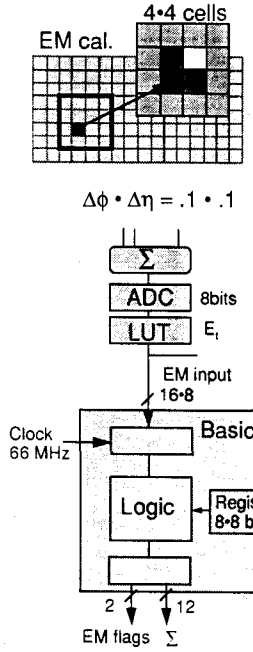
Basic functions :

- 2D clustering and energy cuts
- Segment identification

for inclusive electron, muon and jets identification

A first level calorimeter trigger

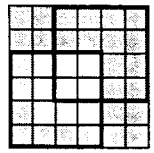
Demonstrator project for a first level calorimeter trigger
(Birmingham, Queen Mary and Westfield College, RAL)



A digital processor chip
• 15ns pipeline < 500 ns latency

Algorithm: > E_t cut
or
> E_t cut
and
< E_t cut

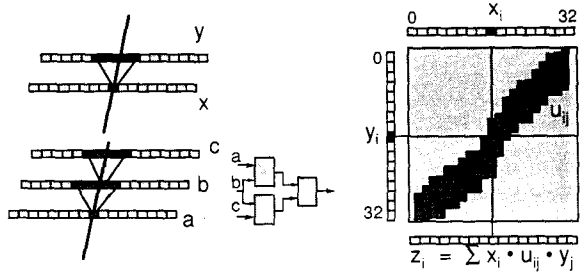
System modularity:
9 cluster finding chips each 36 em channels for 9 reference cells



- .8 μm CMOS gate array (Jan. 92)
- Prototype test and system integration
- Demonstrator system in a test beam at CERN

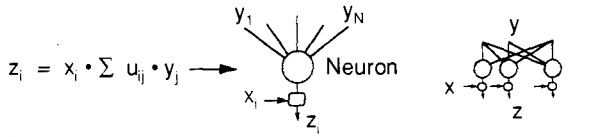
Muon trigger

Segment identification in low occupancy detectors.



- Desy-H1 μ trigger. 32•32matrix 48 ns. 2μ CMOS (RAL)
- CERN-WA92 μ trigger. PAL 25 ns (INFN Rome.)

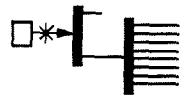
RD5 (CMS collaboration).
Simulation study for a new proposal of a first level muon trigger associated to RPC detectors (INFN Rome)



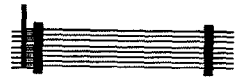
Neural Net for tracking and ASIC implementation (RD11 & RD12)



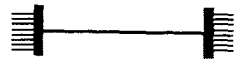
Optoelectronics



Timing and control distribution



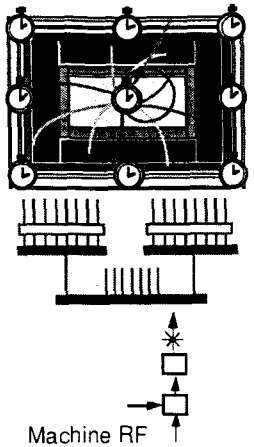
Analog signal readout



Data transmission

Timing & Control.

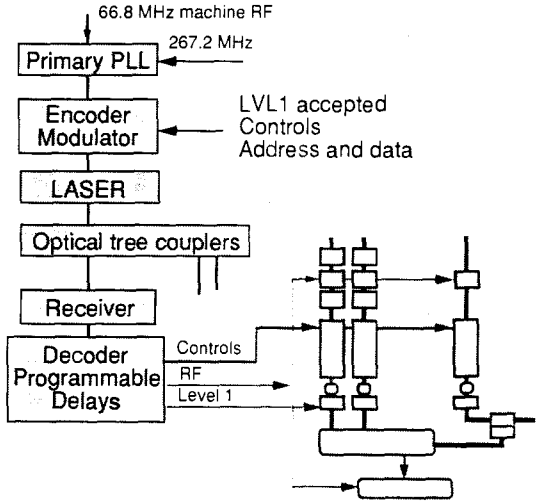
Timing & Control test bench (RD12)
Development of basic hardware and software components of a **multichannel optical-fibre time distribution system** for LHC detector front-end electronics, and investigation of the feasibility of simultaneously exploiting the timing system for transmission of the level-1 trigger acceptance and addressable control information



Need to compensate:
- Variable propagation delays
- Particle TOF • Drift times
- Electronics

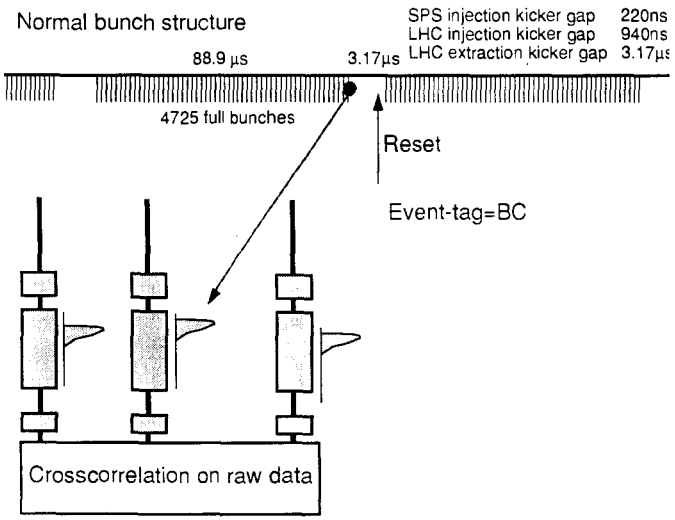
Need to broadcast :
- Bunch crossing
- Trigger-1 acceptance
- Control
- Test pattern

Timing & Control. RD12 Test bench



RD12. Timing test bench :
- Digital modulator demodulators
- Optical couplers
- Receivers
- Clock recovery
- Programmable delays
- Timing calibration
- High power Laser
- CATV, FTTH technologies

Timing calibration



Optoelectronics

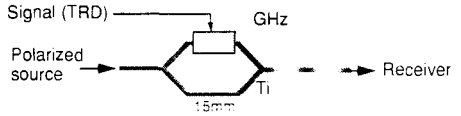
Analog signal transfer

Needs :
- Readout of large number of channels (10^6 .. 10^8)
- Radiation hardness
- Power dissipation and cabling.

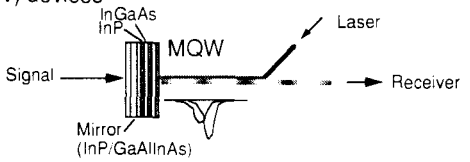
DRDC new proposal for the study of **optoelectronics analog signal transfer** (CERN, Birmingham, EPFL, Imperial College, Oxford, GEC-Marconi)

- Multi-channel electro-optic intensity modulators.
- Optical fibre (ribbon) links and receivers
- Study of engineering, packaging and production processes
- Assess performance with LHC detectors R&D

• Lithium Niobate ($LiNbO_3$) Mach-Zehnder interferometer (BNL)

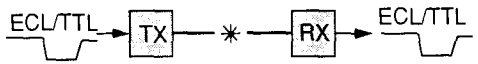


• III-VI semiconductors (GaAs, InP-based) multiple quantum well (MQW) devices



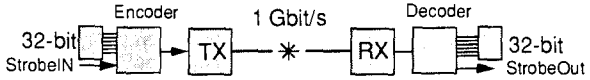
Optoelectronics

Digital signal transmission optical transceivers (RD12-Helsinki)



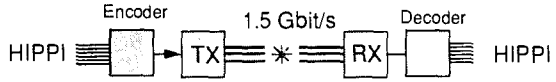
- 8 channels discrete components. ≈200 Mbauds
- GaAs multi channels. Integrated QWL aser arrays, connector etc..

32bit word transfer with GaAs transceivers (INFN Rome)



- Simulation study
- GaAs implementation. (TriQuint)

HFOX. **High Speed Optical Links** (Birmingham, CERN, HP)
1.5 Gb/s optical link for HIPPI data communication

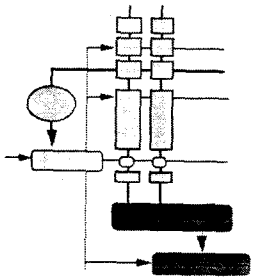


- Test bench development with HP
- Application in the L3 experiment

- Transmitter/Receiver
- Multi-fibre connector
- GaAs integrated optics

Second level trigger

- **Fine measurements**
- **First level trigger complement**
- **Event topology and kynematics**

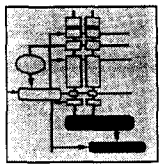


- 10..10^2 rate reduction
- 10..100μs latency
- Asynchronous

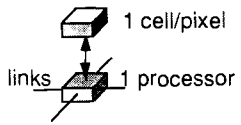
- Multi processor system
- Level 1-2 data routing
- Local/Global communication

SIMD. MPPC

Massive Parallel Processing Collaboration

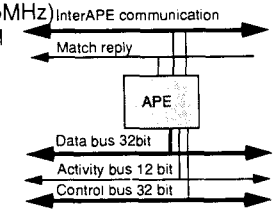


A SIMD machine for second level trigger
fine grain parallelism



SIMD architecture

- String/loop of associative processing elements:
  APE (2μm CMOS 64Ape/chip, 25MHz)
  - 64bit associative memory cell
  - 70bit comparator
  - 1bit processor
  - 10bit activity and flag
  - Communication capabilities
- Programmable structure
- Scalable.

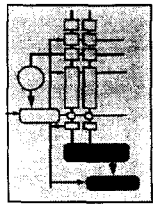


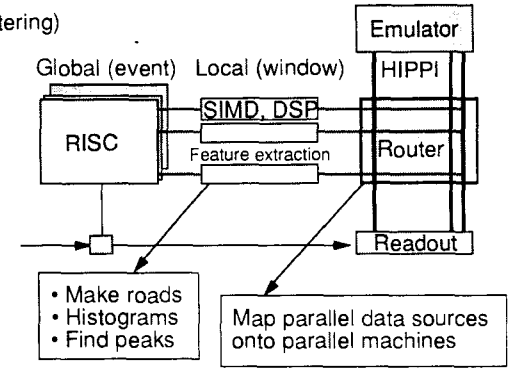
- Chip design (ASPEX UK)
- Preproduction (ES2)
- Algorithm study
  - High p_t electron ≤ 50μs
  - p_t muons (≤ 20μs)
  - TRD electron tracking
  - Calorimetry (SDC) ≤20 μs
- Controller and data communication
- VME interface
- 8K APE prototype
- 4 16K APE machines

Second level trigger. RD11

RD-11 Embedded architecture for second-level triggering in LHC experiments (EAST)

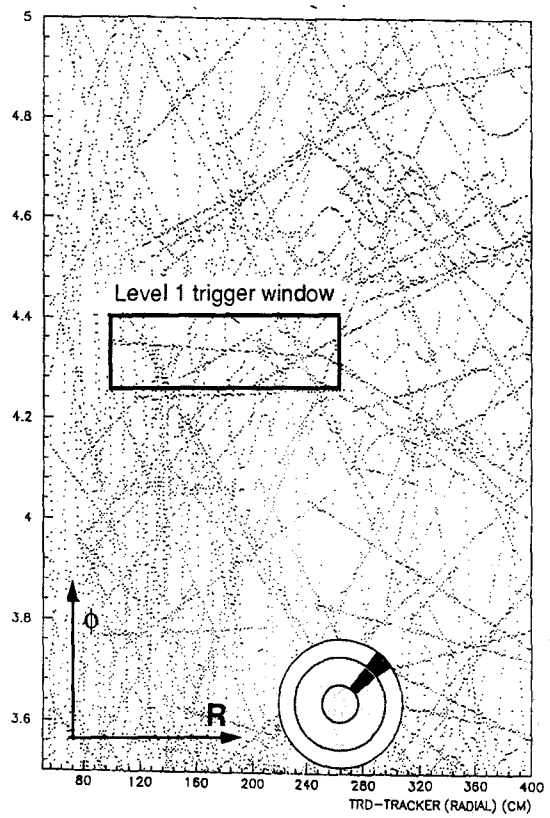
TRD (tracking)
SPACAL (clustering)





- Data emulator
- Point to point link (HIPPI)
- Local/Global LVL 2 simulation
- Image processors (MaxVIDEO)
- DSP and VSP (DAVIS)
- General-purpose SIMD (APS)
- Data router
- Custom Hardware
- MasPAR
- RISC farms

Electron identification. TRD-RD11



DAQ. RD13

RD13. A scalable data taking system at a test beam for LHC

A test beam setup for the simultaneous testing of :
- detector prototypes
- R/O electronics
- trigger architectures
- DAQ software

Introduce UNIX operating system and modern software methods in a data acquisition environment

Basic configuration :
- **SUN work stations**
- VME as I/O interface concentrator and control system
- CES RAID8235 **MIPS3000 VME based processor**
- **LynxOS** as UNIX real time system (adopted by the accelerator division)

Languages :
- Saber C++

Tools :
- Software-through-Pictures
- Virtual Software Factory
- IPSYS

User interface
- Motif
- Teleuse, UIMX, Interviews

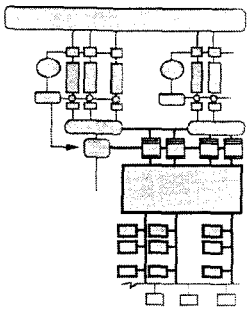
Database
- Oracle
- OODB

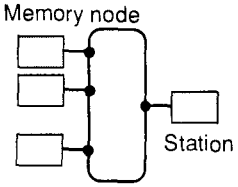
Simulation:
- Verilog
- SIMSCRIPT
- MODSIM

Application of SCI to DAQ

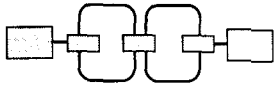
Proposal for the application of SCI at LHC (CERN, Dolphin)

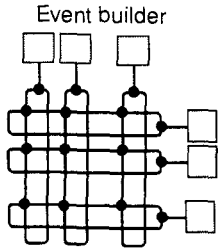
Scalable Coherent Interface protocol (SCI. IEEE standard P1596)
- 1 Gbyte/s diff. ECL node to node (15m)
- 100 MByte/s optical fibre (2km)





Bridges :
SCI-SCI, VME-SCI,Sbus-SCI...





GP-MIMD project

Collaboration of European computer manufactures to produce a general purpose parallel machine from next generation **Transputer** chips. (EC(Esprit), INMOS, MEIKO, PATSYS, TELMAT, CERN and European universities))

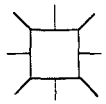
The aims of the project

- To design and build a **message passing parallel computer** with scalable CPU, I/O and communication capability. A GP-MIMD : between 16 and 1024 processors
- To define and implement a standard **Application Support Interface for parallel applications**.

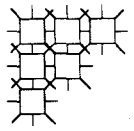
CHORUS for real time and full UNIX V

The role of CERN

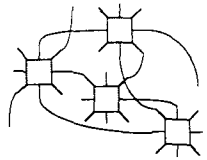
- To identify an appropriate programming paradigm for large **FORTRAN programs**
- To port the **JULIA off-line event reconstruction** program
- To implement a demonstration **On-line Data Acquisition** System
- To receive two Machines:
  - 32 nodes each
  - 16Mb per node
  - 10Gb disk space



> 100 Mips
100 Mb/s links

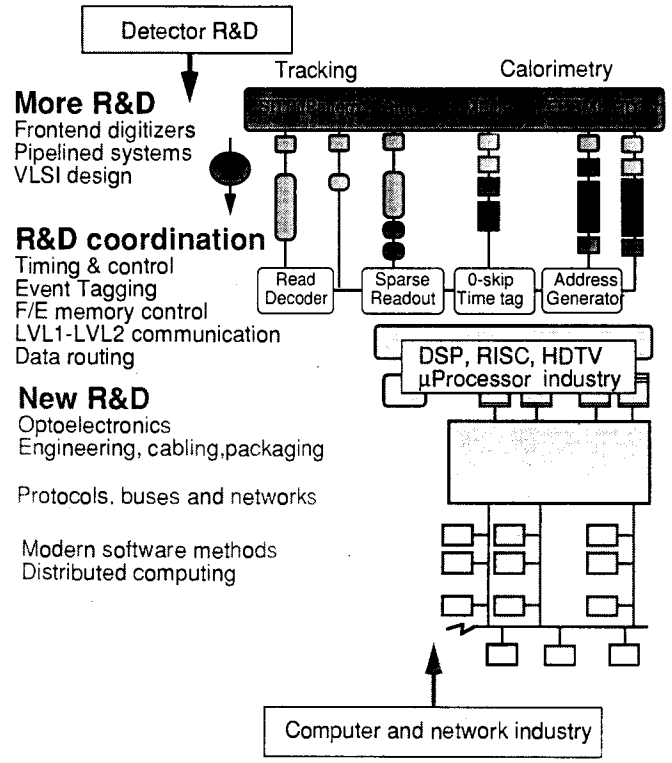


Supercomputer



Local electronics
control&calibration

Future phases...



Muon Systems

J. Bensinger

Muon Systems

Jim Bensinger
Brandeis University and SSCL

Abstract

The designs of both the GEM and SDC muon systems and the technological choices are reviewed. In particular, the chamber options for the detectors are discussed.

Introduction

The development of a muon system for an experiment at the SSCL requires an understanding of the physics objectives for a particular system and how those goals translate into specific requirements for such a system. These requirements are established by the final off-line measurement accuracy needed to provide the necessary resolution for the experiment. It is the trigger requirements which generally determine the on-line placement accuracy that the system components have to achieve. Finally, it is an understanding of backgrounds and the operating environment which sets the operational requirements of the system.

Having established these conditions, one must proceed to systematically develop all parts of a muon system. For muon chambers, this means choice of gas and basic unit cell, choice of chamber size and construction method, as well as the structural system that holds the chambers. For trigger systems, it means choice of technology to provide fast timing to associate the muons with a particular beam crossing and a mechanism to provide an approximate momentum for the trigger track. Triggering is generally done in stages to provide an approximate rate reduction factor of 10^4 in level one and an additional reduction factor of 10 to 100 in level two.

In this paper we will review the GEM and SDC muon systems to understand motivation for the SSCL Subsystem R&D program. Then we will discuss the specific R&D results from the subsystem progress reports #200[1], #207[2], and #218[3,4].

GEM Muon System

The goal for the GEM muon system is a precision momentum measurement outside the calorimeter with high precision tracking chambers in a large magnetic field..The sagitta method for momentum determination is used. Measuring muons outside the calorimeter means the the detector will be robust at the highest luminosities. The expected precision of the GEM muon system is 5% at η=0 and P_μ=0.5 TeV. One possible implementation of the GEM muon system is shown in Figure 1.

Level 1 triggering in GEM is accomplished by requiring that the ϕ difference in track position in the outer two superlayers of the muon system be smaller than a predetermined threshold. Level 2 is then given by calculating the change in slope of the track measured in the outer two muon superlayers. Successful triggers will have a difference below another preset threshold. This is shown in Figure 2.

SDC Muon System

The SDC muon system provides muon identification, a trigger, and augments the central tracker momentum measurement. In the forward direction it provides the primary momentum measurement. Momentum is calculated by measuring the bend in an iron toroid. Figure 3 shows the SDC muon system. Figure 4 shows the expected resolution for muon measurement.

For the SDC muon trigger a road and timing pulse is created by the coincidence of a pair of scintillation counters. Wires (θ measuring) in alternate layers of drift tubes are projective to the interaction point. The time difference between signals arriving at the wires is a measure of the bend in the toroidal magnet. These signals arriving sufficiently close in time, coincident with a scintillator, make a Level 1 trigger. The timing diagram for this trigger is shown in Figure 5.

Chamber Gas and Electrostatic Cell Studies

The requirements for a choice of an electrostatic cell design or a choice of chamber gas is based on several considerations. One wants a gas that is insensitive to the variations in the electrostatic field, ambient pressure, and variations in composition (including impurities). If we have large drift distances, we would like it to have a small longitudinal diffusion but high drift velocity. If the chamber is used in a magnetic field, we would like a small Lorentz angle. Proper cell operation implies that the gas should cause minimal chamber ageing and not be prone to sparking. The large volume of the proposed muon systems implies that the gas should be safe (nonflammable and nontoxic) and affordable both in initial and operating costs.

Systematic studies of various gases to find the optimal combination of gases given the specific requirements of the various systems have been made by all groups. Some typical results (from the MIT group[1]) are shown in figures 6 and 7. Of course it is the behavior of the gas in combination with the electrostatic fields in the chamber and the surrounding magnetic field that determines the quality of the measurement. An example of such a convolution is shown in Figure 8. The arrival time (in 50 nsec steps) of ionization along various field lines is shown by the *'s and o's.

In most cases the groups reported satisfactory solutions to the problem of finding the correct combination of chamber gas and electrostatic cell design. It does not appear that the optimum solution for SSC running has been found in all cases and these studies will continue.

Chamber Studies

The requirements for muon chambers are:

1. They must have reasonably good resolution. This is required to provide good momentum measurements to several hundred GeV transverse momentum.
2. They must have good track pair resolution so that delta rays accompanying muons can be resolved.
3. They must be capable of having a single wire span a distance of up to 9 m.
4. There should be a minimum of dead space within a layer so that level triggers are as robust as possible.
5. They must be easily industrialized. That is, they must be capable of being built at sites with relatively unskilled labor but with good quality control.
6. They must be relatively inexpensive.

The proposed technologies for the GEM system are:

1. For the central region $0<\eta<1.3$ the choice is between Pressurized Drift Tubes (PDT) and Limited Streamer Drift Tubes (LSDT). PDT achieve their accuracy by capturing the wires in precision plates, as is shown in Figure 9.

2. In the endcap region $1.3<\eta<2.5$ Cathode Strip Chambers (CSC) are the technology of choice. The advantage here is that only the cathodes have to be accurately positioned to achieve the required resolution. The backup technology for this region is LSDT.

3. The timing information is provided by Resistive Plate Chambers, essentially a self-quenching spark chamber which uses a resistive glass for electrodes. An illustration of this chamber is shown in Figure 10.

The chamber cell technological choice for SDC is either a single wire cell or a 3-wire jet cell. For the single wire extruded tube one can have a simple round or octagonal tube or more complex tube with field shaping as shown in Figure 8. An example of this is the SSCL/Washington design for a stack of round cells made from Aluminum extrusions, shown in Figure 11. The version shown in the figure contains field shaping electrodes. The wire position is maintained by capture of the tube endcap in a precision milled endplate.

Figure Captions

1) Elevation view of one possible implementation of the GEM muon system.

2) Level 1 and Level 2 muon trigger definition for GEM.

3) Cross section view of the SDC muon system. The barrel and forward (FT) toroids are shown. Tracking chambers are BW - barrel tracking, IW - intermediate tracking, and FW - forward tracking.

4) Expected resolution for the SDC muon system including a central tracker resolution of .25 $(TeV/c)^{-1}$ up to $\eta = 1.7$.

5) Timing diagram for SDC muon Level 1 trigger.

6) Velocity and Lorentz angle for various combinations of Argon and CO_2.

7) Velocity and Lorentz angle for various combinations of CF_4 and Isobutane.

8) Drift time calculation for ionization in cell with field shaping. *'s and o's indicate arrival time in 50 nsec ticks of ionization produced in the cell. The gas is Argon (90%), CF_4 (5%), and CH_4 (5%).

9) Pressurized Drift Tube End Plug Assembly. (GEM)

10) Restive Plate Chambers. (GEM)

11) SSCL/Washington design for a stack of round cells made from aluminum extrusions and containing field shaping electrodes. The wire position is maintained by capture of the tube endcap in a precision milled endplate. (SDC)

---

[1] Progress on the Research and Development Program to Continue the Development of Precision Instrumentation for the Study of Muons in the TeV Region. Charles Stark Draper Laboratories, Harvard University, John Hopkins University, Lawrence Livermore Laboratory, Massachusetts Institute of Technology, Princeton University, Purdue University Contact: Samuel C.C. Ting, M.I.T.

[2] Muon Subsystem R&D 1991 Progress Report. Argonne National Laboratory, University of Colorado, University of Illinois, University of Maryland, University of Michigan, University of Minnesota, Rochester University, University of Washington, and University of Wisconsin. Contact: K. Heller, U. of Minn. and S. Errede, U. of Ill.

[3] Toroidal Spectrometer Group - Progress Report. Joint Institute for Nuclear Research at Dubna, University of Houston, LeCroy Corporation, Louisiana State University, Massachusetts Institute of Technology. Contact: Louis S. Osborne, M.I.T.

[4] Progress Report on Streamer Chamber - Drift Chamber R&D. University of Houston. Contact: R. Weinstein, U of Houston.

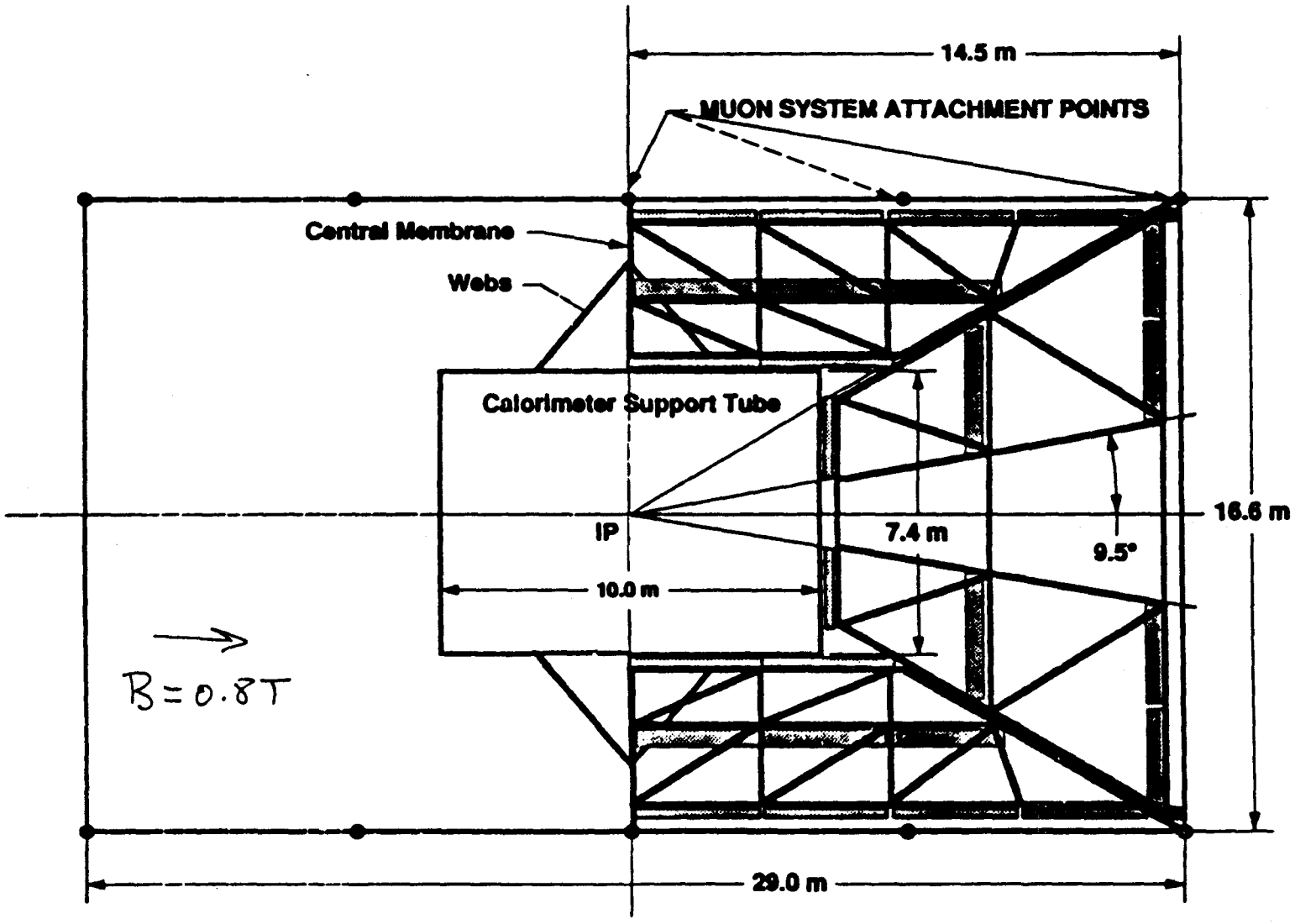


Figure 1 Elevation view of one possible implementation of the GEM muon system.

F. Nimblett
21 August 1991

D P H I AND RAYS TRIGGERS

***

D P H I IS A VALID TRIGGER IF THERE IS A COINCIDENCE BETWEEN PADS PHI3(i) AND ONE OF PHI2(i +/- thr) WHERE thr = 0,1,2,3,....

***

R A Y S IS A VALID TRIGGER IF CALCULATED ANGLE BETWEEN RAY2 AND RAY3 IS SMALLER THAN A GIVEN THRESHOLD

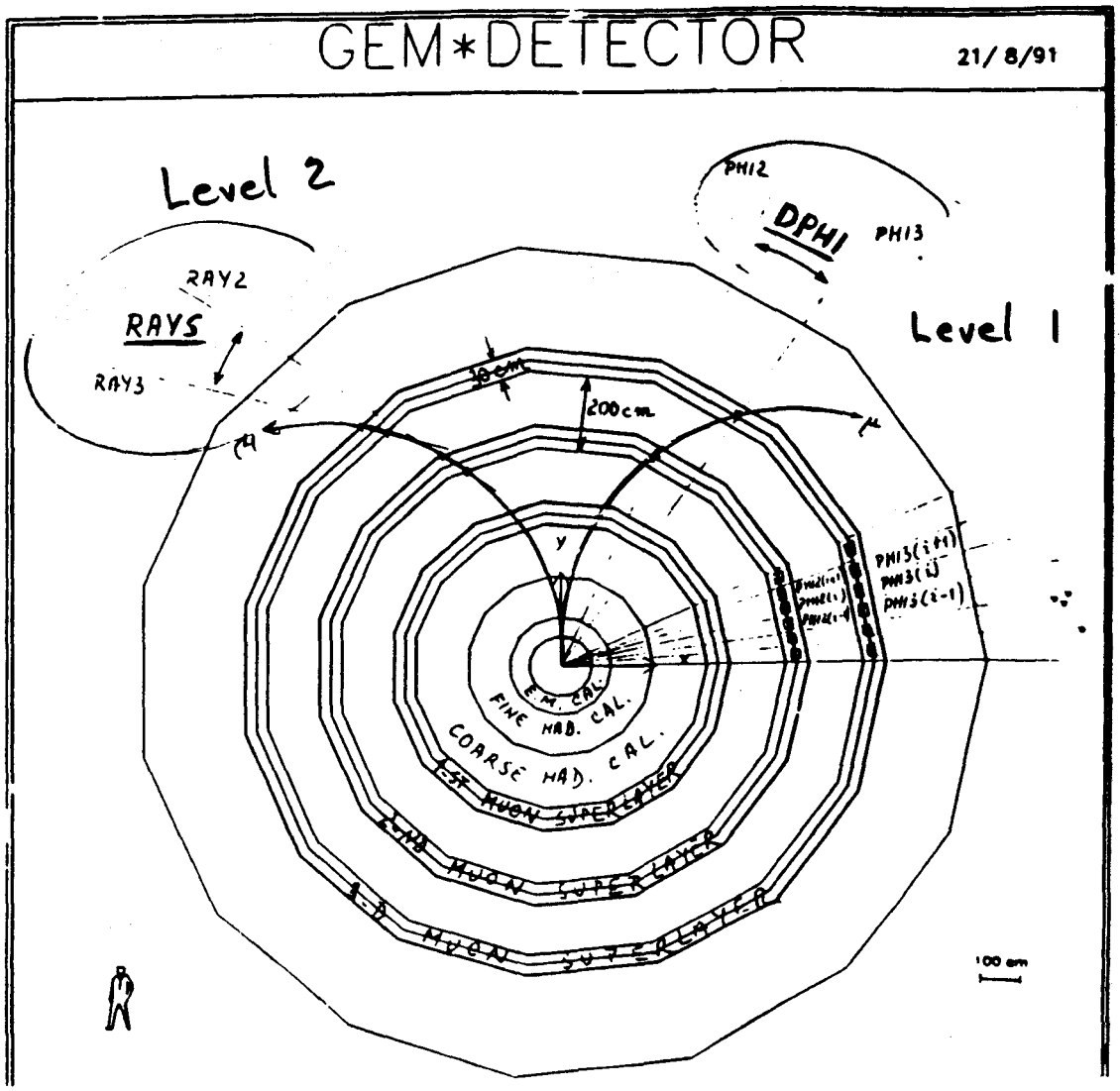


Figure 2 Level 1 and Level 2 muon trigger definition for GEM.

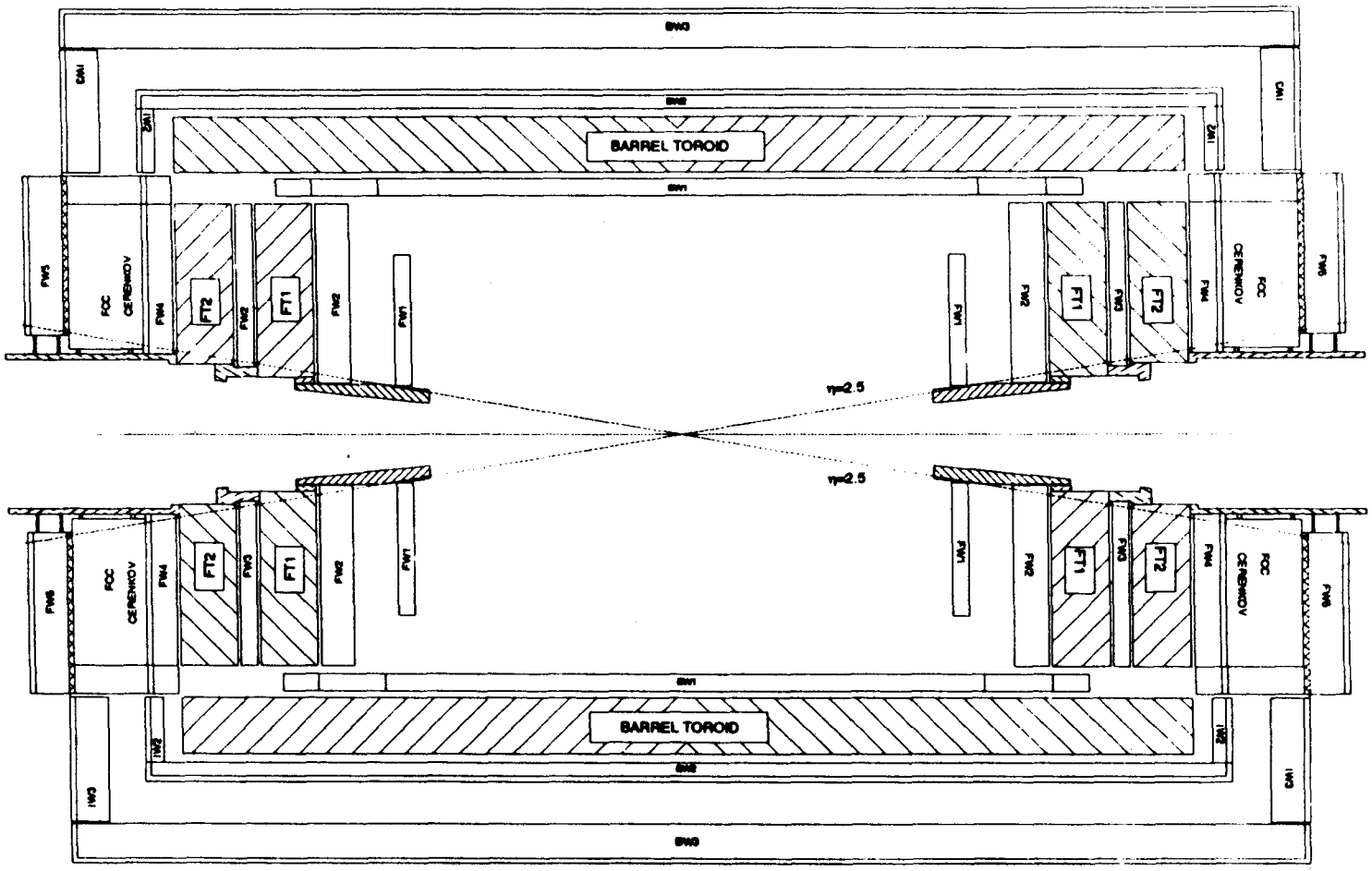
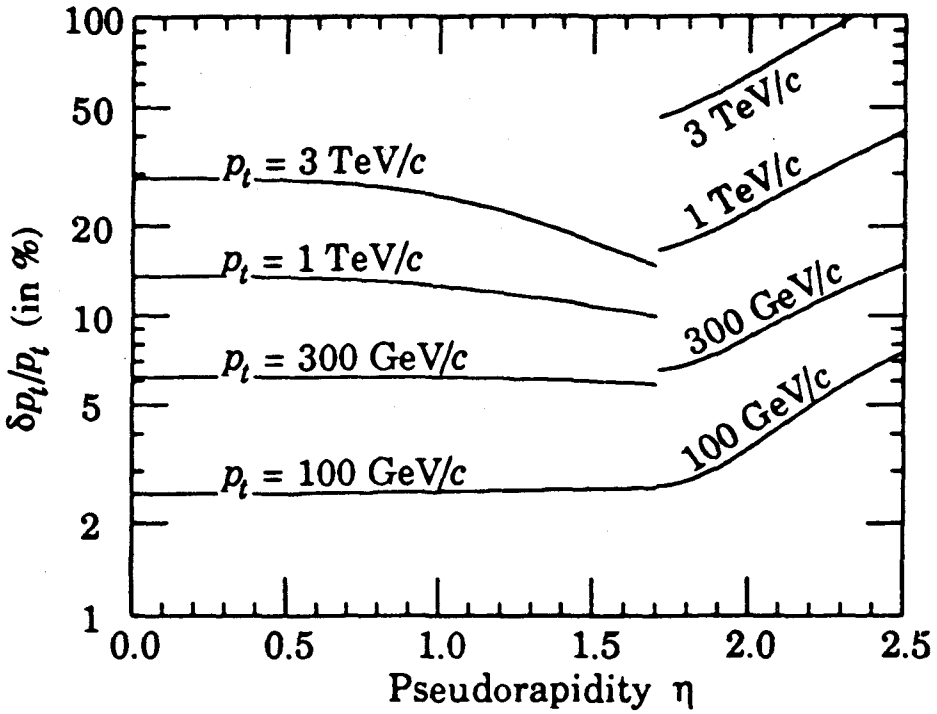


Figure 3 Cross section view of the SDC muon system. The barrel and forward (FT) toroids are shown. Tracking chambers are BW - barrel tracking, IW - intermediate tracking, and FW - forward tracking.



Muon momentum resolution as a function of pseudorapidity for various values of transverse momentum. A resolution of 0.25 $(\mathrm{TeV}/c)^{-1}$ from Table 1 is used to characterize the central tracking performance.

Figure 4 Expected resolution for the SDC muon system including a central tracker resolution of .25 $(\mathrm{TeV/c})^{-1}$ up to η=1.7 .

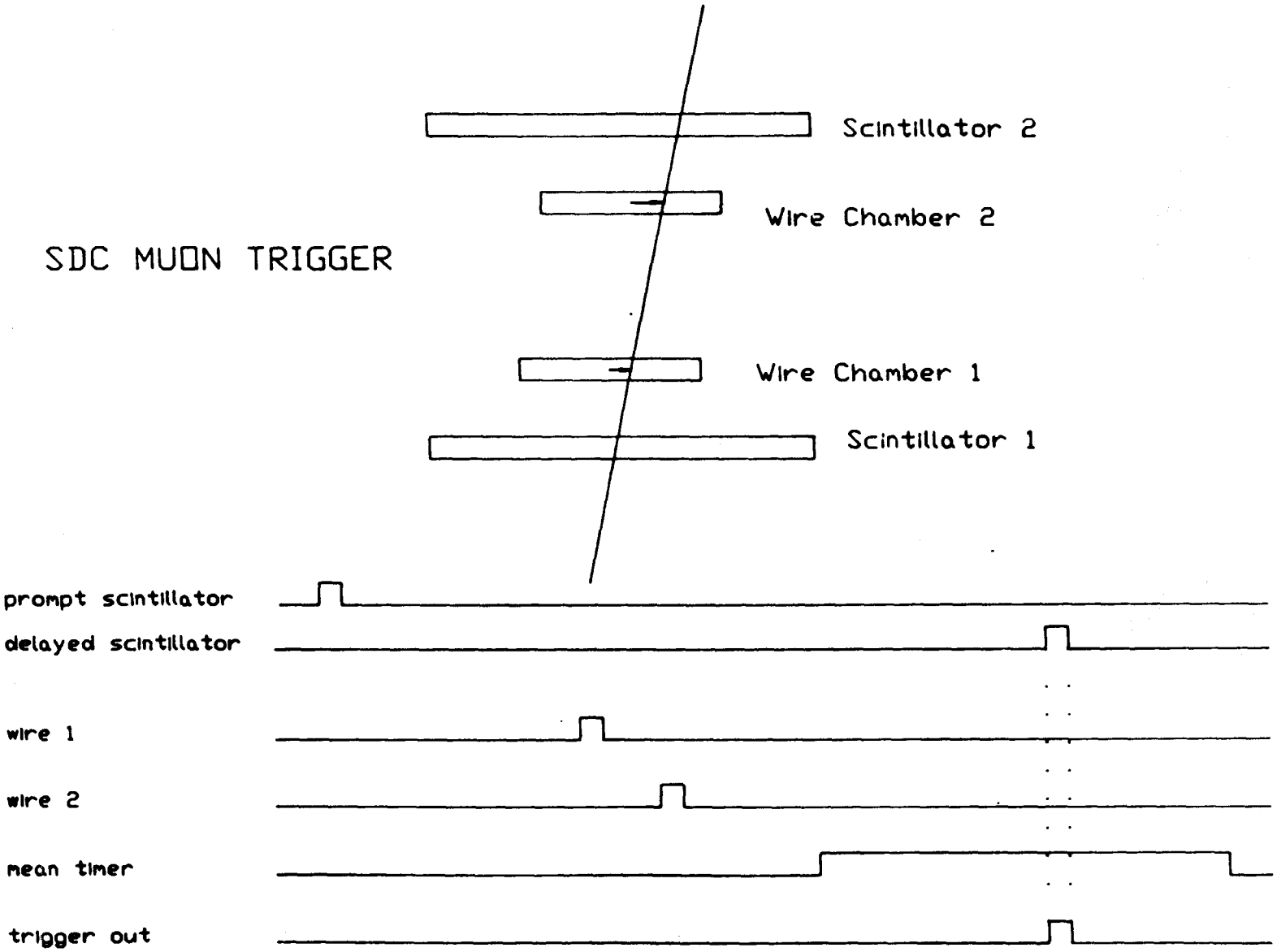


Figure 5 Timing diagram for SDC muon Level 1 trigger.

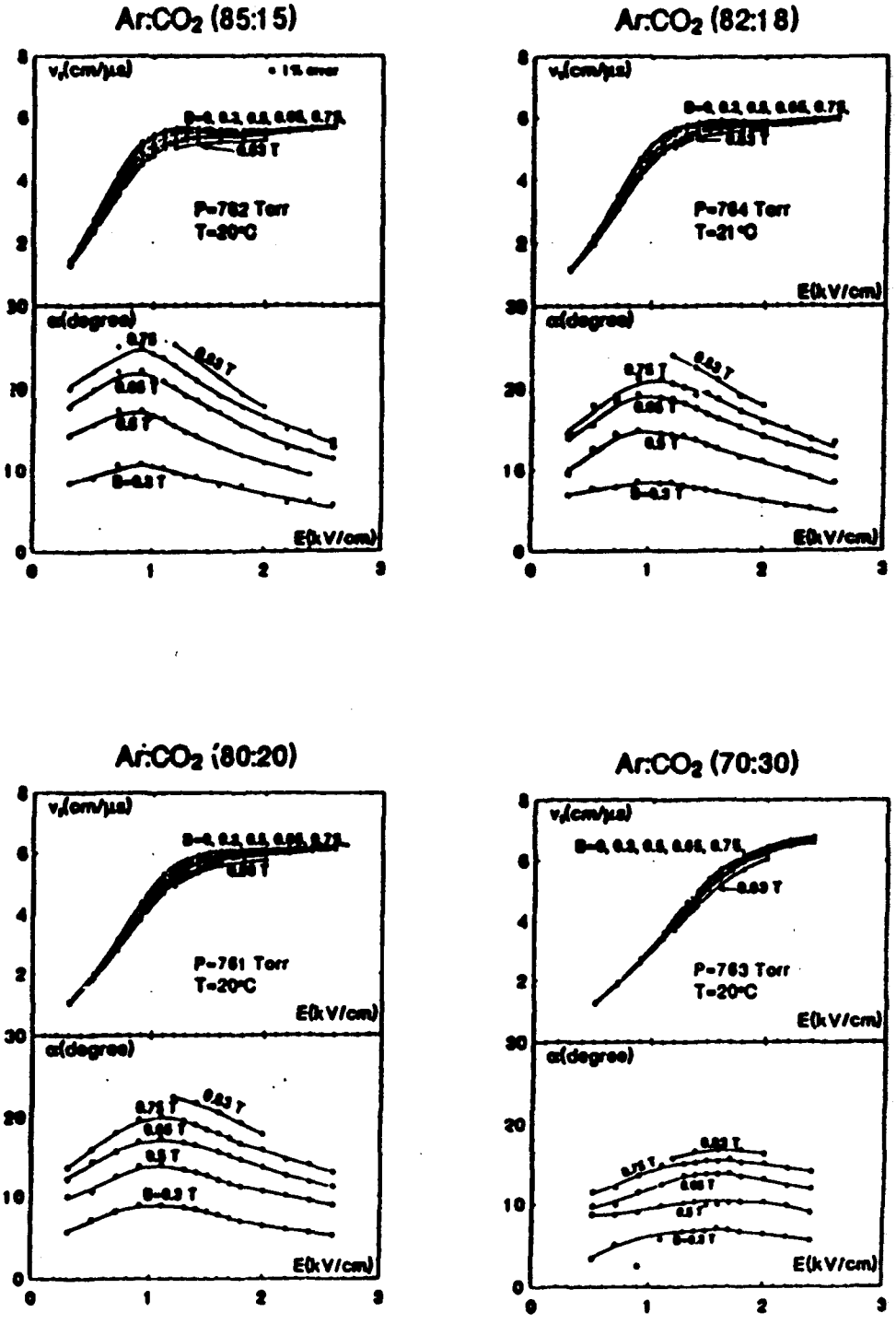


Figure 6 Velocity and Lorentz angle for various combinations of Argon and CO_2.

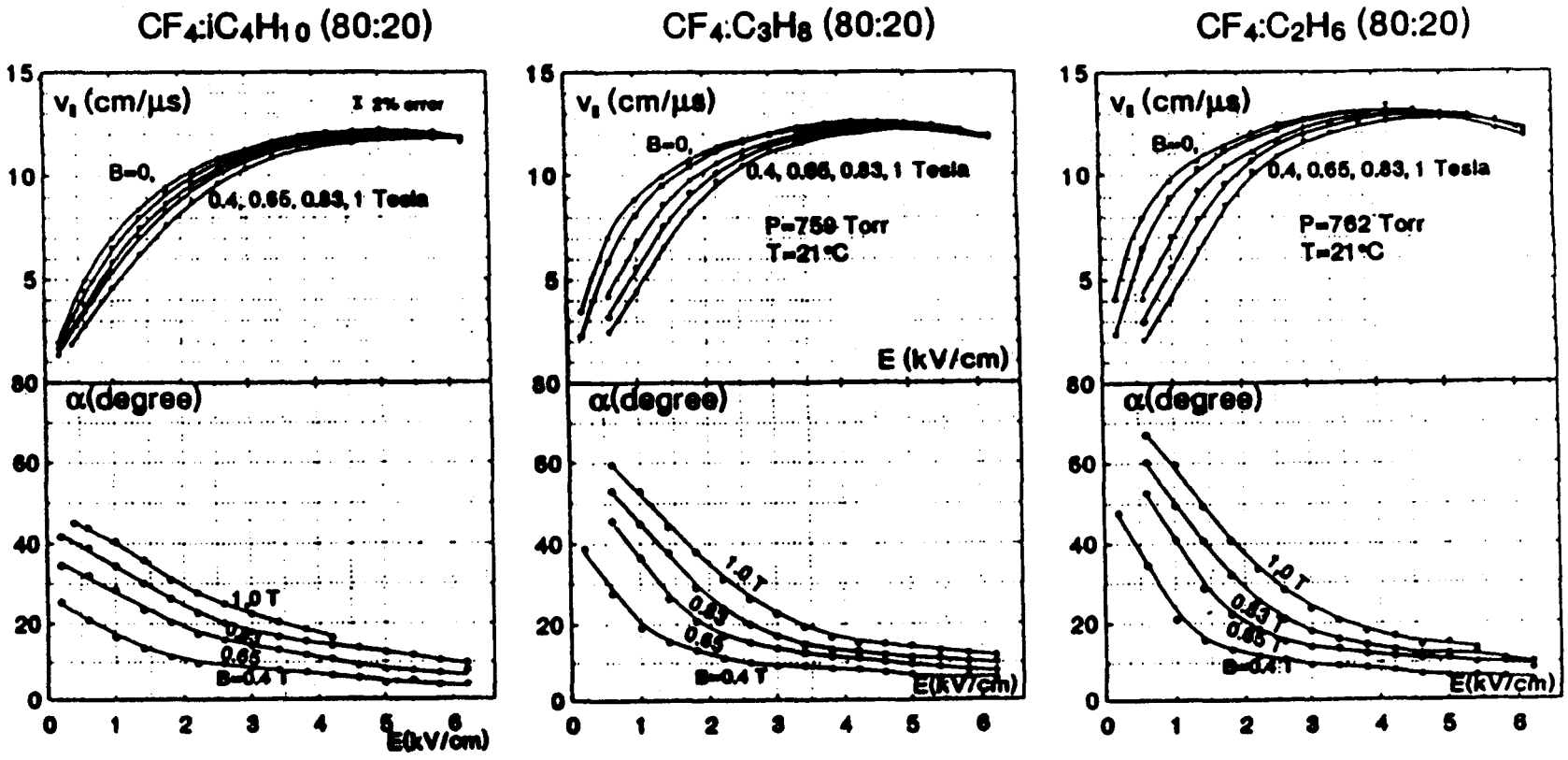


Figure 7 Velocity and Lorentz angle for various combinations of CF_4 and Isobutane.

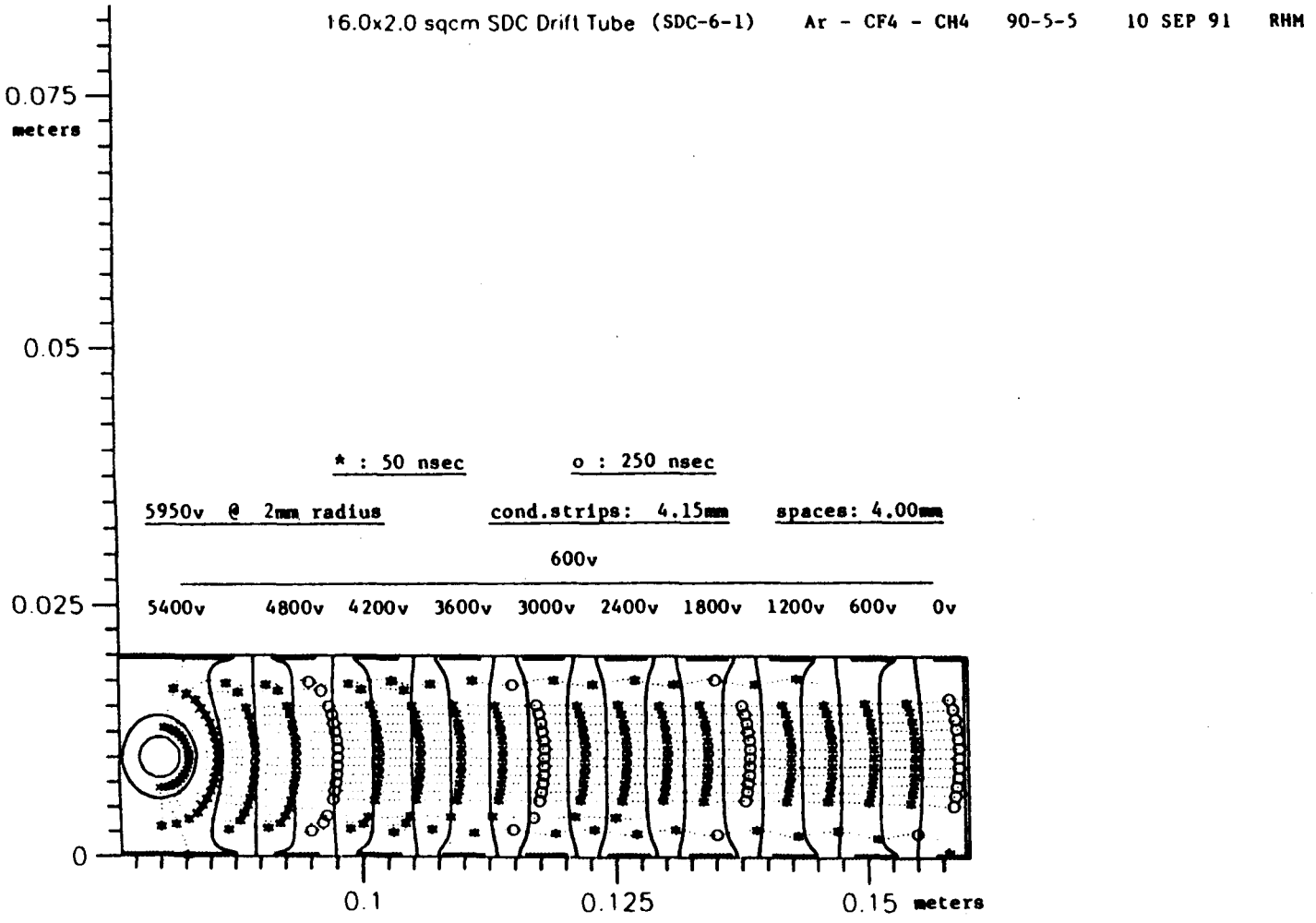


Figure 8 Drift time calculation for ionization in cell with field shaping. *'s and o's indicate arrival time in 50 nsec ticks of ionization produced in the cell. The gas is Argon (90%), CF_4 (5%), and CH_4 (5%).

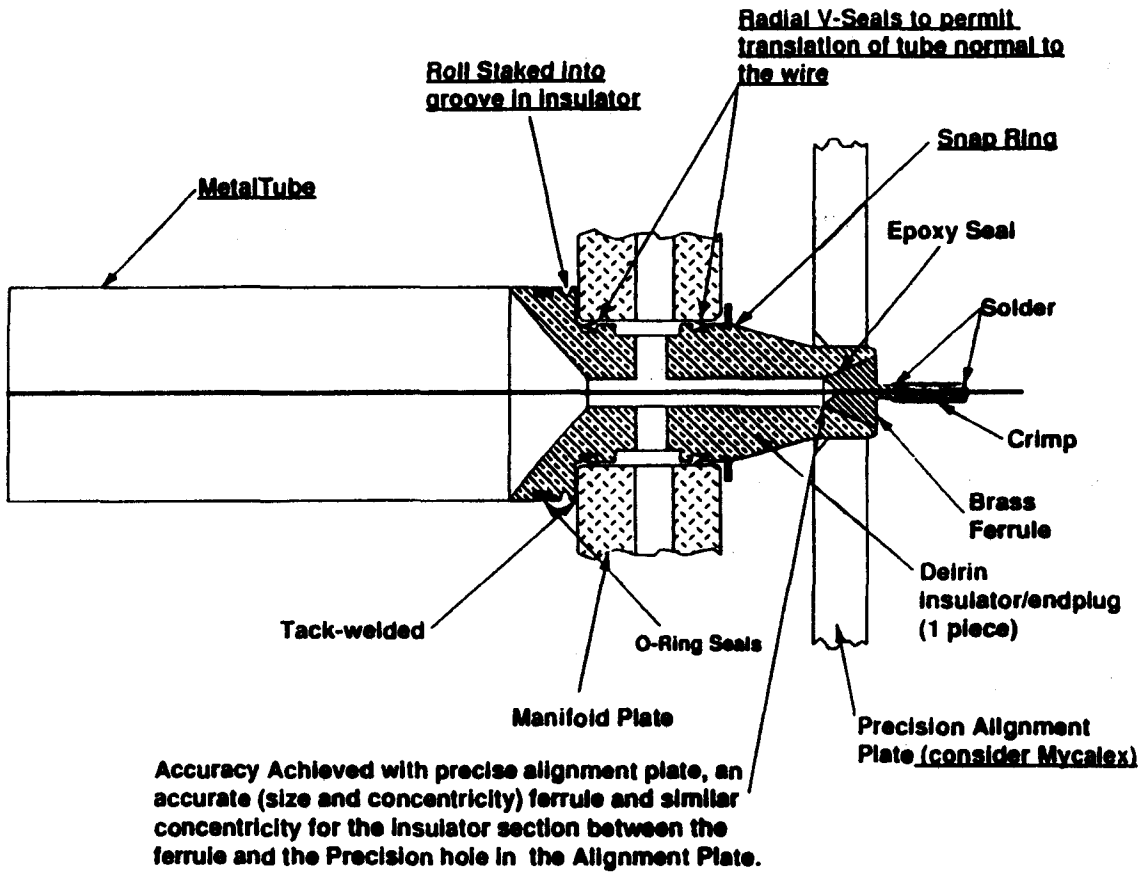
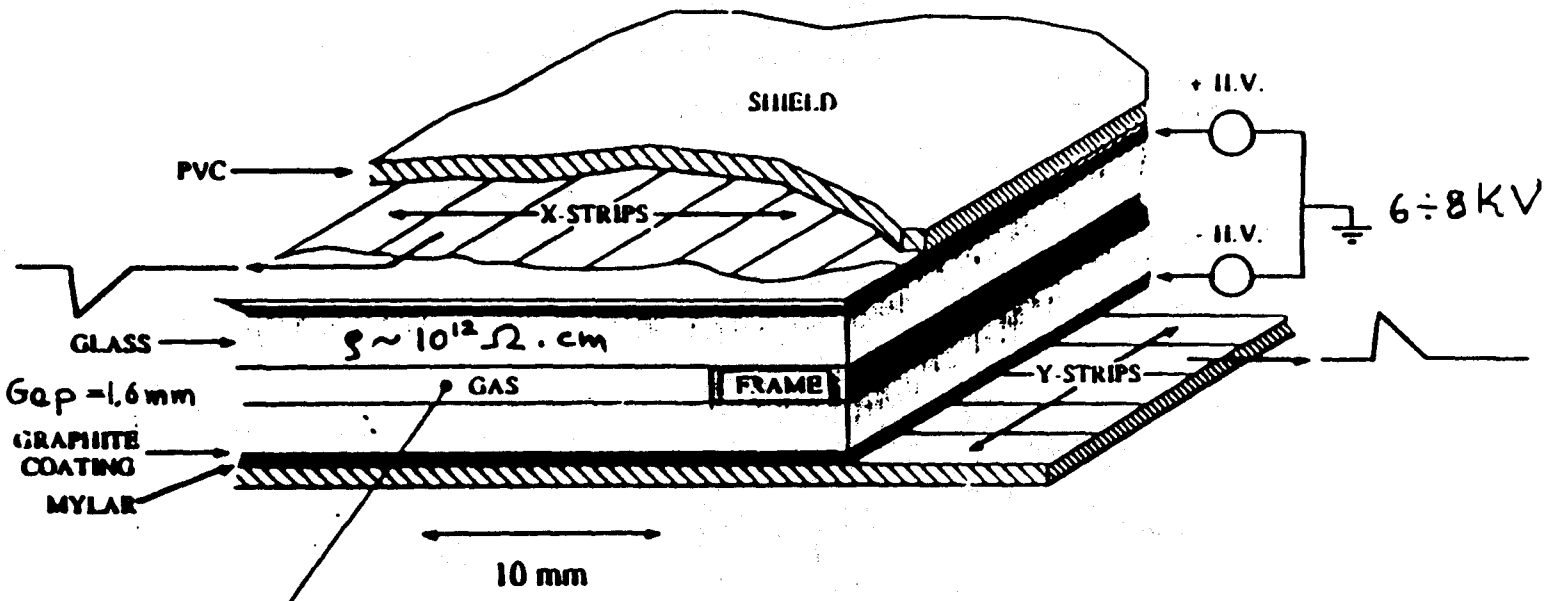


Figure 9 Pressurized Drift Tube End Plug Assembly. (GEM)

Resistive Plate Chambers



Ar/Iso/Freon = 60/38/2

* R&D project for a new version of large gap parallel plate counters (GLASS)

Figure 10 Restive Plate Chambers. (GEM)

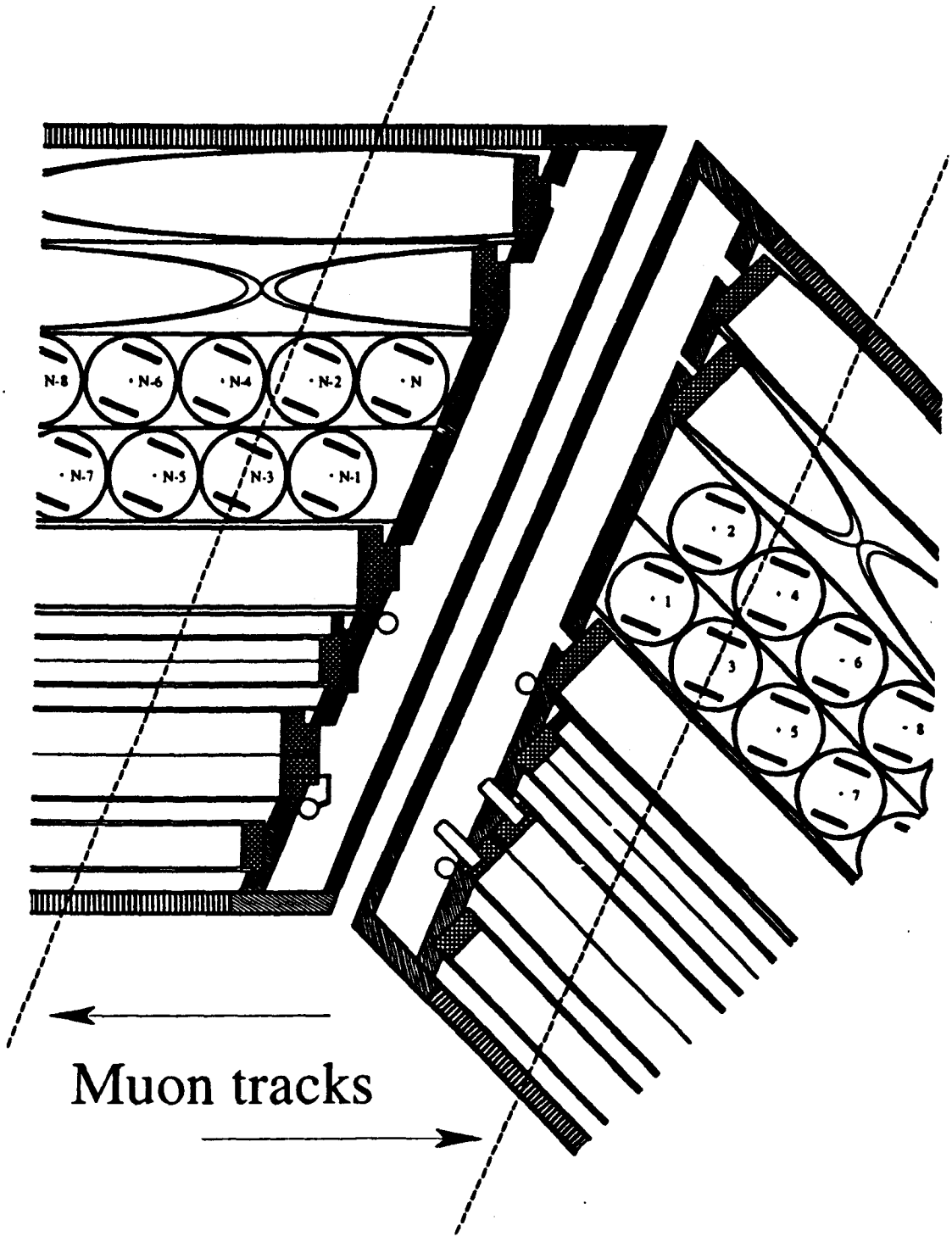


Figure 11 SSCL/Washington design for a stack of round cells made from aluminum extrusions and containing field shaping electrodes. The wire position is maintained by capture of the tube endcap in a precision milled endplate. (SDC)

SSCL R&D in Computing

K. McFarlane

SSCL R & D in Computing

K. McFarlane

Corpus Christi

Oct. 16, 1991

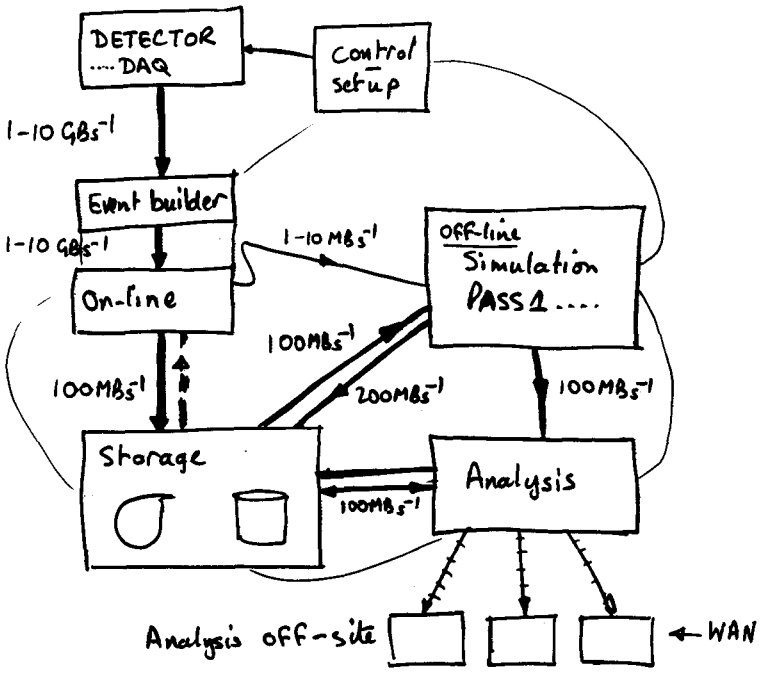
Areas in which Research or Development is needed:

- Total Computing Power
  - ✓ • off-line (Simulation, 'PASS1')
  - ✓ • on-line (Event building, Level 3)
- Networking
- Storage (Capacity, speed)
- ✓ • Data Access (
- Software

Some will happen in any case, some areas will need HEP effort. ✓ = SSCL involvement (FY91)

Schematic of data flows

(2a)



(2b)

HEP dependent on development for other areas:

CPU: Business
Engineering CAD/CAM ..
Defense / Aerospace
Telecommunications

Recording: TV

Future: HDTV, speech recognition
document storage ....

Computing Power Needs

- Simulation in 1992: ≈ 4,000 SSCUPs
  (from present 1,000 SSCUP "ranch")

- On-line (level 3) in 1992:
  - 1-10 kHz of 1MB events, 20-50 SSCUP-sec/evt to reduce to 100 Hz
    → 20,000 - 500,000 SSCUPs

  (Interaction with storage, PASS1)

- Off-line (PASS1...) in 1992:
  - Keep up with 100 Hz of 1MB events.
    CDF: 2,100 VUP-sec/MB
    → ~200,000 SSCUPs
  - Add second PASS1 (updated calibration...)
  - Add simulation in equal amount
    → ≈ 600,000 SSCUPs total

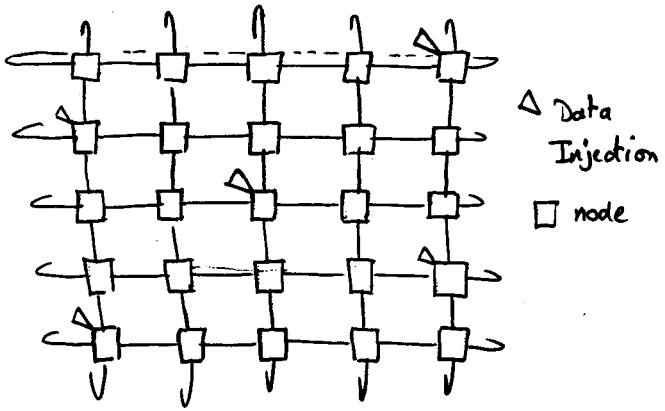
These are large numbers. How to achieve?

- Take advantage of fortunate development:
  - Event processing is separable: every event is independent - no correlations.
  - VLSI processors are both "cheap" and capable of processing an event (complete).
- So, distribute events across many processors.
- Use commercial solutions to reduce cost
  - Complete boxes with network → 'ranch'
  - Single Board Computers in crates (FNAL ACP..)
  - 'Parallel' machine designed for more truly parallel problems, e.g. Intel Touchstone, Connection machine....
    (may also solve event building problem)

Penn-Princeton-SSCL-Intel Parallel Computing Project ⑤

(K. Anupindi, L. Gladney, P. Keener, N. Lockyer, M. Rezaei, J. Heinrich, K.T. McDonald, L.A. Roberts, J. Rattner.) – BCD

Use MESH (prototype on Hypercube)



1992: ~2,000 Nodes, Internode 200 MBs^{-1}

1991: i860 node ≈ 10-15 SSCUPs.
(60 DP MFlops, 33 MIPS)

⑥

1991 Progress

- Ported CERNLIB, BCD GEANT to Hypercube
  - Benchmarked i860 node:

	GEXAM1 sec/event	BCD GEANT sec/event	BCD ISAJET Sec/event
Intel i860	12.33	204.	0.098
Sun Sparc2	11.40	175.	0.069
IBM es/6000 320	11.72	237.	0.059
SGI 4D/35	6.1	139.	0.047
HP 9000/720	4.0	81.	—

- Long-sequence independent random number generators (fast). [$\lesssim 10^4$ random numbers for each ISAJET event]
- Simulation of message passing with Verilog
- Simulation of I/O
  - Injector Model (I/o replaces node)
  - Distributed (I/o to a node)

will add to Intel MESH simulator

- Event building
  - build complete event in a node (data decomposition)
  - have a node dedicated to a detector subsystem (Functional decomposition)
  - Have implemented a tracking-Trigger algorithm (CDF drift chamber) that runs concurrently: divide chamber into cells and assign each cell to a node.
- In '92 will take delivery of 6-node MESH with I/O (Injection)
  - Multi node GEANT
  - data injection studies
  - Event builder / Level 3 rejection studies
  - Vertex trigger (concurrent) algorithm
  - Intel simulator I/O demo.

Used CalTech 512-node Hyper-MESH + systems at Intel, SSCL

Multi-user Ranch — PDSF

SSCL Physics Detector Simulation Facility

- Provide high performance at low cost
- Use volume-production computers linked by networks.
- Open systems and standards (non-proprietary)
  - multi-vendor
  - can evolve
  - use commercial solutions

Means RISC/Unix, Xwindows, TCP/IP ...

- System integration by SSCL
  - sys. management issues
  - I/O issues (disk access ...)
  - networking issues
  - ....

PDSF follows recommendation of

SSCh Computer Planning Committee (L. Price, chm)

L. Cormell, G. Yost, B. Scipioni, M. Marquez,

P. Liebold and others.

Phase I – In operation ≃ 1,000 SSCUPs

Phase II – Jan 1992 ≈ 2,000 SSCUPs

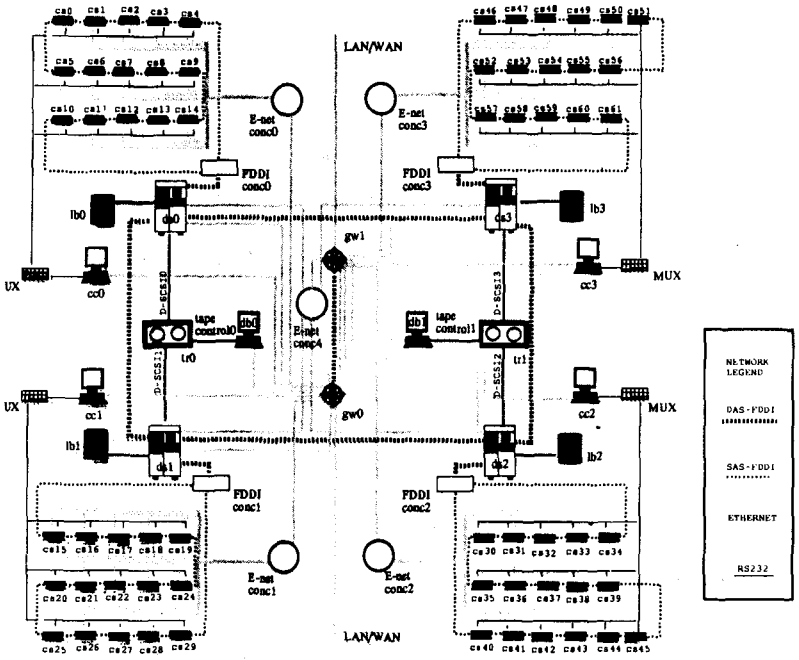
Phase III – mid 1992 ≈ 4,000 SSCUPs

Available to outside users, near-100% availability.

SDC, GEM, accelerator simulations, CDF analysis

Unlike many "single-user" farms, this is a multi-user ranch where a user may vary CPU power applied to his/her problem from 1 to 30 (or more!) CPUs.

PLANNED PDSF WITHOUT OPTION







SSC Laboratory Physics Research Division

PHYSICS and DETECTOR SIMULATION FACILITY

FUNCTIONAL MODEL:

- **Interactive Front-End:** Personal workstation, remote access, editing, debugging, test jobs, data-less configuration, scratch disk
- **File Server:** Centralized data storage, user's codes, libraries, permanent storage
- **Batch Ranch:** Symmetric multi-processors, batch mode, event level parallelism, stage output disks
- **Tape Storage:** Robo-tape, near-line storage of events data

SYSTEM ELEMENTS (cont.):

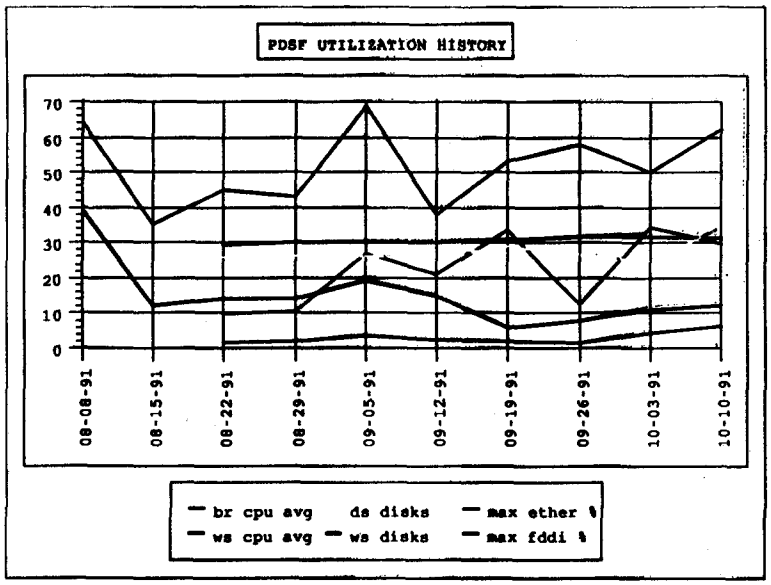
- Data Management System (DMS): FORTRAN interface to Robo-Tape staging and storage, DBMS for user data sets/volumes
- WASH: Workstation Assignment System
- CONCH: Console Concentrator System
- SYSPOLL: System Monitoring Programs
  SYSMAP: Operator Interface to SYSPOLL

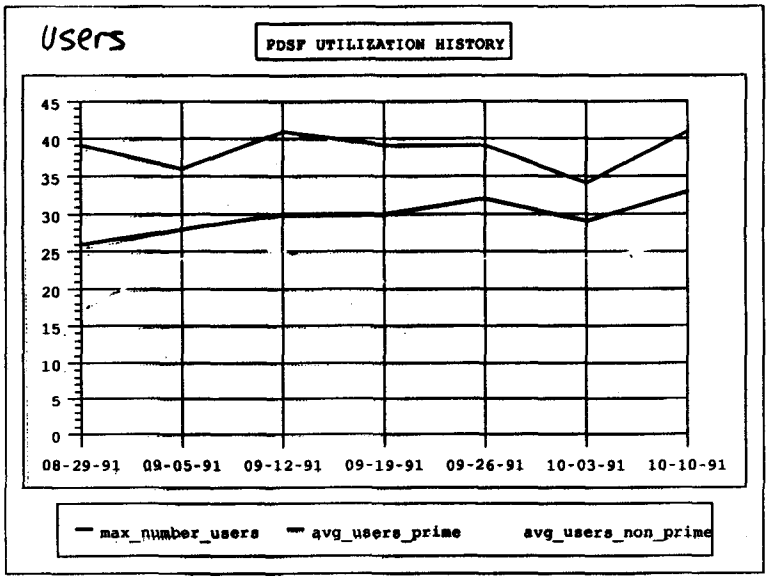
PHYSICS and DETECTOR SIMULATION FACILITY

SYSTEM ELEMENTS:

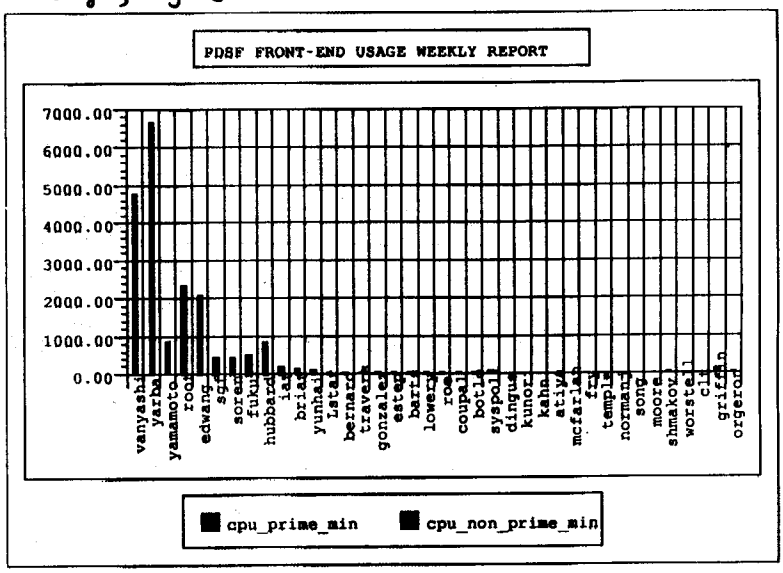
- NFS File Mounting
- Network Information System (NIS) - i.e Yellow Pages
- Network Queuing System (NQS): Batch Submission and Control
- Cooperative Process Software (CPS)
- Net Central - Network monitor layered on Sybase
- CERN Library: PAW, GEANT, etc.

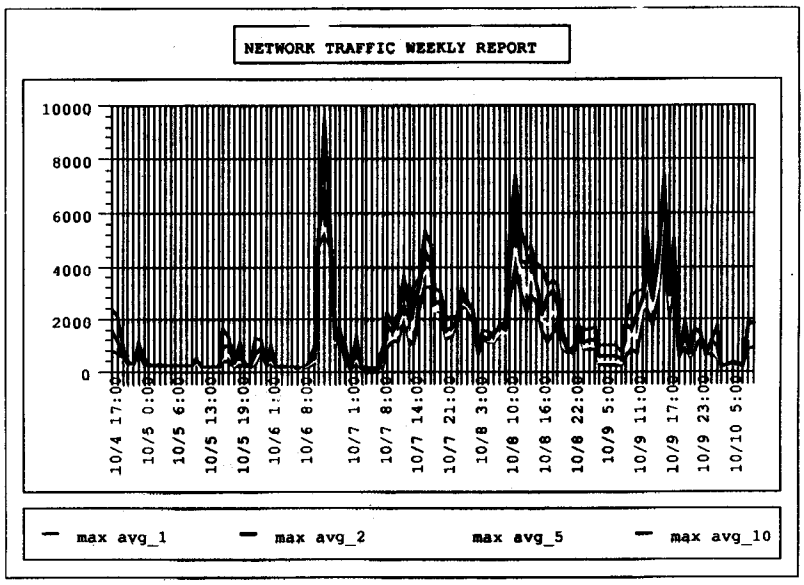
CPU and network Use





Usage, by user





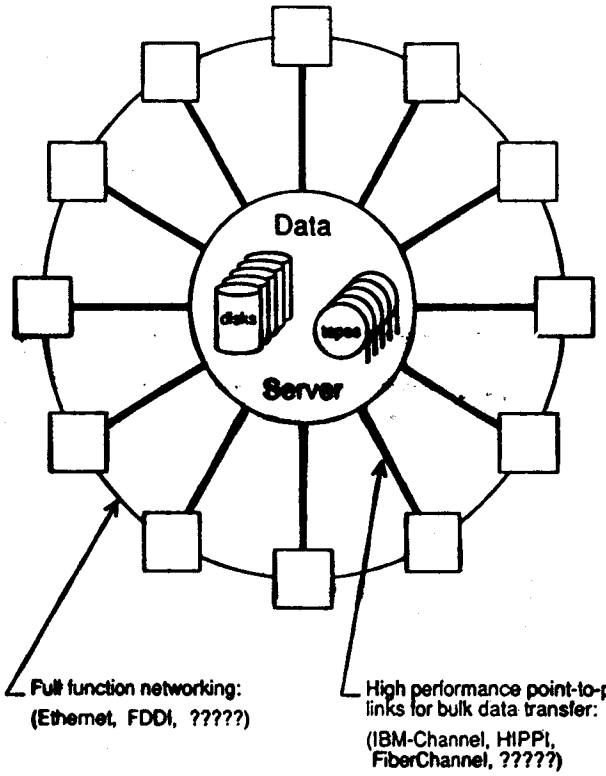
Ethernet
max

1-minute average
2- " "
5- " "
10- " "

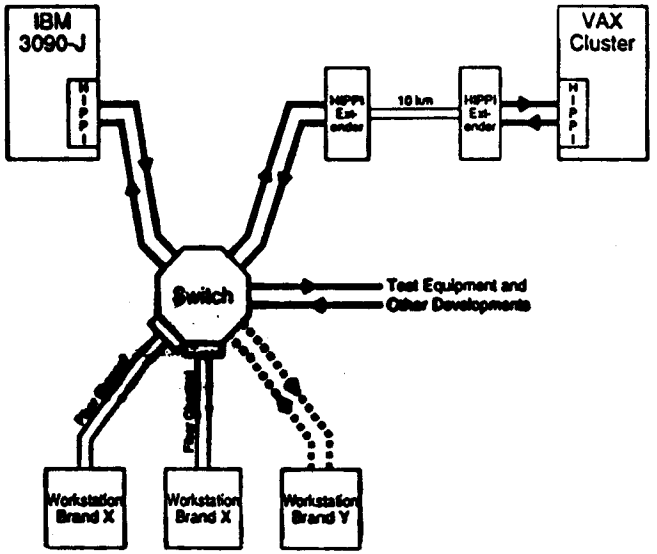
L3 A Model for HEP Computing

L3

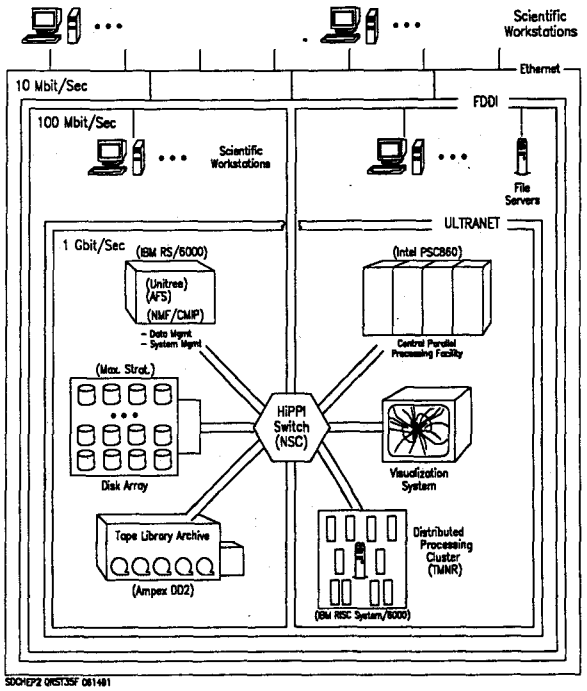
Workstations/CPU Servers and Data Server



R. P. Mount, January 1991



HEP LAB Stage 2



SHIFT

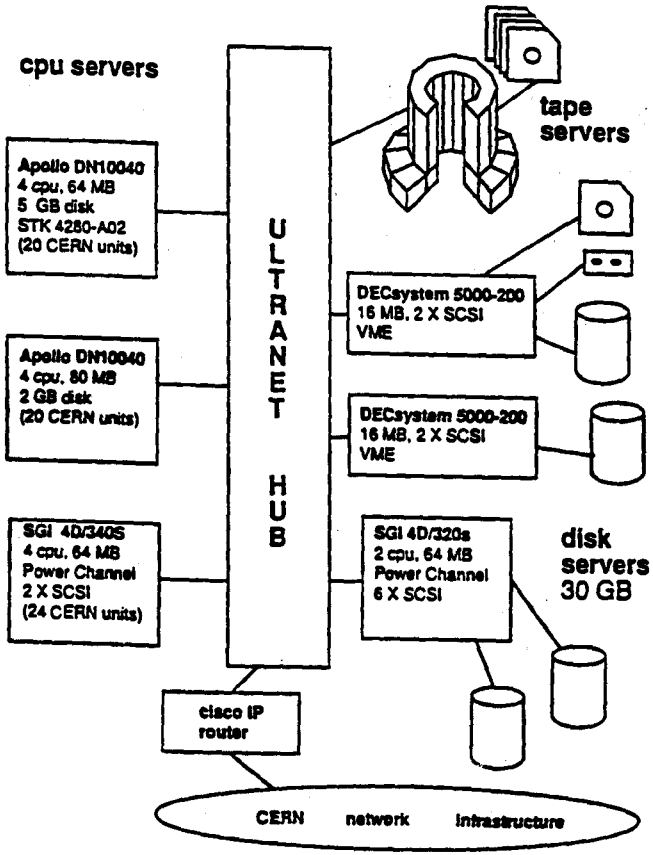
The Scalable Heterogeneous Integrated Facility for HEP Computing

Jean-Philippe Baud Julian Bunn Fabrizio Cane David Foster
Frédéric Hemmer Erik Jagel Gordon Lee Les Robertson Ben Segal
Antoine Trannoy Igor Zacharov

CERN - European Laboratory for Particle Physics
1211 Genève 23, Switzerland
2 March 1991

Abstract

***shift*, the Scalable Heterogeneous Integrated computing FaciliTy, aims to demonstrate that commercially available workstations and associated disk and tape storage products can cheaply and reliably be networked together to provide an integrated computing service, comparable in quality and availability with traditional mainframe services, but suitable for installation in user-operated environments, and smoothly scalable to provide very large computing facilities.**



Conclusions

- System is workable, available (100% in recent weeks).
- Network is close to saturation (Ethernet ≈ 200 kBs^{-1}, FDDI ≈ 2 MBs^{-1})
- Storage needs improvement (speed)

Future (92)

- SGI SMP → File server
- 30 more single-CPU boxes
- FDDI to every box
- Study Ampex DD2 tape (15 MBs^{-1})

(22)

"There is no SSCL computing R&D budget"

Nevertheless there are some projects:

- SDC/SSCL / DOE HPCC – data storage and access
  - Evaluation of relational and object-oriented data bases
  - HEP-specific query language
  - Prototyping of hardware and software (disk arrays, striping)
- SDC/IBM (Houston) – hardware architecture + data flow
  - HPPI switched network
  - Disk arrays
  - DD2 tape system ....
- SDC – study of software development methods

In other places:

- L3/IBM and L3/HP effort on data access and analysis (HPPI, mainframe server)
- CERN 'SHIFT' project

(24)

CONCLUSIONS

- Given budget constraints, HEP will use hardware produced primarily for other markets, assembling systems from components.
- HEP will likely not influence evolution of basic components (CPU's, memory, disks....)

- However, there will be areas where work will be necessary and fruitful and may influence or create commercial products; for example
  - System integration methods and tools
  - High performance I/O (MESH, HPPI ...)
  - Database (software and hardware)
- There will also be a need to import industry approaches to HEP; e.g.
  - Software methodologies
- Lastly, written HEP new tools will be needed to speed up analysis, eg. graphic interfaces

There is much to be done, and much will be done at other places, but SSCL expects to play an increasing role.

Fermilab Collider Program

J. Huth

Electroweak Measurements

Marciano + Sirlin Convention:

$$\sin^2\theta_w = \frac{A}{M_W^2(1-\Delta r)}$$

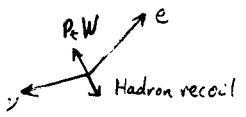
$$A^{\frac{1}{2}} = \left(\frac{\pi\alpha_{em}}{\sqrt{2}G_\mu}\right)^{\frac{1}{2}} = 37.2805 \pm 0.0003 \text{ GeV}/c^2$$

$$\sin^2\theta_w = 1 - \frac{M_W^2}{M_Z^2}$$

$\Delta r \rightsquigarrow$ function of M_{top}, M_{Higgs}

M_W

$W \rightarrow e\nu, \mu\nu$



ν unobserved, unknown longitudinal motion

Impose momentum conservation in transverse

$P_{t\nu}$ from missing E_t (electron + hadronic)

Transverse Mass:

$$M_t^2 = 2 P_{te} P_{t\nu} (1 - \cos(\phi_{e\nu}))$$

UA2

Final M_W, use $e\nu$ mode (2065 evts)

Measure $\frac{M_W}{M_Z} = 0.8813 \pm 0.0036 \text{ (stat)} \pm 0.0019 \text{ (syst)}$

Use LEP M_Z (91.175 GeV/c^2)

$$M_W^{UA2} = 80.35 \pm 0.33 \text{ (stat)} \pm 0.17 \text{ (syst) GeV}/c^2$$

Without LEP M_Z, Syst ~ 0.8 GeV/c^2

CDF

(1130 e)
(592 μ)

In Situ Calibration $\Rightarrow$ 0.1% syst μ, 0.2% e's
(check using J/ψ peak)

Uncertainties Stat: 350 MeV (e) 530 MeV (μ)

Syst		
~150 MeV	W pt resolution	e
~170 "	balancing	e
~ 50	background	e
	PDF's	

Combined $e + \mu$ data set:

$$79.91 \pm 0.39 \text{ GeV}/c^2$$

CDF + UA2 Average:

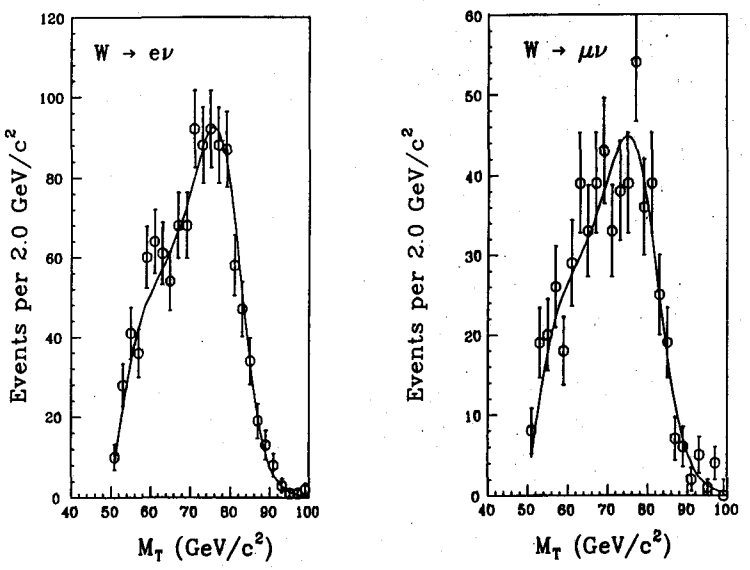
M_W 80.14 ± 0.27

Use LEP M_Z:

$\sin^2\theta_w = 0.2274 \pm 0.0052$

CDF $e\nu, \mu\nu$

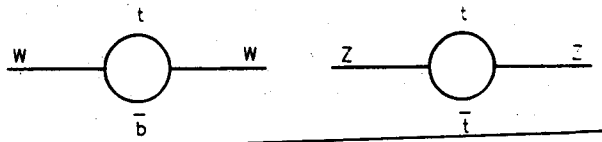
W Transverse Mass Distributions



Constraints on M_{top} (assume S.M.)

$$\Delta r = \Delta\alpha_{em} - f(\alpha_{em}, \theta_W) * \left(\frac{M_{top}}{M_Z}\right)^2 + C(\ln M_H, \ln(m_e))$$

$\Delta\alpha_{em} \rightsquigarrow \alpha(m_u) \rightarrow \alpha(m_W)$



$M_{top} = 130 \pm 40$ GeV/c², $M_{top} < 210$ GeV/c² 95% CL.

$M_{Higg} = 100$ GeV/c², add'l unc. $^{+30}_{-10}$, $M_H - 25 \rightarrow 1000$

L. Nodulman

What is the Ulimate precision of M_W?

~100 pb^{-1} from Tevatron Collider by ~1994

~25 k W's / mode

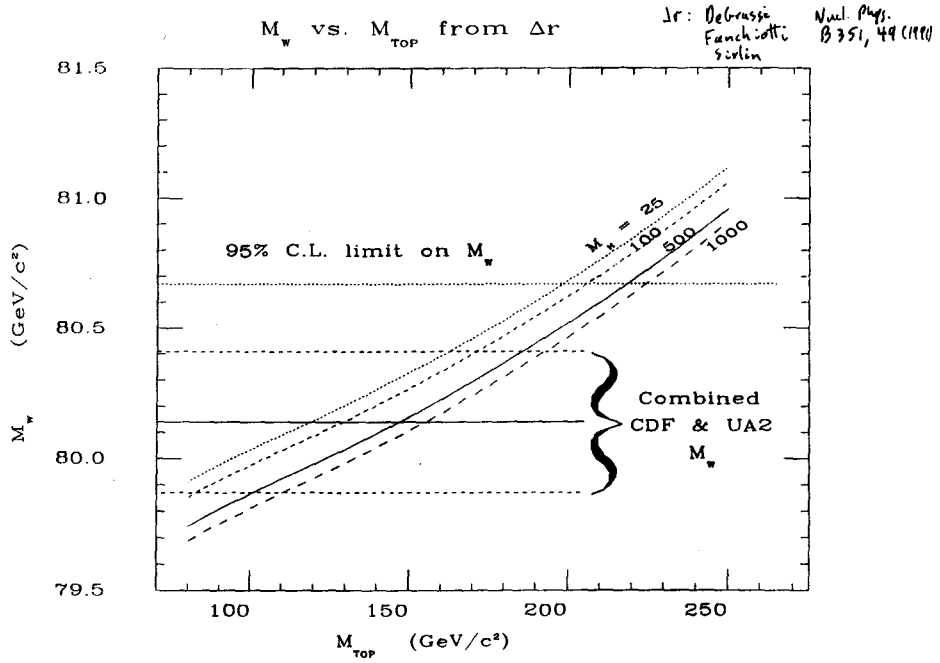
Stat error ~ 70 MeV

Can gain on syst. uncertainties, Z calib sample

est. ~ 100 MeV total uncertainty

with 1000 pb^{-1}?

50 MeV? (Parton Dist. Functions must improve)



Δr: DeGrassi, Fanchiotti, Sirlin — Nucl. Phys. B 351, 49 (1991)

$\Gamma(W)$

Cabibbo Hatzen Mursula

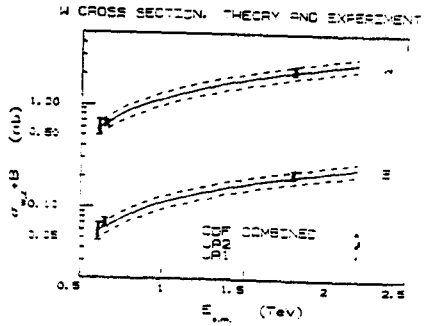
$$R \equiv \frac{\sigma(\bar{p}p \to W) \times Br(W \to \ell\nu)}{\sigma(\bar{p}p \to Z) \times Br(Z \to \ell\ell)}$$

$$\Gamma_W = \frac{1}{R} \frac{\sigma(W)}{\sigma(Z)} \Gamma(Z) \frac{\Gamma(W \to \ell\nu)}{\Gamma(Z \to \ell\ell)}$$

Exp. — Theory (small unc) — LEP — Standard Model

$$\frac{\Gamma(W \to \ell\nu)}{\Gamma(Z \to \ell\ell)} = \frac{M_W^3}{M_Z^3} \frac{2}{1 - 4\sin^2\theta_W + 8\sin^4\theta_W}$$

R:			
	UA1	9.5 ± 1.05	
	UA2	10.4 ± 0.72	Lepton · Photon · Final
	CDF	9.98 ± 0.74	all samples combined



Detail To Find World Average Γ_W

Each experiment uses different values

$\frac{\sigma(W)}{\sigma(Z)}$, Γ_Z, M_W, M_Z

Choose a consistent set

Input $\begin{cases} \frac{\sigma(W)}{\sigma(Z)} = 3.16 \pm 0.05 \quad 0.63\ TeV,\ 3.23 \pm 0.05 \quad 1.8\ TeV \\ \qquad\qquad\qquad\

CDF (T. Liss)

⇒ Combine ee, μμ, eμ

Require $P_{t\ell} > 15$ GeV/c, $20° < \Delta\phi_{ee} < 160°$

Cut out $75 < M_{\ell\ell} < 105$ GeV/c²

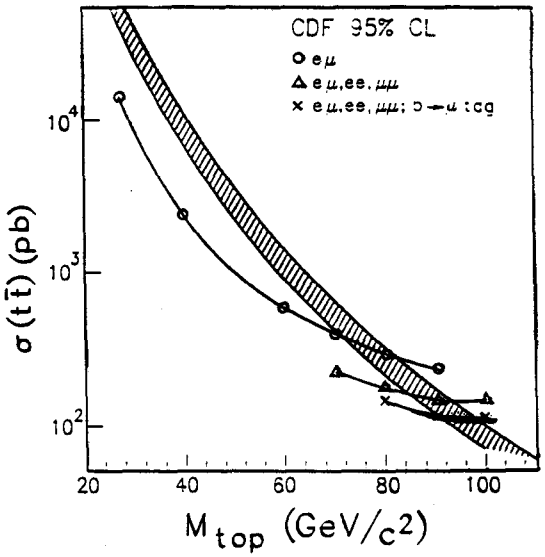
eμ → Observe 1 event, est. 1.5 evt. background

Lepton + Jets

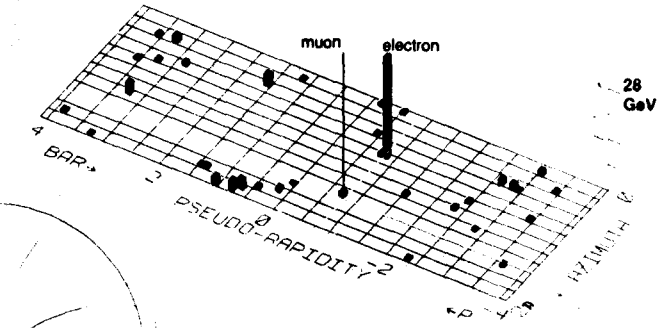
e or μ, $P_t > 20$ GeV/c, Missing $E_t > 20$ GeV

≥ 2 jets, $E_t > 10$ GeV, look for soft muon in jet

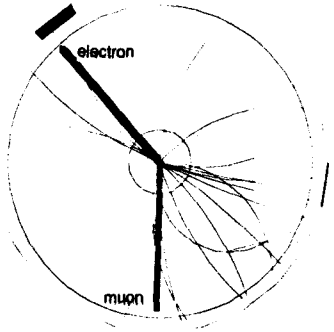
$M_{top} > 91$ GeV/c² 95% C.L.



CDF: t tbar --> e μ + X candidate event from the 1988-89 Collider Run



Calorimeter lego plot



Central Tracking Chamber View

Prospects

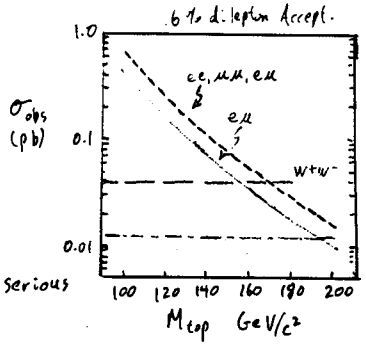
Minimal Discovery

≡ 4 dilepton events

By 1994 est ~ 100 pb^{-1}

⇒ 170 GeV/c^2

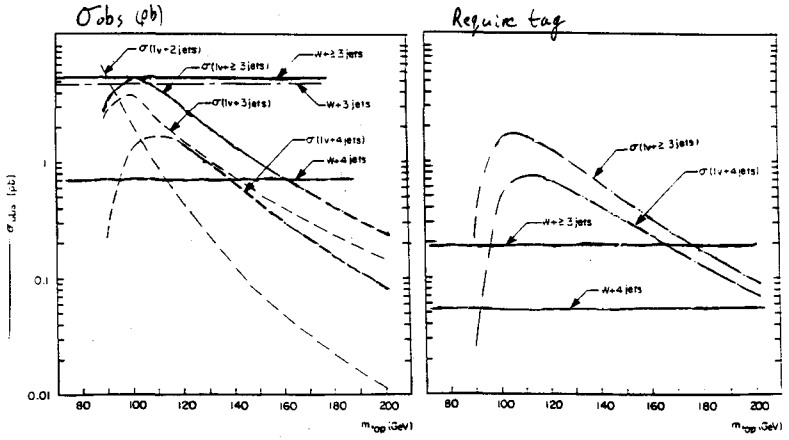
W Pair background becomes serious



In ℓ+jets (Berends et al.)

Requirement of b tag significantly reduces high p_t W bgd.

$\varepsilon_{ff} \approx 50\%$ single, 25% double



Prove It's Top!! What's M_{top}?

$t \to Wb \to j_1 j_2 j_3$

Need jets? M_W M_{top}

dileptons → est ± 20 GeV/c² from rate

From jets,

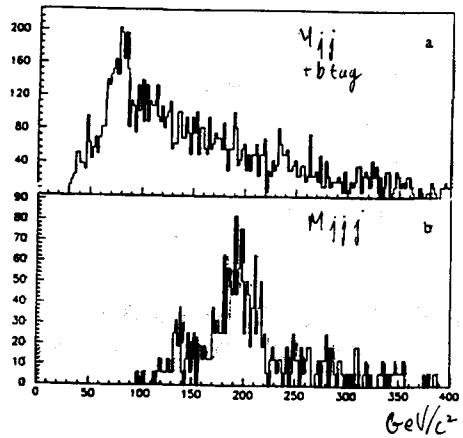
$W \to q\bar{q}$

Estimate ~ ± 8 GeV/c² syst. limit from Escale

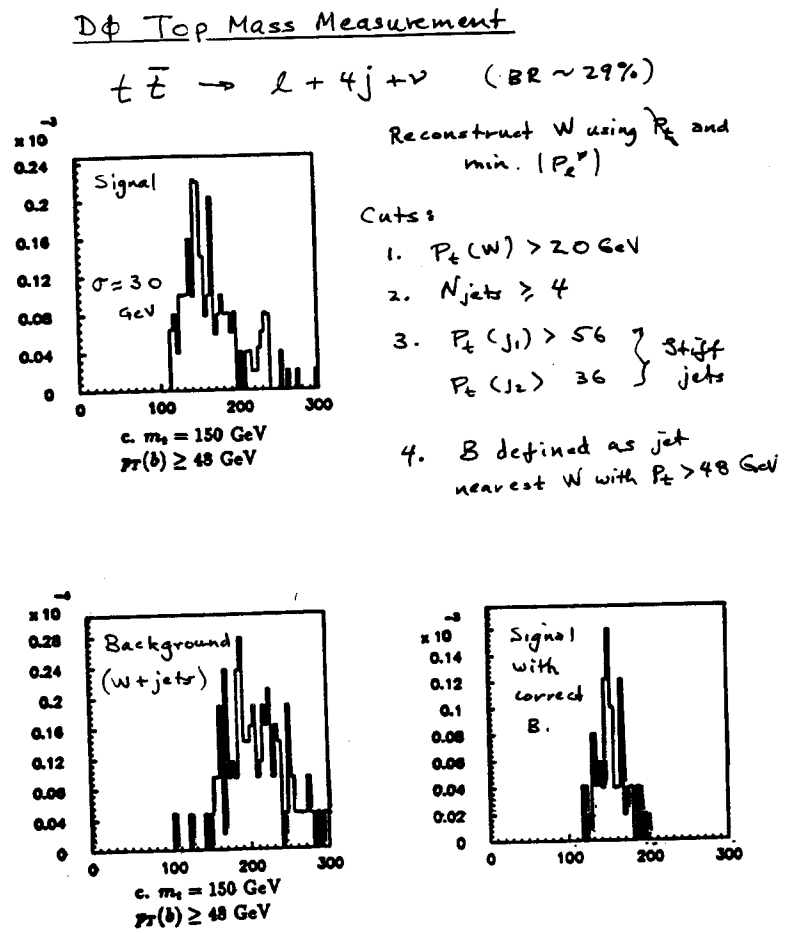
When?

Need ~ 300 ℓ+ν+4 jet events

250 pb^{-1} for M_{top} = 130 GeV/c²



M_{top} = 200



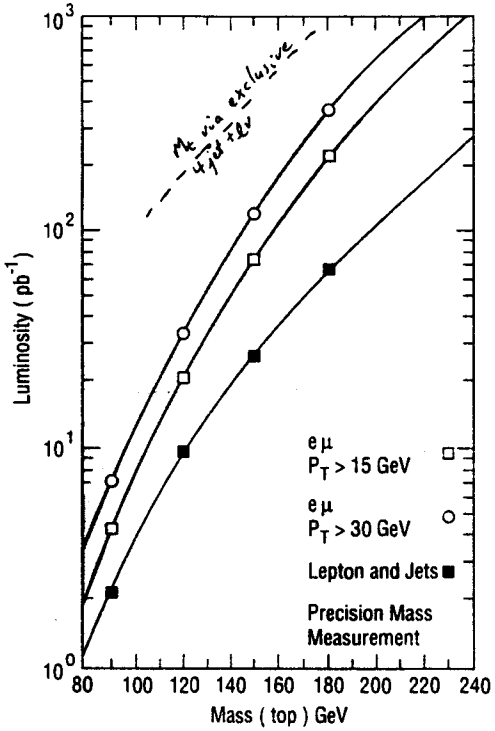
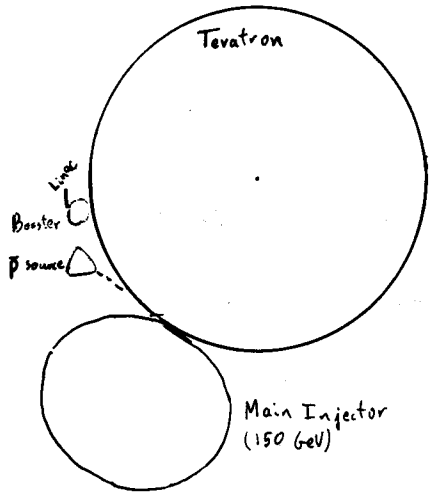


Figure 5: Required luminosity to discover top at 1.8 TeV for various decay modes vs. m_t. (Based on expected performance of D0 detector and upgraded CDF detector)

Tevatron Upgrades

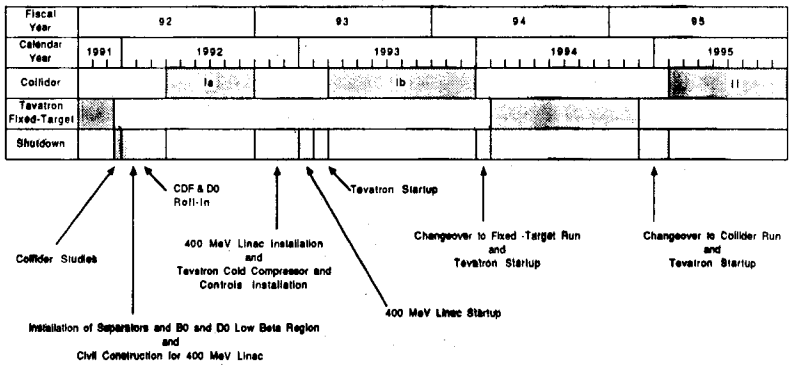
Electrostatic Separators (reduce beam-beam tuneshift)
Low β quads (β^* from 55 to 25 cm)
$\bar{p}$ source bandwidth (2-4 GHz → 4-8 GHz)
Linac Upgrades (200 → 400 MeV)
Cold Compressors (1.8 → 2.0 TeV)
36 bunch operation (reduce multiple interactions)
Main Injector (Increase admittance + cycle time)



October 91

Draft Long Range Schedule

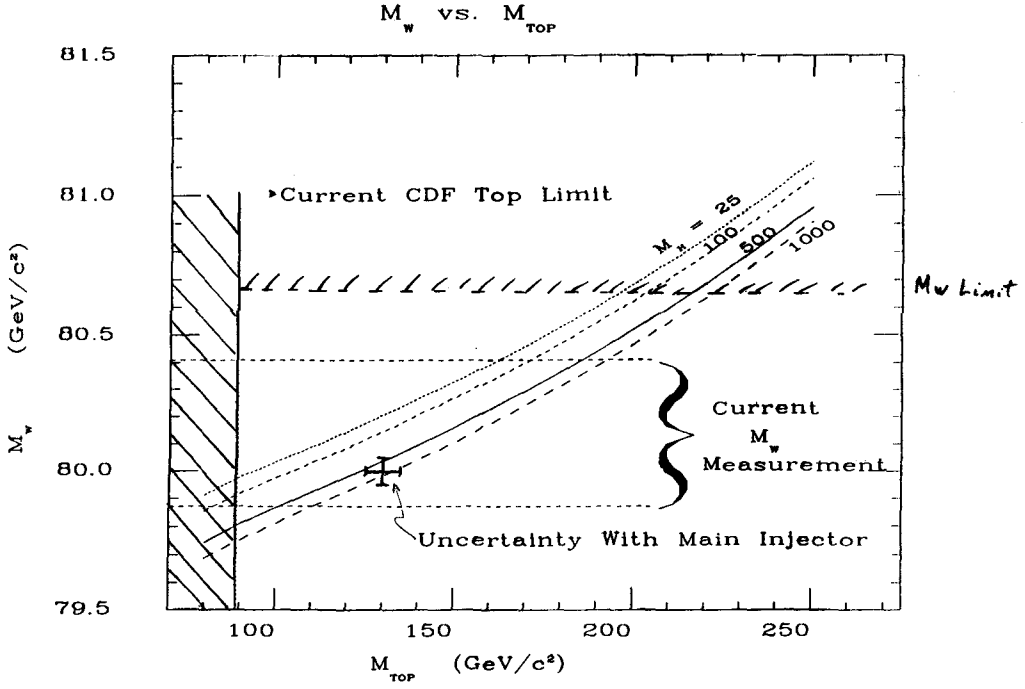
Preliminary



Evolution of Tevatron Luminosity

	1988-89	IA	IB	II	MI
$\sqrt{s}$	1.8 TeV	1.8TeV	1.8TeV →	2.0 TeV	2.0 TeV
p's/bunch$\times N_b$	$7.0\times10^{10}\times6$	$7.0\times10^{10}\times6$	→ $1.2\times10^{11}\times6$	→ $1.2\times10^{11}\times36$	→ $3.3\times10^{11}\times36$
$\bar{p}$'s/bunch$\times N_b$	$2.9\times10^{10}\times6$ →	$7.2\cdot10^{10}\times6$	$7.2\times10^{10}\times6$ →	$1.2\times10^{10}\times36$ →	$3.1\times10^{10}\times36$
ε_p	25 π →	15π	15π	15π →	30 π
$\varepsilon_{\bar{p}}$	18 π	18π	18π	18π →	22 π
β^*	55cm →	50cm	50cm	50cm	50cm
$\mathcal{L}$ (typ)	1.6×10^{30} →	5.7×10^{30} →	1.1×10^{31}	1.1×10^{31} →	5.7×10^{31}
$\Delta\nu$ ($\bar{p}$)	.025 →	.007 →	.012	.012 →	.017
$\int\mathcal{L}dt$	5 pb^{-1}	25 pb^{-1}	75 pb^{-1}	100 pb^{-1} →	1000 pb^{-1}

Separators, Low β magnets, $\bar{p}$ Source — Linac Upgrade, Cold Compressors — 36 bunch — Main Injector



John Huth

Fermilab Collider Program

$\bar{p}p$

Explore Standard Model

Smallest possible error on M_W

Find (or set "serious" limit) Top

Smallest possible error on M_{top}

⇒ Increase Luminosity (+ energy)

⇒ Upgrade Detectors

(Handle Luminosity
b tagging)

In addition

QCD Studies

b physics

Search for exotics

Fixed target

KAMI

NUMI

Volume 31
No. 7
September 1991

The consistency of this information, combined with precision measurements from other experiments, provides powerful limits on the top quark, now confidently predicted to live somewhere between 120 and 160 GeV.

$\bar{p}p$	130 ± 40	GeV	} N.B. Not Independent!
e^+e^-	128 ± 30	GeV	
Global	124 ± 30	GeV	

(Langacker + Hemmdy)

True for minimal Higgs (Similar for M. Susy)

Caveats: Charged Higgs
Extra Doublets

Hard Limit $M_t < 294$ GeV ($Z \to b\bar{b}$)

Outline

I M_W, Γ_W

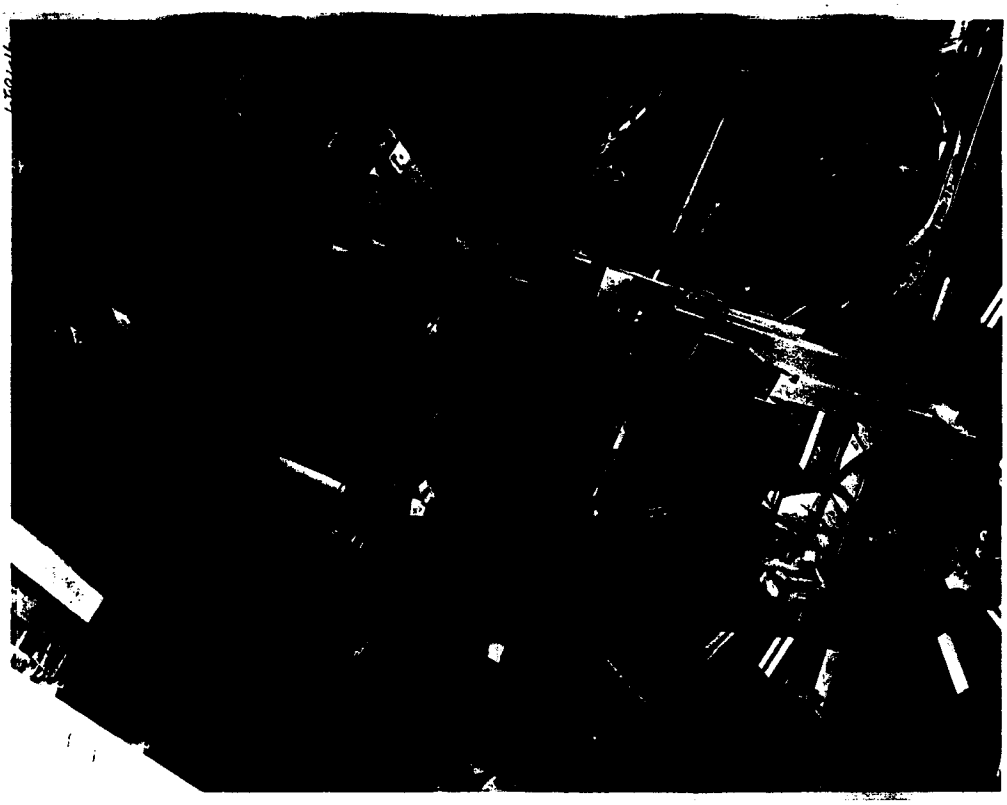
II Top limits, M_{top} (uncertainties of QCD σ)

III Tevatron Upgrades

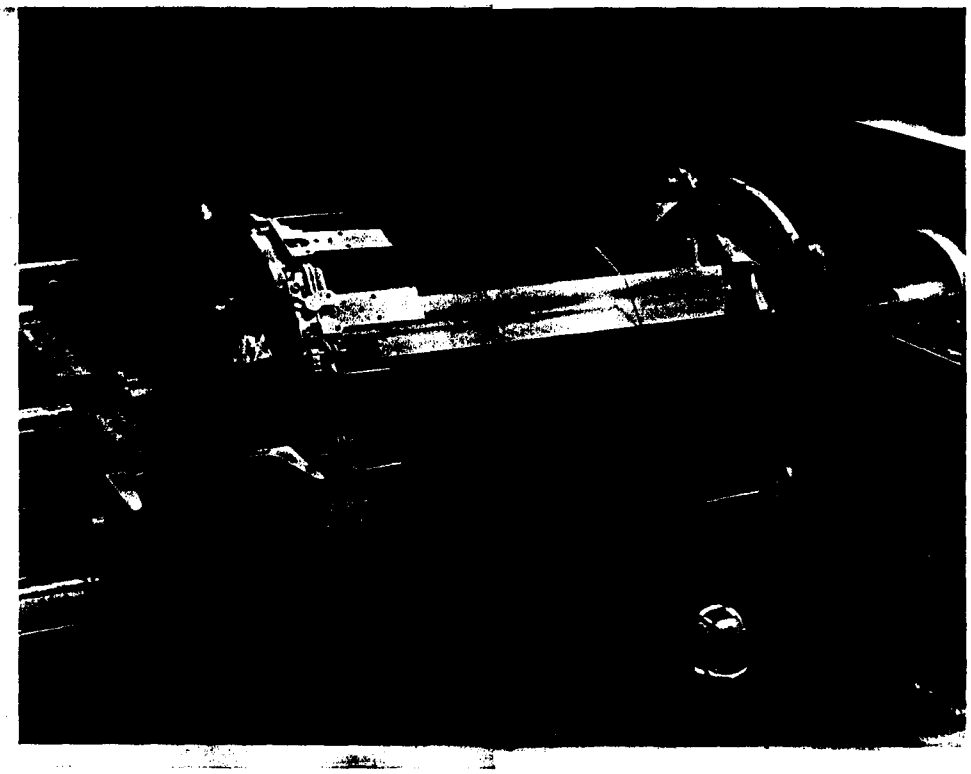
IV CDF + DØ

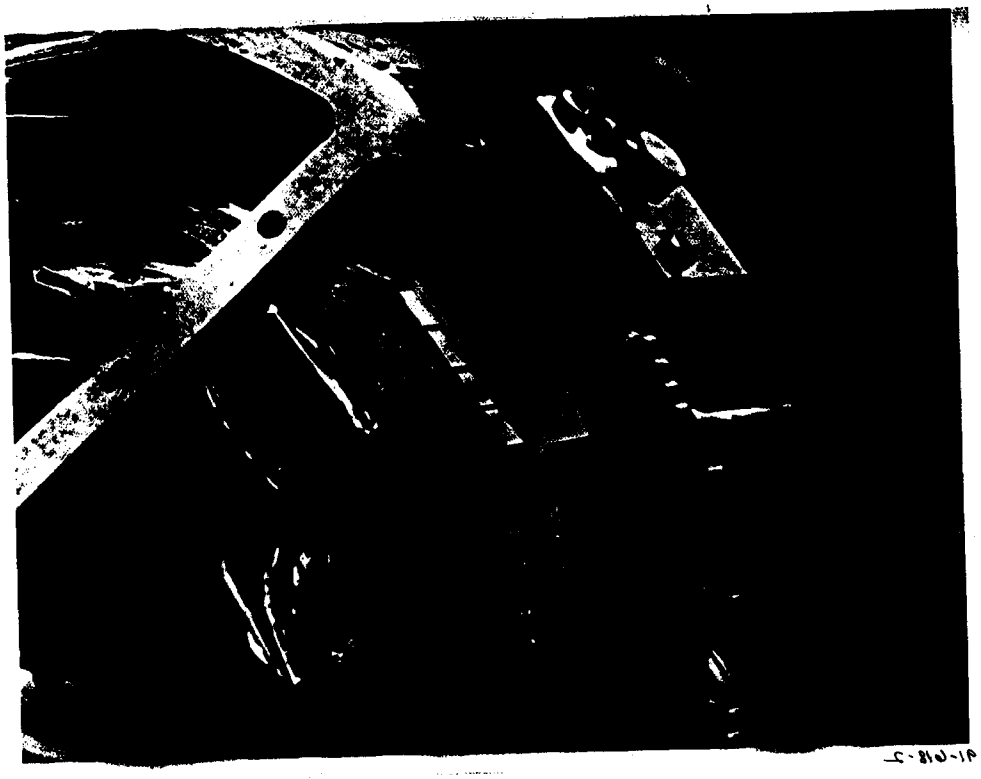
V KAMI + NUMI



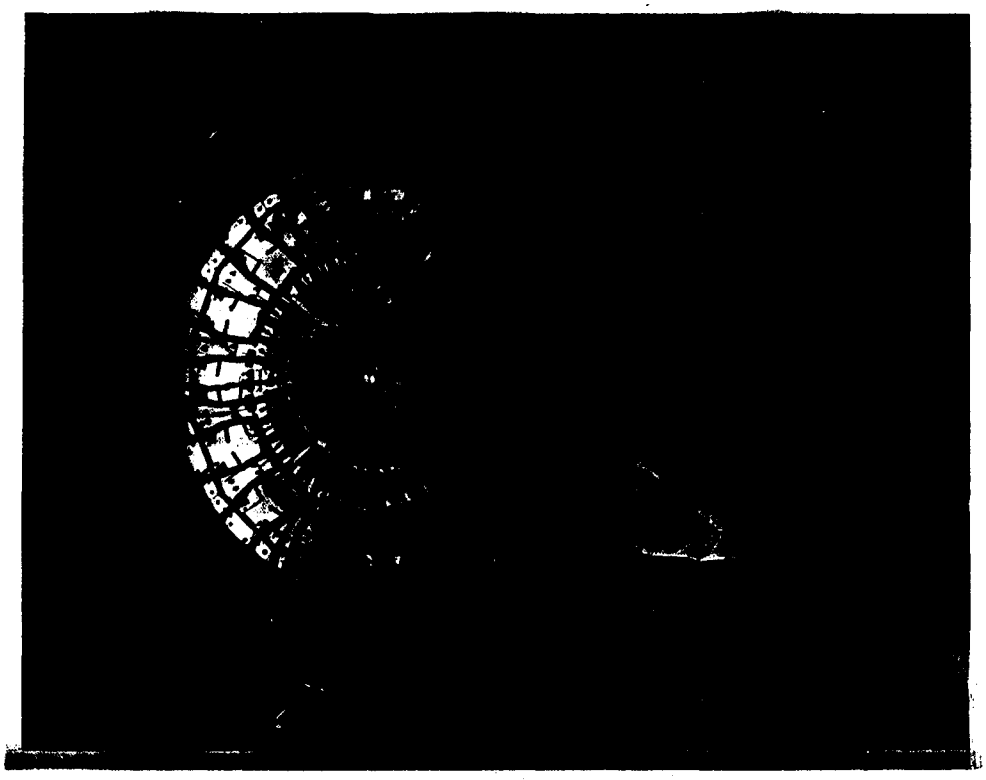


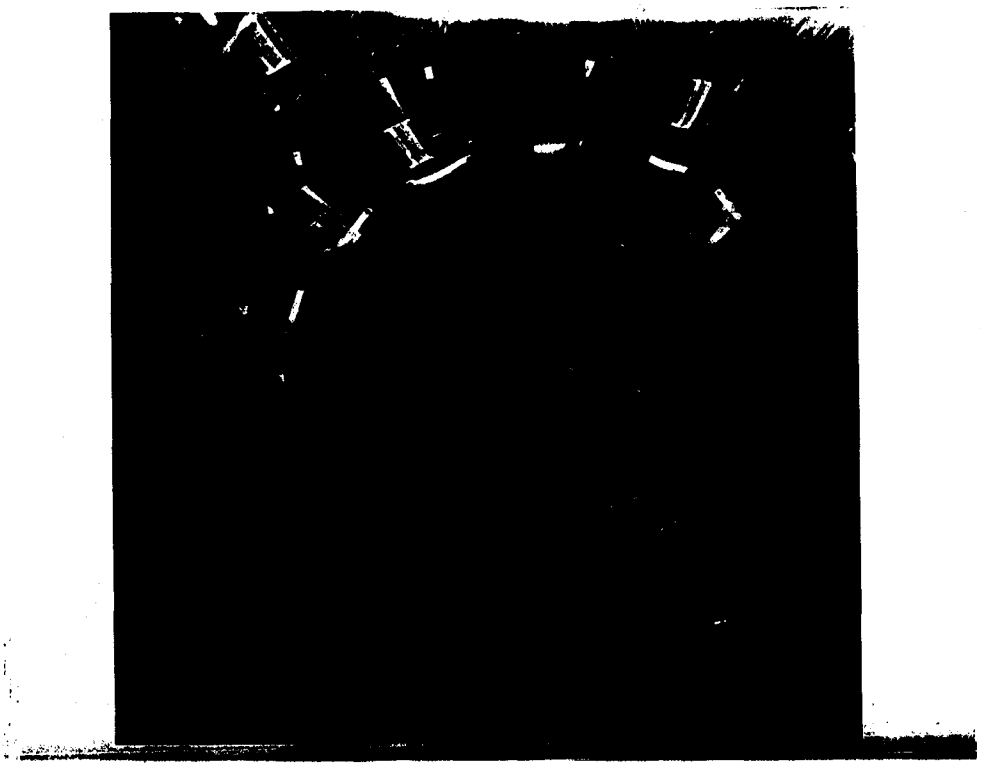




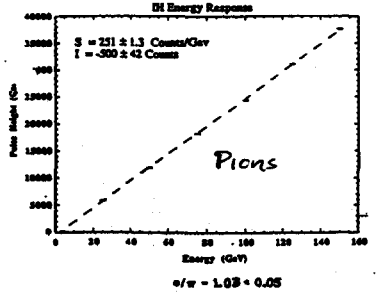


SVX LBL
1991

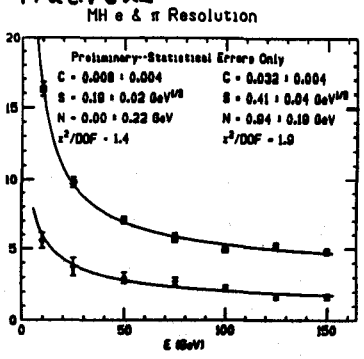




DØ Test Beam Hadrons



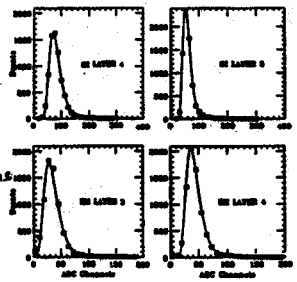
e/π = 1.03 ± 0.05



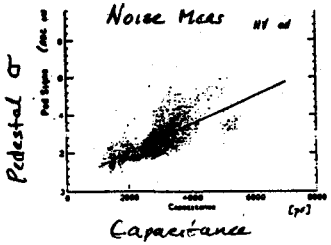
10 ≤ E ≤ 150 GeV

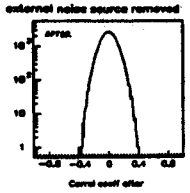
For π's $\frac{\sigma}{E} = \frac{0.41}{\sqrt{E}}$ with 3.2% constant term

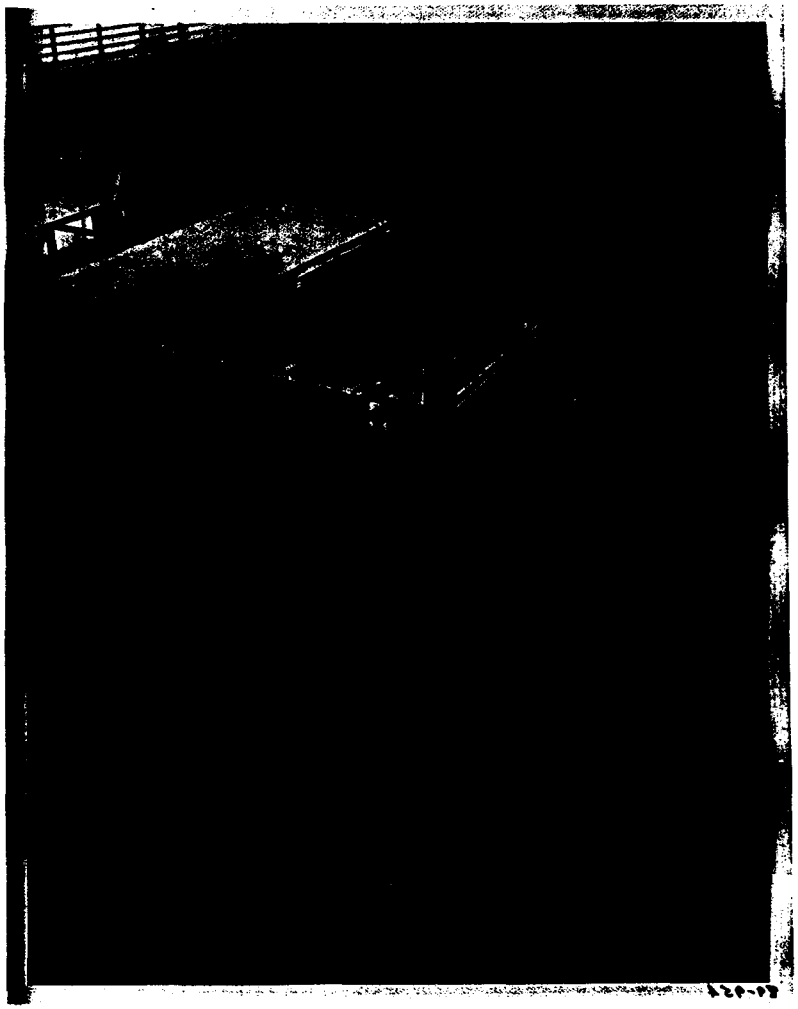
Muon peaks in the 4 long. sects of the EM calor.



Random noise per tower ≈ 50 MeV







Upgrades to Detectors

CDF + DØ: Electronics for 36 bunch operation
(up to 140 nsec)

CDF: Replace gas calorimetry with scintillator
Upgrade Silicon Vertex detector
Complete muon coverage

DØ: Add solenoid (?)
Silicon Vertex detection

Immediate Goals

Extend high p_t Physics
M_W, M_{top}, Exotics, QCD

Further
Explore b physics
B_s
B_s and B_d mixing
Time evolution
CP violation?

b Production

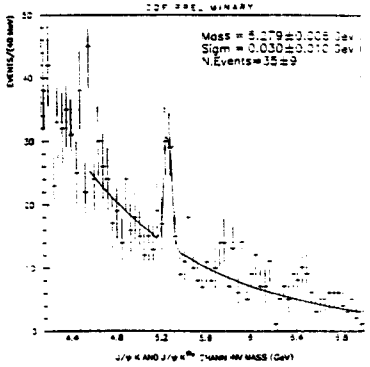
Probes low-x region - gluon fusion
"Engineering" numbers for future studies

CDF

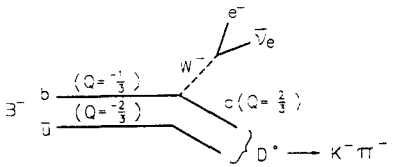
Use inclusive electrons
Subtract out W, Z contributions
Upper limit ~40 GeV (trigger ⇒ Implicit Isolation
Also, $B \to J/\psi K^{\pm}$, $J/\psi K^{*0}$
$M = 5.279 \pm 0.006$ GeV/c^2
~35 events

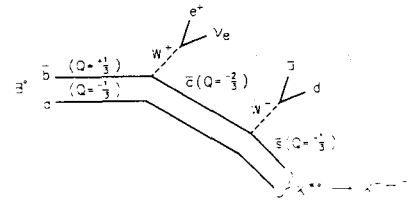
tride

for ~ 100 pb^{-1}
expect ~ 3000 $J/\psi K^{\pm}$'s
(trigger + added $\mathcal{L}$)



Inclusive electrons from b's ?





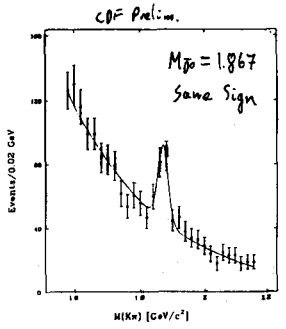
Examine charge sign correlations in

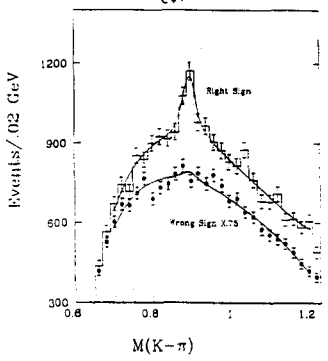
D^0, K^{*0} Production

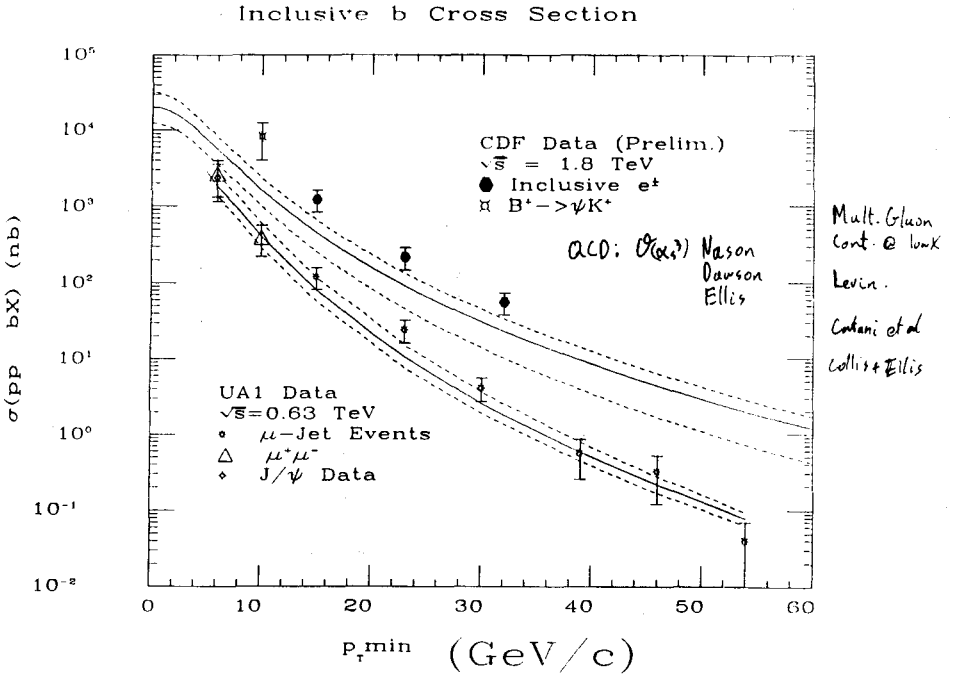
K^-e^- correlation for D^0

like wise

Ke correlation for K^{*0} from b







Mult. Gluon Cont. @ low K

Levin.

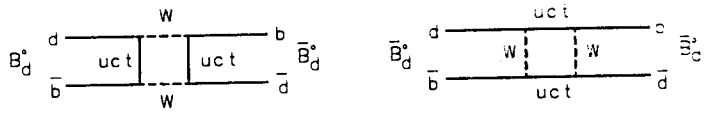
Catani et al

Collins + Ellis

$B^0 - \bar{B}^0$ Mixing

t exchange dominates ($\sim m_{top}^2$)

$|V_{td}|$ and $|V_{ts}|$, V_{ts} larger



$$\chi_{d(s)} \equiv \frac{P(B^0_{d(s)} \to \bar{B}^0_{d(s)})}{P(B^0_{d(s)} \to B^0_{d(s)}) + P(B^0_{d(s)} \to \bar{B}^0_{d(s)})}$$

Measure

$$R = \frac{N(\ell^+\ell^+) + N(\ell^-\ell^-)}{N(\ell^+\ell^-)}$$

$$\Rightarrow \bar{\chi} = \frac{P(b \to \bar{B}^0 \to B^0 \to \ell^+)}{P(b \to \ell^\pm)}$$

{ assumptions @ charm, sequential decay contribution

$$= f_d \chi_d + f_s \chi_s$$

UA1

Use $\mu\mu$ pairs

$$\boxed{\bar{\chi} = 0.158 \pm 0.059}$$

CDF

Use ee, $e\mu$ (no Υ, J/ψ background)

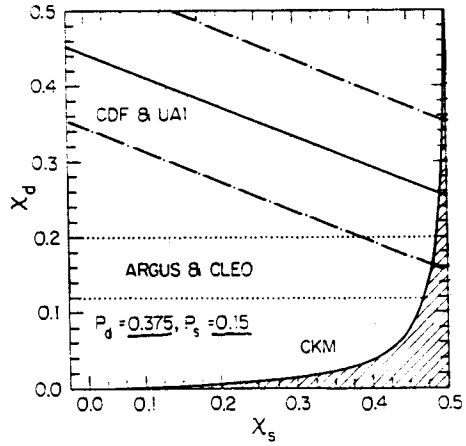
$R_{ee} = 0.573 \pm 0.116 \pm 0.047$

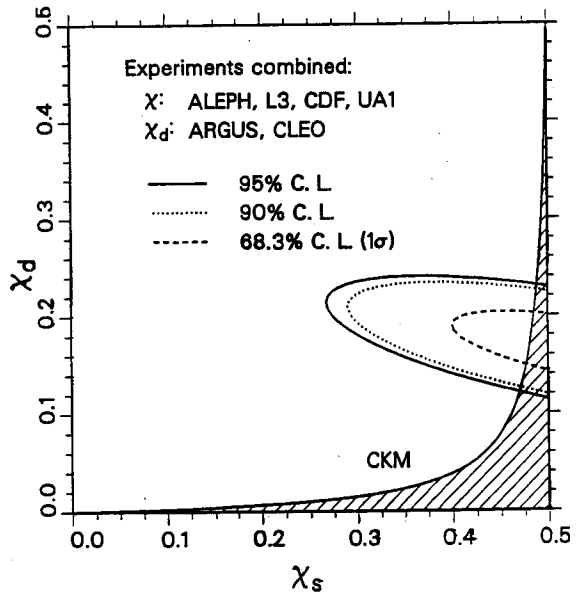
$R_{e\mu} = 0.556 \pm 0.048 \pm {}^{0.035}_{0.042}$

$$\boxed{\bar{\chi} = 0.176 \pm 0.031\ (\text{syst.} + \text{stat}) \pm 0.036\ (\text{M.C.})}$$

CDF + UA1 Average

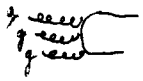
$$\boxed{0.170 \pm 0.031}$$





Where do J/ψ's Come From? @ Tevatron

Expectation: J/ψ direct production suppressed (G Parity)



J/ψ Glover et. al.

2 sources: B, χ decays

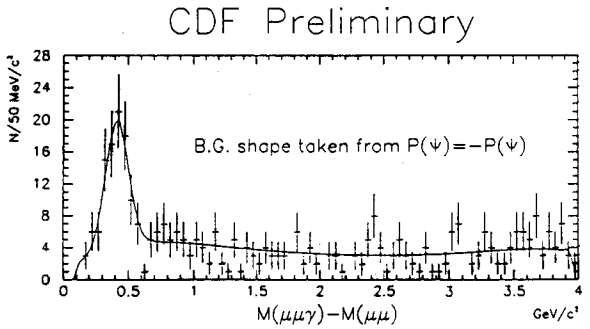
CDF

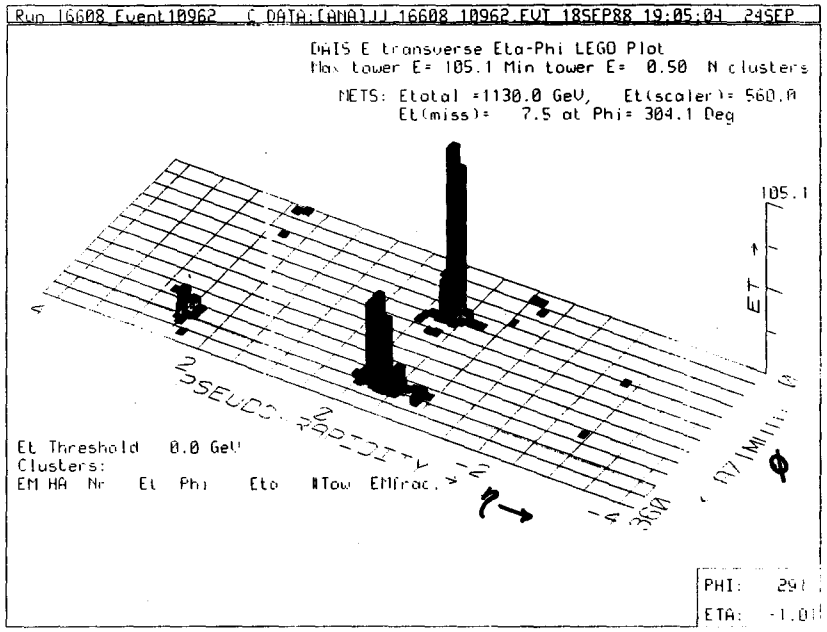
Look for $\chi \to \psi\gamma$

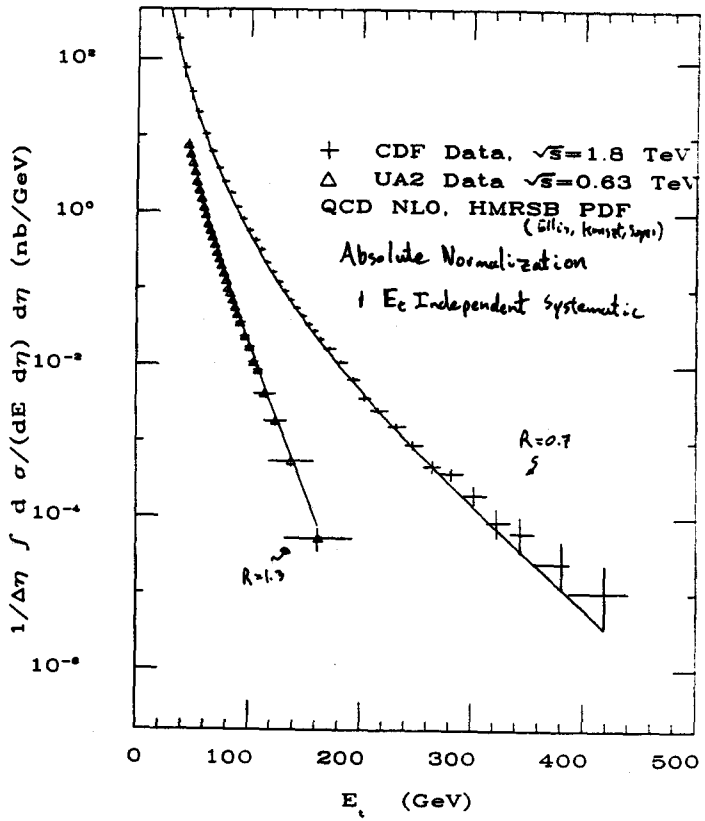
$E_\gamma \gtrsim 2$ GeV

Fraction of ψ from χ is $37 \pm 7 \pm 11\%$

(includes $b \to \chi X$, $\chi \to \psi\gamma$)




Run 16608 Event 10962 C DATA:[ANA]JJ_16608_10962.EVT 18SEP88 19:05:04 24SEP
DAIS E transverse Eta-Phi LEGO Plot
Max tower E= 105.1 Min tower E= 0.50 N clusters
METS: Etotal =1130.0 GeV, Et(scaler)= 560.0
Et(miss)= 7.5 at Phi= 304.1 Deg
105.1
ET
2 SEUDO-RAPIDITY
Et Threshold 0.0 GeV
Clusters:
EM HA Nr Et Phi Eta #Tow EMfrac.
PHI: 29
ETA: -1.0

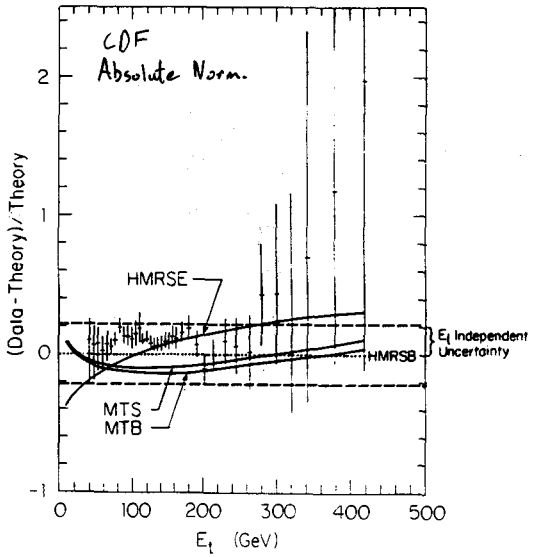

+ CDF Data, √s=1.8 TeV
Δ UA2 Data √s=0.63 TeV
QCD NLO, HMRSB PDF
(Ellis, Kunszt, Soper)
Absolute Normalization
1 Et Independent Systematic
R=0.7
R=1.3
1/Δη ∫ d σ/(dE dη) dη (nb/GeV)
E_t (GeV)
0
100
200
300
400
500

Smaller Exp. Uncertainties

Old: $\gtrsim 50\%$ (CDF, UA1, UA2) } Better understanding of E scale
New: $\sim 20-30\%$ (CDF - UA2) }

Largely E_t Independent (ie. Shape is good to $\sim 4\%$!!) $E_t > 90$

Fits to Parton Distribution Functions:
HRMSB (BCDMS) + MTS + B fit fine
HRMSE excluded >99% C.L. (EMC data) - old



PDF's now limit

Exotics

Compositeness - quarks

Approximate low energy behavior as:

$$\mathcal{L}_{eff} = \frac{g^2}{2\Lambda_c^2} (\bar{q}_L \gamma_\mu q_L)^2 \quad \text{(4 Fermi)}$$

$g^2 = 4\pi$ Convention

Scales like $q\bar{q}$ CMS E^2 (as opposed to $\frac{1}{E^2}$)

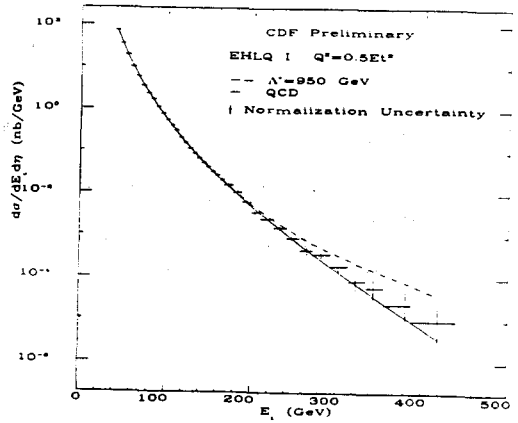
Excess at high jet E_t

UA2 $\Lambda_c > 825$ GeV 95% C.L.

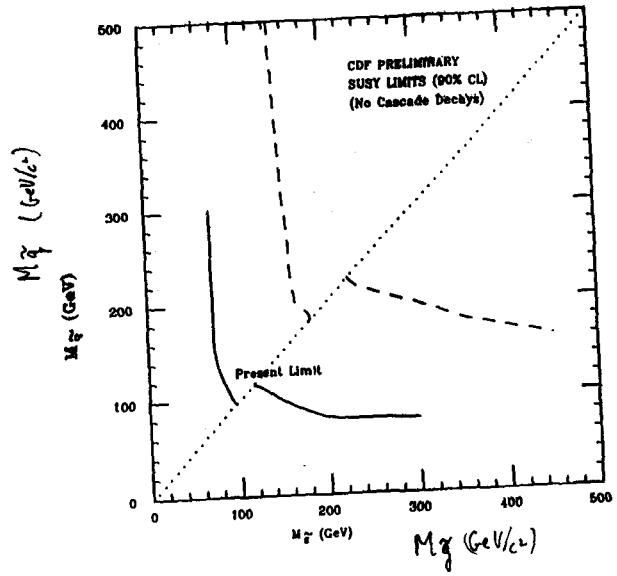
CDF $\Lambda_c > 1.4$ TeV 95% C.L.

Quarks are pointlike to $\sim 1.4 \cdot 10^{-17}$ cm

Sensitivity to $\Lambda_c \sim 2$ TeV with $1\ fb^{-1}$



SUSY Limits



$M(\tilde{g}) > M(\tilde{q})$

E_t miss > 100 GeV

2 jets, $E_t > 15$ GeV

(3 obs, 1.3 exp.)

$M(\tilde{q}) > M(\tilde{g})$

E_t miss > 40 GeV

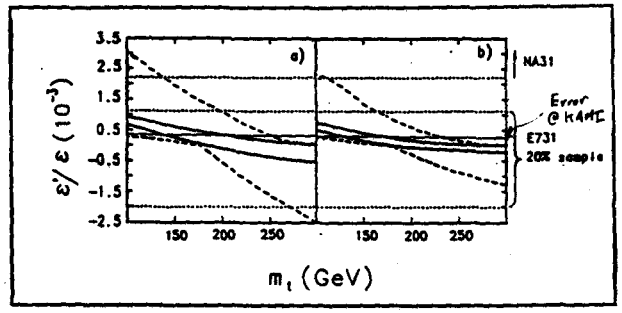
4 jets, $E_t > 15$ GeV

(2 obs, 1.3 exp)

Sensitivity to

~ 200 GeV/c² with 1 fb^{-1}

Kaons at the Main Injector



Measure CP violation in ε'/ε → Mixing or Direct?

Current Sensitivity $\sim 10^{-3}$

Projected Sensitivity $\sim 10^{-5}$

Decay $K_L \to \pi^0 e^+ e^-$



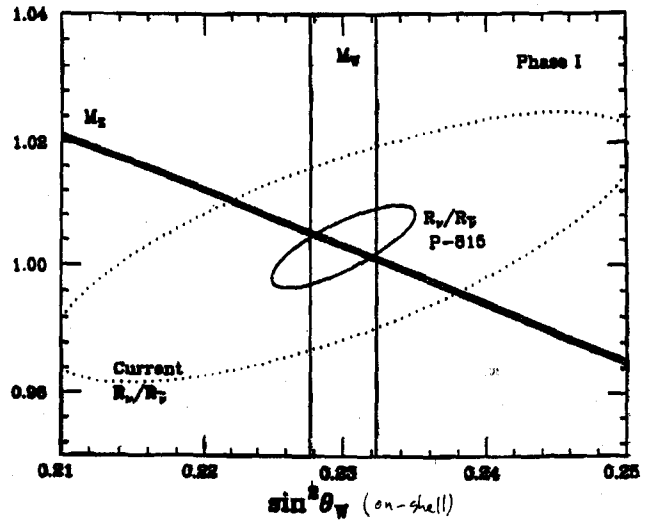
expect $\sim 3 \times 10^{-12}$ B.R. (2-M)

sensitivity $\sim 5 \times 10^{-13}$

Compare $B \to K \mu^+ \mu^-$ at CDF, CLEO, ARGUS

Neutrinos at The Main Injector

$R_\nu = NC/CC$



$$R^- = \frac{\sigma_\nu^{NC} - \sigma_{\bar\nu}^{NC}}{\sigma_\nu^{CC} - \sigma_{\bar\nu}^{CC}} = \rho^2\left(\tfrac{1}{2} - \sin^2\theta_W\right)$$

Many corrections cancel

Precision test of S.M. ⇒ Consistency with high p_t Proc

→ Use of charge tagged beams

Summary

Goals:

→ Explore available mass range for top (~200GeV)

→ Measure M_{top}, M_W with sufficient precision to constrain S.M. (Higgs)

→ b physics

→ Exotics (susy)

→ QCD

→ $\varepsilon'/\varepsilon \sim 10^{-5}$

→ $K \to \pi^0 e^+ e^- \sim 10^{-12}$

→ ρ vs. $\sin^2\theta_W$

Collider Upgrades
(Main Injector, $\bar p$ source, cold compressors, linac)

High Intensity K, ν (charge tagged) beams

Detector Upgrades

The CERN Large Hadron Collider (LHC)

W. Hoogland

THE CERN LARGE HADRON COLLIDER (LHC)
THE PROJECT, THE PROGRESS, THE PHYSICS AND THE PROGRAMME

Walter Hoogland, CERN, Geneva, Switzerland

The LHC is now a well established part of CERN's long range planning. In the December meeting of Council, a Resolution was adopted by unanimous vote, in which it is agreed that the LHC is the right machine for the advance of Particle Physics and and of the future of CERN. Major R&D efforts are underway for both the machine and its experimental programme. The LHC will be a fast and cost effective way to cross the 1 TeV frontier in constituent collisions, generally accept ed to be the energy scale at which the clues for our understanding of electroweak symmetry breaking will be found. It will do so by optimally exploiting the existing infrastructure of CERN in particular by building a SC proton collider in the present LEP tunnel using high field SC magnets. The location of the LHC at the CERN site makes a broad diversified scientific programme possible, in line with CERN's present scientific policy. In particular this foresees that the LHC is used as a heavy ion collider, extending the experimental opportunities presently provided at the SPS, while at a later stage the electrons of LEP and the protons of the LHC may be brought into collision making the LHC a giant electron-proton collider.

Prototypes for the dipole magnets constructed in close collaboration with European industry have now reached the design value of 10 Γ, demonstrating that the compact "2 in 1" has the intrinsic capability to obtain the desired field strength.

Preparations for the experimental programme now involve many hundreds of physicists, engineers and technicians in the framework of various initiatives aiming at laying the foundation of the future experimental programme. These include in particular a Detector R&D programme, coordinated through a CERN Detector R&D Committee (DRDC), and working groups on detector magnets, microelectronics, machine-experiment interface and the homogenization of mechanical CAD. A deliberate cautious approach was taken in establishing the experimental programme, preferring to emphasize common R&D work before going ahead with the procedure for detector approval. In this spirit, and after the October 1990 ECFA Workshop in Aachen on "Physics and Detectors at the LHC", it is now decided to have a joint CERN/ECFA meeting in March in Evian where the experimental community is invited to present "Expressions of Interest". This will be followed in the course of 1992 by a call for Letters of Intent, eventually leading to an approved experimental programme by the end of 1993.

DOE: Laying the Framework for Future Support

J. Decker

TALK BY DR. JAMES F. DECKER
AT THE
1991 SYMPOSIUM ON THE SUPERCONDUCTING SUPER COLLIDER
THURSDAY, OCTOBER 17, 1991
CORPUS CHRISTI, TEXAS

- IT IS A PLEASURE TO BE HERE TO TALK WITH YOU ABOUT THE SUPERCONDUCTING SUPER COLLIDER (SSC) PROJECT.

- THE PAST YEAR HAS BEEN A VERY PRODUCTIVE ONE FOR THE SSC AND I WANT TO SHARE WITH YOU MY PERSPECTIVE ON THE ACCOMPLISHMENTS OF THE SSC PROJECT AND ITS FUTURE PROSPECTS.

- AS SOME OF YOU KNOW, I FIRST BECAME INVOLVED SOME SIX YEARS AGO WITH THIS PROJECT AT THE TIME AL TRIVELPIECE WAS PREPARING TO SELL IT TO THE THEN SECRETARY OF ENERGY, JOHN HERRINGTON.

- THAT SEEMS A LONG TIME AND MANY HURDLES AGO.

- I WANT TO TAKE JUST A FEW MINUTES THIS MORNING TO RECALL SOME OF THE HURDLES THAT WE HAVE FACED AND SUCCESSFULLY CLEARED BECAUSE I BELIEVE IT HELPS PUT THIS YEAR'S PROGRESS IN PERSPECTIVE.

- AFTER SUCCESSFULLY SELLING THE SSC TO SECRETARY HERRINGTON, IT HAD TO BE SOLD TO THE PRESIDENT.

- SECRETARY HERRINGTON AND AL TRIVELPIECE DID A MASTERFUL JOB WORKING THE PROCESS THROUGH THE DOMESTIC POLICY COUNCIL.

- WE HAD BEEN SPENDING MONEY FOR RESEARCH AND DEVELOPMENT AND DESIGN FOR SEVERAL YEARS, BUT OUR FIRST REQUEST FOR CONSTRUCTION FUNDS FROM THE CONGRESS WAS FOR FY1988. WE WERE UNSUCCESSFUL.

- WE DID NOT GET OUR FIRST APPROPRIATED CONSTRUCTION FUNDS UNTIL FY1990, $126,592,000 MILLION DOLLARS.

- WE DID NOT HAVE A SITE FOR THE PROJECT UNTIL 1989.

- THE SITE SELECTION PROCESS REQUIRED ENORMOUS EFFORT BECAUSE WE HAD TO ENSURE FAIRNESS AND THE INTEGRITY OF THE PROCESS. HAD WE MADE AN ERROR IN PROCESS, THE SITE SELECTION COULD HAVE BEEN CHALLENGED AND DELAYED FOR A LONG TIME.

- FINALLY, WE HAD THE TEXAS SITE, A "GREEN FIELD" SITE, BUT WE DIDN'T OWN ANY OF THIS LAND. WE STILL DID NOT HAVE A CONTRACTOR TO BUILD THE SSC.

- UNIVERSITIES RESEARCH ASSOCIATION (URA) WAS CHOSEN AS THE CONTRACTOR IN JANUARY OF 1989, BUT URA HAD TO ACQUIRE A MANAGEMENT TEAM AND A LABORATORY STAFF, NON-TRIVIAL TASKS.

- THE DEPARTMENT OF ENERGY WAS ONLY IN SLIGHTLY BETTER SHAPE WITH REGARD TO STAFF AT THAT TIME.

- WE TOO HAD TO PUT TOGETHER A SITE OFFICE AND A MANAGEMENT TEAM.

- THEN THERE WERE THE TECHNICAL ISSUES.

- ON EVERYONE'S MIND WAS THE SUPERCONDUCTING DIPOLE MAGNETS BECAUSE OF THE ISABELLE PROBLEMS.

- WE WERE ALWAYS CONFIDENT WE COULD DO IT, BUT WE HAD TO PRODUCE - COST INCREASE.

- WHAT HAVE WE ACCOMPLISHED? WHERE ARE WE TODAY? WHERE ARE WE GOING?

- LET ME START WITH THE PROGRESS MADE DURING THE PAST YEAR AT THE SSC LABORATORY. I AM SURE THAT SOME OF THIS HAS ALREADY BEEN COVERED BY OTHERS THIS WEEK AND PAUL REARDON WILL TALK ABOUT THE STATUS OF THE PROJECT SO I'LL BE BRIEF.

- THERE ARE SOME EXAMPLES OF MAJOR CHALLENGES THAT HAD TO BE SURMOUNTED. WHAT I HAVEN'T TOLD YOU ABOUT ARE DOZENS OF EVENTS ANY ONE OF WHICH WERE POTENTIAL SHOWSTOPPERS HAD THEY NOT BEEN HANDLED PROPERLY.

- PROGRESS IN THOSE EARLY DAYS WAS BOTH SLOW AND UNCERTAIN. BUT THROUGH THE DEDICATION AND HARD WORK OF MANY PEOPLE ENORMOUS PROGRESS HAS BEEN MADE AND THAT PROGRESS IS ACCELERATING AT A RAPID RATE.

- THE MANAGEMENT TEAM AT THE LAB WAS STRENGTHENED SIGNIFICANTLY BY THE ADDITION OF A NUMBER OF SENIOR PERSONNEL, INCLUDING THE GENERAL MANAGER, ED SISKIN, AND THE PROJECT MANAGER, PAUL REARDON.

- THE TECHNICAL DIVISIONS WERE STRENGTHENED BY THE ADDITION OF SENIOR MANAGERS.

- IN FACT, THE OVERALL TEAM AND STRENGTH OF THE LABORATORY GREW AT AN IMPRESSIVE RATE.

- THE STAFF AT THE LABORATORY HAS GROWN TO OVER 1400 PEOPLE.

- THE STATE OF TEXAS AND THE LABORATORY PROCURED THE REVCO BUILDING IN ORDER TO PROVIDE OFFICE AND LABORATORY SPACE FOR THE LABORATORY'S RAPIDLY EXPANDING STAFF.

- NOW KNOWN AS THE CENTRAL FACILITY, THIS NEW BUILDING ALREADY HOUSES SEVERAL HUNDRED PEOPLE FROM THE ACCELERATOR DIVISION, PLUS DEPARTMENT OF ENERGY (DOE) PERSONNEL.

- SUPPORT BY THE STATE OF TEXAS HAS BEEN INVALUABLE IN MAINTAINING THE RAPID PROGRESS OF THE PROJECT DURING THE PAST YEAR.

- IN FY1991, THE STATE OF TEXAS ACQUIRED 8,850 ACRES OF THE LAND NEEDED TO BUILD THE COLLIDER AND CONTRIBUTED $149 MILLION DOLLARS TO THE PROJECT; TEXAS IS ALSO EXPECTED TO CONTRIBUTE SUBSTANTIAL ADDITIONAL FUNDS TO THE PROJECT IN FY1992.

- THE DEPARTMENT'S PARTNERSHIP WITH TEXAS IS A GOOD EXAMPLE OF HOW THE FEDERAL AND STATE GOVERNMENTS CAN WORK TOGETHER TO ACCOMPLISH MAJOR ACTIVITIES FOR THE BENEFIT OF THE COUNTRY.

- IN FACT, THE STATE OF TEXAS-DEPARTMENT OF ENERGY-SSC LABORATORY COLLABORATION SHOULD SERVE AS AN EXAMPLE IN THE FUTURE FOR OTHER PROJECTS.

- ALSO THE CONSTRUCTION ACTIVITY BUILT UP RAPIDLY WITH THE SELECTION OF PARSONS, BRINKERHOFF, MORRISON AND KNUTSON, AS THE PROJECT'S ARCHITECTURAL ENGINEERING FIRM.

- THE EXPLORATORY SHAFT, THE MAGNET DEVELOPMENT LABORATORY, THE ACCELERATOR SYSTEM STRING TEST FACILITIES, AND THE MAJOR REFRIGERATOR FACILITIES AT THE E-1 SITE ARE NEARLY COMPLETED.

- OBVIOUSLY, THE SSC IS NO LONGER A PAPER OPERATION - IT NOW HAS REAL FACILITIES; THE CONSTRUCTION PROGRAM IS EXPECTED TO ACCELERATE FURTHER IN FY1992.

- THERE WAS SUBSTANTIAL PROGRESS IN THE MAGNET PROGRAM DURING FY1991.

- THE CONSTRUCTION OF THE 50 MILLIMETER COLLIDER DIPOLE MAGNETS PROGRESSED WELL WITH THE ADDITION OF THE GENERAL DYNAMICS TEAM AT FERMILAB AND THE WESTINGHOUSE TEAM AT BROOKHAVEN NATIONAL LABORATORY.

- FERMILAB AND THE SSC LAB CONDUCTED A SUCCESSFUL STRING TEST OF FIVE 40 MILLIMETER COLLIDER DIPOLE MAGNETS DURING 1991.

- THIS SUCCESSFUL STRING TEST DEMONSTRATED THE PROJECT'S ABILITY TO BUILD MAGNETS AND TO OPERATE THEM IN STRINGS - SUCCESSFULLY POWERING THE MAGNETS TO FULL FIELD AND CONTROLLING MAGNET QUENCHES.

- THIS SIGNIFICANT MILESTONE GIVES US GREAT CONFIDENCE THAT THE 50 MILLIMETER COLLIDER DIPOLE MAGNETS WILL PERFORM SATISFACTORILY WHEN CONNECTED UP IN THE STRING TEST.

- FY 1991 WAS BOTH A DIFFICULT AND REWARDING YEAR FOR THE PHYSICS PROGRAM AT THE LAB.

- THE SOLENOID DETECTOR COLLABORATION WAS CHOSEN BY THE LABORATORY AS THE FIRST MAJOR DETECTOR FOR THE PROJECT.

- AS YOU ALL ARE PROBABLY WELL AWARE, THE BUDGET PROBLEMS FACING THE UNITED STATES GOVERNMENT ARE SIGNIFICANT.

- THE DEFICIT HAS GROWN MORE RAPIDLY THAN EXPECTED AND BUDGET CAPS HAVE BEEN IMPOSED.

- WE ARE VERY PLEASED WITH THE SUCCESSFUL VOTES IN SUPPORT OF THE SSC THAT WERE TAKEN IN THE HOUSE AND THE SENATE ON OUR FY1991 BUDGET REQUEST AND THE DEPARTMENT WAS SUCCESSFUL IN GETTING $454 MILLION DOLLARS FOR THE SSC IN FY1992. THIS WAS IN A DIFFICULT BUDGET CLIMATE.

- IN FY1993, SSC AGAIN NEEDS A SIGNIFICANT INCREASE IN FUNDING IN AN ENVIRONMENT WHERE THERE MAY WELL BE CUTS IN OTHER SCIENCE PROGRAMS.

- THERE ARE, HOWEVER, THINGS THAT WE CAN DO TO MAINTAIN SUPPORT AND KEEP THE SSC ON TRACK.

- FIRST, THE PROJECT MUST BE KEPT ON SCHEDULE AND COSTS MUST BE MAINTAINED WITHIN THE COST ESTIMATES.

- GOOD PROJECT MANAGEMENT AND COST AND SCHEDULE CONTROL ARE REQUIRED TO CONVINCE THE PUBLIC AND THE CONGRESS THAT THIS PROJECT IS BEING WELL MANAGED.

- BESIDES, I HAVE A VET WITH CONGRESSMAN SHERRY BOLERT FROM NEW YORK THAT WE CAN FINISH THE PROJECT ON TIME AND COST. I DON'T LIKE TO LOSE.

- THE PROJECT HAS BEEN WELL MANAGED UP TO THIS POINT, AND WE NEED TO KEEP UP THE GOOD WORK.

- SECOND, TECHNICAL SUCCESS IS CRUCIAL, WE MUST HAVE A SUCCESSFUL STRING TEST OF THE 50 MILLIMETER COLLIDER DIPOLE MAGNETS.

- TESTING AND DEMONSTRATION OF THE COLLIDER MAGNETS IS A CRITICAL ELEMENT BECAUSE MANY THOUSANDS OF MAGNETS WILL BE REQUIRED IN ORDER TO MAKE THE COLLIDER WORK SUCCESSFULLY.

- THE THIRD ELEMENT THAT IS CRITICAL FOR SUCCESS WITH OUR FY1993 BUDGET REQUEST IS OBTAINING INTERNATIONAL SUPPORT.

- ONE OF THE CONDITIONS THAT THE DEPARTMENT AGREED TO WHEN THIS PROJECT WAS APPROVED WAS THAT WE WOULD SEEK ONE-THIRD OF THE FUNDING FROM NON-FEDERAL SOURCES.

- IF WE SUBTRACT THE AMOUNT THAT IS ALREADY BEING PROVIDED BY THE STATE OF TEXAS, THE PROJECT STILL MUST ACQUIRE APPROXIMATELY $1.7 BILLION DOLLARS FROM OTHER NON-FEDERAL SOURCES.

- IT IS OUR INTENT TO MAKE THE SSC LABORATORY TRULY INTERNATIONAL IN CHARACTER. WE WANT OTHER COUNTRIES TO JOIN US AS PARTNERS.

- LET ME ASSURE YOU THAT THE ADMINISTRATION STRONGLY SUPPORTS THE SSC AND HAS BEEN MAKING A MAJOR EFFORT TO OBTAIN INTERNATIONAL PARTNERS.

- HOWEVER, IT IS A SLOW, TIME CONSUMING PROCESS.

- WE ARE PRESENTLY INVOLVED IN DISCUSSIONS WITH THE SOVIET UNION, JAPAN, KOREA, CANADA, AND INDIA.

- PRESIDENT BUSH HAS CLEARLY DEMONSTRATED HIS SUPPORT FOR OBTAINING FOREIGN PARTNERS BY SENDING LETTERS OF INVITATION TO OTHER HEADS OF STATE AND BY RAISING THE ISSUE WITH JAPAN'S PRIME MINISTER KAIFU EARLIER THIS YEAR.

- DR. WILLIAM HAPPER, THE DIRECTOR FOR ENERGY RESEARCH, RETURNED JUST LAST WEEK FROM JAPAN WHERE HE MET WITH LEADERS OF JAPAN'S SCIENTIFIC COMMUNITY, GOVERNMENT AND INDUSTRY.

- DEPUTY SECRETARY HENSON MOORE, AND JOE CIPRIANO, HAVE ACCOMPANIED THE PRESIDENT'S SCIENCE ADVISOR DR. ALAN BROMLEY TO JAPAN THIS WEEK TO AGAIN EMPHASIZE THE IMPORTANCE THE ADMINISTRATION PLACES ON THE SSC.

- FINALLY, THE SECRETARY OF ENERGY, ADMIRAL WATKINS, IS SCHEDULED TO GO TO JAPAN IN NOVEMBER OR DECEMBER.

- ALL OF THIS ACTIVITY ON THE INTERNATIONAL FRONT UNDERSCORES THE ADMINISTRATION'S STRONG COMMITMENT TO FULFILL ITS GOAL OF OBTAINING ONE-THIRD OF THE FUNDING FOR THE SSC FROM NON-FEDERAL SOURCES.

- LAST, IT IS VERY IMPORTANT THAT THE HEP COMMUNITY CONTINUE TO GIVE VIGOROUS SUPPORT TO THE SSC AS ITS NUMBER ONE PRIORITY. THIS IS PARTICULARLY TRUE AS WE HEAD INTO WHAT I PREDICT WILL BE A MOST DIFFICULT FY1993 BUDGET DISCUSSION IN CONGRESS.

- FINALLY, IN CLOSING, I'D LIKE TO SAY THAT THE SSC'S ACCOMPLISHMENTS DURING THE PAST YEAR ARE A TRIBUTE TO THE QUALITY OF LEADERSHIP AND THE MANAGEMENT THAT EXISTS IN THE LABORATORY AND THE DOE PROJECT OFFICE, LEAD BY JOE CIPRIANO, ROY SCHWITTERS, AND ED SISKIN, THE DIRECTOR, AND GENERAL MANAGER FOR THE SSC LABORATORY RESPECTIVELY.

- THE CLOSE WORKING RELATIONSHIP THAT EXISTS BETWEEN THESE INDIVIDUALS, THEIR STAFFS, AND THE STATE OF TEXAS, ARE A FURTHER EXAMPLE OF THE KIND OF COOPERATION THAT IS NECESSARY TO ENSURE THAT THE PROJECT IS SUCCESSFUL.

- I ALSO WANT TO THANK ALL OF YOU WHO ARE PARTICIPATING IN THIS CONFERENCE FOR THE EFFORTS YOU HAVE MADE ON BEHALF OF THE SSC.

- WE LOOK FORWARD TO THE OPERATION OF THE SSC AND THE EXCITING NEW SCIENCE IT WILL PRODUCE.

Status of the Project

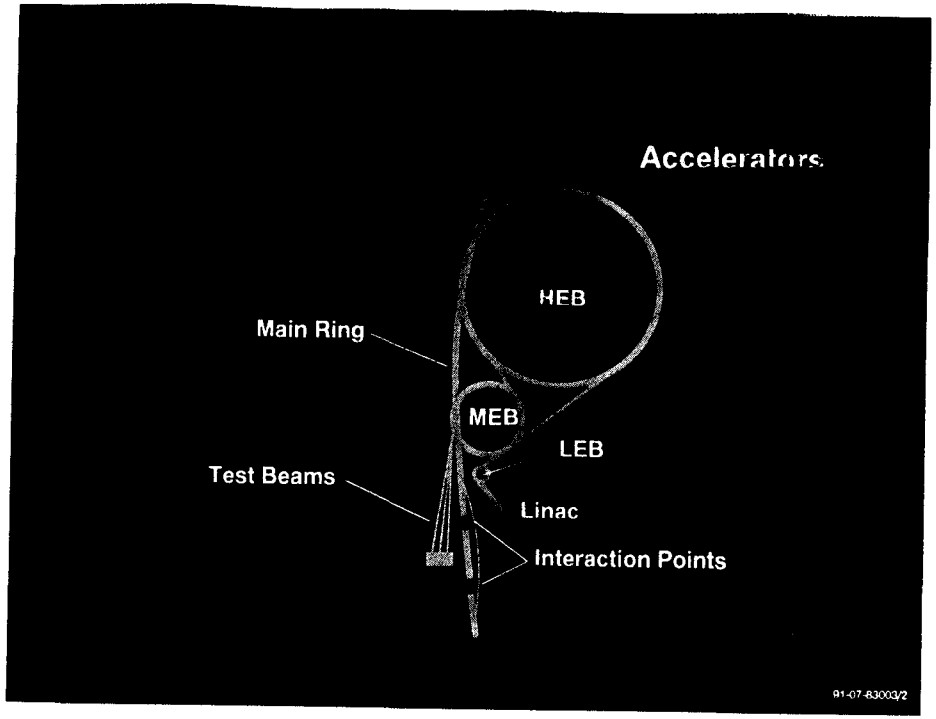
P. Reardon

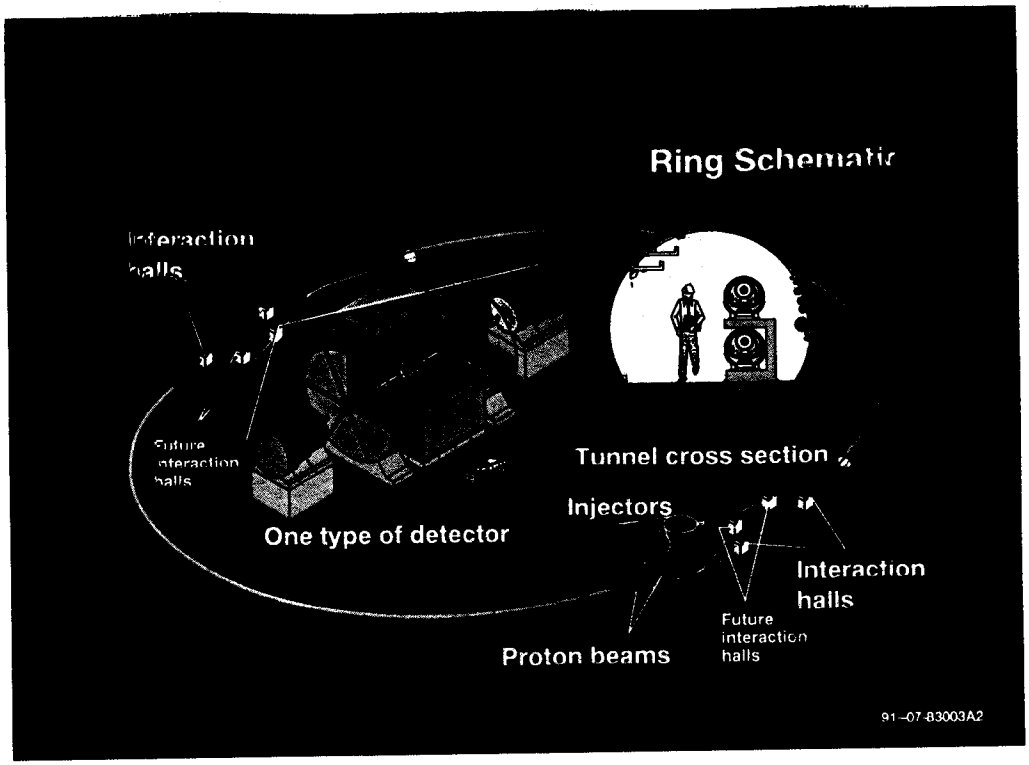
SSCL PROJECT

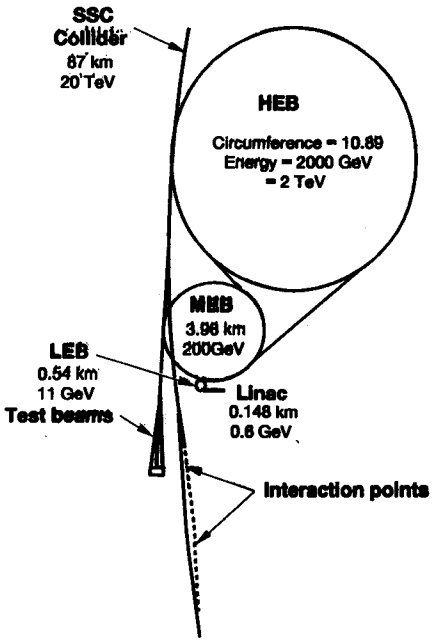
PROBLEMS ADDRESSED IN THE

PAST YEAR

- Final Conceptual Design and location of All Machines and Beam Transport Systems
- Establishment of Sufficient Office and Lab Space for Most of Project to be Co-located and Functioning as a Team
- Establish a Beach-head at the Site of New Facilities That Will Become a Part of Final SSC Complex
- Initiate Master Planning for all Site Activities
- Award Major Contracts for Superconducting Wire and Magnets
- Initiate Other Major Hardware Procurements such as Cryogenic Systems, RFQ, Corrector Magnets, DTL and Klystrons
- Start In-house Development and Test Efforts (Dipole and Quad Models, Corrector Magnets, Ion Source, etc.)
- Accomplish ER String Test at FNAL
- Prepare for Accelerator Systems String Test (ASST) Including Provision of Additional Dipole Magnets and a Back-up Refrigerator
- Work with Physics Research to Define Detector and Detector Hall Requirements
- In Concert with DOE, Develop Specific Approaches to Foreign Participation in the SSCL
- Develop Effective Procedures for Change Control and Configuration Management
- Complete Integrated Project Schedule and Reporting System
- Strengthen Scientific and Technical Staff with Improved Technical Oversight Capabilities







5 Stages of Acceleration	
Linac	0 – 0.6 GeV
LEB	0.6 – 11 GeV
MEB	11 – 200 GeV
HEB	200 – 2000 GeV
Collider	2 TeV – 20 TeV

Schematic layout of the injector complex, a portion of the collider ring and test beam area. The dashed line indicates a future beam bypass.

PROJECT MANAGEMENT STRATEGY ON DEVELOPMENT OF REVISED DESIGN

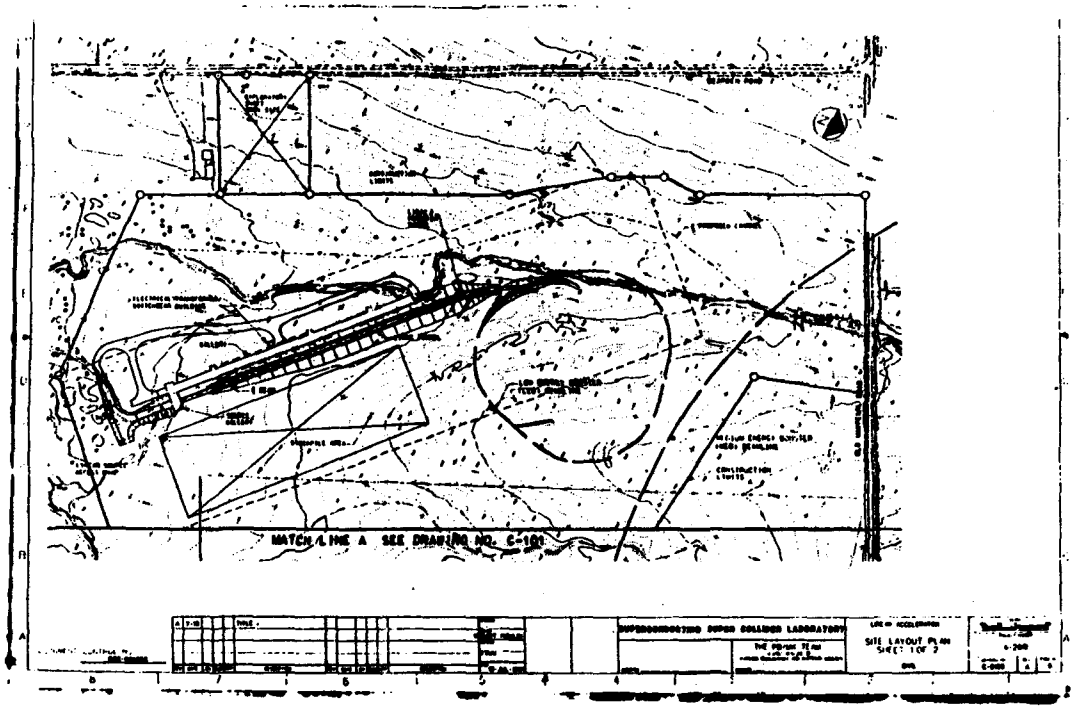
- USED THE SCDR PARAMETERS AS THE BASELINE FOR THE PROJECT
- RECOGNIZED THAT THAT BASELINE WAS A POINT DESIGN, NOT A FINAL DESIGN
- REFINED THAT POINT DESIGN IN A CONTROLLED WAY TO DEVELOP THE PRESENT IMPROVED POINT DESIGN
- PROCEED WITH CRITICAL DECISIONS ON AN AS-NEEDED BASIS TO MEET COST AND SCHEDULE REQUIREMENTS
- CONTINUE TO DEVELOP DESIGN FOR OVERALL OPTIMIZATION

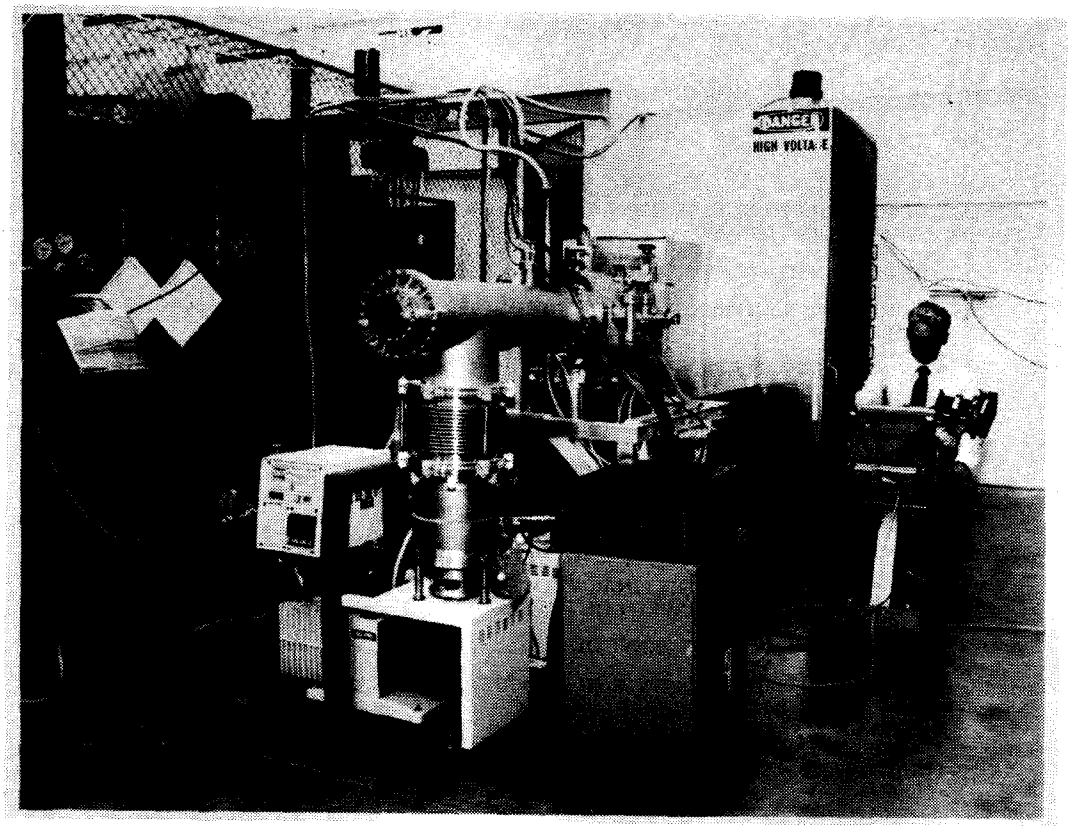
DESCRIPTION OF CONCEPTUAL DESIGN

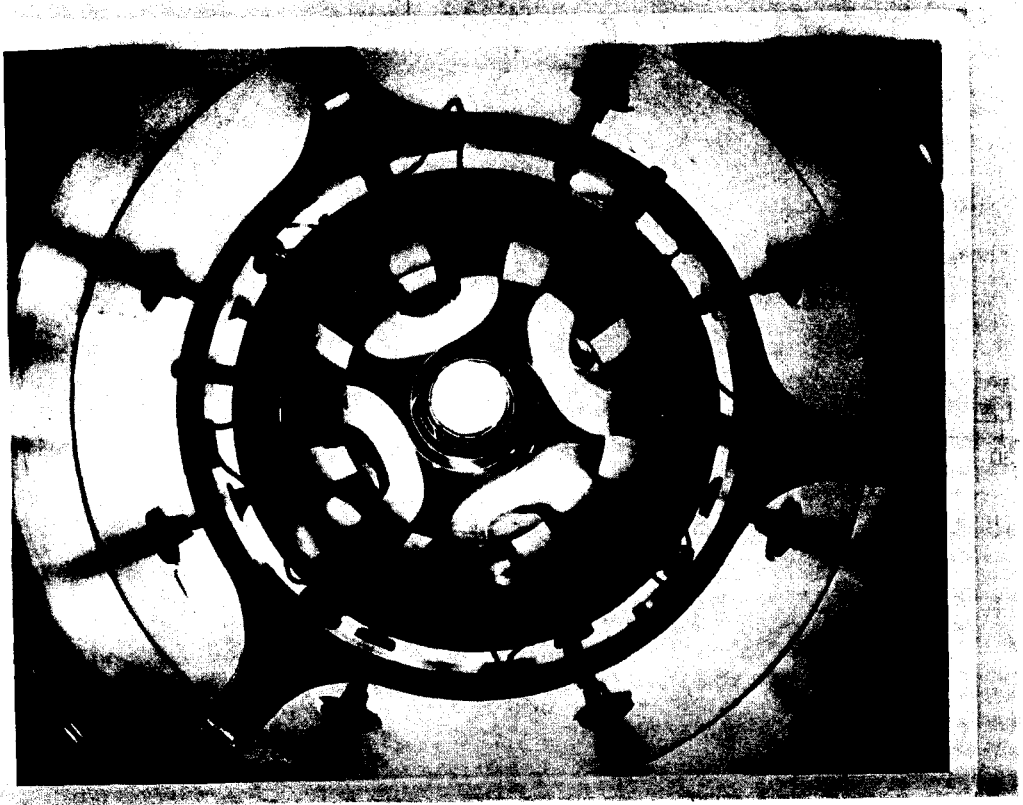
OPTIMIZATION PROCESS

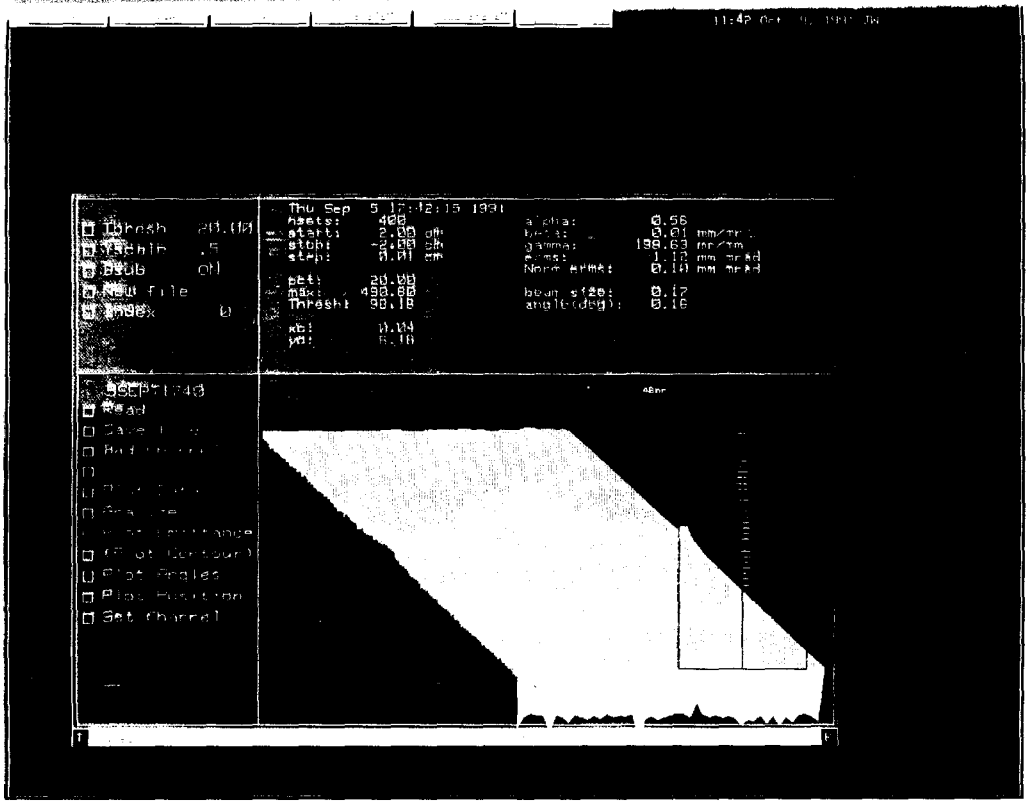
A SMALL NUMBER OF CHANGES TO THE ACCELERATOR PARAMETERS WERE PROPOSED. THE PROPOSALS ADOPTED WERE:

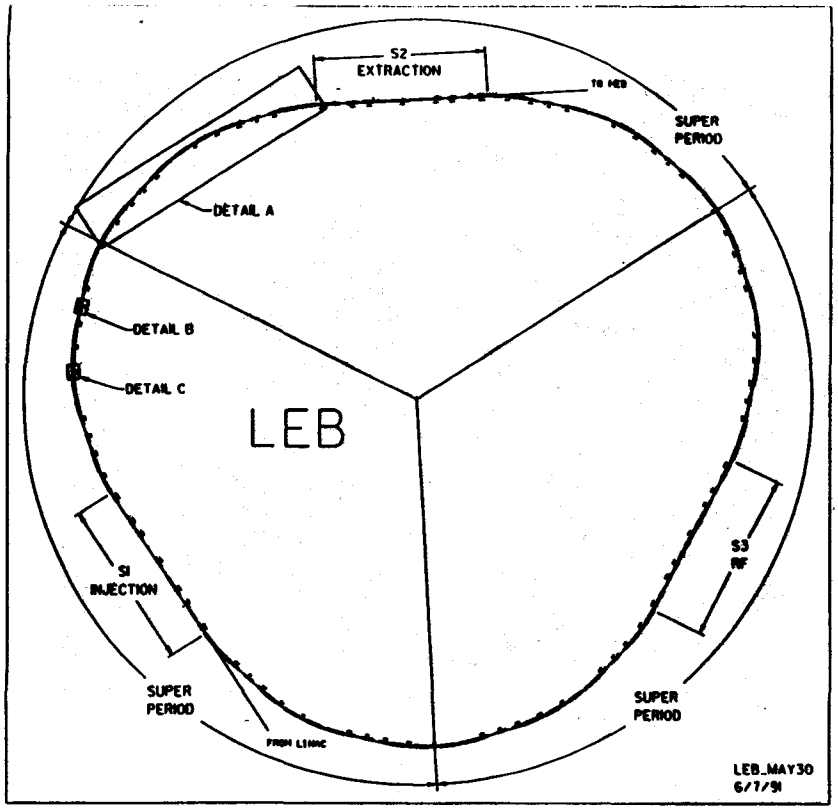
- A HIGH-TRANSITION ENERGY LATTICE IN THE LEB
- A LARGER CIRCUMFERENCE OF LEB TO PROVIDE ADEQUATE STRAIGHT SECTION SPACE.
- MOVING THE TRANSITION ENERGY FURTHER AWAY FROM THE INJECTION IN THE MEB
- MOVE TO A HIGHER TUNE IN THE MEB TO MORE EFFECTIVELY MATCH DIPOLE AND QUAD TRACKING
- A SMALL REDUCTION IN THE HEB CIRCUMFERENCE IN ORDER TO IMPROVE THE INJECTOR/COLLIDER COGGING AND FILLING TIME
- CHANGE THE TUNE OF THE HEB TO MAINTAIN 5CM APERTURE
- ADJUST THE LAYOUT OF THE LINAC AND LEB FACILITIES IN ORDER TO LATER INCREASE THE OUTPUT ENERGY OF THE LINAC FROM .6 TO 1 GeV
- CHANGE THE COLLIDER TUNNEL DIAMETER FROM 12 FT TO 14 FT
- CHANGE THE COLLIDER LATTICE TO PROVIDE ADDITIONAL SPACE FOR LATER INJECTION OF SPECIAL CORRECTORS, ETC.
- PROPOSE THE ADJUSTMENT OF THE COLLIDER ELEVATION TO IMPROVE FOUNDATION MATERIAL FOR BOTH THE COLLIDER AND THE DETECTOR HALLS

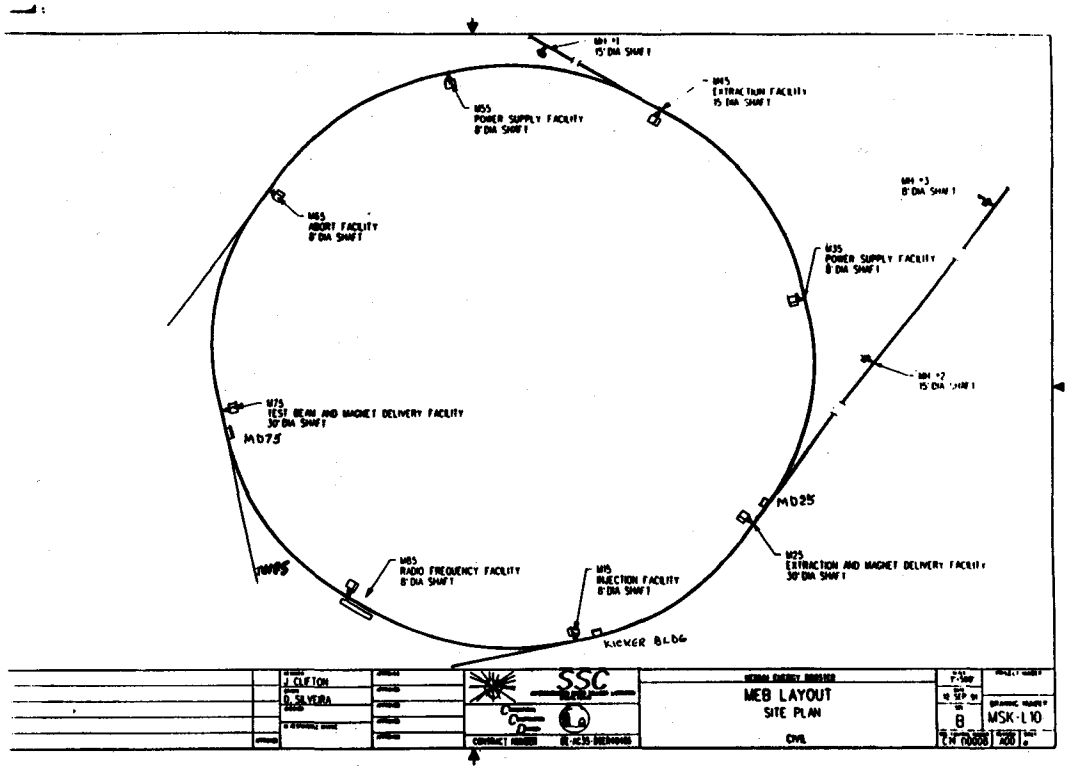

MATCH LINE A SEE DRAWING NO. C-101
SUPERCONDUCTING SUPER COLLIDER LABORATORY
SITE LAYOUT PLAN
SHEET 1 OF 2

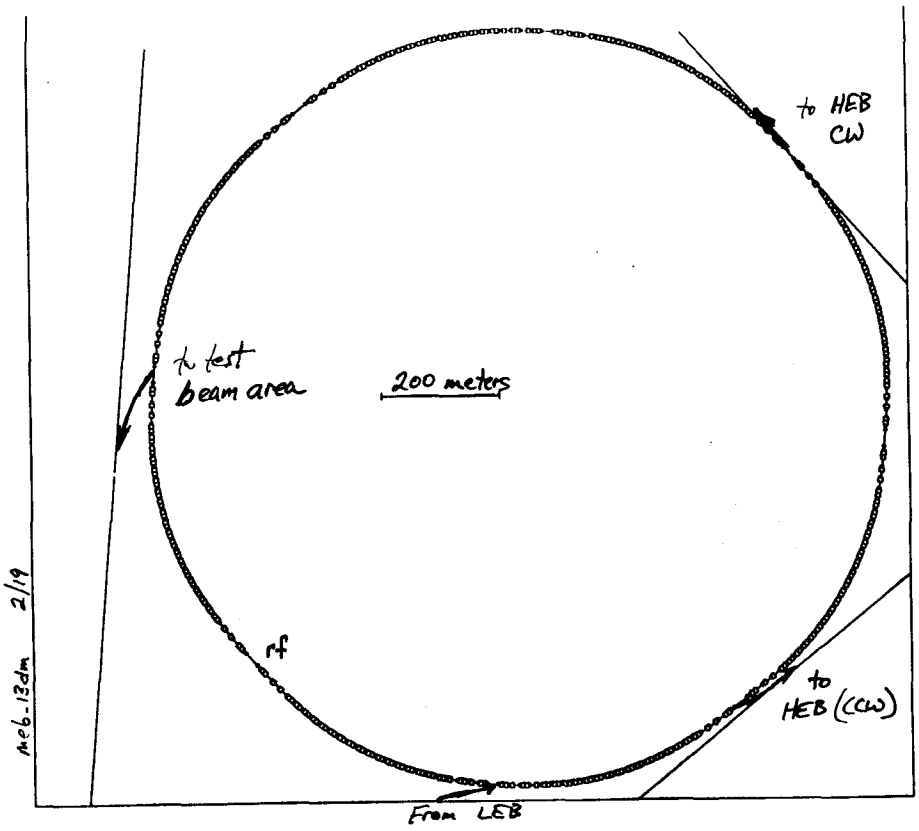


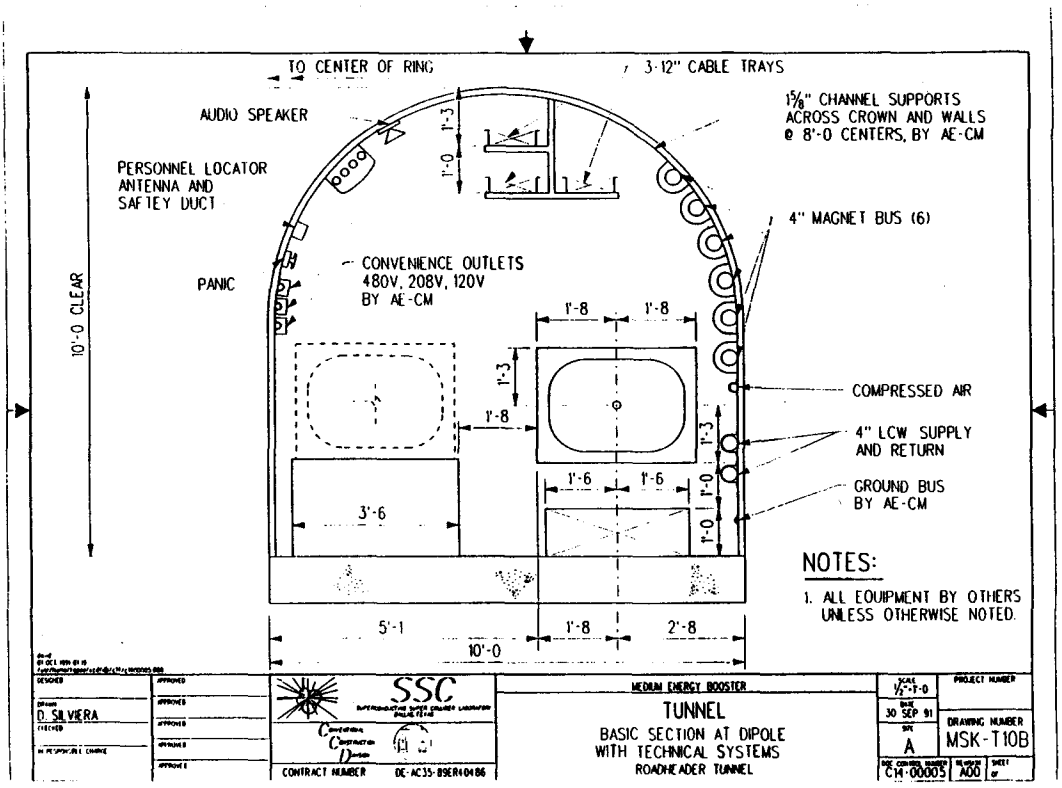



Thu Sep 5 17:42:15 1991
heats: 400
start: 2.00 cm
stop: -2.00 cm
step: 0.01 cm
pct: 20.00
max: 490.60
Thresh: 98.10
xc: 11.04
yc: 6.10
alpha: 0.56
beta: 0.01 mm/mr
gamma: 198.63 mr/cm
emit: 1.10 mm mrad
Norm emmt: 0.14 mm mrad
beam size: 0.17
angle(deg): 0.16
Read
Get Channel


S2
EXTRACTION
TO MEB
SUPER
PERIOD
DETAIL A
DETAIL B
DETAIL C
LEB
S3
RF
SI
INJECTION
SUPER
PERIOD
SUPER
PERIOD
FROM LINAC
LEB_MAY30
6/7/91


M55
POWER SUPPLY FACILITY
8'DIA SHAFT
M45
EXTRACTION FACILITY
15 DIA SHAFT
M65
ABORT FACILITY
8'DIA SHAFT
M35
POWER SUPPLY FACILITY
8'DIA SHAFT
M75
TEST BEAM AND MAGNET DELIVERY FACILITY
30'DIA SHAFT
MD75
MD25
M25
EXTRACTION AND MAGNET DELIVERY FACILITY
30'DIA SHAFT
M85
RADIO FREQUENCY FACILITY
8'DIA SHAFT
M15
INJECTION FACILITY
8'DIA SHAFT
KICKER BLDG
J. CLIFTON
D. SILVEIRA
SSC
MEB LAYOUT
SITE PLAN
CIVIL
8
MSK-L10


to HEB CW
to test beam area
200 meters
rf
to HEB (CCW)
From LEB
meb.13dm 2/19


TO CENTER OF RING
3-12" CABLE TRAYS
AUDIO SPEAKER
1⅝" CHANNEL SUPPORTS ACROSS CROWN AND WALLS @ 8'-0 CENTERS, BY AE-CM
PERSONNEL LOCATOR ANTENNA AND SAFTEY DUCT
4" MAGNET BUS (6)
PANIC
CONVENIENCE OUTLETS 480V, 208V, 120V BY AE-CM
10'-0 CLEAR
COMPRESSED AIR
4" LCW SUPPLY AND RETURN
GROUND BUS BY AE-CM
NOTES:
1. ALL EQUIPMENT BY OTHERS UNLESS OTHERWISE NOTED.
SSC
MEDIUM ENERGY BOOSTER
TUNNEL
BASIC SECTION AT DIPOLE WITH TECHNICAL SYSTEMS
ROADHEADER TUNNEL
D. SILVIERA
CONTRACT NUMBER DE-AC35-89ER40486
30 SEP 91
A
MSK-T10B
C14-00005
A00

NO:E10-000006
REV:
8/7/91

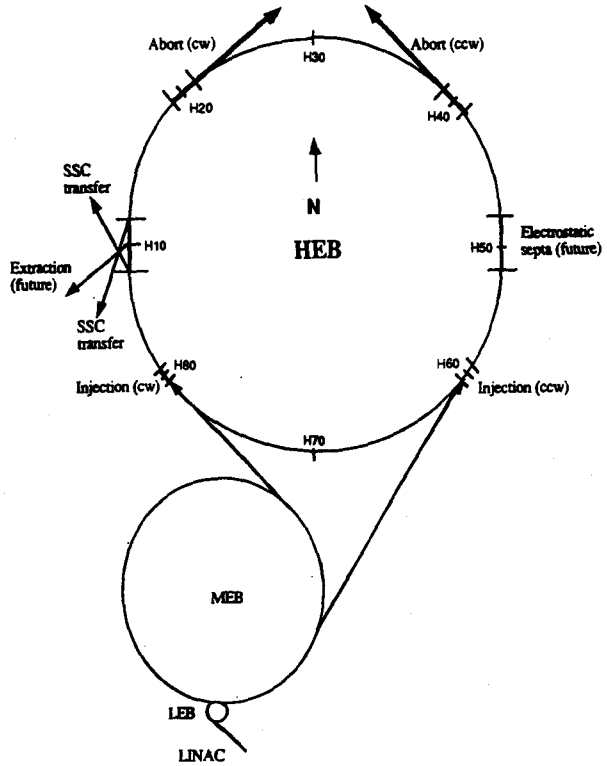
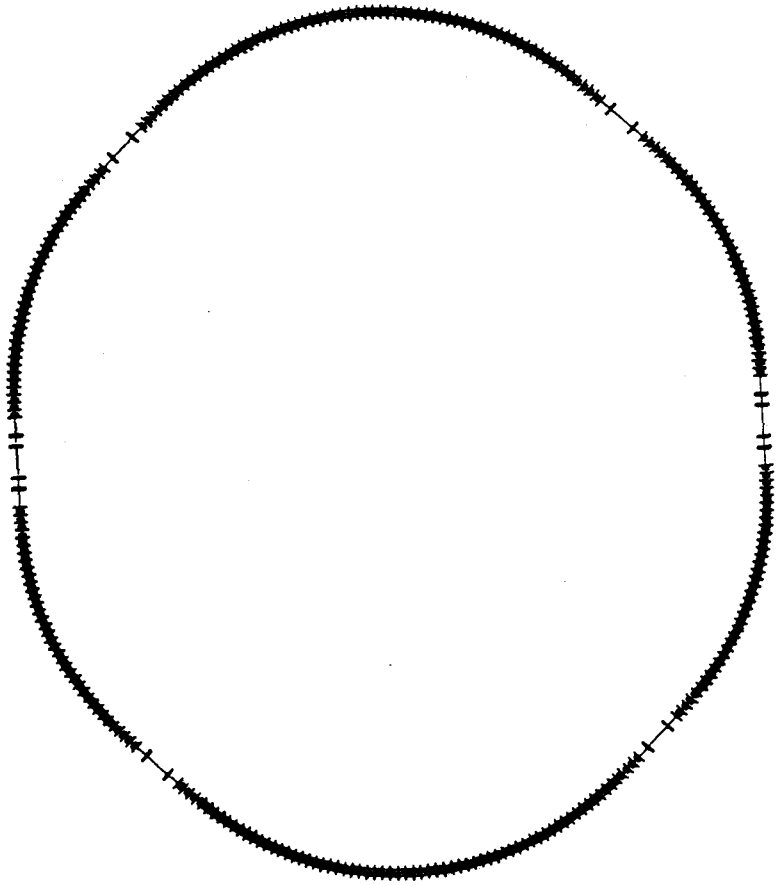
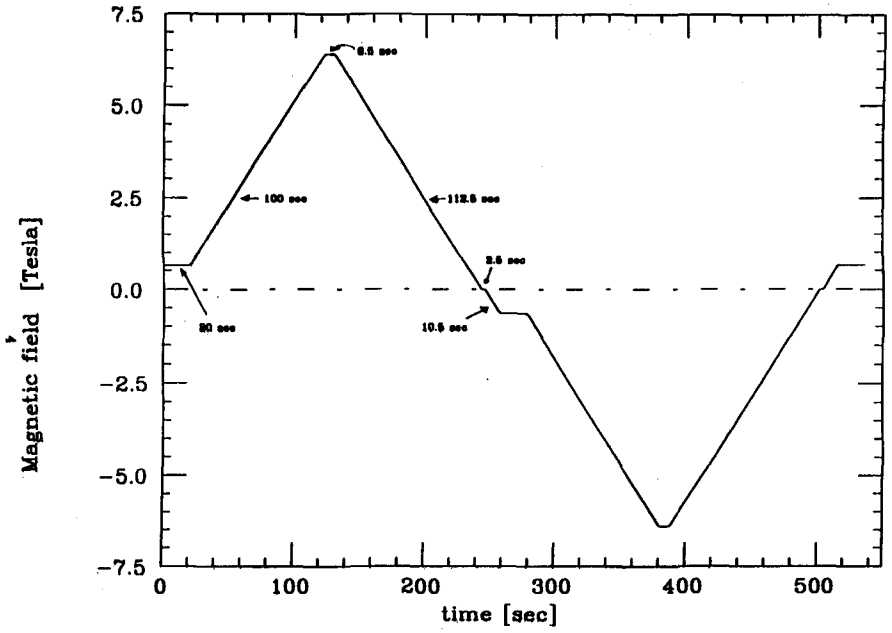


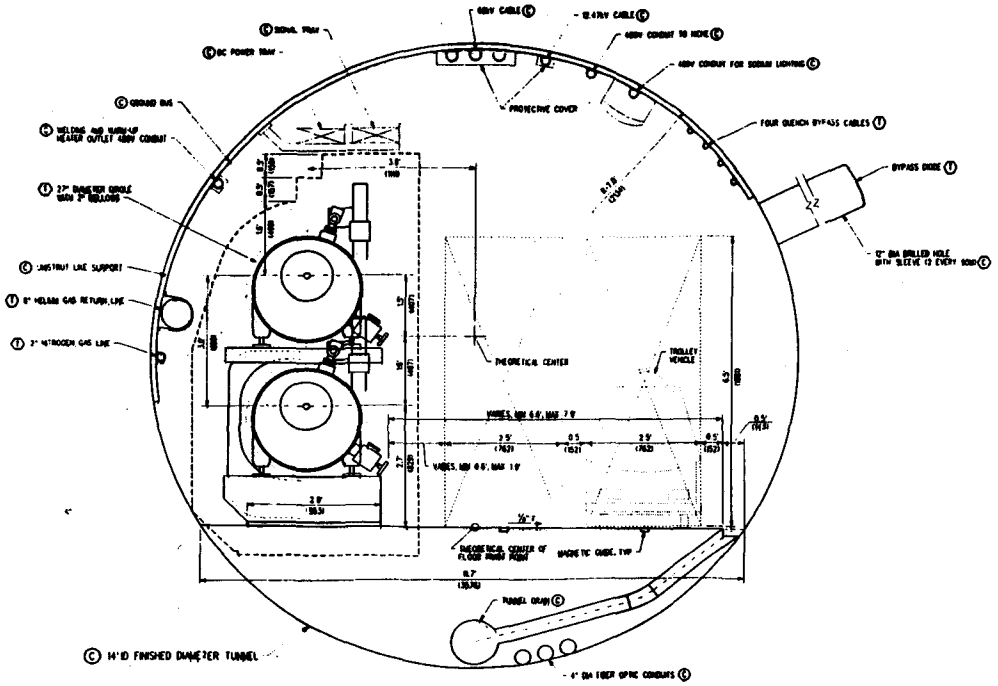
Figure 1.2-1 HEB Ring Layout

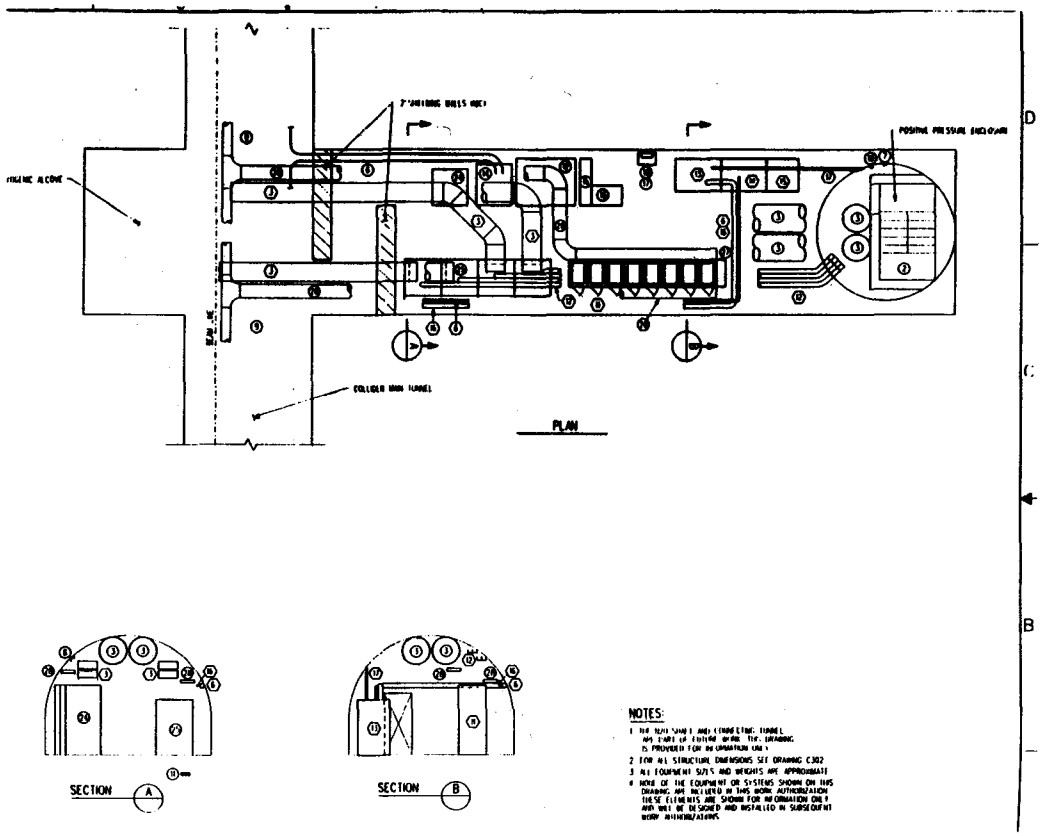


HEB cycle

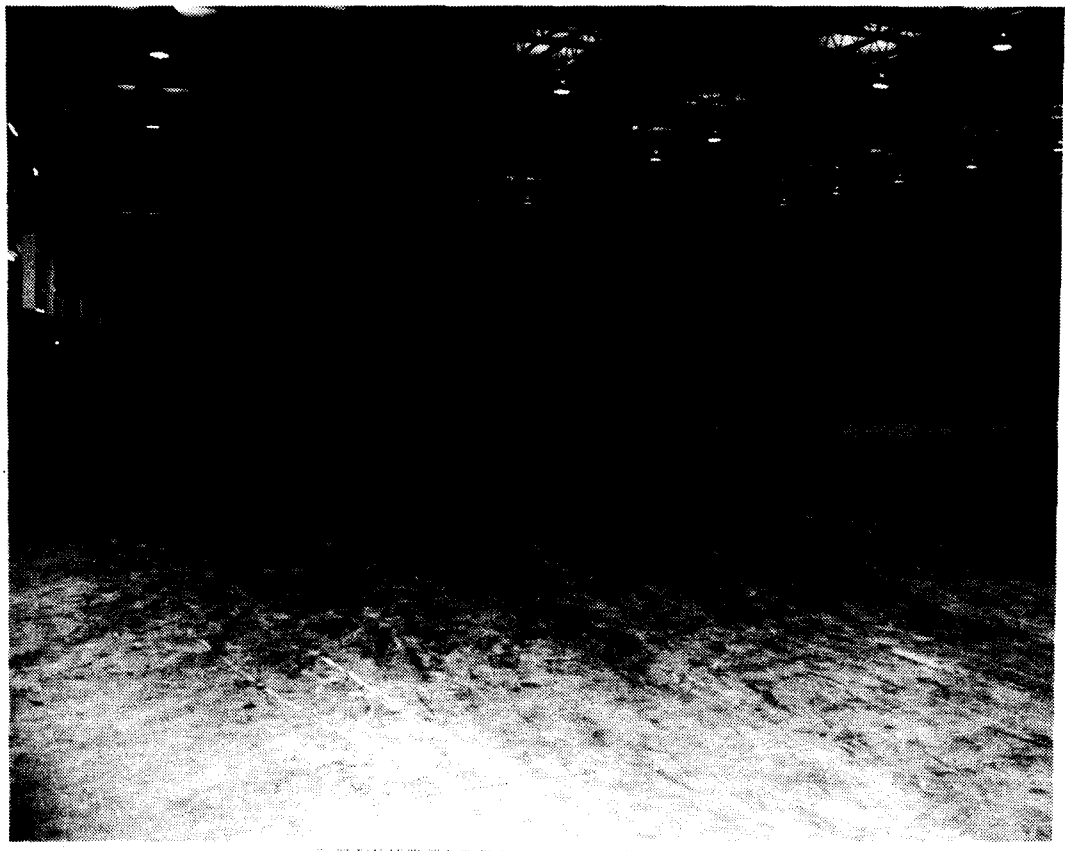


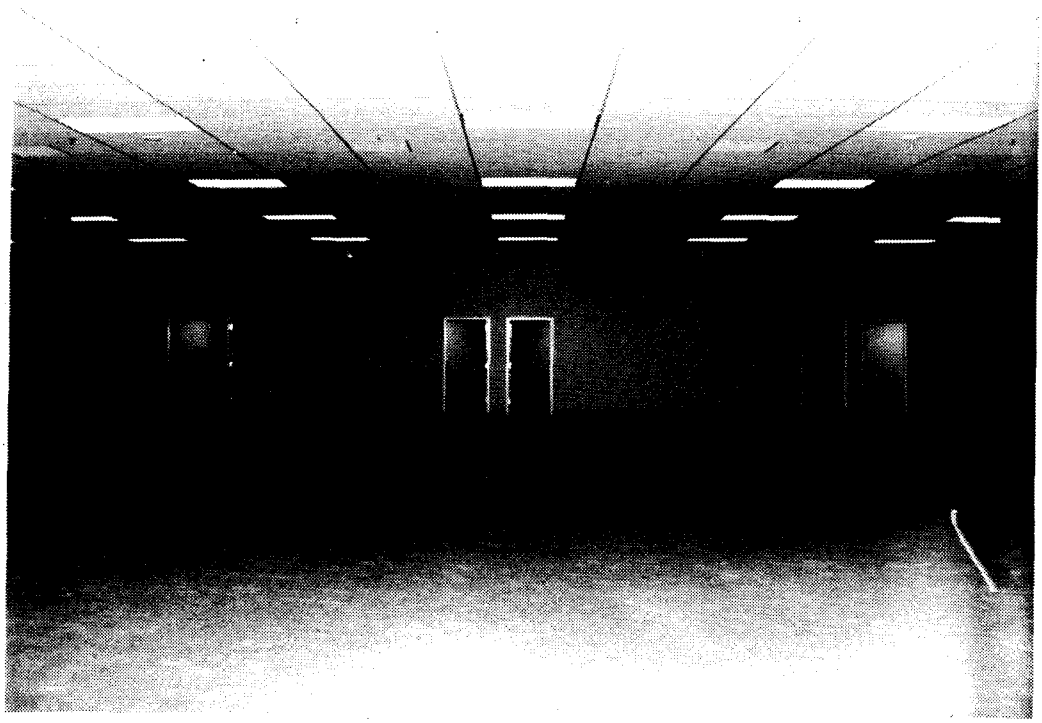
Magnet Task Force
D. E. Johnson
HEB Overview
14 Nov 1990

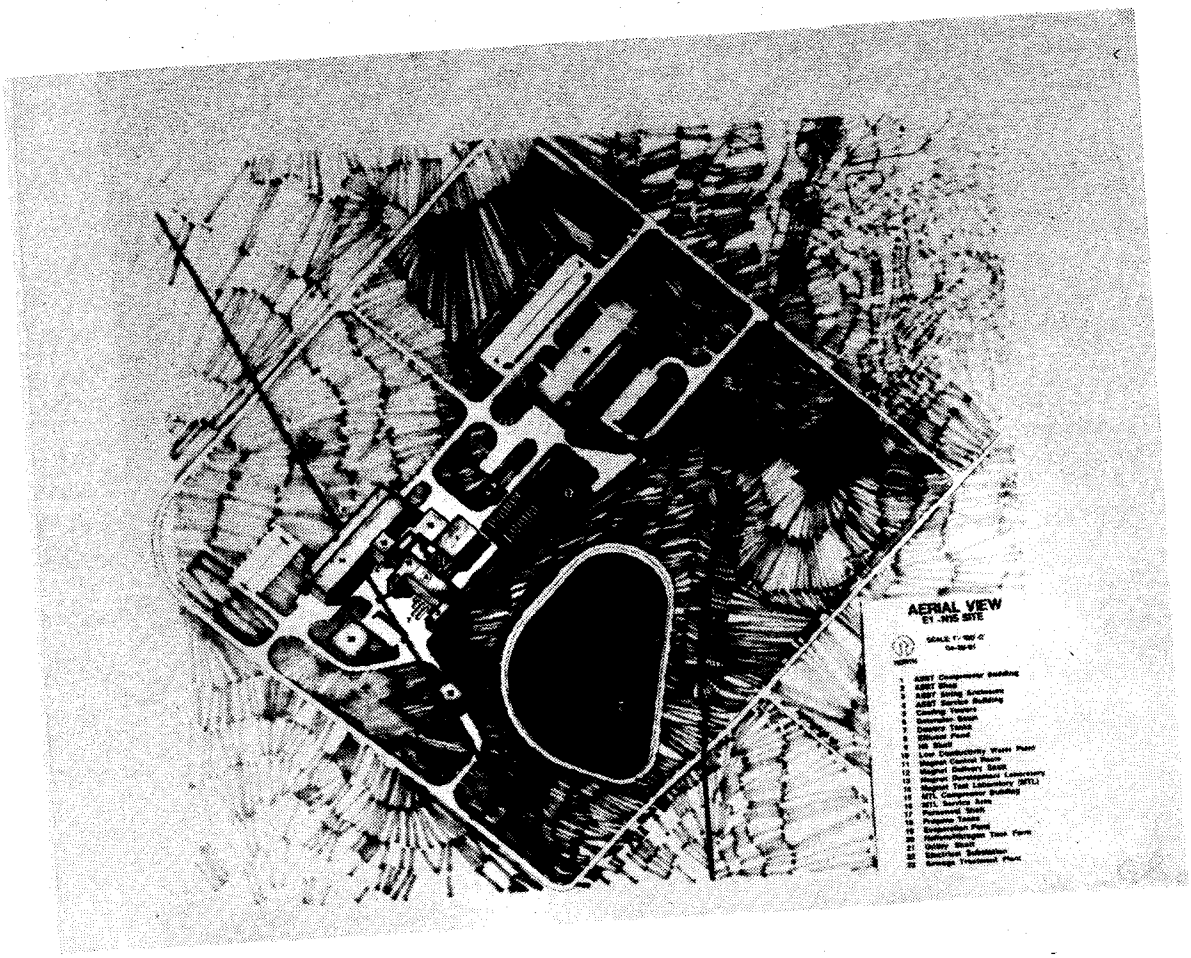



PLAN
SECTION A
SECTION B
NOTES:
2 FOR ALL STRUCTURE DIMENSIONS SEE DRAWING C302
3 ALL EQUIPMENT SIZES AND WEIGHTS ARE APPROXIMATE

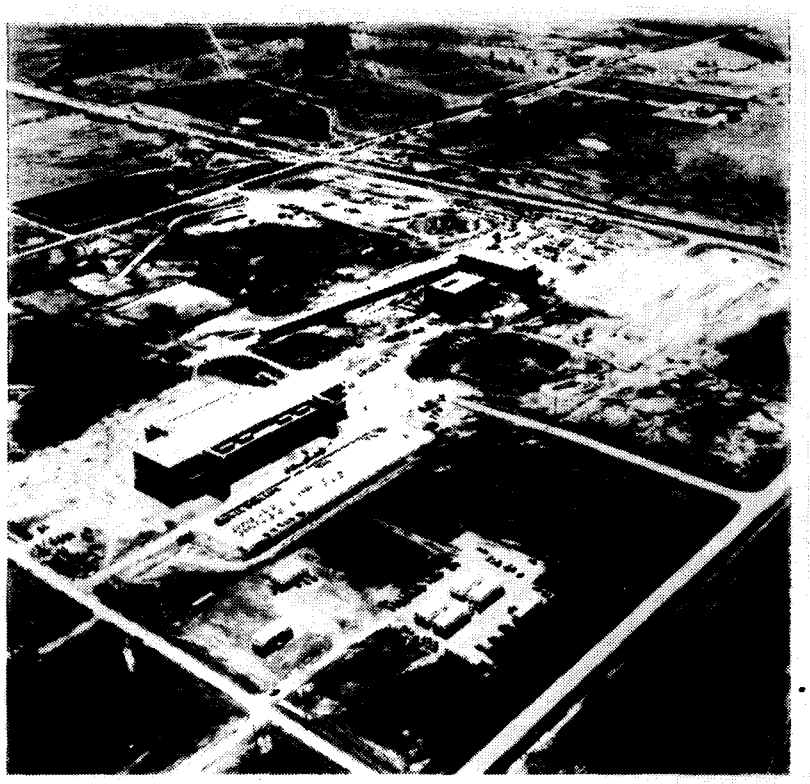







AERIAL VIEW





E1 - COMPARISON OF B.C.E. & CURRENT PLAN

W.B.S		BASELINE SCOPE	BASELINE $K	CURRENT PLAN SCOPE	CURRENT PLAN $K
	FACILITIES				
2.4.2.2	MDL		9,234		9,805
2.4.2.1	MTL		4,570		4,570
	MTL COMPRESSOR BUILDING	(a)	0		1,284
	MTL REFRIGERATOR	(a)	0		614
2.1.6.25	ASST	(b)	3,602		3,802
2.1.6.2.2.1	E1 HEADHOUSES/SERVICE	1-req'd	1,021	3-req'd	1,395
2.1.6.2.2.2	E1 COMPRESSOR	(b)	1,210		1,210
	Subtotal		19,637		22,480
	SHAFTS				
2.1.6.2.1.1	E-1 MAGNET DELIVERY	1-55'	3,424	60 x 30	2,531
	PERSONNEL		0	21' DIA	636
	UTILITY		0	18' DIA	899
2.1.6.2.1.2.2	CONNECTING TUNNELS		983		1,474
2.1.6.2.1.3	INSTALLED SYSTEMS		893		601
	SHAFT COVER/SHEILDING		0	(c)	538
	Subtotal		5,300		6,679
	INFRASTRUCTURE				
2.3.3	ROADS/PARKING/FLATWORK		1,714		1,620
	OFFSITE ROADS		0		982
2.3.3	COMMUNICATIONS		623		200
2.3.3	GAS		118		163
2.3.3	SEWER/STR REGRADING		662		1,403
	SEWAGE TREATMENT PLANT		0		1,117
2.3.3	DOMESTIC WATER		292		364
2.3.3	INDUSTRIAL WATER		540		100
2.3.3	FIRE		1,255		687
2.3.2	ELECTRICAL		587		1,721
2.3.3	SITE LIGHTING		86		50
2.3.2	SPOILS		232	(d)	232
2.3.2	PONDS/COOLING TOWERS		1,708		1,823
2.1.6	E1 TRANSFORMERS & SWITCHGEAR		2,058	(e)	1,500
	Subtotal		10,685		11,942
	EQUIPMENT				
1.2.4.1	MDL EQUIPMENT		7,790		7,790
1.2.4.2	MTL EQUIPMENT		29,984		29,984
1.1.6.0.13.2	INDUSTRIAL WATER		707		707
1.1.6.0.11	ASST CRYO SYSTEMS (also WBS 4.2.1)		21,245	(f)	16,388
1.1.6.8.19	CONTROLS		6,046	(f)	9,046
1.2.3.1.2.3.4	ASST MAGNETS (also 1.2.3.1.1.3)		3,340	(f)	3,340
4.2.1	ASST EQUIPMENT(from R&D)		23,459	(f)	23,459
	Subtotal		92,571		97,714
	MISCELLANEOUS MTL ELECTRIC	(g)	5		1,200
	TOTAL		127,583		130,015

NOTES:

No fees or contingencies are included in the above costs

(a) These facilities were specified as vendor supplied in the SCDR

(b) Money budgeted for ASST includes funds to increase compressor size

(c) Req'd for three shaft alternative

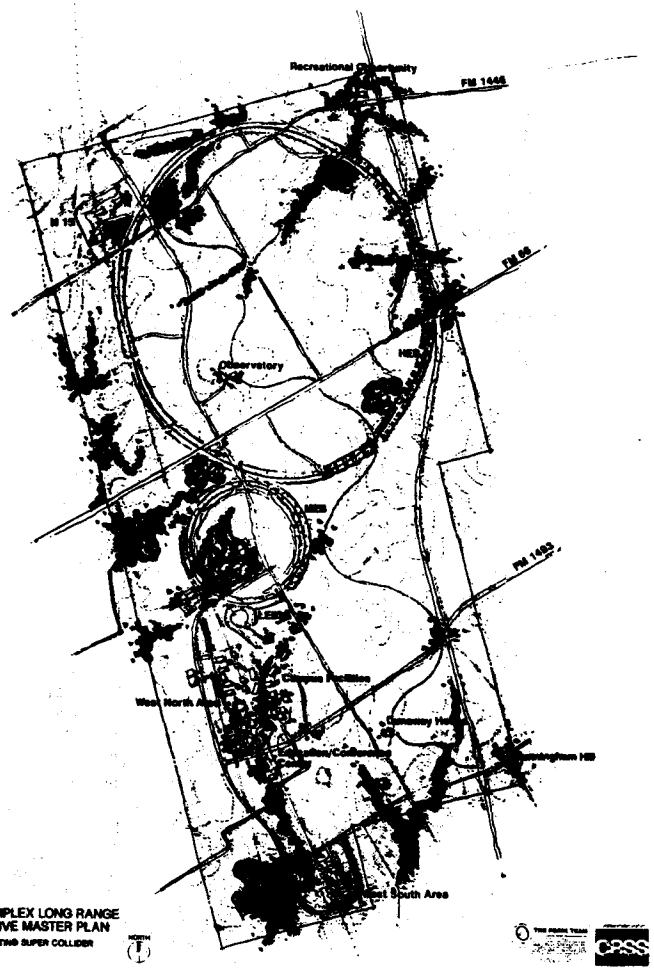
(d) Part of the first collider tunnel contract

(e) Allowance for future collider transformers/switchgear for collider

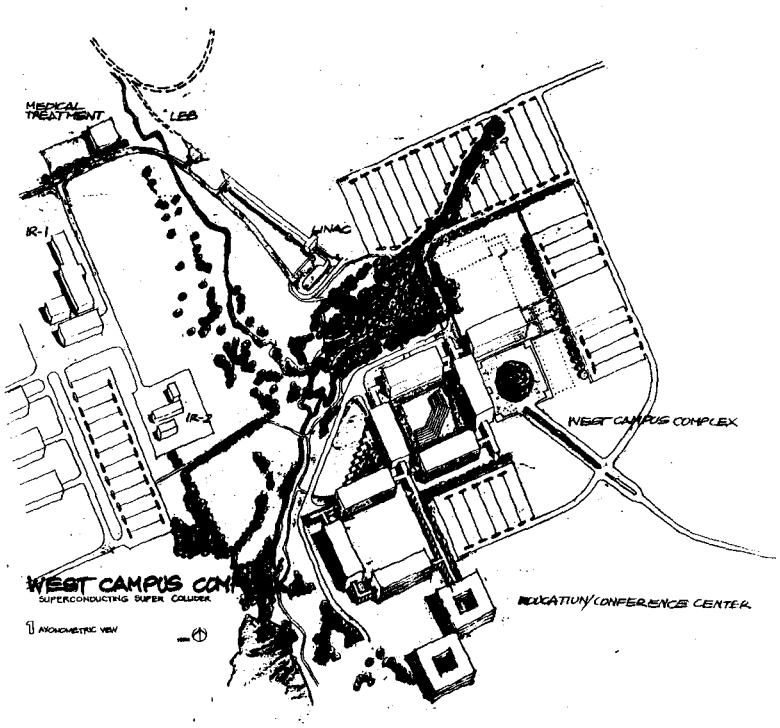
(f) The current numbers represent the figures given to OMB

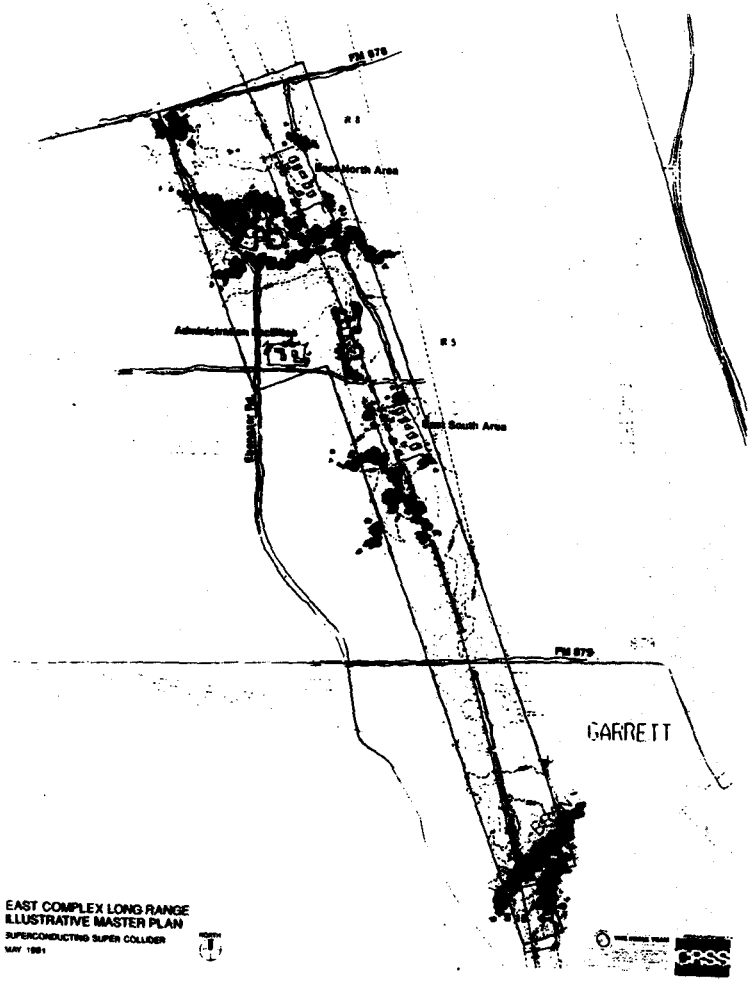
(g) This electrical cost required for transformers, switchgear and cooling req'mnts in the MTL. It was not budgeted in the BCE

8/27/91



WEST COMPLEX LONG RANGE
ILLUSTRATIVE MASTER PLAN
SUPERCONDUCTING SUPER COLLIDER
MAY 1991

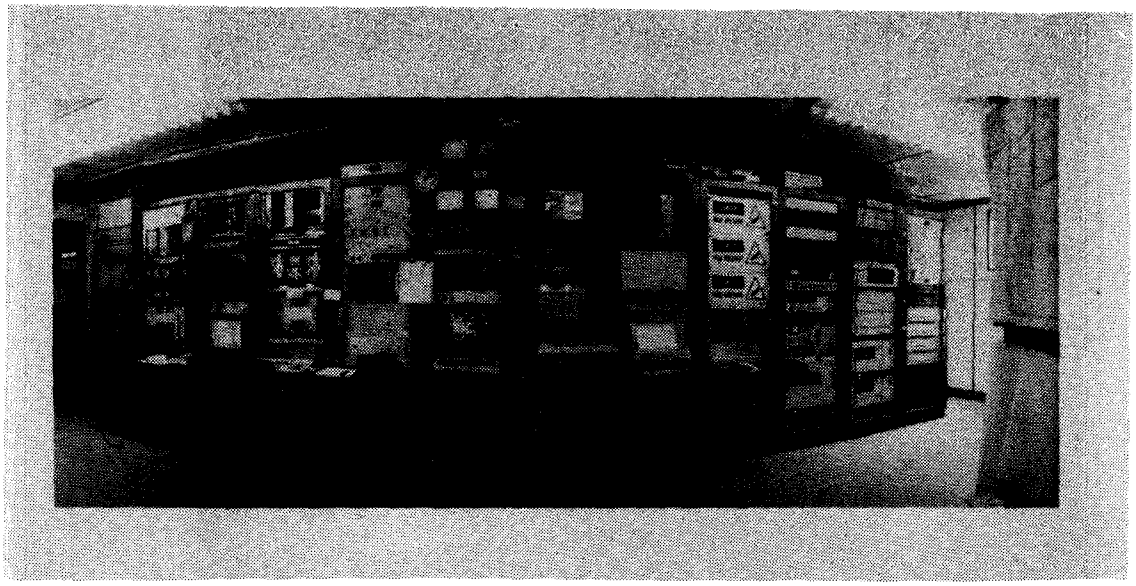

MEDICAL TREATMENT
LEB
IR-1
HVAC
IR-2
WEST CAMPUS COMPLEX
EDUCATION/CONFERENCE CENTER
WEST CAMPUS COM
SUPERCONDUCTING SUPER COLLIDER
AXONOMETRIC VIEW


FM 879
R 4
R 5
FM 879
GARRETT
EAST COMPLEX LONG RANGE
ILLUSTRATIVE MASTER PLAN
SUPERCONDUCTING SUPER COLLIDER
MAY 1991
DPSS

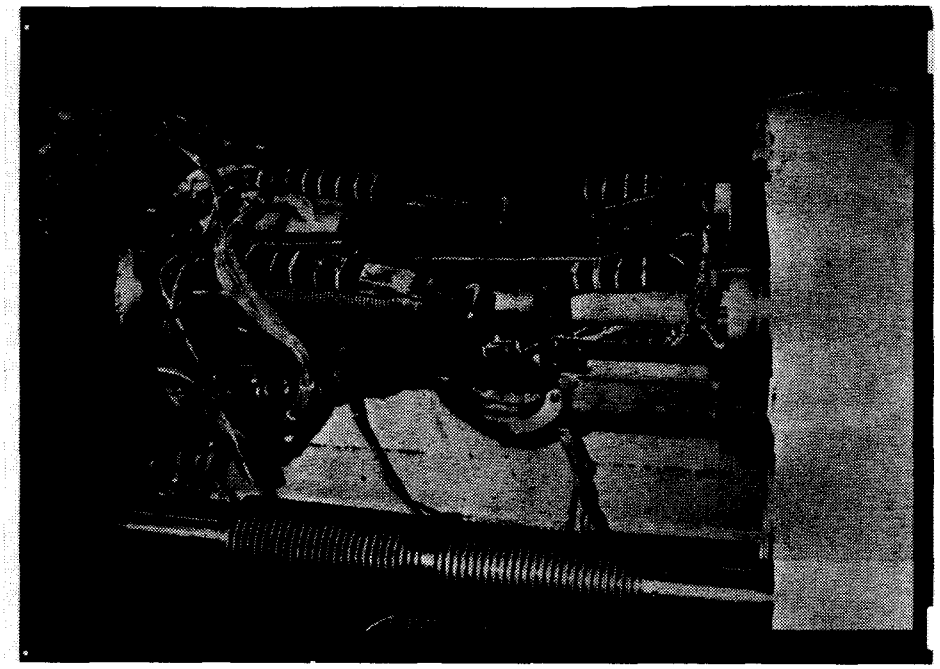
THE SUCCESSFUL COMPLETION OF MAJOR GOALS IN THE 40-mm APERTURE MAGNET STRING TEST

- ON AUGUST 30, SSC LABORATORY, IN CONJUNCTION WITH FERMILAB, SUCCESSFULLY COMPLETED POWER TESTS ON A STRING OF 40-mm APERTURE DIPOLE MAGNETS
  - First Demonstration of a String of Prototypic SSC Magnets Operated At Currents Required for the SSC Collider
  - This String Test Used the Earlier 40-mm Aperture Prototype Magnets, The String Test In Texas Next Fall Will Use the New 50-mm Aperture Magnets Which Are Presently Under Construction
- THESE SLIDES WILL COVER:
  - A Description of the String Test and Facilities
  - The Major Results Obtained to Date From the Test











D-66-3

RESULTS FROM THE 40-mm MAGNET STRING TEST AT FERMILAB

- Cold Mass Region Instrumented, Welded and Vacuum Tested in five Months--Required much Retrofitting with the 40-mm Aperture Magnets
- Required Two Weeks (6 Interconnects/6 People) to Install the Heat Shields--Prototypes for the 50-mm Magnets
- Cool Down Required Five Days (Implies 7 for ASST)
- Refrigerator Modified to Cool to Less Than 4.0K
- Ramped the Magnets to Their Design Goal of 6500A, and Held There for Many Hours
- No Major Surprises--All Data Were Within Manageable Ranges. But There Were Some Unexpectedly High Voltages Generated, Even a Double Quench and Magnet Training
- Preliminary Heat Leak Measurements to 20K Shield Larger Than Budget, But Problems in Old Magnet Insulation Have Been Corrected in 50-mm Magnets
- Using Blow Through of Llquid He at 500 l/hr it took 4 Hours to Recover From a High Current Quench
- Much Data Taken on Pressures and Voltages Generated During Quenches

- CURRENT PLANS:
  - Powering String with First SSCL Power Supply
  - Preparing for ER Spool Installation

THE SSC 1991 SYMPOSIUM AT CORPUS CHRISTI

THE ACCELERATOR SYSTEMS STRING TEST AT THE SSCL

- THE ACCELERATOR SYSTEMS STRING TEST (ASST) WILL TAKE PLACE IN TEXAS NEXT FALL AND WILL USE THE COLLIDER PROTOTYPIC 50-MM APERTURE MAGNETS
  - This String Test Will Use the First Industrially-Fabricated Collider Dipole Magnets
  - The Test Will Demonstrate the Operation of a String of SSC Magnets Comprising the Basic Sub-Unit for the Collider (a Half Cell)
  - Cryogenic, Electrical, and Magnet Safety Systems Will Also Be Demonstrated In This Test

- THESE SLIDES WILL COVER:
  - A Description of the String Test and Facilities
  - The Current Status Of the ASST Components

PROGRESS IN THE ASST--MAGNETS

•THE 50-mm APERTURE DIPOLE MAGNET PROGRAM:

BNL/Westinghouse: Four-1.8 m and Seven-15 m Dipoles

FNAL/General Dynamics: Six-1 m and Thirteen-15 m Dipoles

•DIPOLE MAGNET PRODUCTION:

- •Retooling for the Long 50-mm Dipoles Finished at BNL and FNAL
- •Training of General Dynamics/Westinghouse Personnel at FNAL/BNL Very Successful
- •Six Long 50-mm Dipoles in Various Stages of Fabrication at FNAL; Prototype Ready for Cryostat
- •BNL Prototype Dipole Being Installed in Cryostat
- •Test Stands at BNL/FNAL Converted for 50-mm Dipoles and Had a Test Cooldown at FNAL on October 10

•QUADRUPOLE MAGNET PRODUCTION

- •First Prototype Quadrupole Cold Mass Successfully Tested at LBL; Ready for Cryostat at SSCL

PROGRESS IN THE ASST--ACCELERATOR TECHNICAL SYSTEMS

•REFRIGERATION

- •Fabrication on Schedule, Installation to Begin in November

•POWER SUPPLIES

- •First Power Supply Delivered to FNAL and Successfully Powered 40-mm Aperture Dipole String Test
- •Five Other Supplies Due in October

•QUENCH PROTECTION SYSTEM

- •Final Procurement Begun For All Systems

•SPOOL PIECES

- •Power Lead Design Successfully Tested at FNAL
- •Orders Have Been Placed for All ASST Spools
- •Prototype Spool Delivered to FNAL to Be Installed in 40-mm Aperture Dipole String Test

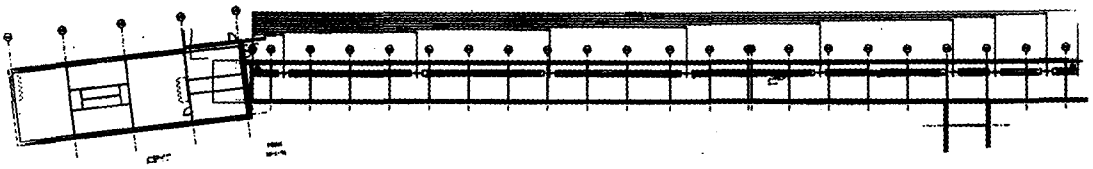
•CONTROLS SYSTEM

- •Electronics Being Installed in Controls Trailer
- •Prototype Electronics Demonstrated at FNAL

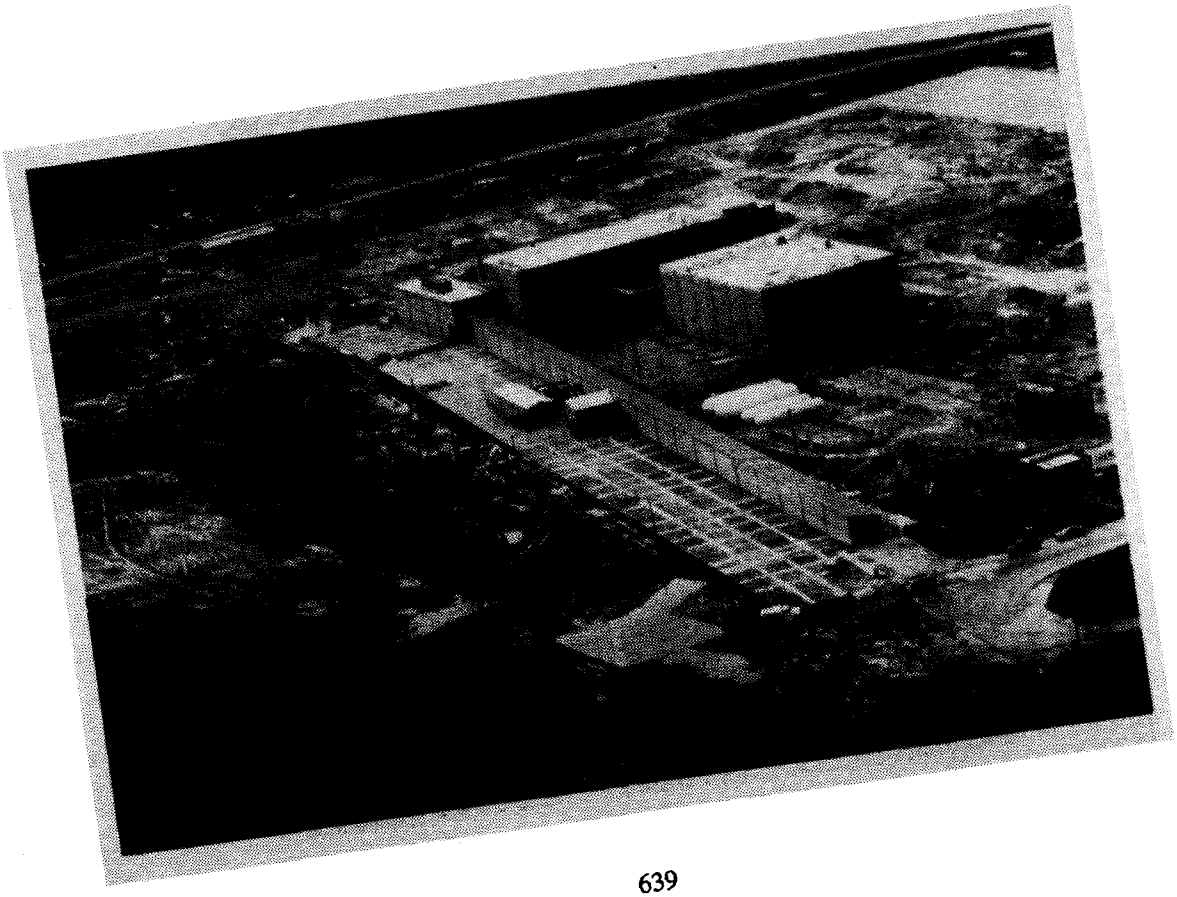
•GENERAL INSTALLATION OF ASST COMPONENTS

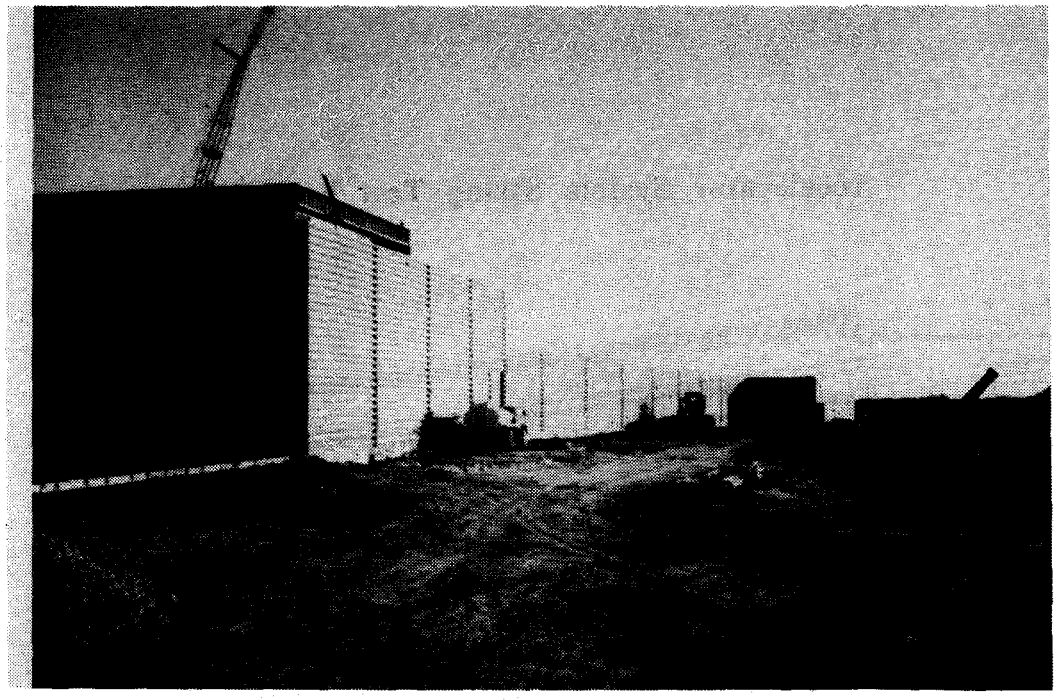
- •Preparing Vacuum Equipment
- •Installation of Magnet Stands, Headers, Cables, etc. to Begin in November

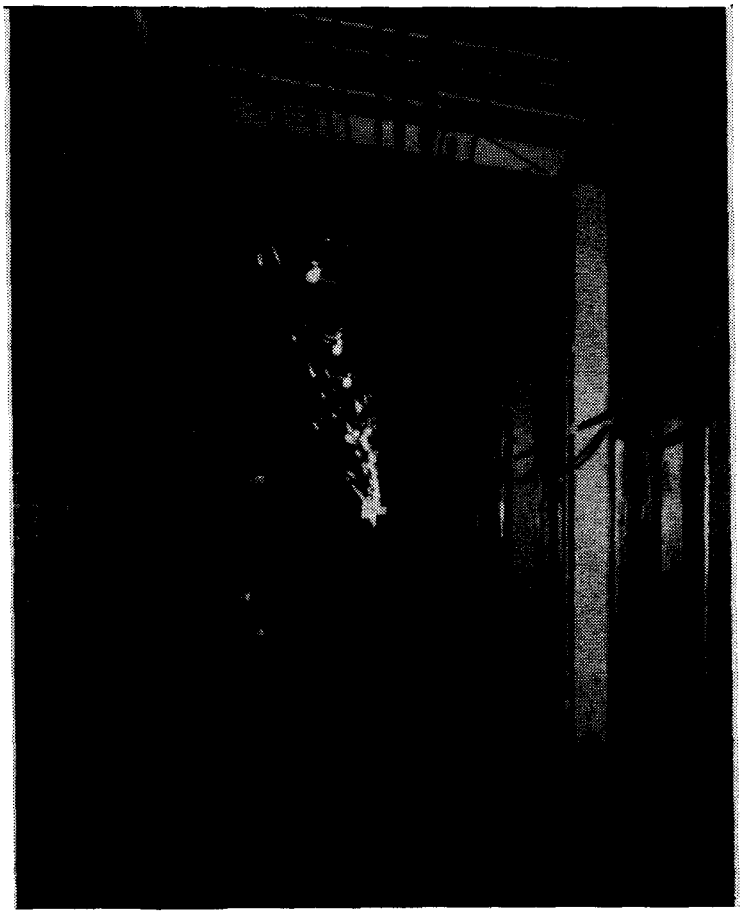
Accelerator System String Test Layout

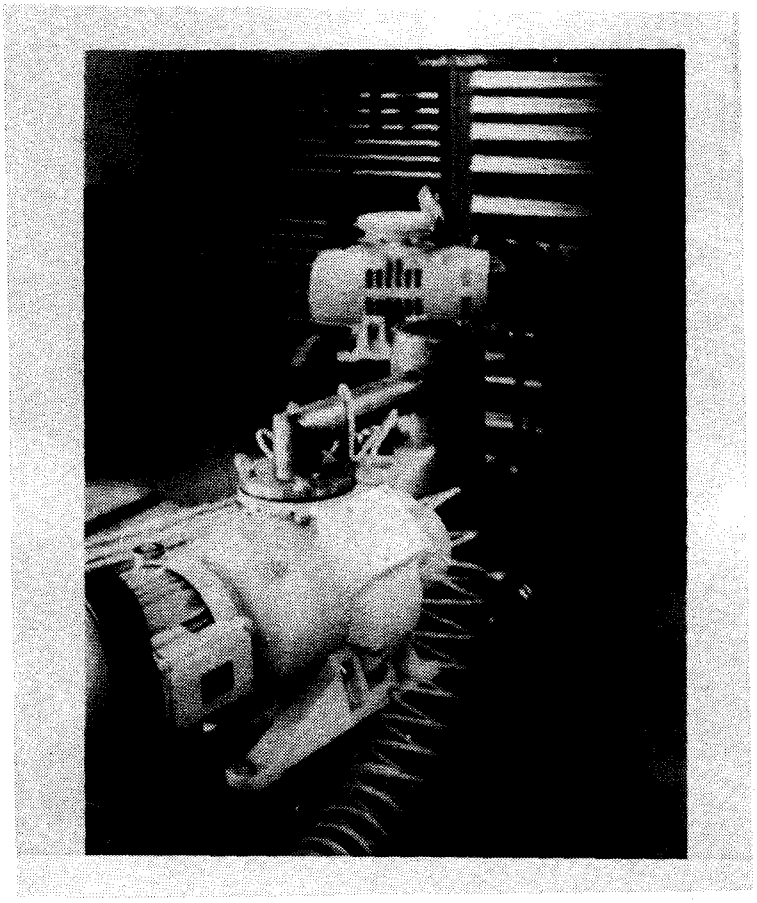


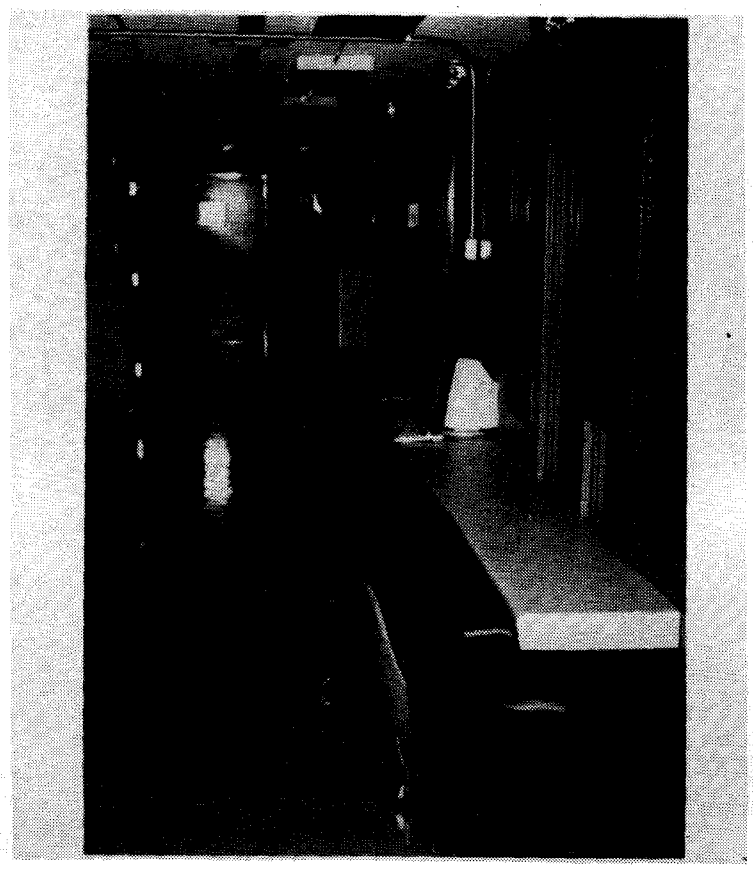
String includes five dipole magnets (each 17-m long), one quadrupole magnet and three spool pieces. Refrigeration and power connections made at the left end of the string.

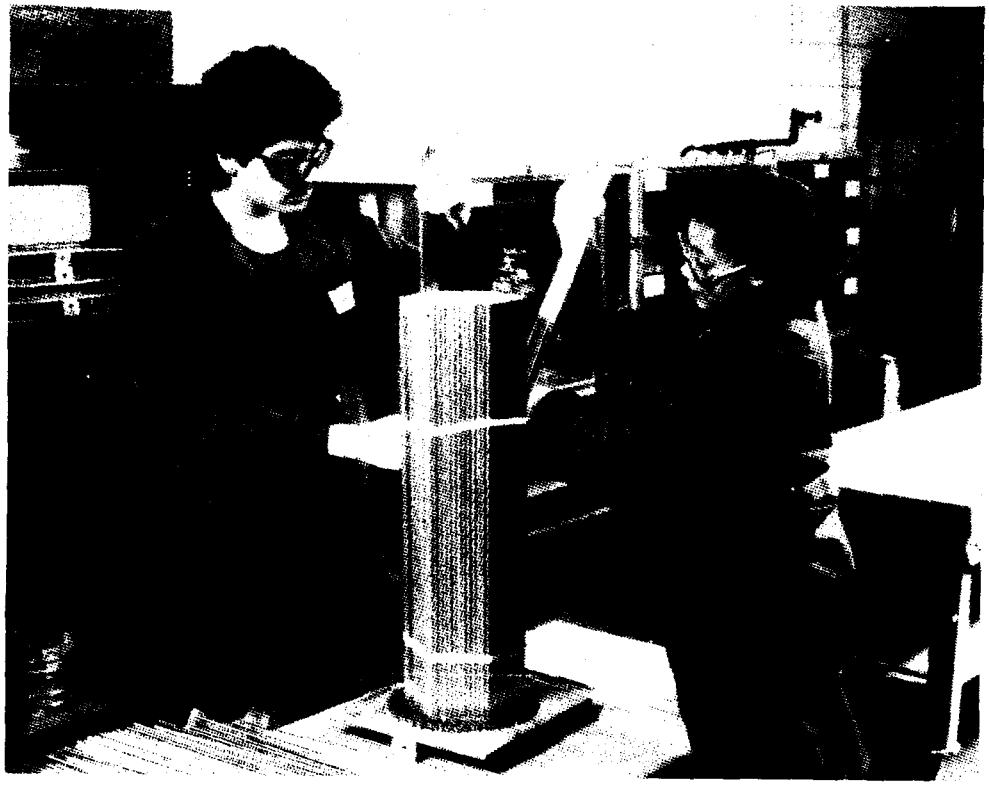


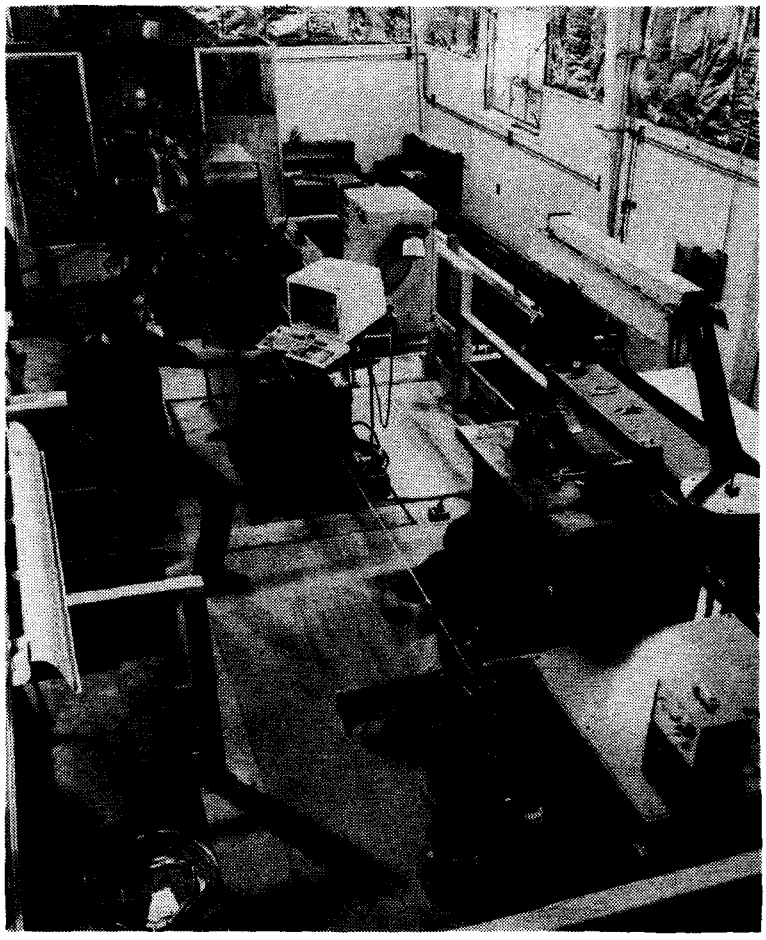


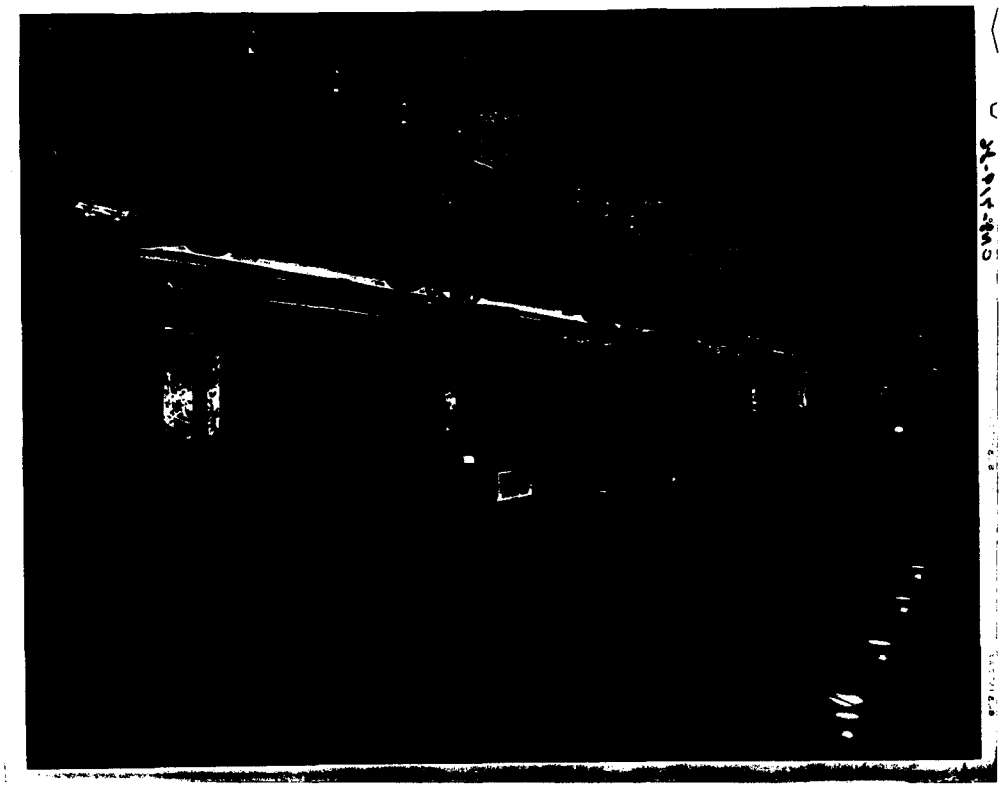








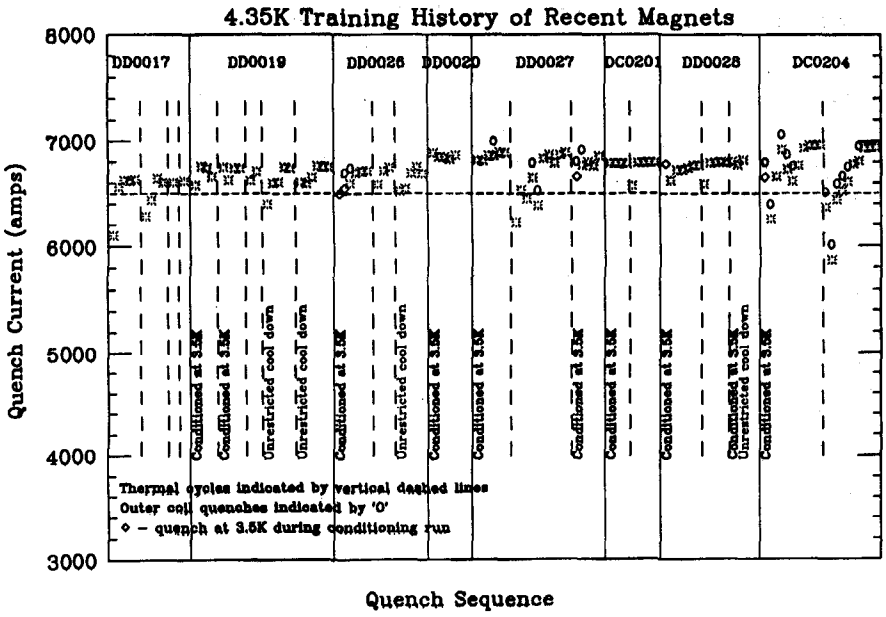


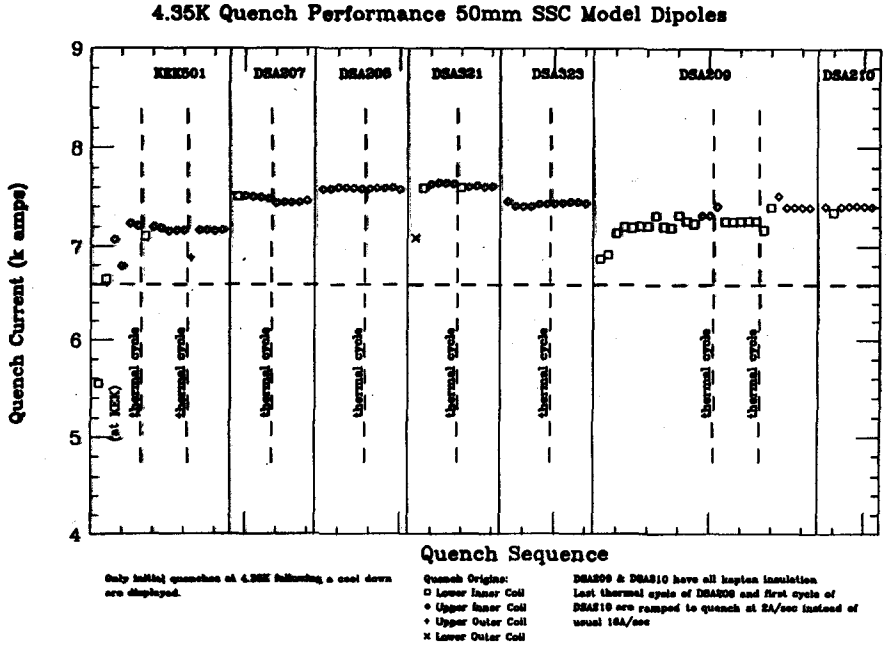


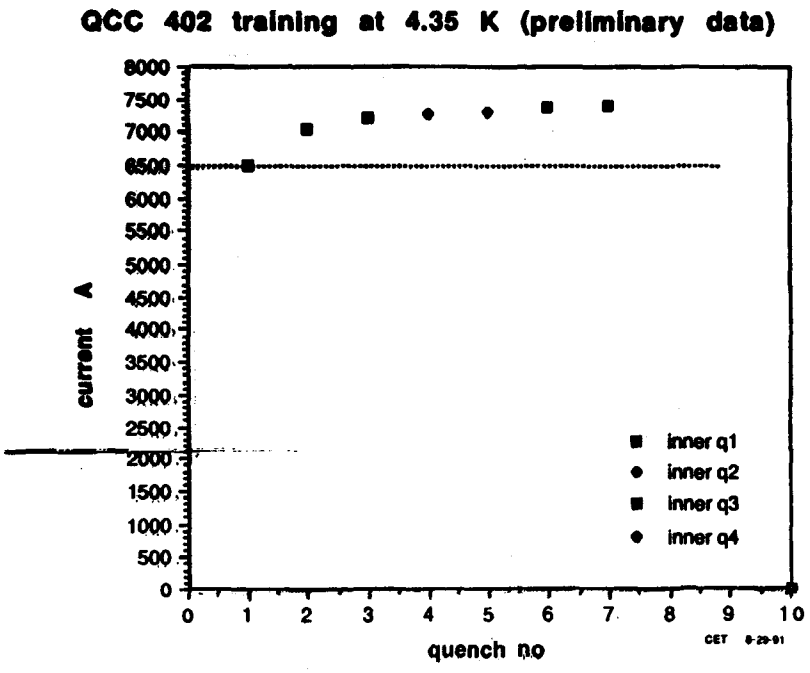


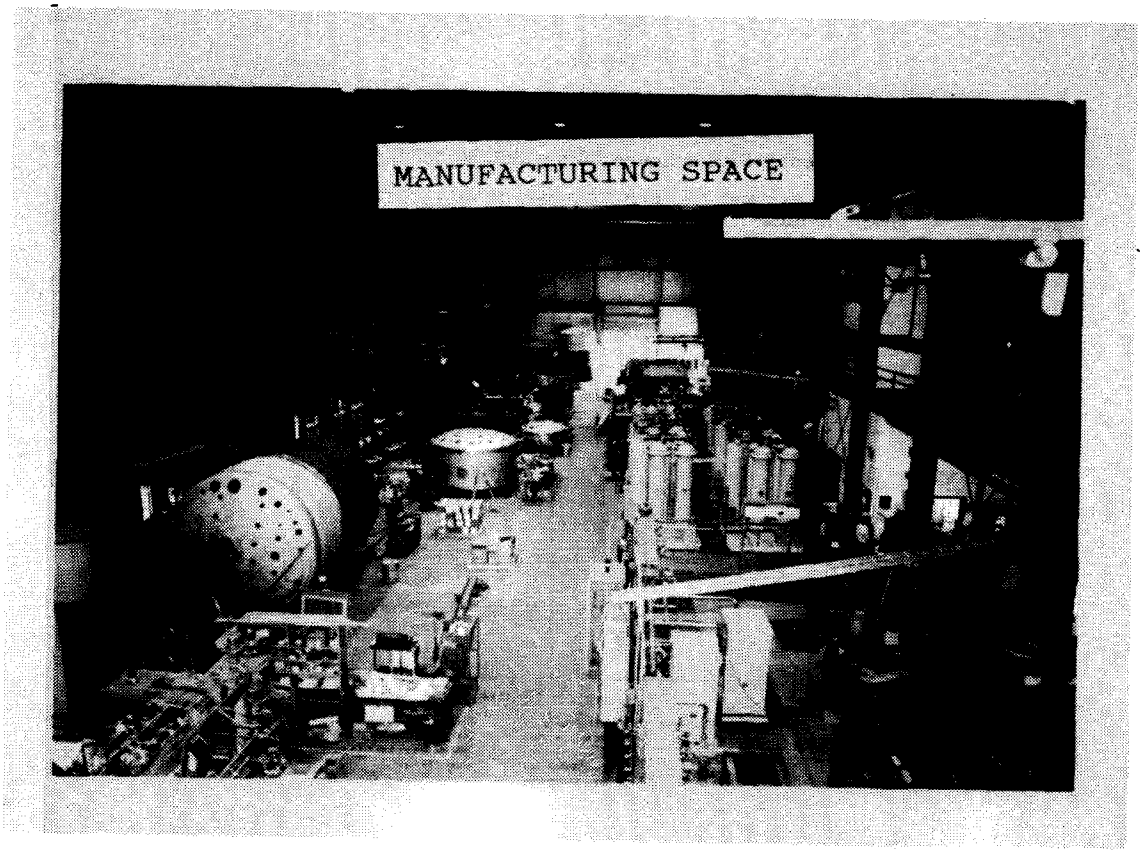


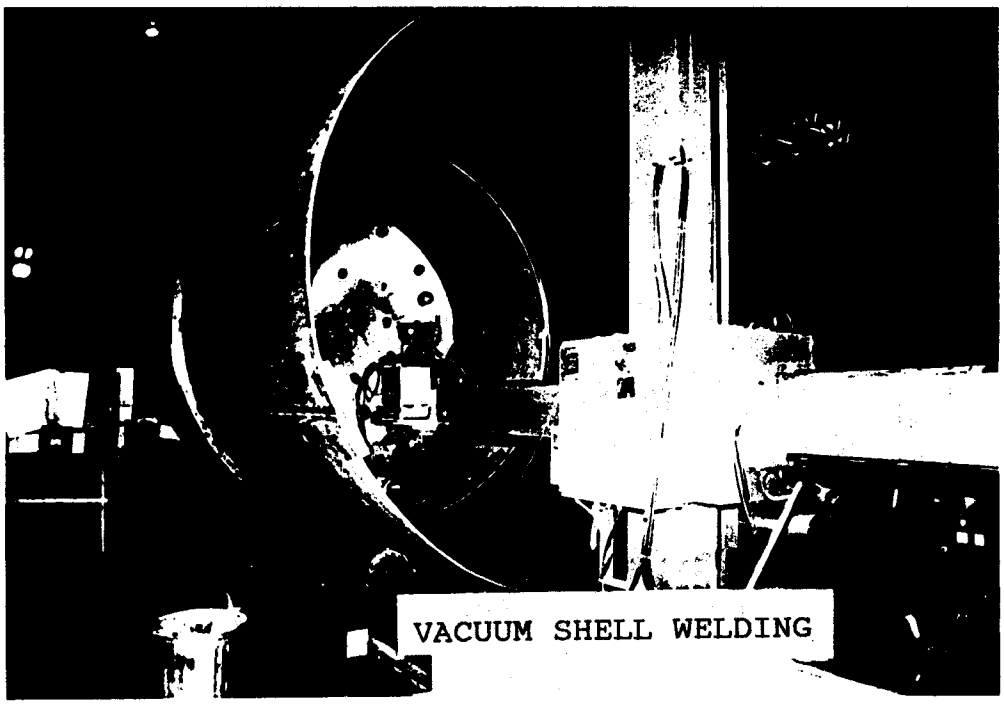


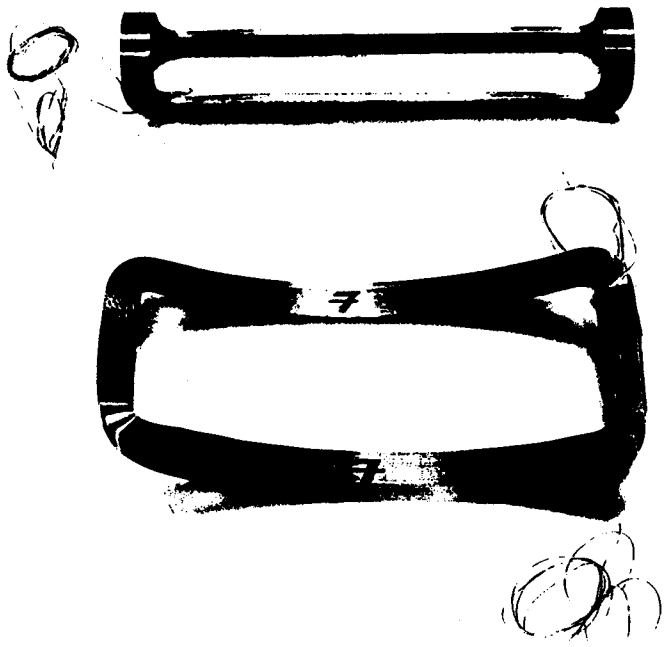

4.35K Training History of Recent Magnets
DD0017
DD0019
DD0026
DD002D
DD0027
DC0201
DD0028
DC0204
Quench Current (amps)
8000
7000
6000
5000
4000
3000
Conditioned at 3.5K
Unrestricted cool down
Thermal cycles indicated by vertical dashed lines
Outer coil quenches indicated by 'O'
◇ – quench at 3.5K during conditioning run
Quench Sequence

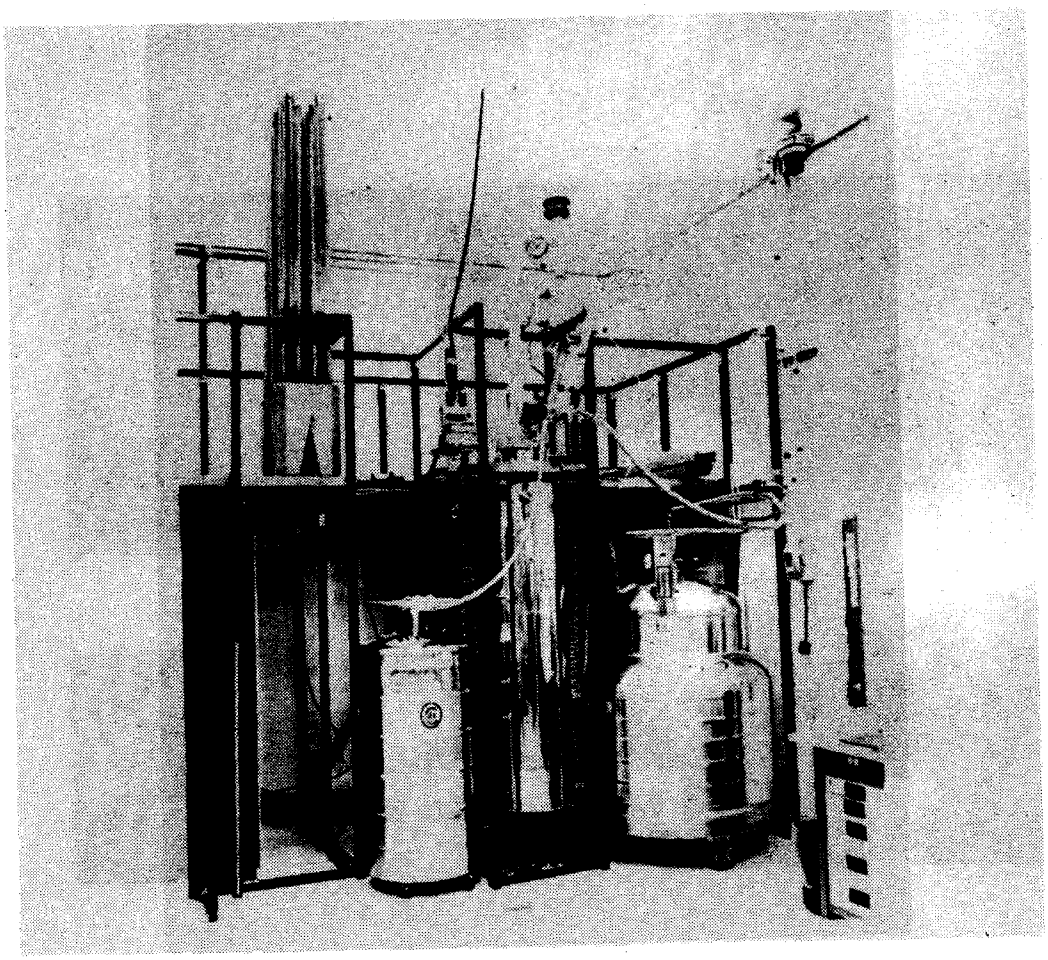

4.35K Quench Performance 50mm SSC Model Dipoles
HEK501
DSA207
DSA206
DSA221
DSA223
DSA209
DSA210
Quench Current (k amps)
9
8
7
6
5
4
(at HEK)
thermal cycle
Quench Sequence
Only initial quenches at 4.35K following a cool down are displayed.
Quench Origins:
□ Lower Inner Coil
◇ Upper Inner Coil
◇ Upper Outer Coil
× Lower Outer Coil
DSA209 & DSA210 have all kapton insulation
Last thermal cycle of DSA209 and first cycle of DSA210 are ramped to quench at 2A/sec instead of usual 10A/sec

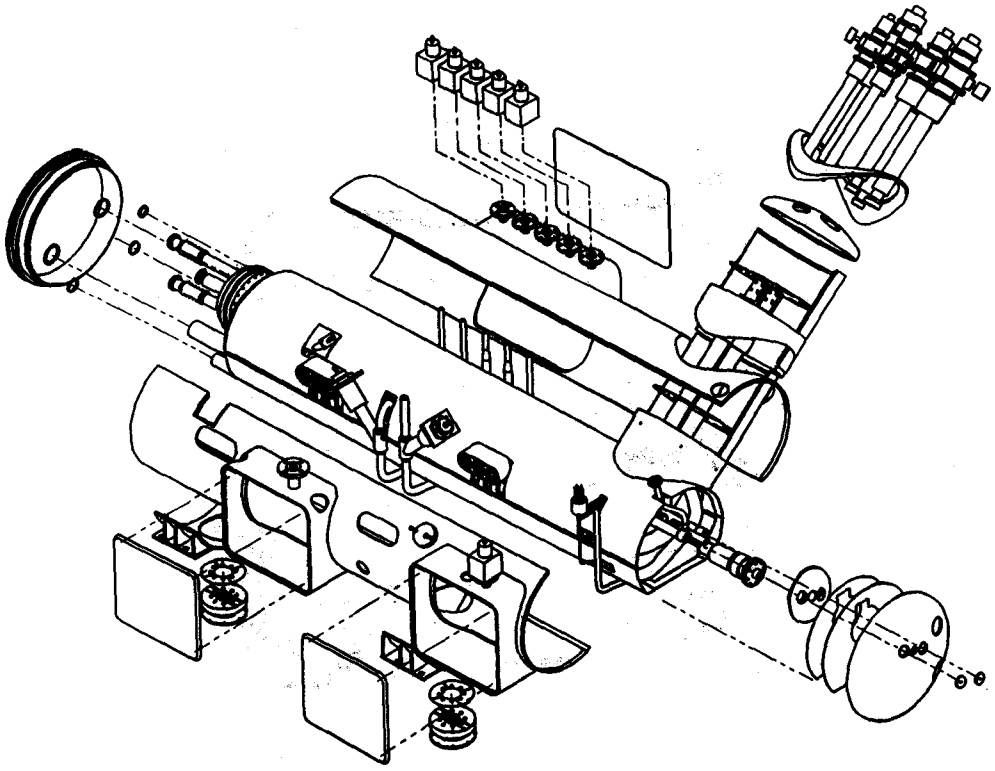

QCC 402 training at 4.35 K (preliminary data)
current A
quench no
inner q1
inner q2
inner q3
inner q4
8000
7500
7000
6500
6000
5500
5000
4500
4000
3500
3000
2500
2000
1500
1000
500
0
0 1 2 3 4 5 6 7 8 9 10
CET 8-29-91


MANUFACTURING SPACE

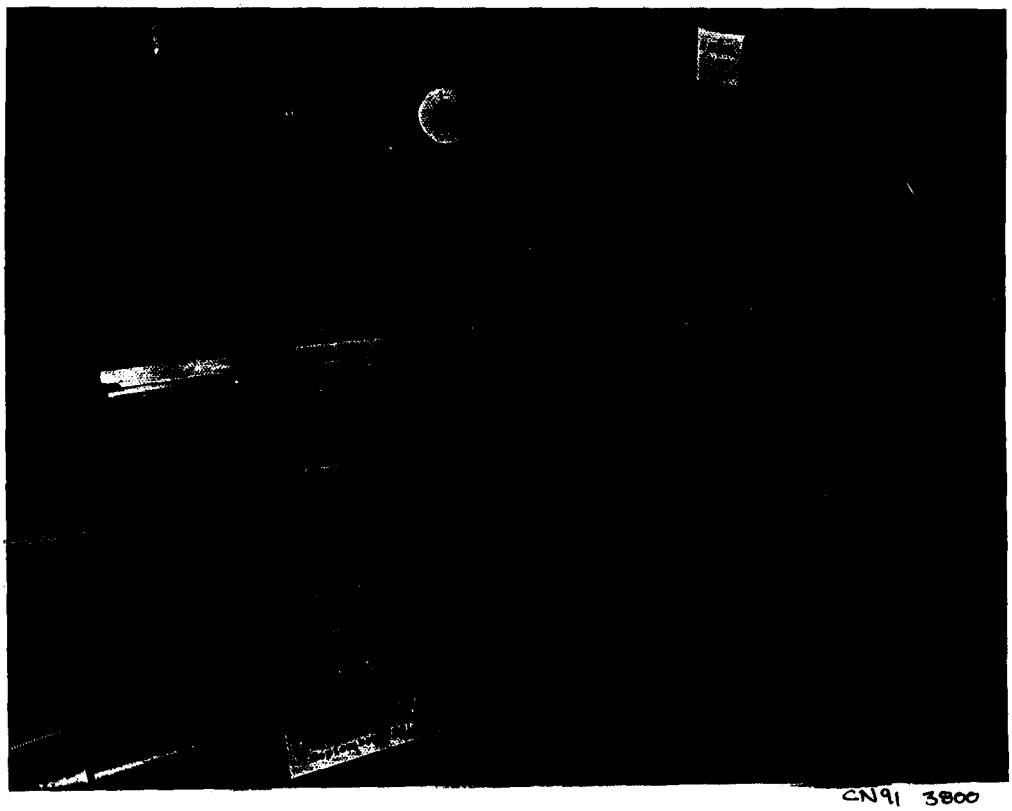

VACUUM SHELL WELDING










CN91 3800

Status of Detector Facilities

- Based on studies by the A/E firm PB/MK, the location of the large general purpose detectors among the four IRs will be determined within the next month.
- Based on this siting decision, user requirements for the SDC detector will be established in preparation for the start of Title I design by PB/MK. This work is well along and needs only a few weeks for completion.
- User requirements for the GEM detector will be ready for start of Title I design in January.
- Establishing requirements for surface facilities is very dependent on the location of the detector. Many models have been developed, and a general knowledge of floor space requirements exists for each detector. The Muon Chamber Assembly building for SDC and the Coil Assembly building for GEM are critical path items.

10/15/91

What Lies Ahead?

J. D. Bjorken

What Lies Ahead?*

James D. Bjorken
Stanford Linear Accelerator Center
Stanford University, Stanford, California 94309

1. Introduction

I begin this talk with a self-introduction. I am a person often asked to give talks with titles like the above. In checking out the record, I found the rate over the last decade is somewhere around two a year. I frankly have gotten a little tired of giving them, and even more tired of having to listen to others give them. You are forgiven if you feel the same way about this one. But this talk may be a little different, just as the SSC experience is a little different from the experiences in physics that have preceded it.

Another part of my history I want to mention has to do with SSC. I am one of the rare birds in U.S. high energy physics that did not support the SSC initiative back in 1983–1984. And here I am, not only giving a closing talk at an SSC jamboree, but also involved in a nontrivial way in expressing interest in its experimental program. So I feel the need to explain myself in a few words as to where I was then and where I am now. The history of those years do condition my present viewpoint, which is after all what I was asked to present.

In 1983 I was advocating a site-filling collider at Fermilab as the next step in the U.S. program, to interpolate between Tevatron and the LHC, with an SSC or something else to come later. The idea went nowhere, although in Europe I find to this day some sympathy for it. My concern about the SSC initiative was not that it was scientifically wrong—on the contrary I have always felt that it is scientifically superb—but that such a large next step was a very high risk to take, and that many years would be required to get the SSC off the ground, with a high probability of failure of the whole venture.

I am happy to admit that my political judgments were off the mark. The SSC initiative has consistently progressed more rapidly and successfully than I guessed it would. The public, be it the grass roots, the state of Texas, the Congress, or the administration, has been supportive to a most impressive degree. And I see this support to large extent as originating from the right reasoning—not from considerations of the quark-barrel or spinoffs, but in terms of fundamental values and the major advances in basic science that the SSC should provide.

So I stand here, delighted to witness the SSC project well underway. There may be delays and obstacles and no shortage of difficulties, but someday those 20 TeV beams will be there colliding with each other. With this reality comes a recognition of the overwhelming obligation the high energy physics community has

* Work supported by the Department of Energy, contract DE-AC03-76SF00515.

in following through in every way possible to help make those collisions occur. And before that happens there are sure to be some pretty tough times.

2. Discoveries

I do not want to dwell on those difficulties, especially since my morbid thoughts regarding SSC in the past were somewhat ill-considered. Rather I prefer to concentrate on the reasons why I have always been highly enthusiastic about the physics of the SSC. They go well beyond the generally cited Big Three of Higgs, supersymmetry, and compositeness. My enthusiasm is based simply on the general, very familiar line of argument for the intangibles; that the increase of a factor 20 in cms energy and 1000 in luminosity from what we now have is an extraordinary advance in sensitivity to new—and old—phenomena. The usual arguments regarding the TeV mass scale are, at the least, strongly suggestive that there will be really new physics available in this new parameter domain. And all the "old" physics, be it bottom quark or W physics or whatever, will be present in much greater abundance at the higher energy. One must keep in mind that thorough study of old physics can be a major avenue to big discoveries. And there are new frontiers at low mass scales as well which cry out for incisive exploration at the SSC. This subject is my preoccupation nowadays and I will return to it later. Putting together all the various opportunities, I believe a well-conceived and well-supported SSC physics program could have the breadth and diversity represented by, say, the entire Fermilab program, fixed target plus collider.

This point is to me central. Hadron-hadron collider physics is really different from electron-positron physics. The SSC program should be qualitatively different from the LEP program. There the event rate is so low that there is only one winning strategy, namely to accept every event and examine it with the best 4π detector one can make. True, the highest-mass scale SSC physics bears similarity to this. But even in that case there is, for the pp collisions, useful supplementary information in the beam directions to be had, possibly demanding novel strategies and unconventional extensions of generic detector design. And there is the ubiquitous problem of event selection to deal with—is the right physics being chosen? Ultimately the answer is that the whole spectrum of SSC physics at all mass scales deserves a thorough examination. This is a big order and may well require a set of detectors with as much variety as one finds in Fermilab/CERN fixed target experiments. For this reason I put the scientific longevity of the SSC as very large, at least 50 years.

Whatever the mass scale, it is the discovery physics, not the programmatic physics, that provides the primary motivation for most experimental physicists to undertake the great hardships involved in mounting experiments. It is interesting that nowadays, with our standard-model conditioning, the very concept of discovery seems increasingly circumscribed. It is the class of discoveries that may be called "engineered" which seem to dominate present thinking. The discovery of the W and Z, as well as the anticipated discoveries of the top quark or standard-

model Higgs, fall into this category. One knows enough about the properties of the hypothesized particle or phenomenon that a well defined search strategy can be defined. With the success of the standard model this mode of discovery becomes increasingly the dominant one. We see large tomes written for the Higgs hunters or SUSY hunters, detailing in advance how to make the Great Discovery. But one thing for sure is that almost all the words in the Higgs Hunter's Guide[1] on how to find a nonstandard Higgs are wrong. There are so many mutually incompatible scenarios that generally what is on one page contradicts what is on another. Is it reasonable to average over a large number of wrong strategies in order to increase the odds of finding the right one?

The earlier history of particle physics abounds with examples of another kind of discovery, which can be called serendipitous. The discovery of strange particles or the muon are examples. The observation of the many hadron resonances in the early 1960's is another. CP violation lies on the edge. More recently I think the J and ψ arguably fall into that category. All these discoveries arrived largely without advance billing, with theoretical prophets having little if any significant part of the action.

In those simpler days the justification for the instrumentation which was responsible for those discoveries was much simpler. I am told that the proposal for the BNL AGS was a model of brevity. I know not whether there was even a proposal for the big Berkeley bubble chamber. But in any case I am pretty sure that it would not contain any simulations of the physics expected to occur. And even if it did, it is pretty certain that it would not have had much to do with the important results. Big bureaucratic SLAC did create fat documents. But again what went into the physics projections for the linac program, and later for SPEAR, bore little resemblance to what turned out to be the memorable experiments and discoveries.

Even some facilities have been in a sense serendipitous. The SPEAR storage ring did not emerge out of the national master plan, but in spite of it. The same can be said for the Cornell storage ring CESR. I know; I was on one of those committees that recommended against it.

Is there a future for the serendipitous discovery? I think the answer is affirmative. The problems of the electroweak sector are ripe for that kind of occurrence. There is much talk about the importance of WW scattering, just as there was much talk about $\pi\pi$ scattering in the early 1960's. The key to strong interactions was to be revealed by study of that process. But it was other degrees of freedom-quarks, gluons, strangeness, charm, ...—which were the real teachers of what goes on. The four Higgs degrees of freedom may well again be only indirect, and relatively uninteresting compared to those which are really behind the origin of particle masses.

It takes very little to change the phenomenology a lot. Yukawa predicted not only the existence of the pion but also its decay mode into electron and neutrino. If only the muon were to weigh twice as much as it does, he would have come out

ok. Certainly Yukawa is not to blame for the bad prediction. It is this kind of thing that makes me indifferent to SUSY phenomenology. Imagine someone telling you that there are three generations of quarks and leptons and that they interact via standard model couplings, with only the information on the mass matrix not given. I think it would be hard to reconstruct anything like the phenomenology we have. The details are everything.

I stumbled on an interesting, if morbid, example while working on my expression of interest for an SSC experiment.[2] I call it the dark Higgs sector.[3] Take the usual four Higgs fields and replicate them with four more which also undergo spontaneous symmetry breaking with similar self-interactions. However, the new particles have no charge or electroweak couplings whatever; they are "dark". So there will be three massless (or nearly massless, if there is some breaking of the new $O(4)$ symmetry) "dark" Nambu-Goldstone bosons I call k, as well as a new massive Higgs-like boson called S. The new "dark" states can interact with the usual Higgs degrees of freedom. The most important effect is the mixing of the heavy S with the usual Higgs. As a consequence of this, not only will the S decay into two k's, which most likely are as invisible as neutrinos, but so also will the ordinary Higgs. For a large range of parameters, this kk channel can overwhelm the usual Higgs decay channels. And were this the case, the usual SSC discovery modes of the Higgs particle would disappear, although the missing mass techniques used in the electron-positron world would still be available.

Yes, this is a priori an unlikely, contrived scenario. But the S and k were carefully named. WW scattering would reveal not only the usual Higgs resonance but also the S, just as $\pi\pi$ scattering reveals not only the σ but also the $S^*(975)$ resonance, coupled strongly to those "unexpected" Nambu-Goldstone modes, the K's. And the presence of an extra $O(4)$ symmetry for the dark sector, which commutes with all known symmetries, is maybe made more credible when one reflects on the fact that the key to the strong interactions as seen in the 1960's lay in a symmetry (color) which commutes with all symmetries known at that time. So the dark Higgs sector is no less incredible than what actually happened for the strong interactions. That does not increase the odds for this specific model, only for the notion that simple twists of the present thinking can change phenomenology and search strategies in a big way.

It is not only at the highest mass scales that the discoveries can occur. The J and ψ were for their time discoveries well below the energy frontier, as was the τ lepton. The b quark discovery was ideal for the Cornell electron-positron machine, much less so for its higher energy cousins at PEP and PETRA (although they made essential contributions to b-physics as well.) For the future, axions and SUSY particles are only two obvious classes of particles which might show themselves somewhere other than at the highest energy scale.

And the new low energy phenomenon need not be a particle discovery. A theorist friend of mine, Vadim Kuzmin, provided an extraordinary example of one to

me.[4] Ever since the 1967 Sakharov paper on the cosmological baryon asymmetry, Kuzmin has explored various aspects of baryon-antibaryon mixings and oscillations. According to him, there could still be a baryon-number violating coupling originating in particles of electroweak masses and coupling strengths, provided all three generations are simultaneously involved. Therefore he exhibits special interest in the Ξ_b (bus) baryon, which according to him might undergo a lot of mixing with its antiparticle. (See Fig. 1 for a little motivation for this craziness.) Yes this is wild, but think how it would change the wonderful world of b-physics were it to occur. Electron-positron b-factories running at the $\Upsilon(4S)$ would be out of it, as well as (probably) Z-factories. A high-powered dedicated b-experiment at a hadron collider would (probably) offer the best chance.

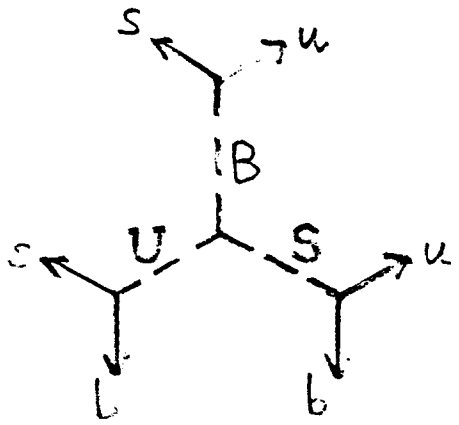


Figure 1. Kuzmin's Krazy Koupling. The dashed lines are color-triplet scalar fields; the solid lines are right-handed quark fields.

Of course there is also the present search for discovery physics in high-precision tests of the standard model. No new particles or striking new phenomena need be seen, only the disagreement of an accurate prediction for a number with an accurate measurement. These methods have been and are now truly beautiful to behold. But ultimately there is no substitute for seeing more directly the reason for a disparity—or for that matter an agreement—if that is what it comes down to.

Finally, there is the possibility of discoveries which do not go beyond the standard model but could be fundamental and interesting in their own right. I came across a possible example when working on the expression-of-interest, and am now exploring the issues together with Marvin Weinstein at SLAC. The measurement is as follows: Select events for which the multiplicity of produced particles is as large

as possible, but where there is no significant jet activity. Now plot the distribution in transverse momentum. At low transverse momentum, say 100 MeV and below, Weinstein and I predict a pion excess. So of course it will be there. Cut on that excess; it should exhibit Centauro and anti-Centauro behavior. That is, there should be large fluctuations in the charged-to-neutral ratio of the anomalous component. There should even be some events where all the anomalous excess is charged and there is no neutral component, and other events where all the anomalous excess is neutral and none is charged.

The idea was motivated by cosmic ray data,[5] although this is not the place to elaborate how that happened. And there are some accelerator experiments which point to phenomena something like this,[6] although I would not cite the evidence as anything except nonnegative "support". A good experiment is clearly not easy. Neither low-p_t charged particles nor neutral pions are easily seen in a generic central barrel detector, although in principle it can be done. It is not easy to dismiss the idea (or support it) on the basis of existing evidence.

What is the physics? The picture is that in a high energy collision with high associated multiplicity the spherical debris-shell emerging from the collision point is relatively thin, perhaps a fermi or so thick, and propagates outward at the speed of light. Eventually this shell turns into the dilute gas of hadrons expanding outwards and into the detector elements. But before the critical distance and/or time of hadronization ("decoupling", "freeze-out") one has an inner volume that has relaxed back to something approximating the vacuum, separated by the debris-shell from the outer vacuum. But the QCD vacuum is approximately degenerate because of the approximate chiral symmetry of the up and down light-quark system. So the chiral orientation of the vacuum, usually in the σ direction (we use the language of the linear σ-model), need not be the same in the volume interior to the debris shell, provided the surface-density of energy in the shell is sufficiently high. The actual orientation will be influenced by details of the specific collision at early times. Suppose the interior-vacuum orientation is deflected in the π^0 direction. Then, when at late times (of order the time of hadronization), the interior vacuum sees the exterior vacuum again, it will relax back to the "correct" vacuum by coherent emission of only neutral pions. Let f be the fraction of anomalous low-p_t pions which for a given event are neutral. Then, assuming that the direction in which the vacuum is disoriented is a random variable, the expected distribution of f should be inverse square-root, very different from what a statistical picture would give.

While this experiment does not require an SSC, it would be best done there. The reason is that the effect is anticipated to be more prominent the higher the associated multiplicity. The higher that is, the larger will be the hadronization radius R. The usual multiplicity of hadrons should scale as the area of the debris ell at decoupling, R^2, while the anomalous, coherent piece scales as the volume in the debris shell, R^3. Also, the quasi-macroscopic semiclassical arguments

used to bolster the theoretical picture are better justified the larger the space-time distance scales involved. In addition, it may be experimentally advantageous to choose a large mean rapidity for observing the low-p_t particles, because they then have a larger laboratory momentum.

This picture of disoriented chiral condensate is quite speculative. But I think it credible enough to merit experimental consideration. Were one able to see such a thing, one might learn useful things about the nature of the QCD chiral vacuum, a subject which is not at all in good shape theoretically at present. And this in turn might lead to useful spinoffs for technicolor theories. Without asking for it this subject therefore could be relevant to electroweak physics beyond the standard model.

3. Some General Concerns

The above examples do not qualify as candidates for serendipitous discoveries, because as soon as they are written down, an engineered search can be defined. On the other hand, had they not been written down, and if by some fluke one or another of them actually turned out to be true, they would qualify as candidates. But it is not so clear to me how well a generic physics program such as one finds in the big design books would do in making the actual discovery.

There is to me a big challenge of a new type facing this and future generations of experiments and machines. One cannot easily defend an expensive machine or detector on the basis of the physics of intangibles and serendipity. There must be an underlying warranty of productivity, not just for programmatic physics, but in fact for programmed searches for "engineered" discoveries. Otherwise the expenditures will not be deemed cost-effective. This in turn influences the design of machines and detectors, quite possibly in ways which inhibit their potential for stumbling on the unexpected.

Even more serious in my mind is the change in attitude this can engender. I see less rugged individualism amongst the newer generations of experimental physicists. This may be a false perception, because it is hard to see into the inner workings of big collaborations and how tolerant they are to those who would venture into unconventional directions. But there are certainly institutional inhibitions that have to be overcome. For example, high-risk innovative instrumentation is hard to incorporate into the large monolithic collider detectors, with their half- to full-decade lead-times and turnaround times. The possibility of failure is unacceptable. I have seen remarkable conservatism in the running of experiments, where not even a small fraction of time at the end of a run was allocated to lower priority triggers or speculative searches. Even in analyses of data there are pressures toward conservatism. In the early Rochester conferences one finds data presented of appalling quality by present standards, but which helped provide leads for further experimentation. Nowadays it is dangerous for a collaboration to exhibit some wild crazy phenomenon even at the 3 and 4 σ level, because so much hoopla is created by the theoretical community, not to mention the press, that

when the effect eventually goes away it can reflect negatively on the reputation of the collaboration.

4. EoI-19: A Full Acceptance Detector

The feelings expressed in the previous section became motivation this year to revive some old work on full acceptance detectors. I decided that the best way to try to attract interest in the approach was to submit an expression-of-interest to the SSC, detailing what is on my mind. It is not appropriate in this talk to go into detail on this enterprise; that was not my charge. But it is difficult for me to ignore it here, since that EoI is a specific expression of what I have tried to say in this talk in more general terms. So in this section I report briefly what the detector is, what has happened to the initiative at the SSC Laboratory, and what the general response of the community has been.

The full-acceptance detector (FAD) is intended to supplement the generic program of high-mass scale physics, by concentrating on lower mass scales, especially the physics in the forward-backward direction. Full acceptance here means good coverage and momentum analysis, for charged particles and photons, over the entire lego plot of $\pm$ 12 units of rapidity or so. A detector which does this is going to look roughly like two 20 TeV fixed-target spectrometers face-to-face, with the circulating beams going through the middle of them, and the final-focus quadrupole magnets integrated into the detector, serving as analyzing magnets for the fast forward charged-particle secondaries. Simple and general considerations then lead to a detector of order one plus one kilometers long, with a width of order meters. A cartoon of a possible detector architecture is exhibited in Fig. 2 and 3 taken from the EoI submitted to the SSC.

The detector is essentially one dimensional, looking something like a beam line. As such, it exhibits a high degree of modularity. Different portions of the detector are labeled by the pseudorapidities to which they are mainly sensitive. I find this feature singularly attractive. It means that the big experiment naturally is subdivided into a set of subexperiments which each enjoy a significant level of autonomy. This happens all the way from the technical level, e.g. the architecture of the data acquisition system, to possibly the social organization of the experiment itself. It means that for many purposes the interdependence of the sundry detection elements is lessened, and therefore there can be more risk-taking in the technologies used in individual detection elements, and faster turnaround times to replace or upgrade those portions of the detector that don't initially work like they are supposed to. If these utopian ideas on modularity have any truth to them, I think that they could be very powerful in allowing the experiment to adapt and respond to changing trends of what is important to measure, with relatively short lead-times.

This modularity also is important with regard to the practicality of the idea. The complete FAD is obviously expensive, and as a lower-priority initiative it is clear that the whole thing will not be supported out of the SSC budget. However,

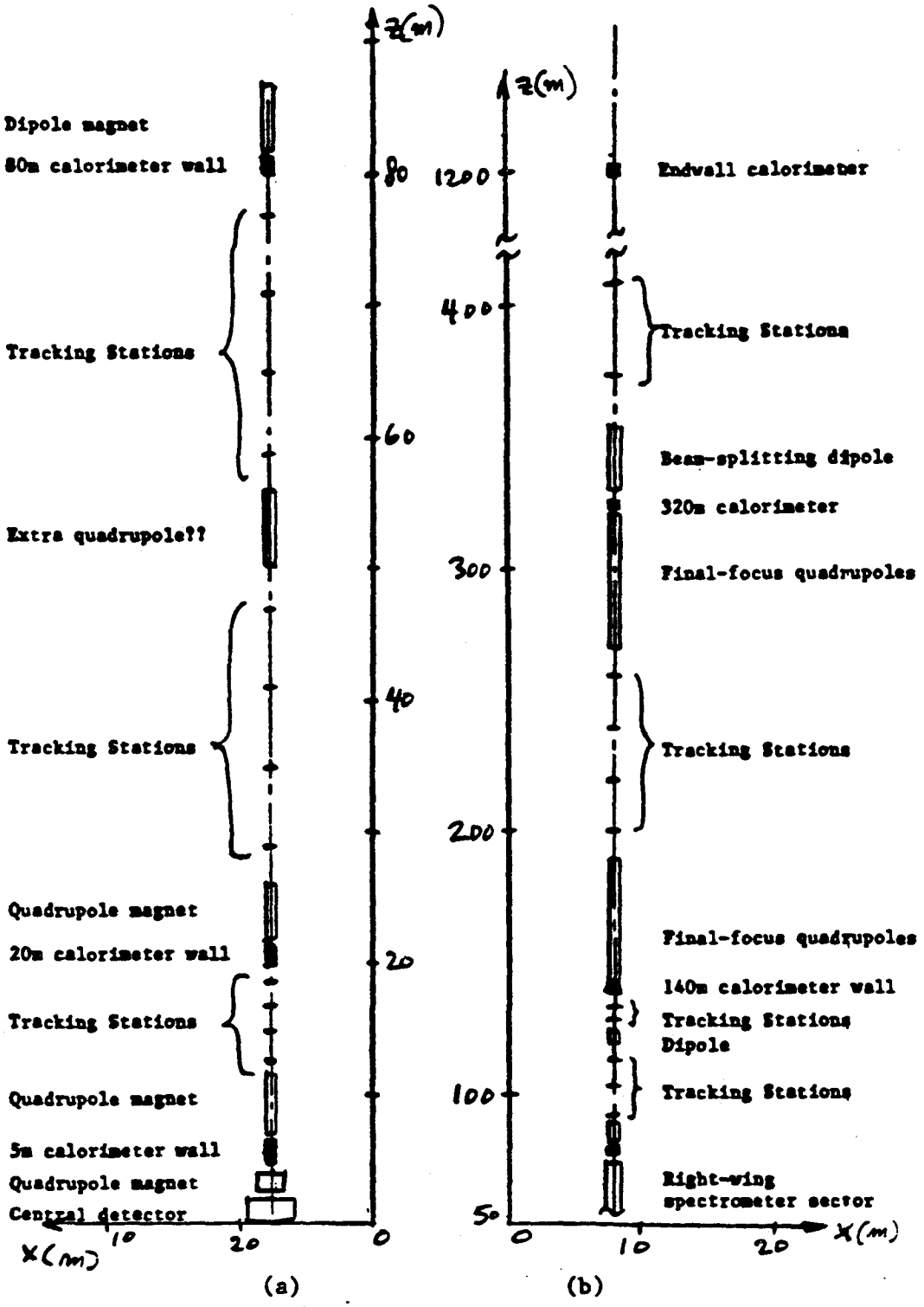


Figure 2. A cartoon of a possible FAD. Only one half is exhibited.

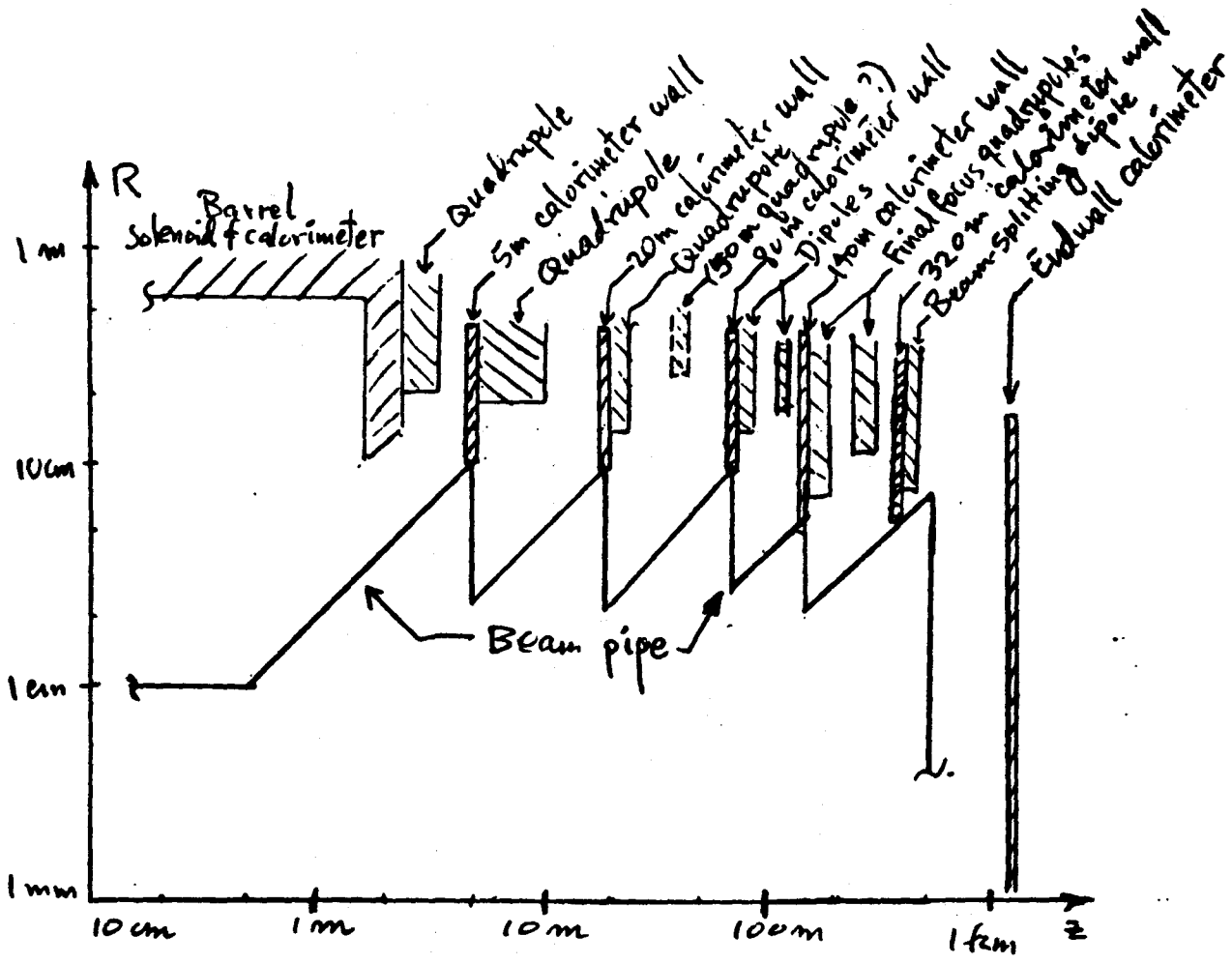


Figure 3. The same as Fig. 2 in log-log coordinates.

because of the modularity it can be staged. One natural scenario is to start with the outer rapidities (greater than about 7). This part of the detector, whose front end is of order 100m away from the collision point, is not especially expensive, of order the cost of a single-stage FNAL/SPS fixed target experiment. It does define the architecture of the final-focus system and therefore the nature of the machine-lattice in the collision region. It also defines the nature of the collision-hall extensions in the beam directions as well.

I believe that if the outer rapidities are instrumented (and it is important to instrument both directions in order to do a good job on diffractive processes) then various institutions, perhaps predominantly non-U.S., should find it attractive to bring in enough resources and manpower to instrument at some level the remainder. In my mind the problem is not whether that will happen, but whether quality control can be maintained, as well as compatibility with satisfactory operation of the outer detectors.

The physics associated with such an initial stage program will be dominated by (but not limited to) the lowest mass scales, e.g. diffraction and minimum-bias phenomenology. There are hard technical problems having to do with backgrounds from beam pipe interactions and other interactions originating from edges of upstream detection elements or other materials. But the biggest problem I see is not these but rather whether this kind of initial physics is worth doing. To me the answer is evident; to most others it seems not to be.

What is happening? This spring I wrote the EoI and submitted it to the SSC Laboratory. It contained three requests to the SSC, all of which have been acted upon. First of all, the lab promptly reviewed it. Secondly, the lab has been most cooperative in helping out on the issues having to do with the interface of detector and machine design, namely lattice and collision hall. The most difficult request I made was to provide space for the detector even were there no community response to the idea. The rationales for this request are that the construction deadlines occur soon and that the opportunity could be lost, and that by providing the hall the laboratory could exercise leadership in stimulating this kind of initiative. Happily, the PAC in July has recommended to the laboratory[7] that $\pm$ 500m of tunnel be enlarged in one of the east collision regions. I am most encouraged by this response from the laboratory and its advisory bodies.

What about the response from the rest of the community? I have received warnings from experts that the detector is technically very difficult. I have also received casual encouragement from some of the theoretical and experimental community. But I seek more than that. In order to make this idea into a real initiative (or to give it a proper burial), individuals must come forward and be willing to put in real time in studying the physics issues, design problems, background simulations, etc. This is not an easy step for an experimentalist to take. At present there are of order ten volunteers, precious few. I would like to see a strong leadership for this initiative emerge. I myself do not want to become an experimentalist, but

believe in the idea and intend to stay with it while it is getting off the ground. Once the enterprise is in motion, I would like to step to the side, and move into at most a "godfather" mode.

5. Concluding Remarks; What Lies Ahead?

One justification for discussing this EoI here is that I see what I am doing as something of a social experiment. In the past, an off-beat approach not in the main line of thinking could get started easier than now. This EoI represents a test of whether that is still possible within a laboratory as big as the SSC. Now using my experience with my own EoI to make more general inferences is sure to be very dangerous. After all, my perceptions are sure to be biased, since I am much less likely to see the deficiencies of what I am doing than anyone else. Maybe the physics is lousy. Maybe the detector can't be made to work. Maybe it is really politically impossible. Maybe I am not going about selling the idea in the right way. Maybe I am too impatient. But taking all that into account I still have days when I feel very discouraged. It is not that more people have failed to sign on. What is most discouraging is lack of feedback. I sense not opposition to the idea but indifference – not by the SSC Laboratory, but by the experimental community. There seems not the sensitivity out there to a new approach. Worst of all, there seems to be indifference to the physics. Half the EoI has to do with nonconventional physics topics, expressed in cryptic, telegraphic form. Even after oral presentation, I hardly ever get queries about what I mean by them. The other half of the EoI has some pretty unconventional ways of looking at detector design. These may indeed be lousy ideas, but hardly anyone is willing to offer an opinion why, no less defend it.

As I mentioned in the introduction, I am a person who is often asked to talk about the future. But it seems that this is not meant to include action on what to do about it.

What lies ahead? We enter a period of extraordinary opportunity. Facilities like the SSC are not going to come our way very often. But its huge size makes it very hard to maintain the variety and creativity that has characterized our field in the past. The non-SSC base program is threatened. The scientific opportunities there and the importance of maintaining its health are enormous. And with respect to the SSC base program, I can't help but feel concern about it. It appears to be nearly saturated by two not very dissimilar detector initiatives, no more dissimilar than CDF and D0 at Fermilab or Aleph and L3 at LEP. There are strong institutional pressures that push the field in this direction. But I share the worries of some of our critics that we are in danger of losing the essence of what makes science so exciting and interesting, as our approach to the physics becomes more and more homogeneous. I believe that for the base program and the SSC program there is no objective reason why this has to happen. The problem originates not in laboratory managements or advisory committees, but in the attitudes of individual physicists themselves. While diversity, and with it serendipitous discovery, is still

very much a possible way of life in the future of high energy physics, I am fearful that the opportunity will be forfeited. I wish I could be more optimistic than I am.

REFERENCES

1. J. Gunion, H. Haber, G. Kane, and S. Dawson, "The Higgs Hunter's Guide," Addison-Wesley (Redwood City, CA), 1990. Please, do not interpret my remarks here as a disparagement of this monumental contribution. What they have done is of great value. It is most necessary—but maybe not sufficient.
2. J. Bjorken, "A full acceptance detector for SSC physics at low and intermediate mass scales: an expression of interest to the SSC," SLAC-PUB-5545, May 1991.
3. R. Barbieri and L. Hall, LBL preprint LBL-30465 (1991).
4. V. Kuzmin, private communication.
5. Chacaltaya and Pamir Collaboration, Tokyo University preprint ICRR-Report-232-91-1 (1991).
6. L. Van Hove, Ann. Phys. (N.Y.) 192, 66 (1989).
7. Specifically, the PAC stated that "it appears prudent to enlarge the collider tunnel in one of the interaction regions in the East Straight Section to have a diameter of approximately 6m and a length of approximately 1000 meters..."

First order tune shift calculations for transverse betatron dynamics[†]

T. Garavaglia

Superconducting Super Collider Laboratory, Dallas, Texas 75237*

An effective Hamiltonian, with non-linear magnetic multipole terms and momentum dispersion contributions, is used to obtain the first order tune-shift results for transverse betatron motion for protons in the Superconducting Super Collider (SSC). This Hamiltonian is represented in terms of action angle variables, and analytical results are obtained using symbolic algebra methods. Mathematical derivations of the transverse multipole expansion and of the transverse betatron equations, using an invariant action and curvilinear coordinates, are given in the appendices. Numerical and graphical tune-space results are given that illustrate the dependence of tune-shifts on injection amplitude and momentum spread.

Tuneshift.tex

[†] Contributed to the *"1991 Symposium on the Superconducting Super Collider", Corpus Christi, Texas October 13-17, 1991.*

I. INTRODUCTION

When protons are injected into the SSC they execute transverse betatron oscillation with betatron numbers (tunes) ν_x and ν_y. In a linear machine, if a proton of initial phase ϕ_0 is observed at the same fixed point along its path for j rotations around a ring of radius R, a transverse position coordinate follows the sinusoidal law $\cos(j\nu_0\omega_r T_0 + \phi_0)$. The phase advance for one rotation is $2\pi\nu_0$, and the betatron frequency is $\omega_r = c/R$, where c is the speed of light. The period for one rotation is $T_0 = 2\pi R/c$. Non-linear multipole contributions to the transverse magnetic field of the SSC dipole magnets can produce changes (tune-shifts) in the transverse betatron numbers. These changes can drive the tunes into regions of ν_x, ν_y tune-space where resonance lines are present. This can result in particle loss and degradation of the dynamic aperture of the beam. Such effects are seen clearly in computer simulation studies [1] done using the tracking code SSCTRK [2]. Using Fourier analysis methods, one can extract values for the betatron tunes from the data produced by SSCTRK. However, it is desirable to have an analytical method which will show the pattern in tune-space produced by particles with different injection positions (x,y) and with different values of momentum spread $\delta|\vec{p}|/\vec{p}|$, where $\delta|\vec{p}| = |\vec{p}| - |\vec{p}_0|$ is the difference between the proton scalar momentum $|\vec{p}|$ and the ideal orbit scalar momentum $|\vec{p}_0|$. The corrections to betatron tune-shifts resulting from higher order magnetic multipole contributions are calculated in first order perturbation theory using a non-linear effective Hamiltonian, represented in terms of action angle variables. The analytical results are obtained from this Hamiltonian using symbolic computational methods, and numerical results are obtained from these expressions. The analytical results are obtained from the REDUCE [3] program TSHIFT which is described in this paper. The results from this program are used in the numerical program TUNESHIFT.FOR to produce graphical results in the Top Drawer [4] file

TUNESHIFT.TOP. These methods have been successfully used to study the spread in tune-space associated with magnetic peaking [5]. Sample graphs resulting from these programs are given in the text, and the method for generating these results is described. For the numerical results, multipole contributions through B_{10} are included; however, the REDUCE code can be used to generate higher order contributions if these are desired. The numerical code TUNESHIFT.FOR is driven by and input file which contains data on the operating point (ν_{0x}, ν_{0y}) for the nominal transverse betatron tunes, values of the multipoles B_1 through B_{10}, and momentum offset $\delta|\vec{p}|/\vec{p}|$.

II. THE ACTION ANGLE EFFECTIVE HAMILTONIAN

The non-linear magnetic field multipole contributions are found from the multipole expansion for the transverse magnetic fields of the SSC dipole magnets

$$B_x(x,y,\bar{s}) + iB_y(x,y,\bar{s}) = \sum_{n=0}(B_n(\bar{s}) + A_n(\bar{s}))(x+iy)^n, \tag{2.1}$$

where $B_n(\bar{s})$ and $A_n(\bar{s})$ are, respectively, the normal multipole and skew-multipole coefficients. As described in Appendix A, these transverse fields are obtained from the real part of the scalar function $A(z,\bar{s})$ according to

$$B_y(x,y,\bar{s}) + iB_x(x,y,\bar{s}) = \bar{\mathcal{D}}ReA(z,\bar{s}), \tag{2.2}$$

where

$$\bar{\mathcal{D}} = \partial_x - i\partial_y,$$

and $z = x + iy$. The coordinates x, y, and $\bar{s}$ are defined in Appendix C.

In terms of the transverse coordinates x and y, the first order perturbed effective Hamiltonian, found from (C38), is written as

$$H = \frac{p_x^2}{2} + \frac{p_y^2}{2} + \frac{|\vec{p}_0|}{|\vec{p}|}\frac{K_x(\bar{s})}{2}x^2 - \frac{|\vec{p}_0|}{|\vec{p}|}\frac{K_y(\bar{s})}{2}y^2 + ReA(z,\bar{s}) + \frac{|\vec{p}_0| - |\vec{p}|}{|\vec{p}|}\frac{x}{\rho(\bar{s})}, \tag{2.3}$$

with

$$Re\mathcal{A}(z,\bar{s}) = Re\sum_{n=0}\frac{\bar{B}_0(\bar{s})}{B(\bar{s})\rho(\bar{s})}\frac{(b_n+ia_n)}{(n+1)}(x+iy)^{n+1}. \tag{2.4}$$

In the above, use is made of the notations

$$K_x(\bar{s}) = \frac{1}{\rho^2(\bar{s})} + \frac{(e/c)\bar{B}_1(\bar{s})}{2|\vec{p}_0|}), \text{ and } K_y(\bar{s}) = \frac{(e/c)\bar{B}_1(\bar{s})}{2|\vec{p}_0|}), \tag{2.5}$$

and the relations $eB(\bar{s})\rho(\bar{s}) = c|\vec{p}|$, and $e\bar{B}_0(\bar{s})\rho(\bar{s}) = c|\vec{p}_0|$. The expression (2.4) represents the error coefficients associated with the multipole components within the dipole magnets of mean strength $\bar{B}_0$. The error coefficients associated with the mean values $\bar{B}_0$ and $\bar{B}_1$ are represented by the expressions

$$B_0(\bar{s}) = \bar{B}_0(\bar{s})(1+b_0)$$

$$B_1(\bar{s}) = \bar{B}_1(\bar{s}) + \bar{B}_0(\bar{s})b_1 \tag{2.6}$$

The other components of the error field are given by

$$B_n(\bar{s}) = \bar{B}_0(\bar{s})b_n \text{ and } A_n(\bar{s}) = \bar{B}_0(\bar{s})a_n, \tag{2.7}$$

where b_n and a_n are, respectively, a measure of the normal multipole and skew-multipole error fields. In deriving (2.3), terms of order B_0x, and B_1x^2 have been retained. However, terms of order B_0x^2/ρ, B_1x^3/ρ, $B_2x^4/\rho\ldots$, and A_0xy/ρ, $A_1x^2y/\rho\ldots$ have been neglected.

An additional non-linear contribution occurs as a result of having sextupole chromatic correctors [6]. This correction is of the form

$$\frac{|\vec{p}_0|}{|\vec{p}|}\frac{S(\bar{s})}{6}(x^3-3xy^2), \tag{2.8}$$

with

$$S(\bar{s}) = \frac{e}{|\vec{p}_0|c}B_2(\bar{s}). \tag{2.9}$$

Neglecting the error field contribution (2.4) and considering only the effect of the sextupole chromatic corrector, the effective Hamiltonian (2.3) becomes

$$H = \frac{p_x^2}{2} + \frac{p_y^2}{2} + (1 - \frac{\delta|\vec{p}|}{|\vec{p}|})\left(\frac{K_x(\bar{s})}{2}x^2 - \frac{K_y(\bar{s})}{2}y^2\right) - \frac{\delta|\vec{p}|}{|\vec{p}|}\frac{x}{\rho(\bar{s})} + (1 - \frac{\delta|\vec{p}|}{|\vec{p}|})\frac{S(\bar{s})}{6}(x^3 - 3xy^2). \tag{2.10}$$

Following the method described in Appendix B, one finds the periodic closed orbit solution for an off-momentum particle to be of the form

$$x_c = \frac{\delta|\vec{p}|}{|\vec{p}|}D(\bar{s}, |\vec{p}|), \tag{2.11}$$

where the periodic dispersion function $D(\bar{s}, |\vec{p}|)$ satisfies

$$D''(\bar{s}, |\vec{p}|) + (1 - \frac{\delta|\vec{p}|}{|\vec{p}|})K_x(\bar{s})D(\bar{s}, |\vec{p}|) + (1 - \frac{\delta|\vec{p}|}{|\vec{p}|})\frac{S(\bar{s})}{2}D^2(\bar{s}, |\vec{p}|) = \frac{1}{\rho(\bar{s})}. \tag{2.12}$$

At this point it is useful to perform a canonical transformation to eliminate certain terms which are linear in $\delta|\vec{p}|/|\vec{p}|$. This is accomplished with the use of the generating function

$$F_2(x, p_{x_0}) = (x - D(\bar{s}, |\vec{p}|)\frac{\delta|\vec{p}|}{|\vec{p}|})(p_{x_0} + D'(\bar{s}, |\vec{p}|)\frac{\delta|\vec{p}|}{|\vec{p}|}), \tag{2.13}$$

which gives the transformed relations

$$\begin{aligned} x &= x_0 + D(\bar{s}, |\vec{p}|)\frac{\delta|\vec{p}|}{|\vec{p}|} \\ p_x &= p_{x_0} + D'(\bar{s}, |\vec{p}|)\frac{\delta|\vec{p}|}{|\vec{p}|} \\ H_0 &= H + \frac{\partial F_2}{\partial \bar{s}}. \end{aligned} \tag{2.14}$$

When these are used with (2.10), one finds

$$\begin{aligned} H_0 = {} & \frac{p_x^2}{2} + \frac{p_y^2}{2} + \frac{K_x(\bar{s})}{2}x^2 - \frac{K_y(\bar{s}))}{2}y^2 + \frac{S(\bar{s})}{6}({x_0}^3 - 3x_0y^2) \\ & - \frac{\delta|\vec{p}|}{|\vec{p}|}\left[(S(\bar{s})D(\bar{s}, |\vec{p}|) + K_x(\bar{s}))\frac{{x_0}^2}{2} - (S(\bar{s})D(\bar{s}, |\vec{p}|) + K_y(\bar{s}))\frac{y^2}{2} + \frac{S(\bar{s})}{6}({x_0}^3 - 3x_0y^2)\right] \\ & + \left(\frac{\delta|\vec{p}|}{|\vec{p}|}\right)^2 \frac{S(\bar{s})D(\bar{s}, |\vec{p}|)}{2}({x_0}^2 - y^2). \end{aligned} \tag{2.15}$$

For the SSC $K_x(\bar{s}) \sim K_y(\bar{s})$, and one can choose the value of $S(\bar{s})$ to eliminate the first two $\delta|\vec{p}|/\vec{p}|$ dependent terms in (2.15). The remaining $\delta|\vec{p}|/\vec{p}|$ dependent term will not contribute to the first order tune-shifts as a result of the averaging process described later in the text. The remaining term coming from the sextupole correction is

$$-\left(\frac{\delta|\vec{p}|}{|\vec{p}|}\right)^2 \frac{K_x(\bar{s})}{2}(x_0{}^2 - y^2), \tag{2.16}$$

and since $K_x(\bar{s}) \sim 1.6 \times 10^{-4}$ for the SSC this term will give a contribution which is small when compared to the $\delta|\vec{p}|/|\vec{p}|$ sextupole correction errors which occur in a real machine.

To obtain the first order tune-shifts, it is convenient to introduce the generating function

$$\begin{aligned} F_1(x_0, \phi_x, y, \phi_y) = &-\frac{x_0{}^2}{2\beta_{x_0}(\bar{s})}\left(\tan\phi_{x_0} - \frac{\beta'_{x_0}(\bar{s})}{2}\right) \\ &-\frac{y^2}{2\beta_y(\bar{s})}\left(\tan\phi_y - \frac{\beta'_y(\bar{s})}{2}\right) \end{aligned} \tag{2.17}$$

and to express the effective Hamiltonian obtained from (2.3), using

$$H_1 = H_0 + \frac{\partial F_1(x_0, \phi_{x_0}, y, \phi_y)}{\partial \bar{s}}, \tag{2.18}$$

in terms of action angle variables J_{x_0}, ϕ_{x_0} and J_y, ϕ_y, which are related to x, y, p_{x_0}, and p_y according to

$$\begin{aligned} x &= \sqrt{2\beta_{x_0}J_{x_0}}\cos\phi_{x_0} + \eta(\bar{s})\frac{\delta|\vec{p}|}{|\vec{p}|} \\ y &= \sqrt{2\beta_y J_y}\cos\phi_y \\ p_{x_0} &= -\sqrt{2J_{x_0}/\beta_{x_0}}(\sin\phi_{x_0} - \frac{\beta'_{x_0}(\bar{s})}{2}\cos\phi_{x_0}) \\ p_y &= -\sqrt{2J_y/\beta_y}(\sin\phi_y - \frac{\beta'_y(\bar{s})}{2}\cos\phi_y), \end{aligned} \tag{2.19}$$

where $D(\bar{s}, |\vec{p}|) \sim \eta(\bar{s})$ is the momentum independent part of the solution of the dispersion equation (2.12) with $S(\bar{s}) = 0$. The effective Hamiltonian (2.3) becomes

$$H_1(J_{x_0}, J_y, \phi_{x_0}, \phi_y) = \frac{J_{x_0}}{\beta_{x_0}(\bar{s})} + \frac{J_y}{\beta_y(\bar{s})} + Re\mathcal{A}(J_{x_0}, J_y, \phi_{x_0}, \phi_y). \tag{2.20}$$

The first order corrected tunes for transverse betatron motion are obtained from

$$\begin{aligned} \nu_x &= \nu_{0x} + \Delta\nu_x \\ \nu_y &= \nu_{0y} + \Delta\nu_y, \end{aligned} \tag{2.21}$$

where the nominal tunes are

$$\nu_{0x,y} = \frac{1}{2\pi}\int_s^{s+C_0} \frac{d\bar{s}'}{\beta_{x,y}(\bar{s}')}, \tag{2.22}$$

and the tune-shifts are

$$\begin{aligned} \Delta\nu_{x,y} &= \frac{C_0}{2\pi}\frac{\partial < Re\mathcal{A}(J_{x_0}, J_y, \phi_{x_0}, \phi_y)}{\partial J_{x_0,y}} > \\ &= \frac{\partial}{\partial J_{x_0,y}}\frac{1}{C_0}\int_0^{C_0} d\bar{s}\frac{1}{n+1}\left(\frac{b_n C_0}{2\pi\rho(\bar{s})}\right)\left(\frac{1}{2\pi}\right)^2\int_0^{2\pi}\int_0^{2\pi} d\phi_{x_0}d\phi_y \\ &\quad Re\left(\sqrt{(2\beta_{x_0}J_{x_0})}\cos\phi_{x_0} + \eta(\bar{s})\frac{\delta|\vec{p}|}{|\vec{p}|} + i\sqrt{(2\beta_y J_y)}\cos\phi_y\right)^{n+1}, \end{aligned} \tag{2.23}$$

where $C_0 \sim 2\pi\rho(\bar{s}) \sim 2NL$ for a ring of N cells each of half-length L. The angular averages appearing in this expression are evaluated using

$$\frac{1}{2\pi}\int_0^{2\pi}(\cos\phi)^{2n}d\phi = \frac{1}{2^{2n}}\binom{2n}{n}. \tag{2.24}$$

The integrals involving odd powers of $\cos\phi$ are zero, and as a result of this no terms containing the skew-multipole coefficients $A_n(\bar{s})$ appear after performing the angular integration. The averaging around the circumference C_0 of the SSC involves integrals of the form

$$< \beta_{x_0}\beta_y^2\eta >= \frac{1}{C_0}\int_0^{C_0}\beta_{x_0}(\bar{s})\beta_y^2(\bar{s})\eta(\bar{s})d\bar{s} \sim \frac{1}{L}\int_0^{L}\beta_{x_0}(\bar{s})\beta_y^2(\bar{s})\eta(\bar{s})d\bar{s}, \tag{2.25}$$

which are evaluated numerically using the program TUNESHIFT.FOR. The symmetry properties and analytical expressions for the lattice functions $\beta_{x_0}(\bar{s})$, $\beta_y(\bar{s})$, and $\eta(\bar{s})$ are given in Appendix D. In a similar manner, an additional contribution to (2.23) is found when the chromatic non-linear term (2.16) is added to (2.20).

III. RESULTS AND CONCLUSIONS

The evaluation of (2.3) is performed using the REDUCE program TSHIFT (see Appendix E). The results agree with those found in [7]; however, there are some errors found in the expressions given in this reference. The REDUCE code has been used to generate FORTRAN code which has been substituted into the numerical code TUNESHIFT.FOR, where corrections up to order B_{10} have been included. The numerical results obtained from TUNESHIFT.FOR are generated from an input file INPUTS.DAT which has values for the multipole errors b_n, $\delta|\vec{p}|/\vec{p}|$ (DELTA), and injection amplitudes x_{max} mm (AMPX) and y_{max} mm (AMPY), which determine the size of the injection grid. In addition, this file contains the nominal tunes dnux and dnuy, the phase advance per cell D(degrees), the lattice tune q, and XIX and XIY, which represent chromaticity tune-shifts errors linear in $\delta|\vec{p}|/\vec{p}|$. These are errors which remain in (2.15) with imperfect cancellation resulting from chromatic correction. For the SSC, these terms are large compared to the quadratic correction (2.16). Particles are injected onto a grid from (0,0) to (x_{max}, y_{max}). Typical result for the points in tune-space are shown in Fig. 1 through Fig. 4, which also show the input file. In these figures, resonance lines up to 7th order are shown, and the cross indicates the location of the nominal SSC tunes $\nu_{0x} = .425$ and $\nu_{0y} = .410$. Fig. 1 and Fig. 2 differ in the values of (x_{max}, y_{max}), which are, respectively, (0.5,0.5) and (0.6,0.6); however, they both result from the same value of $\delta|\vec{p}|/\vec{p}| = 5 \times 10^{-4}$. Comparing these figures, one can see clearly the effect of increased injection amplitude on the location of points in tune-space. Fig. 3 and Fig. 4 have the same injection amplitudes, respectively, as Fig. 1 and Fig. 2; however, they both result from $\delta|\vec{p}|/\vec{p}| = 10 \times 10^{-4}$, and one can see the dependence of the betatron tunes on momentum spread. The result of having a linear momentum error remaining after chromatic correction is seen in

Fig. 5 and Fig. 6, with XIX=XIY=5.0. These are to be compared with Fig. 1 and Fig. 2, respectively, where XIX=XIY=0.0. Here, one can see clearly that a linear momentum error has a large effect on the tune-spread.

In conclusion, one can see that reasonable results are found from the first order calculation. A comparison of the values of ν_x and ν_y obtained from the first order calculation with the values obtained from the tracking code SSCTRK shows good agreement. Results for the injection point $(0.8, 0.8)$, with all $b_n's = 0$ except $b_{10} = 0.05$, and $\delta|\vec{p}|/\vec{p}| = 5. \times 10^{-4}$, are $\nu_x = .426$ and $\nu_y = .409$ from TUNESHIF.FOR, and $\nu_x = .425$ and $\nu_y = .409$ from SSCTRK. Furthermore, one can see the effect of multipole errors on the location of the betatron tunes in tune-space. In the case when the tune-spread crosses lower order resonance lines, one would expect to see a decrease of the dynamic aperture of the SSC during the injection phase. This, indeed, is in agreement with the results obtained from tracking codes.

APPENDIX A: MULTIPOLE EXPANSION FOR TRANSVERSE FIELDS

The transverse magnetic fields are determined easily in the form of complex functions of the variable $z = x + iy$. Defining the operators

$$\begin{aligned} \mathcal{D} &= 2\partial_z, \\ \bar{\mathcal{D}} &= 2\partial_{\bar{z}}, \end{aligned} \tag{A1}$$

one finds from

$$\begin{aligned} x &= \frac{z+\bar{z}}{2}, \\ y &= \frac{z-\bar{z}}{2} \end{aligned} \tag{A2}$$

that

$$\begin{aligned} \mathcal{D} &= \partial_x + i\partial_y, \\ \bar{\mathcal{D}} &= \partial_x - i\partial_y. \end{aligned} \tag{A3}$$

The Laplacian operator is found from (A1) and (A3) as

$$\nabla^2 = \bar{\mathcal{D}}\mathcal{D} = \partial_{xx} + \partial_{yy} = 4\partial_z\partial_{\bar{z}}. \tag{A4}$$

Considering the function

$$f(z) = B_y(x,y) + iB_x(x,y) = \sum_{n=0}^{\infty}(B_n + iA_n)z^n, \tag{A5}$$

one finds

$$\mathcal{D}f(z) = (\nabla \times \vec{B})_3 + i\vec{\nabla}\cdot\vec{B} = 0, \tag{A6}$$

and

$$\bar{\mathcal{D}}\mathcal{D}f(z) = \nabla^2(B_y(x,y) + iB_x(x,y)) = 0. \tag{A7}$$

These equations imply

$$(\vec{\nabla} \times \vec{B})_3 = \vec{\nabla}\cdot\vec{B} = \nabla^2\vec{B} = 0, \tag{A8}$$

and

$$\vec{B} = \vec{\nabla} \times \vec{A}.$$

These give the result

$$\vec{\nabla} \cdot \vec{B} = \vec{\nabla}\vec{\nabla} \cdot \vec{A} - \nabla^2 \vec{A} = 0, \tag{A9}$$

which is satisfied by

$$\vec{A} = (0, 0, A^3(x, y)).$$

Since

$$f(z) = \frac{1}{2}\bar{\mathcal{D}}A(z) = \frac{1}{2}\bar{\mathcal{D}}(A(z) + \bar{A}(z)), \tag{A10}$$

with

$$A(z) = \sum_{n=0}^{\infty} \frac{(B_n + iA_n)z^{n+1}}{n+1}, \tag{A11}$$

one finds

$$B_y(x, y) + iB_x(x, y) = \bar{\mathcal{D}}ReA(z). \tag{A12}$$

This allows the transverse components of the magnetic field to be written as

$$\begin{aligned} B^x(x, y) &= \partial_y A^3(x, y), \\ B^y(x, y) &= -\partial_x A^3(x, y), \end{aligned} \tag{A13}$$

with

$$A^3(x, y) = -ReA(z).$$

APPENDIX B: THE INVARIANT ACTION

The equations of motion for transverse betatron oscillations [8] can be found from a Lorentz invariant Hamiltonian [9]. This Hamiltonian, which is equal to the rest energy of the proton, is also invariant under general curvilinear coordinate transformations [10], and this suggests the introduction of an invariant action. This allows one to represent the special relativistic dynamical equations for betatron motion in the coordinate system related to the curved ideal orbit of a proton in the SSC. In addition, this formulation allows one to explicitly see the various approximations which are made to obtain the usual Courant-Snyder equations. For this invariant Hamiltonian, the Minkowski space contravariant coordinates are defined as the four-vector $q^i = (q^0, q^1, q^2, q^3) = (ct, x, y, z)$, where c is the speed of light. The contravariant components of the four-velocity are defined to be

$$u^i = dq^i/ds, \tag{B1}$$

and those of the four-momentum for a particle of rest mass m are

$$p^i = mcu^i, \tag{B2}$$

where ds is the invariant measure

$$ds = \sqrt{dq_i dq^i}, \tag{B3}$$

where use is made of the Einstein summation convention. The covariant differential components of a four-vector are found from

$$dq_i = g_{ij} dq^j. \tag{B4}$$

The non-zero Minkowski space components of the covariant metric tensor g_{ij} are

$$(g_{oo}, g_{11}, g_{22}, g_{33}) = (1, -1, -1, -1). \tag{B5}$$

The contravariant components of the metric tensor are found from the relation

$$g^{ij}g_{jk} = \delta^i_k \tag{B6}$$

to be

$$(g^{oo}, g^{11}, g^{22}, g^{33}) = (1, -1. - 1, -1). \tag{B7}$$

The invariant Hamiltonian is defined as

$$H(p^i, q^i)/c = p_i u^i - L(u^i, q^i) + mc, \tag{B8}$$

where the invariant Lagrangian for the motion of a particle of mass m and electric charge e in an electromagnetic field with four-potential $A(q)^i$ is defined as

$$L(u^i, q^i) = mc\sqrt{u_i u^i} + (e/c)A(q)_i u^i. \tag{B9}$$

The conjugate four-momentum is

$$p_i = \frac{\partial L}{\partial u^i} = \frac{mcu_i}{\sqrt{u_i u^i}} + (e/c)A(q)_i, \tag{B10}$$

and the Lagrangian (B9) becomes

$$L(u^i, q^i) = p_i u^i. \tag{B11}$$

For this Lagrangian, the action which is invariant under curvilinear coordinate transformations is defined as

$$S = \int L(u^i, q^i)ds. \tag{B12}$$

Using the method of stationary action and the approximations described in Appendix C, one finds equations (C41) and (C42), which describe transverse betatron motion.

As shown in Appendix C, the approximate Hamiltonian for this system may be written in terms of the transverse coordinates x and y and the local radius of curvature $\rho(\bar{s})$ of the ideal orbit as

$$\bar{p}_3 \approx \left(-(e/c)\frac{A^3(x,y,\bar{s})}{|\vec{p}|} - 1 + \frac{(p^x)^2+(p^y)^2}{2}\right) \times (1 + x/\rho(\bar{s})), \qquad (B13)$$

with

$$A^3(x,y,\bar{s}) = -\frac{c|\vec{p}|}{e} Re\mathcal{A}(x,y,\bar{s}), \qquad (B14)$$

and

$$Re\mathcal{A}(x,y,\bar{s}) = Re\sum_{n=0}\frac{e}{c|\vec{p}|}\frac{(B_n(\bar{s})+iA_n(\bar{s}))}{(n+1)}(x+iy)^{n+1}, \qquad (B15)$$

where $A_n(\bar{s})$, and $B_n(\bar{s})$ are, respectively, the normal and skew-multipole coefficients, and $|\vec{p}|$ is found in (C33).

APPENDIX C: THE BETATRON EQUATIONS OF MOTION

In this appendix it is shown how an invariant action is used to obtain the equation for betatron oscillations when these equations of motion are expressed in terms of curvilinear coordinates. This approach is motivated by the consideration of an invariant Hamiltonian. Considering (B8) and the identity

$$\frac{d}{ds}H(p^i,q^i)/c = \frac{1}{c}\frac{\partial H(p^i,q^i)}{\partial p_i}\frac{dp_i}{ds} + \frac{1}{c}\frac{\partial H(p^i,q^i)}{\partial q^i}\frac{dq^i}{ds}$$

$$= \frac{d}{ds}(p_i u^i) - \frac{\partial L(u^i,q^i)}{\partial q^i}u^i - \frac{\partial L(u^i,q^i)}{\partial u^i}\frac{du^i}{ds} = 0, \qquad (C1)$$

one can infer for Minkowski space the equations of motion

$$\begin{aligned} c\frac{dq^i}{ds} &= \frac{\partial H(p^i,q^i)}{\partial p_i}, \\ c\frac{dp_i}{ds} &= -\frac{\partial H(p^i,q^i)}{\partial q^i}, \\ p_i &= \frac{\partial L(u^i,q^i)}{\partial u^i}, \text{ and} \\ \frac{dp_i}{ds} &= \frac{\partial L(u^i,q^i)}{\partial q^i}, \end{aligned} \qquad (C2)$$

where the invariant Hamiltonian becomes

$$H(p^i,q^i) = mc^2 = c\sqrt{(p-(e/c)A(q))_i(p-(e/c)A(q))^i}. \qquad (C3)$$

Using the above, along with

$$\frac{d}{ds}A(q)_i = u^j\partial_j A(q)_i, \qquad (C4)$$

with $\partial_j = \partial/\partial x^j$, one finds the equation of motion

$$\frac{d}{ds}mcu_i = (e/c)u^j F_{ij}, \qquad (C5)$$

where the electromagnetic field tensor is

$$F_{ij} = \partial_i A(q)_j - \partial_j A(q)_i. \qquad (C6)$$

Since

$$F^{oj} = (0, -\vec{E}), \tag{C7}$$

with the electric field defined as

$$\vec{E} = \frac{\partial}{\partial ct}\vec{A}(q) + \vec{\nabla}A(q)^0, \tag{C8}$$

and since for the magnetic field $\vec{B}$ satisfies

$$F_{\alpha\beta} = -\epsilon_{\alpha\beta\gamma}B^{\gamma}, \tag{C9}$$

with $\alpha, \beta = 1$, 2, or 3 and $\epsilon_{123} = 1$ for the completely antisymmetric tensor, it follows that

$$\frac{d}{dt}\gamma mc^2 = \frac{d\mathcal{E}}{dt} = \vec{E} \cdot \vec{v}, \tag{C10}$$

$$\frac{d}{dt}\gamma m\vec{v} = e\vec{E} + (e/c)\vec{v} \times \vec{B}. \tag{C11}$$

The first equation gives the energy $\mathcal{E}$ gain or loss of the particle of rest mass m and velocity $\vec{v}$, and the second is the Lorentz equation. In obtaining these results, use has been made of $u^0 = \gamma, \vec{u} = \gamma\vec{\beta}$, $ds = cdt/\gamma$, $\vec{\beta} = \vec{v}/c$, and $\gamma = (1 - \vec{\beta} \cdot \vec{\beta})^{-1/2}$.

It is usual to express the equations of motion for betatron dynamics in curvilinear coordinates. The curvilinear coordinates used here are x, y, and $\bar{s}$, where x is the horizontal position of the particle relative to the ideal orbit, y is the vertical position coordinate relative to the orbital plane, and $\bar{s}$ is the arc length along the ideal orbit (see Fig. 7). The position vector of the particle, expressed in terms of the right-handed orthonormal basis $\hat{e}_1, \hat{e}_2$, and $\hat{e}_3$, is

$$\vec{r} = (\rho(\bar{s}) + x)\hat{e}_1 + y\hat{e}_2. \tag{C12}$$

The origin of this vector is at the instantaneous center of curvature of the ideal orbit. The coordinates relative to the system with origin at $\vec{r}_0 = \rho(\bar{s})\hat{e}_1$ are x, y,

and z, and they are measured, respectively, along the right-handed orthonormal basis. For motion relative to the torsion-free ideal orbit, the differential of the position vector is

$$d\vec{r} \approx dx\hat{e}_1 + dy\hat{e}_2 + (1 + x/\rho(\bar{s}))d\bar{s}\hat{e}_3 + O(d\theta^2), \qquad (C13)$$

where

$$d\bar{s} = \rho(\bar{s})d\theta, \qquad (C14)$$

with $d\theta$ the angular increment of $\vec{r}_0$ along the ideal orbit. It follows from (C13) that

$$(dr)^2 \approx (dx)^2 + (dy)^2 + (1 + x/\rho(\bar{s}))^2(d\bar{s})^2. \qquad (C15)$$

The contravariant coordinates in the curvilinear system are

$$(\bar{q}^0, \bar{q}^1, \bar{q}^2, \bar{q}^3) = (q^0, q^1, q^2, \bar{s}), \qquad (C16)$$

and it follows from (C15) that

$$d\bar{q}^3 = dq^3/(1 + x/\rho(\bar{s})). \qquad (C17)$$

The invariant space-time measure is

$$ds = \sqrt{\bar{g}_{ij}d\bar{q}^i d\bar{q}^j}, \qquad (C18)$$

and the components of the covariant metric tensor $\bar{g}_{ij}$ are

$$(\bar{g}_{oo}, \bar{g}_{11}, \bar{g}_{22}, \bar{g}_{33}) = (1, -1, -1, -(1 + x/\rho(\bar{s}))^2). \qquad (C19)$$

The curvilinear contravariant components of the four-momentum are

$$(\bar{p}^0, \bar{p}^1, \bar{p}^2, \bar{p}^3) = (p^0, p^1, p^2, p^3/(1 + x/\rho(\bar{s}))), \qquad (C20)$$

and the covariant components are

$$(\bar{p}_0, \bar{p}_1, \bar{p}_2, \bar{p}_3) = (p_0, p_1, p_2, p_3(1 + x/\rho(\bar{s}))). \tag{C21}$$

Similar relations are obtained for the coordinate differential four-vector dq^i and the vector-potential $A(q)^i$.

The betatron equations of motion are found in the curvilinear coordinate system using the fact that the action S is invariant under Lorentz transformations and orthogonal spatial coordinate transformations. The action (B12) is an invariant under the coordinate transformation $q^i \rightarrow \bar{q}^i$ so that

$$S = \int p_i u^i ds = \int \bar{p}_i \bar{u}^i ds. \tag{C22}$$

A variation of this action gives

$$\delta S = \int (\delta \bar{p}_i \bar{u}^i + \bar{p}_i \delta \bar{u}^i) ds. \tag{C23}$$

Using

$$\delta \bar{u}^i = \frac{d\delta \bar{q}^i}{ds}, \tag{C24}$$

and

$$\delta \bar{p}_3 = \frac{\partial \bar{p}_3}{\partial \bar{p}_\alpha} \delta \bar{p}_\alpha + \frac{\partial \bar{p}_3}{\partial \bar{q}^i} \delta \bar{q}^i, \quad \alpha \neq 3, \tag{C25}$$

one finds for δS

$$\delta S = \int \left((\frac{\partial \bar{p}_3}{\partial \bar{p}_\alpha} \bar{u}^3 + \bar{u}^\alpha) \delta \bar{p}_\alpha + (\frac{\partial \bar{p}_3}{\partial \bar{q}^i} \bar{u}^3 - \frac{d\bar{p}_i}{ds}) \delta \bar{q}^i + \frac{d(\bar{p}_i \delta \bar{q}^i)}{ds}) \right) ds. \tag{C26}$$

In the usual manner, this yields the dynamical equations of motion

$$\begin{aligned} \frac{d\bar{q}^\alpha}{ds} &= -\bar{u}^3 \frac{\partial \bar{p}_3}{\partial \bar{p}_\alpha}, \\ \frac{d\bar{p}_i}{ds} &= \bar{u}^3 \frac{\partial \bar{p}_3}{\partial \bar{q}^i}. \end{aligned} \tag{C27}$$

Using the representation of the invariant measure

$$ds = \sqrt{d\bar{q}_i d\bar{q}^i} = \sqrt{\frac{d\bar{q}_i}{d\bar{q}^3}\frac{d\bar{q}^i}{d\bar{q}^3}}\, d\bar{q}^3, \qquad (C28)$$

and the coordinates $(\bar{q}^0, \bar{q}^1, \bar{q}^2, \bar{q}^3) = (q^0, x, y, \bar{s})$, along with

$$\bar{u}^3 = 1/\sqrt{\frac{d\bar{q}_i}{d\bar{q}^3}\frac{d\bar{q}^i}{d\bar{q}^3}}, \qquad (C29)$$

one finds, using the notation $x' = dx/d\bar{s}$ etc., the dynamical equations

$$q^{0\prime} = -\frac{\partial \bar{p}_3}{\partial p^0} \qquad p^{0\prime} = \frac{\partial \bar{p}_3}{\partial \bar{q}^0}$$

$$x' = \frac{\partial \bar{p}_3}{\partial p^x} \qquad p^{x\prime} = -\frac{\partial \bar{p}_3}{\partial x}$$

$$y' = \frac{\partial \bar{p}_3}{\partial p^y} \qquad p^{y\prime} = -\frac{\partial \bar{p}_3}{\partial y}$$

$$(\bar{p}_3)' = \frac{\partial \bar{p}_3}{\partial \bar{s}}. \qquad (C30)$$

It is interesting to note in passing that the conventional form of Hamilton's equations can be found in the Cartesian coordinate system from (C22), if the coordinate $q^0 = ct$ is used in place of $\bar{q}^3$, and if one considers the variation δp_0 in finding the variation of the action. This leads to a system of equations similar to (C30)

$$\frac{dp^0 c}{dt} = \frac{\partial p^0 c}{\partial t}, \quad \frac{d\vec{p}}{dt} = -\frac{\partial p^0 c}{\partial \vec{q}}, \text{ and } \frac{d\vec{q}}{dt} = \frac{\partial p^0 c}{\partial \vec{p}}, \qquad (C30a)$$

where the Hamiltonian is $p^0 c$. These equations lead to (C10) and C(11).

The effective Hamiltonian $\bar{p}_3$ for this system is found from the invariant

$$(mc)^2 = (p-(e/c)A(q))_i(p-(e/c)A(q))^i = (\bar{p}-(e/c)\bar{A}(q))_i(\bar{p}-(e/c)\bar{A}(q))^i. \quad (C31)$$

Defining the energy $\mathcal{E}$ from

$$\mathcal{E}/c = p^0 - (e/c)A(q)^0 = mc\gamma, \qquad (C32)$$

and the scalar three-momentum as

$$|\vec{p}| = \sqrt{\mathcal{E}/c)^2 - (mc)^2}, \tag{C33}$$

one can use

$$\bar{g}^{33} = -(1 + x/\rho(\bar{s}))^{-2}, \tag{C34}$$

and

$$\bar{A}_3 = -(1 + x/\rho(\bar{s}))A^3, \tag{C35}$$

to obtain

$$\frac{\bar{p}_3}{|\vec{p}|} = -(e/c)(1 + x/\rho(\bar{s}))\frac{A^3(x,y,\bar{s})}{|\vec{p}|} - \sqrt{1 - \left(\frac{p^x - (e/c)A^x(x,y,\bar{s})}{|\vec{p}|}\right)^2 - \left(\frac{p^y - (e/c)A^y(x,y,\bar{s})}{|\vec{p}|}\right)^2} \times (1 + x/\rho(\bar{s})). \tag{C36}$$

For constant $|\vec{p}|$, one can introduce the scaled variables for the four-momentum $p^i/|\vec{p}| \to p^i$ in the dynamical equation (C30) and in (C36). These equations simplify for the case of a purely transverse magnetic field, where $A^x = A^y = 0$, and for the approximation

$$\sqrt{1 - (p^x)^2 - (p^y)^2} \approx 1 - \frac{(p^x)^2 + (p^y)^2}{2}, \tag{C37}$$

which is valid for large $|\vec{p}|$. For this case, one finds that (C36) becomes

$$\bar{p}_3 \approx \left(-(e/c)\frac{A^3(x,y,\bar{s})}{|\vec{p}|} - 1 + \frac{(p^x)^2 + (p^y)^2}{2}\right) \times (1 + x/\rho(\bar{s})), \tag{C38}$$

and, neglecting terms of order $p^{x2}/\rho(\bar{s})$, (C30) gives

$$x' = p^x(1 + x/\rho(\bar{s})), \qquad y' = p^y(1 + x/\rho(\bar{s})), \tag{C39}$$

$$\frac{d}{d\bar{s}}\left(\frac{x'}{1 + x/\rho(\bar{s})}\right) = \frac{\partial}{\partial x}\left[(e/c)(1 + x/\rho(\bar{s}))\frac{A^3(x,y,\bar{s})}{|\vec{p}|} + 1 + x/\rho(\bar{s})\right],$$

and

$$\frac{d}{d\bar{s}}\left(\frac{y'}{1+x/\rho(\bar{s})}\right)=\frac{\partial}{\partial y}\left[(e/c)(1+x/\rho(\bar{s}))\frac{A^s(x,y,\bar{s})}{|\vec{p}|}+1+x/\rho(\bar{s})\right]. \qquad (C40)$$

Neglecting terms of order $(x/\rho(\bar{s}))^2$, $x'^2/\rho(\bar{s})$, and skew-multipole errors, one finds using $e\bar{B}_0(\bar{s})\rho(\bar{s})=c|\vec{p}_0|$,

$$x''+\frac{|\vec{p}_0|}{|\vec{p}|}\left(\frac{1}{\rho(\bar{s})^2}+\frac{e\bar{B}_1(\bar{s})}{c|\vec{p}_0|}\right)x=\frac{|\vec{p}|-|\vec{p}_0|}{\rho(\bar{s})|\vec{p}|}\sim 0, \qquad (C41)$$

and

$$y''-\frac{|\vec{p}_0|}{|\vec{p}|}\frac{e\bar{B}_1(\bar{s})}{c|\vec{p}_0|}y=0, \qquad (C42)$$

where $|\vec{p}_0|$ is the three-momentum along the ideal orbit.

APPENDIX D: LATTICE FUNCTIONS

In this appendix, the lattice functions used in the numerical calculations are derived. They are found for a lattice made up of similar cells of the FODO (focusing, drift, defocusing, drift) form. Focusing and defocusing are achieved with thin lens quadrupole magnets, and the drifts occur through bending dipole magnets of length L and strength B_0. These functions have period $2L$, and the functions on the interval $L < \bar{s} < 2L$ are found from those on the interval $0 < \bar{s} < L$ using

$$f(\bar{s})_{L<\bar{s}<2L} = f(2L - \bar{s})_{0<\bar{s}<L}. \tag{D1}$$

The beta functions for a lattice with phase advance μ per cell are found from the $(1,2)$ component of the transfer matrix. The function $\beta_x(\bar{s})$ is found from

$$\beta_x(\bar{s}) \sin\mu = (\mathrm{O}(\bar{s})\mathrm{FO}(L)\mathrm{DO}(L-\bar{s}))_{12}, \tag{D2}$$

where the focusing and defocusing matrices for lenses of focal length f are, respectively,

$$\mathrm{F} = \begin{pmatrix} 1 & 0 \\ -1/f & 1 \end{pmatrix} \text{ and } \mathrm{D} = \begin{pmatrix} 1 & 0 \\ 1/f & 1 \end{pmatrix}. \tag{D3}$$

The matrix for a drift of distance $\bar{s}$ is

$$\mathrm{O}(\bar{s}) = \begin{pmatrix} 1 & \bar{s} \\ 0 & 1 \end{pmatrix}. \tag{D4}$$

The resulting beta function for $0 < \bar{s} < L$ is

$$\beta_x(\bar{s}) = \frac{2L}{\sin\mu}\left(1 + \frac{L}{2f} - (\frac{1}{f} + \frac{L}{2f^2})\bar{s} + \frac{\bar{s}^2}{2f^2}\right), \tag{D5}$$

where $L = 2f\sin(\mu/2)$. The expression for $\beta_y(\bar{s})$ on the same interval is found from $\beta_y(\bar{s}) = \beta_x(L - \bar{s})$.

The dispersion function $\eta(\bar{s})$ can be found when the differential equation (2.12) is approximated by

$$\eta''(\bar{s}) + K(\bar{s})\eta(\bar{s}) = \frac{eB_0(\bar{s})}{c|\vec{p}_0|} = \frac{1}{\rho(\bar{s})}. \tag{D6}$$

For the interval $0 < \bar{s} < L$ where the dipole bending angle is θ, it is found to be

$$\eta(\bar{s}) = \eta(0)(1 - \bar{s}/2f) + C_0\bar{s}^2/8f^2, \qquad (D7)$$

where $\eta(0) = C_0(1+L/4f)$ and $C_0 = 4\theta f^2/L$. Within the dipole magnet, $K(\bar{s}) = 0$, and $B_0(\bar{s}) \sim B_0(L/2)$. If follows from (D6) that

$$\eta''(L/2) = \frac{1}{\rho} = \frac{\theta}{L}. \qquad (D8)$$

Within a focusing quadrupole of width ϵ, $B(\bar{s}) = 0$, and (D6) gives

$$\epsilon\eta''(0) = -\epsilon K(0)\eta(0) = -\eta(0)/f, \qquad (D9)$$

where $\epsilon K(0) = 1/f$. This equation represents the change in the slope of $\eta(\bar{s})$ through the focusing quadrupole, and it is equivalent to the condition

$$\eta'(0) = -\eta(0)/2f. \qquad (D10)$$

A similar argument for the defocusing quadrupole gives the condition

$$\eta'(L) = -\eta(L)/2f. \qquad (D11)$$

From these three conditions, one can determine the quadratic approximation (D7) on the interval $0 < \bar{s} < L$. On the interval $L < \bar{s} < 2L$, $\eta(\bar{s})$ is found from (D1).

APPENDIX E: THE REDUCE CODE TSHIFT

The REDUCE program TSHIFT is given in this appendix, and the FORTRAN results which it produces for the tune-shifts (2.21) are given also. In the results, the notations $epsx = 2J_x$ and $epxy = 2J_y$ have been used. These quantities are related to the injection amplitudes through

$$\begin{aligned} \epsilon_x &= x_{amp}^2/\beta_{xmax} \\ \epsilon_y &= y_{amp}^2/\beta_{ymax}. \end{aligned} \tag{E1}$$

In addition, the notation $DELTA = \delta|\vec{p}|/\vec{p}|$ appears in the results. The angular averaging appearing in (2.23) has been performed in obtaining the results; however, the averaging of the type (2.25) around the circumference is done numerically in the program TUNESHIFT.FOR.

```
comment TSHIFT$
comment This programme calculates the multipole tuneshifs$
comment deltanux and deltanuy for B1 through B19$
comment 20 June 1991$
comment Tshift provides input for Tuneshift.for$
comment The A's are set to zero because they do not contribute$
comment as a result of the averaging on phix and phiy.$
  operator a$
  a(0):=0$
  a(1):=0$
  a(2):=0$
  a(3):=0$
  a(4):=0$
  a(5):=0$
  a(6):=0$
  a(7):=0$
  a(8):=0$
  a(9):=0$
  a(10):=0$
  a(11):=0$
  a(12):=0$

  operator b$
  b(0):=b0$
  b(1):=b1$
  b(2):=b2$
  b(3):=b3$
  b(4):=b4$
  b(5):=b5$
  b(6):=b6$
  b(7):=b7$
  b(8):=b8$
  b(9):=b9$
  b(10):=b10$
  b(11):=b11$
  b(12):=b12$

  operator c$

  let J**2=-1$
  for all n let c(n)=(x+j*y)**n$
  factor j$
  operator potential$
  comment potential=repot+i*impot$
  operator impot$
  operator repot$
  for all n let potential(n)=(b(n)+j*a(n))*c(n+1)/(n+1)$

  for all n let impot(n)=df(potential(n),j)$

  for all n let repot(n)=potential(n)-j*impot(n)$

  factor BO$
  factor a1,a2,a3,a4,a5,a6,a7a,a8,a9,a10,a11,a12$
  factor b1,b2,b3,b4,b5,b6,b7,b8,b9,b10,b11,b12$
  comment This gives the multipole potential for B3.$
  repot(3);

  x:=sqrt(2*betax*jx)*cos(phix)+eta*delta$
  y:=sqrt(2*betay*jy)*cos(phiy)$
  repot(1)$
  operator ix$
  operator iy$
  for all n match cos(phix)**n=ix(n)$
  for all n match cos(phiy)**n=iy(n)$
  match cos(phix)=ix(1)$
```

```
   match cos(phiy)=iy(1)$
   for i:=1 step 2 until 21 do let ix(i)=0$
   for i:=1 step 2 until 21 do let iy(i)=0$
   comment The operator for n!.$
   operator nfac$
   for all n let nfac(n)=for i:=1:n product i$
   comment Evaluate the integral(1/2pi)int(0>2pi)of cos**2m(phix)$
for i:=0 step 2 until 20 do let ix(i)=nfac(i)/(nfac(i/2)*nfac(i/2)*2**i)$
for i:=0 step 2 until 20 do let iy(i)=nfac(i)/(nfac(i/2)*nfac(i/2)*2**i)$
   jx:=epsx/2$
   jy:=epsy/2$
   comment The tune-shift operators.$
   operator dnux$
   operator dnuy$
   comment Tuneshifts$
   for all n let dnux(n)=df(repot(n),epsx)*2$
   for all n let dnuy(n)=df(repot(n),epsy)*2$
   off allfac$
   on div$
   order delta,epsx,epsy,betax,betay,eta$
   on fort$
   out dnux$
   for i:=1:10 do write"dnux(",i,"):=",dnux(i)$
   shut dnux$
   out dnuy$
   for i:=1:10 do write"dnuy(",i,"):=",dnuy(i)$
   shut dnuy$
   end$
```

```
          for i:=1:10 do write"dnux(",i,"):=",dnux(i)$

dnux(1.):=1./2.*B1*BETAX
dnux(2.):=B2*DELTA*BETAX*ETA
dnux(3.):=B3*(3./2.*DELTA**2*BETAX*ETA**2+3./8.*EPSX*BETAX
      . **2-3./4.*EPSY*BETAX*BETAY)
dnux(4.):=B4*(2.*DELTA**3*BETAX*ETA**3+3./2.*DELTA*EPSX*
      . BETAX**2*ETA-3.*DELTA*EPSY*BETAX*BETAY*ETA)
dnux(5.):=B5*(5./2.*DELTA**4*BETAX*ETA**4+15./4.*DELTA**2*
      . EPSX*BETAX**2*ETA**2-15./2.*DELTA**2*EPSY*BETAX*
      . BETAY*ETA**2+5./16.*EPSX**2*BETAX**3-15./8.*EPSX*
      . EPSY*BETAX**2*BETAY+15./16.*EPSY**2*BETAX*BETAY**2)
dnux(6.):=B6*(3.*DELTA**5*BETAX*ETA**5+15./2.*DELTA**3*
      . EPSX*BETAX**2*ETA**3-15.*DELTA**3*EPSY*BETAX*BETAY*
      . ETA**3+15./8.*DELTA*EPSX**2*BETAX**3*ETA-45./4.*
      . DELTA*EPSX*EPSY*BETAX**2*BETAY*ETA+45./8.*DELTA*
      . EPSY**2*BETAX*BETAY**2*ETA)
dnux(7.):=B7*(7./2.*DELTA**6*BETAX*ETA**6+105./8.*DELTA**4
      . *EPSX*BETAX**2*ETA**4-105./4.*DELTA**4*EPSY*BETAX*
      . BETAY*ETA**4+105./16.*DELTA**2*EPSX**2*BETAX**3*ETA
      . **2-315./8.*DELTA**2*EPSX*EPSY*BETAX**2*BETAY*ETA**
      . 2+315./16.*DELTA**2*EPSY**2*BETAX*BETAY**2*ETA**2+
      . 35./128.*EPSX**3*BETAX**4-105./32.*EPSX**2*EPSY*
      . BETAX**3*BETAY+315./64.*EPSX*EPSY**2*BETAX**2*BETAY
      . **2-35./32.*EPSY**3*BETAX*BETAY**3)
dnux(8.):=B8*(4.*DELTA**7*BETAX*ETA**7+21.*DELTA**5*EPSX*
      . BETAX**2*ETA**5-42.*DELTA**5*EPSY*BETAX*BETAY*ETA**
      . 5+35./2.*DELTA**3*EPSX**2*BETAX**3*ETA**3-105.*
      . DELTA**3*EPSX*EPSY*BETAX**2*BETAY*ETA**3+105./2.*
      . DELTA**3*EPSY**2*BETAX*BETAY**2*ETA**3+35./16.*
      . DELTA*EPSX**3*BETAX**4*ETA-105./4.*DELTA*EPSX**2*
      . EPSY*BETAX**3*BETAY*ETA+315./8.*DELTA*EPSX*EPSY**2*
      . BETAX**2*BETAY**2*ETA-35./4.*DELTA*EPSY**3*BETAX*
      . BETAY**3*ETA)
dnux(9.):=B9*(9./2.*DELTA**8*BETAX*ETA**8+63./2.*DELTA**6*
      . EPSX*BETAX**2*ETA**6-63.*DELTA**6*EPSY*BETAX*BETAY*
      . ETA**6+315./8.*DELTA**4*EPSX**2*BETAX**3*ETA**4-
      . 945./4.*DELTA**4*EPSX*EPSY*BETAX**2*BETAY*ETA**4+
      . 945./8.*DELTA**4*EPSY**2*BETAX*BETAY**2*ETA**4+315./
      . 32.*DELTA**2*EPSX**3*BETAX**4*ETA**2-945./8.*DELTA**
      . 2*EPSX**2*EPSY*BETAX**3*BETAY*ETA**2+2835./16.*
      . DELTA**2*EPSX*EPSY**2*BETAX**2*BETAY**2*ETA**2-315.
      . /8.*DELTA**2*EPSY**3*BETAX*BETAY**3*ETA**2+63./256.
      . *EPSX**4*BETAX**5-315./64.*EPSX**3*EPSY*BETAX**4*
      . BETAY+945./64.*EPSX**2*EPSY**2*BETAX**3*BETAY**2-
      . 315./32.*EPSX*EPSY**3*BETAX**2*BETAY**3+315./256.*
      . EPSY**4*BETAX*BETAY**4)
dnux(10.):=B10*(5.*DELTA**9*BETAX*ETA**9+45.*DELTA**7*EPSX
      . *BETAX**2*ETA**7-90.*DELTA**7*EPSY*BETAX*BETAY*ETA
      . **7+315./4.*DELTA**5*EPSX**2*BETAX**3*ETA**5-945./
      . 2.*DELTA**5*EPSX*EPSY*BETAX**2*BETAY*ETA**5+945./4.*
      . DELTA**5*EPSY**2*BETAX*BETAY**2*ETA**5+525./16.*
      . DELTA**3*EPSX**3*BETAX**4*ETA**3-1575./4.*DELTA**3*
      . EPSX**2*EPSY*BETAX**3*BETAY*ETA**3+4725./8.*DELTA**
      . 3*EPSX*EPSY**2*BETAX**2*BETAY**2*ETA**3-525./4.*
      . DELTA**3*EPSY**3*BETAX*BETAY**3*ETA**3+315./128.*
      . DELTA*EPSX**4*BETAX**5*ETA-1575./32.*DELTA*EPSX**3*
      . EPSY*BETAX**4*BETAY*ETA+4725./32.*DELTA*EPSX**2*
      . EPSY**2*BETAX**3*BETAY**2*ETA-1575./16.*DELTA*EPSX*
      . EPSY**3*BETAX**2*BETAY**3*ETA+1575./128.*DELTA*EPSY
      . **4*BETAX*BETAY**4*ETA)

          shut dnux$
```

```
          for i:=1:10 do write"dnuy(",i,"):=",dnuy(i)$

dnuy(1.):=-1./2.*B1*BETAY
dnuy(2.):=-B2*DELTA*BETAY*ETA
dnuy(3.):=-B3*(3./2.*DELTA**2*BETAY*ETA**2+3./4.*EPSX*
     . BETAX*BETAY-3./8.*EPSY*BETAY**2)
dnuy(4.):=-B4*(2.*DELTA**3*BETAY*ETA**3+3.*DELTA*EPSX*
     . BETAX*BETAY*ETA-3./2.*DELTA*EPSY*BETAY**2*ETA)
dnuy(5.):=-B5*(5./2.*DELTA**4*BETAY*ETA**4+15./2.*DELTA**2
     . *EPSX*BETAX*BETAY*ETA**2-15./4.*DELTA**2*EPSY*BETAY
     . **2*ETA**2+15./16.*EPSX**2*BETAX**2*BETAY-15./8.*
     . EPSX*EPSY*BETAX*BETAY**2+5./16.*EPSY**2*BETAY**3)
dnuy(6.):=-B6*(3.*DELTA**5*BETAY*ETA**5+15.*DELTA**3*EPSX*
     . BETAX*BETAY*ETA**3-15./2.*DELTA**3*EPSY*BETAY**2*
     . ETA**3+45./8.*DELTA*EPSX**2*BETAX**2*BETAY*ETA-45./
     . 4.*DELTA*EPSX*EPSY*BETAX*BETAY**2*ETA+15./8.*DELTA*
     . EPSY**2*BETAY**3*ETA)
dnuy(7.):=-B7*(7./2.*DELTA**6*BETAY*ETA**6+105./4.*DELTA**
     . 4*EPSX*BETAX*BETAY*ETA**4-105./8.*DELTA**4*EPSY*
     . BETAY**2*ETA**4+315./16.*DELTA**2*EPSX**2*BETAX**2*
     . BETAY*ETA**2-315./8.*DELTA**2*EPSX*EPSY*BETAX*BETAY
     . **2*ETA**2+105./16.*DELTA**2*EPSY**2*BETAY**3*ETA**
     . 2+35./32.*EPSX**3*BETAX**3*BETAY-315./64.*EPSX**2*
     . EPSY*BETAX**2*BETAY**2+105./32.*EPSX*EPSY**2*BETAX*
     . BETAY**3-35./128.*EPSY**3*BETAY**4)
dnuy(8.):=-B8*(4.*DELTA**7*BETAY*ETA**7+42.*DELTA**5*EPSX*
     . BETAX*BETAY*ETA**5-21.*DELTA**5*EPSY*BETAY**2*ETA**
     . 5+105./2.*DELTA**3*EPSX**2*BETAX**2*BETAY*ETA**3-
     . 105.*DELTA**3*EPSX*EPSY*BETAX*BETAY**2*ETA**3+35./2.
     . *DELTA**3*EPSY**2*BETAY**3*ETA**3+35./4.*DELTA*EPSX
     . **3*BETAX**3*BETAY*ETA-315./8.*DELTA*EPSX**2*EPSY*
     . BETAX**2*BETAY**2*ETA+105./4.*DELTA*EPSX*EPSY**2*
     . BETAX*BETAY**3*ETA-35./16.*DELTA*EPSY**3*BETAY**4*
     . ETA)
dnuy(9.):=-B9*(9./2.*DELTA**8*BETAY*ETA**8+63.*DELTA**6*
     . EPSX*BETAX*BETAY*ETA**6-63./2.*DELTA**6*EPSY*BETAY
     . **2*ETA**6+945./8.*DELTA**4*EPSX**2*BETAX**2*BETAY*
     . ETA**4-945./4.*DELTA**4*EPSX*EPSY*BETAX*BETAY**2*
     . ETA**4+315./8.*DELTA**4*EPSY**2*BETAY**3*ETA**4+
     . 315./8.*DELTA**2*EPSX**3*BETAX**3*BETAY*ETA**2-2835.
     . /16.*DELTA**2*EPSX**2*EPSY*BETAX**2*BETAY**2*ETA**2
     . +945./8.*DELTA**2*EPSX*EPSY**2*BETAX*BETAY**3*ETA**
     . 2-315./32.*DELTA**2*EPSY**3*BETAY**4*ETA**2+315./
     . 256.*EPSX**4*BETAX**4*BETAY-315./32.*EPSX**3*EPSY*
     . BETAX**3*BETAY**2+945./64.*EPSX**2*EPSY**2*BETAX**2
     . *BETAY**3-315./64.*EPSX*EPSY**3*BETAX*BETAY**4+63./
     . 256.*EPSY**4*BETAY**5)
dnuy(10.):=-B10*(5.*DELTA**9*BETAY*ETA**9+90.*DELTA**7*
     . EPSX*BETAX*BETAY*ETA**7-45.*DELTA**7*EPSY*BETAY**2*
     . ETA**7+945./4.*DELTA**5*EPSX**2*BETAX**2*BETAY*ETA
     . **5-945./2.*DELTA**5*EPSX*EPSY*BETAX*BETAY**2*ETA**
     . 5+315./4.*DELTA**5*EPSY**2*BETAY**3*ETA**5+525./4.*
     . DELTA**3*EPSX**3*BETAX**3*BETAY*ETA**3-4725./8.*
     . DELTA**3*EPSX**2*EPSY*BETAX**2*BETAY**2*ETA**3+
     . 1575./4.*DELTA**3*EPSX*EPSY**2*BETAX*BETAY**3*ETA**3
     . -525./16.*DELTA**3*EPSY**3*BETAY**4*ETA**3+1575./
     . 128.*DELTA*EPSX**4*BETAX**4*BETAY*ETA-1575./16.*
     . DELTA*EPSX**3*EPSY*BETAX**3*BETAY**2*ETA+4725./32.*
     . DELTA*EPSX**2*EPSY**2*BETAX**2*BETAY**3*ETA-1575./
     . 32.*DELTA*EPSX*EPSY**3*BETAX*BETAY**4*ETA+315./128.*
     . DELTA*EPSY**4*BETAY**5*ETA)

          shut dnuy$
```

REFERENCES

* Operated by the Universities Research Association, Inc., for the U. S. Department of Energy under Contract No. DE-AC35-89ER40486.

[1] T. Garavaglia, S. K. Kauffmann, R. Stiening, and D. Ritson, in *Supercollider 2*, edited by M. McAshan (Plenum Press, New York, 1990), p. 39.

[2] D. Ritson, in *Nonlinear Problems in Future Particle Accelerators*, edited by W. Scandale and G. Turchetti (World Scientific, Singapore, 1991), p. 304.

[3] A. C. Hearn, *REDUCE User's Manual, Version 3.3* (The Rand Corporation, Santa Monica, California, 1987).

[4] *Top Drawer*, (SLAC Computation Group, Stanford, California, 1980).

[5] T. Garavaglia and R. Stiening, Superconducting Super Collider Laboratory Report No. SSCL-260, 1990.

[6] R. D. Ruth, in *AIP Conf. Proc. No. 153*, edited by M. Month and M. Dienes (American Institute of Physics, New York, 1987) p. 151.

[7] A. Jackson, Superconducting Super Collider Laboratory Report No. SSC-107, 1987.

[8] E. D. Courant and H. S. Snyder, Annals of Phys. (N. Y.) **3**, 1 (1958).

[9] C. Garrod, Phys. Rev. **167**, 1143 (1968).

[10] L. D. Landau and E. M. Lifshitz, *The Classical Theory of Fields* (Pergamon Press, New York, 1987) p. 230.

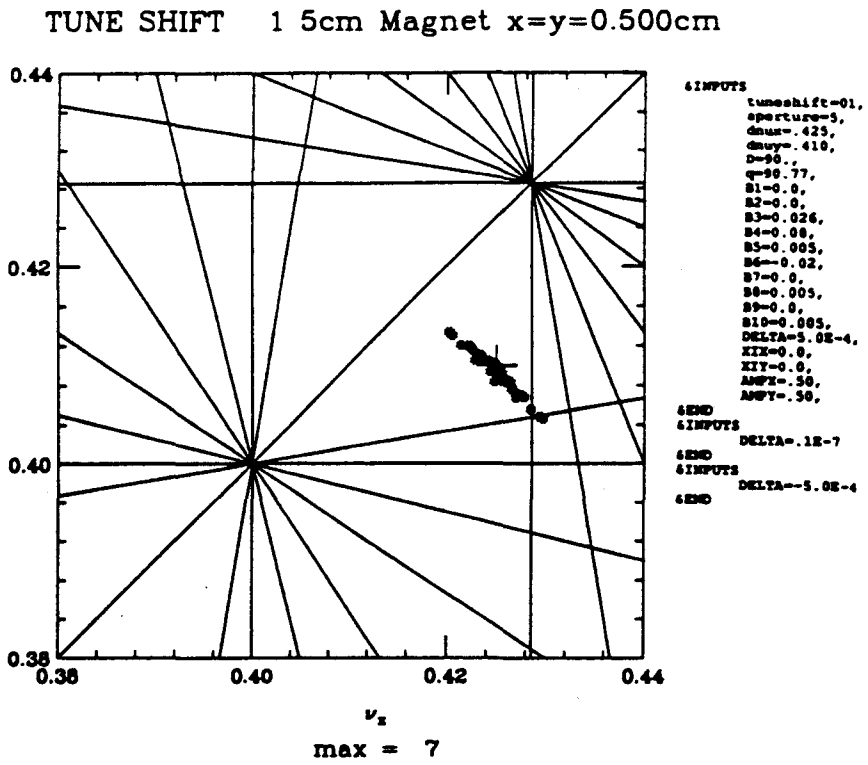


FIG. 1. The tune-spread for $\delta|\vec{p}|/\vec{p}| = 0$, and $\pm 5. \times 10^{-4}$, with injection amplitude grid from (0, 0) to (0.5 mm, 0.5 mm).

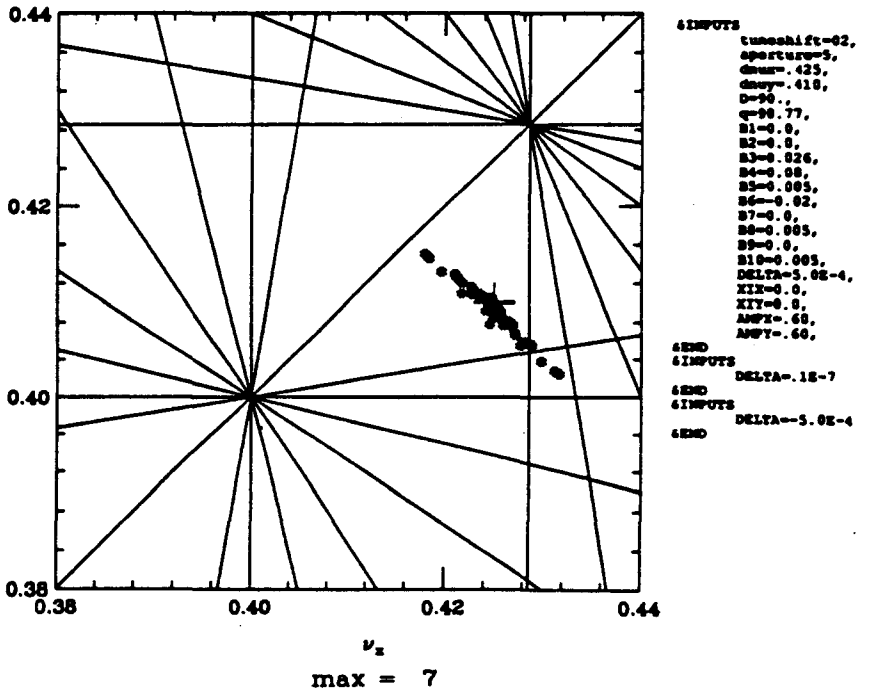


FIG. 2. The tune-spread for $\delta|\vec{p}|/\vec{p}| = 0$, and $\pm 5. \times 10^{-4}$, with injection amplitude grid from (0, 0) to (0.6 mm, 0.6 mm).

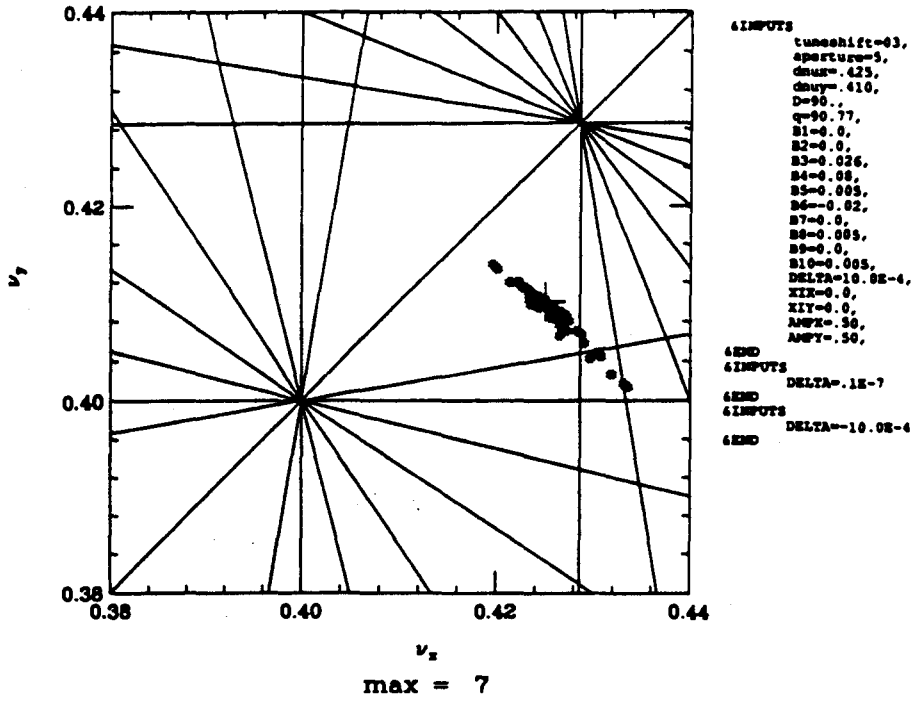


FIG. 3. The tune-spread for $\delta|\vec{p}|/\vec{p}| = 0$, and $\pm 10. \times 10^{-4}$, with injection amplitude grid from (0, 0) to (0.5 mm, 0.5 mm).

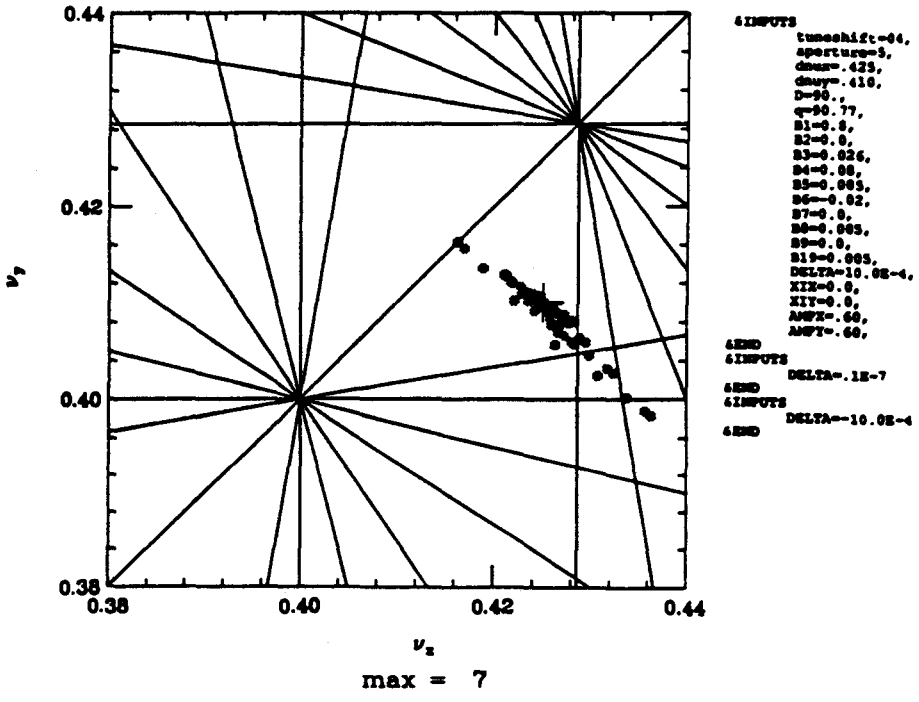


FIG. 4. The tune-spread for $\delta|\vec{p}|/\vec{p}| = 0$, and $\pm 10. \times 10^{-4}$, with injection amplitude grid from (0, 0) to (0.6 mm, 0.6 mm).

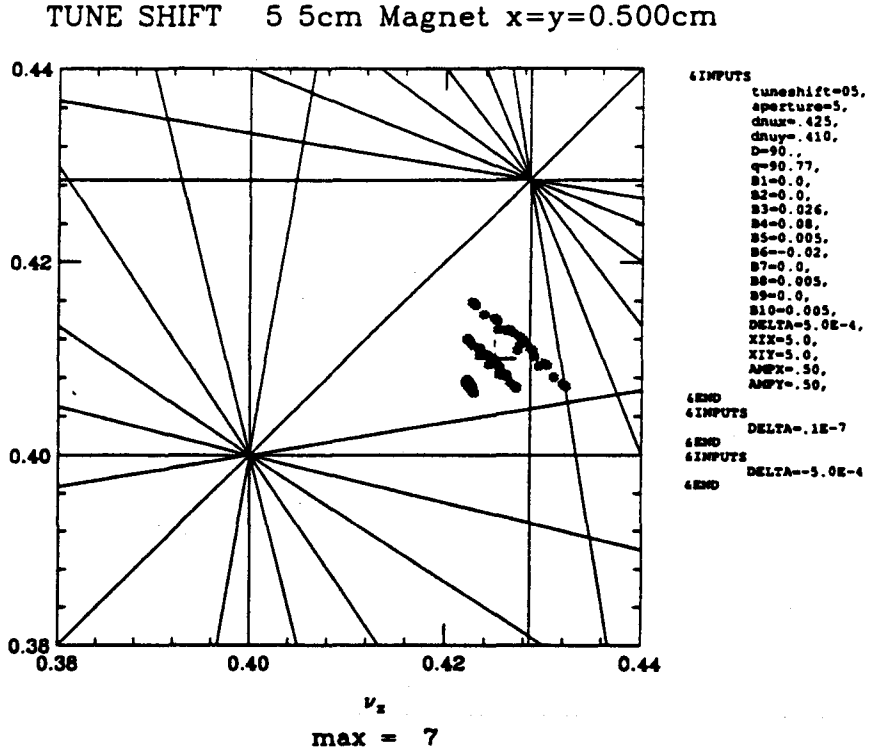


FIG. 5. The tune-spread with linear momentum error for $\delta|\vec{p}|/\vec{p}| = 0$, and $\pm 5. \times 10^{-4}$, with injection amplitude grid from (0,0) to (0.5 mm, 0.5 mm).

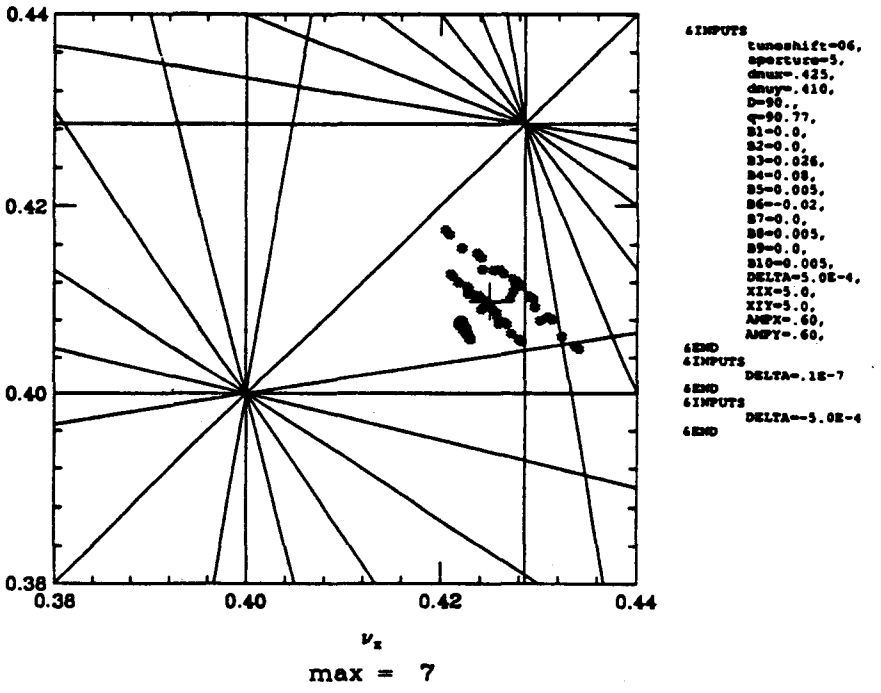


FIG. 6. The tune-spread with linear momentum error for $\delta|\vec{p}|/\vec{p}| = 0$, and $\pm 5. \times 10^{-4}$, with injection amplitude grid from (0,0) to (0.6 mm, 0.6 mm).

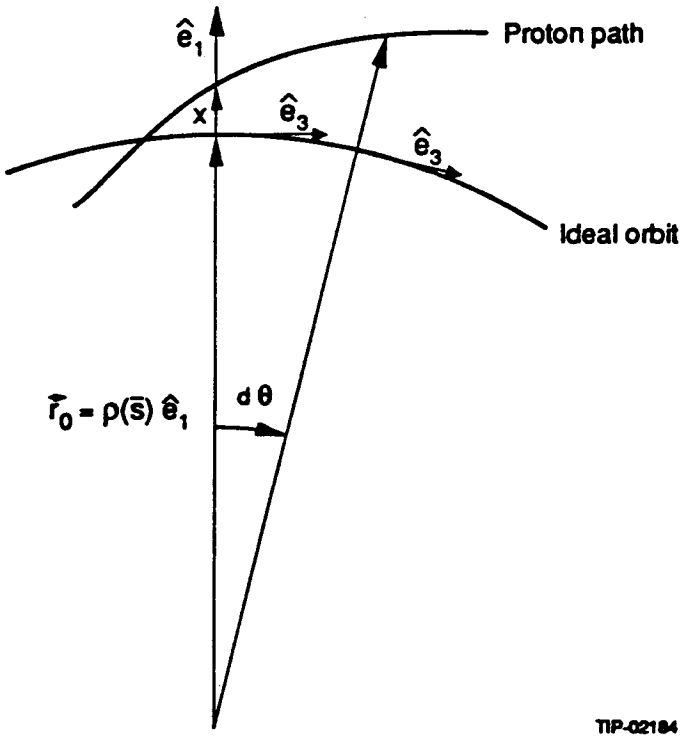


FIG. 7. The curvilinear geometry and coordinate systems for proton motion relative to the ideal orbit.

A FAST VERTEX FITTING METHOD FOR THE EXPERIMENTS AT MULTI-TEV PP COLLIDERS

Pierre BILLOIR
LPNHE, Universités Paris VI et VII, Paris, France

Sijin QIAN
CERN, Geneva, Switzerland/ INFN, Frascati, Italy

Abstract

A fast vertex fitting algorithm using a local parametrization of tracks has been proposed and tested for the experiments with high track multiplicity environment. The parametrization of tracks is around a fixed point which is chosen to be close to the primary and short-lived secondary vertices, or to the decay vertex of a long-lived particle; hence useful approximations may be applied. The parametrization is done once per track, even if the track association procedure needs to be iterated. The time consumption of the method is proportional to the number of tracks (n) instead of n^3 as in a standard least-squares method. Also, the track addition to or the track subtraction from a fitted vertex can be easily performed.

1. Introduction

In the experiments at future multi-Tev pp colliders (e.g. SSC and LHC), the high track multiplicity at the vertices (especially at the primary vertex) requests the fast vertex fitting algorithms. We have developed and tested a promising fast method [1] using a local (i.e. "perigee") parametrization of tracks [2].

The goal of a "full" 3-Dimensional vertex fit is to obtain the vertex position V and n 3-vectors track momenta $\mathbf{p}_i$ (i=1~n) at the vertex as well as the associated covariance matrices. The input information for the vertex fit consists of 5-parameters $\mathbf{q}_i$ (for 3-D tracks curved in a magnetic field) and their covariance matrix C_i of each track at a reference point (Fig.1). The perigee parameters defined in section 2.2 describe the trajectory close to the origin point which is a first approximation of the primary or the short-lived secondary vertices; therefore the relationship between $\mathbf{q}_i$ and $(V,\mathbf{p}_i)$ is simple if the curvature effect may be neglected, or approximated at the first order. In addition, by using the "perigee" parametrization, the "full fit" can be reduced to an even faster "simple fit", which only estimates the vertex position without re-adjusting the track parameters.

In this short paper, section 2 lists the main ingredients of the algorithm. More detailed mathematical derivation can be found in [1,2]. Its performance and promising features are briefed in section 3. See [2,3] for more comprehensive reports about the Monte Carlo test and the implementation in an experiment.

2. Summary of the formalism

The algorithm mainly consists of three parts as described below.

2.1 The "full" vertex fit.

The charged track (i) is characterized by the parameters q_{ij} (j=1~5) and their weight matrix W_i (= C_i^{-1}, i.e. the inverse of the covariance matrix) at a reference point. The q_{ij} are the functions of the vertex position $V \equiv (x_v,y_v,z_v)$ and the track momenta p_{im} (m=1~3) at the vertex, i.e. $q_{ij} = F_j(V,\mathbf{p}_i)$. The aim is to find the V and $\mathbf{p}_i$ which minimize the χ^2,

$$\chi^2 = \sum_i \Delta q_i^T W_i \Delta q_i \text{ , where } \Delta q_i = q_i^{measured} - F(V,p_i). \quad (1)$$

If q_i, within measurement errors, are linearly related to

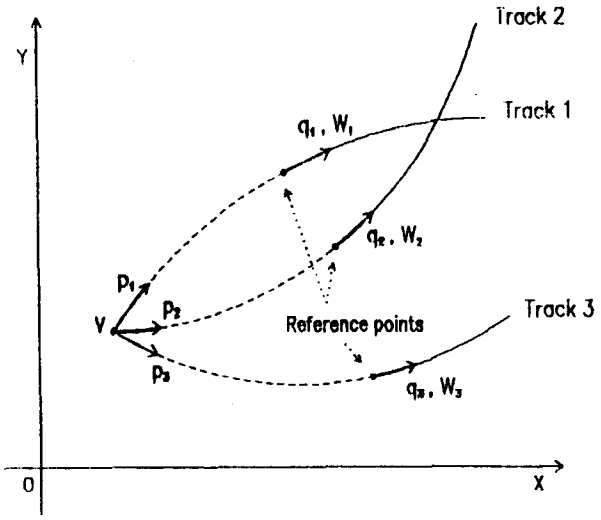


Fig. 1. Relation between q_i and (V, p_i) in a vertex fit.

variations δV and δp_i, i.e.

$$F(V^0+\delta V,\ p_i^0+\delta p_i) = F(V^0,p_i^0) + D_i\delta V + E_i\delta p_i\ , \quad (2)$$

where δV and δp_i are variations around first approximations V^0 and p_i^0,

$$(D_i)_{jn} \equiv \frac{\partial F_j(V,p_i)}{\partial V_n}, \quad (E_i)_{jm} \equiv \frac{\partial F_j(V,p_i)}{\partial p_{im}}\ ,$$

$$(j = 1\sim5,\ n = 1\sim3,\ m = 1\sim3),$$

then Eq.(1) can be expressed as

$$\chi^2 = \sum_i (\delta q_i - D_i\delta V - E_i\delta p_i)^T W_i (\delta q_i - D_i\delta V - E_i\delta p_i)\ , \quad (3)$$

where $\delta q_i = q_i^{measured} - F(V^0,p_i^0)$.

Minimizing the χ^2 w.r.t. V and p_i, we get

$$\begin{cases} A\delta V + \sum_i B_i\delta p_i = T \\ B_i^T\delta V + C_i\delta p_i = U_i \end{cases}\ , \quad (4)$$

where $A \equiv \sum_i D_i^T W_i D_i$, $B_i \equiv D_i^T W_i E_i$, $C_i \equiv E_i^T W_i E_i$,

$$T \equiv \sum_i D_i^T W_i \delta q_i,\ U_i \equiv E_i^T W_i \delta q_i.$$

The solution for vertex position is

$$\delta V = (A - \sum_i B_i C_i^{-1} B_i^T)^{-1}(T - \sum_i B_i C_i^{-1} U_i)\ . \quad (5)$$

Notice that $(A - \sum_i B_i C_i^{-1} B_i^T)^{-1}$ in Eq.(5) is just the covariance matrix (i.e. Cov(V,V)) associated to δV. Substituting δV back into Eq.(4), δp_i and Cov(p_i,p_j) as well as Cov(V,p_i) can be obtained [1].

Standard least-squares method for vertex fitting relies on inverting a (3n+3)x(3n+3) matrix with a number of operations proportional to n^3 (where n is the number of tracks associated at the vertex). In contrast, our method uses only small matrices and the computing time is merely proportional to n (as shown in Table 1). Hence it is particularly suitable to be applied in the environment with high track multiplicity at multi-Tev pp colliders.

Note also that if the matrices A, B_i, C_i, T and U_i are kept in memory, it is easy to add a track to (or to remove a track from) the fitted vertex, without total re-computation from the beginning [1].

2.2 The "perigee" parametrization.

The purpose of this parametrization is to give a precise and simple description of the trajectory in the neighborhood of the expected vertex. The extrapolation of the measured tracks to the vertex region is done once and for all, and the vertex fitting procedure (which may be repeated with different subsets of tracks) uses only a short range propagation.

If the magnetic field is along the beam direction (i.e. the z-axis); we define the "perigee" P (Fig.2) to be the point of the closest approach of the trajectory (a helix) to the z-axis. If the origin O is chosen to be around the interaction region, this point is close to the primary vertex and short lived secondary vertices. The five "perigee" parameters of a track are:

(1) ε: the distance between P and O; by convention, the sign of ε is positive if the angle from OP to the direction of the track is $+\pi/2$;

(2) z_p: z coordinate of P;

(3) θ: polar angle of the trajectory w.r.t. z-axis;

(4) ϕ_p: azimuthal angle of the trajectory at P;

(5) ρ: the signed curvature of the trajectory (the $1/|\rho|$ is the radius of the curvature in the xy projection, and the sign of ρ is positive if the trajectory is anti-clockwise).

To use this parametrization, i.e. $q = (\varepsilon, z_p, \theta, \phi_p, \rho)$, in the vertex fit, we need to express these parameters as functions of the vertex parameters: the coordinates (x_v,y_v,z_v) of vertex V (see Fig.2) and the track parameters $p = (\theta, \phi_v, \rho)$ at V. If we introduce the quantities $Q \equiv x_v\cos\phi_v + y_v\sin\phi_v$ and $R \equiv y_v\cos\phi_v - x_v\sin\phi_v$, calculations at first order in ρ give the matrices of derivatives in Eqs.(2)-(4):

$\partial\downarrow / \partial\rightarrow$	x_v	y_v	z_v	θ	ϕ_v	ρ
ε	s	-c	0	0	Q	$-Q^2/2$
z_p	-tc	-ts	1	$-Q(1+t^2)$	-Rt	QRt
ϕ_p	$-\rho c$	$-\rho s$	0	0	1	-Q
	D matrix			E matrix		

(6)

where $c \equiv \cos\phi_v$, $s \equiv \sin\phi_v$, $t \equiv \cot\theta$.

If one wants to fit a secondary vertex far away from the primary vertex (e.g. the long-lived particle decay), the "perigee" parameters may be computed w.r.t. a displaced origin. The parametrization w.r.t. the origin assures a correct vertex fit within a range of about 15~20 mm [2]. Thus, for most secondary vertices created by the short-lived particles, they may be fitted by using the reconstructed tracks parametrized w.r.t. the main origin without re-parametrization w.r.t. a shifted origin.

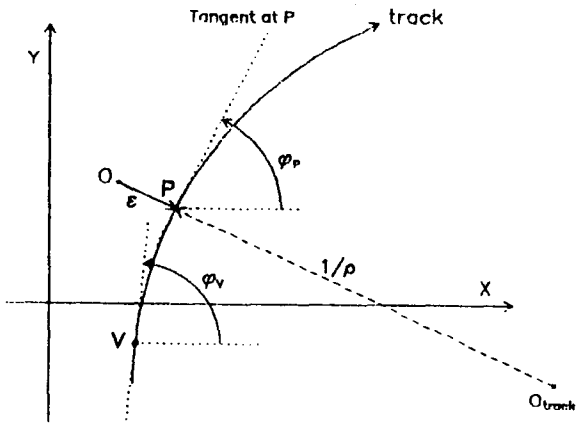


Fig. 2. Definition of the perigee parameters in x-y projection

2.3 The "simple" vertex fit.

By using the perigee parametrization, a simpler algorithm can be derived to estimate the vertex position without re-fitting the track parameters. In this algorithm, the variation of transverse errors along the track is neglected in the neighbourhood of the perigee, and $\mathbf{p} = (\theta, \phi_v, \rho)$ is considered to be constant. Thus the (5x5) covariance matrix C (which is the inverse of W in Eq.(1)) is reduced to its (2x2) submatrix C' corresponding to the variables ε and z_p, and the (5x3) matrix D in Eq.(2) to its (2x3) submatrix D' which is the derivatives of (ε, z_p) w.r.t. (x_v, y_v, z_v), i.e. the first two rows in Eq.(6).

Let W' be the inverse of the C', $w_i = D_i'^T W_i' D_i'$ and $x_{pi} = (x_p, y_p, z_p)_i$ to be the coordinates of the perigee P of the track i, the vertex position can be estimated by

$$V = (\sum_i w_i)^{-1} (\sum_i w_i x_{pi}) \quad . \tag{7}$$

$$\chi^2 = \sum_i (x_{pi}-V)^T w_i (x_{pi}-V) \quad , \tag{8}$$

The error matrix on V is simply $(\sum_i w_i)^{-1}$.

This "simple" method also provides a means to quickly reject the tracks which may not belong to the vertex. While solving V by Eq.(7), the two factors in the right hand side can be stored; then when calculating the χ^2, by Eq.(8), after having obtained V, the contribution to the χ^2 by each individual track i can be examined. If any track (say the track k) would contribute too much to the χ^2, the vertex could be re-estimated by subtracting the w_k and $w_k x_{pk}$ from the two stored factors of Eq.(7), without a complete re-calculation from the beginning.

3. Performance and main features of the method

The algorithm has been implemented in two experiments: DELPHI at LEP and ZEUS at HERA. The detailed Monte Carlo tests are reported in [2]. Table 1 is the speed comparison. For the standard least-squares method, only CPU time for the matrix inversion (i.e. without including any other operation) is monitored. For the fast methods, the column "Interface" indicates the time spent in the perigee parametrization. The absolute value of CPU time is in VAX9000 computer unit.

In conclusion, the following features of the method are observed:

(1) It is indeed fast, especially for the primary vertex with high track multiplicity.

(2) The fitting quality is quite good and can be maintained within a range of 15mm without need of re-parametrization of tracks [2].

(3) It allows to perform the track addition to or the subtraction from a fitted vertex without fully re-fitting. This may be used to build up a vertex finding strategy that seperates the primary and secondary vertices.

Therefore this algorithm hopefully provides an efficient way for the vertex reconstruction in the experiments at multi-Tev pp colliders.

Table 1 Timing Comparison

Track mult. at vertex	Matrix inversion		Fast methods in this paper		
	Dim. of matrix	CPU time	"Simple" fit	"Full" fit	Interface
10	33	4.4 ms	0.1 ms	0.5 ms	1.0 ms
20	63	35 ms	0.2 ms	1.2 ms	1.7 ms
40	123	~280 ms*	0.5 ms	2.9 ms	3.6 ms
80	243	~2200 ms*	1 ms	5 ms	7.1 ms

*) The numbers are estimated by extrapolation from lower dimensions since the subroutine for the matrix inversion in CERNLIB has a dimensional restriction of 100.

References

[1] P. Billoir, R. Frühwirth and M. Regler, Nucl. Inst. and Meth. A241 (1985) 115;

[2] P. Billoir and S. Qian, to be published on Nucl. Inst. and Meth. (A), (1991).

[3] G. Iacobucci and S. Qian, ZEUS Notes 91-020 (1991).

October, 1991

Calorimeter Trigger Applications, Training, and Assessment of a Feed-forward Neural Net

D. Y. Wu, M. K. Campbell
University of Michigan, Ann Arbor
and SSC Laboratory, Dallas, Texas

Abstract

A feed-forward neural net technique is applied to trigger on $B \rightarrow e\bar{\nu}X$ decays in the high background environment of $\bar{p}p$ collisions at E_{cm}=1.8 TeV. For the 1992 data run, we will install electronics into the CDF detector trigger using calorimeter signals as input to a neural net IC chip. We describe our algorithm and network optimization (training) issues, including those unique to $\bar{p}p$ physics and to an electronic implementation. We assess the advantages and problems of using trained neural nets. In addition to the trained mode of operation, the architecture of the analog chip also allows employing it as a massively parallel arithmetic processor for conventional trigger applications. The device may be re-programmed to accommodate changes in trigger requirements and to provide considerable flexibility in trigger design.

Introduction

The large cross section ($o(50)$ mb at E_{cm}=1.8 TeV) from inelastic hadron collisions at $\bar{p}p$ accelerators makes it difficult to trigger on interesting processes which contain low-energy decay products. This is especially true of events requiring calorimetry for identification, such as for $B \rightarrow e\bar{\nu}X$decays. Good pattern recognition is needed to improve the signal–to–background ratio. Such pattern recognition requires analyzing and correlating critical sub-detector signals, which is time consuming to process electronically and therefore typically implemented in secondary-level triggers.

We will implement one particular type of pattern recognition technique based on neural net IC technology, new to triggering in high energy physics, in the CDF detector Level 2 trigger for the 1992 data run at E_{cm}=1.8 TeV. Neural networks are one method to correlate information in order to maximize the separation of signal from background.

Our neural network consists of a non-linear function containing free parameters which must be optimized via a minimization procedure, known as training. There are several reasons for investigating the utility of neural nets. The network can be trained to distinguish very complex patterns. At the trigger level, one of the major assets of neural net IC's is their flexibility. The analog network chip may be re-programmed to accommodate changes in trigger requirements. In addition, neural nets have parallel processing capabilities and are rather insensitive to fluctuations, such as from electronic noise or channel–to–channel differences in detector response. A final reason for pursuing neural nets is that powerful conventional cuts are sometimes difficult to implement electronically. The hope is to realize a similar signal–to–background ratio via a neural net cut for which the electronic capability exists.

Electronics manufacturers have produced IC chips which mimic the function S used in neural nets.[1] One downloads such a device with some set of optimized weights prior to trigger installation for data taking.

We provide an offline study of using a neural net to trigger on $B \rightarrow e\bar{\nu}X$ jets with calorimeter signals, a network application proposed by M. Campbell. We use the feed-forward multi-layer (signals are fed forward through layers of processing nodes) network to separate the $B \rightarrow e\bar{\nu}X$ signal from gluon-jets background. An overview of the trigger, the input signals from the CDF calorimeter, and a brief explanation of our neural net are given in Section I. The expected efficiencies, the event kinematics, and some network issues relevant to triggering are considered here as well. A major aspect of employing neural nets is to first train it to recognize signal from background. Therefore, we describe our algorithm in detail as well as discuss the advantages and problems of using trained neural nets in the Appendix.

There is a second application for neural net chip technology: the circuit architec-

ture provides a unique flexibility that is valuable for trigger development, as suggested by S. Kuhlmann and D. Wu. For trigger design purposes, it is often known in advance which sub-detector (*e.g.*, calorimeter) signals would be useful in forming electronic decisions. However, what the best trigger algorithm for utilizing such signals prior to data-taking at new energy or luminosity regions is less clear. It is possible to design general circuits using the neural net device without having a fixed trigger algorithm in advance. The interconnections in the chip are such that the device may be used as an arithmetic processor, although it is analog, to improve the performance of conventional trigger tasks, allowing re-programming of threshold values and even revision of the type of arithmetic operations needed. For example, conventional electron and photon triggers involve threshold requirements, sums of calorimeter module energies, and ratio checks of hadronic to electromagnetic energy. In 1992, we will try out this second way of using the device to form a conventional isolated-photon trigger, which requires no training and is discussed in Section II. The neural net structure (Fig. 1) processes the input signals and performs the arithmetic operations in parallel, allowing the possibility of fast triggering. While trained-network applications, like for $B \rightarrow e\bar{\nu}$X decays, are mainly feasible only as secondary-level triggers, the parallel-processor applications can be more readily implemented at any level. For example, the chip may be used to make multiple threshold decisions in parallel, an application which is often needed in primary-level triggers.

I. A $B \rightarrow e\bar{\nu}$X Application of Neural Nets at $\bar{p}p$

Although our main goal is to test the utility of neural net technology for triggering, our physics interest lies in studying B's at $\bar{p}p$ where we hope to log more of the large 10–40 μb $B\bar{B}$ production cross section.[2] Measurements of rare B decays, the B lifetime, and $B\bar{B}$ mixing all require as large a sample of B's as possible. Therefore, we select $B \rightarrow e\bar{\nu}$X jets as our signature for the new trigger and use a trained net to try to improve the signal–to-background ratio over that obtained with the conventional electron trigger. The cross section for B physics is about 10^3 times smaller than for the typical inelastic hadron collision ("minimum bias" event) and it decreases sharply as a function of the transverse momentum of the B. In order to trigger on more B's, it is necessary to lower the energy thresholds. However, it becomes difficult to distinguish the B decay particles from the

gluon–jet backgrounds at lower energies.

There is a second, practical reason for choosing to trigger on $B \rightarrow e\bar{\nu}X$ jets. For the CDF detector, calorimeter signals are available more quickly than track momentum information and therefore are better for forming a fast trigger. Such a calorimeter-based pattern motivates selecting a physics process involving electrons, such as $B \rightarrow e\bar{\nu}X$ decays. Using only calorimeter signals to form an efficient trigger for *all* B decay modes is much more difficult. For measurements like $B\bar{B}$ mixing, an electron in the event is also useful because its charge distinguishes the B from $\bar{B}$. Finally, a third reason for selecting $B \rightarrow e\bar{\nu}X$ is that CDF has already collected $B \rightarrow e\bar{\nu}X$ data where the E_t of the electron is > 7 GeV, a useful data sample for trigger development. CDF will also implement a conventional electron trigger, allowing cross checks of the neural net $B \rightarrow e\bar{\nu}X$ results.

We now describe the CDF calorimeter[3] signals which are fed to the neural net. Cylindrically symmetric about the beam axis, the central calorimeters consist of towers which point back to the interaction region. Each tower has an electromagnetic shower counter (lead–scintillator) in front of a corresponding hadron calorimeter (steel–scintillator). The energy resolution for the central electromagnetic calorimeter is $\delta E/E \approx .14/\sqrt{E}$ (E in GeV), and for the hadronic calorimeter is $\delta E/E \approx .5/\sqrt{E}$. Calorimeter signals representing information in bins of 15° in azimuth (ϕ) and 0.2 in pseudorapidity (η) reach the trigger electronics.[4] The neural net $B \rightarrow e\bar{\nu}X$ trigger obtains signals from a $(14\eta \times 24\phi)$ grid area with two layers in depth (electromagnetic and hadronic).

A $B \rightarrow e\bar{\nu}X$ jet where the B has >15 GeV momentum transverse to the beam direction (p_t), would typically deposit all of its energy in a 5×5 grid, subtending 37.5° by 0.5η from the center to the outer edge. At CDF, for a Monte Carlo b-quark jet with >15 GeV p_t, the opening angle between the direction of the parent B and the electron averages less than 10°. The electron energy is normally deposited in a single 1×1 electromagnetic trigger tower which is 18 radiation lengths thick. The particles from the hadronized b-quark jet deposit hadronic and electromagnetic energy in a few towers and the underlying minimum bias event normally deposits little energy.

Our procedure for triggering on the $B \rightarrow e\bar{\nu}X$ decay is to look for central electromag-

netic (CEM) calorimeter trigger towers that pass a certain E_t threshold (seed towers). The signals from the seed tower and from nearby towers (a 5×5 calorimeter grid region centered on the seed tower with coordinates (η_s, ϕ_s)) are fed to to the neural net electronics. There are altogether 50 trigger towers signals, half electromagnetic, half hadronic. The network then decides if the calorimeter pattern indicates the presence of a $B \rightarrow e\bar{\nu}$X jet. After the neural net electronics finish processing, we require a charged track with p_t above some threshold to extrapolate to the seed tower in the ϕ direction, further indicating the presence of an electron.

I-a. A Feed-forward Multilayer Network

Here is a brief explanation of the feed-forward 2-layer neural net (Fig. 1) we use to separate signal from background patterns. The network consists of a non-linear function, S, involving the product of the input values x_i (the 50 calorimeter signals) and of weight parameters w_i, and thresholds (biases) b_j:

$$S \equiv g_k\Big(\sum_j w'_{jk} f_j\big(\sum_i w_{ij} x_i + b_j\big) + b_k\Big)$$

where i is an index over the inputs, j the hidden nodes and k the output nodes (only one is shown). The two layers f and g are of the same mathematical form, a sigmoid function:

$$f(y) = \frac{1}{1 + \mathrm{e}^{-y}}$$

We obtain optimal weight and bias values for S via a minimization procedure which tries to separate signal from background patterns. We use patterns *known* to be either signal or background (*e.g.*, from a Monte Carlo sample) and assign a desired response value "0" or "1" to the pattern during the minimization. This training process is essentially fitting the function S to a surface proportional to the relative fraction of the two sets of patterns such that the surface best "separates" signal from background. The Appendix provides an explanation of the algorithm we use, which is adapted from Rumelhart, *et al.*[5] The procedure is changed slightly to account for the fact that there are many more possible patterns from the background class. We afterwards check the separation efficiency of the *trained* neural net by running it on an independent test sample.

Signal and backgrounds tend to show better separation using a neural net technique than with one-dimensional cuts. Section E in the Appendix gives a simple example. For any set of variables used to characterize events, the actual boundary of best separation between the signal and the background does not normally consist of flat surfaces corresponding to fixed values on each variable; the boundary has some curvature. Using conventional single-valued threshold cuts, which do not account for correlations between variables, leads to needless loss in signal or retention of background. The neural net training procedure finds the parameters of S such that contours of constant S approximate the actual curvature of the boundary. We examine physical quantities which may be formed from the 50 tower energies fed as inputs to the network in order to understand the neural net solution after training. For example, Fig. 2 provides the distribution of neighboring *vs* seed trigger tower electromagnetic energy for test patterns passing and failing the neural net. For both signal and background, the plot demonstrates that a final neural net output threshold cut (cut on a particular value of S) does not necessarily correspond to a flat cut on the values of the input variables. It is worth noting that neural net training can provide insights into the kinematic features of the physics process, useful for optimizing threshold algorithms for *conventional* triggers and analyses.

The very advantage of a neural net algorithm also leads to a possible problem of estimating trigger biases and efficiencies. One must understand the detector response over a large range of values for the input variables because the final network cut corresponds to a cut over a large range ("multi-valued" cut) of those input signal values, as shown in Fig. 2. However, for most conventional, single-valued cuts on a particular variable, one needs to estimate the efficiency of the requirement only mainly near the cut value. If Monte Carlos are used either to train the network or to estimate efficiencies and errors, they must be correct over the broad range of values and correlations among the many input variables. Otherwise, it may be difficult to know if the final estimated efficiencies and systematic errors for a neural net cut are reliable. This problem is reduced by using redundant and other less stringent triggers to measure the neural net trigger efficiency.

I-b. Description of the Training and the Trigger Rates

The results from an offline simulation of the neural net trigger are considered in this section. We train on 1000-2000 events from a Monte Carlo sample containing $B \rightarrow e\bar{\nu}X$ jets and on 4000-5000 Monte Carlo two-jet (gluon-gluon) background event sample, where the jet p_t is >15 GeV, and the pattern contains a seed tower with E_t >4 GeV. The primary-level calorimeter trigger thresholds implemented at CDF precludes reducing the seed threshold below 4–5 GeV for the neural net trigger, which is a secondary-level trigger. Jets with p_t below 15 GeV do not produce enough energetic electron candidates, making the event generation inefficient. The events, produced in $\bar{p}p$ collision where the beam energy is 0.9 TeV, are generated using Isajet with CDF default fragmentation parameters[6] and passed through detector simulation and event reconstruction. New patterns not in the training sample are then used to estimate trigger efficiency after the net is optimized. Both the testing and training patterns must pass the following requirements in addition to CEM seed trigger tower $|\eta|$ <1.0: (a) seed tower $4 < E_t < 15$ GeV, where the upper limit is to have the network improve its efficiency for identifying lower energy B's, (b) a charged track with p_t >3.5 GeV matching the seed tower in ϕ and η, and (c) for Monte Carlo signal events, the seed tower shower must be from an electron from B decay. Fig. 3 shows the distribution of the output values of the trained neural net (the value of last node in Fig. 1) for new test signal and background data. The trigger efficiency will depend on the exact threshold value we select in Fig. 3 to separate signal from background. We choose a value of about 0.8 to reject more than 98% of the background. For Monte Carlo *training* samples, the network accepts $(40.8 \pm 1.4)\%$ of the $B \rightarrow e\bar{\nu}X$ and $(1.4 \pm 0.2)\%$ of the gluon patterns. For Monte Carlo *testing* samples, the values are $(39.4 \pm 1.6)\%$ and $(1.3 \pm 0.2)\%$, indicating that the separation performance generalized to new patterns.

To check inaccuracies in the simulation, we use the data collected by CDF with loose trigger requirements to compare with our Monte Carlo expected efficiencies. For example, we apply the same set of requirements, consisting mainly of stringent electron cuts, to both data and Monte Carlo to obtain a fairly pure sample of $B \rightarrow e\bar{\nu}X$ jets and then pass the pattern through the trained net. For 5 GeV electron E_t data, the efficiency for both real and simulated data is about 56%, and it is about 65% for 7 GeV electrons. The agreement between Monte Carlo and data is generally good and the neural net is not very sensitive

to the deficiencies in the simulation. It is also possible to use previous CDF data instead of the Monte Carlo to optimize the neural net by assigning "1" to those events passing the offline analysis requirements and "0" to those which do not.

Although we have not optimized the neural net on a particular type of $B \rightarrow e\bar{\nu}X$ jets, the sample which passes the neural net requirements turn out to favor cases where the electrons are more isolated and the surrounding jet energy is lower than that of the typical $B \rightarrow e\bar{\nu}X$ jet. The relative values of the weights connecting the input layer and the first hidden layer indicates the significance of a particular input variable. For our patterns, the maximum value amongst all of the weights after training is four times larger than the others and it belongs to the electromagnetic–hadronic seed tower, where the electron candidate is located. Therefore much of what the trained neural net recognizes is the electron. This is not too surprising because the typical pattern is an array of small energy depositions symmetric about a more obvious, larger deposition. This trigger is quite efficient on finding electrons from sources other than from B jets. A smaller 3×3 grid pattern would be more suitable for a general electron trigger. Once the electron p_t is greater than ~7 GeV the B purity of the sample is naturally high for an inclusive electron trigger. Then even simple, conventional electron triggers begin to do as well as a trained neural net trigger in signal-to-background. The network still does better at 7 GeV, providing a factor of two improvement in $B \rightarrow e\bar{\nu}X$ purity over that of the conventional CDF electron trigger.

I-c. Trigger Issues of Neural Nets

For trigger applications, the efficiency of the neural net must be fairly insensitive to the effects of electronic noise, DC offsets, and device variations. This issue is considered in Appendix E. Generally, the efficiency is not much altered except in one case. Positive voltages are used to represent calorimeter energy measurements at CDF; therefore, we operate the neural net circuit in the positive voltage region and train the net with only positive input values. Should there be electronic noise that is negative, even slightly, by about 100 MeV equivalent noise, the efficiency is degraded by about 50%. The chip permits defining a mathematical zero by setting a reference voltage to zero, thus helping us avoid this problem, but small signals near zero volts are then somewhat distorted. To overcome

this problem, we must download our parameters which are optimized offline into the neural net chip and further train with the chip and hardware in the minimization algorithm loop itself.

The current version of the chip unfortunately has a limited dynamic voltage range of 0–3 Volts. This reduces the resolution of the full energy scale we wish to cover by the voltage range. The initially-expected voltage range for the chip was to be double or triple the 3 Volt scale and we had trained the network with such a range in mind. The new, smaller range requires reducing the values of the input variable of the patterns by a factor of about two. Using the network weights actually optimized with the full-scale data, we run new patterns where the inputs are scaled down by a factor of two. We find that the trigger efficiency remains about the same as before. We note however, that if we have to scale the inputs down further by factors of 5 or 20 and run these scaled-down patterns through the full-scale-trained net, then the result is very poor separation. The signal and background network output distributions overlap more than shown in Fig. 3. If instead, we now re-optimize the net by starting with training data that is already scaled down, by 5, 10 or 20, we can achieve a separation efficiency comparable to before by selecting an output threshold requirement different from 0.8. However, the distributions of the network output for new patterns is somewhat different than shown in Fig. 3, with the peak for background data shifted closer to zero and signal data forming a broader peak. The result is that the new cut ends up on the peak or on the higher-end tail of the distribution for *signal* patterns. It turns out the network output distributions resemble that of a 1×1 training pattern where we fed the network only the seed hadronic and electromagmetic E_t's. The scaling down causes the 5×5 pattern to look like only a single electron candidate tower(seed) with energy, and the rest of the tower energies be comparable to values due to noise. Such a scaled-down 5×5 pattern resembles that of the 1×1. For both the 1×1 and the scaled-down 5×5 case, the minimization results in events containing higher seed E_t's to have a higher probability of being identified as signal.

II. Second Application of Neural Net Technology

We now describe an altogether different way of using analog neural net chips – to carry

out conventional, *non-trained* trigger algorithms. The basic architecture of the device processes signals in parallel, permitting a flexibility not existing in other analog or digital IC's. The device may be used to do arithmetic sums, multiplication, fixed ratio checks, and logical AND's and OR's. For the neural net $B \rightarrow e\bar{\nu}X$ trigger we use a 5×5 calorimeter grid centered about a seed electromagnetic (EM) tower with a large energy deposition (electron candidate). When there are no tracks associated with the seed EM tower, then the energy deposition is very likely a photon candidate; *isolated* photons are of particular interest because they probe QCD and are signatures for new physics. We may chose one of the following procedures to implement isolation criteria. The first is a typical example of using the chip to perform sums and threshold requirements, and the second to check whether ratios pass a certain value (*e.g.*, $\frac{A}{B} < 10$).

1. Require the sum of the energy deposited in the 8 calorimeter towers, adjacent to the seed tower, to be small and less than some value α. This is done by setting the weights for the 8 towers in the summation in the sigmoid function to –1.0, and zero for all other towers. The offset parameter b is set to α:

$$\text{Neural Net Output} = \frac{1}{1 + e^{-\left(-\sum_{i=1}^{8} x_i + \alpha\right)}}.$$

   When the value of the output is less than 0.5, then the isolation requirement is satisfied, otherwise not.

2. Alternatively, the energy deposited in the 8 adjacent towers may be required to be only some fraction of that deposited in the seed tower, for example, one-tenth. Now, the weights for the 8 towers should be set to –10, and 1 for the seed tower, and zero for the bias parameter b:

$$\text{Neural Net Output} = \frac{1}{1 + e^{-\left(-\sum_{i=1}^{8} 10x_i - 1x_{seed}\right)}}$$

   Again the output threshold is set to be 0.5.

The neural net chip has several good features which compensate for this awkward way of performing arithmetic. First, our particular chip is very compact (45×45 mm^2), but it allows 64 parallel inputs and contains 64 hidden nodes, permitting 64 individual operations to be carried out simultaneously. Although it is possible to use conventional IC's like op amps to do the same arithmetic, the number of circuit components required would be very much larger. Second, since we are designing circuit boards for the $B \rightarrow e\bar{\nu}X$ trigger, we find it convenient and economical that the exact same design can also handle conventional trigger functions. The third and main reason is the ability to re-program the chip's weights and threshold values via EEPROM technology to accomodate trigger changes. We can design physics trigger circuits around this device with almost no exact algorithm in mind *a priori*, and then afterwards select a particular algorithm. Input voltage ranges may be re-scaled, and offsets may be removed by changing the weights and biases. It is important to note for this *analog* device that one can revise even the *type* of arithmetic operation desired for the algorithm, as shown in the above example for photons. Of course this flexibility is true for the trained network application as well, such as to recognize $W \rightarrow \tau\bar{\nu}$ instead of $B \rightarrow e\bar{\nu}X$ decays.

Depending on application, the current version of the device we use may need to be improved in speed ($\sim 3\mu s$) and in the dynamic range of the input and output voltages (between 0 - 3.5V) for both the trained and untrained use of the chip. For untrained network applications, it is possible to use simpler functions instead of a sigmoid for the nodes, so long as the $\sum_i w_i x_i + b$ structure is retained. This can speed signal processing time, reducing from 3 to 0.8 μs, values based on the characteristics of our chip. The complexity of the chip should be reduced as well which should lead to improved performance and flexibilty. The chip was designed to allow a two layer network by clocking results of the previous layer through the chip again. Chips containing only a single layer network are easier to use and multiple chips may be cascaded for multi-layer network applications.

Conclusion

We have considered the multi-layer feed-forward type of neural net to recognize $B \rightarrow e\bar{\nu}X$ jets at a $\bar{p}p$ collider. These nets must first be optimized with a large data sample,

requiring considerable computing resources. Afterwards we load the weights into an IC chip to operate it in the CDF trigger. We have provided a primer on training the network in the Appendix and have described some short-comings of utilizing trained neural nets. We will also use the analog chip to perform conventional trigger tasks in parallel with the trained neural net. Both the $B \rightarrow e\bar{\nu}X$ and conventional applications will have trigger cross-checks to ensure a full understanding of these new techniques. The technology has great potential because it is intelligent enough to distinguish complex patterns and it allows changes to trigger algorithms in a way never permitted before. We will determine if neural nets can expand our choice of techniques for fast triggering which thus far is limited because sometimes *conventional* cuts may be powerful but are difficult to implement electronically. We look forward to the 1992 data run.

We thank CDF for use of the Monte Carlo and event reconstruction code. We appreciate useful comments from K. Riles and R. Thun. Also, we thank N. Chriss and B. Denby for their useful suggestions, and particularly Zhaoping Li for her advice and insights on training tricks.

Appendix: A. Neural Net Training Algorithm

The type of neural net we use is known as the feed-forward, multi-layer perceptron configuration which accepts patterns with either continuous valued (*e.g.*, particle energies) or binary inputs. The theory of neural nets is discussed extensively in Refs. 5 and 7. We consider here instead the practical aspects of the training procedure. The configuration is widely applicable and basic to some other networks.

We use the algorithm derived in Ref. 5 for obtaining the optimal values for the parameters, weights w's and biases b's, contained in our neural net function S:

$$S_l^k \equiv g_l\Big(\sum_j w'_j f_j\big(\sum_i w_{ij}x_i + b_j\big) + b'\Big) \tag{1}$$

where i indexes the inputs, j the hidden nodes, k the pattern, and l the output node. S defines the neural net configuration, which for us consists of a layer of 50 inputs x_i's (the zeroth layer), a hidden layer f with 10 nodes (the first layer), and an output layer g usually

2. The value of f_j for each node j is calculated using the the current value of the w_{ij}'s and b_j's. This is refered to as presenting the input data to the net. Each input pattern should have a fixed desired response, S^k_{target}, associated with it. During training, we have set the target output value to 0.9 for patterns from signal events, and 0.1 for background.

3. The weights are adjusted at time $(t + 1)$ based on the previous state of the the neural net at time t:

$$w_{ij}(t + 1) = w_{ij}(t) + \eta \Delta w_{ij}(t) + \alpha(w_{ij}(t) - w_{ij}(t-1)) \quad (4)$$

where i indexes the nodes (or inputs) in a previous layer and j, the nodes in the next layer. The biases for each node are varied similarly:

$$b_j(t + 1) = b_j(t) + \eta \Delta b_j(t) + \alpha(b_j(t) - b_j(t-1)) \quad (5)$$

The parameters η and α, scale factors input by hand, are described in Section D. For weights connecting each of the hidden nodes i and the output node j:

$$\Delta w_{ij} = -\sum_k \delta^k_j f^k_i, \quad (6)$$

where k indexes a summation over the total number of patterns and

$$\delta^k_j = f^k_j(f^k_j - S^k_{target})(1 - f^k_j) \quad (7)$$

(note: for the jth output node, f^k_j is the same as the actual final response of the net, S^k_j, from eqn. 1). For the weights connecting the inputs x_i and the j-th node in the hidden layer, the term $\Delta\, w_{ij}$ is:

$$\Delta w_{ij} = -\sum_k \Big(f^k_j(1 - f^k_j) \sum_l \delta^k_l w^k_{jl} \Big) x^k_i, \quad (8)$$

where l is over all nodes in the next higher layer (output) and δ^k_l is the δ^k_j given

with one node (the second layer). The summation is over the number of nodes feeding into each network layer. Both f and g have the same functional form, called a sigmoid function (they are represented by the rectangles in Fig. 1):

$$f_j = \frac{1}{1+\mathrm{e}^{-\left(\sum_i w_{ij}x_i+b_j\right)}} \tag{2}$$

The goal is to separate the training sample into two classes via an appropriate S, *e.g.* to obtain a desired response value(S^k_{target} for the kth pattern) of S be ~0.9 for input signal events and ~0.1 for input background events. The optimum set of weights and biases is found by a least squares minimization of the differences(E) between the actual responses S^k_{actual} and the target responses. The weight values for the minimum point are reached through successive approximations; in each iteration, the weights are changed by an amount proportional to the partial derivatives of the function E with respect to the w's, and similarly for the biases. The choice for the function E in Ref. 5 is:

$$E \equiv \frac{1}{2}\sum_l\sum_k\left(S^k_{target}-S^k_{actual}\right)^2 \tag{3}$$

where k indexes a summation over the number of training patterns, and l over the number of output nodes (for debugging purposes, we sometimes used two output nodes). In short, the training procedure samples the function E in weight space until yielding an optimized function S in input-variable space to separate signal from background. In practice, the procedure consists of the following:

1. The net is started in an arbitrary state by generating different small random values for the w_{ij}'s and b_j's. For a reasonable set of starting weights, the final result does not depend on the initial choice. During the *first* pass of the inputs through the neural net, we check that the response value of S for at least most of the patterns is within the 0.1 – 0.9 region; otherwise we rescale the weights (see Section D on the scale of training parameters). We use initial weight and bias values between –1 and 1, but for the weights there is a multiplicative factor of (average value of the inputs to a particular layer/total number of inputs for that same layer).

above. Similarly, the biases for the output nodes j are modified according to:

$$\Delta\, b_j \;=\; \sum_k \delta_j^k \tag{9}$$

and for the hidden node j:

$$\Delta\, b_j \;=\; \sum_k f_j^k(1-f_j^k)\sum_l \delta_l^k w_{jl}^k, \tag{10}$$

where again, l is over all nodes in the next layer, and k over the number of patterns.

Steps 2 and 3 are repeated when E stops fluctuating and an arbitrarily small value for E is reached. The procedure is slow but fairly stable and is intended for *a priori* training and then later use in a system with pre-determined weights. For an electronic implementation, the fact that the weight changes(derivative of the sigmoid function) depend only on the f_j's and not a different function facilitates placing the actual IC chip in the training loop.

Typically, the neural net weights are updated after pairs of signal and background patterns are presented to the net. Instead, we present *all* of the patterns to the net prior to each weight update (the summation over k). By doing so, we have averaged over the effect of all of the input events every time. Averaging requires scaling η down. For example, we use η values ranging approximately from 10^{-5} to 10^{-4} when a few thousand patterns are presented prior to each weight-update; whereas, when only pairs of patterns are presented, η values from 0.1 to 0.5 are more appropriate. This averaging method allows more flexibility in that (a) the order of the input patterns does not matter, and (b) we can input more patterns from one class than from the other. For a $B \rightarrow e\bar{\nu}$X trigger at a $\bar{p}p$ collider, we expect many more background than signal events and thus to more closely span the larger variety of background patterns, we use about 3–4 times more background than signal events.

B. Training Sample

This section and the next two address how we select our net configuration, the significance of some of the training parameters and their values. Generally, the most important

consideration is the training data themselves. A neural net cannot separate patterns which are intrinsically inseparable. And of course, the choice of input variables matters greatly.

Table I shows how the number of patterns and the relative amount from each class (signal and background) affect the final separation. For the case of a 15 GeV jet p_t with a 4 GeV (E_t) electron candidate, we typically use more than 3000 gluon background (Isajet Monte Carlo) and over 1000 $B \rightarrow e\bar{\nu}X$ signal patterns. It became apparent that more than $\sim$ 1500 background patterns are needed for training when we examine a value for the output threshold that allows the network to accept at most $\sim$1% background (last column of Table I), a level permitted at CDF based on luminosity, cross sections and dead time considerations. We check the acceptance efficiency after fixed intervals (about 200 iterations) of weight-updating. With too few patterns, the efficiency can fluctuate by as much as 40% at successive intervals; whereas, it is typically only 5% by using $>$ 3000 background training patterns. In addition, the net not does generalize so well: the discrepancy between the acceptance of background *training* and *new* test patterns widens by a factor of $>$3, as the number of weight-updating iterations is increased. To investigate whether further increasing the total number of patterns or the ratio of background patterns compared to signal is advantageous, we loosen the output threshold cut to improve the statistics of the background accepted (signal detection efficiency of 50%, column 4 of Table I). There is no significant improvement in doing either. Because it requires much CPU to generate more training data, by assuming that 4224 events adequately spans the set of background patterns, we have checked that a yet larger ratio of background–to–signal patterns shows no improvement by multiplying the effective weight change by ten for background events. Aside from generation time, the CPU needed for training also increases with the number of patterns: for a total of 7000 patterns, 50 inputs per pattern, and one layer of 10 hidden units, it takes about 8 hours on a 7–10 MIP machine; whereas, 2500 patterns take about 3 hours.

It is clear that the intrinsic overlap between signal and background patterns places an upper limit on the network's ability to separate the two. Therefore, if one knows something about the characteristics of the events beforehand, or has other means of enhancing the signal-to-background (other than with a neural net cut), one should limit the diversity of

connections between nodes define the topology.

The number of layers determines what shape the final surface separating the two classes of events may take.[7] Three layers, in addition to the input layer, where the nodes are continuous functions, can provide the most general shape. For instance, if one of the two classes of events occupies disjoint regions in the space of the input variables (*e.g.*, like holes in swiss cheese), then a three layer net configuration along with sufficient number of nodes is needed. Single-layer networks involve only linear combinations of the input variables and are adequate only when the signal and background occupy different sides of a plane in the input variable space. Two layers allow a region of space to be approximated by either an open or closed convex surface. We expect the energy variables for signal and background jets each to occupy a continuous region of space where the surface that best divides them is not necessarily a plane; so, we use only two layers: one hidden layer and one output. Furthermore, extra layers require more CPU time during training and also result in an electronically slower trigger.

We now examine the number of nodes used in each of the layers, which also then determine the number of weights (interconnections). For the input layer, we have 50 units (5×5 grid), a choice determined by the size of the jets. A 6×6 grid yields about the same separation efficiency but requires more electronics channels to implement and CPU-time to train, and a smaller grid is insufficient to contain the typical jet. We use 10 nodes in the hidden layer and one in the output. This results in a total of 510 weights plus 11 biases, 521 parameters to be optimized! Clearly, the amount of training data must be large. However, not all of the weights matter; the larger weight values are usually of order 1.0 and among the 500 weights between the input and hidden layer, about *half* of them are smaller than 0.05. There are pruning techniques to remove extraneous weights and hidden units.[6] Another method is to start with fewer nodes in the hidden layer prior to training; this turns out to result in fewer small-valued weights after training. For instance, for one hidden layer with two nodes, only 12 of the 100 weights connecting the input and the next layer, are less than 0.05. The range in the values of the weights, the separation efficiency and purity are similar to the 10 node case. The response distribution for signal patterns with two hidden units contains two prominent peaks, one centered around 0.14 and the

the patterns and train on only a subset of the data to improve the separation efficiency. As a simple example, we know that $B \rightarrow e\bar{\nu}X$ jets are more similar to gluon jets when the E_t of the electron is lower and thus expect a network to do poorer on lower-energy patterns. With our signal $B \rightarrow e\bar{\nu}X$ patterns and our background gluon jets, we started with training patterns where the seed electromagnetic (CEM) tower energy ranged from (a) 3 to 15 GeV, then narrowed it to (b) 4 to 15 GeV, and finally restricted the sample further by (c) requiring a stiff track be associated with the candidate electron shower. Because of the large background cross section, we must set the neural net trigger thresholds to accept at most about 1% background. For approximately the same amount of training data, network topology and η and α parameters, and after the network performance efficiency has generalized, we find for ~1% background, the neural net efficiency on new signal patterns, passing the same requirements as the training data, improved from (a) ~8%, to (b) ~14%, and finally to (c) ~30%.

Even after we narrow the kinematic characteristics of the training sample, there may still be variations, and the optimized neural net will generally be efficient in distinguishing only a subset of the patterns. Sometimes, the trained-net's response distribution for, say, the signal data, will have several peaks, reflecting the existence of subsets with different kinematic properties within the sample. The distribution can be used to guide the pruning of the training patterns, to try to steer the neural net to recognize a particular data subset if desired.

C. Network Configuration

The topology of the net is important because it helps determine the region of space containing the minima points. Larger nets, with more hidden units and associated weights, can parametrize more characteristics of the training patterns. However, more free parameters also require much more data and CPU to optimize. As with any parameter fitting procedure, too little data forces the parameters to take on a very specific value and "memorize" the input training set, in which case the network performance does not generalize to new test patterns. For the multi-layer perceptron type of network, the number of inputs, the number of layers, the number of nodes within each layer, and the number of weight

other at 0.8, unlike the ten-hidden unit case shown in Fig. 3 which has one main peak. The signal events in the two peaks differ most noticeably in the degree of isolation of the electron. The ten-hidden-unit case favors patterns with isolated electrons in a much more gradual way, producing only one peak. The background distribution for both cases has only one peak, around 0.13. Even with the fewer hidden units, it is still possible to achieve about the same separation efficiency as found for the ten-node case by an appropriate choice for the network output threshold cut - which ends up being around the apex or high-tail end of the second peak around 0.8, making the few-node cases a less desireable trigger than the ten-node one. As the number of hidden nodes is increased from 2 to 10, the signal events in the first peak (at 0.14) diminish and migrate to the second peak. The first peak does not continue to shrink as we go to 15 hidden units for our fixed training sample size.

D. Training Parameters

After defining the network topology and thus the space containing the minima and the total number of variables to optimize, the scale parameters α and η in Eqns. 4 and 5 then determine which of the points of the function E the training samples. The variable η is a "step size" to move the neural net from one point to the next along the direction of the slope of E towards a minimum. The value of η, defined in Appendix A, should be chosen to be small enough so that the minimization samples the points in a fairly smooth fashion. The α term is an optional variable; it further smooths the weight changes since it brings in a term involving the previous weight update. If the scale of these parameters takes S to an extreme end of the sigmoid function, 0.0 or 1.0, the training tends to collapse (the value of E drops to and remains zero suddenly) or to be slow. The weight changes are proportional to the derivative of the sigmoid function, but at the extreme ends, the derivative is very small or zero. We notice for different choices of η, the resulting shape of the network output distribution might vary. However, it may still be possible to select the output threshold cut to achieve approximately the same separation efficiency despite the varying shapes. Perhaps, this indicates the convergence is not final or that there are different minima. To sample as many points as possible, η may be set to smaller values and the training repeated with different initial weights. We prefer smaller values for η also

because the network output distribution seems to be smoother. The training sets with higher η values appear to classify our data (several peaks in the distribution) rather than perform a single separation (two peaks, signal *vs* background). Small changes to the other variable, α, affects the training much less than changes to η[3]. We try values ranging from 0.0 to 0.8, but usually used 0.3 or 0.5 for α.

For each training pattern, we associate a desired scalar response S^k_{target} in equation 3. We use 0.1 for background and 0.9 for signal. Choosing values like 0.05 and 0.95 would presumably create a greater distance of separation; but, for our particular setup, using target values closer to 0.0 and 1.0 does not improve the final results.

One more consideration in training is the number of weight-updating iterations performed. Without enough data to span the diversity of the entire pattern space, it becomes very obvious when we over-train the net. The network acceptance on training and new test data begins to diverge after more weight updates - though this is not true with larger samples of events. The performance efficiency improves from iteration to iteration, but slowly so that it is adequate to check the performance after every 200 updates. We run about 3000 iterations for each training set, but for our patterns, 1000 iterations are usually sufficient to reach the best separation. Further weight updates do not improve the efficiency. In practice, we sometimes use two sigmoid units in the output layer connecting to each one of the hiddden units, although only one is shown in Fig. 1. Training signal patterns are required to be 0.9 from output unit one and 0.1 from the other, and exactly the opposite for background patterns. Once the weight–updating has reached optimum, the two sets of weights connecting the hidden and each of the two output nodes become anti-symmetric (the value of one set is the negative of the other, a likely result of the fact that the sigmoid function equals one minus the sigmoid with the exponent term negated). Reaching this anti-symmetry helps confirm when to stop training. We find that values of the weights between the input and hidden layers grow but do not typically display any obvious symmetry even after many iterations, despite the symmetry of the 5×5 pattern itself; they do not give much of a clue to the number of necessary iterations.

E. Quality and Assessment of Our Neural Net

This section addresses the quality of the results and the nature of the training algorithm itself. We use stability as a measure of the quality of the training results. The general stability of the final "minimum point" is important particularly for an electronic application because of variation among devices and weight-setting precision, or distortions to the input signal. When we adjust the optimized weights by one percent (manufacturer specifications) and then re-evaluate the trigger efficiency on the test data, the rates change by $\sim$ 5%. Similarly, the trigger performance is affected by less than 5% if there is 40MeV-equivalent voltage offset somewhere in the circuit. To check the situation due to electronic noise, we add energy distributed Gaussianly about a mean of 100 MeV to each calorimeter trigger tower in the test patterns. As expected, this noise affects patterns containing low-energy electron candidate more than those with higher energy. For seed tower E_t above 4 GeV, the rates for either noisy signal or background patterns changes by about 20%; whereas, for E_t above 7 GeV, the difference is about 10%. Here, we only consider positive voltages for noise because a reference voltage defines an arithmetic zero for the neural net chip. Unfortunately, if both negative and positive noise are included, our simulation of the trigger performance suffers approximately 50% change in rates instead. We plan to train with patterns allowing for both positive and negative noise to try to reduce the sensitivity to this effect.

There are several issues related to the training algorithm which are still under study.[5,7] For fairly complicated jet patterns like ours, it is not possible to check in advance whether a solution (convergence of the minimization) exists. It is rather cumbersome to determine when the most desireable pattern separation has been achieved or whether further fine–tuning will help. With so many parameters, there may exist many local minima in addition to a global one. Therefore, we make many training runs using different parameters η and α to sample as much of the space containing the minima as possible which is time-consuming. In addition, the training procedure itself does not guarantee reaching the solution even if it does exist – for example, the minimization can collapse which occurred 5–10% of the time for us even after we set the order of magnitude of the training parameters in a reasonable region. It is clear from sections A through D that there is considerable flexibilty; it takes trial and error to determine the best region for the training parameters. There are other

drawbacks in using the algorithm. The optimal technique for our particular set of patterns may or may not fully apply to another application. Finally, there is trial and error because the best separation is not necessarily the most beneficial; it may not yield accepted patterns with the most desirable kinematic characteristics. It is difficult to control the exact nature of the final sample of accepted events; pattern pruning may be required. The saving feature of the algorithm and the network is that in many case studies, a desirable minimum is reached and signal and background patterns are indeed separated, as for the $B \rightarrow e\bar{\nu}X$.

Our primary goal has been to achieve the best separation rather than to obtain a sample of patterns with a particular set of characteristics. All of our good training runs result in approximately the same final separation efficiency, which suggests we have reached a limit. Testing the efficiency and plotting the pattern characteristics every couple hundred of iterations is one way of determining whether desireable separation has been reached. The lack of fluctuations after about 500 weight updates makes it unlikely for us to accidentally skip over the "best" minimization point even though we do not check the efficiency after each update.

Because there is an upper limit for separating two sets of patterns, it is interesting to verify on a simple example that neural net triggers are better able to reach this limit than conventional, one-dimensional threshold requirements. We train on a 1×1 pattern consisting of two inputs, one electromagnetic and one hadronic tower E_t. With only two inputs, there is not much choice in the way of cuts, other than to demand each E_t or the ratio of the two E_t's (HAD/EM) exceed some value. In this example, there are few enough variables that we can optimize the signal-to-background ratio by inspection, and we find that requirements on electromgnetic E_t and HAD/EM to be best. Shown in Fig. 4, is the acceptance curve for different values of HAD/EM for E_t above some fixed threshold; also shown is the neural net's acceptance for different choices of the output value. The neural net does indeed do better than conventional cuts, but with so few variables, the improvement is only slight. For multi-dimensional variables, however, a neural net becomes more effective and practical for achieving the best separation, particularly when the signal is hard to distinguish from background. Knowing this, we can also use neural nets in another way. They can help determine the best range of values to set one-dimensional cuts

for the different variables used in a *conventional* trigger or analysis, or to show whether a particular set of variables has any hope of extracting a signal.

REFERENCES

1. Holler, M., S. Tam, H. Castro, R. Benson, (Intel Inc.) "An Electrically Trainable Artificial Neural Network with 10240 Floating Gate Synapses." International Joint Conference on Neural Networks, June 1989, Washington, D.C.
2. Ellis, N. and A. Kernan. **Physics Reports C**, 195:23-125, 1990.
3. Balka, L. *et al.*, **Nuclr. Instr. and Meth. A**267:272-279, 1988. Bertolucci, S. *et al.*, **NIM A**267:301-314, 1988.
4. Amidei, D. *et al*, **Nucl. Instr. and Meth. A**269:51-62, 1988.
5. Rumelhart, D.E. and J.L. McClelland, **Parallel Distributed Processing Explorations in the Microstructure of Cognition**, Vol I. 1988. Lippmann, R.P. **IEEE ASSP Magazine**, p. 4–22, 1987.
6. Paige, F. and S. Protopopescu, Brookhaven National Lab Rept. BNL 38034, 1986. Abe, F. *et al*, **Phys. Rev. D**43:664-686, 1991.
7. Hertz, J., A. Krogh, R. Palmer, **Introduction to the Theory of Neural Computation**, 1991.

Figure Captions

Fig. 1. A feed-forward neural net containing one layer of input signals, a hidden and an output layer. The processing nodes in the last two layers, represented by rectangles, consist of the sigmoid function described in the text. The lines connecting the inputs x_i and the hidden nodes will multiply the x_i's by a factor w_i, and similarly for the lines between the hidden and output nodes. For the conventional trigger application, the nodes may be thought of as many parallel arithmetic processors.

Fig. 2. The distribution of neighboring *vs* seed trigger tower electromagnetic energy for Monte Carlo signal and background test patterns accepted and rejected by the trained neural net.

Fig. 3. The distribution of the network output value S (last node in Fig. 1) for signal and background patterns, where the curves are normalized to unity. The exact signal-to-background ratio depends on our choice for the trigger threshold; we typically use a value in the range 0.7 – 0.8. When normalized to the estimated cross sections, this trigger is expected to yield a $B \rightarrow e\bar{\nu}$X purity of about 15%.

Fig. 4. A comparision of neural net and threshold cut acceptance for signal and background patterns with only two inputs. The conventional-selection curves correspond to different HAD/EM ratios after requiring the electromagnetic seed E_t to be above some threshold. The neural net curve gives the acceptance for different network output values. Though shown for only two cases, all of the HAD/EM curves only asymptotically approach the network curve, but never crosses. A neural net performs as well as or better than conventional selection requirements, the relative improvement increasing with increasing variables and correlations among variables.

We will implement one particular type of pattern recognition technique based on neural net IC technology, new to triggering in high energy physics, in the CDF detector Level 2 trigger for the 1992 data run at E_{cm}=1.8 TeV. Neural networks are one method to correlate information in order to maximize the separation of signal from background.

Our neural network consists of a non-linear function containing free parameters which must be optimized via a minimization procedure, known as training. There are several reasons for investigating the utility of neural nets. The network can be trained to distinguish very complex patterns. At the trigger level, one of the major assets of neural net IC's is their flexibility. The analog network chip may be re-programmed to accommodate changes in trigger requirements. In addition, neural nets have parallel processing capabilities and are rather insensitive to fluctuations, such as from electronic noise or channel–to–channel differences in detector response. A final reason for pursuing neural nets is that powerful conventional cuts are sometimes difficult to implement electronically. The hope is to realize a similar signal–to–background ratio via a neural net cut for which the electronic capability exists.

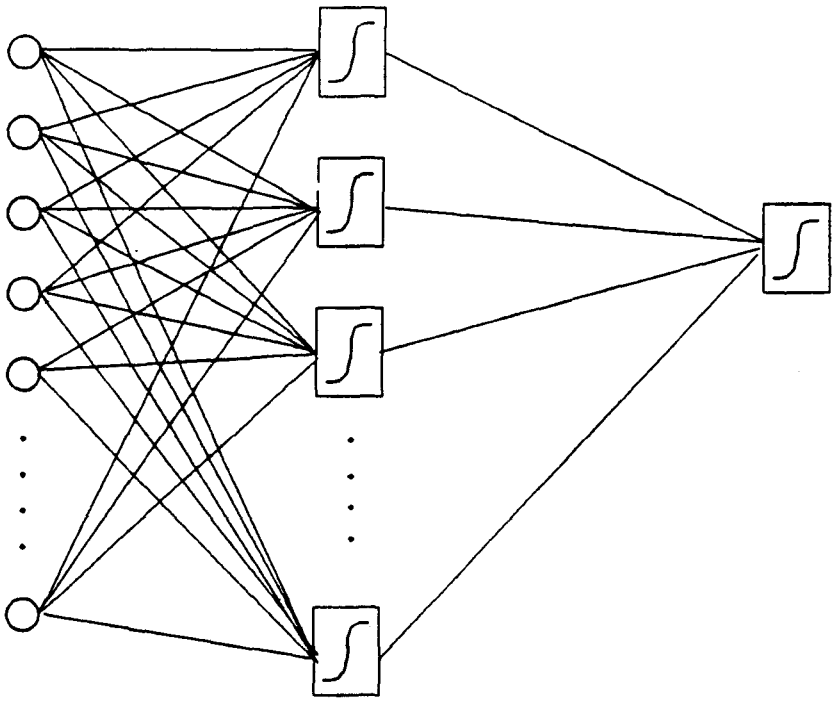
Electronics manufacturers have produced IC chips which mimic the function S used in neural nets.[1] One downloads such a device with some set of optimized weights prior to trigger installation for data taking.

We provide an offline study of using a neural net to trigger on $B \rightarrow e\bar{\nu}X$ jets with calorimeter signals, a network application proposed by M. Campbell. We use the feed-forward multi-layer (signals are fed forward through layers of processing nodes) network to separate the $B \rightarrow e\bar{\nu}X$ signal from gluon-jets background. An overview of the trigger, the input signals from the CDF calorimeter, and a brief explanation of our neural net are given in Section I. The expected efficiencies, the event kinematics, and some network issues relevant to triggering are considered here as well. A major aspect of employing neural nets is to first train it to recognize signal from background. Therefore, we describe our algorithm in detail as well as discuss the advantages and problems of using trained neural nets in the Appendix.

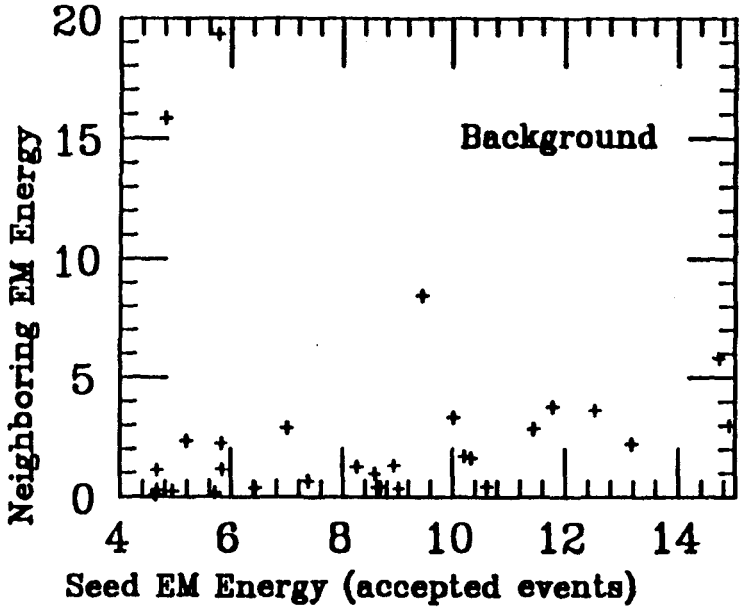
There is a second application for neural net chip technology: the circuit architec-

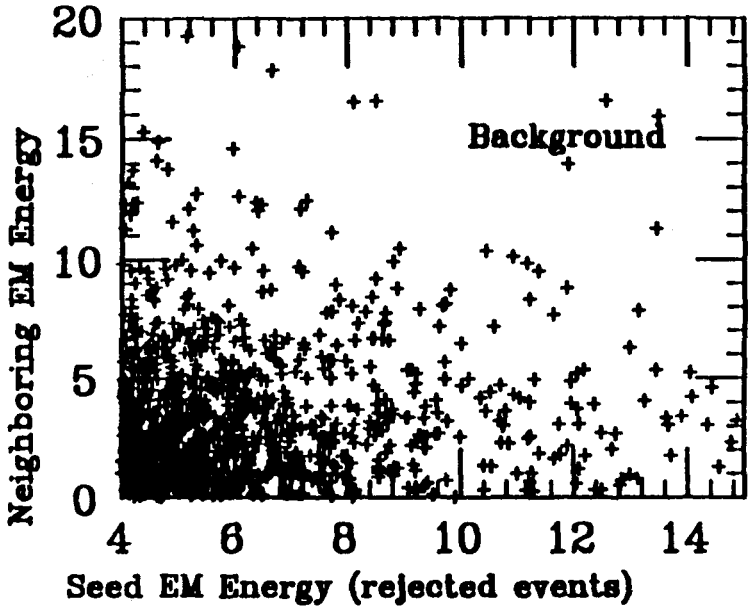
Number of training patterns		Ratio of	Background acceptance	Signal acceptance
(1)background	(2)signal	(1) to (2)	(50% signal)	(1% background)
1452	1213	1.2	3.0 ± 0.2 (%)	~ 20(%)
3109	1213	2.6	2.9 ± 0.2	~ 30
4224	1213	3.5	2.2 ± 0.2	~ 30
42240	1213	34.8	2.6 ± 0.4	~ 25
5122	1777	2.9	2.8 ± 0.2	~ 30
3109	2182	1.4	2.8 ± 0.4	~ 30
4224	2182	1.9	2.7 ± 0.4	~ 30

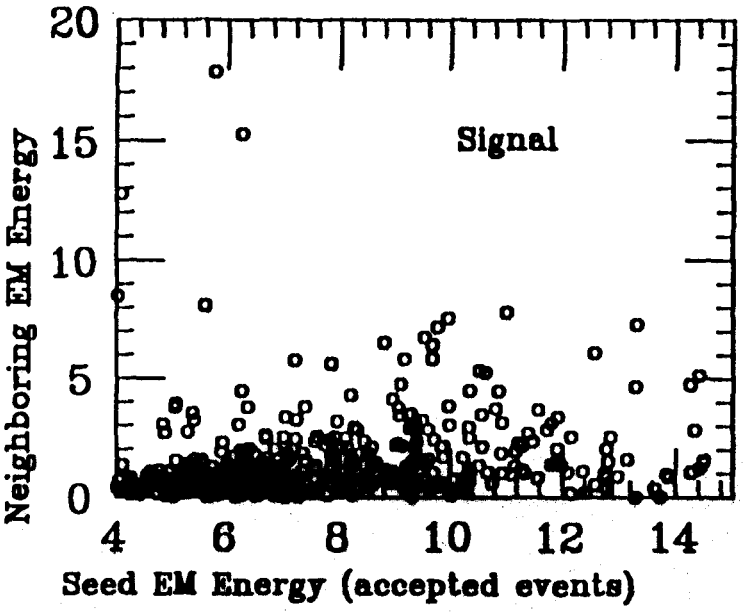
Table 1. The effect of varying the number of training patterns and the relative amounts of signal to background: column 4 shows the acceptance of new background patterns when the trained net passes new signal patterns with 50% efficiency. The last column gives the signal efficiency when the background acceptance is required to be no more than $\sim$1%.

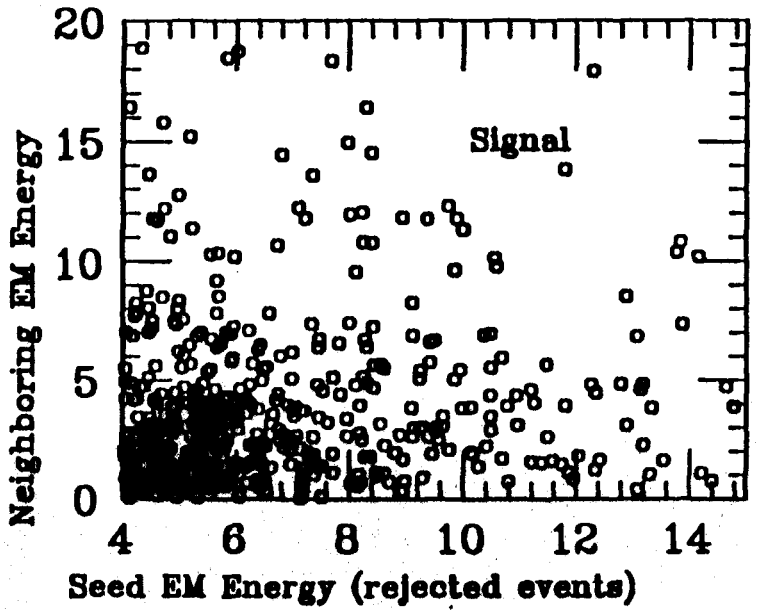


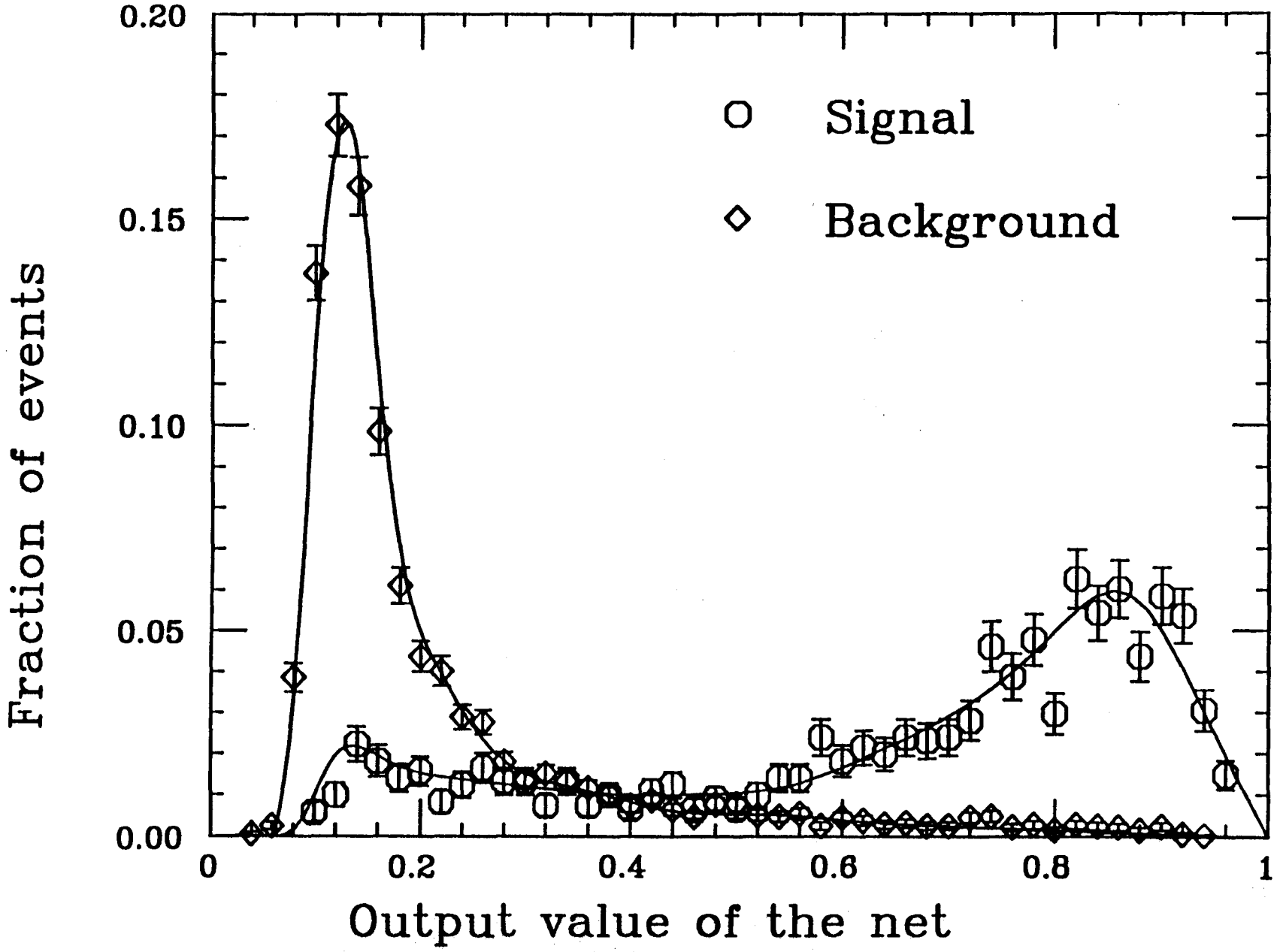
Layer 0:	Layer 1:	Layer 2:
Signal	Hidden	Output
Inputs x_i	Nodes f_j	Node g_k

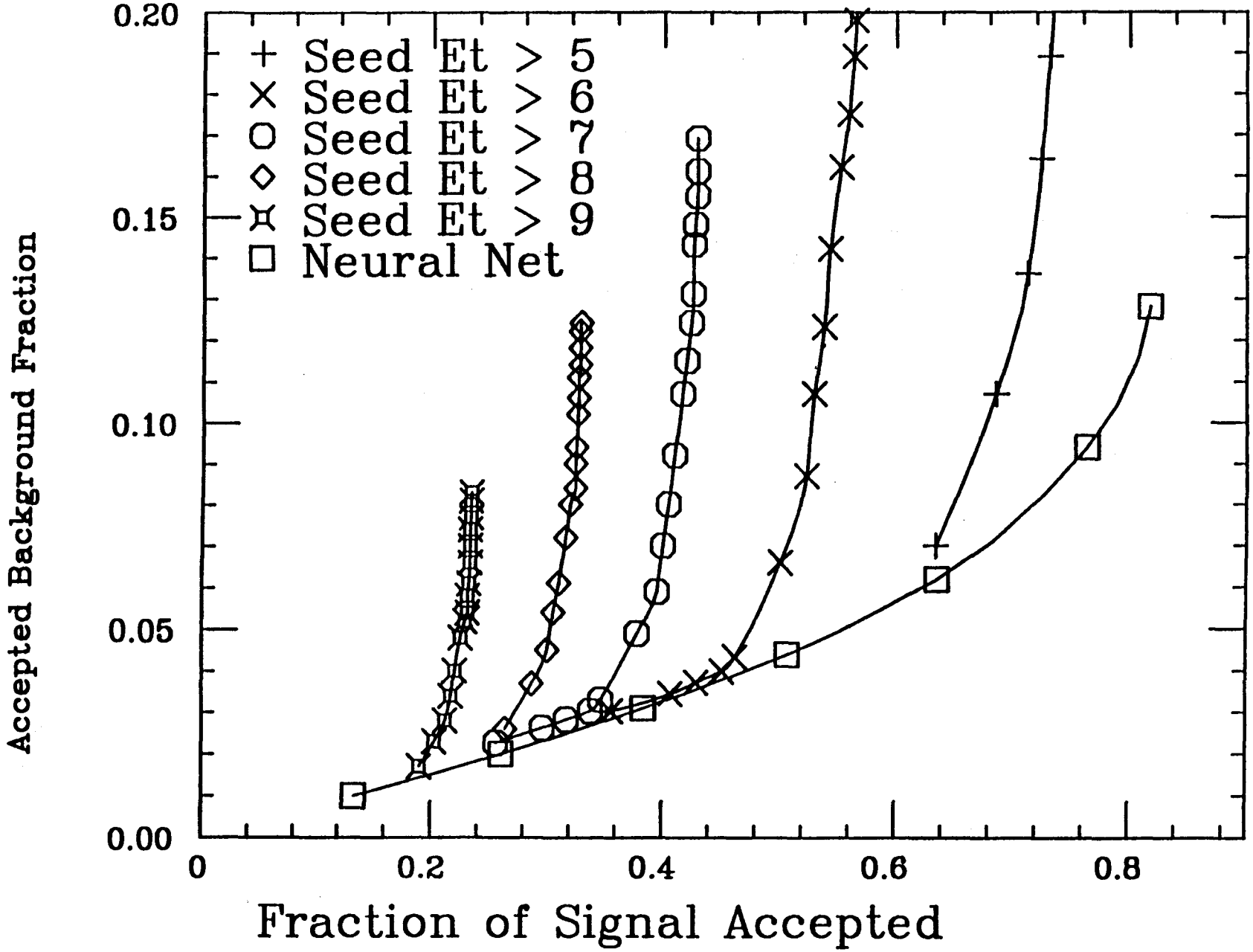

Background
Neighboring EM Energy
Seed EM Energy (accepted events)
0
5
10
15
20
4
6
8
10
12
14


Background
Neighboring EM Energy
Seed EM Energy (rejected events)
0
5
10
15
20
4
6
8
10
12
14


Signal
Neighboring EM Energy
Seed EM Energy (accepted events)
0
5
10
15
20
4
6
8
10
12
14


Signal
Neighboring EM Energy
Seed EM Energy (rejected events)
0
5
10
15
20
4
6
8
10
12
14


0.20
0.15
0.10
0.05
0.00
0
0.2
0.4
0.6
0.8
1
Signal
Background
Fraction of events
Output value of the net


0.20
0.15
0.10
0.05
0.00
0
0.2
0.4
0.6
0.8
+ Seed Et > 5
× Seed Et > 6
○ Seed Et > 7
◇ Seed Et > 8
⋈ Seed Et > 9
□ Neural Net
Accepted Background Fraction
Fraction of Signal Accepted

Development of Diamond Radiation Detectors for the SSC and LHC*

M. Franklin[a], A. Fry[b], K.K. Gan[c], S. Han[d], H. Kagan[c], S. Kanda[e], D. Kania[d], R. Kass[c], S.K. Kim[f], R. Malchow[c], F. Morrow[c], S. Olsen[e], W.F. Palmer[c], L.S. Pan[c], F. Sannes[f], S. Schnetzer[f], R. Stone[f], Y. Sugimoto[g], G.B. Thomson[f], C. White[c], S. Zhao[c]

[a] *Department of Physics, Harvard University, Boston, MA 02138*
[b] *Department of Physics, SSC Laboratory, Dallas, TX 75237*
[c] *Department of Physics, The Ohio State University, Columbus, OH 43210*
[d] *Laser Division, Lawrence Livermore National Laboratory, Livermore, CA 94550*
[e] *Department of Physics, University of Rochester, Rochester, NY 14627*
[f] *Department of Physics and Astronomy, Rutgers University, Piscataway, NJ 08854*
[g] *KEK, Tsukuba-shi, Ibaraki-ken, Japan 305*

* Presented by S.K. Kim

Abstract

Diamond is a nearly ideal material for use as a radiation detector in the high rate and high radiation environments of the SSC and LHC. The recent development of the chemical vapor deposition (CVD) method of diamond growth promises to make feasible the use of diamond in large quantities. We have carried out beam tests of various samples of CVD diamond supplied by several manufactures and have measured signals from ionizing particles. Details of these measurements are presented.

Submitted to Nuclear Instruments and Methods

1. Introduction

In order to realize the experimental goals at the planned high energy, high luminosity hadron colliders (SSC and LHC), it is essential to develop detector technologies that are able to handle the extremely high rates and that can operate in the severe radiation environments. Detectors based on diamond could have advantages over all existing technologies because of diamond's inherent radiation hardness, fast charge collection speed, and potential low cost.

In Table 1, we summarize the relevant properties of diamond and compare with those of silicon. A detailed description of diamond properties can be found in reference [1]. Since diamond has a large band gap, 5.5 eV, it is a very good electrical insulator. The resistivity of high-purity diamond is typically 10^{11} Ω-cm to 10^{16} Ω-cm. Because of this large resistivity, a large electric field ($> 10^4$V/cm) can be applied across the diamond layer without producing significant leakage current. The charge created by the ionization process is collected, or induced, on ohmic contacts on the surface. Lower resistivity materials, on the other hand, require the use of a reversed biased *pn*-junction to prevent a large leakage current whose fluctuations would dominate the signal.

2. Charge Collection Speed

As shown in Table 1, the breakdown electric field for diamond is about 10^7 V/cm. It is, therefore, possible to apply a large enough field to reach the saturation velocity of 2.2×10^7 cm/s. In silicon, because of the *pn*-junction and associated depletion region, the maximum field that can be

applied before avalanche breakdown is only about 10^3 V/cm. This limits the electron velocity to a few times 10^6 cm/s. Since for either diamond or silicon the required detector thickness is a few hundred microns, the collection time would be about 1 ns in diamond compared to about 20 ns and 60 ns for the electrons and holes, respectively, in silicon.

3. Radiation hardness

One of the primary manifestations of radiation damage in solid state detectors is an increase of leakage current due to the production of intra-band states in the depletion region caused by the displacement of atoms from lattice sites. These states then act as current generation sources. The leakage current is given by

$$I_{leak} \sim qAn_i d\Phi$$

where n_i is the intrinsic carrier concentration and Φ is radiation fluence. Due to the absence of a *pn* junction and the extremely small value of n_i, this effect should be negligible in diamond.

Another effect of radiation damage is a decrease in the collected charge due to the production of trapping centers. Because of the relatively large binding energy of atoms in the diamond lattice, the degree of lattice dislocation is much smaller in diamond than in silicon. Also, the neutron transmutation cross section for diamond is more than 20 times smaller than that for silicon. As a result, diamond should be much less sensitive to neutron damage.

Although no data for radiation damage on CVD diamond exists, neutron

damage on natural diamond was reported by Kozlov *et al.* [2] They showed that a diamond detector can survive up to a few times 10^{14} neutrons/cm^2. In another study, no increase in leakage current was observed for exposures up to 10^{16}/cm^2 of 1.5 MeV electrons in a Schottky diode made of diamond [3].

5. CVD Diamonds

Natural diamond has been used as a radiation detector since 1949 [4]. However, it is extremely expensive and cannot be used on a large scale. Also, it contains naturally high level of impurities, such as nitrogen, and crystal defects which limit its carrier lifetime. The recently developed technology of manufacturing diamond by chemical vapor deposition(CVD) [5] has the potential of allowing the economical production of diamond in large sheets and of significantly higher purity than natural diamond.

In the CVD process, a hydrocarbon gas, such as methane, is mixed with a large concentration of molecular hydrogen gas. The gas mixture is then excited by either microwaves, a hot filament, or some other energy source. The resulting reactive gas mixture is brought into contact with a substrate, typically silicon, where the carbon based radicals are reduced and linked together with single bonds (sp^3 hybridized orbitals) forming a diamond crystal. Because of the large number of variables, systematic correlations between growth parameters and diamond quality is one of the main tasks in developing CVD diamond detectors.

6. Beam Tests of Diamond

We have carried out beam tests of single-crystal natural and polycrys-

talline CVD diamonds at the Accumulator Ring (AR) test beam at KEK in Japan and at the M13 beam line at TRIUMF in Canada.

The AR is an 8 GeV storage ring which is a part of the injection system of TRISTAN. By use of a thin internal target, scattered electrons with energies from 0.5 GeV to 5.5 GeV at rates of a few Hertz can be obtained. At TRIUMF the M13 beam line is a tuneable 100 MeV secondary beam line consisting of pions, muons and electrons. At this momentum, minimum ionizing (e's), twice minimum ionizing (μ's), and three times minimum ionizing (π's) particles are available at rates up to 10^6 particles per second.

The samples tested at KEK and TRIUMF included natural diamond (D34) and polycrystalline CVD diamond. The natural diamond sample was 1 mm thick (1x3 mm^2 area) and contained the natural abundance of nitrogen (10-30 ppm). The CVD diamond samples were grown by five manufactures using a variety of growth processes. Under scanning electron microscopy, most samples showed a typical needle-like growth of diamond crystals extending across the layer. Some samples were polished to remove surface roughness from the growth process. Sample thicknesses ranged from 100-500 μm. The total number of samples tested was about 50.

Scintillation counters plus a small (3x3 mm^2) silicon detector defined the incident beam and formed the trigger. A removable lead stack was used to create electromagnetic showers (used at KEK) and thereby increase the numbers of particles traversing the detectors. Signals from a diamond detector and from a silicon detector located just downstream of the diamond were measured and compared. These signals were amplified by a charge sensitive preamplifier [6] and by a shaping amplifier. Figure 1 shows minimum ionizing

signals as seen by the natural diamond detector and by the silicon detector. Figure 2 shows the corresponding signal from a CVD diamond detector and silicon detector. The rise time and shapes of these pulses are determined by the shaping amplifier. The diamond signals themselves have rise times of less than 1 ns.

The quantity used to characterize the diamond in these tests is the charge collection distance. The observed signal results from induced charge on the electrodes due to the movement of the electrons and holes. Because of impurity and defects, the electrons and holes drift on average some distance, (d), before capture. When this distance is much smaller than the diamond thickness, the observed signal is proportional to the ratio of d to the diamond thickness (t). All samples tested to date have fallen into this category. The collection distance can then be determined by:

$$Q_{meas}/Q_{gen} = \quad d/t$$

Here Q_{gen} is the amount of charge generated by the ionizing radiation and Q_{meas} is the measured charge. The generated charge in diamond has been calculated in two ways: (1) by normalizing the diamond pulse height to the silicon pulse height after correction for solid angle and dE/dx, and (2) using the EGS monte carlo. Both methods agree. In these calculations, we used 13 eV of energy deposit per electron-hole pair produced.

The collection distance is also related to the mobility (μ), carrier lifetime (τ), and applied electric field (E) by:

$$d = v\tau = \mu E\tau.$$

Figure 3 compares the collection distance for natural diamond and four CVD samples. At electric fields of 25 kV/cm, the natural diamond reaches a collection distance of 50-60 μm and is still not saturated. At this electric field the signal to noise (S/N) is approximately 6:1. Extrapolating from this data we expect the natural diamond to reach collection distances of approximately 100 μm (S/N = 10:1) at electric fields of 40 kV/cm. At low electric field, one of the CVD diamonds compares well with natural diamond. This is the region where impurities are expected to dominate. As shown in Fig. 3, at higher fields this CVD sample saturates at a collection distance around 10-15 μm; significantly lower than that of the natural diamond. The onset of this saturation is probably related to imperfections and defects in the CVD sample. This effect is being studied and correlated with CVD production parameters.

In addition to studying the charge collection in natural and CVD diamond, we have begun to look at rate effects. In Fig. 4, we show the normalized pulse height as a function of rate in CVD diamond. No degradation of pulse height was observed up to rates of 10^4 particles/cm^2/sec. This is the first indication that diamond will withstand the large rate environment of the SSC.

7. Conclusion

The experiments described above were the first demonstration that CVD diamond can detect charged particle minimum ionizing radiation and handle

large rates. The collection distance is of the order of 10 μm in CVD diamond and 50 μm in natural diamond. These preliminary results based on "off the shelf" CVD diamond are very encouraging. We are at the point now where calorimetry is becoming feasible and tracking is within reach.

Acknowledgements

We are grateful for the cooperation we received from both the KEK and TRIUMF laboratories which made these test beam studies possible. This work was supported in part by grant #RGFY9164 from the Texas National Research Laboratory Commission. In addition, two of us, K.K. Gan and S.K. Kim, would like to acknowledge support of the SSC Fellowship Program funded by the Texas National Research Laboratory Commission.

Table 1: Properties of Diamond

Property	Diamond	Silicon
Band Gap	5.5 eV	1.1 eV
Resistivity	$> 10^{11}$ Ω-cm	10^5 Ω-cm
Breakdown Voltage	10^7 V/cm	10^3 V/cm
Electron Mobility	1800 $cm^2/V/s$	1500 $cm^2/V/s$
Hole Mobility	1200 $cm^2/V/s$	500 $cm^2/V/s$
Saturation Velocity	220 μm/ns	100 μm/ns
Dielectric Constant	5.6	11.7
Neutron Transmutation Cross Section	3.2 mb	80 mb
Energy to create e-h pair	13 eV	3.6 eV
Mass Density	3.5 gm/cm^3	2.3 gm/cm^3
Ave Min Ionizing Signal/100 microns	3,600 e	8,000 e
Ave Min Ionizing Signal/0.1% X_0	4,500 e	7,500 e

References

[1] R. Plano *et al.*, "A Compact Diamond-Based Detector for the SSC", SSC-EOI0009 (1990).

[2] S.F. Kozlov *et al.*, IEEE Trans. Nucl. Sci. **NS-22**, (1975) 160.

[3] M. Geis, MIT Lincoln Laboratory, private communication.

[4] R. Hofstader, Nucleonics, 1949.

[5] J. Angus and C. Hayman, Science **241**, (1988) 913; W. Yarbrough and R. Messier, Science **247**, (1990) 913.

[6] T. Taniguchi, Y. Fukushima, and Y. Yoribayashi, IEEE Trans. Nucl. Sci. **36**, (1989) 657.

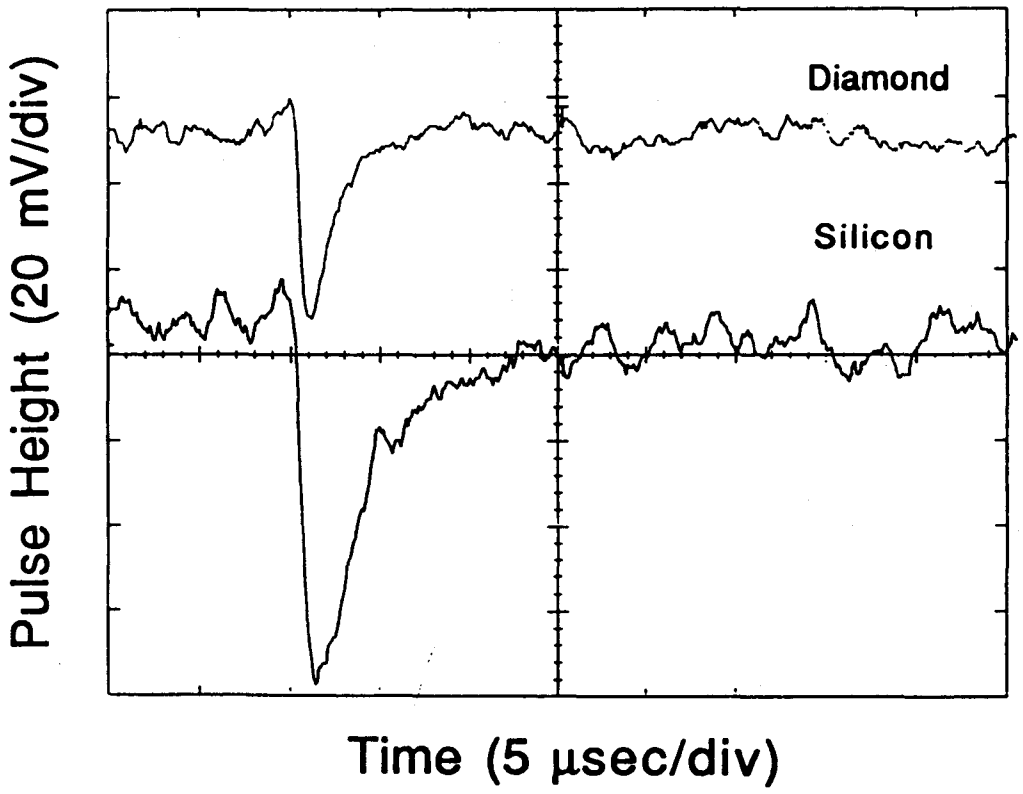
Figure Captions

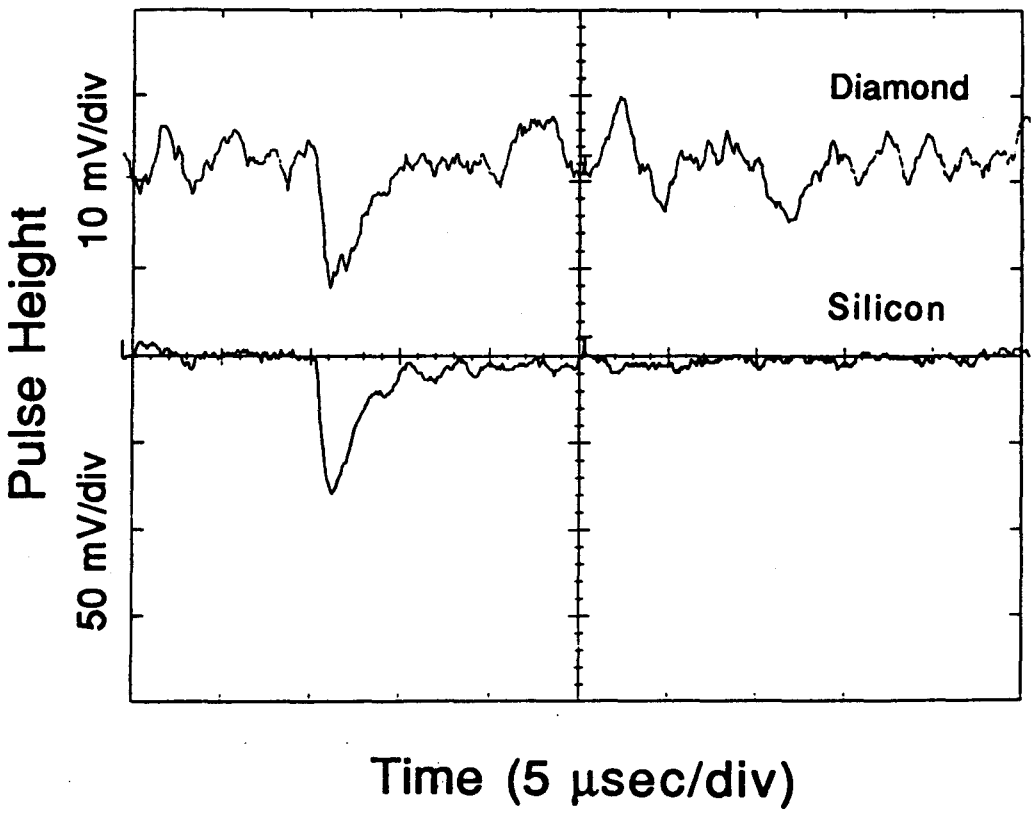
1. Minimum ionizing single pulses in natural diamond (upper trace) and silicon (lower trace). The diamond to silicon pulse height ratio on this particular event was 1:2. The vertical scale is 20 mV/division.

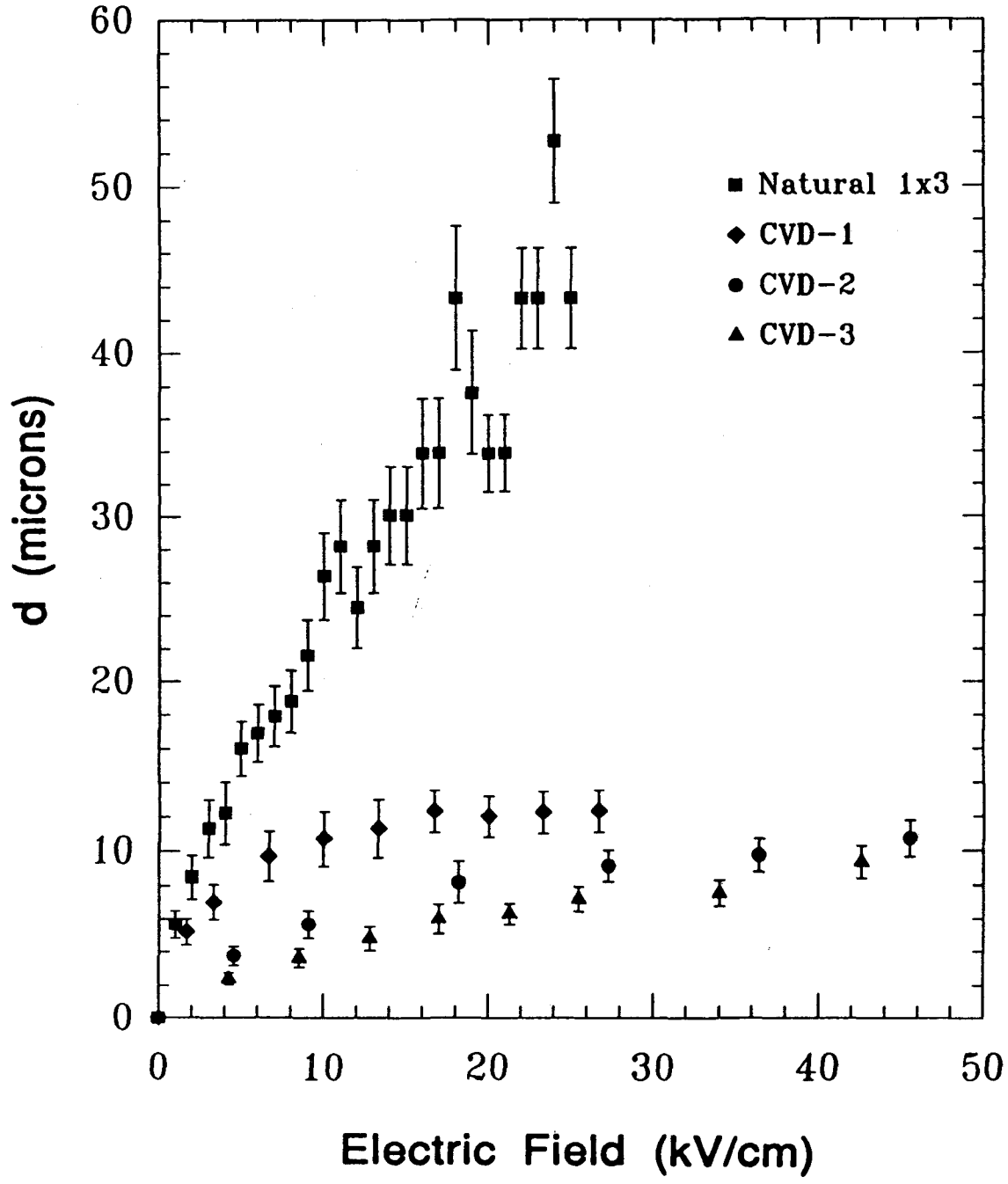
2. Minimum ionizing single pulses in CVD diamond (upper trace) and silicon (lower trace). The diamond to silicon pulse height ratio on this particular event was 1:8. For the diamond trace, the vertical scale is 10 mV/division. For the silicon trace, it is 50 mV/division.

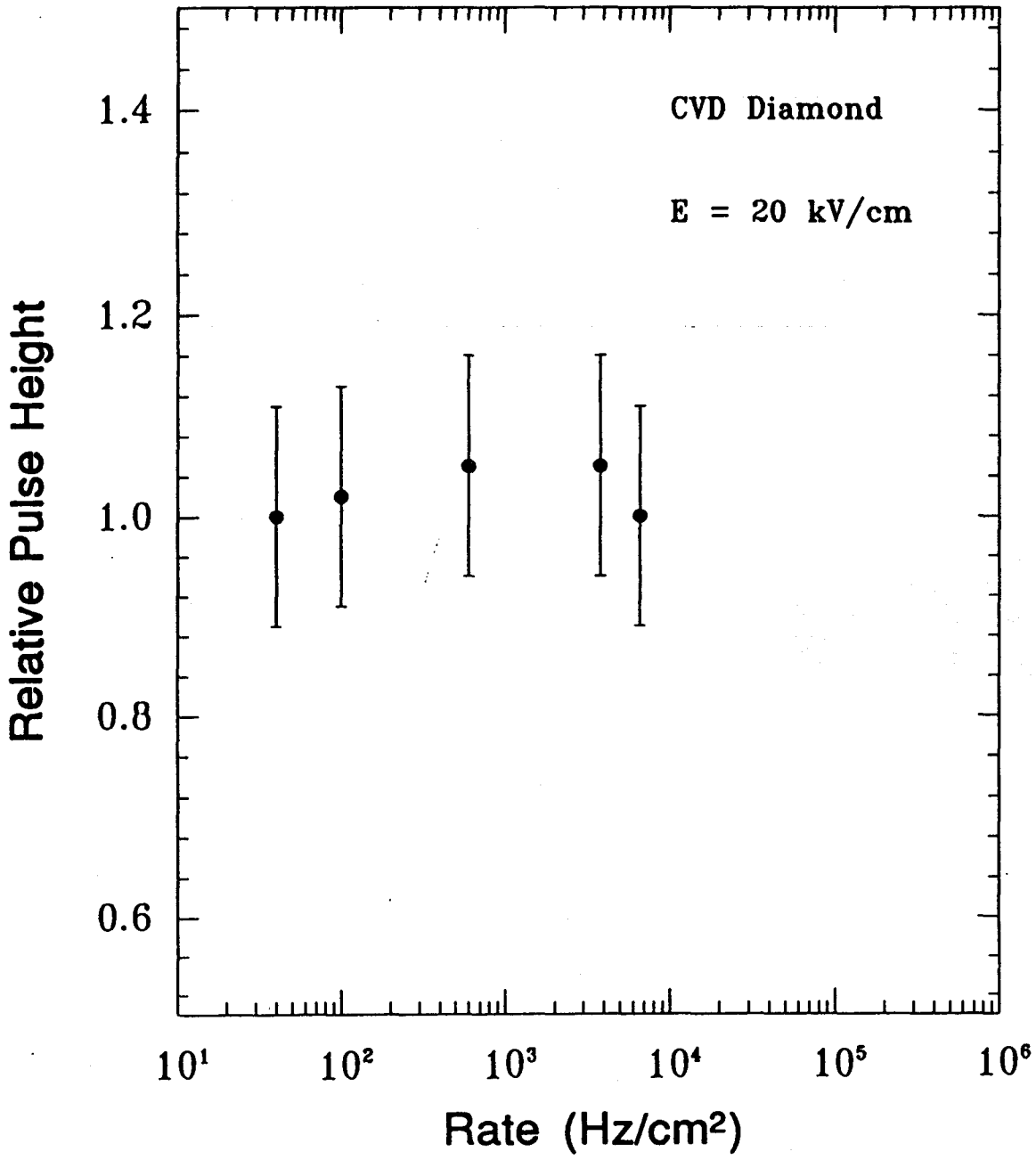
3. Collection distances in natural and CVD diamonds.

4. Pulse height as a function of rate in CVD diamond. The pulse heights are normalized to 1.0 for the lowest rate point.


Diamond
Silicon
Pulse Height (20 mV/div)
Time (5 µsec/div)


Diamond
Silicon
Pulse Height
10 mV/div
50 mV/div
Time (5 μsec/div)


60
50
40
30
20
10
0
0
10
20
30
40
50
d (microns)
Electric Field (kV/cm)
Natural 1x3
CVD-1
CVD-2
CVD-3


CVD Diamond
E = 20 kV/cm
Relative Pulse Height
1.4
1.2
1.0
0.8
0.6
10^1
10^2
10^3
10^4
10^5
10^6
Rate (Hz/cm²)

Conceptual Design for a Parallel Plate LAr and LKr Electromagnetic Calorimeter for GEM

T. Burnett, V. Cook, J. Eisenberg, D. Forbush, P. M. Mockett, F. Toevs
University of Washington, Seattle, WA

J. Rutherfoord, L. Shaver, M. Shupe
University of Arizona, Tucson, AZ

The GEM calorimeter group has endorsed the goal of achieving the very best electromagnetic energy resolution possible in the 100 GeV energy range.The group has advised that we pursue a two prong attack on this goal supporting both the development of a BaF_2 calorimeter and a LAr(LKr) calorimeter. It has emphasized that beam test results are by far the preferred method of demonstrating the resolution that can be achieved. Modeling of the full system incorporating these beam tests is needed for overall comparison.

With the LAr effort there are different paths that might be followed. The 1.8 mm Pb plate accordion technique pioneered by the RD3 group has demonstrated a $10\%/\sqrt{E}$ stochastic term while the 1.5 mm Pb parallel plate calorimeter of NA31 has demonstrated a $7.5\%/\sqrt{E}$ stochastic term. In the latter case a long shaping time was used to process the signals so that it remains to be shown that the same resolution can be obtained with the fast shaping required for GEM. Although it has not been tested, it is believed that substituting LKr for the LAr will further improve the resolution in both cases.

We propose to follow the NA31 path and develop a parallel plate calorimeter with fast signals. To achieve this the signals must be collected and brought to the amplifiers on nearly projective striplines. In this case the thermal noise will be increased by approximately 25% but when added in quadrature to the pileup noise this produces a negligible increase in the total noise.

The striplines must pass through slots in the absorber plates. To minimize the affected area, a four-channel stripline will pass through 1 mm by 10 mm slots. This affects much less than 1% of the total area. A simulation of the effects of these slots on resolution is being carried out at the University of Arizona. Current results show the

effect of the slots on the resolution is less than 0.5%. See Appendix A for the details of the simulation. A schematic of how such a stripline might look is shown in Fig. 1 and an exploded view of the arrangement is shown in Fig. 2. Four towers are serviced by one stripline assembly so that the number of penetrations is minimized. The amplifiers will be placed at the inner and outer radii of the detector to service the inner and outer sections of the calorimeter respectively.

The absorber plates will be constructed of 1.5 mm Pb clad on each side with 0.003" yellow brass sheets. Brass is easier to solder than stainless steel and is a better match to the thermal expansion of Pb. The brass cladding not only supplies substantial strength to the plates but it should greatly reduce the likelihood of lead chips remaining in the gaps that could later produce shorts. For the GEM barrel detector these plates would be formed into concentric arcs of the appropriate radii. The number of degrees subtended by these arcs depends upon a detailed engineering study and the results of construction tests. Ideally they would subtend 180 degrees. This would result in only two small phi cracks. More realistically we imagine 120 degree sections could be produced. The plates would be supported off of a strong back that could also serve as the first plate of the hadron section. The end caps would be composed of flat plate sections having a similar structure.

The electrodes would be etched from copper clad Kapton. These could be strips two towers wide with notches at the appropriate points to allow the striplines to pass. This structure is indicated in Figs. 1 and 2. For the most part, Hexcel could serve as the spacer material and support of the Kapton electrodes. Additional spacers and tie rods from the strong back would be used to give added support as necessary. There would also be support structure at the ends of the plates. It is important that the towers be precisely aligned so that precision position measurements of the showers can be obtained.

The high voltage can be supplied in a couple of ways. It can be produced on a resistive coating separated from the tower electrodes by a dielectric or it can be applied directly to the tower electrodes. In the latter case the amplifiers must be capacitively decoupled from the stripline. The capacitors must have very low inductance and take up little room. We could achieve this by using capacitors formed by layers of copper clad Kapton printed circuits in the outer gap(or gaps). About six such layers would be required to give 90% charge

transfer. A schematic of this concept is shown in Fig. 3. We must be sure that such devices don't distort the wave form on the stripline.

We have looked at fast pulses on a printed circuit model of the proposed structure. The model is shown in Fig. 4. This loaded stripline model is about 20% slower than we expect for the actual EM calorimeter because the dielectric is G10 (k=5) and not Kapton(k=3.5). The loading is also somewhat higher. The total load is expected to come to about 600 pF much less than the 1.2 nF for the model line. We look at these pulses with a high impedance scope probe across the 5 ohm termination. The transmission of these pulses from different places corresponding to different depths in the calorimeter look as expected and encourage us to believe that the electrical challenge can be met. We expect two pulses, one arriving directly at the amplifier and the second arriving at the amplifier after reflection at the far end of the structure. The average time of arrival of the charge is independent of where it is injected. If we designate t=0 as the time of arrival of the charge from the far end of the structure, then when we inject charge at 20 cm from the end two equal pulses are observed. One arrives at -2.5 ns and the other +2.5 ns . The accordion calorimeter being faster would provide two pulses, one being -1.25 ns and one +1.25 ns. But with 40 ns shaping time these small numbers do not present a problem for uniformity of charge collection. We find upon integrating the pulse out to 30 ns, the same amplitude independent of where the charge is introduced. The pulse traces and integrals are shown in Fig. 5-a,b,c,d,e,f. 5-f repeats 5-c which appeared to be 1% low. We attribute the difference to poor probe contact for the 5-c measurement. Such uniformity is substantially greater than is required to prevent the depth fluctuations from degrading the resolution.

We also have reviewed pulse measurements made for our BRITE PAD bench calorimeter. Here charge was injected using a laser, fiber optic link and photodiode in the gap of the plates. The pulses were viewed with a 50 ns RCCR filter. Again the amplitude was independent of the position of the photodiode. Hence, we have good reason to believe that we can bring out fast signals in a uniform way and achieve the resolution goals set for this calorimeter design.

The stack would be assembled in the following fashion. The striplines would be soldered to the absorber serving as the ground plate and a layer of Hexcel placed on the plate. The Kapton PC's providing the tower structure would be added and checked for high voltage

From: IN%"SHUPE@uazhep.physics.arizona.edu" 10-OCT-1991 16:05:16.83
To: MOCKETT <MOCKETT@phast.phys.washington.edu>
CC:
Subj: SLOT NUMBERS, ETC

Received: from ARIZONA by phast.phys.washington.edu; Thu, 10 Oct 91 16:04 PDT
Received: from uazhe0.physics.Arizona.EDU by Arizona.edu with PMDF#10282; Thu, 10 Oct 1991 16:04 MST
Date: Thu, 10 Oct 1991 16:03 MST
From: SHUPE@uazhep.physics.arizona.edu
Subject: SLOT NUMBERS, ETC
To: MOCKETT <MOCKETT@phast.phys.washington.edu>
X-VMS-To: IN%"MOCKETT@UWAPHAST.BITNET"
Message-id: <A36A277FD020111E@uazhep.physics.arizona.edu>
X-Envelope-to: MOCKETT@UWAPHAST.BITNET

Paul,

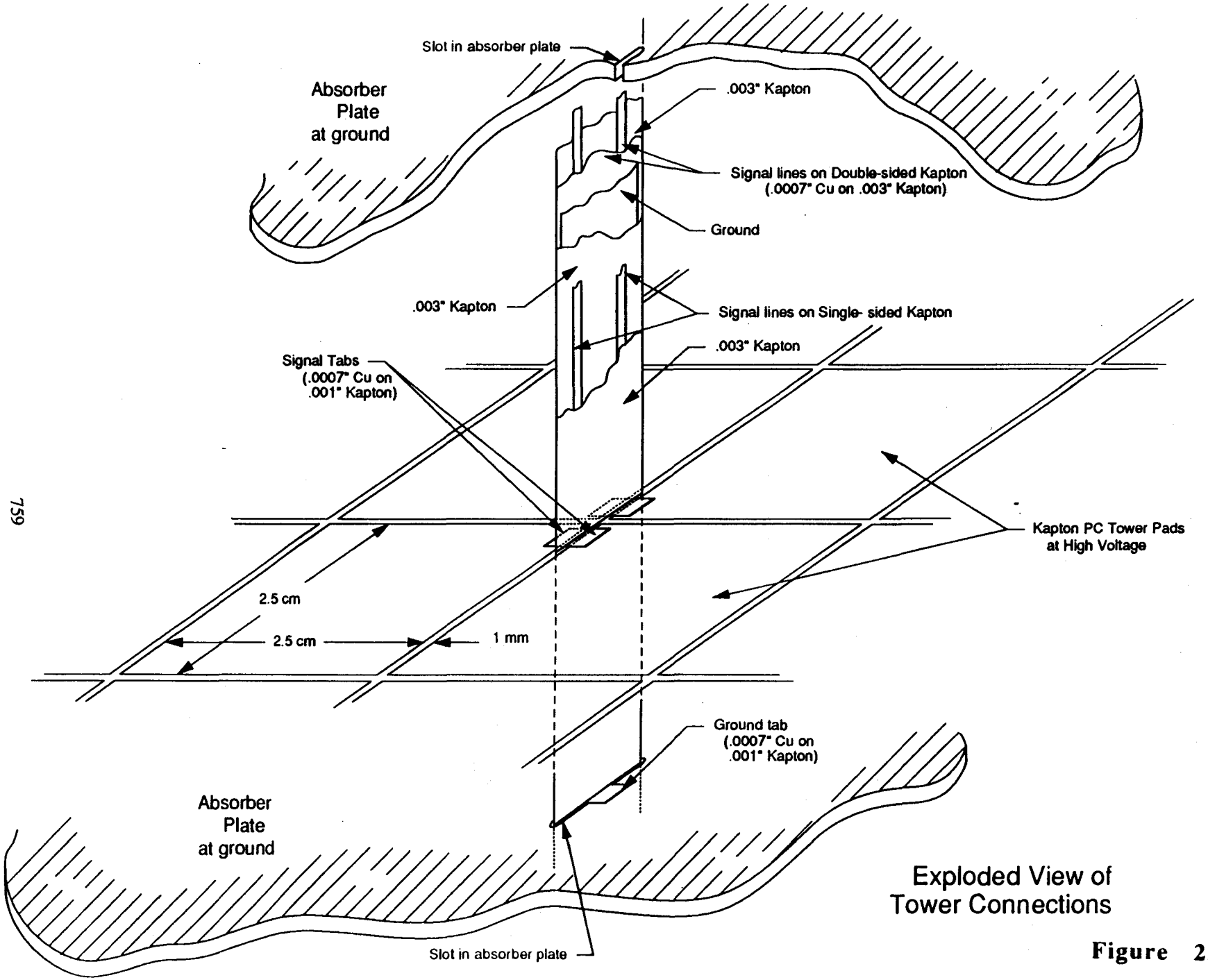
I have finished looking at the slot running for now. Out of 998 events generated, 9 went down the slots. The resulting resolutions in the peak are:

NO SLOTS: GEANT 3.14 SIGMA/SQRT(E) = 5.48 +- .17 %

SLOTS: " " 5.87 +- .13 %

NO SLOTS: EGS4 " 6.33 +- .20 %

So for now you might take the overall number to be about 5.9% plus .9% for the GEANT/EGS effect, and conclude that the slots degrade the resolution by .4%.



Exploded View of Tower Connections

Figure 2.

Decoupling Capacitor Schematic

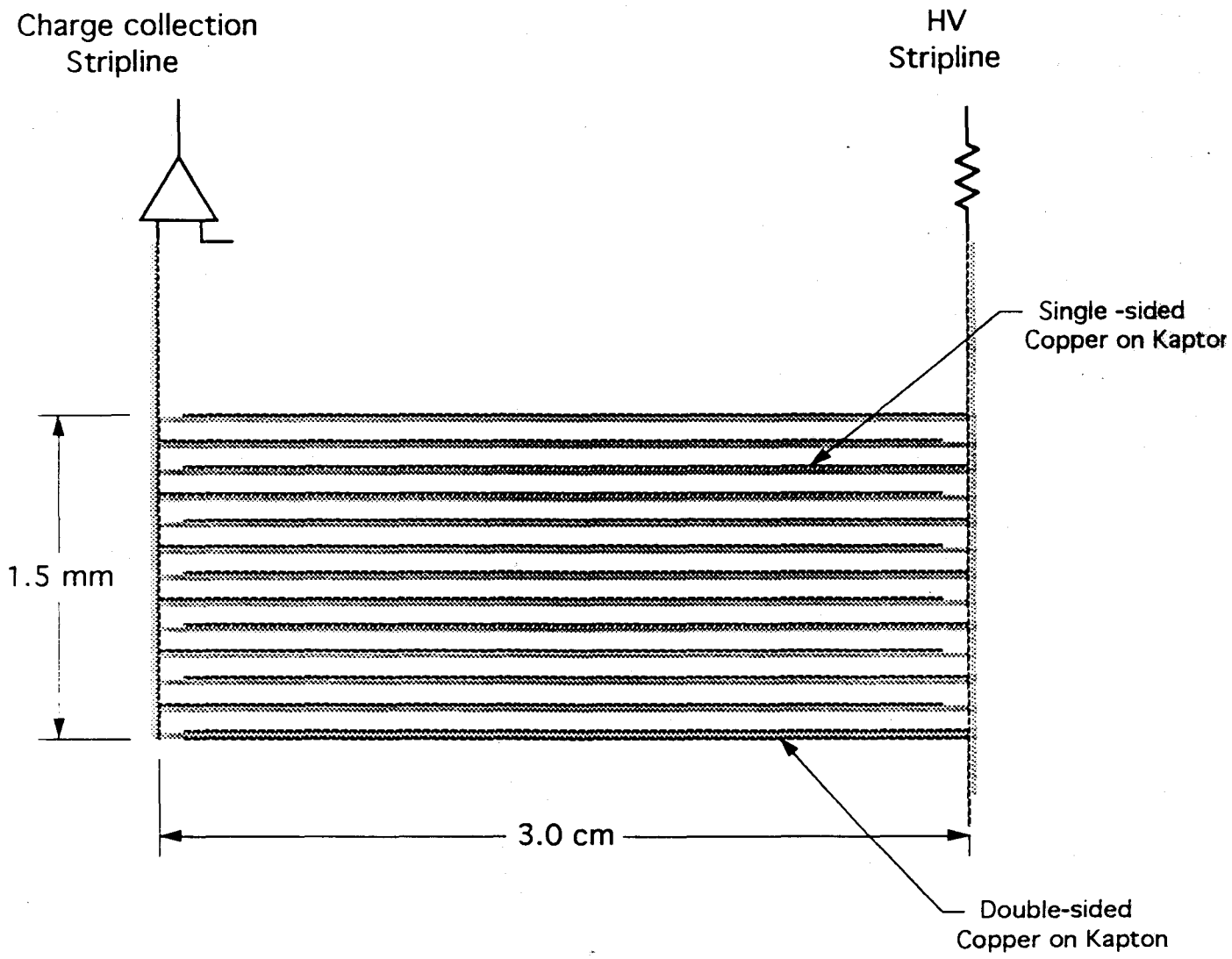
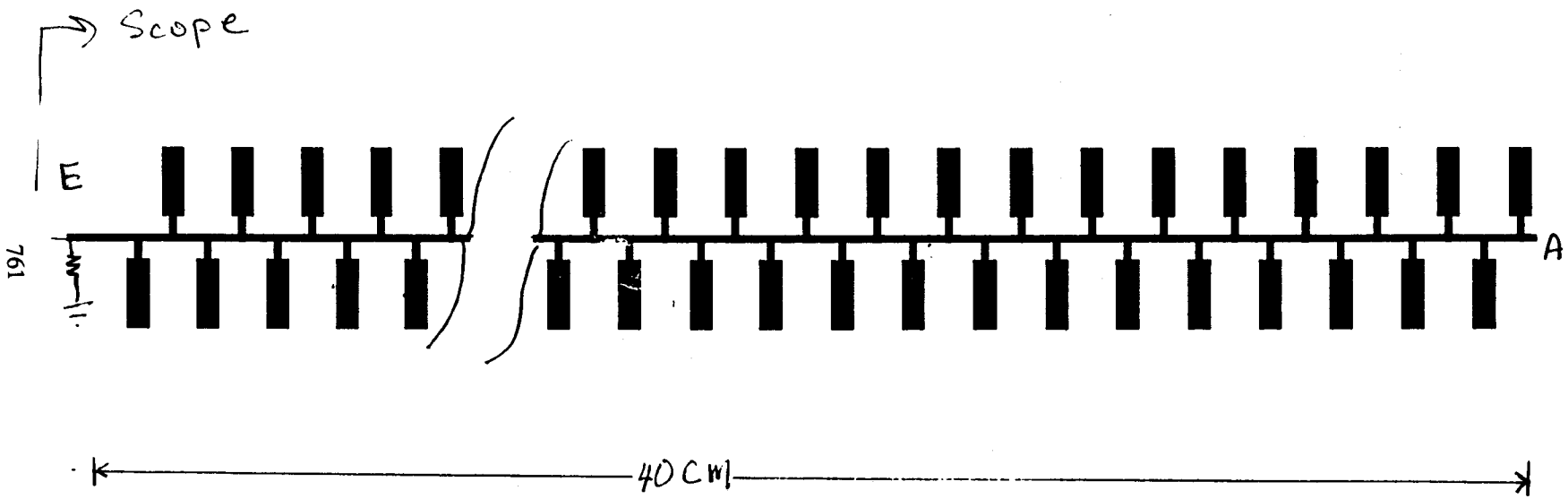


Figure 3.

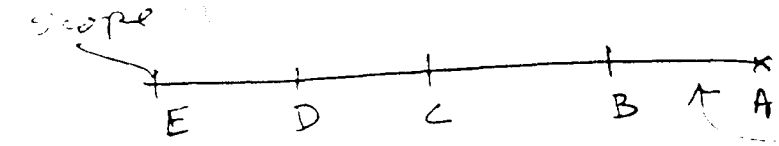


.005" G10 K = 5

1.161 nF

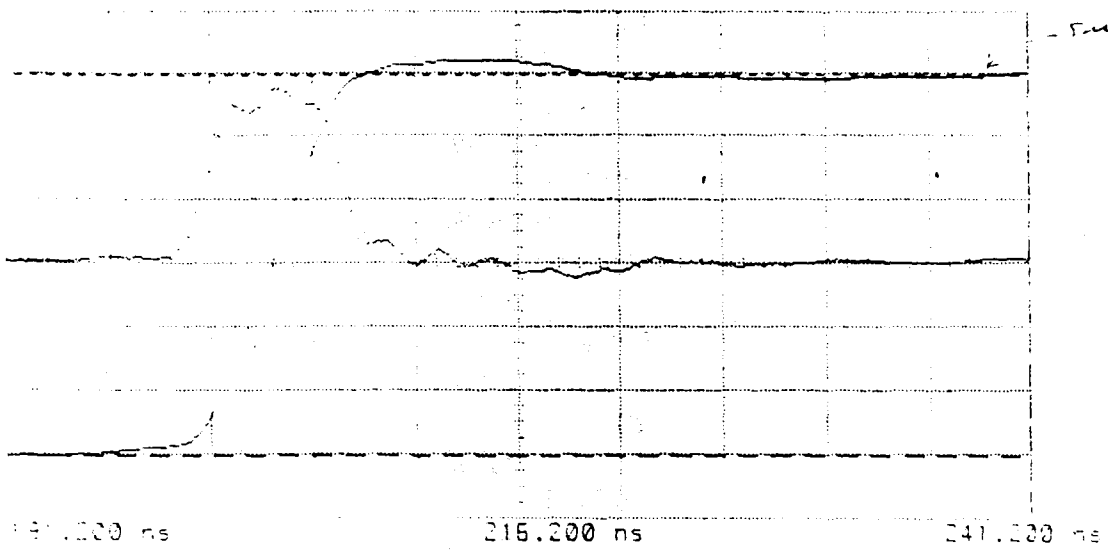
termination 5.1 Ω

Figure 4.



loaded stripline Model on GaAs

input points



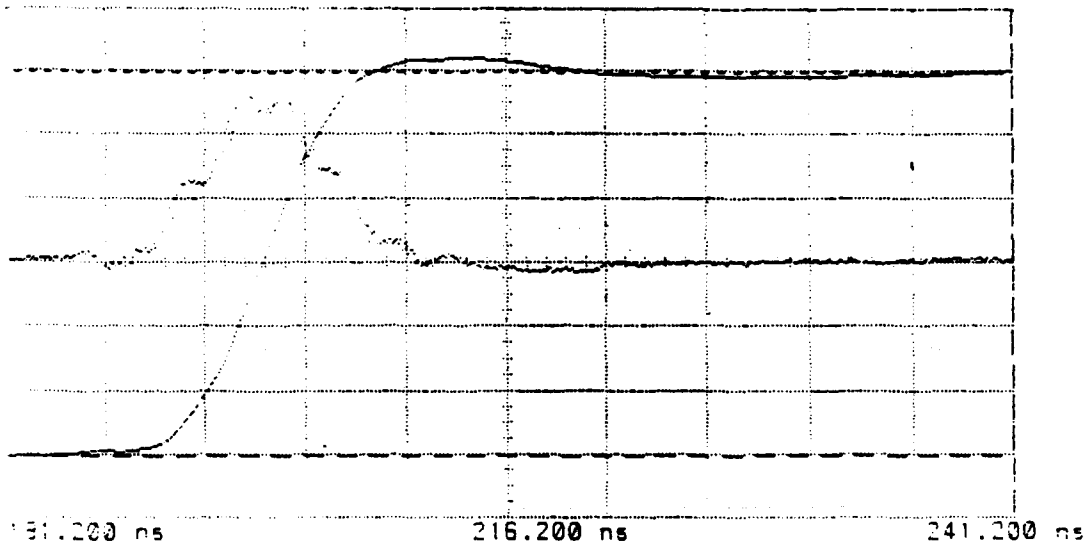
- integrated pulse

Ch. 1	=	100.0 mVolts/div	Offset	=	0.000 Volts
Function2	=	300 pVolts/div	Offset	=	900 pVolts
Timebase	=	5.00 ns/div	Delay	=	216.200 ns
Function 2 Parameters			P-P Volts	=	1.850 nVolts
Rise Time	=	5.850 ns	Overshoot	=	80 pVolts
Preshoot	=	0.000 Volts	Avg Volts	=	1.330 nVolts
Delta V	=	1.780 nVolts			
Vmarker1	=	0.000 Volts	Vmarker2	=	1.780 nVolts
Delta T	=	0.00000 s			
Start	=	691.200 ns	Stop	=	691.200 ns

Trigger mode : Edge
On Pos. Edge on Trig3
Trigger Levels
Trig3 = 0.000 Volts
Holdoff = 70.000 ns

Input at A

Figure 5-a.



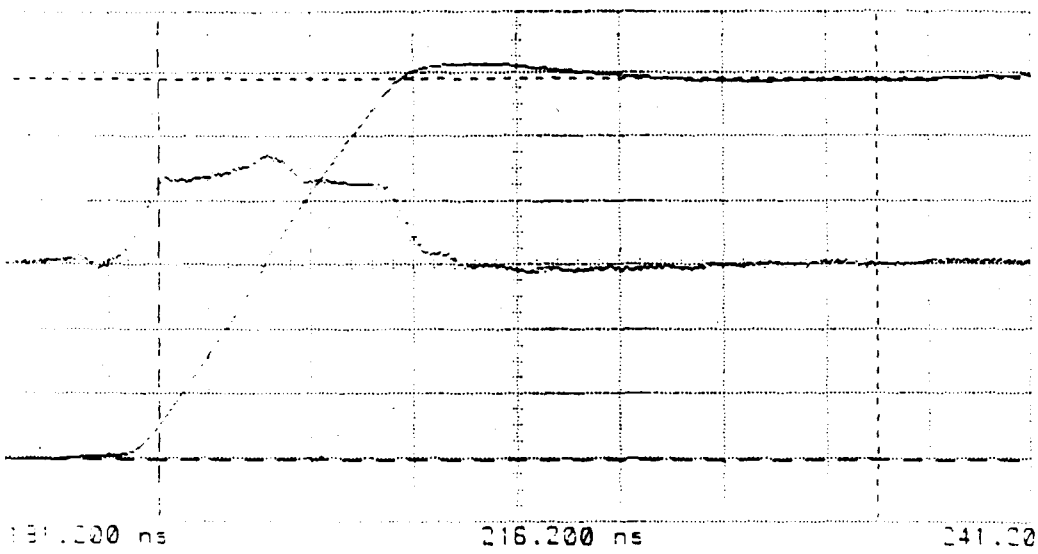
Ch. 1	= 100.0 mVolts/div	Offset	= 0.000 Volts
Function2	= 300 pVolts/div	Offset	= 900 pVolts
Timebase	= 5.00 ns/div	Delay	= 216.200 ns
Delta V	= 1.780 nVolts		
Vmarker1	= 0.000 Volts	Vmarker2	= 1.780 nVolts
Delta T	= 0.00000 s		
Start	= 691.200 ns	Stop	= 691.200 ns

Trigger mode : Edge
On Pos. Edge on Trig3
Trigger Levels
Trig3 = 0.000 Volts
Holdoff = 70.000 ns

(2)

Input at B

Figure 5-b.



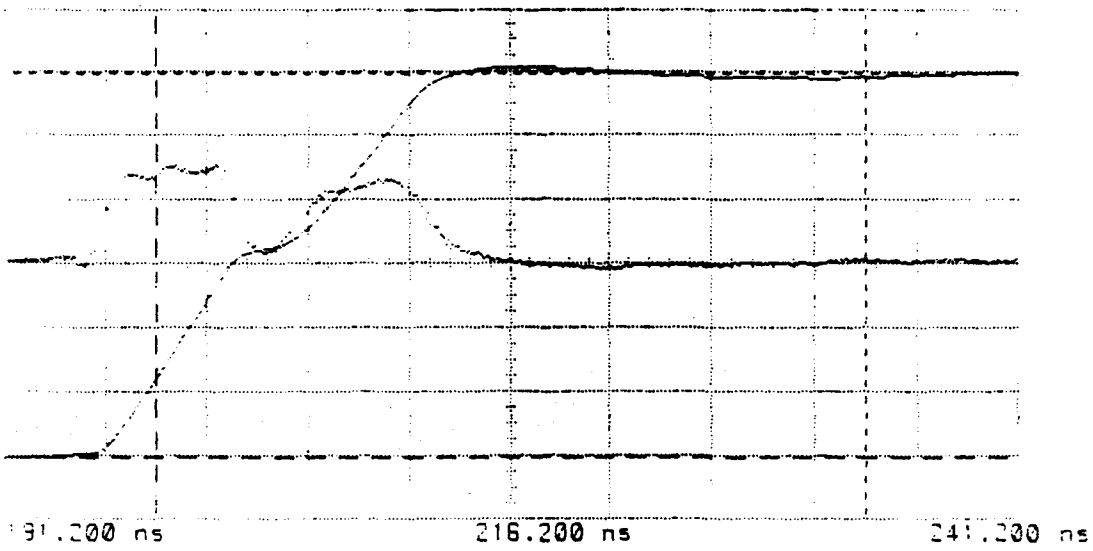
Ch. 1	=	100.0 mVolts/div	Offset	=	0.000 Volts
Function2	=	300 pVolts/div	Offset	=	900 pVolts
Timebase	=	5.00 ns/div	Delay	=	216.200 ns
Delta V	=	1.760 nVolts			
Vmarker1	=	0.000 Volts	Vmarker2	=	1.760 nVolts
Delta T	=	35.000 ns			
Start	=	198.700 ns	Stop	=	233.700 ns

Trigger mode : Edge
On Pos. Edge on Trig3
Trigger Levels
Trig3 = 0.000 Volts
Holdoff = 70.000 ns

(3)

Input at 'C

Figure 5-c.

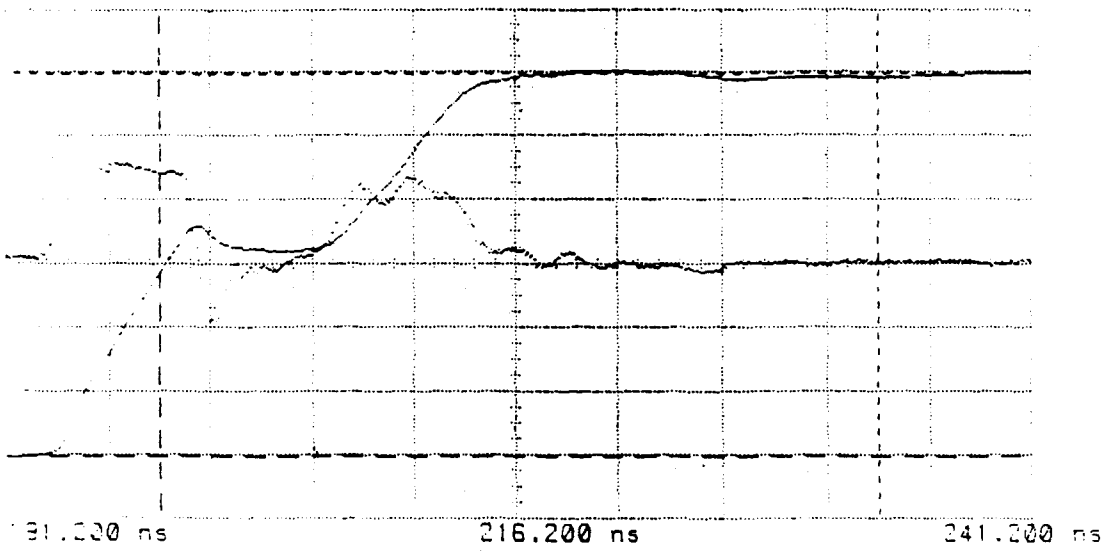


Ch. 1	=	100.0 mVolts/div	Offset	=	0.000 Volts
Function2	=	300 pVolts/div	Offset	=	900 pVolts
Timebase	=	5.00 ns/div	Delay	=	216.200 ns
Delta V	=	1.780 nVolts			
Vmarker1	=	0.000 Volts	Vmarker2	=	1.780 nVolts
Delta T	=	35.000 ns			
Start	=	198.700 ns	Stop	=	233.700 ns

Trigger mode : Edge
On Pos. Edge on Trig3
Trigger Levels
Trig3 = 0.000 Volts
Holdoff = 70.000 ns

(4) (D)

Figure 5-d.



Ch. 1 = 100.0 mVolts/div
Function2 = 300 pVolts/div
Timebase = 5.00 ns/div

Offset = 0.000 Volts
Offset = 900 pVolts
Delay = 216.200 ns

Delta V = 1.780 nVolts
Vmarker1 = 0.000 Volts
Delta T = 35.000 ns
Start = 198.700 ns

Vmarker2 = 1.780 nVolts

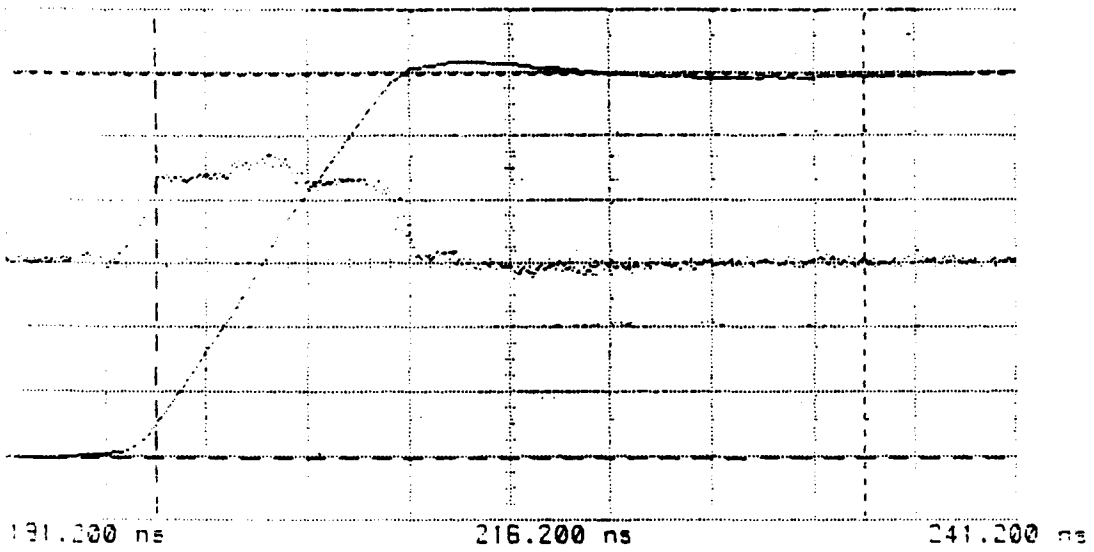
Stop = 233.700 ns

Trigger mode : Edge
On Pos. Edge on Trig3
Trigger Levels
Trig3 = 0.000 Volts
Holdoff = 70.000 ns

5)

E

Figure 5-e.



Ch. 1	=	100.0 mVolts/div	Offset	=	0.000 Volts
Function2	=	300 pVolts/div	Offset	=	900 pVolts
Timebase	=	5.00 ns/div	Delay	=	216.200 ns
Delta V	=	1.780 nVolts			
Vmarker1	=	0.000 Volts	Vmarker2	=	1.780 nVolts
Delta T	=	35.000 ns			
Start	=	198.700 ns	Stop	=	233.700 ns

Trigger mode : Edge
On Pos. Edge on Trig3
Trigger Levels
Trig3 = 0.000 Volts
Holdoff = 70.000 ns

(b) C

Figure 5-f.

A Pizero Identifier for GEM

Jon Eisenberg, Paul M. Mockett
University of Washington, Seattle WA

We are investigating the possibility that the front part of the electromagnetic calorimeter in the liquid argon option for GEM could serve as a pizero detector. This may be feasible without increasing the channel count and therefore the approach may be viewed as a free option.

The pizero detector serves as a front end of the EM stack. There is of course flexibility in the details but we are considering a system about 8 cm by 8 cm(covering 16 towers). A schematic is shown in Fig. 1. It would be about 4 X0 thick with the same plate thickness as the remainder of the stack. Alternate gaps would be viewed by x and y strips. The strips would have a 1 to 2 mm pitch and every sixth strip connected together. The x strips would be read by 6 channels and the y strips would be read by 6 channels. Hence the signals from different sub regions would be folded on top of each other. Using the GEANT Monte Carlo we have been testing an algorithm devised to separate one gamma from the two gammas from pizeros. The first tests look encouraging. We are getting nearly 100% acceptance of one gamma and a good rejection of pizeros. We are still in the process of optimizing the cuts and expect further improvements Table I gives the cuts used in the algorithm and Table II gives the results for a series of photon and pizero energies. The results of these cuts are plotted in Fig. 2. Fig. 3 provides a series of x and y energy profiles for 100 GeV photons and pizeros both in absolute and folded coordinates. These pictures are for photons and pizeros originating 85 cm from the calorimeter. Accompanying each picture are mnemonics showing which if any cut the event fails to pass. The pizero rejection is still about 85% which can substantially reduce the background under the Higgs to gamma gamma signal.

On the simulation side we plan to continue to optimize the algorithm by adding energy dependence to the cuts. On the hardware side we will also construct a test module for bench testing and beam testing. With these hardware tests we plan to verify the simulations as well as demonstrate the feasibility of the construction of such a device.

Preliminary investigations of noise and cross talk indicate they are quite manageable.

We will construct a two by two set of front end towers to identify pizeros. These would require 48 channels of fast electronics. Their exact dimension would be determined by the tower size of the backing EM calorimeter.

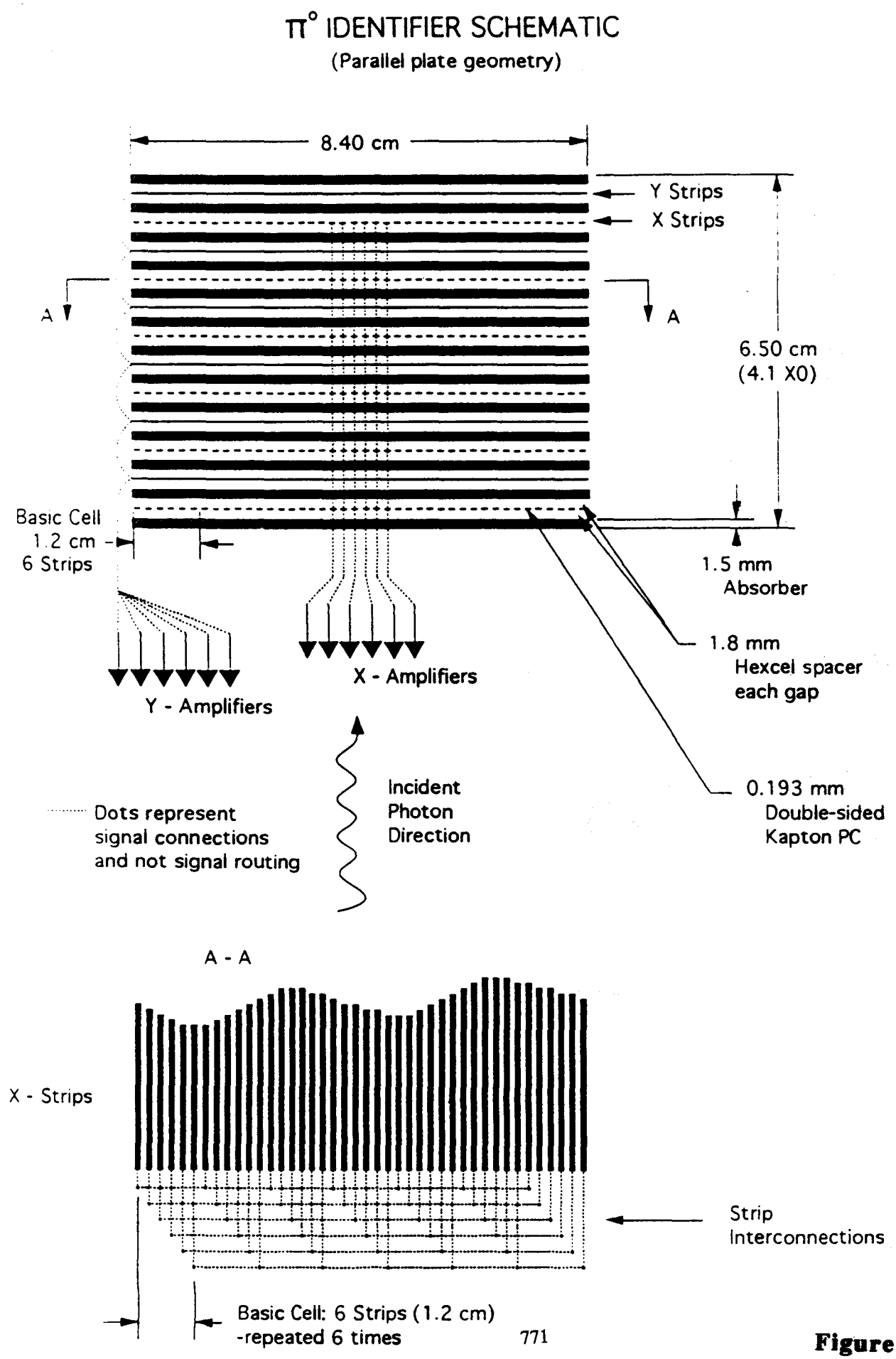

π° IDENTIFIER SCHEMATIC
(Parallel plate geometry)
8.40 cm
Y Strips
X Strips
A
A
6.50 cm
(4.1 X0)
Basic Cell
1.2 cm
6 Strips
1.5 mm
Absorber
1.8 mm
Hexcel spacer
each gap
X - Amplifiers
Y - Amplifiers
Incident
Photon
Direction
0.193 mm
Double-sided
Kapton PC
Dots represent
signal connections
and not signal routing
A - A
X - Strips
Strip
Interconnections
Basic Cell: 6 Strips (1.2 cm)
-repeated 6 times

Figure 1.

Cut Values
1mm strips

Category	Description	Name	Value
Peak definition	Energy required for sum of two highest strips to be considered peaks	ECUT	.015 GeV
	Minimum fraction of highest energy strip that second highest strip must have to be considered a second peak	PEAKCUT	25 %
Width cut	Largest number of adjacent strips not considered a π^0	NCUTWID	3 strips
	Fraction of highest energy strip which NCUTWID+1 adjacent strips must exceed to be considered a π^0	EWIDCUT	50 %
	Total energy above which NCUTWID is replaced by NWCLOWER	WCTHRESH	75. GeV
	Higher energy width cut	NWCLOWER	2 strips
Mean off cut	Mean off constant for π^0 rejection	CUTMEAN	2.83 mm
	Power of energy for mean offset scaling	CUTPOWR	-0.37
	Total energy above which CUTMEAN becomes half the strip width	CUTOFF	75. GeV
Dip cut	Maximum fraction of strip between peaks considered π^0 dip	DIPMAX	50 %

Table I

1mm Strips
Acceptances and Cut Performances

incident particle		accept.	number of photons			number selected by cuts					
E (GeV)		(%)	0 (%)	1 (%)	2 (%)	mean (%)	mean only	dip (%)	dip only	width (%)	width only
5	γ	86.0	6.4	69.6	14.0	2.8	1.6	9.2	8.0	3.6	3.2
5	π^0	77.6	11.6	10.8	77.6	71.2	46.4	17.2	2.8	22.8	3.2
10	γ	94.0	20.4	73.6	6.0	2.0	1.2	4.0	3.2	0.8	0.8
10	π^0	88.4	6.0	5.6	88.4	84.4	51.2	25.6	2.4	20.0	1.6
25	γ	96.8	14.4	82.4	3.2	1.2	0.4	2.8	2.0	0.0	0.0
25	π^0	94.0	4.0	2.0	94.0	89.2	46.0	53.2	4.0	13.2	0.4
50	γ	99.2	15.2	84.0	0.8	0.0	0.0	0.8	0.8	0.0	0.0
50	π^0	92.0	0.4	7.6	92.0	87.6	54.0	40.8	4.0	9.2	0.0
75	γ	98.4	12.8	85.6	1.6	1.6	1.2	0.8	0.0	0.0	0.0
75	π^0	90.0	3.2	6.8	90.0	80.0	34.0	62.4	8.8	15.2	0.4
100	γ	98.0	14.0	84.0	2.0	1.2	1.2	0.8	0.8	0.0	0.0
100	π^0	85.6	2.8	11.6	85.6	68.8	30.8	53.6	12.0	21.2	3.6
125	γ	99.2	12.8	86.4	0.8	0.4	0.4	0.4	0.4	0.0	0.0
125	π^0	81.6	2.0	16.4	81.6	62.4	26.8	46.8	13.2	22.4	4.8
150	γ	97.2	8.8	88.4	2.8	2.8	2.0	0.8	0.0	0.0	0.0
150	π^0	70.0	3.2	26.8	70.0	49.2	24.0	28.4	8.4	23.6	12.4

Table II

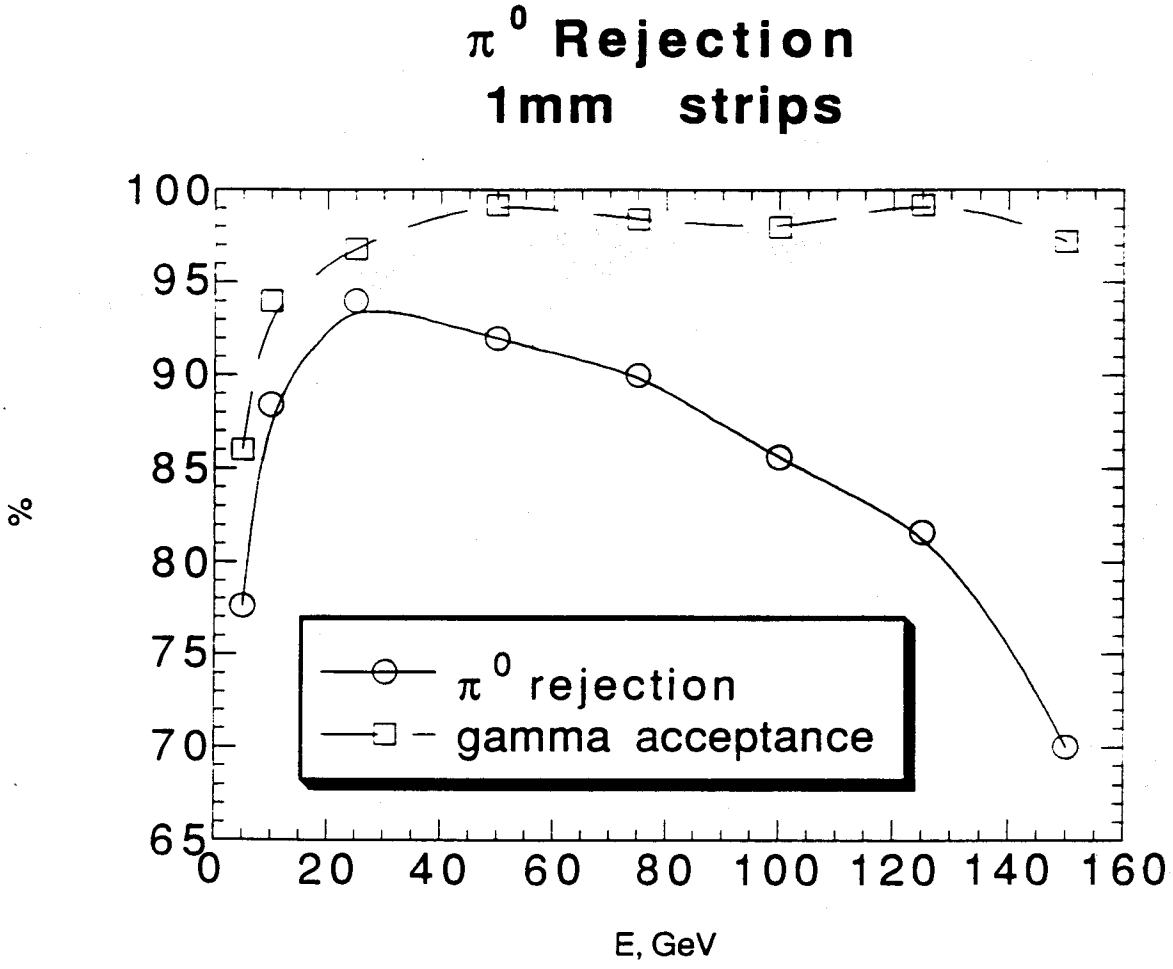

π⁰ Rejection
1mm strips
100
95
90
85
80
75
70
65
%
0
20
40
60
80
100
120
140
160
E, GeV
π⁰ rejection
gamma acceptance

Figure 2

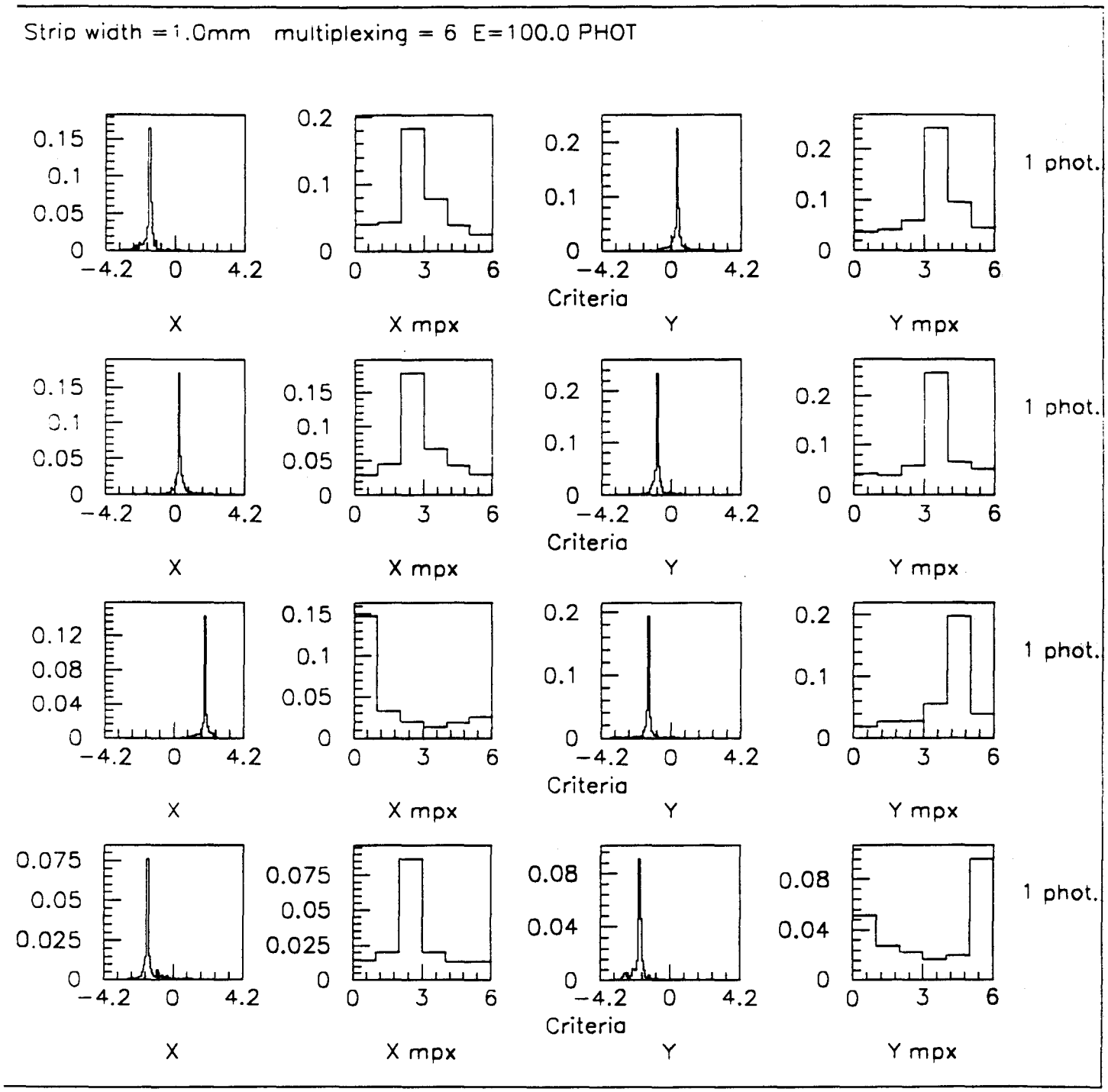
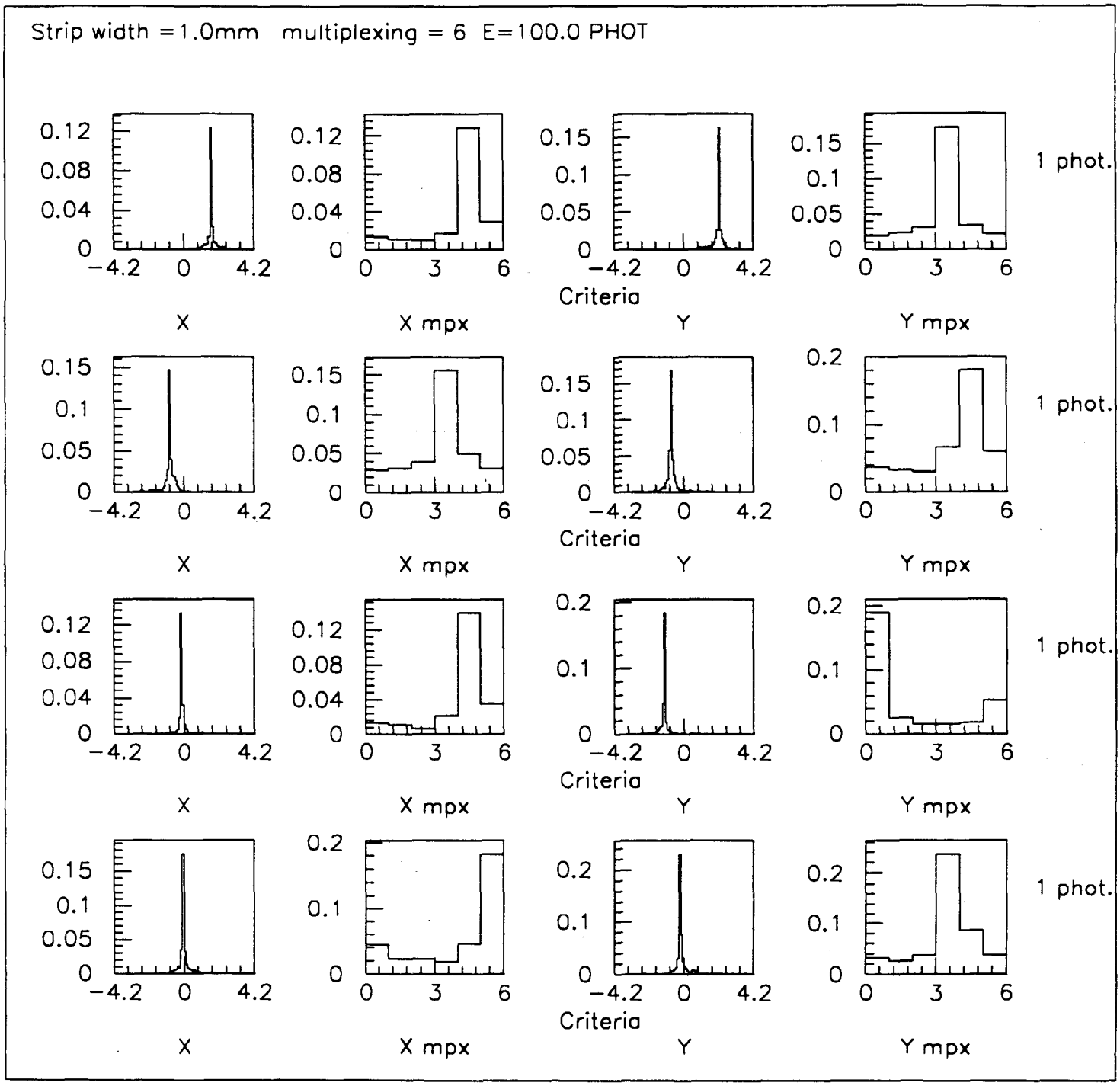
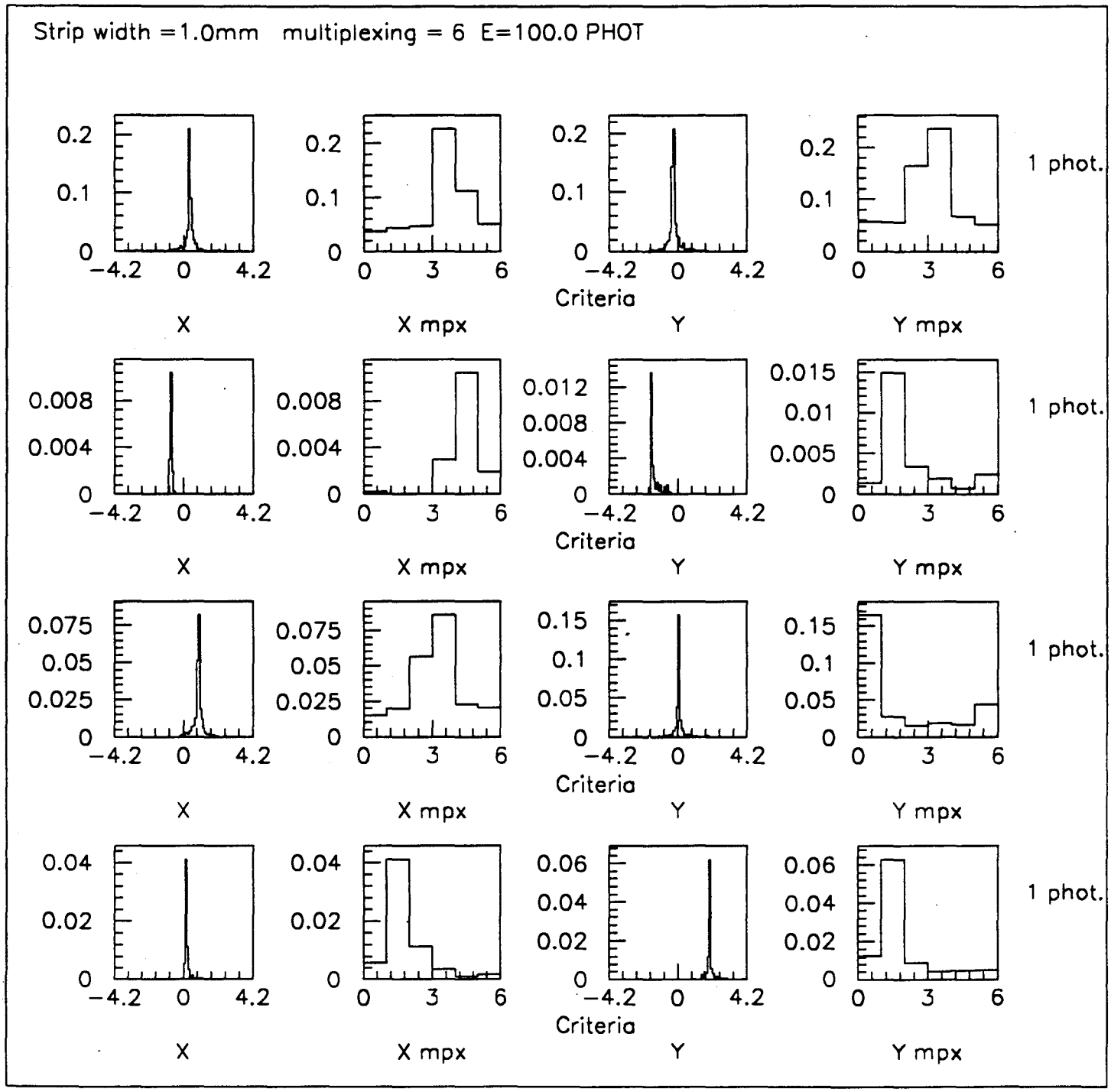
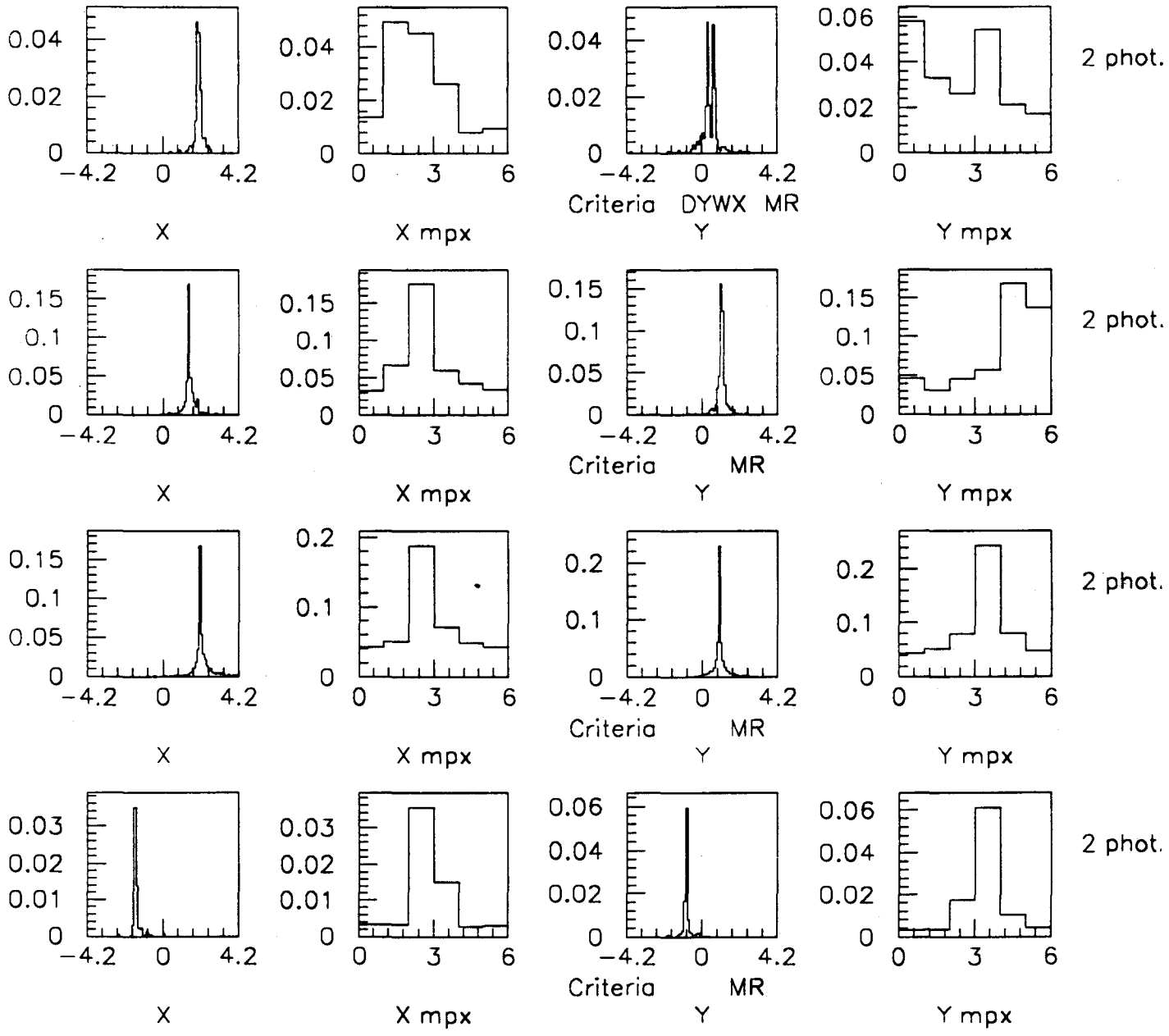

Strip width =1.0mm multiplexing = 6 E=100.0 PHOT
1 phot.
1 phot.
1 phot.
1 phot.
X
X mpx
Criteria
Y
Y mpx

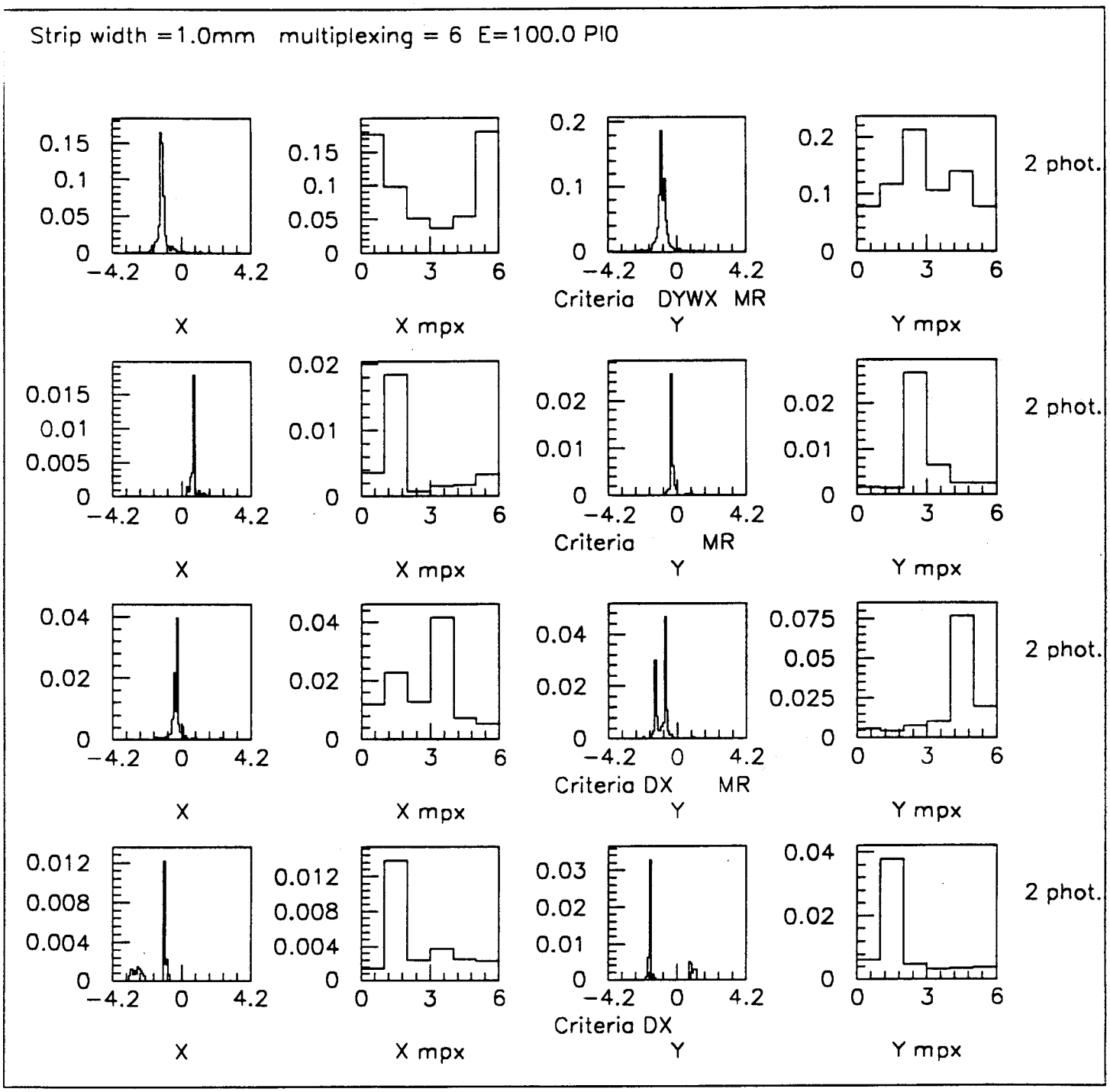
Figure 3.

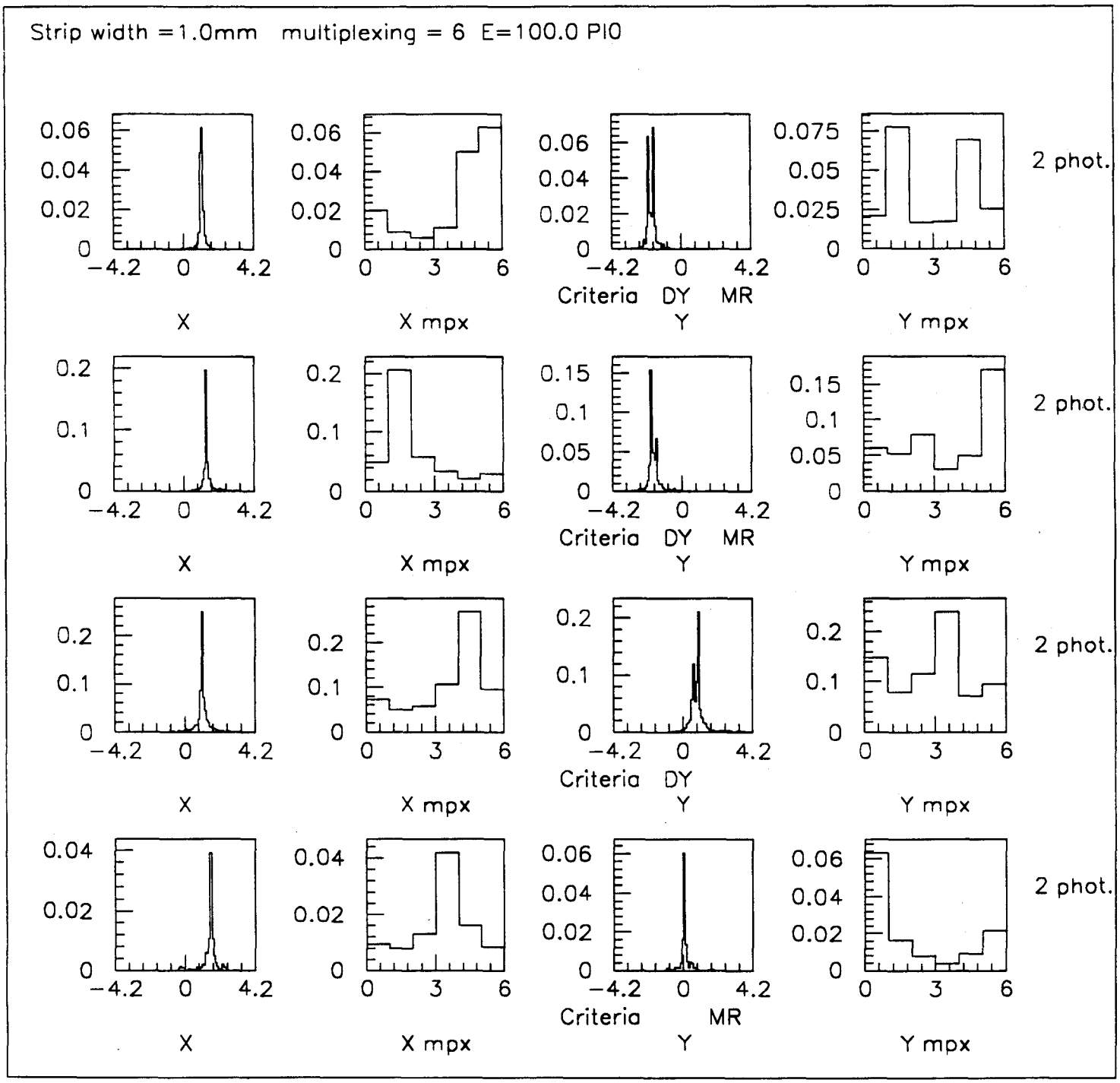

Strip width =1.0mm multiplexing = 6 E=100.0 PHOT
0.12
0.08
0.04
0
−4.2
0
4.2
X
0.12
0.08
0.04
0
0
3
6
X mpx
0.15
0.1
0.05
0
−4.2
0
4.2
Criteria
Y
0.15
0.1
0.05
0
0
3
6
Y mpx
1 phot.
0.15
0.1
0.05
0
−4.2
0
4.2
X
0.15
0.1
0.05
0
0
3
6
X mpx
0.15
0.1
0.05
0
−4.2
0
4.2
Criteria
Y
0.2
0.1
0
0
3
6
Y mpx
1 phot.
0.12
0.08
0.04
0
−4.2
0
4.2
X
0.12
0.08
0.04
0
0
3
6
X mpx
0.2
0.1
0
−4.2
0
4.2
Criteria
Y
0.2
0.1
0
0
3
6
Y mpx
1 phot.
0.15
0.1
0.05
0
−4.2
0
4.2
X
0.2
0.1
0
0
3
6
X mpx
0.2
0.1
0
−4.2
0
4.2
Criteria
Y
0.2
0.1
0
0
3
6
Y mpx
1 phot.


Strip width =1.0mm multiplexing = 6 E=100.0 PHOT
1 phot.
1 phot.
1 phot.
1 phot.
X
X mpx
Criteria
Y
Y mpx

Strip width =1.0mm multiplexing = 6 E=100.0 PIO




Strip width =1.0mm multiplexing = 6 E=100.0 PI0
0.15
0.1
0.05
0
−4.2 0 4.2
X
0.15
0.1
0.05
0
0 3 6
X mpx
0.2
0.1
0
−4.2 0 4.2
Criteria DYWX MR
Y
0.2
0.1
0
0 3 6
Y mpx
2 phot.
0.015
0.01
0.005
0
−4.2 0 4.2
X
0.02
0.01
0
0 3 6
X mpx
0.02
0.01
0
−4.2 0 4.2
Criteria MR
Y
0.02
0.01
0
0 3 6
Y mpx
2 phot.
0.04
0.02
0
−4.2 0 4.2
X
0.04
0.02
0
0 3 6
X mpx
0.04
0.02
0
−4.2 0 4.2
Criteria DX MR
Y
0.075
0.05
0.025
0
0 3 6
Y mpx
2 phot.
0.012
0.008
0.004
0
−4.2 0 4.2
X
0.012
0.008
0.004
0
0 3 6
X mpx
0.03
0.02
0.01
0
−4.2 0 4.2
Criteria DX
Y
0.04
0.02
0
0 3 6
Y mpx
2 phot.


Strip width =1.0mm multiplexing = 6 E=100.0 PIO
0.06
0.04
0.02
0
−4.2 0 4.2
X
0.06
0.04
0.02
0
0 3 6
X mpx
0.06
0.04
0.02
0
−4.2 0 4.2
Criteria DY MR
Y
0.075
0.05
0.025
0
0 3 6
Y mpx
2 phot.
0.2
0.1
0
−4.2 0 4.2
X
0.2
0.1
0
0 3 6
X mpx
0.15
0.1
0.05
0
−4.2 0 4.2
Criteria DY MR
Y
0.15
0.1
0.05
0
0 3 6
Y mpx
2 phot.
0.2
0.1
0
−4.2 0 4.2
X
0.2
0.1
0
0 3 6
X mpx
0.2
0.1
0
−4.2 0 4.2
Criteria DY
Y
0.2
0.1
0
0 3 6
Y mpx
2 phot.
0.04
0.02
0
−4.2 0 4.2
X
0.04
0.02
0
0 3 6
X mpx
0.06
0.04
0.02
0
−4.2 0 4.2
Criteria MR
Y
0.06
0.04
0.02
0
0 3 6
Y mpx
2 phot.

SLAC-PUB-5644
August 1991
(E)

Importance of the $B_s^0 \rightarrow \mu^+\mu^-$ Branching Fraction

A. Fridman[+] and A. Snyder
Stanford Linear Accelerator Center, Stanford University
Stanford, California 94309

Abstract

We discuss the $B_s^0 \rightarrow \mu^+\mu^-$ decay channel which is sensitive to deviations from the standard model. We also consider the B_s^0 mixing information that could be obtained from these decays in the framework of the standard model. Finally we comment the experimental difficulties in observing the $B_s^0 \rightarrow \mu^+\mu^-$ channel.

Submitted to the 1991 Symposium on
The Superconducting Super Collider
Corpus Christi, Texas, October 13 - 17, 1991

* Work Supported by the Department of Energy, Contract DE-AC03-763f00515
[+] LPHHE, Université de Paris VI et VII

1 - Introduction

To illustrate the usefulness of large $B\bar{B}$ data samples, we briefly discuss problems related to the measurement of rare B-decays, specifically, the $B_s^0 \to l^+l^-$ channels where $l \equiv \tau, \mu, e$. These decays are expected to have small branching ratios (see below) but to be sensitive to deviations from the standard model. Moreover, these measurements could give additional information about B_s^0 mixing that could complete our knowledge of the mixing observed first for the B_d^0 case with the $e^+e^- \to \Upsilon(4S) \to B_d^0\bar{B}_d^0$ experiments[1].

Let us recall that in the standard model the B_s^0 mixing parameter[2,3] x_s is expected to be much larger than x_d, the B_d^0 case ($x_s/x_d \sim 14$). Although the measurement of r_s,

$$r_s \equiv \frac{N(B_s^0 \to \bar{B}_s^0)}{N(B_s^0 \to B_s^0)} = \frac{x_s^2}{2+x_s^2} , \tag{1}$$

appears to be possible[4] (N is the number of events), the extraction of the x_s value becomes difficult if x_s is large[5]. The distribution of the time-dependent rate could, in principle, also allow the x_s value to be obtained[2] if the detector can measure the time-dependence with good precision[4]. Because this measurement will be difficult, an indirect estimate of x_s via branching ratio measurements might be very helpful (see below). In any case the comparison of x_s measurements using different methods will be a further test of the standard model.

2 - The $B_s^0 \to l^+l^-$ decay

These decays ($l \equiv \tau, \mu, e$) have been investigated theoretically[6-9]. Estimates of the branching ratios[8] are given in Table 1 for a top quark mass, $m_t = 150$ GeV (here m_k is the mass of the k-type quark or particle). The $B_s^0 \to \tau^+\tau^-$ decay has the largest branching ratio but will not be easily detected (the momentum of the τ must be measured in order to know if they are coming from the same B_s^0 meson). It may eventually be possible to detect the $B_s^0 \to \mu^+\mu^-$ decay in experiments where very large statistics could be obtained. For this decay the theoretical expression for the branching ratios[8,9] is:

$$BR(B_s^0 \to \mu^+\mu^-) = \frac{G_F^2}{2\pi}\left(\frac{\alpha^2}{16\pi^2}\right) f_B^2 m_B \frac{|V_{tb}V_{ts}|^2}{\Gamma_s}\, m_\mu^2\, |C(y)|^2 . \tag{2}$$

Here G_F is the Fermi coupling constant and α is the fine structure constant. The f_B (usually assumed to be ~ 0.2 GeV) is the B_s^0 decay constant and Γ_s is the B_s^0

decay width. The V_{jk} are the CKM matrix elements and $C(y)$ is a function of

$$y = \frac{m_t^2}{m_W^2}$$

given in reference 8. Fig. 1 shows the dependence of $BR(B_s^0 \to l^+l)$ as a function of the top quark mass. One sees that the branching ratio increases rapidly with increasing m_t. Note also from equation (2) that the $B_d^0 \to \mu^+\mu^-$ branching ratio will be much smaller than that expected in the B_s^0. Their ratio should be of the order of $|V_{td}/V_{ts}|^2 \sim 0.06$.

Equation (2) contains several quantities that also appear in the parameter x_s describing the B_s^0 mixing[10]:

$$x_s \equiv \frac{\Delta M}{\Gamma_s} = \frac{G_F^2}{2\pi}\, B_B\, f_B^2 m_B \frac{|V_{tb}V_{ts}|^2}{\Gamma_s}\, m_t^2\, |F(y)|^2 \eta\,. \tag{3}$$

Note that B_B is the bag parameter (~ 1) corresponding to the B_s^0 meson while the QCD correction factor is $\eta \sim 0.85$ (Ref. 11). In this equation the mass of the top quark is not neglected with respect to the W mass. Then, in the standard model, x_s will depend on m_t via the the $m_t \times F(y)$ factor where[10]

$$F(y) = \frac{1}{4}\left[1 + \frac{3-9y}{(y-1)^2} + \frac{6y^2\, ln(y)}{(y-1)^3}\right]$$

Fig. 1 also presents the m_t dependence of x_s. It is much weaker than the m_t dependence of the branching ratio. Using formulas (2) and (3), we obtain

$$BR(B_s^0 \to \mu^+\mu^-) = x_s \left[\frac{3\alpha^2}{16\pi} \times \frac{m_\mu^2}{B_B\, \eta} \times \frac{|C(y)|^2}{m_t^2\, F(y)}\right]. \tag{4}$$

Using this approach, x_s can be obtained by measuring the branching ratio. Moreover, an increase of x_s increases the branching ratio and facilitate its measurement. This is in contrast with r_s and time-dependence rate measurements discussed above.

By using formula (4) with known values of m_t and B_B, one could obtain the value of $r_s = x_s^2/(2 + x_s^2)$ where the error on r_s will be small if x_s is large. For instance, with 100 $B_s^0, \bar{B}_s^0 \to \mu^+\mu^-$ events, one find $\Delta r_s/r_s \leq 4\ 10^{-3}$ for $x_s \geq 10$. Thus, the comparison of the r_s values obtained from formulas (1) and (4) could verify the standard model and, eventually, may be used to obtain x_s.

3 - Experimental Comments

In the case that $BR(B_s^0 \to \mu^+\mu^-) \sim 10^{-9}$ (Table 1), this decay channel could not be studied with e^+e^- colliders[4,12]. For pp interactions with the LHC (c.m. energy of $\sqrt{s} = 16$ TeV) or SSC ($\sqrt{s} = 40$ TeV) colliders the production of events with B mesons is much larger[12,13]. Table 2 indicates the number of $b\bar{b}X$ events (X meaning anything) expected in one year ($10^7 s$) of running with a luminosity of $L = 10^{32} cm^{-2} s^{-1}$. This is the luminosity usually proposed for studying B-physics in order to decrease multiple interactions per bunch crossing[13]. Since tagging is not needed for the measurement of the discussed branching ratio, one could envision a larger luminosity. For instance, with $L = 10^{33} cm^{-2} s^{-1}$ one could obtain at the SSC (LHC) $\sim 1.4\ 10^3$ ($\sim 6\ 10^2$) $B_s^0, \bar{B}_s^0 \to \mu^+\mu^-$ events in one year of running (corresponding, however, to a number of interactions per second of $N_{int}/s \sim 10^8$).

Let us roughly discuss the properties of a μ-detector to be able to give a signal-to-background ratio of S/B$\sim$ 1. Due to the large multiplicity in pp interactions, one expects a large background in the data sample used to study the $B_s^0 \to \mu^+\mu^-$ channel. The background can initially be decreased with kinematical cuts by using only tracks (charged particles) with large momentum ($p > 5$ GeV/c) and transverse momentum ($p_T > 1$ GeV/c). The momentum cut will decrease the contribution of μ's due to the π and K decays. The number of charged particles pairs having an effective mass corresponding to B_s^0 will be reduced by the p_T cut[12]. At $\sqrt{s} = 40$ TeV (and using tracks with $p_T > 1$ GeV/c) we show in Fig. 2 the efficiency (ϵ) for detecting the $B_s^0 \to \mu^+\mu^-$ channel as a function of the maximum value of θ due to the size of the chosen detector. Here θ is the emission angle of the charged tracks with respect to the beam line. A minimum value of $\theta > 1°$ is used in the Monte Carlo calculation[14] because of the beam-pipe cut. Fig. 2 indicates also the influence of the p limits ($p > 0, 5, 10, 20$ GeV/c).

As an example we present in Table 3, ϵ, S/B and the number of $B_s^0 \to \mu^+\mu^-$ events expected in one year of running using the kinematical cuts. The values were obtained with a Monte Carlo calculation at $\sqrt{s} = 40$ TeV. We assumed that the $B_s^0 \equiv \bar{b}q$ production rate is taken to be 0.15 with respect to all particles containing a $\bar{b}$ quark. We also consider that the $B_s^0 \to \mu^+\mu^-$ can be detected after a decay length corresponding to the average B_s^0 lifetime. From Table 3 we see that a background rejection factor of at least $\sim 10^8$ is needed to achieve a workable signal-to-noise (S/B$\sim$ 1). Here, only background due to $B\bar{B}$ events is considered. Thus the detector must have μ identification and B_s^0 vertex reconstruction adequate to obtain this level of background rejection[15]. In any case, detailled investigations have to be done in order to evaluate the possibility of measuring the $B_s^0 \to \mu^+\mu^-$. One must also take into account other sources of background, for instance, Drell-Yan μ pair production as well as $B \to \mu X, \pi^+\pi^-$ reactions.

4 - Conclusions

We discussed the $B_s^0 \to \mu^+\mu^-$ channel which is sensitive to deviations from the standard model. In addition, information about B_s^0 mixing could be obtained in the framework of the standard model. In this approach, large values of the x_s mixing parameter could be measured. We also discussed difficulties of measuring the $B_s^0 \to \mu^+\mu^-$ having theoretical predictions of $\sim 10^{-9}$ for its branching ratio. Clearly, detailled investigations of the various backgrounds have to be made in order to evaluate the possibility of identifying $B_s^0 \to \mu^+\mu^-$ events

Acknowledgements

It is a pleasure to thank A. Ali, L. Dixon and M. Peskin for useful discussions.

Table 1 - Estimates of the $B_s^0 \to l^+l^-$ branching ratios with $m_t = 150$ GeV and $f_B = 200$ MeV (Ref. 8). Here f_B is the B meson decay constant.

$\tau^+\tau^-$	1.8×10^{-7}
$\mu^+\mu^-$	8.3×10^{-10}
e^+e^-	2.0×10^{-14}

Table 2 - The comparison of luminosity (L), total (σ_T) and $b\bar{b}X$ ($\sigma(b\bar{b})$) cross-section of the LHC and SSC colliders[12,13]. Here L is given in $cm^{-2}s^{-1}$. The number of $b\bar{b}X$ interactions per year ($N(b\bar{b})/10^7s$) as well as the number of interactions per second (N_{int}/s) are also given.

	LHC 16 TeV	SSC 40 TeV
L	10^{32}	10^{32}
σ_T	$\sim 110\ mb$	$\sim 120\ mb$
$\sigma(b\bar{b})$	$\sim 200\ \mu b$	$\sim 500\ \mu b$
$\sigma(b\bar{b})/\sigma_T$	1/550	1/240
$N(b\bar{b})/10^7s$	2×10^{11}	5×10^{11}
N_{int}/s	1.1×10^7	1.2×10^7

Table 3 - Kinematical cuts for detecting the $B_s^0 \to \mu^+\mu^-$ decay estimated by using a Monte Carlo calculation [14] at the SSC c.m. energy. Given are the fraction of the events passing the kinematical cuts, ϵ, and the corresponding signal to background ratio, S/B. The cuts are the μ momentum (p), its transverse momentum $p_T \geq 1.5$ GeV/c and $\theta > 1°$. Here $N(\mu\mu)$ is the number of $B_s^0 \to \mu^+\mu^-$ events passing the cuts, in one year of running at $L = 10^{33}cm^{-2}s^{-1}$.

$p \geq$	5 GeV/c	10 GeV/c	20 GeV/c
ϵ	0.27	0.24	0.15
S/B	$\sim 5 \times 10^{-9}$	$\sim 5 \times 10^{-9}$	$\sim 5 \times 10^{-9}$
$N(\mu\mu)$	150	133	84

References

1) H. Albrecht et al. (ARGUS), Phys. Lett. B192 (1987) 245;
M. Artuso et al. (CLEO), Phys. Rev. Lett. 62 (1989) 2233.
2) I.I. Bigi and A.I. Sanda, Nucl. Phys. B193 (1981) 85; Nucl. Phys. B281 (1987) 41.
3) The mixing parameter $x_{d,s} = \Delta M_{d,s}/\Gamma_{d,s}$ for the $B^0_{d,s}$ have the incovenience of having a value between 0 and ∞. Here $\Delta M_{d,s}$ is the mass difference between the heavy and light neutral mesons while $\Gamma_{d,s}$ is their average width; see also the lectures: Mixing and CP Violation in the B-System, A. Fridman, CERN-EP/88-123 Report (1988).
4) The Physics Program of a High-Luminosity Asymmetric B Factory, SLAC 353 Report (1989).
5) For instance, the measurement of the small value of r_d (~ 0.2) allowed one to obtain $x_d = 0.66 \pm 0.11$ (ref. 1).
6) B.A. Campbell and P.J. O'Donnel, Phys. Rev 25D (1982) 1989.
7) G. Eilam and A. Soni, Phys. Rev Lett. 215B (1988) 171.
8) A. Ali, DESY 91-080 Report (1991).
9) M.J. Savage, RU-91-22 Report (1991)
10) CLNS 91-1043 Report (1991) and references therein.
11) A.J. Buras, W. Slominski and H. Steger, Nucl. Phys. B 238 (1984) 529; Nucl. Phys. B 245 (1984) 369.
12) A. Fridman and A. Snyder, Proceedings of the Large Hadron Collider Workshop, Aachen, 4-9 October 1990, CERN 90-10 Report, Vol. II, p.218 (1990).
13) A. Fridman, B-Physics Possibilities with pp Colliders, Invited talk to be published in the Proceedings of the 3rd Topical Seminar on Heavy Flavor, San Miniato, 17-21 June 1991 and references therein.
14) H.-U. Bengtsson and T. Sjöstrand, Comp. Phys. Commun 46 (1987) 43.
15) Vertex reconstructions for $B \rightarrow \mu\mu$ are under investigation, see for instance, Dilepton and Dihadron Production in Proton-Nucleus Collisions at 800 GeV, The E-772 and 789 Collaborations, C.S. Mishra, FERMILAB-Conf-90/100-E (1990).

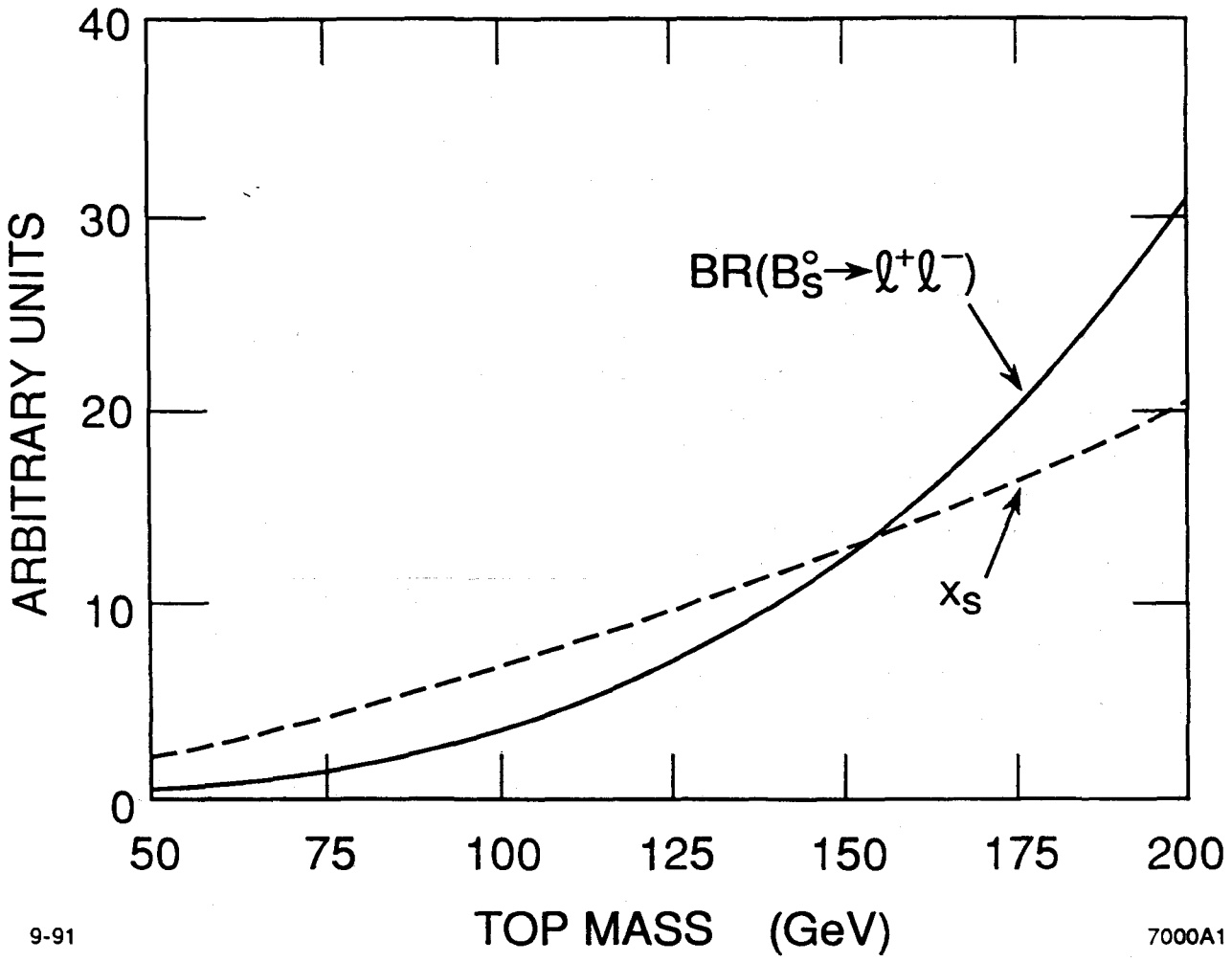


Fig. 1 - The $B_s^0 \to l^+l^-$ branching ratio and the x_s mixing parameter as a function of m_t, the top quark mass.

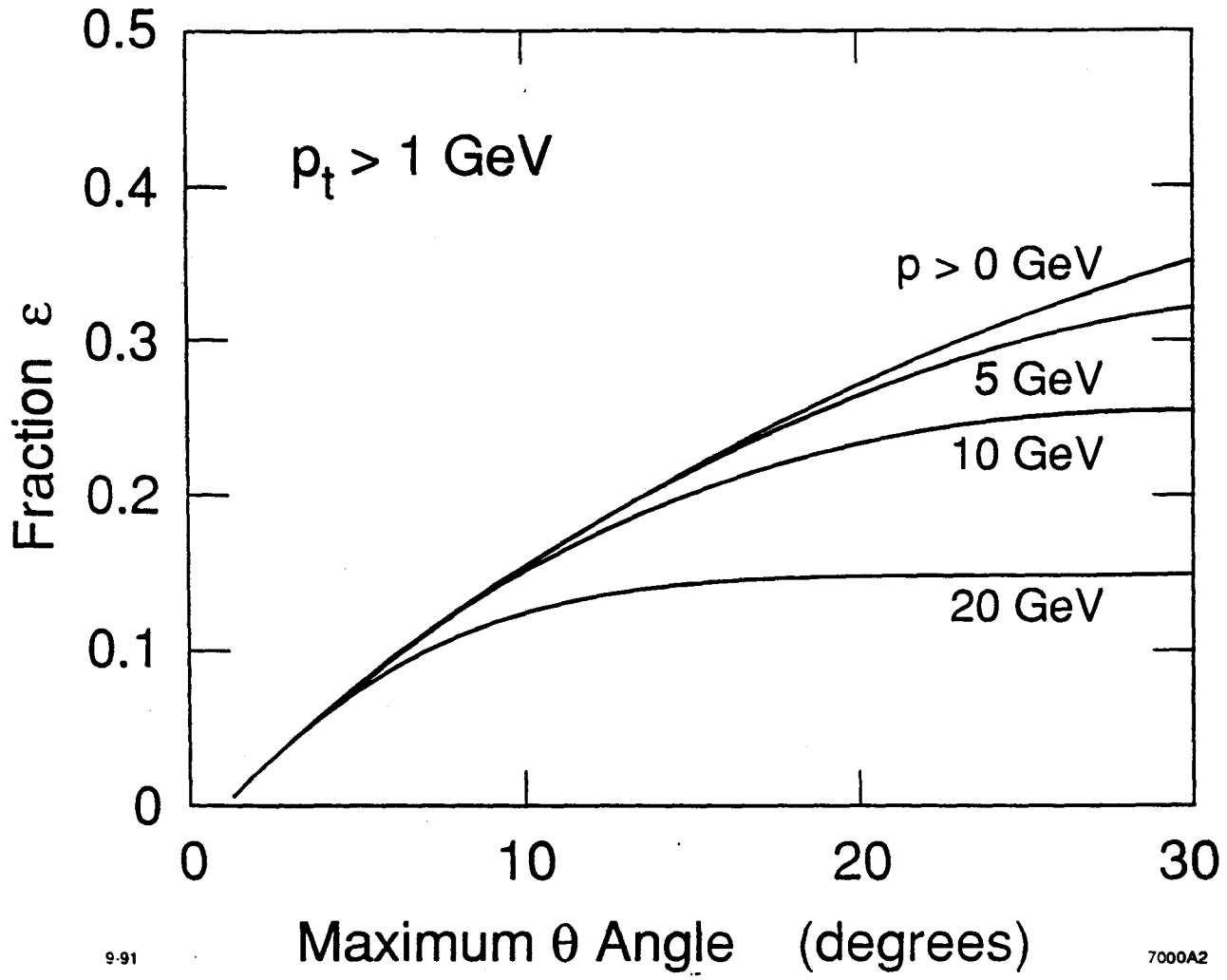
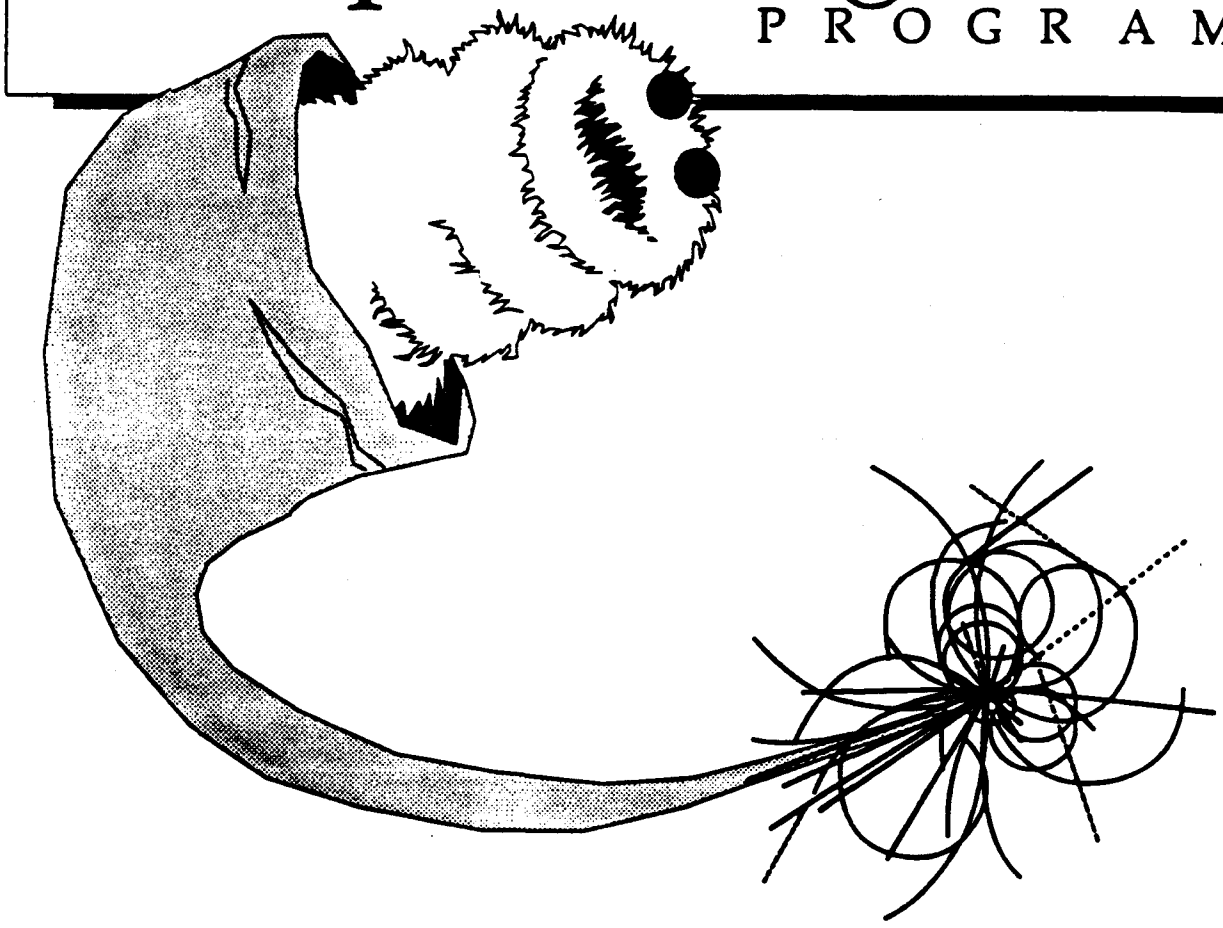


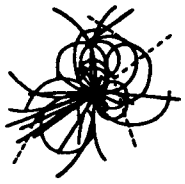
Fig. 2 - The efficiency ϵ of detecting the $B_s^0 \to \mu^+\mu^-$ events as a function of the maximum θ value at $\sqrt{s} = 40$ TeV. Here θ is the μ emission angle with respect to the beam line. The curves are given with μ having $p_T > 1$ GeV/c and various p limits.

Adopt-A-Magnet

PROGRAM



Learning activities from the Superconducting Super Collider



SSC SCIENCE EDUCATION MODULE

ADOPT - A - MAGNET

Program Concept Developer
Dr. Tom O. Bush

Head, SSC Education Office
Dr. Tom Gadsden

Manager of Educational Programs,
SSC Education Office / Program Director
Sherrie "Sam" Kivlighn

Program Coordinator
Lola K. Williamson

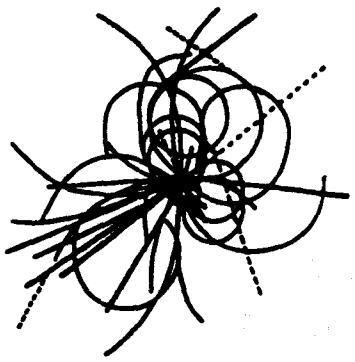
Program Development Group
Regina Bonner
Ed Cannady
Linda Franklin
Suzann Goodman
Annette Moran
Sharron Pearson
Brenda Rentfro
Evelyn Restivo
Brenda Stevenson
Rodney Wetterskog
Dr. George Yost

Graphic Design
Wanda Rice

Acknowledgement just be given to several parties who have been instrumental in helping to make this project a reality. Thanks go the Superconducting Super Collider staff, Texas National Research Laboratory Commission, and the Texas Education Agency. The work, encouragement and support of Tom Bush, Joseph Cipriano, Per Dahl, Doug Fisher, Carl Goodzeit, Jim Gray, Grace Grimes, Marletta Henegar, Raphael Kasper, Ted Kozman, Bob Malnar, Bob Rooney, Roy Schwitters, and John Tompkins are greatly appreciated. A special thanks to other people too numerous to mention who have contributed to the development of the Adopt-A-Magnet program.

The Adopt-A-Magnet Program was developed at the Superconducting Super Collider Laboratory which is operated by the Universities Research Association Inc., under contract with the United States Department of Energy. For information, contact:

Adopt-A-Magnet Program
Superconducting Super Collider Laboratory
2550 Beckleymeade Avenue, MS-2070
Dallas, Texas 75237
(214) - 708 - 1091



Copyright ©1991 by Universities Research Association, Inc. All rights reserved.

This publication has been authored by a contractor of the U.S. Government under Contract No. DE-AC02-89ER40486. Accordingly, the U.S. Government retains a nonexclusive, royalty-free license to publish or reproduce the published form for this contribution, or allow others to do so, for U.S. Government purposes.

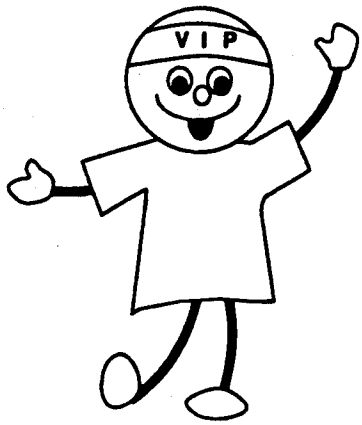
Permission is hereby granted to reproduce designated materials in this book for noncommercial classroom and individual use.

Purpose of Adopt-A-Magnet

Dr. Tom Bush, a nuclear physicist in charge of the Magnet Division of the Superconducting Super Collider (SSC), wanted the young students of Texas and the rest of the United States to become familiar with some interesting work now being carried out in the field of high energy physics. Specifically, he wanted students like you to learn how magnets will be used in the giant Super Collider that will be built surrounding Waxahachie, Texas, which is in Ellis County about 30 miles south of Dallas. Construction is scheduled to begin in 1991 and to be completed by the year 2000. Students who successfully complete this unit of study on magnets and the Super Collider will make their school eligible to have its name placed on an SSC magnet and, in this way, become "adopters" of a magnet.

Many of you boys and girls who are in school today will become the scientists, computer operators, technicians, and lab attendants of the future who will operate this giant machine in the year 2000. It will require thousands of highly trained people to run this huge particle accelerator and to perform the complex research into the basic building blocks of matter. Dr. Bush hopes that you will enjoy working with VIP (the Very Important Proton) as you learn more about the SSC. One day you will want to visit the Laboratory site and see your school's name displayed there.

There is already tremendous interest in the Adopt-A-Magnet program. Schools from forty seven states and eight foreign countries have already requested the modules. Additional letters, calls, and personal requests are received every day. You and the SSC can be proud to be part of this international educational venture.



A Historical Perspective of Magnetism:

Lodestone to Superconducting Super Collider

History confirms man's first association with magnetism occurred some 2,500 years ago with the discovery of a natural iron ore known as magnetite or lodestone, meaning "leading stone." An ancient legend states that on the Greek island of Magnesia, for which magnets were named, a shepherd noticed that his iron-tipped walking staff would attract small pieces of tiny stones, known as lodestones. Not only did the black lodestones have the power to attract iron, but many people during the Middle Ages believed this unique form of iron ore had medical powers. Interestingly, the lodestone was used in navigation by the Norsemen as they invented one of the earliest compasses. The Norsemen found that lodestone, when set in a block of wood and then set afloat in a basin of water, would consistently point north, the direction of the Earth's magnetic field. Today, lodestone or magnetite can be found in several areas such as Norway, Sweden, and the Ural Mountains.

While studying the compass in 1269, Petrus Peregrinus, also known as Peter the Pilgrim of France, located the lines of magnetic force and discovered the two poles of a spherical lodestone. These poles were the areas of strongest force. Further experimentation confirmed that like poles repel and unlike poles attract. Peregrinus' efforts stopped short of the conclusion that the Earth itself is a magnet. In 1600, Sir William Gilbert, a physician to Queen Elizabeth I, continued experimentation with a spherical magnet and discovered the Earth's magnetism.

Another historical milestone was Volta's invention of the "galvanic" battery for producing an electric current in 1800. His famous voltaic "pile" consisted of zinc and copper plates separated by blotting paper moistened with brine. The invention of a constant-current source of electricity was a turning point in practical experimentation, making possible the subsequent discoveries of Oersted, Sturgeon, Ampere and Faraday.

In the 1820's a significant discovery linked magnetism and electricity. Hans Christian Oersted, a Danish physicist, found that an electric current flowing in a wire would move a compass needle. In 1825 an English electrician, William Sturgeon, wrapped a coil of insulated wire around a soft-iron horseshoe, and created the first practical electromagnet.

During the 1830's efforts in electromagnetic induction continued. The British physicist Michael Faraday, and the American physicist Joseph Henry found that moving a magnet around near a closed loop of wire would produce an electric current in the wire.

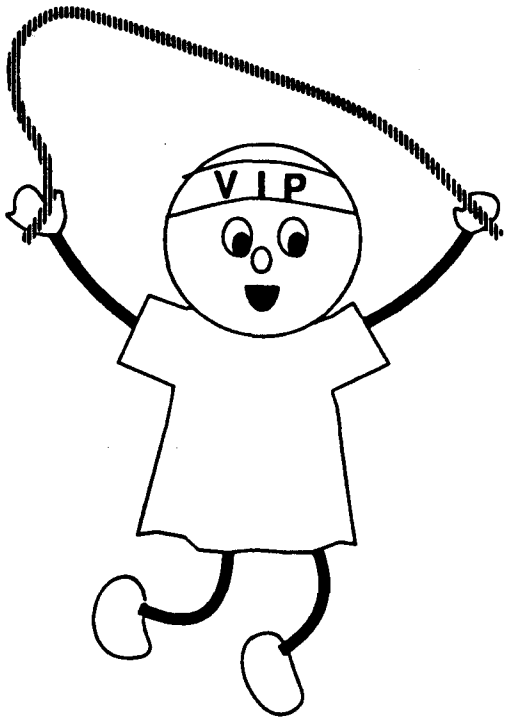
Around 1860, a scientific theory was proposed that correctly brought together and explained the experimental results obtained by the great physicists Oersted, Gauss, Faraday, Henry and Ampere. The unified theory of electromagnetism was developed by James Maxwell. This theory showed for the first time the remarkable fact that light is just a set of rapidly changing electric and magnetic fields propagating through space.

The beginning of the twentieth century held promise for continued discovery in the field of modern electromagnet design. In the early part of the century the materials for making wire appeared to be well understood, but there was a lot of room for improvement in the core over William Sturgen's soft-iron horseshoe. Increased magnetic strength led to the application of electromagnetism in everyday life. Strong magnets were developed that could lift huge beams for building construction, move heavy cars at scrap yards, and carry big containers used for storage.

In 1961 another major breakthrough occurred in magnet technology. It had been well known since 1911 that some materials are able to conduct the flow of electric current with no resistance if the material is maintained at extremely low cryogenic temperatures. This is called superconductivity. This technique allows the wire to carry significantly more electric current which in turn creates a significantly stronger electromagnetic field. This led to the construction of the first superconducting magnet

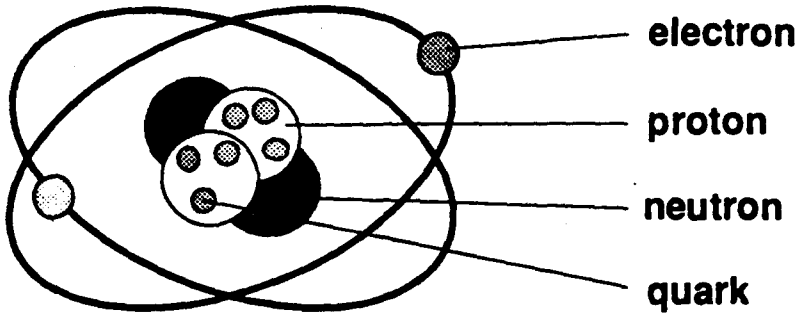
in 1961. During the 1980's, the first successful particle accelerator using superconducting magnets became operational at Fermi National Accelerator Laboratory in Chicago. These superconducting magnets produced magnetic fields twice as strong as those possible with the existing electromagnets using one-half the electrical power, even when the power needed for refrigeration was taken into account. This basic design and associated research led to the present magnet design for the Superconducting Super Collider.

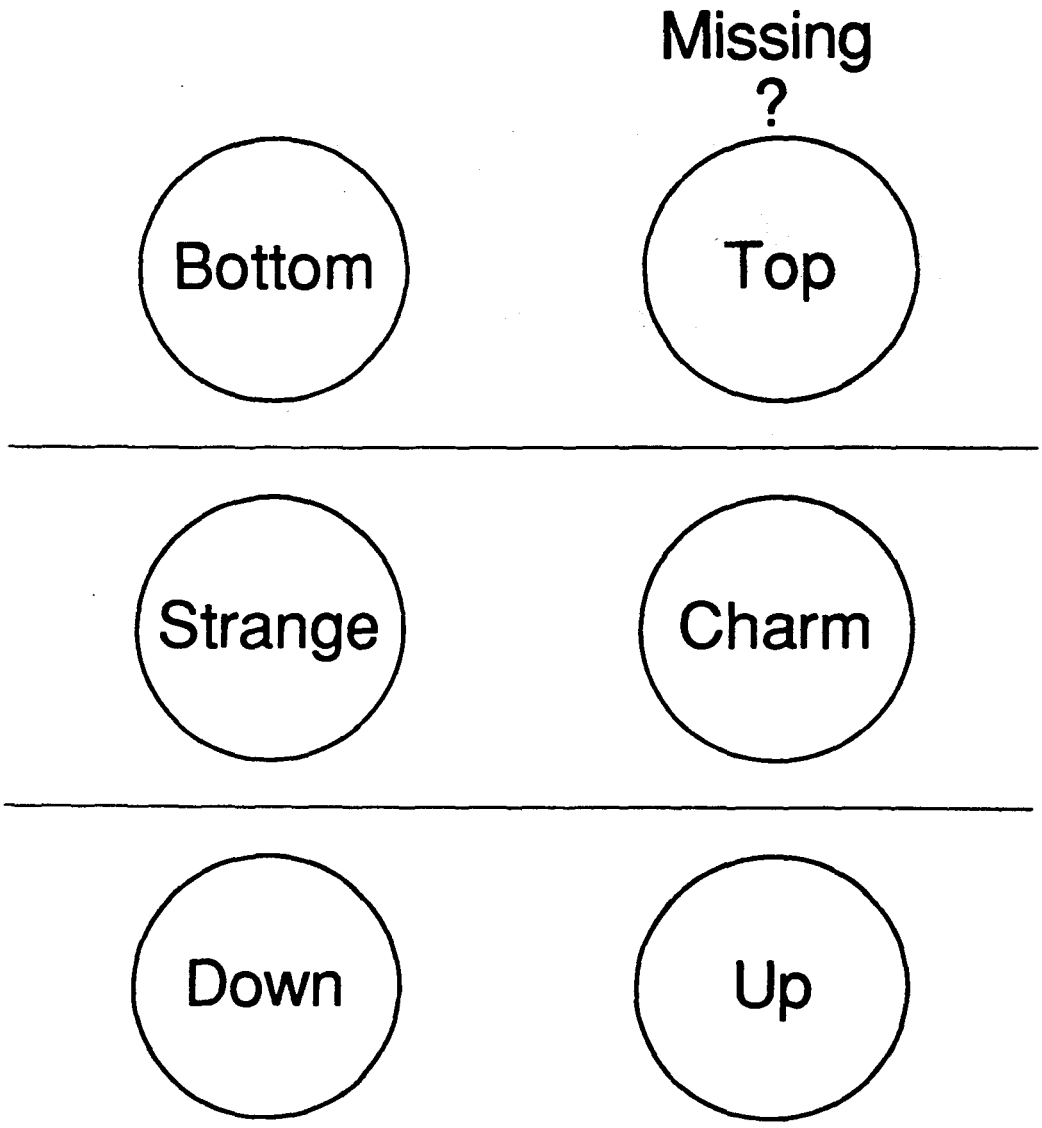
ABC Jump Rope Jingle



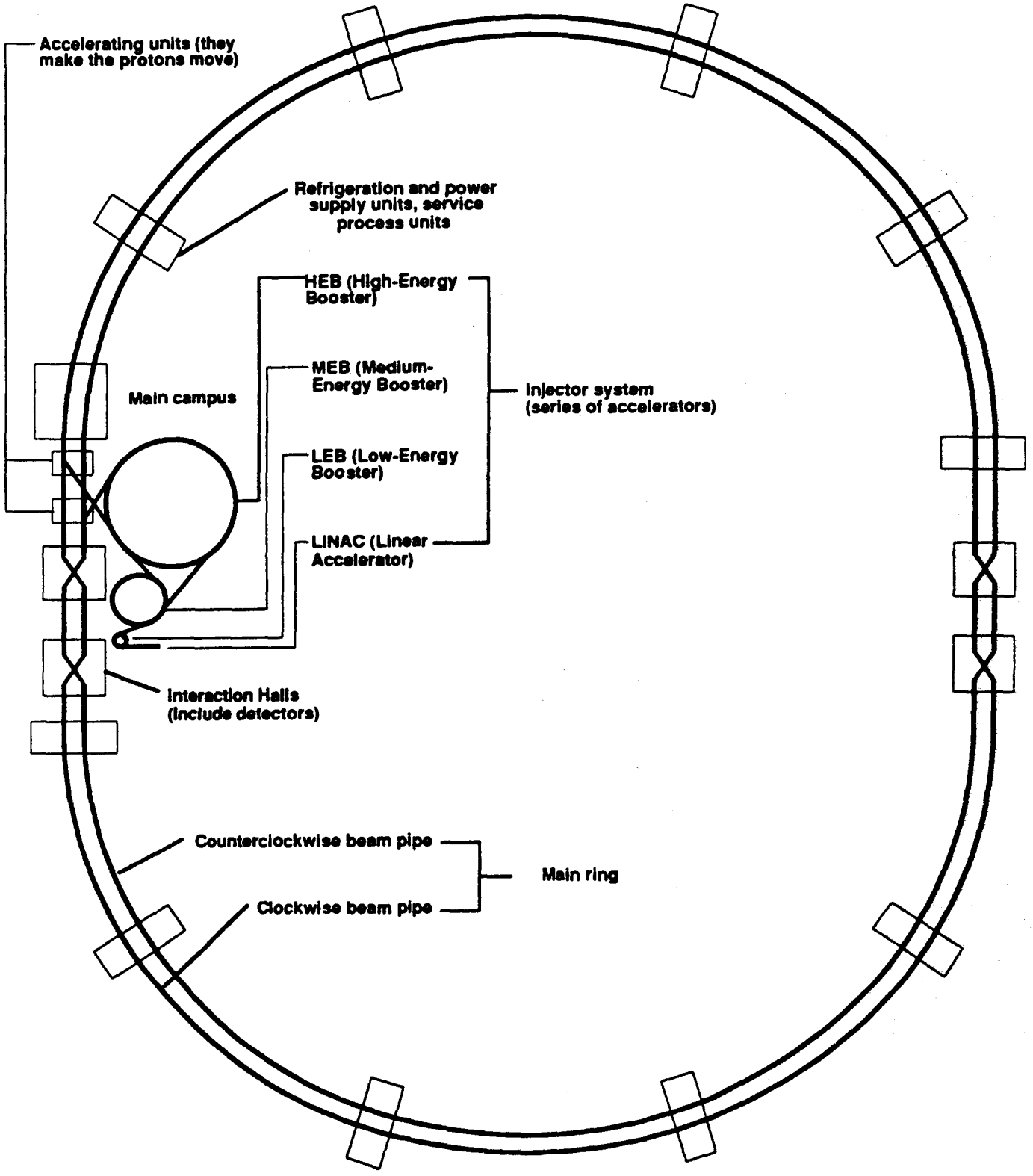
Atoms, Atoms,
Everything's made of Atoms.....

A.....Apples are made of atoms.
B.....Boxes are made of atoms.
C.....Candles are made of atoms.
D.....Dishes are made of atoms.


electron
proton
neutron
quark

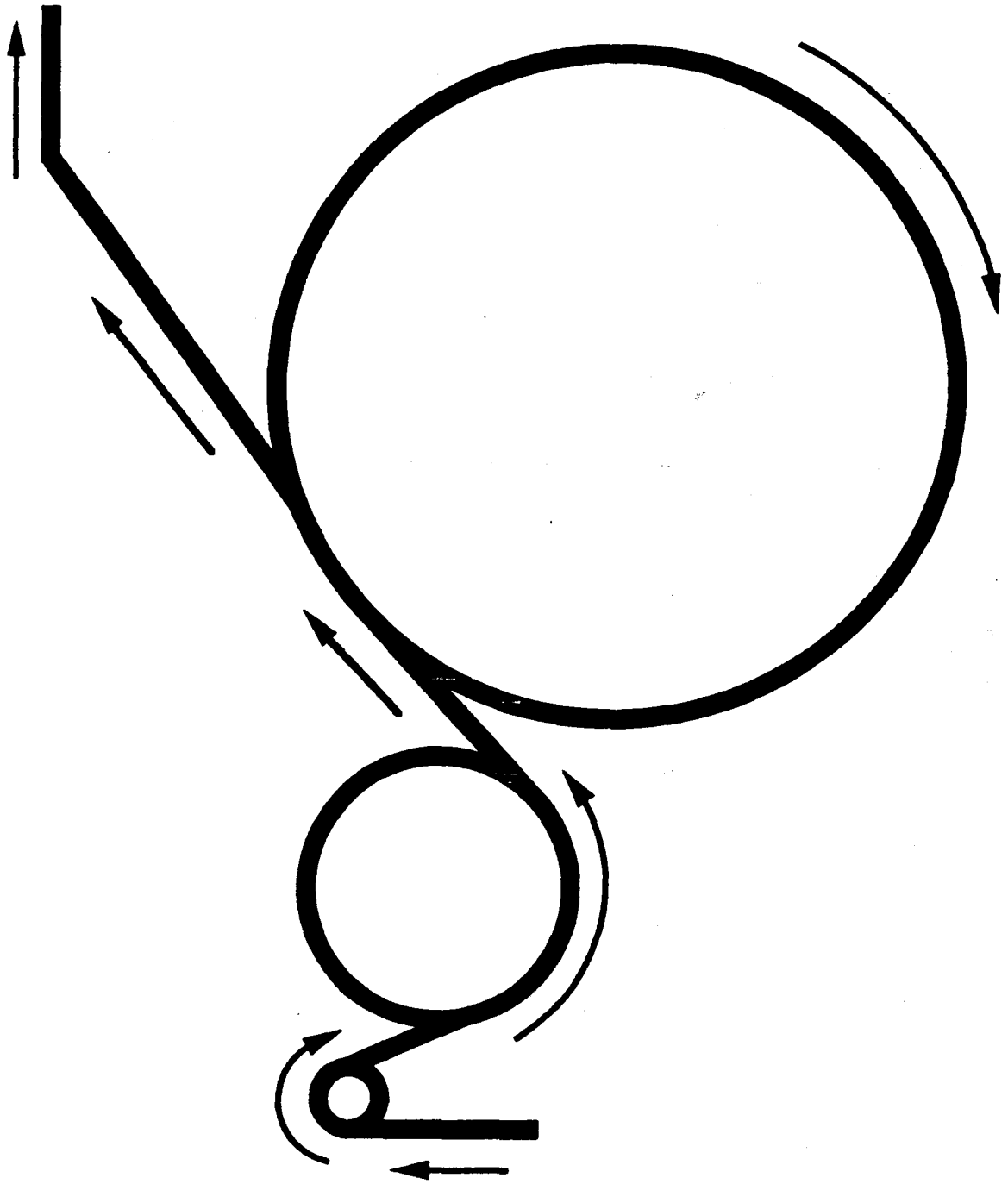

Missing
?
Bottom
Top
Strange
Charm
Down
Up

Flannel Board of simplified SSC layout

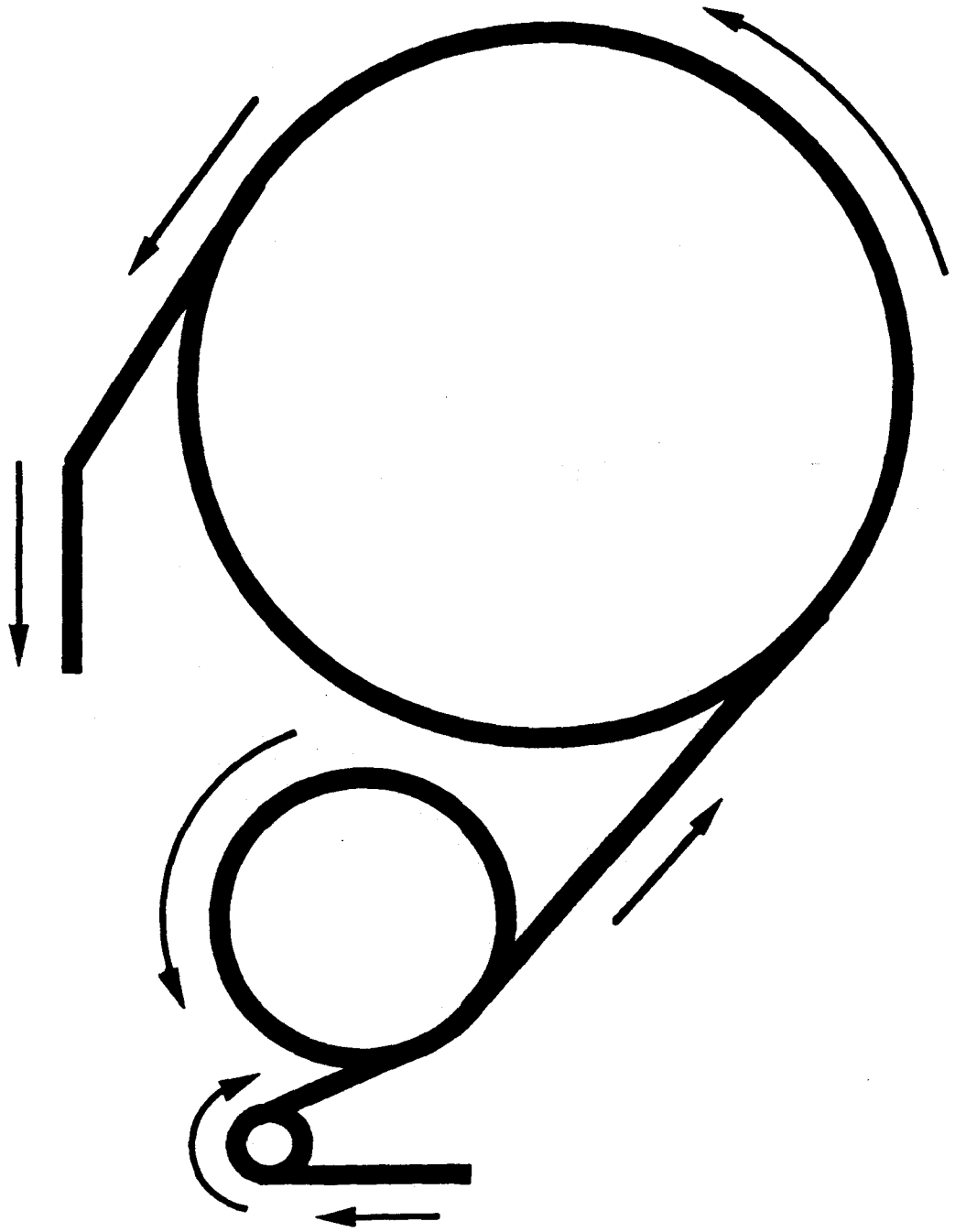


Field Test Copy B

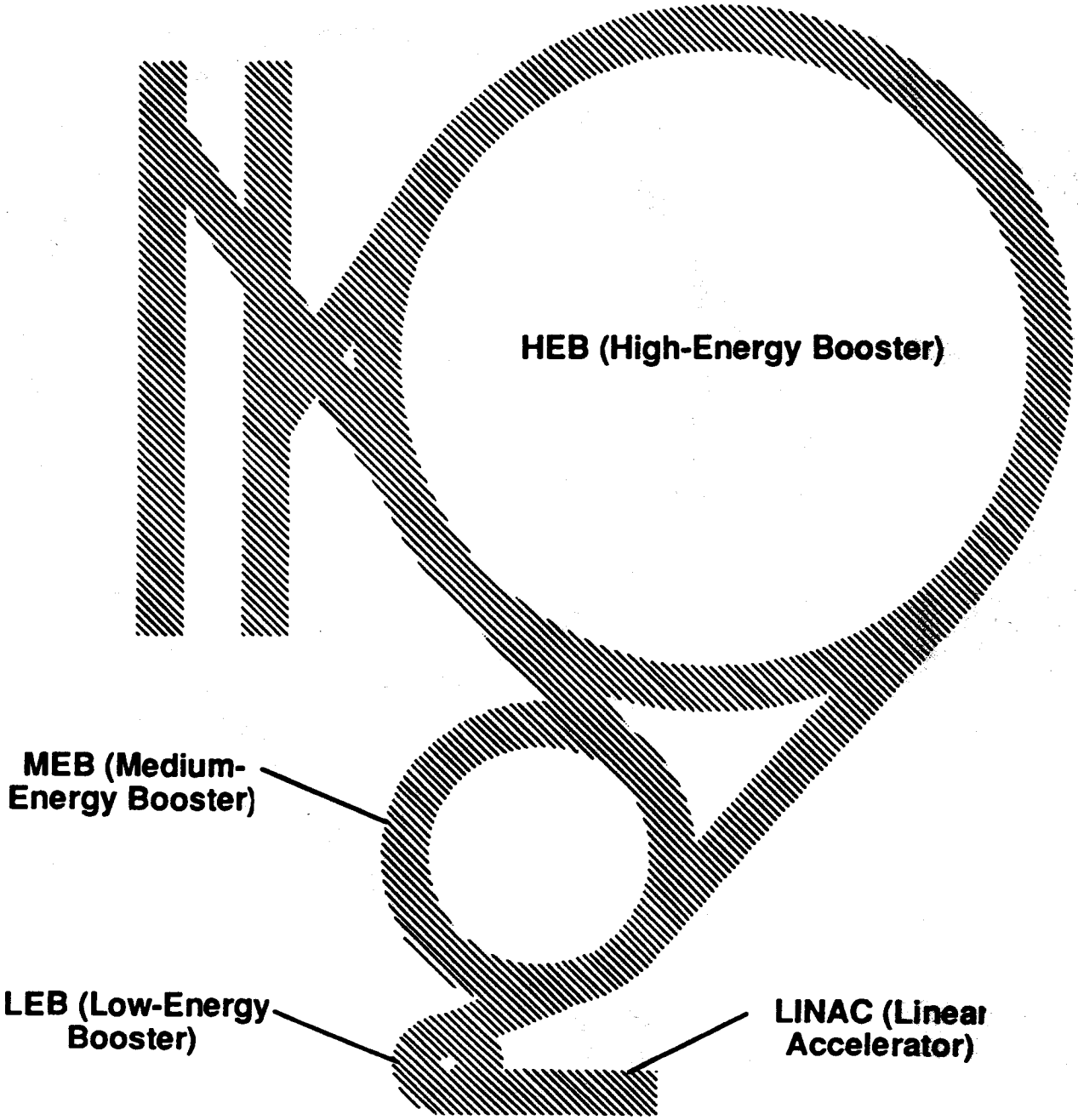
Injector Overlay - Loading Clockwise *2.9.2*



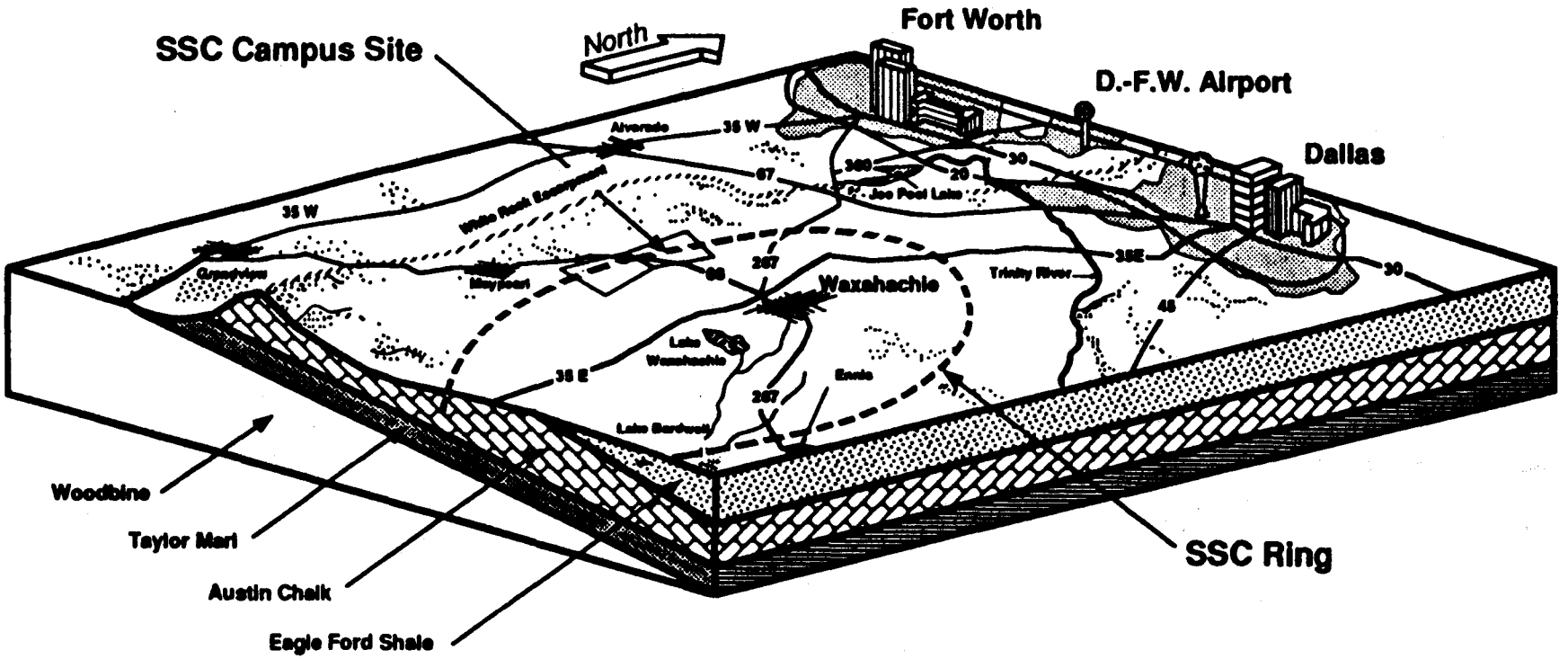
Injector Overlay - Loading Counter Clockwise 2.9.3

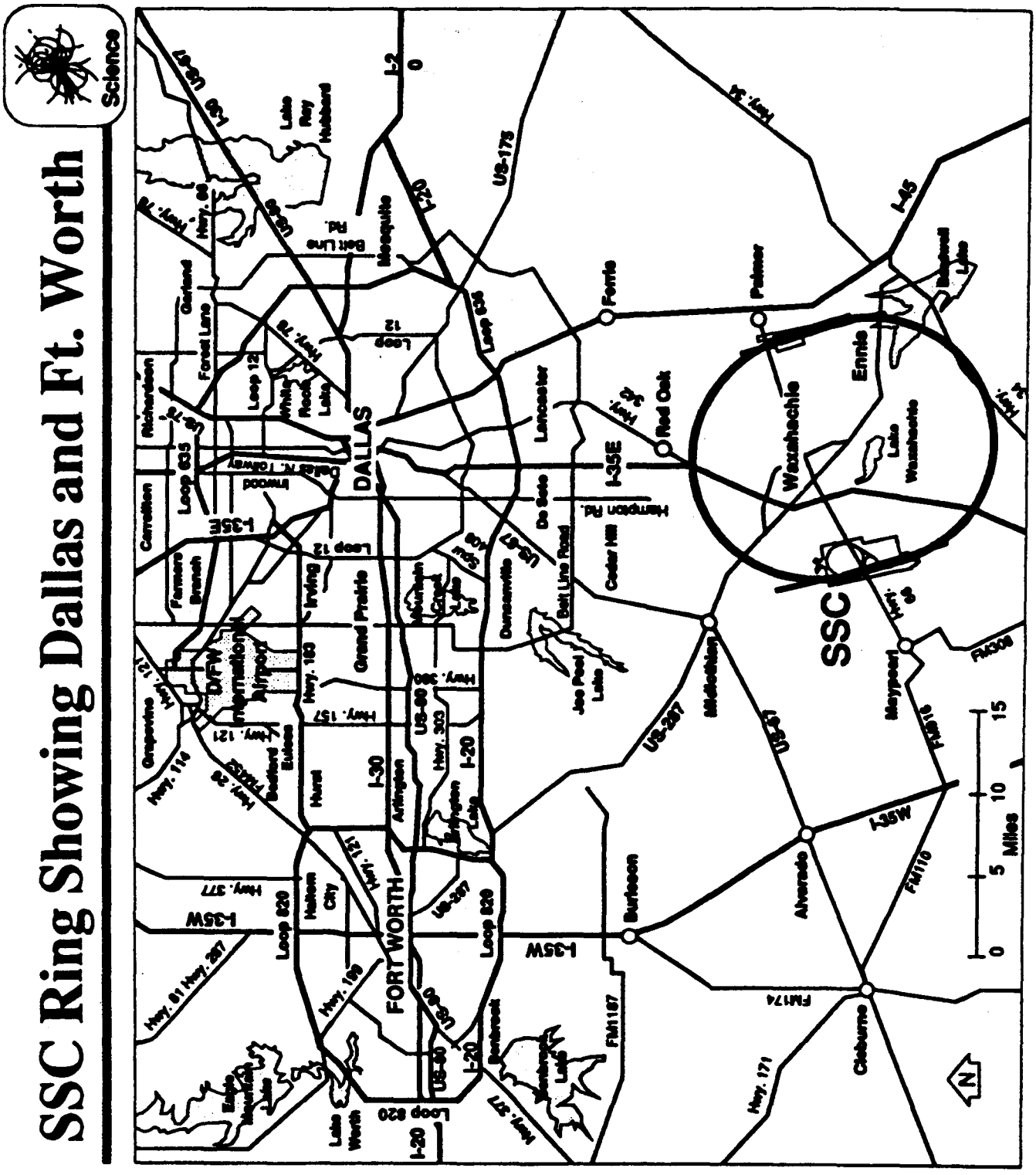


Injector Transparency A

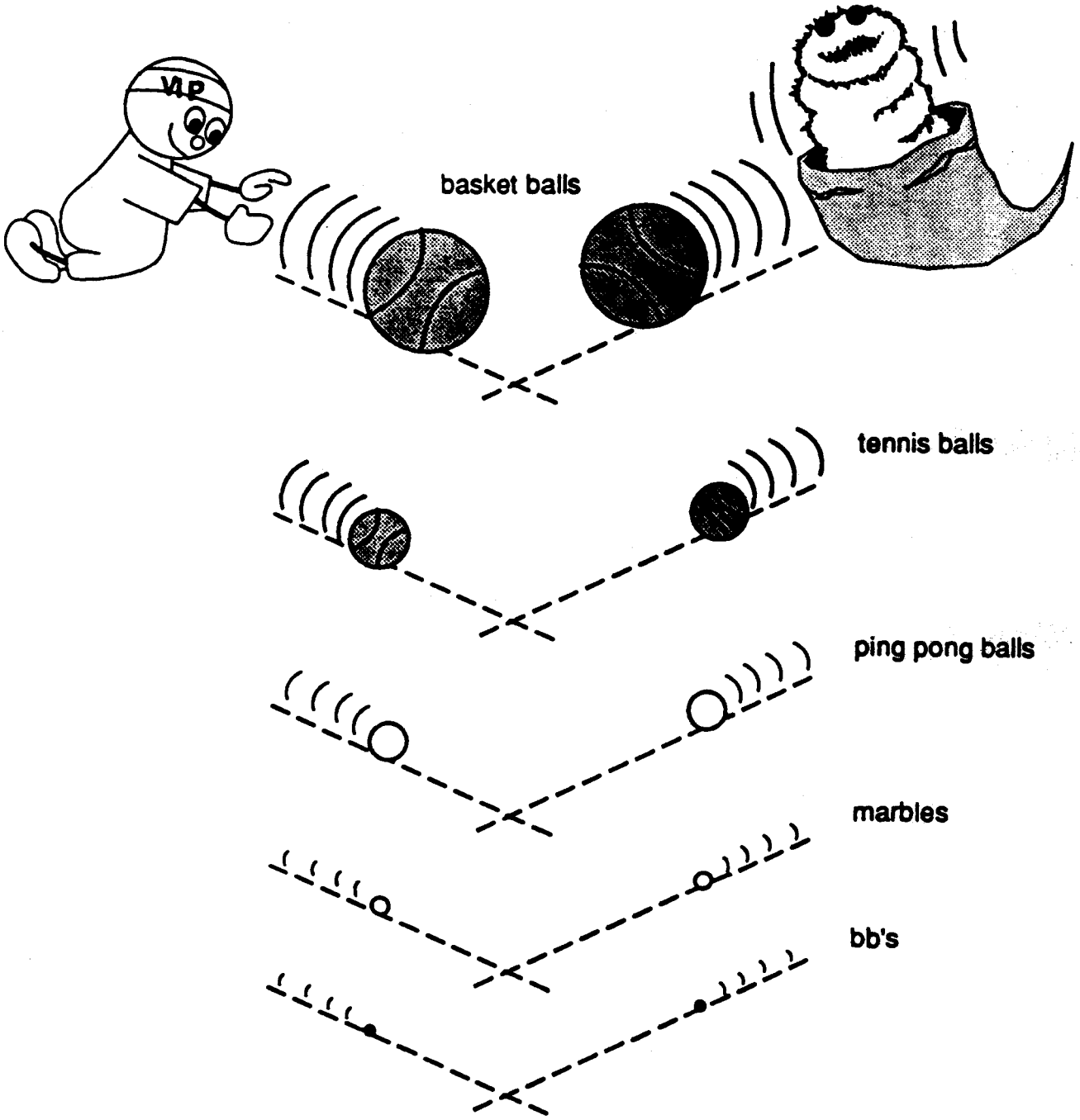


Schematic Location of SSC Facilities




SSC Ring Showing Dallas and Ft. Worth
Science
DALLAS
FORT WORTH
SSC
Waxahachie
Ennis
Lancaster
Ferris
Palmer
Red Oak
Cedar Hill
Midlothian
Mansfield
Burleson
Alvarado
Cleburne
DFW International Airport
Grand Prairie
Irving
Arlington
Hurst
Euless
Grapevine
Carrollton
Richardson
Garland
Mesquite
Balch Springs
Duncanville
De Soto
Joe Pool Lake
Lake Ray Hubbard
Lake Waxahachie
Lake Worth
Eagle Mountain Lake
Benbrook Lake
Meyperan
I-35E
I-35W
I-30
I-20
I-45
US-67
US-287
US-80
US-175
Loop 820
Loop 12
Loop 635
FM1187
FM1774
FM1710
Hwy. 171
Hwy. 157
Hwy. 360
Hwy. 303
Hwy. 377
Hwy. 81 Hwy. 287
0 5 10 15 Miles
N

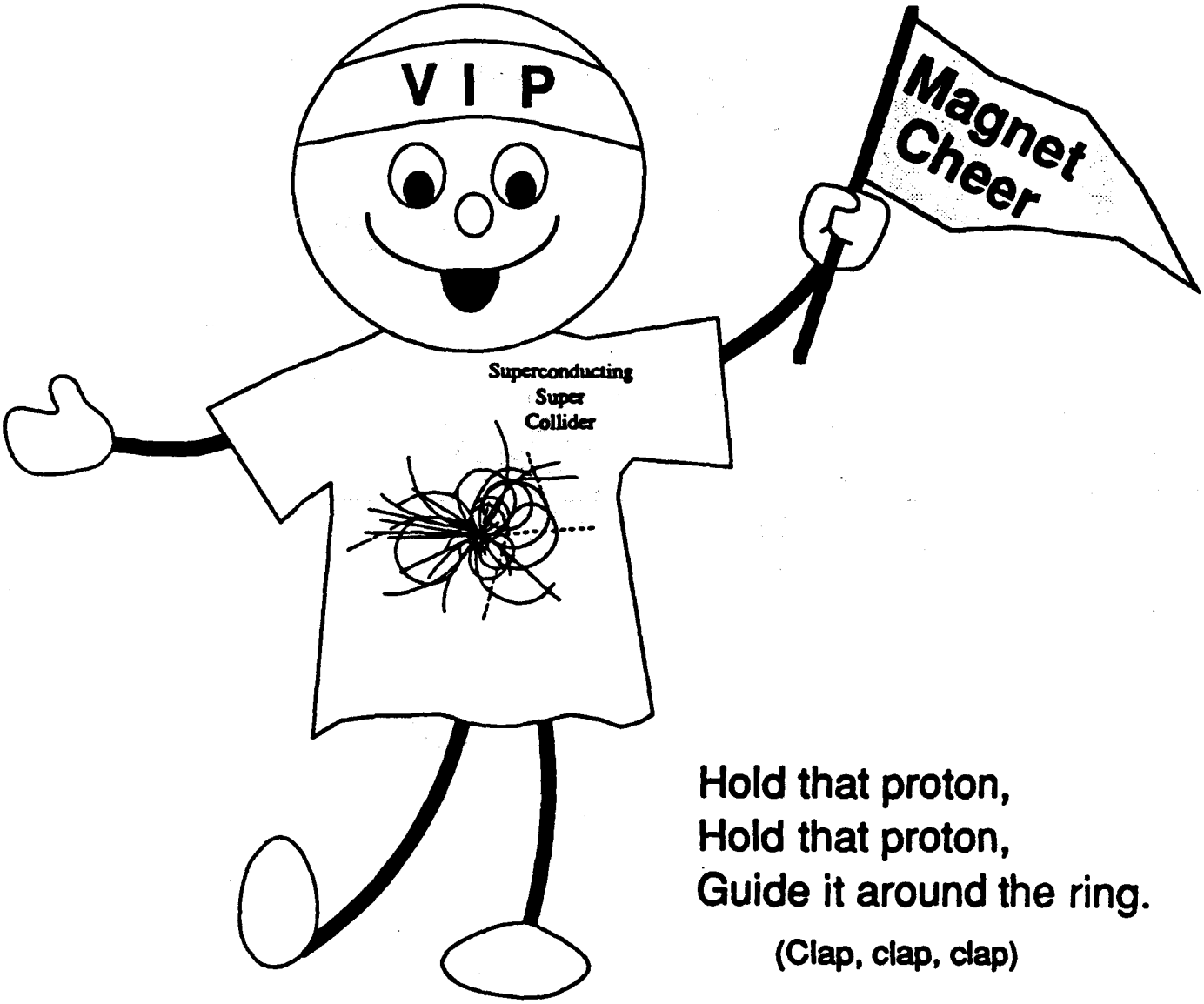
Roll balls to collide like the protons will in the Superconducting Super Collider!



Magnet Cheer

Lesson 1.7.5

Science



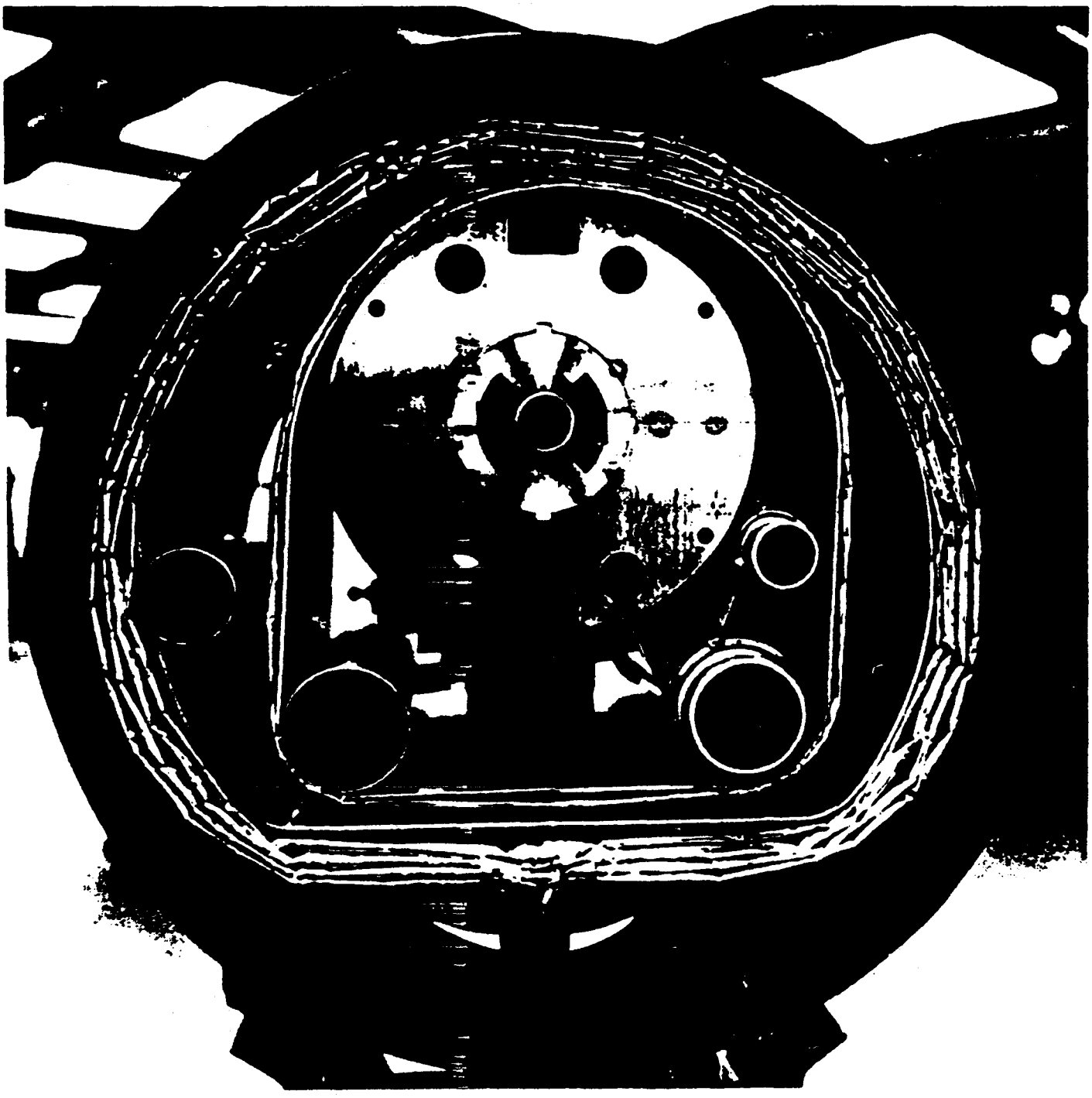
Hold that proton,
Hold that proton,
Guide it around the ring.

(Clap, clap, clap)

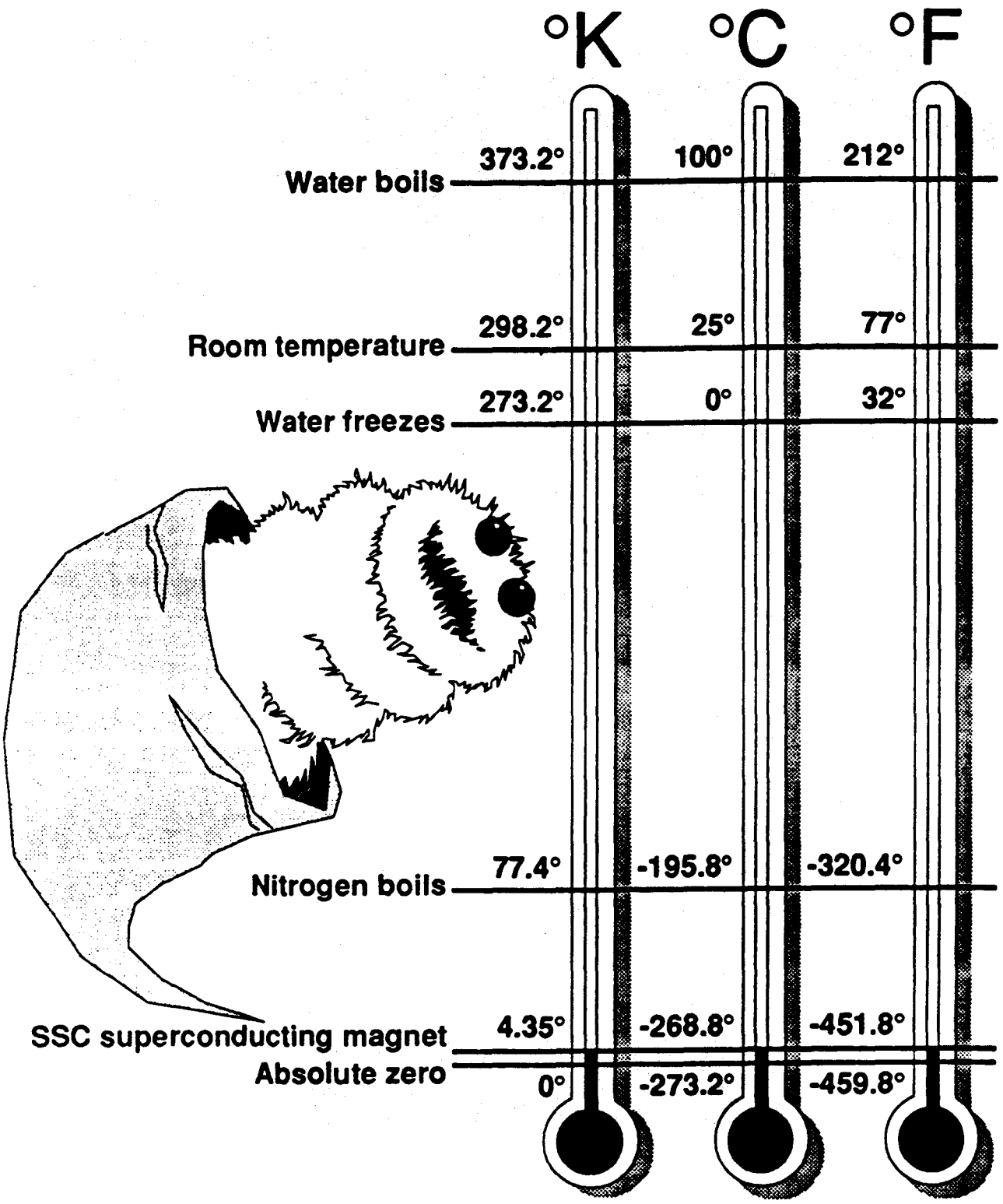
Guide that proton,
Guide that proton,
Magnets – (pause) – a
most important thing.

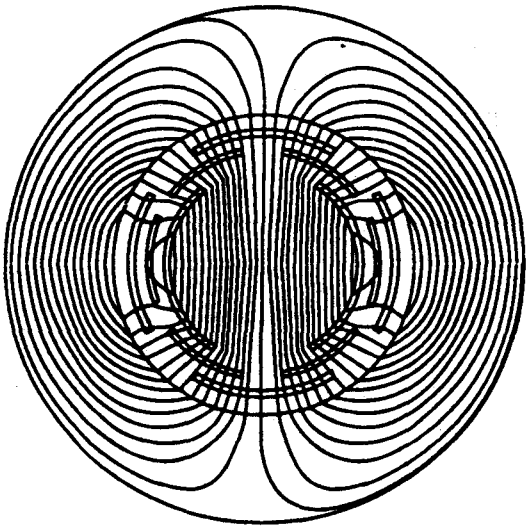
(Clap, clap, put hand
in air and say "yea!")

Cross Section of Complete Magnet Cryostat 5.7.1

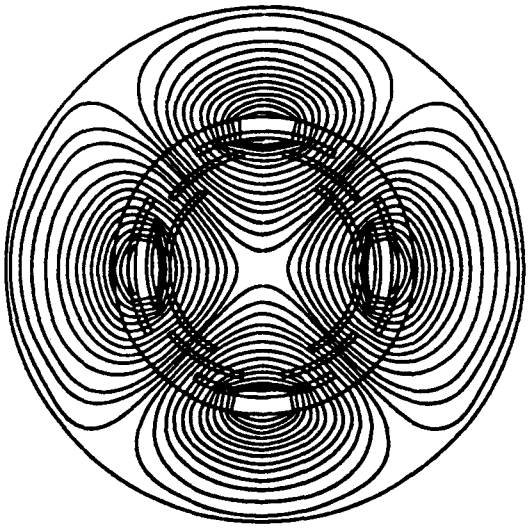


Shivers Scale

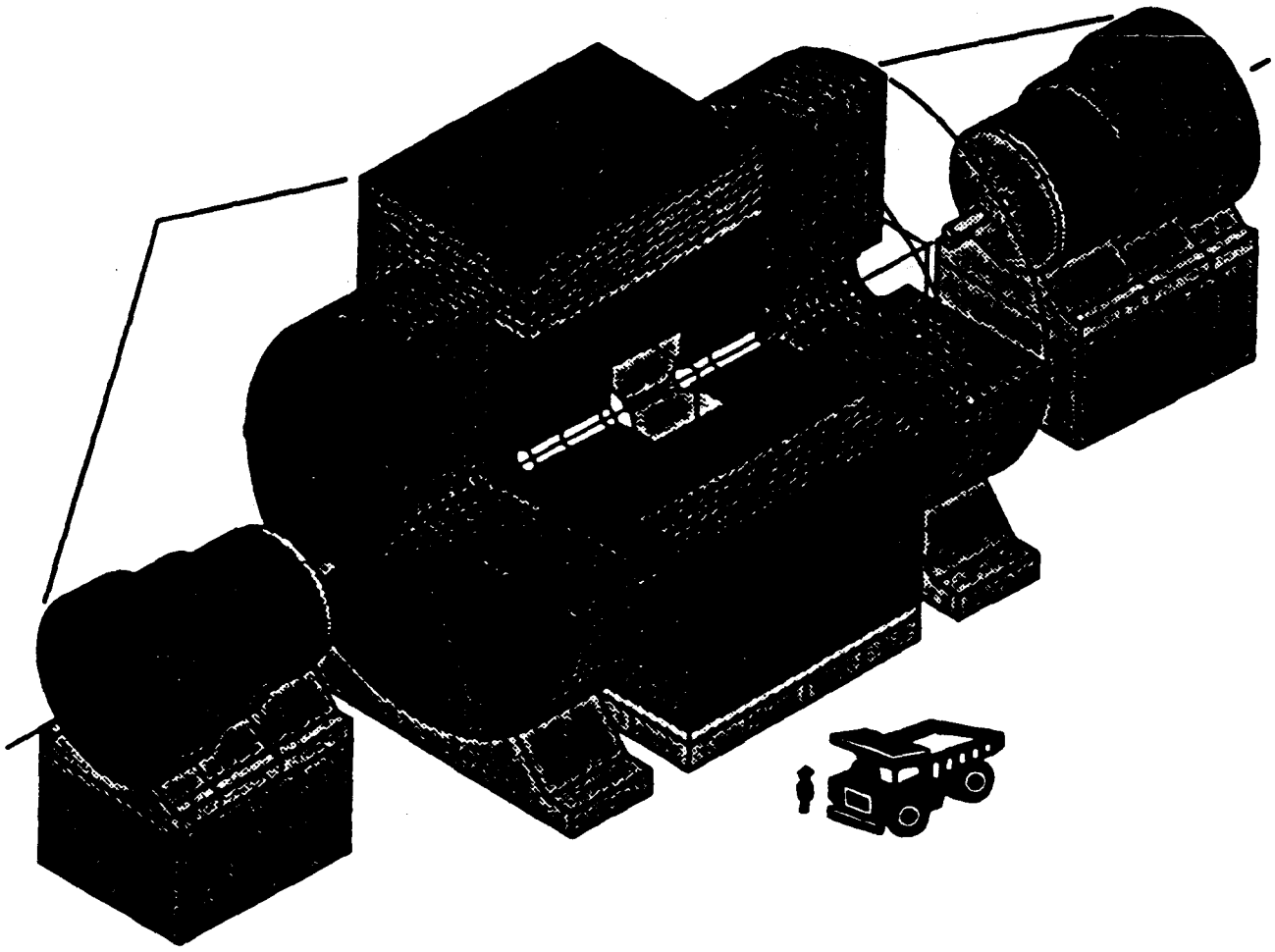


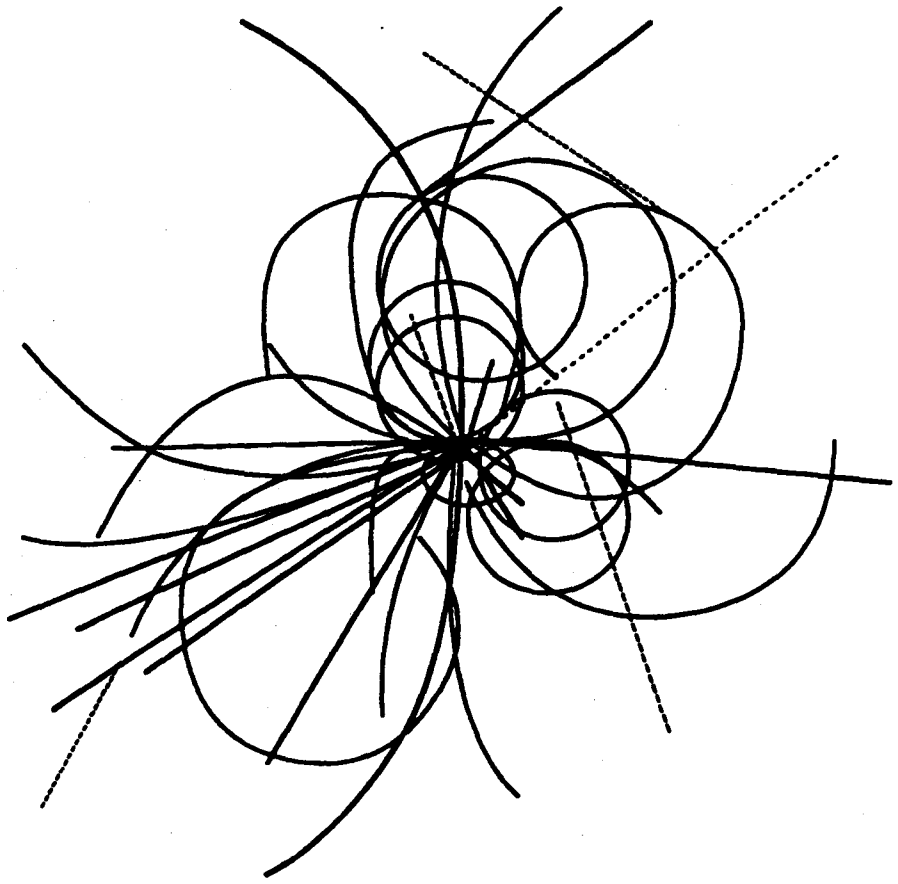


Dipole Magnetic Field

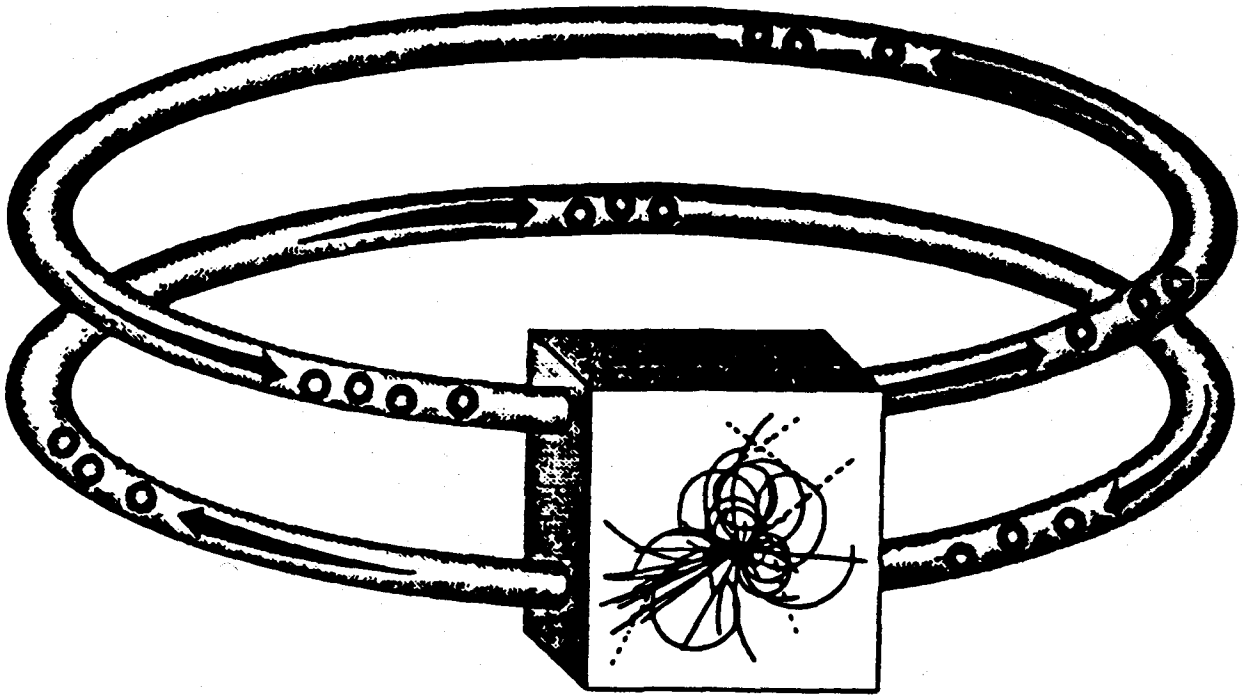


Quadrupole Magnetic Field





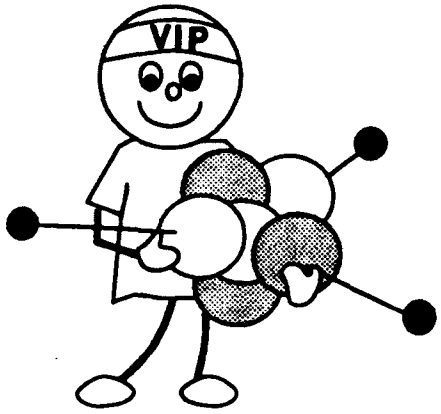
Protons Whirling *1.9.4*



Protons, protons, whirling 'round the ring;
Faster, faster, ZING! ZING! ZING!
Some from the left side,
Some from the right,
Smashing together
With all their might!
Protons, protons, soon we'll know
All that's inside that makes them go!

(to the tune of "Bah, Bah, Black Sheep")

I Want to be a Scientist



I want to be a scientist
When I'm grown,
Searching for answers
To things unknown.

I will dream of ideas
That are not in sight;
Then do experiments
To see if I'm right.

(To the tune of "I'm a Little Teapot")

Hybrid Subsystem Progress Report for FY1991

Results of a Low Dose Rate Irradiation of Selected Plastic Scintillating Fibers

CEBAF, Physics Division
12,000 Jefferson Avenue
Newport News, VA 23606

Brian Kross, Stan Majewski, Randy Wojcik, and Carl Zorn†

† contact person

ABSTRACT

We report on the initial results from the analysis of data from a low dose rate (< 10 Gy/hr) irradiation of a wide variety of plastic scintillating fiber formulations. The results are striking and seem to be the following: (1) those fibers irradiated slowly in air (i.e., oxygenated) suffer the greatest amount of damage, (2) fibers irradiated rapidly in air and then allowed to recover in air, suffer the least amount of damage, and (3) those fibers irradiated slowly in argon (an oxygen-free atmosphere) suffer an intermediate level of damage somewhere between the levels seen in (1) and (2). We note a particular exception: a green-emitting fiber known as SCSF-Y8 which does not display any differences in damages levels. The data analysis continues on such matters as loss in intrinsic light output (as compared to transmission losses), and quantifying the overall losses among the fibers.

Introduction

To our knowledge, this is the first report of a systematic investigation of possible low dose rate effects in plastic scintillating fiber. Current and past investigations of radiation damage effects have used relatively high rates (100 to 10,000 Gy/hr where 1 Gy (Grey) = 100 rad) to achieve the target doses (1 kGy to > 100 kGy) within a realistic time frame. We will briefly summarize the chief characteristic results of such an irradiation [1].

Under high rate conditions, color centers are formed which absorb heavily in the UV and blue, but also in the green and red to some some extent. The concentration of these color centers is proportional to the dose and may saturate at extremely high doses. After completion of the irradiation, an annealing phenomenon is observed. That is, the concentration of color centers decreases with passage of time. This annealing takes place most rapidly in the presence of oxygen which bleaches the scintillator as it diffuses into the plastic (see figure 1). The rate of annealing is consistent with the rate of diffusion of oxygen into the material, and this rate will decrease somwhat with increasing accumulated dose. Annealing can also take place in the absence of oxygen, but at a much smaller rate. An increase of the ambient temperature can increase the rate significantly. After annealing is completed, there is a residual level of damage remaining which is proportional to the accumulated dose. To appreciate the effect of these color centers upon the performance of the scintillator, we proceed to briefly describe the energy transfer mechanisms within the scintillator.

The most popular scintillators consist of a weakly fluorescent plastic solvent (polystyrene) doped with a high concentration of a primary fluor plus a much lower

concentration of secondary fluor. Excited states in the solvent primarily transfer their energy to the primary via a non-radiative dipole-dipole interaction. Subsequently, the fluorescent emission of the primary is absorbed and re-emitted by the secondary at a suitably longer wavelength (> 400 nm).

The residual color centers absorb most strongly in the UV where the primary radiatively transfers energy to the secondary. Hence these color centers compete with the secondary with a resulting decrease in light output being observed. There is also some level of increased absorption at longer wavelengths so that attenuation of the secondary emission also increases. Figure 2 displays the effect of decreased light output and transmission upon a scintillating fiber.

A key concern that has arisen is whether the residual level of damage observed after a high rate irradiation will be the same if the irradiation is performed at a more realistic rate. There is plenty of evidence from studies of *mechanical* damage to polymers that indicates that oxygen diffusion **during** the irradiation can lead to increased levels of residual damage. At high rates, the oxygen does not have time to diffuse into the plastic and participate in deleterious reactions. In fact, extraneous *optical* damage has recently been observed in undoped polystyrene samples [2] in a high rate Co-60 gamma irradiation (0.5 kGy/hr). By using large samples (1 in^3) and a high dose (160 kGy), the researchers were able to observe a thin layer (about 2 mm in thickness) after annealing that had increased color absorption. The thickness of this layer is consistent with the extent to which oxygen would diffuse into the sample during the irradiation.

The Experimental Procedure

In our experiment, we have selected a wide variety of blue and green-emitting fibers (listed in figures 8(a) through 8(t)). The fibers labelled as SCSF-38C, -81C, and -Y8C are special formulations of the fibers SCSF-38, -81, and -Y8 that use a new low refractive index cladding resulting in higher light collection efficiency. There were a total of ten fiber types with 12 samples of each fiber. All fibers were 150 cm long and 1 mm in diameter. The latter is typical for fibers and the length was sufficient for measuring attenuation changes. All fibers were shipped in straight lengths as curled samples would produce a wider variation in attenuation behavior. One end of each fiber was hand-polished and a 3 cm long strip of flat-black paint applied to that end to eliminate any contributions from light

propagating in the cladding (as this light is a known source of noise). The other end was blackened to eliminate reflections.

The attenuation characteristics (and relative brightness) of the fibers were measured on a scanning device shown in figure 3. A continuous x-ray source from X-Tech was used as the excitation source. This device generated 8 keV x-rays which could penetrate the 1 mm diameter fiber. The generated light was detected by a bialkali phototube set in DC mode, and the current measured with a Keithley picoammeter. The scan is controlled via a personal computer. By using the DC mode, the many necessary measurements could be made fairly quickly. A bialkali tube was used for several reasons: (1) it was readily available, (2) although the goal is to use highly efficient green and red-sensitive photodetectors, they are still a research curiosity at present, (3) most of the fibers are blue-emitting in any case, (4) bialkali tubes may still be used in calorimeter applications, and (5) the use of optical filters can qualitatively simulate the effect of green-sensitive photodetectors, and most importantly (6) any low dose rate effects will not qualitatively change by use of an improved photodetector.

In terms of what dose and dose rate one should use, one can use the recent study by Groom for guidance [3]. The central tracking chamber is envisioned to cover the radial region from about 0.6 to 1.6 meters. At the design luminosity of 10^{33} $cm^{-2}s^{-1}$, one can estimate doses of 15 (outer radius) to 110 Gy (inner radius) per year. At the high luminosity option of 10^{34} $cm^{-2}s^{-1}$ for ten years, this becomes 1.5 to 11 kGy which is not a negligible dose. Since it seems likely that a fairly appreciable dose is required to create significant changes in attenuation, it was decided to choose somewhat extreme doses so as to clearly see a low dose rate effect, namely 5 and 20 kGy. With such doses, the information obtained could also be useful to calorimeter researchers who will be dealing with such doses (and worse) in the forward region. In choosing a dose rate, we wanted something low enough that oxygen would have time to permeate the fibers during the irradiations. Other researchers [4] found that for dose rates below 45 Gy/hr, oxygen would permeate their 2.6 mm thick sheets of polystyrene-based scintillator (SCSN-38). Hence we aimed for a dose rate below 10 Gy/hr.

Figure 4 is a schematic of the irradiation setup at the Nuclear Reactor Facility of the University of Virginia. A set of depleted Co-60 line sources was used to create the low rate radiation field. The fiber sets were divided into 4 subsets (3 fibers of each type per subset for statistics), and placed in four stainless steel tubes sealed with gas-tight enclosures. Besides splitting them into the two dose subsets, one tube from each dose subset was tied

into the same gas circulation system: two with dry argon gas, and two with dry air. The two subsets closest to the line source experienced a dose rate of 6.7 Gy/hr. These were taken to 20 kGy. The outer ones were irradiated to 5 kGy at a rate of 5.5 Gy/hr. Note that the first 30 cm of the fiber samples were shielded with a lead annulus with sufficient thickness to give a factor of 200 less in accumulated dose. This was done so that one can obtain a measure of intrinsic light output loss by looking for a "step" beyond 30 cm in the attenuation curve after the irradiations.

In addition to the low dose rate irradiations, another two subsets of fibers were irradiated at a typical high rate at the 3 MeV electron beam facility of Florida State University. One subset was irradiated to 5 kGy and the other to 20 kGy. From past experience with irradiating such fibers at a high rate, one week of recovery in air was allowed before measurements were made. (For the low rate data, the fibers were also re-measured 2-3 weeks later to see if any recovery effects were present. None were found.)

Finally, some measurements (for the 5 kGy low rate) were made with a set of optical filters. These filters had several purposes: (1) for green-emitting fibers, an appropriate filter can qualitatively simulate the use of a green-sensitive photodetector (this was verified by using a multialkali green and red-sensitive phototube), (2) the extent of damage as a function of wavelength can be ascertained, and (3) the use of an optical filter can qualitatively simulate the effect of natural optical filtration by long lengths of undoped readout fiber. Figure 5 displays the transmission characteristics of the filters. As a point of reference, the blue fibers emit in the range of 400 to 440 nm. The green-emitting 3HF fiber emits at 530 nm and the SCSF-Y8 fiber emits at 500 nm.

The Preliminary Results

Figure 6 displays the relative light outputs of the fibers as measured with the bialkali phototube. BCF-10 was used as the reference. The second set of columns displays the light output after 1.5 meters of attenuation is allowed to take place. Again BCF-10 (at 1.5 meters) is used as the reference. Figure 7 displays typical attenuation data. Fits to the double exponential function $y = A_1 * \exp(-x/\lambda_1) + A_2 * \exp(-x/\lambda_2)$ were used to quantitatively describe the attenuation behavior.

Figures 8(a) through 8(t) display the results of the low and high rate irradiations. The upper graphs are the results for the 5 kGy irradiations and the lower for 20 kGy for

each fiber type. Only changes in attenuation are shown as changes in the intrinsic light output are currently under investigation. Finally, figure 9(a) through 9(o) display the effects of using an optical filter for the low rate 5 kGy data. (Note that all the light outputs in figures 8 and 9 were normalized to the same value at 0 cm (0.5) in order to best display the attenuation changes. Figure 6 is a guide to how the actual light output would change when using a bialkali phototube.)

We see two primary effects. For the low dose data, we see that in fact oxygen does introduce an increased level of damage. Furthermore, there seems to be an additional low dose rate effect independent of the presence of oxygen. The high rate data shows considerably less damage for many of the fibers than for those irradiated slowly in argon. The one exception is SCSF-Y8 and -Y8C which do not display this hierarchy. We are currently investigating the possibility of some systematic effect creating the difference between the fibers irradiated slowly in argon and those irradiated quickly. However, as of this point in time, we see no reason to disbelieve the results as shown.

Closing Remarks

The analysis of the data is continuing, particularly in the area of ascertaining any loss in intrinsic light output, and in quantifying the overal light output losses (transmission and intrinsic) over the length of the fiber. In particular, we wish to compare the performance of the PMMA-clad Kuraray fibers with the new versions clad in lower refractive index material.

As to the implication of the results as they stand at present, it seems clear that high dose rate experiments may seriously underestimate the levels of damage to be expected with scintillating fibers. It will be interesting to compare the results reported here for fibers with those of an ongoing experiment on low dose rate effects upon *plate* scintillator [5].

REFERENCES:

[1] For details (including a complete bibliography), the interested reader is referred to a new review *Fast Scintillators for High Radiation Areas* by Stan Majewski and Carl Zorn. It will be published as a chapter in an upcoming book *Instrumentation in High Energy Physics* edited by Fabio Sauli and will be published by World Scientific. Copies of the preprint version of the review may be obtained from either of the authors.

[2] J.S. Wallace, Sandia National Laboratories, private communication.

[3] D.E. Groom, "Ionizing Radiation Environment in SSC Detectors," *Proceedings of the Workshop on Radiation Hardness of Plastic Scintillator*, ed. K.F. Johnson (March 19-21, 1990, Tallahassee, Florida) pp. 69-75.

[4] B. Bicken et al., *IEEE Trans. Nucl. Sc.* **38** (1991) 188.

[5] N.D. Giokaris, Fermilab, private communication.

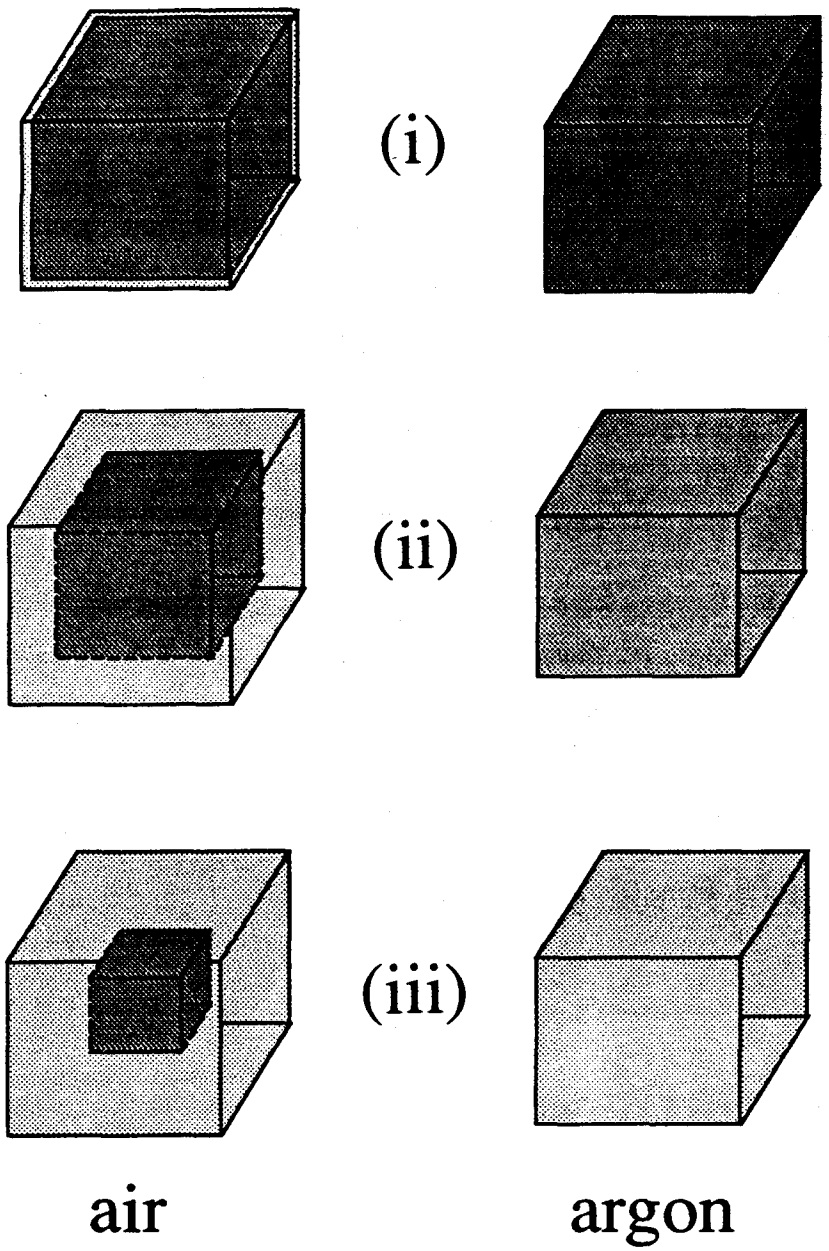
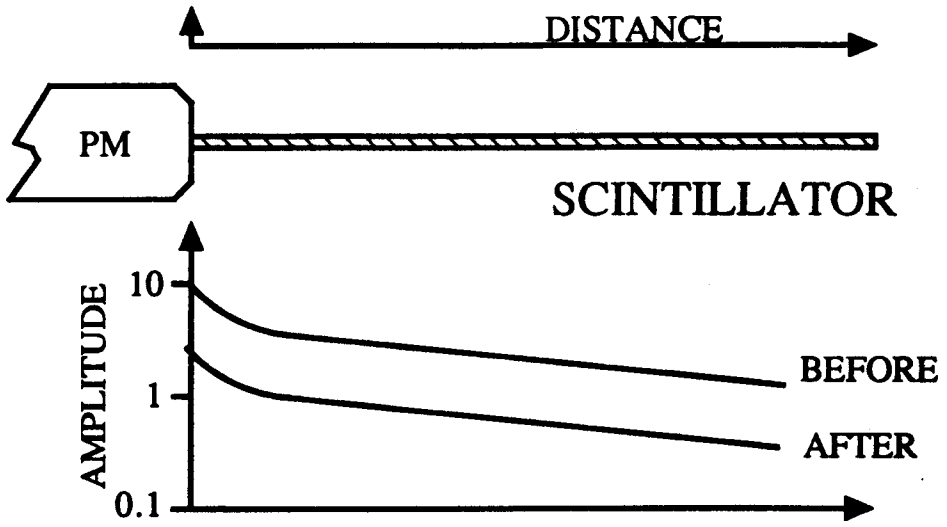
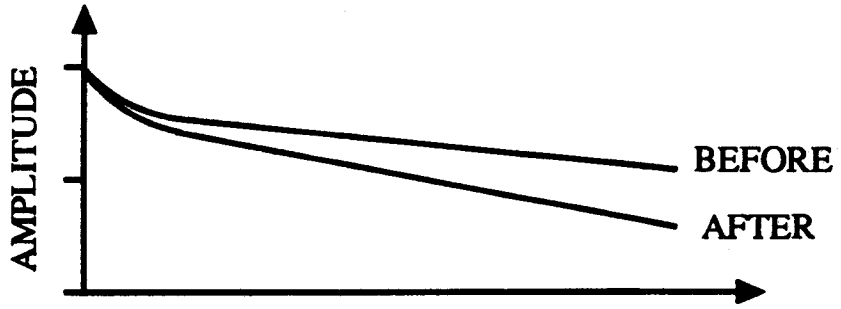


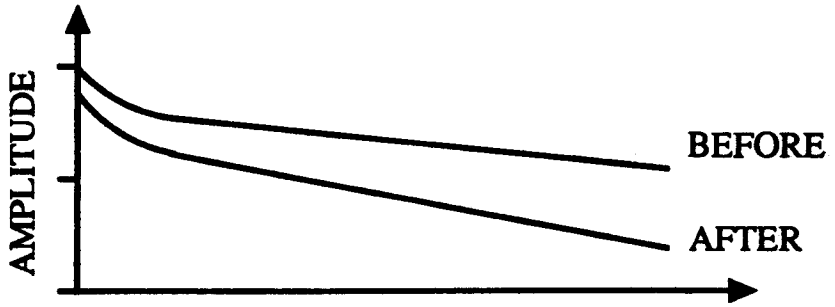
FIGURE 1: A pictorial representation of post-irradiation annealing in polystyrene cubes after a high dose rate irradiation. In air, oxygen diffusion drives the bleaching process at a rapid rate while in an oxygen-free atmosphere (e.g., argon), color center relaxation takes place slowly throughout the volume of the material. In air, the time scale from (i) to (iii) can be a matter of days while in argon the relevant time scale can be several months.



CASE 1: DAMAGE TO LOCAL SCINTILLATION YIELD ONLY



CASE 2: DAMAGE TO TRANSMISSION ONLY



CASE 3: TYPICAL DAMAGE OBSERVED IN EXPERIMENTAL CONDITIONS

FIGURE 2: Effect of radiation damage upon optical performance of scintillators.

SCINTILLATING FIBER SCANNER

(4 meter scan)

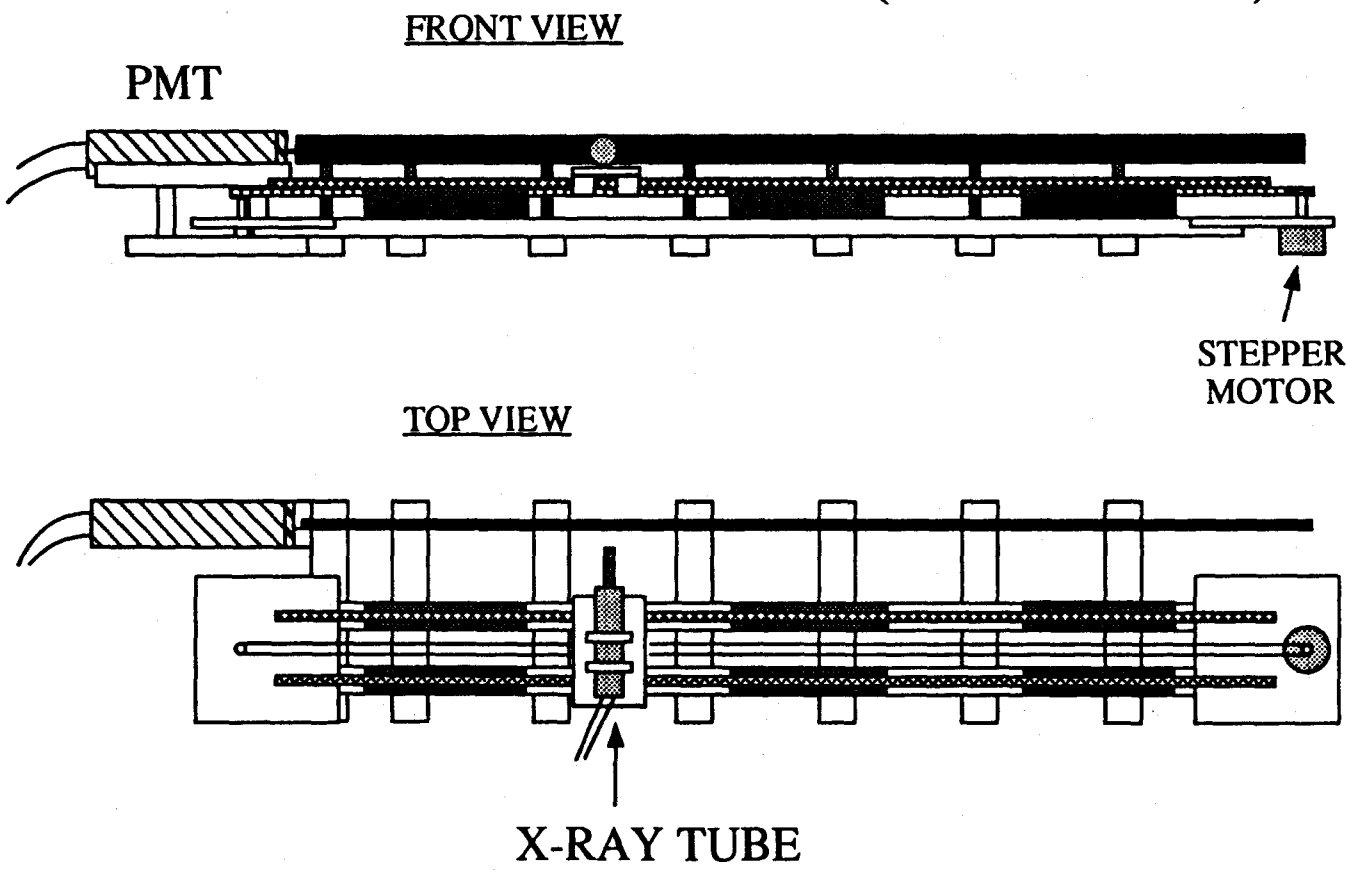


Figure 3: Schematic of the PC-controlled scanner used in measuring the attenuation curves for the fiber sample set.

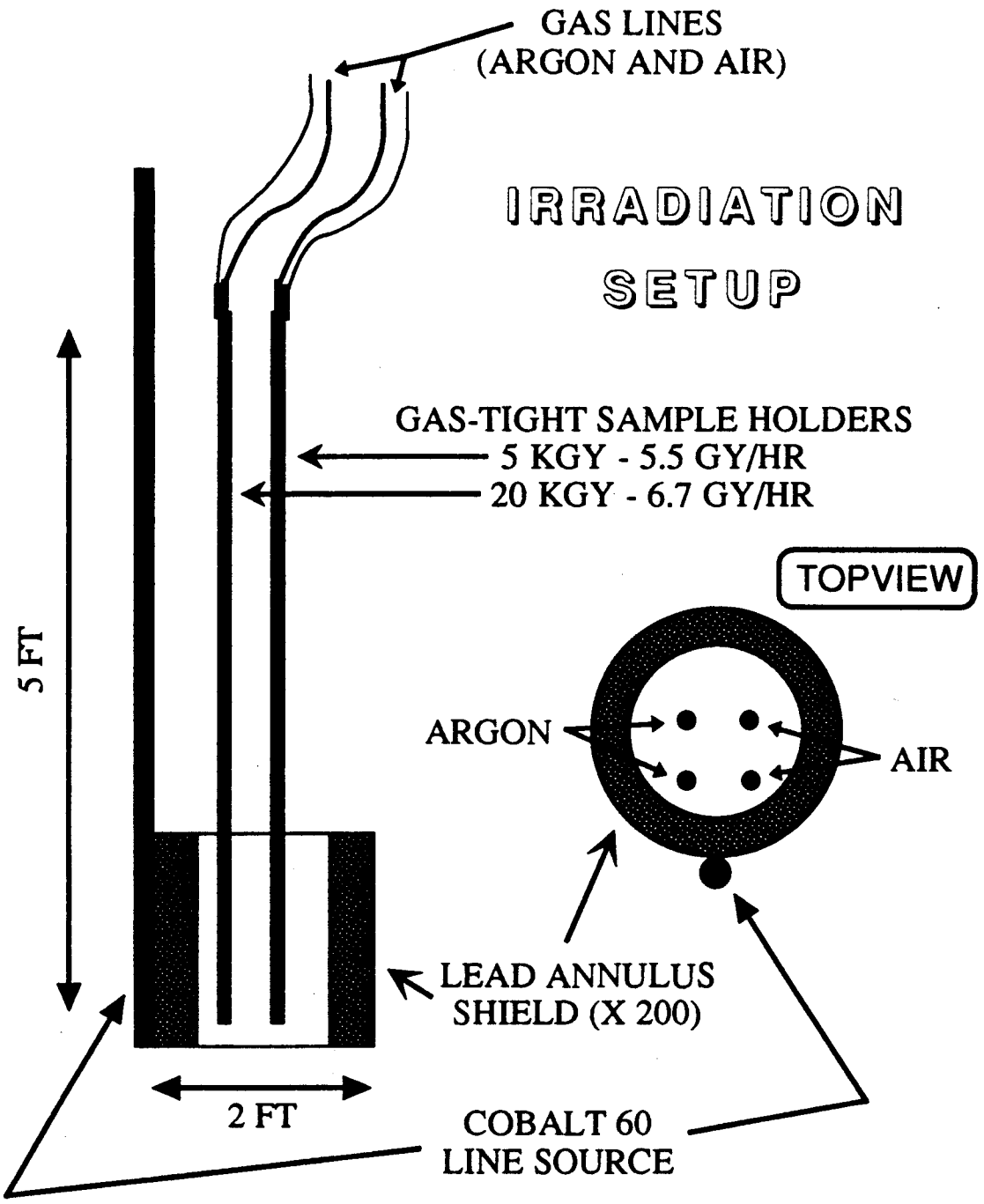


Figure 4: Schematic of the irradiation setup for the low dose rate irradiation.

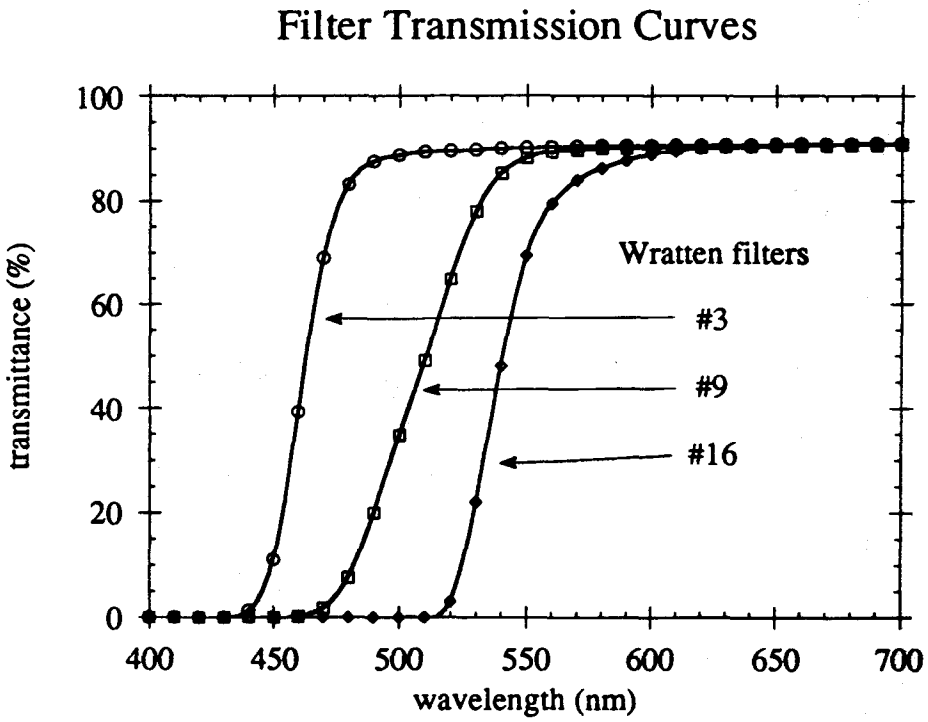


Figure 5: Transmission spectra for optical filters. Wratten #3 was used for the blue-emitting fibers while #9 and #16 were for the green-emitting fibers SCSF-Y8, -Y8C and 3HF.

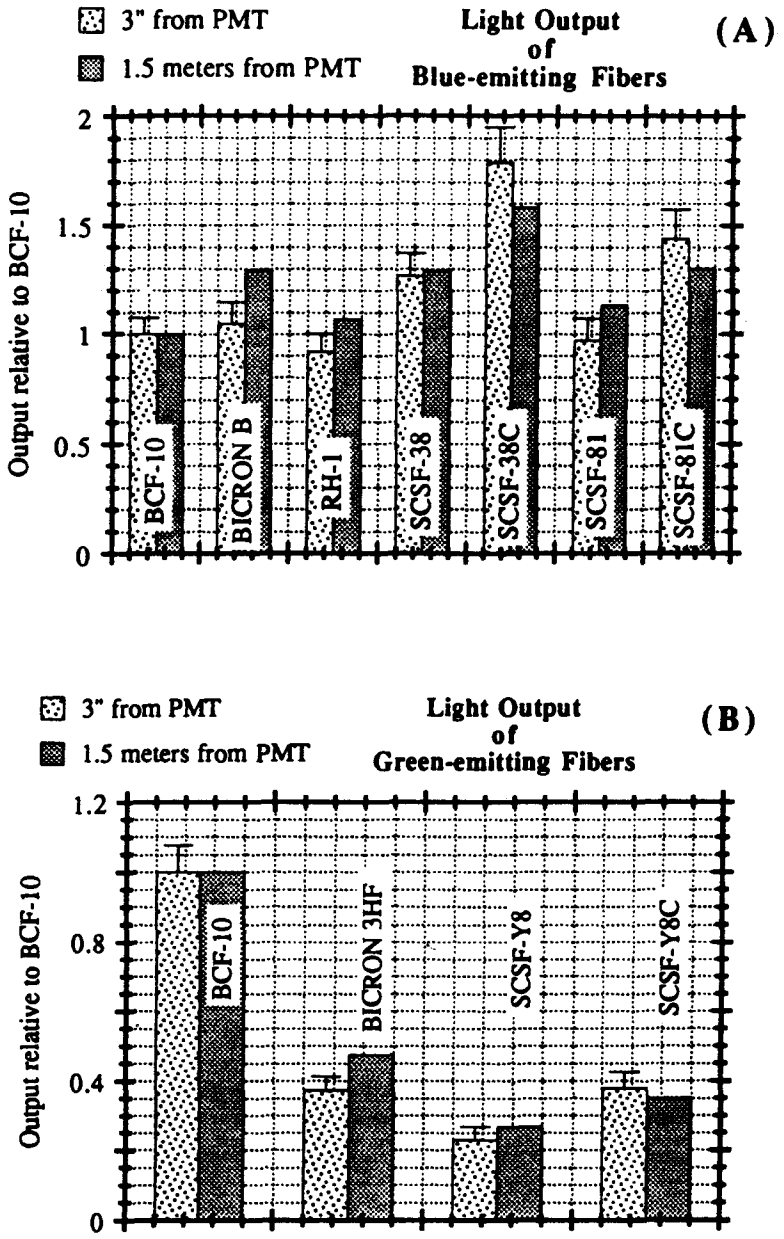


Figure 6: Relative light output of fibers as measured with a bialkali phototube. BCF-10 is used as the standard. The second set of columns show the light output after 1.5 m of attenuation with BCF-10 at 1.5 m used as the reference output.

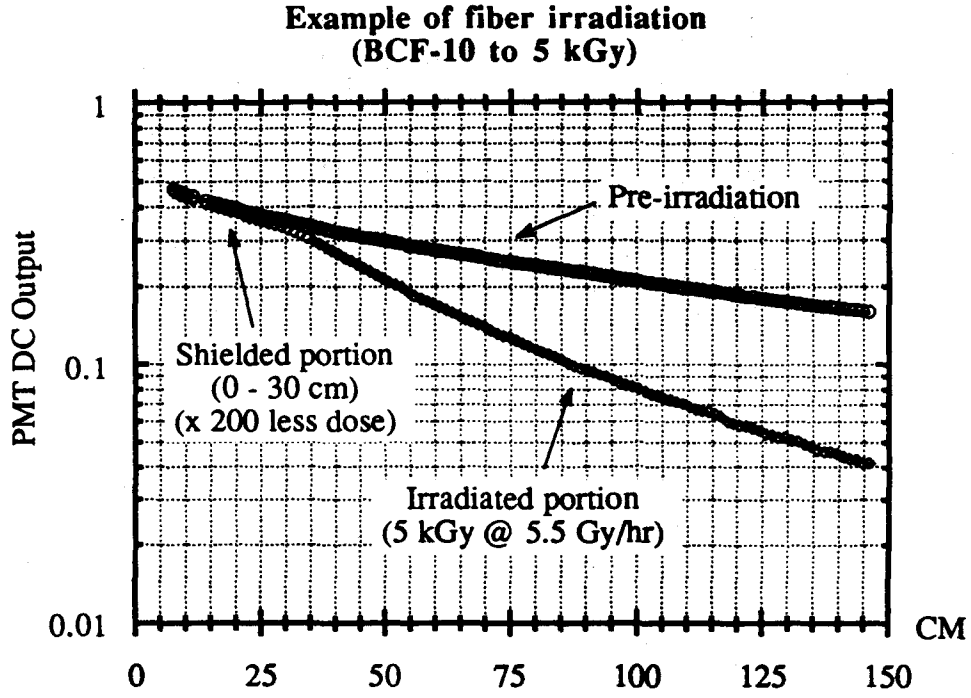


Figure 7: Example of typical data from the low dose rate irradiation experiment. Functional fits were made to function $y = a_1 * \exp(-x/\lambda_1) + a_2 * \exp(-x/\lambda_2)$ to quantitatively describe the data.

Figure 8(a): BCF-10 5 kGy

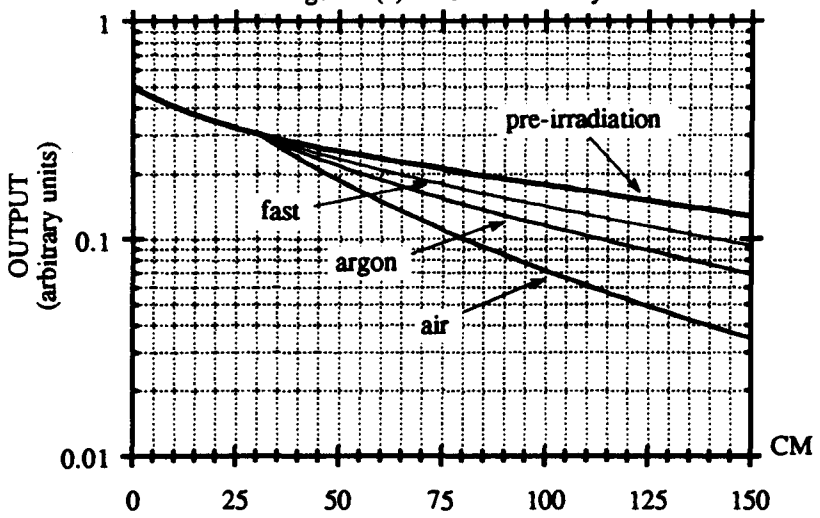


Figure 8(b): BCF-10 20 kGy

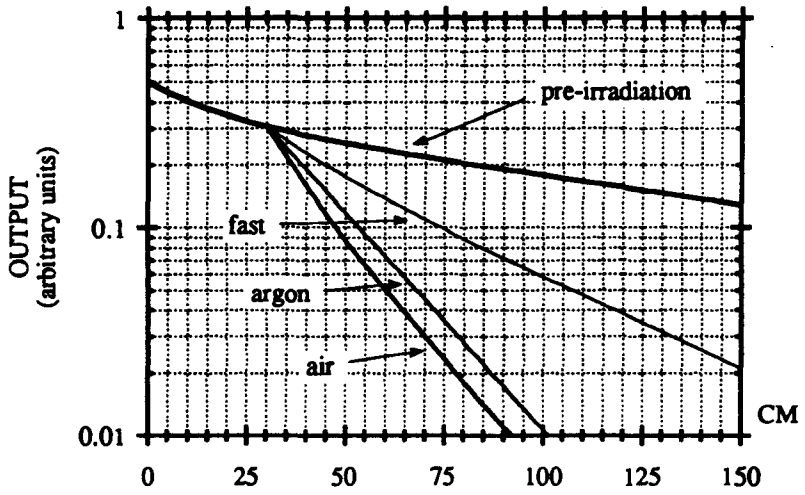


Figure 8(c): Bicron B 5 kGy

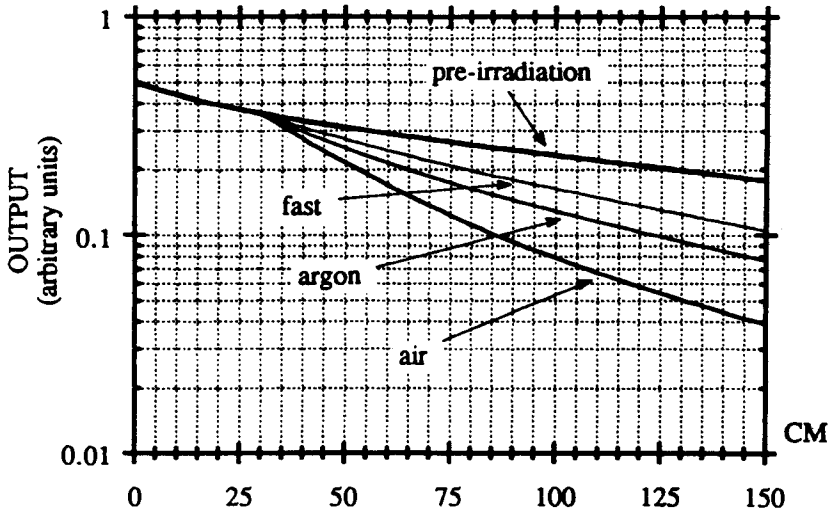


Figure 8(d): Bicron B 20 kGy

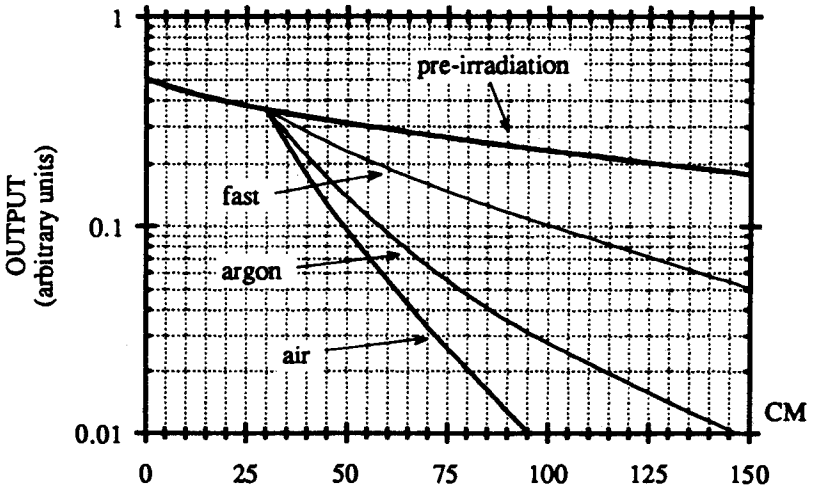


Figure 8(e): Bicron RH-1 5 kGy

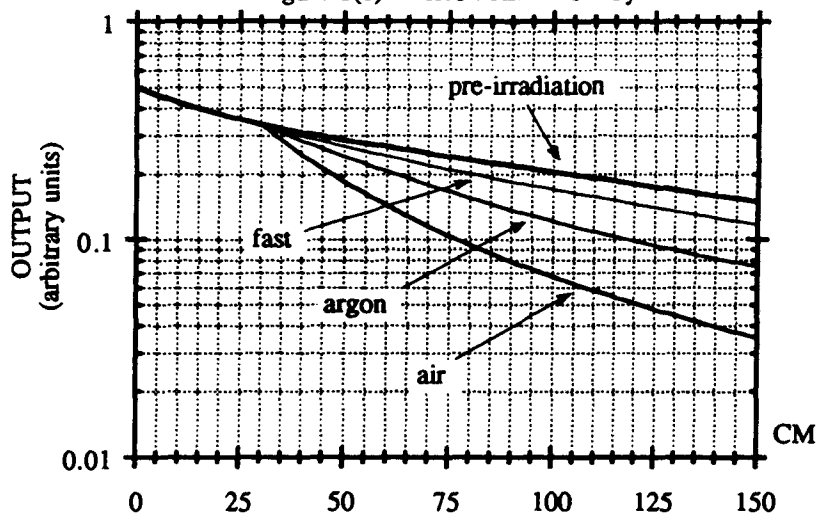


Figure 8(f): Bicron RH-1 20 kGy

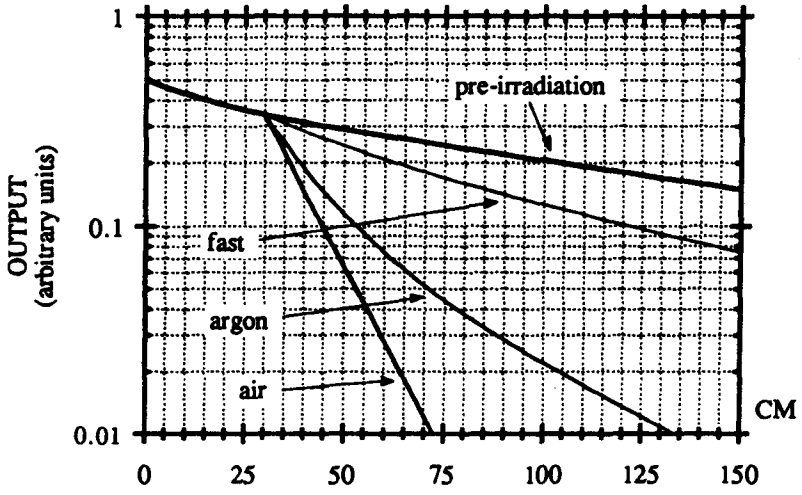


Figure 8(i): SCSF-81 5 kGy

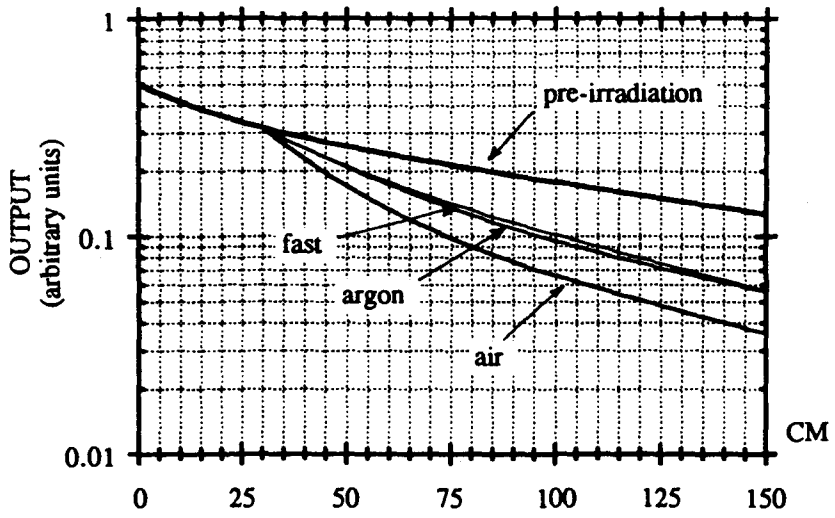


Figure 8(j): SCSF-81 20 kGy

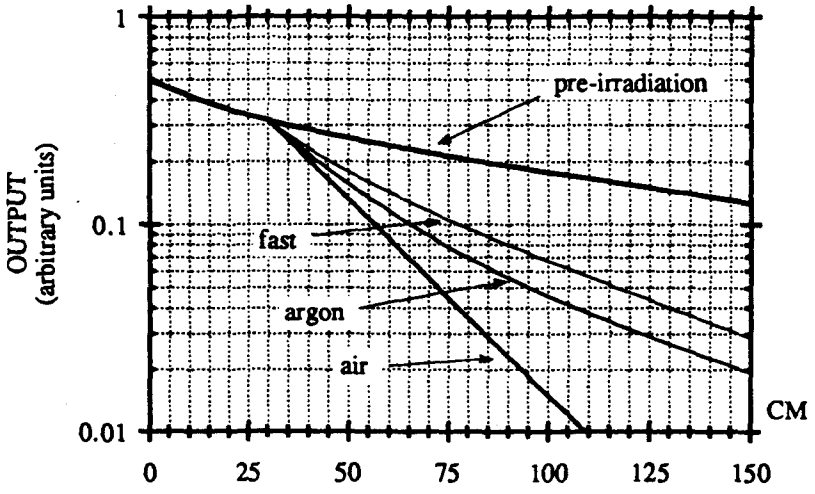


Figure 8(k): SCSF-38C 5 kGy

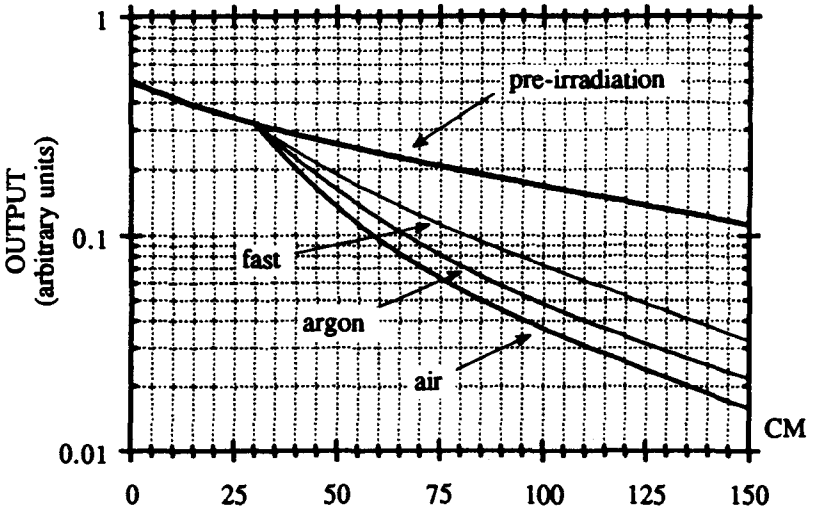


Figure 8(l): SCSF-38C 20 kGy

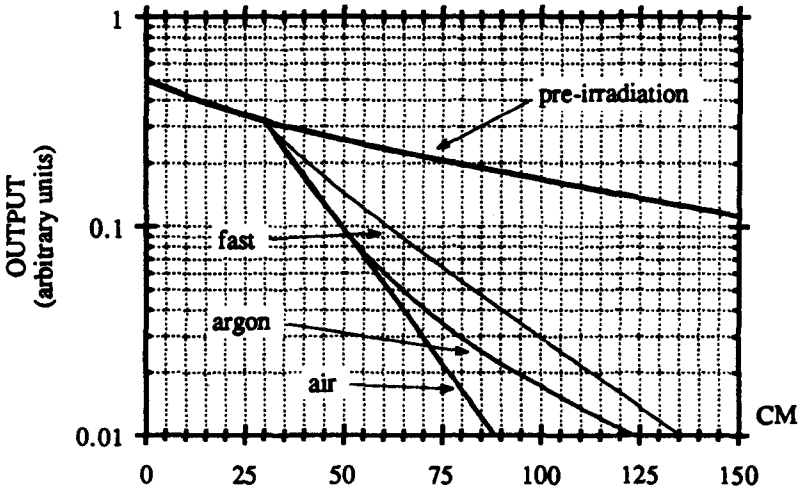


Figure 8(m): SCSF-81C 5 kGy

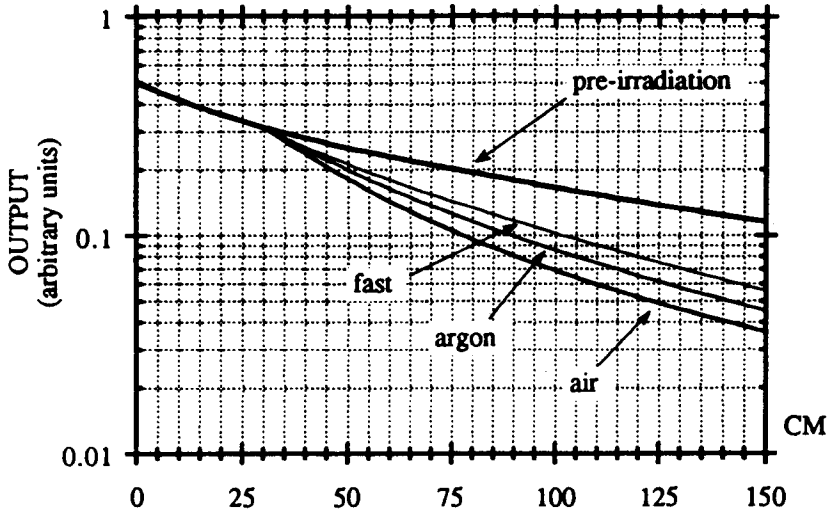


Figure 8(n): SCSF-81C 20 kGy

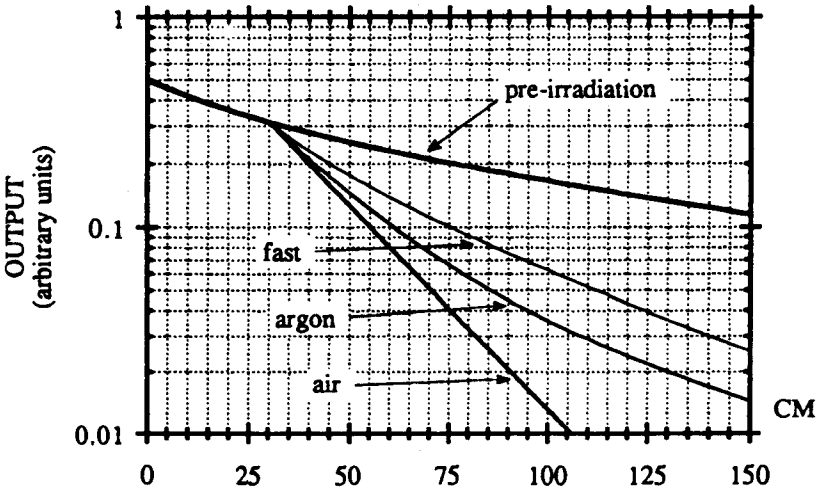


Figure 8(g): SCSF-38 5 kGy

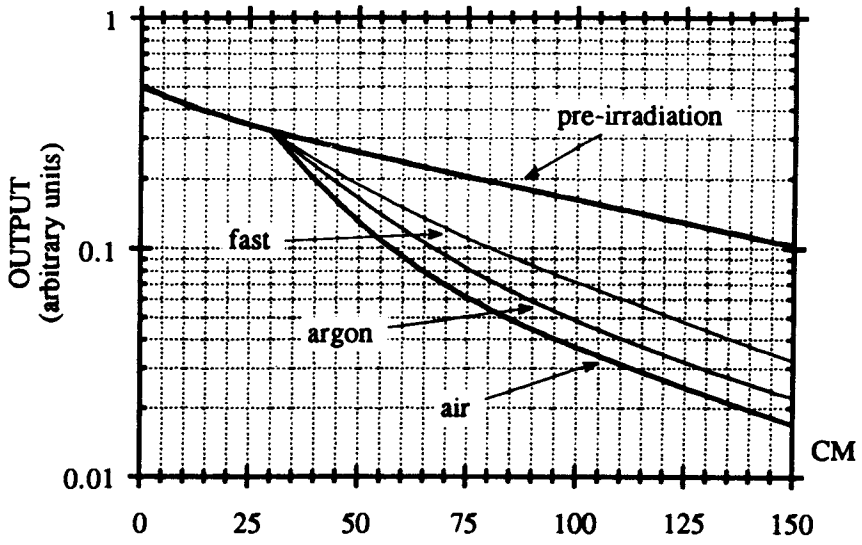


Figure 8(h): SCSF-38 20 kGy

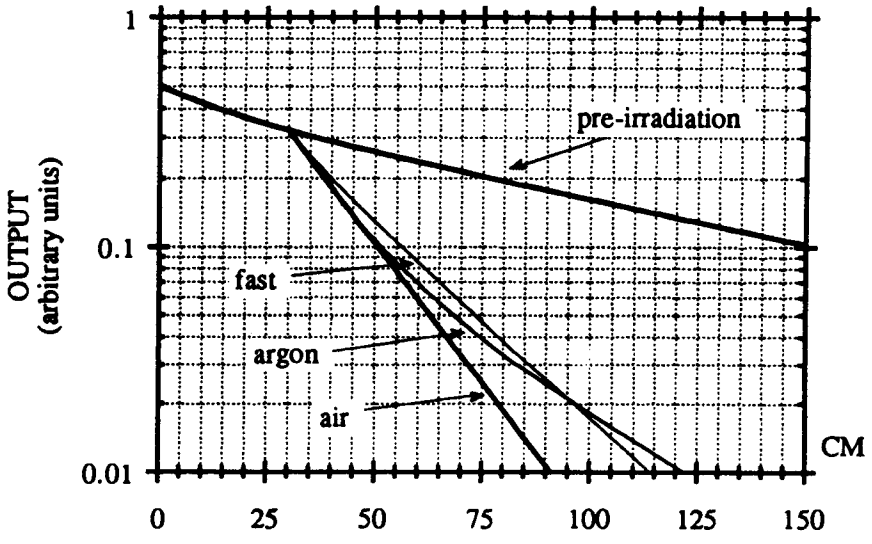


Figure 8(o): Bicron 3HF 5 kGy

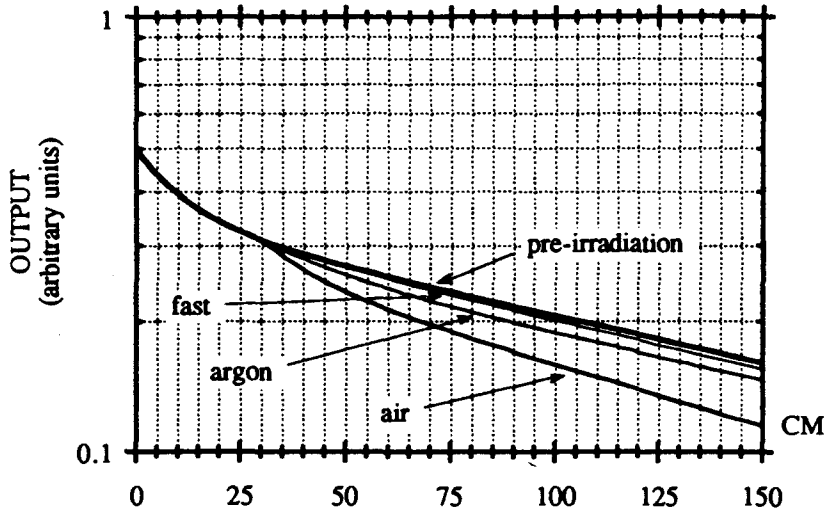


Figure 8(p): Bicron 3HF 20 kGy

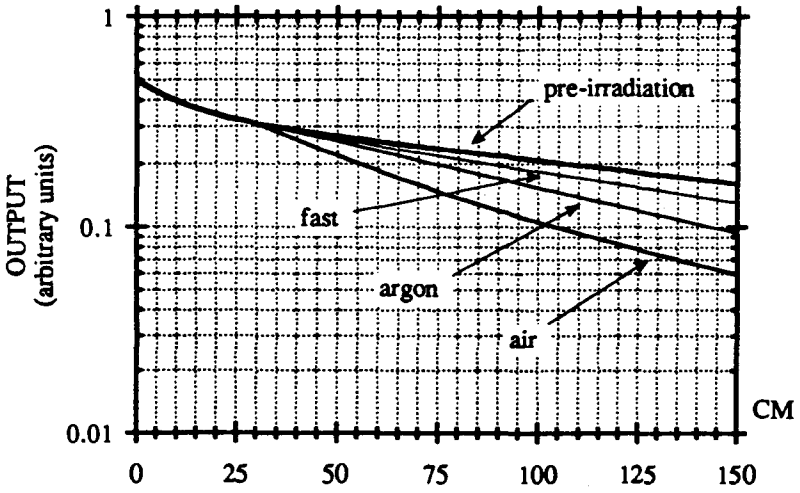


Figure 8(q): SCSF-Y8 5 kGy

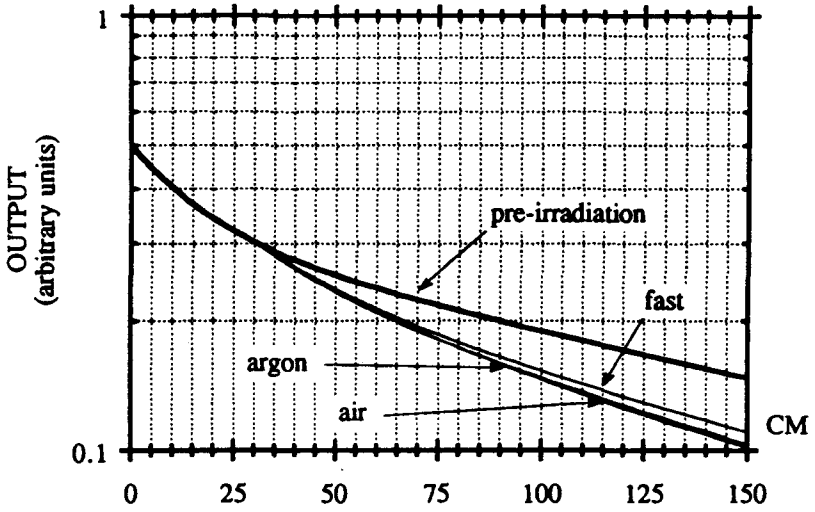


Figure 8(r): SCSF-Y8 20 kGy

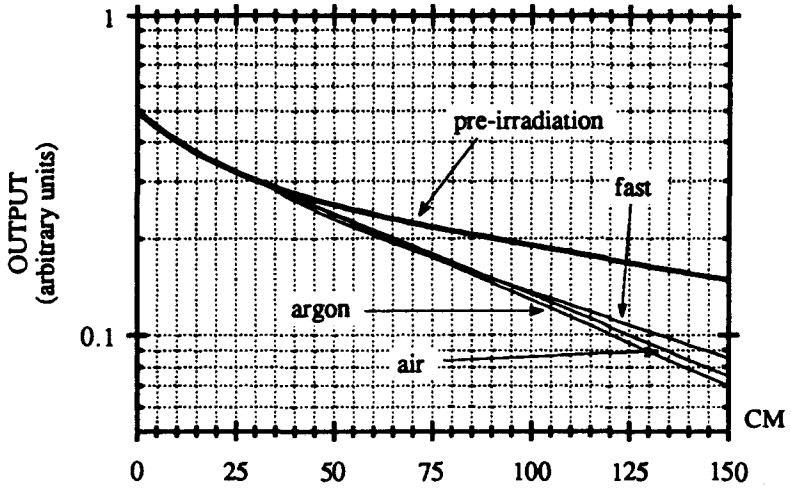


Figure 8(s): SCSF-Y8C 5 kGy

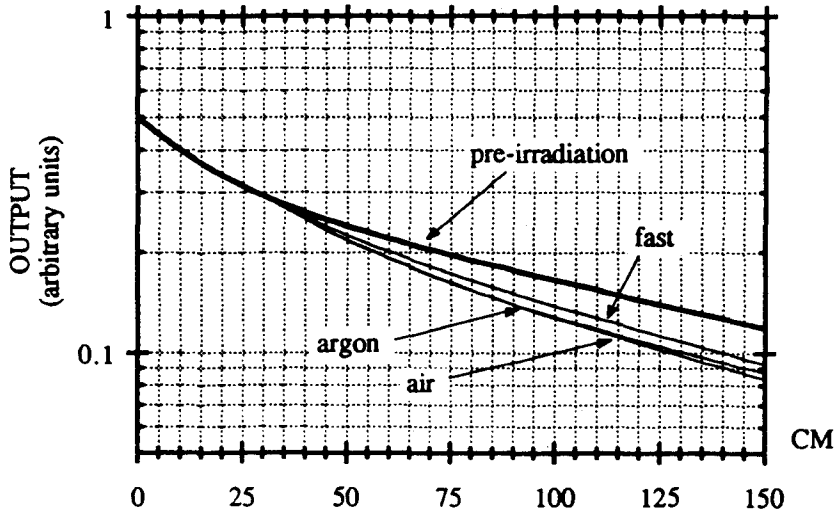


Figure 8(t): SCSF-Y8C 20 kGy

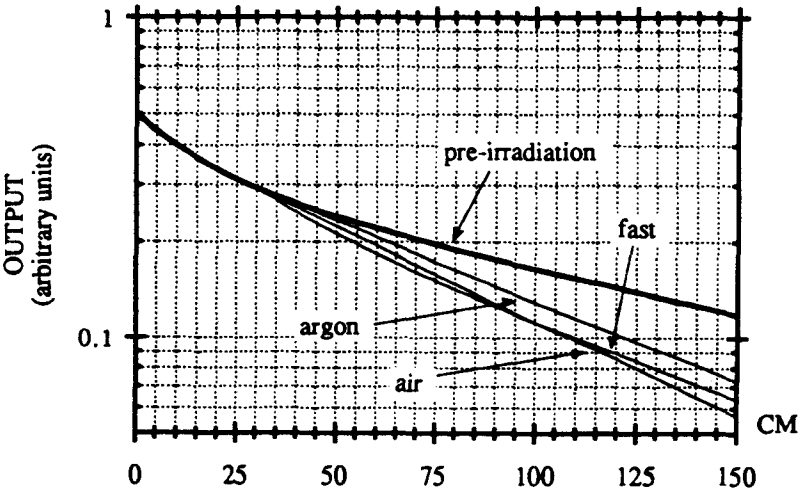


Figure 9(a)
BCF-10 5 kGy Wratten #3

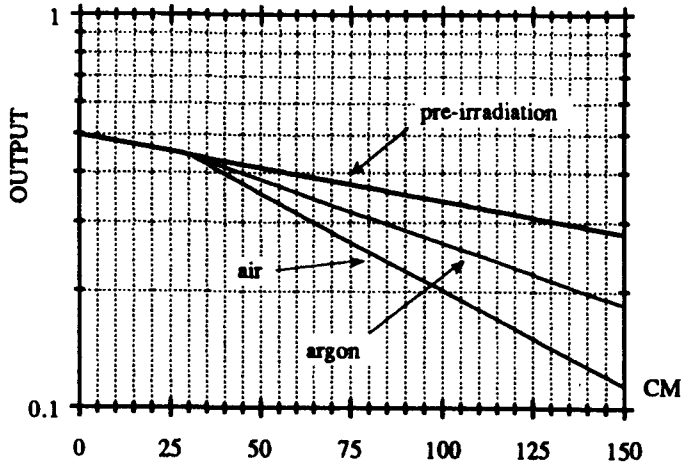


Figure 9(b)
Bicron B 5 kGy Wratten #3

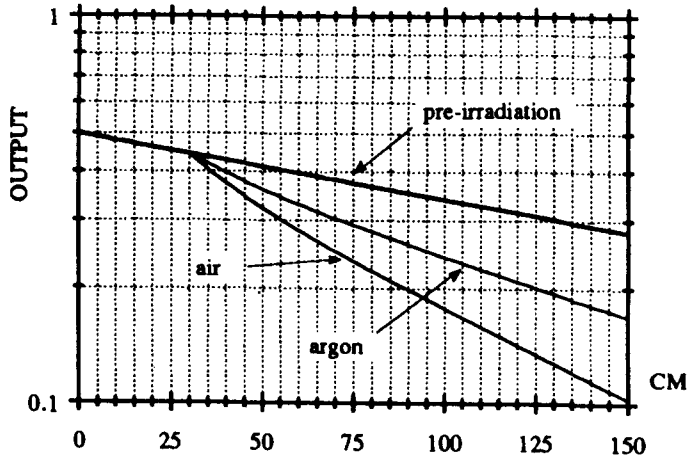


Figure 9(c)
Bicron RH-1 5 kGy Wratten #3

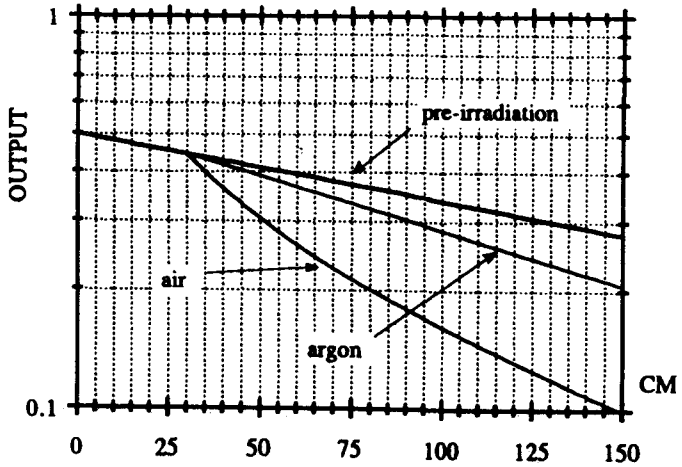


Figure 9(d)
SCSF-38 5 kGy Wratten #3

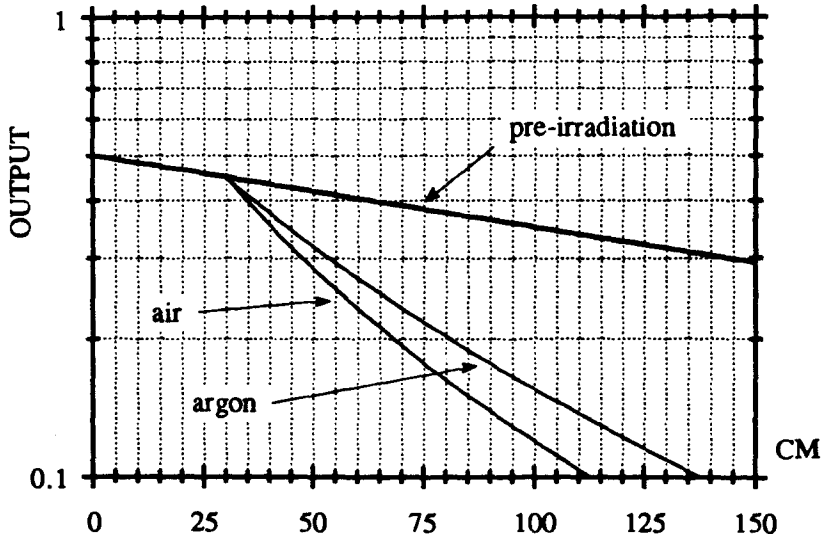


Figure 9(e)
SCSF-81 5 kGy Wratten #3

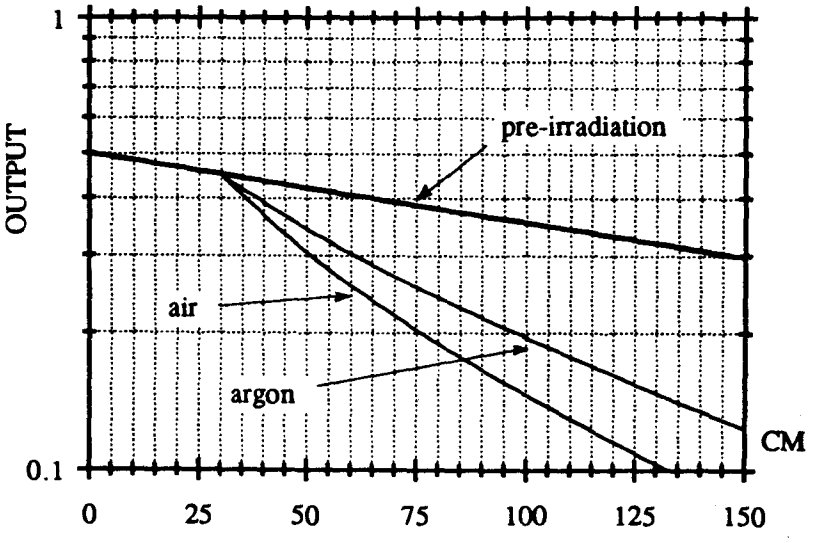


Figure 9(f)
SCSF-38C 5 kGy Wratten #3

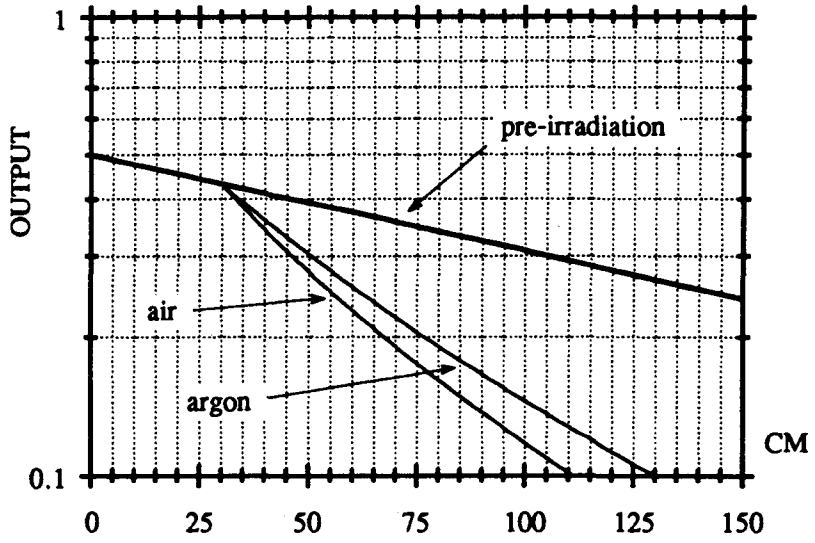


Figure 9(g)
SCSF-81C 5 kGy Wratten #3

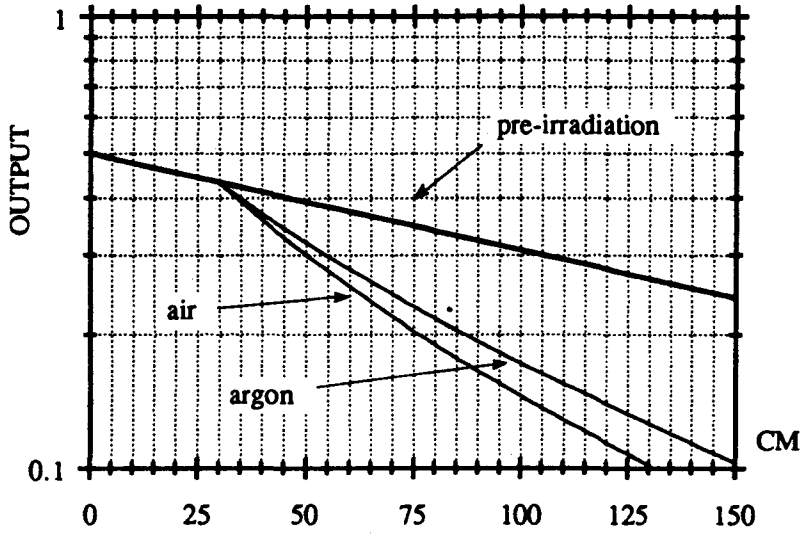


Figure 9(h)
Bicron 3HF 5 kGy Wratten #9

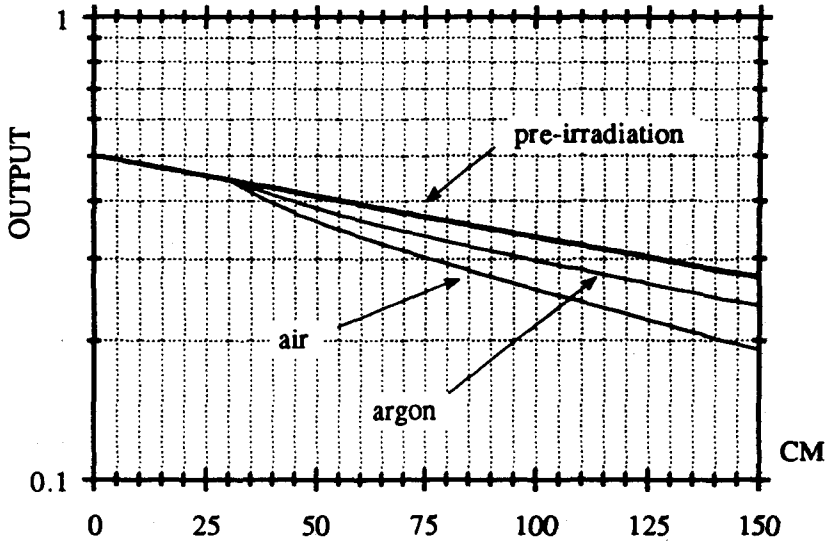


Figure 9(i)
Bicron 3HF 5 kGy Wratten #16

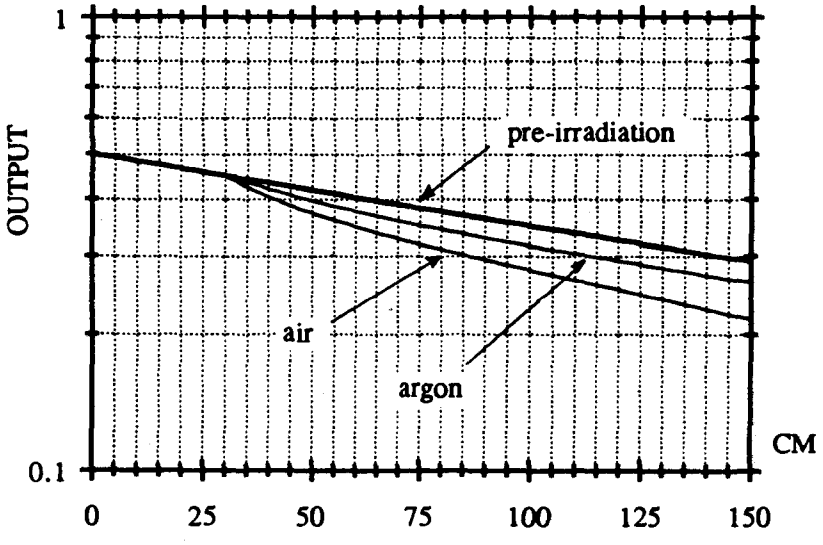


Figure 9(j)
SCSF-Y8 5 kGy Wratten #9

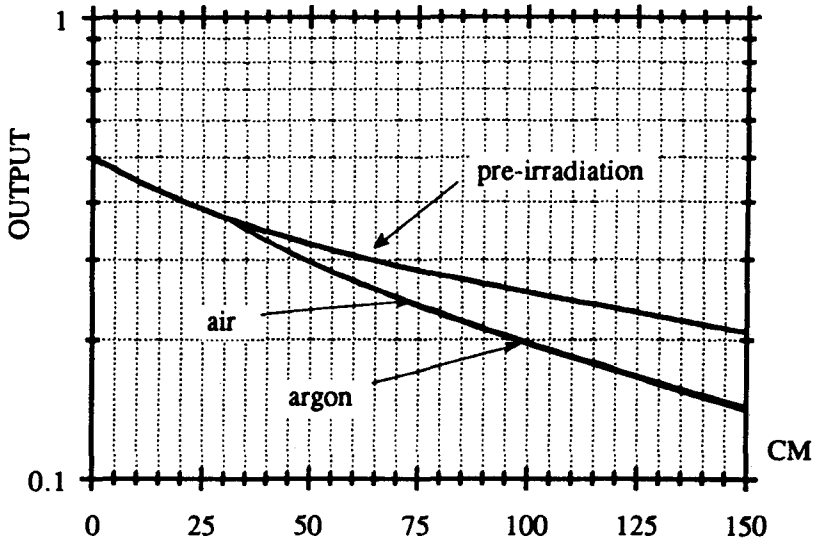


Figure 9(k)
SCSF-Y8 5 kGy Wratten #16

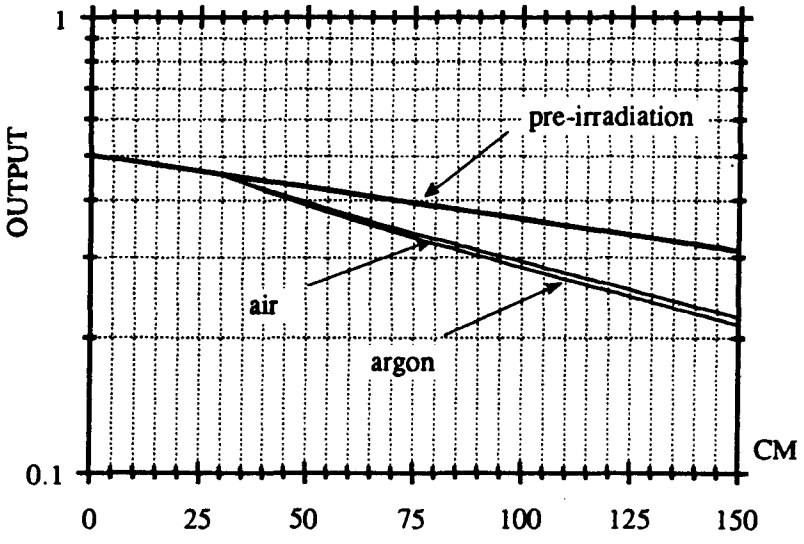


Figure 9(l)
SCSF-Y8C 5 kGy Wratten #9

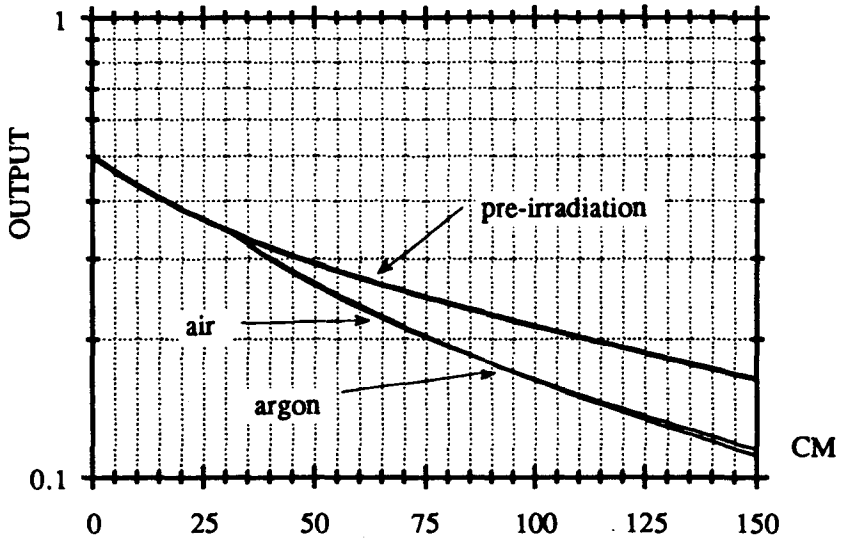
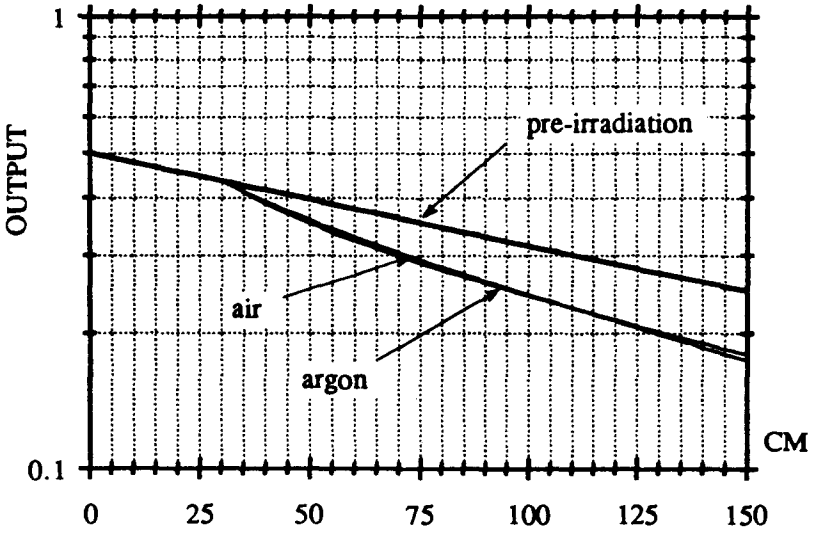


Figure 9(m)
SCSF-Y8C 5 kGy Wratten #16



Study of Hadron Punchthrough and Muon Rates at the SSC

Yuan-Hann Chang
Physics Dept., M.I.T., Cambridge, MA 01239
Bing Zhou
Physics Dept., Boston University, Boston, MA 02215
Oct., 1991

ABSTRACT

Hadron punchthrough probabilities as functions of hadron energy and absorber length (in terms of interaction length) at the SSC are studied in detail using GEANT Monte Carlo simulations. Energy epectra, charged multiplicity and the angular spread distributions of the punchthroughs are presented. Total muon rates including prompt muons and the punchthroughs are calculated as functions of muon transverse momentum and the rapidity coverage with GEM detector baseline design.

1 Introduction

Experiments at the next generation of hadron colliders (SSC/LHC), operating at very high luminosities ($10^{33} - 10^{34} cm^{-2} s^{-1}$), will allow us to explore the physics behind the electroweak symmetry breaking. This implies the search for the Higgs boson, technicolor, supersymmetry, as well as the search for new gauge bosons, new leptons and quarks. Leptonic/photonic final states will be detected as the most sensetive signatures for new physics. At the extremely high luminosities, muons offer an advantage over electrons/photons since the trigger and the measurement can be performed outside of the calorimeters (as absorbers of hadrons), where the particle

flux is low. For high luminosity hadron colliders, muon detections is therefore the first principle in optimizing the detector design.

Very broad physics topics at the TeV energy scale require the muon detection at the SSC to cover large range of the muon momentum, from few GeV to few TeV, and large solid angle, down to few degrees (rapidity larger than 2.5). Understanding the hadron punchthroughs and muon rates is crucial for muon detector and trigger design. However, punchthrough simulations need enormouse amount of computer time: in order to obtain reasonablly good spectra, we need to simulate in total about 13 million shower developments in the calorimeters. Our strategy for the simulations is therefore:

(1) To obtain punchthrough probabilities for single hadron (mainly pions) with different energies and incident angles (therefore different calorimeter thickness) using full GEANT[1] simulations;

(2) The total hit distributions in muon chambers and the muon trigger rates are obtained using ISAJET[2] Monte Carlo program to generate pp collision events. The punchthrough probabilities and the muon energy loss were then for each μ, π and k according to the spectra obtained from the GEANT simulations.

It is the goal of this study to provide detailed information on punchthroughs which should be easily used for total muon rate calculations of any detector configuration for high luminosity hadron colliders. We have used this information and calculated total muon rate with the GEM detector baseline design.

In this paper we will first describe the main parameters of the detector model and the physics processes set for hadronic shower simulation in GEANT programs. In section three we will report the results on simulations of single muon and pion with different energies and incidence angles. Section four reports the results of total muon rate calculations with GEM detector at the SSC. Discussions on the calculation uncertainties and the conclusions will be given in the last section.

2 Detector and Physics Parameters for GEANT Simulation

We have used a simplified detector model for GEANT (version 3.14), which uses the GHEISHA[3] collision model for a full shower simulations. Figure 1 shows the detector geometry set up:

(1) 1.5 mm Berillium beam pipe located at a distance(R) of 10 cm from the beam line;

(2) A simple Silicon central tracker from R=13-75 cm, with length=300 cm;

(3) BaF_2 EM calorimeters from R=78-130 cm in barrel, Z=210-262 cm in endcaps. It has in total 25 radiation lengths (X_0), corresponding to 1.7 interaction lengths (λ);

(4) Fe/Pb/scintillator sandwitch hadron calorimeter located between R=145-335 cm in the barrel, and Z=330-558 cm in the endcaps. Its total interaction length equals to 10.1λ in the barrel ($|\eta| < 1.4$), and 12.3λ in the endcaps.

(5) Three layers of Aluminum muon chambers located at R=370, 600, 830 cm in the barrel, Z=600, 1025, 1450 in the endcaps. Inner and outer chambers have 10% radiation length, and the middle chamber has 20% radiation length.

(6) All the subsystem detectors are located in a large magnetic field (1.0 T) with the field direction along the beam line.

Table 1 lists the values of the particle energy cutoff and the physics processes setup in the GEANT program to control the shower development and the tracking of the secondary particles in the detector.

3 Results from GEANT Simulations

Table 1: Parameters used in GEANT Monte Carlo Simulations

```
***** G E A N T     Version 3.1416       DATE/TIME 911005/2008 ******
*************************************************************
*                                                           *
*              Standard TPAR for this run are               *
*              ------------------------------               *
*                                                           *
*  CUTGAM=  1.00 GEV  CUTELE=  1.00 GEV  CUTNEU=  1.00 GEV  *
*  CUTHAD=500.00 MEV  CUTMUO=100.00 MEV                     *
*  BCUTE =  1.00 GEV  BCUTM =  1.00 GEV                     *
*  DCUTE =  1.00 GEV  DCUTM =  1.00 GEV  PPCUTM= 10.00 MEV  *
*  IPAIR =        1.  ICOMP =        1.  IPHOT =        1.  *
*  IPFIS =        1.  IDRAY =        1.  IANNI =        1.  *
*  IBREM =        1.  IHADR =        1.  IMUNU =        1.  *
*  IDCAY =        1.  ILOSS =        1.  IMULS =        1.  *
*  IRAYL =        0.                                        *
*                                                           *
*************************************************************
```

3.1 Hadron Punchthrough Probabilities

To obtain the punchthrough probabiliteis, we simulated the shower development of single pions and kaons incidented to the detectors from the interaction point. We have parallelly used about 10 VAX workstations, 2 DEC-5000 workstations and 10 SGI CPUs to run the computing jobs for about 6 weeks to study the hadron punchthroughs using GEANT full shower simulations. Table 2 lists number of hadron showers simulated in our studies.

In the following, we present main results which are needed for total muon rate calculations:

- **Single π^+ punchthrough probability:** It is defined as N_{out}/N_{total} where N_{out} is the number of events with charged particles leaking out of the calorimetry and N_{total} is the total number of pions simulated. N_{out}/N_{total} versus pion energies at several different interation lengthes are shown in Figure 2. π^- and $k^{\pm}$

punchthrough probilities at 90 degrees are compared with π^+ in Figure 3.

- **Single pion punchthrough charged multiplicity:** It is defined as the number of hits in the inner layer of the muon chambers from a single incident pion. Note that if a low energy particle loops in the magnetic field and hits the chamber twice, we have counted it twice. Figure 4 shows single pion punchthrough charged multiplicities at different pion energies and calorimetry thickness (in terms of λ).

- **Normalized momentum spectra:** It is defined as $p_{out}/p_{incident}$, where p_{out} is the momentum of the punchthrough particle and $p_{incident}$ is the momentum of the incident particle. For leading energy punchthrough charged particles the spectrum is shown in Figure 5. Figure 6 and Figure 7 show the spectra for the second and the third leading energy punchthrough particles, respectively. The spectra of low $p_{incident}$ at large λ show clear enhancement at high $p_{out}/p_{incident}$ values. These are contributions from the flight decays.

- **Punchthrough particle angular spread:** It is defined as the angles between the out-going punchthrough particles and the incident hadron. The angular spread is correlated to the normalized momentum. Figure 8 shows 2-dimension histograms, $\Delta\theta$ versus $p_{out}/p_{incident}$, for different incident pion energies.

3.2 Muon Energy Loss Spectra

The purpose to study muon energy loss in the calorimeters is:

(1) To obtain correct prompt muon spectra out of the calorimetry by taking into account muon energy loss in the calorimeters.

(2) To learn how to correct the energy loss for total muon energy measurement.

Figure 9 shows the energy loss spectra for muons with different muon energies at different calorimetry thickness (in terms of λ). The spectra peaks correspond to

the dE/dx energy loss, and the tails mainly come from muon bremsstrahlung energy loss in the calorimeter. For high energy muons such energy loss is significant, which implies that we have to collect the muon energy loss in the calorimeter to improve total muon energy resolution.

We have studied the method to correct the muon energy loss for total muon energy measurements:

$$E^{\mu}_{total} = P_{\mu-chamber} + \Delta E$$

where $P_{\mu-chamber}$ is the muon momentum measured in the muon chambers out side of the calorimeters, ΔE is the muon energy loss in the calorimeters. From the studies we determined that if $\Delta E < 1.27 \times E_{peak}$, we used E_{peak} to correct for the muon energy loss; otherwise we used ΔE measured by the calorimeters assuming an energy resolution of $\Delta E/E = 50\%/\sqrt{E} + 2\%$.

Figure 10 shows $\Delta p^{\mu}/p^{\mu}$ distributions using the above mentioned method compared with using only the calorimetry measured ΔE to correct for the muon energy losses. It is clear that the method we used improves the muon energy resolution significantly.

4 Total Muon Rate Calculations

We have used ISAJET Monte Carlo program to generate events for various processes of pp reactions. The final state particles then pass through the GEM detector (baseline design) simulation by parametrizations from the results of the GEANT simulations. Figure 11 shows the calorimeter material thickness (in λ) versus rapidity, η, for muon energy loss and the punchthrough rate calculations.

The following procedure was used in our simulation to calculate the total muon rate:

- ISAJET generate events with selected physics processes. For this study we included TWOJET(6 quarks and gluon jets, with 140 GeV Top mass), W+JET, Z+JET, and DRELL-YAN processes. Table 3 shows the number of generated events for each process.

- For each prompt muon, we calculated the pass-through thickness of calorimetry material according to the incident angle. The energy loss is simulated by the energy loss spectrum obtained in GEANT simulation of muons that are closest in both momentum and incident angle. dE/dx energy loss is corrected according to the calorimetry thickness.

- For each charged pions and kaons, the following procedures were used to generate the punchthrough particles:

  1. We first check if the particle should yield punchthrough particles in the muon chambers. The probability is calculated according to the spectra in figures 2 and 3.
  2. If there are charged punchthroughs in the muon chambers, the charged multiplicity was generated according to the distribution extrapolated from the distributions in Fig. 4.
  3. The energies and angular spread of the punchthrough particles are calculated according to the spectra shown in Figures 5, 6, 7 and 8. If there are more than three particles, their energies were generated based on the spectrum of the third leading energy particle (Fig. 7).
  4. The difference of punchthrough rates between outer layer and inner layer of the muon chambers were taken care by the difference of the first few bins of the normalized momentum spectra of inner and outer layers.
  5. For π^- and $k^\pm$ we used the spectra for π^+ of the same energy and incident angle.

- The total muon rates are calculated by combining the spectra from each physics process weighted by the cross section.

Fig. 12 shows the total rates in the inner layer muon chambers as functions of muon transverse momentum, p_T, in different rapidity ranges. Spectra from different physics processes were plotted to show their relative contributions.

Fig. 13 shows the total rates versus the rapidity, η, with different muon p_T cut. Without p_T cut, punchthroughs dominate the total rate. However with $p_T > 10$ GeV, the prompt muons dominate.

Fig. 14 shows the rate/cm^2 as functions of θ, with different hadron calorimeter thicknesses in the barrel region. We have assumed that the barrel inner layer muon chambers located at a distance of 3.7 m from the beam line, and endcap inner layer located at z=5.5 m (the beam line is along the z coordinate). We found that in the barrel region, the muon rate is roughly constant at 0.3 Hz/cm^2 for 12λ absorber, and about factor of 3 higher in the case of 10λ. In the endcap region, 14λ is necessary, since the rate increase exponentially as the angle decreases.

As a summary, Table 4 lists the muon rates in the inner layer of the muon chambers at several θ angles, with different p_T cuts, and Table 5 lists the integrated muon rates in various η regions. Table 6 lists the multi-muon event rates with different muon p_T cuts.

5 Discussions and Conclusions

5.1 Rate Calculation Uncertainties

Muon chamber and trigger design need to know the total muon rates. It is important to understand the calculation uncertainties for the designs. We list the calculation uncertainty contributions in the following:

- GEANT simulation energy cut off: we set the shower development energy

cut off at 0.1, 0.5 and 1.0 GeV for muons, hadrons and electron/photon respectively to speed up the simulations (if the GEANT default energy cutoff values were used, at least 5 times more CUP hours would be needed). In order to check our calculation uncertanties, we have used the GEANT default energy cutoff values (see Table 2) to study the punchthrough probabilities with 10 GeV and 20 GeV pions at different angles. We compared the punchthrough probabilities from low cutoff runs with our standard cutoff runs, and found that the differences were at 30% level. We therefore estimated our punchthrough probability calculations with an uncertainty of $\sim$ 30% for energy less then 0.5 GeV charged particles. It is clear that this uncertainty will not affect the muon trigger rates if we consider triggering on muons with p_T >5 GeV. However muon inner chamber hit occupancy should be higher than what we have presented.

- **Extrapolation of punchthrought spectra:** We have used momentum spectra obtained from pions at certain incident angles. Particles with incident angles different from these values can have different flight decay probabilities. We also used only spectra of 50, 100, 200, and 500 GeV pions. The punchthrough spectra of low energy pions (<20 GeV) show significantly increase of flight decays, which are not in the 50 GeV spectrum. We estimated that these effects can cause an rate uncertainty of $\sim$ 10%.

- **Theoretic model:** quark hadronization, which determines charged multiplicity of jets, in ISAJET program was tuned by UA1 data, extrapolation to the SSC energy scale gives uncertainties. It is not clear to us how much does this contribute to the rate uncertainties.

- **Small angle detector geometry:** for $|\eta| > 2.5$, the rate calculation using parametrization method has large uncertainty since hadronic showers spread into the detector hole around the beam. Also charged particles interacting with the beam pipe in the small angle will knock out many showered particles and increase the occupancy of the small angle muon chambers. Therefore, without detail detector and beam pipe shielding design and using full GEANT

simulation, the calculation is not reliable. In this study, we used only the calculation results above 9° .

- **Cosmic rays and beam spread :** The calculation reported in this paper doesn't include the contributions from cosmic rays and beam spread.

In summary, considering the above uncertainties in our calculations the real occupancy rate in the muon chamber will be higher than our results. A safety factor of ~3 should be used for chamber and trigger designs based on these results.

5.2 Applications of the Results

- *Muon Level-1 Trigger*

The GEM collaboration proposed to use Resistive Plate Counters "RPC's", which have a response time of less than 10 nanoseconds, and Cathod Strip Chamber "CSC's", which have a response time of less than 15 nanoseconds (wire spacing for 'CRC's" is 2.5 mm), as the fast muon trigger devices for the barrel and the endcap regions respectively. The "RPC's" can handle a rate of 40 Hz/cm^2, which is limited by chamber dead time. The "CSC's" in principle can handle a rate up to 100 kHz/stripe, which is limited by signal integration time. Figure 14 shows that even at $10^{34}/cm^2/s$ luminosity, the total muon rate in the barrel region is about 3 Hz/cm^2, "RPC's" certainly can hadle this rate with large safety factor. In the endcap regions, the total muon rate in inner muon chambers can be as high as 200 Hz/cm^2 at the $10^{34}/cm^2/s$, the "CSC's" can be easily designed to work on such rate.

Fast muon trigger is generated from roads in three layers of "RPC's" or "CSC's". Roads are formed by few centimeter wide strips in the central "RPC's", and by radial cathod strips and vertical wires in the endcaps. According to Table 5, the total muon rate ($| \eta |< 2.5$) with $p_T^\mu > 5$ GeV is about 10 kHz, and with $p_T^\mu > 25$ GeV is about 1 kHz at the SSC standard luminosity. If the Level-1 trigger is designed to handle a few tens of kHz, then it is possible to trigger on muons with 5 GeV p_T threshold at

$10^{33}/cm^2/s$ luminosity, and with 25 GeV p_T threshold at $10^{34}/cm^2/s$.

• *Muon Chamber Occupancy*

Assuming that the barrel muon chambers are made of 4 meters long drift tubes with 4 cm diameters. Based on Fig. 14, the rate per tube would be about 500 Hz at the SSC standard luminosity. The occupancy can be estimated as $rate \times T_{max}$, where T_{max} is the maximum drift time of the tube. Assuming $T_{max} = 1\mu s$, the occupancy would be about 5×10^{-4} at $10^{33}/cm^2/s$ luminosity, and 5×10^{-3} when the luminosity increases by a factor of 10.

If the endcap muon chambers are made of "CSC's" (also called PAD chambers) with 0.5 cm wide and 1 meter long cathod strips. The occupency would be less than 0.1% at the standard luminosity. Here we assumed the strip integration time to be 1 μs, and that one charged particle signals three pads. From this result we believe that it will also work at higher luminosities.

5.3 Conclusions

We conclude, based on our simulations, that:

- At the high luminosity hadron colliders, muons certainly offer an advantage over electrons/photons due to the low particle rate outside of the calorimeter. We can trigger on muons with the p_T cut as low as 5 GeV. Such low p_T cut is very important for increasing the event acceptance in events like $H^0 \rightarrow ZZ^* \rightarrow \mu\mu\mu\mu$.

- Muon chamber located outside the calorimeter can certainly work at the $10^{34}/cm^2/s$ luminosity.

- Except from the uncertainties in the theoretical models, this simulation should be accurate to within a factor of 2 for $|\eta| < 2.5$. For small angle $|\eta| > 2.5$ muon chamber and trigger design, one needs full GEANT simulation with completely

defined detector geometry.

Acknowledgement

We would like to thank the Texas National Research Laboratory Commission for their support through the SSC fellowship program, and providing essential computer equipements for this study. We thank the Laboratory for Nuclear Science of MIT and the SSC lab. for supporting our calculations.

References:

[1] R. Brun et al., GEANT (version 3.14) CERN DD/EE/89-1, Sept. 1990;

[2] F. Paige and S. D. Protopopescu, ISAJET (v. 6.36) A Monte Carlo Event Generator for PP and $P\bar{P}$ reactions, July, 1991.

[3] H. Fesefeldt, GHEISHA, RWTH Aachen preprint PITHA 85/02 (1985).

Figure Captions

Figure 1 Side view of detector geometry set up for GEANT Monte Carlo simulations.

Figure 2 Singel π^+ punchthrough probabilities as functions of energy of the incident π^+ and the absorber thickness.

Figure 3 Comparison of the punchthrough probabilities of π^+, π^-, k^+, and k^-.

Figure 4 In total 12 figures show the single pion punchthrough charged multiplicity distributions at different pion energy and absorption length. Shaded histograms show the muon component in the punchthrough particles.

Figure 5 In total 12 figures show the normalized momentum spectrum of the leading energy punchthrough particle. Open histogram corresponds to the inner chamber spectrum, and shaded histogram corresponds to the outer chamber spectrum. The difference is due to the low energy particle looping inside the magnetic field.

Figure 6 In total 12 figures show the normalized momentum spectrum of the second leading energy punchthrough particle. Open histogram corresponds to the inner chamber spectrum, and shaded histogram corresponds to the outer chamber spectrum. The difference is due to the low energy particle looping inside the magnetic field.

Figure 7 In total 12 figures show the normalized momentum spectrum of the third leading energy punchthrough particle. Open histogram corresponds to the inner chamber spectrum, and shaded histogram corresponds to the outer chamber spectrum. The difference is due to the low energy particle looping inside the magnetic field.

Figure 8 In total 12 figures show the punchthrough particle angular spread correlated to the normalized momentum.

Figure 9 In total 12 figures show the muon energy loss distributions for differnt muon energies and absorber thicknesses.

Figure 10 Muon energy resolution distributions for 20 GeV and 50 GeV muons. Solid histograms were obtained using the method described in section 3.2. Dashed histograms were obtained by adding energy loss measured in the calorimeters only.

Figure 11 Calorimeter interaction length as a function of the rapidity used in our total rate calculations.

Figure 12 Total muon rates versus muon transverse momentum (p_T). Contributions from different physics processes are also shown. (a) $\mid \eta \mid < 1.5$, (b) $1.5 < \mid \eta \mid < 2.0$, (c) $2.0 < \mid \eta \mid < 2.5$, (d) total rate with $\mid \eta \mid < 2.5$.

Figure 13 (a) Total muon rates as functions of the rapidity with different muon p_T cuts. (b)-(f) show the total muon rates as well as contributions from different physics processes, with different muon p_T cuts. Note that the rates at the positive and negative rapidity have been folded together in this figure.

Figure 14 Inner muon chamber hits rate per cm^2 versus the polar angle, θ. For this figure we assumed that the inner barrel chambers are located at 3.7 meters from the beam line in the case of 12λ, and 3.5 meters in the case of 10λ. The inner endcap chambers were assumed to be located at 5.5 meters from the interaction point.

Table 2: **List of Number of Single Hadron Simulated**

cutoff energy: 0.1, 0.5, 1.0 GeV for μ, hadron and γ/e respectively								
P (GeV)	10	20	50	100	200	300	400	500
θ=90° (λ=11.8)	250k	200k	620k	415k	126k	64k	53k	110k
θ=15° (λ=14.5)	1070k	11k	1385k	782k	413k	100k	100k	164k
θ=25° (λ=15.5)	100k	13k	2132k	100k	50k	50k	10k	10k
θ=45° (λ=17.0)	89k	16k	1494k	23k	10k	10k		
θ=70° (λ=12.8)	100k	100k	100k	100k	100k	100k	100k	
θ=90° (λ=10)	1100k	100k	100k	100k	80k		40k	40k
cutoff energy: 0.01, 0.01, 0.001 GeV for μ, hadron and γ/e respectively								
θ=90° (λ=11.8)	100k	50k						
θ=15° (λ=14.5)	100k	50k						
θ=25° (λ=15.5)	100k	50k						
θ=45° (λ=17.0)	100k	50k						
θ=70° (λ=12.8)	100k	50k						

Table 3: **Simulated MC Events in Various Physics Processes**

process	P_T^{jet}**(GeV)**	cross section(mb)	N_{MC}
Minimal bias	4-20	7.4×10^{1}	1000k
$PP \rightarrow$ 2 jets (q, g)	20-9000	0.2×10^{1}	9700k
$PP \rightarrow t\bar{t}$	10-5000	1.6×10^{-5}	1150k
$PP \rightarrow W + X \rightarrow \mu\nu X$	10-5000	3.1×10^{-5}	1770k
$PP \rightarrow Z + X \rightarrow \mu^+\mu^- X$	10-5000	3.1×10^{-6}	800k
$PP \rightarrow \gamma(Z) + X \rightarrow \mu^+\mu^- X$	10-5000	5.1×10^{-6}	432k

Table 4: **Particle Rate (Hz/degree) at Several Angles**

Angle	90°	70°	45°	25°	15°
no p_T cut	2.4k	3.0k	10k	23k	45k
$p_T > 5$ GeV	13	24	45	70	140
$p_T > 10$ GeV	4	5	8	20	30
$p_T > 15$ GeV	1.5	2.2	3.3	4.5	7
$p_T > 20$ GeV	0.8	1.1	1.5	2.0	3.0

Table 5: **Integrated Rate (Hz) in Several η Regions**

Region	$\mid \eta \mid < 2.5$	$\mid \eta \mid < 1.5$	$1.5 < \mid \eta \mid < 2$	$2 < \mid \eta \mid < 2.5$	di-muon $\mid \eta \mid < 2.5$
no p_T cut	2467k	1042k	660k	760k	230k
$p_T > 5$ GeV	9.31k	4.84k	2.23k	2.23	91
$p_T > 10$ GeV	1.92k	1.08k	440	403	19
$p_T > 15$ GeV	630	372	136	120	9.9
$p_T > 20$ GeV	280	166	52	58	6.3
$p_T > 25$ GeV	140	50	26	24	

Table 6: **Multi-Muon Event Rate (Hz) for $\mid \eta \mid < 2.5$**

multi-μ state	1μ/event	2μ/event	3μ/event	4μ/event	$> 4\mu$/event
no p_T cut	1274k	144.7k	42.7k	19.3k	24.1k
$p_T > 5$ GeV	9.14k	88	1.84	0.17	0.022
$p_T > 10$ GeV	1.91k	17.4	0.52	0.14	0.016
$p_T > 15$ GeV	629	8.36	0.30	0.12	0.014
$p_T > 20$ GeV	280	4.95	0.20	0.092	0.013

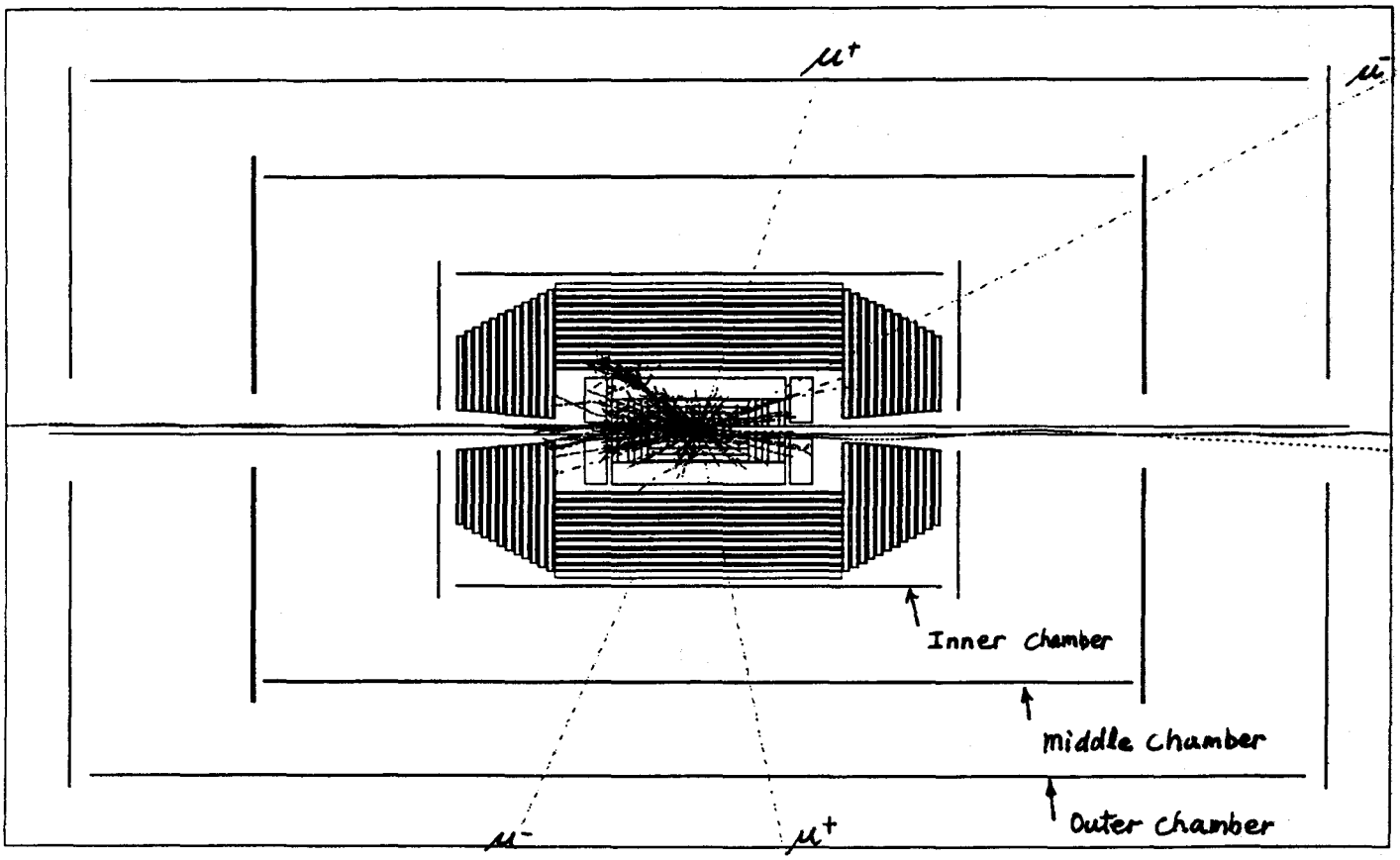


Figure 1 Side view of detector geometry set up for GEANT Monte Carlo simulations.

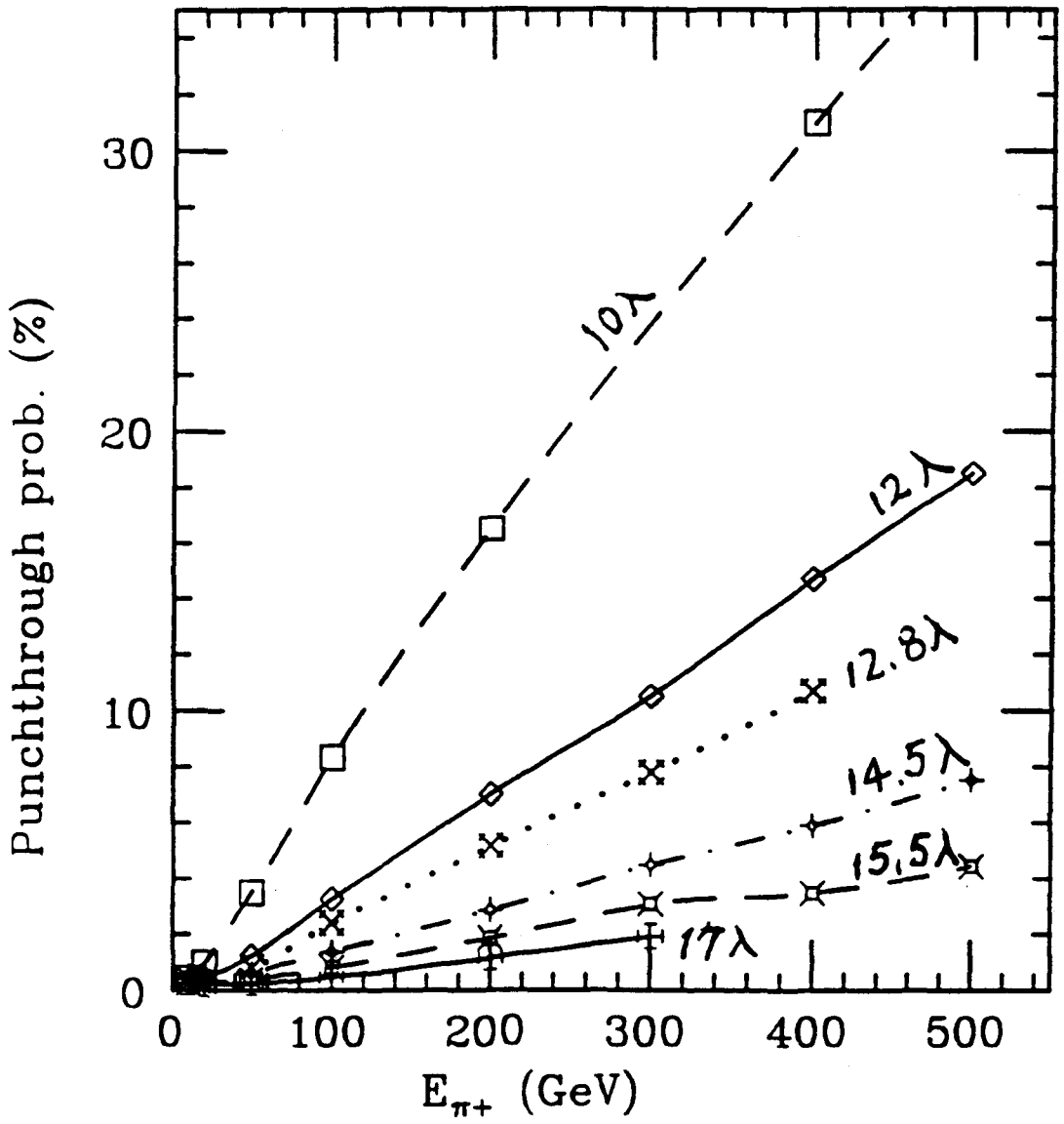


Figure 2 Singel π^+ punchthrough probabilities as functions of energy of the incident π^+ and the absorber thickness.

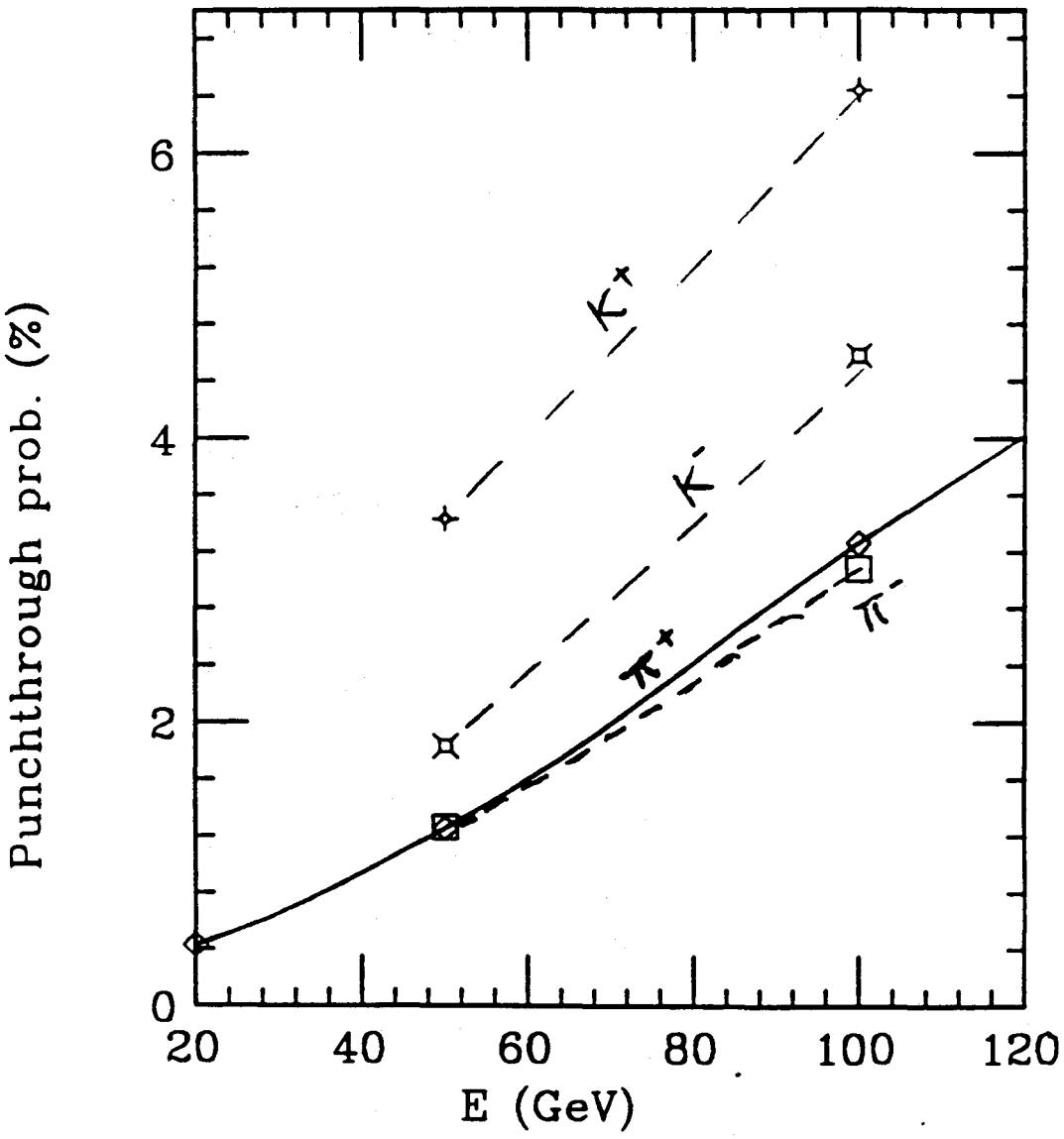


Figure 3 Comparison of the punchthrough probabilities of π^+, π^-, k^+, and k^-.

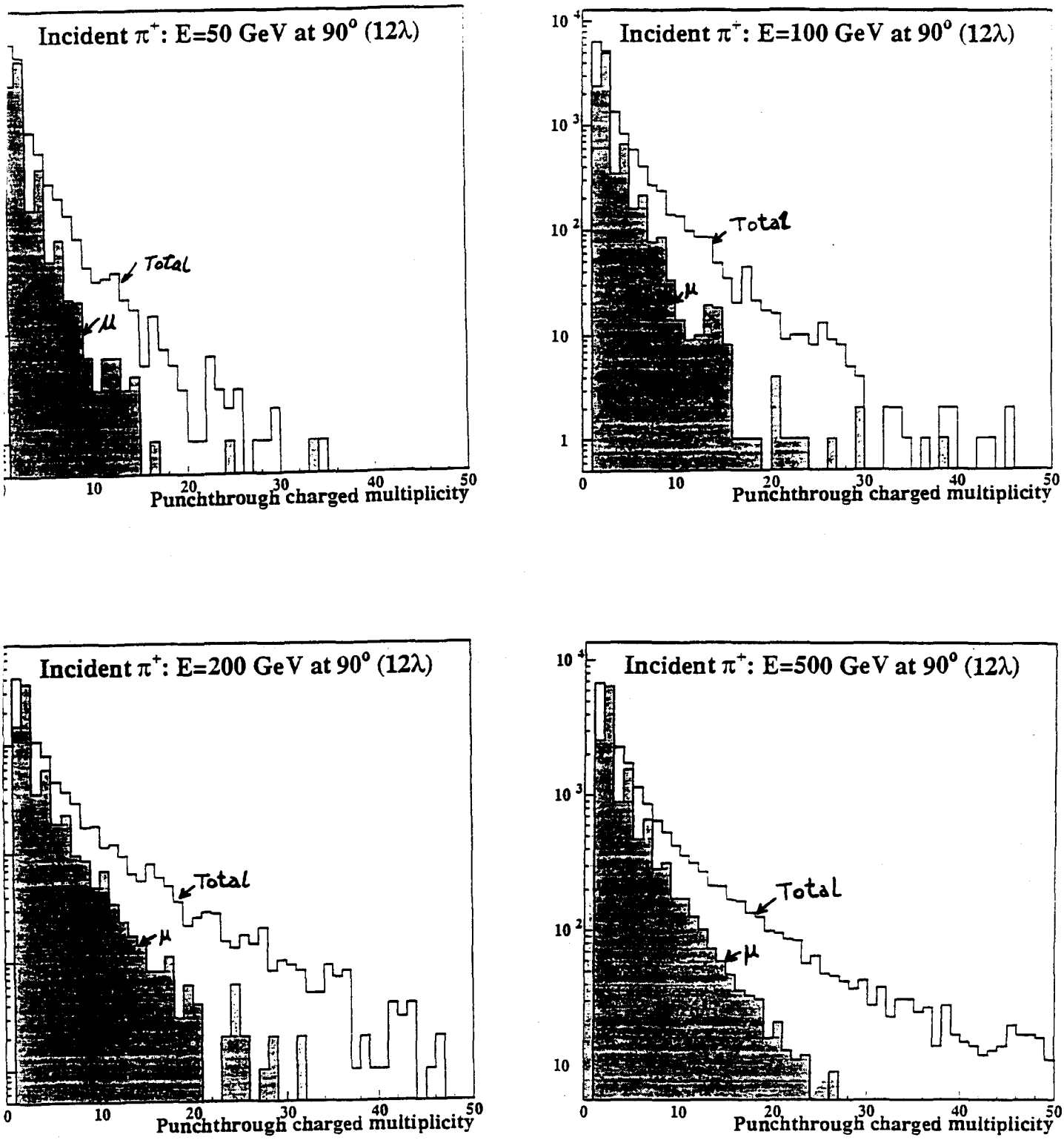
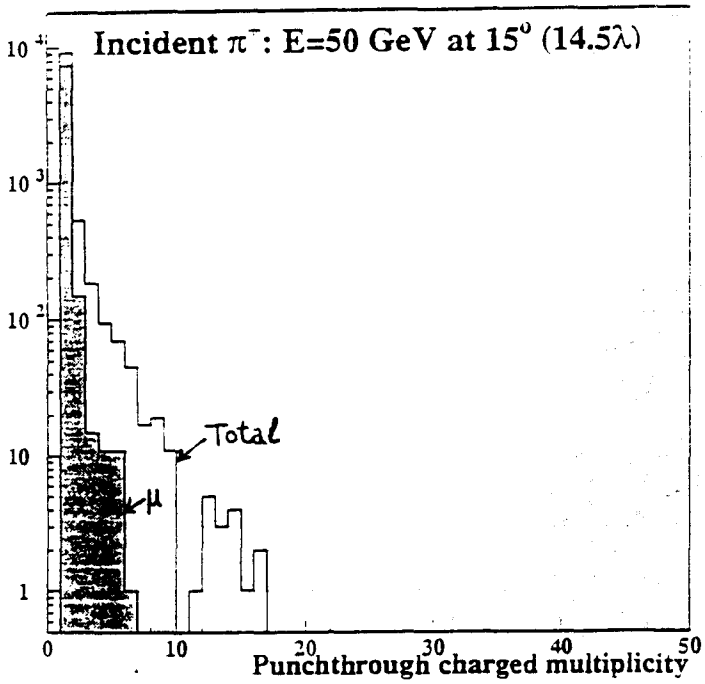
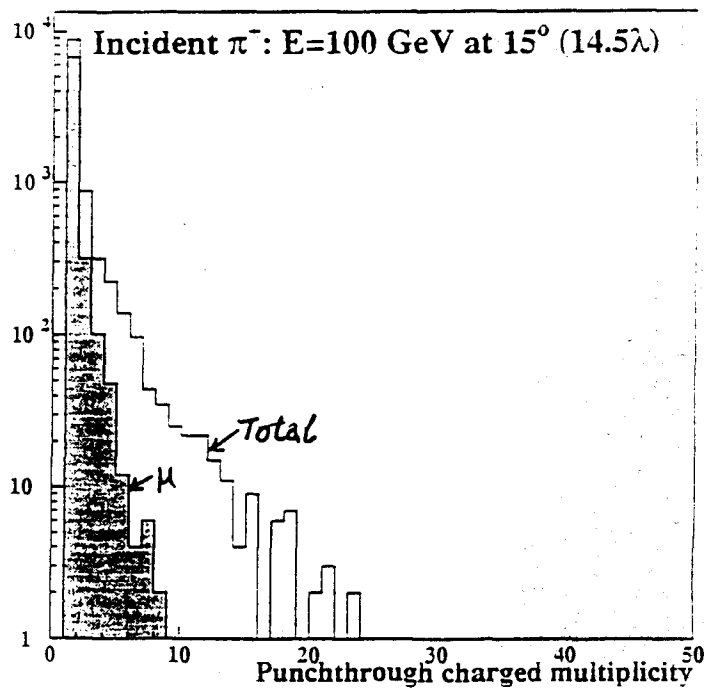
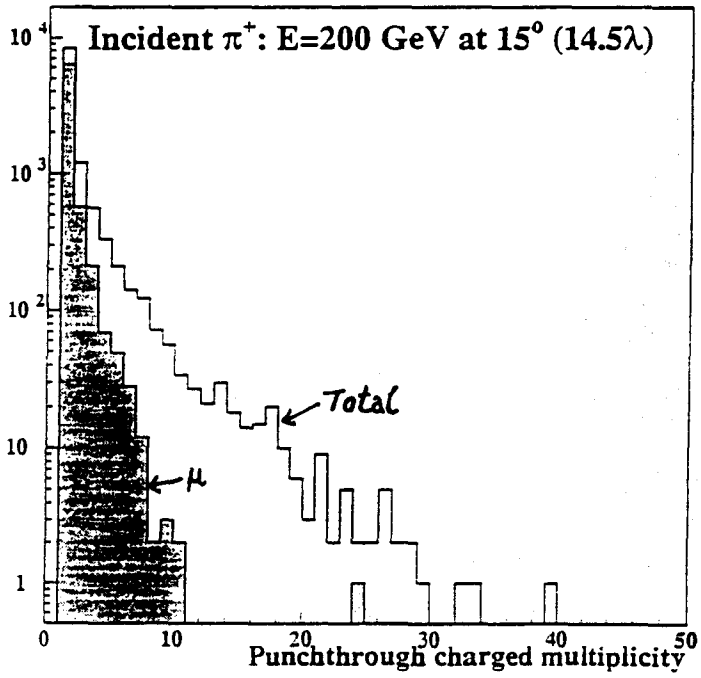


Figure 4 In total 12 figures show the single pion punchthrough charged multiplicity distributions at different pion energy and absorption length. Shaded histograms show the muon component in the punchthrough particles.







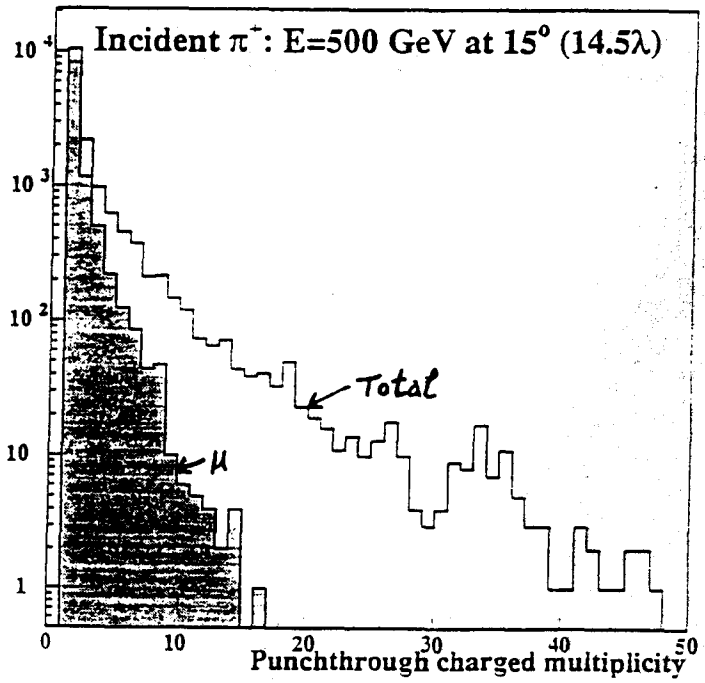
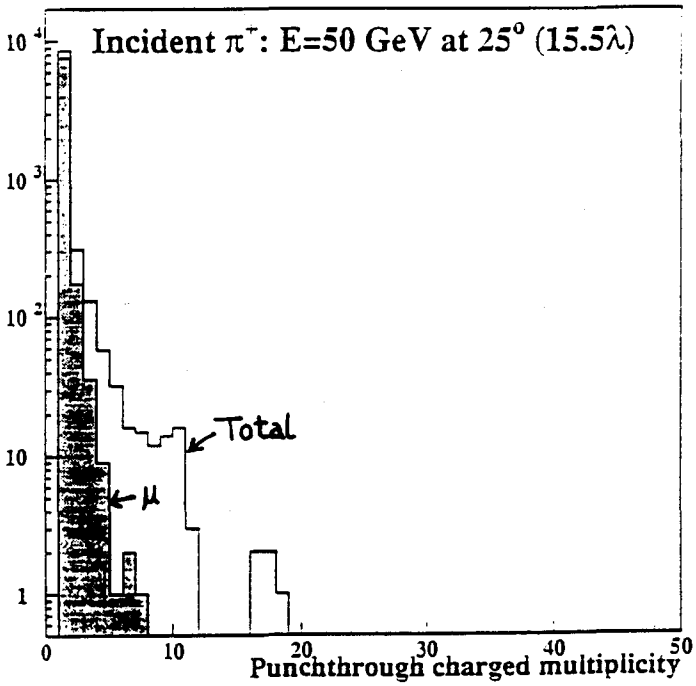
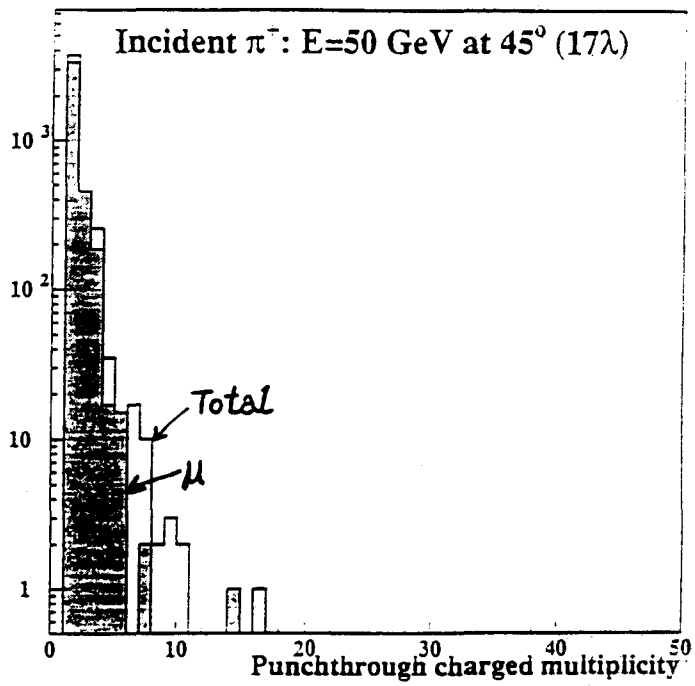
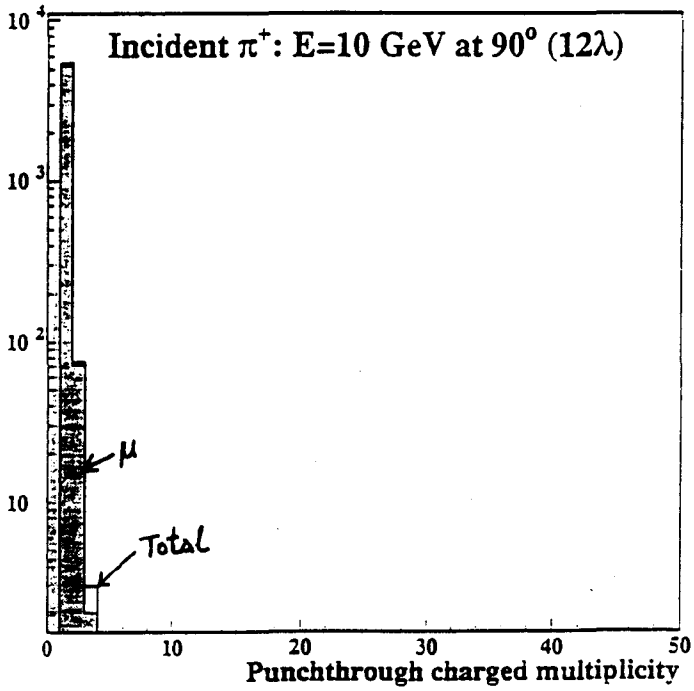


Fig. 4 Contine







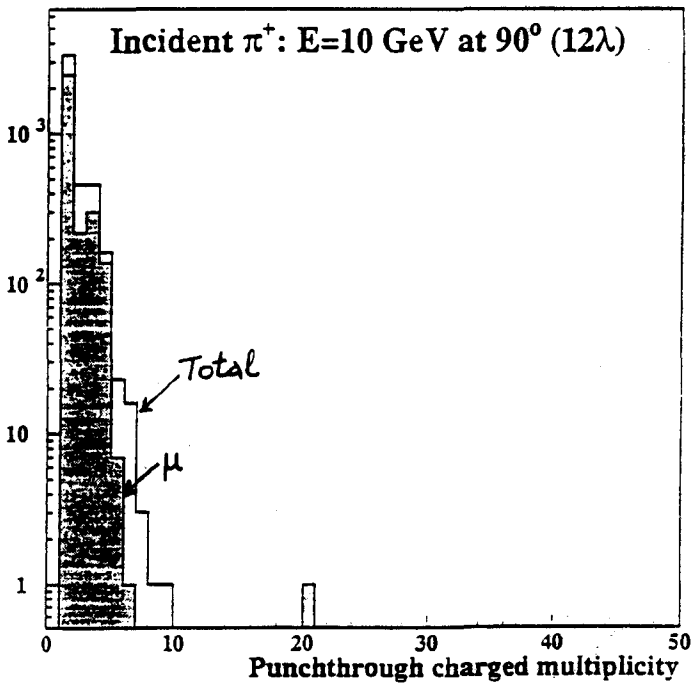
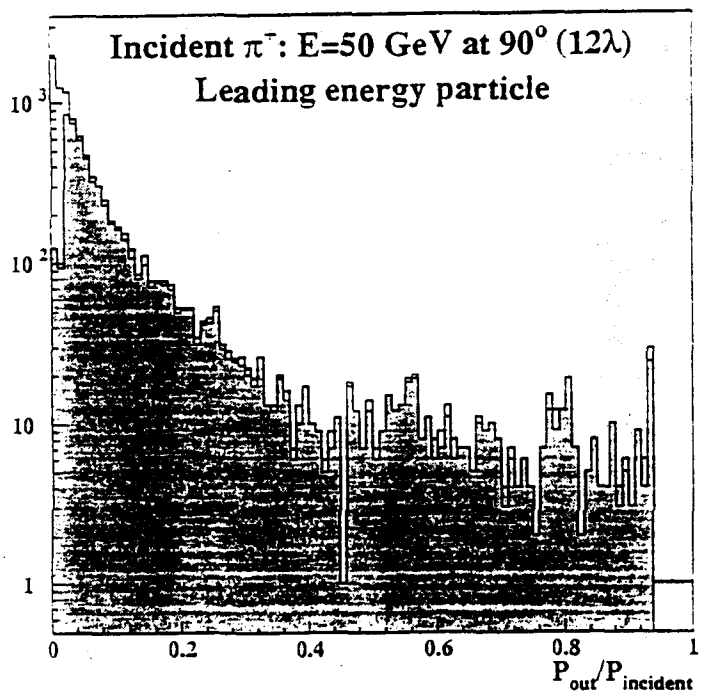
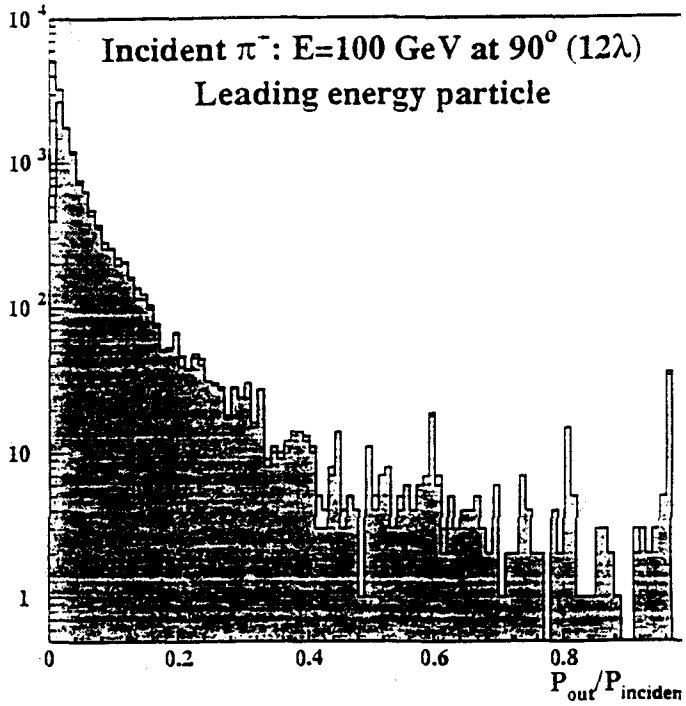
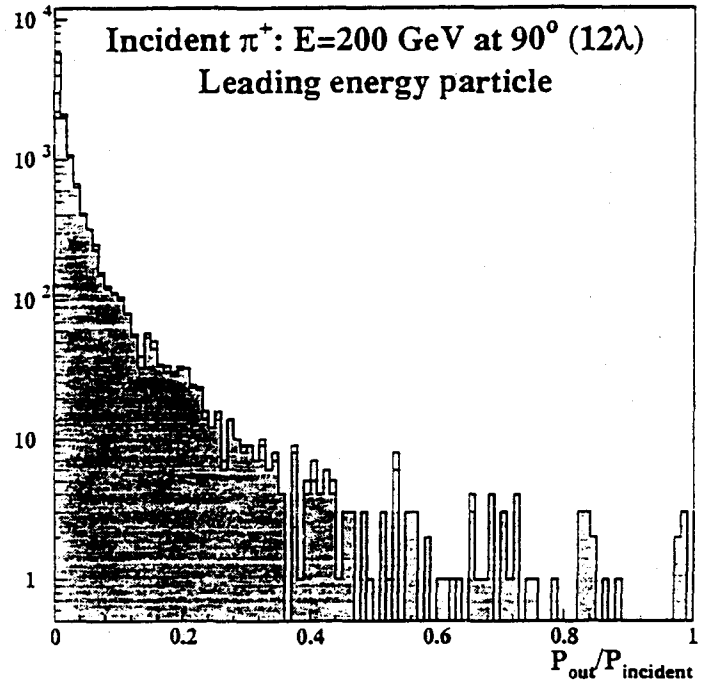


Fig. 4 Continue







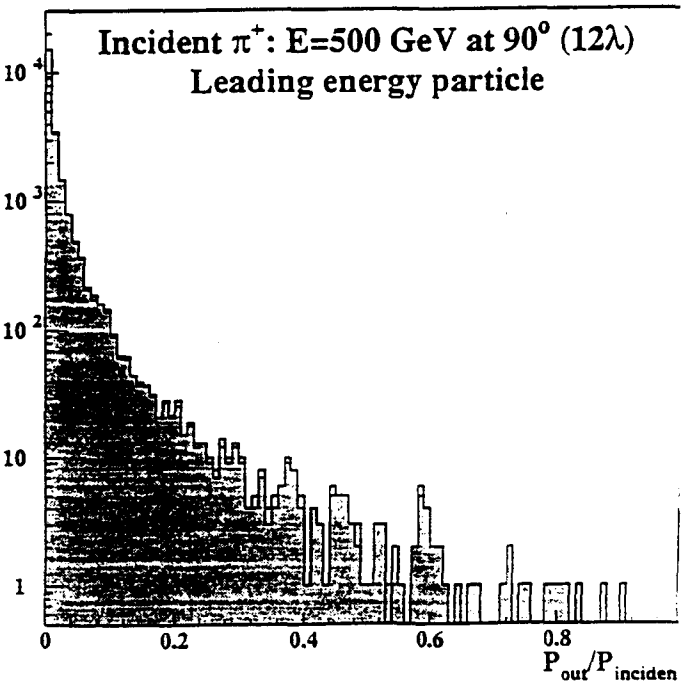
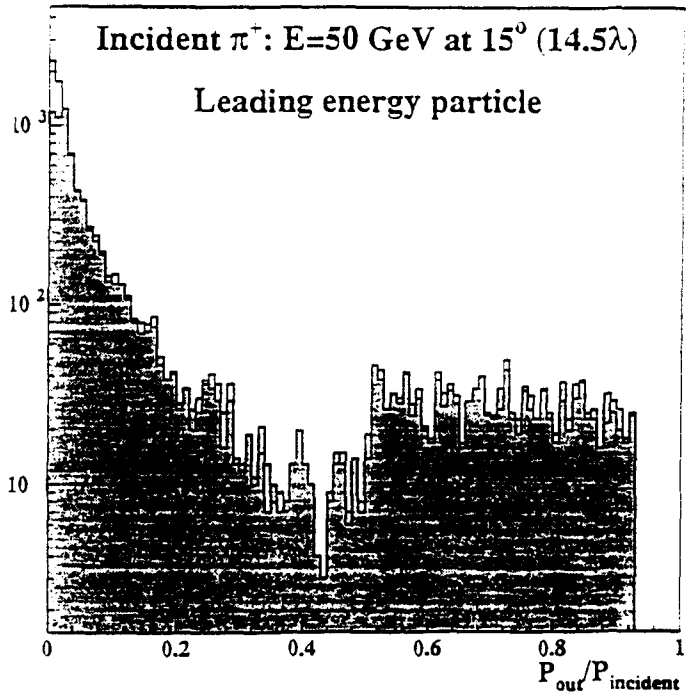
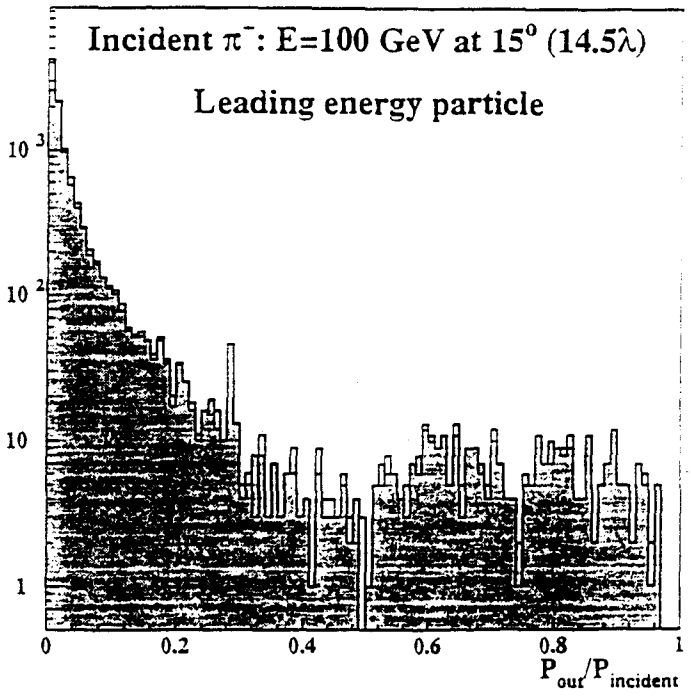
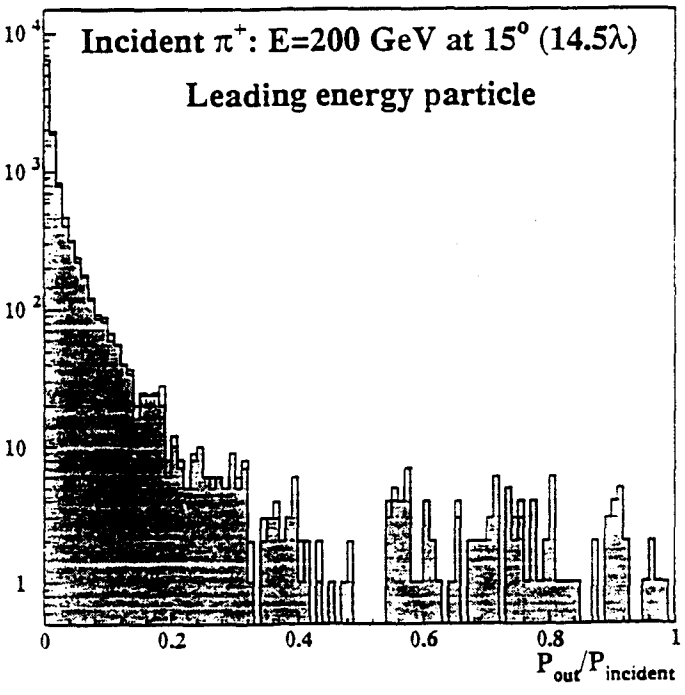


Figure 5 In total 12 figures show the normalized momentum spectrum of the leading energy punchthrough particle. Open histogram corresponds to the inner chamber spectrum, and shaded histogram corresponds to the outer chamber spectrum. The difference is due to the low energy particle looping inside the magnetic field.







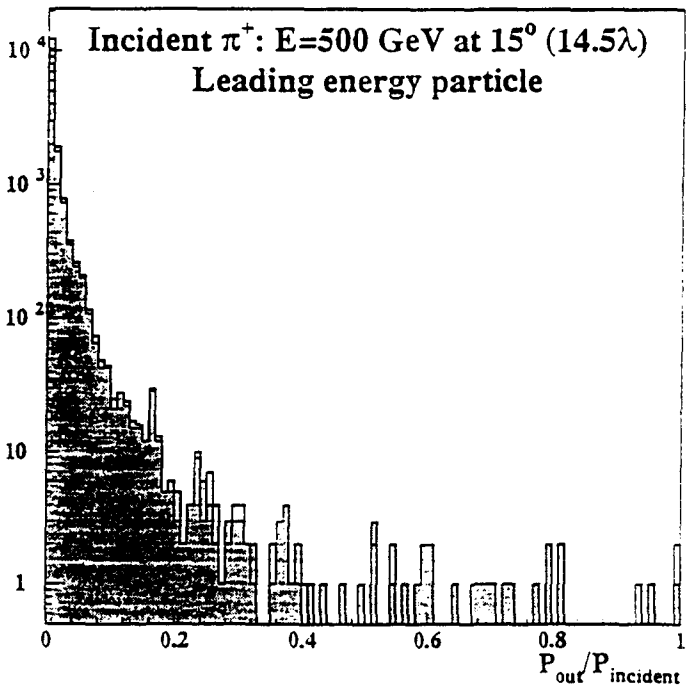
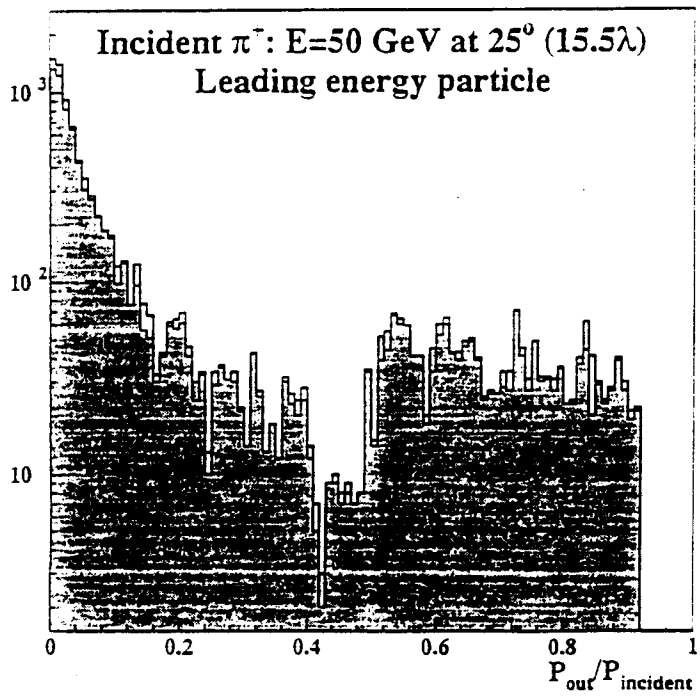
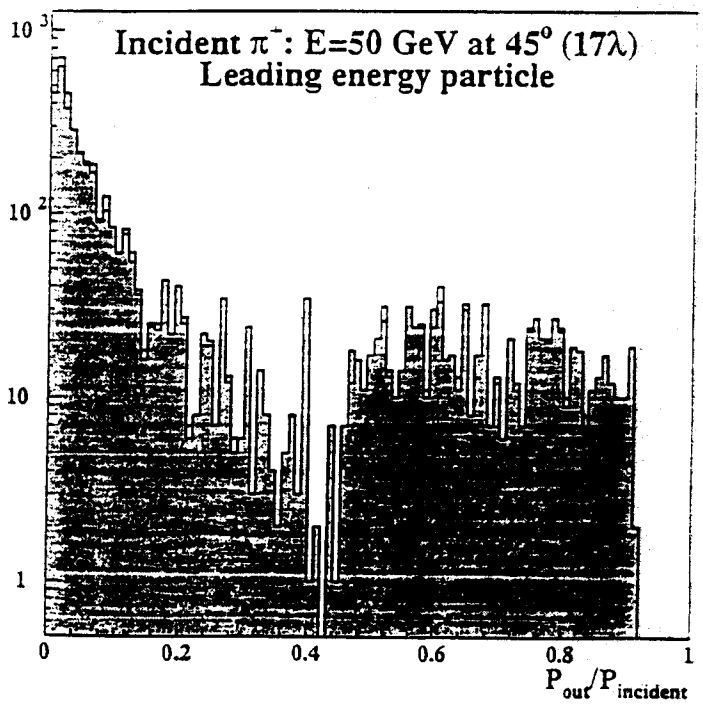
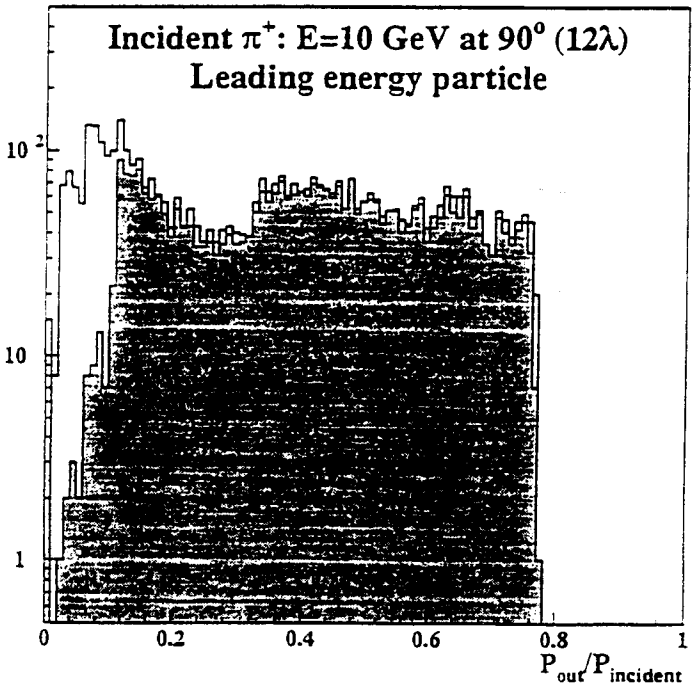


Fig. 5 Continue







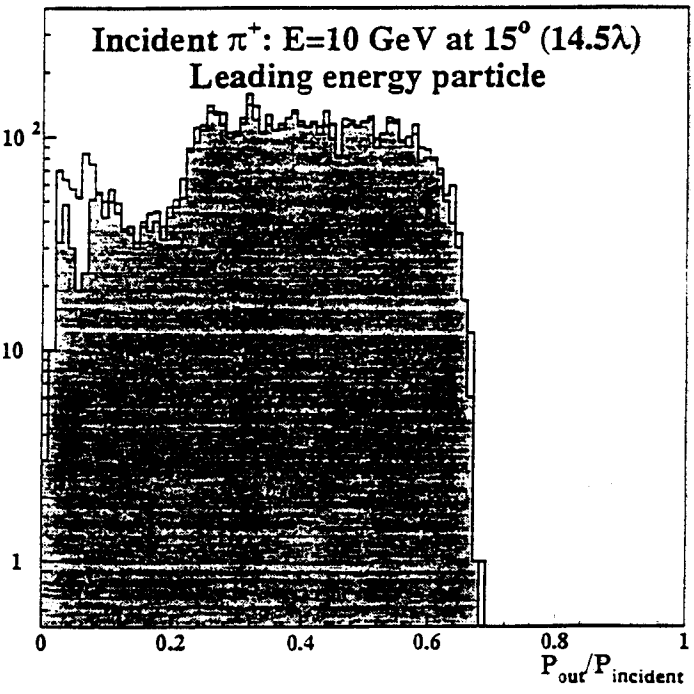
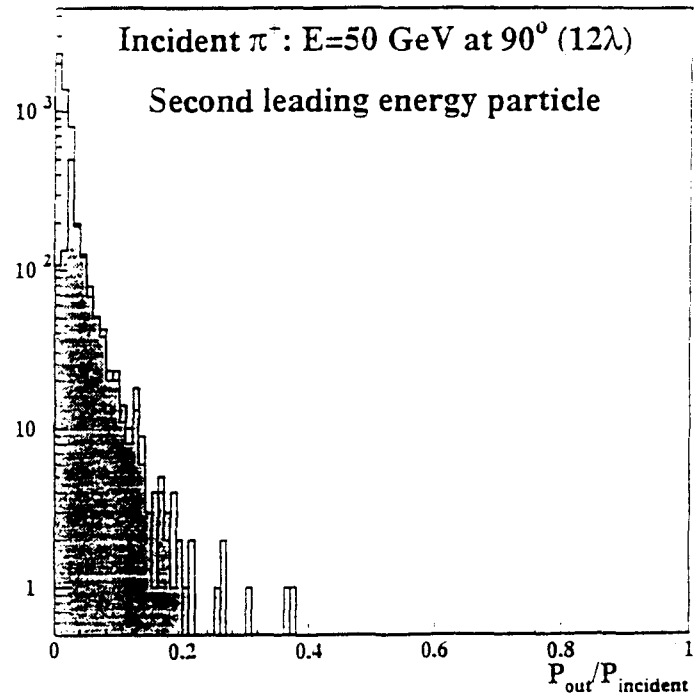
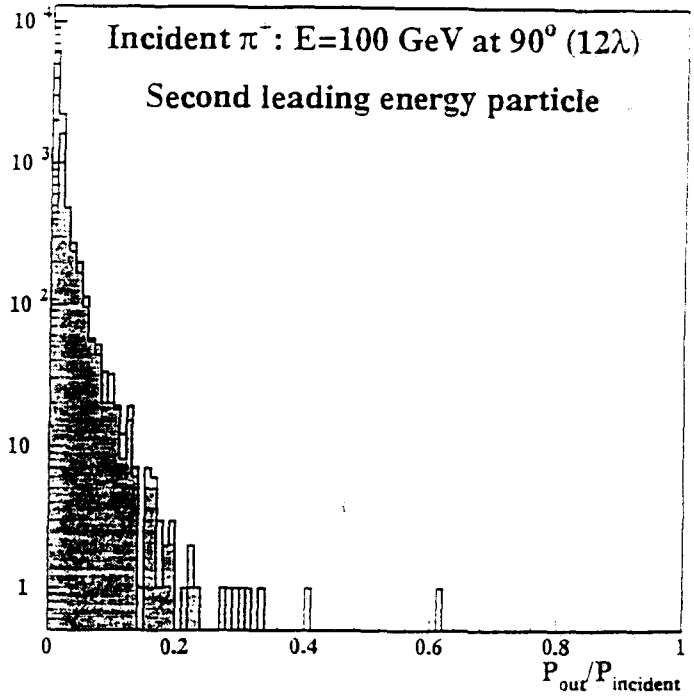
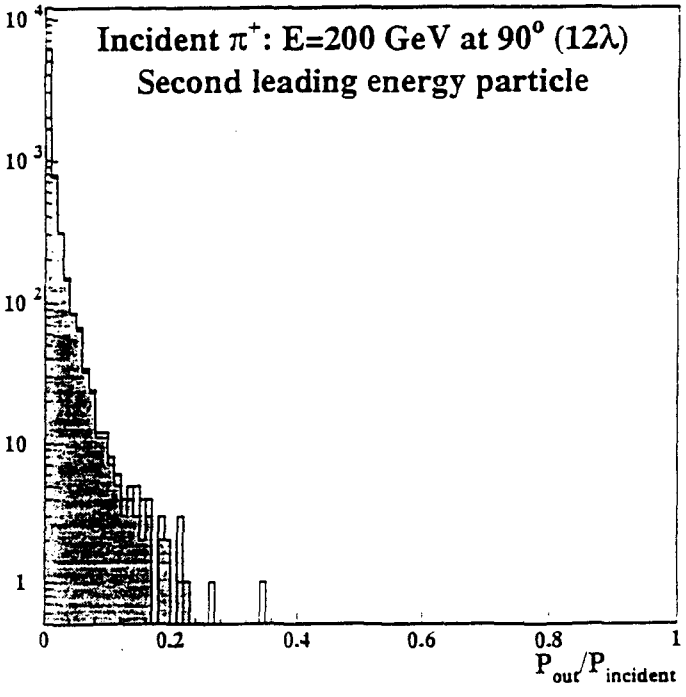


Fig. 5 Continue







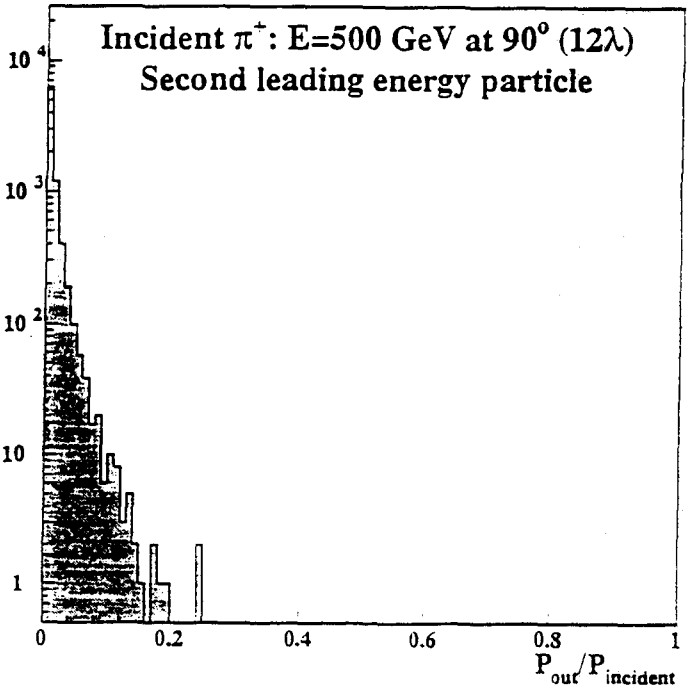
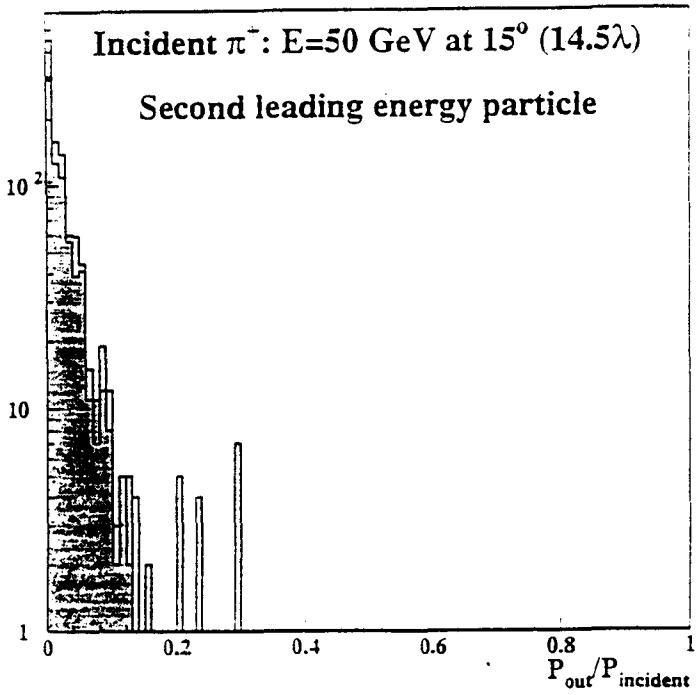
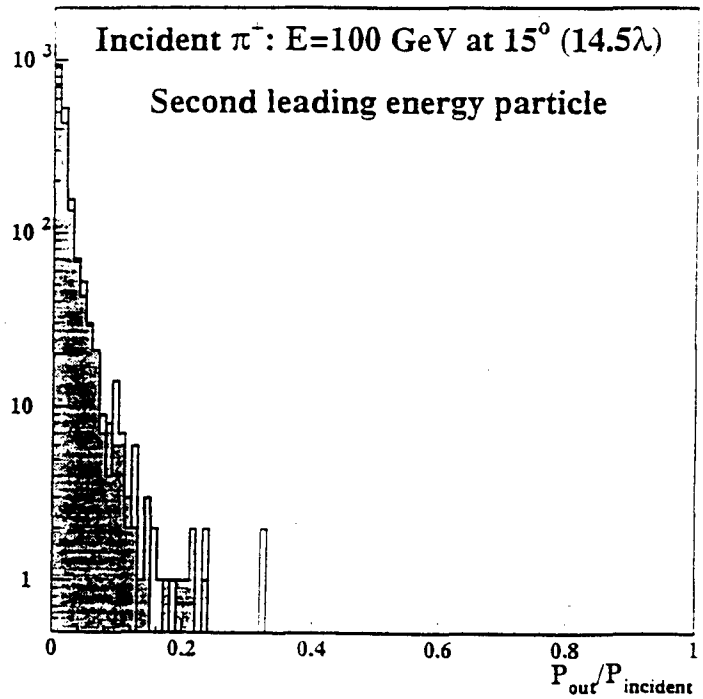
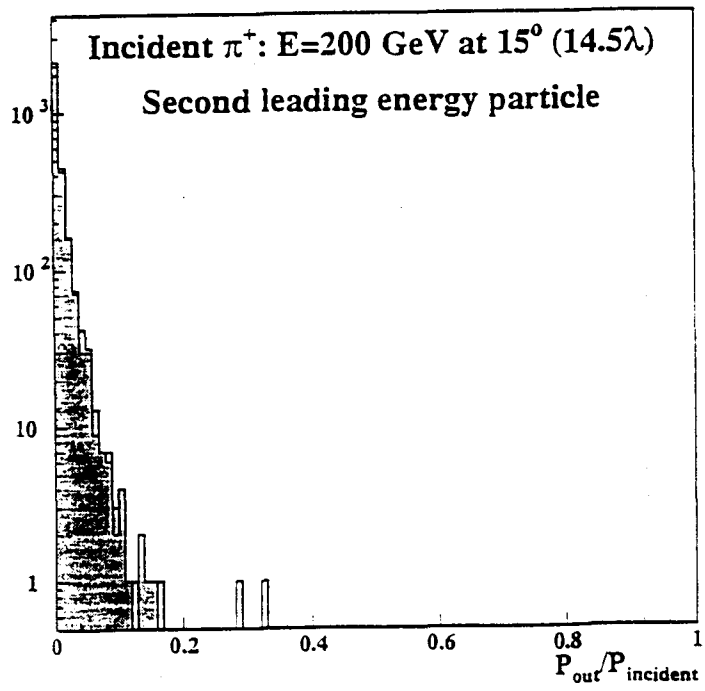


Figure 6 In total 12 figures show the normalized momentum spectrum of the second leading energy punchthrough particle. Open histogram corresponds to the inner chamber spectrum, and shaded histogram corresponds to the outer chamber spectrum. The difference is due to the low energy particle looping inside the magnetic field.







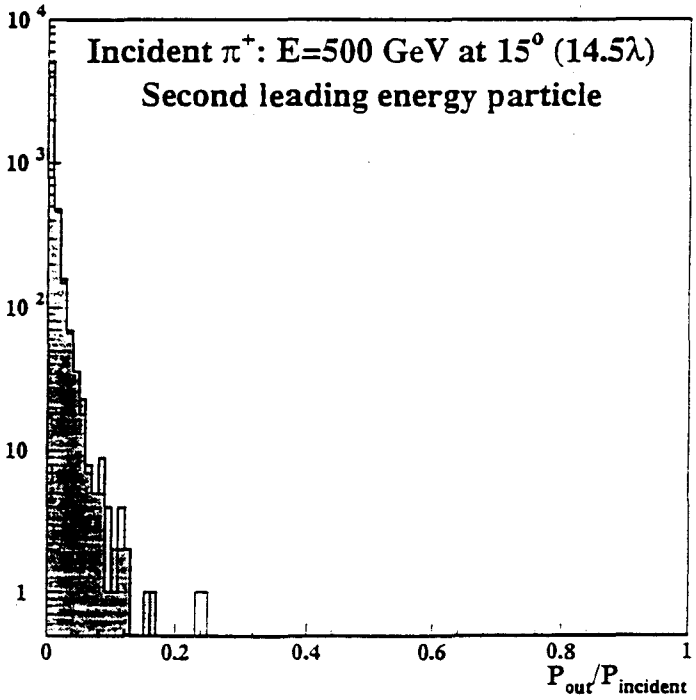
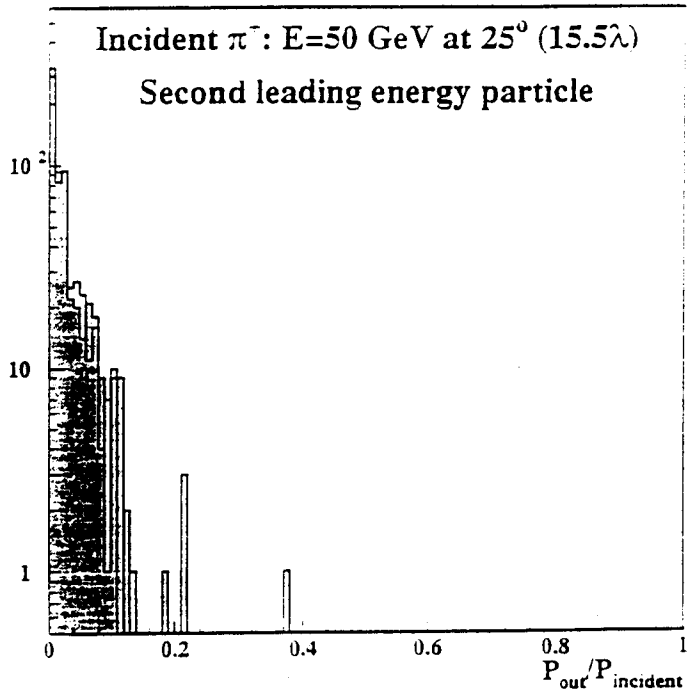
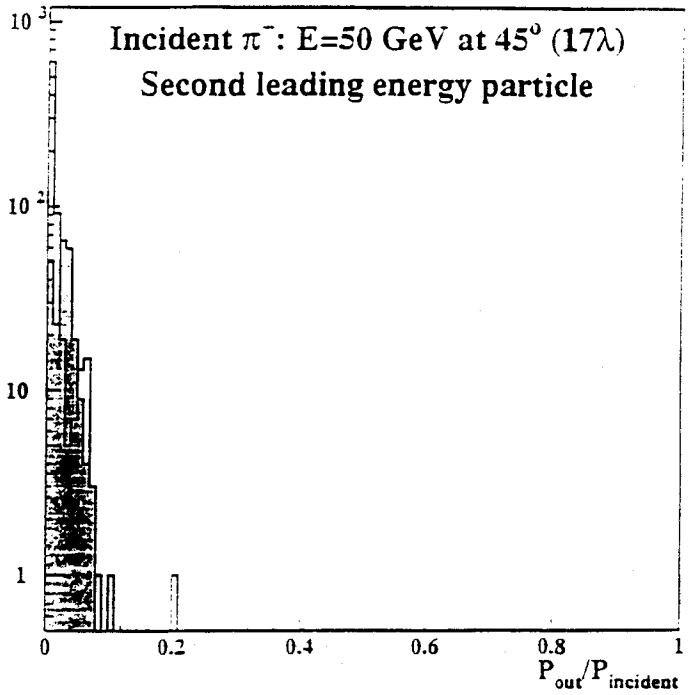
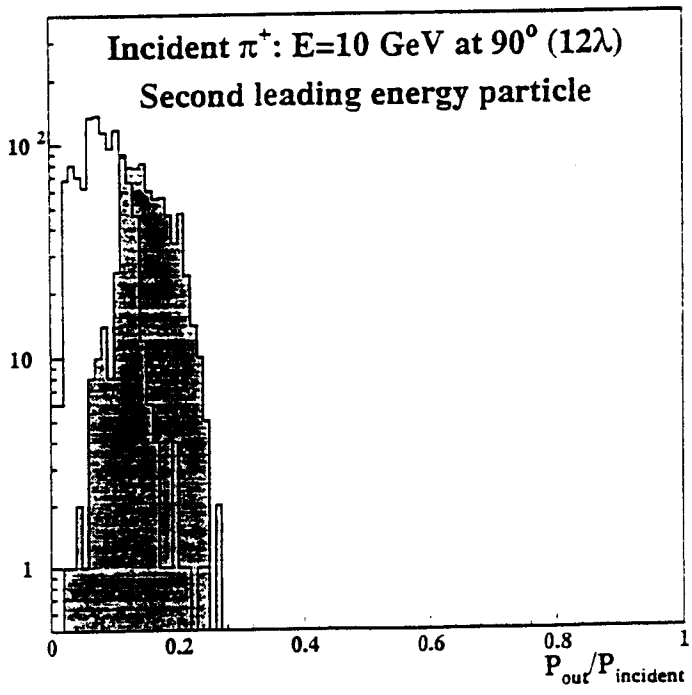


Fig. 6 continue







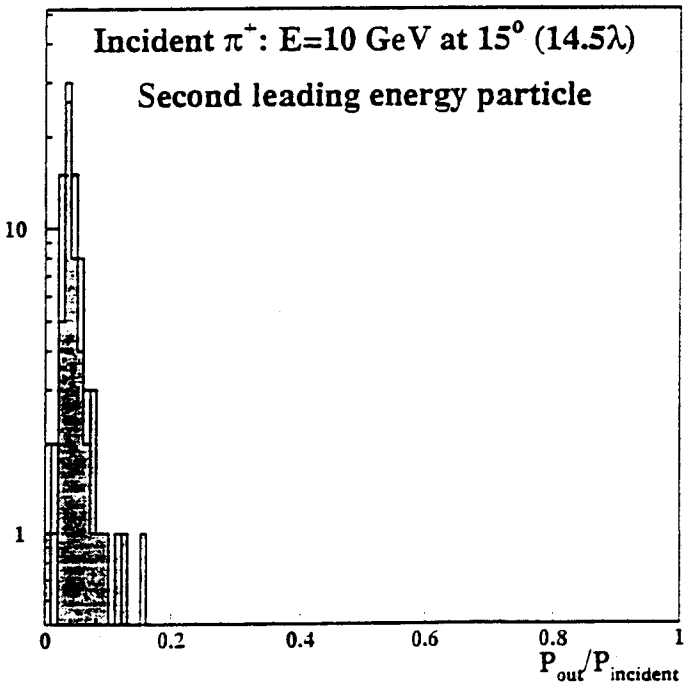
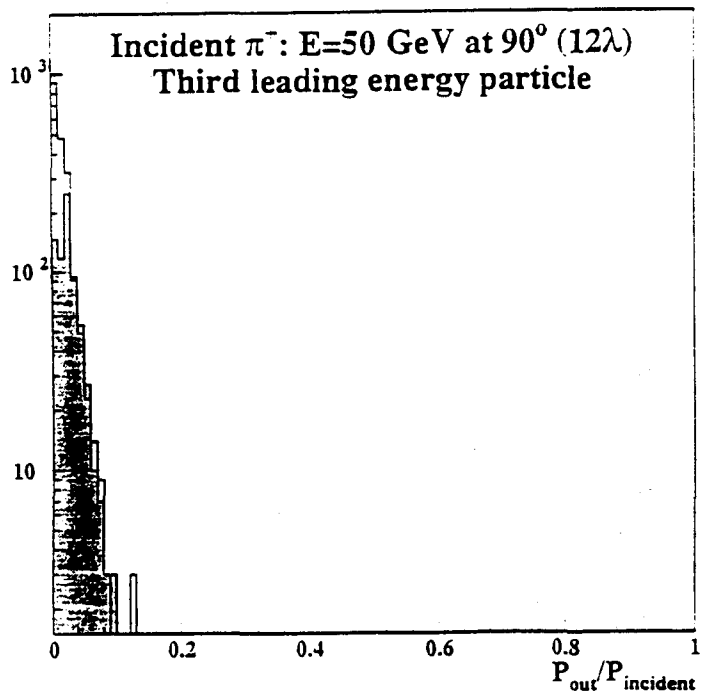
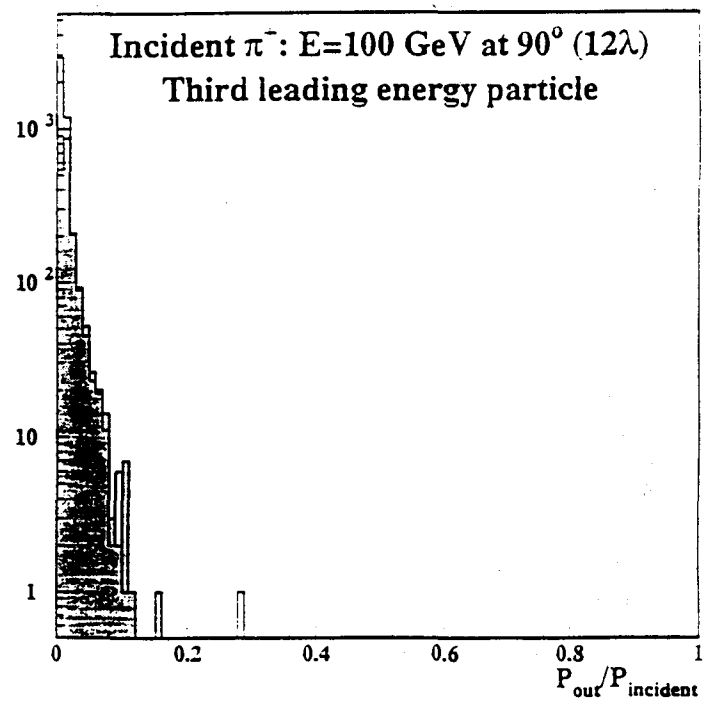
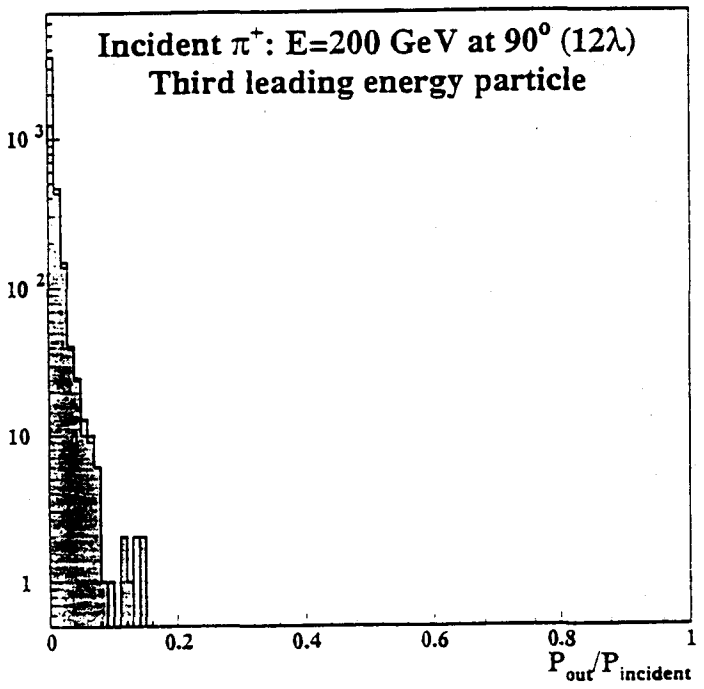


Fig. 6 continue







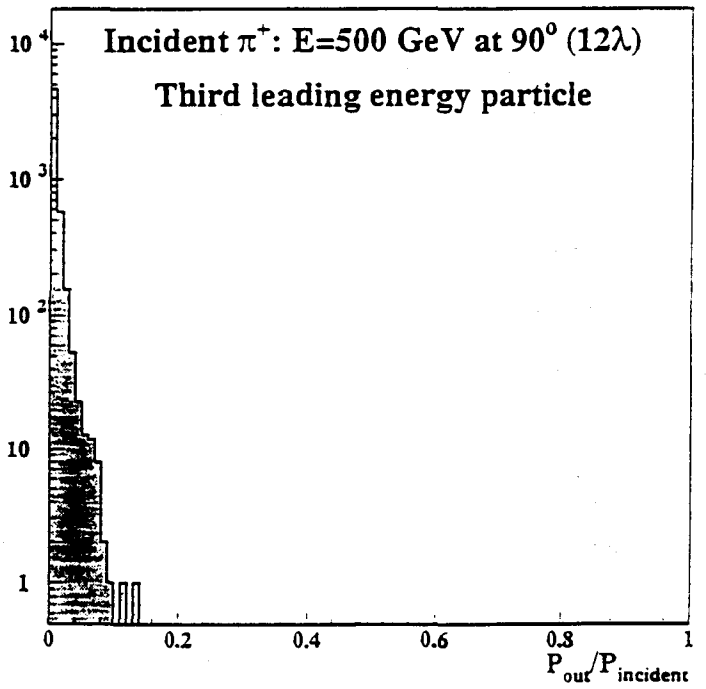
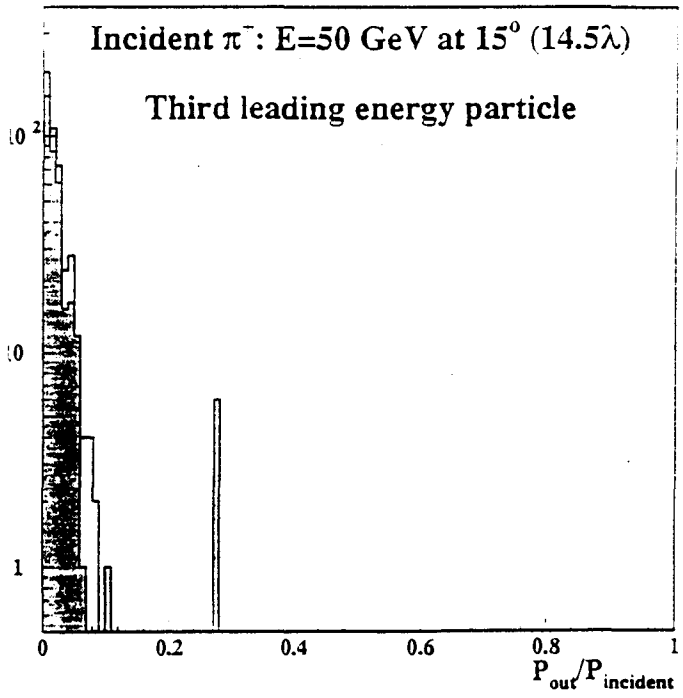
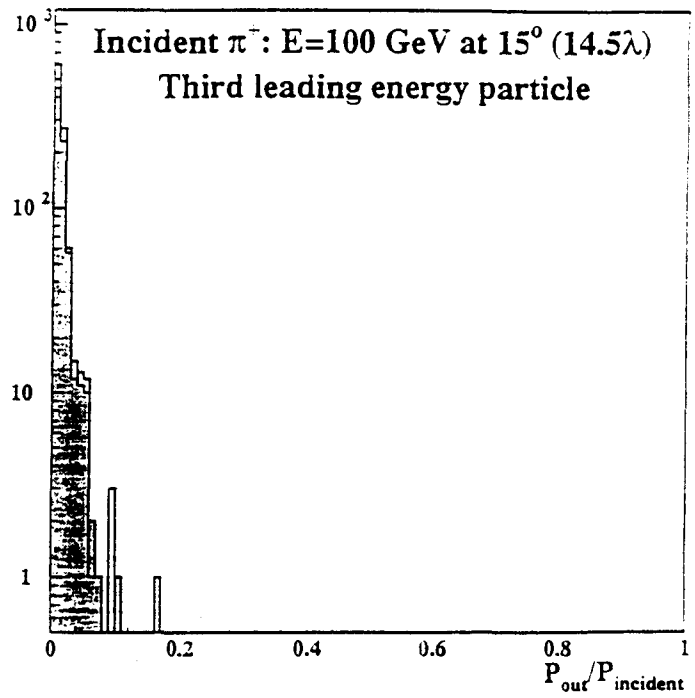
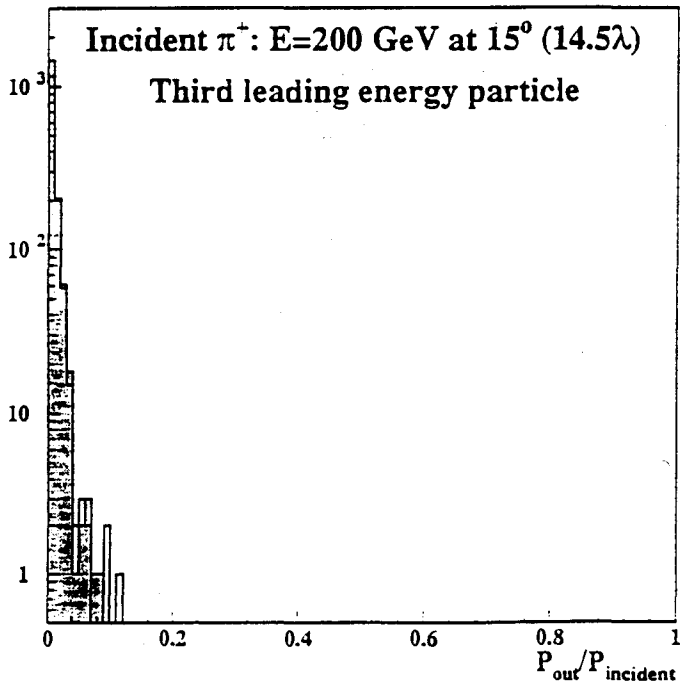


Figure 7 In total 12 figures show the normalized momentum spectrum of the third leading energy punchthrough particle. Open histogram corresponds to the inner chamber spectrum, and shaded histogram corresponds to the outer chamber spectrum. The difference is due to the low energy particle looping inside the magnetic field.







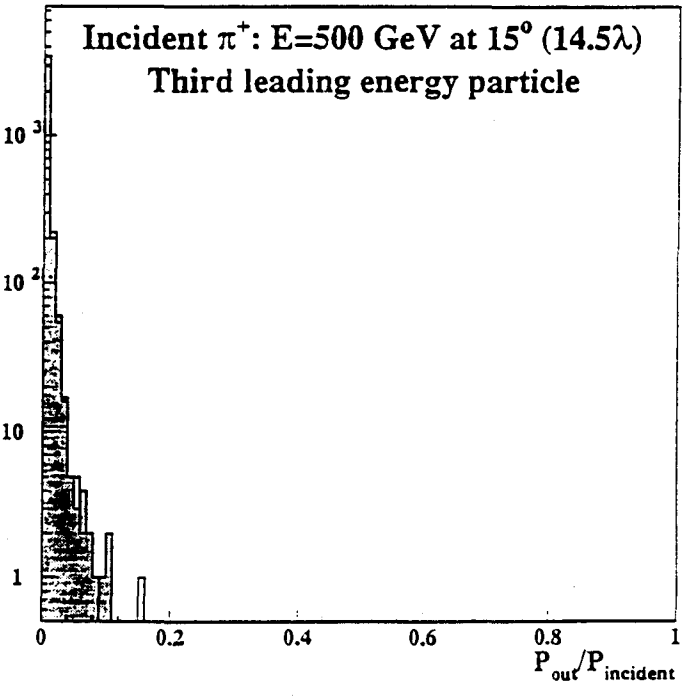
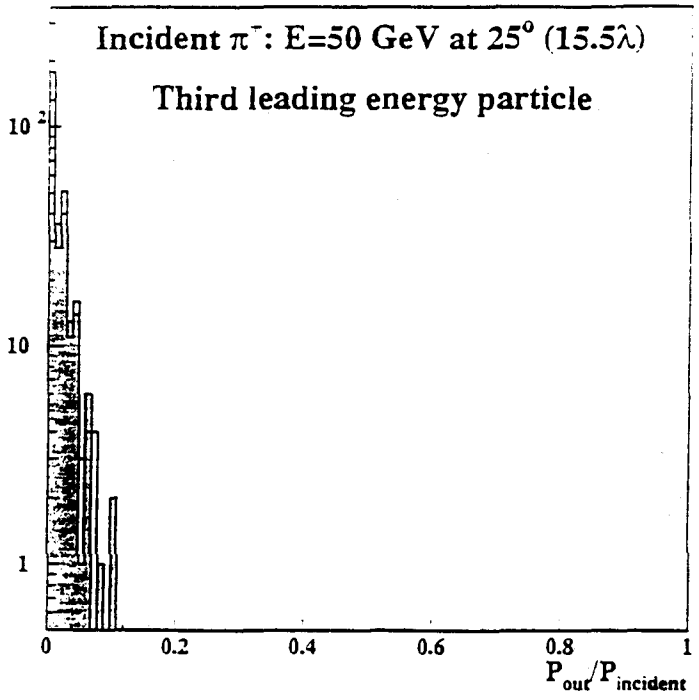
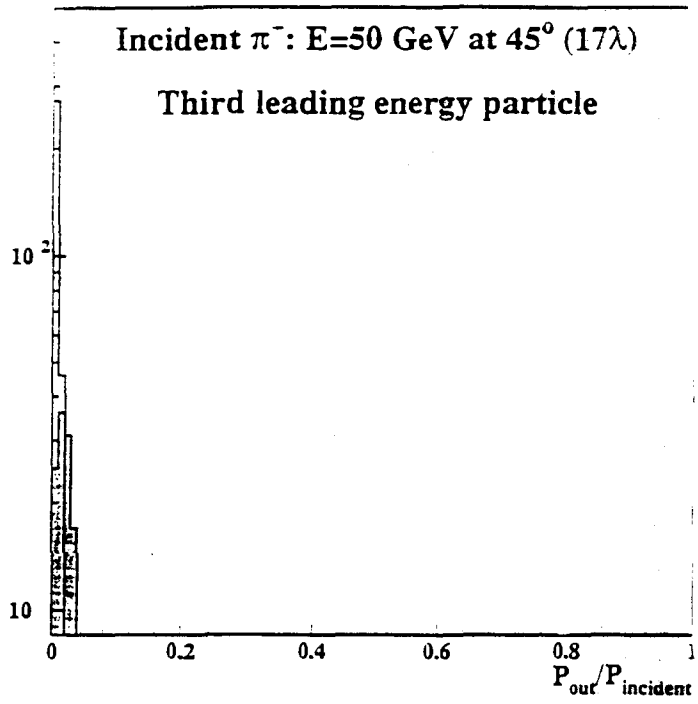
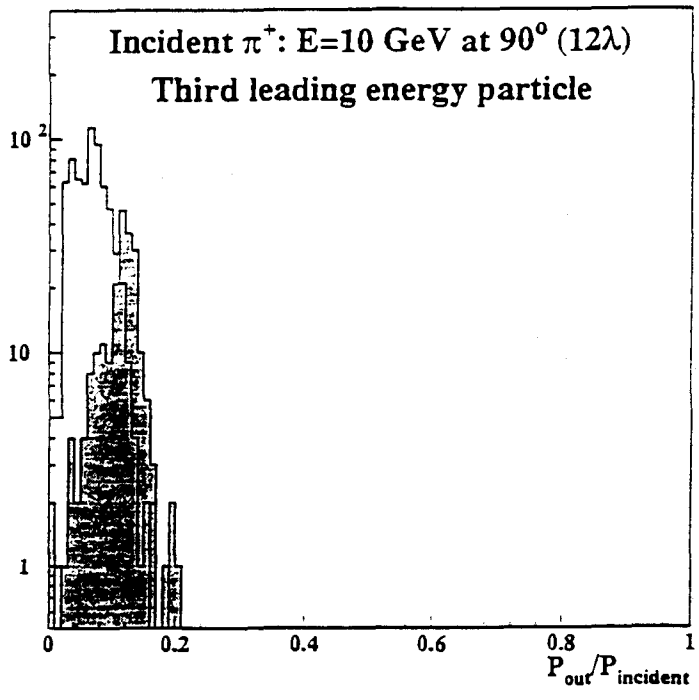


Fig. 7 continue







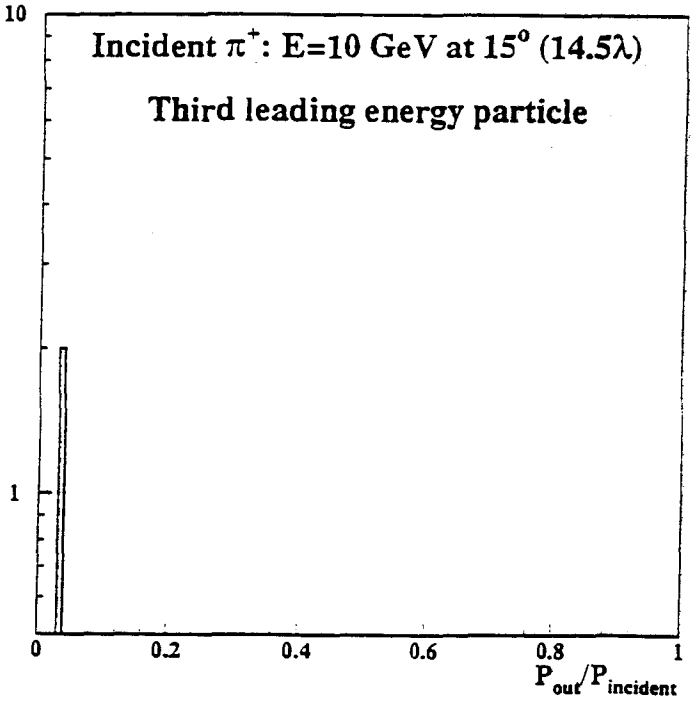
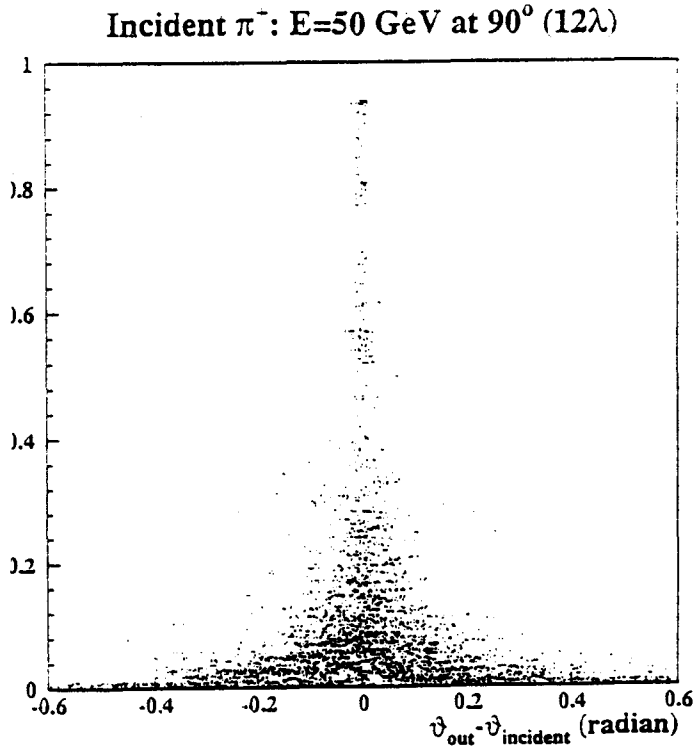
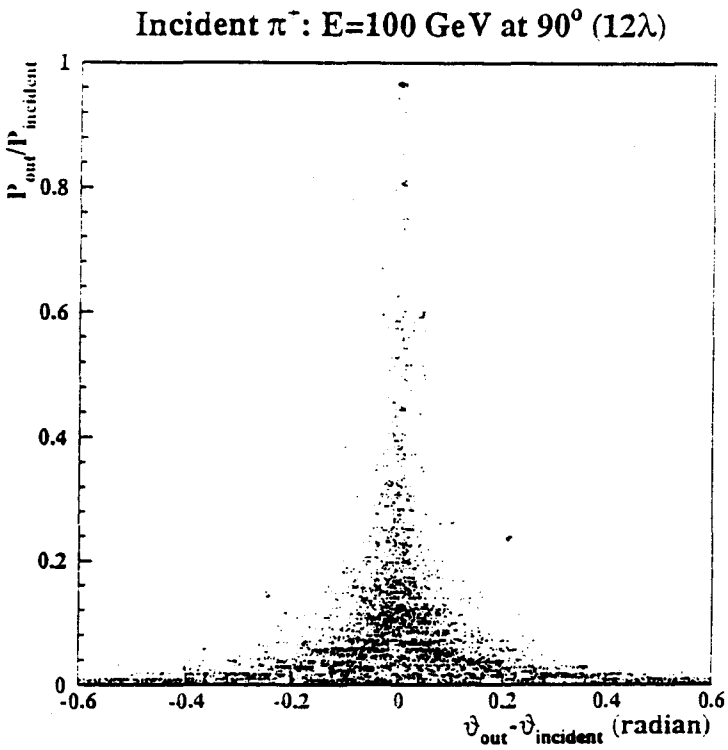
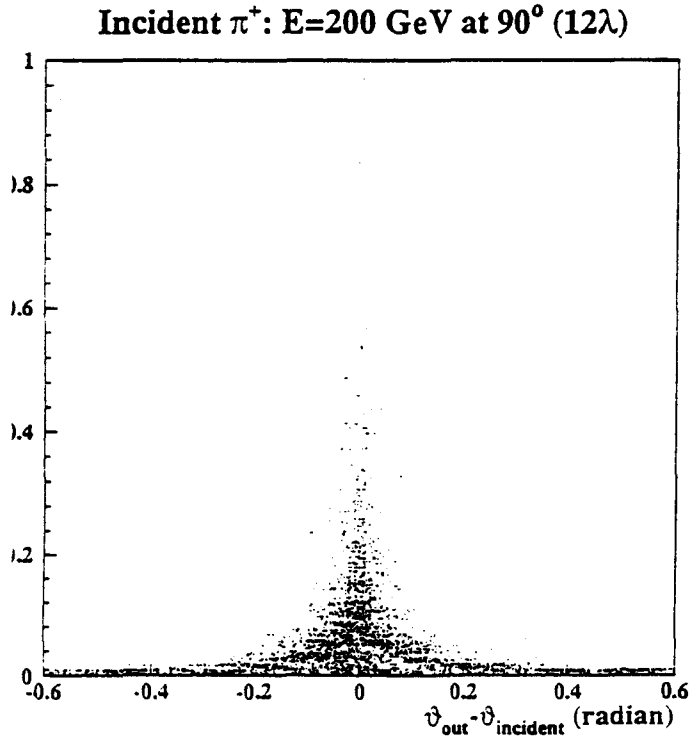


Fig. 7 continue







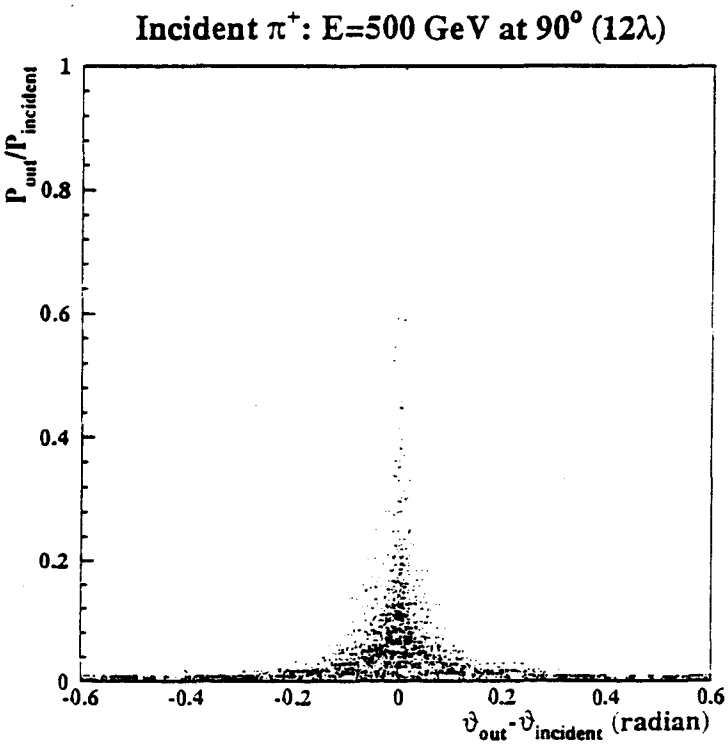
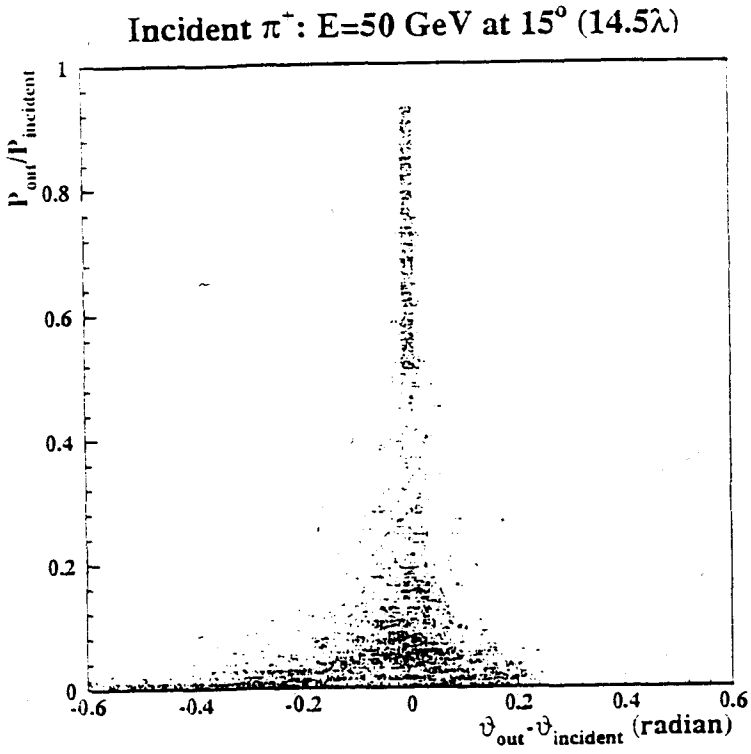
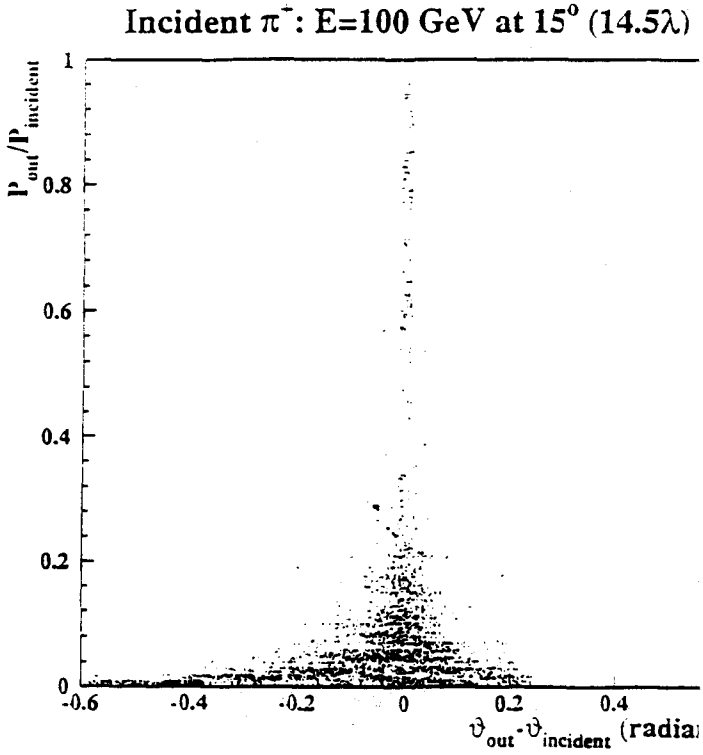
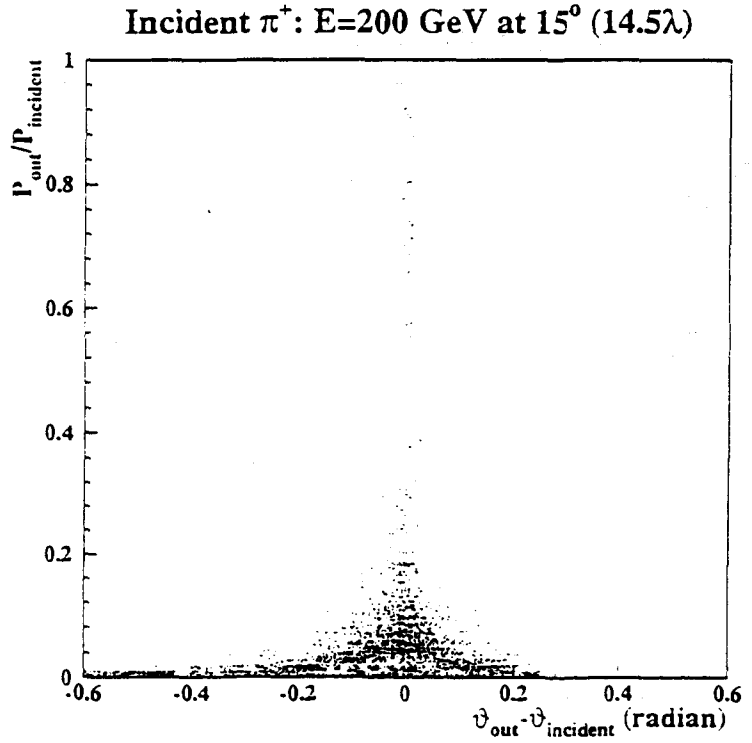


Figure 8 In total 12 figures show the punchthrough particle angular spread correlated to the normalized momentum.







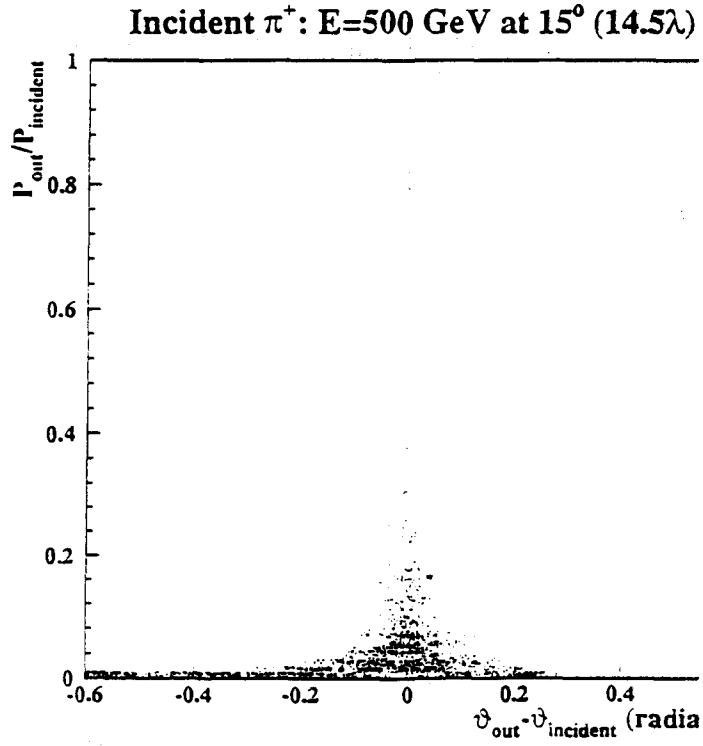
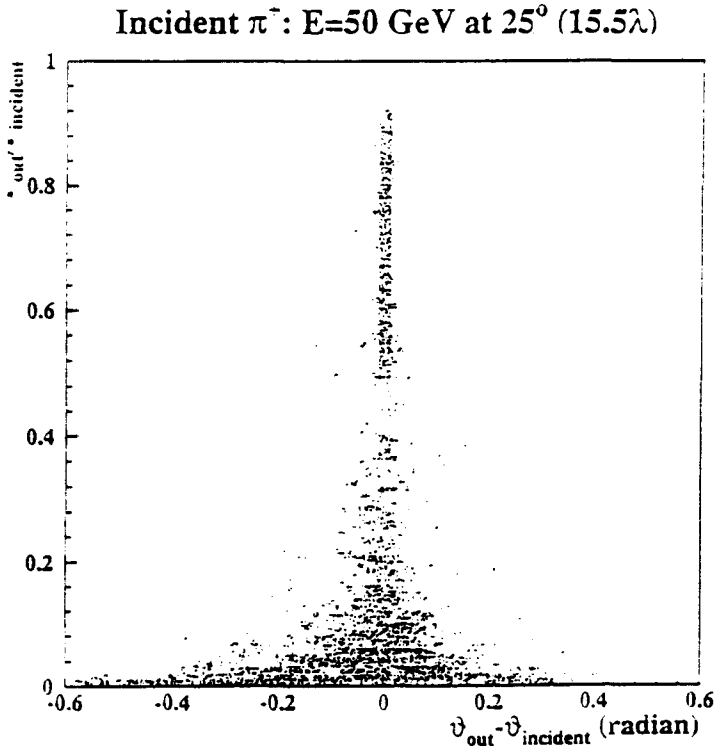
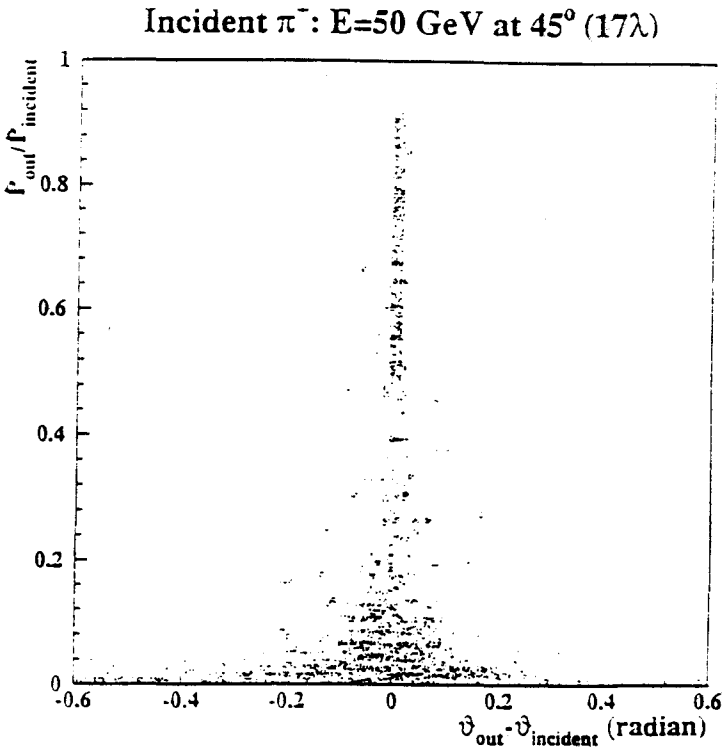
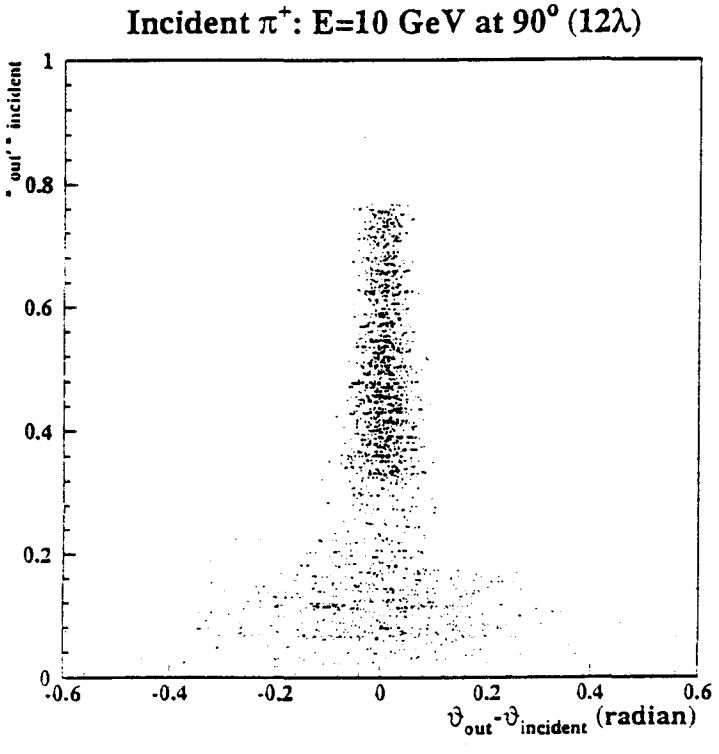


Fig. 8 continue







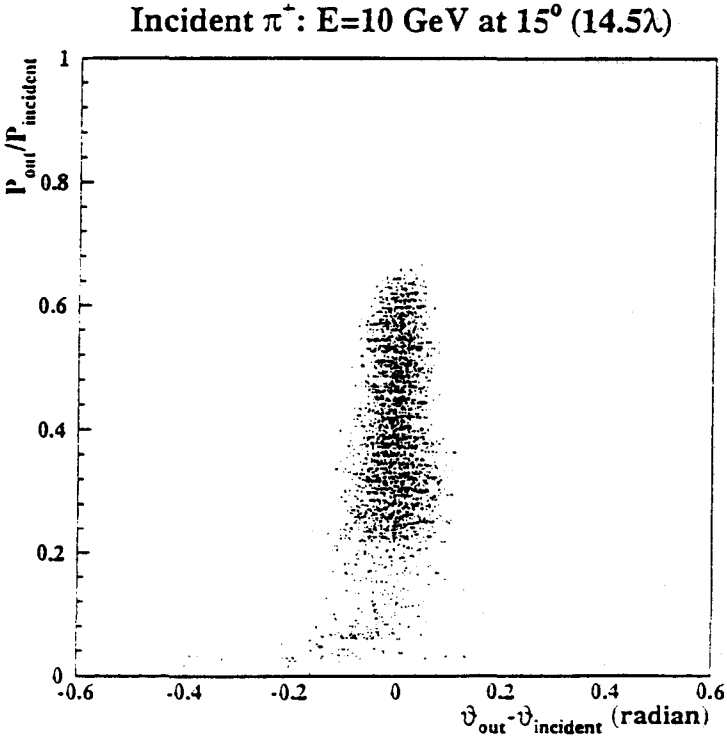
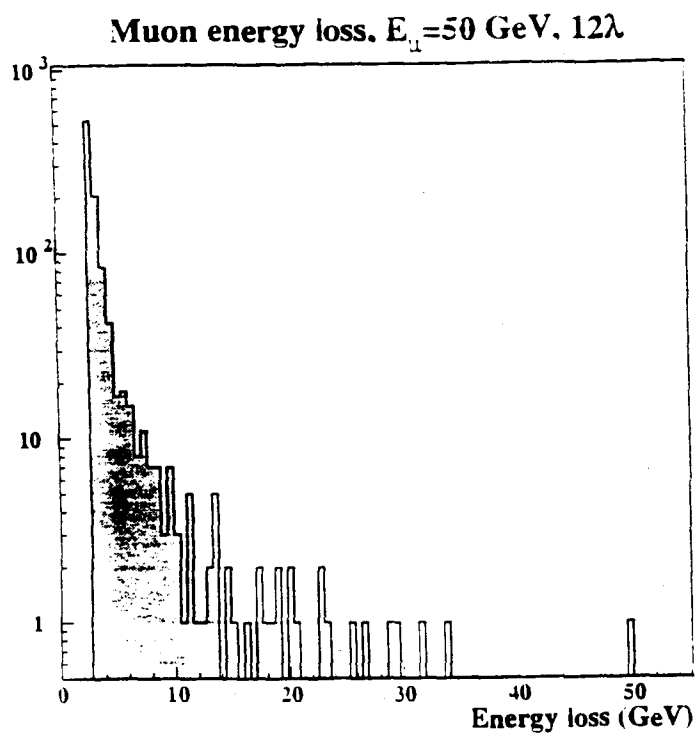
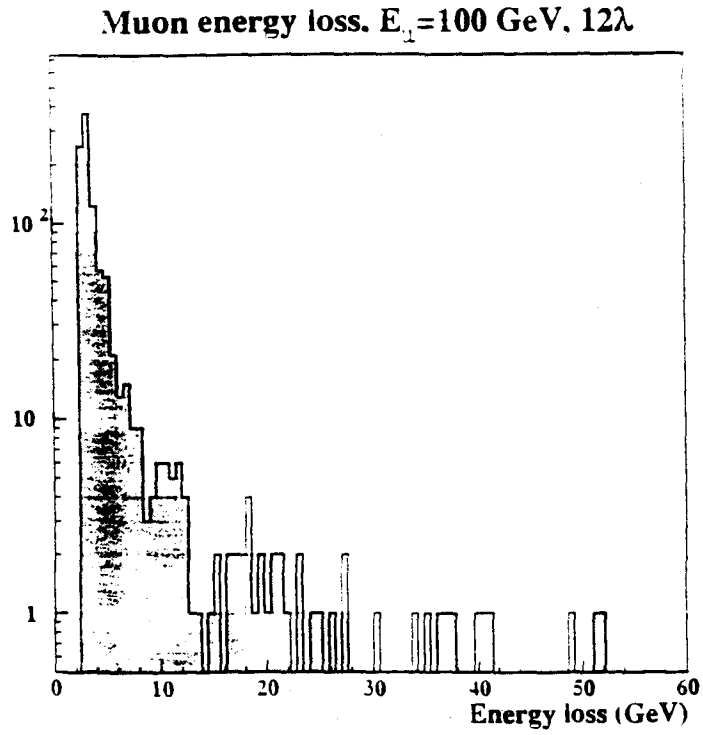
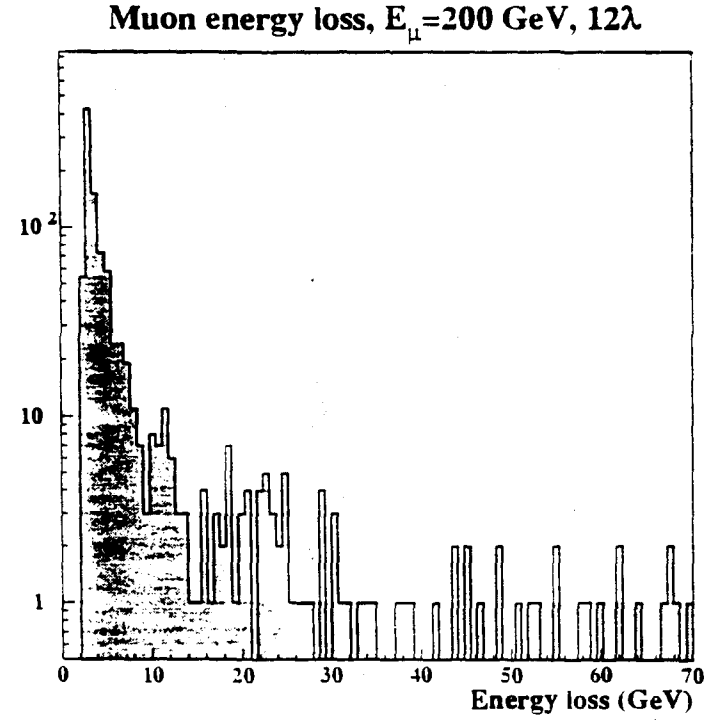


Fig. 8 continue







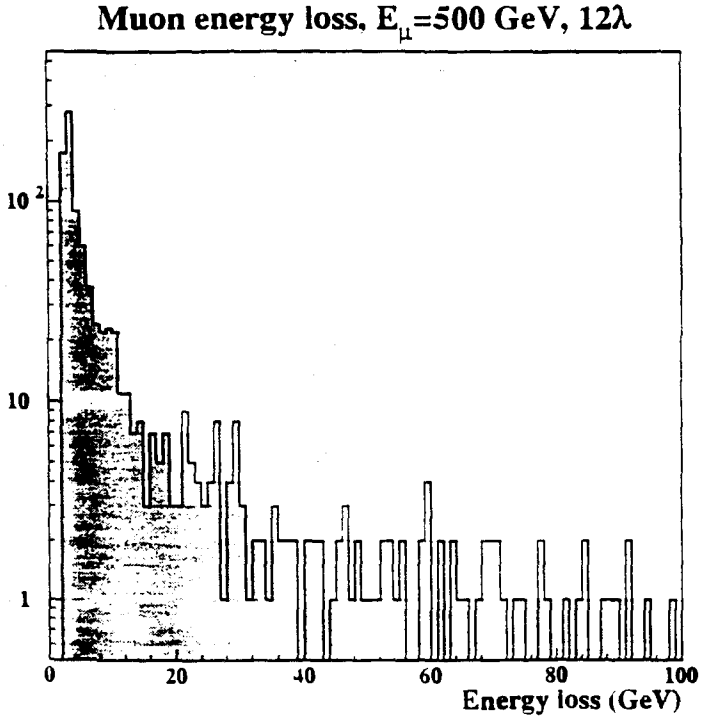
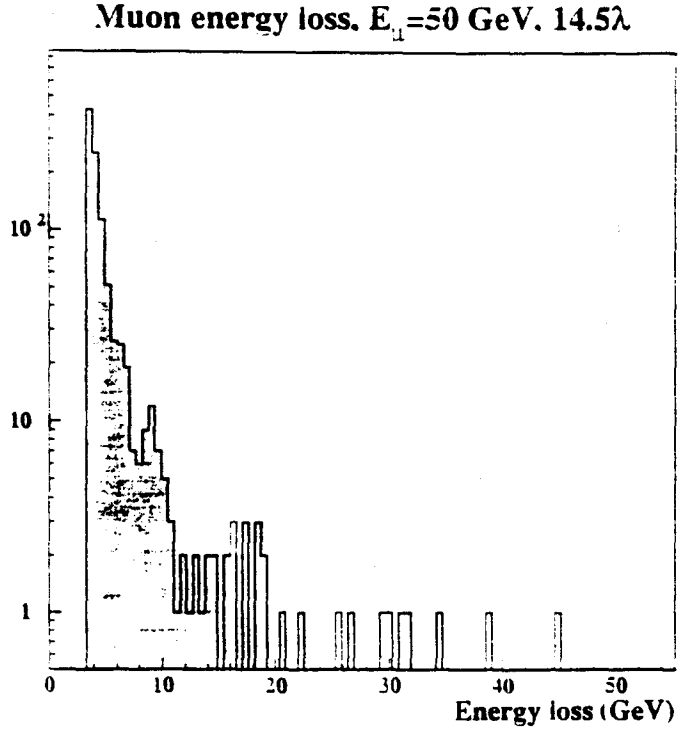
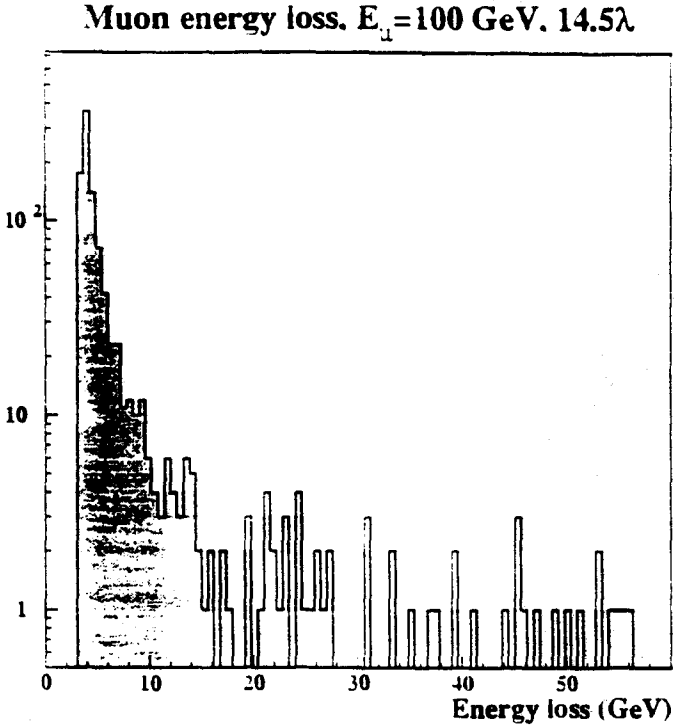
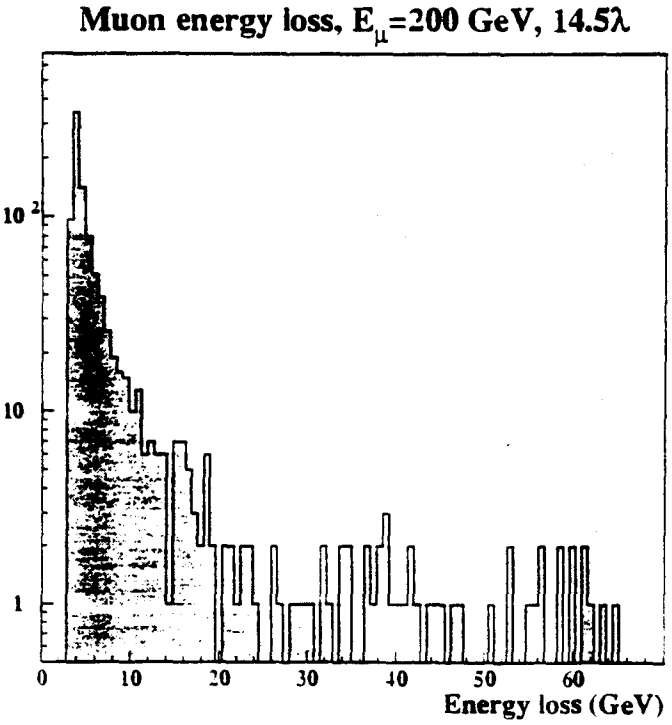


Figure 9 In total 12 figures show the muon energy loss distributions for differnt muon energies and absorber thicknesses.







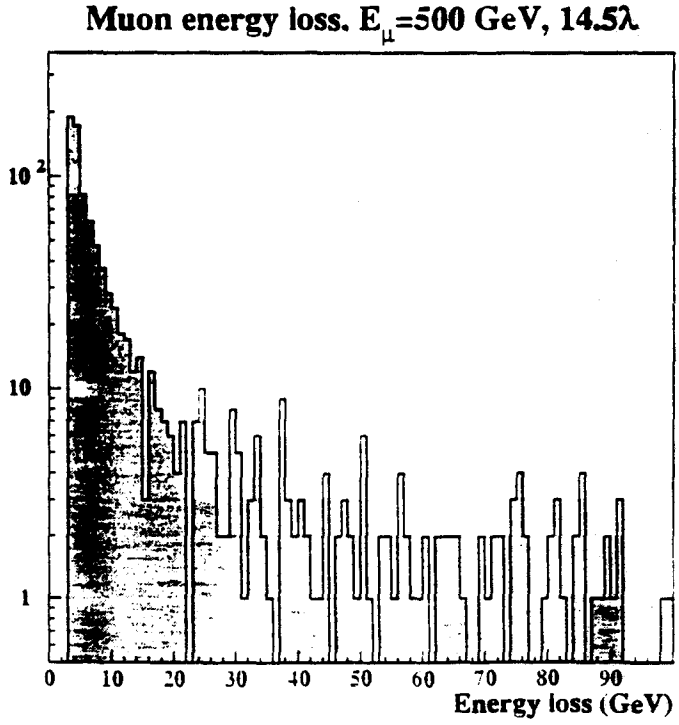
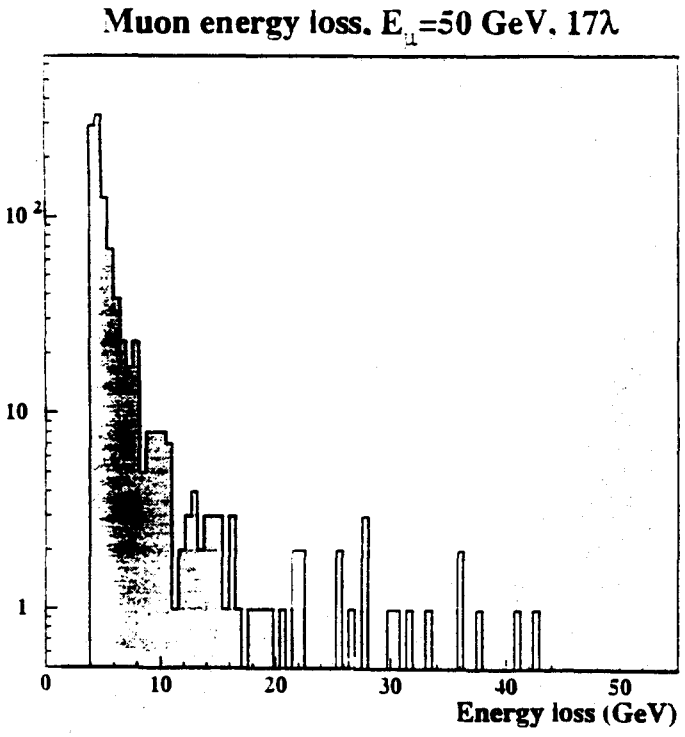
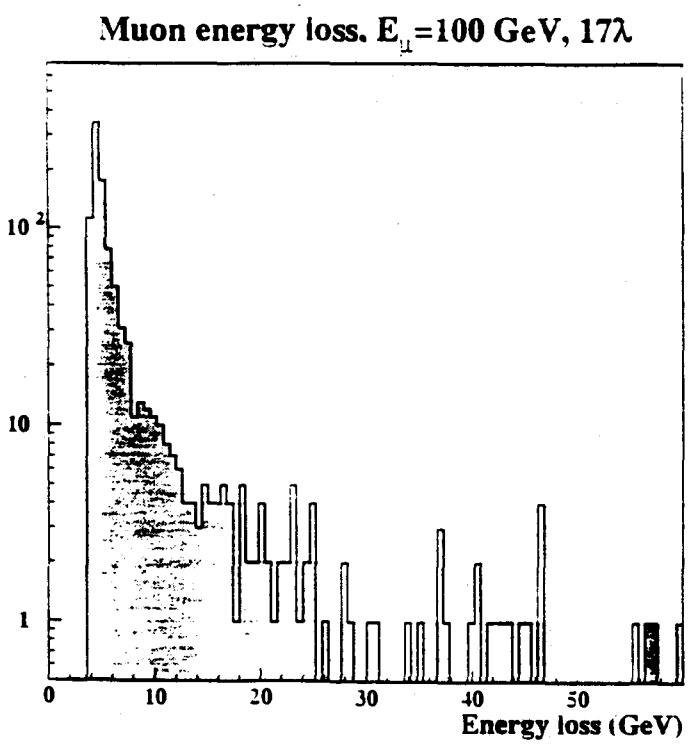
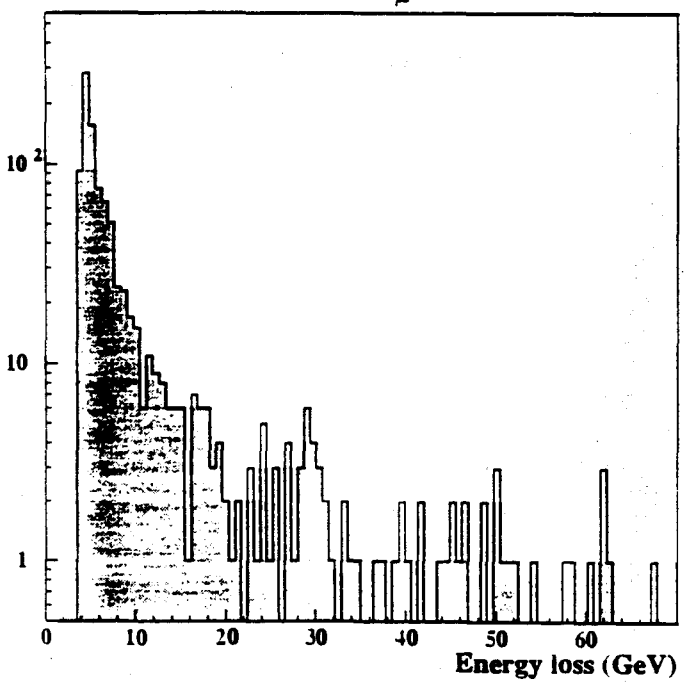


Fig. 9 Continue







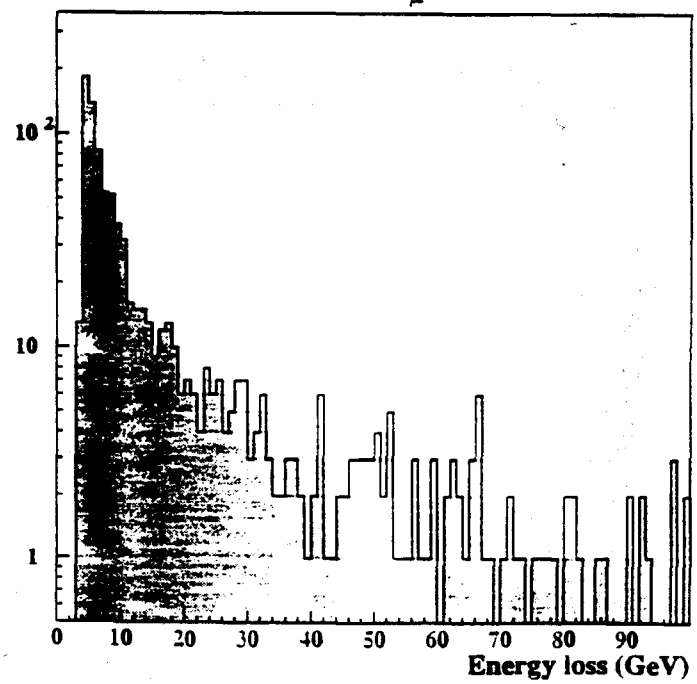


Fig. 9 continue

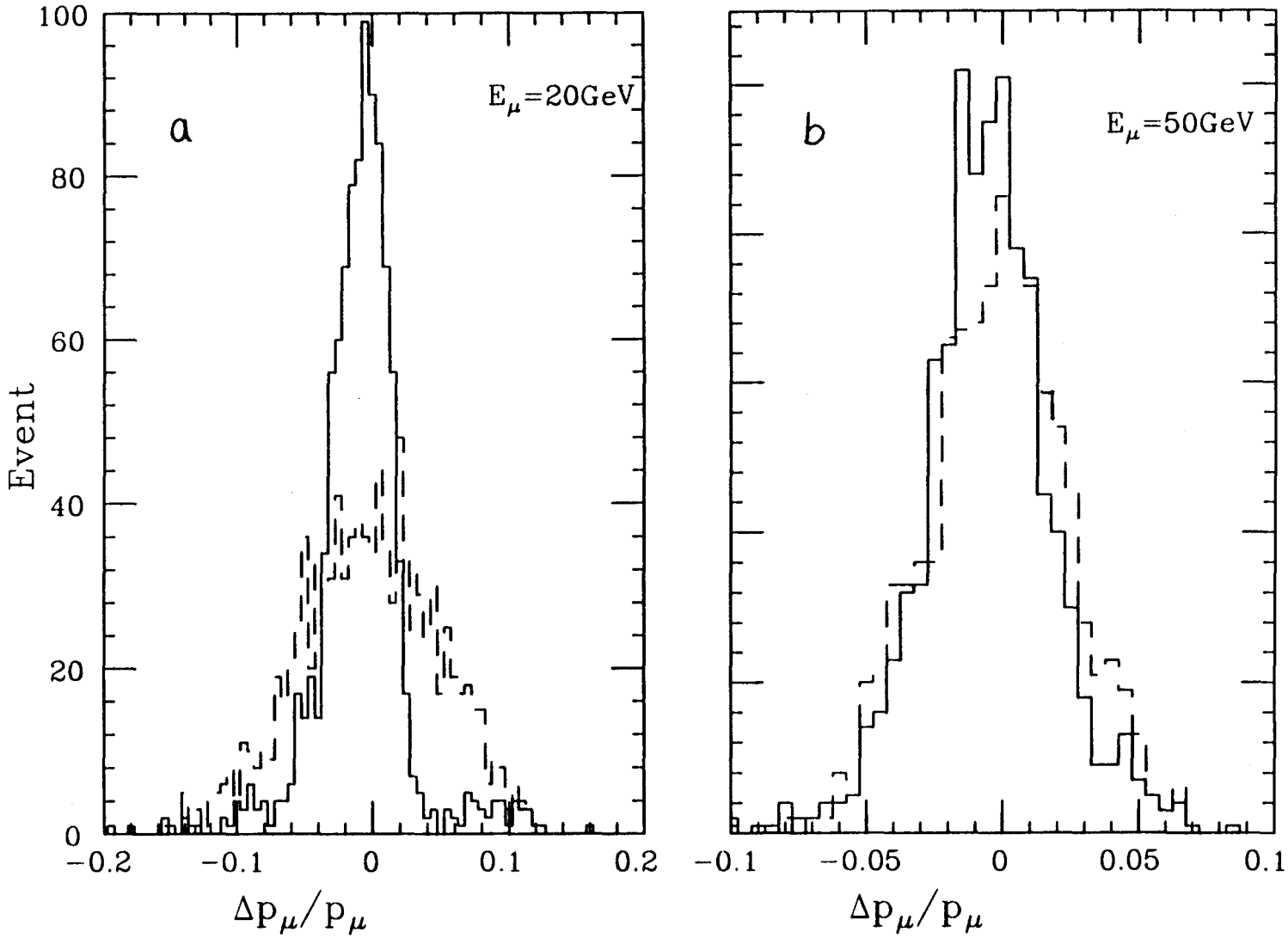


Figure 10 Muon energy resolution distributions for 20 GeV and 50 GeV muons. Solid histograms were obtained using the method described in section 3.2. Dashed histograms were obtained by adding energy loss measured in the calorimeters only.

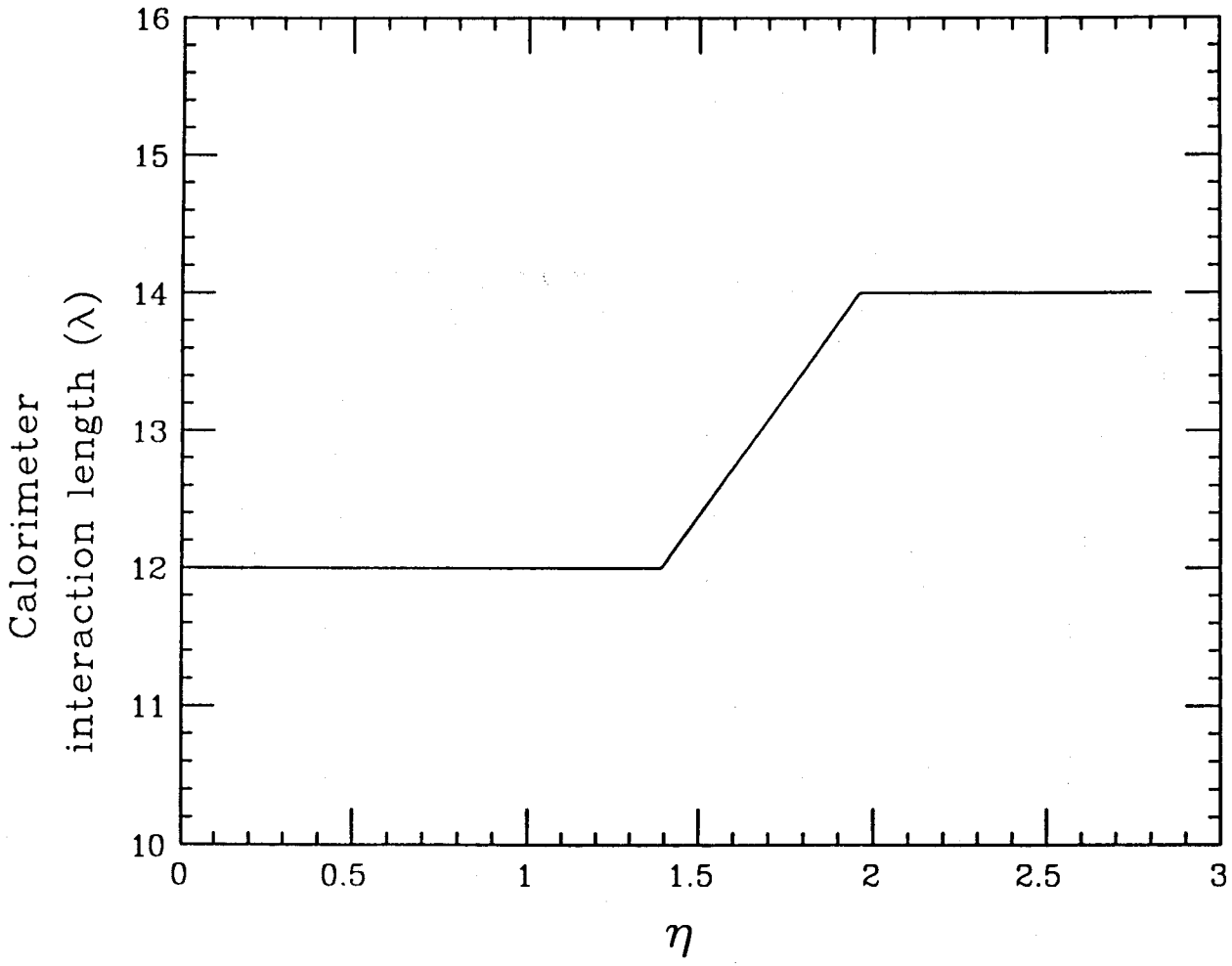
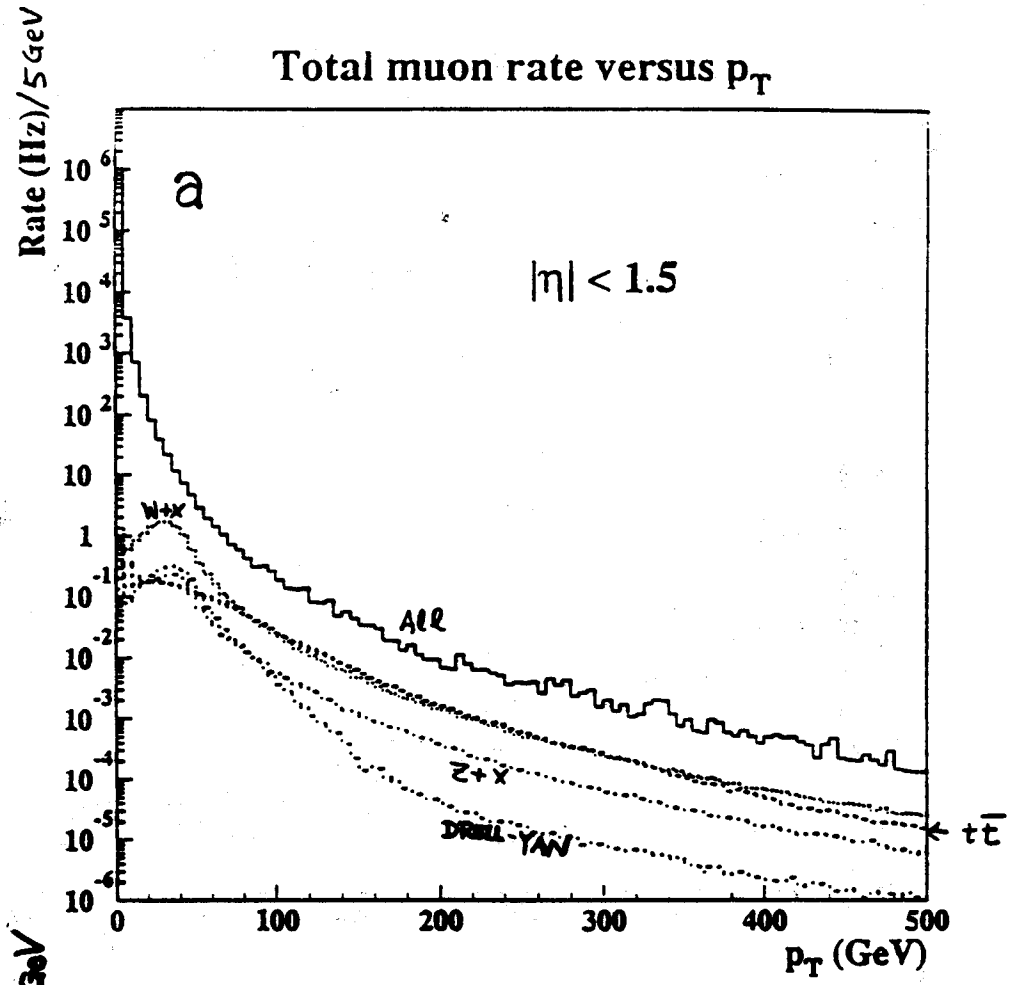


Figure 11 Calorimeter interaction length as a function of the rapidity used in our total rate calculations.


Total muon rate versus p_T
Rate (Hz)/5GeV
a
$|\eta| < 1.5$
All
W+X
Z+X
DRELL-YAN
$t\bar{t}$
p_T (GeV)

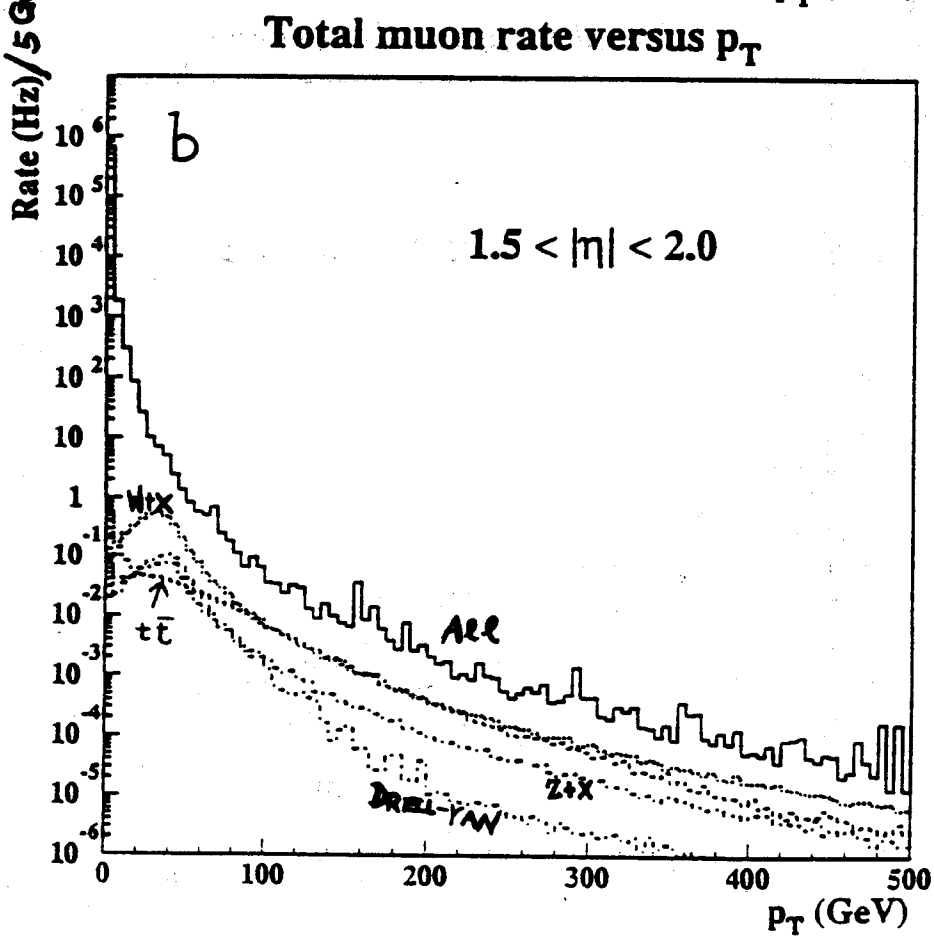
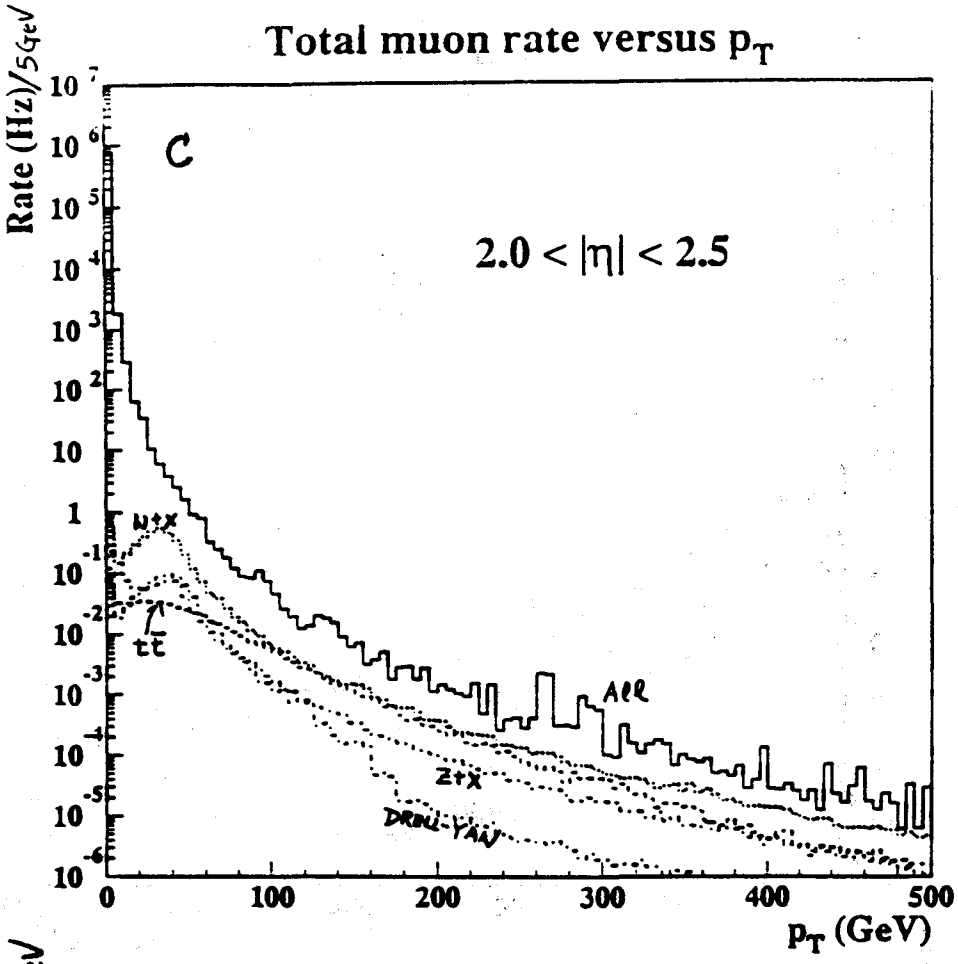

Total muon rate versus p_T
Rate (Hz)/5 GeV
b
$1.5 < |\eta| < 2.0$
All
W+X
$t\bar{t}$
Z+X
DRELL-YAN
p_T (GeV)

Fig. 12



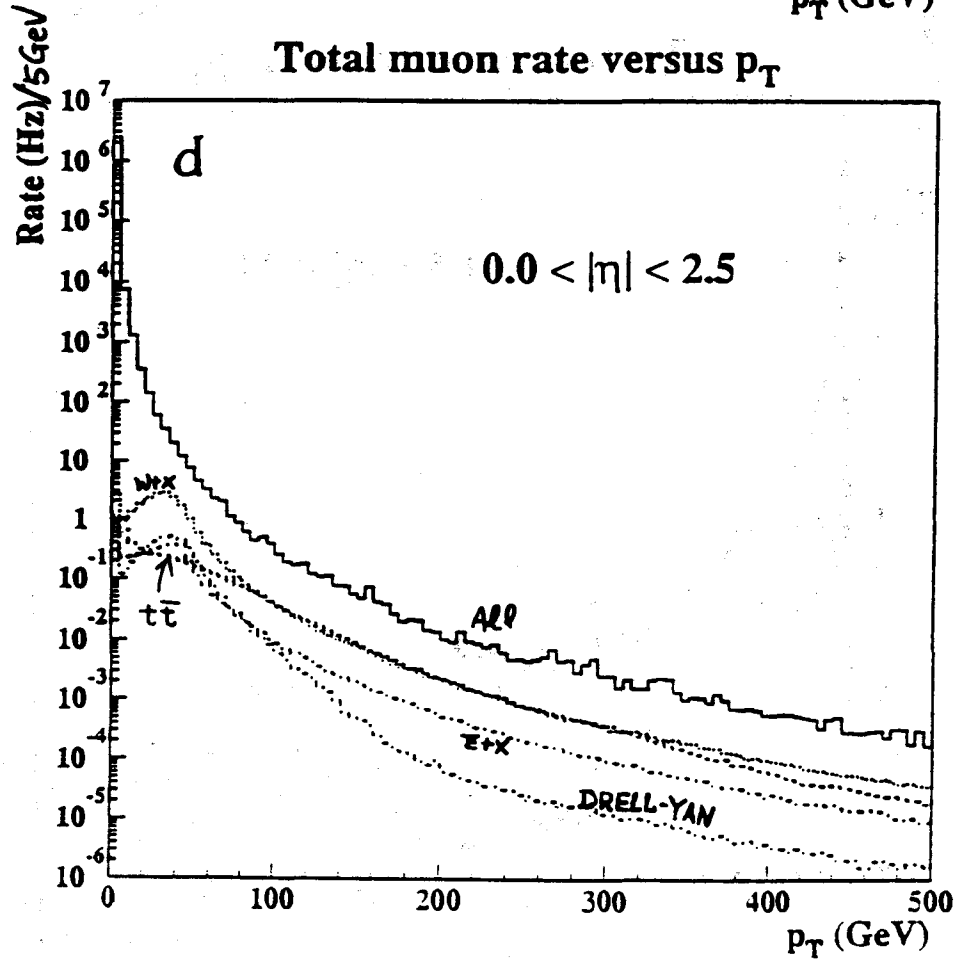
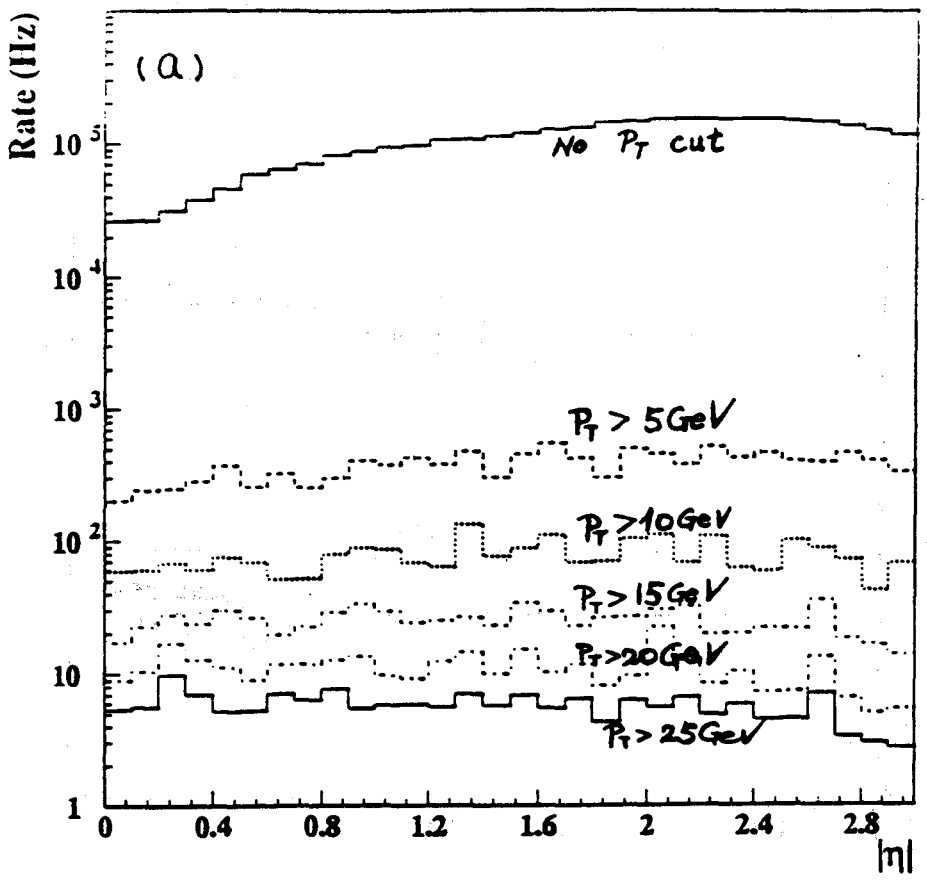


Fig. 12 continue


Total muon rates versus η
(a)
Rate (Hz)
No P_T cut
$P_T > 5$GeV
$P_T > 10$GeV
$P_T > 15$GeV
$P_T > 20$GeV
$P_T > 25$GeV
|η|

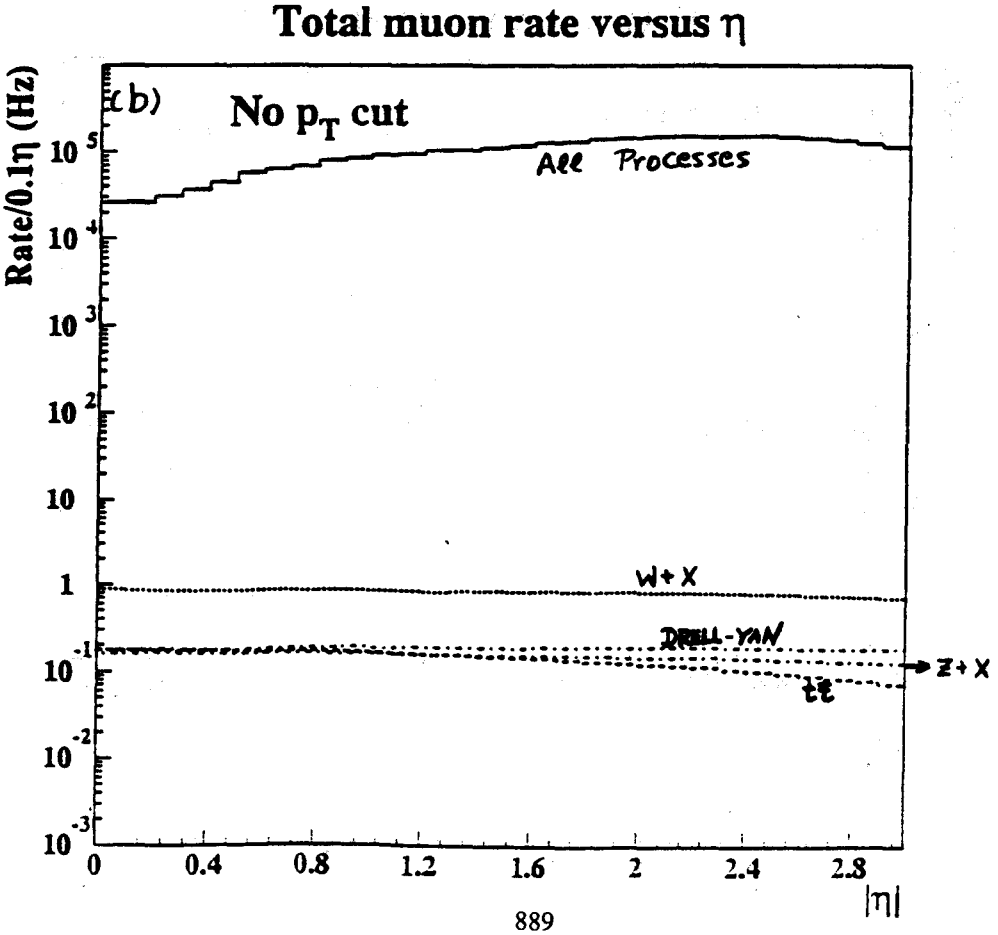
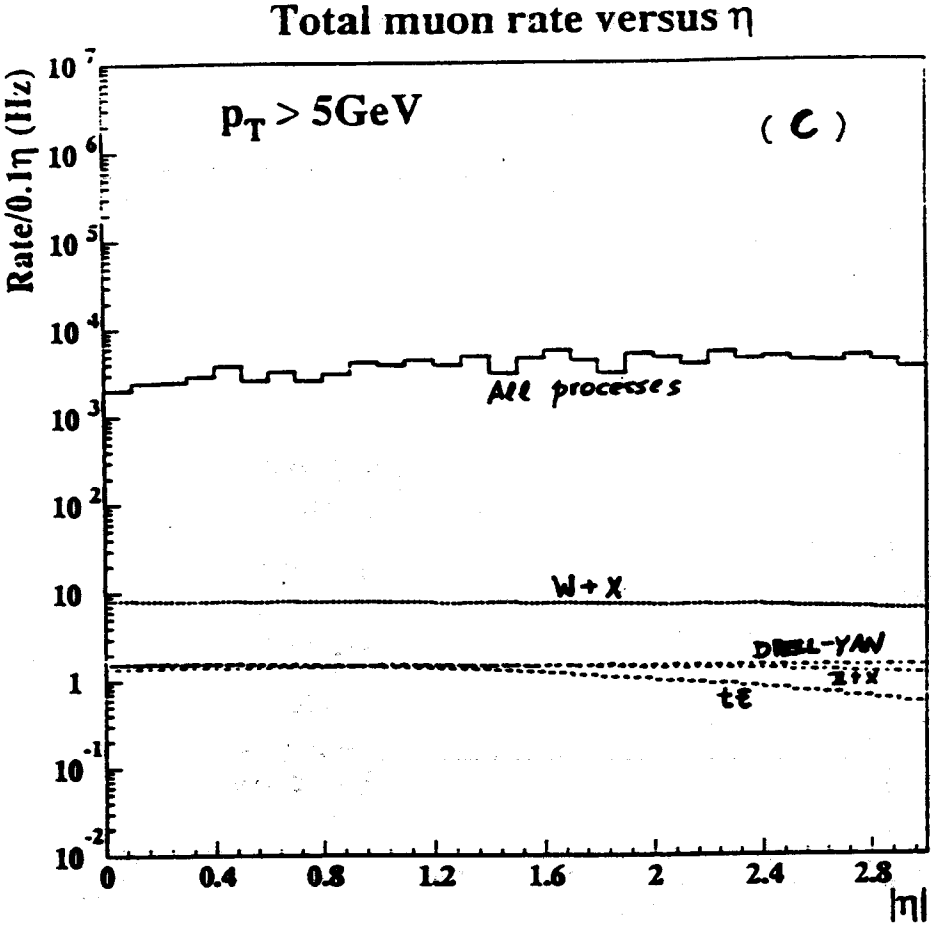

Total muon rate versus η
(b)
No p_T cut
Rate/0.1η (Hz)
All Processes
W+X
DRELL-YAN
Z+X
tt̄
|η|

Fig. 13



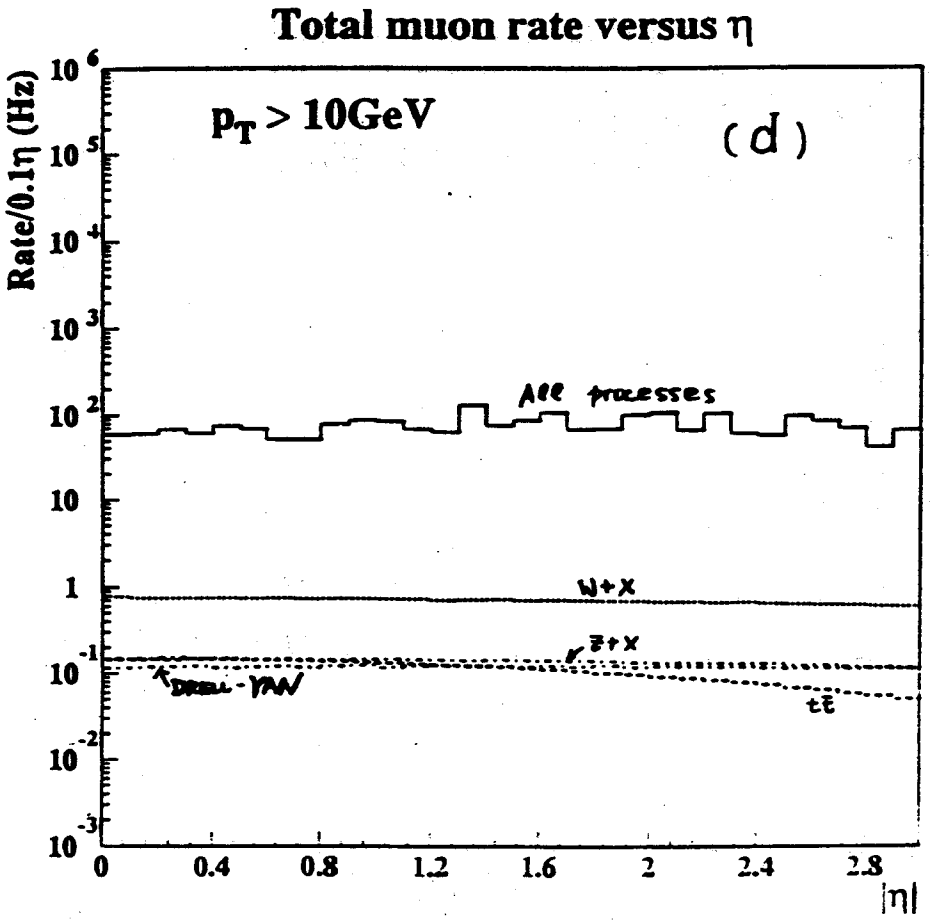
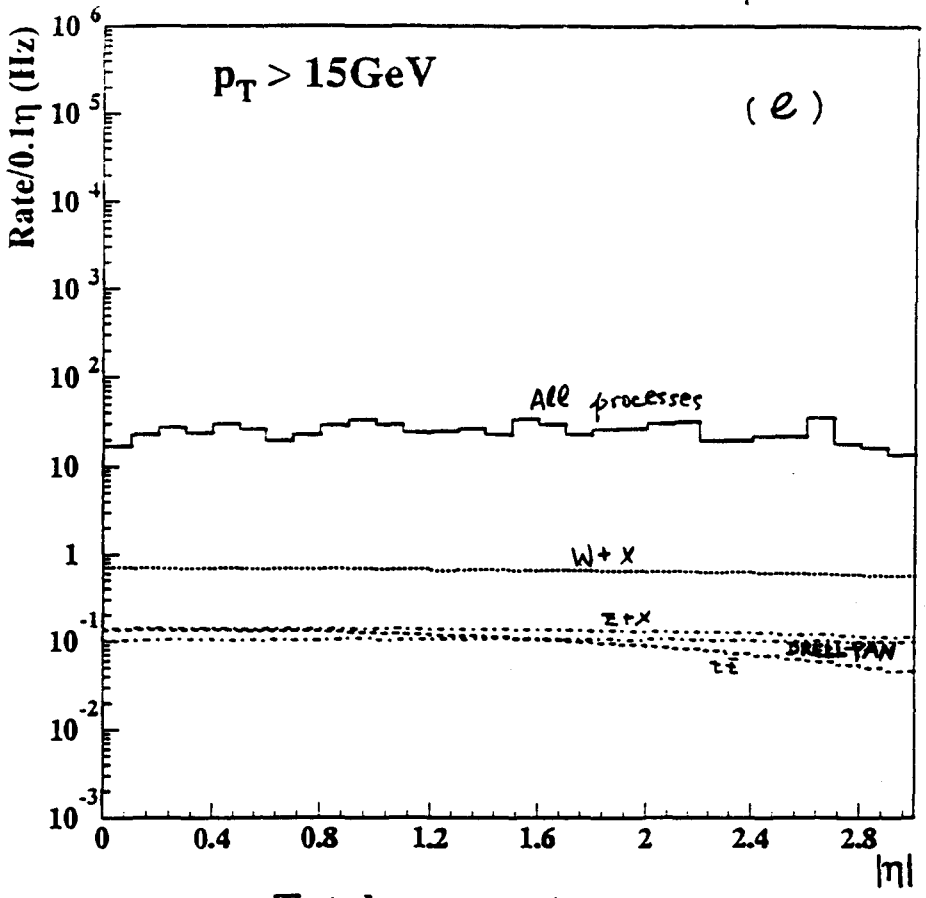


Fig. 13 continue



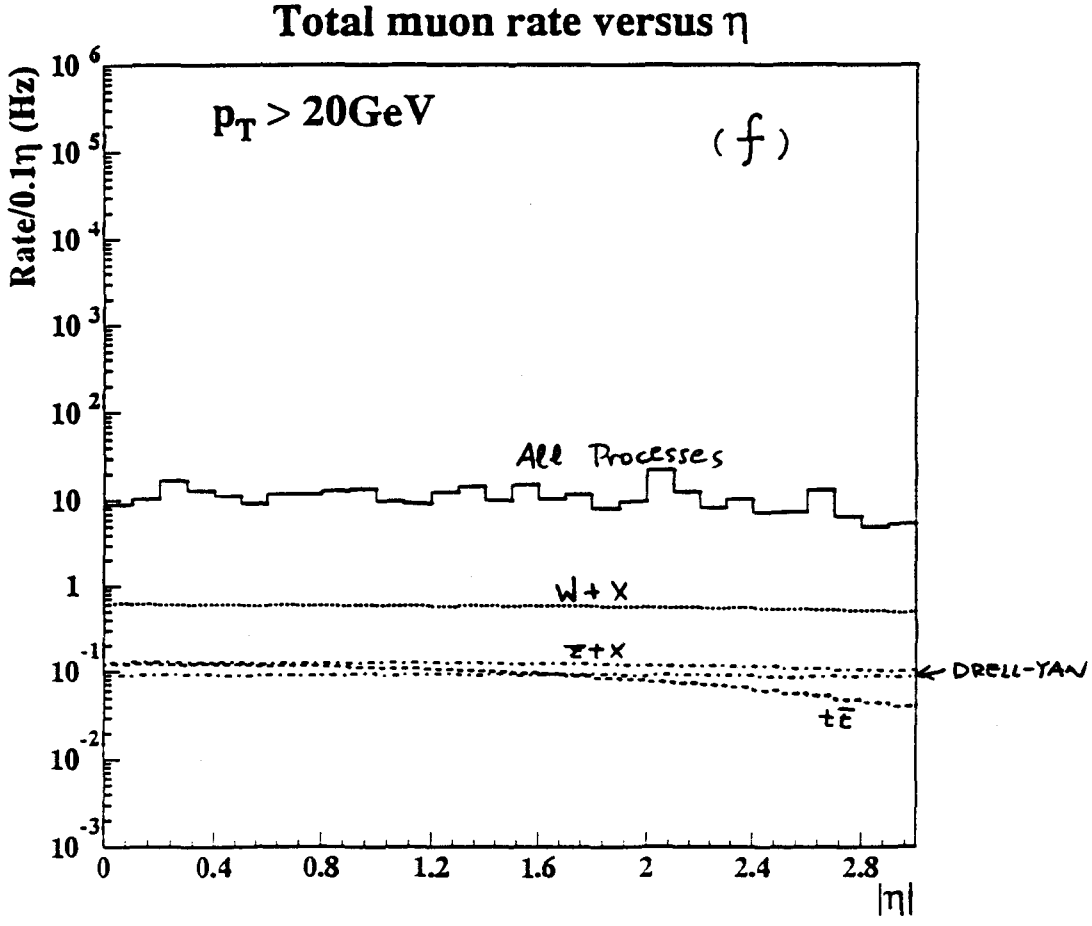


Fig. 13 continue

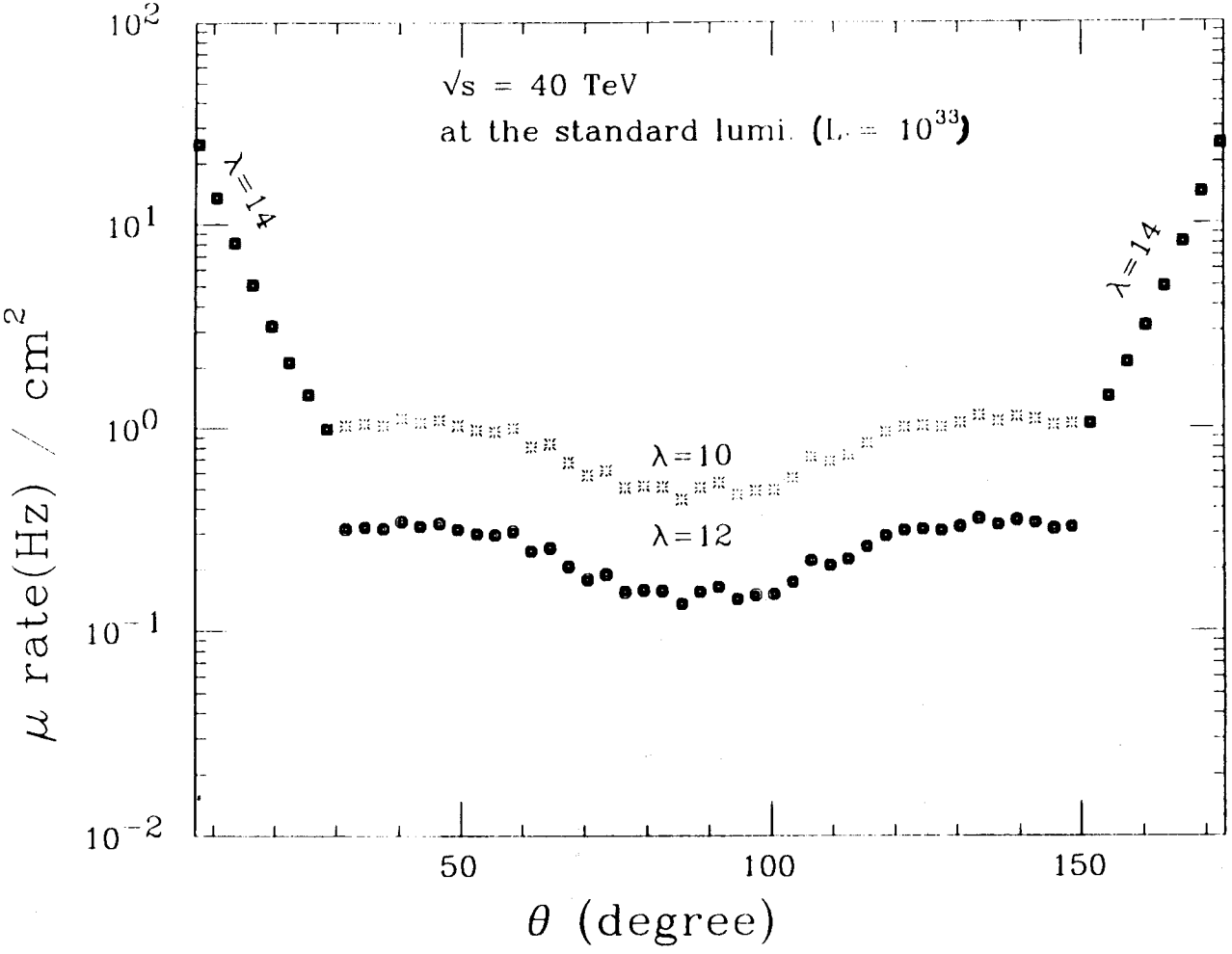


Figure 14 Inner muon chamber hits rate per cm^2 versus the polar angle, θ. For this figure we assumed that the inner barrel chambers are located at 3.7 meters from the beam line in the case of 12λ, and 3.5 meters in the case of 10λ. The inner endcap chambers were assumed to be located at 5.5 meters from the interaction point.

ATTENDEES

LIST OF ATTENDEES

Kenneth A. Abbott	High Tech Services, Inc.
Robert K. Adair	Yale University
Anatoliy Ageyev	Inst. for High Energy Physics, IHEP - Serpukhov
Hiroaki Aihara	Lawrence Berkeley Laboratory
Mohammad S. Alam	State Univ. of New York at Albany
Robert E. Allen	U.S. General Accounting Office
Gary T. Alley	Oak Ridge National Laboratory
Dan Amidei	Fermilab / University of Michigan
Farinaz Amirani	Mitsui Plastics, Inc.
Kathy Anderson	SSC Laboratory
Eric J. Anderson	Rockwell International
Sumikatsu Arima	U.S. General Accounting Office
Muzaffer Atac	University of California - Los Angeles/Fermilab
Neil Baggett	SSC Laboratory
Samuel I. Baker	SSC Laboratory
Jon Bakken	Martin Marietta
Valeri I. Balbekov	Inst. for High Energy Physics, IHEP - Serpukhov
Joseph Ballam	Stanford Linear Accelerator Center
William A. Bardeen	Fermilab
Barry C. Barish	California Inst. of Technology
Martin Bauer	Oak Ridge National Laboratory
James Bensinger	SSC Laboratory
Steve Berridge	University of Tennessee
P.J. Besser	Rockwell International
Fred Bird	SSC Laboratory
James Bjorken	Stanford Linear Accelerator Center
Regina Bonner	SSC Laboratory
Franz V. Boos	Michigan Precision Ind., Inc.
Walter L. Borst	Texas Tech University
Hugh R. Brashear	Oak Ridge National Laboratory
James E. Brau	University of Oregon
William M. Bugg	University of Tennessee
Paul Burnham	Burle Industries, Inc.
Catherine Burns	SSC Laboratory
Thomas O. Bush	SSC Laboratory
David G. Cassel	Cornell University
Clara Castoldi	Fermilab / University of Milano
Coby Chase	SSC Laboratory
Min Chen	Massachusetts Institute of Technology
William Chinowsky	University of California - Berkeley
Sergio Cittolin	CERN
Peter Clee	Rutherford Appleton Laboratory
Mark J. Clemen	Carnegie-Mellon University
Hans O. Cohn	Oak Ridge National Laboratory
Laird R. Cormell	SSC Laboratory
Gerardo Herrera Corral	CINVESTAV, Mexico
Billy Covington	Sam Houston State University
Dennis Cox	SSC Laboratory
Joe Coyne	SSC Laboratory
Nasser Danesh	SSC Laboratory
Cornelis Daum	CERN
James Decker	U.S. Department of Energy
David Delaney	University of Tennessee
Yarosav Derbenev	University of Michigan

Robert E. Diebold	U.S. Department of Energy
Nicholas Joseph DiGiacomo	Martin Marietta Astronautics Group
Jheroen P. Dorenbosch	SSC Laboratory
Paul A. Draper	University of Texas at Arlington
Eduardo Duek	SSC Laboratory
Bryan Edwards	SSC Laboratory
Karston Eggert	CERN
Tom Elioff	SSC Laboratory
Carlos O. Escobar	Universidade de São Paulo
Christian Fabjan	CERN
Orrin D. Fackler	Lawrence Livermore National Laboratory
Werner Farr	LeCroy Corporation
Howard C. Fenker	SSC Laboratory / Northeastern University
Ervin J. Fenyves	University of Texas at Dallas
Thomas Ferbel	University of Rochester
Tom Ferguson	Carnegie-Mellon University
Paolo Franzini	Columbia University
Alfred Fridman	SSC Laboratory
Jerome I. Friedman	Massachusetts Institute of Technology
William R. Frisken	Lawrence Berkeley Laboratory / York University
Toru Fukui	SSC Laboratory
Yasuo Fukui	Fermilab / Nat'l Lab. for High Energy Physics (KEK)
Koichiro Furuno	University of Oregon
Tony A. Gabriel	Oak Ridge National Laboratory
Tom Gadsden	SSC Laboratory
Kock Gan	Ohio State University
Theodore Garavaglia	SSC Laboratory
Marvin Gettner	Department of Energy
Paul Gilbert	PB/MK Team
Fred Gilman	SSC Laboratory
Nikos Giokaris	Fermilab / Rockefeller University
George Glass	Los Alamos National Laboratory / Texas A&M University
Michael J. Glaubman	Northeastern University
Jacques Goldberg	Technion
Howard Gordon	Brookhaven National Laboratory
Alfred T. Goshaw	Duke University
David Green	SAES Getters USA, Inc.
Ben Grinstein	SSC Laboratory
Wiley Guinn	SSC Laboratory
Gennady Gurov	Inst. for High Energy Physics, IHEP - Serpukhov
Ahmet Gursoy	PBMK Team
H. Richard Gustafson	University of Michigan
Gregory M. Haas	U.S. Department of Energy
Phyllis Hale	SSC Laboratory
Maurizio Hamel	Laben SPA
Wilmot N. Hess	U.S. Department of Energy
Hans J. Hilke	CERN
Tatsushige Hirose	Tokyo Metropolitan University
Walter Hoogland	CERN
Richard Hubbard	CEN-Saclay
Michael Humbert	THT Sales Company
Joey W. Huston	Michigan State University
John Huth	Fermilab
Jon Ives	SSC Laboratory
Goran Jarlskog	Lund University
Norman P. Johnson	University of Texas at Dallas
Dave Johnson	Standard Mfg. Co., Inc.
Donald Jordan	Spaulding Composites Co.

Dennis J. Judd	Prairie View A&M University
Yuri Kamyshkov	Oak Ridge National Laboratory / Inst. for Theor. and Exper. Physics, (ITEP)
Alvin S. Kanofsky	Lehigh University
Mika Karhu	SEFT Finland
Raphael G. Kasper	SSC Laboratory
Henry Kendall	Massachusetts Institute of Technology
Anne Kernan	University of California - Riverside
Sun Kee Kim	Rutgers University
Elizabeth Kittrell	Oak Ridge Associated Universities
Sherrie Kivlighn	SSC Laboratory
Quintin W. Kneen	CBI Na-Con, Inc.
Takahiko Kondo	Nat'l Lab. for High Energy Physics (KEK)
John R. Laage	Phelps Dodge Copper Products
Horace N. Lander	Nippon Steel USA, Inc.
Karol Lang	University of Texas at Austin
Alexei Lebedev	Inst. for High Energy Physics, IHEP - Serpukhov
Phil Leibold	SSC Laboratory
Lawrence Leipuner	U.S. Department of Energy
Dennis Lieurance	General Dynamics Space Systems
Ta-Yung Ling	Ohio State University
David Lissauer	Brookhaven National Laboratory
Nigel S. Lockyer	University of Pennsylvania
Stewart C. Loken	Lawrence Berkeley Laboratory
Henry Lubatti	SSC Laboratory
Harvey Lynch	SSC Laboratory
Chris Lyndon	Louisiana State University
Stanley Majewski	CEBAF
Joseph P. Marcus	Martin Marietta Astronautics Group
Seymour Margulies	University of Illinois - Chicago
Hans Mark	The Univ. of Texas Systems
Manlio Marquez	SSC Laboratory
Alfred W. Maschke	SSC Laboratory
Lyle Mason	Martin Marietta Science Systems
Lewis May	CRSS
Kenneth McFarlane	SSC Laboratory / Temple University
Charles Meitzler	Sam Houston State University
Dario Menasce	INFN-Milano
Sydney Meshkov	SSC Laboratory
Gena Mitselmakher	SSC Laboratory
Paul M. Mockett	University of Washington
Nikolai V. Mokhov	Inst. for High Energy Physics, IHEP - Serpukhov
Suhas Mookerjee	Asea, Brown, Boveri, Technology, Inc.
Kate Morgan	SSC Laboratory / Boston University
Norman Morgan	Virginia Polytechnic Institute
Taisuke Mori	Kawasaki Steel Corp.
Raul Munoz	University of Alabama
Kirill P. Myznikov	Inst. for High Energy Physics, IHEP - Serpukhov
Yorikiyo Nagashima	Osaka University
Harvey B. Newman	California Inst. of Technology
Kiyohiko Nohara	Kawasaki Steel Corporation
Joe O'Loughlin	Rector Assoc. Int'l
Pier J. Oddone	Lawrence Berkeley Laboratory
Frank Paige	SSC Laboratory
Steve Paxton	Hewlett-Packard Laboratories
Jack M. Peterson	SSC Laboratory / Lawrence Berkeley Laboratory
Vincent Z. Peterson	University of Hawaii
Aihud Pevsner	Johns Hopkins University

Nicolaus Porschek	PEC
Lawrence E. Price	Argonne National Laboratory
Sijin Qian	CERN / NFN - Frascati
Myrna Ramos	Hewlett-Packard Laboratories
Sergio P. Ratti	University of Pavia
Neville William Reay	Ohio State University
William Rector	Rector Associates International
Thomas O. Regan	SSC Laboratory
Larry A. Rehn	Interfet Corp.
James J. Reidy	University of Mississippi
Keith Rich	SSC Laboratory
Rick Riney	Martin Marietta Astronautics Group
Michael Riordan	Universities Research Association, Inc.
Lee Alan Roberts	SSC Laboratory
Byron Roe	SSC Laboratory
S. Peter Rosen	University of Texas at Arlington
Eli I. Rosenberg	Iowa State University
Alessandro G. Ruggiero	Brookhaven National Laboratory
Evgeny Rybakov	Efremov Instititute of Electrophysical Apparatus
Richard D. Saam	Proteus Systems Inc.
Angela Sala-Grabar	INFN-Milano
Gary H. Sanders	Los Alamos National Laboratory
James R. Sanford	SSC Laboratory
Felix Sannes	Rutgers University
Fay Saremi	SSC Laboratory
Frank Schmidt	CERN
Michael P. Schmidt	Yale University
Roy Schwitters	SSC Laboratory
Brian L. Scipioni	SSC Laboratory
Abraham Seiden	University of California –Santa Cruz
James Shank	Boston University
Edward I. Shibata	Purdue University
Chehyon Shio	University of Tennessee
Ram K. Shivpuri	University of Delhi
Konstantine Shmakov	Oak Ridge National Laboratory / Inst. for Theor. and Exper. Physics, (ITEP)
James Siegrist	SSC Laboratory
George Siopsis	University of Tennessee
Dane Skow	Fermilab
Anna Jean Slaughter	Fermilab / Yale University
Ray Stefanski	Fermilab
Jack Steinberger	SSC Laboratory
Zdenek J. Stekly	Intermagnetics General Corporation
Frank Stocker	SSC Laboratory
Sheldon Stone	Syracuse University
Jack Story	SSC Laboratory
Karl Strauch	Harvard University
Lawrence R. Sulak	Boston University
James D. Sullivan	Massachusetts Institute of Technology
Chih-Ree Sun	State Univ. of New York at Albany
Veniamin Sytnik	Inst. for High Energy Physics, IHEP - Serpukhov
Greg Tanimoto	C. ITOH Pipe & Tube, Inc.
Bob Taussig	Bechtel
Geoffrey N. Taylor	University of Melbourne
Vic Teplitz	Southern Methodist University
Harry B. Thacker	University of Virginia
John S. Toll	Universities Research Association, Inc.
Marc Turcotte	SSC Laboratory

Yoshinobu Unno	Nat'l Lab.for High Energy Physics (KEK)
Kashyap Vasavada	Purdue University
Luis Villasenor	SSC Laboratory / University of Guanajuato
Patrick M. Visintainer	Airco/British Oxygen Co.
David E. Wagoner	Prairie View A&M University
Bennie Ward	University of Tennessee
William Watson	U.S. Department of Energy
Terence L Watts	Rutgers University
Gene Weckler	EG&G Solid State Products Group
Andy White	University of Texas at Arlington
Bruce R. Wienke	Los Alamos National Laboratory
Hugh H. (Brig) Williams	University of Pennsylvania
Lola Williamson	SSC Laboratory
Robert D. Williamson	SSC Laboratory
Kenneth F. Wilson	CVI Incorporated
Phillip Winkler	Air Products and Chemicals, Inc.
Ed Womble	Draper Laboratory
Dolly Wu	University of Michigan
Julia Yarba	SSC Laboratory / Moscow State University
Edward Yeh	Naval Weapons Center
George P. Yost	SSC Laboratory
Haruo Yuta	Tohoku University
Arnulfo Zepeda	CINVESTAV-IPN, Mexico
Ren-yuan Zhu	California Inst. of Technology
Marek Zielinski	University of Rochester
Alexander Zlobin	Inst. for High Energy Physics, IHEP - Serpukhov
Gus T. Zorn	University of Maryland